Equine MRI

Edited by

RACHEL C. MURRAY MA, VetMB, MS, PhD, MRCVS, Diplomate ACVS

Senior Orthopaedic Advisor, Animal Health Trust, Newmarket, UK

WILEY-BLACKWELL

A John Wiley & Sons, Ltd., Publication

Equine MRI

Equine MRI

Edited by

RACHEL C. MURRAY MA, VetMB, MS, PhD, MRCVS, Diplomate ACVS

Senior Orthopaedic Advisor, Animal Health Trust, Newmarket, UK

WILEY-BLACKWELL

A John Wiley & Sons, Ltd., Publication

This edition first published 2011

Blackwell Publishing was acquired by John Wiley & Sons in February 2007. Blackwell's publishing program has been merged with Wiley's global Scientific, Technical and Medical business to form Wiley-Blackwell.

Registered office: John Wiley & Sons Ltd, The Atrium, Southern Gate, Chichester, West Sussex, PO19 8SQ, UK

Editorial offices: 9600 Garsington Road, Oxford, OX4 2DQ, UK
The Atrium, Southern Gate, Chichester, West Sussex, PO19 8SQ, UK
2121 State Avenue, Ames, Iowa 50014-8300, USA

For details of our global editorial offices, for customer services and for information about how to apply for permission to reuse the copyright material in this book please see our website at www.wiley.com/wiley-blackwell.

Library of Congress Cataloging-in-Publication Data

Equine MRI / edited by Rachel C. Murray.
p. ; cm.
Includes bibliographical references and index.
ISBN 978-1-4051-8304-8 (hardback : alk. paper) 1. Horses–Diseases–Diagnosis. 2. Magnetic resonance imaging. 3. Veterinary diagnostic imaging. I. Murray, Rachel C.
[DNLM: 1. Horses–anatomy & histology. 2. Magnetic Resonance Imaging–methods. SF 765 E64 2011]
SF951.E577 2011
636.1'089607548–dc22
2010022799

A catalogue record for this book is available from the British Library.

This book is published in the following electronic formats: ePDF 9781444329193; ePub 9781444329209

Set in 10.5 on 14pt Times by Toppan Best-set Premedia Limited

1 2011

Contents

Contributors

Fabrice Audigié
CIRALE-IPC, Ecole Nationale Vétérinaire d'Alfort, RD 675, 14430, Goustranville, France

Andrew P. Bathe
Rossdales Equine Hospital, Cotton End Road, Exning, Newmarket, Suffolk CB8 7NN, UK

Nick Bolas
Hallmarq Veterinary Imaging Ltd, Unit 5, Bridge Park, Merrow Lane, Guildford, Surrey GU4 7BF, UK

Matthew T. Brokken
Cleveland Equine Clinic, 3340 Webb Rd, Ravenna, OH 44266, USA

Simon Collins
Animal Health Trust, Lanwades Park, Kentford, Newmarket, Suffolk CB8 7UU, UK. School of Veterinary Science, The University of Queensland, Gatton Campus, Gatton, Queensland 4343, Australia

Jean-Marie Denoix
CIRALE -IPC, RD 675, 14430, Goustranville, France

Sue Dyson
Centre for Equine Studies, Animal Health Trust, Lanwades Park, Kentford, Newmarket, Suffolk CB8 7UU, UK

Katherine S. Garrett
Rood and Riddle Equine Hospital, PO Box 12070, Lexington, KY 40580, USA

Shannon Holmes
College of Veterinary Medicine, University of Georgia, Athens, GA 30602-7382, USA

Carter E. Judy
Alamo Pintado Equine Medical Centre, 2501 Santa Barbara Avenue, PO Box 249, Los Olivos, CA 93441, USA

Elizabeth Leece
Department of Veterinary Clinical Medicine, University of Cambridge, Madingley Road, Cambridge, CB3 0ES, UK

Tim Mair
Bell Equine Hospital, Butchers Lane, Mereworth, Maidstone, Kent ME18 5GS, UK

Rachel C. Murray
Animal Health Trust, Lanwades Park, Kentford, Newmarket, Suffolk CB8 7UU, UK

Annamaria Nagy
Animal Health Trust, Lanwades Park, Kentford, Newmarket, Suffolk CB8 7UU, UK

Henrik Nyberg
ATG Horse Hospital, Grabrodragatan 6, 53231 Skara, Sweden

Sarah Powell
Rossdales Equine Hospital, Cotton End Road, Exning, Newmarket, Suffolk CB8 7NN, UK

Stephen Reed
Rood and Riddle Equine Hospital, PO Box 12070, Lexington, KY 40514, USA

Michael Schramme
North Carolina State University of Veterinary Medicine, Department of Clinical Sciences, 4700 Hillsborough Street, Raleigh, NC 27606, USA

Thorben Schulze
Pferdeklinik Burg Müggerhausen, 53919 Weilerswist, Germany

Ceri Sherlock
Department of Large Animal Medicine, University of Georgia, Athens, GA 30602, USA

Meredith Smith
Animal Health Trust, Lanwades Park, Kentford, Newmarket, Suffolk CB8 7UU

Bert Van Thielen
33, rue Philippe Lebon, 80000, Amiens, France

Russell Tucker
College of Veterinary Medicine, Washington State University, Pullman, Washington 99164-7010, USA

Natasha Werpy
Orthopaedic Research Centre, Colorado State University, 300 West Drake Road, Fort Collins, Colorado 80523-1678, USA

Foreword

No aspect of medical imaging requires the understanding of such complex physics as that required for magnetic resonance imaging (MRI). However, since Röntgen first produced a radiographic image of his wife`s hand, no imaging technique has excited such interest nor presented such potential opportunities. MR scanning owes its origin to a number of scientists and physicians during a period of over a hundred years. These include Tesla, Lamor, Rabi, Bloch, Purcell, Lauterbur and Mansfield, who all contributed to the recognition and application of the phenomenon we call nuclear magnetic resonance. However, it was not until 1977 that Damadian, Goldsmith and Minkoff produced the first human MR scanner. Since then the technique has come to occupy a central role in medical imaging throughout the developed world.

MRI was first used in veterinary medicine in the 1990s, predominantly for the evaluation of anaesthetised or heavily sedated small animal patients. The high field magnets employed in imaging human patients were also adapted to be used on anaesthetised horses and ponies. However it was the development of low field magnets which could be used on standing equine patients, which really saw widespread recognition of the potential value of the technique for equine use. Initially restricted to the foot and distal limb, the development of software packages to correct for patient movement, plus increasing expertise of clinicians in obtaining and interpreting the images, now allows examination of the more proximal limb to include the carpus and hock.

This is not to say that the high field magnet has been superseded. The superior image quality possible makes it the diagnostic method of choice along with computed tomography for imaging the equine head. However, risks associated with general anaesthesia in equine patients have encouraged the use of MRI in standing patients whenever possible. Numerous clinics around the world have introduced MR scanning into their protocols for investigating equine lameness. Consequent understanding of the technique, with its benefits and limitations, has accelerated dramatically in the last few years.

As a surgeon benefitting from the skill of those who obtain and interpret MR images of patients with orthopaedic problems, it never ceases to astonish just what information about tendon, ligament, bone and articular cartilage can be collected. Exquisite detail of the anatomy and pathology of, for example, the foot is clear, provided one is equipped with an expert in the sophisticated language so alien to those of us brought up solely on a diet of radiographic and ultrasound images. This allied to additional information obtained by complementary techniques such as radiography, computed

tomography, ultrasound, arthroscopy or gamma scintigraphy and of course underpinned by a thorough physical examination, has armed the modern clinician with investigative powers undreamt of by veterinary predecessors.

The future is hard to predict. It is likely that improvements in both hard and software will enable imaging of more proximal portions of the limb or other parts of the body. We can anticipate the development of a standing system using a more powerful magnet, new sequences and further improvements in motion correction by the physicists, with concurrent clinical research to enable more accurate interpretation of the images. For those of us being carried along by and experiencing the benefits of this wave of development of MR imaging, it is difficult to believe that the momentum will cease. Whilst inevitably there may be practical limitations to further progress, imagination should not be allowed to constrain those enthusiasts who have taken up the challenge of this technology and created a valuable diagnostic resource.

This first book dedicated to equine MRI will I am quite certain assume its rightful role as the "bible" of equine MR imaging. It endeavours to explain some of the complex physics which underpin the technology and gives practical guidance to obtaining and interpreting images of the limbs and head. At the current speed of development, I am certain that future editions will be necessary to keep pace with this.

Tim Greet
President, World Equine Veterinary Association

Preface

When I started clinical veterinary diagnostic work in the horse, I could only have dreamed of an imaging modality that could provide detailed anatomical and physiological information of both soft tissues and bone. Using magnetic resonance imaging (MRI) in the horse has transformed my expectations of how much can potentially be evaluated and how much more there is to learn about normal structure, normal variation and pathology. There are increasing demands on the athletic horse, and improvements in diagnosis and management are constantly being sought. Application of MRI has revolutionized our understanding of foot pathology and demonstrated the presence of numerous previously unrecognized or poorly understood conditions in the limbs and head. Early work with MRI was focused on validation and investigation into the significance of MRI findings. However, expanding clinical knowledge, improvements in technology and practical application of MRI to the standing and recumbent horse has meant that MRI has become an integral and essential part of the diagnostic evaluation in lameness, and a realistic option for investigation of ophthalmological, neurological and cranial pathology. Despite the rapidly expanding use of MRI for equine clinical investigation, until now there has been no reference book that covers this field. This book seeks to fill that gap.

The aim of *Equine MRI* is to provide a comprehensive guide to MRI in the horse, based on the information currently known worldwide. It aims to cover information from the basics of MRI to the practicalities of image acquisition and interpretation, to describe normal anatomy and normal variations, to describe different types of pathological change and to discuss options for clinical management and prognosis for different conditions. MRI produces large amounts of data with great potential for over-interpretation due to image acquisition problems or insufficient knowledge or experience. This book should help the reader understand the best ways to achieve good-quality images, and give a guide to the problems that may occur. As image interpretation is based on an understanding of MR physics, normal variation and detection of pathology, this book should guide the inexperienced reader towards their initial steps in interpretation; it also provides considerable detail, with numerous examples of both common and uncommon problems to expand knowledge for the more advanced reader. The information given is based on previous validation work and clinical experience of many experts, which should allow the reader to improve their understanding and clinical application of MRI faster than the trial and error often needed in clinical practice.

Equine MRI is for the radiologist interpreting MR images from horses, for the diagnostic imaging technician who is acquiring MR images in the

horse, for the clinical veterinarian using MRI for diagnosis, and for veterinary and science students. The clinical aspect of the book is of particular use for the practising and specialist veterinarian, and the diagnostic imaging technician. The detailed anatomy and image interpretation is for the specialist and practising veterinarian who is either using MRI or referring to a centre with MRI, and for both scientists and students. The detailed anatomy visible on the images make MR images ideal for teaching anatomy to veterinary and equine science students. As the book is divided into sections based around the principles of MRI and image acquisition, normal anatomy, pathology and clinical outcome, with use of numerous examples in each section it should be clear for the reader to navigate around the sections most applicable for their specific uses.

We are still on a steep learning curve in our understanding of the applications of MRI in the horse. I hope that this book provides a small step forward in distributing current knowledge as a basis for future work with MRI and in helping our patient – the horse.

Rachel C. Murray

Acknowledgements

I would like to thank the individuals who have provided their time and expertise in contributing to this book. We are continuing to learn with every patient, and it is this combined information that is improving our understanding to help future patients, so I am grateful to everyone who has given permission for use of images and material. Many people have been involved in developing MRI in the horse, and it is their dedication and skill that has led to the recognition of MRI as a vital diagnostic tool in the horse – and from which this book has been derived. I am grateful to so many of these people for passing on their knowledge and for questioning what the images actually represent in the horse. These include the authors of the chapters in this book, the veterinary surgeons who have been involved in validation and clinical use of MRI, and the medical radiologists who have helped translate MRI from the veterinary field. I need to mention in particular the members of the diagnostic imaging and clinical teams at the Animal Health Trust, the MR radiologists and physicists from Addenbrookes Hospital, University of Cambridge, and Russ Tucker from Washington State University, who have been integral in developing my understanding of high field MRI and its applications. I am indebted to the physicists from Hallmarq for continually improving my understanding of MRI physics and interpretation during development of practical MRI in the standing horse.

On a personal basis, I will be forever grateful to my parents for showing me that editing a book is achievable, and to Duncan, Ruth and Clare for allowing me the time to do so.

Section A
Principles of MRI in horses

Chapter 1
Basic MRI principles

Nick Bolas

INTRODUCTION

Since its introduction into human medicine in the early 1980s, magnetic resonance imaging (MRI) has become established as the gold standard for orthopaedic and neurological diagnostic imaging. The first scans on live equine patients were performed in the late 1990s, and since that time more than 20,000 horses have been scanned, primarily for investigation of pain in the foot.

As a diagnostic imaging technique MRI has some features in common with other imaging modalities, such as radiography, computed tomography (CT), nuclear scintigraphy and ultrasound. But it also has unique characteristics related to the underlying physics behind the generation of signal and the formation of the image.

MRI:

- forms images of radically different appearance depending on the adjustment of key settings on the scanner
- is inherently of low sensitivity, and therefore the images are usually suboptimal in some respect. Improving any one aspect involves understanding the trade-offs and how they will affect features of the resulting image
- poses unique hazards related to magnetic and electrical effects on common tools, equipment and surgical implants.

The origin of the MRI signal relies on exotic quantum physics, which unfortunately is impossible to describe fully in terms of the behaviour of familiar objects. A formal description requires a mathematical approach. Fortunately, however, such a rigorously correct approach is not necessary to obtain enough understanding for the purposes of medical imaging. The purpose of this introductory chapter is to explain how the image is produced, how it is influenced by scanner settings and the environment, and to lay the foundations for the descriptions of image acquisition and interpretation in later chapters.

HOW THE IMAGE IS CREATED

Overview

At about the time Xenophon (431–355 BC) was writing the first recorded discourse on horsemanship and conformation, his contemporary Democritus

Equine MRI, edited by Rachel C. Murray.

(ca. 460–370 BC) was expanding on the idea that all matter is made up of various imperishable 'indivisible units', termed atoms. The Greek word *tomos* (from the verb to cut) has given the English language both *atom* and *tomography*.

Today we are familiar with the idea that all material is made up of atoms, and that atoms themselves are composed of protons, neutrons and electrons. The protons and neutrons are condensed together to form a nucleus at the core, surrounded by a cloud of electrons. Magnetic resonance imaging depends on the manner in which that nucleus interacts with external magnetic fields.

The key principles are as follows.

1 In the presence of a static magnetic field, certain nuclei (including the proton, ^{1}H) become sensitive to oscillating magnetic fields and resonate in a synchronized manner.

2 The frequency of magnetic oscillations at which such nuclei resonate is *exactly* proportional to the strength of the static field.

3 At commonly used static field strengths of about 1 Tesla, the nuclei resonate at the MHz range of radio frequencies. Magnetic oscillations of this frequency are easy to create and detect electrically. Thus magnetic resonance provides a way to:

(a) create and detect signal using the biological tissue itself, using the ^{1}H in water (H_2O) and fat (with many $–CH_2–$ chains)

(b) very precisely measure the magnetic field at the location of the biological tissue.

4 By applying a linear magnetic field gradient, so that the magnetic field is stronger on one side of an object than on the other, the position of the resonating nuclei can be determined by measuring the exact resonance frequency.

5 A mix of signals from nuclei all resonating at different frequencies (e.g. because they are in different places in a field gradient) would almost immediately cancel each other out. Special methods are needed to make the signals refocus, or echo, so that they can be detected.

6 To locate a position in the three dimensions of space, three field gradients are required. However, they can only be applied one at a time (otherwise only a single gradient at a diagonal angle would result), so special techniques are needed to code the three dimensions of space by a succession of gradients applied in the three directions, one after the other.

7 Other properties of the nuclei, called relaxation times, give additional clinically useful information, and imaging techniques are adapted to make this information available.

MRI physics

Nuclei

The nucleus has a positive electrical ***charge***,[1] carried by ***proton***s. The ***mass*** of the nucleus comes from these protons and also from almost equally heavy,

[1]Words in bold italic are further defined in the Glossary.

electrically neutral, ***neutron***s. As well as these familiar concepts of charge and mass the sub-atomic protons and neutrons have a property called ***spin***. While this spin is not really caused by a physical rotation of the particles, it does create some properties comparable to those of rotating charged bodies; properties that give rise to the phenomenon of nuclear magnetic resonance (NMR).

Magnetic resonance signals can be detected from a wide range of nuclei with odd ***atomic number***s[2] (MR active nuclei), and NMR has been used in chemistry and physics since the 1950s. The amount of detectable signal varies between nuclei, with hydrogen (^{1}H) being almost the most sensitive of all.[3] Hydrogen is a component of water (H_2O) and of fat (with many $–CH_2–$ chains), both of which are very common in biological tissue, so images of patients can be created without a need to add any external substance. In normal biological tissue the natural abundance of the ^{1}H ***isotope*** is almost 100%,[4] and the resulting high sensitivity makes hydrogen (or almost synonymously the proton, the nucleus of the hydrogen atom) by far the most important nucleus for clinical magnetic resonance imaging. With the commercialization of clinical magnetic resonance imaging the word 'nuclear' was dropped and the abbreviation MRI introduced.

The quantum property of spin causes the nucleus to generate its own magnetic field (or magnetic moment), rather like the earth's magnetic field. This will interact with an externally applied static magnetic field and cause the nucleus to respond to other, varying magnetic fields; but only those that vary at a precisely defined frequency of oscillation or ***precession*** (the Larmor frequency). This frequency is exactly proportional to the external field strength, related by the ***gyromagnetic ratio*** (or magnetogyric ratio). Different nuclei have different gyromagnetic ratios; for the proton the value is 42.577 $MHzT^{-1}$. At a field strength of 1.5T this corresponds to a resonance frequency of about 64 MHz, and at 0.26T one of about 11 MHz. Because the nuclear oscillations can be detected electrically, and their frequency can be measured to better than 1 Hz, the signal created by the spinning and rotating (***precessing***) nucleus provides an exquisitely sensitive means to measure changes in magnetic field.

The cause of the interaction, and its characteristics, can be considered by two different analogies (see Box 1.1). The first considers the nuclei as rotating, spinning objects where the oscillation is viewed as precession of a spinning ball. The second is comparable with optical and other forms of spectroscopy, where the frequency corresponds to the energy of a photon emitted or absorbed by a transition between energy states. The resulting frequency is identical in either case.

[2]For example ^{1}H, ^{13}C, ^{19}F, ^{31}P, ^{131}Xe. Within the nucleus the spins of two protons will pair up and cancel out, and similarly for neutrons, but when there is an unequal number of protons and neutrons the nucleus carries a residual spin.
[3]The only exception being tritium (^{3}H), which is radioactive with a half-life of 12.3 years and has decayed over geological time to negligible natural abundance.
[4]^{2}H constitutes less than 0.02% of hydrogen atoms, and the amount of ^{3}H is negligible.

Box 1.1 Origin of the MR signal

The spinning sphere analogy

Each nucleus can be considered as a spinning sphere, the spin causing it to possess both its own magnetic field (or magnetic moment) and angular momentum. When placed in an external magnetic field (termed the B0 field) the magnetic moment of the nucleus causes it to experience a force, which, if the nucleus had no spin, would move it into alignment (like a compass needle aligning with the earth's magnetic field). However, by the law of conservation of angular momentum, the spin of the nucleus causes it to move at right angles to the applied force, like a gyroscope. As soon as it has moved a little, the tendency to move will now be at 90° to the new direction. This carries on forever, so the movement is a continuous rotation called precession (Figure 1.1).

If a second magnetic field is applied at right angles to the first, and is also rotated at the same speed as the nucleus so that it continuously 'keeps up' with its precession, then the nucleus will precess about this too (Figure 1.2). This causes the magnetization to tip over. The second, rotating field is created by passing an alternating current through a coil around the sample and is called the B1 field to distinguish it from the main or B0 field.

If this second field is stopped just when the magnetization has tipped by 90°, then the resulting net magnetization is at right angles to the B0 field, still precessing about the B0 field direction. Such a burst of rotating magnetization exactly sufficient to tip the magnetization through a right

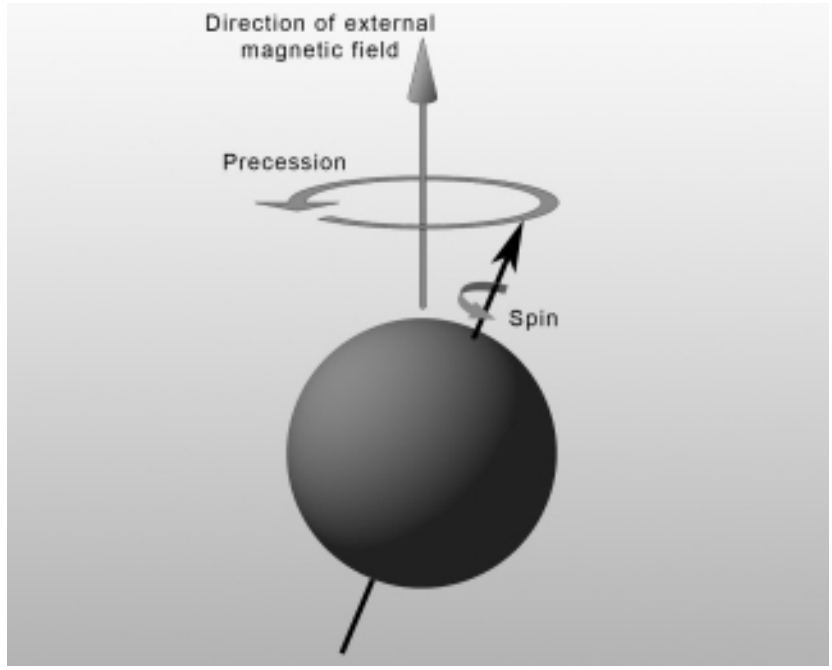

Figure 1.1 Nuclear spin. The classical analogy of the nucleus as a small sphere, spinning about a tilted axis which is itself precessing about the axis of an external magnetic field.

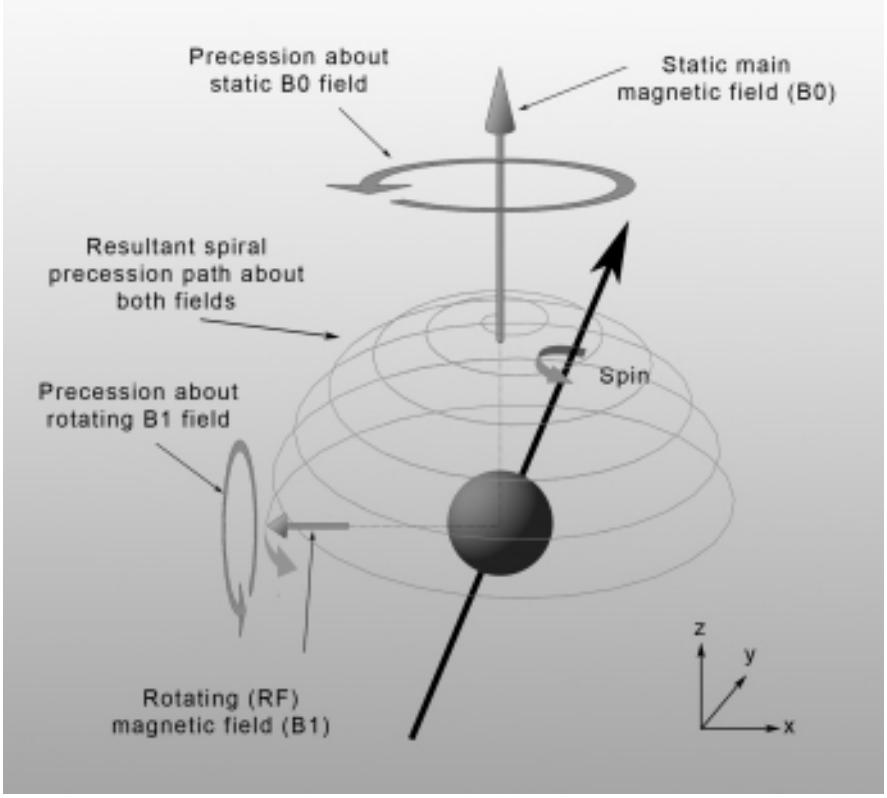

Figure 1.2 Precession about a rotating RF field. When a rotating (or oscillating) magnetic field that is exactly synchronized with the precessing nuclei is applied, then the nuclei will follow a spiral path (light grey trace), precessing about both the static main magnetic field (B0) and the rotating RF field (B1).* If this rotating field is stopped when the axis of the bulk magnetization has rotated exactly into the x-y plane, then the burst of radio waves that has been applied is called a 90° pulse. Similarly, rotation can be through 180°, 270° or any arbitrary flip angle α, depending on the strength and duration of the applied pulse.

angle is called a '90° pulse'. Typically the B1 field is much weaker than the B0 field, and it will commonly take several milliseconds for the magnetization to precess through 90° around B1.

Because the current generating the B1 field oscillates at the precession frequency of several MHz, which is in the range of radio waves, and is used in short bursts to control the tipping of nuclear magnetization, it is referred to as a radiofrequency or RF pulse.

A single gram of water contains many billions of hydrogen nuclei. Not all of them align with the external field due to thermal interactions and other effects, but quantum rules prevent anything other than alignment with, or opposed to, the external field. The effect of a large number of nuclei is to produce a cone of magnetism. Along the B0 field direction there is a resultant net (or bulk) magnetization, but at right angles to the B0 field the individual nuclei are randomly oriented and cancel out.

*To simplify the mental gymnastics required to visualize all these spins MR physicists often refer to a 'rotating frame of reference' in which the imaginary observer is sitting on a nucleus and rotating at the precession frequency due to the main magnet. In this frame the main field (B0) becomes zero and only the rotating field (B1) need be considered.

(*continued*)

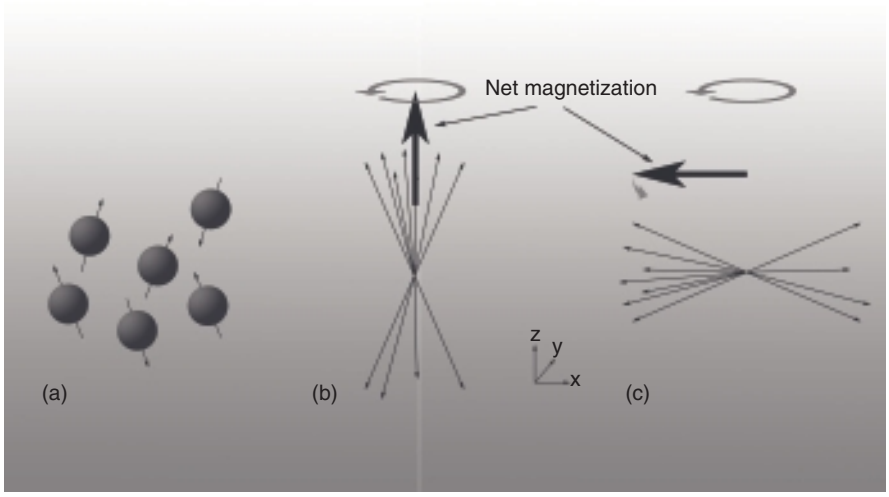

Figure 1.3 Net magnetization. (a) In material with many nuclei, the tilt angles are random, creating a cone of magnetization with more nuclei aligned with, rather than opposing the B0 field, thus creating (b) a net magnetization in the z direction (along B0) but cancelling out any net magnetization in the x-y plane (transverse magnetization). After a 90° pulse (c), the cone, and thus net magnetization, rotates through 90° and tips the net magnetization into the x-y plane, where it rotates as the individual nuclei continue to precess about the B0 field.

An applied RF pulse tips over the entire cone (Figure 1.3), and when it stops the tipped-over cone of magnetization precesses again about the main field direction. The rotating nuclear magnets generate a detectable voltage in a coil around the sample, in the same way that a rotating magnet in a dynamo generates electricity.

Magnetic resonance as spectroscopy

The spin of the nucleus causes it to generate its own magnetic field (or magnetic moment), which interacts with an externally applied magnetic field to put the nucleus in one of two energy states. A nucleus with its magnetic field aligned *with* the external field is in the lower energy state (energy is released as the fields align). Conversely, when the fields are aligned in *opposite* directions the nucleus is in the higher energy state (energy must be applied to overcome the repulsive magnetic interaction). Because of the quantum nature of the spin, and thus its magnetic moment, intermediate states are not allowed.

Transitions between states will either absorb or release energy, which will be in the form of photons of electromagnetic radiation. As with any electromagnetic radiation there is a direct relationship (given by the Planck equation $e = h\nu$) between the amount of energy and the frequency of the electromagnetic wave. For MRI the electromagnetic radiation is commonly in the shortwave (3–30 MHz) or VHF (30–300 MHz) radio frequency bands. This is very small (about 10 million times less than the energy of a visible light photon), which has two consequences.

1 Unlike other common electromagnetic waves (e.g. gamma rays, x-rays, ultraviolet light) radio waves do not have sufficient energy to dislodge

electrons from their orbits around the nucleus. They are therefore non-ionizing and do not create a safety hazard from damage to cells or DNA.

2 At room, or body, temperature the energy gap is comparable to the thermal kinetic energy of the atoms moving about. In material with a large number of nuclei, frequent random transitions caused by thermal collisions make the populations in the high and low energy states very nearly equal. This makes MRI very insensitive, less so as the magnetic field increases, but even at 1.5 T the imbalance is fewer than one in 10,000 nuclei.

T1 relaxation

When a patient is initially placed into a magnetic field, each individual nucleus can be in one of only two states, aligned with or opposed to the external field. Initially the populations of the two states are equal and therefore the overall (commonly called net, or bulk) magnetization of the material is zero. Once in the magnetic field, however, the net magnetization starts to align parallel to the external field, as more nuclei align with the external field than in the opposite direction. This alignment takes some time, because each individual nucleus must wait until a packet of energy (either thermal or electromagnetic) of just the right size comes along to stimulate a transition between its two possible states. Eventually there will be more transitions to lower than to higher levels and a new equilibrium will be achieved with a stable net magnetization.

The time constant for the progress towards the new equilibrium is called T1, and the process is called T1 relaxation. It is also known both as ***spin-lattice relaxation*** to reflect the fact that it depends on energy transfers through the structure of the material, and as ***longitudinal relaxation*** to reflect the fact that the nuclear magnetization aligns along the axis of the main magnetic field.

Of course, diagnostic MRI is never carried out by moving samples rapidly into a strong field. Instead, the sample is positioned stationary in the magnet, and the magnetization is rotated by the application of one or more radiofrequency (RF) pulses. Whatever the cause though, once away from equilibrium the net magnetization will gradually return to alignment with the main field by T1 relaxation.[5]

In gases, where there are few opportunities for interactions, T1 can be seconds or even minutes. In biological tissue, T1 is generally in the range 10–1000 ms, and is faster in fat and slower in fluid (water). This can be used to distinguish between fat and water on images. By applying pulses in quick succession the water nuclei never get a chance to recover, tip and become detectable, but the fat nuclei do so repeatedly and generate a strong signal.

[5]Though the radiation is at the Larmor frequency, corresponding to the quantum energy gap, only a tiny fraction of the energy released as the nuclei return to alignment is radiated. The vast majority is lost to thermal vibrations in the structure of the material.

T2 and T2 relaxation*

Immediately following a 90° pulse all the individual nuclei are precessing together, and average to generate a rotating bulk magnetization that can be detected. After the pulse stops they gradually lose synchronization and the signal fades. This loss of synchronization is called ***transverse relaxation*** and has two causes.

1 Transfer of a quantum of energy directly from one nucleus to another. While this does not affect the total energy of the system, the two spins concerned are no longer in phase with the others. This is called spin-spin relaxation and makes the main contribution to the relaxation time T2.

2 Some nuclei will simply be in a slightly higher local magnetic field than others, and will therefore precess slightly faster and gradually lose phase coherence with the slower ones. Local magnetic field variation can be due to imperfect uniformity of the main magnet, local magnetic influences such as iron in blood, and very local influences due to the electron distribution in the molecule surrounding the nucleus concerned. Under the influence of these extra factors the spins dephase more quickly, with a time constant T2* (pronounced T-two-star).

Loss of signal due to local magnetic influences that are reasonably constant can be reversed using a spin-echo sequence (Figure 1.4), while signal loss due either to inherent spin-spin energy transfer or to local variations that are not constant over the spin-echo time period (e.g. diffusion, flow), cannot be refocused in the same way.

T2 relaxation is sensitive to the degree of mobility of a substance, being much longer in mobile fluids and shorter in more solid material. In biological tissue, it ranges from microseconds (in solid bone and tendon) to tens of milliseconds. The sensitivity of T2 relaxation to the local environment, and in particular the increase in T2 relaxation time with increased water content, makes image contrast weighted according to T2 a particularly valuable diagnostic aid.

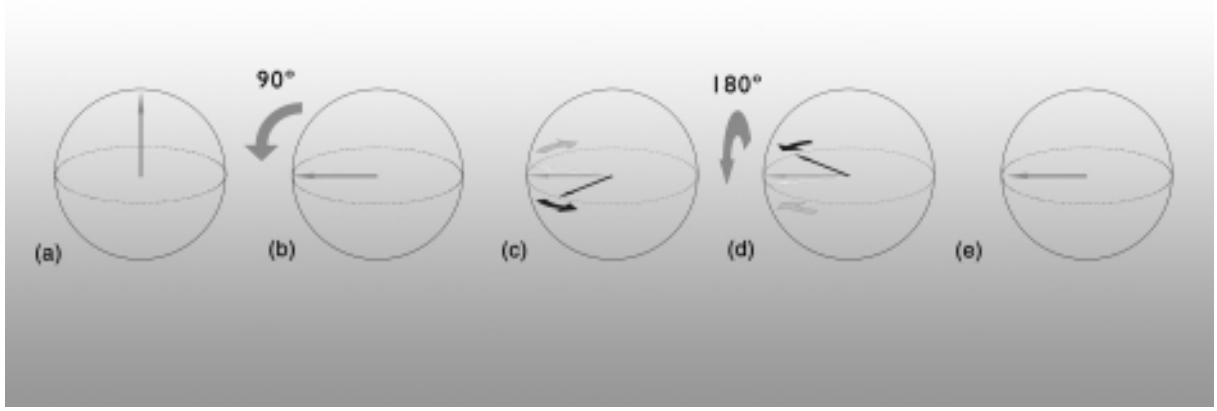

Figure 1.4 Spin-echo. (a) In the fully relaxed state all the spins are aligned with the main magnetic field. (b) Following a 90° pulse the spins are all in the same direction. (c) After a period of time some have rotated faster, some slower, and the individual nuclei lose phase coherence. (d) An RF pulse is applied which flips all the nuclei by 180°. Those that were rotating faster continue to do so and catch up with the slower nuclei. (e) After an equal period of time all the spins are back in phase, but some signal has been lost due to irreversible processes.

It is sometimes faster and more convenient to collect images using gradient-echo sequences, in which the contrast is dependent on T2* relaxation, rather than spin-echo images, which give a T2-weighted contrast. The two relaxation mechanisms are similar and in some ways give comparable biological information, but they are not identical and do not result in fully equivalent images.

Fourier transform

Early magnetic resonance instruments detected the signal by sweeping a transmitter across a range of radio frequencies, detecting separate peaks from nuclei resonating at different frequencies. But it was soon recognized that following a short pulse of RF power all the signals appear together, in much the same way as hitting a piano with a hammer will start all the strings vibrating simultaneously. This allows for much faster data collection and an entire range of techniques for manipulating nuclear spins by applying one or more pulses in carefully timed succession, termed a pulse sequence. The mixture of signals can then be separated back out into its component frequencies by a mathematical process known as the Fourier transform (Figure 1.5).[6] An efficient computer algorithm exists[7] for performing the Fourier transform, known as the Fast Fourier Transform or FFT [1], and since this requires the number of data points to be a power of two, MR data acquisitions commonly use 128, 256 or 512 points.

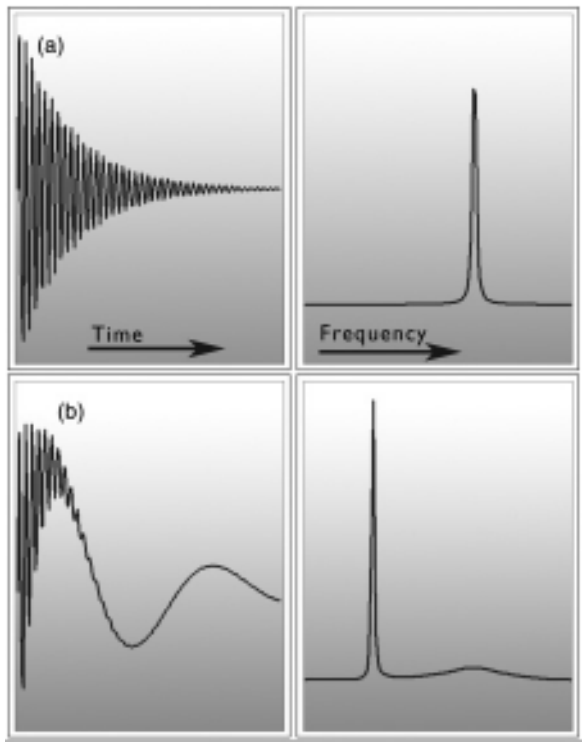

Figure 1.5 Fourier transform. (a) A single resonance, shown as both the oscillating signal decaying in time (left) and its Fourier transform, a plot of signal intensity against frequency (right). This might correspond to the signal from, for example, synovial fluid. (b) Two resonances of the same initial amplitude. The high-frequency signal decays away rapidly on the time domain plot (left) corresponding to a broad, low resonance on the Fourier transformed frequency domain plot (right). It is clear that with a small amount of additional noise the broad signal would be difficult to detect. These might correspond to signals from, for example, synovial fluid (narrow line) and tendon (broad line, with a very short T2 so becoming essentially undetectable).

[6]After Jean Baptiste Joseph Fourier, 1768–1830, who determined, during investigations of heat transfer, that any function can be expressed as the sum of a series of sine waves.
[7]Developed during the Cold War to help analyse seismic waves for the detection of nuclear explosions.

In MRI the intensity of the Fourier transform, representing the strength of the signal, is converted to the brightness of a point on the image.

Quadrature

MRI signals are normally digitized not at their original MHz frequency,[8] but after subtraction of a reference frequency in the receiver electronics. If the reference frequency is placed in the centre of the expected range of received signals, the receiver bandwidth can be kept to a minimum, and since a narrower bandwidth reduces the amount of random noise in the image (and so improves image quality) this is generally preferred. However, this means that some nuclei are now resonating faster, and some slower, than the reference frequency. To distinguish the direction of rotation the MRI instrument internally detects two signals, one delayed by one-quarter of a cycle. The resulting related sine and cosine waveforms are effectively views of the rotating resonance from two positions at right angles to each other (i.e. the waves are in quadrature to one another). The corresponding Fourier transform also has two parts. The mathematics of these calculations are performed using ***complex numbers*** and the parts are known as the ***real*** and ***imaginary*** components, which are combined together in the final MR image, as the brightness is calculated as the square root of the sum of the squares of the real and imaginary parts (the ***magnitude***).

Shimming

In a precisely uniform magnetic field identical nuclei will all resonate at the same frequency, with the resulting signal slowly decaying with a long time constant T2*. The Fourier transform of the signal will be well defined and intense. If the field is very variable the individual resonances will be at different frequencies and will rapidly get out of phase, the mixed signal will quickly disappear (short T2*), and the Fourier transform will be weak and spread out. Hence it is important in MRI to ensure that the field is uniform, and MRI systems incorporate a means to adjust it before collecting the image. The adjustment process uses electrical currents passed through coils inside the magnet, but is often known as shimming, in a reflection back to the days when magnets were adjusted literally with thin metal shims.

RF pulse modulation

The reverse Fourier transform relationship between the spread of frequencies (or ***bandwidth***) and the duration in time can also be used in determining the shape and duration of the transmit RF pulse. A well-defined frequency range, and thus a long pulse, is required to image slices with sharp edges or to irradiate fat resonances in fat-saturated sequences without stimulating the water resonances. Conversely a short pulse is needed to stimulate a large volume for three-dimensional imaging or uniform inversion. To obtain

[8]Though modern digital receivers are beginning to operate this fast.

uniform excitation within a slice, and a sharp drop at the edges, the RF pulse is commonly modulated with a combination of ***Gaussian*** and ***sinc***-shaped profiles, or a more complex numerically optimized wave shape.

Image formation

The potential biological value of MR was discovered in 1970 by Raymond Damadian [2] who found that T1 and T2 relaxation times differed between normal and cancer tissues. The first MR images of a living animal were published in 1976 by Damadian and colleagues [3], using an instrument in which the magnetic field was only uniform over a small region that was moved around the body of a mouse. These were followed in 1977 by images from a person resolved into 64 sensitive volumes, and in 1980 by the first commercial MRI scanner. But this technique was very slow, and further innovations (for which the Nobel prize was awarded to Paul Lauterbur and Sir Peter Mansfield in 2003) were necessary to bring MRI to the speed and resolution we use today.

Field gradients

By controlling the magnetic field so that it is stronger on one side of the magnet than the other, the nuclei in material on that side can be made to resonate at a higher frequency. Using linear field gradients in all three orthogonal axes allows the resonance frequency to be precisely controlled in a three-dimensional volume to locate the source of signal to within less than 1mm. The ability to generate field gradients that are accurately linear, strong, switch to a precise strength quickly and do not incur side effects such as eddy currents in the magnet is one of the critical challenges for an MR system manufacturer.

By applying a field gradient at the same time as a shaped RF pulse, signal will be returned from only a narrow slice of the sample, because only spins that resonate at the frequencies stimulated by the pulse will be excited. Such a gradient is termed the ***slice select gradient***. If a second field gradient is applied while the RF signal is being collected, the signal generated by material on one side of the magnet will be detected at a different frequency from that generated on the other side (Figure 1.6). Such a field gradient is called the ***read gradient*** and can be used to resolve one direction of the final image. Although imaging using this type of gradient alone was the basis of Lauterbur's early images [4], in which he used the field adjustment shim coils to create a series of linear gradients that were progressively rotated around the sample in a similar way to the x-ray projections used in CT, it has been superseded today in all but special applications.

Spin-warp imaging

The standard technique for resolving the third dimension in space (the second dimension of a single slice) was invented by Edelstein and colleagues in Aberdeen [5] using concepts from chemical and biochemical applications

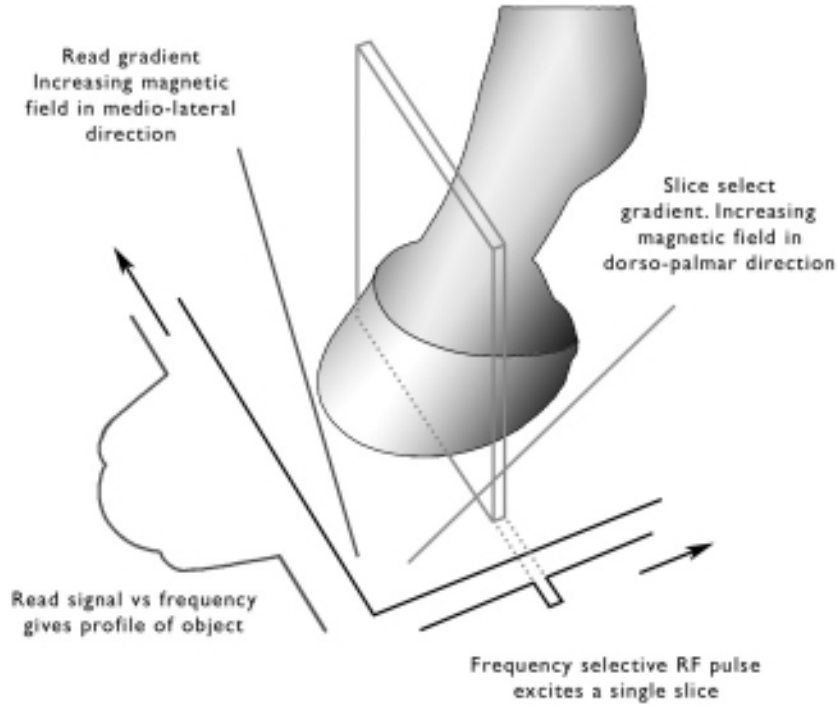

Figure 1.6 Slice select and read gradients. Magnetic field gradients provide the link between position and frequency. A gradient in the slice direction causes a frequency selective RF pulse to stimulate nuclei in only a thin slice of tissue. A gradient in the read direction causes the resulting signals to vary in frequency according to their position. The actual physical directions of the gradients are controlled to produce oblique slices.

of NMR developed in Zurich (for which Richard Ernst was awarded the Nobel Prize in 1991).

Applying a field gradient for a short period of time will cause those nuclei in the stronger field to precess faster, and at the end of that time to have advanced slightly in phase ahead of those in a weaker field. By collecting signals following a succession of gradient pulses, on each occasion incrementing the strength of the field gradient slightly, those nuclei in the strong parts of the field will advance further and further at each repeat compared to those in the weaker field. With a gradient balanced about the magnet centre, those nuclei exactly at magnet centre will not advance at all, and those on the other side of the magnet will progressively lag further behind.

The field gradient used to progressively increment the phase of the signals is known as the ***phase encode*** gradient (Figure 1.7).

Considering the collected signal point-by-point, with respect to the incrementing field rather than to time, the nuclei in the stronger field will be seen to progress more rapidly from one cycle to the next (Figure 1.8). With a second Fourier transform this second apparent 'frequency' is converted to the second dimension of the image.

Again, the transformation requires the number of data points to be a power of two (128, 256, 512…), but because each point takes a considerable length of time to collect (limited by T1) it is common to collect fewer and to fill in the missing points either with zero ('zero filling') or by sophisticated algorithms to guess the missing data ('partial Fourier'). However, if fewer than two points are collected per cycle, the waveform will be insufficiently

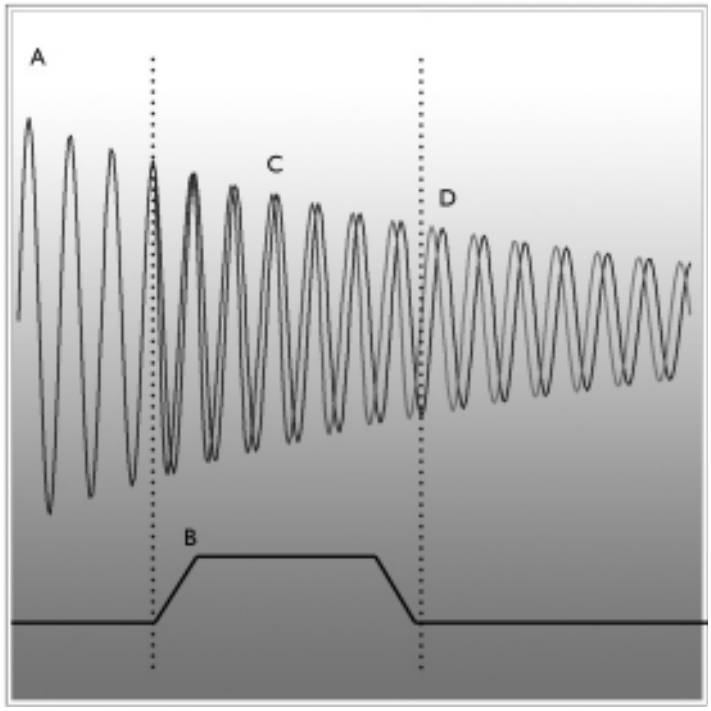

Figure 1.7 Phase encode gradient. Initially at A nuclei resonate at a single frequency. During the phase encode gradient pulse B, those nuclei that are located towards one edge of the magnet experience a higher field and will precess faster (light grey), C, advancing ahead of nuclei at the centre of the magnet (dark grey) where the field is unchanged. If the gradient is switched off after a short period, all nuclei will return to the same frequency, but the phase of those that experienced the higher field will be advanced, D.

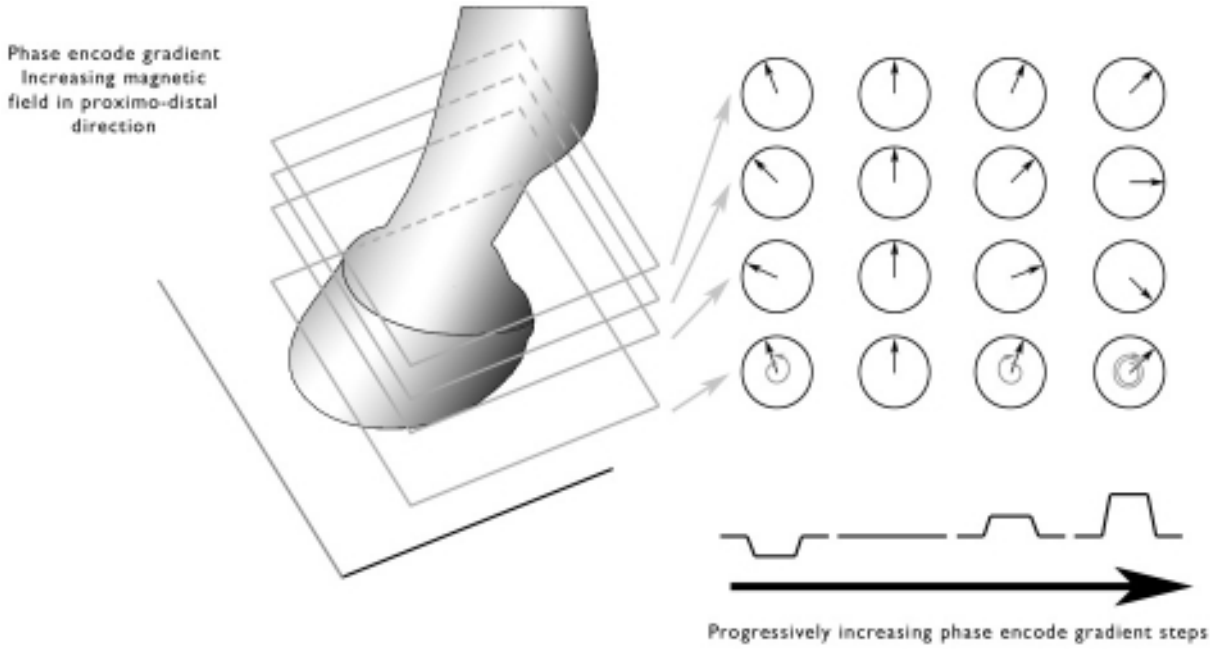

Figure 1.8 Phase encoding. At successive steps during the pulse sequence the phase encode gradient is progressively strengthened. At each step the phase of the signal is incremented. At a level close to the centre of the magnet (top) the phase increments are small. Further from the magnet centre each step is larger, and a Fourier transform with respect to the successive steps will transform to a higher 'frequency', and thus a different position. At a level further away still (bottom, not to scale) the phase will rotate so far at each step that it goes right around, and so will appear to be progressing at a slower rate and be transformed to the wrong location.

digitized[9] and parts of the object far away from the magnet centre will appear in the wrong location – an effect known as phase wrap, aliasing or undersampling. To minimize this artefact it is preferable to orient the phase encode direction across one of the shorter dimensions of the object being imaged (i.e. dorsal-palmar/plantar or medial-lateral rather than proximal-distal for the equine distal limb). Where this is not possible, the MR instrument may have to be set to collect more samples (phase encode oversampling or anti-aliasing), but this will be at a cost of a longer imaging time, lower resolution or more noisy images.

True three-dimensional images are collected by dispensing with the slice select gradient and repeating all the phase encode steps for a two-dimensional image again multiple times, while incrementing a third orthogonal gradient, to produce a second Fourier transformable phase encode direction.

k-space

The raw data for an MRI image consists of digitized signal amplitudes collected at successive time points, repeated many times for the different phase encoding steps, to build up a two-dimensional grid of points. The centre of this data set consists of points collected at the middle of the echo, with zero amplitude phase encode gradients, so the signal is at its strongest. Further from the centre the signal oscillates and becomes weaker. On Fourier transformation the central points dominate the brightness and contrast of the image, while the outer points fill in the detail and determine the ultimate resolution. The term 'k-space' is often used to describe the raw data and its Fourier transform relationship with the transformed image. By analogy, the raw k-space data is comparable to light in the centre of a camera lens, while its Fourier transform is comparable to the focused image. Using a larger lens gives a clearer image, not a larger image.

PULSE SEQUENCES

MR image formation involves:

- one or more stimulating RF pulses
- field gradients in all three directions, switched on and off and varied in amplitude
- acquisition of the resulting RF signal.

The succession of activities is under precise computer control and is termed the pulse sequence. The most fundamental conceptual sequence could be considered as in Figure 1.9, although *in reality this would not work*, as the oscillations from spins at different frequencies (due to being in different places in the field gradient) would all muddle up and cancel each other out before the data could be collected.

Real sequences include a number of further important practical modifications. There are two basic types of pulse sequence using different methods to correct for the dephasing of signals: gradient echo and spin echo. For each

[9]Two points per cycle is known as the Nyquist criterion.

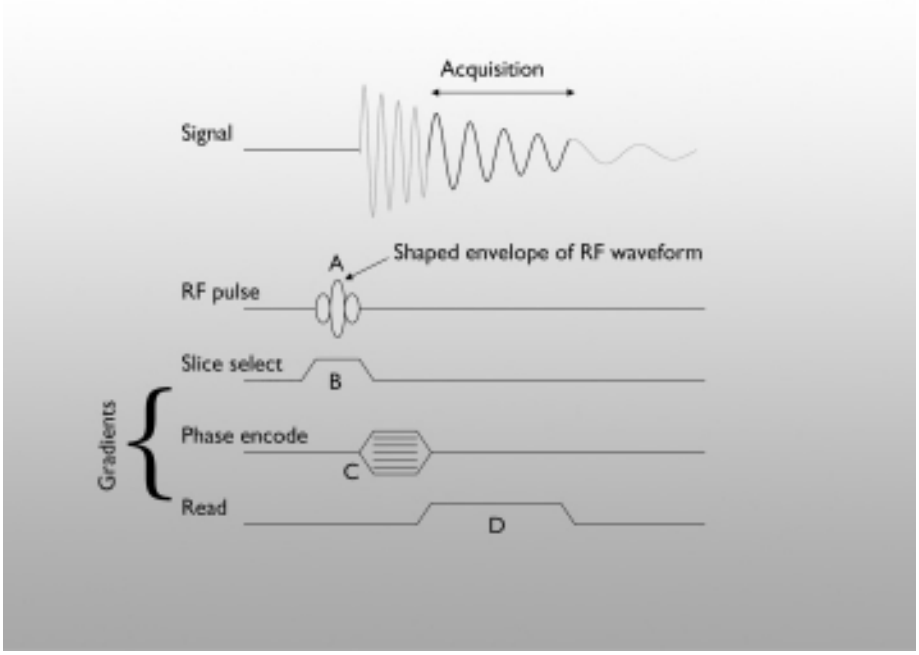

Figure 1.9 Conceptual MR imaging pulse sequence. The most basic conceptual MR imaging pulse sequence, consisting of an RF pulse A at the same time as a gradient pulse B used for slice selection, followed by a short phase encode pulse C, and then a read gradient D. The entire pulse train is repeated a number (e.g. 128) of times with the strength of the phase encode pulse C incremented each time.

of these there are common extensions to the basic form, including inversion recovery, fat saturation and fast imaging. Some clinical sequences combine elements of more than one sequence type. Additional features such as flow compensation, magnetization transfer, crusher gradients and navigator echoes can also be added, and the phase of successive RF pulses may be alternated or rotated. Writing fully optimal sequences is a complex task, and a practical clinical pulse sequencer is a sophisticated piece of real-time computing equipment.

It has become something of an MRI tradition to name pulse sequences with an acronym, and system vendors have become increasingly creative not only in creating acronyms but also in disguising the fact that many rival sequences are almost identical, varying only in minor details. It is helpful therefore in comparing systems and images from different vendors to understand the fundamental types of sequence rather than rely on the proprietary name or acronym alone.

Gradient echo

The gradient echo is the closest practical implementation to the prototype described in Figure 1.9. Gradient-echo sequences were initially abbreviated to GE, but with the entry of General Electric into the MRI market were renamed GRE (gradient recalled echo).

The gradient-echo imaging sequence (Figure 1.10) can be very fast because a low ***flip angle*** (a short or weak) RF pulse can be applied, sampling only part of the magnetization on each cycle with no need to wait for the magnetization to recover fully with the time constant T1. This was the basis of the first implementation of rapid imaging, called FLASH (fast low-angle

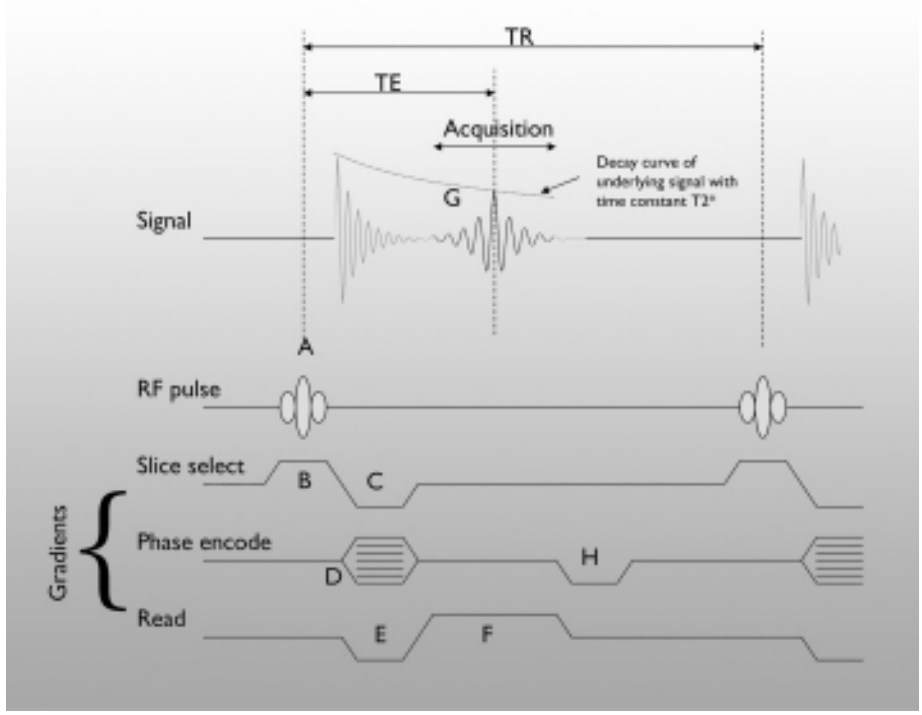

Figure 1.10 The basic gradient echo imaging sequence. Following the slice select RF pulse A and gradient B, the slice select gradient is inverted, C, so that all the spins in the excited slice are returned to the same phase. The phase encode gradient D is applied in the same time slot. At the same time a read dephase gradient is applied, E, so that when the read gradient is applied later the phase of all spins will come together in the middle of the echo. The read gradient F is applied at the same time as the data collection receiver is enabled, G. Rephase or spoiler gradients H may be applied (on any gradient axis) after the data acquisition and before the next cycle. The time period between the initial RF pulse and the data collection is termed TE, and that between successive cycles is TR. The sequence is repeated with the phase encode gradient incremented, until a complete 2D data set is collected. The complete set is then repeated a number (NA or NEX) of times, with the acquired data being averaged to improve image quality. During the time period TE the signal is decaying with time constant T2*, so a gradient-echo image will to some degree be T2* weighted.

shot) [6]. As the flip angle increases, the recovery of magnetization becomes more important and those spins that relax more quickly (short T1) give more signal, while those that relax more slowly (long T1) remain saturated. The image intensity of a gradient-echo image with large flip angle and short TR (repetition time) therefore depends on T1 and is said to be ***T1 weighted***.

During the time between the pulse and the data collection, termed the echo time or TE, the signal from regions with a short T2* decays more quickly. These areas become dark on the resulting image, while parts of the image corresponding to tissue regions with a long T2* remain bright. Increasing TE creates an increasingly ***T2*-weighted*** image, but also decreases the image quality as more signal decays away before it is collected.

Spins outside the selected slice are not stimulated by the frequency-selective RF pulse. While magnetization in the first slice is recovering (with time constant T1) during the repetition (or relaxation) time TR between

successive pulses, signal can be collected from other slices. The maximum number of slices in a multi-slice sequence depends therefore on TR, as this determines the time available to scan all other slices before returning to the first.

Gradient-echo sequences are usually run with a short TR compared to T1, so the magnetization does not fully recover between RF pulses. Spoiled GRE sequences aim to reduce T2* weighting by destroying the residual transverse magnetization using a semi-random gradient pulse (FLASH) or by randomizing the phase of successive RF pulses (Spoiled GRASS, SPGR). Varying TR, TE and flip angle produces a range of useful contrast weightings:

TR	**TE**	**Flip angle**	**Contrast**
Long	Short	Small	***Proton density***
Short	Short	Large	***T1 weighted***
Long	Long	Small	***T2* weighted***

With a short TE, a decrease in TR can be compensated for with an increase in flip angle, increasing T1 weighting and imaging speed at the expense of SNR. Increasing the number of averages to compensate for the decreased SNR produces an almost constant SNR per unit time, for any given T1, TR and selection of the optimum flip angle (the ***Ernst angle***).

Coherent GRE sequences do not use spoiling, so that successive pulses act on a mix of longitudinal and transverse magnetization. By using a phase unwinding gradient to refocus the transverse magnetization, and alternating the phase of successive RF pulses (GRASS, FISP, TrueFISP, FFSP), the magnetization can be kept close to the longitudinal axis. At low flip angles these sequences show similar proton density and T1-weighted characteristics to spoiled GRE sequences, but at larger flip angles they show increased T2* weighting.[10]

Spin echo

Spin-echo images compensate for the T2* signal decay due to local magnetic field inhomogeneity by refocusing the signals that have dephased. The spin-echo sequence (Figure 1.11) results in a stronger signal than the gradient echo, but it is slower because the period TR must be long enough to allow for substantial T1 relaxation before repeating the sequence.

With a short TE (so T2 decay is negligible) and long TR (so T1 relaxation is complete) the spin echo gives a proton density-weighted (PD) image. As TE increases the image becomes progressively more ***T2 weighted***. The T2-weighted image is the mainstay of clinical imaging, as the T2 of water in biological tissue is sensitive to its environment and increases in regions of inflammation and oedema.

[10] At large flip angles it is also possible to create a chaotic state where no steady state is ever reached.

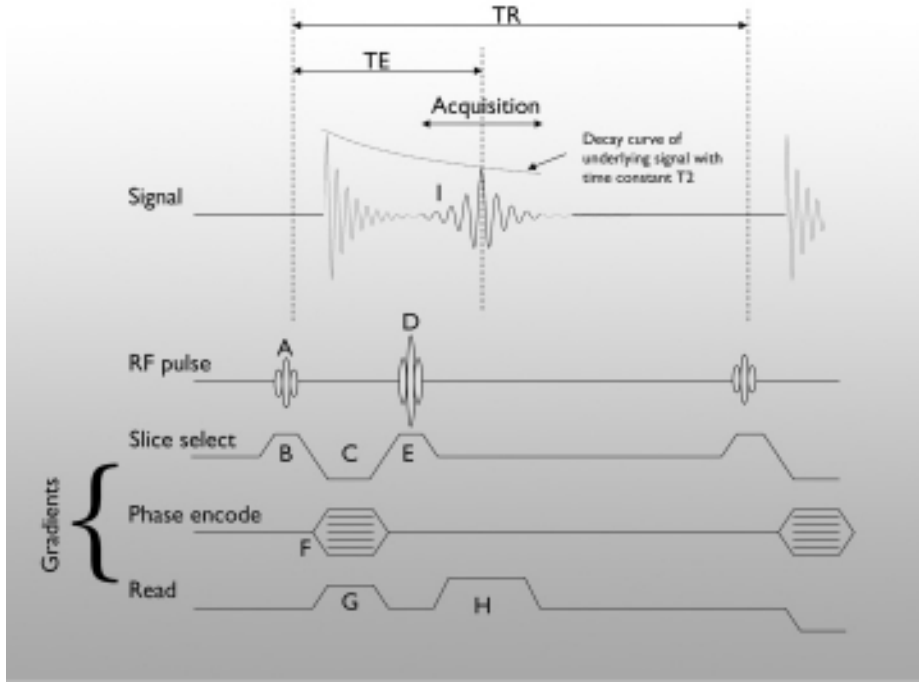

Figure 1.11 Basic spin-echo imaging sequence. Following the slice select RF pulse A and corresponding gradient B, the slice select gradient is inverted for a rephasing lobe C, before a further slice select pulse D and gradient E. This second pulse is of greater amplitude than the first and flips the spins through 180°, creating a spin echo. The phase encode gradient F, and a read dephase gradient G, are applied at the same time. The read gradient H is applied after the inversion pulse and the data is collected at the same time I. Over the period TE signal decays with time constant T2, so to some degree spin-echo images will always be T2 weighted.

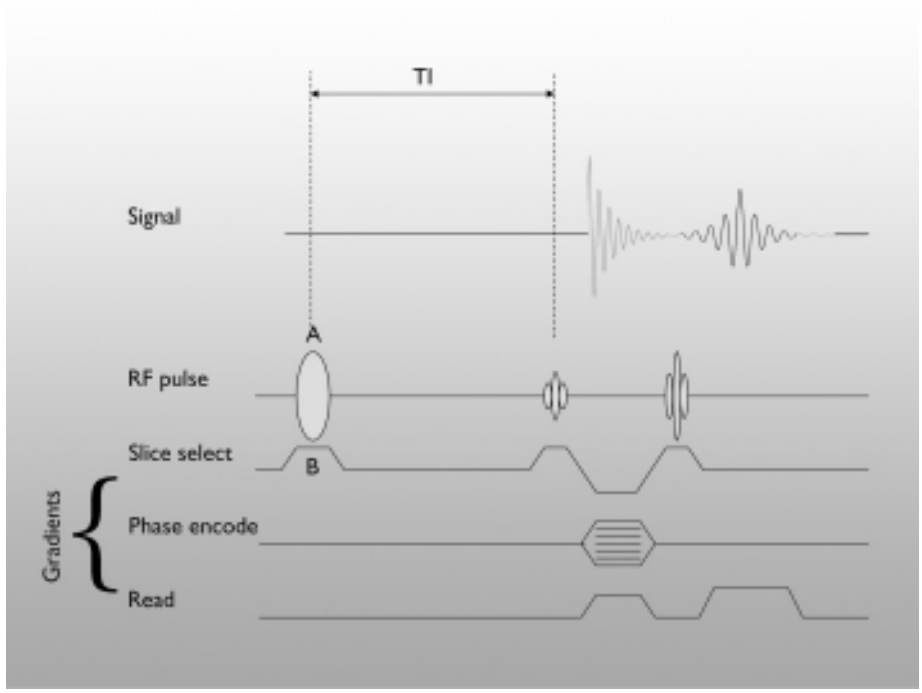

Figure 1.12 Inversion recovery. The basic inversion recovery imaging sequence with spin-echo readout. An inversion pulse A is applied, with an associated slice select gradient B. Normally the shape of the pulse A is different to the imaging pulses, and the thickness of the slice selected by A and B is thicker, to ensure good quality suppression. The inversion pulse is followed by the inversion time TI and then the standard imaging sequence. The repetition time TR is the time between successive inversion pulses.

Inversion recovery and STIR fat suppression

Both gradient-echo and spin-echo imaging sequences can be preceded by an additional 180° pulse and delay period (Figure 1.12). The 180°, or inversion, pulse flips the magnetization completely, from which it starts to recover with time constant T1 during the delay period TI.

[20]

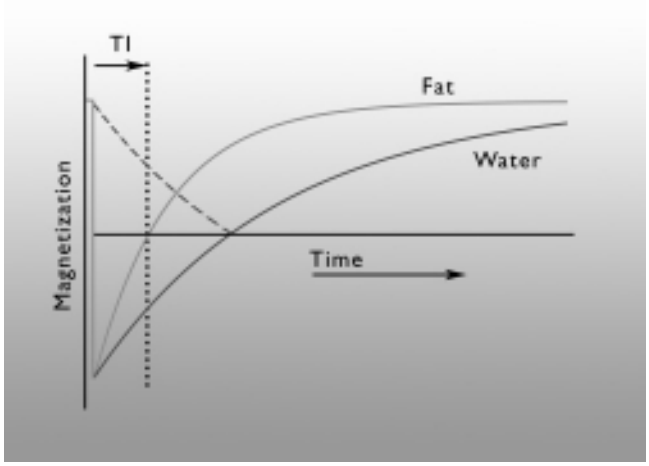

Figure 1.13 STIR fat suppression. Following the initial inversion pulse the magnetization from both fat and water becomes negative, and recovers towards the initial value with time constant T1. As T1 is shorter for fat, the magnetization from fatty tissue crosses zero after a time TI, while that of water and other tissues is still negative. Data collected at this point will give an image from water (the dotted line representing the fact that all image data is made positive during the image formation process) while suppressing any signal from fat.

If an image were to be collected immediately after the inversion pulse, then the signal would be negative (though the image would still be white as the sign is eliminated during the image generation process). During the recovery from complete inversion (negative signal) to complete relaxation (positive signal), the system passes through a null point where no signal is detected. The time taken to reach this point is shorter for material with a short T1 (e.g. fat) than for material with a longer T1 (e.g. water), so by carefully choosing the exact inversion time the signal from fat or from water can be suppressed (Figure 1.13). The STIR (short τ inversion recovery, where τ is an alternative denotation for TI) sequence is a common way to suppress fat signal and increase the ability to detect water in the presence of fat (e.g. in bone). Its complement, FLAIR (fluid attenuated inversion recovery) can be used to suppress the signal from water (e.g. for brain imaging).

The RF pulse shape applied for the inversion pulse is often of a complex form in which the magnetization spirals down to the inverted state and remains inverted even if the pulse continues. Using such pulses with a well-tuned coil and a high transmit power ensures a good inversion across the whole sample, even if the coil does not produce a perfectly uniform distribution of RF.

Inversion recovery fat suppression is slow, partly because while the fat signal is decaying to zero the water signal is also decaying, so the signal is weak, and partly because TR has to be sufficiently long for the magnetization to recover before it can be inverted again. It works reasonably well at low field, where the T1 of fat and water are well separated, but is less commonly used at high field.

STIR images are particularly sensitive to motion because of the long TI period (~80 ms). If the horse leg moves between the inversion and the

detection pulses then clearly the signal will not be properly prepared, and fat suppression will not be good.

T1 of fat in tissue is also sensitive to temperature, and possibly to other factors such as the age and breed of the horse. Some fine-tuning of the TI period may be needed in individual cases to get the best suppression. An equine foot image with generally poor suppression, for example covering the distal and middle phalanges and the navicular bone, is more likely to be the result of an instrument artefact than genuine pathology.

Fat saturation

The chemical environment in which a hydrogen nucleus resides has a slight influence on the exact magnetic field at the nucleus, as the surrounding electrons in the nearby atoms and molecules provide a weak shielding effect. This effect is known as ***chemical shift***, and results in the resonant frequency of fat being slightly higher than that of water. The chemical shift between fat and water (measured in parts per million compared to a standard reference) is only about 3.5 ppm, but in a high-field magnet it can be sufficient to produce separate peaks for the fat and water signals. This can be a problem, producing images from fat and water that are slightly shifted apart and distorting signal at the boundaries between them, a phenomenon termed the chemical shift artefact. But it can also be exploited in a number of ways to suppress the fat signal while retaining the full strength of the water signal.

The most common method is fat saturation (fat-sat) in which a frequency-selective pulse is applied to stimulate only the fat signal, followed by spoiler gradients to completely dephase it. The following image sequence then only detects signal from water.

Newer techniques [7, 8] are also beginning to be seen in which two images are collected, one with the fat and water signals in phase, and one, by adjusting a delay, with the two out of phase. Summing the two cancels the fat while adding the water signals, giving good fat suppression.

Fast spin echo

Image quality is largely determined by the amount of signal that can be collected in a given time, compared to the unavoidable level of electrical noise due to thermal motion of electrons in the sample, coil and RF receiver. The limit on time is generally the need to wait between phase encode cycles while the magnetization recovers with time constant T1.

Fast spin echo (FSE; also known as turbo spin echo) is a method for speeding up the image by collecting several phase encode steps in one TR period, following only one initial RF pulse. The principle is to follow the first RF pulse with a train of 180° pulses, collecting echoes and rewinding the phase encode gradients between each one. However, because the different echoes are not all collected at the same time they do not each have the same T2 weighting. Data are collected in an order, and reshuffled in the computer, so that the phase encode steps that dominate the image contrast

are collected close to the desired nominal TE, while those that fill in the detail are collected at shorter or longer times. Even taking this precaution, the image contrast of a FSE sequence is not quite identical to that of a conventional spin echo.

Fast spin-echo sequences can be 10 times or more faster than conventional spin-echo sequences but are very demanding on an MRI system, requiring both fast and precise operation to allow the train of echoes to be collected without accumulating slight errors and distorting the signal.

Variations on the same theme include the following.

- Dual echo imaging, in which only two echoes are collected with one at a short TE (giving a proton density image) and one at a longer TE (giving a T2-weighted image) at the same time.
- Inversion recovery with FSE readout, using one inversion for several phase encode steps.
- Echo planar imaging (EPI), which is a multi-echo gradient echo technique comparable to FSE that can obtain an entire image in a few milliseconds. It is used in human brain and cardiac imaging but not commonly in equine imaging.
- Hybrid imaging, in which a few gradient echoes are collected before a 180° pulse is used to refocus the spins, and the process repeated.

Sequence choice

With such a wide variety of sequence types and parameters within each sequence, images can be collected in many different ways. The choice often comes down to the preference of the individual radiologist, but guidelines include the following.

- Gradient-echo sequences generally have greater signal to noise ratio but lower T2-weighted contrast than spin-echo sequences. Gradient-echo sequences are most useful:
  - to obtain high anatomic resolution (where the increased signal allows for thinner slices in a given time)
  - where time constraints make rapid imaging essential
  - for T1-weighted images of bone, especially at low field.
- The T2* weighting obtained from a gradient-echo sequence is not identical in either origin or characteristics to the T2 weighting of a spin-echo or fast spin-echo sequence, so care is needed in interpreting one on the basis of experience gained with the other. The lower contrast of the gradient-echo sequence can lead to pathology being overlooked if a greater change in image intensity is expected.
- Fat/water cancellation must be properly recognized to correctly interpret T2*-weighted gradient-echo sequences, but can be a very useful guide to regions of the image worthy of more detailed attention.
- Gradient-echo sequences are more susceptible to magnetic susceptibility artefacts. They should be avoided where, for example, a nail fragment causes magnetic distortion, but can be useful to determine the track of an injury from the magnetic susceptibility 'black line' of blood breakdown products.

- Fast sequences trade time against signal to noise ratio, resolution or both, so care must be taken when interpreting questionable features. In some cases a low resolution combined with a sharp change in contrast can cause features to appear larger or smaller than they truly are, and care is needed in interpreting small features. For example, the bright appearance of cartilage in T1-weighted GRE sequences can mask thin regions or defects.
- Spin-echo images show T2-weighted contrast more clearly, and so are theoretically preferable for T2-weighted sequences and for fat suppression. However, the lower signal to noise ratio can degrade image quality and necessitate reduced spatial resolution and increased slice thickness, so care is needed in assigning the anatomical origin of the observed signal changes.
- Long T2 spin-echo and fast spin-echo images are much more resistant to magic angle artefact and are essential to interpret images of structures that are at an angle to the main magnetic field.

Interaction between parameters

When examining an individual patient the radiologist or radiographer may wish to adjust some of the timing parameters in the pulse sequence, for example to minimize imaging time for a difficult patient or obtain thin slices over a particular region. However, each parameter is linked to others by a complex network of interactions, so the planned change may not be possible or may cause unexpected side effects. Table 1.1 shows some common interactions.

Most commercial sequences are highly optimized to image the maximum number of slices in the minimum time, and adjustment of key parameters generally requires one or more compensating adjustments. Some system software provides tools to help, indicating for example with red and green

Table 1.1 Interactions between parameters

Parameter increased	SNR	Resolution	Acquisition time	Distance covered by slices	Maximum number of slices
FOV (Field of view)	↑	↓	No change	No change	No change
Slice thickness	↑	↓	No change	↑	No change
Slice separation	↑	↓	No change	↑	No change
Number of slices	No change	No change	↑[1]	↑	No change
No. averages	↑	No change	↑	No change	No change
TR	↑	No change	↑	No change	↑
TE	↓	↓	No change	No change	↓
Matrix size	↓	↑	↑	No change	No change
Bandwidth	↓	No change	No change	No change	↑

[1] Up to a certain number of slices (batch size) can be collected without changing the acquisition time, as some slices can be imaged in the TR of others. Beyond this limit acquisition time will increase.

bars the available ranges. Other manufacturers provide a wider range of optimized sequences, but discourage individual adjustments.

MRI HARDWARE

There are five vital components of an MRI system.

1 A magnet, sufficiently strong to give a useful signal, and sufficiently large to accommodate the patient.

2 A means of modifying the field strength according to location within the magnet. This is done by passing electrical currents through coils wound inside the magnet.

3 A method to stimulate, and to detect, the interaction between nuclei in the patient and the magnetic field. This is a form of radio transmitter and receiver, with a coil surrounding part of the patient as the radio aerial.

4 A computer to control and to process the necessary electrical signals.

5 An electrical screen, or screened room, to prevent interference from external radio waves.

While many of these can be adapted from products designed for human MRI, the shape and nature of the equine patient imposes some special demands.

Magnet

The strength of the MRI signal, a strong influence on the quality of the final image, increases roughly in proportion to the strength of the magnet. Imaging is technically possible at the earth's magnetic field (0.05 mT), but to obtain a reasonable image in a reasonable time requires a strength of at least 0.2 T. Currently the most common human MRI systems operate at 1.5 T, with some of the most recent at 3 T or 4 T, and cutting edge research at up to 9.4 T (400 MHz).

The earliest MRI magnets were constructed with high electric currents flowing through coils of copper wire, cooled by air or water. This technology cannot be used beyond about 0.2 T as the cost of the power supply, the electricity and the cooling system become too high, and it is only seen now in a few older or second-hand systems.

At high fields, electromagnets are wound using superconducting wire, which must be kept at close to the temperature of liquid helium. By joining the ends of a continuous loop (using a special switch), once a suitable power supply has started an electric current of several hundred amps flowing around the coil the current will continue without loss. To maintain the low temperature the superconducting magnet is built into a large stainless steel cryostat and cooled using a reservoir of liquid helium and a refrigeration device called a cryopump. Modern magnets require only occasional cryogen gas refills, while older ones need regular top-ups and the very old ones also use liquid nitrogen to cool the outer layers of the cryostat. The cost of liquid helium, and of electricity to run the cryopump, is a significant factor in considering the economics of a high-field MRI system.

Conventional human MRI magnets are in the form of a tube, about 60–70 cm in internal diameter and 2–3 m in external diameter. The most

common field strength is 1.5T, although 3T magnets are becoming well established in human MRI. The most modern magnets have a flared end and a short bore of only 1–1.5 m, while older magnets are longer. Because the equine patient is a different shape to the human, only the extremities of an adult horse can be fitted into the tube, and for all but the most recent wide-bore magnets even the carpus, tarsus and head can be difficult to image.

General anaesthesia is necessary to keep the patient still, and because ferromagnetic material is strongly attracted to a high-field magnet, special equipment is required. This includes a non-magnetic table and MR-compatible anaesthetic machine, ventilator and monitoring devices (MR-compatible devices are also designed so as not to produce radio frequency interference).

The standard patient bed may well be incapable of supporting the weight of a horse, so it may be necessary to fit the equine patient in from the rear of the magnet. Most human MRI systems incorporate safety interlocks to ensure that the patient and the RF coil are correctly positioned, which can cause problems when the patient is not human-shaped. Overriding such safety interlocks will generally require the co-operation of the system manufacturer.

Current international regulations require restriction of public access to areas with a magnetic field strength of 0.5 mT (5 G) and above. Further close control is needed nearer to the magnet to reduce the risk of flying metal objects. Modern superconducting magnets are designed with an outer, counter-wound coil to reduce the external field and constrain the area within the 0.5 mT isocontour (to minimize siting costs) but this has the effect of increasing the attractive power close to the magnet opening. Great care is needed to ensure that no metal objects (e.g. scissors, stethoscopes, gas cylinders) are brought anywhere near the magnet by the horse or its attendants.

As an alternative to the tubular form, magnets can also be designed with two flat poles separated by a gap of about 20–40 cm. In some cases the poles are held apart by four posts in the corners, in others the magnet is a 'C' or 'U' shape open on one side. For human MRI this technology has been promoted for claustrophobic patients, but for equine MRI the advantage is in improved access. High-field versions of such 'open' magnets using superconducting technology are at the very edge of current technology and are only just beginning to be seen in human MRI, but at lower fields of 0.2–0.3T they can be built economically using permanent magnets and used for veterinary imaging. Permanent magnet products originally designed for human limb imaging are marketed for small animal and anaesthetized equine applications by Esaote (Genoa, Italy), while Hallmarq Veterinary Imaging (Guildford, UK) manufactures a unit with thin poles and a vertically oriented gap especially designed for the distal limb of the standing horse.

Gradients

Magnetic field gradients are created by passing an electric current through coils wound inside the magnet bore or gap. They are characterized by their maximum strength and the rise-time from zero to near maximum strength:

the stronger and faster the gradients the quicker the images can be acquired, but at an increased cost. Gradient performance, and the compensation of unwanted eddy currents, has a significant impact on image quality and is one of the more critical factors to consider when comparing alternative products from different manufacturers, and old versus new systems.

High mechanical forces are generated on the gradient coil during the pulse sequence (due to the electric motor effect of an electric current in a magnetic field) and the resulting slight motion creates audible noise, which can be uncomfortably loud in a high-field system but is usually negligible in an open, low-field one.

RF coils

RF coils are used both to transmit and to receive radio waves. They generally consist of a copper winding tuned to the resonant frequency with high-quality, non-magnetic capacitors and enclosed in a plastic housing. Fine-tuning may be mechanical or electrical.

The transmitter coil must be able to handle high power and generate a uniform field over the entire sample. In high-field magnets it is usually built into the bore of the magnet, on a tube just inside the gradient coils.

The receiver coil (which may be combined with the transmitter coil) effectively collects signal from the sample and noise from its entire volume. The smallest coil that will fit the sample should therefore always be used, and the uniformity of the field (and thus uniformity of the image brightness) is to some extent sacrificed to achieve the best signal to noise ratio.

The B1 field generated by the RF coil must be orthogonal to the B0 field of the main magnet. In an open magnet this is straightforward, and a simple one-turn coil can be fitted around the sample. In a cylindrical magnet the B0 field direction is along the magnet bore, so the RF coil cannot also be a simple concentric coil. Instead, a variety of configurations are used, the simplest being a 'saddle' or 'Helmholtz' design with two shaped windings either side of the sample. Because none of the closed magnet designs is as efficient as the simple solenoid coil, open magnet systems generate images of about 30% higher quality than would be expected from a simple scaling of the image quality obtained from the relative difference in field strengths.

Spine coils and flexible coils consist of an array (phased array) of separate coils with their mutual interaction carefully configured to reinforce their sensitivity inside the sample, and cancel outside.

The origin of the MR signal is the rotation of the bulk magnetization caused by precessing nuclei. A simple RF coil is sensitive to an alternating field, which could be produced by rotation in either direction. Effectively, this means it will pick up the signal from the precessing nuclei in one direction, but only noise in the other direction. By combining two coils at right angles to each other, and combining the two signals together with an exact quarter-cycle delay between them, a composite coil can be made which is sensitive to the field rotating only in one direction. Such a combination is termed a ***quadrature coil***, and can improve the detected signal to noise ratio by up to a theoretical factor of $\sqrt{2}$.

The conventional RF coil is not necessarily the most effective way to detect the MR signal, and interesting advances may be seen in future from the use of cryogenically cooled coils, high temperature superconducting coils or SQUIDs (superconducting quantum interference devices).

RF hardware

RF hardware is generally the province of the system manufacturer and not visible to the operator. The transmitter must generate precisely timed, shaped and phase- or frequency-modulated waveforms, and amplify them to a high power (several kW). The receiver must handle very weak signals (nV–μV) from one or more coils and have a uniform sensitivity over a narrow bandwidth with a very sharp fall-off outside the target range. Modern receivers are almost entirely digital, digitizing the signal either at the raw RF frequency or after conversion to an intermediate frequency of a few MHz, and processing it in customized silicon chips.

Computer

Hardware

The MR system computer usually comprises at least two components: the pulse sequencer and the user interface controller.

The pulse sequencer is again the domain of the manufacturer, but older systems may not be capable of running modern sequences such as fast spin echo or Dixon method fat suppression.

The user interface controller is normally a generic computer running Microsoft Windows or one of the Unix-type operating systems, presenting the user with a single program or suite of programs for routine control of the system. The same computer will usually run a number of diagnostic and monitoring programs, generally password protected for use only by the manufacturer or service engineer.

MRI software

The user interface generally consists of a number of pages, grouped by function. Control may be by mouse, keyboard or a combination of the two. Each manufacturer has developed its own software, and the grouping, terminology and functions available will vary from system to system, but the key functions are:

- entering the patient details or retrieving them from a central database (e.g. a DICOM worklist server)
- selecting the sequence or list of sequences (protocol) to be applied
- adjusting or fine-tuning the parameters of individual sequences
- initializing the scanner and performing manual and automatic safety checks and calibrations
- collecting a scout, or pilot, scan for initial orientation
- setting up the physical position and angle of the image slices to be collected

- starting, stopping or pausing the scan in progress
- viewing the image
- storing the images and/or passing them on to another image store (e.g. a DICOM PACS server).

Most systems allow multiple operations at the same time, so while one set of images is being collected the operator can be setting up the next patient or reviewing the last set of images.

The Hallmarq standing MRI systems incorporate motion compensation software, which monitors the motion of the limb in real time. Where possible, the apparent position of the image is corrected and the imaging continues. Where the object moves too fast, or too far, to be corrected, the system goes into a 'free-wheel' mode waiting for the object to return, at which point the imaging continues where it left off.

MR system software is also responsible for the Fourier transformation that converts the raw data into images, and for image-processing functions such as trimming the edges of the image to the defined field of view, and advanced image filtering to improve the signal to noise ratio. Other data such as the patient name, date, pulse sequence used, etc., are associated with the image, normally in a protected manner so that any later alterations can be prevented, or at least detected.

A full set of MR images from one examination can easily consist of 500 or more separate images. Once collected, they are generally reviewed using DICOM viewing software, which allows for zoom and pan, brightness and contrast adjustment, and side-by-side comparison of different images. The direct comparison is particularly critical in MRI where much of the clinical information is derived from the relationship between the different contrast weightings (PD, T1, T2, fat suppressed) of the same feature. Merge Efilm Workstation (Merge Healthcare, Milwaukee, WI, available for veterinary applications from Sound-Eklin, Carlsbad, CA) for Microsoft Windows and Osirix (free, available at www.osirix-viewer.com) for the Apple Macintosh are popular third-party DICOM viewers suitable for MRI.

RF screened room

To reduce RF interference the MRI system is installed inside a metal-walled room, with the walls made from a conductive metal such as aluminium, steel, copper or even gold-coated fabric. Copper and galvanized (zinc-coated) steel are the most common, although if steel is used it must be kept well away from the magnet. Copper is most commonly used on the floor, as it is non-magnetic, resistant to corrosion and easy to solder into a continuous electrically conductive sheet around corners. Door openings are electrically sealed using either conductive springs or a conductive tube inflated by air pressure when the door is closed. Rubber flooring and plastic or wooden panels on the walls are often used to protect the metal and provide a more aesthetic environment inside the room.

Penetrations through the walls must be insulated or pass through electrical filters. All mains cables entering or leaving the room must be filtered, and because the room walls are metal, special attention is needed to provide

safe earthing. Cables for special equipment must also be filtered. Ethernet cable carries signals that interfere with MRI, but both 802.11 wireless internet and Bluetooth operate sufficiently far from the MR frequencies that they can often be used. Copper pipes for plumbing or air conditioning must pass through a panel that is well connected to the metal walls, or alternatively services must pass through plastic pipes. Air ducting, or any non-conductive penetrations, must pass through a waveguide, which is a conductive tube or grid of tubes of a length and diameter that attenuates RF waves.

Even though the radio frequencies used may be well away from the MR frequency, devices such as mobile phones and laptop computers may generate noise internally, and these and other electrical equipment such as blood pressure monitors, ECG monitors and CD players must be kept out of the room, or at least checked and not used during the actual scanning time.

IMAGE QUALITY AND ARTEFACTS

Image quality is primarily determined by four factors: signal, noise, contrast and artefacts. Signal and noise are often considered together as the signal to noise ratio or SNR.

Signal

The MR signal is generated by nuclei in the sample in the magnet. Increased field strength, and increased amounts of material, give more signal. The amount of signal in any one image pixel is reduced sharply as the image resolution increases: a resolution of 1 mm x 1 mm with 1 mm slice thickness has only one-eighth the signal of the same sample at 2 mm x 2 mm x 2 mm resolution, so there is a practical limit beyond which improving resolution will not improve the image quality.

The amount of signal is also increased by repeating the scan and averaging the data together. The overall signal to noise ratio increases as the square root of the number of averages. This is expensive in time, requiring a factor of four increase in time to compensate for a factor of two loss in signal. Extending the resolution example above, it would require a factor of 64 increase in time to obtain the same signal to noise ratio at double the spatial resolution in each direction. This of course also works the other way, providing dramatically faster images for modest reductions in spatial resolution.

Noise

Electrical noise is generated by thermal motion of electrons in any conductor, including the sample, coil and amplifiers. Even with cryogenic cooling this can never be completely eliminated, and the thermal noise from the sample sets an absolute lower limit on the noise level. Because the MR signal is very weak, care must be taken not to allow any external sources of noise to further degrade the image.

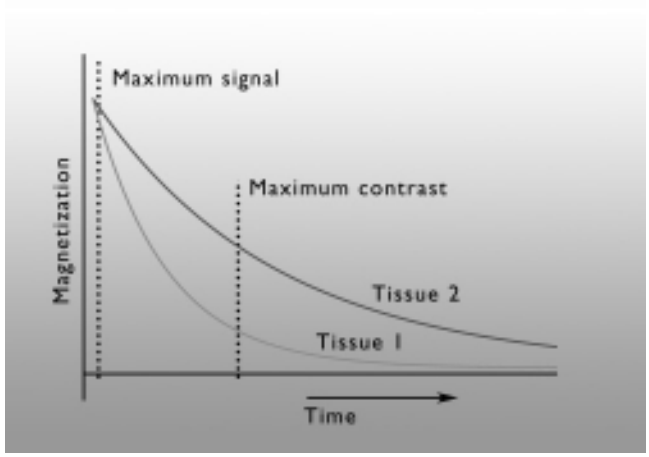

Figure 1.14 Image contrast vs image signal strength. For two different tissue types maximum contrast is obtained at a specific point in time, and this is not the point at which maximum signal is available. The time axis could relate to either TR (T1 weighting) or TE (T2/T2* weighting). A range of sequences is needed to obtain both high signal and high contrast.

Contrast

No image would be of value if it consisted of a uniform grey intensity; the only value is from the contrast between lighter and darker areas. Contrast in an MR image comes from the amount of signal (proton density) and from deliberately introduced weighting. Signal is lost by T2 and T2* relaxation processes, and can only be detected following T1 relaxation. Image contrast weighting works by throwing away unwanted signal, but in so doing reduces the total amount of signal and thus the image quality. Thus for the highest anatomical resolution, the higher signal from a proton density image, or a T1-weighted image using the short T1 components, is often more valuable than the higher contrast of a T2-weighted image. Conversely, for diagnostic interpretation a greater contrast is obtained at lower signal strengths. Advance knowledge of the specific tissue types is important to optimize the image weighting for maximum contrast (Figure 1.14). Collateral ligaments for example are indistinguishable from the surrounding tissue on some sequences while being clearly visible on others.

In general, gradient-echo images have more signal but less contrast, and spin-echo images more contrast but less signal. The choice is often a matter of individual preference, though the T2-weighted spin echo or fast spin echo is such a valuable sequence that it should always be considered.

Artefacts

An artefact is the name used to describe a feature of the image that does not truly represent the object being imaged. Care is needed to eliminate artefacts where possible at the time the images are collected, and not to misinterpret artefacts as potential pathology when viewing images. MR imaging is particularly susceptible to artefacts because the underlying signal to noise ratio is low, the data collection takes a long time (seconds to minutes) and so is sensitive to motion, and MR itself introduces some unusual characteristics.

Signal to noise-related artefacts include spots, stripes and lines across the image, and are most often due to external interference.

Motion and blood flow cause smearing or ghosting, where faint copies of all or part of the image are repeated. Motion can be created not only by the sway or movement of the standing horse but also by the breathing motions and heartbeat of an anaesthetized animal. Metal objects moving near the magnet (e.g. steel toecapped boots) can also give the appearance of a motion artefact.

Other MR specific artefacts include the following.

- *Partial volume averaging.* MR signal is obtained from volumes of tissue with dimensions of the order of 1mm in each direction. If this volume contains signals of more than one intensity the final image brightness will be the average. This is particularly important when interpreting images of fine features on curved surfaces (e.g. cartilage). For best results the image plane should be aligned parallel or perpendicular to the structure under examination.
- *The magic angle effect.* The signal from aligned molecular structures such as collagen fibres increases when they are close to a specific angle (54.7°) to the main magnetic field. This is seen, for example, where the deep digital flexor tendon passes around the distal sesamoid bone in images collected using a high-field magnet, and in the collateral ligaments of the distal interphalangeal joint in a low-field magnet. The magnet dependence is not due to the field strength, but instead to the direction of the field and thus the structures which are aligned at approximately 55°. The magic angle effect is reduced as TE increases, so is seen less on T2-weighted spin-echo images.
- *Magnetic susceptibility effects.* Magnetic objects such as nail fragments will distort the local field, creating both position and brightness artefacts. Dirt caught in the frog or on the coat around the limb, and blue Play-Doh used as packing for x-ray examinations, are also known to create susceptibility artefacts. Blood breakdown products (e.g. haemosiderin) influence the magnetic field and produce dark regions on the image that can be useful to determine the extent of a penetrating injury.
- *Chemical shift artefact.* Fat and water resonate at slightly different frequencies, causing a slight sideways shift of the image from fat relative to that from water, and distortion of the boundaries between them. This is only significant at high field, while at low field the two signals overlap sufficiently to be indistinguishable.
- *Phase wrap.* The sharp edges of the displayed image are a somewhat artificial construction based on the processing of the data, and rely on there being nothing outside the field of view. Objects just outside will appear wrapped around to the other side, a phenomenon known as aliasing or phase wrap. This can be particularly disturbing with a moving object or pulsatile flow outside the imaging region. The effect can be eliminated or reduced by changing the orientation of the gradients, or alternatively by selecting appropriate oversampling options in the software at the expense of a slight reduction in image quality or increase in time. In 3D images phase wrap artefacts may appear in different slices and be difficult to recognize.
- *Flow artefact.* Phase encoding depends on preparing spins at one point in time to be detected at a later time. If the material is moving, the signal will be detected in a location different to where it was prepared, causing an

artefactual displacement in the phase encode direction. Pulsatile flow can create a series of displaced locations as the pulse rate interacts with the repetitive nature of the pulse sequence, creating a row of spots or a smear across the image.

- *Gibbs ringing.* Without collecting an infinite amount of data, sharp edges cannot be represented precisely, instead appearing as a steep transition followed by a series of wiggles. This can produce an artefactual bright line within a dark region close to a sharp boundary between bright and dark objects. This can sometimes be seen, for example as a grey line running along the deep digital flexor tendon, and care must be taken not to misdiagnose it as tendonitis. It can often be distinguished by looking for the symmetrical artefact on the other side of the sharp bright/dark edge.
- *Fat/water cancellation.* Because (as for the chemical shift artefact) the resonant frequency of fat and water are slightly different, at the time the echo is collected in some T2*-weighted imaging sequences the phase of the signal from fat is opposite to that of water. Under these circumstances the signals subtract. This creates a hypointensity where both water and fat are present (e.g. with bone oedema) where a hyperintensity would be expected. The true presence of water can be determined using a fat-suppressed sequence (e.g. STIR), but care must be taken not to misdiagnose the hypointensity as sclerosis.

GLOSSARY

	Atomic number	The number of protons in the nucleus of the atom. Equal to the number of electrons in the uncharged atom and thus determines the chemical properties and the chemical element
α	**Flip angle**	The amount by which the initial RF pulse tips the bulk magnetization
BW	**Bandwidth**	The frequency range over which the data is collected (set by the gradient strength and the field of view)
	Charge	A fundamental property of matter, in both positive form (carried by protons) and negative form (carried by electrons)
	Chemical shift	A small change in resonant frequency caused by the shielding effect of electrons in the atoms and molecules surrounding the resonating nuclei. In biological MRI a small chemical shift separates the resonant frequencies of fat and water
	Complex number	A mathematical convention for representing two-dimensional numbers. One component (real) is a normal number, the other (imaginary) is a number multiplied by the square root of –1 (i or j according to physics or engineering conventions)
DW	**Dwell time**	Sampling time of the data acquisition. The inverse of bandwidth

	Ernst angle	The flip angle producing optimum signal to noise ratio (SNR) for a given T1 and TR. α_E: cos α_E = exp(–TR/T1)
G	**Gauss**	cgs unit of magnet field strength. 1T = 10,000 G
	Gaussian	A smooth bell-shaped curve. The Fourier transform of a Gaussian is another Gaussian. Gaussian-shaped RF pulses are short and an efficient way to stimulate signal from a slice of tissue, but the edges of the slice are not sharply defined
	Gradient or field gradient	Manipulation of the magnetic field so that it is stronger in one location than another, with a linear relationship between position and field strength. Normally three orthogonal gradients are used to collect an image, the *slice select*, the *read* and the *phase encode* gradients. The actual physical orientation can be controlled by mixing components of physical gradients in the x, y and z orientations with the correct sine and cosine scaling
γ	**Gyromagnetic ratio**	The ratio of precession frequency to magnetic field strength
	Isotope	Atoms with the same number of protons but different numbers of neutrons are termed different isotopes of the same element. They behave essentially identically chemically, but have a different atomic mass and are identified by the mass number written as a superscript prefix
	Longitudinal relaxation	Synonymous with T1 relaxation. Realignment of the net magnetization with the direction of the main magnetic field with time constant T1
	Mass	A fundamental property of matter, carried largely by the protons and neutrons in the atomic nucleus
	Magnetic moment	A measure of the strength of a source of magnetism
	Neutron	One of the sub-atomic particles in the nucleus of the atom, possessing mass and spin but no electrical charge. The number of neutrons in the nucleus affects the mass of an atom, giving rise to different isotopes with the same number of protons, and thus of the same atomic number and same chemical element, but different atomic weights. The nuclei of isotopes with an odd atomic weight can give rise to magnetic resonance effects
NA NEX	**Number of averages** **Number of excitations**	Number of times the whole sequences is repeated and the data averaged together. Also abbreviated NSA or ACQ by other manufacturers

Phase encode gradient Field gradient applied between the RF pulse and the data acquisition. Spins precessing faster or slower under the influence of this field gradient cause a change in the phase of the detected signal

Precession The change in direction of the axis of rotation of a spinning object, normally itself a rotation so that the axis transcribes a cone shape over time

Proton (1) One of the sub-atomic particles in the nucleus of the atom, possessing mass, a positive charge and spin. The number of protons in the nucleus of an atom gives its atomic number and determines the chemical element of the atom

(2) The sole component of the nucleus of the most common isotope of hydrogen, ^{1}H. The terms 'proton' and 'hydrogen' in MRI terminology are almost synonymous

Proton density The concentration of protons in the tissue

Proton density weighted Type of image in which the brightness depends only on the concentration of protons, and the effect of T1, T2* and T2 are minimized. Only effective to a limited degree, as material with a very short T2 (e.g. tendon) still appears dark even though its molecular structure contains protons

Quadrature The means by which the direction of rotation is determined by observing from two locations at right angles. Used (a) inside the MR receiver, where errors can produce ghost images reflected about the centre line, and (b) for RF coils which combine two receiver elements and can gain up to 40% improvement in image quality per unit time

Read gradient Field gradient applied during the data acquisition period, so that signal in stronger parts of the gradient is detected at a higher resonant frequency

Sinc The shape of the function sin(x)/x, which consists of a central lobe surrounded by a succession of decreasing wiggles. The Fourier transform of a sinc shape is a rectangle, so sinc-shaped RF pulses can be used to create sharp-edged slice profiles, but as the wiggles take time to transmit they cannot be used for the fastest pulse sequences. The inverse can also be seen as an image artefact causing a succession of bright and dark bands on the image close to a sharp edge (Gibbs ringing)

	Shim	Fine adjustment of the uniformity of the main magnetic field, either by using small magnets or by passing electrical currents through specially wound coils positioned on the inside of the main magnet
	Slice select gradient	Field gradient applied during one or more RF pulses, so that only nuclei in a defined slice resonate at the frequency stimulated by the pulse(s)
	Spin	A quantum property of atomic nuclei and sub-atomic particles, somewhat analagous to rotation about an axis but constrained to be only at quantized values whichever axis of rotation is considered
	Spin-lattice relaxation	Synonymous with T1 relaxation. Realignment of the net magnetization with the direction of the main magnetic field with time constant T1 as energy is exchanged with the 'lattice' of surrounding material
T	**Tesla**	SI unit of magnetic field strength
T1		Time constant for realignment of the net magnetization with the direction of the main magnetic field
	T1 weighted	Type of image in which the brightness relates to T1. Brighter for *shorter* values of T1 (e.g. fat)
T2 T2*		Time constant for the loss of coherence of the rotating magnetization in the x-y plane, and thus loss of detectable signal. T2 relaxation is caused by interactions between nearby nuclei. T2* relaxation also includes the overall signal loss when some nuclei are experience a different local field strength
	T2 (or T2*) weighted	Type of image in which the brightness relates to T2 (or T2*). Brighter for *longer* values of T2 (e.g. water)
	Transverse relaxation	Synonymous with T2 or T2* relaxation. Loss of coherence of the rotating magnetization in the x-y plane, and thus loss of detectable signal
TE	**Echo time**	Time between the initial RF pulse and the centre of the data collection time
TR	**Relaxation time or Repetition time**	Interval between repeats of the pulse-acquire sequence
TI	**Inversion time**	Time between the inversion pulse and data acquisition
τ	**Inversion time**	An alternative designation to TI

ACKNOWLEDGEMENTS

The author would like to thank the veterinary and MR physics colleagues he has worked with at Hallmarq Veterinary Imaging, and in particular Dr Steve Roberts, for their helpful reviews of the text and figures in early drafts of this chapter.

REFERENCES AND RESOURCES

[1] Cooley JW, Tukey JW. An algorithm for the machine calculation of complex Fourier series. *Math Comput* 1965; **19**: 297–301.
[2] Damadian R. Tumor detection by nuclear magnetic resonance. *Science* 1971; **171**: 1151–3.
[3] Damadian R, Minkoff L, Goldsmith M, Stanford M, Koutcher J. Field focusing nuclear magnetic resonance (FONAR): visualization of a tumor in a live animal. *Science* 1976; **194**: 1430–2.
[4] Lauterbur PC. Image formation by induced local interactions: examples employing nuclear magnetic resonance. *Nature* 1973; **242**: 190–1.
[5] Edelstein WA, Hutchison JMS, Johnson G, Redpath T. Spin warp NMR imaging and applications to human whole-body imaging. *Phys Med Biol* 1980; **25**(4): 751–6.
[6] Haase A, Frahm J, Matthaei D, Hänicke W, Merboldt KD. FLASH imaging: rapid NMR imaging using low flip angle pulses. *J Magn Reson* 1986; **67**: 258–66.
[7] Dixon WT. Simple proton spectroscopic imaging. *Radiology* 1984; **153**: 189–94.
[8] Glover GH, Schneider E. Three-point Dixon technique for true water/fat decomposition with B0 inhomogeneity correction. *Magnet Reson Med* 1991; **18**: 371–83.

MR-Technology Information Portal: www.mr-tip.com

Chapter 2
High-field MRI in horses: practicalities and image acquisition

2A Practicalities and image acquisition

Rachel Murray

MRI SAFETY

Although magnetic resonance imaging (MRI) is an amazing diagnostic tool, there are potential hazards associated with its use, particularly where high-field MR systems are used [1]. Safety must always be paramount wherever an MR system is installed, and local rules must be put into place to ensure precautions are taken at all times [2]. Warning signs should be positioned in high visibility locations and a standard employee training programme should be implemented. It is important to remember that training should not only include staff who are involved in handling patients or acquiring scans, but also any maintenance, cleaning or other staff who may be required to enter the room. The MRI room must have restricted access and be entered through a lockable door, with warning signs (Figure 2.1). The 5 and 10 gauss lines should be clearly marked within the room, but it is essential that the 5 gauss isomagnetic contour is entirely contained within the controlled area. Hazards include ferromagnetic projectiles, radiofrequency waves, magnetic field gradients and use of cryogens in superconducting magnets.

The most common life-threatening hazard is that of ferromagnetic projectiles [3, 4]. Any ferromagnetic object that moves near to the magnet will be attracted strongly to the magnet at increasing speed as it gets closer to the magnet, and may then oscillate within the magnet bore. Metallic objects are therefore a potential hazard to a patient within the magnet or a member of staff between the metal object and the magnet. To avoid this, strict procedures and staff training must be put into place to avoid any ferromagnetic object entering the MRI room. Ferromagnetic objects include medical equipment such as gas cylinders, non-MRI-safe anaesthetic equipment, trolleys, scalpels, clippers, hobbles and head collars with metal fittings. Steel toecap boots are attracted to the magnet, which may cause issues for horse handlers, and if these are used too close to the imaging portion of the magnet they can cause artefacts resulting from magnetic field disruption. Personal effects that can be ferromagnetic include coins, jewellery, watches, hairpins, hearing aids, cameras, tape recorders, laptops and mobile phones. It must be routine for staff entering the MRI room to remove all personal effects as they can not only cause safety issues, but may also be damaged by close apposition

Equine MRI, edited by Rachel C. Murray.

Figure 2.1 Warning sign on a door to the MRI room.

to the magnetic field – having a credit card wiped does not usually go down well. Maintenance and cleaning equipment such as tape measures and mops or buckets should not be discounted as these can make rapid projectiles, particularly in the hands of untrained staff inadvertently entering the room. It is essential that no metallic object is allowed to enter the MRI room unless it has been confirmed to be non-magnetic using a hand magnet.

Magnetic material implanted into a patient can act as a hazard to the patient or have its function disrupted by the external magnetic field [4]. Even ferromagnetic objects that may not provide a mobile hazard, for example minute nail fragments in the hoof wall, can cause problems with creation of artefacts. Staff with pacemakers, vascular clips or other implants that have not been approved should not enter the MRI room, and those with metallic orthopaedic implants should be evaluated for the type of implant before they are allowed to enter. Although it is less likely that an equine patient would have such devices implanted, they should be ruled out prior to MRI examination.

There is a risk of burns to a patient as a result of the radiofrequency (RF) pulses required to generate the MRI signal, which are transferred through free space from the transmit RF coil to the patient. Burns can occur if conducting materials are placed within the RF field, resulting in a concentration of electrical currents that are sufficient to cause excessive heating and tissue damage [5, 6]. These effects may be seen at attachment of electrodes and in association with cables, despite apparent insulation, and are more likely where there are closed loops, so equipment should be minimized

as far as possible and loops and crossing of cables should be avoided [7]. For anaesthetic monitoring, it is recommended that only MRI-compatible electrocardiogram (ECG) leads and electrodes are used.

During MR procedures, gradient magnetic fields may stimulate nerves or muscles by inducing electrical fields in patients [8]. However, the risk of damage associated with this in most MRI systems used for clinical imaging of horses appears to be quite low. Acoustic noise results from changing currents within the gradient coils and is louder in higher field strength magnets. For staff remaining in the MRI room with a patient in a high field strength MRI system, it advisable to use earplugs or MRI-compatible headphones.

Superconducting magnets are cooled using liquid helium, so hazards including asphyxiation and cold burns can result from leakage of the cryogen or vent failure. Release of cryogen could inadvertently occur during servicing or happen accidently following impact from a ferromagnetic projectile, an explosion or fire, so staff should be aware of the risks in these circumstances. If there is sudden quenching of the magnet and the liquid helium boils off, then the oxygen is displaced from the air in the room and there is potential risk of asphyxiation to anyone in the room. There is value to having an oxygen sensor located within the MRI room, which sounds an alarm if the oxygen level drops below safe levels. As a sudden quenching increases pressure in the room, this may prevent opening of an inward-opening door, so if there are any concerns the door to the MRI room should not be closed. In the case of a system with a permanent or resistive magnet, cryogen hazards do not have to be addressed.

DESIGN OF THE MRI FACILITY AND MRI EQUIPMENT

When designing an MRI facility it is useful to position the induction/recovery room adjacent to the MRI room. However, this can present some issues as any doors and equipment that enters the MRI room controlled area must be MRI safe. Recovery box doors that open into a high-field MRI room have been made successfully using primarily wood and fibreglass, with MRI-safe stainless-steel mountings. If there is expected to be a high patient throughput for the MRI, then having both an induction and recovery room in the vicinity of the MRI room will avoid delays between patients.

For operation of the MRI system, the MRI room needs to have RF shielding, usually incorporated as a copper cage. This is continuous through the doorways, so the shielding is incorporated into the door, and is connected at the edges of the door with copper ‘fingers’ and a copper strip in the base. As these shielded doors must not be damaged, it is advisable for them to be separate from the recovery box door, which can withstand the forces of a horse falling during recovery and thus protect the shielding. As the shielding must not be damaged as the horse and table pass through the doorway, a smooth run over the base and plenty of room in the doorway for table, patient (including limbs) and staff is required.

The MRI room must be large enough to allow movement and turning of the table with the horse in both left and right lateral recumbency, and the floor must be smooth enough to keep clean and move the table easily.

Equipment that has to enter the room includes the table and that required for anaesthetic maintenance and monitoring (see section on general anaesthesia for MRI). Testing of metals for ferromagnetic properties is necessary prior to use in any equipment entering the MRI room. A table is required because the standard patient table provided with medical high- or low-field imaging units is of insufficient size and strength to support a horse. Various designs of tables have been used for equine MRI, including those made from wood, glass fibre composite with brass screws and MRI compatible stainless steel (e.g. Shanks MRI table). There is value in having this table capable of moving up and down, which can be done manually or using piped, compressed air, although this is generally not essential, depending on the MR system being used. For some high-field MRI systems, locking of the medical table to the magnet may be required to start scanning. In that case, disabling the MRI system table software or creating an artificial docking mechanism is required in order to start acquiring images, which can make initial setting up of the system a little more problematic but is usually possible to work with.

PATIENT SELECTION

It is generally possible to carry out MRI on the limbs and head of an equine patient provided that these areas of the horse can be positioned within the imaging portion of the magnet. Usually, the limitations are limb length, chest width and depth (for forelimbs, head and neck), quarters width (for hind limbs) and neck length (for head and neck). In general, the limbs up to and including the carpus and tarsus can be imaged with a short bore, high-field magnet with a sloping gantry or an open low-field magnet [9]. However, it is possible to image up to and including the stifle and cranial neck of selected horses using an ultra-short, wide bore MR system [10] and in some open, low-field MR systems [11].

Preparation of the patient

Prior to undertaking MRI, the patient history should be reviewed to confirm the absence of implants or other ferromagnetic devices. Shoes should be removed, ensuring that there is complete removal of all nails and nail fragments, particularly where imaging of the foot is to take place [12]. Prior to MRI of the foot, some clinics routinely use radiography to confirm removal of nail fragments. In my experience, this is not of high enough benefit to justify purely on the basis of checking for nail fragments, unless there is a known problem or suspicion of a fragment. In various horses where a nail fragment artefact was clearly present on MR imaging, no radioopacities could be detected. It can be useful to pare and smooth the foot to ensure removal of any debris, and scrubbing the foot is necessary. Where imaging is of a limb proximal to the foot, washing of the limb can be useful to remove any possible dirt that may lead to artefacts.

Prior to anaesthetic induction, a full pre-anaesthetic clinical examination should be performed. At our clinic, we routinely apply a silicone-based show shine preparation to the hair coat on the dependent side for anaesthesia to assist in smooth movement of the patient on the table during positioning.

The patient should be induced and positioned on the table outside the controlled MRI area. For imaging the head, either lateral or dorsal recumbency is possible and this may be determined by the suspected pathology. Provided positioning is done outside the controlled area, this can be achieved using a winch and hobbles to lift the horse onto a padded MRI-compatible table. Any clipping must be done prior to entering the MRI room, along with catheter placement or any procedure involving scalpel blades, needles or other potentially ferromagnetic objects. These must be detached and removed before entering the MRI room.

Once all ferromagnetic objects have been removed, and the patient is stabilized, the table can be moved manually into the MRI room and positioned with the patient close to the magnet. The area of interest can be moved into the magnet using ropes. Depending on the type of table and MR system set-up, this may be done by pulling the patient and mat into the magnet, pulling the patient onto another padded mat (Figure 2.2) or rotating

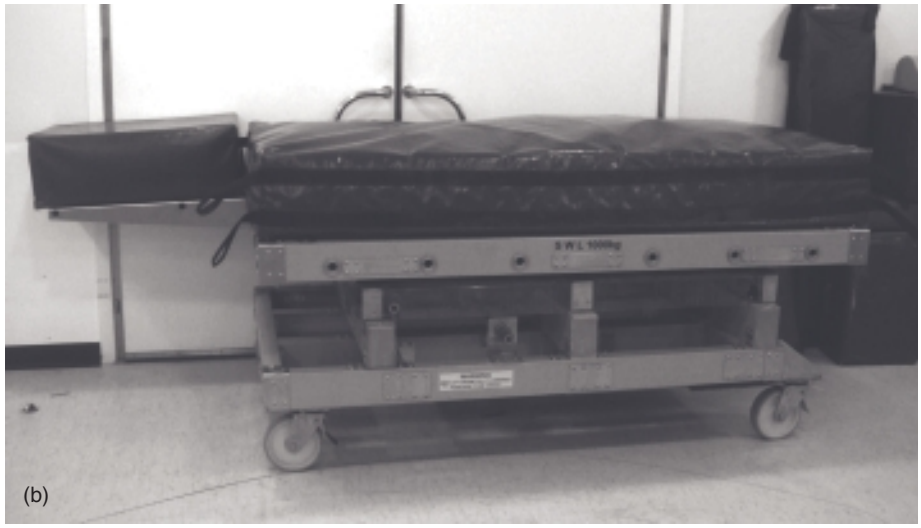

Figure 2.2 (a) A purpose built table constructed from glass fibre composite, brass screws and MRI-compatible stainless steel. This is covered by a thick plastic-covered foam pad with handles. (b) The table with an MRI-compatible stainless-steel head support attached. The pads behind the table are useful for padding limbs during the procedure. The table is positioned in front of radiofrequency shielded double doors through which the horse is pushed on the table.

the table into the magnet (Figure 2.3). For low-field open magnets, it is often easier to rotate the patient into the magnet, but this is not an option with a closed bore high-field magnet. It is important that the dependent eye is protected and lubricated during handling.

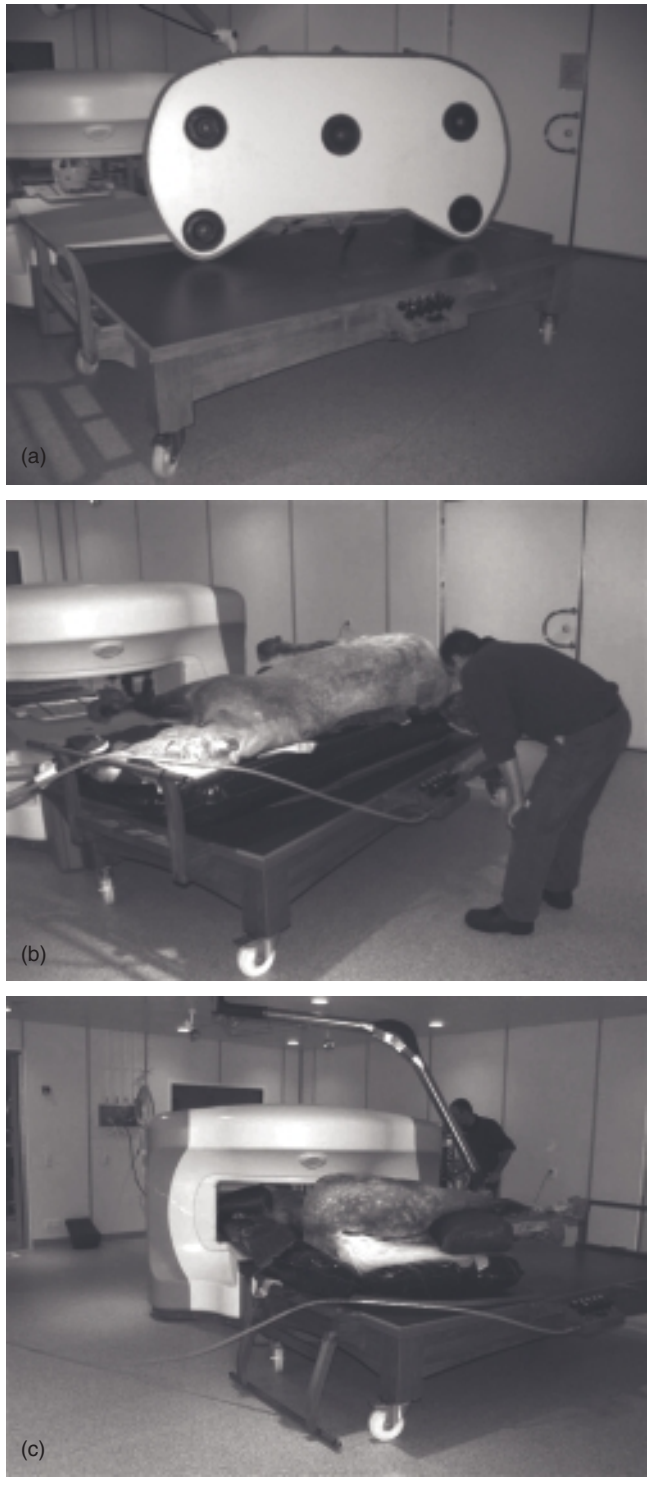

Figure 2.3 Use of a wooden table for MR imaging in Skara, Sweden. (a) A specially designed wooden MRI table with brass screws, stainless steel and plastic wheels. For ease of movement, there is a board with air cushions underneath, each of which can be adjusted individually. The board is made just big enough for the horse's torso so that the legs, head and most of the neck are as mobile as possible inside the magnet gantry. For this reason, the air mattress is also of the same size as the mobile board. (b) Positioning a horse adjacent to the magnet, ready for imaging of the limbs. (c) Rotation of the table top allows the head to be easily positioned into the magnet.

Positioning of the patient

Positioning in lateral recumbency with the limb of interest on the dependent side is recommended to minimize limb movement during scanning, i.e. for a horse with right forelimb lameness it is most appropriate to position the horse in right lateral recumbency, even if the left is being scanned as a comparison. However, for some systems and in the more proximal limb, it may be more practical for the upper limb to be positioned into the magnet isocentre or the stifle imaged in dorsal recumbency (Figure 2.4).

The area of interest must be positioned within the imaging portion of the magnet, ideally at the isocentre, where the magnetic field is most uniform. It is important to immobilize the limbs as far as possible to avoid movement artefact, but it is also important to ensure that positioning does not lead to risk of post-anaesthetic problems. Having a variety of shape, size and thickness of padded cushions is important. Sandbags are useful to weight the limbs and minimize limb movement related to respiration or cardiac function.

Radiofrequency coils should be selected on the basis of being as close as possible to the size of the area of interest, to maximize the MR signal received (Figure 2.5). However, for a high-field system in particular, there can be physical limitations on what can fit into the magnet bore. An extremity RF coil may be placed over a single distal limb being scanned, and then changed onto the contralateral limb between sequences. More proximally it may be necessary to include more than one limb in a larger or flexible RF coil in order to fit everything into the magnet bore. For the head or neck, it may be most suitable to use a body coil that is incorporated into the MR system housing.

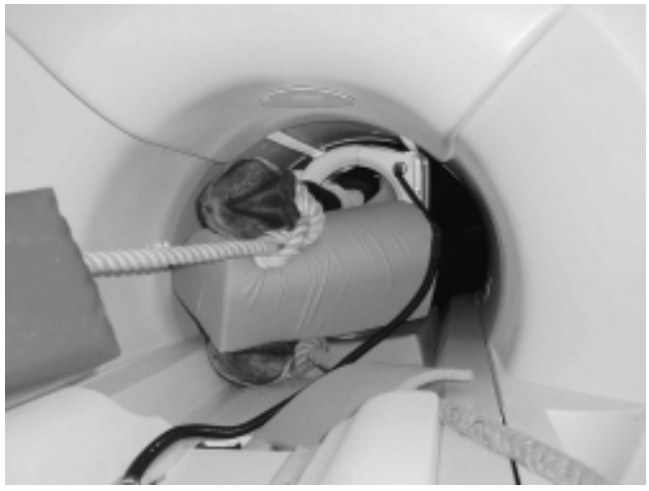

Figure 2.4 The metatarsal region positioned for scanning in the bore of a high field MR imaging system. There is little room for the two limbs and radiofrequency coil within the magnet bore. Note the ropes and padding that have been used to assist with positioning.

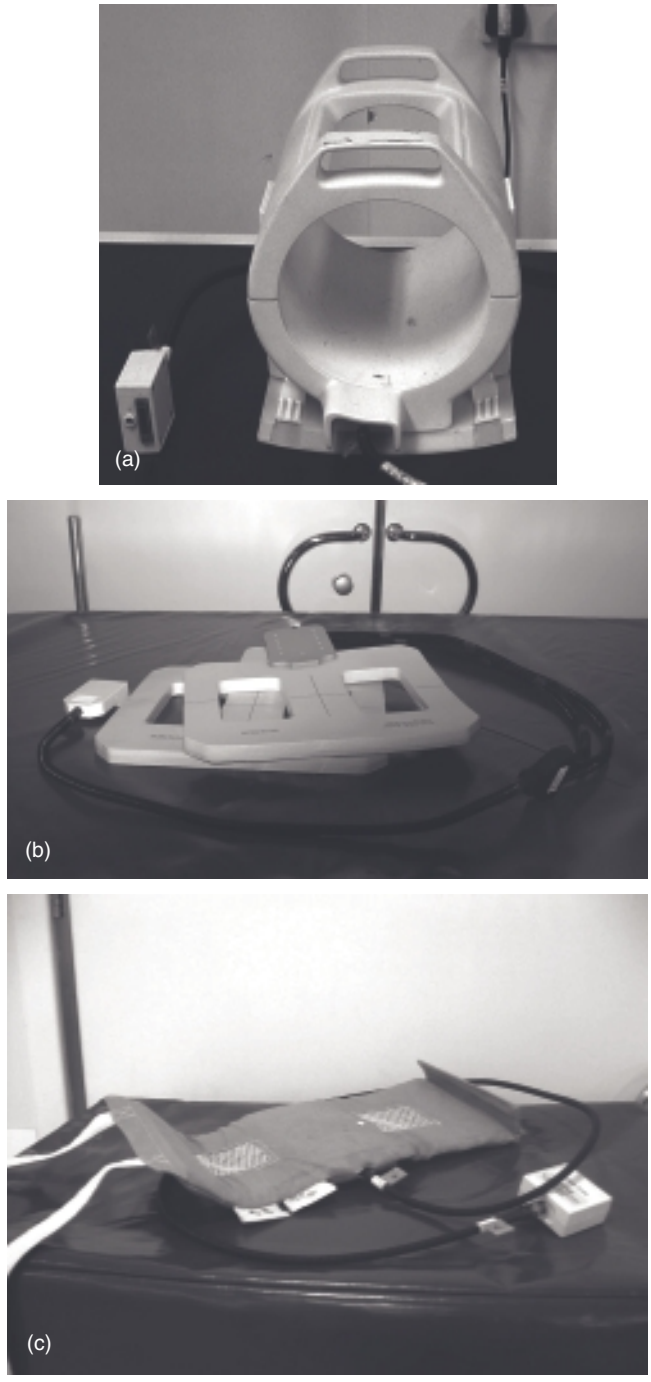

Figure 2.5 Examples of radiofrequency (RF) coils used in one high field imaging system to optimize signal from different areas of the patient. A body coil incorporated into the magnet bore can be used for larger areas such as the head or neck. (a) Quadrature extremity RF coil, which is suitable for the distal limb. (b) Torso phased-array RF coil, which may be useful for the more proximal limb. (c) Flexi RF coil ,which can be wrapped around areas of the limb.

IMAGE ACQUISITION

The scans acquired need to be good enough to enable a diagnosis to be made, so scan selection and quality are important, but this must be balanced against total scan time. For any horse, time under general anaesthesia needs to be minimized, so selection of scan sequences and planes that optimize diagnostic capability is essential. Scan sequences may either be chosen beforehand as a standard protocol for a particular region or type of problem,

or they may be selected during the scan dependent on the ongoing findings. In clinics where a radiographer or MR technician acquires the images, it is usually normal practice to have a standard protocol that is likely to detect most types of pathology in this region. An experienced technician should be able to detect reasons for extending beyond the current field of view or be aware of the need to request additional sequences. Where a radiologist is involved in image acquisition, images may be interpreted during acquisition. This will allow decisions about further scan planes and sequences to be made during the scan, and a standard protocol may be less necessary. This has particular advantages at earlier stages of scanning with a new unit, when scanning a less routine area or where there is limited knowledge about the type of problem. However, having standard sequence parameters saved for particular areas, RF coils and types of sequences is useful to minimize the time required for image acquisition.

The best sequences and imaging parameters to select are dependent on the MR system, and knowledge of your own system with respect to its strengths and limitations is essential. Optimizing imaging sequences prior to scanning live patients is important when a new system is installed, and worth reassessing after software upgrades or with respect to new RF coils or other equipment. Specific advice on optimizing image sequences for specific regions is covered within the relevant chapters. However, in general, scans should be acquired in at least three planes: sagittal, dorsal (frontal/coronal) and transverse (axial). There may also be value to acquiring images in additional planes positioned perpendicular to different points on a curved articular surface. A mixture of scan sequences including high and lower resolution, with low and high contrast, is likely to be beneficial. It may be necessary to focus on a particular area of suspected pathology and acquire additional high-resolution scans of this location. Including three-dimensional sequences into the protocol improves the ability to reformat images in different planes and can often be acquired in higher resolution than two-dimensional scans. It is important to include fat-suppressed images, particularly where bone is being assessed. Use of gradient-echo scans are of particular benefit where there may be suspicion of haemorrhage, so should be included in both orthopaedic and neurological assessments. Where possible a scan should include at least T1 weighted, T2 weighted and fat-suppressed (fat-saturated or short τ inversion recovery [STIR]) sequences, plus proton density in a variety of imaging planes.

Personnel

Required during scanning:

- anaesthesiologist/anaesthesia technician
- radiographer/MRI technician/radiologist
- technicians for moving the horse into and out of the MRI (number dependent on table and handling facilities).

For interpretation (either during scanning or after scan already acquired):

- MR radiologist or trained and experienced veterinary MRI interpreter.

Tips for image acquisition

For optimal image acquisition, the person acquiring images must have:

- training
- experience
- knowledge of equine anatomy for the region of interest
- an understanding of MRI physics in relation to image acquisition
- an understanding of MRI safety.

To set up image sequences:

- position the area of interest as close as possible to the isocentre of the magnet
- centre the field of view over the area of interest
- to save time, set up further scans while previous scans are running
- aim for as high resolution as possible within the constrictions of signal to noise ratio and imaging time
- use a variety of sequences, including T1- and T2-weighted scans
- include gradient echo to detect haemorrhage, and give fast, high-resolution scans
- use fast spin echo to increase contrast
- use long echo time (TE, generally T2 weighted) sequences to reduce magic angle effect
- include fat-suppressed sequences to avoid interference from fat signal.

To standardize image planes:

- ensure that the limb is positioned with joints as close as possible to a standard angle
- always align parallel to a specific structure, e.g. mid-flexor cortex of the navicular bone or dorsal cortex of the third metacarpal bone.

To avoid obliquity:

- position the limb or head/neck as straight as possible in the scanner. This may require padding at different levels
- set up sequences based on three image planes.
- compare specific anatomical markers between medial and lateral
- if a horse has a marked conformational angular abnormality, there may be value to acquiring transverse scans in more than one orientation, aligned with the areas proximal and distal to the angular change.

To avoid artefacts:

- to avoid magnetic susceptibility artefacts, clean and check the area for any magnetic debris prior to scanning, and recheck and clean if there is evidence of a problem
- to minimize problems with magnetic field inhomogeneities, position the area of interest as close as possible to the isocentre of the magnet and avoid touching the edges of the magnet
- minimize gross movement of the area of interest by padding and positioning, use of sandbags, correct level of anaesthesia and temporarily stopped intermittent positive pressure ventilation (IPPV) if necessary
- many artefacts are in the phase direction, so ensure that the frequency and phase directions are set up to prevent artefacts (including flow artefacts from large vessels) covering structures of particular interest. If there is a

concern, then the scan should be repeated with frequency and phase directions reversed

- to test for magic angle effects, alter the positioning of the limb relative to the static magnetic field
- to minimize magic angle effects, use a long TE sequence.

REFERENCES

[1] McRobbie DW, Moore EA, Graves MJ, Prince MR. *MRI: from picture to proton*. Cambridge: Cambridge University Press, 2003.
[2] Kanal E, Barkovich AJ, Bell C *et al*. ACR Blue Ribbon Panel on MR Safety. ACR guidance document for safe MR practices: 2007. *Am J Roentgenol* 2007; **188**(6):1447–74
[3] Chaljub G, Kramer LA, Johnson RF III, Johnson RF Jr, Singh H, Crow WN. Projectile cylinder accidents resulting from the presence of ferromagnetic nitrous oxide or oxygen tanks in the MR suite. *Am J Roentgenol* 2001; **177**: 27–30.
[4] Shellock FG. *Reference Manual For Magnetic Resonance Safety, Implants, and Devices*. Los Angeles, CA: Biomedical Research Publishing Group, 2006.
[5] Dempsey MF, Condon B. Thermal injuries associated with MRI. *Clin Radiol* 2001; **56**: 457–65.
[6] Dempsey MF, Condon B, Hadley DM. Investigation of the factors responsible for burns during MRI. *Journal Magnetic Resonance Imaging* 2001; **13**: 627–31
[7] Shellock FG. Radiofrequency-induced heating during MR procedures: a review. *J Magn Reson Imaging* 2000; **12**: 30–6.
[8] Schaefer DJ, Bourland JD, Nyenhuis JA. Review of patient safety in time-varying gradient fields. *J Magn Reson Imaging* 2000; **12**: 20–9.
[9] Murray RC, Mair TS. The use of magnetic resonance imaging in lameness diagnosis in the horse. *In Practice* 2005; **27**: 138–46
[10] Judy C, Saveraid T, Rick M, Herthel D. Magnetic resonance imaging of the equine stifle in a clinical setting. *Proceedings, American College of Veterinary Surgeons Surgical Summit*, Chicago, IL, 2007.
[11] Dyson S, Murray R, Schramme M *et al*. Magnetic resonance imaging of the equine foot: 15 horses. *Equine Vet J* 2003; **35**: 18–26.
[12] Judy C. MRI of the equine stifle. *Proceedings 5th European Veterinary MRI-User Meeting*, 2009.

2B General anaesthesia for MRI

Elizabeth Leece

INTRODUCTION

The continuous strong magnetic field in a magnetic resonance imaging (MRI) unit presents unique problems for the anaesthetist. Coupled with the problems associated with equine anaesthesia and limited access to the patient, anaesthesia for equine MRI can be extremely challenging. The physical effort involved in positioning the equine patient for scanning requires fully trained personnel.

Equine anaesthesia in the MRI environment presents further problems for the anaesthetist. However, for some conditions this technique is preferable to standing MRI. It can be less time-consuming and produce better image quality, but it involves greater expense and manpower. General anaesthesia for healthy, surgical horses presents a 0.63–0.9% risk of mortality. One study reported a mortality rate of 0.6% in 350 horses undergoing MRI under general anaesthesia, suggesting the risk was similar between MRI and surgery [1]. The two deaths in that study were attributed to post-anaesthetic myopathy/neuropathy syndrome (PAMNS). However, in the institution reporting this previous study, the anaesthetic problems were encountered within the first 6 months of MR imaging, and no further anaesthetic-related mortality has occurred in 400+ cases following on from the original study of 350 horses. This suggests that although MRI-associated anaesthetic problems should be considered when recommending MRI, the level of risk is likely to be reduced as institutions become more experienced with the practicalities of general anaesthesia for MRI.

THE MRI ENVIRONMENT AND ANAESTHESIA

- The type of scanner used often dictates many of the problems associated with anaesthesia for MRI. Low-field magnets present less ferromagnetic potential, making the use of standard monitoring equipment possible. Also positioning and access to the patient is more straightforward. Much of this chapter will consider equine anaesthesia for high-field MR scanners (1.5 Tesla and above)

Equine MRI, edited by Rachel C. Murray. © 2011 by Blackwell Publishing Ltd.

- The strong ferromagnetic field means that any metal objects should be removed from the horse. Nails from shoes can cause signal drop-out and interfere with signal quality.
- Hobbles or other metal equipment used, such as mouth gags, should always be removed before entering the MRI room.
- Due to the ferromagnetic field, specialized non-ferrous anaesthetic machines should be used. If normal machines are used then they must be secured outside the 5 Gauss line and long breathing hoses used. These machines represent an enormous potential for projectile damage. Only aluminium medical gas cylinders should be used within the scanning room and ideally piped gases should be installed when the MRI unit is built.
- Monitoring equipment can be positioned outside the scanning room and tubing adapted, but it is preferable to use MRI-compatible equipment.
- All personnel should be fully trained for working in the MRI environment. Any loose ferromagnetic items should be removed from pockets. The steps involved in positioning the patient should be rehearsed to allow a rapid preparation time. Procedures to be followed in an emergency (anaesthetic problems, movement of the patient, event of fire) should also be in place.
- Duration of scanning should be kept to a minimum and repetition of scans avoided. Anaesthetic time for MRI was reported to be approximately 110 minutes in one study [1], which is greater than the 90-minute period that has been found to be associated with a ninefold increase in the risk of myopathy. Careful positioning and preventing movement artefact is important from the outset.
- To obtain the best image quality, movement should be avoided. Due to the vicinity of expensive equipment, depth of anaesthesia should be kept as stable as possible. However, accessibility to the patient may be limited. Extension sets from the jugular intravenous catheter should be used for emergency drug administration or a hind limb catheter placed when scanning the head. Access for monitoring depth of anaesthesia is limited during head scans.
- The use of the intravenous contrast agent gadolinium has not been associated with problems in horses, but reactions in dogs and humans have been reported and careful monitoring should be undertaken following its administration.

ANAESTHETIC EQUIPMENT

The table must be custom made in non-ferrous material and have sufficient padding (foam or air mattress) to minimize pressure on muscle compartments. The table should be at the correct height to 'dock' with the magnet. A foam mattress with handles can be used to allow the patient to be moved on the mattress itself once in the scanning room (Figure 2.2). To move the patient more easily separate from the mattress it can be useful to use show shine silicon-based liquid or spray.

Non-ferrous anaesthetic machines can easily be custom made. The small amount of ferrous material present in modern vaporizers does not present

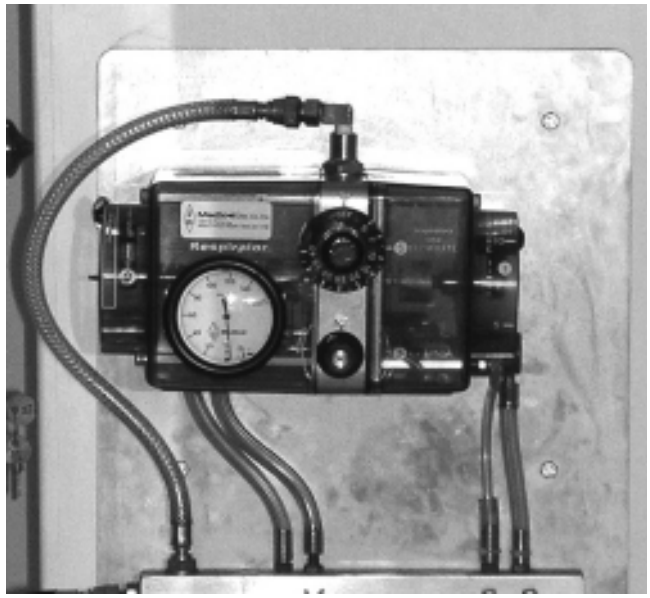

Figure 2.6 Any ferromagnetic equipment that must be in the scanner room, such as a Bird ventilator, should be placed outside the 5 Gauss line and ideally secured to a wall.

a problem, but the machine should be kept at a distance from the bore and vaporizers should be filled outside the scanning room. Intermittent positive pressure ventilation (IPPV) can be performed either manually or by using a bag-in-bottle technique. Bird ventilators can be used outside the 5 Gauss line and used to drive the bellows on the anaesthetic machine; however, they should be secured to the wall for safety (Figure 2.6). Oxygen cylinders in the scanning room should only be made of aluminium. Projectile accidents have resulted from normal medical gas cylinders being taken into the scanning room and could result in serious damage to personnel, the patient or the MR scanner itself.

MONITORING EQUIPMENT

If horses are to be anaesthetized for MRI then the same standard of monitoring used in the surgical suite should be employed. Some equipment can be modified to suit the MRI environment. Monitors may be positioned outside the Faraday cage and non-electrical conducting tubing passed from the patient through the waveguide. This is a hollow tube, typically 25–50 mm in diameter, made of brass that forms a conduit through the RF shielded wall. However, MRI-compatible equipment should be used if possible. Despite high capital costs and service contracts, it is beneficial to have reliable monitoring for such challenging procedures if the caseload is high. A number of companies now produce MRI-compatible monitoring systems. It is important to avoid any coiling of cables within the magnet as this can set up a conductive coil resulting in overheating and potential burns. Cables should not be placed directly against the patient due to the potential for burns and should be separated by insulation or padding.

Equipment may be either MRI safe or MRI compatible. MRI safe implies that there is no safety hazard to patients or personnel if taken into the scanning room. However, there is no guarantee of correct function of the equipment or lack of interference with the imaging equipment and so image degradation may result. MRI-compatible equipment is MRI safe and functions normally while not interfering with MR imaging if instructions are followed. This is primarily due to radiofrequency (RF) shielding. If this shielding is degraded the equipment may interfere with image quality. Standard intravenous fluid bags should not be hung over the telemetry monitoring units as any leaks from the bag or giving set could result in damage to the shielding over time.

Any monitoring equipment located within the scanning room should be positioned in such a way that it cannot be inadvertently damaged when the table and horse are being manoeuvred into the room and scanner. During the scan it is advisable that the equipment is kept as far as possible from the scanner and not in direct line with the coil. Remote monitoring allows the anaesthetist to monitor the patient from the control room. However, apparent depth of anaesthesia can change once image acquisition starts, probably due to the increase in noise associated with gradient manoeuvres, and so some anaesthetists may prefer to stay in the scanning room with the patient. Headphones or earplugs should be available for acoustic protection and a clear signal to stop imaging should be known in case of an emergency. MRI-compatible equipment usually consists of a telemetry unit which transmits through to the monitoring display box in the control room (Figures 2.7 and 2.8).

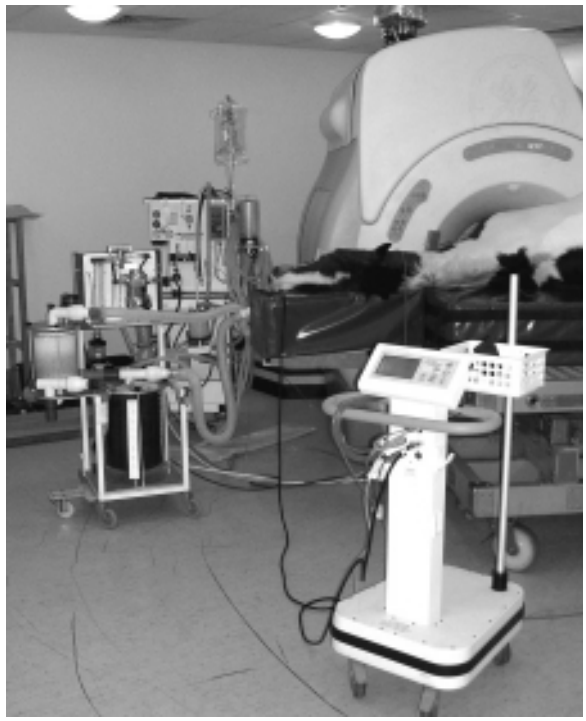

Figure 2.7 Telemetry unit of MRI compatible monitoring equipment. Note that it is not advisable to 'hang' fluids over such equipment as the sheer forces can damage the RF shielding, as can intravenous fluids if they leak.

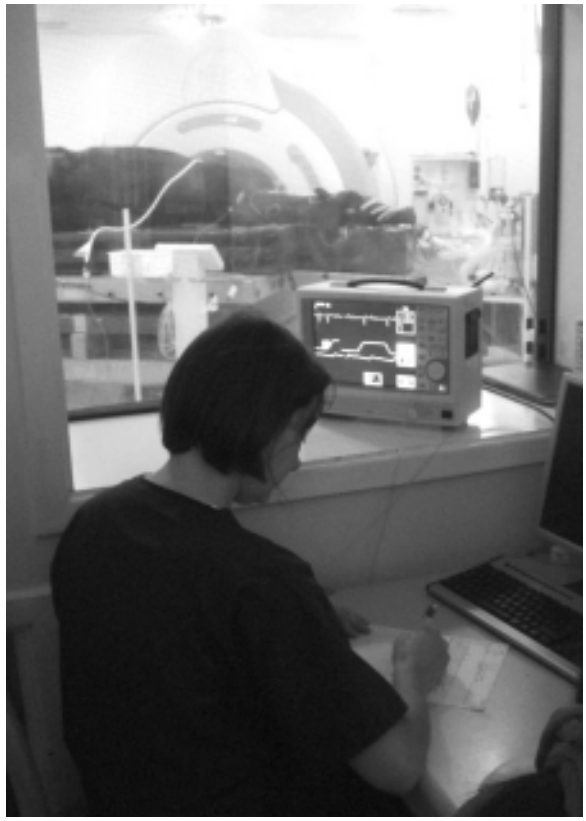

Figure 2.8 Remote monitoring of anaesthesia from the control room.

Anaesthetists monitoring from the control room should have an unobstructed view of the patient and anaesthetic machine, since audible alarms within the scanner room are useless. Equipment should not be moved once image acquisition has started.

The magnetic field generated by the magnet decreases in strength with distance from the bore. Generally, ferromagnetic materials can be positioned outside the 5 Gauss line. This area will differ for different strength magnets and with different shielding. It is vital that equipment outside this line should be secured to prevent it crossing into the magnetic field.

Monitoring equipment may be blamed for poor image quality, but if guidelines are followed correctly this is rarely the case. Interference from monitoring equipment gives a typical distortion at the edges of the image. To rule out problems, test scans should be taken with and without the monitoring equipment.

The various aspects of anaesthetic monitoring are discussed below.

Depth of anaesthesia

Depth of anaesthesia may be difficult to assess during head scans due to inaccessibility. Cranial nerve reflexes can only be assessed intermittently and the anaesthetist is much more dependent on other parameters such as arterial blood pressure.

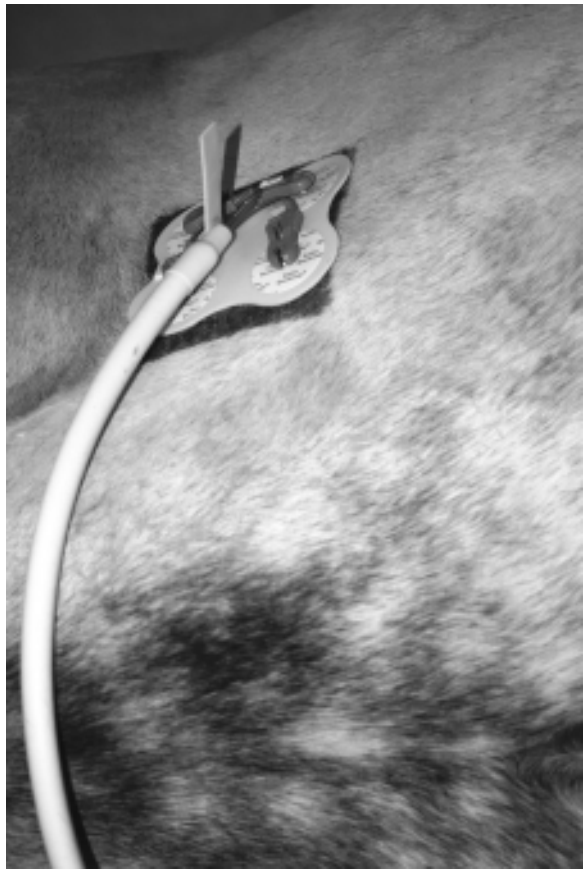

Figure 2.9 MRI-compatible electrocardiograph pad positioned on the thorax. Note the insulated cable in contact with the patient.

Electrocardiogram

Standard electrocardiogram (ECG) monitors can cause distortion of the images due to the wires acting as antennae. Voltage induced in the wires may also result in burns and so MRI-compatible ECG leads are preferable. These are insulated where they cross the patient's thorax (Figure 2.9). A small area of hair needs to be clipped prior to entering the scanning room. The electrodes are placed close together to minimize electrical artefacts; however, RF pulses can still interfere with the ECG signal, particularly in STIR (short τ inversion recovery) and FLAIR (fluid attenuated inversion recovery) sequences.

Blood pressure monitoring

Monitoring of blood pressure is vital, as in many cases it appears to be a sensitive monitor of depth of anaesthesia during MRI scanning, and hypotension should be avoided where post-anaesthetic myopathy/neuropathy syndrome is likely. The oscillometric technique can be used with a tail cuff, although this method is unreliable. If necessary, the oscillometric tubing can be passed through the waveguide and linked to a monitor outside the scanning room. Invasive blood pressure monitoring is advisable and there are several non-ferrous transducers available. The length of saline column should not exceed 1.5 m to limit damping effect on the blood pressure trace

and MRI-compatible transducers are readily available. Some scans (gradient echo) can interfere with the blood pressure trace and also the readings given and so attention must be paid to the timings of these scans.

Capnography

Sidestream capnography can be a useful tool during MRI, although due to the length of sampling tubing required there is a long lag time (usually at least a 20 s delay). It is important to position the sampling line in a non-dependent position to avoid water contamination of the tubing, as over time this can damage the capnograph pump. Unfortunately, in horses, the end tidal concentration may not be an accurate indication of arterial carbon dioxide partial pressure.

Pulse oximetry

Fibre-optic or non-ferromagnetic cabled pulse oximeters are recommended, although the sensors are rarely suitable for use on the equine tongue. Burns are still possible and care must be taken, particularly if scanning the head, to avoid coiling of the cable. Arterial blood gas sampling can be performed to help indicate adequate oxygen content. Once again the inversion recovery sequences can interfere with the pulse oximeter trace displayed.

Respiratory gas monitoring

Anaesthetic gas monitoring and inspired oxygen concentration can often be monitored in conjunction with the capnograph from the sidestream sampling line and can be useful for detecting breathing system or vaporizer problems.

ANAESTHETIC TECHNIQUE

Planning is possibly the most important factor for the anaesthetist when performing equine anaesthesia for MRI. Each person should have a designated role in positioning or preparing the patient so that the transfer of the patient from induction to the scanning room is rapid, and positioning of the patient allows for image acquisition without repeating scans. Great care should be taken when positioning both the limbs to be imaged and those outside the scanner, since there is a risk of PAMNS. Hypotension should also be managed. An adequate plane of anaesthesia is imperative to avoid movement of the patient within the confines of the coil. Movement artefact may also result from minor movement associated with breathing or even when the heart beats. Adequate padding to minimize such movement is particularly important when scanning the non-dependent limb. For this reason the horse should be positioned with the limb to be investigated dependent where this is possible.

The usual anaesthetic care should be taken, but the following steps may be particularly important during MRI.

Patient preparation

Care must be taken to remove shoes and nails and to thoroughly clean the hooves before scanning takes place. The jugular catheter should be placed in the uppermost jugular vein and an extension set is extremely useful during the procedure. If the forelimbs are to be scanned then it is useful not to place the catheter too low. For imaging of the head, another catheter can be placed in the femoral vein to allow intravenous access.

Following induction of anaesthesia, prior to entering the MRI room, hair should be clipped from sites required for arterial catheterization, additional venous catheters and the ECG pad. Any ferrous mouth gags used during intubation should be removed, as should metal hobbles used to hoist the horse onto the table. Catheters can be placed in the scanner room as long as needles, stylets and scalpel blades are not allowed near the scanner. Placing catheters within the scanner room will reduce anaesthetic time, but equipment must only be moved by the anaesthetist.

Positioning

Careful positioning of the patient within the scanner is important to allow imaging of the area required without having to waste time repeating scans. Each member of the team should have a set role during positioning. Well-muscled or heavier horses may be at more risk of developing PAMNS and adequate padding and positioning is imperative. The area within the magnet bore should also be padded (Figure 2.10). Padding should be used for any

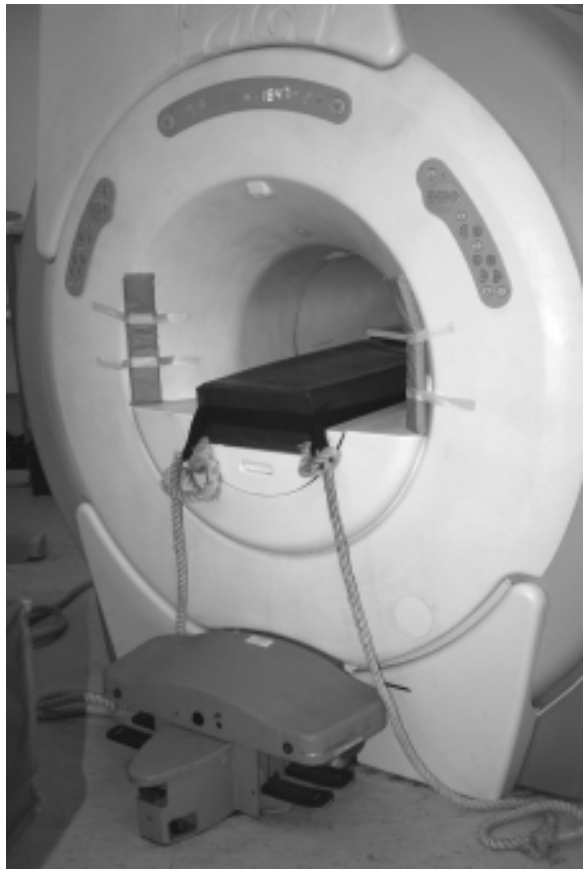

Figure 2.10 The magnet bore should contain padding and any areas of contact with horse should also be padded around the bore.

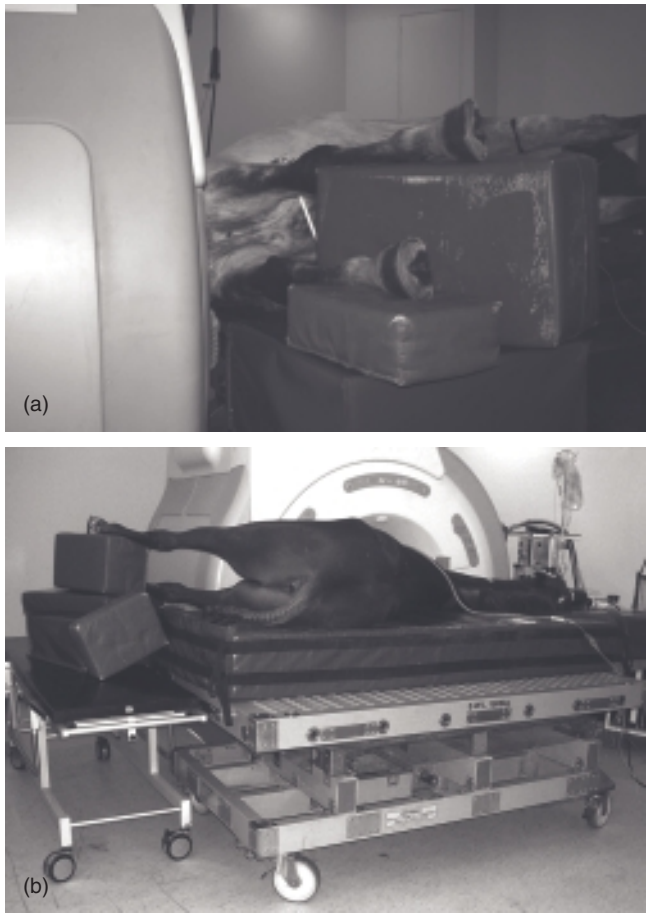

Figure 2.11 (a) and (b) As with any horse under general anaesthesia, limbs that are not being scanned need to be carefully positioned and padded.

areas of the patient in contact with the scanner. The limbs being scanned cannot be positioned as normal but every care should be taken to improve their position within the magnet bore, particularly when the hind limbs are scanned. Interestingly, PAMNS following MRI is more common in the limbs not being scanned. It is important to pay attention to positioning these limbs, which may be done using non-ferrous attachments for the table or cushions to raise the upper limb adequately (Figure 2.11).

When scanning the head the eyes should be protected and if a head collar or halter is used, this should not have any pressure points or metallic attachments.

Movement artefact

This can be minimized by putting sandbag weights over the limbs and placing padding around them. Movement artefact can result from respiratory motion, and scan quality for certain scans may be improved by limiting this movement. In one centre, IPPV is imposed throughout the imaging and the ventilator stopped for certain scans, such as the T2-weighted scans, for

a matter of minutes to allow image acquisition without respiratory movement artefact. IPPV may be used to allow better control of depth of anaesthesia while scanning.

SPECIFIC ANAESTHETIC CONSIDERATIONS

Anaesthesia for horses with intracranial disease

MR imaging of the head may be necessary for horses with a history of seizures, neurological signs or head trauma. Exophthalmus may result from retrobulbar masses that may extend intracranially. It is important to perform a full neurological assessment on these patients to localize lesions. Full blood work to rule out other causes of neurological problems should be performed.

Acepromazine has been suggested to lower the seizure threshold, but this is unsubstantiated and the drug has been used in small animals with no increased incidence in seizure activity. It may be advisable to avoid ketamine in seizure patients if an alternative is available. Lowering of the head following sedation may cause an increase in intracranial pressure. In patients with suspected intracranial disease, either isoflurane or sevoflurane may be used. There is some suggestion that sevoflurane is the better agent in human medicine for such cases and it may be helpful for recovery. IPPV should be employed, but moderate hypocapnia ($PaCO_2 < 28$ mmHg) should be avoided as this can result in cerebral vasoconstriction and possible ischaemia to compromised brain tissue.

Patients can be positioned in lateral or dorsal recumbency. Intravenous access should be secured. A hind-limb catheter allows easier access than a jugular catheter when the patient is positioned in lateral recumbency. Depth of anaesthesia may be difficult to monitor due to limited access to the head (Figure 2.12), and the anaesthetist must be very close to the bore to establish

Figure 2.12 Access to the head is limited when this area is scanned and other monitors of depth of anaesthesia can be helpful, such as anal tone.

the palpebral response. Using anal tone is a useful substitute for cranial nerve reflexes in this situation. Breathing system hosing should be long to allow for positioning through the magnet bore, depending on the layout of the room.

Resuscitation

Resuscitation is extremely difficult within the scanner room. The patient will need to be removed from the scanner and ideally moved back to the induction/recovery area. If there are problems during anaesthesia the scan should be cut short.

PLANNING AN EQUINE MRI FACILITY

Involving the anaesthetist during the early planning stages of an MRI facility is necessary to minimize problems. It is important to plan the location to fit in with the current hospital set-up and to avoid having to transport animals. The induction area should be adjacent to the scanning room if possible, to minimize transport time. There should be easy access to this room to allow clipping and further diagnostics, such as CSF sampling, to be performed.

The scanning room itself should be large enough to house all of the equipment when not in use and also to allow the table to be turned as necessary during positioning. The control room should be positioned so that the anaesthetist can have a clear view of the patient in the coil and the anaesthetic machine. There should be immediate access to the scanning room.

Piped gases should be installed as well as active scavenging. A waveguide should be built into the Faraday cage to allow sampling lines to be passed through.

Provision for the capital costs and ongoing maintenance of MRI-compatible anaesthetic machine and monitoring equipment should be made from the outset.

REFERENCE

[1] Franci P, Leece EA, Brearley JC. Post anaesthetic myopathy/neuropathy in horses undergoing magnetic resonance imaging compared to horses undergoing surgery. *Equine Vet J* 2006; **38**(6): 497–501.

FURTHER READING

Provision of Anaesthetic Services in Magnetic Resonance Units. The Association of Anaesthetists of Great Britain and Ireland, 2002. www.aagbi.org/publications/guidelines/docs/mri02.pdf

2C Contrast agents in equine MRI

Carter Judy

INTRODUCTION

Approximately 30% of magnetic resonance imaging (MRI) scans in human patients are performed with the addition of an intravenously administered contrast agent [1], and their use is well established in humans. The first approved contrast agent for use in human MRI examinations was gadopentetate dimeglumine (Magnevist, Bayer Health Care Pharmaceuticals Inc, Wayne, NJ), which was approved in 1988. This first generation of contrast agents are considered extracellular fluid agents. Subsequently, a wide variety of contrast agents has been developed to target specific tissues, be administered via different routes and even provide contrast enhancement at the molecular level.

The goal of this chapter is to focus on those agents that have been used in the horse and provide insight into how contrast agents can be used to better understand the pathological processes occurring in these patients.

MAGNETIC AND BIOLOGICAL PROPERTIES OF CONTRAST AGENTS

It is useful to classify MRI contrast agents into two broad groups based on whether the contrast agent increases the transverse relaxation rate (1/T2) by roughly the same amount that it increases the longitudinal relaxation rate (1/T1) or whether the transverse relaxation rate is altered to a much greater extent. Those that act in the first category are considered T1 agents. These agents alter the 1/T1 of tissue more than the 1/T2 due to the fast transverse relaxation rate of tissue. This lowering of T1 gives rise to increases in signal intensity on most pulse sequences and hence they are considered positive contrast agents. The T2 agents largely increase 1/T2 and cause a reduction in signal intensity and are considered negative contrast agents.

Gadolinium-based contrast agents such as gadopentetate dimeglumine (Magnevist) are considered examples of T1 agents. Ferromagnetic iron oxide particles are an example of a T2 agent. Generally, gadolinium-based agents increase signal intensity as a function of contrast dose until it is present in such a high concentration that the T2 effects begin to decrease the signal intensity. Iron oxide particles have some effect on T1, but the T2

Equine MRI, edited by Rachel C. Murray. © 2011 by Blackwell Publishing Ltd.

Table 2.1 Gadolinium-based contrast agents approved for use in humans for MRI examination in the United States

Generic name	Product name	Chemical abbreviation
Gadopentetate	Magnevist	Gd-DTPA
Gadoterate	Dotarem	Gd-DOTA
Gadodiamide	Omniscan	GD-DTPA-BMA
Gadoteridol	Prohance	GD-HPD03A
Gadobutrol	Gadovist	GD-Do3A-Butrol
Gadoversetamide	Optimark	Gd-DTPA-BMEA
Gadobenate	Multihance	Gdd-BOPTA
Gadoxetic acid disodium	Primovist	Gd-EOB-DTPA

effect is much greater and these agents cause signal loss at all concentrations. An excellent example in the horse of this T2 effect is that of shoe nail fragments or debris from nails from horse shoes within the nail tracts and the void of signal that results. The remainder of this chapter will focus on the use of agents that are predominantly T1 agents, since T2 agents have not been utilized extensively to this author's knowledge.

There are currently six approved gadolinium-based contrast agents available for use in humans (Table 2.1). All contain gadolinium, an 8-coordinate ligand binding to gadolinium and a single water molecule coordination site to the gadolinium. The ligand provides thermodynamic stability and makes the heavy metal (gadolinium) inert, preventing metal loss and thereby allowing for the agent to be excreted safely from the body. The water molecule and gadolinium are the components that provide the contrast effects in tissue. In humans, all of the available agents have nearly identical signal effects on tissue, plasma half-life and bio-distribution. The half-life and bio-distribution in the horse is unknown. A limited pilot study performed in the horse (Judy CE, Saveraid TC, unpublished observations) identified that a steady state of contrast distribution within the foot of gadopentetate dimeglumine (Magnevist) occurred 60s after intravenous administration in the jugular vein of adult horses and continued past the termination of the evaluation at 15 minutes (Figure 2.13).

The safety record of the four longest-used agents in humans is exceptionally good (gadopentetate dimeglumine, gadodiamide, gadoteridol and gadoterate meglumine). In humans, the most common side effects are nausea (1–2% of patients) and urticaria (1%). Almost all adverse events with these agents are reported to be transient and mild. There are reports of serious adverse reactions in humans, including anaphylactoid reactions and death for these agents. The estimate of the rate of these events is between 1 in 200,000 and 1 in 400,000 [1] in humans. In the horse, administration of contrast agents has been much more limited. In the author's practice more than 500 horses have been administered gadopentetate dimeglumine (Magnevist) intravenously and no adverse effects have been observed to date (summer 2009).

Gadopentetate dimeglumine (Magnevist) has been the most extensively used agent in the horse. It is considered an extracellular fluid agent, as are the agents in Table 2.1. The major use in humans of these non-specific agents

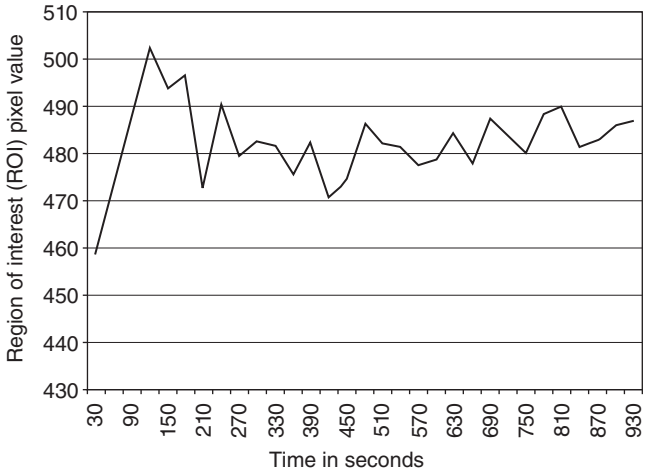

Figure 2.13 Signal intensity over time of the medial palmar digital artery and vein at the level of the navicular bone after injection of 25 ml (0.05 ml/kg) gadopentetate dimeglumine (Magnevist) intravenously in the jugular vein of a horse. Repeat T1 VIBE FS sequences were acquired at 30s intervals for the duration of the evaluation. Notice the rapid rise in signal intensity followed by a steady state that continues beyond the 15-minute study window.

is the detection of capillary breakdown or enhancement of tissues with increased extracellular volume. Tissues that have a larger fraction of extracellular volume will give an increased signal change post contrast because there is more contrast agent within the given voxel. This results in a brighter image after contrast administration in damaged or diseased tissues. This localization of contrast within diseased or pathologic tissue increases the signal to noise ratio such that subtle lesions may be more accurately detected.

The recommended dose for gadopentetate dimeglumine (Magnevist) in humans and small animals is 0.20 ml/kg (1ml per 10lb of body weight) intravenously. This would equate to approximately 100ml in a 500 kg horse. At a current (summer 2009) wholesale cost of US$450/100 ml, this makes the use of contrast agents fairly expensive. An unpublished study (Judy CE *et al*. Development of an effective dosage of gadopentetate dimeglumine for contrast enhanced equine orthopedic magnetic resonance imaging [in preparation]) determined that the most effective dose of contrast agent that provided good contrast enhancement of the tissues was a dose of 0.10 ml/kg of gadopentetate dimeglumine (Magnevist). This equates to 50 ml of contrast intravenously for an average 500 kg horse. A separate study advocated the use of a single 20 cc (0.02 mmol/kg) dose of gadolinium-diethylentriaminepentaacetic acid (Omniscan, Nycomed Inc, Pinceton, NJ) per adult horse and 0.1 mmol/kg for foals, to evaluate neurological diseases in the brain of horse [2]. This dose was empirically chosen by the authors due to the fact that a single vial of gadopentetate dimeglumine (Magnevist) was provided in a single-use 20 cc vial (Saveraid TC, personal communication). It is the author's perspective that contrast enhancement increases significantly at increasing dosages (Figures 2.14 and 2.15).

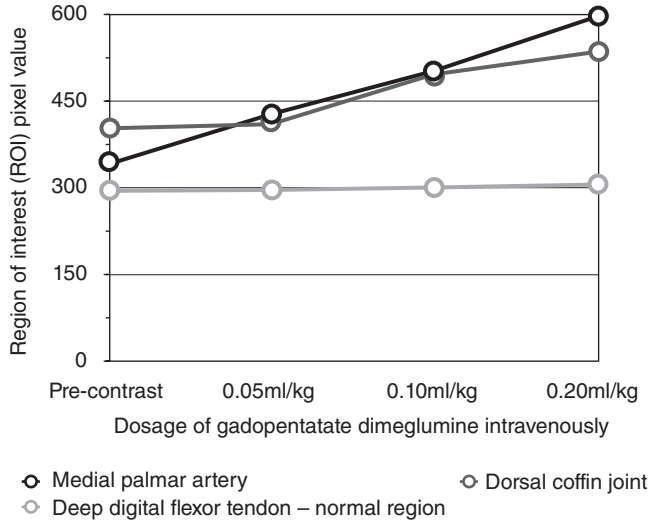

Figure 2.14 This graph depicts the relative contrast enhancement of the identified normal regions based on a variable dosage of the intravenously administered contrast agent. These data are derived from the average Region Of Interest (ROI) of 25 horses administered additive doses of the contrast agent. Notice the linear increase in contrast enhancement of the digital palmar artery and dorsal aspect of the coffin joint with increasing contrast dosage. This is to be expected in vascular tissues such as the synovium or digital artery. Notice the lack of enhancement of the deep digital flexor tendon. This is to be expected in a relatively avascular region of tissue and the relative lack of permeability in undamaged tendon. Source: Judy CE *et al*. Development of an effective dosage of gadopentetate dimeglumine for contrast enhanced equine orthopedic magnetic resonance imaging (in preparation).

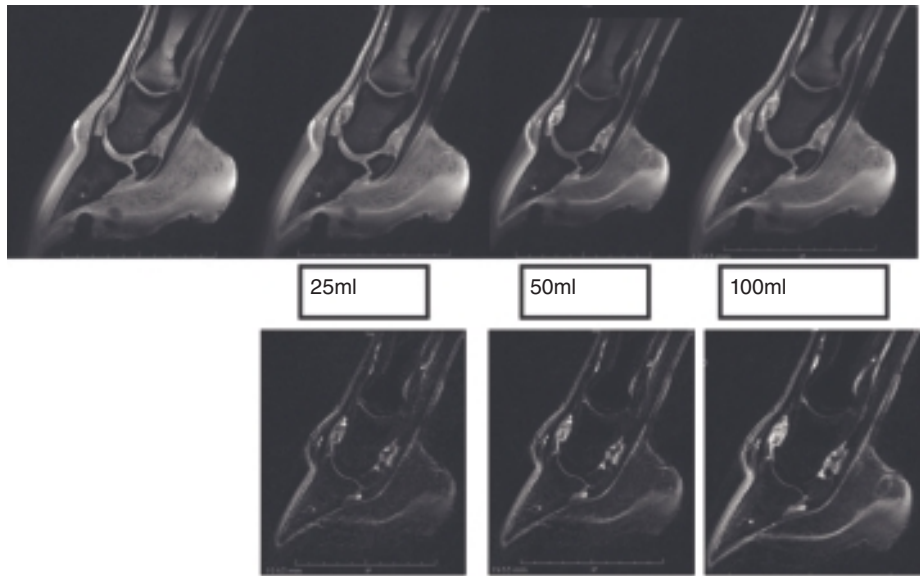

Figure 2.15 T1 VIBE FS mid-sagittal images of a normal foot showing the effects of various dosages of gadopentetate dimeglumine (Magnevist) intravenously. Top row (left to right): no contrast (pre-contrast image); post 25 ml (0.05 ml/kg) intravenous contrast; post 50 ml (0.10 ml/kg) contrast; post 100 ml (0.20 ml/kg). Bottom row: digital subtractions of the pre- and post-contrast images at their respective dosages. Note the increase in signal intensity as the dosage increases.

Intrasynovial contrast agents have been used in humans to detect subtle changes in articular cartilage defects, bursal abnormalities and tendon sheath issues. Both positive and negative contrast agents have been used, but one of the most popular techniques is the use of saline within the joint to increase distention and provide separation between distinct tissues, allowing for better visualization of adjacent structures. While the use of T1 and T2 contrast agents inside synovial structures of the horse has not been explored currently, the use of saline as a positive contrast agent within the navicular bursa to detect the presence or absence of adhesions between the deep digital flexor tendon and the navicular bone and bursa has been reported [3]. The report states that this technique allowed for better determination of the presence or absence of the bursa and surrounding structures and was dependent on the severity of the abnormalities detected [3].

CONTRAST USE IN CLINICAL EQUINE PRACTICE

There are two main areas in which contrast agents have been used in the horse. The first is in the evaluation of neurological diseases, specifically the brain, central nervous system and adjacent structures of the head. The second is in orthopaedic conditions.

Contrast agents in neurological disease evaluation

Contrast agents have been helpful in identifying space-occupying masses of the brain, inflammatory conditions of the brain and peripheral nerves as well as pituitary disorders [3]. Normal brain will have contrast enhancement of the choroid plexus and vascular structures, but due to the blood–brain barrier should not have any significant enhancement of the parenchyma of the brain (Figure 2.16).

In pathological conditions T1 contrast agents will become localized in the regions of increased extracellular volume and in regions with breaks in the blood–brain barrier or increased vascularity. In the case of the pituitary gland and pituitary adenoma formation, the combination of increased size, increased vascularity and increased extracellular volume, results in significant contrast enhancement (Figures 2.17 and 2.18).

With masses of the head, contrast enhancement tends to be more variable, with some masses contrast enhancing (Figure 2.19) and others resulting in no contrast enhancement at all. Again the combination of increased vascularity, extracellular volume or break in the blood–brain barrier results in the detection of contrast in the region of a pathological problem. Often there will be a rim of enhancement surrounding a mass, instead of generalized uptake within a given mass.

Contrast agents in orthopaedic disease evaluation

Contrast enhancement of T1 agents depends on the absolute concentration of the agent in the desired tissue and the selectivity of the distribution to other tissues [1]. Extracellular fluid agents such as gadopentetate

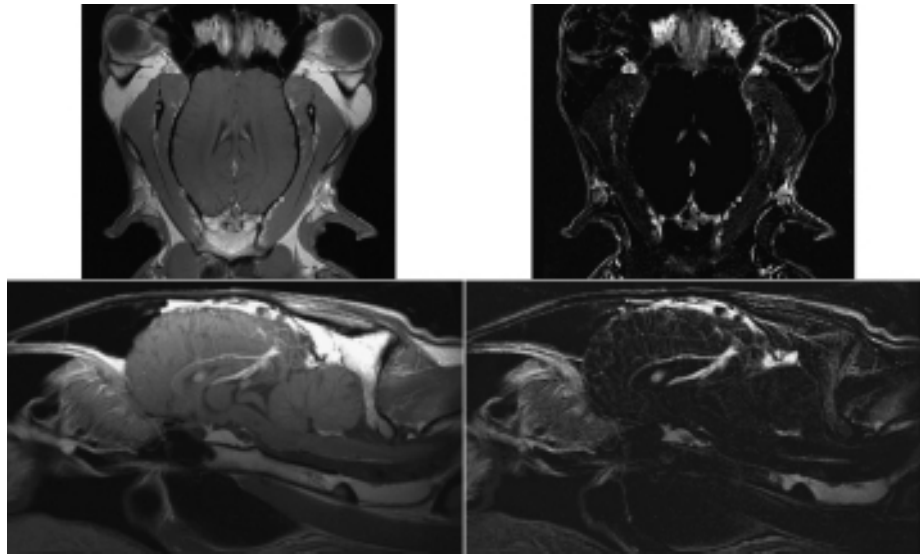

Figure 2.16 Normal brain post 0.20 ml/kg intravenously of gadopentetate dimeglumine (Magnevist). Top row: dorsal images. Bottom row: mid-sagittal images. The images on the left are post-contrast T1-weighted images and the images on the right are post-contrast digital subtractions of the pre- and post-contrast T1-weighted images. On the dorsal images, notice the lack of contrast uptake in the parenchyma of the brain with normal moderate uptake in the choroid plexus and vascular regions of the ventricles. On the mid-sagittal projections notice the delicate, intricate contrast within the normal vasculature.

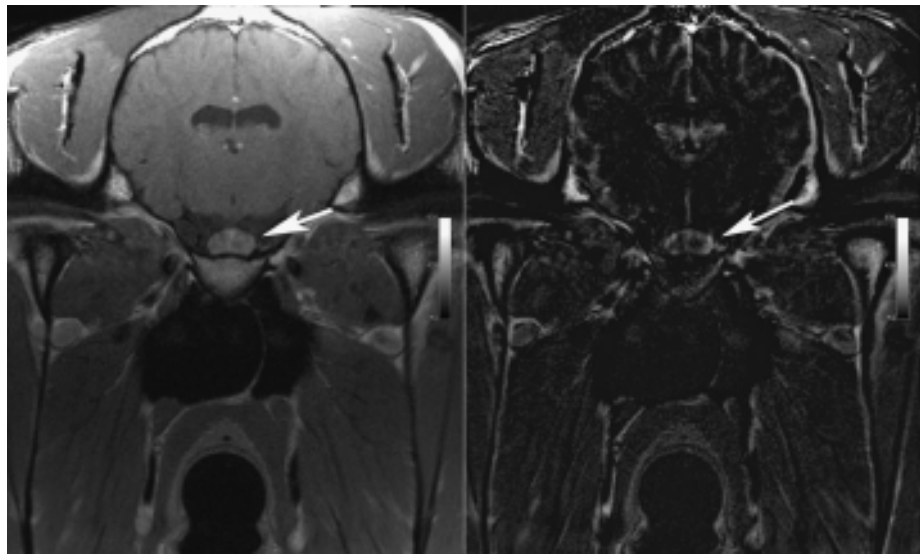

Figure 2.17 Normal pituitary after intravenous administration of 0.20 ml/kg of gadopentetate dimeglumine (Magnevist). Left: T1-weighted transverse image. Right: digital subtraction of the same region derived from the pre- and post-contrast T1-weighted images. Note the normal contrast enhancement and size of the pituitary gland (arrow).

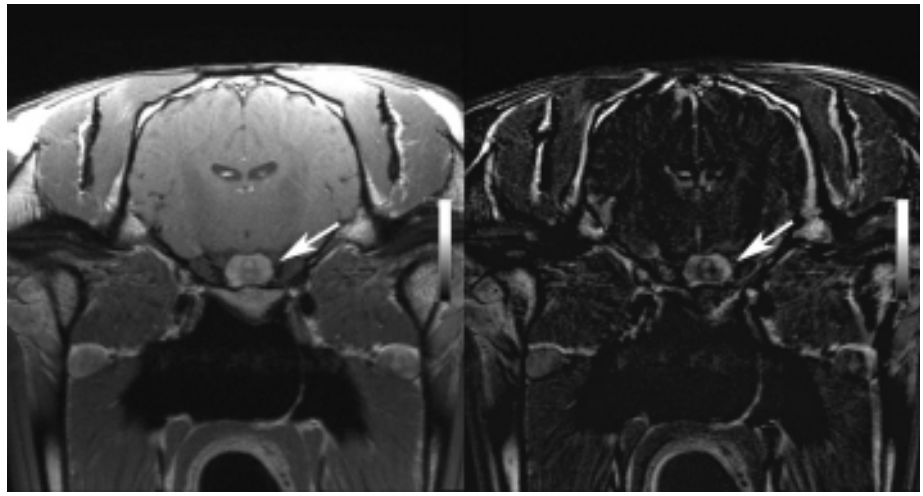

Figure 2.18 Abnormal pituitary after intravenous administration of 0.20 ml/kg of gadopentetate dimeglumine (Magnevist). Left: T1-weighted transverse image. Right: digital subtraction of the same region derived from the pre- and post-contrast T1-weighted images. There is gross enlargement of the pituitary gland (arrow) with increased contrast enhancement.

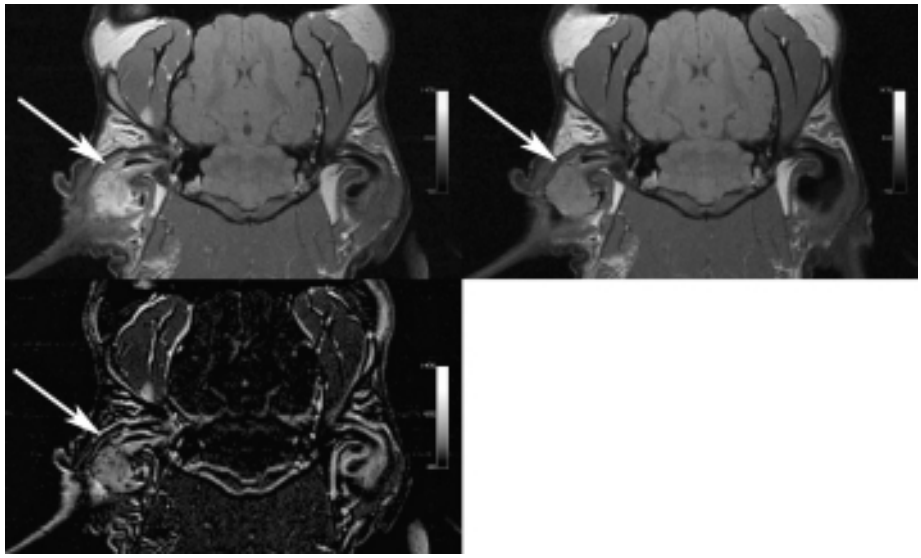

Figure 2.19 Aural mass within the middle and inner ears. Left: T1-weighted dorsal image of the calvarium after intravenous administration of 0.20 ml/kg of gadopentetate dimeglumine (Magnevist). Top right image: pre-contrast administration. Top left: post-contrast image. Bottom left: digital subtraction of the left and right top images. There is a contrast enhancing mass (arrow) in the aural canal and middle and inner ear.

dimeglumine (Magnevist) have been recently used to explore lesions in the distal limb of the horse [4]. In this study, 24 horses underwent contrast enhancement with gadopentetate dimeglumine (Magnevist) of the lamest limb after a routine MRI examination. Contrast enhancement was noted in normal regions, such as the vessels of the limb, the synovial lining of the joints and navicular bursa. Contrast enhancement was not noted in normal structures with low vascularity, such as the deep digital flexor tendons or cortical bone of the distal limb. In comparison, pathological regions of contrast enhancement were noted to be significantly increased in the deep digital flexor tendon where tearing had occurred, the collateral sesamoidean ligament and the impar ligament. Horses with more chronic injuries or longer durations of lameness had significantly less contrast enhancement of the pathological regions than those with more acute lesions or shorter durations of lameness. The authors concluded that contrast administration helped to detect subtle lesions and stage the current state of a detected signal abnormality. In addition the authors postulated that recheck MRI procedures with contrast would help determine the relative healing of the affected tissues.

Much like lesions of the brain, T1 contrast agents localize in areas of increased extracellular volume or increased vascularity. Therefore acute or active lesions in tendons and ligaments appear as regions of high signal within the ligament or tendon (Figures 2.20 and 2.21). Conversely regions of low extracellular volume or low vascularity do not contrast enhance (Figure 2.22). This can be used to help determine the current status of a lesion within a given structure.

For example, in Figure 2.22, significant signal abnormalities are present on both the medial and lateral lobes of the deep digital flexor tendon (DDFT) on the pre-contrast T1-weighted VIBE sequences. The current

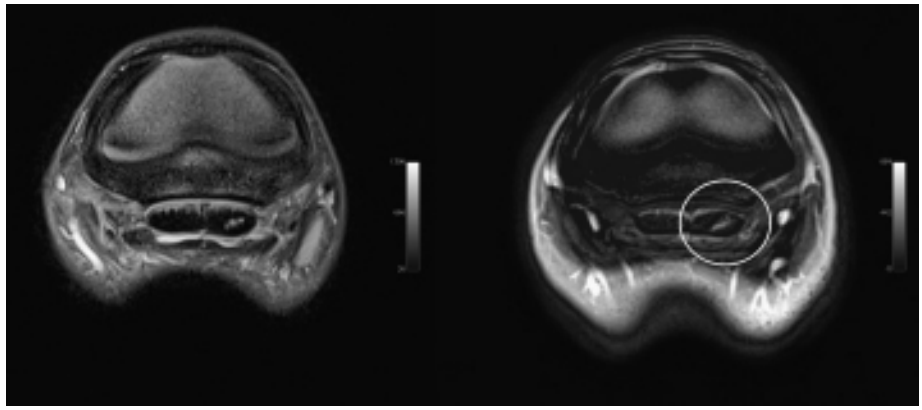

Figure 2.20 Deep digital flexor tendonitis with a tear of the lateral lobe. Left: proton density transverse image. Right: postcontrast T1weighted FS subtraction of the same axial section after administration of 0.20 ml/kg of gadopentetate dimeglumine (Magnevist). There is significant contrast enhancement within the lateral lobe of the deep digital flexor tendon (circle). This lesion can also be seen clearly in the same location on the proton density image.

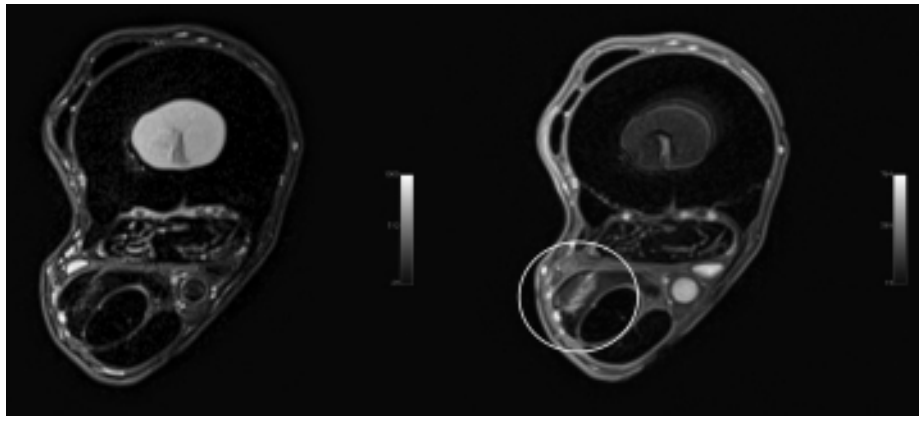

Figure 2.21 Desmitis of the accessory ligament of the deep digital flexor tendon. Right: T1-weighted FS post-contrast transverse image after administration of 0.20 ml/kg of gadopentetate dimeglumine (Magnevist). Left: digital subtraction at the same location of the pre- and post-contrast images. There is significant contrast enhancement of the ligament (circle).

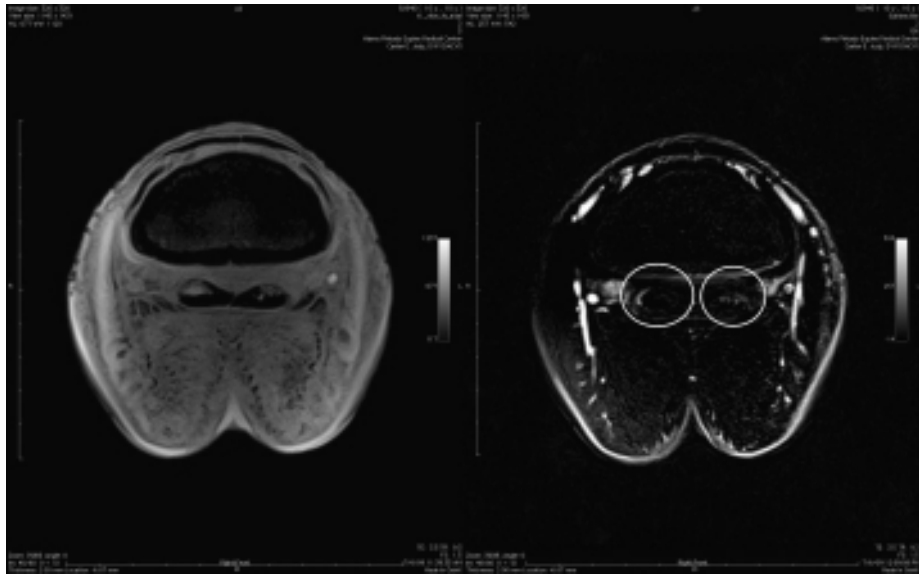

Figure 2.22 Deep digital flexor tendonitis of the lateral lobe of the tendon and healed injury of the medial lobe of the tendon. Left: pre-contrast T1-weighted FS transverse image. Right: post-contrast subtraction of the same region. The left circle represents the region of no contrast enhancement and the right circle depicts significant contrast enhancement. The lack of contrast enhancement of the medial lobe is consistent with a healed deep digital flexor injury while the lateral lobe's significant contrast enhancement is consistent with an active tendonitis.

clinical relevance of each lesion is difficult to determine, and given the relative size of the lesion on the lateral lobe (left side of the image) of the DDFT, it would seem to be the more significant of the two lesions. However, with the lack of contrast enhancement of the lateral lobe of the DDFT on the post-contrast subtraction images, the current clinical relevance of this lesion comes into question and is most consistent with a previously injured but likely healed injury. Conversely, the medial (right side of image) lobe of the DDFT shows significant contrast enhancement, indicating increased vascularity and extracellular volume consistent with an active lesion. This distinction becomes important when determining potential treatment options that require very accurate placement of therapeutic modalities.

The use of contrast agents in the proximal suspensory region has been helpful in distinguishing regions of normal musculature, which often appear as regions of high signal on all sequences, from regions of pathologic change (Figure 2.23). Contrast enhancement of the normal muscular fibres within the ligament appears minimal on post-contrast subtraction images. However, regions of pathologic change will appear to have increased signal intensity within the ligament and musculature. This can be very helpful for identifying subtle lesions of the proximal suspensory ligament.

Contrast agents in bone have similar enhancement characteristics as that of soft tissues. Regions of increased vascularity and extracellular space will regularly contrast enhance (Figures 2.24 and 2.25). In rare instances, regions of high signal intensity on STIR (short τ inversion recovery) images will fail to contrast enhance or will contrast enhance significantly less than anticipated (Figure 2.26). The cause of this is unknown, but may be related to increased intra-osseous pressure within the bone resulting in failure of adequate perfusion within the affected tissues. This results in a region devoid

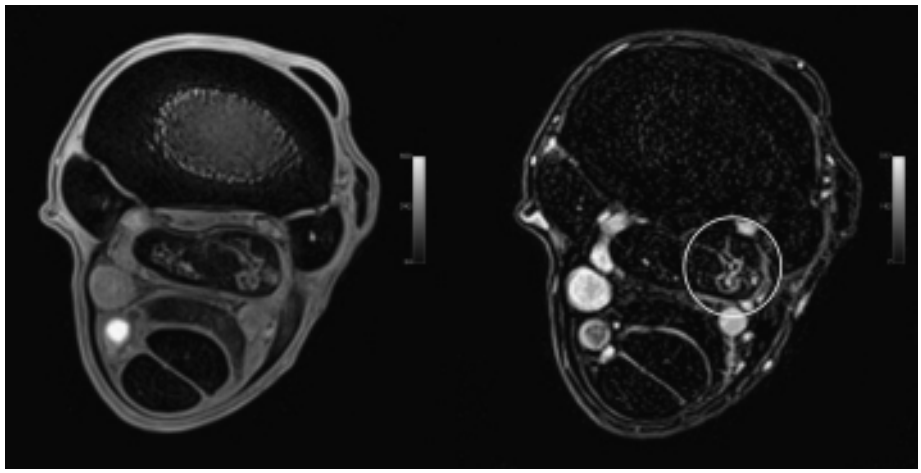

Figure 2.23 T1 FS VIBE transverse images of proximal suspensory desmitis. Left: pre-contrast. Right: post-contrast digital subtraction of the same region after administration of 0.20 ml/kg of gadopentetate dimeglumine (Magnevist). There is a region of significant contrast enhancement within the suspensory ligament (circle). Note the lack of contrast enhancement of the normal musculature within the ligament which appears as a high signal intensity region on the pre-contrast image. The contrast allows for easy distinction between normal and abnormal tissues.

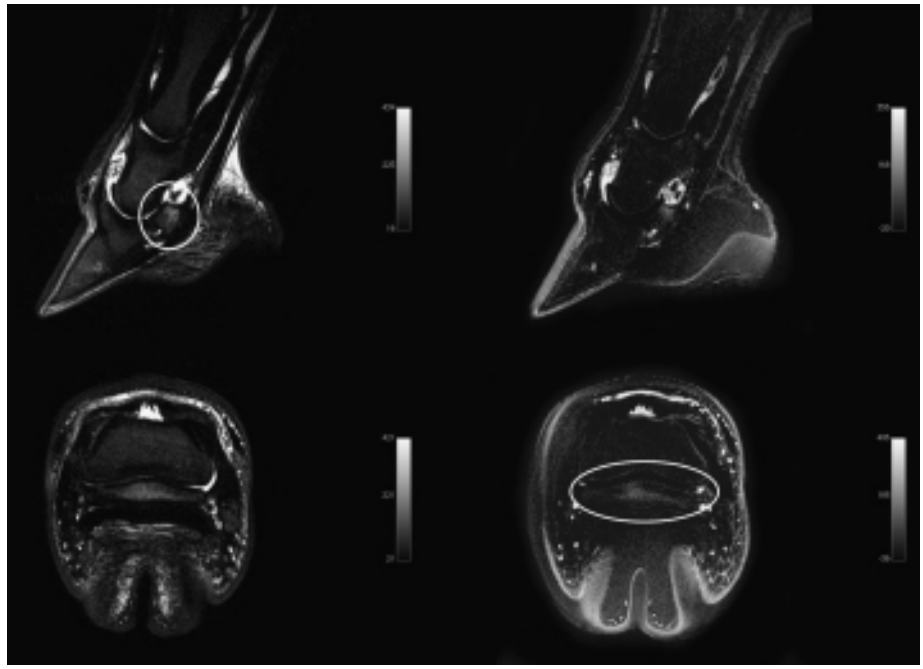

Figure 2.24 Contrast enhancement of the navicular bone. Top left : T2 STIR sagittal. Bottom left: T2 STIR transverse. Right are post-contrast T1 FS VIBE digital subtractions of the same region after administration of 0.20 ml/kg of gadopentetate dimeglumine (Magnevist). There is increased signal intensity within the navicular bone on T2 STIR image (circle) at the same location as the enhancement evident post-contrast administration.

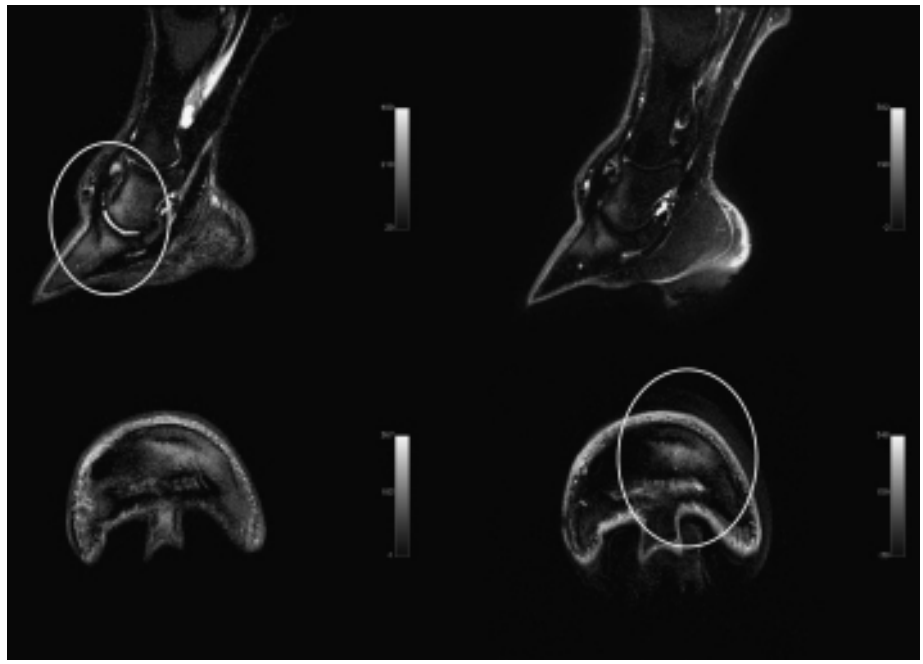

Figure 2.25 Contrast enhancement of the distal and middle phalanx. Top left: T2 STIR sagittal. Bottom left: T2 STIR axial. Right: post-contrast T1 FS VIBE digital subtractions of the same region after administration of 0.20 ml/kg of gadopentetate dimeglumine (Magnevist). There is increased signal intensity on the T2 STIR sequence at the same location as the enhancement evident following contrast administration.

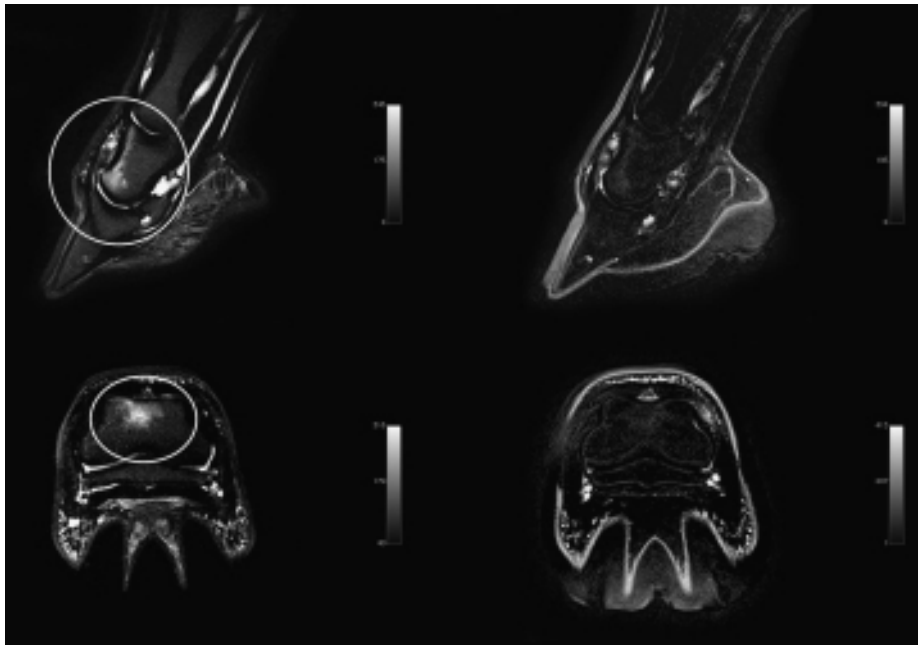

Figure 2.26 Dorsal middle phalanx bone 'oedema' showing low contrast enhancement of bone. Top left: T2 STIR sagittal. Bottom left: T2 STIR transverse. Right: postcontrast T1 FS VIBE digital subtractions of the same region after administration of 0.20 ml/kg of gadopentetate dimeglumine (Magnevist). The circles on the left images depict the region of increased signal on T2 STIR sequences. Note the relative lack of contrast enhancement of the corresponding regions on the post-contrast digital subtractions compared to the relatively intense T2 STIR images.

of contrast but relatively high signal intensity on T2 STIR images. Most of the cases with this lack of contrast enhancement have acute histories of lameness, which may represent a more significant inflammatory reaction in the medullary cavity resulting in higher intra-osseous pressure.

Recheck examinations can be aided greatly by the use of contrast agents (Figure 2.27). By using a contrast agent, the current status of the lesion can be more clearly defined. Since tendon and ligament healing can result in misaligned collagen fibres that are very noticeable on T1-weighted images, the use of contrast agents can clarify the activity within the collagen matrix and help determine if the lesion has become quiescent or remains in the active remodelling phase. This can help to guide rehabilitation and either expedite the return of a horse to performance or keep a horse in rehabilitation to further heal an injured tendon or ligament.

CONCLUSION

The use of MRI contrast agents in horses is in its infancy. Early work has shown that it is a useful adjunctive tool to further characterize and clarify diagnoses and helps to further identify subtle lesions. Changes in contrast enhancement over time are proving helpful in further classifying the current state of an injury and helping to make a more educated diagnosis that will further benefit the horse.

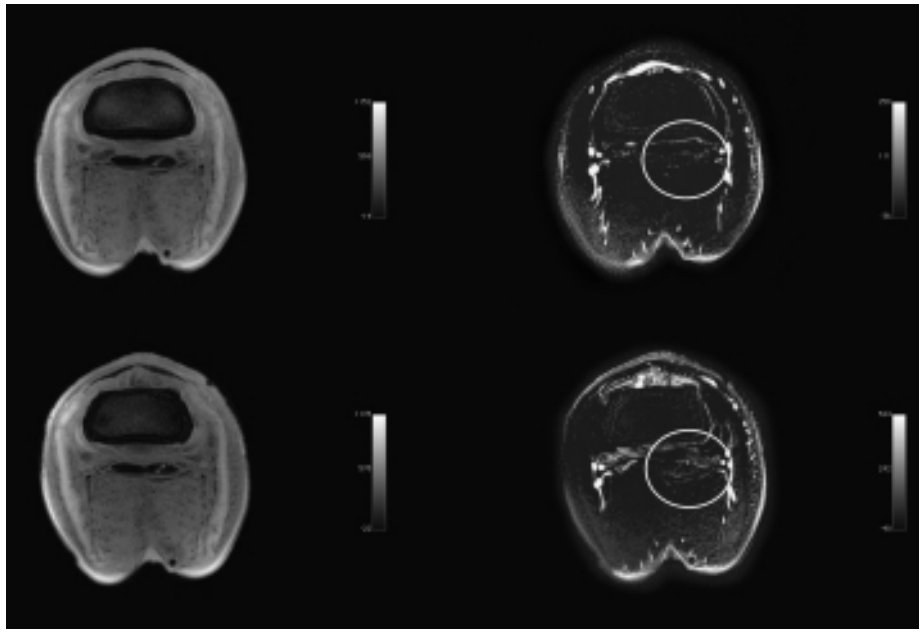

Figure 2.27 Original and recheck images of a deep digital flexor injury taken 8 months apart. Bottom: original images taken at the time of injury. Bottom left: T1-weighted FS VIBE transverse image. Bottom right: post-contrast digital subtraction of the same region after administration of 0.20 ml/kg of gadopentetate dimeglumine (Magnevist). Top: images of the same area 8 months post injury. The circle on the bottom right image depicts the region of significant contrast enhancement within and around the lobe of the deep digital flexor tendon. Notice the lack of contrast enhancement on the upper right image in the circle in the same area. This lack of contrast enhancement is consistent with inactivity and likely healing of the injury. The continued presence of high signal on the T1-weighted FS VIBE image in the upper left is likely a result of misaligned collagen (probable scarring) within the tendon.

REFERENCES

[1] Caravan P, Lauffer RB. Contrast agents: basic principles. In: Edelman RR, Hesselink JR, Zlatkin MB, Crues JV (eds) *Clinical Magnetic Resonance Imaging*, 3rd edn. Philadelphia, PA: Saunders, 2007, pp. 358–76.

[2] Ferrell EA, Gavin PR, Tucker RL, Sellon DC, Hines MT. Magnetic resonance for evaluation of neurologic disease in 12 horses. *Vet Radiol Ultrasound* 2002; **43**: 510–16.

[3] Maher MC, Werpy NM, Goodrich LR *et al*. Distention of the navicular bursa to determine the presence of adhesions using magnetic resonance imaging. *Proceedings of the 54th American Association of Equine Practitioners Meeting*, Lexington, KY, 2008, p. 460.

[4] Judy CE, Saveraid TC, Rodgers E *et al*. Characterization of foot lesions using contrast enhanced equine orthopedic magnetic resonance imaging. *Proceedings of the* 2008 *Veterinary Symposium – The Surgical Summit – American College of Veterinary Surgeons*, Germantown, MD, 2008.

Chapter 3
Low-field MRI in horses: practicalities and image acquisition

Natasha Werpy

INTRODUCTION

Magnetic resonance imaging (MRI) provides excellent visualization of soft tissue and osseous injuries. Currently, greater numbers of low-field systems are available for imaging equine patients compared with the number of high-field systems in use. Although high-field systems have superior image quality, low-field systems offer many advantages when diagnosing injury in equine patients. Low-field MR systems are defined as having a field strength of up to 0.3T [1]. The currently available equine-specific low-field MRI systems utilize U-shaped permanent magnets ranging in field strength from 0.2 to 0.3T. Permanent magnets create a magnetic field using the ferromagnetic properties of certain metal alloys [2]. The magnetic field is induced into the materials at the time of manufacturing. The reasonable cost of low-field systems has made MRI accessible to many practices in the United States and Europe. These systems have allowed imaging of horses that may not have otherwise had access to this modality. Human low-field systems can be adapted for equine use, and several systems are currently in use. Currently, two companies provide low-field MR systems specifically designed for equine patients: the Hallmarq distal limb scanner (0.28T) for standing sedated or anesthetized patients and Universal Medical Systems (02–0.3T), which can image under general anaesthesia from carpus/tarsus distally, plus the head, cranial neck and stifle in the larger units (Figure 3.1).

Many important differences between high- and low-field MRI systems exist. Understanding these differences is important when considering all the aspects of using a low-field system. This knowledge should be used to maximize image quality and ensure accurate interpretation of studies produced by low-field systems. Field strength is the greatest determinant of image quality in a MR system. A normally functioning high-field MR system will consistently produce images of substantially greater quality when compared to images produced by low-field systems. However, low-field systems can produce diagnostic quality images for numerous different types of pathologic change in many different anatomic regions. The ability to produce diagnostic quality images from a low-field system is dependent on knowledge of the system, including its limitations, in conjunction with an understanding of basic MR principles and detailed knowledge of equine anatomy.

Equine MRI, edited by Rachel C. Murray. © 2011 by Blackwell Publishing Ltd.

Figure 3.1 Horses undergoing MRI of the foot in the Hallmarq distal limb scanner (a), and of the head in the Vet-MR Grande XL (b) from Universal Medical Systems, the currently available equine-specific low-field MRI systems. The Hallmarq distal limb scanner can obtain images from the carpus and tarsus distally. The Vet-MR Grande XL can obtain images from the carpus and stifle distally, as well as the head and cranial cervical spine.

Optimizing image acquisition begins with appropriate patient positioning, continues with meticulous study planning and is completed by thorough scrutiny of the images. This process results in production of the highest quality images possible by the system, providing the greatest probability that a lesion will be visible on the study.

The difference in image quality and image acquisition time between high- and low-field systems arises from disparities in field strength, magnetic field homogeneity and maximum field of view. The differences between high- and low-field systems have a direct impact on how the limb should be positioned in the magnet, what dimensions of an anatomic region can be imaged in one study, how much of that study will be of diagnostic quality and what area within the study will have reliable fat suppression. These factors impact image acquisition time because they determine how many studies will be required to produce diagnostic images in an area of interest. To maximize the anatomy imaged per study it is critical that the system operator understands these factors. Furthermore, assessment of image quality and accurate interpretation of the images by the reader requires an understanding of these factors.

Image acquisition and interpretation requires an understanding of the process of fat suppression when using a low-field system. In MRI, fat suppression is most commonly accomplished by two methods: frequency-selective fat saturation and inversion recovery. However, because the difference between the resonating frequency of adipose tissue and water is

considerably less in a low-field system than it is in a high-field system, frequency-selective fat suppression is not performed using low-field systems. Consequently, low-field systems use inversion recovery sequences for fat suppression (Figure 3.2). The fat suppression produced using inversion recovery sequences is most reliable at the isocentre of the magnet. Images produced at the periphery of the field of view will have less reliable fat suppression, reduced signal to noise and less detail due to field inhomogeneity.

Evaluation of high-field images compared to low-field images gives a clearer understanding of the limitations of low-field systems and can be used

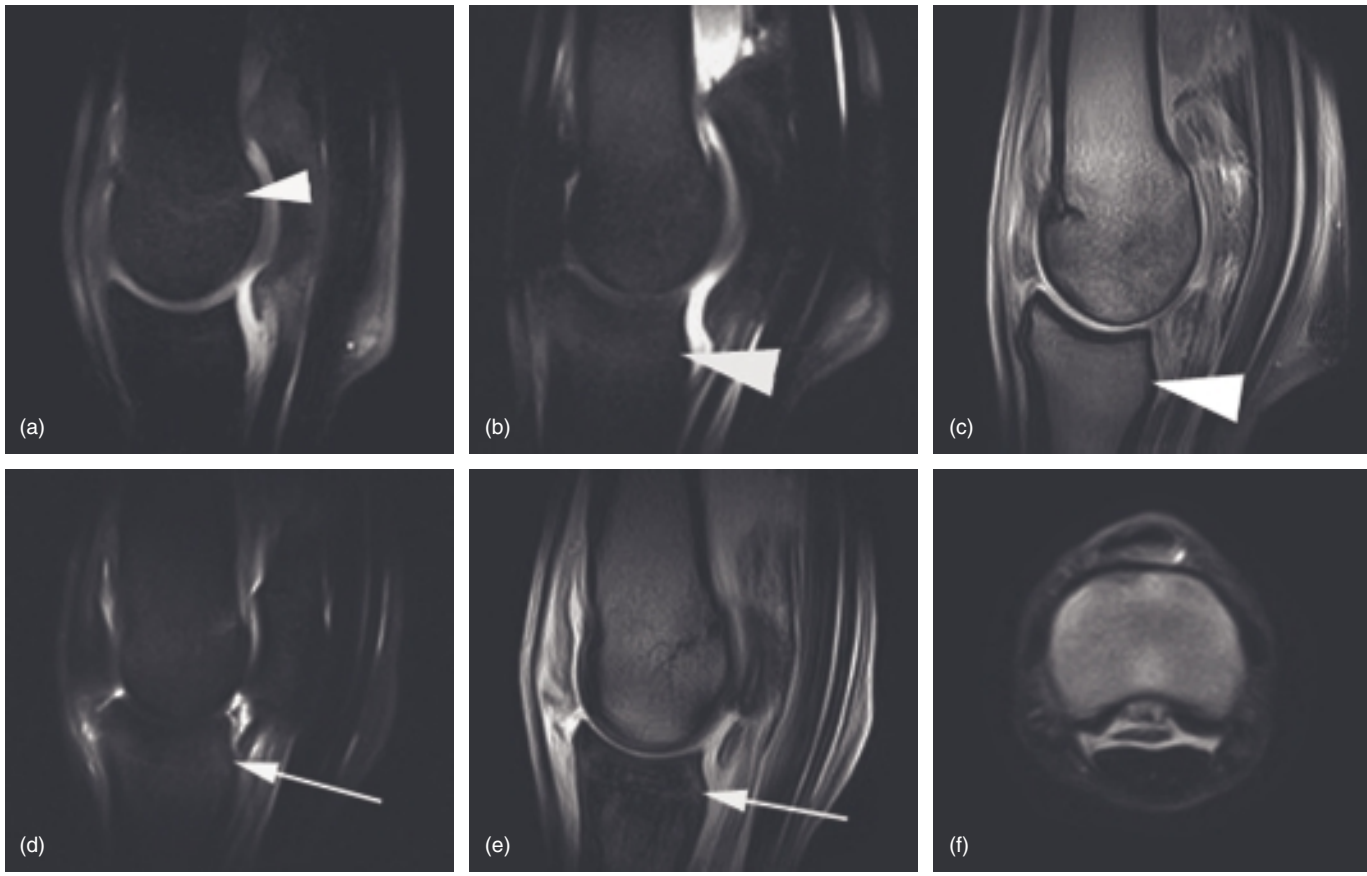

Figure 3.2 Inversion recovery sequences are most commonly used by low-field systems to produce fat-suppressed images, which are useful for detecting fluid in bone and soft tissue. (a) Uniform magnetic field homogeneity along with proper limb placement in the magnet and centring of the coil in the field of view produces diagnostic quality fat suppressed images. A diagnostic quality fat-suppressed image has consistent pattern of low signal intensity in areas of the limb that contain fat and do not contain fluid. Normal vasculature within bone will still be detectable as linear areas of increased signal intensity (arrowhead). (b) Incomplete fat suppression produces images with variable signal intensity, and areas of increased signal intensity do not necessarily represent regions of fluid (arrowhead). Comparison with other sequences can help differentiate incomplete fat suppression from the presence of fluid. (c) A lack of any abnormal signal intensity on T2 FSE images confirms the signal pattern is a result of incomplete fat suppression (arrowhead). Currently, with images obtained using the Hallmarq system, comparing T2* gradient echo and T2 FSE images to STIR images provides the best method for differentiating incomplete fat suppression from the presence of fluid. Areas of increased signal intensity on STIR images (d) with corresponding low signal intensity on the T2*-weighted images (e) that do not have low signal intensity on T2 FSE (f) images are the result of phase cancellation artefact/effect and indicate the presence of fluid (white arrows).

as a learning tool to improve image interpretation [3] (Figure 3.3). Several criteria can be used when comparing images from high- and low-field systems. These include spatial resolution, contrast resolution and noise, which are affected by sequence parameters as well as the hardware and software available. In addition, it is imperative to understand and recognize motion artefacts as they can both create the appearance of lesions and obscure true lesions. The person interpreting the images must be able to recognize when sequences need to be repeated or additional images are necessary because the initial study did not answer the question set forth by the clinician.

Field strength is the major determinant of image quality. The amount of data extracted from the anatomy by the MR system being used to produce images is based on field strength. As a result, MR systems with similar field strengths will have comparable image quality. Nevertheless, differences in the appearance of the images that are not related to image quality can be identified on studies produced by different MR systems of similar field strength. These differences are due to both hardware and software factors. Specific hardware components, such as the radiofrequency (RF) coils, can significantly impact image quality. However, each company attempts to maximize these components of the system, so the quality is similar between systems. The size of the magnet determines the maximum field of view and will affect the area of anatomy that can be imaged with one study. A larger

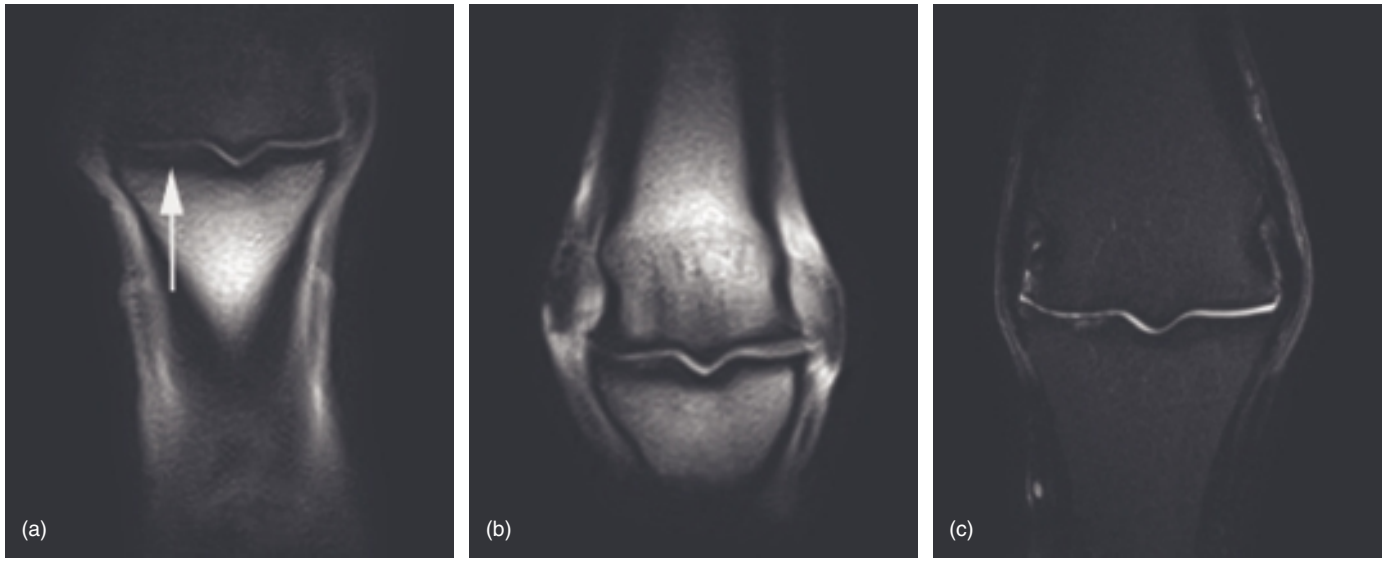

Figure 3.3 Images from a 10-year-old warmblood jumper with a grade 3/5 left forelimb lameness that resolved with an abaxial nerve block, diagnosed with damage to the proximal medial subchondral bone of the proximal phalanx. Low-field standing T1-weighted gradient-echo frontal images at the level of the pastern joint (a) and at the level of the fetlock joint (b). High-field proton density fat-saturated frontal image at the level of the fetlock joint (c). A lesion was suspected in the proximal medial aspect of the proximal phalanx on the pastern study due to a small area of mild increased signal intensity in the subchondral bone (arrow). Due to the amount of noise and signal drop-off at the periphery of the field of view, the field of view was raised and centred over the fetlock joint. The lesion then becomes a more clearly demarcated area of increased signal intensity within the subchondral bone in the proximal medial aspect of the proximal phalanx, demonstrating the importance of centring the region of interest in the field of view. On the high-field image the lesion is larger with well-defined margins. In addition, the soft tissues associated with the fetlock joint can be easily visualized on the high-field image in contrast to the low-field images. The low-field images demonstrated the lesion in the proximal phalanx; however, accurate visualization of the soft tissues is difficult. This, in combination with difference between lesion margins, demonstrates a difference in resolution between high- and low-field systems.

magnet has a bigger and more homogenous field of view, leading to improved fat suppression and fewer artefacts compared with a smaller magnet.

The software used for image acquisition and processing affects the overall appearance of the images. Following data acquisition, the degree to which the data are manipulated, or post-processed, is determined by each individual manufacturer. Low-field images undergo additional post-processing, such as filtering or smoothing, when compared with high-field systems. Software manipulation and the degree of smoothing affect the appearance of images. This process is used to prevent individual pixels from being visualized in the images and to decrease the appearance of noise. The end result of this process creates images that appear as an accurate representation of the anatomy and are more aesthetic to the reader. However, this process does result in loss of information. This difference is apparent when comparing the trabecular bone pattern between high- and low-field systems. In most cases, the signal intensity pattern overlying the trabecular bone in an image from a low-field system does not represent the trabeculae and is influenced by the noise pattern in the image. The signal intensity pattern in the bone should be compared to the noise pattern present in the background outside the margins of the imaged anatomy. This can be accomplished by adjusting the contrast of the image to reveal the noise pattern. It is difficult to accurately represent the trabecular bone on most low-field images due to resolution limitations. As a consequence, differentiating diffuse fluid with intact trabecular bone from fluid accumulation with loss or destruction of the trabeculae can be difficult to impossible, depending on the severity of the injury.

Given that low-field systems will produce images of similar quality, selecting the best system for a practice is determined by evaluating several factors. The available systems are capable of imaging different regions of the anatomy and require different anesthetic protocols. Overall caseload and the desire of the clinicians in the practice to image the head, neck and stifle should be weighed against the advantage of imaging feet in a standing patient. In addition, financial considerations that must be understood include equipment cost or lease arrangements, construction costs, ancillary equipment for studies requiring general anaesthesia, service contracts and warranties. Once a system has been selected, great effort should be given to a room design that encompasses all the possibilities for use of that system. Once the room is built and the shielding is in place it is very expensive to change the size of the room or add features, such as oxygen or scavenge lines. It is much less expensive to plan for all the possibilities in the initial building design. This planning should include dimensions that allow both right and left lateral recumbency with the patient positioned to image both the front and hind limbs.

MACHINE PREPARATION, PATIENT PREPARATION AND SEDATION TECHNIQUE

Prior to imaging the patient, several preparations must be made. A clear understanding of the area to be imaged should be established. It is best to

communicate with the clinician using specific anatomic landmarks, such as from the base of the sesamoid bones to the laminar tissues of the distal phalanx, to avoid confusion. The MR system should be calibrated based on the requirements of the manufacturer to ensure it is working properly before the patient is sedated or anaesthetized. In the standing system, the appropriate magnet height can be determined by measuring the height of the area of interest using a wooden ruler and then using the measurement to correctly set the magnet height prior to placing the horse in the magnet. Anything that can be done to minimize movement of the magnet once the horse has stepped forward into the magnet should be done. Moving the magnet up or down can scare the horse so it should be avoided wherever possible. Taking these steps will reduce the amount of time required to position the horse in the magnet. Ideally, the lateral aspect of the limb should be marked prior to positioning the horse in the magnet. This can be done with a vitamin E capsule or oil in an extension set. Although in many joints the orientation of the limb is apparent, this a good practice to maintain.

Sedation technique will vary from practice to practice. Currently, a number of sedation protocols are being used for imaging the standing horse. The goal is to have the patient relaxed with the feet planted, but not oversedated resulting in leaning and swaying. Positioning the horse in the magnet is best accomplished with premedication. This should be followed by a continuous rate infusion of sedative drugs to maintain a consistent plane of relaxation for the duration of the study [4, 5]. In preparation for the MR study an intravenous catheter is placed in a jugular vein. Commonly used drugs for premedication include romifidine, detomidine and butorphanol. Premedication drugs are usually administered to the patient prior to entering the room. Very nervous or potentially claustrophobic patients, as determined by willingness to load in the trailer or walk into a small room, can benefit from intramuscular acepromazine at the recommended premedication dose. Once the horse has entered the MRI room, a continuous rate infusion (CRI) is started. A CRI frequently used contains 10–15 mg of detomidine per 500 ml of 0.9% sodium chloride or lactated Ringer's solution and is titrated to effect. A higher rate of administration is usually required for the first 10–15 minutes that the horse is in the room. The rate of administration of the CRI can be reduced once the horse has reached an appropriate plane of sedation. In certain patients, achieving a consistent plane of relaxation may require higher rates of infusion. Changing fluid bags because of an increased rate of infusion can distract the patient and cause them to move. In these cases, increasing the dose of detomidine in the CRI will allow a reduced rate of infusion and eliminate the need to change bags during the study. As with any anaesthetic situation, guidelines are in place that must be constantly adjusted based on the patient response to the drugs administered.

Creating an environment that encourages patient co-operation is imperative for producing diagnostic quality images. When positioning a horse for a standing study, the patient must be relaxed and able to stand comfortably for an extended period of time. Minimal noise, or consistent low-level noise, facilitates this process. A stable head support that is adjustable should be

used so the head position can easily be maintained. The head support should be removable because it could interfere with positioning a horse for an anaesthetized study. A freestanding headrest can be used when scanning hind limbs. However, a headrest that is positioned over the top of the magnet should be used when scanning the forelimbs. The head should be maintained at the level that allows the horse to be relaxed. It should not be positioned so low that the horse drifts or leans forward.

Prior to positioning the horse in the magnet for a study, it is important to evaluate the patient's conformation, so that the area of interest is placed perpendicular to the main magnetic field. This will make study planning easier and facilitates the production of diagnostic images. Due to the size of the magnet, most horses must stand base wide when positioned for a front limb study in the standing system. This stance creates several difficulties with study planning and can affect the anatomic appearance of certain structures. Minimizing the base-wide stance as much as possible without making the horse uncomfortable will reduce artefacts resulting from asymmetrical positioning of the anatomy relative to the axes of the magnet. The base-wide stance can be reduced by placing the limb that is not being imaged as close as possible to the magnet. However, contact between the magnet and the limb can be irritating to the patient and cause the horse to pick up the leg and reposition it, leading to unnecessary motion. The degree of contact between the limb and the magnet that will be tolerated by each patient must be assessed in the context of each patient's personality. A small amount of additional firm rubber padding placed under the foot of the contralateral limb may more closely align the limb with the main magnetic field, and so can be useful in some situations. This places the feet at different heights and should only be done to the point at which it straightens the leg, but not enough to make the horse feel unbalanced or uncomfortable.

The wide-based stance that occurs with the standing system often causes some degree of rotation to the limb, which the operator should try to correct. When positioning the patient, as much attention should be paid to the opposite end of the horse as is paid to perfecting the position of the limb being imaged. Many horses will shift and cause motion artefact if their hind end is not comfortably positioned prior to beginning the exam. If the horse is walked straight into the magnet to position the front limbs, the limbs are often rotated by the operator to align them with the magnet axes. This correction can create curvature in the spine, which may be uncomfortable for the patient. To avoid this, once the front limbs are positioned in the magnet but prior to the fine-tuning of the imaged limb, the position of the hind end should be evaluated and properly adjusted so the neck and spine are straight. This increases the likelihood that the horse will stand in the same position for the duration of the exam. Adjusting the front and hind end together ensures that once the front limbs are well positioned it is not necessary to further adjust the hind end. Considerations for positioning of the limb in the magnet for an anaesthetized study using a low-field system are similar to those for a standing study.

Vitamin E capsules, and other forms of enclosed fat or water, can be used to mark specific locations on the limb. This is especially helpful when

there are no obvious landmarks to determine medial versus lateral. Another circumstance where this is beneficial is an area such as the mid-metacarpus, where limited landmarks are available to determine appropriate slice block overlap or complete coverage of the anatomy. Artificial landmarks can be created using vitamin E capsules proximal to distal on the limb, while sequentially increasing the number of vitamin E capsules at each level.

The smaller magnet bore used in low-field systems provides the opportunity for circumferential padding of the limb, which decreases the effects of physiologic patient motion. The benefits from circumferential padding are most apparent on anaesthetized studies. When padding the limb, care should be taken to maintain the position of the RF coil and excessive pressure on the RF coil should be avoided. In a standing patient, high-motion joints, such as the fetlock, can be placed in a bandage to help stabilize the limb, discouraging flexion and extension of the joint, and maintain the positioning of the RF coil. Stabilizing the fetlock joint should also be considered when imaging anatomical regions proximal to it, as small flexion and extension movements of the fetlock in a standing sedated horse can often result in motion of the entire limb. A contralateral limb bandage can be useful, as the horse is less likely to feel the magnet if it brushes up against it during limb positioning.

To maximize image quality it is imperative to choose the smallest RF coil that will fit around the region of the interest. The RF coil must be stable and secure around the site of interest throughout the entire scan. Excessive padding around the region to be imaged for the purpose of joint or coil stabilization can require the use of a larger RF coil, which has a negative impact on image quality. In these cases, the concern of motion artefact versus the impact of the larger coil on image quality must be prioritized to optimize image quality. In certain cases, both options must be tried before the best decision is apparent.

In addition to stabilizing the joint with a bandage, sponge pieces may be useful between the RF coil and the limb to stabilize the coil. Once the horse is in position and the coil is in place, any existing gaps between the limb and the coil can be filled with small sponge pieces. It is best to pad the space between the coil and the limb evenly so there is less chance of the coil slipping or changing orientation. For more proximal regions of the limb, larger sponge pieces can be used to fill the gap proximal to the coil between the limb and the magnet bore. This can reduce the degree of sway and help secure the coil, but is not as restrictive to the horse as bandaging.

Anaesthetized studies require extreme attention to the padding of musculature as well as the position of the limbs. Any contact between the patient and the magnet housing should be minimized and appropriately padded. Low-field studies have long acquisition times and precautions should be taken to prevent any negative effects of anaesthesia. If two consecutive studies are required on the same side of the patient, this side should be placed up when the horse is positioned in lateral recumbency. When the down side of the patient is imaged, proper positioning of the limb in the magnet bore precludes extension of the limb, which is necessary to decrease the risk of radial nerve paralysis. In this situation, positioning the horse with

the imaged limb on the upper side allows proper positioning for both studies as well as full extension of the dependent limb.

IMAGE ACQUISITION AND OPTIMIZING IMAGE QUALITY

Protocol design

In most institutions, MR protocols are designed based on the anatomic region that will be imaged. Designing a protocol requires understanding the characteristics of the available MR sequences. MR sequences have advantages and disadvantages specifically related to spatial and contrast resolution as well as acquisition time. These factors should be considered when selecting sequences for a protocol. Different protocols are used with musculoskeletal imaging than would be selected for imaging of the head and neck in studies with a specific interest in the neuroanatomy. These differences are based on the strengths and weakness of the individual sequences as well as the pathologic changes most commonly encountered in the anatomic region being imaged.

Images acquired with low-field systems have longer acquisition times than high-field systems resulting in increased motion artefacts. Thus, the fast acquisition time of gradient-echo sequences is advantageous in low-field imaging. Although these sequences have the highest spatial resolution, they have the lowest contrast resolution relative to comparable sequences of similar tissue weighting. This characteristic is accentuated on low-field images. Gradient-echo sequences provide an overall view of the anatomy, and in most cases will provide evidence of an abnormality, but do not necessarily characterize the abnormality well. For example, the difference between fluid and tissue is not well shown on gradient-echo sequences when compared to fast or turbo spin-echo sequences. However, exceptions exist. For example, gradient-echo sequences show the laminar tissues of the hoof wall better than fast or turbo spin-echo sequences.

In a research setting where the study goal is three-dimensional modelling, computer software programs performing the data analysis require the use of gradient-echo sequences due to their acquisition parameters. In many research articles gradient-echo sequences are selected for that reason. However, the characteristics desirable for clinical imaging are quite different from those required for research data analysis. Distinguishing different tissue types is a highly desirable characteristic for clinical imaging. Although gradient-echo sequences can be produced rapidly with three-dimensional image acquisition, the decreased contrast resolution of these sequences makes distinguishing different tissue types more challenging and is an undesirable characteristic for clinical imaging.

Images with two-dimensional acquisition, such as fast spin-echo, turbo spin-echo and inversion recovery sequences, have decreased resolution compared to gradient-echo sequences. They take longer to obtain and consequently are more susceptible to motion artefact. Their decreased spatial

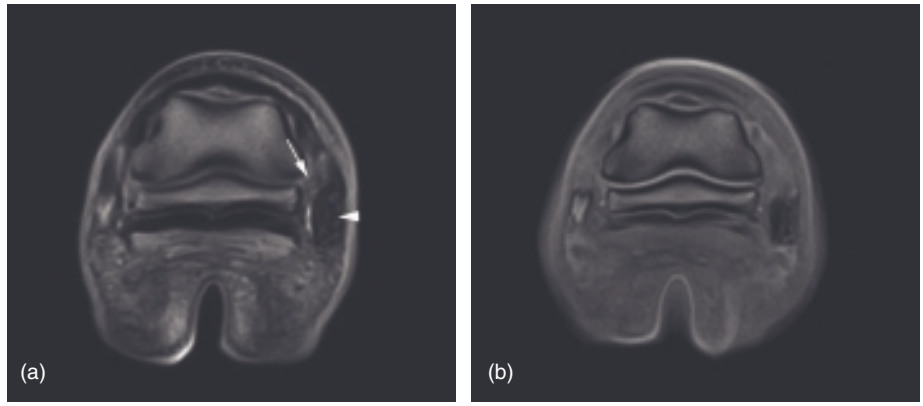

Figure 3.4 Transverse proton density (a) and T1-weighted gradient-echo (b) images of the foot at the level of the navicular bone. The osseous structures and the deep digital flexor tendon are well defined on the T1-weighted gradient-echo image. However, the remaining soft tissue structures are primarily intermediate grey with poorly defined margins. The proton density image has superior soft tissue contrast. The margins of the ligamentous structures can be clearly defined on the proton density image. The lateral chondrosesamoidean ligament (arrow) is diffusely enlarged. This is well demonstrated on the proton density image. In contrast, it is not evident on the gradient-echo image. The cartilages of the foot are incompletely ossified and the lateral cartilage is sclerotic (arrowhead).

resolution is accompanied by better contrast resolution, allowing clearer identification of different tissue types and a more detailed characterization of injury. Proton density sequences provide an overall view of the anatomy with more contrast compared with T1-weighted images. This difference in contrast occurs because T1-weighted images have low signal intensity fluid compared to proton density images. On T1-weighted images the low signal intensity fluid provides less distinction at the interface between fluid and soft tissue structures compared with proton density images (Figure 3.4). Inversion recovery and T2-weighted images have greater contrast and are superior for characterizing many types of lesion. STIR (short τ inversion recovery) images have the lowest spatial resolution and are the most susceptible to magnet field inhomogeneity and motion artefact. They are specifically made to show areas of fluid in bone and soft tissue and are necessary for detecting many types of pathologic change. T2-weighted images have greater spatial resolution compared with STIR images and are comparatively more resilient to motion artefact. They demonstrate fluid in the soft tissue, but typically not in bone.

All categories of sequences, when used in combination, result in a protocol that is designed for speed and tissue contrast. Generalizations regarding advantages and disadvantages can be made about all sequences. However, in the end, the sequence that will best show the lesion is dependent on the character of that lesion. Other considerations for selecting sequences to complete a protocol include artefact identification. Magic angle effect can cause problems with image interpretation. To identify whether this phenomenon is present, it is important to include a long time of echo sequence,

which will be minimally affected by the magic angle effect. The minimum time of echo required to identify magic angle artefact in tendons has been reported to be 28 ms. Although in high-field systems STIR sequences can be used to minimize magic angle effect, often the time of echo of this sequence on a low-field system is not long enough to meet this requirement. Under these circumstances, a T2-weighted sequence is required in the protocol to identify magic angle effect.

Study planning

When using any MR system, image acquisition and optimization require an appropriate grasp of basic MR physics as well as a solid understanding of the strengths and weakness of the system being used. The operator applies this knowledge during study acquisition to produce the best possible images. In general, study planning in low-field imaging is similar to high-field imaging. However, low-field studies have thicker slices and a smaller field of view. This requires more precise patient positioning and study planning to ensure the appropriate area is imaged and the images are correctly positioned. Appropriate study planning requires localization of the lameness to as specific an anatomic region as possible. Once this has been established, knowledge of the location and orientation of the soft tissue and osseous structures in that region facilitates accurate patient positioning and study planning.

When placing the limb in the magnet, the area of interest should be positioned as close to the isocentre of the magnet as possible (Figure 3.5). Knowledge of the field of view and the area of reliable fat suppression within the field of view will impact the positioning of the limb. MR studies are performed because a lesion has not been identified on other imaging modalities or more information about a previously identified lesion is desired. In the latter case, the lesion should be placed in the centre of the cross hairs that represent the isocentre of the magnet. In cases where a lameness has been localized but a lesion has not been identified, place the most commonly injured structures within that localized region in the isocentre of the magnet. In general, statistical incidence of disease is used to prioritize positioning of the limb. However, adjustments to the limb's position are made if the clinical exam or history indicates that the site of injury is likely to fall outside the norm. Additional steps in study planning may be required if the initial images do not provide the desired information or demonstrate evidence of a lesion that correlates well with the clinical examination.

Once the limb is positioned with the region of interest centred in the cross hairs, pilot images are obtained. The quality of the pilot images is dependent on correct positioning of the limb in the magnet as well as correct placement of the RF coil. Pilot images show the anatomy that will be included in the study using a limited number of slices compared to a standard sequence. Improper coil placement will obscure the anatomy even if it is in the isocentre of the magnet due to inadequate signal generation from

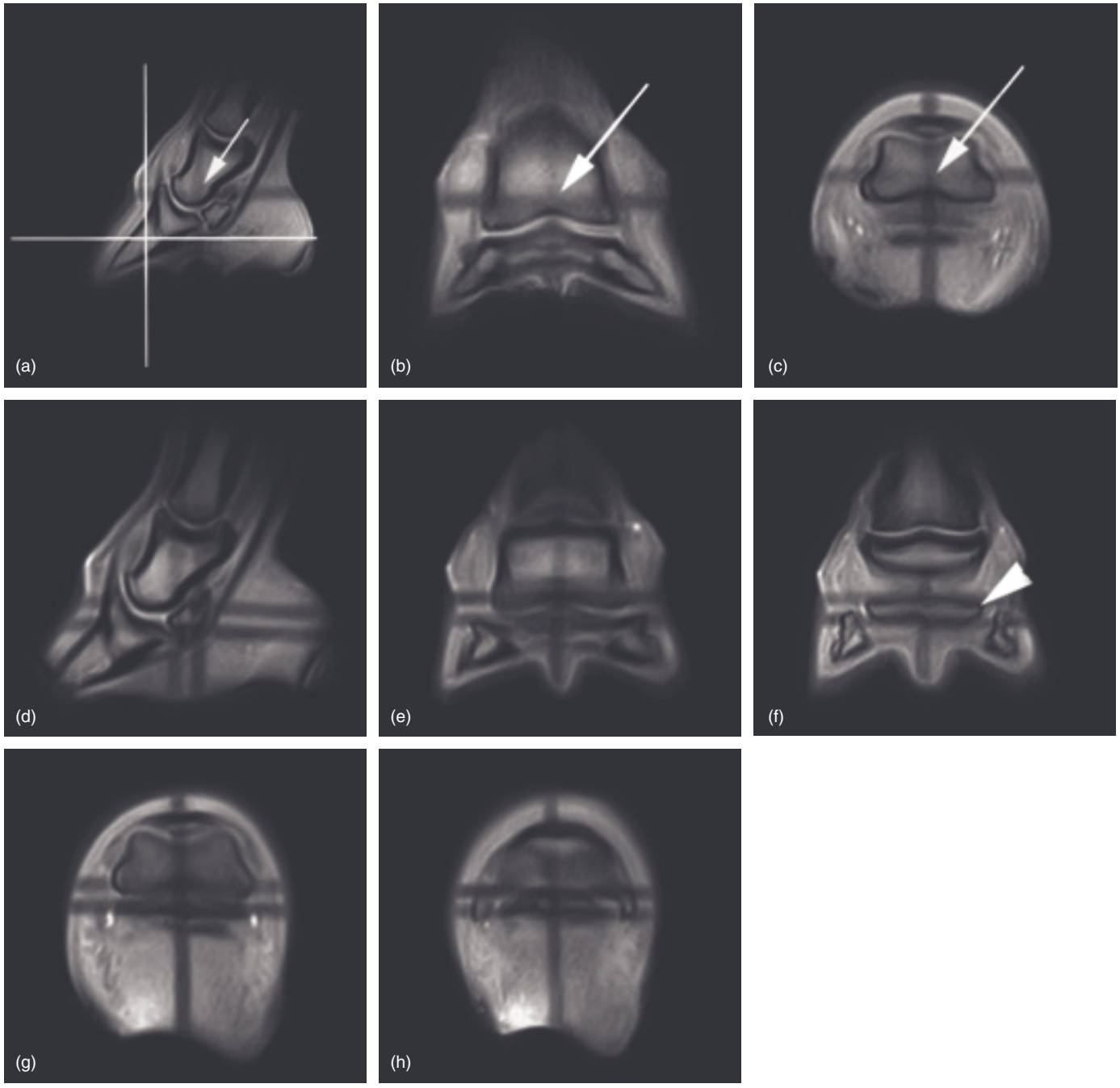

Figure 3.5 Pilot images are used to ensure that the anatomy and coil are placed in the isocentre of the magnet and provide the anatomic landmarks necessary for study planning. Using the Hallmarq system, a properly positioned three-plane pilot, designated by two black lines or cross hairs on the saggital image, provides one gradient-echo image in each of the imaging planes (a–c). The cross hairs on an image identify the position of the other two images in the remaining planes. In addition, the centre of the cross hairs (white arrows) identify the isocentre of the magnet and are overlying the palmar distal aspect of the middle phalanx. Centring on the foot in this manner maximizes image quality and fat suppression associated with the deep digital flexor tendon, navicular bone and distal interphalangeal joint. A five-plane pilot, designated by four lines on the sagittal image, will provide additional landmarks often required for study planning (d–h). When properly positioned, additional pilot images allow visualization of important landmarks, including the navicular bone (arrowhead) on the frontal plane images, which is essential for properly positioned transverse images. In a case where laminitis or a distal phalanx lesion is strongly suspected, in addition to the normal foot protocol, images should also be obtained with the cross hairs centred lower in the foot (white cross hairs on (a)).

the tissues (Figure 3.6). Pilot images are most often acquired using gradient-echo sequences making visualization of certain soft tissue structures challenging due to decreased contrast. Correct study planning requires that important landmarks can be visualized. If these landmarks cannot be seen on the pilot images because of positioning, the pilot should be repeated following repositioning of the limb. If, however, critical landmarks are not visible on the pilot images because of the type of sequence used, additional sequences are necessary to plan the study. The exact process used to accomplish this is system dependent. Accurate pilot images result from proper limb positioning and facilitate precise study planning. Precise study planning

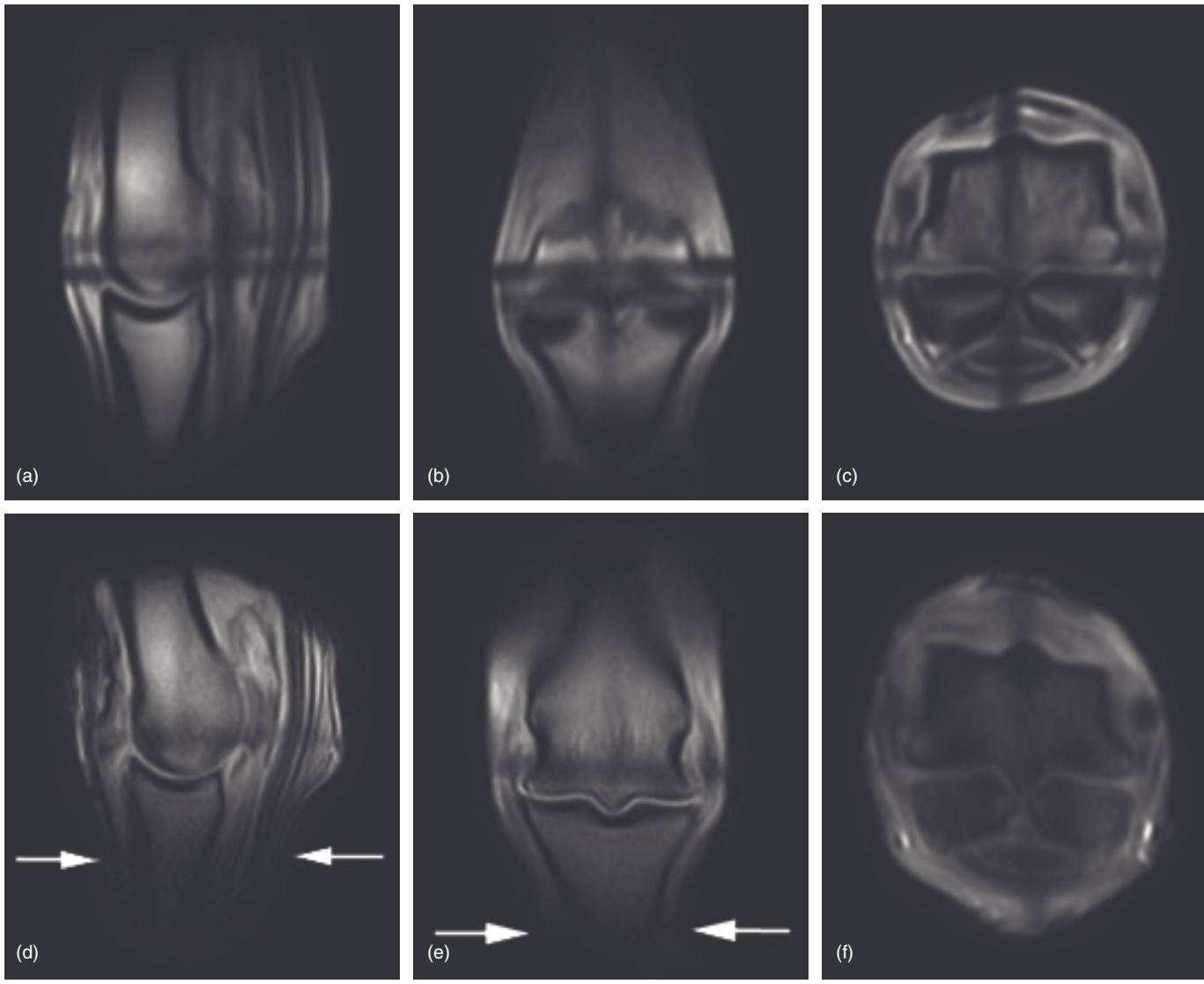

Figure 3.6 Pilot images from a fetlock study where both the coil and the area of interest are properly aligned with the isocentre of the magnet (a–c). The cross hairs should be centred in the palmar distal aspect of the third metacarpus. Both the distal aspect of the third metacarpus and proximal aspect of the first phalanx are well visualized on the images with minimal noise. In contrast is a second set of pilot images without proper coil placement (d–f). The anatomy is properly centred in the magnet as the cross hairs are over the distal palmar aspect of the third metacarpus. However, significant noise and signal drop-off are present in the proximal phalanx (arrows). The low signal intensity in the proximal phalanx is present because the coil is not centred relative to the isocentre of the magnet and this will result in poor image quality in this region of the study.

creates symmetrical, well-positioned images. Symmetry and correct positioning of images are the most important factors in determining the degree of confidence the reader has for assessing true findings versus artefact.

Regardless of whether the study is performed in a standing or anaesthetized patient, perfect positioning of the limb is not always possible. In recumbent horses the limbs tend to rotate. In standing horses the base-wide stance creates angulation of the limb and asymmetrical joint spaces due to compression of the joints on the side closest to the magnet. In addition, rotation is often present in standing horses. These difficulties with positioning of the limbs create challenges for study planning. With rotation or angulation of the limb, the slice cannot be oriented correctly for all the different levels of the anatomy. Adjustments in slice positioning may be required if rotation or angulation is detected on the pilot images (Figure 3.7). Often the important landmarks visible on the pilot images are located in the central aspect of the

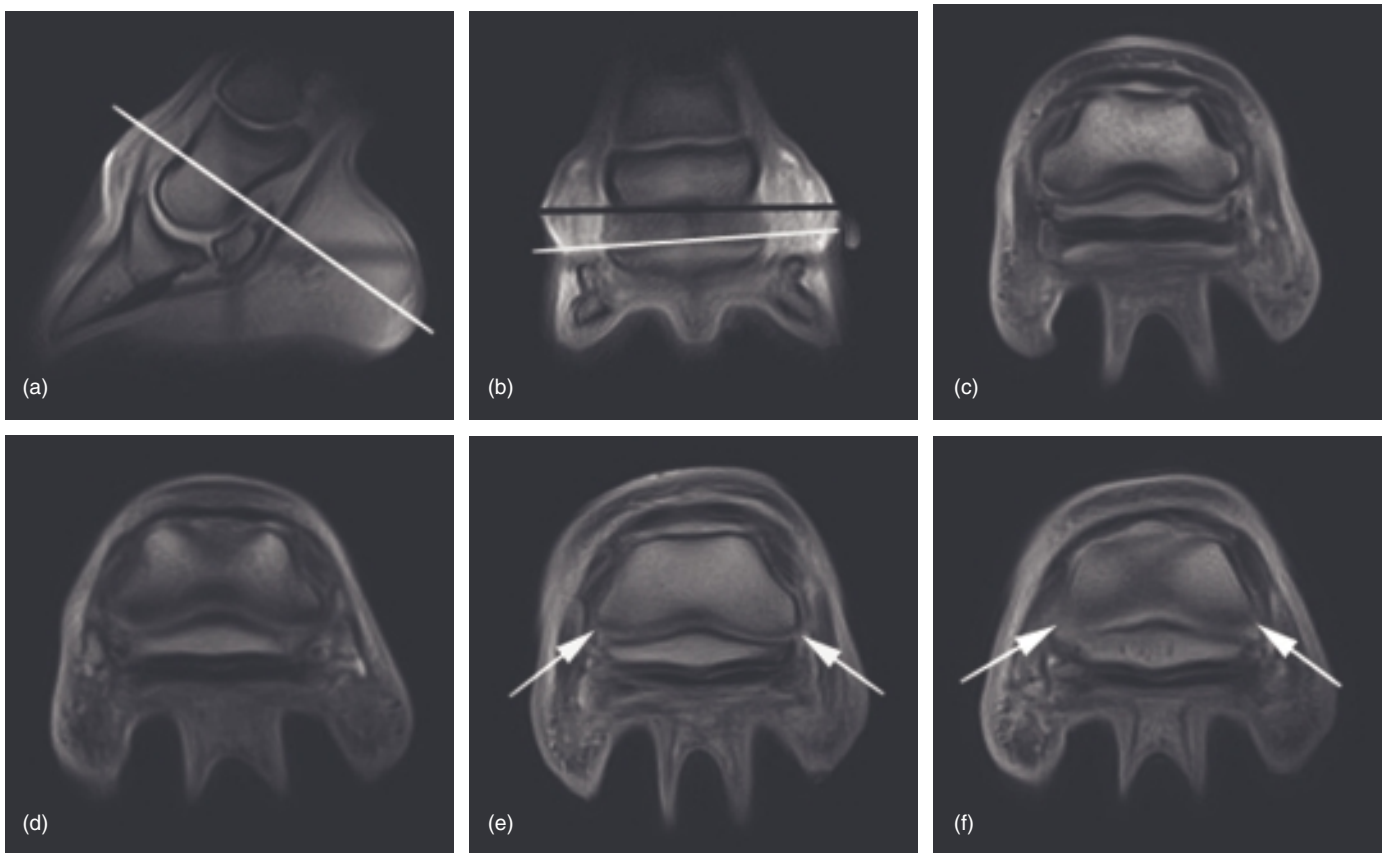

Figure 3.7 Sagittal and frontal pilot images of a foot acquired using the Hallmarq system (a, b). Transverse images are produced by positioning slices on the sagittal and frontal images. Most horses stand base wide in the magnet causing the limb to be angled on the frontal image (b). To produce symmetrically positioned transverse images (c, d) the slices should be aligned perpendicular to the long axis of the limb and parallel with the proximal and distal margins of the navicular bone as well as the distal interphalangeal joint on the frontal image (white line on (b)). Slices that are not positioned parallel to the long axis of the limb (black line on (b)) will produce oblique transverse images (e, f). Image obliquity can cause normal structures to appear abnormal, making image interpretation more difficult. Image obliquity is most evident in structures that rapidly change shape or at bone margins. The medial and lateral sides of the distal palmar aspect of the middle phalanx are asymmetrical (arrows on (e) and (f)) because the slices were produced from the angle shown by the black line on the frontal image. To decrease the effects of partial volume averaging on the transverse images, the slices should be oriented perpendicular to the structures of the interest on the sagittal pilot image (white line on (a)).

anatomy. Unfortunately, the degree of rotation or angulation of the limb is often not as apparent in the central aspect of a limb as it is in the periphery. Therefore, using the centrally located landmarks can create image obliquity even though the slice orientation appears correct on the pilot images.

Evaluation of the pilot images, or any images used for slice positioning, is very important prior to orienting the slices. Obliquity on the pilot images due to malpositioning of the limb must be recognized and attempts should be made to correct for this. Adjustments in slice orientation will be required if repositioning of the limb is not possible or will not be productive due to patient temperament. To detect abnormalities in position, areas that rapidly change shape should be selected and evaluated. In general, the central aspect of the anatomy is the least likely to show poor positioning of the limb or slices because those areas are more uniform in shape. Thus, assessment of the degree of obliquity, rotation or angulation on the images should be done in regions of the anatomy that rapidly change shape. These regions will most readily show imperfections in limb and image positioning. In general, the proximal and distal aspects of the bone have more shape changes than the mid-aspect of the bone. Soft tissue attachments or fossae also provide good landmarks. Once the slices are oriented, it is important to look through all the pilot images to determine how each slice lines up with the anatomy. If there is angulation or rotation, the slices and the anatomy will not consistently line up throughout the entire sequence. A compromise must be made between the proximal and distal, medial and lateral, or dorsal and palmar aspects of the anatomy. This is done while still prioritizing the areas that are of the most concern and only making adjustments with these principles in mind.

Planning each individual sequence in a protocol is accomplished by manipulating the position and orientation of the block of slices for that sequence. This should be done in a specific order to improve efficiency. First, rotate the slices to the appropriate orientation based on the structures that are the priority for that sequence. Place the block of slices over the anatomy of interest. Verify that the block of slices covers the structures of interest by evaluating the position of the block on all the pilot images or all the images used to plan that sequence. If necessary, make changes to the position of the block to cover the region of interest. The last step is to fine-tune the position of the slices. The margins of individual slices should be positioned to line up with specific structures of interest, decreasing the effects of partial volume averaging.

If adjustments in the position of the slice block will not completely cover the region of interest, add additional slices to the sequence or plan to do an additional sequence in that plane. When producing images using the Hallmarq Distal Limb MRI, the sequences have a preset slice block with a specific number of slices. In most cases, the number of allowed slices in the slice block will not cover the entire anatomic region. In general two slice blocks are required to completely cover the anatomy. In this circumstance, slices should be overlapped. Overlap of two slices in the central portion of the anatomy provides the greatest opportunity for differentiating artefact versus anatomy.

As part of the study protocol, images should be acquired in sagittal, frontal and transverse planes. When planning studies it is important to understand how each plane can be used to best position the desired images. In general, the desired image plane is produced using the two remaining planes. For example, sagittal images are produced by setting up the slice orientation on the frontal and transverse planes concurrently. Sagittal images are the easiest to position, and are minimally affected by obliquity in positioning. When positioning sagittal images from a frontal plane, the slices should be placed parallel to the long axis of the limb. When positioning sagittal images from a transverse plane, the slices should be parallel to medial and lateral cortices of the bones, and the position of the central slice should be separating the bone into two equal halves.

Obliquity due to slice positioning is easier to detect on frontal images compared with sagittal images. Producing frontal images that accurately represent the anatomy requires correct slice positioning on the transverse plane. If the slices are not properly prescribed on the transverse plane, the medial and lateral aspects of the anatomy will appear asymmetrical. Positioning frontal images on the sagittal plane requires prioritizing the structures of interest. Frontal images show joint surfaces as well a longitudinal view of many soft tissue structures. However, the bones and soft tissue structures can be angled slightly differently. Therefore, it may not be possible to have slices aligned parallel to both bone and soft tissue. Most often frontal images are oriented perpendicular to the joint surfaces, while the transverse images are oriented with the soft tissue structures as the priority. However, this can change depending on the joint. When positioning frontal images from a transverse plane, the slices should be placed parallel to the dorsal/cranial and palmar/plantar/caudal margins of the structures in the region of interest. When positioning frontal images from a sagittal plane, the slices should be parallel to dorsal/cranial and palmar/plantar/caudal margins of the osseous and soft tissue structures.

Transverse images most readily reveal obliquity in slice positioning. Evaluation of soft tissue structures is often the priority when positioning transverse images. Correct positioning of transverse images is a requirement for accurate assessment of the anatomy. Symmetry of the anatomy on a transverse image is determined by the positioning of the slices on the frontal plane. When planning transverse images from the frontal plane the slices should be placed such that they are perpendicular to the long axis of the bones and soft structures that are oriented parallel to the long axis of the bones. The slices should be oriented parallel with the joint surfaces and should cross the joint surfaces at exactly the same level on the medial and lateral aspects of the joint. The sagittal plane is used to visualize the structures of priority. On the sagittal plane the slices are oriented perpendicular to their dorsal/cranial and palmar/plantar/caudal margins creating true transverse images of the majority of soft tissue structures.

In addition to standard sagittal, frontal and transverse images, images positioned oblique to the standard planes are used to visualize important structures that are not oriented parallel or perpendicular to a limb. These structures are more susceptible to partial volume averaging due to their

orientation with images produced from the standard imaging planes. In this instance, the term oblique is used to describe a deviation in angle from the standard imaging planes, but the slices are still aligned with the anatomy to produce symmetrical images at non-traditional angles. Partial volume averaging should also be considered when planning a study because this artefact can prevent detecting abnormalities that are present on the first and last slice of a sequence. Structures of interest should not be placed in the first or last slice of a sequence unless additional sequences with overlapping slices are performed.

For each joint, specific landmarks should be established and consistently used when planning a study. These landmarks are selected by prioritizing the areas within the anatomic region that are most commonly injured. This consistency improves the MR studies in many different ways. Consistently using the same landmarks and evaluating the anatomy in relation to those landmarks improves the ability to make corrections for angulation and rotation of the limb that result from patient positioning. Using consistent landmarks creates similarity between studies making them more comparable for the reader, potentially allowing detection of less obvious structural abnormalities. This method of consistency in study planning creates a greater library of information for each hospital and is imperative for recheck examinations.

Image acquisition for specific regions

Foot study

The structures in the foot that have the highest incidence of disease on MR images are the navicular bone and the palmar soft tissues, so in the absence of information suggesting abnormalities at a different location, these structures are a priority when orienting slices during study planning for the foot (Figure 3.5). In addition, the collateral ligaments of the distal interphalangeal joint and the joint itself should also be considered when prescribing slice positions. When positioning the limb relative to the isocentre of the magnet, the navicular bone and the palmar soft tissues should be placed in the region of the field of view that has the best fat suppression. This positioning will ensure that the collateral ligaments of the distal interphalangeal joint and the joint have adequate fat suppression. This positioning may not provide good fat suppression in the distal phalanx. If complete fat suppression of the distal phalanx is desired, additional sequences with the central aspect of the distal phalanx placed at the isocentre of the magnet are required (Figures 3.3, 3.4 and 3.5).

Sagittal images are produced by aligning slices parallel to the midsagittal ridge of the navicular bone, and the medial and lateral cortices of the middle phalanx on transverse images. When positioning sagittal plane slices using frontal plane images, slices should be aligned parallel to the longitudinal axis of the limb. The central slice on the transverse and frontal images should be positioned such that it divides the bones into equally sized and shaped medial and lateral halves.

Frontal plane images are produced by aligning slices parallel with the navicular bone flexor surface and palmar margin of the middle phalanx on transverse images. In addition, the slices should be oriented such that they cross the medial and lateral aspects of the distal phalanx at the same level, creating symmetrical images. When orienting frontal plane slices using sagittal images, slices should be aligned parallel to the longitudinal axis of the limb, parallel to the dorsal and palmar margins of the middle phalanx, taking into account the dorsal and palmar margins of the deep digital flexor tendon. Alternatively, the slices can be oriented parallel to the navicular bone flexor surface.

Transverse images are produced by aligning slices parallel with the proximal and distal margins of the navicular bone and the distal interphalangeal joint on frontal images. Orienting the slices so that they cross the medial and lateral aspects of the middle and distal phalanges, as well as the navicular bone at the same level, determines the degree of symmetry on the images. Anatomic symmetry on images is important as it allows the reader to compare paired structures. When using the frontal images to align slices for transverse images, the proximal and distal margins of the navicular bone provide good landmarks. It is important to remember that the proximal aspect of the lateral wing of the navicular bone can be more prominent than the medial wing. The central aspect of the proximal margin of the navicular bone, excluding the proximal margin of the wings, provides the best landmark. This method will produce straighter images of the navicular bone and often correlates well with the orientation of the distal interphalangeal joint. When producing transverse images, slices on the sagittal image should be oriented perpendicular to the palmar soft tissues proximal to the navicular bone and the navicular bone flexor surface.

Fine-tuning of the slice positioning can be accomplished by aligning slice margins with the proximal and distal cortices of the navicular bone. The exact angle of the slices on the sagittal images will depend on the angle of the deep digital flexor tendon relative to the navicular bone. The conformation of the feet may dictate the need for additional sequences or a compromise between the two different angles. Horses with extremely low heels or club feet usually have greater disparity between the position of structures in the feet, such as the deep digital flexor tendon and navicular bone. Horses with rotational deformity, medial/lateral foot imbalance or a base-wide stance will have asymmetry in the position of the medial and lateral aspects of the limb relative to the main magnetic field. It is important in these cases to make sure that the slices are oriented as closely as possible to the standard imaging planes. If necessary, multiple slice blocks oriented at different angles can be used to correct for the asymmetry of the limb. A standard positioning protocol that takes into consideration the anatomic structures in the foot should be in place. However, the conformation and anatomy of each patient should be evaluated and adjustments made to slice orientation in order to keep the slices aligned with the important structures.

In the feet, the collateral ligaments of the distal interphalangeal joint and the impar ligament are best visualized using sequences angled specifically for their orientation. The collateral ligaments can be visualized in

parasagittal images. The slices can be oriented parallel with and perpendicular to the ligament margins, producing longitudinal and transverse images of the ligaments. These ligaments are often not well visualized on the pilot images because they are located at the periphery of the anatomy. In addition, these ligaments do not have contrasting signal intensity compared to the adjacent tissues on gradient-echo images. If the ligament margins cannot be well visualized on the pilot images or from a different sequence, slices oriented parallel and perpendicular to the solar margin of the distal phalanx will produce similarly oriented images. However, alignment of the collateral ligament margins relative to the solar margin of the distal phalanx for the purpose of slice positioning can be influenced by the conformation of the feet.

Additional steps are necessary to image the impar ligament due to its small size and normal fluid pattern resulting from the interdigitations of the distal interphalangeal joint. The impar ligament should be specifically visualized on the pilot images. The palmar margin of the impar ligament is usually parallel with the dorsal margin of the deep digital flexor tendon, which can also be used as a reference. To produce a true transverse image of the impar ligament requires positioning the slices perpendicular to the ligament on sagittal images. Frontal or transverse images are used to ensure the slices are symmetrical with the anatomy. The impar ligament is thickest on midline, so midline images will often provide the best view (Figure 3.8). After obtaining the correct perpendicular angle on the sagittal images, the sagittal images should be magnified so the proximal and distal margins of the ligament can be identified. A single slice should be positioned in the central aspect of the ligament. This slice should not contain any bone from either the distal phalanx or navicular bone. In low-field images, only one

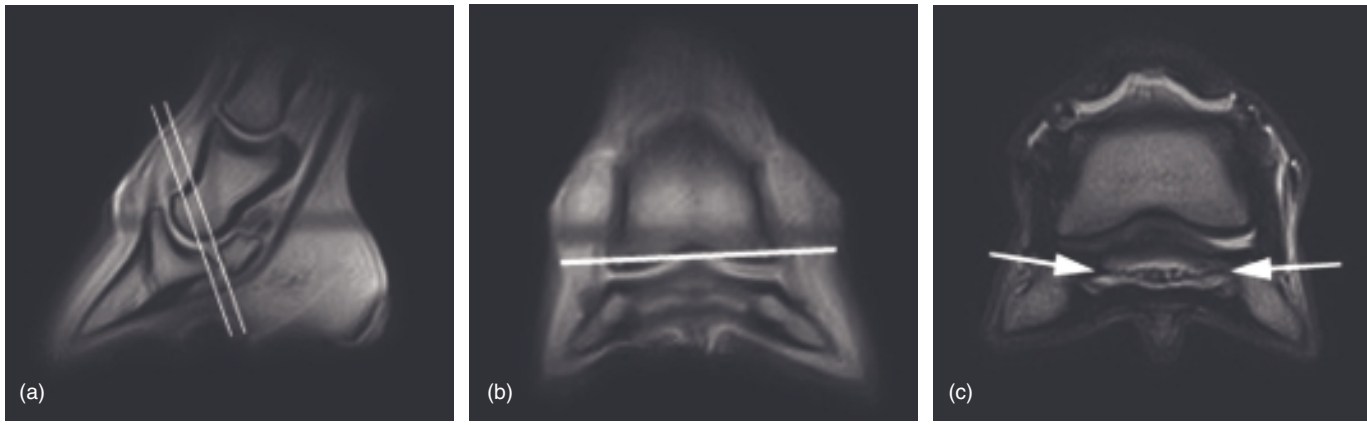

Figure 3.8 Sagittal and frontal pilot images of a foot to demonstrate slice positioning for the impar ligament. A midline sagittal image is used to provide the best opportunity to visualize the impar ligament. The margins of the impar ligament can be difficult to visualize on the gradient echo pilot images. The margins of the deep digital flexor tendon can be used for slice positioning as they are usually parallel with the impar ligament. The slices are angled perpendicular to the dorsal and palmar margins of the ligament. The correct medial to lateral orientation is determined on the frontal images. A single slice is positioned in the central aspect of the ligament, excluding any bone from either the navicular bone or distal phalanx (white lines on (a)). This slice positioning produces a true transverse image of the impar ligament, which has multiple small areas of fluid signal intensity resulting from the synovial invaginations of the distal interphalangeal joint and is thicker in the central aspect of the ligament compared to the medial and lateral aspects of the ligament which are thinner (c).

true transverse slice of the impar ligament is usually possible. Great care should be taken to ensure it is properly positioned.

Pastern study

In general, a pastern study should include the base of the sesamoid bones and continue distally to the middle of the middle phalanx. Sagittal images are produced by orienting slices such that the central slice on the transverse image divides the proximal phalanx into two equally sized and shaped halves. Positioning of sagittal slices using frontal images is done by orienting slices perpendicular to the longitudinal axis of the proximal and distal phalanges. The central slice on the transverse and frontal images should be positioned such that it divides the bones into equally sized and shaped medial and lateral halves.

Frontal images are produced by orienting slices parallel with the dorsal and palmar margins of the phalanges and palmar soft tissues on sagittal images. Using transverse images, frontal images are produced by orienting slices perpendicular to the dorsal and palmar margins of the phalanges and palmar soft tissues. The dorsal and palmar margins of the phalanges and palmar soft tissues structures usually have a similar orientation at the level of the pastern.

Transverse images are produced by orienting slices perpendicular to the longitudinal axis of the proximal phalanx on frontal images. Using sagittal images, transverse slices are oriented perpendicular to the dorsal and palmar margins of the proximal phalanx and the palmar soft tissues. When planning transverse images, special attention should be paid to the shape of the base of the sesamoid bones and the position of the origin of the oblique sesamoidean ligaments. The abaxial and dorsal aspects of the sesamoid bones are located proximal relative to the rest of the bone. The pilot images are usually centrally located so these images may not allow visualization of the oblique sesamoidean ligament origin. If the pilot images are centrally located and do not allow visualization of the oblique sesamoidean ligament origin, the slices should be positioned further proximally than apparently necessary, to make sure the oblique sesamoidean ligament origin is included on the transverse images. Transverse images should include one slice of the base of the sesamoid bones followed by the origin of the distal sesamoidean ligaments (Figure 3.9).

Fetlock study

Sagittal images are produced by orienting slices such that the central slice on the transverse image divides the third metacarpus or metatarsus and the proximal phalanx into two equally sized and shaped medial and lateral halves. Positioning of sagittal slices using frontal images is done by orienting slices perpendicular to the longitudinal axis of the third metacarpus or metatarsus, and the proximal phalanx such that the central slice divides the bones into two equally sized and shaped medial and lateral halves (Figure 3.6).

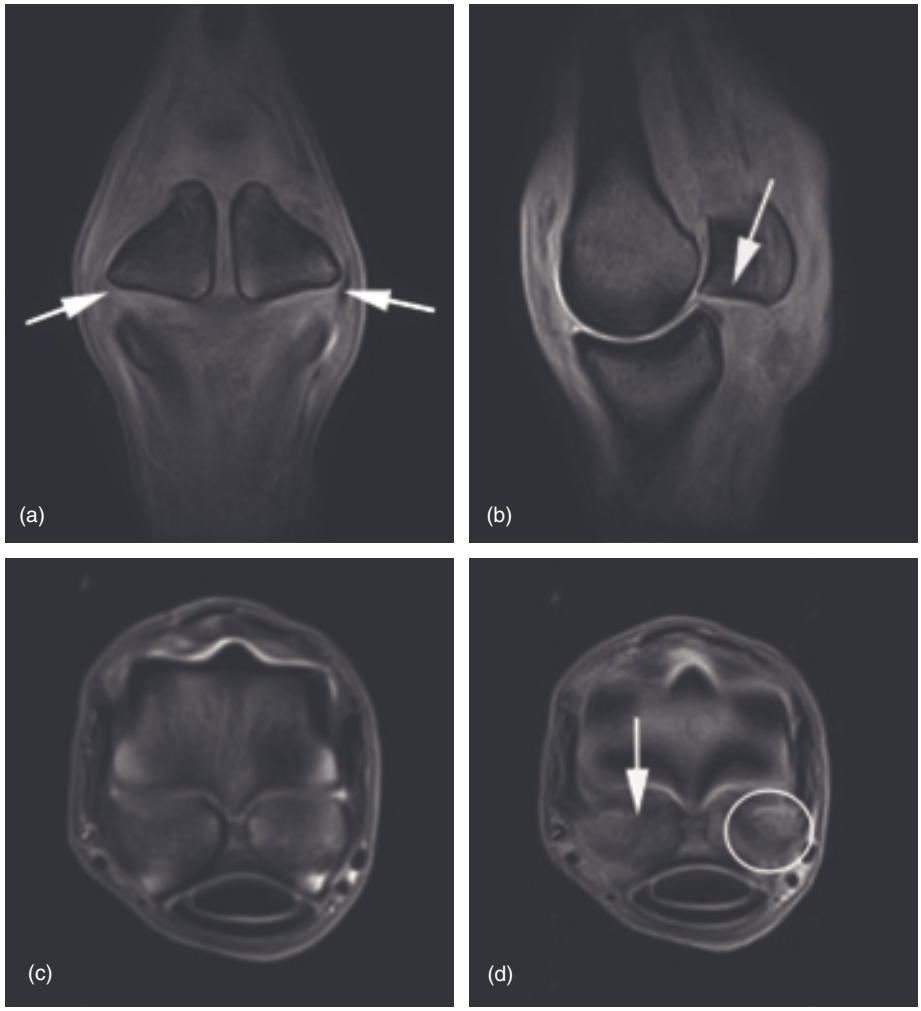

Figure 3.9 The technique for accurate slice positioning to ensure visualization of the origin of the oblique sesamoidean ligaments on transverse images. When planning transverse images, special attention should be paid to the shape of the base of the sesamoids and the position of the origin of the oblique sesamoidean ligaments. The abaxial and dorsal aspects of the sesamoid bones at the origin of the ligaments are located proximal relative to the rest of the bone (arrows on (a) and (b)). If the pilot images are centrally located and do not allow visualization of the oblique sesamoidean ligament origin (see Figure 3.6), the slices are positioned further proximally than apparently necessary to ensure that the oblique sesamoidean ligament origin is included on the transverse images. Transverse images should include one slice of the base of the sesamoid bones (c) immediately followed by the origin of the distal sesamoidean ligaments (d) to demonstrate the entire ligament has been imaged. On the transverse image of the origin of the oblique sesamoidean ligaments (d), the lateral ligament is outlined by a circle, while an arrow denotes the division between the axial margin of the medial ligament and the sesamoid bone.

Frontal images are produced by orienting slices parallel to the palmar or plantar margin of the condyles of the third metacarpus or metatarsus on transverse images. Using sagittal plane images, frontal slices should be oriented perpendicular to the distal articular margin of the third metacarpus or metatarsus as it articulates with the proximal phalanx.

Transverse images are produced by orienting slices parallel to the joint space on frontal plane images. Using sagittal plane images, transverse slices

are oriented perpendicular to the margins of the palmar soft tissues. In general, the soft tissues are parallel with the adjacent bone. The degree of extension of the joint is greater in a standing horse compared to an anaesthetized horse, resulting in a large disparity between the longitudinal axis of the metacarpus or metatarsus in relation to the proximal phalanx. Thus, two different sets of transverse images, positioned at different angles, should be obtained. This division between sets of images should occur at the level of the joint with a small amount of slice overlap. When planning transverse images, special attention should be paid to the shape of the base of the sesamoid bones and the position of the origin of the oblique sesamoidean ligaments as previously described in the pastern section.

Injury to the palmar or plantar aspect of the distal condyles of the third metacarpus or metatarsus commonly occurs in the fetlock, thus it is an important region to image accurately. The curvature of the distal aspect of the third metacarpus or metatarsus causes it to be extremely susceptible to partial volume averaging. Additional views oriented perpendicular to the palmar margin of the condyles will decrease partial volume averaging and show in greater detail the articular margins on the palmar aspect of the joint. Previously described transverse slice positioning will produce images that are perpendicular to the soft tissues as well as to the dorsal articular surface at the level of the third metacarpus or metatarsus. Previously described frontal slice positioning will produce images perpendicular to the distal articular surface of the third metacarpus or metatarsus. Therefore, both of these planes will already have maximized visualization of the joint surfaces in these regions.

The only remaining portion of the joint that may not be accurately imaged due to partial volume averaging is the dorsal distal aspect of the third metacarpus. If potential abnormalities are identified in this region on other imaging planes, additional views oriented perpendicular to the dorsal distal aspect of the third metacarpus or metatarsus may better characterize the findings.

Metacarpus/Metatarsus

A metacarpus or metatarsus study should begin at the distal row of carpal or tarsal bones. The distal extent of the study will be determined by the size of the horse and the blocking pattern. Sagittal images are produced by orienting slices such that the central slice on the transverse image divides the third metacarpus or metatarsus into two equally sized and shaped halves. Using frontal images, sagittal slices should be oriented parallel to the longitudinal axis of the third metacarpus or metatarsus. The central slice on the transverse and frontal images should be positioned such that it divides the third metacarpus or metatarsus into equally sized and shaped medial and lateral halves.

Frontal images are produced by orienting slices parallel to the margins of the suspensory ligament on sagittal images. The palmar or plantar margin of the third metacarpus or metatarsus should not be used to orient the frontal slices because it is not aligned with the margins of the suspensory ligament or the longitudinal axis of the bone. Use of this landmark results

in slice obliquity relative to the margins of the suspensory ligament and the carpometacarpal or tarsometatarsal joint. Frontal images are produced by orienting slices such that the central slice on the transverse image divides the third metacarpus or metatarsus into two equally sized and shaped medial and lateral halves.

Transverse images are produced by orienting slices parallel to the carpometacarpal joint and perpendicular to the margins of the suspensory ligament on sagittal images. Transverse images are produced by orienting slices parallel to the carpometacarpal joint and perpendicular longitudinal axis of the third metacarpus or metatarsus on frontal images. Transverse images of the opposite limb must be obtained for comparison in order to reliably evaluate the suspensory ligament. The nutrient artery can be well visualized and is a helpful anatomic landmark for the study planning.

It is important to remember that the fourth metatarsal bone is larger than the second metatarsal bone. This difference in size should be ignored when orienting slices on the transverse plane for production of sagittal and frontal images. Some degree of asymmetry will appear in correctly positioned images due to the difference in size between these two bones.

Carpus

A carpus study should begin at the distal aspect of the radius and end at the proximal aspect of the third metacarpus. If the primary concern is radial carpal bone disease, sagittal images are produced by orienting slices parallel to the margins of the radial carpal bone on transverse images. If the primary area of concern is the palmar soft tissues or central aspect of the carpus, sagittal images are produced by orienting slices perpendicular to the dorsal and palmar margins of the soft tissues on the palmar aspect of the carpus, or parallel with the margins of the centrally located osseous structures on transverse images. Positioning of sagittal slices using frontal images is done by orienting slices parallel to the longitudinal axis of the limb such that the central slice divides the distal aspect of the radius and proximal aspect of the third metacarpus into equally sized and shaped medial and lateral halves.

Frontal images are produced by orienting slices parallel to the longitudinal axis of the limb on sagittal images. If the limb is positioned straight in the magnet the slices will be parallel to both the dorsal margin of the carpus and the dorsal and palmar margins of the palmar soft tissues. Similar to sagittal images, planning of frontal images can vary depending on the primary area of concern. Alignment with the dorsal margin of the radial carpal bone on transverse images can be used to produce frontal images. However, this orientation will produce obliquity to the more centrally located osseous structures and palmar soft tissues. Alternatively, frontal images can be produced by orienting slices parallel with the dorsal and palmar margins of the palmar soft tissues in the centrally located osseous structures on transverse images.

Transverse images are produced by orienting slices parallel to the radiocarpal, middle carpal and carpometacarpal joints on sagittal images. Using frontal images, transverse images slices are oriented parallel to the

radiocarpal, middle carpal and carpometacarpal joints as well as perpendicular longitudinal axis of the limb.

Tarsus

A tarsus study should begin at the distal aspect of the tibia and end at the proximal aspect of the third metatarsus. The plantar soft tissues of the tarsus are located medially, adjacent to the calcaneal tuber. Therefore, the profile of the limb on transverse images does not necessarily provide the correct landmarks for slice positioning. When producing sagittal images, the margins of the osseous structures should be used for slice positioning on transverse images. Sagittal images are produced by orienting slices parallel to the medial and lateral margins of the talus at the distal aspect of the talocalcaneal ligament. At this level the depressions in the medial and lateral margins of the talus deep to the collateral ligaments creates flat surfaces that facilitate slice orientation. Positioning of sagittal slices using frontal images is done by orienting slices parallel to the longitudinal axis of the limb. Although the calcaneus is parallel with the longitudinal axis of the limb, rotation of the limb can cause confusion when planning a study. The lateral position of the calcaneus in conjunction with rotation of the limb can obscure the normal landmarks. In this case, the calcaneus should be ignored and the talus and distal rows of tarsal bone should be used to orient the slices.

Frontal images are produced by orienting slices parallel to dorsal margin of the central and third tarsal bones, as well as to the dorsal margin of plantar soft tissues distal to the curvature over the sustentaculum tali on sagittal images. If the primary area of concern is the tibiotarsal joint, slices should be aligned perpendicular to the joint space on sagittal images. Frontal images are produced by orienting the slices perpendicular to the medial and lateral margins of the talus.

Using frontal images, transverse images are produced by orienting slices parallel to the proximal and distal intertarsal joints as well as perpendicular longitudinal axis of the limb. Transverse images are produced by orienting slices parallel to the proximal and distal intertarsal joints on sagittal images.

A NORMAL MRI STUDY IN A LAME HORSE

In certain cases lameness will be localized to an anatomic region and the images will not reveal any abnormalities consistent with the clinical findings. What possibilities should be considered in these cases? The possibilities are numerous and all should be considered and correlated with the history and clinical findings. First, the lesion could be located outside the field of view of the study. As we continue to learn more about the localization of lameness using regional analgesia, it must be considered that the lesion is not located within the imaged anatomy. Second, structures or tissues that are not well visualized on low-field images should be considered. Articular cartilage is thin and difficult to resolve on low-field images. Injury to the articular cartilage should be considered in these cases. In certain joints, such as the fetlock joint, injury to the articular cartilage usually results in

abnormality in the adjacent bone. However, this is not necessarily the case in every joint. The distal interphalangeal joint can have extensive articular cartilage damage without abnormalities in the adjacent subchondral or trabecular bone. Therefore, the absence of osseous abnormalities on a study does not necessary preclude articular cartilage damage, depending on the joint imaged. Third, laminitis without substantial laminar thickening or rotation should be considered in these cases. Normally, the distal phalanx and the laminar tissue have a marked vascular pattern with extensive regions of increased signal intensity on STIR images. Moderate to severe injury, such as fluid accumulation or findings associated with disruption of the vasculature, in the periphery of the distal phalanx and the laminar tissues would be required to produce a detectable change in signal intensity on low-field images.

Many different lesions likely exist that we do not yet recognize on MR studies. Neuritis and nerve impingement are commonly identified as a clinically significant findings on human MR studies. Certain stages of injury have also not yet been recognized. Ligaments normally have a varied signal pattern. How much variation in the signal pattern of the collateral ligament of the distal interphalangeal joint indicates clinically significant pathologic change? Sole bruising or pain in the digital cushion is diagnosed in equine patients but is yet to be described on MR images. Is this source of pain detectable on MR images? Scarring of tendons and ligaments is reported by human patients to be quite painful. Mature scar tissue has low signal intensity on MR images and can be difficult to diagnose if it is not associated with changes in size or shape of the affected structure. This is also a concern in cases where no pathologic change is identified. Small or low contrast lesions that are divided between two slices represent yet another situation that may not be detectable on low-field images. It is difficult to determine the significance of these findings that cannot be recognized. Therefore, we must make every attempt to continue to compare high-field and low-field studies, as well as correlate lesions identified with physical exam findings.

REFERENCES

[1] Bushberg JT. Magnetic resonance imaging (MRI). In: *The Essential Physics of Medical Imaging* (vol. 1, edn 2). Philadelphia, PA: Lippincott, 2002, pp. 415–67.
[2] Bushberg JT. Nuclear magnetic resonance. In: *The Essential Physics of Medical Imaging* (vol. 1, edn 2). Philadelphia, PA: Lippincott, 2002, pp. 373–413.
[3] Gluckert K, Swoboda B *et al.* Comparison of low-field (0.2 Tesla) and high-field (1.5 Tesla) magnetic resonance imaging of the knee joint. *Arch Orthop Trauma Surg* 1995; **114**: 281–6.
[4] Peroni JF, Horner NT *et al.* Equine thoracoscopy: normal anatomy and surgical technique. *Equine Vet J* 2001; **33**(3): 231–7.
[5] Cruz AM, Kerr CL *et al.* Cardiovascular effects of insufflations of the abdomen with carbon dioxide in standing horses sedated with detomidine. *Am J Vet Res* 2004; **65**(3): 357–62.

Chapter 4
Image interpretation and artefacts

Rachel Murray and Natasha Werpy

INTRODUCTION

Magnetic resonance imaging (MRI) produces large amounts of data, which can provide detailed diagnostic information, but may also be very confusing to understand. There are many artefacts and variations that can confuse the interpreter, and need to be understood, so a basic knowledge of MR physics is important. A wide range of contrasts and detail can be produced using different pulse sequences, so the same tissue may appear very different on images acquired using different acquisition parameters. It is therefore important for the interpreter to be aware of, and understand, these variations, including the idiosyncrasies of any particular imaging system. Skill in image acquisition is also essential, because image obliquity, artefacts and poor positioning in the magnetic field can cause considerable problems with image interpretation. Any MR system has advantages and limitations, so an understanding of the features of the MR system used to acquire images is important in order to make judgements during image interpretation.

The high degree of anatomical detail visible on MR images makes an in-depth knowledge of tissue structure and tissue inter-relationships essential for the interpreter [1]. The wide range of normal anatomy within the horse population means that experience in reading equine images and use of concurrent clinical diagnostic evaluation is crucial for determining the significance of a potential lesion [2].

MAGNETIC RESONANCE IMAGE APPEARANCE

MR images are produced in a grey scale with a varying range of contrasts that are the result of level of signal intensity. The appearance of a tissue is affected by its nature, the MR system, pulse sequence and acquisition parameters. When a tissue is injured, changes in tissue structure, biochemical composition or water distribution result in alterations in the MR image appearance [3–6].

Signal contrast is created from tissue properties based on the proton density and relaxation processes of spin-lattice (T1) relaxation and spin-spin (T2) relaxation [3, 4]. The mobility and density of hydrogen nuclei in the tissue are therefore important in determining its appearance on MR images. Overall, most MR signal in the patient is derived from fat and water, where hydrogen nuclei are abundant and freely mobile. Structures that have few

Equine MRI, edited by Rachel C. Murray.

hydrogen nuclei or where the nuclei are tightly bound produce very little or no signal, which is why cortical bone and tendon generally appear as black on an image.

By manipulating the echo time and repetition time of the pulse sequence, contrast in the images can be determined by proton density (PD), T1 and T2 properties to different extents. For images referred to as T1 or T1-weighted images, contrast is dependent mainly on T1 relaxation properties. For images referred to as T2 or T2-weighted images, contrast is dependent mainly on T2 relaxation properties, and for PD or PD-weighted images, contrast is dependent on the proton density or number of mobile hydrogen nuclei in the tissue. A tissue may therefore have a different appearance on T1, T2 and PD images [3–6] (Figure 4.1).

Fluids have long spin-lattice relaxation times (T1), while fat-based tissues have short T1. On T1-weighted images, water therefore appears dark unless it is moving fast. Water-based tissues are mid-grey, the position on the grey scale being determined by the water content along with the other constituents of the tissue and parameters used during image acquisition. In contrast, fat-based tissues are very bright (Figure 4.1). T1-weighted images usually have good anatomical detail. Tissue with higher water content, oedema or increased capillary content due to injury or disease will appear darker than the surrounding normal tissue. Consequently fluid-based damage to medullary bone will generally appear as an area of lower signal intensity compared to normal fat-based marrow tissue, which has intermediate to high signal intensity.

On T2-weighted images, fluid appears bright. Water-based and fat-based tissues have intermediate signal intensity (Figure 4.1). T2-weighted images often have less anatomical detail than T1-weighted images, but can be very useful in detection of fluid-based pathology, including oedema and inflammation. Fluid-based pathology can be clearly detected as areas of high signal intensity against darker normal tissue. However, if there is increased fluid content in a fat-based tissue such as medullary bone, it can be difficult to detect a difference in signal intensity between normal fat-based tissue and fat-based tissue with pathological fluid using T2-weighted images. The sequence parameters used to acquire the images will dictate whether fluid can be detected in fat-based tissues on T2-weighted images. Sequence parameters can be adjusted to improve the detection of fluid in fat-based tissues.

Fat is generally shown as high signal intensity on MR images, except for some T2 spin-echo sequences. To detect the presence of pathologic fluid in fat-based tissues it is useful to suppress the fat signal. Suppression of the fat signal makes fat or fat-based tissues appear as low signal intensity on images. This allows the interpreter to differentiate high signal from fluid within the tissues or fat. For some tissues, such as bone marrow or cancellous bone, pathologic change is frequently fluid based so it is important to include sequences utilizing fat suppression as part of a routine scan protocol. When fat-suppression techniques are used, medullary bone is difficult to differentiate from adjacent cortical bone as they both have low signal intensity on the images (Figure 4.2) [1–6].

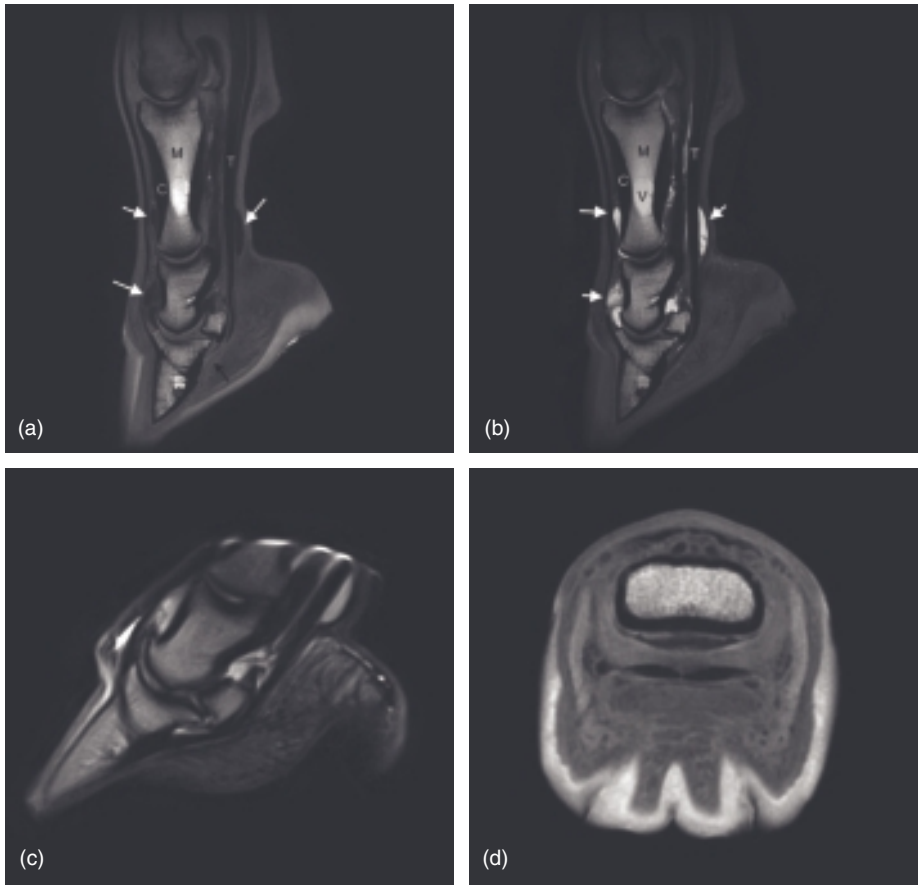

Figure 4.1 Images of different weightings have different appearance and contrast. (a) Sagittal plane T1 gradient-echo high-field image of the foot and pastern of a horse. There is marked distension and synovial proliferation in the proximal and distal interphalangeal joints and effusion within the digital flexor tendon sheath. There is also increased dorsal laminar thickness distally, in conjunction with slight distal rotation and modelling of the tip of the distal phalanx. On T1-weighted images, synovial fluid has very low signal intensity (white arrows). The fibrotic synovium separating the dorsal pouch of the distal interphalangeal joint is of relatively higher signal intensity. Cortical (C) and subchondral bone have very low signal intensity. Tendons should have homogeneous low signal intensity (T). Magic angle effect in the distal deep digital flexor tendon gives artefactual high signal intensity within the tendon, which is particularly evident on short TE sequences (black arrow). The distal aspect of the normal straight distal sesamoidean ligament has heterogeneous signal intensity (white arrow), probably associated with the cartilaginous tissue within this part of the ligament. The cancellous bone (M) has high signal intensity while articular cartilage has a moderate to high signal intensity, clearly marginated by the synovial fluid. (b) Sagittal plane T2* gradient-echo image of the same limb. The synovial fluid in the proximal and distal interphalangeal joints, the navicular bursa and digital flexor tendon sheath has high signal intensity (white arrows), as does the nutrient foramen/vascular channels within the bone. The fibrotic synovium has lower signal intensity than the surrounding synovial fluid. Bone marrow/cancellous bone has relatively slightly lower signal intensity than on T1-weighted images, but remains moderately high signal intensity (M). The tendons (T) and cortical bone (C) have very low signal intensity, similar to other imaging sequences. The magic angle effect is less prominent in this sequence, but still visible near the insertion of the deep digital flexor tendon. (c) Sagittal T2 fast spin-echo image obtained standing in a low-field MR imaging system. As the patient's foot was very large and extended beyond the ideal imaging portion of the magnet, the edges of the image have some distortion. (d) Transverse T1 gradient-echo high-field image at the level of the collateral sesamoidean ligament. Note the synovial fluid has within the distal interphalangeal joint has low signal intensity.

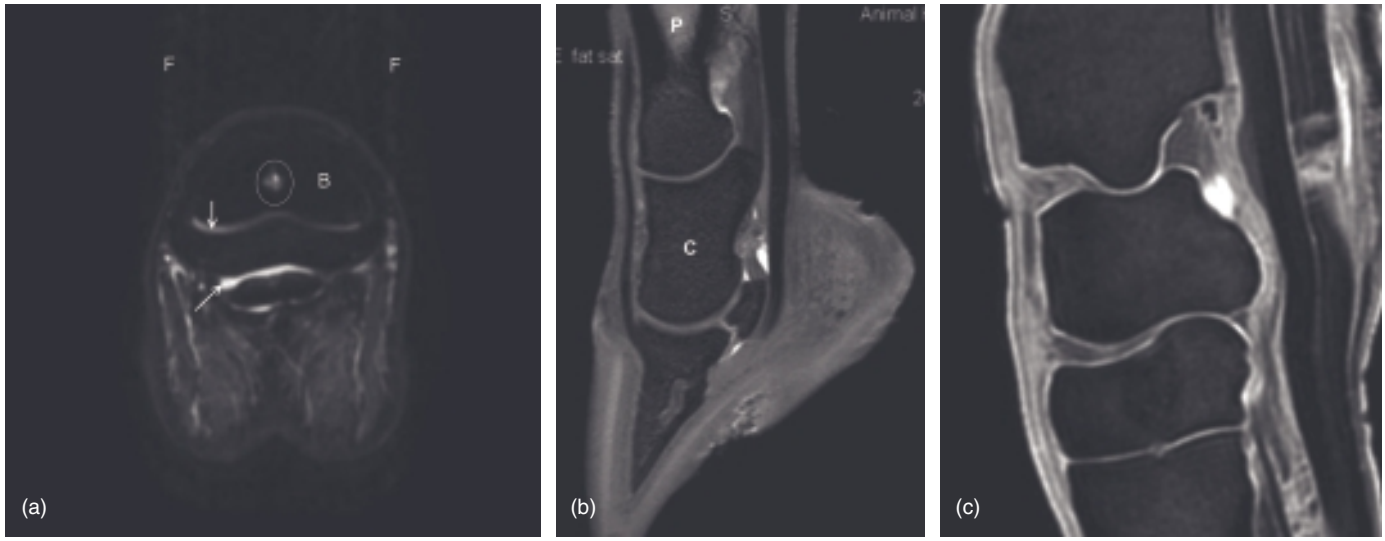

Figure 4.2 Fat-suppressed images. (a) Transverse STIR (short τ inversion recovery) image of a non-lame limb at the level of the proximal interphalangeal joint, in an anaesthetized horse in a 1.5 T MR imaging system. Fat suppression results in low signal intensity throughout both the cancellous (B) and the cortical bone, so any fluid present in the cancellous bone can be visualized without being masked by a high fat signal. The high signal of an osseous cyst-like lesion (circle) and of synovial fluid in the proximal interphalangeal joint and the digital flexor tendon sheath (white arrows) is clearly seen as these images have high contrast, but there is relatively lower resolution than in three-dimensional gradient echo images. A flow artefact from the digital vessels is present in the phase direction, running vertically in this image (F). (b) Sagittal T2 fat-saturated high-field image of a normal foot. There is low signal intensity throughout the cortical and cancellous bone, similar to the STIR image, but it is of higher resolution and shows structures in more detail. It may be difficult to get homogeneous fat suppression in some anatomical sites, such as the proximal phalanx, which is seen as higher signal intensity (P) than the more distal bones in this image (C). (c) Sagittal T1 fat-saturated high-field image of the carpus. Fat suppression can be useful for improving contrast with articular cartilage as well as detection of bone marrow lesions.

IMAGE ACQUISITION TO OPTIMIZE INTERPRETATION

The positioning of the patient and region of interest within the scanner will influence image appearance, as will the imaging parameters. It is important to obtain and analyse images in three planes and to ensure that images are set up taking into account all three planes of the localizer images to minimize obliquity.

Positioning of the patient within the scanner to allow the area of interest to be placed at the isocentre of the magnet is necessary to optimize image quality. Careful orientation of slices during study planning of a standardized protocol is very important to optimize assessment of anatomical structures. In addition to the images obtained using a standardized protocol, it may be necessary to acquire higher resolution images of a smaller, specific area, or to obtain images in an additional plane. These methods can be used to improve interpretation or provide specific answers to a particular query that arises during imaging. Obliquity in image acquisition can be very misleading as the shape, size and appearance of the structure can be altered by image obliquity (Figure 4.3). Post-processing manipulation of 3D images can be used to eliminate the image obliquity, but at the expense of image quality, as the best resolution occurs in the original acquisition plane. If a horse has marked conformational misalignment, then it may be difficult to avoid obliquity in a part of the region of interest, especially when planning transverse images. However, acquiring transverse images in more than one orientation

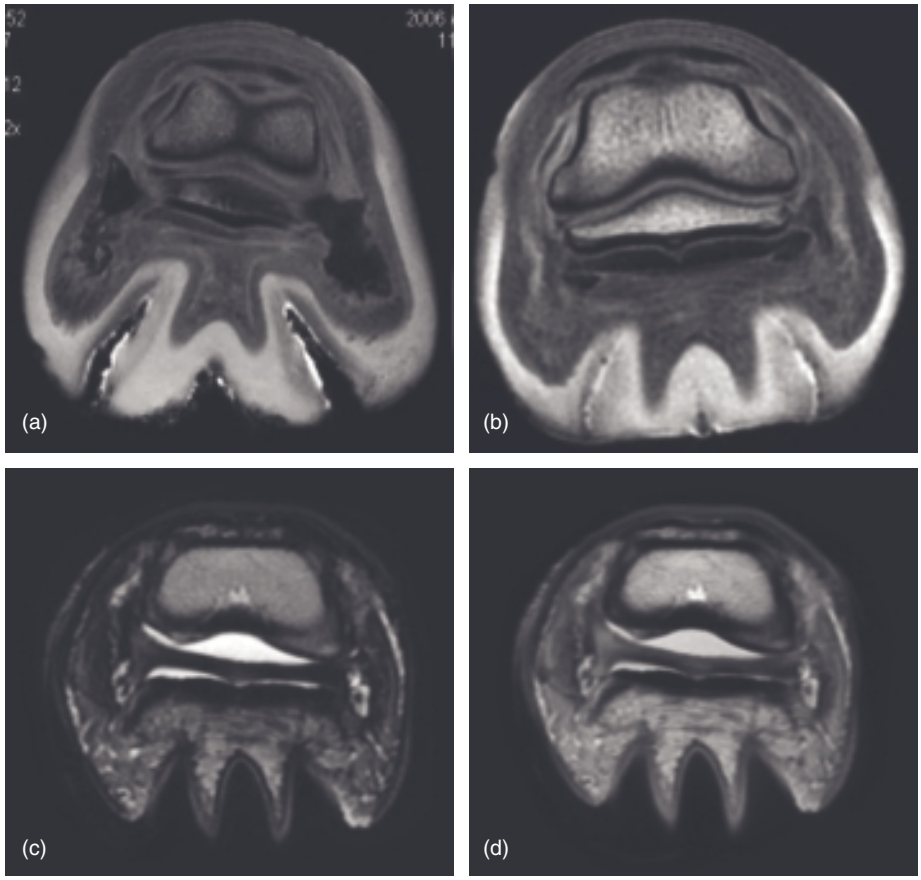

Figure 4.3 (a) Transverse T1-weighted image of the foot at the level of the distal interphalangeal joint collateral ligaments and palmar processes of the distal phalanx. There is obliquity of the image which makes it difficult to evaluate the integrity of the collateral ligaments and deep digital flexor tendon. However, there is abnormal low intensity in the palmar processes which is evident despite the image obliquity. (b) A straight image obtained at the same level makes is easier to assess structures within a limb. Shape and size of tendons and ligaments is generally symmetrical within a limb and between limbs, unless there are conformation features associated with altered biomechanical loading directions. (c) Transverse T2 fast spin-echo image at the level of the collateral sesamoidean ligament. The ligament appears asymmetric, which is an artefact related to oblique image acquisition. (d) Proton density images at the same level and location as (c), demonstrating the same image obliquity.

over different parts of the area of interest can be used to overcome this problem.

Use of different pulse sequences for imaging the same area provides more information about the anatomical and pathological features of the tissues [1, 2]. Routine use of T2-weighted, T1-weighted and/or proton density and fat-suppressed images at each site is beneficial for interpretation [1, 8–10]. Slice matching, which occurs when slices in each plane are identically positioned during study planning, provides the most information when comparing different sequences. This should be done during study planning whenever possible and cannot be accomplished if the patient moves during the course of the study. Use of particular imaging sequences for specific regions or suspected pathology can add further information [5, 6, 11–13]. Use of a mixture of high-resolution and lower-resolution scans allows

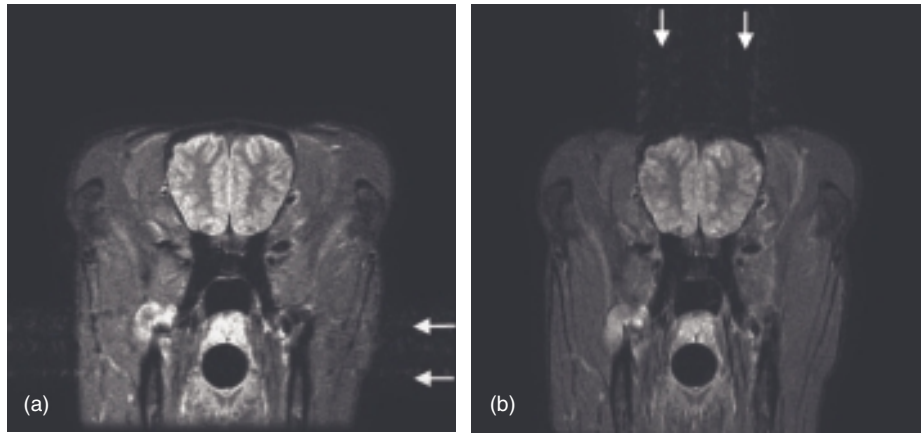

Figure 4.4 Transverse STIR images of the head. There is a flow artefact from the large arteries oriented in the phase direction, which may obscure structures that need to be assessed. (a) The frequency direction is vertically and the phase direction is horizontally so the flow artefact is seen running across the image (arrow). (b) In this image, the phase-frequency directions are reversed so the flow artefact runs vertically over the image (arrow), so interfering with the appearance of different structures.

coverage of a greater area and may be used to improve contrast. However, it may be necessary to focus on improved detail at particular locations within the area of interest.

Magnetic field homogeneity, which dictates the quality of the images and reliability of the fat suppression obtained during a study, is best in the centre of the field of view and is lowest along the peripheral margin. Therefore, it is important to centre the structures of particular interest in the centre of the field of view to maximize all aspects of image quality. Artefacts from blood flow and motion should be considered when selecting phase and frequency directions during study planning. Typically, the phase direction is dorsal to palmar on transverse images to avoid flow artefact crossing the soft tissues on the palmar aspect of the limb due to the high incidence of injury in this region. However, unusually located injuries could then have overlying flow artefact. In any case where phase direction artefacts could be obscuring pathologic change, it is useful to acquire additional scans with the phase and frequency directions reversed (Figure 4.4). This will remove the artefact from the area of interest.

ARTEFACTS

Artefacts can occur commonly in MR images [3, 4]. These can be caused by patient-related factors, acquisition technique, nature of MR imaging and imperfections in the design of any MR system, for example a lack of uniformity in the magnetic field of the MR scanner or a slight variation between the pulse programming and pulse produced. Occasionally they can result from equipment failure. Causes of artefacts can be classified into motion, magnetic field inhomogeneity and digital imaging artefacts. Motion artefacts generally result in ghosting, or repeated picturing of a structure throughout the entire image. Inhomogeneity artefacts lead to image distortion or altera-

tions in signal intensity. Digital imaging artefacts relate to the methods of data manipulation during processing.

Motion artefacts

Movement during the acquisition of MRI data may be due to gross patient motion or physiological motion, such as respiratory motion or pulsatile movement in vessels. It results in blurring of margins or ghosting, the repetition of a single structure multiple times across the image (Figure 4.5). Gross patient motion can occur in an anaesthetized patient, but is more likely to cause a problem in a standing, sedated patient where there may be sway or voluntary movement. Continuous movement leads to generalized blurring of the image, which may render the entire scan non-diagnostic. However, subtle movements may only result in a small amount of image ghosting with the majority of the study remaining adequate, at which point it is important that these image ghosts or blurring of margins are not misinterpreted as alterations within the tissues.

The most effective way to avoid motion artefacts is to minimize motion of the area of interest. This can be achieved by padding and immobilizing the region in an anaesthetized horse, but it presents more of a challenge in the sedated patient. In the Hallmarq standing MR system, motion insensitive scans have been developed to minimize the effects of small movements in a sedated horse [14]. These scans use navigator echoes [15] within the imaging pulse sequence to monitor patient motion during data acquisition. If patient motion is detected, the image slices can be repositioned and/or data segments can be reacquired in real time. Essentially, these motion insensitive scans allow the system to acquire data only when the horse is stationary. This has made it practical to acquire images with minimal motion artefact in the standing horse up to and including the level of the carpus or tarsus. The trade off for minimizing artefact is generally a longer scan acquisition time if there is continual movement of the area of interest. Unfortunately, despite these technical advances, large movements and the horse walking out of the scanner cannot be accounted for!

Physiological motion that is most likely to affect images in equine orthopaedic or head scans is due to respiration and blood flow [1, 2, 11]. These

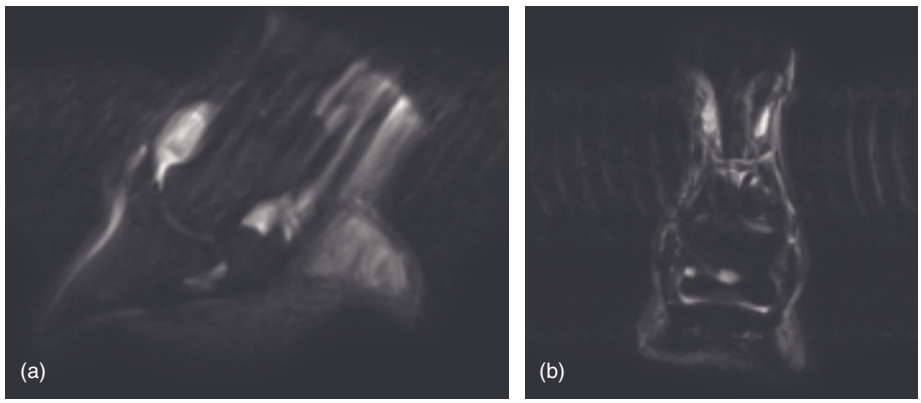

Figure 4.5 Motion artefact. (a) Gross patient movement under sedation in a standing low-field system results in ghosting or repetitions through this sagittal STIR image of a horse's foot. Marked distension of the distal interphalangeal joint is evident despite the artefacts, but it is difficult to evaluate other structures. (b) In an anaesthetized horse in a high-field system, movement of the chest during respiration leads to movement of the forelimbs which needs to be minimized through positioning and control of ventilator movement.

motion artefacts show as multiple ghost images in the phase-encoding direction. Respiratory motion is most likely to be a problem when scanning the forelimbs of anaesthetized patients because respiratory chest movement causes large displacements of the upper forelimb during imaging. However, the lower forelimb and hind limbs may also be affected. Motion can be minimized by weighting the limb with sand bags or reducing respiratory excursion by avoiding mechanical ventilation. Alternatively techniques such as respiratory compensation (or phase reordering) or respiratory triggering (or gating) can be used, but these can prolong scan times considerably and may not always improve image quality.

Moving protons in blood vessels cause artefacts by two effects [3–6]. Ghost images of both arteries and veins occur in the phase-encoding direction, and result from movement of the protons through the vessels. The direction of flow does not alter the direction of the artefact. In-flow (or time of flight) effects occur due to replacement of protons within the imaging portion during the repetition time, and cause a particular problem in gradient-echo sequences where the blood is seen as high signal intensity. Use of flow compensation options or saturation bands during image acquisition can reduce the effect considerably. However, it is important to be aware of the position of vascular structures relative to particular tissues of interest during scan acquisition and to ensure that any flow artefact in the phase-encoding direction will not affect the appearance of the particular tissues of interest. If there is a query or concern over a flow artefact, it is most useful to reacquire the images with the phase and frequency directions reversed so that the flow artefact runs in a direction perpendicular to that in the original images (Figure 4.4).

Magnetic field inhomogeneity artefacts

To create diagnostic images, MR systems need as homogeneous a magnetic field as possible. Field heterogeneity can lead to distortions and artefacts, so it is important that routine shimming of the magnet is done to improve magnet homogeneity and reverse these effects. Temperature fluctuations can affect homogeneity and should be avoided within the scan/MRI room housing the magnet. Metal within the magnet will be attracted to the magnetic field, creating inhomogeneities within the field. This metal in the magnet can also be a source of heat and potentially burn the patient. Magnetic susceptibility or metal artefacts severely distort the image. These occur because metals create large magnetic field inhomogeneities around them, and are more severe on gradient-echo than spin-echo sequences. Metal artefacts are seen as an area of zero signal, often with a high intensity rim and distortion in adjacent tissues (Figure 4.6). Magnetic susceptibility artefacts are generally less severe, with reduced and not necessarily zero signal, and adjacent geometric distortion may be absent, for example in an area of haemosiderin deposition (Figure 4.6).

It is therefore essential that any metal is removed from the patient or any equipment located near to the patient. For example, a head collar with metal fittings would be a particular problem during scanning of the head,

but would also have safety implications when another area is being scanned. Steel toecap boots positioned near the scanner may distort the image, so a handler of a horse being imaged standing needs to be aware of their positioning and footwear. Shoes and nails should be removed from the limbs of the horse that are being placed inside the magnet. For foot studies, nail fragments must be removed from the feet and dirt cleaned from the sulci

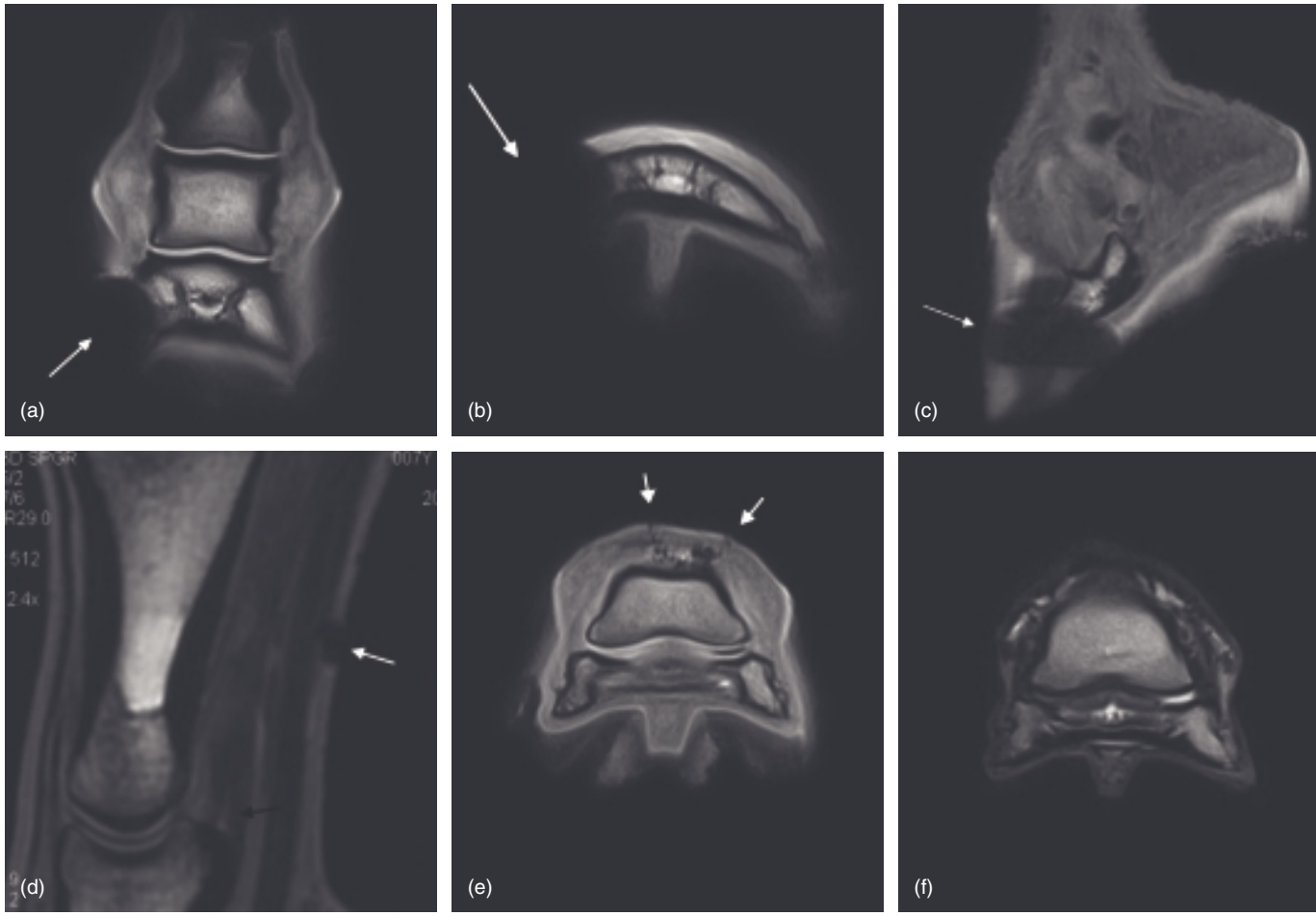

Figure 4.6 Magnetic susceptibility artifacts. (a) Low-field dorsal plane T1 gradient-echo image of the foot. A nail fragment left in the hoof wall leads to considerable distortion of the magnetic field and image. This is seen most obviously on gradient-echo scans of the foot, where there is complete loss of the image around the fragment and distortion of the structures adjacent to the signal void. (b) Transverse T1 gradient-echo image of the same foot as (a). (c) High-field sagittal plane T2* gradient-echo image of a foot with a magnetic susceptibility artefact (arrow), likely nail residue in the hoof wall. No metal was visible on radiography of the area. (d) High-field sagittal plane T1 gradient-echo image of the pastern region. There is a magnetic susceptibility artefact on the skin (white arrow), which was lost from the image after washing the area. Note the high signal intensity within the insertion of the straight distal sesamoidean ligament, which represents presence of cartilaginous tissues within the ligament. (e) Low-field, transverse plane T1 gradient-echo image of the foot of a horse with no history of lameness attributable to the distal interphalangeal joint. There is haemosiderin deposition within the distal interphalangeal joint, located in a triangular pattern consistent with previous arthroscopic surgery. Haemosiderin may remain within the tissues for months and years after trauma. Metal shavings may also be deposited following arthroscopic surgery which will create a similar artefact. Surgery in this horse had taken place more than 3 years prior to MR imaging of the region. (f) T2 fast spin-echo image of the same foot as (e). The haemosiderin is difficult to visualize in the FSE scan because it is less sensitive to magnetic field inhomogeneities than a gradient-echo scan. (g) Fat-suppressed STIR image of the same foot as (e). The haemosiderin is visible in this image, but less obvious than in the gradient-echo scan. (h) Transverse T2* gradient-echo image of the head, acquired with the dorsal part of the head pushed against the left side of the magnet. There is distortion of the image in the dorsal aspect on the left side of the head (arrow). (i) Transverse T1 fast spin-echo image of the same horse and location as (h). Using this pulse sequence, there is minimal distortion of the image.

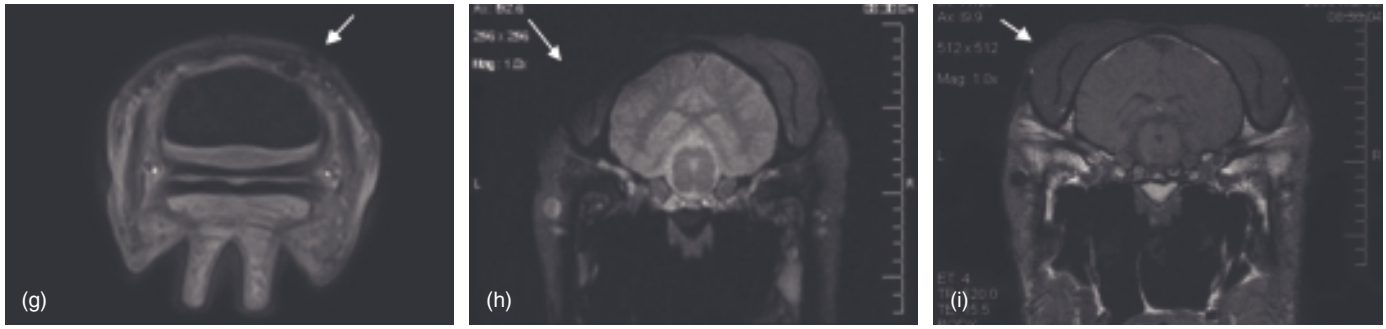

Figure 4.6 *Cont'd*

of the frog. Nail fragments left after shoe removal can produce severe metal artefacts, and render a portion of the image uninterpretable [1, 2, 11]. These nail fragments may be too small to detect on radiographic examination, but still cause a large artefact. Even if radiographic identification of nail fragments is possible, physical removal is often not possible without drilling out the entire nail hole. It appears that hoof filler may also set up similar problems, possibly related to contained metal fragments so it is recommended that any hoof filler is also removed where the foot is entering the scanner. Even some wound sprays or frog packing material (including blue Play Doh) used for radiography may result in magnetic susceptibility artefacts, so complete cleaning and possibly rasping of the hoof wall may be required [16]. Fine metal particles or grit on the skin surface, or debris contaminating a wound, can lead to magnetic susceptibility artefacts, which may be eliminated by cleaning the affected area (Figure 4.6).

At the edge of the imaging portion of the magnet, there may be distortion of the magnetic field, resulting in artefactual disruption of the image. It is therefore important to ensure that the region of interest is placed within the imaging portion of the magnet and that the patient is not positioned against the edge of the magnet housing (Figure 4.6).

Chemical shift artefact

Chemical shift artefact occurs when fat and water are adjacent to each other in the imaged tissue. Under normal conditions, the protons in fat and water precess at different frequencies when placed in the main magnetic field. The MRI system computer is set up to assume the protons in all tissues precess at the same frequency. During image reconstruction the computer interprets the difference in frequency between fat and water as a difference in location within the imaged anatomy and not a result of normal tissue properties. Consequently, it shifts the signal intensity to a different pixel resulting in spatial misregistration (i.e. the pixel that signal was obtained from is not where it was placed during image reconstruction). Due to this frequency difference between fat and water, the position of the fat signal is shifted in the frequency-encoding direction. The artefact can appear as a light and dark band on either side of a structure or as a ghost image, depending on the receive bandwidth used. This artefact occurs in both high and low

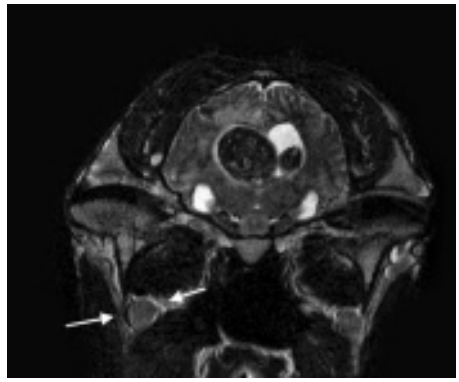

Figure 4.7 Transverse T2 fast spin-echo image of the head. Chemical shift artefact is evident in the frequency direction at the margins of the salivary gland to the left of the picture (arrows). The artefact results in high signal intensity to the right, and low signal intensity to the left side of the gland. Note this horse also has a large mass lesion (a cholesterol granuloma) formed from the choroid plexus, and secondary hydrocephalus.

field strength systems. The precessional frequency of tissue and the resultant frequency shift is field strength dependent, therefore this artefact is more obvious on high-field images than it is on low-field systems. The artefact is more apparent on a high-field system because the distance that the fat signal is displaced on the image is greater due to the larger frequency shift. This artefact is generally only a problem at high field strengths, and may be more of an issue where accurate measurements of particular structures are required [17, 18]. Locations where chemical shift artefact should be considered include articular cartilage margins and within the head (Figure 4.7).

Phase cancellation artefact

If the phase signal for fat and water are collected at specific intervals, then it is possible for their signals to cancel out, leading to an artefactual void signal on the image, known as phase cancellation artefact. When observed in bone, the artefactual signal void can mislead the interpreter into reading this area of low signal intensity as sclerosis or cortical bone, when it actually represents fluid. It important to be aware of and understand phase cancellation artefact and the influence of chemical shift on this artefact [3, 19]. This artefact occurs on gradient-echo sequences that have a time of echo (TE) that falls into certain intervals. For a low-field system these intervals are approximately 13, 39 and 52 ms, but similar can occur on a high-field system. The parameters of the current T2* gradient-echo scans on the Hallmarq system are subject to this artefact, which has both advantages and disadvantages for the interpreter. As long as the interpreter is aware of the artefact, the presence of phase cancellation artefact is a clear signal to the interpreter of the presence of fluid within a normally fat-based tissue. However, the interpreter must be aware that this may or may not also represent sclerosis.

The interpreter should consider that a sequence that would normally produce images with an obvious difference between sclerosis and fluid now requires a more complex interpretation to properly identify and characterize

abnormalities. On images obtained using a sequence subject to this artefact, the appearance of the bone will vary dependent on the proportion of fat and water in the bone. Areas on the T2*-weighted gradient-echo images in which the amount of water and fat in the bone are equal appear black due to phase cancellation (Figure 4.8). When the amount of fluid exceeds the amount of fat the area of bone will retain the traditional appearance with intermediate to high signal intensity fluid. This phenomenon occurs in injured bone where fluid and fat can both occupy the trabecular spaces.

To determine the difference between true sclerosis and phase cancellation artefact requires assessment of various image sequences. Sclerosis has low signal intensity on all sequences. Fluid is seen as intermediate to high signal intensity on T2-weighted, fat-suppressed, STIR (short τ inversion recovery) and proton density images. A T1-weighted sequence does not differentiate areas of fluid from sclerosis because they can have a similar signal intensity pattern. The STIR sequence can be used to definitively identify fluid. However, identifying sclerosis on this sequence is not possible because the low signal intensity in the fat-suppressed areas is similar to the appearance of sclerosis. If there is a rim of sclerosis at the edge of the fluid it would be difficult to differentiate from a region that had low signal intensity as a result of the fat suppression. Proton density and T2-weighted FSE sequences provide a definitive way to identify sclerosis, when compared with the T2* gradient-echo images as there is no overlap between the appearance of fluid and sclerosis on these sequences. Comparison of these sequences to the STIR and T2* gradient-echo images will allow identification of the area of fluid and sclerosis as well as areas where both abnormalities are present (Figure 4.8).

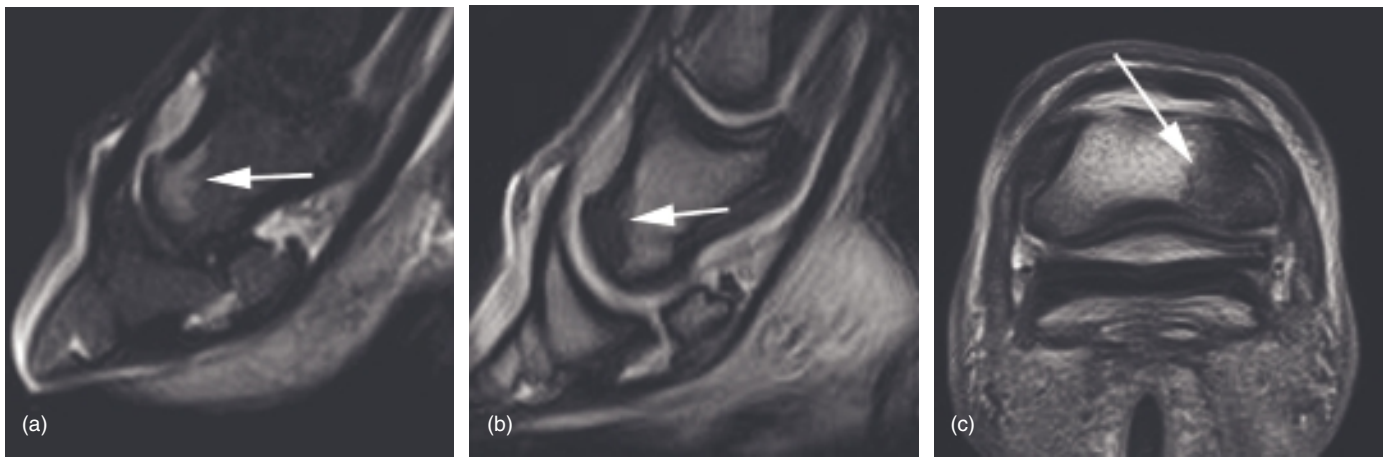

Figure 4.8 Phase cancellation artefact. Sagittal STIR (a) and T2*-weighted gradient echo (b) images with a corresponding transverse proton density image (c) of a foot. An area of well-defined increased signal intensity is present in the distal aspect of the middle phalanx on the STIR image. On the T2*-weighted gradient-echo image an area of uniform low signal intensity is present in the same region. The transverse proton density image has an area of low signal intensity that corresponds to the abnormal signal intensity on the STIR and T2-weighted gradient-echo images. The area of increased signal intensity on the STIR image with corresponding low signal intensity on the T2*-weighted gradient-echo image represents an area of fluid in the middle phalanx. This area has uniform low signal intensity on the T2*-weighted gradient-echo image because the amount of fat and water in the bone are equal, resulting in phase cancellation. The low signal intensity on the proton density image indicates sclerosis in the distal aspect of the middle phalanx in the same region which contains fluid. It would not be possible to detect areas of sclerosis associated with these types of lesions without using a T2-FSE or proton density sequence because the artefact resulting from phase cancellation would not allow differentiation between fluid and sclerosis on the T2*-weighted gradient-echo image.

In cases where there is excessive motion or lack of fat suppression on the STIR images, the T2* gradient echo can provide a method for detecting the presence of fluid when compared to the T2 FSE. Low signal intensity on a T2* gradient-echo image that does not correspond to low signal intensity on a T2 FSE is the result of phase cancellation and indicates the presence of an equal amount of fluid as fat. This method will not work when fluid exceeds fat. However, in many of these cases the fluid usually decreases at the periphery of the lesion creating a rimming effect and gives an indication of the presence of fluid. It is important to recognize that phase cancellation occurs because of chemical shift and can result in shifting and distortion of margins.

Magic angle effect

Magic angle effect is seen when collagen fibres are aligned at the magic angle (54.7° +/– 10) to the static magnetic field [4, 6, 20–26]. Magic angle effect causes an artefactual increase in signal intensity in fibres aligned with the magic angle, which can be mistaken for pathologic change. This is most important in ligaments and tendons, although it has also been reported to occur in cartilage. This artefact is reduced by increasing the echo time, so is less evident on T2-weighted images.

The magic angle artefact is clearly observed at the insertion of the deep digital flexor tendon (DDFT) in a recumbent horse within a high field MR system [1, 2, 11, 12, 24] where the static magnetic field is longitudinal to the limb (Figure 4.9). Increased signal intensity resulting from magic angle

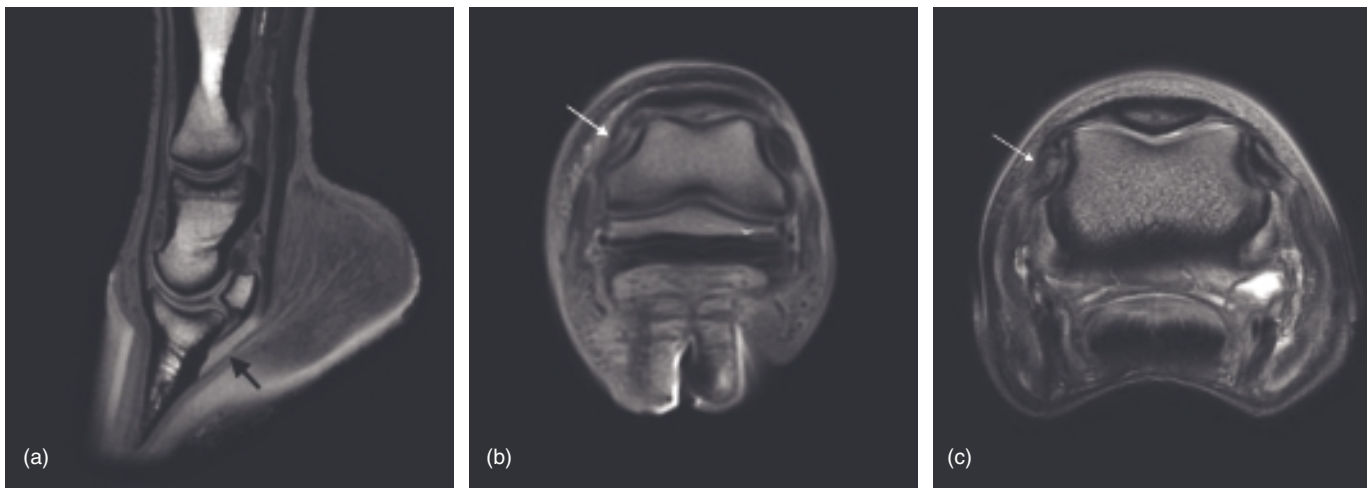

Figure 4.9 Magic angle artefacts occur when collagen fibres are oriented at approximately 55° to the static magnetic field. (a) Sagittal T1-weighted image of a foot obtained in a high-field MR imaging system, where the static magnetic field is oriented longitudinally in relation to the limb. The high signal intensity near the insertion of the deep digital flexor tendon (arrow) is due to a magic angle effect and not pathology. Note there is also evidence of mild distal rotation of the distal phalanx with mild dorsal laminar disruption. (b) Transverse low-field proton density image of the distal interphalangeal joint collateral ligaments. The high signal intensity in the ligament to the left of the picture is due to magic angle effect which affects the entire length of the ligament. (c) Transverse high-field proton density image at the origin of the collateral ligaments of the distal interphalangeal joint. There is high signal intensity within the collateral ligament to the left of the picture (arrow) related to the magic angle effect and not pathological change, which is only seen in the fibres at the origin of the ligament.

effect at the insertion of the DDFT often allows evaluation of the bone–tendon interface because the margin of the distal phalanx can be distinguished. Without magic angle effect in this region evaluation of the osseous margin at the tendon insertion is more difficult because both the tendon and the bone have low signal intensity. In low-field systems with the static magnetic field perpendicular to the limb, magic angle artefacts can cause problems for interpretation of structures that come close to 55° to the main magnetic field. These structures include the collateral ligaments of the distal interphalangeal joint, the oblique sesamoidean ligaments, the abaxial aspect of the DDFT and distal digital annular ligament [26] (Figure 4.10). This is most likely to occur in the lateral collateral ligament, lateral lobe of the DDFT and medial oblique sesamoidean ligament of a horse standing with the limb abducted, which is a common position under sedation. It is therefore recommended that careful positioning of a standing horse, with the horse standing as squarely as possible on all four limbs, is done before starting scan acquisition, and that efforts are made to minimixe leaning during image acquisition.

Careful evaluation of the horse's conformation and foot balance should be made prior to image interpretation. If there is concern about the presence of a magic angle artefact, it is useful to test for a change in signal intensity with different relative positions of the limb and magnet by moving the limb relative to the magnet, by either repositioning the limb or tilting the magnet. Long TE sequences, such as T2 FSE are the least susceptible to magic angle effects and short TE sequences, such as T1-weighted and proton density sequences are the most susceptible. It is important to note that STIR sequences can be susceptible to magic angle effect, and these sequences often have a short TE on low field systems. The TE of the sequence should be taken into account when setting up imaging protocols and interpreting scans, particularly when the signal pattern and affected structure are consistent with the characteristics of magic angle effect [20–22, 26].

Partial volume effects

Partial volume artefacts occur when there is a mixture of different tissue types within a single voxel, causing misleading pixel intensities in the image (Figure 4.11). This can cause problems for any structure with an edge or curved surface crossing multiple voxels or small structures, which are either lost within one slice or partially cross, cut between or are separated into two slices (Figure 4.11). In these cases, margins tend to appear less clearly defined and small structures may be missed completely. On low-field imaging where there are likely to be compromises required between time of acquisition, slice thickness or proximity of data collection points, and signal to noise ratio, there is a potentially higher risk of partial volume effects causing problems. This is often a particular problem for curved articular surfaces or small structures such as the distal sesamoidean impar ligament.

The interpreter should be aware that small structures could be missed or margins appear less distinct, particularly where there are thicker slices or structures crossing the imaging plane at an oblique angle. It is important

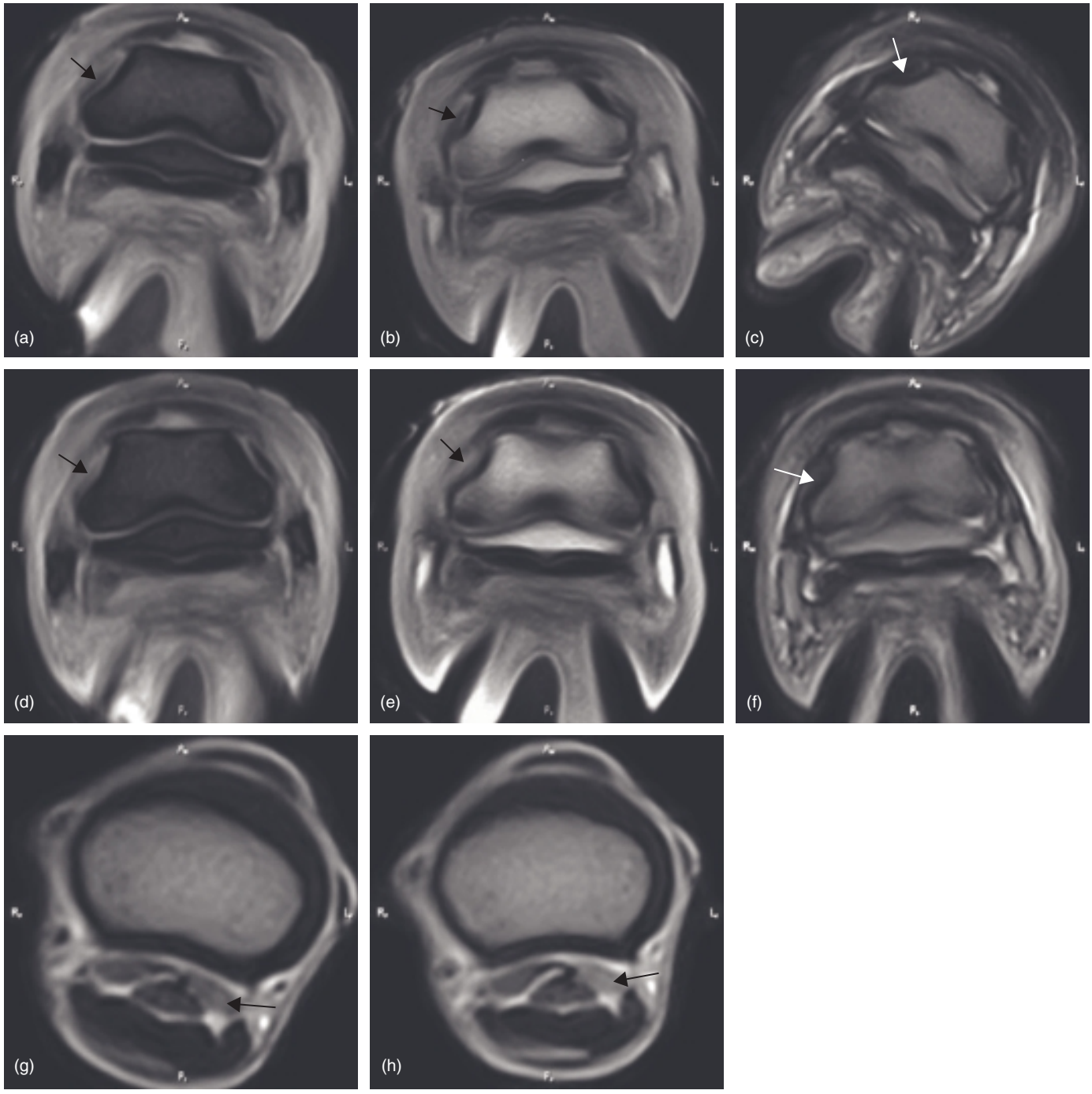

Figure 4.10 Effect of changing angle of limb on different image sequences in a standing low field MRI system. (a) Transverse T2* GRE, (b) T1 SE and (c) T2 FSE MR images of the foot obtained with the limb vertical. The lateral collateral ligament (arrow) of the distal interphalangeal joint was at approximately 77° to the static magnetic field in this image. In all image sequences, the signal intensity within the lateral and medial collateral ligaments of the distal interphalangeal joint is comparable and the ligaments are symmetrical in appearance. (d) Transverse T2* GRE, (e) T1 SE and (f) T2 FSE MR images of the same limb, with the limb tilted relative to the magnet so that the lateral collateral ligament of the distal interphalangeal joint (arrow) was at approximately 65° to the static magnetic field. In the T2* GRE and T1 SE images, the signal intensity within the lateral collateral ligament of the distal interphalangeal joint is now greater than that of the medial collateral ligament, with asymmetry in ligament appearance and loss of definition of the lateral collateral ligament. In contrast, in the T2 FSE images, the ligament appearance remains nearly symmetrical showing the importance of using long TE sequences for evaluation of structures potentially affected by the magic angle effect. (g) A transverse T1 SE MR image of the pastern obtained with the limb vertical. The medial oblique sesamoidean ligament (arrow) was at approximately 73° to the static magnetic field in this image. The signal intensity within the lateral and medial oblique sesamoidean ligaments is comparable and the ligaments are symmetrical in appearance. (h) When the limb is tilted so that the medial oblique sesamoidean ligament (arrow) was at approximately 65° to the static magnetic field, the signal intensity within the medial oblique sesamoidean ligament is greater than that of the lateral oblique sesamoidean ligament, the ligaments are asymmetrical in appearance, and there is loss of definition of the medial oblique sesamoidean ligament. (Images courtesy of Dr Meredith Smith)

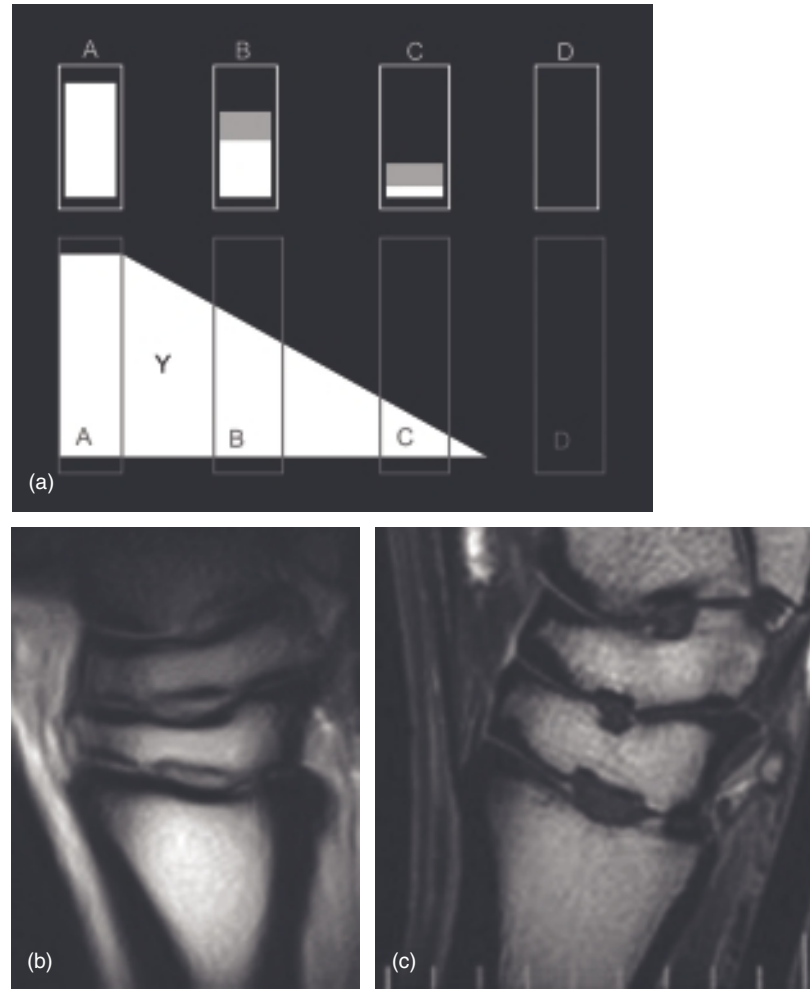

Figure 4.11 Partial volume effect. (a) Obtaining an MRI image of an object with a sloping surface can create problems with the partial volume effect. If an object (Y) is imaged with slices at the locations of letters A, B, C and D (bottom), then the corresponding image appearance for each letter is shown at the top of the picture. Where the edge of the object runs obliquely through the slice, the image appears grey instead of having a sharp white margin. (b) Sagittal image of the distal tarsal joints obtained with large slices and low resolution. The margins of the bones, joints and intertarsal ligaments appear poorly defined associated with partial volume effect. (c) Sagittal image of the distal tarsal joints obtained with narrow slices and high resolution. In contrast to (b), the margins are sharper and more clearly defined.

that the interpreter assesses images from all planes and sequences where there may be queries. For the operator, reducing the slice thickness to a level appropriate for the tissues being imaged will minimize this effect, and using a combination of sequences including a higher-resolution scan over a particular area of query may be beneficial. Positioning and orientation of slices during study planning is particularly important for curved surfaces or small structures, and if comparison between limbs or sides is to be used for assessment. For curved articular surfaces, it is useful to acquire images perpendicular to the articular surface at multiple points across the joint surface so that the articular surface can be evaluated with minimal partial volume

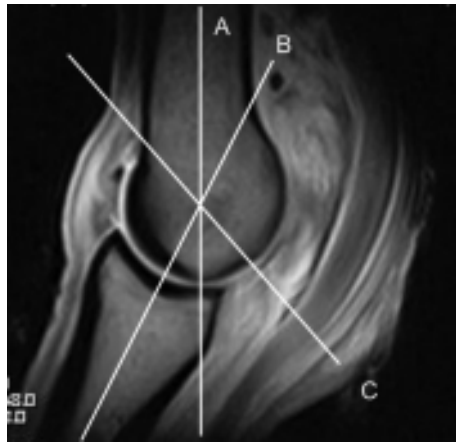

Figure 4.12 Sagittal image of the fetlock joint. The lines (A to C) represent multiple imaging planes perpendicular to the articular surface at different points along the articular surface. Acquiring images perpendicular to the articular surface minimizes partial volume effects.

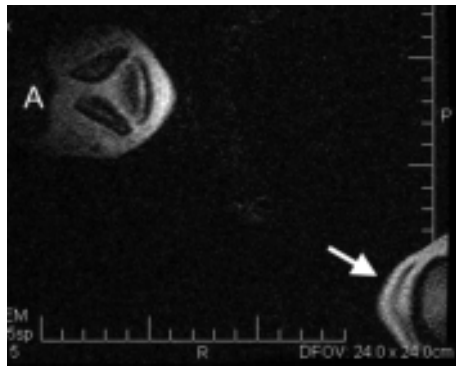

Figure 4.13 Transverse T2* gradient-echo image of a limb at the level of the proximal sesamoid bones. Phase wrap around of the original image (A) is seen as an image (arrow) of the 'missing' part of the limb positioned in the phase direction. This part of the limb was placed near the edge of the imaging portion of the magnet. There is poor signal to noise ratio overall.

effects (Figure 4.12). For assessment of small structures such as the distal sesamoidean impar ligament, it is important for transverse images to be oriented perpendicular to the ligament at the midpoint of the ligament, and avoiding any medial to lateral obliquity (Figure 4.13). When comparing structures such as the collateral ligaments of a joint, orienting and positioning the scan perpendicular to the ligament and without medial to lateral obliquity minimizes the risk of being misled by partial volume effects.

Phase sampling artefacts

Phase sampling artefacts include phase wrap around and Gibbs (truncation) artefact [3, 4] (Figure 4.14). If part of the patient is just outside the field of view but produces a signal that is detected by the receiver coil, then this may be shown incorrectly within the field of view; this is known as aliasing or phase wrap around. It can be avoided by using spatial saturation bands

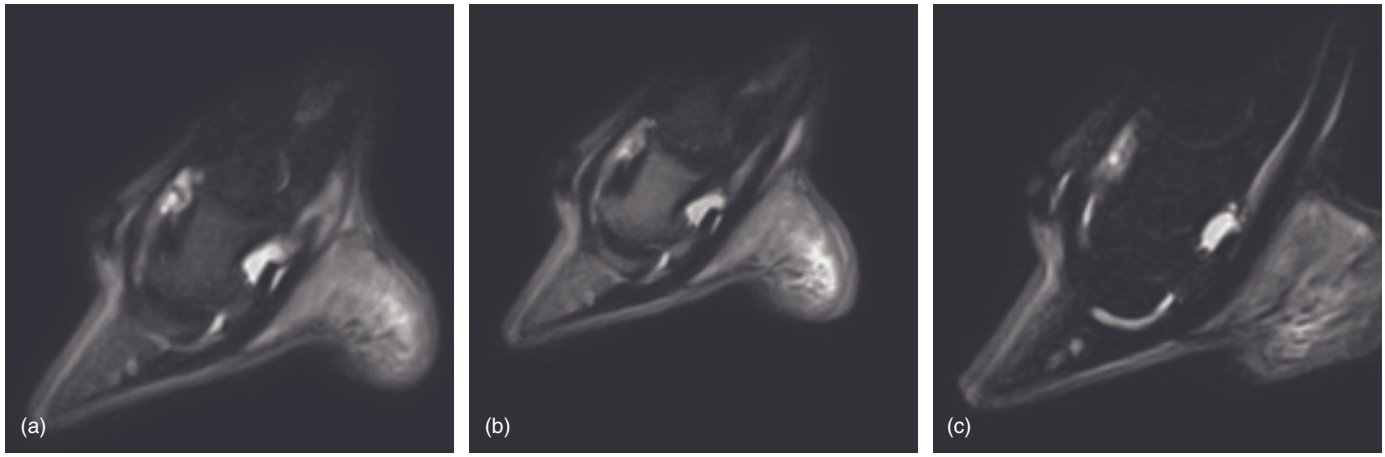

Figure 4.14 Sagittal STIR images of the hind foot of a patient with moderate lameness, obtained standing using a low-field imaging system. The limb appeared warm to touch in relation to the other limbs. Degree of fat suppression on STIR images is affected by the temperature of the region of the interest of the patient. To obtain optimal fat suppression, it is important to optimize the inversion time of the STIR sequence. This is necessary for clinical cases where variation in local temperature may occur, and when scanning at other than body temperature (for example scanning cadaver limbs at room temperature). In this horse, using an inversion time at a regular clinical setting led to insufficient fat suppression, reducing the inversion time reduced the level of fat suppression and increasing the inversion time improved the level of fat suppression, revealing mildly increased signal intensity on the dorsal aspect of the middle and distal phalanges. (a) STIR image obtained with a standard clinical inversion time (80 ms). (b) STIR image obtained with a shorter inversion time (55 ms). (c) STIR image obtained with a longer inversion time (95 ms).

or phase oversampling (the 'no phase wrap' option during image acquisition). The Gibbs effect (truncation artefact) results from undersampling of data and occurs when bright or dark lines are seen parallel and adjacent to borders of abrupt intensity change, for example a line of low signal is incorrectly shown running through a high-intensity area. This can be avoided by increasing the phase-encoding matrix or decreasing the field of view.

Temperature effects

Temperature of the magnet and tissues can affect imaging parameters and image appearance, and this should be considered by the interpreter if there are problems with expected signal intensity variations. This is of particular importance where STIR or FLAIR (fluid attenuated inversion recovery) sequences are being used because the optimal inversion time for fat suppression or fluid attenuation is affected by temperature [17, 27, 28] (Figure 4.15). This has implications for tissues that are at higher or lower temperatures than normal, related to external temperature, local inflammation or alterations in vascularity. Where the tissue temperature varies from the 'normal' clinical temperature that the MR system is optimized for, the fat signal may not be sufficiently suppressed, which could mislead an interpreter into suspecting pathology. In these cases, it may be necessary to select different inversion times dependent on whether the temperature of the tissues is greater or lower than normal clinical body temperature. In general, the optimal inversion time for a particular temperature is the point where the signal intensity for fat (on a STIR image) or fluid, such as cerebrospinal fluid (CSF) (on a FLAIR image) is the lowest. For cadaver limbs at room

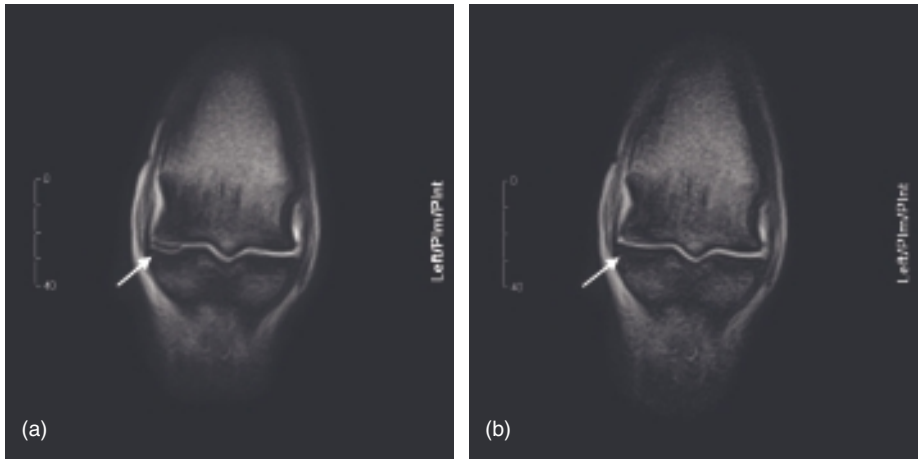

Figure 4.15 Dorsal plane T2* gradient-echo image of the fetlock from a horse with lameness localized to this region, obtained as the last image in one sequence, showing the potential for misinterpretation of images at the ends of a series. (a) Image obtained as the last image of the series demonstrates an apparently severe cartilage and bone defect (arrow). However, this 'lesion' could not be seen using other sequences or planes. When the data is reconstructed correctly (b), it is clear that the original 'lesion' was an artefact (arrow) associated with reconstruction of the data in the last image of the series.

temperature or below, there is a need to alter the inversion time from a clinical protocol if fat suppression or fluid attenuation are required [17, 27, 28].

COMPARISON OF HIGH- AND LOW-FIELD IMAGES

Although recently the term high field strength is sometimes applied to magnets of 3.0 Tesla or greater, traditionally use of the term has implied having a field strength of ≥1.0T, which is clinically applicable for the equine patient under general anaesthesia [19]. Low-field MR systems are defined as having a field strength of up to 0.3T [19]. Both standing and anaesthetized low-field MR units are in use in horses. It is important that the interpreter is aware of the limitations and advantages of both high- and low-field systems, in relation to image acquisition, image appearance and artefacts [19, 29, 30].

In general, for images acquired with optimized sequence parameters for each system while minimizing the acquisition time, high-field images have relatively better resolution and detail. This makes anatomy more clearly defined on high-field images, and subtle pathology may be better detected. When learning image interpretation skills, there is considerable value to training on high-field images in order to understand anatomy and pathology. Once the interpreter is confident in their knowledge of MR anatomy and pathology using high-field images, it is easier to apply this experience to low-field images that have lower resolution.

There are differences between high- and low-field systems in relation to imaging parameters and protocols, acquisition times, signal to noise ratio (SNR), contrast to noise ratio and artefacts. Overall, image quality is dependent on SNR, contrast to noise ratio and artefacts [19]. SNR is most affected

by field strength as it increases almost linearly with field strength. Increased SNR is associated with improved resolution, detail and information present within each pixel/voxel, so a high field strength magnet is able to deliver improved image quality within a shorter acquisition time than a low field strength magnet. Thus, a low-field system takes longer to acquire images of the same resolution. This increased acquisition time has implications for anaesthetized and standing patients. If comparable sequences are used the longer acquisition time increases the risk of motion artefacts and therefore does not achieve a comparable overall increase in the SNR. The noise increases at a rate such that there is a diminishing return relative to the increase in signal gained from a longer acquisition time. Contrast to noise ratio is used to differentiate between tissues, and is better on optimized images produced by a high-field system. Although chemical shift artefacts are more likely in high-field systems, field homogeneity artefacts tend to be more of a problem with low-field systems. In low-field systems where there is a smaller field of view, a greater proportion of the study cannot be accurately evaluated because images at the periphery of the sequences or at the edge of the field of view are prone to artefacts. This can be accounted for by acquiring overlapping sequences, but this increases time of acquisition. As it is more difficult to maintain SNR in a low-field system compared with a high-field system without increasing pixel size, slice thickness or acquisition time, this sets limitations on the ability to improve resolution and quality within the same acquisition time. Lower resolution and increased slice thickness are likely to increase partial volume effect, so the margins of some lesions and structures may be less clearly defined on a low-field system, and some small lesions may not be detected.

In one study comparing MR images of equine cadaver limbs acquired using a high- (anaesthetized) and low-field (standing) system, differences in image appearance resulted from selection of imaging parameters, limitation of the size of the field of view and different acquisition angles [31]. The potential field of view in a high-field system can be considerably larger as a result of the system capabilities and the radiofrequency (RF) coil size so multiple fields of view may be required in a low-field system to cover the same area. The difference in positioning of a limb between standing and general anaesthesia affected the anatomical arrangement and appearance of structures between the two systems.

Magic angle effect can lead to differences in the appearance of the DDFT, distal sesamoidean impar ligament, collateral sesamoidean ligament, the collateral ligaments of various joints and oblique sesamoidean ligaments between high- and low-field images, due to differences in the orientation of the static magnetic field. With the longitudinal orientation of the static magnetic field in a high-field magnet, the DDFT distal to the navicular bone [7, 24, 32], impar ligament and collateral sesamoidean ligament may be susceptible to magic angle effects [32]. The distal interphalangeal joint collateral ligaments and oblique sesamoidean ligaments may be at risk in a low-field system with a transverse magnetic field [23, 26]. Using pulse sequences with a long TE and reducing the flip angle in gradient-echo sequences minimizes magic angle effects.

There is considerable debate in the human medical literature about the relative diagnostic accuracy of high- and low-field systems. Many studies that have compared high-field and low-field MRI in human musculoskeletal disease have shown comparable diagnostic accuracy [33–37]. Although comparable diagnostic accuracy has been reported between field strengths when imaging the shoulder, in another study lesions were identified on high-field images that were not identified on low-field images leading to a significant change in patient management [38]. Studies comparing the results of MRI of the human knee with the results of surgery and/or comparing the results of high-field and low-field MRI have generally shown little difference in the sensitivities and specificities of the two systems for the diagnosis of meniscal and anterior cruciate lesions [39–47]. However, the lesions evaluated in these studies were substantial and included full-thickness meniscal tears and complete anterior cruciate ligament rupture.

There has been relatively little study of the differences between high- and low-field systems in use for equine patients. In one study, the appearance of normal tissues was very similar between high- and low-field systems, but it was possible to define small structures and their margins more clearly on high-field images [31]. Both high- and low-field imaging successfully detected the presence or absence of damage in tendon, ligament, bone and other soft tissues, but high-field imaging detected some small lesions or described the configuration of lesions more clearly than low-field imaging. However, it was not clear whether this would have affected the final clinical recommendations. For example, this was reported to affect the ability to detect irregularity of the distal sesamoidean impar ligament margins. However, as all cases diagnosed with impar ligament pathology had associated changes that were detected on low-field images, including soft tissue accumulation in the navicular bursa and increased signal intensity on STIR images at the origin and insertion of the ligament, it was considered that the final diagnosis would have been the same with both systems. These findings were similar in another study comparing sensitivity and specificity of high- and low-field imaging for detection of lesions in the navicular bone, oblique sesamoidean ligaments and fetlock joint with histological detection of pathology [48].

Evaluation of articular cartilage can be a challenge with both low- and high-field imaging. Significant differences in the detection of articular cartilage lesions between high and low field strength has been reported in both human and equine joints [1, 49, 50]. In cadaver studies using equine joints, high-field imaging was able to detect cartilage abnormality in the absence of subchondral bone damage that was undetectable in low-field images, although severe damage and subchondral bone damage was detectable on both systems [31, 48]. Use of multiple imaging sequences improved the sensitivity and specificity of both high- and low-field images for detection of articular cartilage abnormality [49].

IMAGE EVALUATION

There is a huge quantity of information contained within a series of MR images. To put this information into context, a detailed knowledge of the

anatomy of the region of interest is required, along with experience or understanding of the normal variations that may occur [1, 2]. Not all apparent abnormalities are associated with pain and lameness, so the presence of abnormalities must be interpreted in the light of the clinical findings [10, 32].

As with any imaging modality, the large volume of information may be misleading. It is easy for the eye to be caught by a visually obvious abnormality and miss other, perhaps more clinically significant, abnormalities. This is avoided by routine, systematic image evaluation. Checking all the imaging sequences and planes in a repeatable order, and evaluating each structure in a standard order for each image is useful to prevent inadvertently missing an important finding.

To determine the significance of signal alterations or changes in surface contour or shape on images from a single pulse sequence in a single orientation, it is important to compare these with the same anatomical site evaluated using other pulse sequences or in other orientations. This can be done using image cross-referencing software to determine the exact site in question. If an abnormality is only seen in one pulse sequence in one orientation, and cannot be reproduced, then there is a high likelihood that the finding is an artefact and not a true finding, so should not be considered significant. Under these circumstances, it may be advisable to undertake further acquisitions to rule out artefacts.

It can be more difficult to evaluate some anatomical locations than others. Volume averaging can cause particular problems on curved articular surfaces, such as the distal interphalangeal joint, while the flatter surface of the carpal bones can be more clearly assessed. Evaluation of parts of tendons and ligaments at 55° to the static magnetic field can be difficult due to the magic angle effect. In a closed, high-field magnet, this can cause problems in the distal aspect of the DDFT and parts of the collateral sesamoidean and distal sesamoidean impar ligaments. In a low-field system, this can be more problematic for the distal interphalangeal joint collateral ligaments and oblique distal sesamoidean ligaments.

NORMAL APPEARANCE OF TISSUES AND DETECTION OF PATHOLOGICAL CHANGE

Individual tissues and structures have characteristic appearances on MR images. This appearance is affected by particular pulse sequences and imaging parameters, but in a standard pattern. Anatomical variation does occur, and there can be age and exercise-related differences in structure between individuals and locations that should be taken into account, so the detail for individual structures should be looked at within later chapters of this book. However, it is possible to provide some overview of the standard patterns seen within normal tissues. Normal tissues generally have clearly defined margins and characteristic signal intensity patterns. Signal intensity can be described as zero (or signal void), seen as black on images; low (or hypointense), appearing as dark grey or black; intermediate, appearing as grey; or high (hyperintense), seen as white on images.

Bone

Normal cortical and subchondral bone appears black (zero signal intensity) on all sequences, and has clearly defined endosteal, periosteal or osteochondral margins (Figure 4.16). Cancellous bone has a more heterogeneous appearance because the mineralized trabecular struts emit minimal signal in a similar way to cortical bone, but the bone marrow fat and connective tissues distributed throughout are generally of high signal intensity, making the overall appearance of cancellous bone more heterogeneous. This appearance is influenced by the fat content, bone mineral density and distribution, and by the image acquisition parameters (Figure 4.16) [1, 2, 5, 6, 51].

The thickness of cortical and subchondral bone, and cancellous bone density are affected by age, exercise history and location, so it is important to consider normal variation when evaluating these tissues [52–54]. Neonatal bones have minimal subchondral bone, which increases into a standard pattern of thickness across the articular surface following loading [55]. Horses worked on a soft surface with low training intensity are likely to have thinner cortical and subchondral bone at articular surfaces and less dense cancellous bone than horses with a history of strenuous galloping exercise [52]. In horses with a history of racing or strenuous galloping training, there is frequently smooth enlargement or modelling of the dorsal aspect of the carpal bones, increased thickness of the dorsal cortex, and a pattern of increased palmar subchondral bone thickness and trabecular bone density in the metacarpal condyles, which is generally symmetrical with smooth endosteal margins [54, 56].

The presence of bone spurs or osteophytes is frequently incidental in a variety of joints [53, 57], but should also be considered as a potential indicator of osteoarthritic change when lameness is isolated to the joint and in the

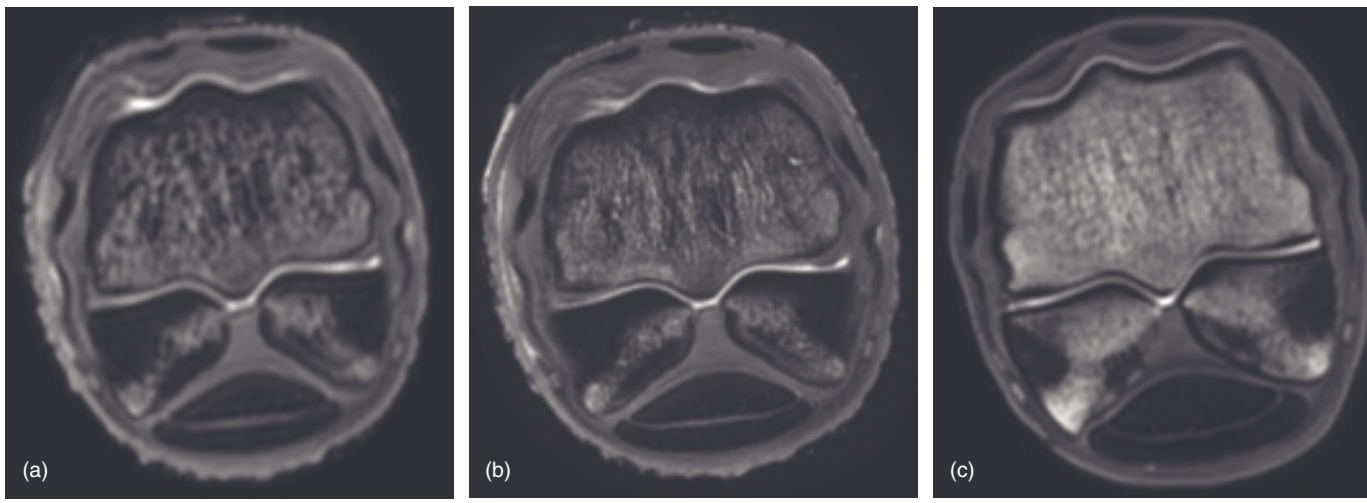

Figure 4.16 The appearance of different tissues is influenced in part by acquisition parameters. Cancellous bone appearance can be affected by fat content, bone mineral density and distribution, and also by image acquisition parameters. These high-field transverse T1 GRE images of the distal metacarpus and proximal sesamoid bones show the different appearance of cancellous bone when the number of excitations is increased. The effect of this is to increase the SNR, but increasing NEX will also increase the acquisition time. As the number of excitations increases, the clarity and uniformity of the cancellous bone becomes more obvious. (a) Image acquired at 2NEX. (b) Images acquired at 8NEX. (c) Image acquired at 16NEX.

presence of concurrent synovial proliferation, fluid distension or other pathology. In an MR study of tarsi from horses without lameness, it was reported that incidental findings of osseous cyst-like lesions, irregularity of subchondral and cortical bone margins, and variable signal intensity in the cancellous bone occurred [57]. The significance of these findings may be dependent on the athletic demands of the horse, so MR interpretation should be done in the light of the normal variation within the population with a similar exercise history.

Tendon

Evaluation of tendons can be done using multiple sequences. However, because of the risk of magic angle effect it is important to include long TE sequences, such as a T2 fast spin-echo sequence, in a musculoskeletal protocol to avoid confusion for the interpreter. Normal tendons emit no signal and therefore appear black on T1-weighted, T2-weighted and proton density images [1, 2, 5, 6] (Figures 4.1 and 4.2). The connective tissue between tendon fibrils and at the boundaries of the tendon emits more signal, so the tendon may appear slightly mesh-like in appearance when imaged on certain sequences using higher-resolution sequence parameters [7, 13]. The margins of normal tendons are clearly defined, smooth and uniform in appearance [5, 7]. Where images are obtained in the plane of a tendon, it should be possible to visualize the structure continuously through the image without any disruption [5]. On transverse images, any changes in shape or size should relate to the anatomy of the limb, without abrupt alterations. Moderate increase in signal intensity over anatomical prominences may be a normal finding, representing chondroid metaplasia as an adaptive response to compressive forces. This is frequently seen in the dorsal aspect of the DDFT at the level of the metacarpophalangeal joint, and in my experience this finding may be more obvious in the older horse with a history of high-intensity exercise.

Normal variation in tendon size, appearance and symmetry occurs as a reflection of horse size and adaptation to loading. Cross-sectional area of the DDFT increases with horse weight, and symmetry between tendons in contralateral limbs or between tendon lobes within the same limb is an indication of normality [7]. However, if there is conformation asymmetry in a limb, then adaptive changes in tendon size and shape may occur, which are not a reflection of pathology.

Ligament

As with tendons, use of a long TE sequence in the protocol for ligament evaluation is recommended to avoid confusion with magic angle effect. Normal ligaments are likely to have areas of low signal intensity on T1-weighted, T2-weighted and proton density images, but many ligaments have a more heterogeneous signal intensity and more variable appearance and structure than tendons. This is particularly evident in the distal sesamoidean ligaments [58] and suspensory ligament [59]. Near the origin of the oblique distal sesamoidean ligaments there is considerable variation in connective tissue composition and ligament fibre orientation, leading to a variability in

signal intensity pattern by different contributions of tissue to signal intensity and magic angle effect [48]. Muscle and adipose tissue is clearly seen within the proximal part of the suspensory ligament, but there is often individual variation and differences between fore and hind limbs. The presence of muscle tissue within a ligament is seen as an area of moderate signal intensity that is relatively higher than the surrounding dense collagenous tissue, but is usually quite clearly defined within the ligament [60]. As the suspensory ligament divides into branches, the muscle tissue and ligament structure becomes less defined and more variable until the branches are fully separated. The presence of cartilaginous tissue within a ligament is seen as moderate to high signal intensity in comparison with the low signal intensity of the ligament. This can be observed near the insertion of the straight distal sesamoidean ligament, and can vary in size, appearance and signal intensity between horses without abnormality [1, 2, 13] (Figures 4.1 and 4.2).

Normal ligaments should be continuous from origin to insertion, and the margins should be smooth and well defined [5, 7]. Collateral ligaments often have multiple ligament fibres joining from different origins or parting to different insertions, therefore it is important to evaluate the ligament fibres in multiple orientations to confirm their continuity. The cortical bone at the origin and insertion of the ligament should be smooth on both endosteal and periosteal aspects. For ligaments within a joint, such as the intertarsal ligaments, the subchondral bone and adjacent articular surface should be smooth and well defined [57].

Normal variations in ligament size and appearance may occur. Length of the distal interphalangeal joint collateral ligaments increases with horse weight and hoof circumference [61]. In general, symmetry between structures in contralateral limbs or between structures within the same limb is an indication of normality, and this has been shown in the collateral ligaments of the distal interphalangeal joint and carpus [61]. However, if there are conformational features such as rotational deformity or medial to lateral asymmetry of a limb then there may be adaptive changes in size and appearance of ligaments [62].

Articular cartilage

Evaluation of articular cartilage requires adequate quality and resolution of images or it is easy to be misled into false positive or negative findings. Use of fat-suppression techniques can improve differentiation of the articular cartilage, and fat-saturated, spoiled gradient-echo and proton density fat-saturated sequences have been found to be particularly useful for defining margins of the articular cartilage [18, 63, 64]. Evaluation of the articular cartilage margins is most useful where the two articular surfaces of a joint are not in contact, so the proximal and distal articular surfaces can be visualized separately. This can be difficult in a standing horse bearing weight on a limb, but in the anaesthetized horse, partial flexion, distraction or saline distension of a joint can improve separation of the surfaces.

Articular cartilage has an intermediate to high signal intensity on T1-weighted images, and intermediate to low signal intensity on T2-weighted

images, and can be clearly defined from the adjacent subchondral bone (no signal) and synovial fluid (high signal on T2 and low signal on T1) [1, 5, 6]. Normal cartilage has smooth articular and chondro-osseous margins, and is generally of uniform thickness [18, 51, 65, 66] (Figures 4.1, 4.2 and 4.6).

It is important to consider normal variation when evaluating articular cartilage. In one MR study in 31 horses without lameness, minor MR abnormalities were detected on the cartilage surface of the middle carpal joint in 11 limbs and within the hyaline cartilage on 13 limbs. These included slight irregularity of the cartilage surface, small cartilage defects and linear, focal or generalized alterations in signal intensity within the articular cartilage [53]. Tarsi from horses without lameness were reported to have multiple mild abnormalities in cartilage surface, signal intensity and osteochondral junction [57]. However, it is possible that these abnormalities represent subclinical problems that may have progressed to lameness at a later stage.

Synovial fluid, synovium and joint capsule

Normal synovial fluid is seen as high signal intensity on T2-weighted and STIR images, low signal intensity on T1-weighted images and intermediate signal intensity on proton density images. (Figures 4.1, 4.2 and 4.6). Normal synovium is a connective tissue that has a lower signal intensity than the surrounding synovial fluid on T2-weighted and proton density images, and slightly higher signal intensity than the synovial fluid on T1-weighted images. Capsular tissue clearly defines the margins of the synovial fluid. It is seen as a thin, smooth band of uniform thickness, which has lower signal intensity than the synovial fluid on T2-weighted and proton density images, and slightly higher signal intensity than the synovial fluid on T1-weighted images [1, 2, 51].

Synovial plica and/or collections of synovium occur at characteristic locations within some joints. These are commonly seen in the dorsal aspect of the distal interphalangeal joint and metacarpo/tarso phalangeal joints.

Muscles

Muscles have medium to low signal intensity on T1-weighted and proton density images with low signal intensity on T2-weighted images. They have clear margins separated by fibrous connective tissue [5, 6]. Musculotendinous junctions can be recognized as well-defined areas of low signal intensity within the muscle tissue. The patterns of the musculotendinous junctions vary with each anatomic region.

Arteries and veins

Arteries and veins can vary in signal intensity appearance on MR images, depending on imaging parameters and blood flow characteristics. The lumen of a normal vessel may appear low intensity, high intensity or mixed intensity [5, 6]. To outline anatomy more clearly, use of presaturation pulses in spin-echo sequences give a low-intensity lumen. Use of gradient-echo imaging, gradient-moment dephasing or administration of contrast gives a high-

intensity lumen [4]. In general, vessels should have smooth margins and run in line with normal anatomy.

Nerves

Nerves have medium signal intensity on T1-weighted and proton density images and low signal intensity on T2-weighted images [1, 2, 5, 6]. They have smooth margins and can be visualized along their length without any interruptions. Nerve fibres are susceptible to magic angle effect, and this should be considered by interpreting variations in signal pattern on short TE sequences [67].

Central nervous tissue

On T1-weighted images, the cranioencephalic structures have intermediate signal intensity; the cortical grey matter is hypointense compared to white matter. On T2-weighted and proton density images, the cortical white matter is hypointense compared with grey matter. CSF appears black on T1-weighted images, intermediate signal intensity on proton density images and high signal intensity (white) on T2-weighted images.

DETECTION OF PATHOLOGICAL CHANGE

Disruption of a tissue frequently leads to an alteration in structure, composition and proton mobility, resulting in an alteration in tissue MR characteristics. Pathological processes are frequently associated with increase in free water within and around the affected tissues. These changes can easily be detected with MRI, as an increase in signal intensity on proton density and T2-weighted images or decrease in signal intensity on T1-weighted images. Although these changes may be most easily seen on T2-weighted images, the combined information from proton density,T2-weighted, T1-weighted and fat-suppressed images is the most useful for interpretation. Proton density and T1-weighted images are particularly useful for evaluation of tissue contours and anatomy, while fat-suppressed techniques are required for evaluation of bone medullary tissues. In general, fluid (and oedema) is hypointense on T1-weighted and hyperintense on T2-weighted images. However, it is important to note that increased protein content in the fluid changes the appearance from hypointense to intermediate or hyperintense on T1-weighted images. The degree of signal increase is dependent on the protein concentration in the fluid. On T2-weighted images, presence of blood leads to a relative decrease in signal intensity compared to oedema. Immature granulation tissue has high signal intensity on T2-weighted images, while mature fibrotic tissue has a low intensity on T2-weighted images [6].

Bone

Although cortical bone has low signal intensity, MRI is extremely useful for detecting bone pathology. Alterations in periosteal or endosteal surface

contour may indicate abnormalities or bone disruption [1, 2, 5, 6, 8] (Figure 4.17). In joints, osteophytes are detected as altered surface contour on MR images [68]. Trabecular architecture can be visualized with high-resolution MRI, and this can be used to monitor trabecular changes [65].

Severe pathologic change in bone can usually be detected on all sequences, including proton density, T1-weighted, T2-weighted and STIR (Figure 4.18). The sequence that will best characterize the lesion is dependent on the nature of the lesion. Pathologic change in bone is frequently

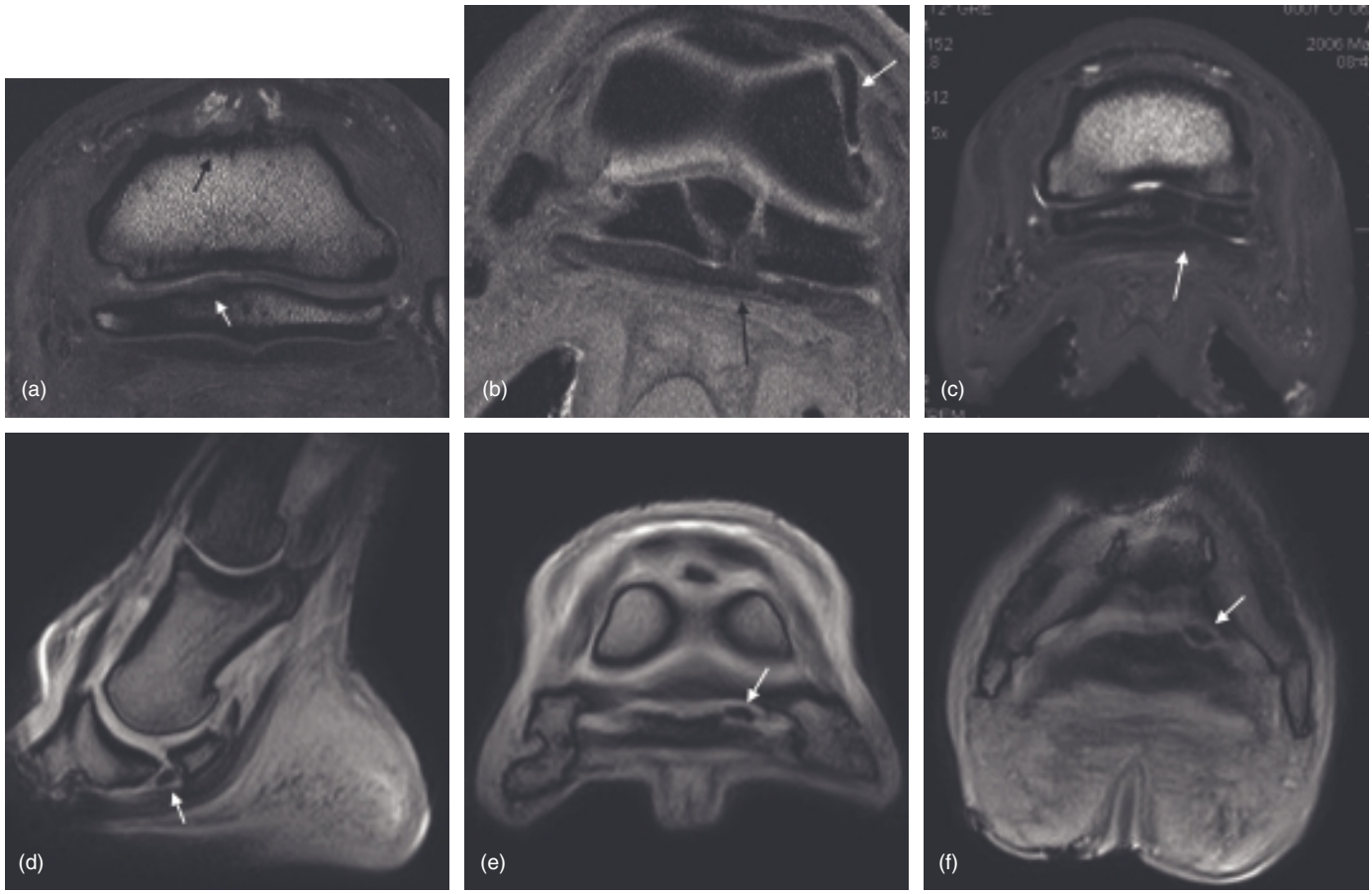

Figure 4.17 Cortical bone abnormalities can be detected as irregularity of surface contour, defects or alterations in signal intensity. It is important to assess the adjacent soft tissues as well as bone damage, in the light of the clinical picture. (a) Transverse high-field T2* gradient-echo image at the level of the navicular bone in a horse with chronic lameness localized to the foot. There is irregularity of the dorsal cortex of the middle phalanx (black arrow) adjacent to evidence of chronic synovitis and synovial proliferation within the distal interphalangeal joint. There is also irregularity of the subchondral bone on the dorsal aspect of the navicular bone at its articulation with the middle phalanx (white arrow). (b) Transverse high-field image at the level of the navicular bone. There is an acute, comminuted fracture of the navicular bone (black arrow) with damage to the adjacent deep digital flexor tendon, which has been lacerated, and the lacerated portion apposed between the fracture fragments. There is also a fracture of the middle phalanx (white arrow). (c) Transverse high-field T2* gradient-echo image at the level of the navicular bone. There is evidence of a chronic fracture of the navicular bone, which had been present for 3 years without clinical problems following recovery from the initial injury, and had no uptake on scintigraphic imaging. There is an adhesion to the adjacent deep digital flexor tendon (arrow), and recent pain was attributed to active damage and tearing further proximally in the tendon. (d) Low-field sagittal plane T2* gradient-echo images of a navicular bone distal border fragment. To assess the configuration of this fragment and its relationship to other tissues, other imaging planes must be examined. (e) Low-field transverse plane T2* gradient-echo image of the same horse as (d), oriented perpendicular to the flexor border of the navicular bone showing the medial to lateral extent of the fragment. (f) Low-field transverse plane T2* gradient-echo image of the same horse as (d) oriented parallel to the sole, providing further information on fragment configuration.

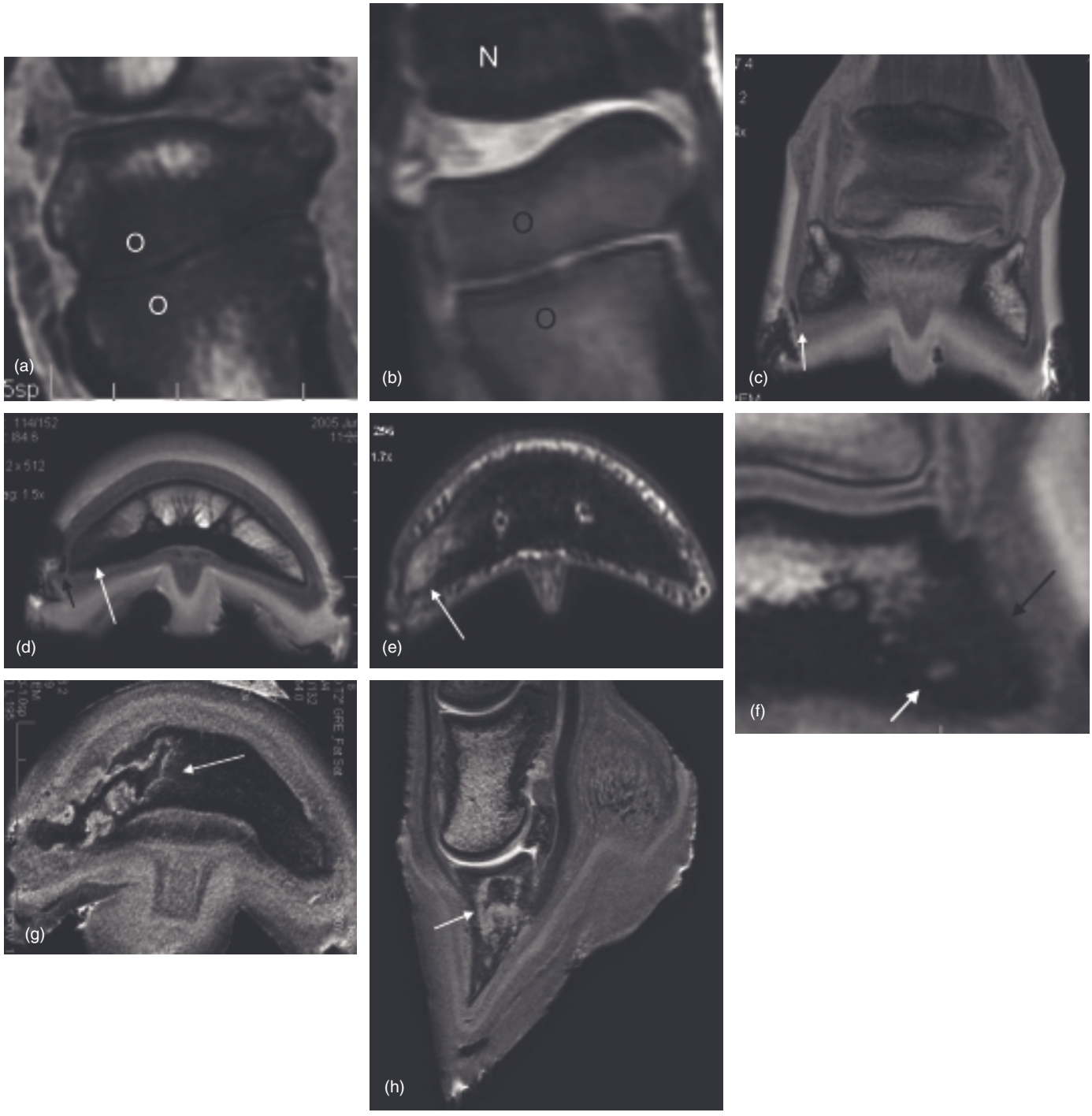

Figure 4.18 Damage to medullary bone can be seen as alterations in signal intensity, which can reflect a variety of types of pathological change. (a) Sagittal T1-weighted image of the third carpal and third metacarpal bones following severe trauma to the carpometacarpal joint. There is low signal intensity in the bones adjacent to the joint (O), indicative of bone damage. The intermediate signal intensity of synovial fluid in the middle carpal joint indicates haemarthrosis or infection. (b) This is supported by the high signal intensity (O) at the same location as (a) on a sagittal STIR image of the same region. (c) Dorsal and (d) transverse T1-weighted image of the foot from a horse with damage to the distal phalanx secondary to trauma from a horseshoe nail. Damage is seen as low signal intensity in the bone (white arrow) adjacent to a linear area of low signal intensity in the laminae (black arrow). (e) Transverse STIR image showing high signal intensity at the same location (arrow), confirming bone damage. (f) Dorsal plane T1-weighted image of the distal phalanx of a horse with chronic lameness with a previous history of solar penetration. There is evidence of focal abscess formation (high signal intensity on T1, T2 and fat-suppressed images) surrounded by reactive bone changes seen as low signal intensity on T1 and high signal intensity on fat-suppressed images. (g) Transverse plane fat-saturated T2* gradient-echo image of a sequestrum (arrow) in the distal phalanx. The sequestered bone is of low signal intensity while the surrounding purulent fluid has high signal intensity. (h) Sagittal plane T2* gradient-echo image of the sequestrum seen in (g).

detected as an increase in signal intensity on T2-weighted and STIR or fat-suppressed images, and decrease in signal on T1-weighted images. Fat-suppression techniques may be required to distinguish fluid from the fat in cancellous bone on most image sequences, although long TR sequences cause fat signal to drop off and show fluid in bone without the need for fat suppression.

These changes are found in bone adjacent to fractures sites, as well as for other types of pathologic change. This combination of an increase in signal intensity on fat-suppressed images, low signal on T1-weighted images and high signal on T2-weighted spin-echo images has been referred to as bone oedema, bone bruising, bone contusion, and more recently as bone marrow or bone marrow oedema-like lesions (Figure 4.8). This signal intensity pattern has been shown to reflect bone necrosis, inflammation, trabecular microdamage, subchondral bone impaction, fracture, stress fracture, haemorrhage, fibrosis, tumour, infarct and bone oedema [1, 2, 29, 69–71]. Focal lesions in the cortical or subchondral bone may be associated with large areas of signal abnormality in the local cancellous bone [10, 72].

It can be impossible to distinguish between some types of pathological processes using MRI alone, so the use of other diagnostic techniques, such as scintigraphic imaging, may be required. Although increased signal intensity in the cancellous bone can continue during the healing process, often the resolution of increased signal intensity on fat-suppressed images correlates with improvement of clinical signs. However, this does not occur in every instance, so in certain cases it may be difficult to use MRI to monitor healing. In humans, abnormalities in bone on MR images can lag behind clinical findings. Depending on the type of injury, residual changes in the signal pattern of the bone on human MR images has been reported to be present for months after clinical recovery [5, 6]. In our clinical experience, this appears less likely to occur in horses.

Fractures show as defects in bone outline and structure, and may show as lines of increased signal intensity on proton density, STIR and T2-weighted images (Figure 4.17). There may be a decrease in signal intensity (usually on T1, possibly T2) dependent a little on the stage of the fracture. Stress fractures are usually low signal intensity on both T1- and T2-weighted images. A fracture is clearly active when it is surrounded by high signal intensity on STIR images, low signal intensity on T1-weighted images and/or high signal on T2* gradient echo possibly with a hypointense rim (due to phase cancellation artefact). However, in the very acute stages of a fracture, this surrounding bone 'oedema' may not yet be present.

Bone abnormality may also be reflected by increased bone density, or sclerosis. This has been reported in the navicular bone [32, 69, 73]. Increased bone density is most apparent when the fat signal in cancellous bone has been replaced by low signal intensity on proton density, T1-weighted and T2-weighted images.

Tissues adjacent to the bone should be carefully evaluated. Periosteal thickening or reaction can be seen as an alteration in surface contour. At an inflammatory, reactive stage this is likely to have increased signal intensity on T2 and proton density images, while at a later stage the ossified

periosteum will have low signal intensity. This is likely to be present in the early stages of a stress fracture or trauma to the bone surface. Altered or increased signal in adjacent soft tissues indicates inflammatory or traumatic damage. Osseous abnormalities at the origin or insertion of a ligament or tendon may reflect damage within these soft tissue structures as well as in the bone. In joints, subchondral bone abnormalities may reflect overlying cartilage damage. Therefore, when osseous abnormalities are present examination of adjacent soft tissues should always be undertaken.

The clinical importance of certain osseous characteristics may not be clear until all the abnormalities on the MR study are obtained and considered together. For example, it has been suggested that dorsoproximal osteophytes on the navicular bone may reflect either primary pathologic change of the navicular bone, osteoarthritic change in the joint, or an adaptive change. Assessment of adjacent structures is therefore important to put these findings into the context of the wider clinical and MRI picture.

Tendon

Like cortical bone, normal tendons and ligaments have primarily low signal intensity on proton density, T1-weighted and T2-weighted images. If muscle tissue is present within the tendon or ligament, such as within the proximal suspensory ligament, then focal areas of moderate/intermediate signal intensity will be contained within the structure [60]. Increased signal intensity indicates tendon or ligament damage. In acute stages or in the presence of inflammatory change, damage is detected as swelling and increased signal intensity on proton density, T1-weighted and T2-weighted images [5, 8, 73–75] (Figure 4.19).

Marked thinning or discontinuity of the tendon contour can indicate an impending or complete tear. At later stages of healing and fibrosis, the lower inflammatory fluid component results in lower signal intensity on T2-weighted and STIR images, but signal intensity on proton density and T1-weighted images remains higher than that of normal tendon [5, 8, 69, 73–77]. It is also recognized in humans/horses that increased signal intensity observed primarily on T1-weighted and only minimally on T2-weighted images can reflect tendon or ligament degeneration rather than tendonitis or desmitis [5]. However, increase in signal intensity on T2 and STIR images can be seen with severe degeneration and necrosis [78]. Tendon lesions must be evaluated carefully on all sequences. The signal intensity within the lesion on the proton density or T1-weighted image must be compared to fluid-sensitive sequences, such as a T2-weighted or STIR image.

Lesions of different severity may appear similar on the proton density or T1-weighted image, but appear significantly different on the T2-weighted or STIR image based on the degree of fluid content within the lesion. Although the size and extent of the lesion can be evaluated well on T1-weighted images, the severity of the lesion should be assessed using the fluid-sensitive sequences. This process is accomplished by comparing the signal intensity of the lesion to the region of known fluid such as the navicular bursa or distal interphalangeal joint. The difference in signal intensity

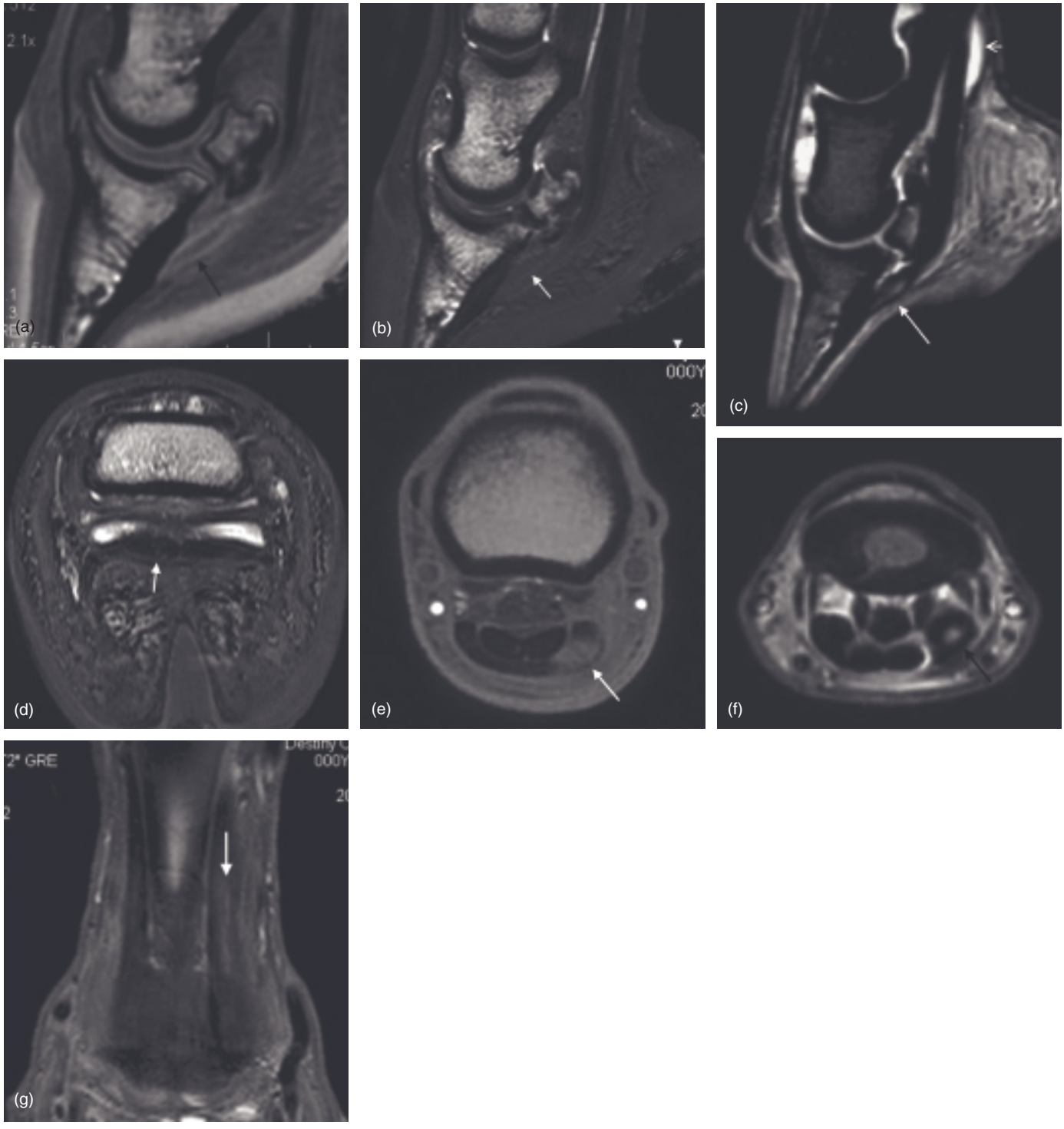

Figure 4.19 Damage to tendons can be seen as increased signal intensity, enlargement or disruption of normal architecture. (a) T1-weighted high-field image of a horse with a necrotic fluid core to the deep digital flexor tendon immediately proximal to the insertion on the distal phalanx. This is seen as low signal intensity within the region of high signal intensity attributable to a magic angle effect in this region. There is also marked disruption to the flexor aspect of the navicular bone. (b) T2* gradient-echo image at the same location. The necrotic core is seen as high signal intensity. (c) STIR image of a horse with a similar lesion. The necrotic core is seen as high signal intensity with marked enlargement of the tendon at this location. (d) Transverse T2* gradient-echo images at the level of collateral sesamoidean ligament, showing adhesions between the ligament and the deep digital flexor tendon, crossing the navicular bursa. The tendon is enlarged with some disruption of the normal architecture. (e) Transverse T1-weighted image at the level of the pastern, showing damage near the medial insertion of the superficial digital flexor tendon. There is increased signal intensity and enlargement of the tendon to the right of the image (arrow). (f) A transverse STIR image immediately distal to (e) confirms a large core lesion in the tendon (arrow). (g) A dorsal plane T2* gradient-echo image of the same region as (e) and (f) is useful to demonstrate the length and extent of the lesion.

between the lesion and a known area of fluid provides a basis for determining the degree of fluid associated with the lesion which can then be correlated with severity.

Other reasons for increased signal in tendon may not reflect pathology, and need to be understood. At compression sites, normal cartilage metaplasia (such as the deep digital flexor tendon at the level of the metacarpophalangeal joint) results in slightly increased signal intensity.

Changes to the peritendonous tissues may also reflect pathologic change. At the level of tendon sheaths, there may be synovial distension. Where there is no tendon sheath, oedema, thickening or proliferation of the peritendonous tissues may be detected [5].

Ligament

Ligament damage can be detected by the presence of periligamentous signal alteration, intraligamentous increase in signal intensity (either focal or diffuse) and ligament thickening [5, 78] (Figure 4.20). Periligamentous oedema is most evident on T2-weighted or STIR images. Periligamentous tissue proliferation or scarring can be detected on all sequences.

For partial tears there may be ligament thinning, elongation, wavy contour or focal retraction of ligament fibres. For complete tears, there is usually a completely interrupted contour, with defects or stumps at the

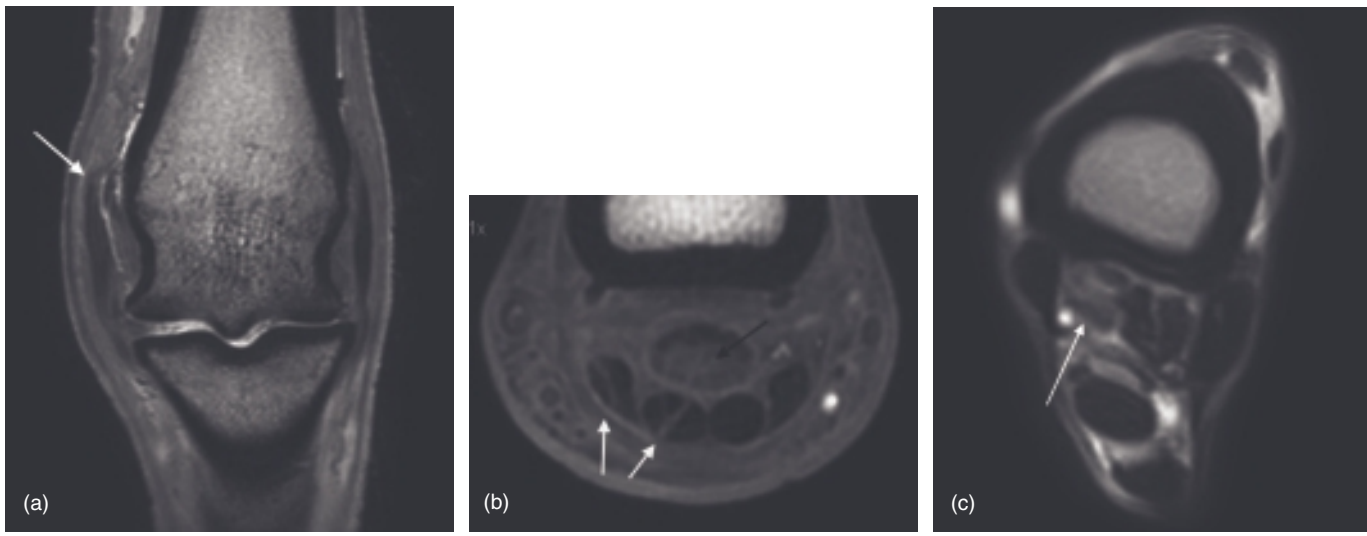

Figure 4.20 Ligament pathology. (a) Dorsal plane image of the metacarpophalangeal joint. The lateral collateral ligament (to the left of the picture) (arrow) is severely disrupted. Relative to the normal medial ligament (to the right of the picture), the damaged ligament has increased signal intensity, loss of continuity and altered size and shape. Periligamentar oedema is indicated by the increased signal intensity and swelling of the soft tissues adjacent to the lateral collateral ligament. The severity of ligament damage is also indicated by the evident joint subluxation. (b) Transverse T1-weighted image of a damaged straight distal sesamoidean ligament. The ligament is enlarged with high signal intensity and loss of normal architecture (black arrow). Note the needle tracts from previous injection through the superficial and deep digital flexor tendons (white arrows). (c) Damage to the proximal suspensory ligament can be difficult to evaluate due to the presence of normal muscle tissue within the ligament, but in this transverse T1-weighted image near the origin of the hind suspensory ligament, the medial lobe has marked increase in signal intensity and loss of normal separation between the muscular and ligamentar tissue.

ligament ends (Figure 4.20). There may be evidence of damage at the ligament origin or insertion characterized by abnormal signal intensity in the ligament fibres, abnormal contour of the adjacent osseous margin or abnormal signal intensity within the adjacent bone. We have observed increased signal intensity in the distal interphalangeal collateral ligaments in association with vacuolar degeneration and chondroid metaplasia [33]. In chronic injuries, there may be ligament thickening during the healing period, which may then be retained long term [5]. In our experience, ligament thickening may also reflect a long-term adaptive response to conformation characteristics, for example with asymmetrical thickness of distal interphalangeal collateral ligaments [78].

Damage to the bone at the origin or insertion of the ligament should be assessed and may show as increased signal intensity on fat-suppressed T2-weighted images in the cortical or cancellous bone with decreased signal on T1-weighted images in the cancellous bone. Enthesiophyte formation or endosteal reaction at the origin or insertion of a ligament can also reflect ligament abnormality. Osseous cyst-like lesions can occur at a ligament insertion with the remainder of the ligament being apparently normal, which has been noted at the insertion of the distal interphalangeal collateral ligaments [78, 79]. Subchondral fracture, cartilage injury and subluxation may also be associated with ligament damage.

Articular cartilage

Cartilage damage can be visualized directly using MR images, as changes in signal and/or alterations in contour (Figure 4.21). Cartilage thickening and increased signal intensity on proton density, T2-weighted and fat-suppressed images (potentially with decreased signal intensity on T1-weighted images) may be seen with increased water content and cartilage swelling. Loss of collagen can lead to focal signal loss, while matrix damage may be indicated by increased signal intensity on T2-weighted images [18, 36]. Surface irregularity

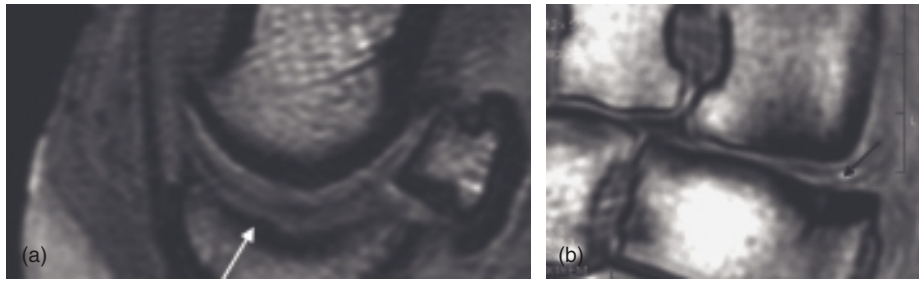

Figure 4.21 Cartilage pathology. (a) Sagittal T1-weighted image of the distal interphalangeal joint. There is irregularity of the cartilage surface and osteochondral irregularity on both aspects of the distal interphalangeal joint (arrow). (b) Sagittal three-dimensional T1 gradient-echo image of the middle carpal joint. This type of image sequence is reported to be particularly useful for assessing articular cartilage. There is a linear defect through the cartilage (arrow) overlying focal subchondral bone abnormality.

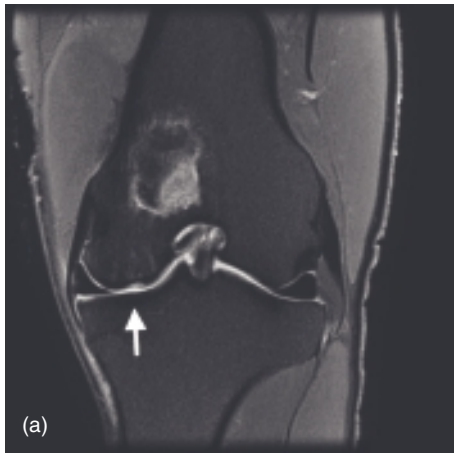

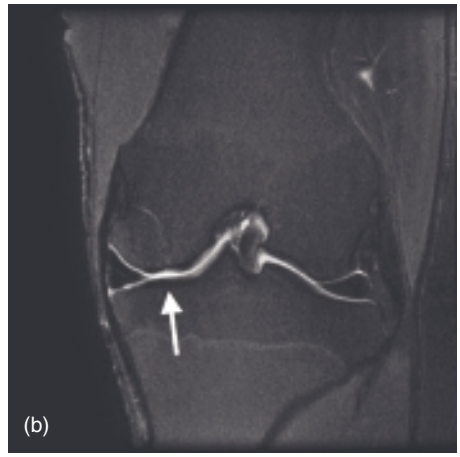

Figure 4.22 Dorsal fat-saturated proton density images of the stifle (a, b).There is increased signal intensity in the subchondral bone at the site of an articular cartilage defect (arrow).

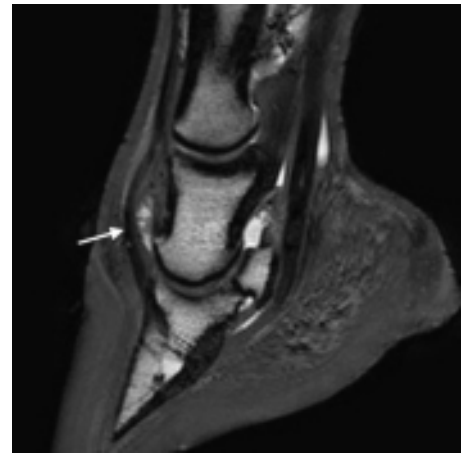

Figure 4.23 Sagittal T2* gradient-echo image of the foot of a horse with marked displacement and thickening of the dorsal aspect of the joint capsule of the distal interphalangeal joint (arrow). There is also a focal increase in signal intensity within the common digital extensor tendon, related to previous intra-articular injection.

on MR images indicates cartilage fibrillation and superficial defects. Deeper defects in the articular cartilage can be visualized as a defect in the cartilage surface contour, while fissures show as a linear defect or linear alteration in signal intensity. Full-thickness defects are usually associated with altered signal intensity, contour or thickness in the subchondral bone [1, 65, 80–82]. Use of fat-suppressed images not only improves contrast in the cartilage itself, but also highlights subtle areas of subchondral bone damage, which may draw attention to a defect in the overlying articular surface [9,83] (Figure 4.22).

Synovial fluid, synovium and joint capsule

Synovial distension results in displacement of the capsular margin. Damage to the capsular tissues may be observed as thickening of the capsule with or without irregular margins (Figure 4.23), while rupture or herniation are seen as a break in the margin with extravasation of fluid. Acute synovial hyperplasia with haemorrhage and oedema may be difficult to differentiate from the adjacent synovial fluid, due to the high fluid content. However, with chronic synovial proliferation, the reduced fluid content and increased fibrosis leads to relatively higher signal intensity of the synovium compared to fluid on T1-weighted images, and decreased signal intensity relative to the fluid on T2-weighted and proton density images. Increased protein content in the synovial fluid is seen as an increase in signal intensity on T1-weighted images compared to normal. Acute haemarthrosis results in a generalized increase in signal intensity of the synovial fluid on T1-weighted images and decrease on T2-weighted images (Figure 4.17). In chronic haemorrhage, presence of haemosiderin within the synovium is seen as small magnetic susceptibility artefacts, appearing as focal areas of signal void. These are particularly obvious on gradient-echo images.

Muscles

Muscular inflammation or contusion appear as increased signal intensity on T2-weighted and STIR images related to elevated water content (oedema) and loss of collagen. Sequelae to muscle injury such as fibrosis or ossification can be detected on MR images. Fibrosis and ossification will be hypointense compared to normal muscle tissue on T2-weighted and proton density images [5, 65]. Muscle tearing can be detected by discontinuity of muscle fibres with associated retraction and bunching of fibres. Muscle tears are often associated with haemorrhage or haematomas, which will have a characteristic appearance over time.

Arteries and veins

Inflammation and damage are frequently associated with increased blood flow, which may be observed as an altered pattern of blood vessels and increased blood vessel size. Haemorrhage is clearly detected on MR images, and can be differentiated into acute or chronic stages. In the hyperacute stage, the relative loss of clotting factors and increase in plasma leads to increased fluid characteristics, with hypointense signal intensity on T1-weighted images and hyperintense signal intensity on T2-weighted images [5]. After 1–3 days, the reduced fluid component and deoxygenated haemoglobin lead to decreased signal intensity on T2-weighted images. After approximately a week, the methaemoglobin leads to increasing T1 signal and a subsequent increasing T2 signal. In the chronic stage, the methaemoglobin hyperintense signal on T1-weighted and T2-weighted images may remain visible in the centre of the haemorrhage, but the periphery appears as a halo of zero or very hypointense signal due to the presence of peripheral haemosiderin (Figures 4.24 and 4.25).

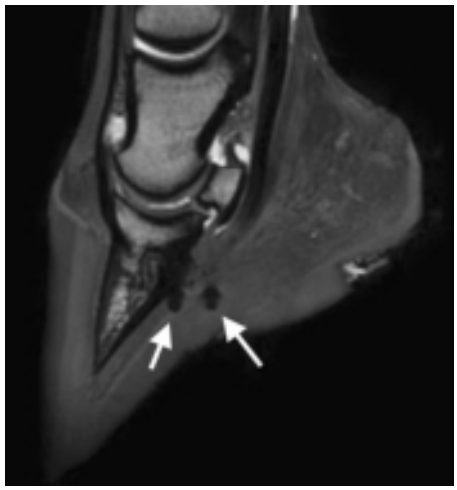

Figure 4.24 Sagittal plane T2* gradient-echo image of the foot of a horse that sustained a penetrating wound to the foot more than 6 months prior to magnetic resonance imaging. There is evidence of haemosiderin deposition in the tissues solar to the insertion of the deep digital flexor tendon, seen as pockets of low signal intensity (arrows) that is clearly visible on gradient echo images.

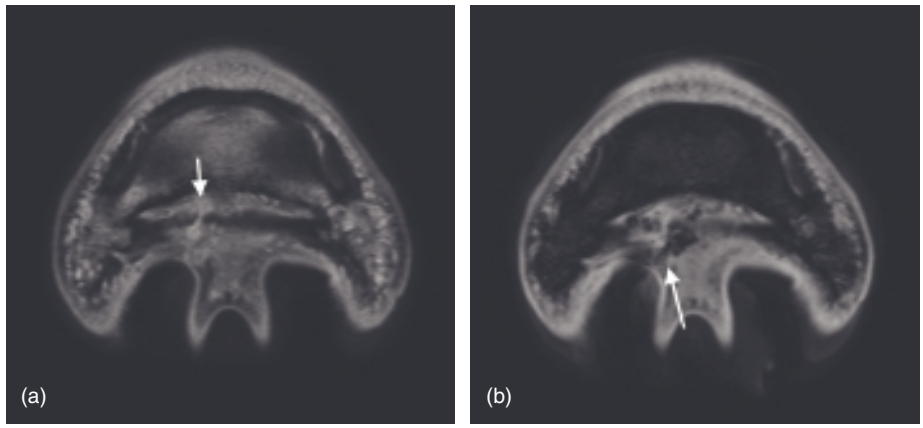

Figure 4.25 Transverse proton density (a) and T2* gradient-echo (b) low-field images of the foot of a horse with severe trauma to the deep digital flexor tendon. There is considerable haemorrhage and haemosiderin accumulation in the tissues around the damaged tendon, which is seen as high signal intensity on proton density and low signal intensity on T2* gradient-echo images (arrow).

Haemosiderin can remain in the tissues for considerable periods of time. Cases of penetrating injury to the foot have been reported where penetration has occurred 6–12 months prior to detection of a linear haemosiderin tract on MRI [84]. Other cases have been seen with evidence of haemosiderin remaining present in tissues for years, and it has been suggested that this may remain almost indefinitely (Figure 4.26). Haemosiderin is shown best on GRE (gradient echo) images due to its magnetic susceptibility artefact, so a GRE sequence should be included in a routine scan of any location where trauma or haemorrhage is potentially involved, including the brain. Although identifying susceptibility artefact is best done on gradient-echo sequences, evaluation of the tissues adjacent to the region of haemorrhage should be done on fast spin-echo or turbo spin-echo images. These sequences will minimize the size of the artefact, thereby increasing visualization of the surrounding tissues.

Relationships between tissues

When assessing any particular tissue or structure, its relationship to other tissues should be considered with respect to both anatomy and function. If there is damage to one structure, then potentially related structures should be assessed completely to rule out damage and to gain further information about potential types and mechanisms of injury. This, in turn, could influence management decisions and prognosis. In the foot, it has been reported that there are relationships between the presence and severity of injury for the navicular bone and surrounding soft tissue structures, including the collateral sesamoidean ligament and distal sesamoidean impar ligament [32, 85]. The same study identified an association between lesions of the distal interphalangeal joint or DDFT, and navicular bone pathology, likely related to both their proximity and biomechanical function.

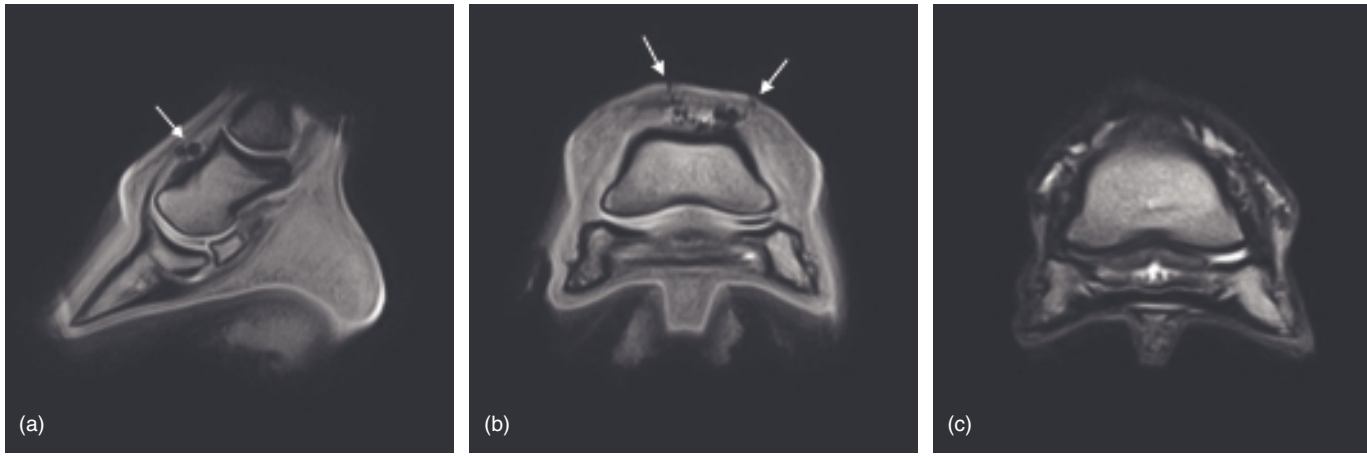

Figure 4.26 Sagittal (a) and transverse (b) T1 gradient-echo images of the distal interphalangeal joint of a horse more than 2 years after previous arthroscopy had been performed, with no lameness associated with the joint. Low signal intensity from remaining haemosiderin remains in the synovium, joint capsule and periarticular tissues (arrow). On a T2 fast spin-echo transverse image (c), the haemosiderin is not visible.

A study comparing scintigraphic and MRI findings concluded that scintigraphy was a useful tool to help determine the significance of MR lesions especially if more than one lesion was identified on MRI that may be contributing to lameness [86]. However, it has also been shown that a lack of scintigraphic abnormality does not preclude MR detection of significant pathological change. Information clarifying the relationship between scintigraphy and MRI has not yet been established. Therefore, the absence of scintigraphic uptake does not necessarily deem a MR finding insignificant. For example, acute contusions that have scintigraphic examination at or close to the time of injury may not necessarily have increased radiopharmaceutical uptake. However, scintigraphic examination performed 2–4 weeks following injury will have scintigraphic uptake. More information must be acquired to understand the timing between stage and severity of injury in relation to increased radiopharmaceutical uptake on scintigraphy examination and correlation with MR findings.

Recheck examinations

Recheck examinations following diagnosis of injury using MRI provide invaluable information. Most lesions that are healing well follow a predictable change in signal pattern during specific time frames. Recheck examinations can be used to determine if an injury is healing appropriately, or if it is not progressing in a manner that would allow the patient to resume exercise. The information gained from recheck examination will dictate any alterations in the rest and rehabilitation programme or the need for additional treatment. Furthermore, lesions of questionable significance can be assessed over time, improving our ability to make a determination of their importance.

Deciding when to perform a recheck examination is based on several factors. The type and severity of the injury and the current understanding of time frames associated with healing of that injury should be considered. Recheck examination performed at approximately 6 months post injury has shown visible improvement on MR images in most soft tissue lesions that are progressing appropriately. This time frame allows assessment about the quality of healing of the injury. However, the owner's goals with regard to recheck examination and treatment should also be taken into account.

The most information about the progression of healing in cases with soft tissue lesions is often gained at approximately 6 months post injury (Figures 4.27 and 4.28). However, a lack of a progression of healing can often be detected sooner than 6 months. Therefore, if additional treatments would be considered at an earlier time frame should the lesion not be progressing and the opportunity for more than one recheck examination is present, examination at 3–4 months post injury should be considered. Obtaining information at 6 months post injury for any type of lesion that is not progressing appropriately could decrease the efficacy of certain types of interventions.

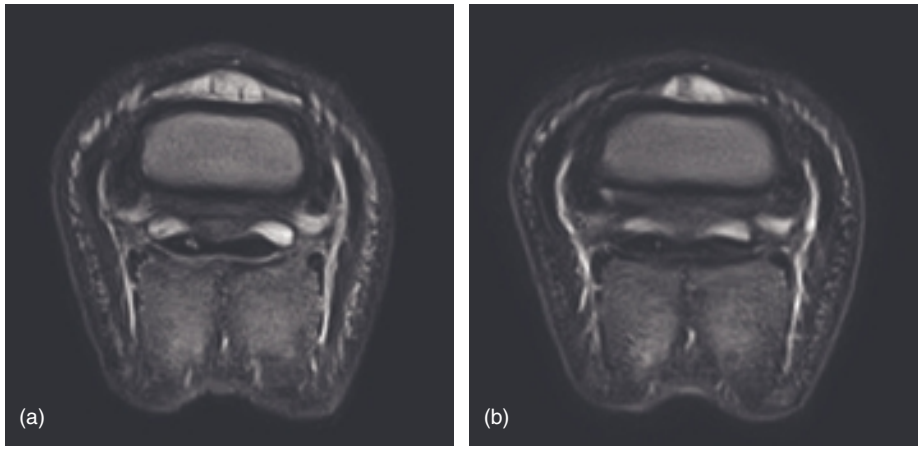

Figure 4.27 Transverse T2-weighted images of a foot at the level of the middle phalanx. On the initial study (a) a core lesion is present in the medial lobe of the deep digital flexor tendon characterized by focal increased signal intensity. The mesotendon is thickened and there is moderate bursitis of the proximal recess of the navicular bursa characterized by increased fluid. On the 6 month follow-up study (b) the lesion in the medial lobe of the deep digital flexor tendon has decreased in size and signal intensity indicating improvement, but not complete resolution of the injury.

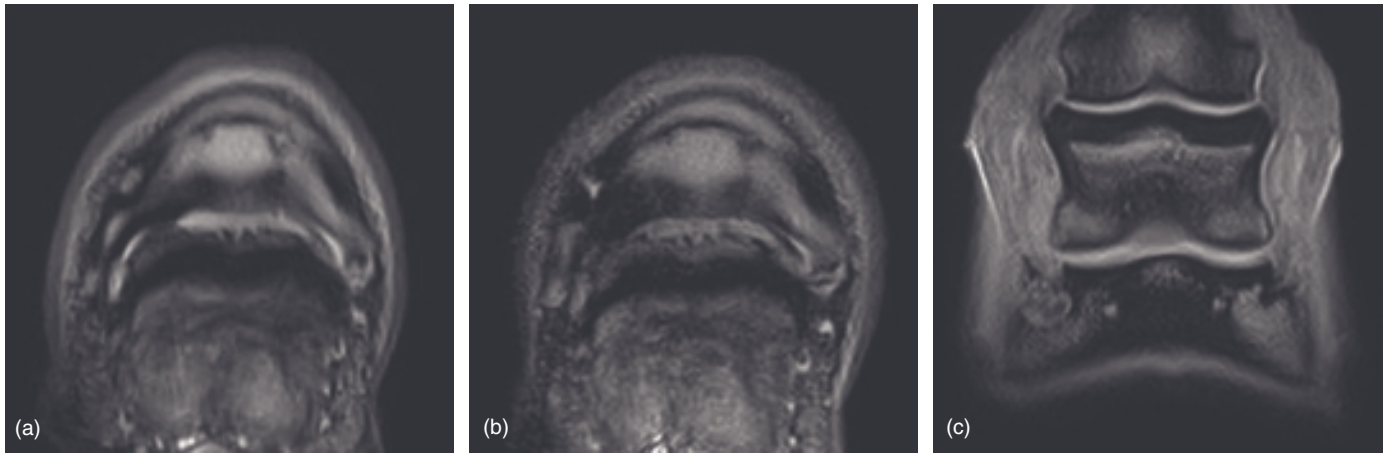

Figure 4.28 A transverse T2-weighted image (a) of a foot with a severe tear in the medial collateral ligament of the distal interphalangeal joint at the level of the insertion on the distal phalanx on the initial study. A T2-weighted transverse image (b) and a T1-weighted gradient-echo frontal image (c) on the 7-month follow-up study. The tear has decreased in size. However, a complete tear can still be identified in the central aspect of the collateral ligament at the level of the insertion on the distal phalanx. The osseous cyst-like lesion in the distal phalanx associated with the collateral ligament tear did not improve on the follow-up study. Although the collateral ligament tear may continue to improve, the greater concern in this case is the lack of bone at the attachment which may make it impossible for the ligament insertion to completely heal.

Uncomplicated bone contusions will show improvement or resolution on MR images between 3 and 6 months (Figure 4.29). This time frame usually correlates well with improvement in clinical signs. For cases that have associated soft tissue injury it is generally beneficial to select the time frame for recheck examination based on the soft tissue injury. Cases that have severe bone contusion or undetected microfracture may develop

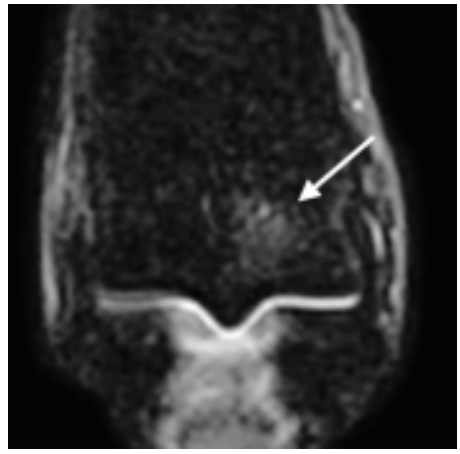

Figure 4.29 Dorsal plane STIR image of the distal metacarpus of a 12-year-old endurance horse examined for lameness localized to the metacarpophalangeal joint. There is increased signal intensity in the lateral parasagittal groove region (arrow). Two months after the initial MR imaging was performed there was complete resolution of the lameness and loss of the increased signal intensity on STIR images.

osteonecrosis and have prolonged lameness and persistent abnormal signal intensity on MR images. Therefore, a seemingly uncomplicated bone contusion that has persistent or worsening lameness should be rechecked a minimum of 3–4 months post injury. The same process can be applied to more complicated fractures. The normal time frame of expected healing should be elongated in cases with severe sclerosis, displacement or associated soft tissue injury.

Certain lesions would not be expected to improve on recheck examination. These include navicular bone flexor surface erosion, full-thickness articular cartilage defect, subchondral bone defect on a weight-bearing articular surface, rotation of the distal phalanx associated with laminitis and extensive trabecular bone sclerosis. Marked improvement would not be expected in cases with adhesions and/or fibrosis of tissue, even though some degree of remodelling can occur over time. For example, chronic proliferative bursitis of the navicular bursa with adhesions to the DDFT rarely improves in appearance on recheck examination. In cases where improvement is not expected, potential worsening of the injury can be monitored with recheck examination and can have important clinical significance. This is especially pertinent in cases where progression of a lesion carries the risk of catastrophic injury. For example, in cases that have had a neurectomy following an injury in the foot, worsening of disease can often be identified, resulting in retirement of the patient prior to catastrophic injury.

Infection vs inflammation

Assessment of lesions is made by comparing the signal pattern, size, shape and margins of the lesion on the original study to those of the recheck examination. If, on the original study, the lesion had increased signal intensity on the fluid-sensitive sequences (T2-weighted or STIR sequences),

improvement would be characterized by a decrease or resolution of the abnormal signal intensity on the recheck examination. Abnormal signal intensity on T1-weighted or proton density images can be present in soft tissue structures in asymptomatic patients, but it can also be associated with lameness. Therefore, to help ensure that this lesion is not a clinically significant finding, recheck examination is used to determine if the appearance of the lesion remains static over time. However, this does not guarantee that the lesion is not contributing to lameness. In fact, certain static lesions indicate a lack of healing. As an example, focal high signal intensity on STIR images within a tendon lobe that is static over 6 months or longer often represents mucoid fluid or a focal area of necrosis within the tendon which is not able to heal. It is important to communicate with owners the information that may be gained from recheck examination. Owners may feel the recheck examination was not beneficial when a lesion is static. However, knowing that the lesion is static allows the veterinarian to make further recommendations about the rehabilitation programme and additional treatments, if indicated.

It should be noted that chronic inflammation in a synovial structure may require more than one treatment to effect a change in the degree of distension.

USING INFORMATION FROM SCINTIGRAPHIC IMAGING TO ASSIST MR IMAGE INTERPRETATION

Bone phase scintigraphic images provide a sensitive marker for bone turnover and can be used to identify primary bone pathology or remodelling secondary to soft tissue damage. Scintigraphy can be used concurrently with MRI to improve understanding of the current activity of different potential lesions seen on MRI. In a comparison of MRI and scintigraphic imaging in the foot, there were significant positive correlations between MR and scintigraphic abnormality for the navicular bone [87]. For MR-detected DDFT lesions or lesions in the collateral sesamoidean ligament, distal sesamoidean impar ligament and navicular bursa, there was increased radiopharmaceutial uptake in the navicular bone in the majority of cases. Use of scintigraphic images may therefore provide information that supports the activity of an osseous or soft tissue, as well as providing an indicator of the site for MR investigation [86]. In my experience, for example, for active or recent DDFT lesions there is commonly increased radiopharmaceutical uptake in the navicular bone adjacent to the site of DDFT damage. This tends to resolve over time in line with clinical improvement, and along with resolution of any increased signal intensity in the navicular bone on fat-suppressed images.

CONCLUSION

MRI can be invaluable for diagnosis, monitoring and study of injury and disease in various parts of the limb, head and neck. It is essential that MRI findings are always interpreted in the light of clinical findings and other diagnostic information. An interpreter must be aware of the limitations of

MRI to avoid overinterpretation or misintepretation of contrast changes observed on MR images, and must have sufficient training to understand their significance.

REFERENCES

[1] Tucker R, Sande RD. Computed tomography and magnetic resonance imaging in equine musculoskeletal conditions. *Vet Clin N Am – Equine* 2001; **17**: 145–57.
[2] Mair TS, Murray RC. The use of magnetic resonance imaging in lameness diagnosis in the horse. *In Practice* 2005; **27**: 138–46.
[3] Graves MJ, McRobbie DW, Moore EA, Prince MR. *MRI: from picture to proton*. Cambridge: Cambridge University Press, 2003.
[4] Kraut C, Westbrook C. *MRI in Practice*, 2nd edn. Oxford: Blackwell Scientific, 1998.
[5] Breitenseher M. *MR Imaging Strategies for the Lower Extremities*. Stuttgart: Thieme, 2005.
[6] Ehman RL, Heaney MD. Interpretation of magnetic resonance images. In: Berquist TH. *MRI of the Musculoskeletal System*, 4th edn. Philadelphia, PA: Lippincott, Williams & Wilkins, 2001, pp. 30–57.
[7] Murray RC, Roberts BL, Schramme MC *et al.* Quantitative evaluation of equine deep digital flexor tendon morphology using magnetic resonance imaging. *Vet Radiol Ultrasound* 2005; **45**(2): 103–11.
[8] Scheider RK, Tucker RL, Zubrod CJ. Use of magnetic resonance imaging to identify suspensory desmitis and adhesions between exostoses of the second metacarpal bone and the suspensory ligament in four horses. *J Am Vet Med Assoc* 2004; **224**: 1815–20.
[9] Scheider RK, Tucker RL, Zubrod CJ *et al.* Use of magnetic resonance imaging for identifying subchondral bone damage in horses: 11 cases (1999–2003). *J Am Vet Med Assoc*; **224**: 411–18.
[10] Dyson S, Murray R, Schramme M. Lameness associated with foot pain: results of magnetic resonance imaging in 199 horses (January 2001–December 2003) and response to treatment. *Equine Vet J* 2005; **37**: 113–21.
[11] Dyson S, Murray R, Schramme M *et al.* (2003) Magnetic resonance imaging of the equine foot: 15 horses. *Equine Vet J* 2003; **35**: 18–26.
[12] Dyson SJ, Murray R, Schramme M *et al.* Magnetic resonance imaging of the equine digit with chronic laminitis. *Vet Radiol Ultrasound* 2003; **44**(6): 609–17.
[13] Kleiter M, Kneissl S, Stanek C *et al.* Evaluation of magnetic resonance imaging techniques in the equine digit. *Vet Radiol Ultrasound* 1999; **40**: 15–22.
[14] Roberts S. Correction of motion artefacts in MRI of the standing horse. *Proceedings 2nd European Veterinary MRI User Meeting*, 2006.
[15] Ehman RL, Felmee JP. Adaptive technique for high-definition MR imaging of moving structures. *Vet Radiol Ultrasound* 1989; **173**: 255–63.
[16] Bolas NM, Jones RD, Kinns J, Mair TS. Magnetic resonance imaging of the distal limb of the standing horse. *Equine Vet Educ* 2005; **17**: 74–8.
[17] Branch MV. How is adaptive change related to pathology in the equine distal tarsal osteochondral unit? PhD thesis, University of London, 2005.
[18] Branch MV, Murray RC, Tranquille C *et al.* Validation of magnetic resonance imaging for measurement of equine articular cartilage and subchondral bone thickness. *Am J Vet Res* 2005; **66**(11): 1999–2005.
[19] Werpy NM. Magnetic resonance imaging of the equine patient: a comparison of high and low field systems. In: Dyson S, Orsini JA. *Clinical Techniques in Equine Practice*. Philadelphia, PA: Elsevier Saunders, 2007, pp. 37–46.
[20] Carrera GF, Cox IH, Erickson SJ *et al.* Effect of tendon orientation on MR imaging signal intensity: a manifestation of the 'magic angle' phenomenon. *Vet Radiol Ultrasound* 1991; **81**: 389–92.
[21] Erickson SJ, Prost RW, Timins ME. The 'magic angle' effect: background physics and clinical relevance. *Vet Radiol Ultrasound* 1993; **188**: 23–5.
[22] Genant HK, Janzen DL, Peterfy CG *et al.* 'Magic angle' phenomenon: a cause of increased signal in the normal lateral meniscus on short-TE MR images of the knee. *Am J Roentgenol* 1993; **163**: 149–54.

[23] Spriet M, Mai W, McKnight A. Asymmetric signal intensity in normal collateral ligaments of the distal interphalangeal joint in horses with a low field MRI system due to the magic angle effect. *Vet Radiol Ultrasound* 2007; **48**: 95–100.
[24] Busoni V, Snaps F. Effect of deep digital flexor tendon orientation on magnetic resonance imaging signal intensity in isolated equine limbs-the magic angle effect. *Vet Radiol Ultrasound* 2002; **43**: 428–30.
[25] Werpy N, Ho C, Kawcak C. Magic angle effect in normal collateral ligaments of the distal interphalangeal joint in horses imaged with a high-field magnetic resonance imaging system. *Vet Radiol Ultrasound* 2010; **51**: 2–10.
[26] Dyson S, Murray RC, Smith M. Is a magic angle effect observed in the collateral ligaments of the distal interphalangeal joint or the oblique sesamoidean ligaments during standing magnetic resonance imaging? *Vet Radiol Ultrasound* 2008; **49**(6): 509–15.
[27] Dyson SJ, Milmine R, Murray RC, Smith MA. Optimisation of STIR sequences for equine standing low field MRI. *Proceedings Voorjaarsdagen European Veterinary Conference* 2008; p. 323.
[28] Cercignani M, Fox NC, Jackson JS *et al.* Imaging cadavers: cold FLAIR and non-invasive brain thermometry using CSF diffusion. *Magnet Reson Med* 2008; **59**(1): 190–5.
[29] Roemer FW, Frobell R, Hunter DJ *et al*. MRI detected subchondral bone marrow signal alterations of the knee joint; terminology, imaging appearance, relevance and radiological differential diagnosis. *Osteoarthr Cartilage* 2009; **17**: 1115–31.
[30] Crowley C, Crues JV, Ghazinoor S. Low-field musculoskeletal MRI. *J Magn Reson Imaging* 2007; **25**: 234–44.
[31] Blunden T, Mair T, Murray RC, Sherlock C. Comparison of high-field and low-field magnetic resonance images of cadaver limbs of horses. *Vet Rec* 2009; **165**: 281–8.
[32] Dyson S, Murray R, Schramme M *et al.* MRI characteristics of the foot in horses with palmar foot pain and control horses. *Vet Radiol Ultrasound* 2006; **47**(1): 1–15.
[33] Marti-Bonmati L, Kormano M. MR equipment acquisition strategies: low-field or high-field scanners. *Eur J Radiol* 1997; **7**(Suppl. 5): 263–8.
[34] Gerhardt P, Langer M, Laubenberger J *et al.* Results of a prospective multicentre study for evaluation of the diagnostic quality of an open whole-body low-field MRI unit. A comparison with high-field MRI measured by the applicable gold standard. *Eur J Radiol* 1999; **30**: 43–53.
[35] Bert J, Crues JV 3rd, Easton R *et al.* Evaluation of the rotator cuff and glenoid labrum using a 0.2-Tesla extremity magnetic resonance (MR) imaging system: MR results compared to surgical findings. *J Magn Reson Imaging* 2001; **14**: 763–70.
[36] Brody J, Entzian DG, Green A, Tung G. High-field and low-field MR imaging of superior glenoid labral tears and associated tendon injuries. *Am J Roentgenol* 2000; **174**: 1107–14.
[37] Hoffman C, Shellock F, Zlatkin M. Assessment of the rotator cuff and glenoid labrum using an extremity MR system: MR results compared to surgical finding from a multi-centre study. *J Magn Reson Imaging* 2004; **19**: 623–63.
[38] Magee T, Shapiro M, Williams D. Comparison of high-field-strength versus low-field-strength MRI of the shoulder. *Am J Roentgenol* 2003; **181**: 1211–51.
[39] Barnett M. MR diagnosis of internal derangements of the knee: effect of field strength on efficacy. *Am J Roentgenol* 1992; **161**: 115–18.
[40] Cevokol C, Karaali K, Esen G, Apaydin A, Ozenci M, Senol U. MR imaging of meniscal tears at low-field (0.35T) and high-field (1.5T) MR units. *Tani Girisim Radyol* 2004; **10**: 316–19.
[41] Boukhelifa M, Boutry N, Chastanet P *et al.* MR imaging of the knee at 0.2 and 1.5 T: correlation with surgery. *Am J Roentgenol* 2000; **174**: 1093–7.
[42] Barden H, Franklin P, Lemon R. Accuracy of imaging the menisci on an in-office, dedicated, magnetic resonance imaging extremity system. *Am J Sports Med* 1997; **25**: 382–8.
[43] Ahovuo J, Bondestam S, Kinnunen J, Kivioja A, Toivakka S, Tulikoura I. Diagnostic performance of low field MRI in acute knee injuries. *J Magn Reson Imaging* 1994; **12**: 1155–60.
[44] Hunink M, Myriam Z, Nikken J, Oei E, Verstijnen AG. MR imaging of the menisci and cruciate ligaments: a systematic review. *Vet Radiol Ultrasound* 2003; **226**: 837–48.

[45] Hof N, Kersting-Sommerhoff B, Merl T, Riel K, Reinisch M. 0.2-Tesla magnetic resonance imaging of internal lesions of the knee joint: a prospective arthroscopically controlled clinical study. *Knee Surg Sport Traumatol Arthroscopy J* 1999; **7**: 37–41.

[46] Lee D, Rutt B. The impact of field strength on image quality in MRI. *J Magn Reson Imaging* 1996; **6**: 57–62.

[47] Dunlavy S, Eliasziw M, Hewett L, Munk P, Vallet AL. Anterior cruciate ligament tear: prospective evaluation of diagnostic accuracy of middle- and high-field-strength MR imaging at 1.5 and 0.5 Tesla. *Vet Radiol Ultrasound* 1995; **197**: 826–30.

[48] Smith M. A comparison of a high-field and a low-field magnetic resonance imaging system for the evaluation of structures of the equine distal limb. PhD thesis, University of London, 2009.

[49] Beyer W, Gluckert K, Kladney B, Swoboda B, Weseloh G. Comparison of low-field (0.2 Tesla) and high-field (1.5 Tesla) magnetic resonance imaging of the knee joint. *Arch Orthop Trauma Surg* 1995; **114**: 281–6.

[50] Ho C, Kawcak C, Pease A, Werpy N. Preliminary study on detection of osteochondral defects in the fetlock joint using low and high field strength MR imaging. *Proceedings of the American Association Equine Practitioners*, 2008.

[51] Baker GJ, Clarkson RB, Martinelli MJ *et al.* Correlation between anatomic feature and low field magnetic resonance imaging of the equine metacarpophalangeal joint. *Am J Vet Res* 1996; **57**: 1421–6.

[52] Birch HL, Murray RC, Vedi S *et al.* Subchondral bone thickness, hardness and remodelling are influenced by short term exercise in a site specific manner. *J Orthop Res* 2001; **19**: 1035–42.

[53] Murray RC. Magnetic resonance imaging of the equine carpus. *Clin Tech Equine Pract* 2007; **6**(1): 86–95.

[54] Dyson SJ, Murray RC. Magnetic resonance imaging of the equine fetlock. *Clin Tech Equine Pract* 2007; **6**(1): 62–77.

[55] Blunden TS, Branch MV, Dyson SJ *et al.* Evaluation of age-related changes in the structure of the equine tarsometatarsal osteochondral unit. *Am J Vet Res* 2009; **70**(1): 30–6.

[56] Dyson SJ, Murray RC. The carpus. In: Thrall D. *Textbook of Veterinary Diagnostic Radiology*, 5th edn. Philadelphia, PA: Elsevier, 2007.

[57] Branch M, Dyson SJ, Goodship A, Murray RC. Magnetic resonance imaging of the equine tarsus. *Clin Tech Equine Pract* 2007; **6**(1): 96–102.

[58] Dyson S, Murray R, Smith S. Magnetic resonance imaging of distal sesamoidean ligament injury. *Vet Radiol Ultrasound* 2008; **49**(6): 516–28.

[59] Bischofberger AS, Geyer H, Konar M *et al.* Magnetic resonance imaging, ultrasonography and histology of the suspensory ligament origin: a comparative study of normal anatomy of warmblood horses. *Equine Vet J* 2006; **38**(6): 508–16.

[60] Baines EA, Bathe AP, Fereday SRJ. Magnetic resonance imaging of the proximal suspensory ligament in the hindlimbs of the horse. *Proceedings of the British Equine Veterinary Association* 2003; **42**: 297.

[61] Branch MV, Dyson SJ, Murray RC, Schramme M. Validation of magnetic resonance imaging use in equine limbs. *Clin Tech Equine Pract* 2007; **6**(1): 26–36.

[62] Blunden T, Dyson S, Murray R. The collateral ligaments of the distal interphalangeal joint: magnetic resonance imaging and post mortem observations in 25 lame horses and 12 control horses. *Equine Vet J* 2008; **40**(6): 538–44.

[63] Asbeutah A, Cicuttini F, Forbes A *et al.* Comparison and reproducibility of fast and conventional spoiled gradient-echo magentic resonance sequences in the detemination of knee cartilage volume. *J Orthop Res* 2000; **18**: 580–4.

[64] Disler DG, McCauley TR, Wirth CR *et al.* Detection of knee hyaline cartilage defects using fat-suppressed three-dimensional spoiled gradient-echo MR imaging: comparison with standard MR imaging and correlation with arthroscopy. *Am J Radiol* 1995; **165**: 377–82.

[65] Jiang Y, Peterfly CG, Zhao JJ *et al.* Magnetic resonance imaging in osteoarthritis. In: Reginster JY, Pelletier JP, Martel-Pelletier J, Henrotin Y. *Osteoarthritis. Clinical and Experimental Aspects*. New York: Springer-Verlag, 2000, pp. 268–95.

[66] Drape JL, Pessis E, Sarazin L *et al.* MR imaging of articular cartilage. *J Radiol* 1998; **79**: 391–402.

[67] Kim YS, Resnick D, Trudell D, Yeh LR. MR imaging of the major nerves about the elbow: cadaver study examining the effect flexion extension of the elbow and pronation supination of the forearm. *J Skeletal Radiol* 1998; **27**: 419–26.
[68] Abraham-Zadeh R, Resnick D, Yu JS. Central (inferior) osteophytes of the distal femur: imaging and pathological findings. *Invest Radiol* 1994; **29**: 1001–5.
[69] Blunden AS, Murray RC, Schramme MC *et al.* How does magnetic resonance imaging represent histological findings in the equine digit? *Vet Radiol Ultrasound* 2006; **47**(1): 16–31.
[70] Freund M, Kathrein A, Rangger C *et al.* Bone bruise of the knee. Histology and cryosections in 5 cases. *Acta Orthopaedica Scandinavia* 1998; **69**(3): 291–4.
[71] Bruder E, Romero J, Zanetti M *et al.* Bone marrow edema pattern in osteoarthritic knees: correlation between MR imaging and histologic findings. *J Radiol* 2000; **215**: 835–40.
[72] Boado A, Dyson S, Kristoffersen M *et al.* Magnetic resonance imaging to diagnose chronic penetrating wounds in the equine foot. *Equine Vet Educ* 2005; **17**: 62–8.
[73] Busoni V, Heimann M, Trenteseaux J *et al.* Magnetic resonance imaging findings in the equine deep digital flexor tendon and distal sesamoid bone in advanced navicular disease – an ex vivo study. *Vet Radiol Ultrasound* 2005; **46**(4): 279–86.
[74] Crass JR, Genovese RL, Render JA *et al.* Magnetic resonance, ultrasound and histopathologic correlation of acute and healing equine tendon injuries. *Vet Radiol Ultrasound* 1992; **33**: 206–16.
[75] Kasashima Y, Katayama Y, Kuwano A *et al.* Magnetic resonance imaging application to live horse for diagnosis of tendonitis. *J Vet Med Sci* 2002; **64**: 577–82.
[76] Dyson S, Murray R, Schramme M *et al.* Lameness in 46 horses associated with deep digital flexor tendonitis in the digit: diagnosis confirmed with magnetic resonance imaging. *Equine Vet J* 2003; **35**: 681–90.
[77] Kumer B, Threepuraneni G, Tolat A *et al.* The role of magnetic resonance imaging in late presentation of isolated injuries of the digitorum profundus tendon in the finger. *J Hand Surg* 2000; **25B**: 95–7.
[78] Blunden A, Dyson S, Murray R *et al.* Histological findings in horses with chronic palmar foot pain and age-matched control horses. Part 1: The navicular bone and related structures. *Equine Vet J* 2006; **38**(1): 15–22.
[79] Dyson S, Murray R, Schramme M *et al.* Collateral desmitis of the distal interphalangeal joint in 18 horses (2001–2002). *Equine Vet J* 2004; **36**: 160–6.
[80] Juretschke HP, Raiss RX, Wachsmuth L. Can magnetisation transfer magnetic resonance imaging follow proteoglycan depletion in articular cartilage? *Magnet Reson Mater Phy* 1997; **5**: 71–8.
[81] Anastasiou A, Ekman S, Skoldergrand E *et al.* Ex vivo magnetic resonance imaging of the distal row of equine carpal bones: assessment of bone sclerosis and cartilage damage. *Vet Radiol Ultrasound* 2003; **44**: 501–12.
[82] Bergman AG, Lindstrand AL, Willen HK *et al.* Osteoarthritis of the knee; correlation of subchondral MR signal abnormalities with histopathologic and radiographic features. *J Skeletal Radiol* 1994; **23**: 445–8.
[83] Denoix J-M, Crevier N, Roger B *et al.* Magnetic resonance imaging of the equine foot. *Vet Radiol Ultrasound* 1993; **34**: 405–11
[84] Boado A, Dyson S, Kristoffersen M, Murray R. Use of nuclear scintigraphy and magnetic resonance imaging to diagnose chronic penetrating wounds in the equine foot. *Equine Vet Educ* 2005; **17**: 62–8.
[85] Dyson S, Murray R. Magnetic resonance imaging evaluation of 264 horses with foot pain; the podotrochlear apparatus, deep digital flexor tendon and collateral ligament of the distal interphalangeal joint. *Equine Vet J* 2007; **39**: 340–3.
[86] Dyson S, Murray R. Verification of scintigraphic imaging for injury diagnosis in 264 horses with foot pain. *Equine Vet J* 2007; **39**: 350–5.
[87] Dyson S, Murray R. Use of concurrent scintigraphic and magnetic resonance imaging evaluation to the improve understanding of the pathogenesis of injury of the podotrochlear apparatus. *Equine Vet J* 2007; **39**: 365–9.

Section B
Normal MRI anatomy

Chapter 5
The foot and pastern

5A Adult horse

Sue Dyson

INTRODUCTION

Magnetic resonance imaging (MRI) has revolutionized our knowledge of the spectrum of injuries that can cause foot pain and lameness [1–13]. However, accurate interpretation of MR images requires an in-depth knowledge of anatomy and an understanding of the types of abnormality that can be seen in clinically sound horses. Based on a previous study [14], we know that low-grade pathological abnormalities may be seen using MRI in horses currently free from lameness (Table 5.1). These signal abnormalities have generally corresponded well with abnormalities detected by gross and histopathological postmortem examination [15–18]. Lesions detected using MRI have been graded in severity from 0 to 3 [14], and are considered more likely to be associated with pain and lameness if ≥2. We have recognized that advanced pathological change can be present relatively soon (6–8 weeks) after the recognition of lameness, and it is presumed that these abnormalities may have been pre-existing [5]. However, once pain associated with such lesions has been triggered it appears to be persistent. Pathological changes to one or more structures of similar severity are sometimes seen in both limbs of a unilaterally lame horse, supporting the hypothesis that lesion development may predate the onset of pain and lameness.

The purpose of this chapter is to describe normal anatomy with reference to both low-field and high-field images. High-field images tend to have greater resolution and be acquired using much thinner slice thickness than low-field images and therefore give potentially more detailed anatomical information. The appearance of each anatomical structure varies somewhat according to the sequence type e.g. three-dimensional (3D) T2* gradient-echo (GRE) versus two-dimensional (2D) fast spin-echo (FSE), and it is beyond the scope of this text to provide detailed information for each sequence type for all structures. However, some tendonous and ligamentous structures are susceptible to the magic angle effect and this is influenced by sequence type and is discussed where relevant. Likewise, the apparent shape of structures is altered in transverse and dorsal plane images depending on the orientation of the slices during acquisition. It is beyond the scope of this

Equine MRI, edited by Rachel C. Murray. © 2011 by Blackwell Publishing Ltd.

Table 5.1 Proportion (%) of limbs graded 0 (normal) to 3 (severe abnormality) for signal irregularities on MR imaging in 27 limbs from horses without lameness (Group N)

Group N (n = 27)	Grade 0	Grade 1	Grade 2	Grade 3
DDFT	85	15	0	0
NB	19	69	12	0
CSL	88	12	0	0
DSIL	69	19	12	0
Navicular bursa	85	15	0	0
DIP joint	81	19	0	0
PIP joint	89	7	4	0
CL of the DIP joint	85	7	7	0
Middle phalanx	100	0	0	0
Distal phalanx	37	41	22	0
Laminae	70	19	11	0
Cartilages of the foot	100	0	0	0
CDE	100	0	0	0
Digital cushion	100	0	0	0
SSL	100	0	0	0

DDFT, deep digital flexor tendon; NB, navicular bone; CSL, collateral sesamoidean ligament; DSIL, distal sesamoidean ligament; DIP, distal interphalangeal; PIP, proximal interphalangeal; CL, collateral ligament; CDET, common digital extensor tendon; SSL, straight sesamoidean ligament. Adapted from: Murray R, Schramme M, Dyson S *et al*. MRI characteristics of the foot in horses with palmar foot pain and control horses. *Vet Radiol & Ultrasound* 2006; **47**: 1–16.

text to discuss all possible variants. It can be difficult to acquire perfectly aligned sagittal, dorsal (frontal) and transverse images depending on the shape of the distal limb. Image obliquity alters the appearance of a structure and potentially compromises its assessment. Mention is made of some incidental variants, or lesions that are considered to be of unlikely clinical significance.

NAVICULAR BONE

A normal navicular bone has clearly demarcated proximal, distal, dorsal and palmar (flexor) cortices, of low signal intensity in all image sequences, with a variable number of small similarly sized indentations of the distal cortex (Figures 5.1–5.3). These indentations may be synovial invaginations, and synovial fluid has high signal intensity in T2-weighted images. The most variable feature of the navicular bone is the number, size and shape of these cortical irregularities along the distal border. The flexor cortex is usually of uniform thickness from proximal to distal and has a smooth endosteal margin. In a transverse image there may be a crescent-shaped area of relatively high signal intensity within the cortex at the sagittal ridge, corresponding to the radiolucent area described radiologically [19]. The spongiosa (medulla) has relatively high signal intensity in all except fat-suppressed images, in which there is uniformly low signal intensity. The fibrocartilage can be seen as a thin layer of intermediate signal intensity in high-resolution

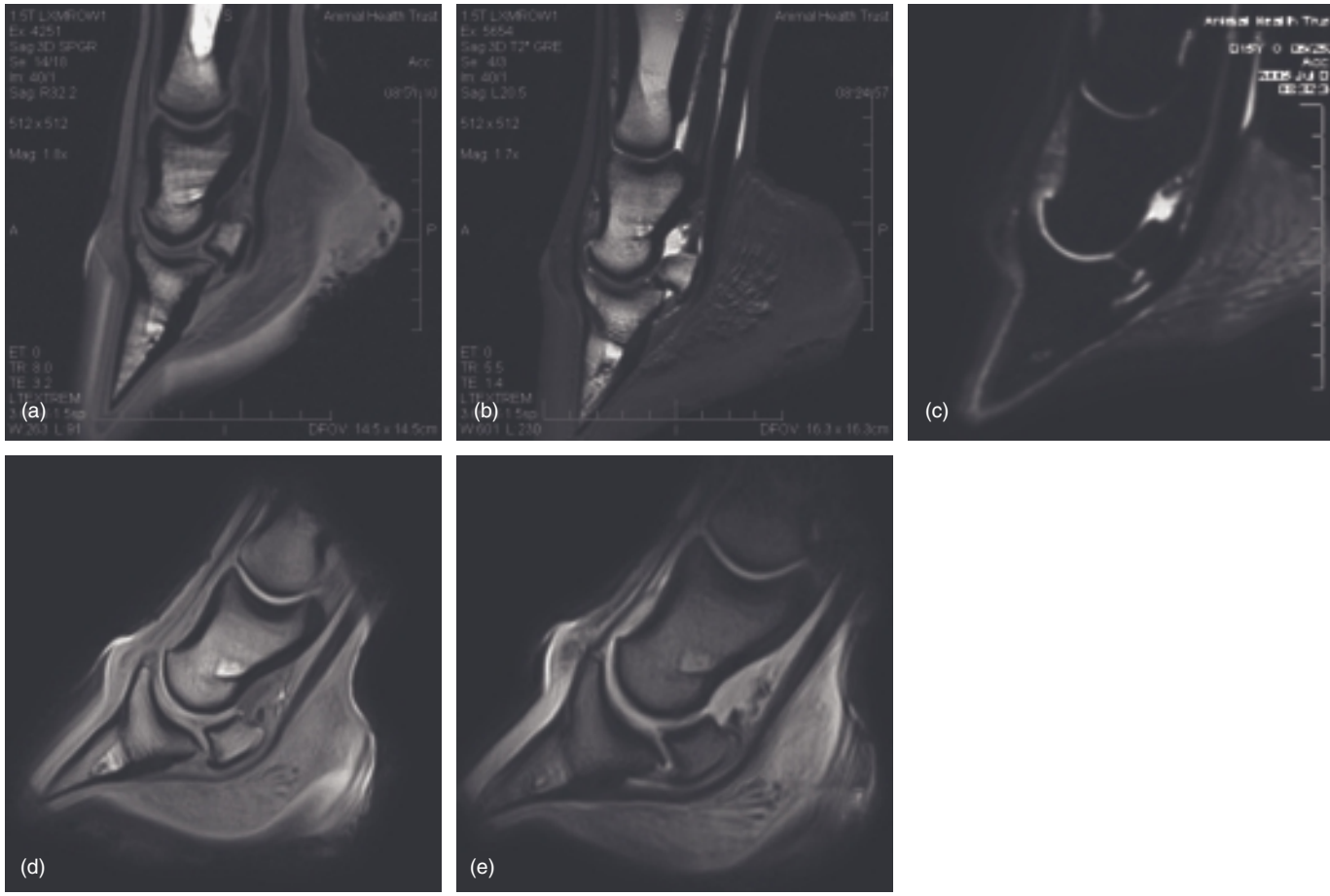

Figure 5.1 (a) Normal sagittal 3D T1-weighted spoiled gradient-echo (SPGR) high-field image of a foot. Note the bulbous appearance of the insertion of the straight sesamoidean ligament (SSL) on the middle phalanx and its heterogeneous signal intensity. The deep digital flexor tendon (DDFT) distal to the navicular bone and the distal sesamoidean impar ligament (DSIL) have a hyperintense signal due to the magic angle effect. (b) Normal sagittal 3D T2* gradient-echo (GRE) high-field image of a foot. The hyperintense fluid signal in the navicular bursa clearly separates the collateral sesamoidean ligament (CSL) and the deep digital flexor tendon (DDFT), and the distal sesamoidean impar ligament (DSIL) and the DDFT. The DDFT distal to the navicular bone and the DSIL have mildly increased signal intensity due to the magic angle effect. There is focal higher signal intensity in the straight sesamoidean ligament close to its insertion. (c) Normal sagittal 2D STIR high-field image of a foot. In contrast to (a) and (b) the DDFT and DSIL have uniform low signal intensity. (d) Normal sagittal T1-weighted 3D GRE low-field MR image of a foot acquired standing. (e) Normal sagittal T2*-weighted 3D GRE low-field MR image of the same foot as (d).

transverse T2* GRE images, but is poorly defined in low-resolution images, particularly due to partial volume effect.

An isolated distal border fragment at the medial or lateral angle of the distal border of the navicular bone is sometimes seen as an incidental finding (Figure 5.2e) in the absence of any reaction in the parent bone, and with no structural abnormality of the distal sesamoidean impar ligament (DSIL). The detection of distal border fragments and assessment of associated bone reaction in the navicular bone is more difficult in images with greater slice thickness, where lesions may be missed as a result of partial volume effect.

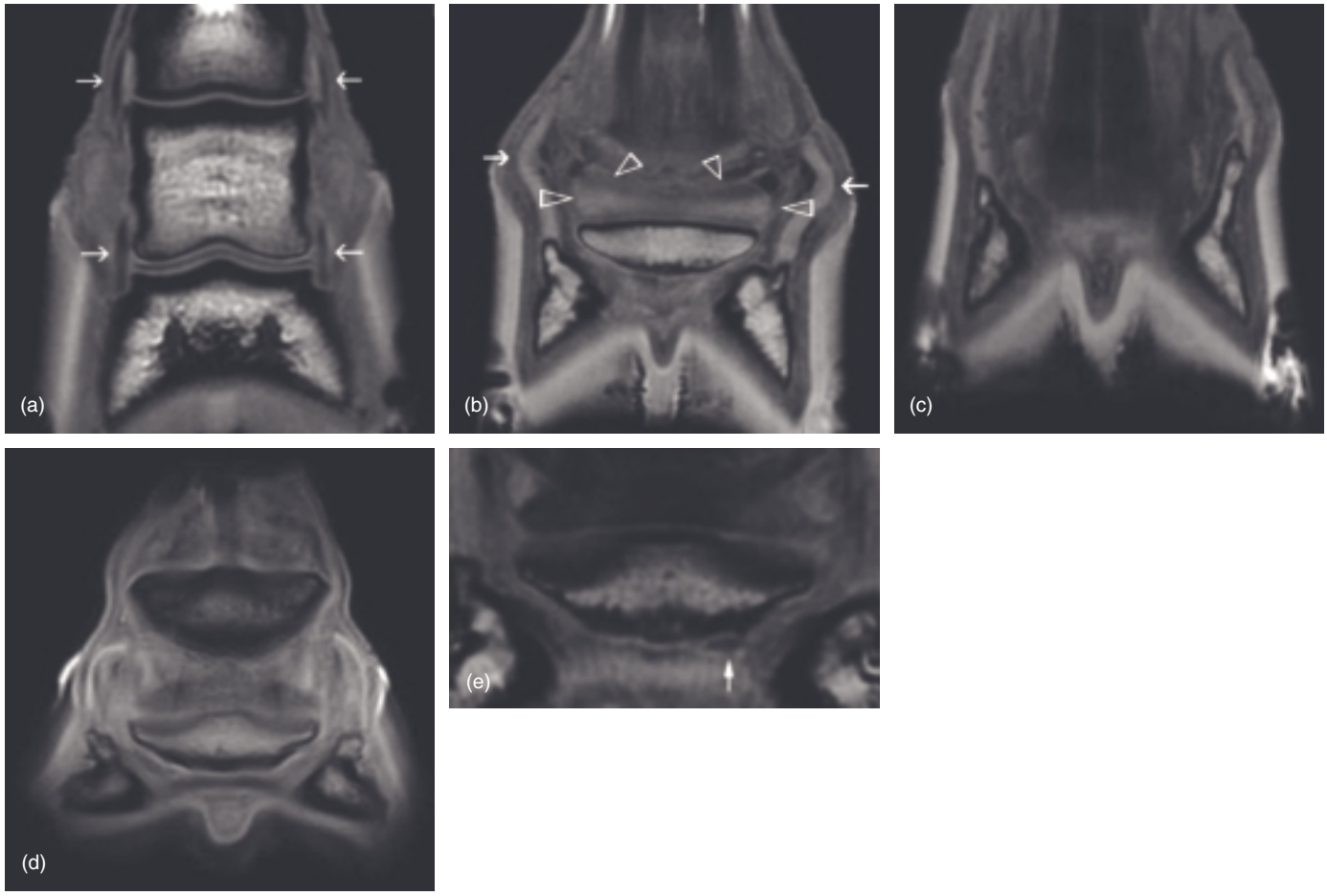

Figure 5.2 (a) Normal dorsal (frontal) 3D T1-weighted SPGR high-field image of a foot at the level of the interphalangeal joints. Medial is to the left. Note the relatively uniform thickness of the subchondral cortical bone from medial to lateral and the symmetrical size and signal intensity of the collateral ligaments of the proximal and distal interphalangeal (DIP) joints (arrows). The undulating black line between the middle and distal phalanges is fluid in the DIP joint. (b) Normal dorsal (frontal) 3D T1-weighted SPGR high-field image of a foot at the level of the navicular bone and cartilages of the foot. Medial is to the left. There are multiple relatively uniform indentations of the distal cortex of the navicular bone. The curved unossified cartilages of the foot (arrows) extend proximally from the palmar processes of the distal phalanx. The outline of the collateral sesamoidean ligaments (CSLs) can be seen (arrow heads). There is slightly reduced signal intensity on the trabecular bone of the medial palmar process of the distal phalanx. (c) Normal dorsal high-field T1-weighted SPGR image of a foot. Medial is to the left. There is moderate ossification of the lateral cartilage of the foot and mild ossification of the medial cartilage of the foot. (d) Normal dorsal T1-weighted 3D GRE low-field MR image of a foot at the level of the navicular bone and cartilages of the foot. The oblique lines of high signal intensity to the left and right of the image are artefacts. (e) Dorsal high-field 3D T1-weighted SPGR MR image of a navicular bone. Medial is to the left. There is a fragment (arrow) distal to the lateral angle of the distal border of the navicular bone, but little alteration in architecture of the navicular bone, which has a slightly thickened distal cortex. This was an incidental finding of unlikely clinical significance.

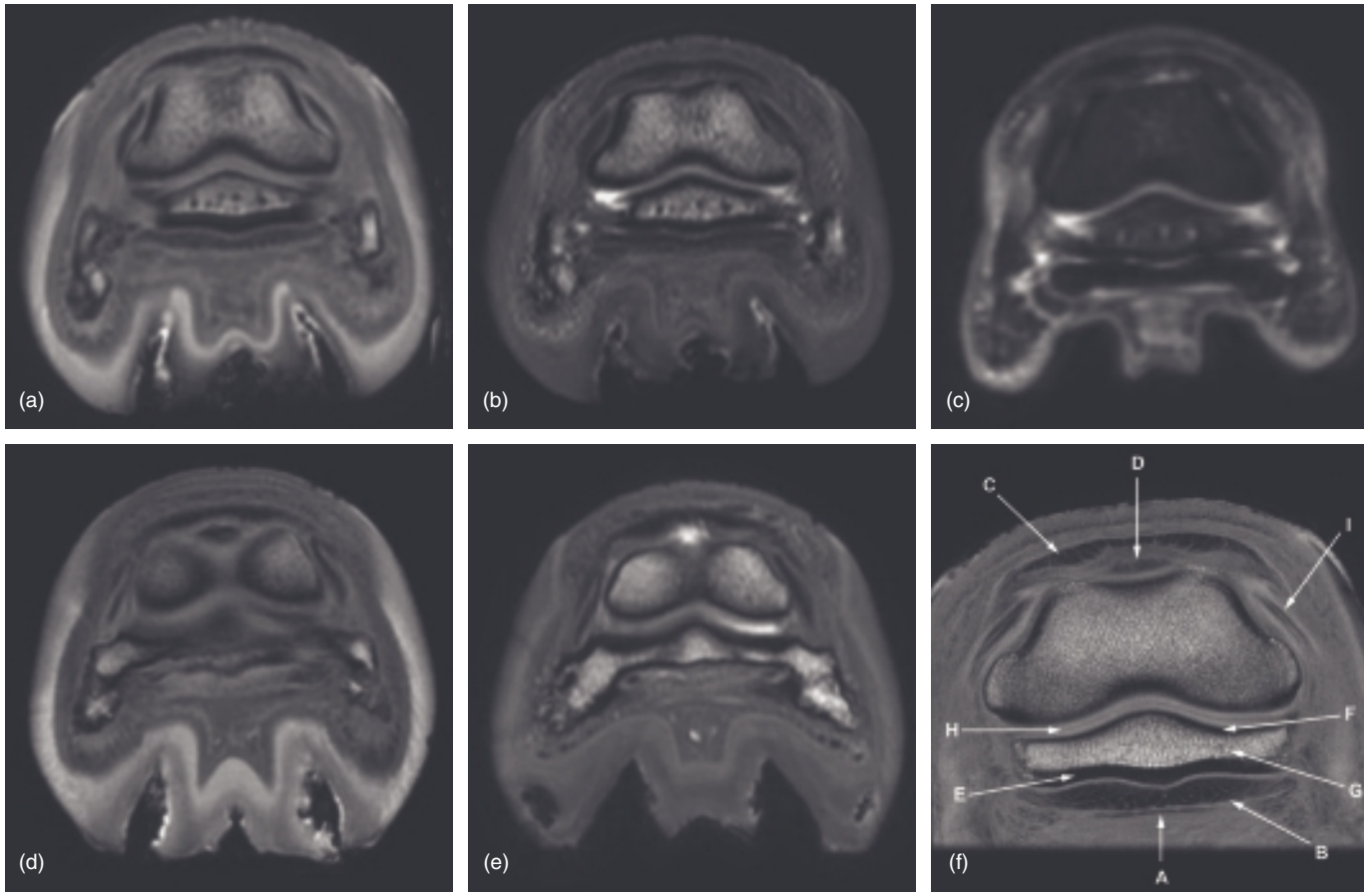

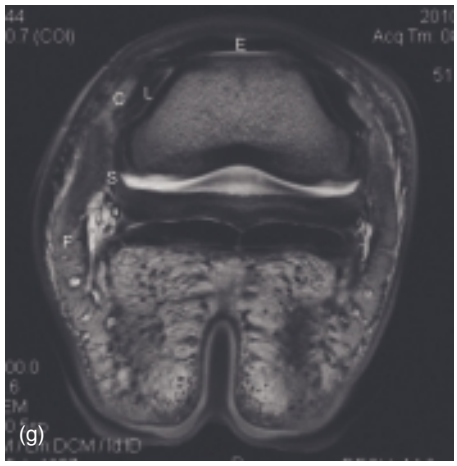

Figure 5.3 (a) Normal transverse 3D T1-weighted SPGR high-field image at the level of the distal aspect of the middle phalanx. Medial is to the left. The collateral ligaments (CLs) of the distal interphalangeal (DIP) joint have uniform low signal intensity, although the medial CL is slightly thicker than the lateral CL, which has slightly higher signal intensity around it. (b) Normal 3D T2* GRE high-field image of the same foot as (a). (c) Normal transverse 2D STIR high-field image of the same foot as (a) and (b). (d) Normal transverse high-field 3D T1-weighted SPGR image at the level of the distal phalanx. Medial is to the left. The collateral ligaments (CLs) of the distal interphalangeal joint are of low signal intensity, although there is a thin rim of higher signal intensity around the periphery of the medial CL. The distal sesamoidean impar ligament is thickest axially. (e) Normal transverse high-field 3D T2* GRE image at the level of the distal phalanx, the same foot as (d). Medial is to the left. The collateral ligaments of the distal interphalangeal joint have low signal intensity and are similar in shape and size. The cortical margin of the medial palmar process is somewhat irregular, with reduced signal intensity in the underlying trabecular bone. There is a small amount of fluid in the distal recess of the navicular bursa separating the deep digital flexor tendon and the distal sesamoidean impar ligament. (f) High-resolution transverse high-field T1 SPGR image. Note the detail seen within the deep digital flexor and common digital extensor tendons. A, distal digital annular ligament; B, deep digital flexor tendon showing fascicular structure; C, common digital extensor tendon showing fascicular structure; D, dorsal pouch of the distal interphalangeal joint; E, palmar (flexor) cortex of the distal sesamoid bone; F, dorsal (articular) cortex of the distal sesamoid bone; G, cancellous bone of the distal sesamoid, showing trabecular bone structure and hyperintense MR signal of the inter-trabecular fat deposits; H, articular cartilage of the middle phalanx and the distal sesamoid bone (hyperintense MR signal), separated by synovial fluid of the distal interphalangeal joint (hypointese MR signal). Image courtesy of Dr Simon Collins, Animal Health Trust. (g) Transverse high field proton density image at the proximal aspect of the collateral ligaments with the lateral structures labelled. Note the close relationship between the collateral ligament (L), the chondrocoronal ligament (C) with its attachment to the common digital extensor tendon (E), the chondrosesamoidean ligament (S) and the cartilage of the foot (F).

DEEP DIGITAL FLEXOR TENDON

A normal deep digital flexor tendon (DDFT) has a uniform, low signal intensity, with tendon fascicles separated by lines of higher signal intensity seen in transverse high-resolution images [20] (Figures 5.1–5.7). At areas of marked biomechanical compression of the DDFT, where there is fibrocartilaginous change within the dorsal aspect of the tendon, the dorsal aspect of the tendon has intermediate signal intensity. Proximally, in transverse images the DDFT is oval-shaped (Figure 5.6a), but it rapidly becomes a bilobed structure (Figures 5.3–5.5 and 5.6b–e). In sagittal plane images acquired in a closed-bore high-field magnet the distal aspect of the DDFT may have relatively high signal intensity in T1-weighted images, and to a lesser extent in T2-weighted GRE images, due to the magic angle effect [21] (Figures 5.1a and b). This feature is not seen in images acquired using a low-field system, whether images are obtained standing (Figure 5.1d) or under general anaesthesia as the static magnetic field, B_0, is perpendicular to the limb. In a low-field system, linear areas of increased signal intensity on the palmar aspect of one lobe of the DDFT in the region of the navicular bone may be seen if the limb is not perpendicular to B_0. A linear hyperintense band may also be seen on the on the dorsal aspect of the other lobe [22]. This is due to local variations in fibre alignment on the dorsal and palmar aspects of the DDFT and focal manifestations of the magic angle effect.

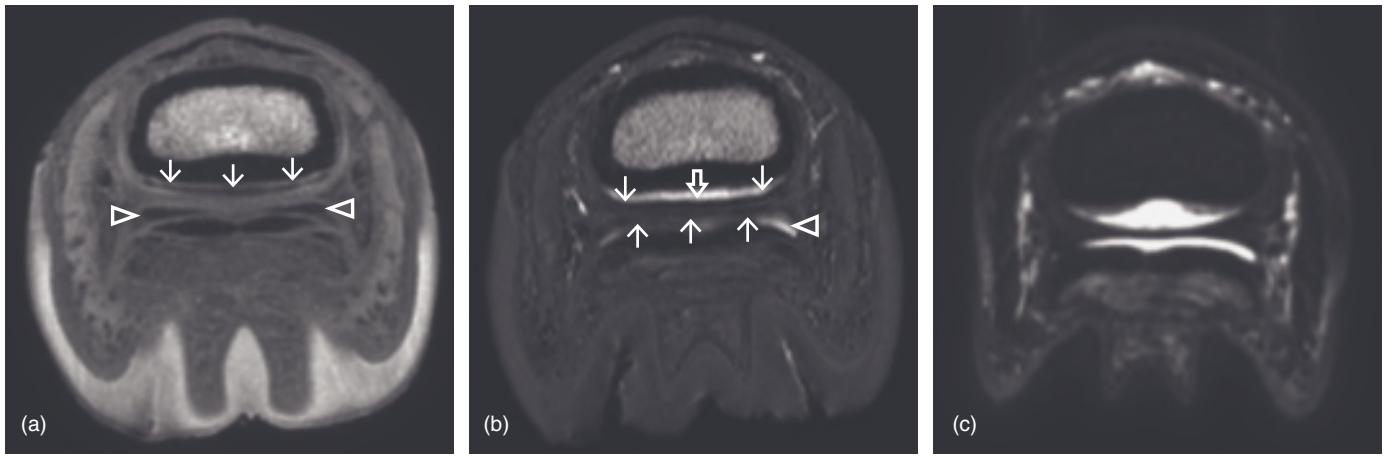

Figure 5.4 (a) Normal transverse 3D SPGR high-field image at the level of the middle phalanx. Dorsal is proximal. Hypointense fluid in the palmar recess of the distal interphalangeal (DIP) joint (arrows) and in the navicular bursa (arrow heads) provide demarcation for the collateral sesamoidean ligament (CSL), which has intermediate signal intensity. The deep digital flexor tendon (DDFT) is the bilobed hypointense structure palmar to the navicular bursa. The broad common digital extensor tendon is seen dorsally as a thin subcutaneous structure of hypointense signal, palmar to which are three foci of hypointense signal, loculated fluid in the dorsal recess of the DIP joint. (b) Transverse 3D T2* GRE high-field image at the same level as (a). The collateral sesamoidean ligament (CSL) (arrows) is clearly outlined by the fluid in the palmar recess of the distal interphalangeal (DIP) joint (open arrow) and fluid in the navicular bursa (arrow head), palmar to which is the bilobed deep digital flexor tendon. There are strands of soft tissue in the dorsal recess of the DIP joint. (c) Transverse 2D STIR high-field image at the same level as (a) and (b). The collateral sesamoidean ligament (CSL) is clearly outlined by fluid in the palmar recess of the distal interphalangeal joint and fluid in the navicular bursa. The middle phalanx and the deep digital flexor tendon (DDFT) have low signal intensity, whereas the CSL has intermediate signal intensity.

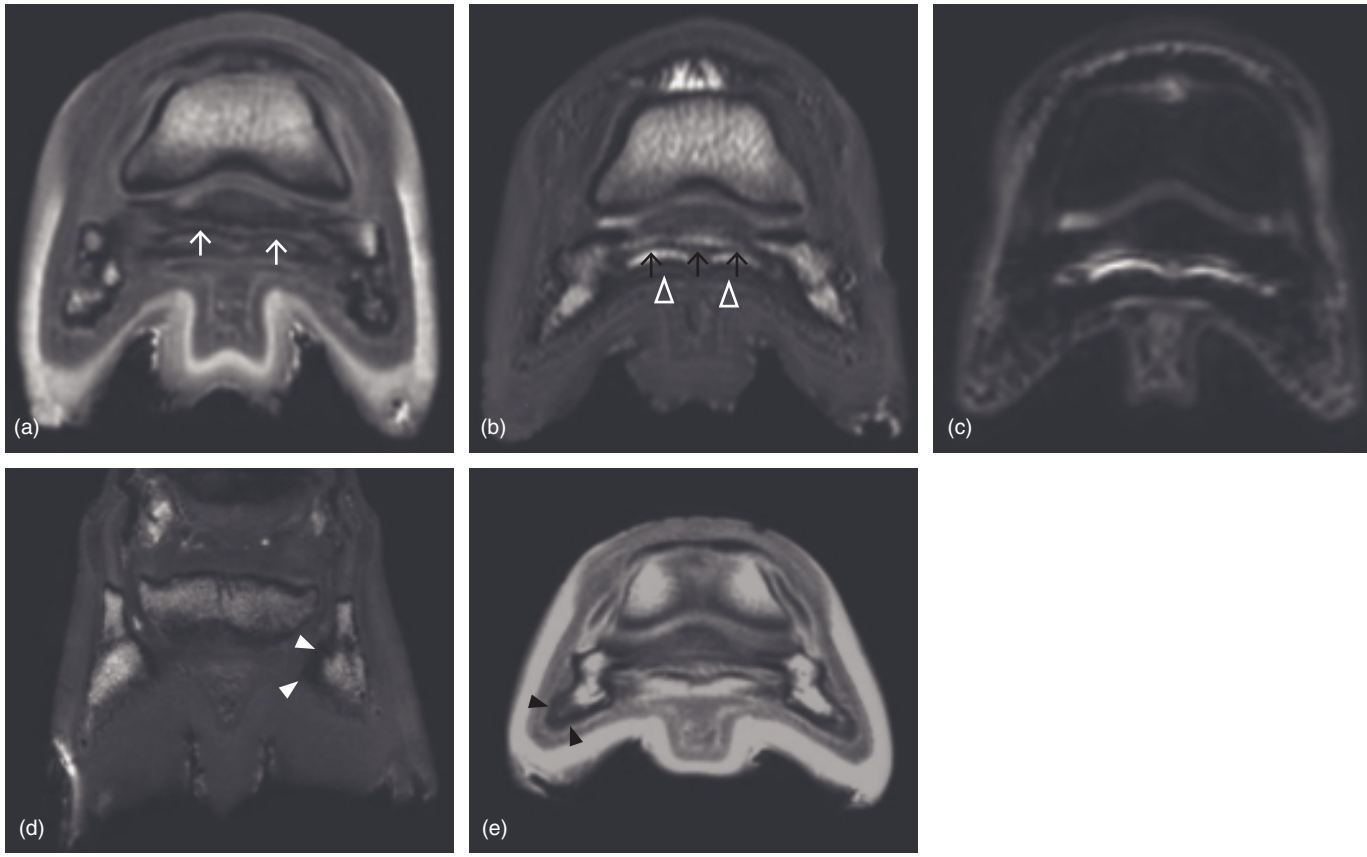

Figure 5.5 (a) Normal transverse high-field 3D SPGR high-field image of a foot distal to the navicular bone. Medial is to the right. The distal sesamoidean impar ligament (DSIL) (arrows) is of uniform thickness from medially to laterally and is clearly separated from the deep digital flexor tendon (DDFT). Note that the abaxial margins of the medial collateral ligament of the distal interphalangeal joint have increased signal intensity, possibly reflecting degenerative change. (b) Normal transverse high-field 3D T2* GRE image of the same foot as (a). Medial is to the right. The DSIL (black arrows) has a uniform architecture, with thin hypointense fascicles separated by interdigitated pockets of hyperintense fluid in the DIP joint. In some horses the fascicles are considerably thicker, with little fluid seen. The DSIL is clearly separated from the DDFT (arrow heads) by hyperintense fluid in the navicular bursa. (c) Normal transverse high-field 2D STIR image of the same foot as (a) and (b). Medial is to the right. The DSIL is of uniform thickness from medially to laterally and has a largely hyperintense signal because of fluid pockets of the DIP joint interdigitated between the narrow fascicles of the DSIL. (d) Dorsal high-field 3D T2* GRE image of the palmar aspect of the distal phalanx. Medial is to the right. There is mild diffuse decreased signal intensity in the medial palmar process, which was also present in T2-weighted images, and a thickened axial cortex (arrow heads). The cartilages of the foot are ossified to the level of the navicular bone. (e) Transverse high-field 3D SPGR image of the palmar aspect of the distal phalanx. Medial is to the left. There is focal marked reduced signal intensity in the medial palmar process (arrows), which was also present in T2-weighted images, but not fat-suppressed images, reflecting mineralization. Note also the increased signal intensity around the periphery of the medial collateral ligament of the distal interphalangeal joint, which may reflect degenerative change. The distal sesamoidean impar ligament is thickest axially, a normal variant.

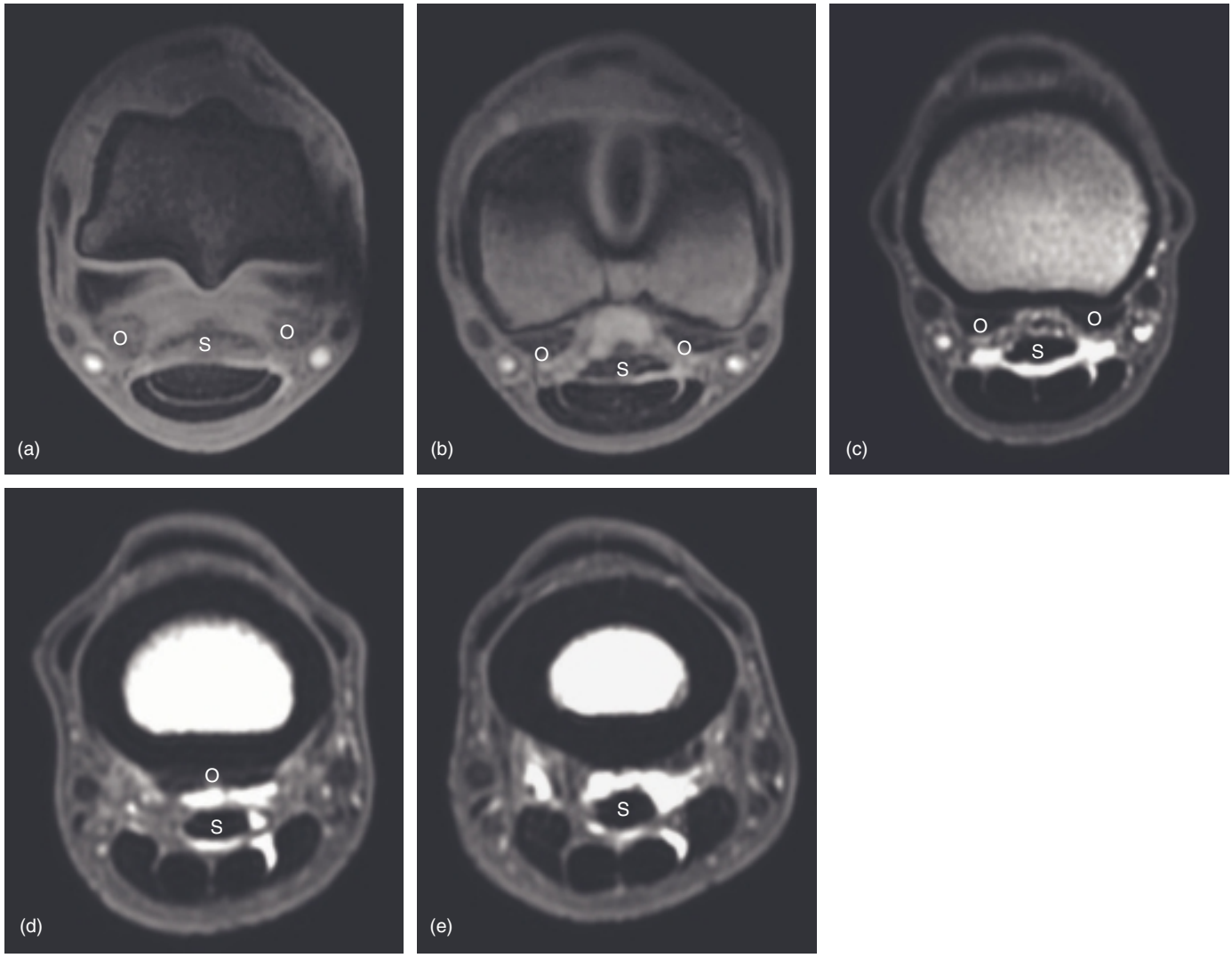

Figure 5.6 Normal transverse high-field 3D T2* GRE images showing the straight (SSL, S) and oblique (O) sesamoidean ligaments from proximal to distal (a–d). Dorsal is to the top and lateral to the right of the images, which are all of similar magnification. (a) The deep digital flexor tendon (DDFT) is oval and the superficial digital flexor tendon (SDFT) is broad and thin. (b) Adjacent and dorsal to the SSL is a circular area of uniform low signal intensity, the accessory ligament of the SSL. (c) There is hyperintense fluid within the digital flexor tendon sheath. The DDFT is bilobed. (d) The SDFT is dumb-bell-shaped. (e) The SDFT has separated into medial and lateral lobes.

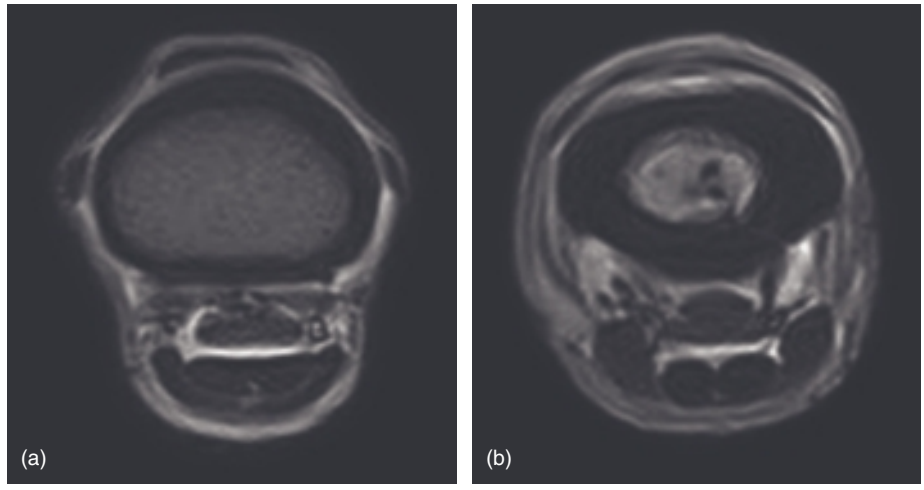

Figure 5.7 (a) Transverse T2* GRE 3D low-field MR image at the level of the proximal phalanx. The superficial and deep digital flexor tendons have low signal intensity. The straight and oblique sesamoidean ligaments have intermediate signal intensity. (b) Transverse T2* GRE 3D low-field MR image at the level of the distal aspect of the proximal phalanx. The superficial and deep digital flexor tendons have low signal intensity. The straight and oblique sesamoidean ligaments have intermediate signal intensity.

The medial and lateral lobes change in shape from proximally to distally, but are generally symmetrical in size and shape [20]. The DDFT has strong left right symmetry in size, and cross-sectional area is positively associated with body weight [20]. The DDFT is clearly separated from the collateral sesamoidean ligament (CSL) and the DSIL by hyperintense fluid within the proximal and distal recesses of the navicular bursa (Figures 5.1b, 5.4b, 5.5b and c).

Isolated sagittal plane splits or focal dorsal abrasions without other signal intensity changes in the tendon, can be seen as incidental findings in clinically normal horses. There may be some endosteal irregularity at the insertion of the DDFT on the distal phalanx.

DISTAL SESAMOIDEAN IMPAR LIGAMENT

A normal DSIL has a heterogeneous appearance on transverse images, with fluid-filled pockets of synovium in the DIP joint interdigitated between the fibres of the ligament (Figure 5.5). The axial region of the ligament may be larger (thicker) than abaxially. There is clear separation between the DSIL and the DDFT. Some endosteal irregularity at the insertion on the distal phalanx may be seen in clinically normal horses [13]. The DSIL is much more difficult to evaluate in low-resolution images with thick slices because often there is only one transverse slice of each image sequence in which the ligament can be identified. If there is image obliquity, then partial volume effect is likely to result in a misleading appearance if there is superimposition of bone over the ligament on one side when only one slice of the ligament is obtained. This can cause problems with low-field images acquired in a sedated standing horse if higher resolution sequences are not used. If there is not exact placement of the slices in 2D imaging, the exact site of a single slice may vary between sequences, making direct comparison difficult. In sagittal high-field T1- and T2*-weighted images the DSIL is susceptible to the magic angle effect, and therefore may have relatively high signal intensity (Figures 5.1a and b). In sagittal T2 and T2 fat-suppressed images there can be considerable variation in signal intensity depending on whether the slice passes through fibres of the ligament or through a fluid-filled synovial pocket.

COLLATERAL SESAMOIDEAN LIGAMENT

A normal CSL has a uniform low-intensity signal in T1- and T2-weighted image sequences and is symmetrical in thickness medially and laterally. It may have intermediate signal intensity in fat-suppressed images. Its borders are clearly demarcated by the high signal intensity of fluid in the palmar recess of the distal interphalangeal (DIP) joint and the navicular bursa in proton density, T2, T2* GRE and STIR sequences (Figure 5.4).

COLLATERAL LIGAMENTS OF THE DISTAL INTERPHALANGEAL JOINT

Some asymmetry in size (width in dorsal plane images and cross-sectional area in transverse images) of the collateral ligaments (CLs) of the DIP joint

may be seen within and between limbs of the same horse and does not necessarily signify injury. This probably reflects adaptation to the biomechanical loading of the limb, in part as a reflection of conformation or foot balance. A normal ligament has uniform, low intensity signal throughout most of its length, with clearly demarcated margins and uniform thickness of overlying soft tissues (Figures 5.2a, 5.3 and 5.7). The lateral CL is significantly longer than the medial CL [23]. There is a close relationship to the chondrocoronal ligament which runs abaxially and dorsally (Figure 5.3g). There are smooth endosteal and periosteal margins of the middle and distal phalanges at the origin and insertion of each CL.

In images obtained with B_0 perpendicular to the limb, the lateral CL of the DIP joint may appear to have relatively high signal intensity, despite being of normal shape and size, as a result of the magic angle effect (Figures 4.9 and 4.10) [24, 25]. The lateral CL of the DIP joint is at a more acute angle to the horizontal than the medial CL, and may therefore approach 55° to the static magnetic field. Images obtained with short echo times (generally T1-weighted images, T2* GRE and proton density [PD] images) are particularly susceptible to this artefact, while T2 FSE sequences, having longer echo times, are less susceptible.

DISTAL INTERPHALANGEAL JOINT

The DIP joint usually has smoothly curved cortical surfaces, although some flattening towards the palmar aspect of the joint is a normal variant. The cortical bone has a homogeneous low signal intensity, with a uniform endosteal surface (Figures 5.1 and 5.2). A smoothly outlined depression in the cortical bone of the distal phalanx axially, covered by thick cartilage, is a normal variant. The articular cartilage has an intermediate signal intensity and in T2-weighted images is clearly defined by the adjacent high-intensity signal of synovial fluid. However, the curved articular surfaces make this joint prone to artefacts due to volume averaging, so that focal cartilage defects may be missed unless there are associated changes in the adjacent subchondral bone. The articular cartilage is much easier to evaluate in higher resolution images, particularly where narrow slices minimize the partial volume effects associated with the curved articular surfaces.

Some distension of the DIP joint capsule with fluid is a very common finding. However, the synovial lining should be smooth, with minimal soft tissue proliferation within the joint.

PROXIMAL INTERPHALANGEAL JOINT

The proximal interphalangeal (PIP) joint usually has smoothly curved cortical surfaces, and the cortical bone has homogeneous low signal intensity, with a uniform endosteal surface (Figures 5.1 and 5.2). The articular cartilage has an intermediate signal intensity and in T2-, T2*- and PD-weighted images is clearly defined by the adjacent high-intensity signal of synovial fluid. In T1-weighted images, the articular cartilage has high signal intensity compared to the low signal intensity of the synovial fluid. However, the

curved articular surfaces also make this joint prone to artefacts due to volume averaging, so focal cartilage defects may be missed unless there are associated changes in the adjacent subchondral bone.

PROXIMAL, MIDDLE AND DISTAL PHALANGES

The cancellous bone of the proximal, middle and distal phalanges usually has a uniform intermediate intensity signal in T1- and T2-weighted images, except in the region of nutrient vessels where there is higher signal intensity and in the middle third of the proximal phalanx (Figures 5.1 and 5.2). The trabecular architecture is seen better in high-resolution than low-resolution images, so may be better defined in high-field image sequences. The cancellous bone is well demarcated from the homogeneous hypointense signal intensity of cortical bone. In fat-suppressed images the cancellous bone has a hypointense signal, although there may be difficulty achieving complete suppression in the proximal phalanx in fat-saturated images associated with the anatomical configuration of the limb. It is important to be aware that where there are magnetic susceptibility artefacts in the hoof wall, these may result in signal inhomogeneity in adjacent parts of the distal phalanx. Abnormalities are quite commonly seen in the palmar processes of the distal phalanx, including mild diffuse decreased signal intensity in both T1- and T2-weighted images, especially medially [26] (Figure 5.5d). Other common abnormalities include focal mineralization with marked decrease in signal intensity in T1- and T2-weighted images and a thick axial cortex (Figure 5.5e). Less commonly there is irregularity of the cortical margin and disruption of the adjacent laminar architecture. Such lesions are usually seen in conjunction with other causes of lameness and their contribution to pain and lameness is currently speculative [26, 27].

Osseous cyst-like lesions (OCLLs) are quite commonly seen as incidental abnormalities in the distal aspect of the proximal phalanx, the proximal and distal aspects of the middle phalanx and the proximal aspect of the distal phalanx (Figure 5.8). These are characterized by well-circumscribed areas of increased signal intensity, surrounded by a narrow rim of mineralized bone

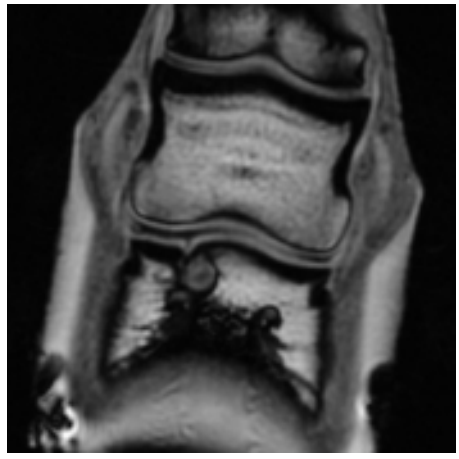

Figure 5.8 Dorsal high-field 3D SPGR image of a foot; medial is to the left. There is an incidental, well-demarcated osseous cyst-like lesion in the distal phalanx medial to the midline. There is a smoothly outlined concave depression in the overlying subchondral bone, with a similar indentation in the articular cartilage, which is intact.

of low signal intensity. There may be a smoothly marginated depression in the articular cortex overlying the OCLL, mirrored sometimes by a depression in the articular cartilage, but the articular cartilage is intact.

THE CARTILAGES OF THE FOOT

The appearance of the cartilages of the foot varies depending on whether or not they are ossified. If unossified, the cartilages extend to the level of the coronary band and are seen as thin, oval-shaped structures of uniform high signal intensity in transverse images (Figure 5.4) and long oblong structures in dorsal plane images (Figure 5.2b). If ossified, each cartilage has a clear cortex of low signal intensity (Figure 5.2c). There may be discrete separate centres of ossification. Mineralization, characterized by low signal intensity in T1- and T2-weighted images, may be seen as an incidental abnormality within an ossified cartilage, or in association with previous trauma [27].

LAMINAE

Normal laminae are clearly defined, with relatively high signal intensity in the deeper layers on T1- and T2-weighted images (Figures 5.9a–d). There is a well-defined, smooth junction between the cortex of the distal phalanx and the adjacent laminae.

Abnormalities can be observed in horses in which other lesions were determined to be the primary source of pain, and include disruption of interlamellar alignment and separation of laminar layers by linear or focal decrease in signal intensity, consistent with gas accumulation (Table 5.1). In some feet there is focal or more generalized disruption of the junction between the laminae and cortex of the distal phalanx, sometimes with increased signal intensity in the area on both T1- and T2-weighted images. In association with local trauma, focal or linear haemosiderin accumulation can be seen as a signal void, particularly on gradient-echo images.

STRAIGHT SESAMOIDEAN LIGAMENT

The straight sesamoidean ligament (SSL) changes in shape from proximally to distally in transverse images, being triangular proximally with the apex pointing palmarly, becoming oval further distally and then round towards its insertion (Figures 5.6a–e). Proximally and axial, dorsal to the ligament is an accessory ligament of uniform low signal intensity, which further distally gets closer to the SSL and merges with it (Figure 5.6b). The SSL often has a rather bulbous appearance distally in sagittal plane images, and may have a focal central triangular area of higher signal intensity close to its insertion in normal horses (Figures 5.1a and b) [28]. This is generally bilaterally symmetrical. In transverse images the ligament has a regular reticular pattern, with low-intensity signal interspersed with lines of intermediate signal intensity. Small (<1 mm) focal hyperintense spots are sometimes seen. There are often thin strands of tissue extending from the dorsal and palmar

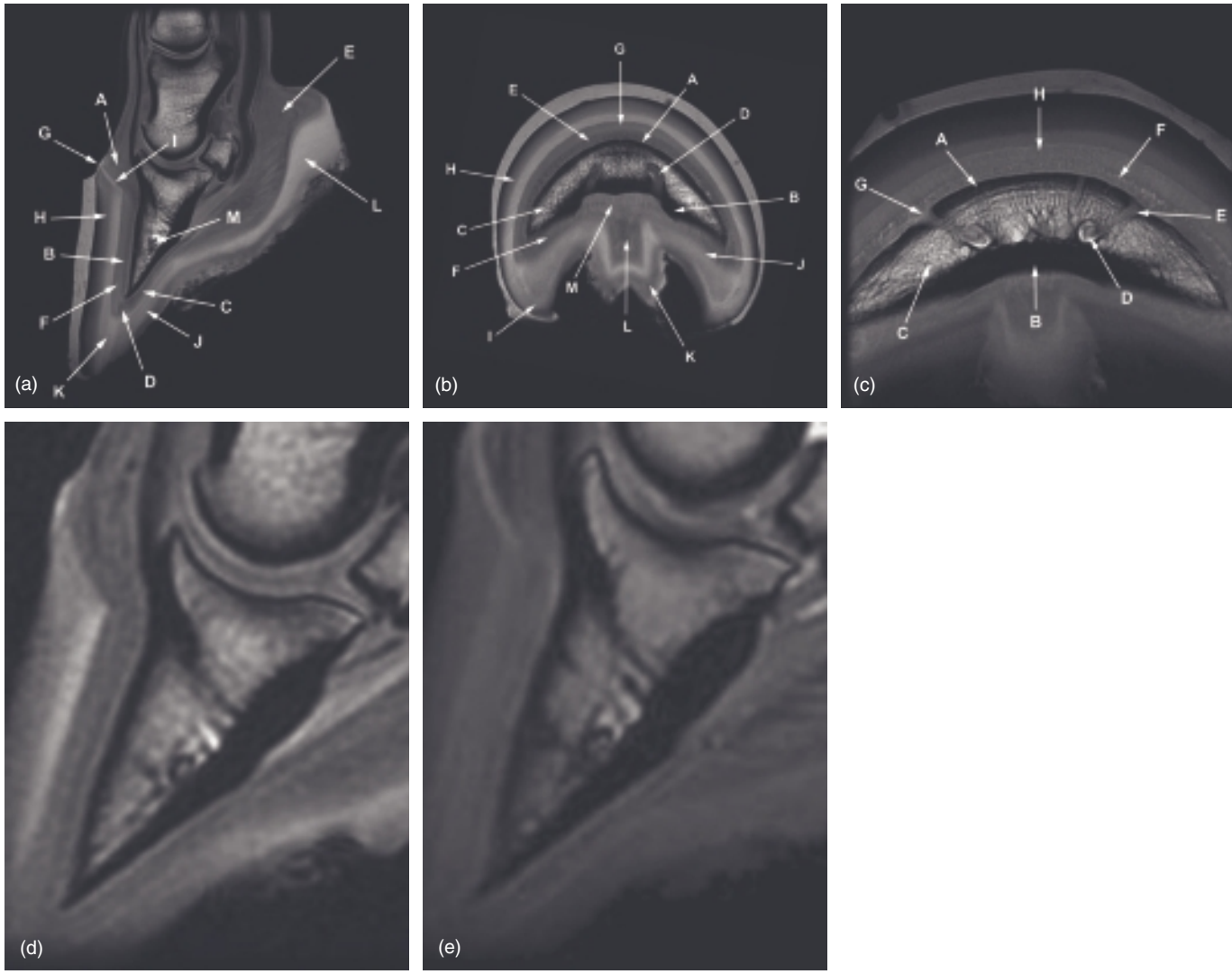

Figure 5.9 (a) High-resolution sagittal transverse T1-weighted 3D SPGR image to show the normal architecture of the laminae and corium. Note the dorsal aspect of the hoof wall has been discriminated by Play-Doh. A, coronary dermis and vascular plexus; B, sublamellar dermis and vascular plexus; C, solar dermis and vascular plexus; D, circumflex vessels; E, digital cushion; F, lamellar interface formed by interdigitating dermal and epidermal lamellae; G, perioplic horn (*Stratum exterum*); H, hoof wall (*Stratum medium*) showing a progressive dorsopalmar change in signal intensity which reflects a corresponding gradient of moisture content, water binding strength, and lipid content; I, keratinization zone within the proximal hoof wall; J, sole horn; K, white line forming the hoof wall–sole junction; L, frog; M, terminal arch and artery. Image courtesy of Dr Simon Collins, Animal Health Trust. (b) High-resolution transverse T1-weighted 3D SPGR image of the distal aspect of the distal phalanx acquired in a 1.5 T MR imaging system. Note the dorsal aspect of the hoof wall has been discriminated by Play-Doh. A, dorsal cortex of the distal phalanx; B, palmar cortex of the distal phalanx; C, cancellous bone of the distal phalanx, showing trabecular bone structure and hyperintense signal of the inter-trabecular fat deposits; D, terminal arch and artery; E, sublamellar dermis and lamellar vascular plexus; F, solar dermis and vascular plexus; G, lamellar interface formed by interdigitating dermal and epidermal lamellae; H, hoof wall (*Stratum medium*) showing a progressive dorsopalmar change in signal intensity which reflects a corresponding gradient of moisture content, water binding strength, and lipid content; I; *Pars reflexa* of the hoof wall; J, sole horn; K, frog; L, digital cushion; M, insertion of the deep digital flexor tendon with the palmar surface of the distal phalanx. Note magic angle artefact and heterogeneous MR signal within the tendon. Image courtesy of Dr Simon Collins, Animal Health Trust. (c) High-resolution 3D SPGR high-field MR image of the distal aspect of the distal phalanx to show the normal architecture of the laminae and corium. Note the dorsal aspect of the hoof wall has been discriminated by Play-Doh. A, dorsal cortex of the distal phalanx; B, palmar cortex of the distal phalanx; C, cancellous bone of the distal phalanx, showing trabecular bone structure and hyperintense MR signal of the inter-trabecular fat deposits; D, terminal arch and artery; E, branching artery from the terminal artery emerging on the dorsal aspect of the distal phalanx; F, lamellar vascular plexus; G, anastomosis of branching artery from the terminal artery with the lamellar vascular plexus; H, lamellar interface formed by interdigitating dermal and epidermal lamellae. Note the homogenous MR signal intensity. Image courtesy of Dr Simon Collins, Animal Health Trust. (d) Sagittal T1-weighted 3D SPGR high-field MR image of the distal aspect of the distal phalanx to show the normal architecture of the laminae and corium. (e) Sagittal 3D T2* gradient-echo high-field MR image of the distal aspect of the distal phalanx to show the normal architecture of the laminae and corium.

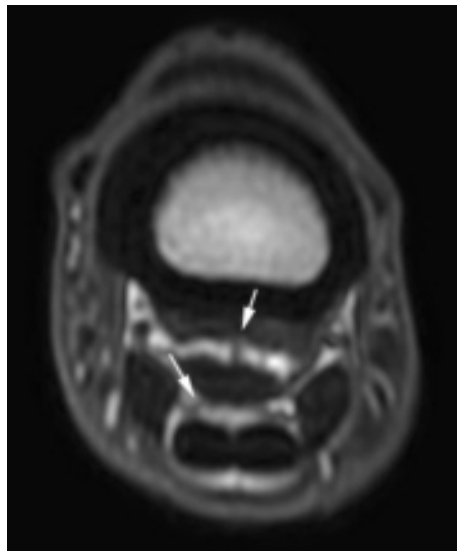

Figure 5.10 Normal transverse 3D high-field T2* GRE image at the level of the insertion of the oblique sesamoidean ligament showing periligamentar tissue as linear strands (white arrows) and broad regions originating from the straight sesamoidean ligament. Lateral is to the right.

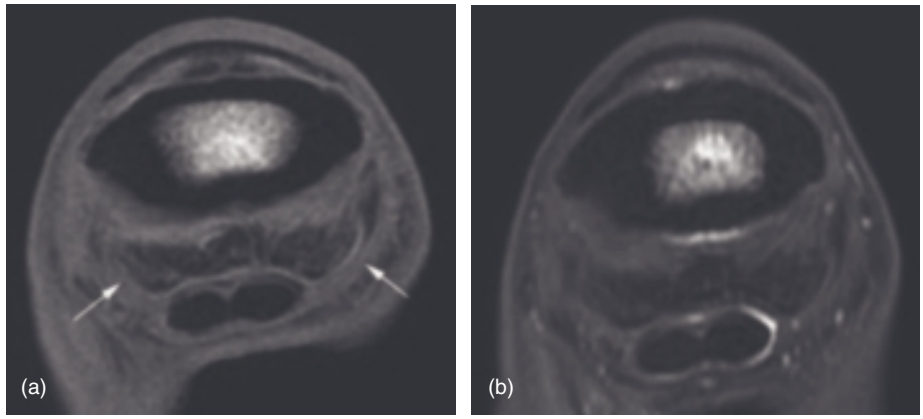

Figure 5.11 (a) Transverse T1-weighted 3D SPGR high-field MR image at the level of the distal aspect of the proximal phalanx close to the insertion of the straight sesamoidean ligament via the middle scutum (arrows), which has a rather heterogeneous internal architecture. (b) Transverse 3D T2* GRE high-field MR image at the level of the distal aspect of the proximal phalanx close to the insertion of the straight sesamoidean ligament via the middle scutum (arrows), which has a rather heterogeneous internal architecture. There is a small amount of fluid in the digital flexor tendon sheath surrounding the deep digital flexor tendon. Hyperintense fluid in the proximal palmar recess of the proximal interphalangeal joint is seen palmar to the proximal phalanx.

aspects of the ligament (Figure 5.10). The SSL inserts via the middle scutum onto the middle phalanx (Figure 5.11).

OBLIQUE SESAMOIDEAN LIGAMENTS

The oblique sesamoidean ligaments (OSLs) have an intermediate signal intensity, and change in shape from proximal to distal, being two discrete

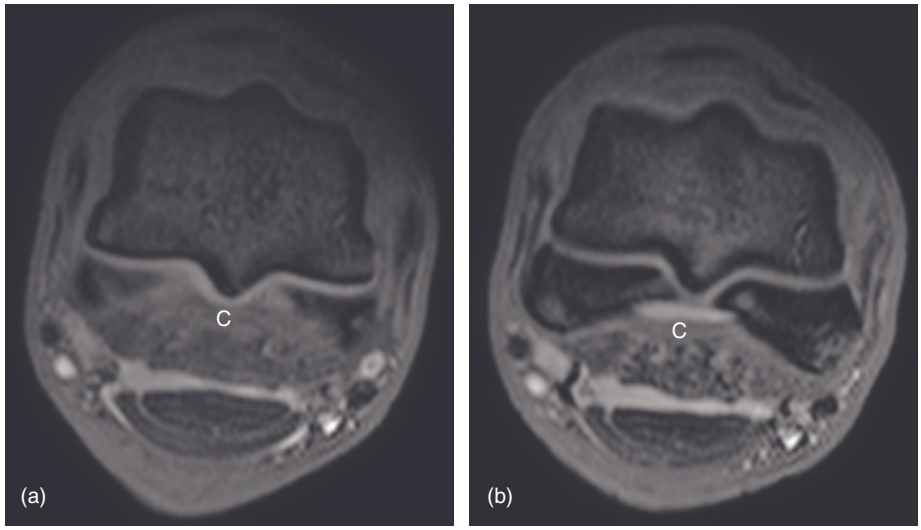

Figure 5.12 (a) Normal transverse high-field 3D T2* GRE images showing the cruciate sesamoidean ligament (c) proximally, which is of intermediate signal intensity. Medial is to the right. (b) Normal transverse high-field 3D T2* GRE images showing the cruciate sesamoidean ligament (c) at the insertion. Medial is to the right.

triangular-shaped structures proximally in transverse images, merging to become a single rectangular structure close to their insertion [28] (Figures 5.6 and 5.10). In high-field images there is slight, inconsistent variation in size and signal intensity between lateral and medial OSLs. In images acquired using a magnet when B_0 is perpendicular to the limb (e.g. low-field magnet in a standing sedated horse), the OSLs may have increased signal intensity in T1-weighted, T2* GRE and PD images due to the magic angle effect [25]. The proximal aspect of the medial OSL is particularly susceptible related to the variable fibre pattern of the ligament in this region.

CRUCIATE SESAMOIDEAN LIGAMENTS

The cruciate sesamoidean ligaments are a challenge to identify in transverse low-field images unless the slice is in exactly the appropriate position. In high-field transverse images the cruciate sesamoidean ligaments are seen as a single horizontal strip with flared ends medially and laterally, with homogeneous signal intensity [28] (Figure 5.12). However, in images acquired in a standing horse, relative extension of the fetlock joint may facilitate identification of the cruciate sesamoidean ligaments, which may be more clearly defined in both transverse and sagittal plane images.

SUPERFICIAL DIGITAL FLEXOR TENDON

The superficial digital flexor tendon (SDFT) has a uniformly low signal intensity until close to its insertion, where it becomes more heterogeneous. Proximally it is a broad, narrow structure that becomes dumb-bell-shaped and then divides into medial and lateral branches (Figures 5.6, 5.11, 5.13 and 5.14).

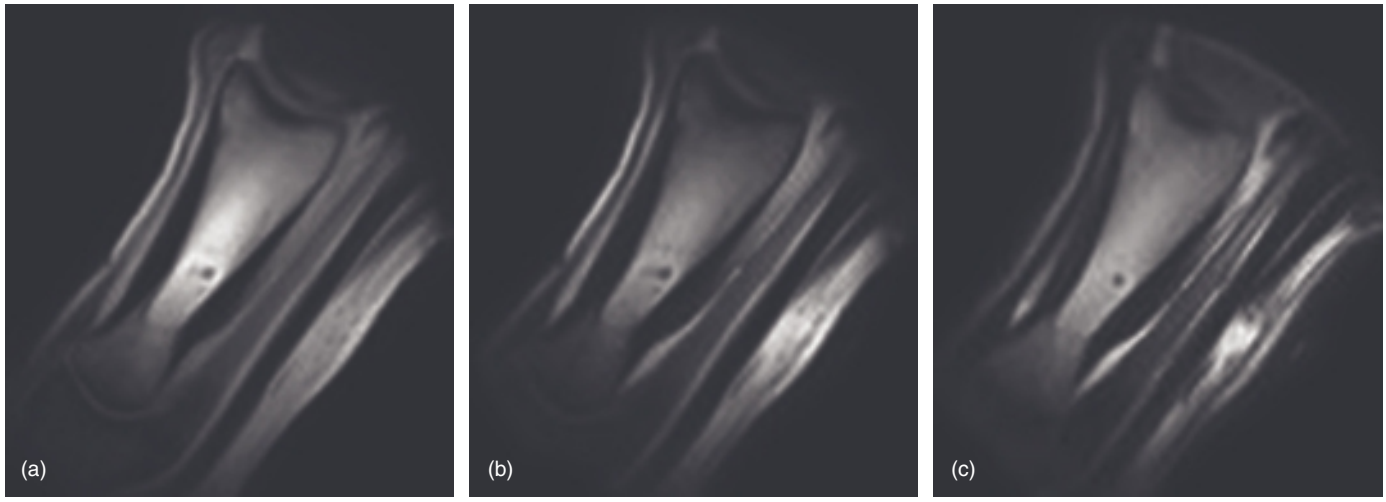

Figure 5.13 (a) Parasagittal T1-weighted GRE motion insensitive low-field MR image of a normal pastern centred on the proximal phalanx. Dorsal is to the left. The deep digital flexor tendon has uniform low signal intensity. The common digital extensor tendon and straight sesamoidean ligament have intermediate signal intensity. (b) Sagittal T2* GRE motion-insensitive low-field MR image of a normal pastern centred on the proximal phalanx. Dorsal is to the left. The deep digital flexor tendon has uniform low signal intensity. The common digital extensor tendon and straight sesamoidean ligament have intermediate signal intensity. (c) Sagittal T2-weighted fast spin-echo motion-insensitive low-field MR image of a normal pastern centred on the proximal phalanx. Dorsal is to the left. The straight sesamoidean ligament has intermediate signal intensity; the common digital extensor and deep digital flexor tendons have low signal intensity.

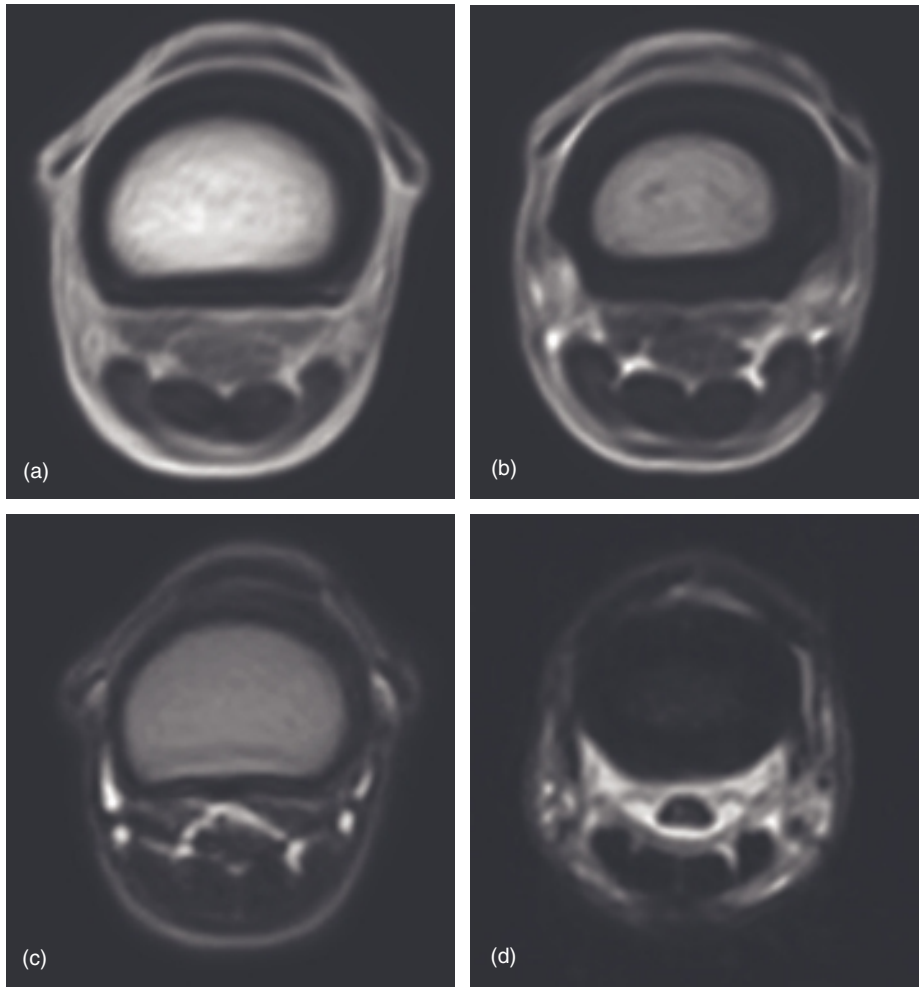

Figure 5.14 (a) Transverse T1-weighted GRE motion-insensitive low-field MR image of a normal pastern at the level of the middle third of the proximal phalanx. Medial is to the left. The oblique and straight sesamoidean ligaments have intermediate signal intensity. The superficial and deep digital flexor tendons have low signal intensity. (b) Transverse T2* GRE motion-insensitive low-field MR image of a normal pastern at the level of the middle third of the proximal phalanx. Medial is to the left. (c) Transverse T2-weighted fast spin-echo motion-insensitive low-field MR image of a normal pastern at the level of the middle third of the proximal phalanx. Medial is to the left. The medial oblique sesamoidean ligament has a slightly heterogeneous signal intensity, whereas the lateral oblique sesamoidean ligament, the straight sesamoidean ligament and the superficial and deep digital flexor tendons have fairly uniform low signal intensity. (d) Transverse STIR fast spin-echo motion-insensitive low-field MR image of a normal pastern at the level of the middle third of the proximal phalanx.

DIGITAL FLEXOR TENDON SHEATH

The amount of fluid within the digital flexor tendon sheath (DFTS) is very variable. There is a normal vinculum between the dorsal aspect of the DDFT and the DFTS, which is seen as a homogeneous band of low signal intensity. The synovial lining of the DFTS is smooth.

COMMON DIGITAL EXTENSOR TENDON

The common digital extensor tendon is a dorsopalmarly flattened structure of uniform low signal intensity throughout its length (Figures 5.1 and 5.3). Occasionally a focal or linear area of high signal intensity is seen reflecting previous needle puncture.

PROXIMAL AND DISTAL DIGITAL ANNULAR LIGAMENTS

The proximal and distal digital annular ligaments are thin structures of uniform low signal intensity that may not be easy to distinguish in a clinically normal horse, unless there is distension of the DFTS.

DIGITAL CUSHION

The digital cushion has a characteristic architecture of mixed low and intermediate signal intensity (Figures 5.1, 5.2 and 5.3). In some horses there are quite large focal areas of low signal intensity.

It is beyond the scope of this text to describe every anatomical structure and the reader is strongly advised to refer to a three-dimensional atlas of anatomy [29] to identify all structures.

REFERENCES

[1] Dyson S, Murray R, Schramme M, Branch M. Magnetic resonance imaging of the equine foot: 15 horses. *Equine Vet J* 2003; **35**: 18–26.

[2] Dyson S, Murray R, Schramme M, Branch M. Lameness in 46 horses associated with deep digital flexor tendonitis in the digit: diagnosis confirmed with magnetic resonance imaging. *Equine Vet J* 2003; **35**: 681–90.

[3] Dyson S, Murray R, Schramme M, Branch M. Collateral desmitis of the distal interphalangeal joint in 18 horses (2001–2002). *Equine Vet J* 2004; **36**: 160–6.

[4] Dyson S, Murray R. Collateral desmitis of the distal interphalangeal joint in 62 horses (January 2001–December 2003). *Proc Am Assoc Equine Pract* 2004; **50**: 248–56.

[5] Dyson S, Murray R, Schramme M. Lameness associated with foot pain: results of 199 horses (January 2001–December 2003) and response to treatment. *Equine Vet J* 2005; **37**: 113–21.

[6] Zubrod C, Schneider R, Tucker R, Gavin P, Ragle C, Farnsworth K. Diagnosis of subchondral bone damage using magnetic resonance imaging in eleven horses. *J Am Vet Med Assoc* 2004; **24**: 411–18.

[7] Schneider R. Lameness problems in the foot: advances in diagnosis. *Proceedings 13th Annual Congress American College of Veterinary Surgeons*. Washington DC, October 2003 (CD-Rom).

[8] Schneider R, Gavin P, Tucker R. What magnetic resonance imaging is teaching us about navicular disease. *Proc Am Assoc Equine Pract* 2003; **49**: 210–19.

[9] Mair T, Kinns J, Jones R, Bolas N. Magnetic resonance imaging of the distal limb of the standing horse. *Equine Vet Educ* 2005; **17**: 74–82.
[10] Mair T, Kinns J. Deep digital flexor tendonitis in the equine foot diagnosed by low-field magnetic resonance imaging in the standing patient: 18 cases. *Vet Radiol Ultrasound* 2005; **46**: 458–66.
[11] Dyson S, Murray R. Magnetic resonance imaging of the equine foot. *Clin Tech Equine Pract* 2007; **6**: 46–61.
[12] Sampson S, Schneider R, Tucker R, Gavin P, Zubrod C, Ho C. Magnetic resonance imaging features of oblique and straight distal sesamoidean desmitis in 27 horses. *Vet Radiol Ultrasound* 2007; **48**: 303–11.
[13] Sherlock C, Kinns J, Mair T. Evaluation of foot pain by low-field magnetic resonance imaging in the standing horse: results in 41 cases with long term follow up. *Vet Rec* 2008; **161**(22): 739–44.
[14] Murray R, Schramme M, Dyson S, Branch M, Blunden A. MRI characteristics of the foot in horses with palmar foot pain and control horses. *Vet Radiol Ultrasound* 2006; **47**: 1–16.
[15] Schramme M, Murray R, Blunden A, Dyson S. A comparison between MRI, pathology and radiology in 34 limbs with navicular syndrome and 25 control limbs. *Proc Am Assoc Equine Pract* 2005; **51**: 348–58.
[16] Murray R, Blunden A, Schramme M, Dyson S. How does magnetic resonance imaging represent histological findings in the equine digit? *Vet Radiol Ultrasound* 2006; **47**: 17–31.
[17] Blunden A, Dyson S, Murray R, Schramme M. Histological findings in horses with chronic palmar foot pain and age-matched control horses. Part 1: the navicular bone and related structures. *Equine Vet J* 2006; **38**: 15–22.
[18] Blunden A, Dyson S, Murray R, Schramme M. Histological findings in horses with chronic palmar foot pain and age-matched control horses. Part 2: the deep digital flexor tendon. *Equine Vet J* 2006; **38**: 23–7.
[19] Berry C, Pool R, Stover S *et al*. Radiographic/morphologic investigation of a radiolucent crescent within the flexor central eminence of the navicular bone in Thoroughbreds. *Am J Vet Res* 1992; **53**: 1604–11.
[20] Murray R, Roberts B, Schramme M, Dyson S, Branch M. Quantitative evaluation of equine deep digital flexor tendon morphology using magnetic resonance imaging. *Vet Radiol Ultrasound* 2004; **45**: 103–11.
[21] Busoni V, Snaps F. Effect of deep digital flexor tendon orientation on magnetic resonance imaging signal intensity in isolated equine limbs – the magic angle effect. *Vet Radiol Ultrasound* 2002; **43**: 428–30.
[22] Spriet M, Knight A. Characterization of the magic angle effect in the equine deep digital flexor tendon using a low-field magnetic resonance system. *Vet Radiol Ultrasound* 2009; **50**: 32–6.
[23] Murray R, Dyson S, Branch M, Schramme M. Validation of magnetic resonance imaging use in equine limbs. *Clinical Tech Equine Pract* 2007; **6**: 26–36.
[24] Spriet M, Mai W, McKnight A. Asymmetric signal intensity in normal collateral ligaments of the distal interphalangeal joint in horses with a low field MRI system: a manifestation of the magic angle effect. *Vet Radiol Ultrasound* 2007; **48**: 95–100.
[25] Smith M, Dyson S, Murray R. Is a magic angle effect observed in the collateral ligaments of the distal interphalangeal joint or the oblique sesamoidean ligaments during standing low field magnetic resonance imaging? *Vet Radiol Ultrasound* 2008; **49**: 509–15.
[26] Nagy A, Dyson S, Murray R. Radiographic, scintigraphic and magnetic resonance imaging findings in the palmar processes of the distal phalanx. *Equine Vet J* 2008; **40**: 57–63.
[27] Dyson S, Murray R. Lameness and diagnostic imaging in the sports horse: recent advances related to the digit. *Proc Am Assoc Equine Pract* 2007; **53**: 262–75.
[28] Smith S, Dyson S, Murray R. Magnetic resonance imaging of distal sesamoidean ligament injury. *Vet Radiol Ultrasound* 2008; **49**: 516–28.
[29] Denoix J-M. *The equine distal limb. An atlas of clinical anatomy and comparative imaging*. London: Manson Publishing, 2000.

5B Foal anatomical development

Bert Van Thielen and Rachel Murray

INTRODUCTION

This section describes the normal magnetic resonance imaging (MRI) anatomy of the foal foot, illustrating this with images collected from foals aged from birth to 7 months (Figures 5.15–5.18). The reference images presented in this chapter were obtained with a 1.5T Siemens Symphony-Advento MRI using a human extremity coil. When obtaining images of foal feet, it may be more difficult to achieve a high signal to noise ratio (SNR) than with adult feet. It is therefore important to use radiofrequency (RF) coils that are as close as possible in size to the limb, and not just use RF coils that are optimized for the adult horse.

THE NAVICULAR BONE

Adaptive and maturational changes in the navicular cartilage and bone are evident from birth. At birth the navicular bone appears as a rounded structure in sagittal plane images. This shape starts to be less rounded from the age of 2.5 months. At day 1, the navicular bone is mainly cartilaginous, with ossification detected only at the centre, and homogeneous cartilage thickness on both dorsal and palmar aspects, and on both proximal and distal aspects. At day 2, the flexor cartilage border is already of less thickness than the dorsal articular cartilage, and this difference increases through week 3. Ossification of the flexor cortex is seen as low signal intensity on T1-weighted images, first evident at approximately 3 weeks to 1 month of age. By 5.5 months, subchondral bone is present on the dorsal aspect and there is ossification of the medial and lateral cortices. At that age, some epiphyseal cartilage still remains.

THE DISTAL PHALANX

Ossification of the extensor process of the distal phalanx is observed on MR images between 2.5 months and 4 months of age. The articular cartilage of the distal phalanx is thickest at birth and then decreases significantly in thickness between 1 and 1.5 months of age. In a sagittal plane, this cartilage

Equine MRI, edited by Rachel C. Murray.

Images of foal feet obtained using T1-weighted fast spin-echo (T1 FSE), T2-weighted spin echo with fat suppression (T2 TIRM) and T2*-weighted 3D gradient-echo pulse sequences (T2* GRE). Anatomical features in all images are labelled using the following coding.

1 Distal phalanx: **a** non-ossified extensor process; **b** articular cartilage surface; **c** palmar articular cartilage border; **d** ossified part of the distal phalanx; **e** ossified dorsal cortex; **f** ossified solar cortex; **g** cartilaginous part of the distal phalanx; h cartilaginous palmar processes.
2 Middle phalanx: **a** distal epiphysis; **b** distal physis; **c** diaphysis; **d** proximal physis; **e** proximal epiphysis; **f** palmarodistal articular cartilage border; **g** early ossified cortex.
3 Proximal phalanx: **a** distal epiphysis; **b** distal physis; **c** diaphysis; **d** bone marrow of the diaphysis; **e** proximal physis; **f** proximal epiphysis (ossified part); **g** proximal epiphysis (cartilaginous part); **h** early ossified cortex; **i** articular cartilage of the proximal interphalangeal joint.
4 Navicular bone: **a** ossified part; **b** flexor cartilage; **c** dorsal articular cartilage; **d** lateral cartilage border; **e** medial cartilage border; **f** ramus naviculares; **g** distal cartilage border.
5 Deep digital flexor tendon (DDFT): **a** distal part of the tendon showing the magic angle artefact; **b** developing lateral lobe; **c** developing medial lobe; **d** insertion of the DDFT onto the solar surface of the distal phalanx.
6 Superficial digital flexor tendon.
7 Common digital extensor tendon.
8 Distal interphalangeal joint.
9 Proximal interphalangeal joint.
10 Digital cushion.
11 Metacarpophalangeal joint
12 Third metacarpal bone: a distal epiphysis; b distal physis.
13 Collateral ligament of the distal interphalangeal joint.
14 Cartilages of the foot.
15 The frog: a dermal papillar layer of the frog; b epidermal papillar layer of the frog.
16 Distal digital annular ligament.
17 Ungular cartilage ligament.
18 The hoof: **a** epidermal lamellar layer; **b** dermal lamellar layer; **c** horny hoofwall; **d** dermal papillar layer of the sole; **e** horny solar surface; **f** epidermal papillar layer of the sole; **g** dermal papillar layer of the coronary wall.
19 Collateral ligament of the proximal interphalangeal joint.
20 Terminal arch of the digital artery.
21 Collateral ligament of the metacarpophalangeal joint.
22 Skin.
23 Collateral sesamoidean ligament.
24 Straight sesamoidean ligament.

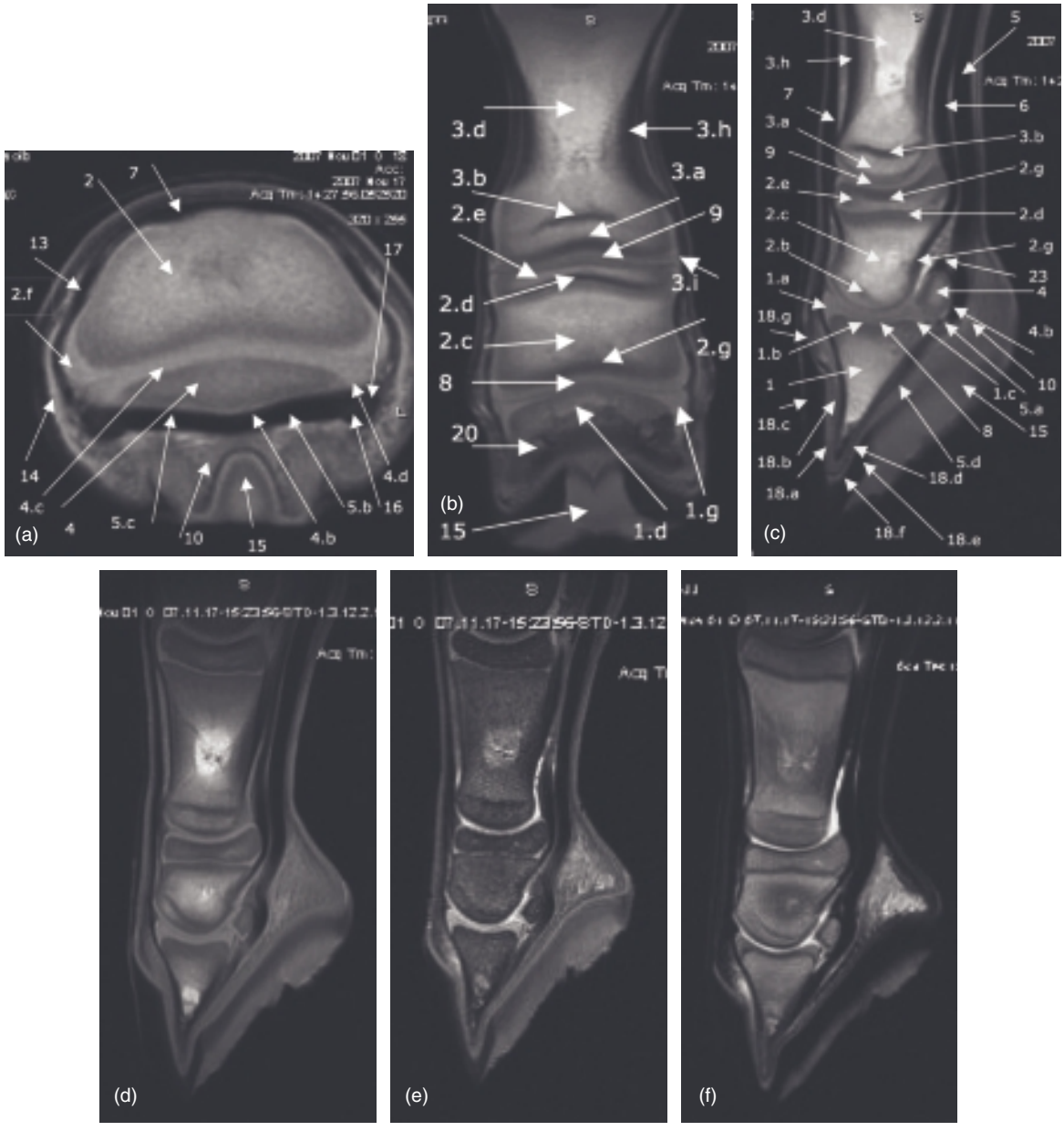

Figure 5.15 Images acquired at 1–2 days of age. (a) T1-weighted transverse image at the level of the navicular bone, with anatomical labels. (b) T1-weighted dorsal image, with anatomical labels. (c) T1-weighted sagittal image, with anatomical labels. (d) T1 FSE sagittal image. (e) T2* GRE sagittal image. (f) T2 TIRM sagittal image.

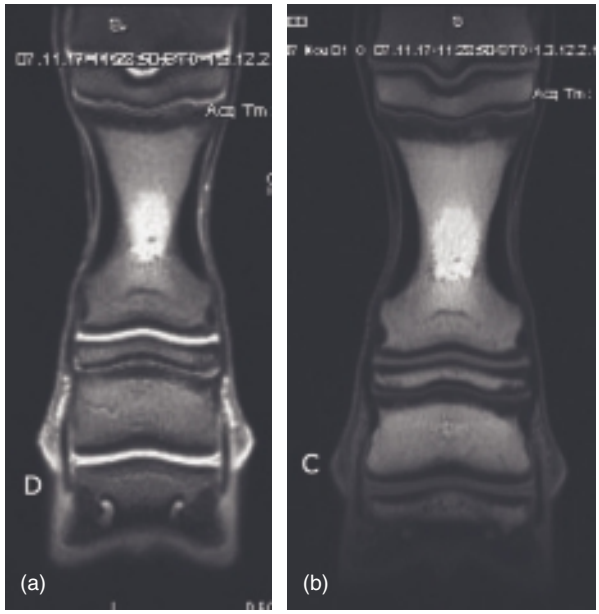

Figure 5.16 Images acquired at age 2.5 months. (a) T2* GRE dorsal image. (b) T1 FSE dorsal image.

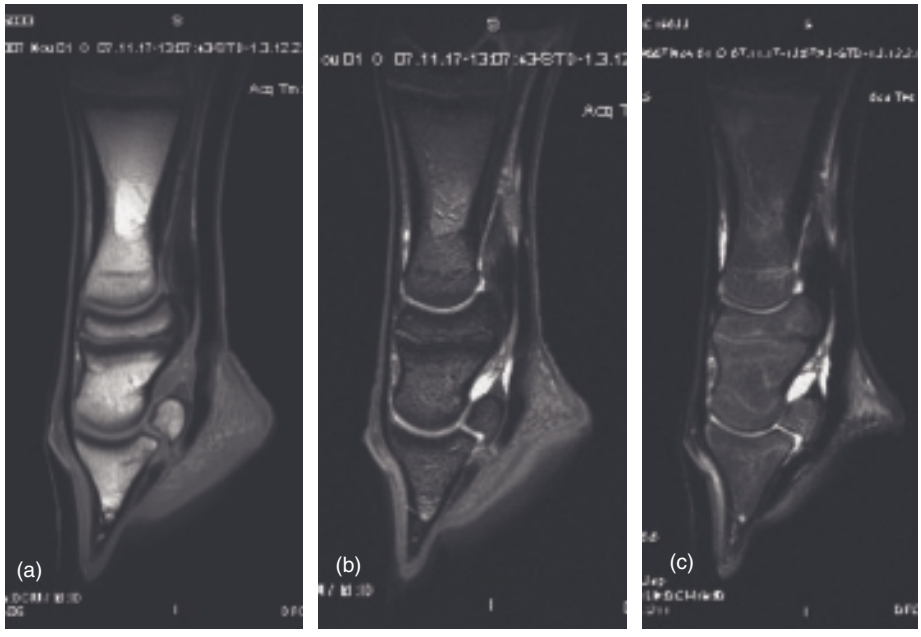

Figure 5.17 Images acquired at age 4 months. (a) T1 FSE sagittal image. (b) T2* GRE sagittal image. (c) T2 TIRM sagittal image.

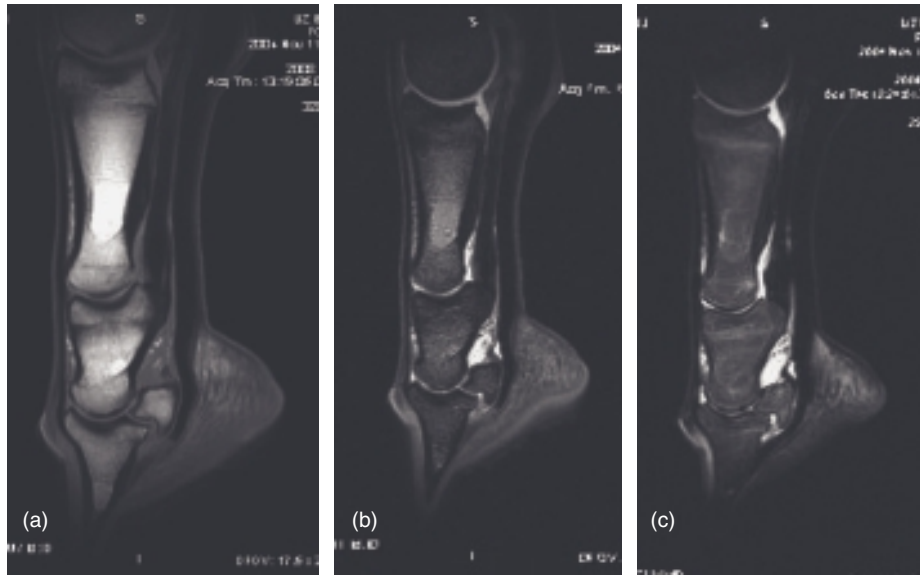

Figure 5.18 Images acquired at age 7 months. (a) T1 FSE sagittal image. (b) T2* GRE sagittal image. (c) T2 TIRM sagittal image.

layer is of maximal thickness at the palmar border; in a frontal plane, this cartilage layer is of maximal thickness on the lateral and medial margins, with increasing thickness towards the palmar aspect.

Dorsal and solar cortical bone and articular subchondral bone of the distal phalanx is visible on MR images as hypointense signal at week 3. Deep to the subchondral bone, there is linear hyperintense and hypointense signal seen on T1 fast spin-echo (FSE) and linear hyperintense signal seen on T2* gradient-echo (GRE) and T2-weighted spin-echo with fat suppression (T2 TIRM) images from day 1, which decreases until only discrete signs of these lines remain until month 7.

THE DISTAL INTERPHALANGEAL JOINT

The articular surfaces of the distal interphalangeal joint are clearly visible from birth. The dorsal and palmar recesses of the distal interphalangeal joint can be seen on MR images from the age of 3 weeks, and from the age of 2.5 months they can be more clearly defined on MR images.

THE COLLATERAL LIGAMENTS OF THE DISTAL INTERPHALANGEAL JOINT

At day 1, the ligaments are visible on MR images as very fine ligaments, which are considerably more substantial at 3 weeks. From day 2, a thickening of the cartilage around the middle phalanx can be seen at the origin of the collateral ligaments on the middle phalanx. The thickening of the cartilage around the distal phalanx can be seen at 1 month for heavy breeds and at 1.5 to 2 months for other breeds. Osseous fossae for the ligaments on the middle phalanx can be seen at the age of 1 to 2 months, which is evident as

cortical bone from 2.5 months, while ossification at the insertion in the distal phalanx is seen at 2 months.

THE SOFT TISSUES OF THE PODOTROCHLEAR APPARATUS

At birth, the navicular bursa is poorly defined with minimal contrast against the adjacent tissues, and a hypointense signal on T1 and hyperintense signal on T2-weighted images. From 3 weeks, the navicular bursa is clearly visible on MR images and the deep digital flexor tendon is clearly separated from the navicular flexor cartilage.

In a neonatal foal, the distal sesamoidean impar ligament is just visible as a very fine structure with hypointense signal. From the age of 1 to 2 months, the ligament is more obvious and there is greater separation at the articulation of the distal phalanx and the navicular bone.

The collateral sesamoidean ligament is clearly visible as a structure with hypointense signal from birth.

THE DEEP DIGITAL FLEXOR TENDON

The deep digital flexor tendon (DDFT) appears well developed in a newborn foal, with hypointense signal in all image sequences. In a transverse plane, the distal digital annular ligament and ungular cartilage ligament are difficult to separate from the DDFT. However, these ligaments can be separated from the tendon as they are less hypointense in signal intensity than the DDFT with less well-defined margins.

THE MIDDLE PHALANX

The proximal physis of the middle phalanx is still visible at month 7, whereas radiographic and scintigraphic closure is described at 6 months [1,2]. At birth, the distal physis of the middle phalanx appears as two lines: one of hyperintense and one of hypointense signal on T1-weighted images and as a line of hyperintense signal on T2* GRE images. These lines can disappear from the age of 1.5 months or can be still present at the age of 7 months. Radiographically this physis is not visible or only very discretely visible at birth [1, 3].

THE PROXIMAL PHALANX

From the age of 3 weeks to 1 month, formation of cortical bone is visible at the proximal and distal border of the epiphysis. At month 7, the proximal physis is still visible in contrast to the reported radiographic closure time of 7 months [1]. At day 1, the distal physis of the proximal phalanx appears as lines of hyperintense and hypointense signal on T1-weighted images, and hyperintense signal on T2* GRE images, which is still slightly visible at 7 months, in contrast to the reported radiographic closure [3]. Cortex at the proximal and distal end of the diaphysis is clearly visible at week 3, and appears well developed from the age of 1.5 months.

THE HOOF

The dermal and epidermal lamellar layer are clearly visible at birth on T1 FSE images, but the external hoof wall is more difficult to visualize.

REFERENCES

[1] Smallwood JE, Albright SM, Metcalf MR, Thrall DE, Harrington BD. A xeroradiographic study of the developing quarterhorse foredigit and metacarpophalangeal region from birth to six months of age. *Vet Radiol* 1989; **30**(3): 98–100.
[2] Metcalf MR, Sellett L, Smallwood JE, Thrall DE, Harrington BD. Scintigraphic characterization of the equine foredigit and metacarpophalangeal region from birth to six months of age. *Vet Radiol* 1989; **30**(3): 111–18.
[3] Crevier N, Denoix JM, Collobert C, Perrot P. Radiographie des members chez le poulain de 0 à 6 mois – images normales et pièges anatomiques. V – Pied et Paturon. *Pratique Vétérinair Equine* 1994; **26**(1): 31–9.

Chapter 6
The fetlock region

Meredith Smith and Sue Dyson

ANATOMY

The distal articular surface of the third metacarpal or third metatarsal bone, the proximal articular surface of the proximal phalanx, and the lateral and medial proximal sesamoid bones make up the bones of the metacarpophalangeal/metatarsophalangeal (MCP/MTP) or fetlock joint [1, 2, 3] (Figure 6.1a). The joint capsule is comparatively large, extending just proximal to the distal physis of the third metacarpal or third metatarsal bone on the dorsal aspect and palmarly/plantarly to the level of the distal ends of the second and fourth metacarpal/metatarsal bones, to accommodate the extensive range of motion of the joint. There is a capsular fold within the dorsal pouch [1]. The lateral and medial collateral ligaments of the fetlock joint are well developed [3]. The superficial collateral ligaments originate from eminences on the distal, lateral and medial aspects of the third metacarpal or third metatarsal bone and insert on the lateral and medial aspects of the proximal phalanx [2]. Proximal and distal to the joint the collateral ligaments merge into the periosteum of the respective bones. A deeper, more oblique component to each collateral ligament originates from slightly more distal depressions on the distal, lateral and medial aspects of the third metacarpal or third metatarsal bone, and also from the adjacent abaxial border of the respective sesamoid bone, and inserts onto the proximal phalanx [1, 3] (Figure 6.1b). Both the superficial and the oblique components have a synovial lining on their axial aspect, and synovial fluid can be found between the deep and superficial collateral components at dissection. The intersesamoidean ligament attaches the proximal sesamoid bones to one another, and covers their palmar/plantar surface, but also provides a proximal fibrocartilaginous extension against which the flexor tendons lie, on its concave, palmar/plantar aspect (Figure 6.1c). The dorsal aspect of the intersesamoidean ligament is in direct communication with the palmar/plantar synovium and synovial fluid of the MCP/MTP joint.

The palmar/plantar annular ligament (PAL) arises from the abaxial borders of the proximal sesamoid bones, fuses with the digital flexor tendon sheath (DFTS) over the palmar/plantar surface of the superficial digital flexor tendon (SDFT) and binds the flexor tendons within the DFTS to the palmar aspect of the MCP/MTP joint on the lateral and medial aspects. The tendons run, within the DFTS, between the PAL and the fibrocartilage of the intersesamoidean ligament of the proximal sesamoid bones [2, 4]. Just proximal to the MCP/MTP joint the deep digital flexor tendon (DDFT) is

Equine MRI, edited by Rachel C. Murray. © 2011 by Blackwell Publishing Ltd.

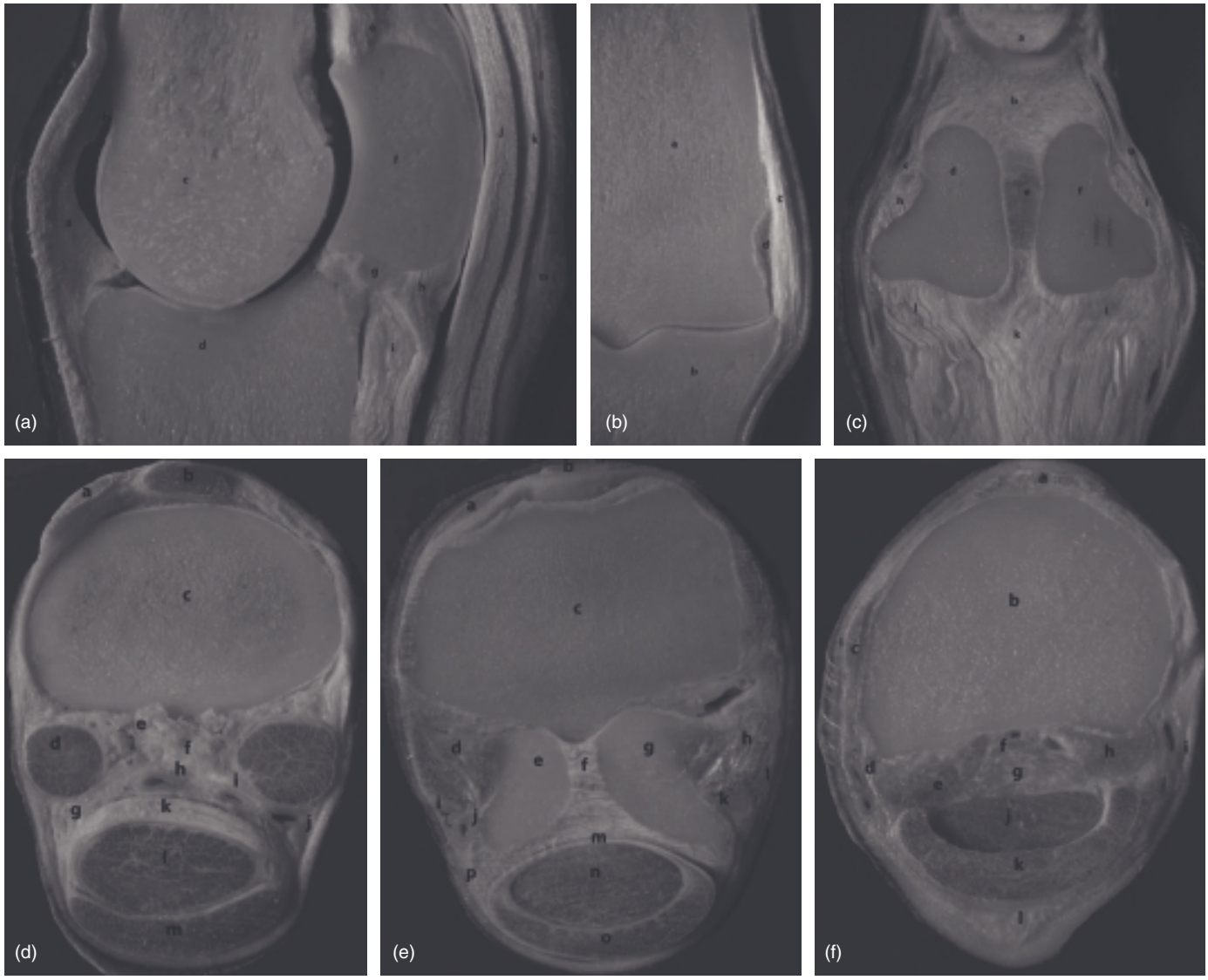

Figure 6.1 (a) A parasagittal section of a metacarpophalangeal joint. Dorsal is to the left of the picture: **a**, joint capsule; **b**, dorsal synovial plica of the metacarpophalangeal joint; **c**, third metacarpal bone; **d**, proximal phalanx; **e**, insertion of branch of suspensory ligament; **f**, proximal sesamoid bone; **g**, cruciate sesamoidean ligament; **h**, oblique sesamoidean ligament; **i**, straight sesamoidean ligament; **j**, deep digital flexor tendon; **k**, superficial digital flexor tendon; **l**, palmar annular ligament; **m**, ergot cushion. (b) A dorsal section of the lateral aspect of a metacarpophalangeal joint. Lateral is to the right of the picture: **a**, third metacarpal bone; **b**, proximal phalanx; **c**, superficial medial collateral ligament of the metacarpophalangeal joint; **d**, deep component of medial collateral ligament of the metacarpophalangeal joint. (c) A dorsal section of a metacarpophalangeal joint. Lateral is to the left of the picture: **a**, cut border of superficial digital flexor tendon; **b**, proximal scutum of the intersesamoidean ligament; **c**, lateral palmar digital artery; **d**, lateral proximal sesamoid bone; **e**, intersesamoidean ligament; **f**, medial proximal sesamoid bone; **g**, medial palmar digital artery; **h**, insertion of the lateral branch of the suspensory ligament; **i**, insertion of the medial branch of the suspensory ligament; **j**, lateral oblique sesamoidean ligament; **k**, straight sesamoidean ligament; **l**, medial oblique sesamoidean ligament. (d) A transverse section at a level 2 cm proximal to the proximal aspect of a metacarpophalangeal joint. Lateral is to the left of the picture: **a**, lateral digital extensor tendon; **b**, dorsal digital extensor tendon; **c**, third metacarpal bone; **d**, lateral branch of the suspensory ligament; **e**, palmar metacarpal vein; **f**, synovium of proximopalmar aspect of the metacarpophalangeal joint; **g**, lateral palmar digital artery and vein; **h**, lateral palmar metacarpal artery; **i**, medial palmar artery; **j**, medial palmar digital artery and vein; **k**, manica flexoria; **l**, deep digital flexor tendon; **m**, superficial digital flexor tendon. (e) A transverse section at the level of a metacarpophalangeal joint. Lateral is to the left of the picture: **a**, lateral digital extensor tendon; **b**, dorsal digital extensor tendon; **c**, third metacarpal bone; **d**, lateral branch of the suspensory ligament; **e**, lateral proximal sesamoid bone; **f**, intersesamoidean ligament; **g**, medial proximal sesamoid bone; **h**, medial branch of the suspensory ligament; **i**, lateral palmar digital vein; **j**, lateral palmar digital artery; **k**, medial palmar digital artery; **l**, medial palmar digital vein; **m**, manica flexoria; **n**, deep digital flexor tendon; **o**, superficial digital flexor tendon; **p**, lateral attachment of palmar annular ligament and digital flexor tendon sheath. (f) A transverse section just distal to a metacarpophalangeal joint. Lateral is to the left of the picture: **a**, common digital extensor tendon; **b**, proximal phalanx; **c**, lateral collateral ligament of the metacarpophalangeal joint; **d**, lateral palmar digital artery and vein; **e**, lateral oblique sesamoidean ligament; **f**, sagittal branch of the straight sesamoidean ligament; **g**, straight sesamoidean ligament; **h**, medial branch of the oblique sesamoidean ligament; **i**, medial palmar digital artery and vein; **j**, deep digital flexor tendon; **k**, superficial digital flexor tendon; **l**, ergot cushion.

surrounded by a thin sleeve of SDFT tissue, the manica flexoria, which continues for approximately 2 cm in a distal direction [2, 5] (Figures 6.1d and e). The proximal rim of this tissue is thicker than the distal rim. The proximal digital annular ligament arises from the proximal tubercles of the proximal phalanx and inserts on the distal tubercles of the proximal phalanx. The body of this X-shaped ligament fuses with the palmar/plantar surface of the SDFT [1].

The suspensory apparatus of the MCP/MTP joint includes the suspensory ligament (SL) (interosseous muscle) and its extensor branches, the proximal sesamoid bones and the distal sesamoidean ligaments [2]. The suspensory ligament branches at the junction of the mid and distal thirds of the third metacarpal or third metatarsal bone, and the lateral and medial branches insert onto the abaxial surface of the lateral and medial proximal sesamoid bones respectively (Figure 6.1e). The extensor branches of the suspensory ligament are comparatively thin distal extensions of each branch of the suspensory ligament that continue distal to the MCP/MTP joint in a dorso-distal direction, wrapping around the proximal phalanx and inserting on the common digital extensor tendon at the level of the proximal interphalangeal joint [1]. The distal sesamoidean ligaments originate at the base of the proximal sesamoid bones and run dorsal to the DDFT and palmar to the proximal and middle phalanges (Figure 6.1f). The straight sesamoidean ligament (SSL) inserts onto the palmar fibrocartilage extension of the proximal middle phalanx [2]. Some authors [1, 2] refer to the oblique sesamoidean ligament (OSL) as a single ligament, while other authors refer to a lateral and a medial oblique sesamoidean ligament [6], which is more consistent with findings during ultrasonography and at dissection. The OSL's insert onto the palmar distal aspect of the proximal phalanx, and the much shorter cruciate sesamoidean ligaments (CSL) sit deep to the SSL and cross one another to insert on palmar eminences on the proximal aspect of the proximal phalanx [2].

The large palmar recess of the MCP/MTP joint extends proximally between the third metacarpal bone and the branches of the suspensory ligament (Figure 6.1d). This portion of the MCP/MTP joint capsule is thicker than the dorsal pouch. The common and lateral digital extensor tendons pass over the dorsal aspect of the joint. On either side there is a large, palpable out pouching of the dorsal joint capsule [1, 2].

MRI OF THE METACARPOPHALANGEAL AND METATARSOPHALANGEAL REGIONS

The appearance of the structures of the equine fetlock joint on magnetic resonance images was first accurately described in 1996, prior to the clinical application of magnetic resonance imaging (MRI) in the equine veterinary profession [7, 8]. Since that study, the further development of sequences optimized for equine limbs on both high-field and low-field MR systems in routine clinical use has enabled us to more consistently interpret the appearances of structures such as cartilage and subchondral bone with MRI [9, 10]. The descriptions in this chapter are based on clinical experience, together

with high- (1.5 Tesla) and low-field (0.27 T) MR imaging, dissection and histology of 20 limbs from horses (aged 5 months to 26 years) that were known to be sound prior to euthanasia. All horses were euthanized for reasons unrelated to this study.

THE THIRD METACARPAL/METATARSAL BONE AND PROXIMAL PHALANX

Within the MCP/MTP joint, there is regional variation in the thickness of the cartilage and subchondral bone, and in the density of the underlying trabecular bone of the third metacarpal or third metatarsal bone and proximal phalanx, as a result of adaptational changes in response to exercise [11–14].

Cartilage

Cartilage is composed of collagen, proteoglycans and water. On MR images at resolutions commonly in clinical use, it is not possible to detect regional differences in cartilage thickness. Depending on the slice thickness and sequence selected, some parts of the cartilage surface are more clearly visualized than in other areas. On images from spoiled gradient-echo (SPGR), T1-weighted gradient-echo (GRE) or spin-echo (SE) sequences, the articular (hyaline) cartilage layer in the MCP/MTP joint appears as a thin (<5 mm) layer of homogeneous intermediate to high signal intensity (SI), overlying the junction between calcified cartilage and subchondral bone, which is of homogeneous low SI (Figure 6.2a). The cartilage surfaces within a joint can be seen due to the presence of synovial fluid of low SI on SPGR or T1-weighted sequences.

Two distinct layers of cartilage are often visible on high-field images because of the high resolution and because the horse is non-weight-bearing during image acquisition. On images from a low-field system, for example during standing MRI, the separate articular surfaces within the MCP/MTP joint cannot always be clearly defined at the weight-bearing aspect of the joint, but two layers are more apparent at the joint margins (Figure 6.2b). On low-field images on some sequences a low to intermediate, slightly heterogeneous SI is more representative of the cartilage layer. This variation in appearance is due to differences in sequence parameters, and volume averaging across the tissues, which occurs as a result of the greater slice thickness. On T2-weighted GRE and fast spin-echo (FSE) sequences, synovial fluid and cartilage are both of high SI, and the ability to distinguish the articular surfaces of the bones is lost (Figure 6.2c). On fat-suppressed sequences such as STIR (short τ inversion recovery) sequences, the cartilage layer has high SI, because of its water content; however, definition is lost due to the high SI of synovial fluid (Figure 6.2d). In any given sequence from any system, when interpreting thicker slices and slices with separation between them, the cartilage layer, where visible, is likely to appear slightly heterogeneous in SI due to volume averaging across the curved surface of the bones within the joint.

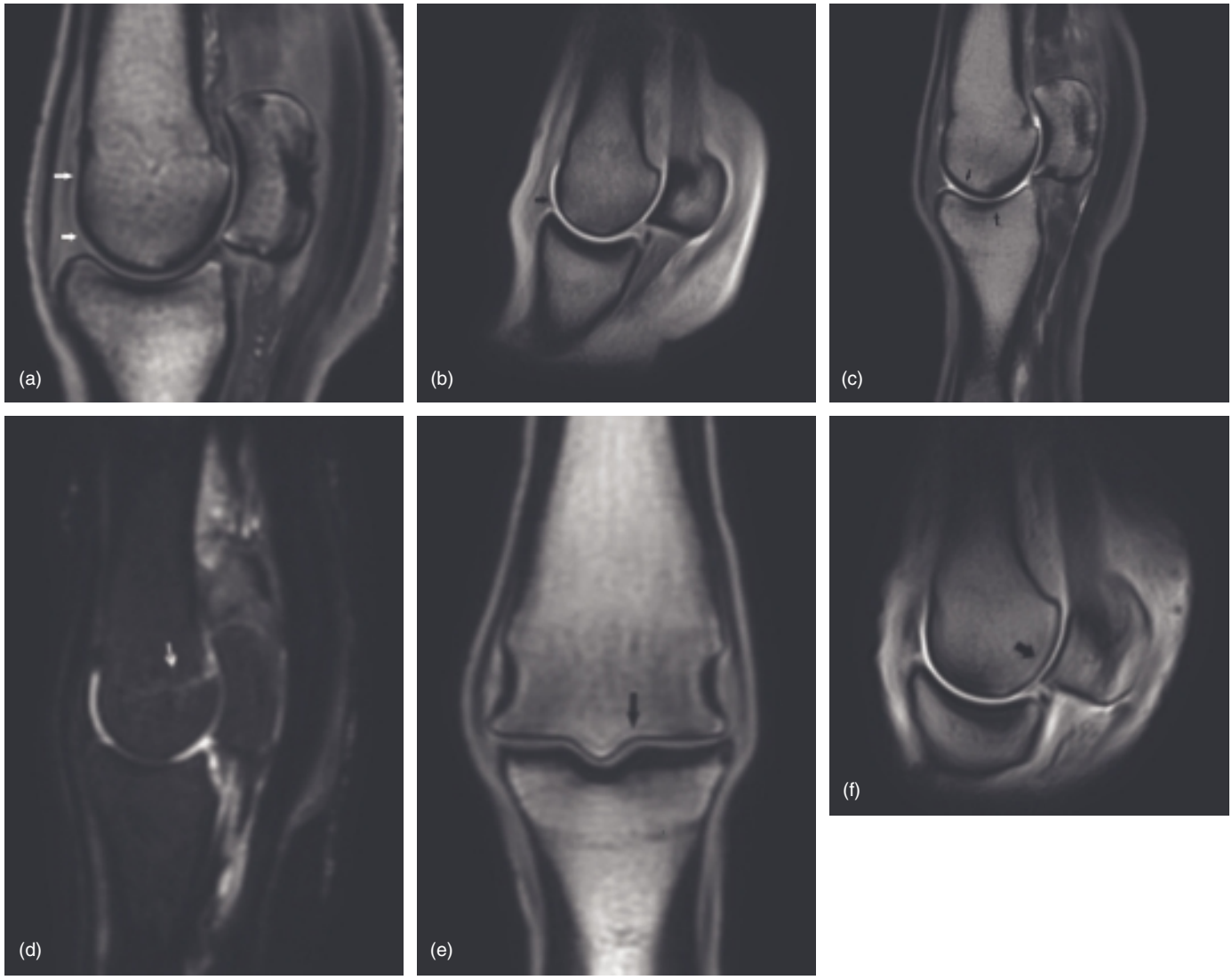

Figure 6.2 (a) A parasagittal T1-weighted 3D gradient-echo MR image of a metacarpophalangeal joint obtained using a high field (1.5T) MRI system (General Electric). Dorsal is to the left of the image. The cartilage layers have intermediate to high signal intensity (arrows). (b) A parasagittal T1-weighted 3D gradient-echo MR image of a metacarpophalangeal joint obtained with a low field (0.27T) MRI system (Hallmarq Veterinary Imaging). Dorsal is to the left of this image. In this image, the cartilage layers have high signal intensity (arrow). (c) A parasagittal T2*-weighted 3D gradient-echo MR image of a metacarpophalangeal joint obtained using a high-field MRI system. Dorsal is to the left of this image. The subchondral bone thickness of the lateral condyle of the distal third metacarpal bone and lateral aspect of the proximal phalanx is within normal regional variation (arrows). Note that the subchondral bone on the palmar, distal aspect of the third metacarpal bone is thicker than dorsally. (d) A parasagittal STIR (short τ inversion recovery) MR image of a metacarpophalangeal joint of a 3-year-old Thoroughbred gelding obtained using a high-field (1.5T) MRI system (General Electric). Dorsal is to the left of this image. The remnant of the distal physis of the third metacarpal bone is visible as intermediate signal intensity (arrow). On this image synovial fluid within the palmar recess of the metacarpophalangeal joint is clearly visible, having high signal intensity with this sequence. (e) A dorsal T1-weighted gradient echo MR image of a metacarpophalangeal joint obtained using a high-field MRI system. Lateral is to the left of this image. A Gibb's or truncation artefact is present on this image appearing as a thin line of intermediate signal intensity parallel with and just deep to the subchondral bone interface (arrow). (f) A parasagittal T1-weighted 3D gradient-echo MR image of a metacarpophalangeal joint obtained with a low-field MRI system. Dorsal is to the left of this image. A Gibb's or truncation artefact is present on this image appearing as a thin line of intermediate signal intensity parallel with and just deep to the subchondral bone interface (arrow). Note that the subchondral bone on the dorsal, distal aspect of the medial condyle of the third metacarpal bone is thicker than palmarly.

Subchondral bone

Subchondral bone is a thin (<10 mm), dense, plate of bone that supports the articular cartilage within a joint. In an adult horse that has not undergone intensive work such as race training, the normal MR appearance of the subchondral bone of the third metacarpal or third metatarsal bone is of a band of homogeneous low SI of varying thickness on SPGR, T1-weighted and T2-weighted GRE sequences and FSE sequences (Figures 6.2b and c). The endosteal interface should be smooth. The subchondral bone layer is clearly delineated by cartilage of high SI on the articular side and trabecular bone of intermediate to high SI on the endosteal side. There is often a Gibbs or truncation artefact associated with this band of low SI on GRE and FSE sequences in the sagittal and dorsal or frontal planes. In the MCP/MTP joint, the artefact appears as a thin line of intermediate SI parallel with and just deep to the subchondral/endosteal bone interface (Figures 6.2e and f). This artefact occurs as a result of under sampling of data so that interfaces of high and low SI such as cartilage and subchondral bone, are misrepresented on the image [15].

On fat-saturated and STIR sequences, the component of the SI attributable to fat within the trabecular bone has been nulled, and so differentiation of subchondral and trabecular bone is lost, giving an appearance of homogeneous low SI throughout (Figures 6.2d and 6.3a).

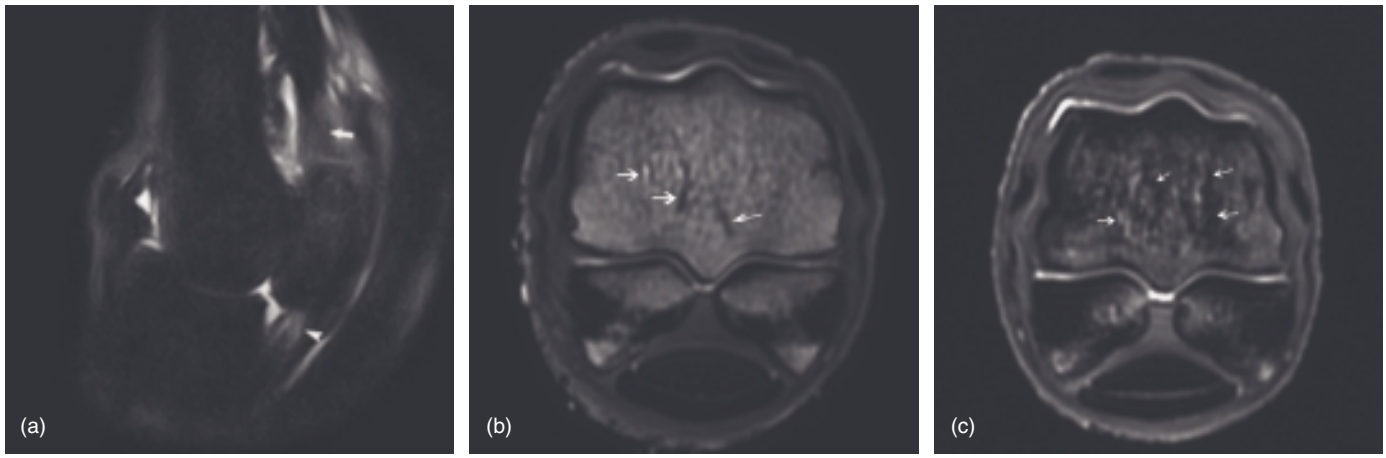

Figure 6.3 (a) A parasagittal STIR MR image of a metacarpophalangeal joint obtained using a low-field (0.27T) MRI system (Hallmarq Veterinary Imaging). Dorsal is to the left of this image. On this image there is a region of diffuse, intermediate signal intensity within the branch of the suspensory ligament that continues distally to the insertion onto the proximal sesamoid bone (arrow). The proximal third of the oblique sesamoidean ligament also has diffuse, intermediate SI (arrow head). The increased signal intensity in these regions is due to fibre divergence and volume averaging and is normal in appearance. (b) A transverse 3D T2*-weighted gradient-echo MR image of a metacarpophalangeal joint at the level of the proximal sesamoid bones obtained using a high-field MRI system. Lateral is to the right of this image. A small number of well-delineated irregular spots of high signal intensity and short lines of low signal intensity are present within the trabecular architecture (arrows). (c) A transverse 3D T2*-weighted gradient-echo MR image of a metacarpophalangeal joint at the level of the proximal sesamoid bones obtained using a high-field MRI system. Lateral is to the right of this image. An increased number and size of well-delineated irregular spots of high signal intensity and irregular lines of low signal intensity are present within the trabecular architecture compared with (b) (arrows); these subclinical changes are common in horses in race training.

The subchondral bone thickness of the distal aspect of the third metacarpal or third metatarsal bone was measured on sagittal T1-weighted MR images from 19 sound horses aged from 2 to 26 years. The subchondral bone was thickest in the dorsal third of the sagittal ridge compared with the mid and palmar or plantar thirds of the sagittal ridge (range of thickness 0.1–0.7 cm). In horses aged 7–26 years ($n = 12$), the subchondral bone at the midpoint of each condyle was also thickest over the dorsal third of the condyle (range 0.1–0.9 cm). In horses younger than 7 years of age that had not undergone race training ($n = 4$), the subchondral bone was thicker in the palmar or plantar third of the lateral condyle (range 0.1–0.5 cm), and the dorsal third of the medial condyle (range 0.4–0.9 cm). In horses younger than 7 years of age that had undergone race training (n = 3), the dorsal thirds of both the lateral and medial condyles as well as the sagittal ridge were the thickest (range 0.3–0.6 cm).

The subchondral bone thickness of the proximal aspect of the proximal phalanx was measured on sagittal T1-weighted MR images from 19 sound horses aged from 2–26 years. At the level of the sagittal groove, the subchondral bone was thickest in the dorsal third of the sagittal groove compared with the mid and palmar or plantar thirds (range 0.2–0.3 cm). There was more uniformity in thickness of subchondral bone throughout the dorsal to palmar or plantar curvature of the glenoid cavity of the proximal phalanx compared with the distal aspect of the third metacarpal or third metatarsal bone. There was a slight increase in thickness of the palmar or plantar third of the lateral glenoid cavity compared with the mid and dorsal thirds (range 0.1–0.7 cm). Within the medial glenoid cavity of the proximal phalanx there was a slight increase in thickness of the dorsal third of the glenoid cavity compared with the mid and palmar or plantar thirds of the glenoid cavity (range 0.1–0.5 cm). These regional changes in thickness mirror those of subchondral bone of the distal aspect of the third metacarpal or metatarsal bone (Figure 6.4e). On dorsal or frontal images, the subchondral bone is thickest towards the midpoint of the palmar aspect of the glenoid cavity of the proximal phalanx, and this pattern is approximately symmetrical on each side of the sagittal groove (Figures 6.2e and 6.4e).

Trabecular bone

The structure of trabecular or cancellous bone is that of an organized, interlacing bone scaffold which is mineralized, with the spaces between the scaffolding contain haematopoietic or fatty marrow [16]. This mixture of mineralized bone and fatty tissue means that trabecular bone is represented by a heterogeneous intermediate to high signal intensity on T1-weighted GRE sequences. On T2-weighted GRE and FSE sequences, the heterogeneity is still present but overall the appearance is darker. On fat saturated and STIR sequences the differentiation of subchondral and trabecular bone is lost, and the medulla of bones has low SI (Figures 6.2d and 6.3a).

The regional differences in density within the trabecular bone in sound horses aged 2–26 years (excluding horses that have undergone race training)

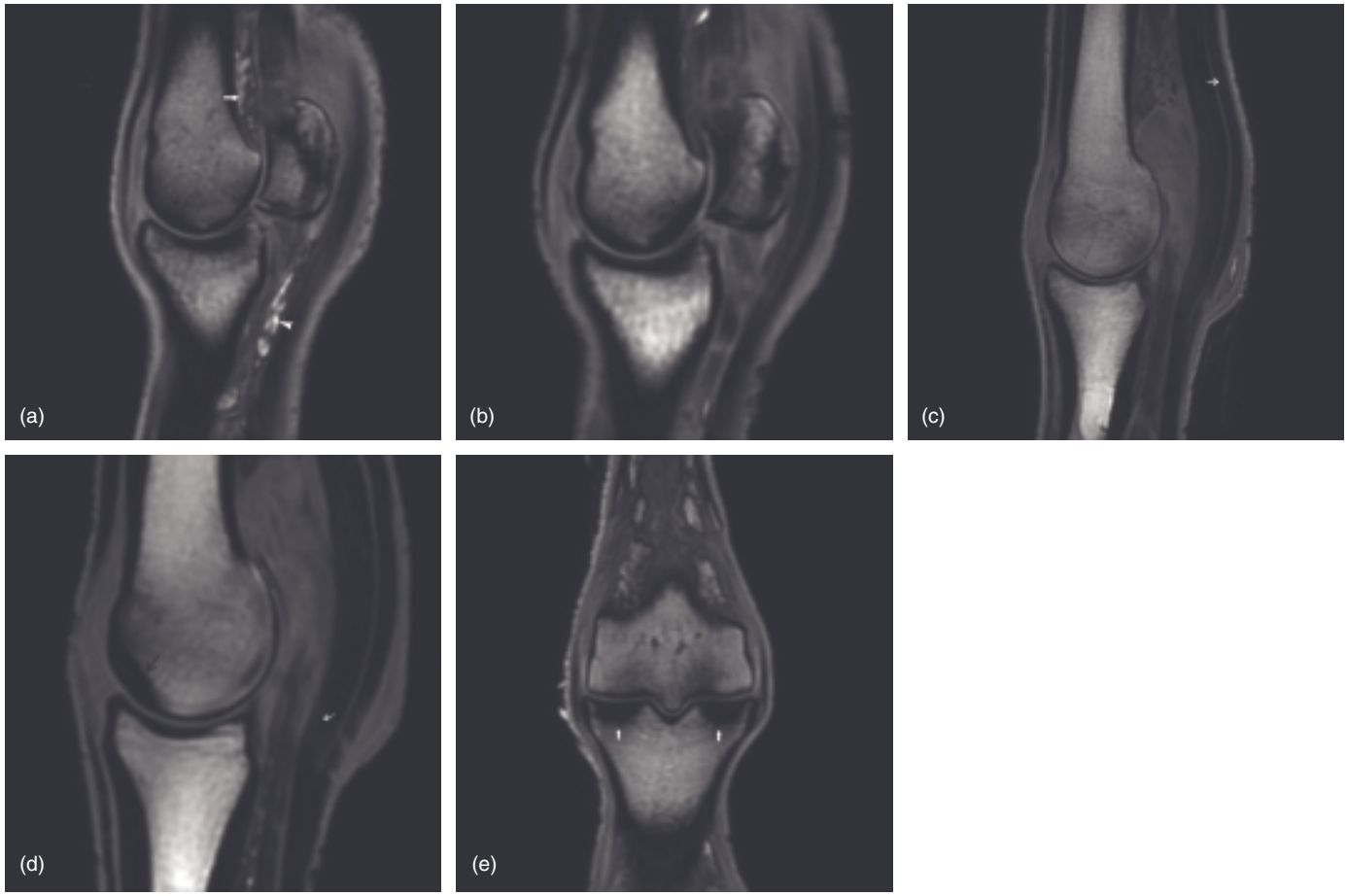

Figure 6.4 (a) A parasagittal 3D T1-weighted gradient-echo MR image of a metacarpophalangeal joint of a 3-year-old horse at the level of the mid-point of the medial condyle obtained using a high-field MRI system. Dorsal is to the left of this image. There are regions of low signal intensity within the proximal sesamoid bone at sites of insertion of ligaments onto the bone. There is intermediate to high signal intensity associated with synovial tissue within the palmar recess of the metacarpophalangeal joint (white arrow) and with fat and fascia palmar to the oblique sesamoidean ligament (white arrow head). Synovial fluid has low signal intensity on this type of sequence. The subchondral bone is marginally thicker in the dorsal region compared with the mid and palmar regions of the distal third metacarpal bone, but at this age, in horses undergoing only light exercise, minimal regional adaptation in subchondral bone thickness has developed (black arrows). (b) A parasagittal 3D T1-weighted gradient-echo MR image of a metacarpophalangeal joint of a 12-year-old horse at the level of the mid-point of the lateral condyle from a sequence obtained using a high-field MRI system. Dorsal is to the left of this image. On this image the subchondral bone is thicker in both the dorsal and the palmar regions of the distal third metacarpal bone compared with the image in (a), consistent with regional adaptation for an older horse (black arrows). (c) A sagittal 3D T1-weighted gradient-echo MR image of a metacarpophalangeal joint of a 3-year-old horse at the level of the sagittal ridge of the distal third metacarpal bone obtained using a high-field MRI system. Dorsal is to the left of the image. The subchondral bone layer is thin and of uniform thickness throughout the condyle from dorsal to palmar. This is a normal appearance for subchondral bone at this level in horses of this age that have undergone only light exercise. A fine line of increased signal intensity is seen within the SDFT (arrow), and is consistent with an edge artefact. (d) A sagittal 3D T1-weighted gradient-echo MR image of a metacarpophalangeal joint of a 12-year-old horse at the level of the sagittal ridge of the distal third metacarpal bone obtained using a high field MRI system. Dorsal is to the left of the image. The subchondral bone of the dorsal aspect of the distal third metacarpal bone is considerably thicker than the subchondral bone of the mid and palmar aspects, which is consistent with regional adaptation for an older horse (black arrow) (compare with (c)). There is linear intermediate signal intensity in the dorsal aspect of the DDFT at the level of the proximal sesamoid bones due to structural change within the tendon secondary to compressive forces (white arrow) in this location. (e) A dorsal 3D T1-weighted gradient-echo MR image of the palmar aspect of a metacarpophalangeal joint of a 5-year-old horse obtained using a high-field MRI system. Medial is to the left of this image. There is regional increased thickness of the subchondral bone of the palmar proximal aspect of the proximal phalanx (arrows).

mirror the differences described above for subchondral bone thickness in both the distal aspect of the third metacarpal or metatarsal bone and the proximal aspect of the proximal phalanx. Increased density within the trabecular bone appears as areas of heterogeneous intermediate to low SI on MR images. Within the lateral and medial condyles of the third metacarpal or metatarsal bone there is normally some mild variation in SI, with lower SI being present within the dorsal and palmar or plantar thirds of each condyle compared with the middle third when viewed on a sagittal image. At the level of the sagittal ridge of the distal aspect of the third metacarpal or metatarsal bone, the trabecular bone density is of uniform, intermediate SI throughout the sagittal ridge (Figures 6.4a–d). On either side of the sagittal ridge, a small number of vascular channels may be present within the condyles of the third metacarpal or metatarsal bone. These are represented by well-delineated irregular spots of high SI on T2*-weighted sequences and/or short lines of low SI on T1- and T2*-weighted sequences within the trabecular architecture (Figure 6.3b). In horses that have undergone race training, or other forms of intensive exercise, the adaptational changes described above are more marked, with increased density of trabecular bone (low SI) extending further into the condyles of the third metacarpal or third metatarsal bone in all three planes. The number and distribution of irregular lines of low SI increases throughout the trabecular architecture, and the pattern and distribution of these lines in those horses may be increased with subclinical trabecular damage (Figure 6.3c).

In mature horses, a remnant of the distal physis of the third metacarpal or third metatarsal bone persists as an irregular line of low SI on T1- and T2-weighted GRE and FSE sequences, and is usually most noticeable extending from the palmar/plantar cortex into the trabecular bone of the palmar/plantar condyle. On STIR sequences, the physis is represented by an irregular line of intermediate SI due to the greater fluid component compared with trabecular bone (Figure 6.2d).

Cortical bone

Cortical bone consists of hard and compact woven bone covered in periosteum, and has homogeneous low SI on MR images. It is not normally possible to differentiate the periosteum from the underlying cortical bone on MR images. The periosteal and endosteal surfaces should normally appear smooth on MR images. During interpretation the inner and outer surfaces of bones must be evaluated for changes in the periosteal or endosteal surfaces. This is possible on T1 GRE, PD and SE/FSE sequences, where there is good contrast between the trabecular bone and the dense cortical bone. Horses that have undergone intensive training show adaptational changes in the thickness of the cortices of the third metacarpal or third metatarsal bone and the proximal phalanx. In particular the dorsal cortex of these bones becomes thicker in response to exercise compared with the palmar/plantar, lateral or medial cortices (Figure 6.4d).

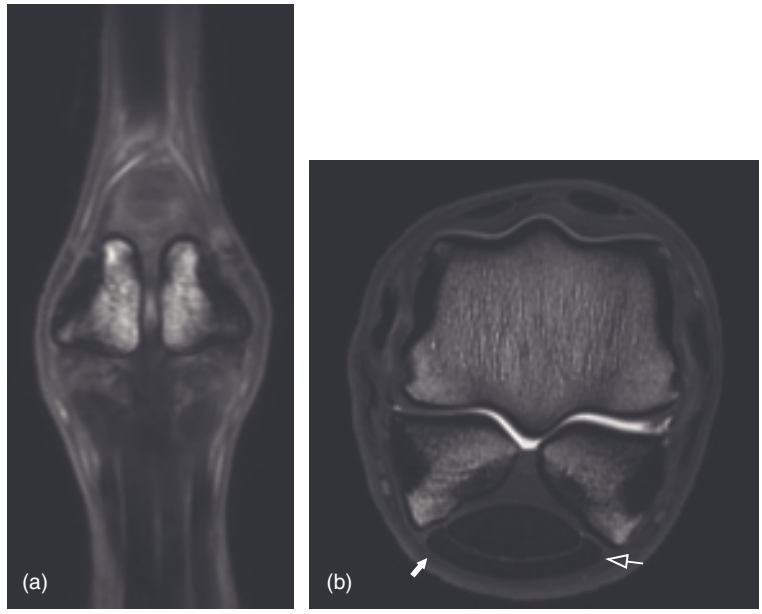

Figure 6.5 (a) A dorsal 3D T2*-weighted gradient-echo MR image of the palmar aspect of a metacarpophalangeal joint from a sequence obtained using a high-field MRI system. Medial is to the left of this image. (b) A transverse 3D T2*-weighted gradient-echo MR image of a metacarpophalangeal joint at the level of the proximal sesamoid bones obtained using a high-field MRI system. Lateral is to the left of this image. The palmar annular ligament (filled arrow) and the digital flexor tendon sheath (open arrow) are visible.

THE PROXIMAL SESAMOID BONES

The articular cartilage over the dorsal surfaces of the proximal sesamoid bones is difficult to visualize. The trabecular bone of the proximal sesamoid bones is generally of heterogeneous intermediate to low SI. Occasional small, focal areas of high SI on T2-weighted and STIR sequences are present, representing vascular channels. The density of cortical and trabecular bone is greater at the insertion of the respective branch of the SL (Figures 6.5a and b), and can appear irregular. There is also increased density of trabecular and cortical bone over the palmar/plantar and abaxial aspects of these bones, represented by decreased SI on MR images at these locations (Fig 6.2c). The cortical margins of the proximal sesamoid bones should appear even, with smooth insertions of the collateral sesamoid ligaments on the abaxial aspect, smooth insertions of the branches of the suspensory ligaments on the abaxial and palmar or plantar aspects and smooth origins of the distal sesamoidean ligaments from the base of each sesamoid bone.

SOFT TISSUE STRUCTURES OF THE FETLOCK REGION

For all tendons and ligaments, the angle of the structure relative to the static magnetic field must be considered. The magic angle effect is most obvious when a structure is at 55° to the static magnetic field [17, 18], but it has been demonstrated that even when the collateral ligaments of the distal

interphalangeal joint and the oblique sesamoidean ligaments are at lesser angles to the static magnetic field, it is still possible for a magic angle effect to be present within these structures (Figure 6.8c) [19]. Using a protocol that includes a mixture of GRE, FSE/SE and PD sequences can help differentiate artefacts from pathology.

The suspensory ligaments

The lateral and medial branches of the SL are well-defined structures of intermediate SI on all sequences. In the transverse plane, the branches may consist of several components (commonly two), due to bands of connective tissue of intermediate to high SI that are present (Figure 6.6a). In a sagittal plane, at the palmar/plantar aspect of the branches of the SL, level with the MCP/MTP joint, there is often a region of diffuse, high SI, which continues distally to the insertion onto the proximal sesamoid bone (Figures 6.2b and f). The dorsal border of each branch of the SL is well defined due to its proximity to synovium (intermediate SI) and synovial fluid (high SI) within the palmar/plantar pouch of the MCP/MTP joint, and with fat, also of high SI, between the branches of the SL, palmar/plantar to the third metacarpal or third metatarsal bone (Figure 6.6b).

The extensor branches of the SL are thin structures that are difficult to identify on MR images. On sagittal images, provided the field of view is wide enough, they are visible as bands of low to intermediate SI, running in an oblique palmaro/plantaroproximal to dorsodistal direction towards the proximal interphalangeal joint.

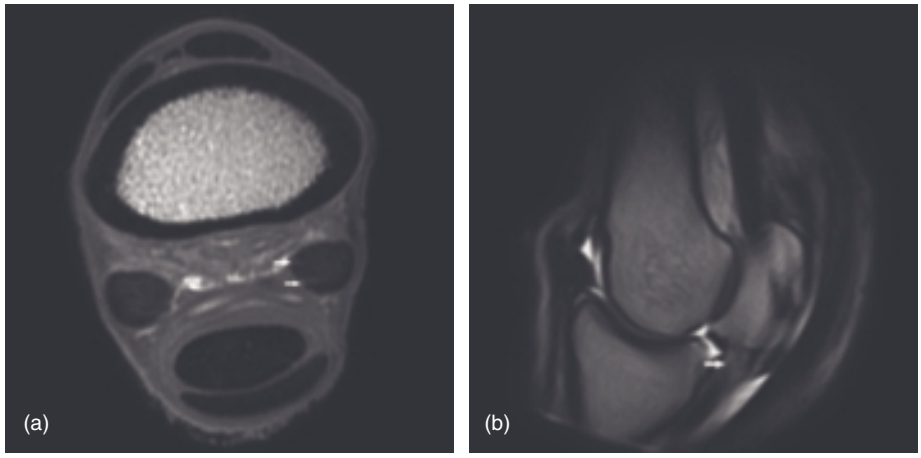

Figure 6.6 (a) A transverse 3D T2*-weighted gradient-echo MR image just proximal to the proximal sesamoid bones of a metacarpophalangeal joint from a sequence obtained using a high-field MRI system. Lateral is to the left of this image. There are two areas of linear, intermediate signal intensity within the medial branch of the suspensory ligament (arrows). This compartmentalization within the branches of the suspensory ligaments is a normal variation. (b) A parasagittal T2-weighted fast spin-echo (FSE) MR image of a metacarpophalangeal joint obtained using a low-field MRI system. Dorsal is to the left of this image. There is intermediate signal intensity within the proximal aspect of the oblique sesamoidean ligament due to divergence of fibre orientation and volume averaging at this location (arrow).

Collateral ligaments of the metacarpophalangeal joint

The collateral ligaments of the MCP/MTP joint are homogeneous structures of low SI, with margins that are clearly delineated due to the presence of synovial fluid on their axial aspect, and subcutaneous tissue and fascia of intermediate SI on the abaxial aspect of each ligament. Some mild asymmetry in thickness between lateral and medial superficial collateral ligaments is a normal variation. The superficial components are thicker and longer than the deeper oblique components. The deep and superficial components of the collateral ligaments may be separated by synovial fluid (bright SI on T2* and T2 FSE sequences), and this must not be mistaken for pathology within one ligament. The origins and insertions of the collateral ligaments should be smooth with no irregularity of the periosteal or endosteal bone surfaces at the origin or insertion (Figures 6.2e and 6.4e). Care should be taken in interpretation of changes in SI within the collateral ligaments from images in a sagittal plane, because volume averaging affects the appearance.

Digital flexor tendons

The SDFT and DDFT have homogeneous low SI, except at the level of the MCP/MTP joint itself, where, as the tendons conform around the angle of the joint, there is often linear, intermediate SI noticeable within the dorsal third of the DDFT on sagittal images (Figure 6.7a). This is attributed to structural change within the DDFT secondary to compression against the palmar/plantar aspect of the MCP/MTP joint. More subtle changes may also be present in the SDFT. There may also be a fine, linear artefact (seen on sagittal images) present towards the dorsal or palmar/plantar margins of either flexor tendon, which is recognized as an edge artefact (Figure 6.4c). Increased SI that extends throughout the dorsal to palmar/plantar width of the flexor tendons in the sagittal plane is an abnormal finding.

On transverse images, the palmar/plantar surface of the DDFT is connected at midline by fascia to the dorsal border of the SDFT, and these surfaces of the tendons may have a thicker paratenon compared with the dorsal surface of the DDFT and the palmar/plantar surface of the SDFT. This fibrous connective tissue extends a short way into the body of the DDFT tendon on midline, at the level of the MCP/MTP joint, and has an intermediate SI compared with tendonous tissue. These anatomical features may give the palmar/plantar border of the DDFT an irregular appearance on MR images (Figure 6.7b). Very small, linear areas of increased SI may be present within the DDFT on transverse images, which represent the normal fascicular architecture of the DDFT (Figure 6.5b). The connective tissue that divides the lateral and medial lobes of the DDFT also appears of intermediate SI, and should not be mistaken for a lesion. Areas of high SI on transverse images may represent blood vessels within the tendon tissue and at the margins of the tendons.

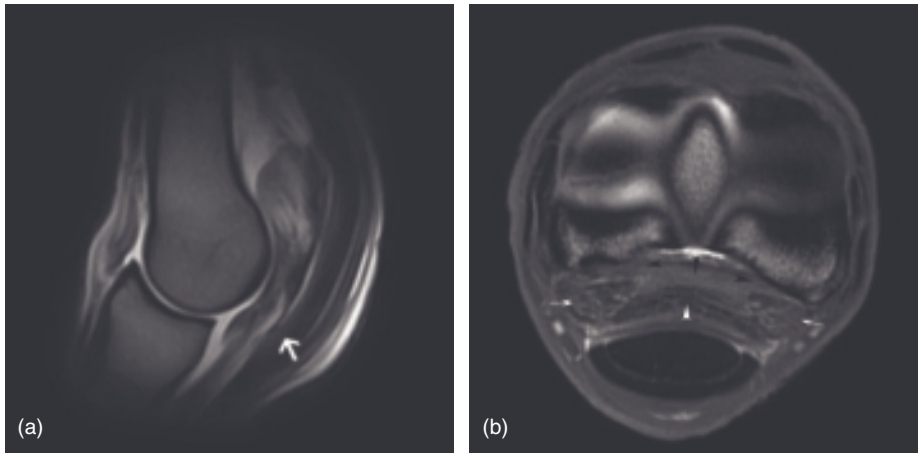

Figure 6.7 (a) A parasagittal T2*-weighted 3D gradient-echo MR image of a metacarpophalangeal joint obtained using a low-field MRI system. Dorsal is to the left of this image. There is linear, intermediate signal intensity within the dorsal third of the deep digital flexor tendon at the level of the proximal sesamoid bones due to structural change within the tendon secondary to compressive forces (white arrow) in this location. (b) A transverse T2*-weighted 3D gradient-echo MR image at the level of the proximal aspect of the proximal phalanx obtained using a high-field MRI system. Lateral is to the left of this image. The oblique sesamoidean ligaments (white arrows) and straight sesamoidean ligament (white arrow head) have heterogeneous signal intensity due to their fascicular construction, and the presence of fat surrounding these ligaments. The fibres of the cruciate sesamoidean ligaments (black arrow heads) are oriented more closely to the plane of this image, and have a more homogeneous signal intensity as a result.

Digital flexor tendon sheath

The DFTS is best seen on transverse images, as a thin (<2 mm diameter) structure of low SI (Figure 6.5b). Fluid within the DFTS can help to delineate this structure on T2-weighted sequences.

Extensor tendons

The dorsal, lateral and common digital extensor tendons all have homogeneous low SI. The margins of the tendons are clearly defined and they are surrounded by fascia, which has intermediate SI on all sequences.

Intersesamoidean ligament

The intersesamoidean ligament is of heterogeneous, intermediate SI, with small, focal areas of intermediate to high SI on T2*-weighted images often being present between and just proximal to the proximal sesamoid bones on dorsal/frontal images (Figure 6.5a). These areas represent areas of increased fluid within the ligament. With age, this structure undergoes thinning, and at dissection there is gross evidence of dystrophic mineralization, which if present, is contributory to the appearance of heterogeneous SI on MR images.

Joint capsule and synovium

The margins of the MCP/MTP joint capsule are most clearly delineated by the synovium, which has intermediate SI on both T1- and T2-weighted sequences, and the synovial fluid, which has high SI on T2-weighted sequences. The capsular tissue is seen as a fine line of intermediate SI on the dorsal aspect of the joint on sagittal images. The synovium at the palmar or plantar aspect of the joint is prolific and appears as tissue of heterogeneous intermediate to high SI with pockets of synovial fluid (high SI) in between (Figures 6.2d and 6.4a).

Palmar/Plantar annular ligament

The palmar/plantar annular ligament is best seen on transverse images as a thin (<2 mm diameter) structure of low SI (Figure 6.5b).

Proximal digital annular ligament

The proximal attachment of the proximal digital annular ligament may be seen as a thin (<2 mm) rim of tissue of low SI on transverse images obtained just distal to the fetlock joint.

Distal sesamoidean ligaments

These structures are discussed further in the section on the pastern. The cruciate sesamoidean ligaments are small and can be difficult to identify. The bright SI of synovial fluid in T2-weighted sequences, which is present on their dorsal surface, helps to differentiate the 'cross' shape (intermediate SI) of these ligaments on transverse images, at a level just distal to the MCP/MTP joint (Figure 6.8a). The oblique sesamoidean ligaments are triangular at their origin on transverse images, and of heterogeneous SI due to the

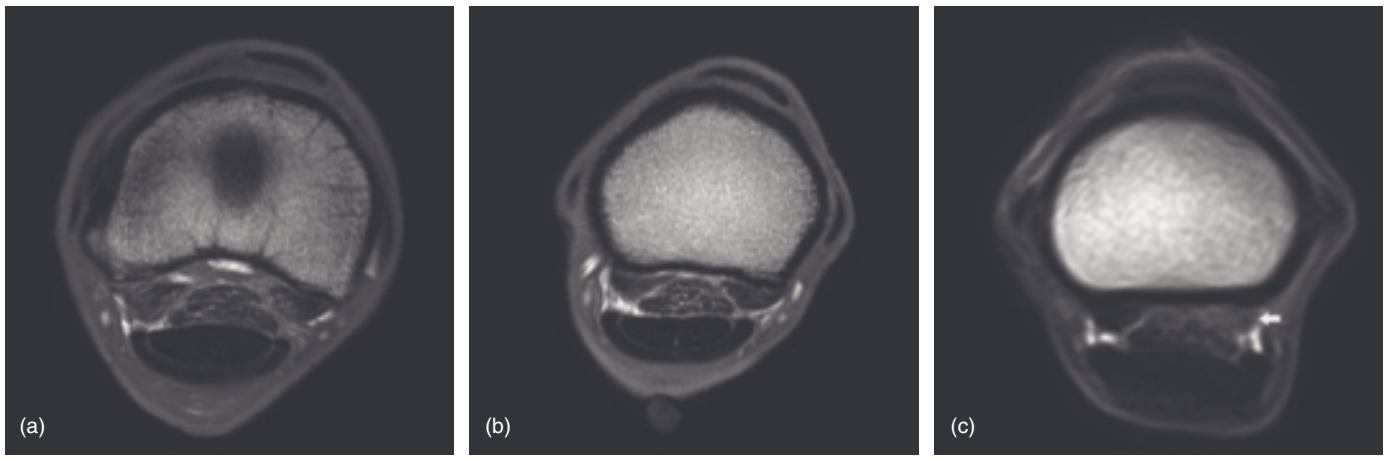

Figure 6.8 (a) A transverse T2*-weighted 3D gradient-echo MR image of the proximal aspect of the proximal phalanx, close to the origin of the distal sesamoidean ligaments obtained using a high field (1.5T) MRI system (General Electric). Lateral is to the left of this image. (b) A transverse T2*-weighted 3D gradient-echo MR image of the proximal aspect of the proximal phalanx obtained using a high-field MRI system. This image is just distal to the image in (a). Lateral is to the left of this image. (c) A transverse T1-weighted spin-echo (SE) MR image of the proximal aspect of the proximal phalanx with the long axis of the limb angled at 8° to vertical, obtained using a low-field MRI system. Lateral is to the left of this image. There is increased signal intensity within the medial oblique sesamoidean ligament as a result of a magic angle effect (arrow).

fascicular nature of these ligaments (Figures 6.8a and b). They are clearly defined due to the presence of fat closely associated with their margins. There is often some asymmetry in size of the lateral and the medial oblique sesamoidean ligaments [20]. The origin of each of the oblique sesamoidean ligaments can be identified towards the abaxial aspect on sagittal images, and is particularly clear on sagittal images from low-field standing MRI as these structures are under tension during weight bearing (Figure 6.2b). The presence of fat and fascia around the soft tissue structures of the palmar/plantar pastern can make the body of these ligaments difficult to evaluate. The origin of the straight sesamoidean ligament is oval on transverse images. There is a smaller sagittal component palmar to the main body of the straight sesamoidean ligament, which is also referred to as the sagittal component of the oblique sesamoidean ligaments [5]. The origins of the oblique and straight sesamoidean ligaments are best evaluated on dorsal/frontal in combination with sagittal images.

NORMAL VARIATION IN APPEARANCE ON MR IMAGES

Immature horses

The distal physis of the third metacarpal or third metatarsal bone is most active up to 2 months of age, and closes at approximately 4–6 months of age. For some time after closure, in skeletally immature horses (<4 years of age), the physis still appears as a clear, irregular structure of intermediate to high SI running in a dorsal to palmar/plantar direction (Figures 6.9a–c).

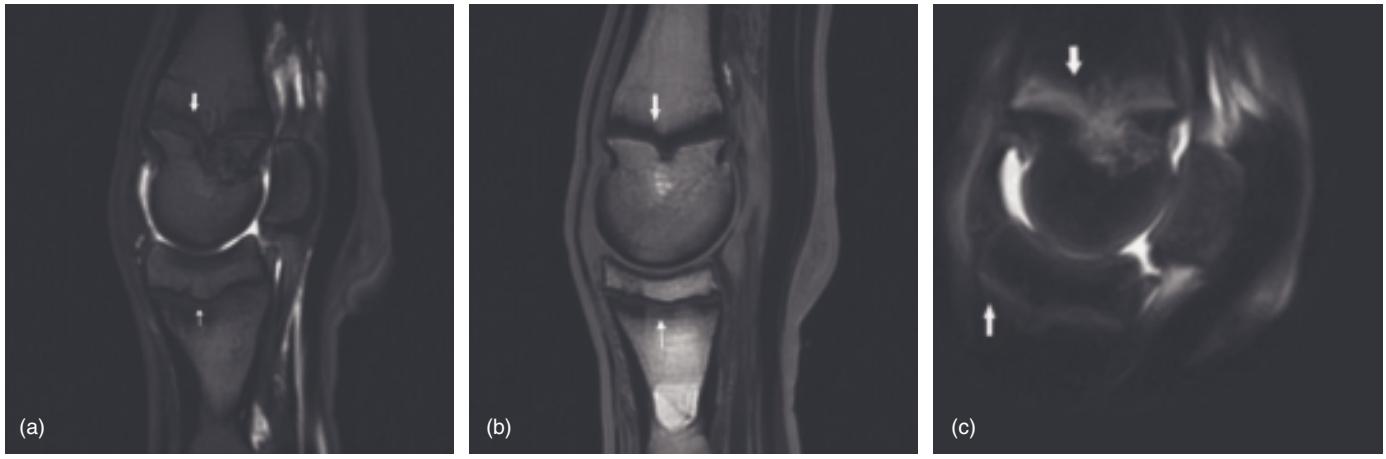

Figure 6.9 (a) A parasagittal T2*-weighted 3D gradient-echo MR image of a metacarpophalangeal joint of a 5-month-old filly at the level of mid condyle, from a sequence obtained using a high-field MRI system. Dorsal is to the left of this image. The distal physis of the third metacarpal bone (fat arrow) and the proximal physis of the proximal phalanx (thin arrow) are distinct. Note the immature shape of the distal aspect of the third metacarpal bone. There is a clearer separation between the articular surfaces of the distal third metacarpal bone and the proximal phalanx compared with an adult, due to the thicker articular cartilage present in this immature horse. (b) A sagittal 3D T1-weighted gradient-echo MR image of a metacarpophalangeal joint of a 5-month-old filly at the level of the sagittal ridge of the distal third metacarpal bone obtained using a high-field MRI system. Dorsal is to the left of this image. The distal physis of the third metacarpal bone (fat arrow) and the proximal physis of the proximal phalanx (thin arrow) are distinct. (c) A parasagittal STIR MR image of the metacarpophalangeal joint of a 5-month-old filly obtained using a low-field MRI system. Dorsal is to the left of this image. The distal physis of the third metacarpal bone (fat arrow) and the proximal physis of the proximal phalanx (thin arrow) have high signal intensity due to the presence of fluid in these structures.

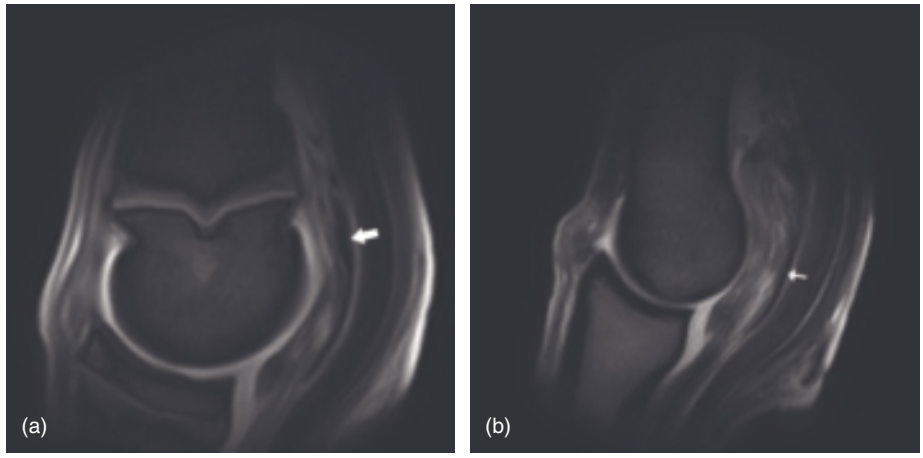

Figure 6.10 (a) A sagittal T2*-weighted 3D gradient-echo MR image of a metacarpophalangeal joint of a 5-month-old Percheron filly obtained using a low-field MRI system. Dorsal is to the left of this image. The manica flexoria has low signal intensity and is prominent in this immature horse (arrow) abutting the palmar margin of the intersesamoidean ligament. (b) A sagittal T2*-weighted 3D gradient-echo MR image of a metacarpophalangeal joint of a 6-year-old Thoroughbred cross mare obtained using a low-field MRI. Dorsal is to the left of this image. The manica flexoria is a thinner structure compared with (a) (arrow).

Increased density of trabecular bone on either side of the physeal scar is also present, represented by decreased SI on MR images. The proximal physis of the proximal phalanx closes at approximately 1 year of age and is also prominent in skeletally immature horses.

Lack of change in trabecular bone density due to regional load distribution is also noticeable in immature horses (Figures 6.9a and b), with the exception of horses that have undergone race training. The manica flexoria may appear more obvious on sagittal images in immature horses compared with mature horses (Figures 6.10a and b).

REFERENCES

[1] Dyce K, Sack W, Wensing C. *Textbook of Veterinary Anatomy*. Philadelphia, PA: WB Saunders Company, 1987.
[2] Kainer RA. Functional anatomy of equine locomotor organs. In: Stashak TS (ed.) *Adams' Lameness in Horses*. Philadelphia, PA: Lippincott, Williams and Wilkins, 1998, pp. 1–72.
[3] Richardson DW. The metacarpophalangeal joint. In: Ross MW, Dyson SJ (eds) *Diagnosis and Management of Lameness in the Horse*, 1st edn. Philadelphia, PA: Saunders, 2003, pp. 348–62.
[4] Schramme MC, Smith RKW. Diseases of the digital synovial sheath, palmar annular ligament and digital annular ligaments. In: Ross MW, Dyson SJ (eds) *Diagnosis and Management of Lameness in the Horse*, 1st edn. Philadelphia, PA: Saunders, 2003, pp. 674–83.
[5] Denoix J-M. Functional anatomy of tendons and ligaments in the distal limbs (manus and pes). *Vet Clin N Am: Equine Pract* 1994; **10**: 273–322.
[6] Reef VB, Genovese RL. Soft tissue injuries of the pastern. In: Ross MW, Dyson SJ (eds) *Diagnosis and Management of Lameness in the Horse*, 1st edn. Philadelphia, PA: Saunders, 2003, pp. 716–23.
[7] Martinelli MJ, Baker GJ, Clarkson RB *et al*. Correlation between anatomic features and low-field magnetic resonance imaging of the equine metacarpophalangeal joint. *Am J Vet Res* 1996; **57**: 1421–6.

[8] Martinelli MJ, Kuriashkin IV, Carragher BO, Clarkson RB, Baker GJ. Magnetic resonance imaging of the equine metacarpophalangeal joint: three-dimensional reconstruction and anatomic analysis. *Vet Radiol Ultrasound* 1997; **38**: 193–9.
[9] Dyson SJ, Murray RC. Magnetic resonance imaging of the equine fetlock. In: *Clinical Techniques in Equine Practice*. Philadelphia, PA: Elsevier Saunders, 2007, pp. 62–78.
[10] Murray RC, Dyson SJ, Branch M, Schramme M. Validation of magnetic resonance imaging use in equine limbs. In: *Clinical Techniques in Equine Practice*. Philadelphia, PA: Elsevier Saunders, 2007, pp. 26–37.
[11] Brama PA, Tekoppele JM, Bank RA, Barneveld A, Van Weeren PR. Functional adaptation of equine articular cartilage: the formation of regional biochemical characteristics up to age one year. *Equine Vet J* 2000; **32**: 217–21.
[12] Brama PA, Tekoppele JM, Bank RA, Barneveld A, Van Weeren PR. Biochemical development of subchondral bone from birth until age eleven months and the influence of physical activity. *Equine Vet J* 2002; **34**: 143–9.
[13] Brama PA, Tekoppele JM, Bank RA, Barneveld A, Van Weeren PR. Development of biochemical heterogeneity of articular cartilage: influences of age and exercise. *Equine Vet J* 2002; **34**: 265–9.
[14] Brama PA, Tekoppele JM, Bank RA, Karssenberg D, Barneveld A, Van Weeren PR. Topographical mapping of biochemical properties of articular cartilage in the equine fetlock joint. *Equine Vet J* 2000; **32**: 19–26.
[15] Westbrook C, Kaut C. Artefacts and their compensation. In: Westbrook C, Kaut C (eds) *MRI in Practice*. Oxford: Blackwell Science, 1998, pp. 175–6.
[16] Markel MD. Bone structure and the response of bone to stress. In: Nixon AJ (ed.) *Equine Fracture Repair*. Philadelphia, PA: WB Saunders, 1996, pp. 3–18.
[17] Erickson SJ, Cox IH, Hyde JS, Carrera GF, Strandt JA, Estkowski LD. Effect of tendon orientation on MR imaging signal intensity: a manifestation of the 'magic angle' phenomenon. *Radiology* 1991; **181**: 389–92.
[18] Erickson SJ, Prost RW, Timins ME. The 'magic angle' effect: background physics and clinical relevance. *Radiology* 1993; **188**: 23–5.
[19] Smith MA, Dyson SJ, Murray RC. Is a magic angle effect observed in the collateral ligaments of the distal interphalangeal joint or the oblique sesamoidean ligaments during standing magnetic resonance imaging. *Vet Radiol Ultrasound* 2008; **49**: 509–15.
[20] Smith S, Dyson SJ, Murray RC. Magnetic resonance imaging of distal sesamoidean ligament injury. *Vet Radiol Ultrasound* 2008; **49**: 516–28.

Chapter 7
The metacarpal/metatarsal region

Matthew Brokken and Russell Tucker

INTRODUCTION

The metacarpal/metatarsal region is a common site for performance-limiting lameness in the horse [1]. Several types of injuries can be localized with diagnostic analgesia and diagnosed with radiographs, ultrasound and nuclear scintigraphy or a combination thereof. However, magnetic resonance imaging (MRI) has been shown to be extremely useful in the detection of lesions that cannot be diagnosed with confidence with other imaging modalities [2]. These injuries will be discussed in greater detail in Chapter 14.

The use of MRI in the metacarpal/metatarsal region is extremely useful because of the difficulties encountered with ultrasonographic and radiographic evaluation of the suspensory ligament (SL) and the accessory ligament of the deep digital flexor tendon (ALDDFT). Ultrasonographic examination of the proximal suspensory ligament (PSL) is technically challenging, especially in the hind limb, due to the limited acoustic accessibility and large vessels plantarolateral to the suspensory ligament that result in broad linear anechoic artifacts within the SL [3]. The overlying digital flexor tendons create edge-enhancement artefacts that result in anechoic defects in the PSL. The axial and abaxial margins are partially obscured by the oblique angles inherent in ultrasound imaging of the PSL. These problems can make detection of abnormalities in fibre pattern difficult as well as causing inaccuracies during measuring [4–6]. Ultrasonographic evaluation of the ALDDFT also has limitations. The proximal insertion of the ligament on the palmar third carpal bone and palmar carpal fascia is difficult to evaluate sonographically because the contour of the accessory carpal bone inhibits optimal 90° contact of the transducer with the ligament [7].

Radiographs are useful for marked osseous changes at the suspensory ligament attachment or exostoses of the splint bones but limited for any other type of evaluation of the region. Nuclear scintigraphy in this region can be beneficial but results can be confusing and should be interpreted with a combination of ultrasonographic and radiographic findings [8]. MRI allows superior visualization of the soft tissue and osseous anatomy of this area. Sectional images allow assessment of both size and signal within the PSL and ALDDFT, both of which are difficult to evaluate by palpation.

Equine MRI, edited by Rachel C. Murray.

MR EXAMINATION AND IMAGE ACQUISITION

There are a number of factors that can make examination of the metacarpal/metatarsal region with MRI challenging. Positioning of the horse in a high-field strength magnet for imaging of the metacarpal/metatarsal region can be difficult due to the fact that the horse has to be moved further into the bore of the magnet to reach the area of interest (Figure 7.1). If the horse is too large or there are not enough people to position the horse, the region of interest will not be at the isocentre and poor image acquisition will result. To help with the positioning of the horse, we apply a hair coat grooming spray to the recumbent side of the horse before induction of anaesthesia. This has proved to be very beneficial in helping to slide the horse on the MR table pad and place the horse further into the magnet and also when removing the horse from the bore of the magnet after the examination is completed. Another useful technique when imaging more areas than just the metacarpus/metatarsus (i.e. fetlocks and metacarpus) is to try to image the most proximal structure first. The reason for this is that the horses under general anaesthesia tend to perspire and this, along with the conforming of the pad underneath the horse, makes it much more difficult to push the horse into the magnet to image the other anatomic regions after time has elapsed.

When imaging the metacarpal/metatarsal regions, the horse is positioned in such a way that some of the limbs are not padded or they may be in an awkward position during the examination. This illustrates the need for a very efficient and swift examination in order to prevent post-anaesthetic myopathy or neuropathy. In our experience, the more proximal the area imaged in the magnet, and the longer the horse remains in this position, the greater the risk for myopathy/neuropathy. Therefore, the size and anaesthetic parameters of the horse during MR examination must also be taken into consideration [9].

Figure 7.1 Positioning of a horse for MR examination of the proximal metatarsal region. Examination of the proximal metacarpal/metatarsal region can be difficult depending on the bore size of the MR unit and the size of the patient.

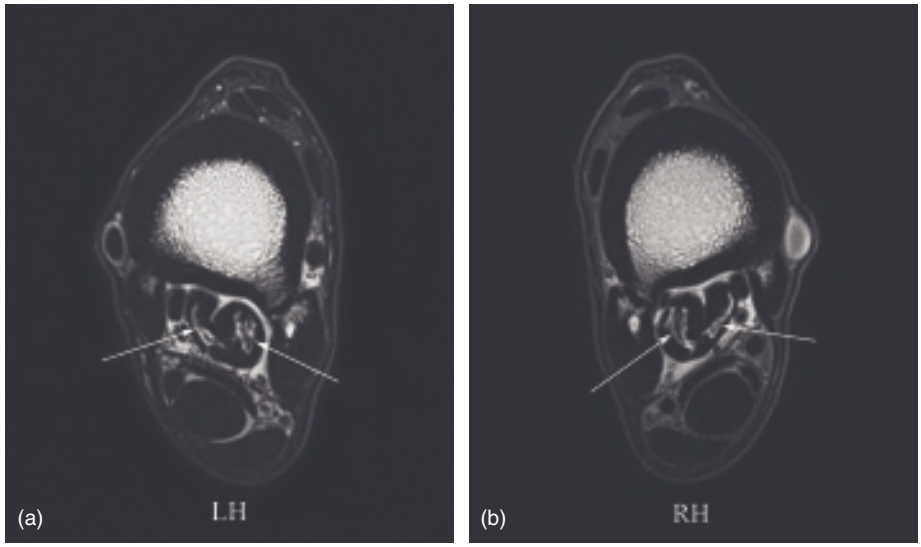

Figure 7.2 Left (a) and right (b) hind transverse proton density images of the proximal metatarsal region. Note the characteristic high-signal muscle/adipose tissue within the proximal suspensory ligament (arrows). This high-signal tissue can make image interpretation difficult, which emphasizes the importance of contralateral limb comparison in this anatomic area.

Advances in technology have made it is possible to acquire images of the proximal metacarpal and metatarsal region in the standing horse under sedation. To maximize image quality, it can be useful to stabilize the limb using padding between the limb and the magnet, or between the limbs.

When considering image acquisition of the metacarpal/metatarsal region, it is critically important that the contralateral limb be imaged as often as possible. Subtle changes in the size of structures, specifically the SL and ALDDFT, may be the only abnormality present. Also, the characteristic appearance of the suspensory ligament with its muscle tissue can be difficult to interpret if there is pathology associated with this area of normally high signal (Figure 7.2). This fact emphasizes the need for careful and systematic examination of both limbs as an internal control to detect subtle differences on MR images.

ARTEFACTS

The most common artefacts are vascular flow and motion artefacts. Due to the number and size of vessels in this region, it is important to acknowledge the presence of flow artefact throughout the images and not to confuse the flow with an area of injury (Figure 7.3). Flow artefact is most apparent on transverse, fat-suppressed sequences (Figure 7.4). It can be difficult to differentiate flow artefact from a lesion within the SL, the ALDDFT, flexor tendons or bone. A technique that has helped evaluation is to change the direction of flow (the direction of the phase encoding acquisition) from anterior-posterior (dorsal to palmar/plantar) to left to right on the fat-suppressed transverse images. The fast-spin echo (FSE) sequences (proton density (PD) and T2-weighted (T2)) will have flow in an anterior-posterior

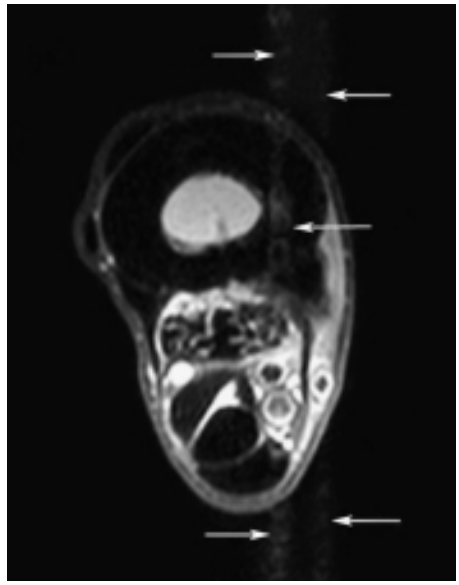

Figure 7.3 Transverse proton density image of the proximal metacarpal region. Note the vessel flow artefact running in the A to P (dorsal-palmar) direction throughout the entire image (arrows).

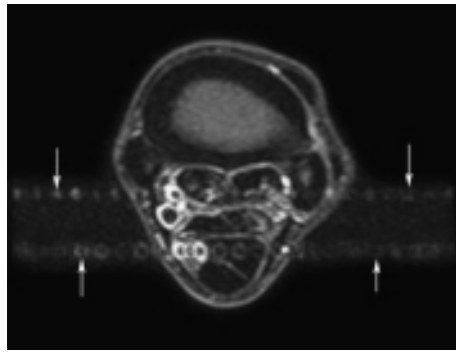

Figure 7.4 Transverse short τ inversion recovery (STIR) image of the proximal metacarpal region illustrating the vessel flow in the left-to-right direction (arrows).

direction because it allows more accurate evaluation of the soft tissues. In the fat-suppressed images, the osseous attachment at the origin is the area of most concern and switching the flow to left to right allows improved evaluation of the osseous attachment of the SL on the transverse images. Also, some newer high-field magnets have flow-suppression software that may lessen the interference of the flow with image interpretation.

Patient motion artefacts are common when imaging the metacarpal/metatarsal region (Figure 7.5). This is mainly due to the respiration/heart beat of the horse under general anaesthesia or sway in the standing horse. Motion can be reduced by stabilization of the limbs by use of pads, sandbags and ropes in the anaesthetized horse. In the standing horse, bandaging of the fetlock to stabilize the degree of extension may be useful to limit motion and stabilize coil positioning.

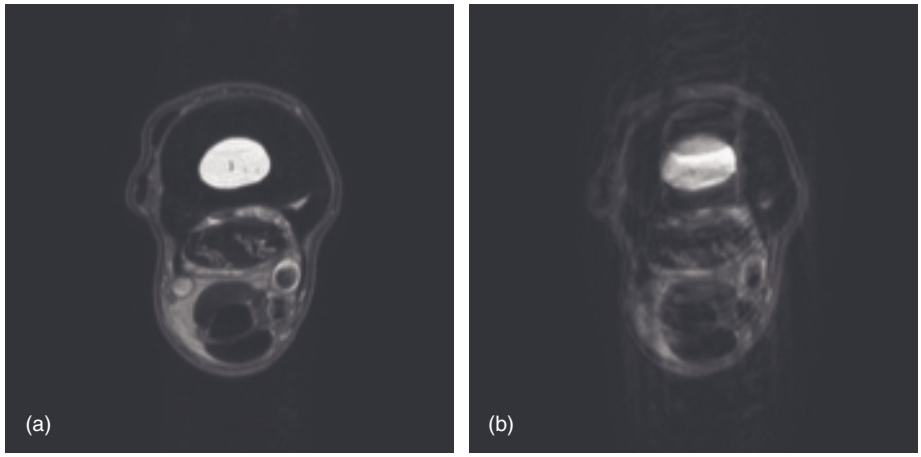

Figure 7.5 Sequential [(a), (b)] transverse proton density images of the proximal metacarpal region, illustrating the presence of motion (b) in alternating MR images. The cause of the motion was not the depth of anaesthesia but the heart beat of the horse. Stabilization with sandbags and additional padding resolved the artefact.

PULSE SEQUENCES

MR examination of the metacarpal/metatarsal region can be performed with a limited number of pulse sequences that allow accurate assessment of the structures in an expedient manner. Scanning protocols should include dual echo (PD and T2) transverse and sagittal sequences, as well as fat-suppressed transverse and sagittal sequences, and fat-suppressed dorsal sequences [10] (Figure 7.6). It is generally agreed that in this region, transverse images usually yield the most information. The sagittal and dorsal sequences are useful in determining the exact location and extent of a particular lesion in conjunction with the findings on transverse sequences.

In the first author's experience, the sequences that yield the most information are the PD and fat-suppressed transverse sequences. Normal tendons and ligaments should be hypointense on all sequences (Figure 7.7). The PD-weighted sequence allows clear visualization of the borders of the tendons and ligaments and detection of abnormal signal within these structures. It is also useful in detection of subtle increases in size and irregularity and adhesions of the borders of the structures. In addition, the PD-weighted sequences provide good anatomic detail of the ALDDFT with minimal interference from vessel flow artefact [2]. Due to the normal variation of the high-signal SL muscle fibres, systematic comparison to the contralateral limb is important to identify mild signal changes in the SL. The transverse PD-weighted images are also helpful in identifying abnormal low signal (sclerosis) in the third metacarpal/metatarsal bone at the PSL attachment (Figure 7.8). The fat-suppressed sequences are most useful in identifying abnormal high signal within the bone at the PSL attachment (Figure 7.9). On fat-suppressed sequences, the normal high signal of fat in the marrow cavity is suppressed, allowing detection of bone lesions that would be inconspicuous on other sequences. Evaluation of the PSL and its proximal attachment with transverse fat-suppressed images is essential; however, the vessel flow artefact is

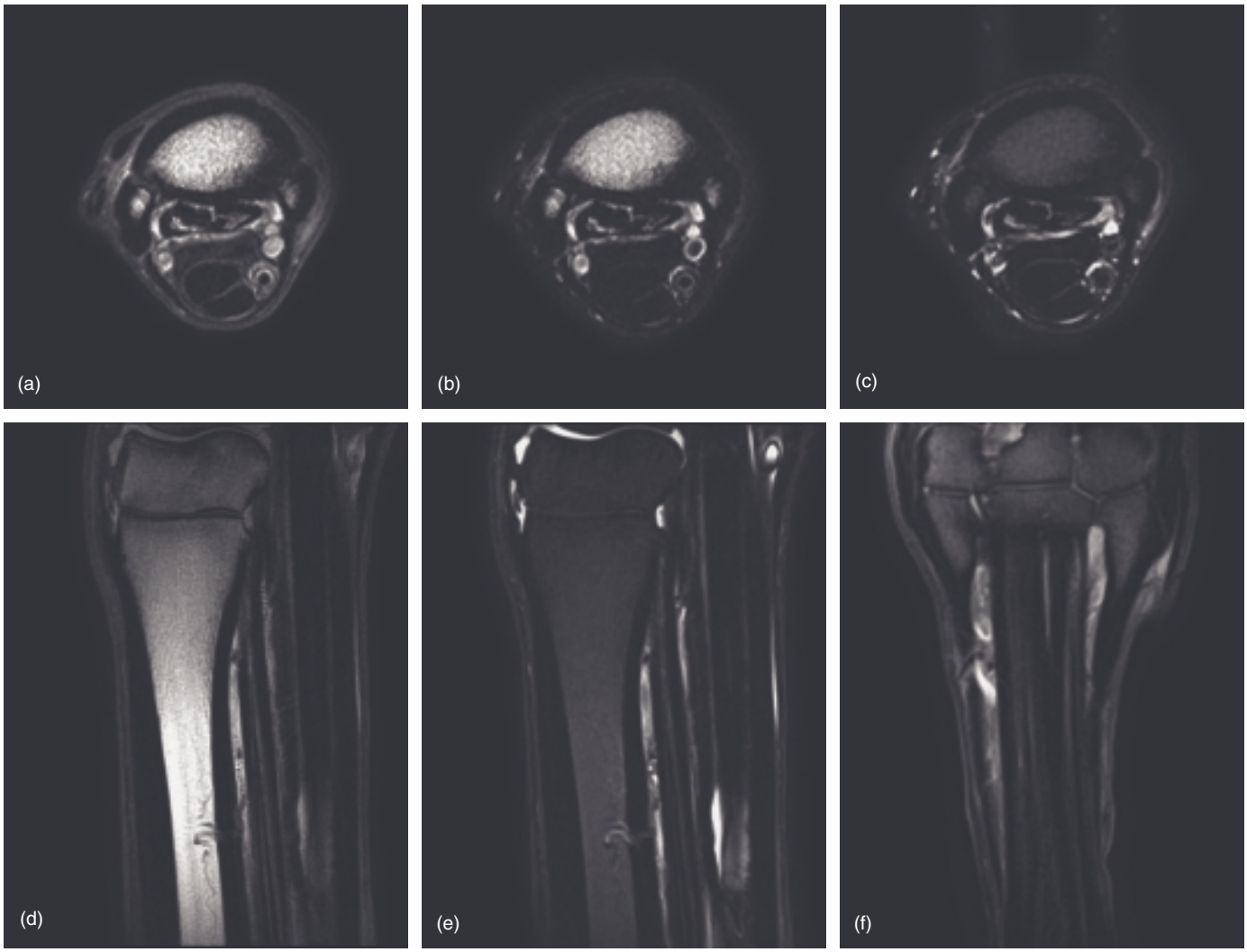

Figure 7.6 Typical protocols for metacarpal/metatarsal imaging. Proton density (a), T2 (b), and STIR (c) transverse images; proton density (c), and STIR (e) sagittal images; and proton density fat-saturated dorsal images (f).

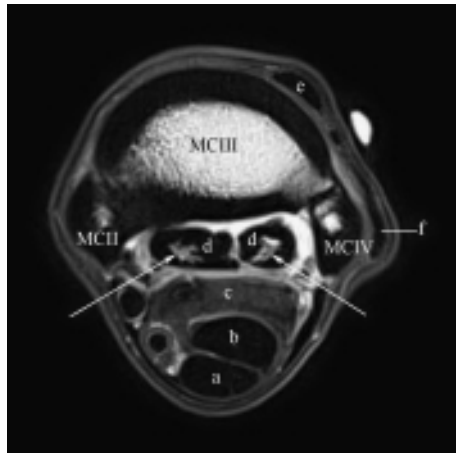

Figure 7.7 Transverse proton density image of the proximal metacarpal region: **a**, superficial digital flexor tendon; **b**, deep digital flexor tendon; **c**, accessory ligament of the deep digital flexor tendon; **d**, suspensory ligament; **e**, common digital extensor tendon; and **f**, lateral digital extensor tendon. Note the characteristic high signal muscle/adipose tissue in the suspensory ligament (arrows). **MCII**, Second metacarpal bone; **MCIV**, fourth metacarpal bone; **MCIII**, third metacarpal bone.

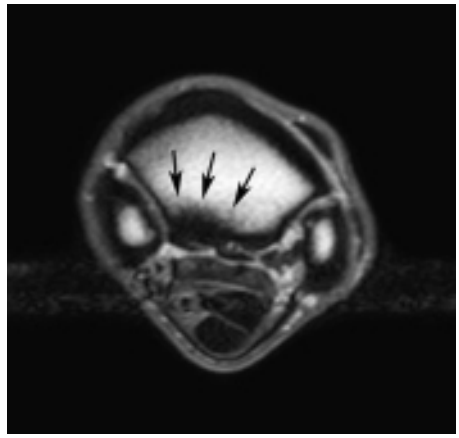

Figure 7.8 Transverse proton density image of the proximal metacarpal region in a horse with abnormal low signal (sclerosis) at the PSL attachment to the third metacarpal bone (arrows).

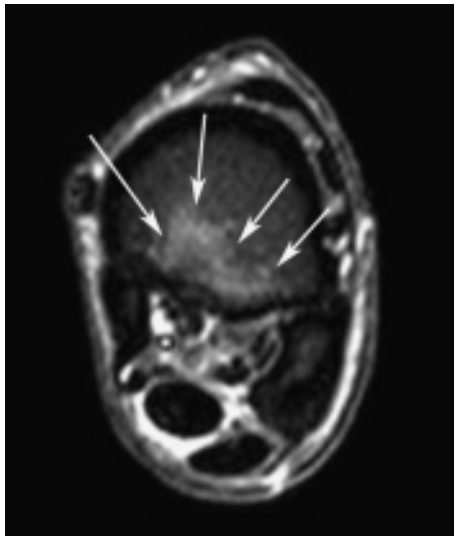

Figure 7.9 Transverse STIR image of a horse with abnormal high signal in the third metatarsal bone (arrows).

more pronounced and can affect image interpretation [2]. Gradient-echo sequences are useful for higher resolution images and can provide more variation in grey scale detail of different structures. They can be used if very thin slices are desired through targeted regions for higher resolution images of specific structures such as the peripheral adhesions occurring along the abaxial margins of the SL.

In the standing horse, motion-insensitive and fast sequences are the most useful to limit the effects of motion. It is useful to acquire fat-suppressed, T1, T2* gradient-echo and T2 fast-spin echo sequences in a transverse plane to provide maximal information for soft tissue and osseous structures, with addition of limited sequences in frontal and sagittal planes. The phase cancellation artefact seen on the T2* gradient-echo sequence can be particularly useful to highlight fluid-based pathology in the bone, which can be confirmed by comparison with other image sequences.

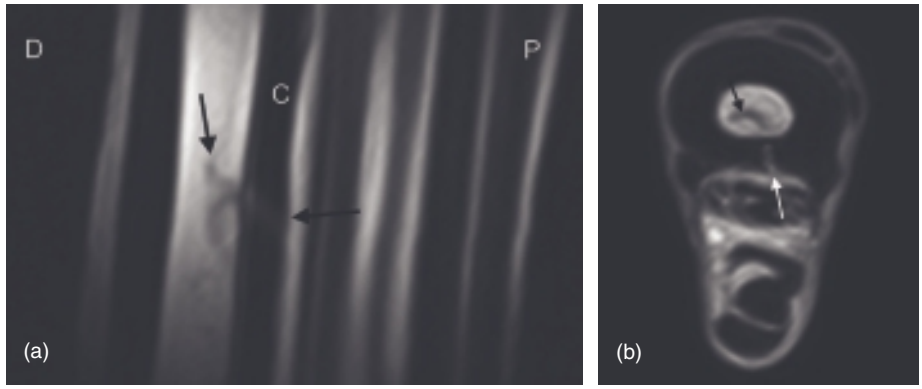

Figure 7.10 The nutrient foramen and vessel (arrows) of the third metacarpal bone seen on T2* gradient-echo images acquired standing in a sagittal (a) and transverse (b) plane. This should not be confused with bone damage, although considerable reaction around or expansion of the foramen and nutrient vessel may be associated with other pathological change. **D**, dorsal; **P**, palmar; **C**, palmar cortex.

ANATOMY: METACARPAL REGION

Metacarpal bones

The third metacarpal bone is flattened in a dorsal to palmar direction and has a close relationship with the second and fourth metacarpal bones. These may be clearly separated throughout their length or the presence of an old synostosis may mean that there is apparent fusion of the cortices distally or throughout the entire length of one or both articulations. The nutrient foramen is clearly seen within the medulla and as high signal intensity crossing the palmar cortex and should not be confused with pathology (Figure 7.10). The second and fourth metacarpal bones generally appear reasonably equal in size, in contrast with the hind limb.

Metacarpal interosseous ligaments

The metacarpal interosseous ligament connects the small metacarpal bones to the large third metacarpal bone and attaches along the proximal two-thirds of the metacarpus [11]. The ligament is narrow proximally where it is located intra-articularly in the intermetacarpal joint [12]. The dense fibrous tissue in the ligament shows intermediate signal intensity in gradient-echo sequences when compared to the low signal intensity in the digital flexor tendons. Small pockets of fluid can be present between the fibre bundles in the ligament or surrounding it at the level of the joint and just distal to the joint. These fluid pockets most likely represent joint recesses (Figure 7.11). More distally, the ligament becomes shorter and wider and the dense fibrous tissue is interspersed with loose connective tissue and fat, giving it a striated appearance [12].

In many horses the ligament is not visible distal to the level of the origin of the SL due to fusion of the metacarpal bones. The cortex of the third metacarpal bone at the attachment of the metacarpal interosseous ligament has low but often slightly heterogeneous signal intensity and there may be some mild irregularity of the endosteal and periosteal margins. The thickness

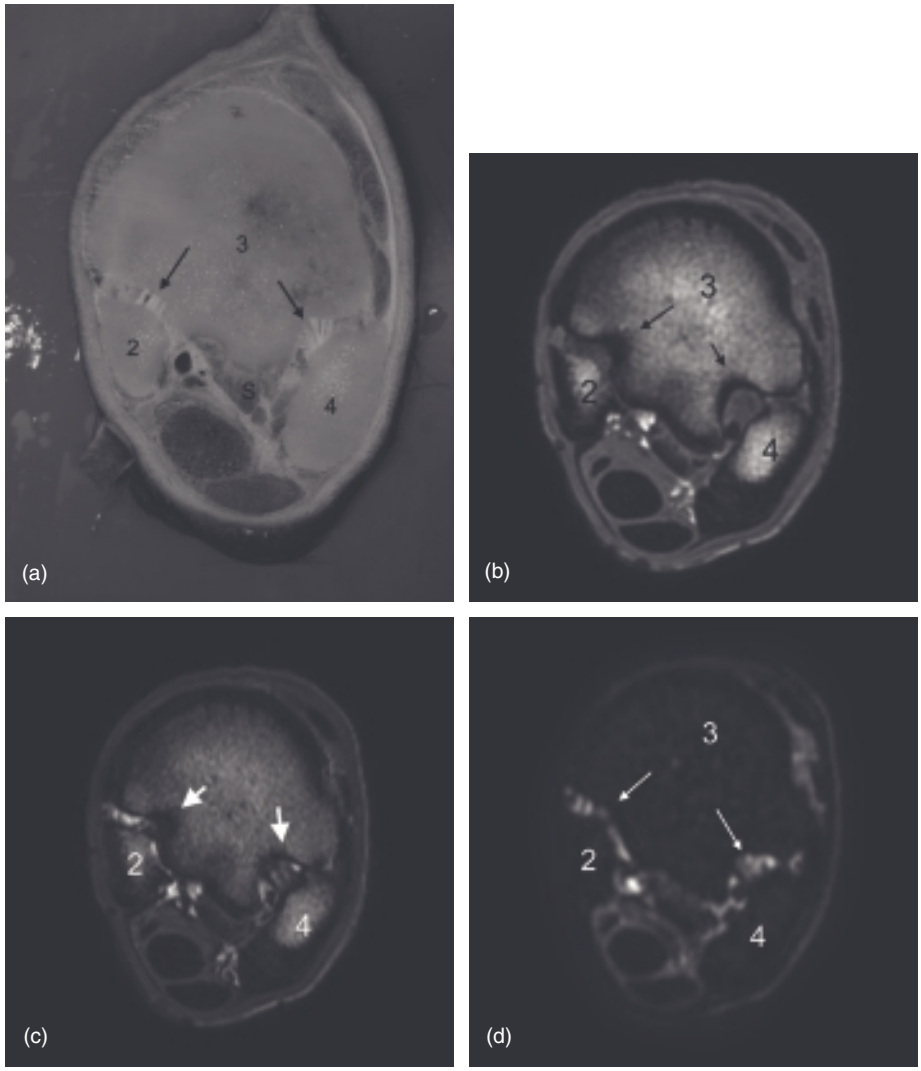

Figure 7.11 (a)Transverse section through the proximal metatarsus showing the anatomical relationships between the second, third and fourth metatarsal bones and the metatarsal interosseous ligaments (arrows) in a horse without lameness. (b) Transverse T1 gradient-echo, (c) T2* gradient-echo and (d) STIR high-field images at the same location. Note the linear pattern of the ligament fibres separated by synovial recesses, and the mild endosteal irregularity at the origin and insertion of the ligaments. **2**, second metatarsal bone, **3**, third metatarsal bone, **4**, fourth metatarsal bone, **S**, suspensory ligament lateral lobe.

of the cortex is variable and can be slightly thicker centrally at the site of attachment at the level of the intermetacarpal joint. More distally the cortex can sometimes be thinner at the site of the attachment. The cortical thickness rarely exceeds 5 mm in the region proximal to the origin of the suspensory ligament. The attachment on the second and fourth metacarpal bones is variable with heterogeneous appearance. Small areas of very low signal intensity in all sequences can be seen in the metacarpal interosseous ligament; this most likely represents mineralization of the ligament, which is a common finding in horses without clinical signs [13]. Mild or moderate changes in the ligament or attachment should be interpreted with caution

as they can be seen in horses without clinical signs. Intra-limb differences most likely due to anatomical variation or asymmetric loading patterns can make it difficult to use the lateral and medial ligaments as references when interpreting images [14].

Suspensory ligament

The suspensory ligament (interosseous medius) is a modified ligament that contains sparse muscle fibres [15]. Therefore, the proximal suspensory ligament is a non-homogenous structure when evaluated on MR imaging. The normal appearance of the PSL on all sequences described above is low signal ligamentous fibres, interspersed with more centrally located high signal muscle tissue (Figures 7.12–7.14). Through examination of histologic and gross sections of the SL, it has been shown that the muscle bundles are well defined with little other tissue. There are nerves, vessels, and adipose tissue within the bundles, but their composition is considered insignificant compared to the content of muscle [16] (Figure 7.15). The borders of the ligament are high signal and the enthesis to the third metacarpal bone is low signal blending with the cortical bone (Figure 7.12). Entheses such as the proximal suspensory attachment are termed 'MR invisible'. Invisible in this sense means that little or no MR signal is detectable and that they appear dark on MR images [17].

The proximal suspensory ligament attaches primarily to the palmar cortex of the third metacarpal bone with a less extensive attachment to the

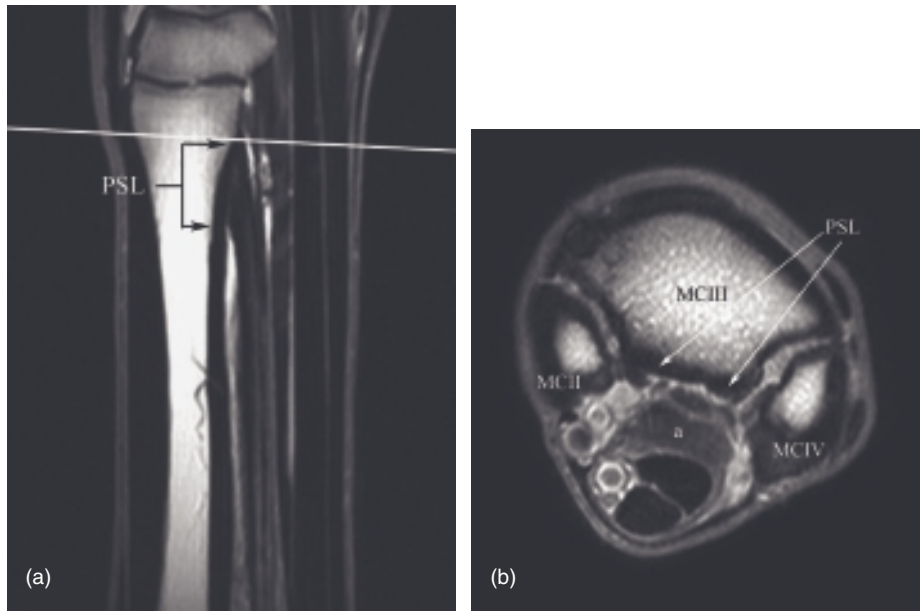

Figure 7.12 (a) Sagittal proton density image of the proximal metacarpal region and (b) the transverse proton density image corresponding to the solid white bar. The extent of the proximal suspensory ligament (PSL) attachment to the third metacarpal bone is indicated by the black arrows on the sagittal image. **a**, Accessory ligament of the deep digital flexor tendon; MCII, second metacarpal bone; MCIII, third metacarpal bone; MCIV, fourth metacarpal bone.

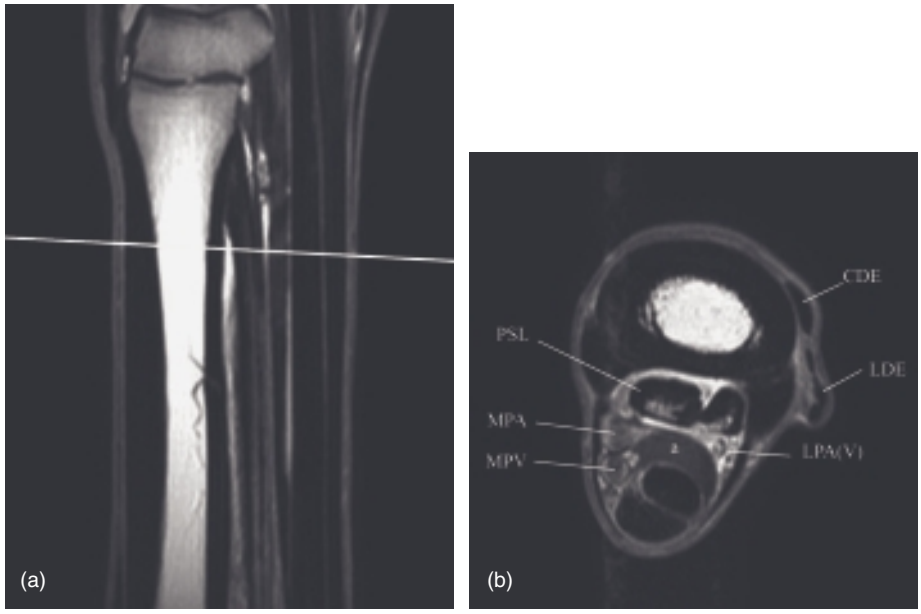

Figure 7.13 (a) Sagittal proton density image of the proximal metacarpal region and (b) the transverse proton density image corresponding to the solid white bar. **a**, accessory ligament of the deep digital flexor tendon; **PSL**, proximal suspensory ligament; **CDE**, common digital extensor tendon; **LDE**, lateral digital extensor tendon; **MPA**, medial palmar artery; **MPV**, medial palmar vein; **Figure**, lateral palmar artery and vein.

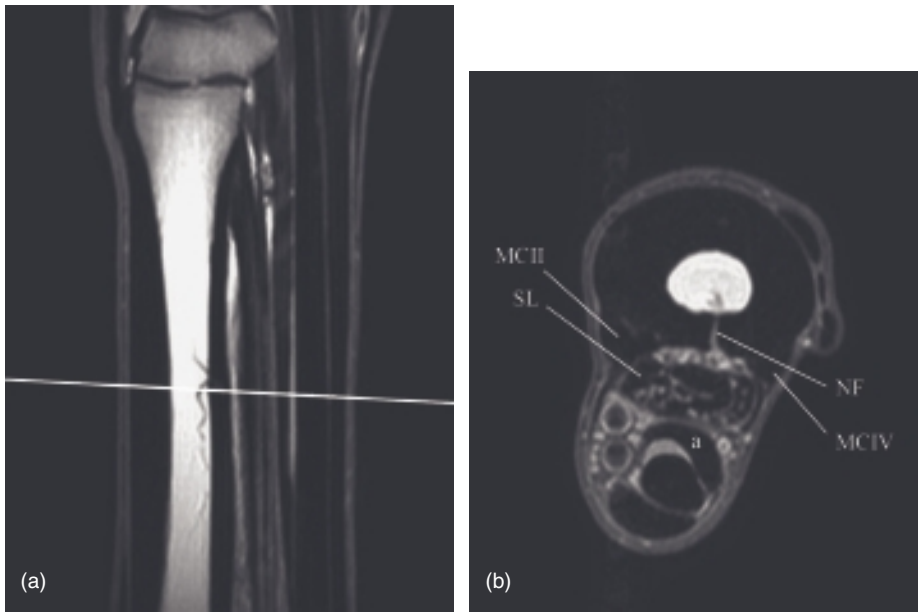

Figure 7.14 (a) Sagittal proton density image of the proximal metacarpal region and (b) the transverse proton density image corresponding to the solid white bar. **a**, accessory ligament of the deep digital flexor tendon; **SL** suspensory ligament; **NF** nutrient foramen; **MCII**, second metacarpal bone; **MCIV**, fourth metacarpal bone.

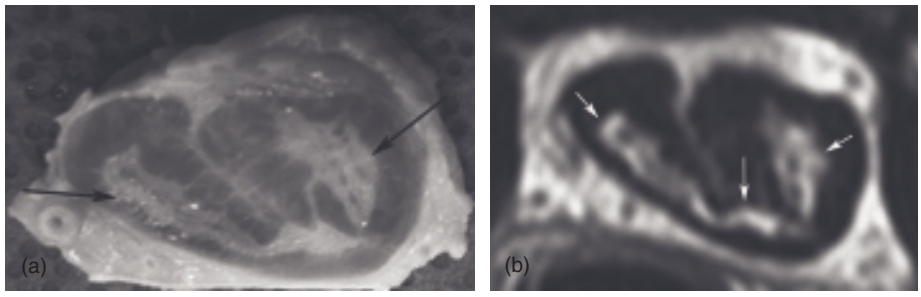

Figure 7.15 (a) Gross specimen of the proximal suspensory and (b) corresponding proton density MR image. Note the normal muscular tissue in the gross specimen (black arrows) and the high signal of the tissue on the MR image (white arrows).

distal row of carpal bones. There is a midline structure of high signal (connective/adipose tissue) that originates from the dorsal border of the proximal suspensory that serves to divide the proximal suspensory into medial and lateral bundles (Figure 7.13). This septum appears to disappear at the level of the nutrient foramen where the ligament takes a more bulbous, oval appearance (Figure 7.14). The medial portion of the proximal suspensory is mostly oval in appearance, whereas the lateral portion is more circular and larger in the dorsopalmar direction. The border between the second and fourth metacarpal bones is very distinct with high signal delineating the boundary of the ligament. The muscular tissue is more organized at the proximal portion of the suspensory. This tissue is primarily in the mid to palmar region of the ligament. Distally, the tissue forms thin strands coursing through the entire ligament.

As the suspensory bifurcates the ligament appears less well organized with heterogeneous signal intensity in all sequences. The branches are generally symmetrical in size, more homogeneous in signal intensity than further proximally and clearly defined from the surrounding connective tissue.

Accessory ligament of the deep digital flexor tendon

The distal ALDDFT is a homogenous low-signal structure on all sequences. On transverse images, the distal aspect of the ALDDFT is crescent shaped, and wraps around the dorsal aspect of the deep digital flexor tendon (Figure 7.14). The lateral aspect of the ligament extends more palmar than the medial side. As the ALDDFT extends more proximal to its third carpal bone and palmar fascial attachment, the overall signal intensity increases to intermediate signal. This change in signal intensity occurs approximately at the level of the proximal suspensory ligament attachment to the third metacarpal bone (Figure 7.12). The borders of the ligament are very distinct high signal.

Tendons

The deep digital flexor tendon (DDFT) is a homogenous low-signal structure on all sequences. It is mostly oval in shape until the proximal metacarpal region and then the medial aspect becomes slightly flattened (Figure 7.12). The superficial digital flexor tendon (SDFT) is a homogenous low-signal structure on all sequences. It is crescent shape for most of the metacarpal region and then becomes more round proximally (Figures 7.12–14). The common digital extensor tendon is the principle tendon dorsally, along with the smaller lateral digital extensor. Both of these extensor tendons are homogenous low signal on all MR sequences.

Neurovascular structures

Vasculature in the metacarpal region consists of the medial and lateral palmar artery and vein, medial and lateral palmar metacarpal artery and

vein, and the lateral and medial dorsal metacarpal artery and vein. The medial palmar vein and artery, as well as the lateral palmar vein and medial palmar metacarpal artery and vein, can be readily identified on MR examination. The nerves present include the medial and lateral palmar metacarpal nerves and the medial and lateral palmar nerves. The nerves are difficult to identify on MR examination but the medial palmar and lateral palmar nerves can be identified on some horses as low to intermediate signal intensity on proton density sequences and high signal on T2 and fat-saturated sequences.

ANATOMY: METATARSAL REGION

The structures in the metatarsal region are similar to the metacarpal region, with some differences. The soft tissue structures include the SL, ALDDFT, deep and superficial flexor tendons, long and lateral digital extensor tendons, and the medial digital flexor tendon (medial head of DDF muscle). Osseous structures include the third metatarsal bone and the second and fourth metatarsal bones.

Metatarsal bones

The third metatarsal bone is longer in a dorsal to plantar direction relative to the third metacarpal bone. The fourth metatarsal bone is larger in comparison with the second, and it generally appears closer to the lateral origin of the suspensory ligament than the second does to the medial origin.

The metatarsal interosseous ligaments

The appearance of the metatarsal interosseous ligaments is similar to the appearance of the metacarpal interosseous ligaments [14] (Figure 7.11). However, interpretation of images in the dorsal plane can be more difficult in relation to the fibre orientation in the ligament. Interpretation in a dorsal plane can be most problematic in the metatarsus because the small metatarsal bones are located in a more plantar then lateral position relative to the third metatarsal bone. Another anatomical difference between the metatarsus and the metacarpus is a more or less pronounced bony ridge on the third metatarsal bone protruding in a plantarolateral direction towards the fourth metatarsal bone distal to the level of the intermetatarsal joint, giving an asymmetric appearance to the metatarsus.

Suspensory ligament

The hind limb suspensory attaches primarily to the proximal plantar aspect of the third metatarsal bone (Figure 7.16). The lateral aspect of the proximal suspensory also has fibres that attach to the distal row of tarsal bones, mainly the fourth tarsal bone. This gives a somewhat asymmetric appearance to the shape and size of the two lobes at the origin (Figure 7.11). The SL in the hind limb is similar in MR signal intensity to that in the forelimb.

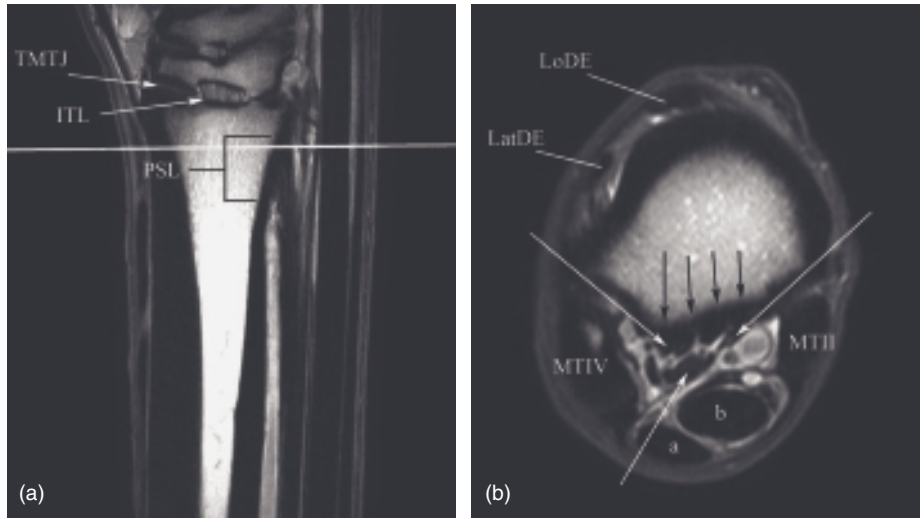

Figure 7.16 (a) Sagittal proton density image of the proximal metatarsal region and (b) the transverse proton density image corresponding to the solid white bar on the sagittal image. TMTJ, tarsometatarsal joint; **ITL** intertarsal ligament; **PSL**, proximal suspensory ligament attachment to the third metatarsal bone. On the transverse image, the black arrows indicate the attachment of the origin of the proximal suspensory ligament (PSL) to the third metatarsal bone. The white arrows indicate the PSL. **a**, superficial digital flexor tendon; **b**, deep digital flexor tendon; **MTII**, second metatarsal; **MTIV**, fourth metatarsal bone; **LatDE** lateral digital extensor tendon; **LoDE**, long digital extensor tendon.

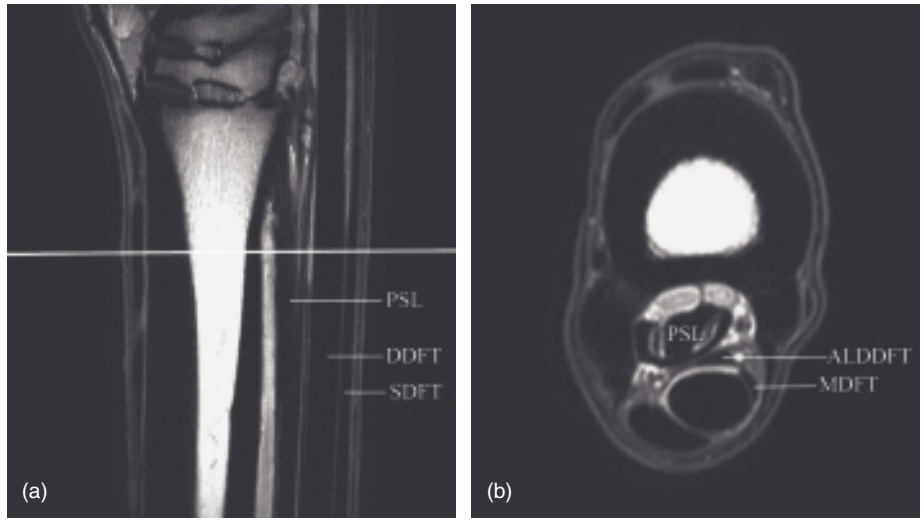

Figure 7.17 (a) Sagittal proton density image of the proximal metatarsal region and (b) the transverse proton density image corresponding to the solid white bar on the sagittal image. **PSL**, proximal suspensory ligament; **DDFT**, deep digital flexor tendon; **SDFT**, superficial digital flexor tendon; **ALDDFT**, accessory ligament of the deep digital flexor tendon; **MDFT**, medial digital flexor tendon.

The ligament is rounder than in the forelimb (Figure 7.17) and is slightly bi-lobed at its proximal aspect just distal to its origin on the third metatarsal bone (Figure 7.17). The muscle tissue bundles extend throughout the entire dorsoplantar length of the ligament and, beginning a few centimetres distal

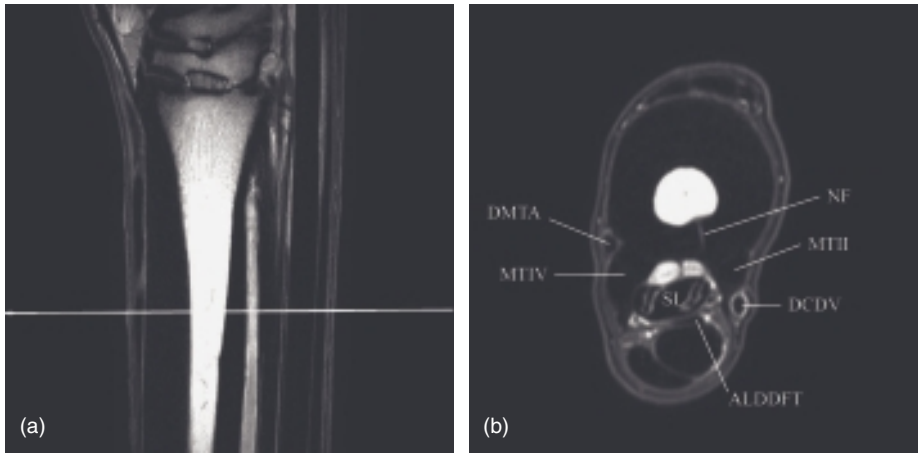

Figure 7.18 (a) Sagittal proton density image of the proximal metatarsal region and (b) the transverse proton density image corresponding to the solid white bar. **SL**, suspensory ligament; **ALDDFT**, accessory ligament of the deep digital flexor tendon; **DCDV**, dorsal common digital vein; **DMTA**, dorsal metatarsal artery; **NF**, nutrient foramen; **MTII**, second metatarsal bone; **MTIV**, fourth metatarsal bone.

to the third metatarsal bone attachment, the fibres become two distinct thin bands for each bundle.

Accessory ligament of the deep digital flexor tendon

The ALDDFT in the hind limb is significantly smaller than in the forelimb. The ligament is thin, with its largest part on the medial side of the limb (Figures 7.17 and 7.18). This ligament has homogenous low signal on all sequences.

Tendons

The DDFT and SDFT have a similar appearance to in the metacarpal region. Adjacent to the ALDDFT on the medial aspect of the limb is the small medial digital flexor tendon (Figure 7.17). This tendon appears to blend with the DDFT at the level of the nutrient foramen (Figure 7.18). Proximally, the tendon courses medially and plantar to the second metatarsal and tarsal bones. The tendon has homogenous low signal intensity throughout its length in the metatarsus. The long and lateral digital extensor tendons are present at the dorsal aspect of the limb and have homogenous low signal intensity similar to the extensors in the metacarpal region.

Neurovascular structures

Vascular structures include the large dorsal metatarsal artery, the medial and lateral plantar metatarsal artery and vein, medial and lateral plantar artery and vein, the medial dorsal metatarsal vein and the dorsal common digital vein. Nerves include the lateral plantar, medial and lateral plantar metatarsal, and the medial and lateral dorsal metatarsal.

REFERENCES

[1] Dyson S. Proximal suspensory desmitis-clinical, ultrasonographic and radiographic features. *Equine Vet J* 1991; **23**: 25–31.
[2] Brokken MT, Schneider RK, Sampson SN, Tucker RL, Gavin PG, Ho CP. Magnetic resonance imaging features of proximal metacarpal and metatarsal injuries in the horse. *Vet Radiol Ultrasound* 2007; **48**: 507–17.
[3] Dyson SJ, Arthur RM, Palmer SE, Richardson D. Suspensory ligament desmitis. *Vet Clin N Am: Equine Pract* 1995; **11**: 177–215.
[4] Dyson S. Suspensory apparatus. In: Rantanen NW, McKinnon AO (eds) *Equine Diagnostic Ultrasonography*. Baltimore, MA: Williams & Wilkins, 1998, pp. 447–73.
[5] Dyson S. Proximal metacarpal and metatarsal pain: a diagnostic challenge. *Equine Vet Educ* 2003; **15**: 134–8.
[6] Bischofberger AS, Konar M, Ohlerth S *et al*. Magnetic resonance imaging, ultrasonography and histology of the suspensory ligament origin: a comparative study of normal anatomy of Warmblood horses. *Equine Vet J* 2006; **38**: 508–16.
[7] Genovese R, Rantanen N. Suspensory apparatus. In: Rantanen NW, McKinnon AO (eds) *Equine Diagnostic Ultrasonography*. Baltimore, MA: Williams & Wilkins, 1998, pp. 399–445.
[8] Dyson SJ, Weeks JS, Murray RC. Scintigraphic evaluation of the proximal metacarpal and metatarsal regions of horses with proximal suspensory desmitis. *Vet Radiol Ultrasound* 2007; **48**: 78–85.
[9] Franci P, Leece EA, Brearley JC. Post-anaesthetic myopathy/neuropathy in horses undergoing magnetic resonance imaging compared to horses undergoing surgery. *Equine Vet J* 2006; **38**: 497–501.
[10] Sampson SN, Tucker RL. Magnetic resonance imaging of the proximal metacarpal and metatarsal regions. *Clin Tech Equine Pract* 2007; **6**: 78–85.
[11] Jackson M, Geyer H, Fürst A. Anatomie der Griffelbeine und ihrer Umgebung unter besonderer Berüchsichtigung der Fasziern. *Schweizer archiv fur Tierheilkunde* 2005; **147**(11): 473–81.
[12] Les CM, Stover SM, Willits NH. Necropsy survey of metacarpal fusion in the horse. *Am J Vet Res* 1995; **56**(11): 1421–32.
[13] Rooney JR, Prickett ME. Foreleg splints in horses. *Cornell Vet* 1996; **56**: 259–69.
[14] Nasvall KE, Dyson SJ, Murray RC. The appearance of the proximal part of the metacarpal/metatarsal interosseous ligaments in MRI of horses with no history of lameness. *Proceedings British Equine Veterinary Association Annual Congress*. 2008. Newmarket: Equine Veterinary Journal.
[15] Gibson K, Steel C. Conditions of the suspensory ligament causing lameness in horses. *Equine Vet J* 2002; **14**: 39–50.
[16] Wilson DA, Baker GJ, Pijanowski GJ, Boero MJ, Badertscher RR. Composition and morphological features of the interosseous muscle in Standardbreds and Thoroughbreds. *Am J Vet Res* 1991; **52**: 133–9.
[17] Benjamin M, Milz S, Bydder GM. Magnetic resonance imaging of entheses. Part 1. *Clin Radiol* 2008; **63**: 691–703.

Chapter 8
The carpus

Annamaria Nagy and Sue Dyson

INTRODUCTION

Magnetic resonance imaging (MRI) is becoming more frequently used in the investigation of carpal pain. However, there is limited information available on normal MRI anatomy of the carpus [1, 2]. It is possible to acquire MR images of the carpus in either low-field or high-field MR systems. High-field images provide more detail and knowledge of high-field anatomy is helpful for interpretation of low-field MR images.

The anatomical description in this chapter is based on high-field and low-field MRI examinations of 30 cadaver carpi of mature horses with no history of carpal or proximal metacarpal pain. High-field MR images were acquired in a 1.5 T cylindrical short bore GE magnet and included 3D T1-weighted spoiled gradient-echo (GRE), 3D T2*-weighted GRE and short tau inversion recovery (STIR) sequences in sagittal, dorsal and transverse planes. Low-field images were obtained in a 0.27 T open magnet (Hallmarq) and included motion-insensitive (MI) 3D T1- and T2*-weighted GRE, 2D T2-weighted fast spin-echo (FSE), MI STIR and proton density (PD) sequences in sagittal, dorsal and transverse planes. The sequences were those used routinely in clinical scanning at the Animal Health Trust.

ANATOMY

Normal MRI anatomy is described by comparison with anatomical specimens [3, 4] and is illustrated by sequential transverse plane high-field MR images from proximal to distal (Figures 8.1–8.4), sagittal plane images from medial to lateral (Figures 8.5–8.7) and dorsal plane images from dorsal to palmar (Figures 8.8–8.11). Normal variants are shown in Figures 8.12 and 8.13. Comparative low- and high-field images are shown in Figures 8.14 and 8.15. The same numbering system is employed to indicate each anatomical structure in each figure (see Key to figures, pp. 218–9). All transverse and dorsal images are oriented with lateral to the right; sagittal images are oriented with dorsal to the left.

Osseous structures

The medulla of the distal aspect of the radius has intermediate to high signal intensity on T1- and T2-weighted images. The cortex has low signal intensity and may be slightly irregular and have uneven thickness, especially at the

Equine MRI, edited by Rachel C. Murray.

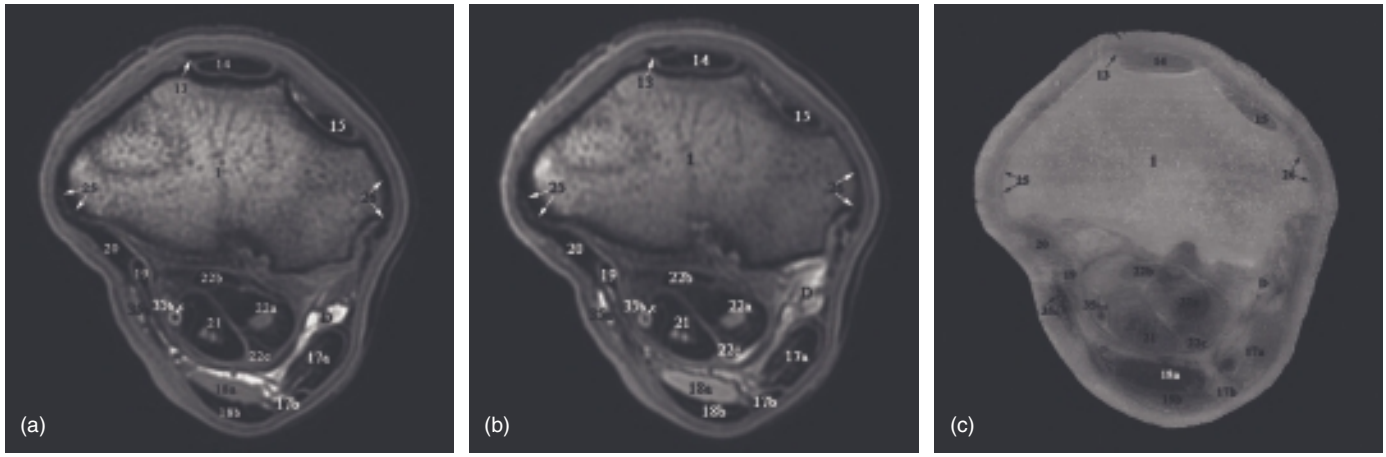

Figure 8.1 Transverse high-field images at the level of the distal aspect of the radius. (a) 3D T1-weighted spoiled gradient-echo (SPGR) MR image. (b) 3D T2*-weighted gradient-echo (GRE) MR image. (c) Anatomical specimen. Note the areas of intermediate signal intensity in the superficial and deep digital flexor tendons reflecting the presence of muscle within the tendons. Note also the tendonous and muscular parts of flexor carpi ulnaris.

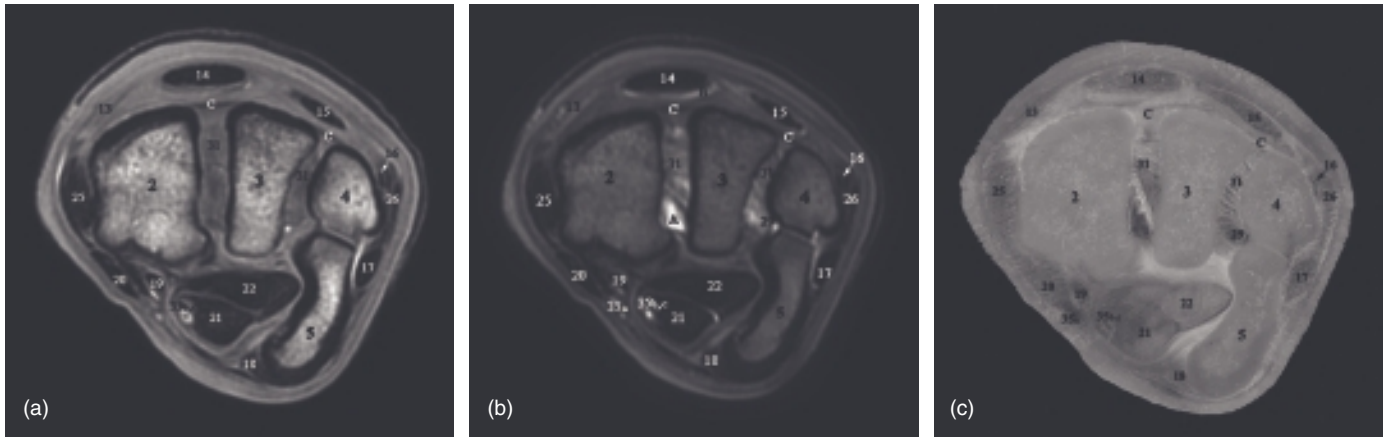

Figure 8.2 Transverse high-field images at the level of the proximal row of carpal bones. (a) 3D T1-weighted SPGR MR image. (b) 3D T2*-weighted GRE MR image. (c) Anatomical specimen.

caudal aspect of the radius. The distal physeal line is often identified on transverse and sagittal images as a fine line of low signal intensity. The subchondral bone is usually slightly thicker in the medial facet of the distal articular surface than in the intermediate or lateral facets. The articular cartilage has intermediate signal intensity on both T1- and T2-weighted images and is best evaluated at the dorsal aspect of the antebrachiocarpal joint in sagittal images.

In the bones of both the proximal and distal rows of the carpus, the subchondral bone is slightly thicker on the dorsal than on the palmar aspect, and medially compared with laterally. Care should be taken in interpretation of signal intensity of the medulla in transverse images close to the proximal or distal subchondral bone plate, because part of the slice may

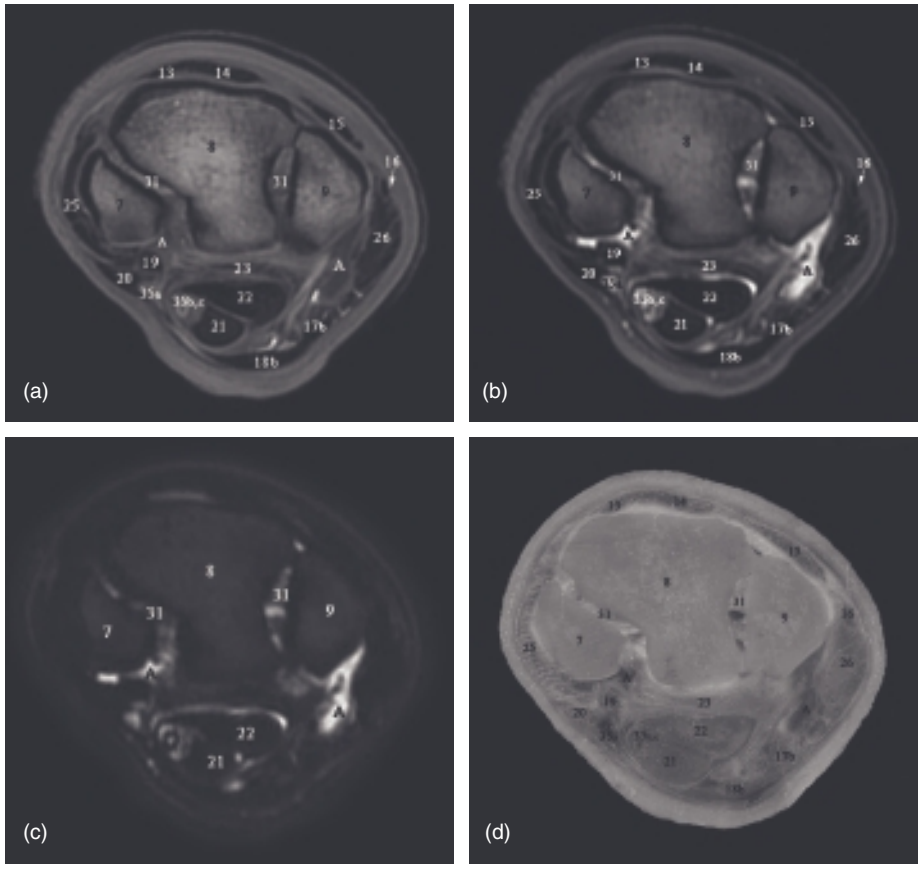

Figure 8.3 Transverse high-field images at the level of the distal row of carpal bones. (a) 3D T1-weighted SPGR MR image. (b) 3D T2*-weighted GRE MR image. (c) STIR image. (d) Anatomical specimen.

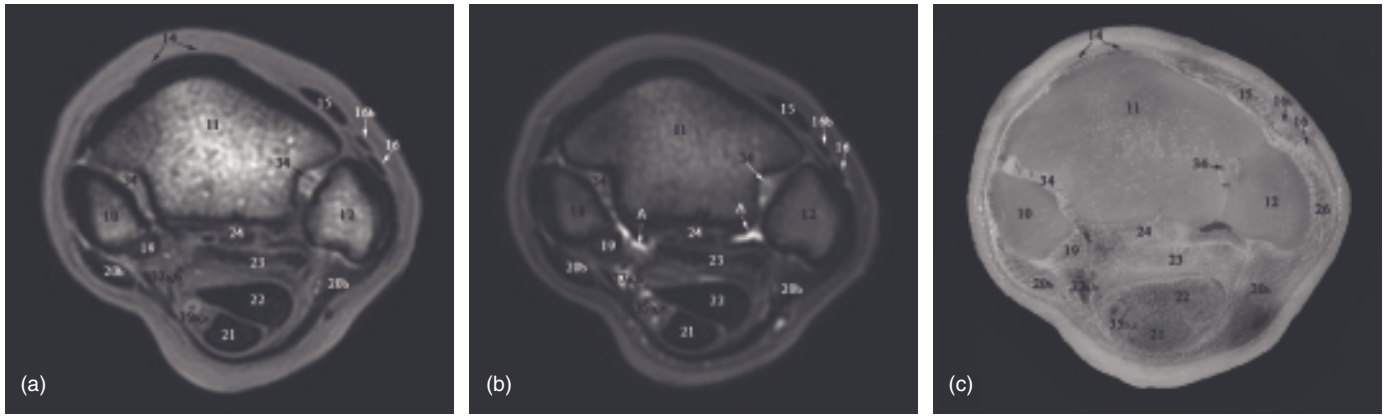

Figure 8.4 Transverse high-field MR images at the level of the proximal aspect of the third metacarpal bone. (a) 3D T1-weighted SPGR MR image. (b) 3D T2*-weighted GRE MR image. (c) Anatomical specimen.

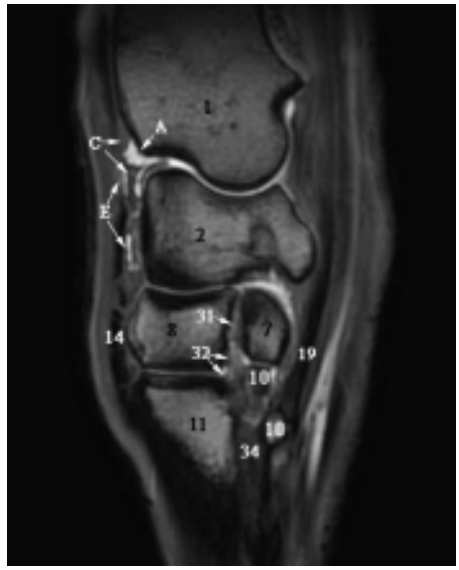

Figure 8.5 Parasagittal 3D T2*-weighted GRE high-field MR image at the medial aspect of a normal carpus.

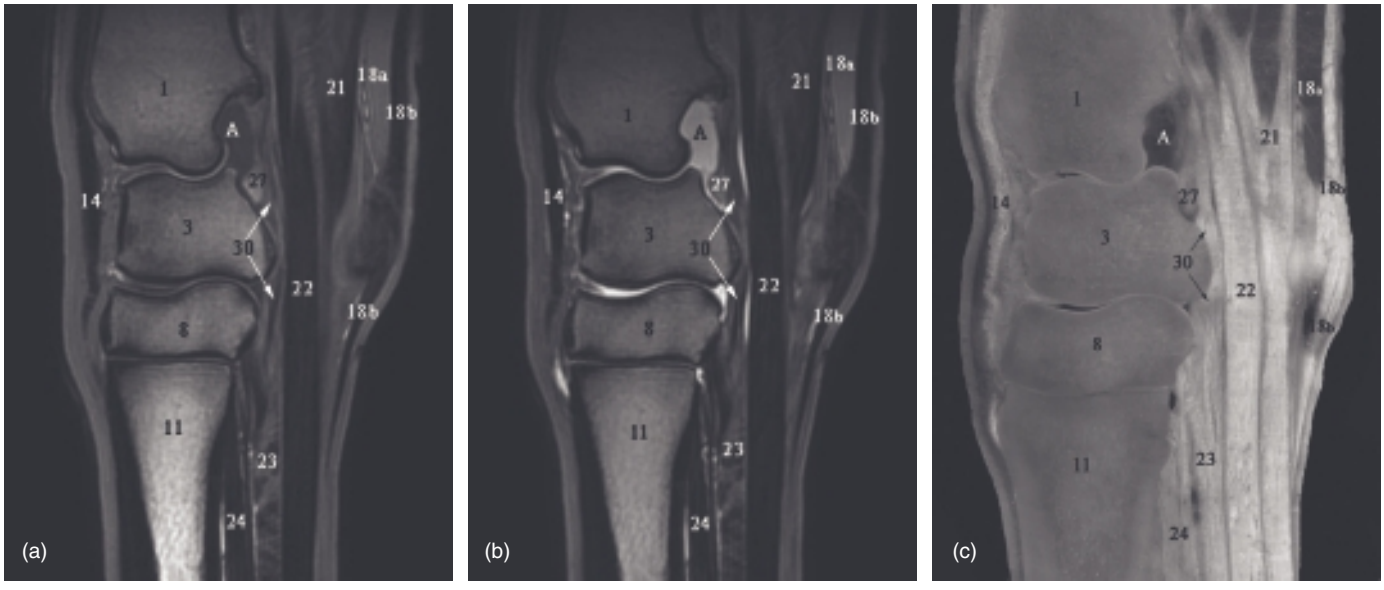

Figure 8.6 Sagittal 3D T1-weighted SPGR (a) and T2*-weighted (b) high-field MR images of a normal carpus. (c) Anatomical specimen.

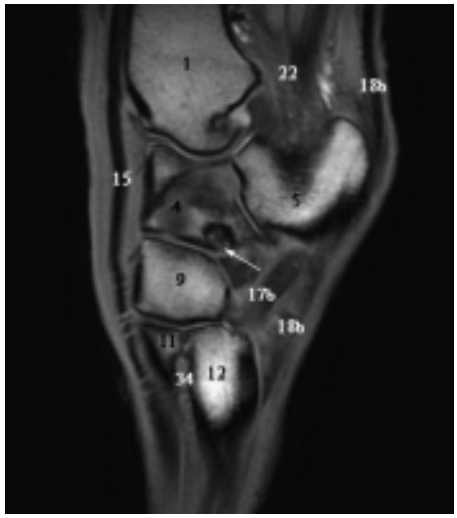

Figure 8.7 Lateral parasagittal 3D T1-weighted SPGR high-field MR image of a normal carpus. There is a small osseous fragment separated from the medial palmar aspect of the ulnar carpal bone (arrow).

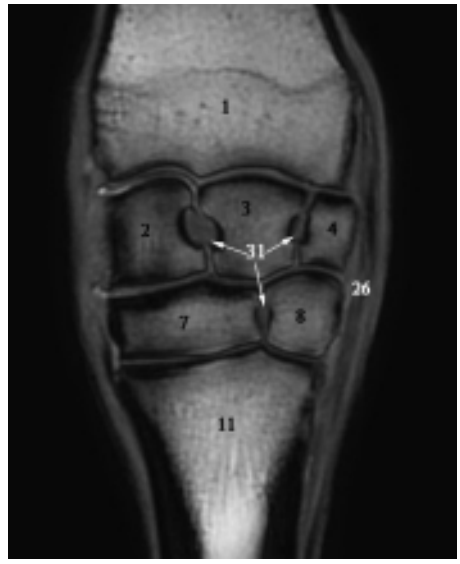

Figure 8.8 Dorsal 3D T1-weighted SPGR high-field MR image at the dorsal aspect of a normal carpus.

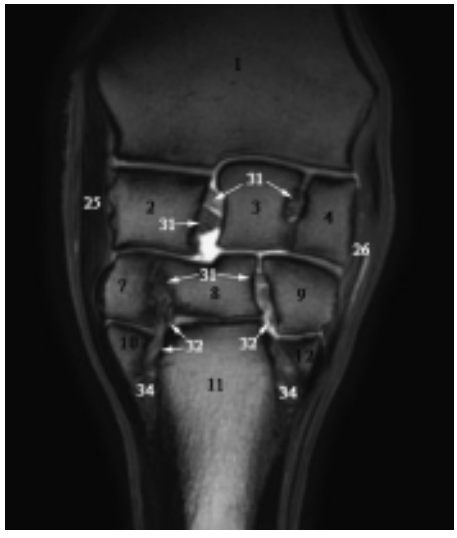

Figure 8.9 Dorsal 3D T2*-weighted GRE high-field MR image midway between the dorsal and palmar aspects of a normal carpus.

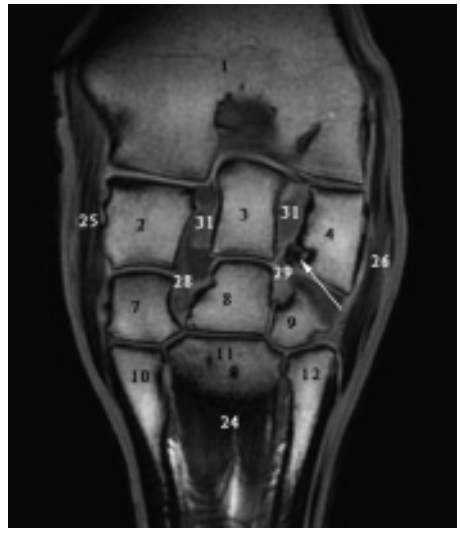

Figure 8.10 Dorsal 3D T2*-weighted GRE high-field MR image towards the palmar aspect of a normal carpus. Note the mineralized fragment on the distal medial aspect of the ulnar carpal bone (arrow).

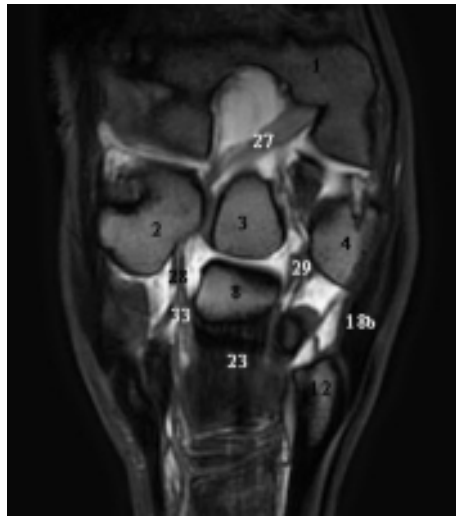

Figure 8.11 Dorsal 3D T2*-weighted GRE high-field MR image at the most palmar aspect of a normal carpus.

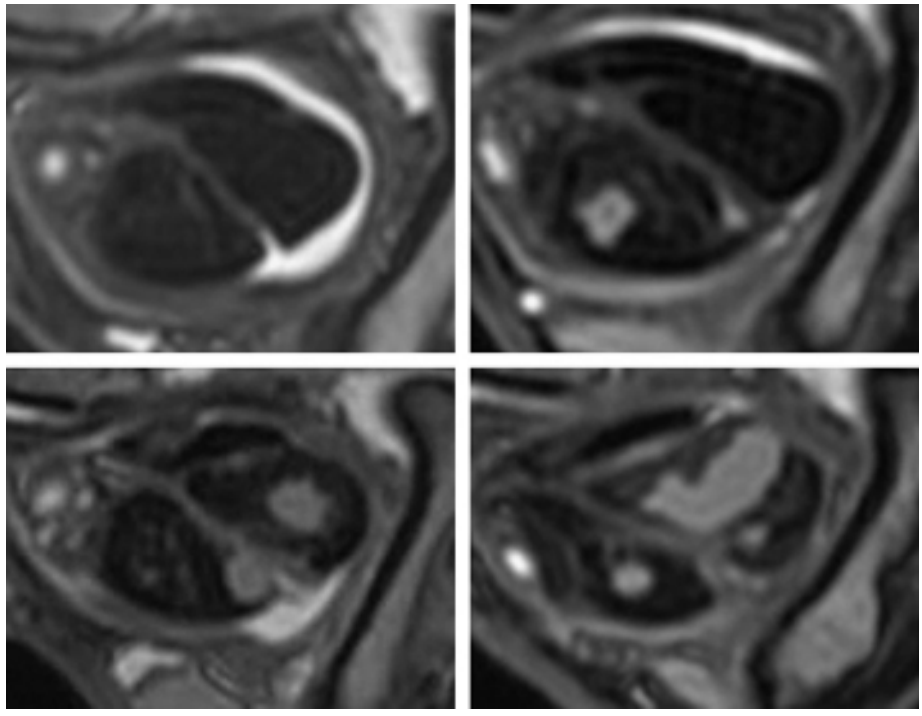

Figure 8.12 Transverse 3D T1-weighted SPGR and T2*-weighted high-field MR images of the carpal canal of four normal horses to show variations in muscle content in the superficial and deep digital flexor tendons at the level of the proximal row of carpal bones. See also Figure 8.1.

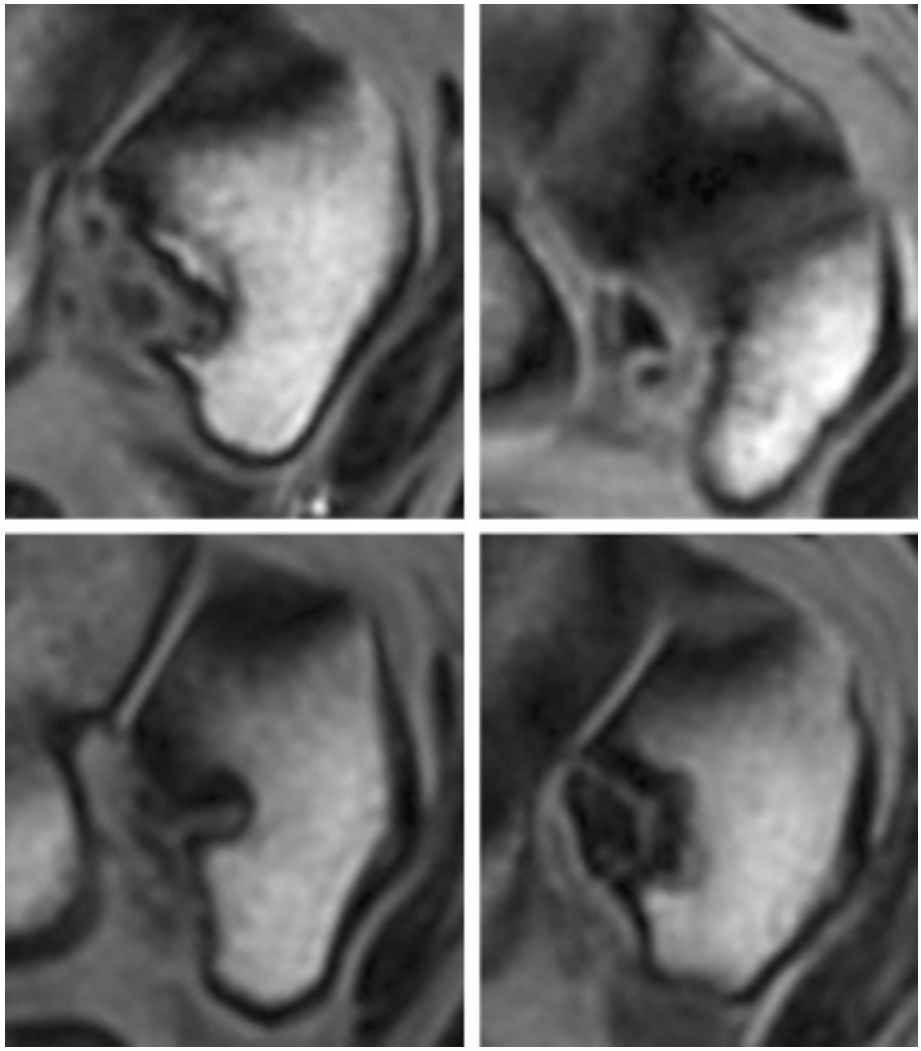

Figure 8.13 Transverse 3D T1-weighted SPGR high-field MR images of the lateral aspect of the proximal row of carpal bones to show variations in shape of the ulnar carpal bone and fragments separated from its distal medial aspect in clinically normal horses.

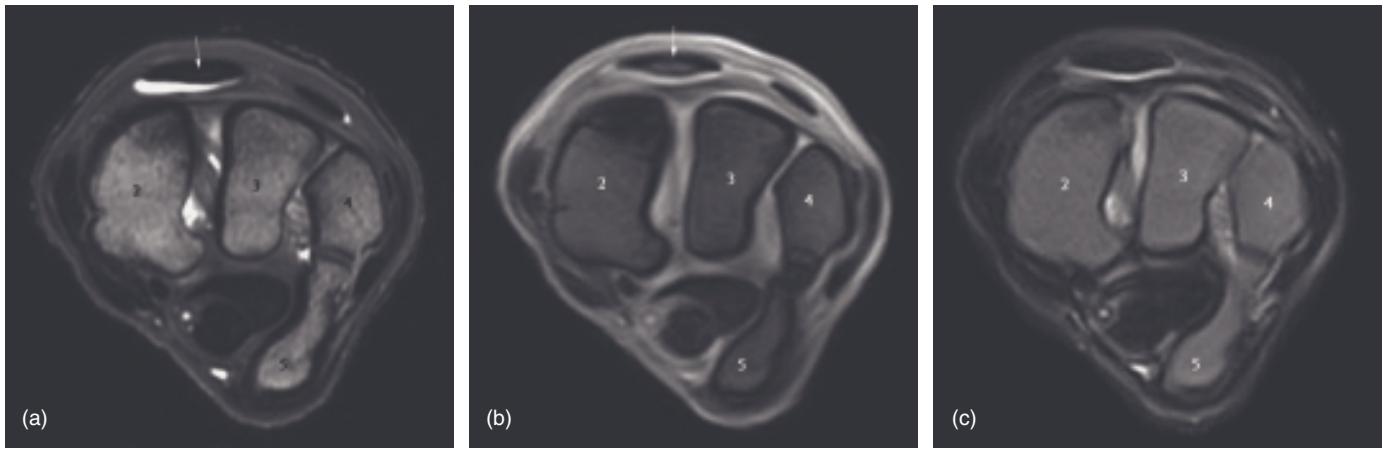

Figure 8.14 (a) 3D T2*-weighted GRE high-field MR image at the level of the proximal row of carpal bones. Note the fine line of high signal intensity in the extensor carpi radialis tendon (arrow). This corresponded to the location of a high signal intensity band in the sagittal image. (b) 3D T2*-weighted GRE low-field MR image at the level of the proximal row of carpal bones of the same horse shown in (a). Note that the linear high signal area seems much larger than on the high-field image (compare with (a)). The transverse intercarpal ligaments are less clearly defined than on the high-field image. (c) Fast spin-echo low-field MR image at the level of the proximal row of carpal bones of the same horse shown in (a) and (b). The extensor carpi radialis tendon has homogeneous low signal intensity (compare with (a) and (b)). The transverse intercarpal ligaments are better defined than on the T2-weighted gradient-echo low-field image.

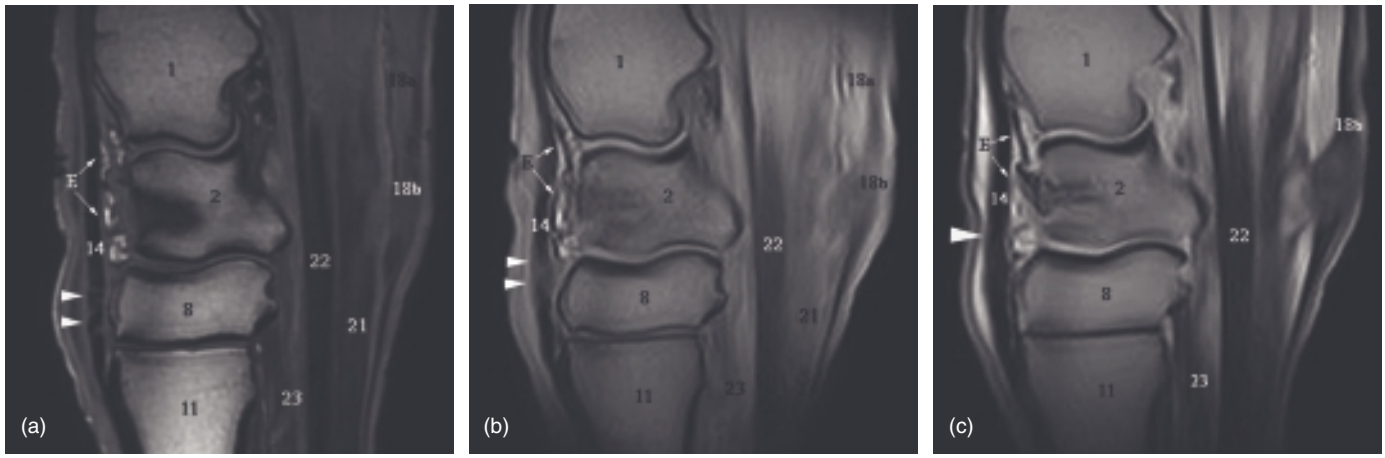

Figure 8.15 (a) Sagittal 3D T1-weighted SPGR high-field MR image of a normal carpus. There are linear high signal intensity bands in the extensor carpi radialis tendon, resulting in 'stripy' appearance (arrowheads). (b) Sagittal 3D T1-weighted low-field MR image of the carpus of the same horse as shown in (a). There is an area of intermediate signal intensity in the extensor carpi radialis tendon (arrowheads), which corresponds to the location of intermediate signal intensity bands identified in the high-field MR image (compare with (a)). (c) Sagittal proton density low-field MR image of the carpus of the same horse as shown in (a) and (b). There is an area in the extensor carpi radialis tendon, which has slightly higher signal intensity than other parts of the tendon, but the difference is much less obvious than in the gradient-echo images (compare with (a)). This area corresponds to the intermediate signal intensity bands identified in the high-field MR images (compare with (a)). Note that the distal articular surface of the radial and third carpal bones cannot be clearly identified (compare with (a) and (b)).

pass through the subchondral bone and thus has low signal intensity. The endosteal surfaces of the subchondral bone and cortical bone are smooth, although in the centre of the palmar aspect of the third carpal bone at the origin of the accessory ligament of the deep digital flexor tendon (ALDDFT) there is often slight irregularity. The articular cartilage can be evaluated on the dorsal aspect of the middle carpal joint in the sagittal images. In more palmar locations and in the carpometacarpal joint, the proximal and distal articular cartilage cannot be differentiated. The signal intensity of the medulla of the dorsal aspect of the small carpal bones is slightly lower in both T1- and T2-weighted images compared with the radius or the third metacarpal bone. In the proximal articular surface of the third metacarpal bone, the subchondral bone thickness is slightly greater medially than laterally.

Muscles and tendons

The extensor carpi radialis (ECR) tendon runs over the dorsal aspect of the carpus and inserts on the metacarpal tubercle of the third metacarpal bone. The tendon has clearly defined margins, is oval-shaped in cross section and is surrounded by a tendon sheath, which may or may not contain a minimal amount of fluid. The tendon has low signal intensity, interrupted by variable numbers of oblique bands of intermediate signal intensity (on both T1- and T2-weighted images). Due to these bands the tendon has a 'stripy' appearance on sagittal and dorsal high-field images and can have low or intermediate signal intensity on the transverse images depending on whether the image coincides with the plane of a band or not. This is more obvious on

high-field images than low-field images (Figure 8.15). The small tendon of the extensor carpi obliquus muscle runs across from the lateral distal aspect of the radius to the medial aspect of the third metacarpal bone. It is not always identifiable, even in transverse images. It has an elongated cross-sectional shape, ill-defined margins and its signal intensity can be low or intermediate, the latter probably due to its position related to the magnet, resulting in magic angle artefact.

The common digital extensor (CDE) tendon is located lateral to the ECR tendon. It is oval in cross-section, with well-defined margins and has low signal intensity. The CDE tendon is smaller than the ECR tendon and may contain some bands of intermediate signal intensity (Figure 8.7). The small lateral digital extensor tendon has uniform low signal intensity. It runs under the lateral collateral ligament of the carpus and the two structures cannot always be distinguished clearly. The ulnaris lateralis tendon has two branches. The short branch runs on the distal caudolateral aspect of the radius and inserts on the accessory carpal bone. It has low to intermediate heterogeneous signal intensity, especially in its axial aspect, and poorly defined margins. The short, smaller branch runs dorsal to the long branch and inserts on the base of the fourth metatacarpal bone. The flexor carpi ulnaris is clearly divided into a cranial muscular and a caudal tendonous parts (Figures 8.1 and 8.6a). The greatest part of the structure inserts on the accessory carpal bone, but there is an additional small distal tendon running on the palmarolateral aspect of the carpus, which inserts on the axial aspect of the base of the second metacarpal bone. It has small cross-sectional area, well-defined margins and low signal intensity. The flexor carpi radialis muscle's small tendon runs along the palmaromedial aspect of the carpus and inserts on the axial aspect of the second metacarpal bone. It has uniform low signal intensity and well-defined margins.

The superficial digital flexor tendon (SDFT) contains a variable amount of muscle tissue at the level of the distal aspect of the radius (Figures 8.1 and 8.12) and less frequently at the level of the proximal row of carpal bones, which appear as areas of intermediate signal intensity in T1- and intermediate to high signal intensity in T2-weighted images. At the level of the distal row of carpal bones, the tendon has uniform low signal intensity. Its signal intensity may be slightly higher than that of the deep digital flexor tendon (DDFT); this difference is most obvious on low-field T1-weighted images. The SDFT is located medial to the DDFT and is oval or tear-shaped on transverse images at the level of the distal aspect of the radius. Further distally, it becomes more rounded in cross-section and is located more palmaromedial, palmar to the DDFT (Figures 8.2 and 8.3). The DDFT's three heads usually join at the level of the distal aspect of the radius. In most horses, all three heads can be identified (Figure 8.1). The largest humeral head is divided by muscle septa. The humeral and the ulnar heads contain variable amounts of muscle tissue of intermediate signal intensity at the level of the distal aspect of the radius and proximal row of carpal bones, which is located centrally in both heads (Figure 8.1). The most dorsal radial head is tendonous in the entire carpal region and therefore has uniform low signal intensity. The DDFT is tear-shaped in cross-section at the level of the

distal aspect of the radius and becomes more oval further distally (Figures 8.2 and 8.3).

Ligaments and fasciae

There is a strong carpal fascia, which is attached to the medial and lateral aspects of the distal aspect of the radius, to the accessory carpal bone and to the collateral ligaments of the carpus. The dorsal part forms the extensor retinaculum and cannot always be identified in MR images. The thicker palmar part, the flexor retinaculum, forms the palmar wall of the carpal canal and can be identified on both T1- and T2-weighted images (Figure 8.4). The flexor retinaculum is the palmar part of the fascia; it surrounds the palmar aspect of the carpus and continues distally to the proximal metacarpal region and forms the palmar wall of the carpal canal. It extends from the accessory carpal bone to the medial collateral ligament of the carpus and to the proximal palmar aspects of the second and fourth metacarpal bones. It has strong fibres joining the medial collateral ligament and it can be difficult to differentiate between the two structures. In the medial aspect of the carpal region the flexor retinaculum is composed of three layers. The superficial layer is superficial to the medial palmar vein. It is thicker medially and easier to identify than the deep layers. The two deeper layers are separated by the flexor carpi radialis tendon and cannot always be clearly identified. The flexor retinaculum has homogeneous intermediate to low signal intensity in all pulse sequences.

The collateral ligaments of the carpus have heterogeneous low signal intensity and slightly irregular margins (Figures 8.3 and 8.8). The medial collateral ligament is rounded proximally and becomes narrower and more oval-shaped distally, while the lateral collateral ligament is narrow close to its origin and gets wider distally. The superficial and the deep parts of the collateral ligaments cannot be distinguished clearly, and this explains why fibres can be seen running in different directions on dorsal images. The small lateral digital extensor tendon runs under the lateral collateral ligament of the carpus and the two structures cannot always be distinguished clearly.

The palmar carpal ligament is best evaluated on sagittal images, but it can sometimes also be identified on transverse images. On sagittal images, its continuation into the ALDDFT can be clearly seen, especially on T2-weighted images (Figure 8.6). Not all small palmar carpal ligaments can be identified, even on high-field images. There is a strong radiocarpal ligament running from the distal lateral aspect of the radius to the proximal medial aspect of the radial carpal bone within the antebrachiocarpal joint (Figure 8.11). It has intermediate signal intensity on both low-field and high-field T1- and T2-weighted images and is best seen on dorsal images, but may also be identified on transverse and sagittal images. Occasionally another radiocarpal ligament can be identified between the distal medial aspect of the radius and the radial carpal bone.

A more distal palmar carpal ligament may be seen on dorsal images, running distally from the palmar aspect of the third carpal bone. The transverse intercarpal ligaments of the carpal bones have intermediate signal

intensity (Figures 8.2, 8.3, 8.9 and 8.10). In high-field images the fibre pattern can be assessed and in some ligaments synovial fluid of high signal intensity interdigitates between fibres. However, in low-field images these ligaments are difficult to differentiate from the synovial fluid. On low-field images, the transverse intercarpal ligaments are best assessed on FSE and STIR images. The medial and lateral palmar intercarpal ligaments have intermediate to high signal intensity. They can be identified on transverse and dorsal images. There are two small ligaments towards the palmar aspect of the carpometacarpal joint. The medial ligament originates from between the second and third carpal bones and inserts in between the third metacarpal bone and the base of the second metacarpal bone. The lateral ligament originates from between the third and fourth carpal bones and inserts in between the third metacarpal bone and the base of the fourth metacarpal bone. These ligaments have intermediate signal intensity in all pulse sequences in both low-field and high-field images. Their fibre structure can only be well evaluated in T1- and T2-weighted high-field images. The majority of the fibres are oriented proximodistally, therefore the carpometacarpal ligaments are best evaluated on dorsal and sagittal images.

The ALDDFT is a continuation of the palmar carpal ligament, and also has fibres originating from the palmar aspect of the third and fourth carpal bones. The ligament has heterogeneous low to intermediate signal intensity and can contain variable bands of intermediate signal intensity, which result in a 'stripy' appearance on the sagittal images, similar to that which is observed in the ECR and CDE tendons (Figures 8.3a and 8.6b). The major part of the suspensory ligament (SL) originates from the proximal aspect of the palmar cortex of the third metacarpal bone, but there are additional fibres originating from the palmar cortex of the third carpal bone (Figures 8.4 and 8.6b) and the axial aspect of the fourth metacarpal bone. The proximal aspect of the SL is a bilobed structure and is surrounded by variable amount of connective tissue of intermediate to high signal intensity.

Joints and tendon sheaths

The antebrachiocarpal joint has a small dorsal pouch and a large palmar pouch, which always contains some synovial fluid. The middle carpal joint also has a small dorsal pouch with a minimal amount of synovial fluid, and a larger palmar pouch. The lateral palmar pouch may extend markedly in a palmar direction and can be identified distal to the accessory carpal bone between the lateral collateral ligament and the ulnaris lateralis tendon (Figure 8.3). The dorsal pouch of the carpometacarpal joint contains minimal synovial fluid. Its palmar pouch extends distally to a variable degree on both medial and lateral sides. It is not always possible to differentiate the synovial fluid from the intermediate to high signal intensity connective tissue around the origin of the suspensory ligament. The dorsal joint capsules of all three joints can easily be identified. A variably sized fat pad is seen in the dorsal aspect of the carpus at the level of the antebrachiocarpal and middle carpal joints, which has intermediate to high signal intensity on T1-weighted images and high signal intensity on T2-weighted images.

Synovial fluid in the tendon sheaths is most commonly seen in the tendon sheath of the ECR and the CDE tendons.

NORMAL VARIATIONS AND SOME DIFFERENCES BETWEEN LOW-FIELD AND HIGH-FIELD MR FINDINGS

The thickness of the subchondral bone in the distal aspect of the radius, in the carpal bones and in the proximal aspect of the third metacarpal bone is variable and is related to the exercise history of the horse. Slight osteochondral irregularity or uneven cartilage thickness can be seen in clinically normal horses.

The SDFT and the DDFT contain variable amounts of muscle tissue in the proximal aspect of the carpus (Figure 8.12). By the level of the distal row of carpal bones, both tendons have uniform low signal intensity.

Variability in shape of the distal medial aspect of the ulnar carpal bone and discrete osseous fragment(s) were seen in 5 out of 30 horses (Figure 8.13). The high frequency of occurrence in non-lame horses suggests that this finding is likely to be a developmental abnormality.

In some tendons (ECR, CDE and occasionally in extensor and flexor carpi radialis) stripy areas were identified, caused by bands of intermediate to high signal intensity. On low-field GRE images, solitary bands may be identified, but if multiple bands are located in close proximity, it results in intermediate signal intensity of the entire cross-section of the tendon. In the majority of limbs, these bands were not obvious on low-field SE sequences. On transverse low-field GRE images focal areas of intermediate to high signal intensity can mimic a core lesion (Figure 8.14); however, they coincide with the bands identified on sagittal and dorsal planes and were absent on the transverse SE images. These bands are the result of an artefact caused by relaxation of the tendons, and can also be seen in lame horses.

The articular cartilage is less well-defined in low-field images compared with high-field images and the infrastructure and clarity of the margins of the transverse intercarpal ligaments are less distinct. In both high- and low-field images the ALDDFT has greater signal intensity than the SDFT, DDFT and SL.

Key to figures

1 Radius
2 Radial carpal bone
3 Intermediate carpal bone
4 Ulnar carpal bone
5 Accessory carpal bone
6 First carpal bone
7 Second carpal bone
8 Third carpal bone
9 Fourth carpal bone

10 Second metacarpal bone
11 Third metacarpal bone
12 Fourth metacarpal bone
13 Extensor carpi obliquus tendon
14 Extensor carpi radialis muscle/tendon
15 Common digital extensor tendon
16 Lateral digital extensor tendon
b, branch from the lateral digital extensor tendon to the common digital extensor tendon
17 Ulnaris lateralis tendon
a, short branch
b, long branch
18 Flexor carpi ulnaris
a, muscle
b, tendonous part
19 Flexor carpi radialis
20 Carpal fascia
b, flexor retinaculum
21 Superficial digital flexor tendon
22 Deep digital flexor tendon
a, humeral head
b, radial head
c, ulnar head
23 Accessory ligament of the deep digital flexor tendon
24 Suspensory ligament
25 Medial collateral ligament of the carpus
26 Lateral collateral ligament of the carpus
27 Radiocarpal ligament
28 Medial palmar intercarpal ligament
29 Lateral palmar intercarpal ligament
30 Palmar carpal ligament
31 Transverse intercarpal ligaments in the proximal and distal rows of carpal bones
32 Carpometacarpal ligament
33 Palmar carpometacarpal ligament
34 Interosseous ligaments between McII and McIII and between McIV and McIII
35 **a,** Medial palmar vein
b, Medial palmar artery
c, Medial palmar nerve
36 Lateral palmar artery, nerve and vein
37 **a,** Radial artery
b, Radial vein
A Synovial fluid in joint
B Synovial fluid in tendon sheath
C Joint capsule
D Connective tissue
E Fat pad

ACKNOWLEDGEMENTS

We thank the Bransby Trust for generous financial support.

REFERENCES

[1] Kaser-Hotz B, Sartoretti-Schefer S, Weiss R. Computed tomography and magnetic resonance imaging of the normal equine carpus. *Vet Radiol Ultrasound* 1994; **35**: 457–61.
[2] Murray RC. Magnetic resonance imaging of the equine carpus. *Clin Tech Equine Pract* 2007; **6**: 86–95.
[3] Getty R. *Sisson and Grossman's The anatomy of the domestic animals*, 5th edn. Philadelphia, PA: WB Saunders, 1975.
[4] Budras KD, Sack WO, Rock S. *Anatomy of the Horse*, 3rd edn. Hannover: Schlutersche, 2001.

Chapter 9
The tarsus

Sue Dyson and Rachel Murray

INTRODUCTION

Magnetic resonance imaging (MRI) of the equine tarsus is still in its infancy. The tarsus is an anatomically complex structure comprising the tarsocrural, talocalcaneal, talocalcaneal-centroquartal (proximal intertarsal), centrodistal (distal intertarsal) and tarsometatarsal joints, and the closely related articulations between the second, third and fourth metatarsal bones. The biomechanical function of these joints and the influence of loading on structure and function are also complex, and recently the effects of age, exercise history and use on osteochondral architecture in the distal hock joints have been described [1–3]. There is a complex of soft tissue structures on the plantar aspect of the tarsus, comprising the tarsal sheath, the deep (DDFT) and superficial (SDFT) digital flexor tendons, the accessory ligament of the DDFT, the accessory ligament of the suspensory ligament (SL) and the plantar ligament. Dorsally there are the tendons of tibialis cranialis, fibularis (peroneus) tertius, and the long and lateral digital extensor tendons. Knowledge of detailed three-dimensional (3D) anatomy is crucial for accurate interpretation of MR images.

An overview of equine tarsal anatomy using low-field MRI has been published [4]. Mid-field MRI has been used to investigate the effect of treadmill training on the tarsal bones of Thoroughbreds [5]. Factors influencing the osteochondral structure of horses with no history of hock-related pain detected using high-field MR images have been documented [6]. A variety of subclinical lesions affecting interosseous ligaments, articular cartilage and subchondral bone have recently been described [7].

The objectives of this chapter are to describe normal anatomy of the equine tarsus using high-field MRI and variations that might be expected in clinically normal horses [6]. The results described were obtained from the review of 74 cadaver tarsi, collected from horses with a variety of exercise histories but no history of hind limb lameness: (1) Low-level exercise, 5 to 17 years of age (n = 20); (2) Welsh section A ponies subject to pasture exercise only, 11 days of age (n = 10), 6 to 9 months (n = 6), 3 to 6 years (n = 4), 11 to 16 years (n = 4), 24 to 25 years (n = 3); (3) racehorses in training, 3 to 12 years of age (n = 15); (4) elite competition horses, 9 to 13 years of age (n = 12). Some comparative low-field images are also illustrated.

Equine MRI, edited by Rachel C. Murray.

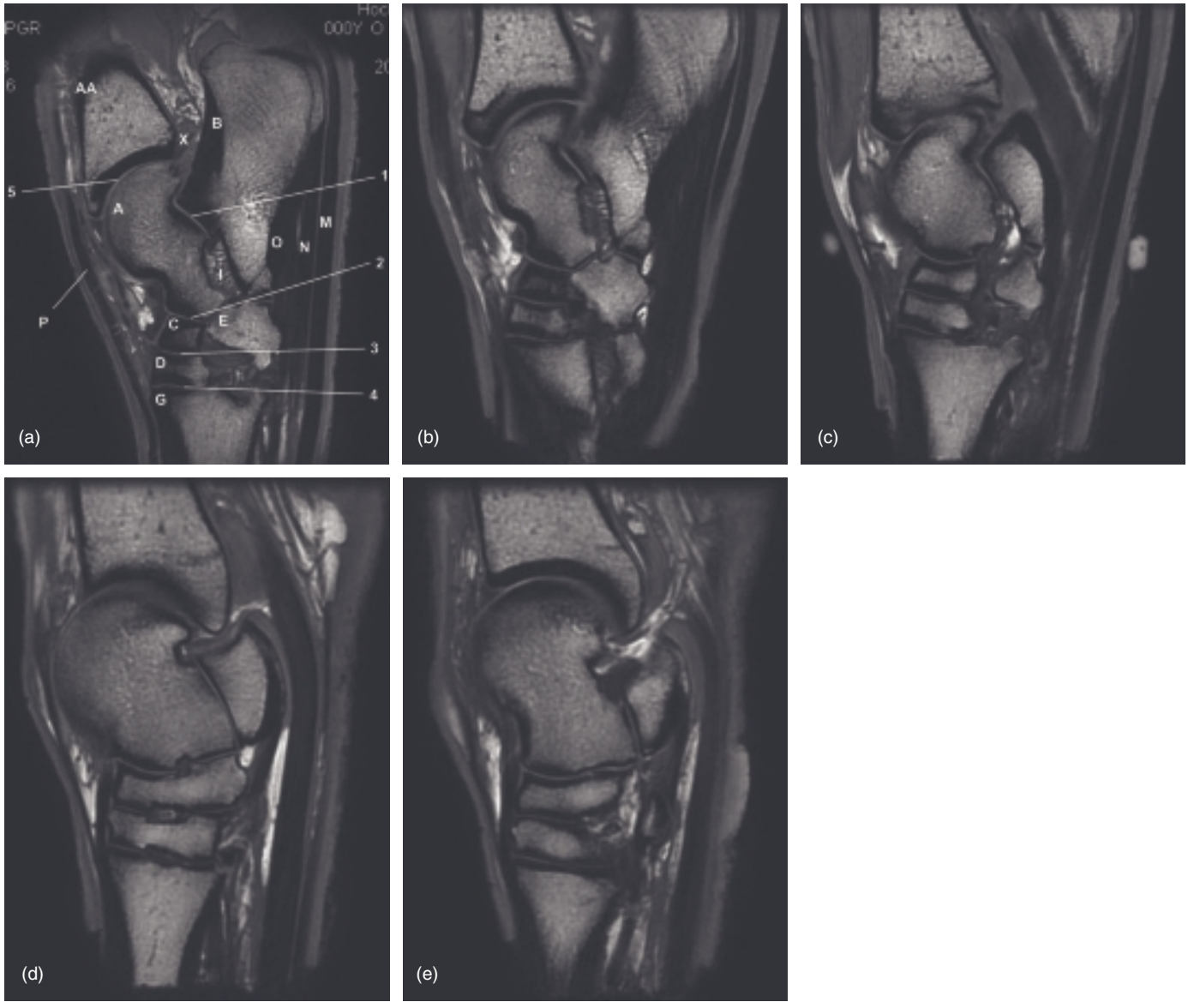

ANATOMICAL DESCRIPTION OF THE NORMAL TARSUS

Normal high-field MR anatomy of the equine tarsus is illustrated in Figures 9.1–9.12. Articular cartilage is a layer of homogeneous intermediate signal intensity on T1, T2* and PD images, with a smooth osteochondral junction in all joints. In the tarsocrural joint, it is usually possible to define the cartilage surface, particularly of the talus, depending on the imaging sequence and plane. However, the very thin cartilage and a narrow joint space prevent distinction of proximal and distal cartilage layers in the talocalcaneal-centroquartal, centrodistal (CD) and tarsometatarsal (TMT) joint spaces. On lower-resolution 2D scans, articular cartilage in these joints may be difficult to visualize as a very thin layer of intermediate signal intensity sandwiched between the low signal intensity of the subchondral bone of each articular surface. However, at the midline and laterally, in the dorsal aspect of the talocalcaneal-centroquartal joint and in the tarsocrural joint, the proximal and distal layers of articular cartilage may be defined on higher-resolution scans (Figure 9.1).

[222]

Figure 9.1 (a) Lateral parasagittal 3D T1-weighted gradient echo high-field MR image of a tarsus from a mature horse with no history of hind limb lameness, which had undergone low-level exercise. Dorsal is to the left and plantar to the right. **AA**, tibia; **A**, talus; **B**, calcaneus; **C**, central tarsal bone; **D**, third tarsal bone; **E**, fourth tarsal bone; **G**, third metatarsal bone; **I**, talocalcaneal ligament; **M**, superficial digital flexor tendon; **N**, plantar tarsometatarsal ligament; **O**, deep branch of plantar tarsometatarsal ligament; **P**, long digital extensor tendon; **X**, tarsocrural synovium; **1**, talocalcaneal joint; **2**, talocalcaneal-centroquartal joint; **3**, centrodistal joint; **4**, tarsometatarsal joint; **5**, tarsocrural joint. (b) to (e) Lateral to medial parasagittal 3D T1-weighted gradient-echo MR images of a tarsus from a mature horse with no history of hind limb lameness. Dorsal is to the left. Compare (c and d) with Figure 9.3 and (c) with Figure 9.4.

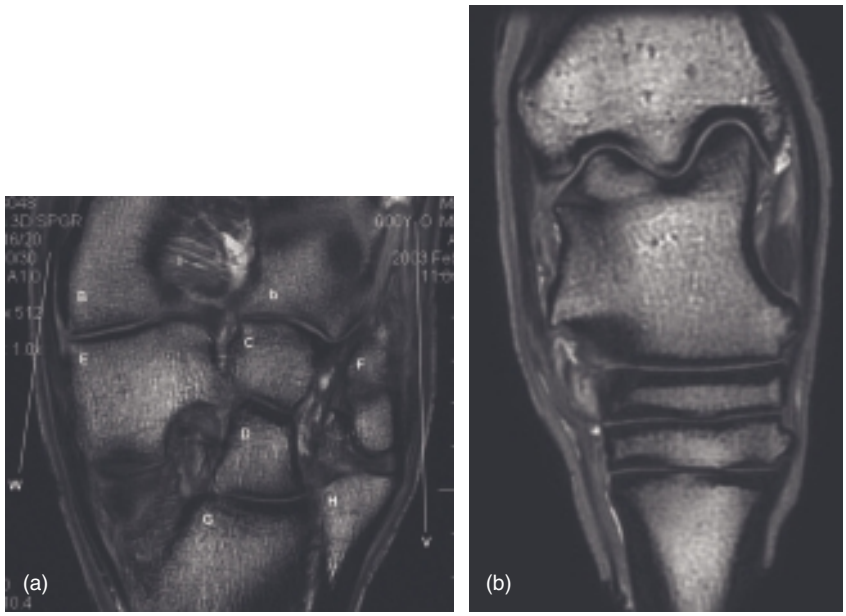

Figure 9.2 (a) Dorsal (frontal) plane 3D T1-weighted gradient echo MR image of the plantar aspect of a tarsus from a mature horse with no history of hind limb lameness, which had undergone low-level exercise. Lateral is to the left and medial to the right. **B**, calcaneus; **b**, sustentaculum tali; **C**, central tarsal bone; **D**, third tarsal bone; **E**, fourth tarsal bone; **F**, fused first and second tarsal bones; **G**, third metatarsal bone; **H**, second metatarsal bone; **I**, talocalcaneal ligament; **V**, medial collateral ligaments; **W**, lateral collateral ligaments. (b) Dorsal (frontal) plane 3D T1-weighted gradient-echo MR image of the dorsal aspect of a tarsus from a mature horse with no history of hind limb lameness, which had undergone low-level exercise. Lateral is to the left.

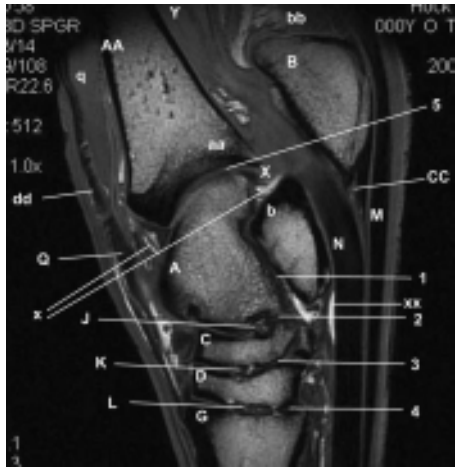

Figure 9.3 Midline sagittal 3D T1-weighted gradient-echo high-field MR image of a tarsus from a mature horse with no history of hind limb lameness, which had undergone low-level exercise. Dorsal is to the left and plantar to the right. **AA**, tibia; **aa**, caudal aspect of the intermediate ridge of the tibial cochlea; **A**, talus; **B**, calcaneus; **b**, sustentaculum tali; **C**, central tarsal bone; **CC**, fatty tissue; **D**, third tarsal bone; **G**, third metatarsal bone; **J**, talocalcaneal-centroquartal ligament; **K**, centrodistal ligament; **L**, tarsometatarsal ligament; **M**, superficial digital flexor tendon; **N**, deep digital flexor tendon; **Q**, tibialis cranialis tendon; **q**, tibialis cranialis muscle; **dd**, fibularis tertius tendon; **X**, tarsocrural synovium; **x**, fat tissue; **xx**, fat tissue dorsal to the deep digital flexor tendon; **Y**, deep flexor muscle; **1**, talocalcaneal joint; **2**, talocalcaneal-centroquartal joint; **3**, centrodistal joint; **4**, tarsometatarsal joint; **5**, tarsocrural joint.

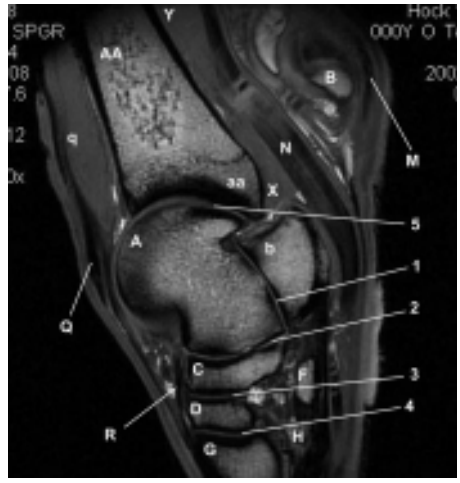

Figure 9.4 Medial parasagittal 3D T1-weighted gradient-echo high-field MR image of a tarsus from a mature horse with no history of hind limb lameness, which had undergone low-level exercise. Dorsal is to the left and plantar to the right. **AA**, tibia; **aa**, caudal aspect of the intermediate ridge of the tibial cochlea; **A**, talus; **B**, calcaneus; **b**, sustentaculum tali; **C**, central tarsal bone; **D**, third tarsal bone; **F**, fused first and second tarsal bones; **G**, third metatarsal bone; **H**, second metatarsal bone; **M**, superficial digital flexor tendon; **N**, deep digital flexor tendon; **Q**, tibialis cranialis tendon; **q**, tibialis cranialis muscle; **R**, dorsal tarsal ligament; **X**, tarsocrural synovium; **Y**, deep digital flexor muscle; **1**, talocalcaneal joint; **2**, talocalcaneal-centroquartal joint; **3**, centrodistal joint; **4**, tarsometatarsal joint; **5**, tarsocrural joint.

Figure 9.5 (a) Midline sagittal 3D T2* gradient-echo high-field MR image of the distal aspect of a tarsus from a mature horse with no history of hind limb lameness, which had undergone low-level exercise. Dorsal is to the left and plantar to the right. **A**, talus; **b**, sustentaculum tali; **C**, central tarsal bone; **D**, third tarsal bone; **G**, third metatarsal bone; **J**, talocalcaneal-centroquartal ligament; **K**, centrodistal ligament; **L**, tarsometatarsal ligament; **M**, superficial digital flexor tendon; **N**, deep digital flexor tendon; **Q**, tibialis cranialis tendon; **R**, dorsal tarsal ligament; **RR**, suspensory ligament; **1**, talocalcaneal joint; **2**, talocalcaneal-centroquartal joint; **3**, centrodistal joint; **4**, tarsometatarsal joint. (b) Lateral parasagittal 3D T2* gradient-echo high-field MR image of a tarsus from a mature horse with no history of hind limb lameness, which had undergone low-level exercise. Dorsal is to the left.

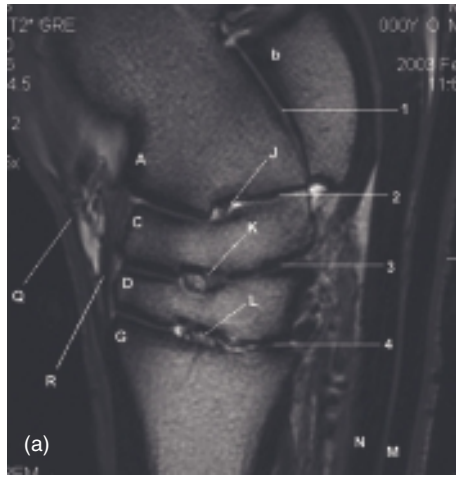

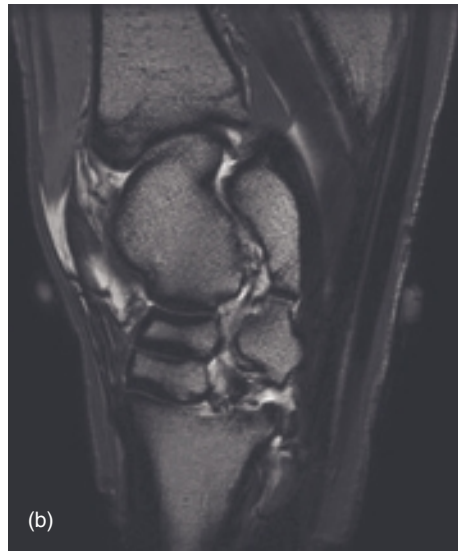

Figure 9.6 (a) Transverse 3D T1-weighted gradient-echo high-field MR image at the level of the proximal third of the third tarsal bone from a mature horse with no history of hind limb lameness, which had undergone low-level exercise. Dorsal is to the top and plantar to the bottom. Lateral is to the right. **D**, third tarsal bone; **E**, fourth tarsal bone; **F**, fused first and second tarsal bones; **M**, superficial digital flexor tendon; **N**, lateral head of the deep digital flexor tendon; **O**, plantar tarsometatarsal ligament; **o**, accessory branch of suspensory ligament; **P**, long extensor tendon; **p**, fibularis tertius tendon; **Q**, tibialis cranialis tendon; **R**, dorsal tarsal ligament; **S**, medial head of the deep digital flexor tendon; **T**, lateral digital extensor tendon; **U**, deep fibular nerve and cranial tibial vessels; **V**, medial collateral ligament; **Z**, oil capsule marking plantar aspect. (b) Transverse 3D T1-weighted gradient-echo high-field MR image of the tarsus of a clinically normal horse, at the proximal aspect of the talus. Lateral is to the left. **T**, talus; **C**, calcaneus; **DDFT**, deep digital flexor tendon; **S**, superficial digital flexor tendon. The deep collateral ligaments (CLs) of the tarsocrural joint have intermediate signal intensity (arrow heads), whereas the superficial CLs have low signal intensity (arrows). The plantar metatarsal ligament originates from the plantar aspect of the calcaneus. (c) Transverse 3D T1-weighted gradient-echo high-field MR image of the tarsus of a clinically normal horse, at the mid level of the talus. Lateral is to the left. **PL**, plantar metatarsal ligament (which has slightly heterogeneous signal intensity). The talocalcaneal interosseous ligament has fascicular structure of intermediate signal intensity. (d) Transverse 3D T1-weighted gradient-echo high-field MR image of the tarsus of a clinically normal horse, at the distal aspect of the talus. Lateral is to the left. (e) Transverse 3D T1-weighted gradient-echo high-field MR image of the tarsus of a clinically normal horse, at the level of the central tarsal bone. Lateral is to the left. **A**, accessory ligament of the suspensory ligament.

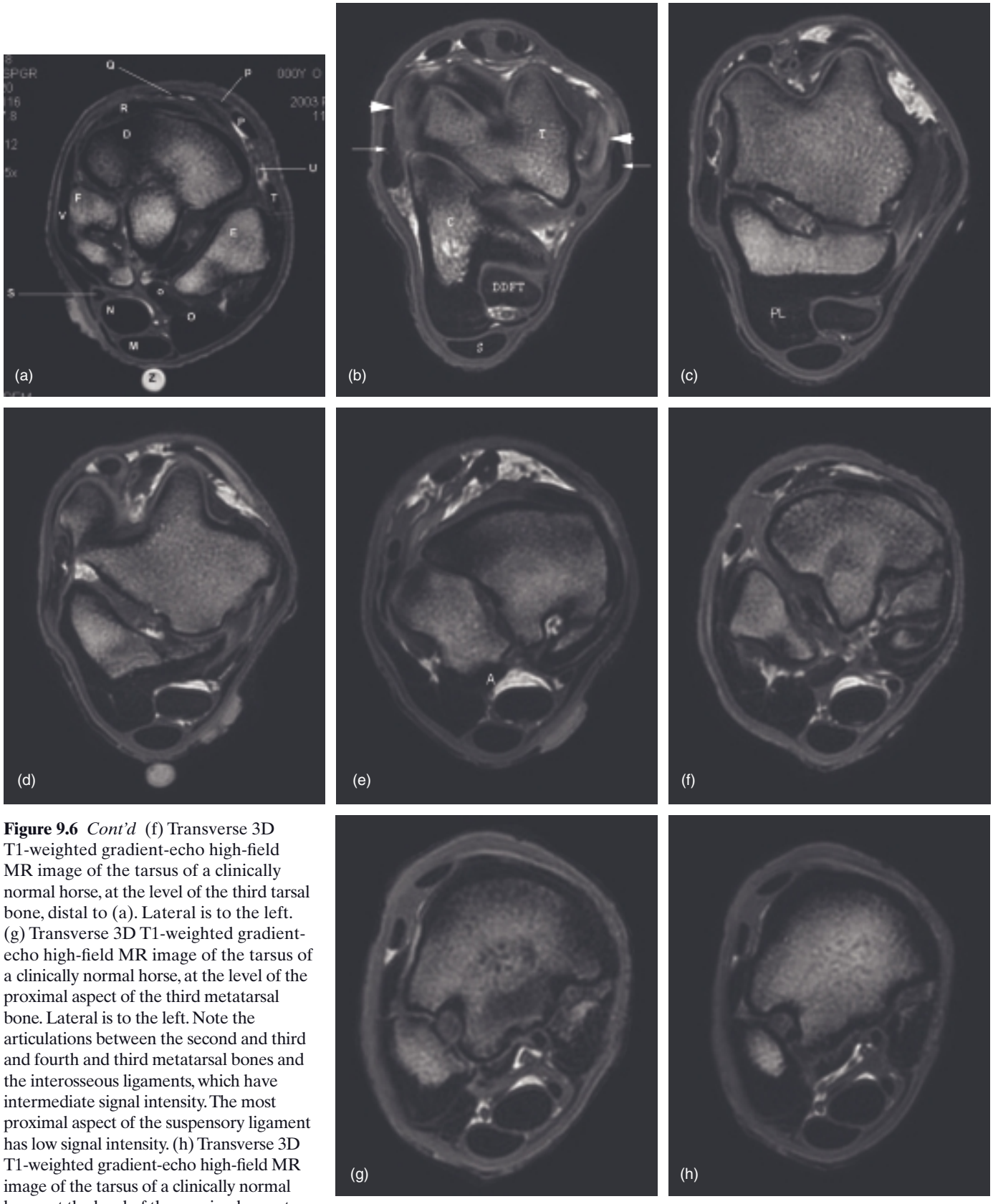

Figure 9.6 *Cont'd* (f) Transverse 3D T1-weighted gradient-echo high-field MR image of the tarsus of a clinically normal horse, at the level of the third tarsal bone, distal to (a). Lateral is to the left. (g) Transverse 3D T1-weighted gradient-echo high-field MR image of the tarsus of a clinically normal horse, at the level of the proximal aspect of the third metatarsal bone. Lateral is to the left. Note the articulations between the second and third and fourth and third metatarsal bones and the interosseous ligaments, which have intermediate signal intensity. The most proximal aspect of the suspensory ligament has low signal intensity. (h) Transverse 3D T1-weighted gradient-echo high-field MR image of the tarsus of a clinically normal horse, at the level of the proximal aspect of the third metatarsal bone. Lateral is to the left.

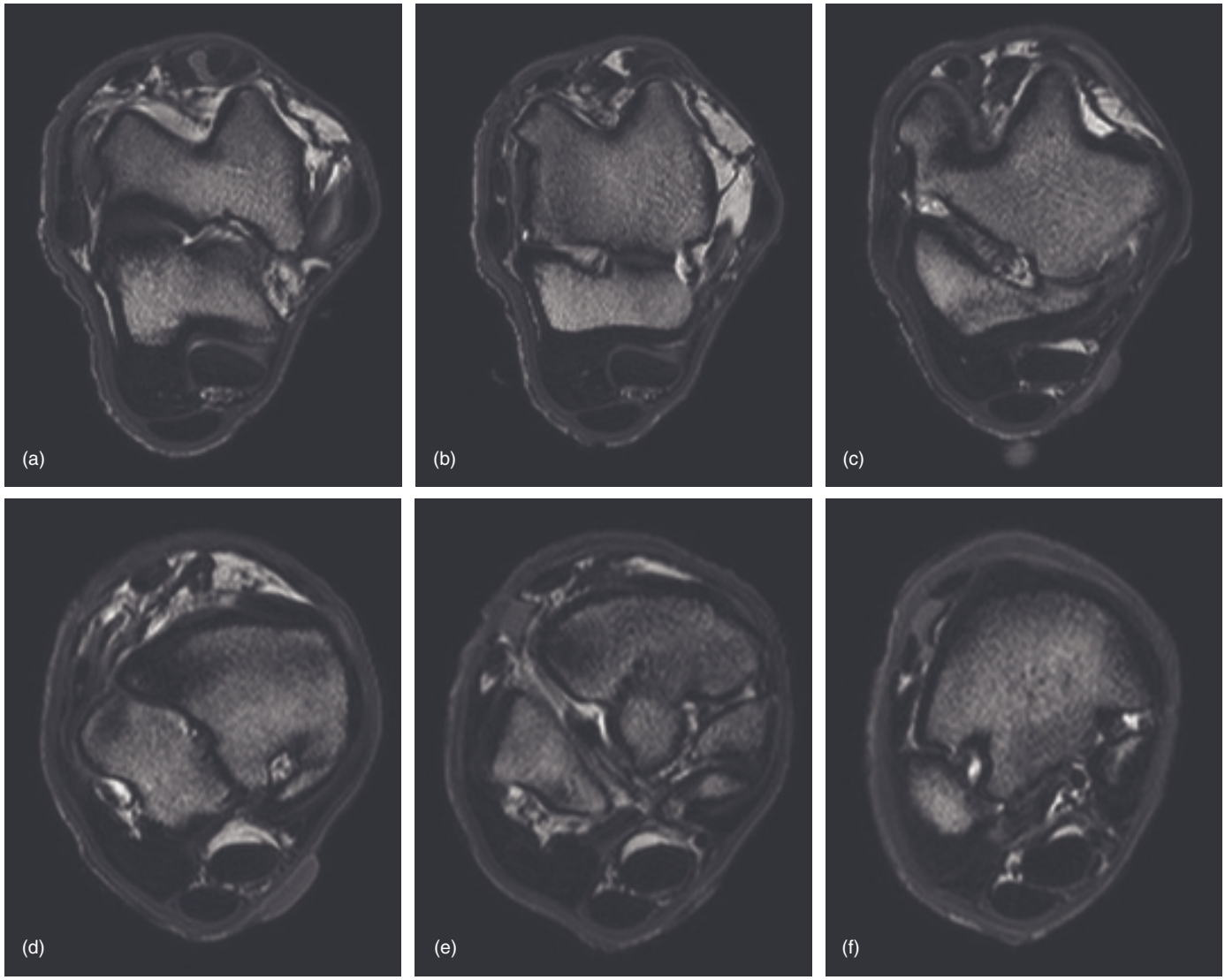

Figure 9.7 (a) Transverse 3D T2* gradient-echo high-field MR image of the tarsus of a clinically normal horse at the level of the proximal aspect of the talus. Lateral is to the left. (b) Transverse 3D T2* gradient-echo high-field MR image of a hock of a clinically normal horse at the level of the mid talus. Lateral is to the left. (c) Transverse 3D T2* gradient-echo high-field MR image of a hock of a clinically normal horse at the level of the distal aspect of the talus. Lateral is to the left. (d) Transverse 3D T2* gradient-echo high-field MR image of a hock of a clinically normal horse at the level of the central tarsal bone. Lateral is to the left. (e) Transverse 3D T2* gradient-echo high-field MR image of a hock of a clinically normal horse at the level of the third tarsal bone. Lateral is to the left. (f) Transverse 3D T2* gradient-echo high-field MR image of a hock of a clinically normal horse at the level of the proximal aspect of the third metatarsal bone. Lateral is to the left.

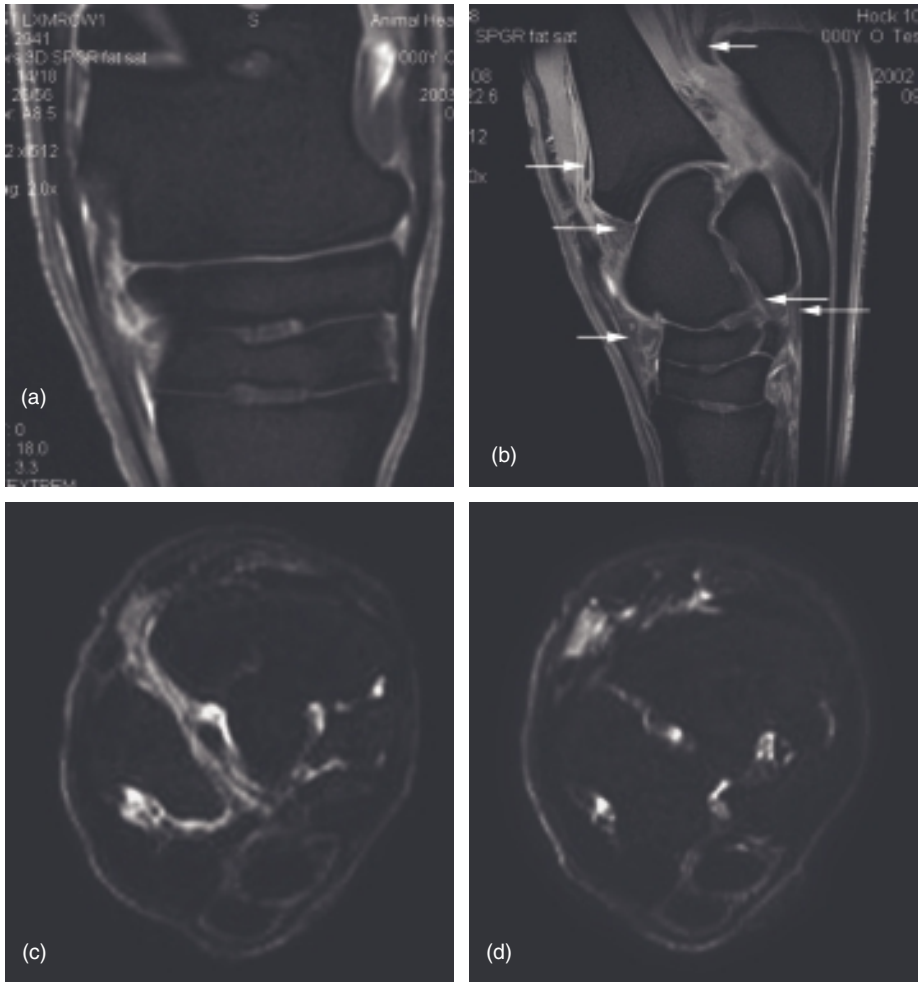

Figure 9.8 (a) Dorsal fat-saturated T1-weighted gradient-echo high-field MR image of a clinically normal horse. Lateral is to the left. Note the intermediate signal intensity of the intertarsal ligaments. (b) Midline sagittal T1-weighted gradient-echo fat-saturated high-field MR image of the hock of a mature horse with no history of hind limb lameness. Dorsal is to the left. The arrows signify areas of fatty tissue, which had high signal intensity on T1-weighted image but a much lower signal intensity on the fat-saturated image. (c) Transverse STIR high-field MR image of a normal hock at the level of the central tarsal bone. Lateral is to the left. (d) Transverse STIR high-field MR image of a normal hock at the level of the third tarsal bone. Lateral is to the left.

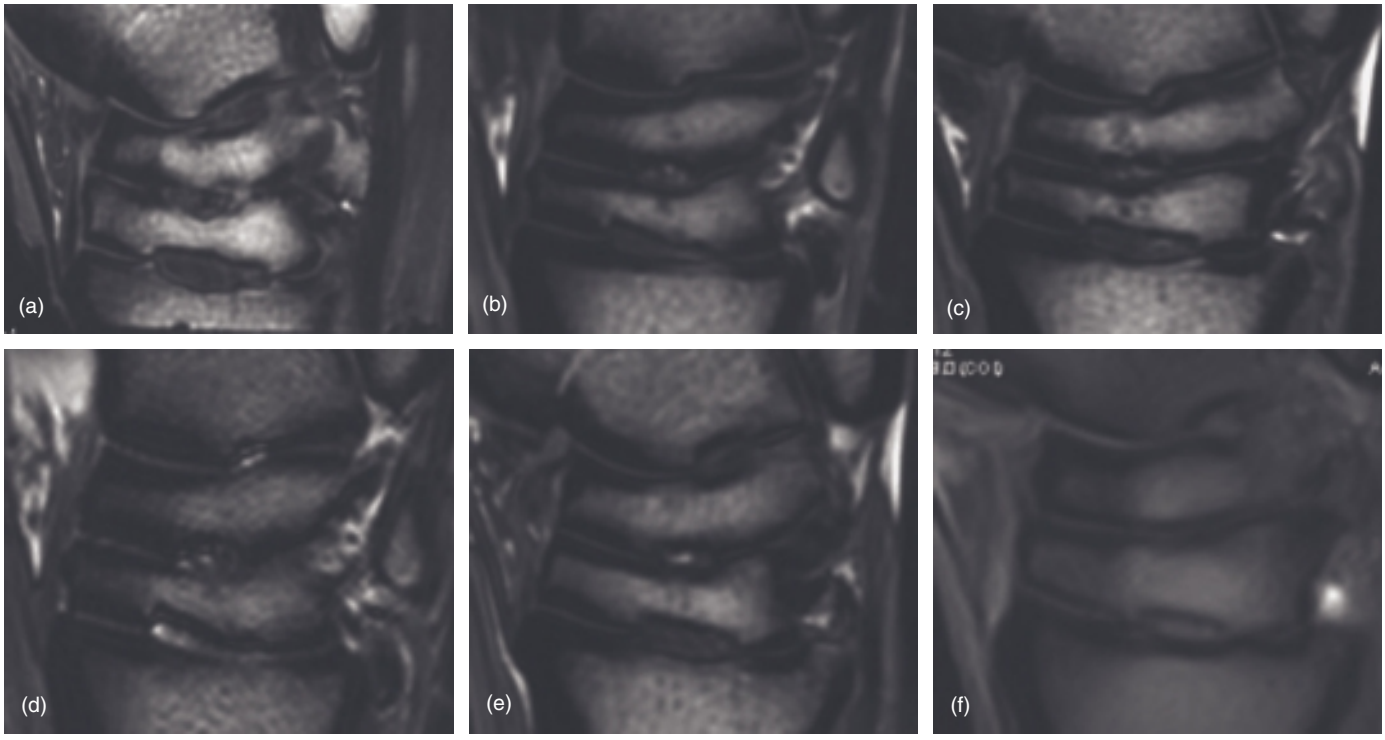

Figure 9.9 (a) Parasagittal T1-weighted gradient-echo high-field MR image of the distal hock joints to show the normal appearance of the intertarsal ligaments between the talus and central tarsal bone, the central and third tarsal bones and the third tarsal and third metatarsal bones. Dorsal is to the left. (b) Parasagittal T1-weighted gradient-echo high-field MR image of the distal tarsal joints of a clinically normal adult horse. Dorsal is to the left. There are small focal areas of high signal intensity within the centrodistal intertarsal ligament. (c) Parasagittal T1-weighted gradient-echo high-field MR image of the distal tarsal joints of a clinically normal adult horse, the same limb as in (b). Dorsal is to the left. There are small focal areas of high signal intensity within the centrodistal intertarsal ligament. (d) Parasagittal T2* gradient-echo high-field MR image of the distal tarsal joints of a clinically normal adult horse, the same limb as in (a), (b) and (c). Dorsal is to the left. There are small focal areas of high signal intensity within each of the intertarsal ligaments, reflecting synovial fluid between fascicles of the ligament. (e) Parasagittal T1-weighted gradient-echo high-field MR image of the distal tarsal joints of a clinically normal adult horse. Dorsal is to the left. There is focal increased signal intensity in the centrodistal intertarsal ligament. (f) Parasagittal T1-weighted gradient-echo low-field MR image of a clinically normal mature horse. The intertarsal ligaments have a homogeneous intermediate signal intensity.

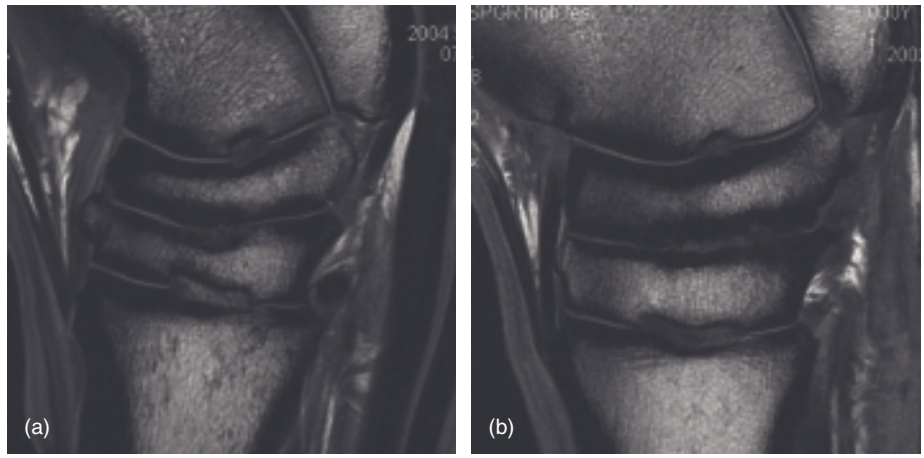

Figure 9.10 (a) Parasagittal 3D T1-weighted gradient-echo high-field MR image of a hock of a clinically normal mature horse. Dorsal is to the left. Note the variability of cortical bone thickness adjacent to the insertions of the intertarsal ligaments between the talus and central tarsal bone, the central and third tarsal bone, and the third tarsal and third metatarsal bone. Compare with Figures 9.9a–e. (b) Parasagittal T1-weighted gradient-echo high-field MR image of a hock of a clinically normal mature horse. Dorsal is to the left. Note the variability of cortical bone thickness adjacent to the insertions of the intertarsal ligaments between the talus and central tarsal bone, the central and third tarsal bone, and the third tarsal and third metatarsal bone. Compare with Figures 9.9a–e.

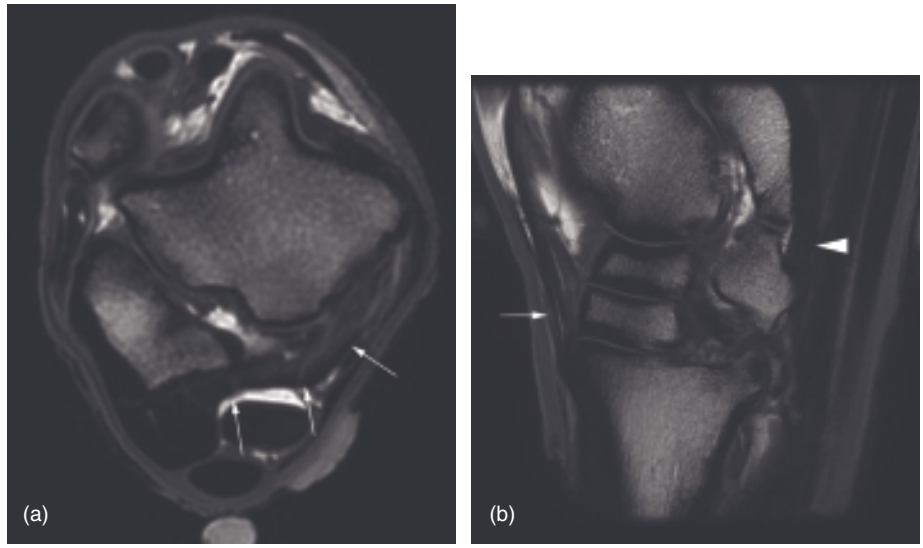

Figure 9.11 (a) Transverse 3D T1-weighted gradient-echo high-field MR image of the tarsus of a normal horse at the level of the third and fourth tarsal bones. Lateral is to the left. There is a broad ligament extending from the plantar axial aspect of the fourth tarsal bone across the plantar aspect of the third tarsal bone (arrows), which attaches to this and the fused first and second tarsal bones. (b) Lateral parasagittal T1-weighted gradient-echo high-field MR image of a normal tarsus. Dorsal is to the left. Dorsally the tendon of fibularis tertius inserts on the proximodorsal aspect of the third metatarsal bone (arrow). Note the broad ligament extending between the plantar aspect of the calcaneus and the fourth tarsal bone (arrow head).

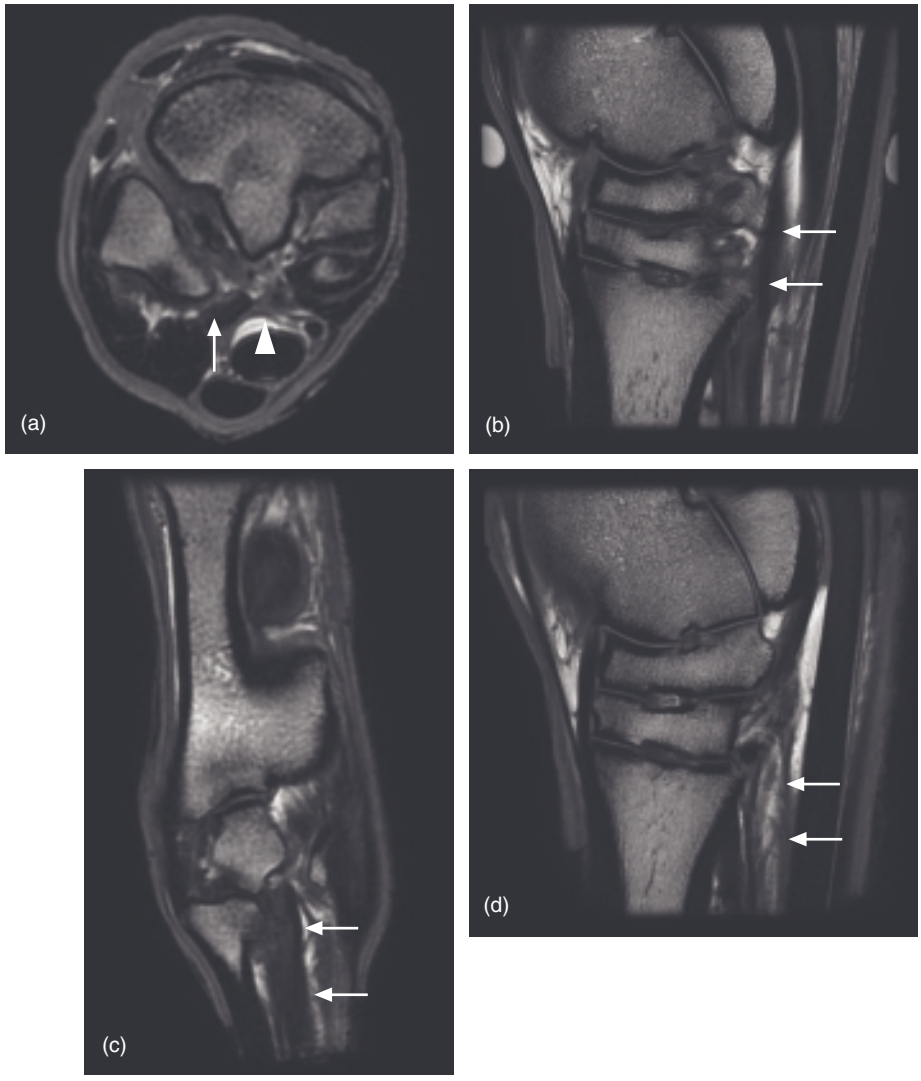

Figure 9.12 (a) Transverse 3D T1-weighted gradient-echo high-field MR image of the tarsus of a normal horse. Lateral is to the left. The accessory ligament of the suspensory ligament originates on the plantar aspect of the fourth tarsal bone (arrow). Plantar and medial to the accessory ligament of the suspensory ligament is the accessory ligament of the deep digital flexor tendon (arrow head). (b) Lateral parasagittal 3D T1-weighted gradient-echo high-field MR image of the same hock as (a). The accessory ligament of the suspensory ligament extends from the plantar aspect of the fourth tarsal bone (arrows). (c) Dorsal 3D T1-weighted gradient-echo high-field MR image of the same hock as in (a) and (b). Lateral is to the left. The accessory ligament of the suspensory ligament extends distally from the plantar aspect of the fourth tarsal bone (arrows). (d) Midline sagittal 3D T1-weighted gradient-echo high-field MR image of the same hock as in (a), (b) and (c). The accessory ligament of the deep digital flexor tendon (arrows) originates from the plantar aspect of the ligament between the calcaneus and the central and third tarsal bones.

The subchondral bone plate has homogeneous low signal intensity, with a regular osteochondral junction and a smooth, but undulating deep border on T1, T2 and PD images. The subchondral bone plate is easily defined from articular cartilage on one border and cancellous bone on the other, with clear margins in higher-resolution 3D scans, although the subchondral bone can be identified even on lower-resolution scans. The osteochondral junction often appears poorly defined, particularly where there is curvature of the articular surface predisposing to partial volume effect. On fat-suppressed images it is not possible to define the subchondral bone plate from cancellous bone.

Cortical bone also has homogeneous low signal intensity, with a regular and clearly defined corticocancellous junction on PD-, T1-, T2- and T2*-weighted images. It is not possible to define a boundary between cortical bone and subchondral bone. The dorsal cortices of the central and third tarsal bones have an irregular contour at ligamentar and capsular insertions. On fat-suppressed images it is not possible to define cortical from cancellous bone.

Cancellous bone has heterogeneous signal intensity on PD-, T1- and T2-weighted images, with a well-defined trabecular pattern on higher-resolution 3D T1 GRE and T2* GRE images. On fat-suppressed images the high signal intensity of fat is suppressed and cancellous bone has a homogeneous low signal intensity that cannot be distinguished from subchondral or cortical bone.

There are interosseous ligaments, connecting the talus and the calcaneus (Figure 9.1), talus and central tarsal bone, the central and third tarsal bones, the central and fourth tarsal bones, the calcaneus and fourth tarsal bone, the third tarsal and third metatarsal bones, and the third tarsal bone and the fused first and second tarsal bones (Figure 9.4). The interosseous ligaments have a somewhat variable appearance within and among horses, depending on the site in the tarsus, slice thickness, image sequence, angle in relation to the static magnetic field (therefore affecting magic angle artefacts) and inherent differences in structure. Some ligaments have a relatively homogeneous intermediate signal intensity, whereas others have heterogeneous signal intensity on PD, 3D T1 GRE and T2* GRE images, with higher signal intensity on 3D T2* GRE images (Figure 9.5). Some ligaments have an obvious fascicular pattern, with bands of low signal intensity running obliquely in the talocalcaneal intertarsal ligament and proximodistally in the other interosseous ligaments, interspersed with bands of high signal intensity. On short τ inversion recovery (STIR) images interosseous ligaments have a heterogeneous, but mostly high signal intensity. The cortical bone at the attachments of the interosseous ligaments should have a smooth endosteal and ligamentar margin, but varies somewhat in thickness, especially in the centrodistal joint.

On the plantar aspect of the tarsus there is a broad ligament extending from the fourth to the third and fused first and second tarsal bones. This has homogeneous low signal intensity in PD-, T1- and T2-weighted images (Figure 9.11a). There are short plantar ligaments extending between the calcaneus and the central and third tarsal bones (Figure 9.12d) and between

the calcaneus and fourth tarsal bone (Figure 9.11b), which have homogeneous low signal intensity in PD-, T1- and T2-weighted images.

Tendons (e.g. superficial and deep digital flexor tendons, fibularis tertius, cranialis tibialis, long digital extensor tendon), ligaments (e.g. plantar ligaments, collateral ligaments of the tarsocrural joint, dorsal tarsal ligaments) and joint capsules generally have homogenous low signal intensity in all image sequences. Fluid in the surrounding sheaths has high signal intensity on PD, T2, T2* GRE and STIR images. The cunean bursa can be difficult to identify in a normal horse, although on T2 and PD images it may be possible to visualize small amounts of fluid near the proximal and distal extents (see Figure 17.6). Proximally in the tarsus, the tibialis cranialis has mixed low and intermediate signal intensity due to the presence of muscle tissue (Figure 9.6b). There are paired medial and lateral collateral ligaments of the tarsocrural joint; the deep and superficial branches are oriented differently. The deep branches usually have an intermediate signal intensity, whereas the superficial branch has uniform low signal intensity. The plantar metatarsal ligament is comprised of a number of fascicles, separated in some horses by lines of slightly higher signal intensity. In some horses it has multiple small foci of increased signal intensity. The SL has a fairly substantial accessory ligament that originates on the plantar aspect of the fourth tarsal bone and is of uniform low signal intensity (Figures 9.12a–c). This is in contrast to the architecture of the SL per se, which is of mixed low and intermediate signal intensity proximally, becoming bilobed further distally, with acentric areas of high signal intensity surrounded by tissue of uniformly low signal intensity. The ALDDFT is a much thinner structure than in forelimbs and is more variable in size between horses (Figure 9.12a). It has intermediate signal intensity and extends distally from the plantar ligament between the calcaneus and the fourth tarsal bone (Figure 9.12d).

In images without fat suppression there are focal areas of heterogeneous or homogeneous high signal intensity on the dorsal aspect of the tarsocrural joint, the plantar distal aspect of the tibia and the dorsal aspect of the deep digital flexor tendon representing fatty tissue (Figures 9.1, 9.3 and 9.5). This is most obvious on T1-weighted images, where there is contrast between the high signal intensity of the fat and low signal intensity of synovial fluid. In fat-suppressed images these tissues have intermediate signal intensity.

There are substantial interosseous ligaments between the second and third, and fourth and third metatarsal bones, which have intermediate signal intensity (Figures 9.6g and h, and 9.7f), and the fascicles may be separated by hyperintense synovial fluid in T2-weighted sequences. Dorsal and palmar facets on the proximal aspect of the second and fourth metatarsal bones articulate with the third metatarsal bone (Figure 9.6g).

INCIDENTAL FINDINGS IN THE DISTAL ASPECT OF THE TARSUS OF NORMAL HORSES

In 20 tarsi considered to be clinically normal, 80% had abnormalities visible on MR images [6] (Figures 9.13–15). Seven tarsi had a mildly irregular or poorly defined osteochondral junction (Figure 9.14); eight tarsi had a minor

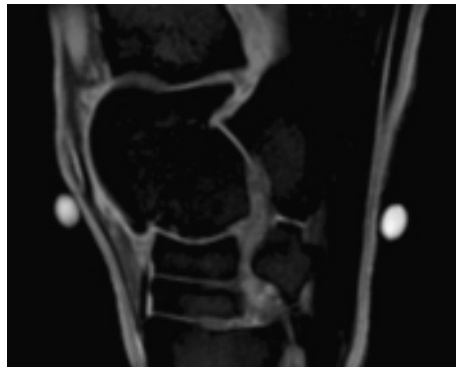

Figure 9.13 Lateral parasagittal fat-saturated T1-weighted gradient-echo high-field MR image of a clinically normal mature horse.

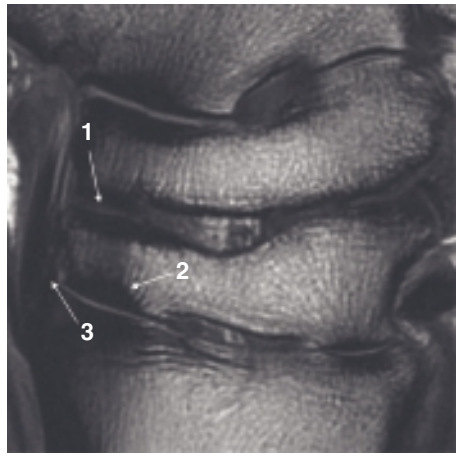

Figure 9.14 Midline sagittal 3D T1-weighted gradient-echo high-field MR image of the distal aspect of a tarsus from a mature horse with no history of hind limb lameness, which had undergone low-level exercise. Dorsal is to the left and plantar to the right. There is a diffuse reduction in cartilage signal intensity and an irregular, poorly defined osteochondral junction dorsally in the centrodistal joint (1). There is also an irregular deep border to the subchondral bone plate in the central and third tarsal bones (2), and a small osteophyte on the proximodorsal aspect of the third metatarsal bone (3).

focal osteochondral junction defect; four tarsi had a small focal increase in subchondral signal intensity; one tarsus had a moderate focal subchondral abnormality; one tarsus had abnormally increased intertarsal ligament signal intensity (Figure 9.15); seven tarsi had a focal increase or reduction in articular cartilage signal intensity (Figure 9.15); seven tarsi had diffuse reduced cartilage signal intensity (Figure 9.14); seven tarsi had mild osteophyte formation (Figure 9.14); five tarsi had mild new bone formation at the dorsal capsular attachments, altering the dorsal contour of central tarsal and, or third tarsal bones; four tarsi had a mildly abnormal areas of low signal intensity in the cancellous bone of the central and third tarsal bones with trabeculae still visible dorsally; and two tarsi had large cystic lesions in the third tarsal bone.

[232]

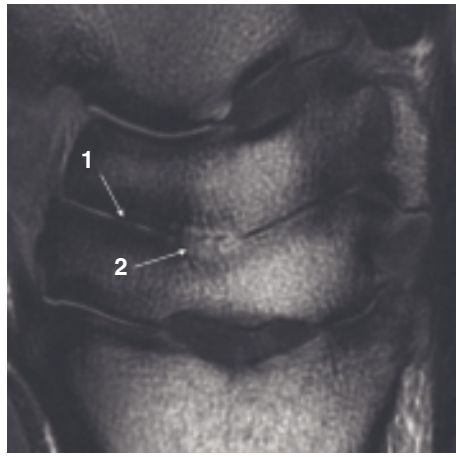

Figure 9.15 Midline sagittal 3D T1-weighted gradient-echo high-field MR image of the distal aspect of a tarsus from a mature horse with no history of hind limb lameness, which had undergone low-level exercise. Dorsal is to the left and plantar to the right. There is a focal reduction in cartilage signal in the centrodistal joint (1), and an abnormal increase in centrodistal ligament signal intensity (2).

Normal subchondral bone thickness pattern in the distal tarsus

In tarsi from skeletally mature (>5 years of age) horses with no history of hind limb lameness, exercised at a low level, a repeatable mediolateral subchondral thickness pattern was seen [1]. Low-level exercise was defined as hacking and unaffiliated competition. On the proximal aspect of the central tarsal bone, medial and lateral subchondral bone thickness was significantly greater than midline ($p < 0.001$). On the distal aspect of the central tarsal bone, the distal aspect of the third tarsal bone and the proximal aspect of the third metatarsal bone, lateral subchondral bone thickness was significantly greater than medially ($p \leq 0.017$) [5].

Effects of age and exercise on the osseous structures of the distal aspect of the tarsus

Effect of age

There were no significant mediolateral differences in subchondral thickness in 11-day old (neonatal) tarsi [6, 8]. In 6- to 9-month-old tarsi the mediolateral subchondral bone thickness pattern mimicked that of mature horses exercised at a low level, with lateral thickness significantly greater than medial ($p \leq 0.004$). The subchondral bone thickness pattern continued to vary with increasing age. There was no distinct mediolateral pattern in the oldest groups.

Effect of exercise intensity

In elite competition horses and horses that underwent high-intensity race training, subchondral bone thickness was greater medially in the CD joint and laterally in the TMT joint, compared with general purpose riding horses

[2]. Subchondral bone thickness was significantly greater on the proximal aspect of the third metatarsal bone than at other sites.

In high-field MR images normal subchondral and cortical bone have homogeneous low signal intensity on both T1 GRE and T2* GRE images, which agreed with the results from low-field MRI of the equine tarsus [4] and our clinical experience using a 0.27 T magnet (Figures 9.16a and b). Using a 0.064 T system, cancellous bone in the equine tarsus had high signal intensity on T1-weighted images due to the fat content of the bone marrow, and intermediate signal intensity on T2-weighted images [4]. A trabecular pattern was not described; this may be due to the poor resolution of their images produced with a low-field system. Our experience with a low-field 0.27 T magnet is that detailed trabecular architecture cannot be reliably assessed (Figures 9.16a and b). High-field imaging allows clear definition of trabecular architecture in cancellous bone, with heterogeneous signal intensity. Trabecular bone has low signal intensity, and fat in the bone marrow filling the trabecular spaces has high signal intensity. In horses with a history of tarsal pain the endosteal surface of the subchondral bone may be more irregular and the normal thickness pattern may be lost irrespective of age and exercise history [9].

In high-field images interosseous ligaments have heterogeneous signal intensity on both T1 GRE and T2* GRE images. In contrast, ligaments had low signal intensity on both T1- and T2-weighted images using a low-field imaging system [4]. Different imaging parameters were used that could have affected the signal intensity and contrast. In a low-field 0.27 T magnet, signal

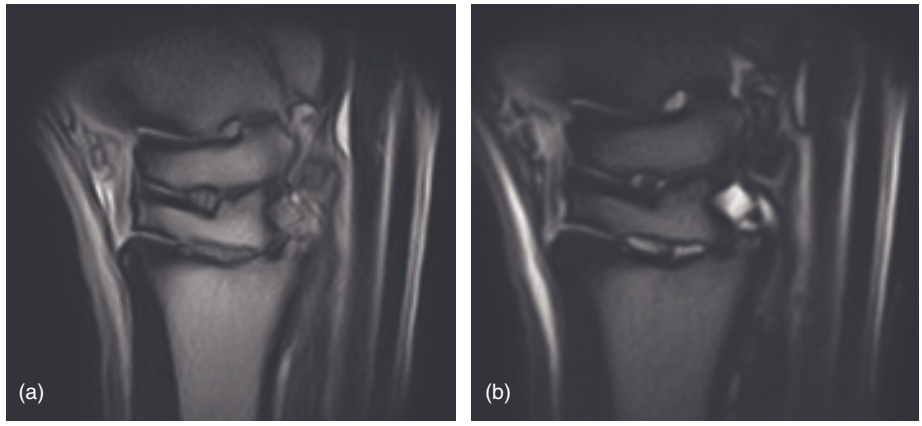

Figure 9.16 (a) Sagittal T1-weighted gradient-echo low-field MR image of the distal tarsal joints of a normal mature horse. Dorsal is to the left. The interosseous ligaments of the talocentral and tarsometatarsal joints have relatively uniform intermediate signal intensity. The interosseous ligament of the centrodistal joint has heterogeneous signal intensity. The articular cartilage has intermediate signal intensity. The endosteal (deep) surface of the subchondral bone is smooth in all bones. (b) Sagittal T2* gradient-echo low-field MR image of the distal hock joints of a normal mature horse. Dorsal is to the left. The interosseous ligaments of the centrodistal and tarsometatarsal joints have relatively uniform low signal intensity, surrounded by a region of high signal intensity. The articular cartilage has intermediate signal intensity. The endosteal (deep) surface of the subchondral bone is smooth in all bones.

intensity of the interosseous ligaments varies with sequence type (Figures 9.16a and b).

In this study, mild interosseous ligament abnormalities were seen in all groups of tarsi from clinically normal horses. More severe abnormalities have been seen in horses with tarsal pain [6, 7]. We speculate that interosseous ligament injury may create low-grade instability and predispose to the development of osteoarthritis.

Lesions affecting bone, cartilage and ligaments detected on MR images have been confirmed by gross postmortem examination and histology [5, 7]. Homogeneous increased signal intensity of the intertarsal ligaments and loss of normal ligament shape on both T1- and T2-weighted images was associated with loss of normal shape, definition and arrangement of ligament fibres seen histologically. An increased area of low signal intensity in adjacent bone on MR images was associated with increased dense bone histologically. Loss of joint space definition with some remaining irregular regions of high signal intensity on MR images was associated with cartilage erosion and loss of joint space, with some remaining pockets of degenerate cartilage on gross postmortem examination and histology.

It appears that structural abnormalities of the tarsus can be seen in clinically normal horses, and therefore interpretation of the clinical significance of minor changes in lame horses may not be easy. Ideally, comparison with the contralateral limb should be performed. Knowledge of normal anatomy and variations with age and exercise history is important for accurate interpretation.

REFERENCES

[1] Branch MV, Murray RC, Dyson SJ, Goodship AE. Is there a characteristic distal tarsal subchondral bone plate thickness pattern in horses with no history of hind limb lameness? *Equine Vet J* 2005; **37**: 450–5.

[2] Murray R, Branch M, Dyson S, Parkin T, Goodship A. How does exercise intensity and type affect equine distal tarsal subchondral bone thickness? *J Appl Physiol* 2007; **102**: 2194–200.

[3] Branch M, Murray R, Dyson S, Goodship A. Magnetic resonance imaging of the equine tarsus. *Clin Techniques Equine Pract* 2007; **6**: 96–102.

[4] Blaik MA, Hanson RR, Kincaid SA, Hathcock JT, Hudson JA, Baird DK. Low-field magnetic resonance imaging of the equine tarsus: normal anatomy. *Vet Radiol Ultrasound* 2000; **41**: 131–41.

[5] Whitton RC, Murray RC, Buckley C, Goodship AE, Lekeux P. An MRI study of the effect of treadmill training on bone morphology of the central and third tarsal bones of young thoroughbred horses. *Equine Vet J* 1999; **Suppl 30**: 258–61.

[6] Branch M. How is adaptive change related to pathology in the equine distal tarsal osteochondral unit? PhD thesis, University of London, 2005.

[7] Branch MV, Murray RC, Dyson SJ, Goodship AE. Magnetic resonance imaging of distal tarsal osteochondral structure: normal variation or pathological change? *Workbook from the American Association of Equine Practitioners, Focus on Joints Meeting, 22-24 July 2004*, pp. 28–41.

[8] Murray R, Blunden T, Branch M, Dyson S, Goodship A. Age-related changes in the structure of the equine osteochondral unit. *Am J Vet Res* 2009; **70**: 30–6.

[9] Branch M, Murray R, Dyson S, Goodship A. Alteration of distal tarsal subchondral bone thickness in horses with tarsal pain. *Equine Vet J* 2007; **39**: 101–5.

Chapter 10
The stifle

Rachel Murray, Natasha Werpy and Simon Collins

INTRODUCTION

Magnetic resonance imaging (MRI) is considered a gold standard for diagnostic imaging of the human knee, but there have been few publications covering MRI of the equine stifle [1]. The stifle includes three joints with a varying degree of intercommunication: the medial and lateral femorotibial and the femoropatellar joint [2]. This region includes the cranial and caudal cruciate ligaments, the medial and lateral menisci and meniscal ligaments, the collateral ligaments of the stifle joint and distal patellar ligaments. Within the stifle joint, the articular cartilage is thick compared with other locations within the horse and therefore it may be easier to visualize articular cartilage in the stifle than at some other locations. Currently, there are very few MR systems being used to image the stifle joint and they are limited to a dedicated equine low-field system (Universal Medical Systems) and a high-field system (Siemens Magnetom Espree) [3, 4]. Both systems require the limb to be positioned in extension for imaging the stifle joint, which places the femur and tibia in greater longitudinal alignment compared with their relationship in the standing horse. Imaging under high field ideally requires the patient to be a long-legged, thin, small horse.

PROTOCOLS FOR STUDY PLANNING

Two considerations should be made when planning sagittal images for a stifle study. If the primary area of interest is the cranial cruciate ligament, then the slices can be oriented such that the entire cranial cruciate ligament will be present in one sagittal image. This allows evaluation of the continuity of ligament fibres in one image as opposed to trying to follow them through multiple images. However, the slice positioning required to produce this image will be oblique to the longitudinal axis of the bones. Therefore, the images will not represent the true sagittal plane of the joint. To produce true sagittal images, the margins of the osseous structures should be used for slice positioning on transverse images. Sagittal images are produced by orienting slices parallel to the medial and lateral margins of the femur and tibia at the level of the collateral ligaments (Figure 10.1). Positioning of sagittal slices using frontal images is done by orienting slices parallel to the longitudinal axis of the femorotibial joint. Although the extensor fossae of femur and tibia are parallel with the longitudinal axis of the limb, rotation of the limb can cause confusion when planning a study. The lateral position

Equine MRI, edited by Rachel C. Murray.

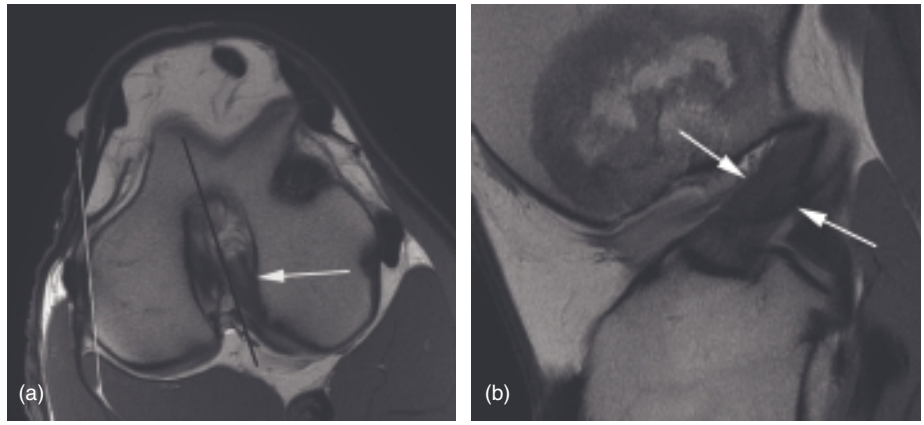

Figure 10.1 Transverse (a) and sagittal (b) images demonstrating the technique for accurate slice positioning when planning sagittal images for a stifle study. The slices can be oriented with the margins of the cranial cruciate ligament or in a true sagittal plane to the joint. To produce true sagittal images, the margins of the osseous structures should be used for slice positioning on transverse images. Sagittal images are produced by orienting slices parallel to the medial and lateral margins of the femur and tibia at the level of the collateral ligaments on the transverse images (white line on (a)). Positioning of sagittal slices using frontal images is done by orienting slices parallel to the longitudinal axis of the limb. This will show the cranial cruciate ligament in multiple sagittal images, making it somewhat more challenging to evaluate fibre continuity. To produce sagittal images that include a complete longitudinal image of the cranial cruciate ligament (white arrows on (b)), slices should be angled from craniomedial to caudolateral beginning at the intercondylar eminence of the tibia parallel to the margins of the cranial cruciate ligament ending at the intercondylar fossa of the femur (black line on (a)). Multiple abnormalities are present in the distal aspect of the femur on the sagittal image.

of the extensor fossae in conjunction with rotation of the limb can obscure the normal landmarks. In this case, the osseous margins located caudal to the extensor fossa in the region of the collateral ligaments should be used to orient the slices. To produce sagittal images that include a complete longitudinal image of the cranial cruciate ligament, slices should be angled from caudolateral in the intercondylar fossa of the femur craniomedial along the margin of the intercondylar eminence of the tibia, visualizing the ligament margins through multiple transverse images. If both orientations are desired and time allows, a full true sagittal series of images can be obtained as well as a limited number of oblique sagittal images for the cranial cruciate ligament. Positioning of sagittal slices using frontal images is done by orienting slices parallel to the longitudinal axis of the femorotibial joint.

Frontal images are produced by orienting slices parallel to the longitudinal axis of the femorotibial joint on sagittal images. Frontal images are produced by orienting the slices perpendicular to the caudal margin of medial and lateral femoral condyles distal to the origins of the collateral ligaments on transverse images. To produce a frontal image with the attachments of the cranial tibial meniscal ligaments on the tibia in one image, the slices must be oriented parallel to the ligament margins on transverse images (Figure 10.2). The caudal margin of the femoral condyles and the cranial tibial meniscal ligament margins may not be parallel. In this circumstance

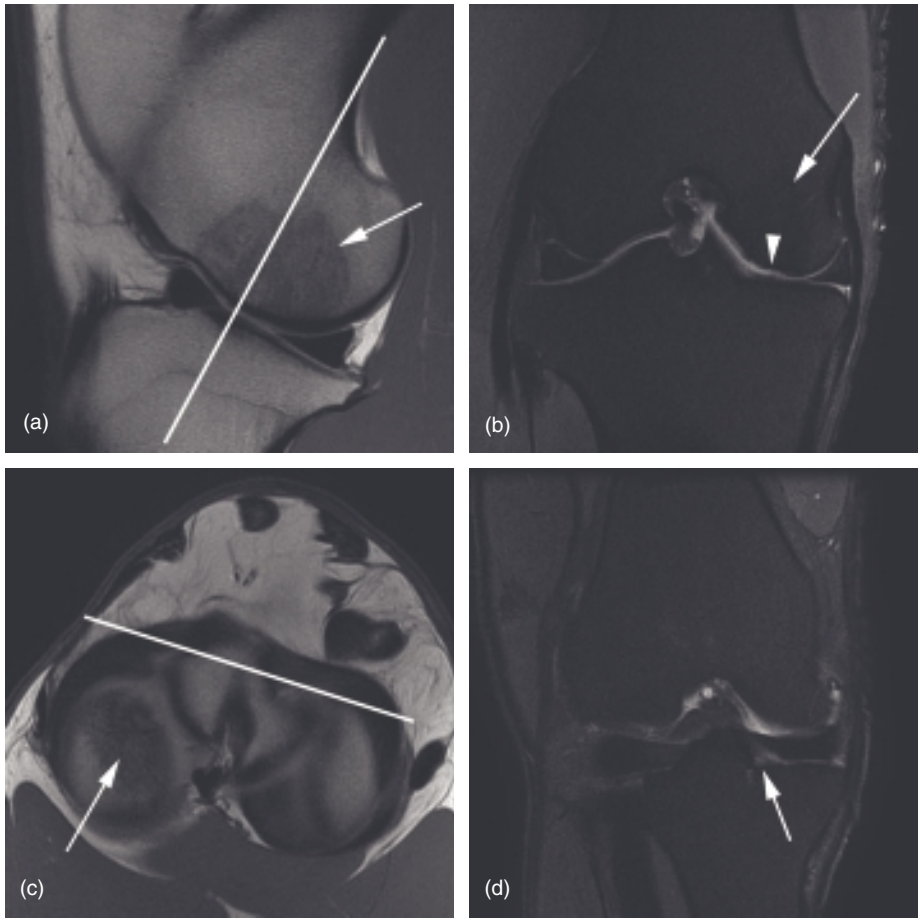

Figure 10.2 Positioning frontal plane images in the stifle. (a) Sagittal proton density image; (b) frontal fat suppressed proton density image positioned at the centre of the joint; (c) transverse proton density image; (d) frontal fat-suppressed proton density image at the cranial aspect of the joint. If the primary site of interest is the articular surface of the femorotibal joint, frontal plane images are produced by orienting slices perpendicular to the distal articular surface of the femur and proximal articular surface tibia on sagittal images (a). This increases the conspicuity of articular cartilage and subchondral bone lesions (arrowhead) in this region (b). On the transverse images positioning slices parallel to the attachments of the cranial tibial meniscal ligaments on the tibia (c) allows comparison of the medial and lateral ligaments and their insertions (d). A partial thickness tear of the medial cranial tibial meniscal ligament and stress-related bone resorption of the insertion on the tibia can be clearly identified (arrowhead on (d)). Sclerosis is identified by arrows on images (a)–(c).

a compromise can be made between the two angles, or the area of greater interest can be used for study planning. It is important to remember that because the medial trochlear ridge is larger than the lateral trochlear ridge, the trochlear ridges should not be used to determine the longitudinal or transverse axes of the limb.

Using frontal images, transverse images are produced by orienting slices parallel to the joint space (Figure 10.3). A single slice should be positioned such that it includes both menisci and cranial tibial meniscal ligaments. This is done to allow evaluation of the transition from the meniscus to the cranial tibial meniscal ligament, as well as fibre continuity in the ligament as it

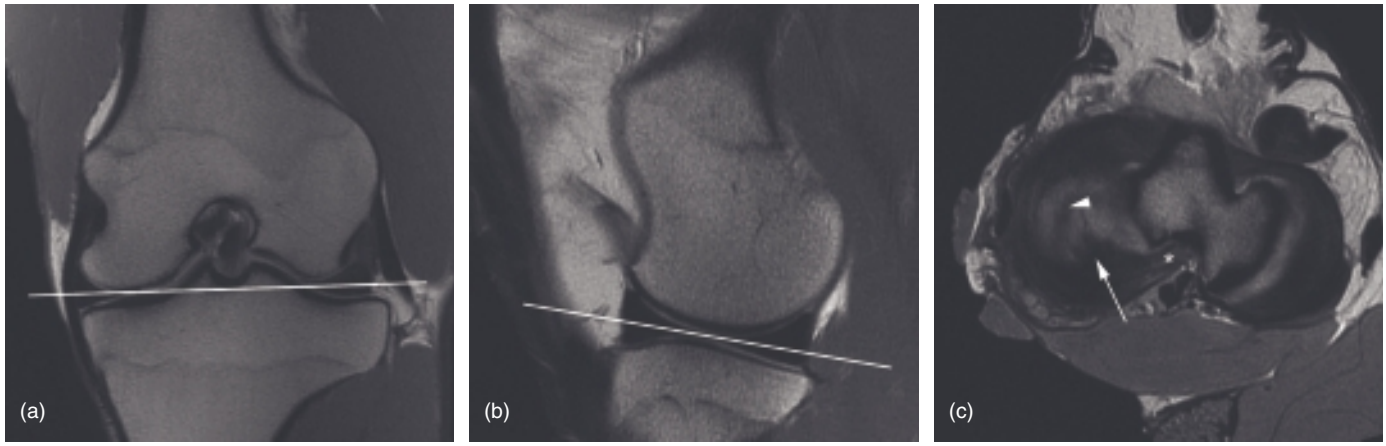

Figure 10.3 Positioning of transverse images. (a) Frontal plane proton density image; (b) sagittal plane proton density image; (c) transverse plane proton density image. Transverse images are produced by orienting slices parallel to the joint space on frontal (a) and sagittal (b) images. On the transverse image (c) there is a large meniscal tear resulting in loss of meniscal tissue in the joint space (arrowhead). Adjacent to the tear the meniscus has severely frayed axial margins (arrow). The caudal ligament of the medial meniscus can be identified inserting on the tibia (asterisk).

inserts on the tibia. Transverse images are produced by orienting slices parallel to the joint space on sagittal images. Disregard the appearance of the joint at the intercondylar eminence of the tibia and select sagittal images that show the cranial and caudal horns of the menisci as individual triangles with a thin linear connection. A sagittal image that shows these landmarks should be selected in the medial half of the joint as well as one in the lateral half of the joint. The slices should be oriented such that they will transect the cranial and caudal horns of the menisci into equally sized and shaped proximal and distal halves.

The degree of extension of the limb required to position the stifle joint in the magnet will vary between horses and alter the relationship between the femur and the tibia. When planning a stifle study, the degree of extension must be evaluated and when necessary slice positioning should be altered so that the structures of primary interest are well visualized.

MRI ANATOMY

The description given within this chapter is based on our experience with MRI of the stifle, previous descriptions of the MRI anatomy of the stifle, and specifically the anatomy and normal variation seen within nine immature ponies and nine mature horse cadaver limbs, which were compared with the macroscopic examination [5].

Adult (Figures 10.4–10.18)

The normal ligaments and menisci of the stifle should have homogeneous low signal intensity in all images sequences. However, magic angle effects may lead to increased signal intensity within normal structures (Figure 10.4). The medial collateral ligament appears more lobulated and generally has a

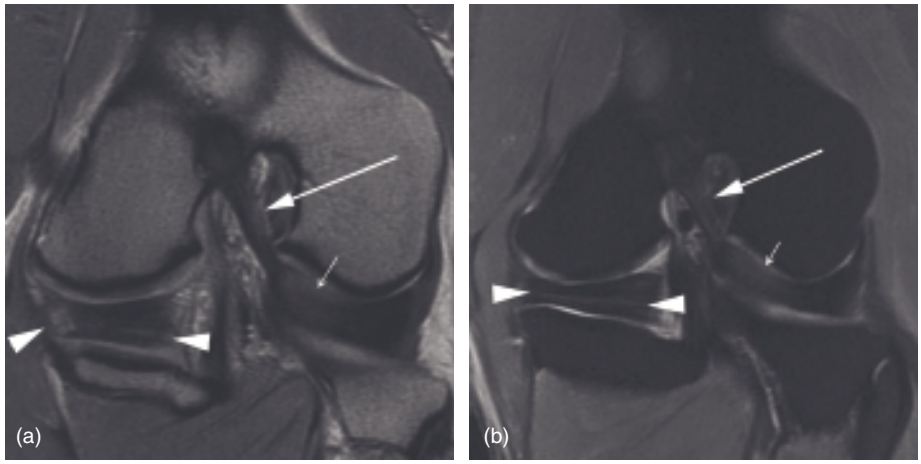

Figure 10.4 Frontal proton density (a) and fat-saturated proton density (b) images from a horse with lameness localized to the stifle. The normal mensicofemoral ligament (large arrow) can be identified extending from the caudal horn of the lateral meniscus proximally to the caudal aspect of the intercondylar fossa of the femur. There is a large tear in the medial margin of the medial meniscus. This lesion continues axially as a horizontal tear in the caudal horn of the medial meniscus (arrowheads). Magic angle effect can be identified in the caudal horn of the lateral meniscus (small arrow); this sequence was acquired with a time of echo of 30 ms.

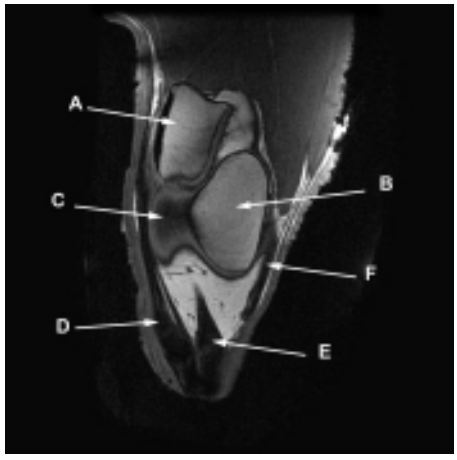

Figure 10.5 Frontal 3D T1 gradient echo image of the cranial aspect of the stifle. **A**, patella; **B**, medial femoral trochlea; **C**, lateral femoral trochlea; **D**, lateral patellar ligament; **E**, intermediate (middle) patellar ligament; **F**, medial patellar ligament.

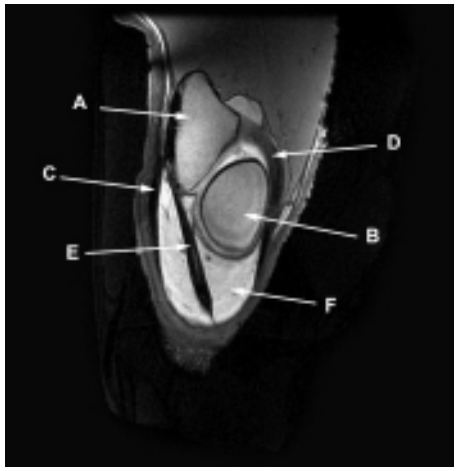

Figure 10.6 Frontal 3D T2* GRE image of an adult stifle at a similar location to Figure 10.6. **A**, patella; **B**, medial femoral trochlea; **C**, lateral patellar ligament; **D**, medial patellar ligament showing origin on the medial aspect of the patellar; **E**, intermediate (middle) patellar ligament showing origin on the dorsodistal aspect of the patellar; **F**, subcutaneous fat.

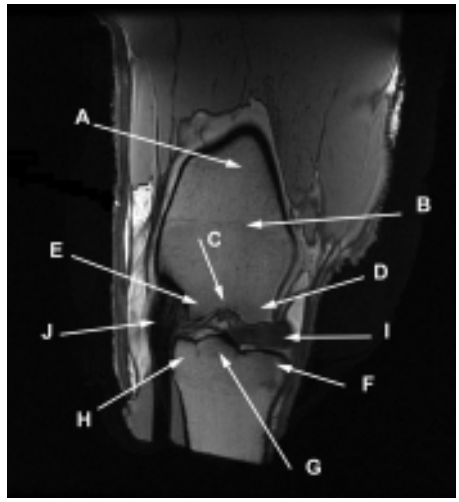

Figure 10.7 Frontal 3D T2* GRE image of an adult stifle. **A**, diaphysis of femur; **B**, fused growth plate; **C**, intercondylar notch (fossa); **D**, medial femoral condyle; **E**, lateral femoral condyle; **F**, medial tibial condyle; **G**, intercondylar eminence of the tibia; **H**, lateral tibial condyle; **I**, medial meniscus; **J**, long digital extensor tendon showing origin in the extensor fossa of the lateral femoral condyle.

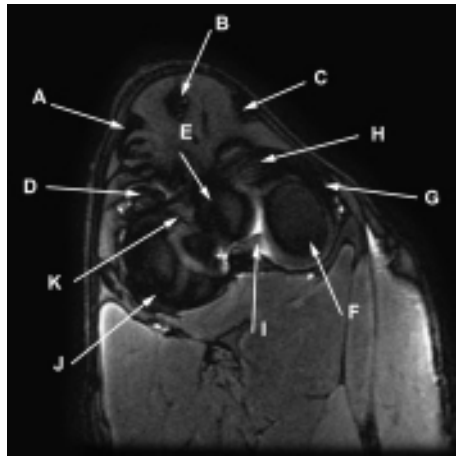

Figure 10.8 Transverse STIR image of an adult stifle. **A**, lateral patellar ligament; **B**, intermediate (middle) patellar ligament; **C**, medial patellar ligament; **D**, long digital extensor tendon; **E**, medial intercondylar eminence of the tibia; **F**, medial femoral condyle; **G**, medial meniscus; **H**, cranial tibial ligament of the medial meniscus; **I**, caudal tibial ligament of the medial meniscus; **J**, lateral meniscus; **K**, cranial tibial ligament of the lateral meniscus.

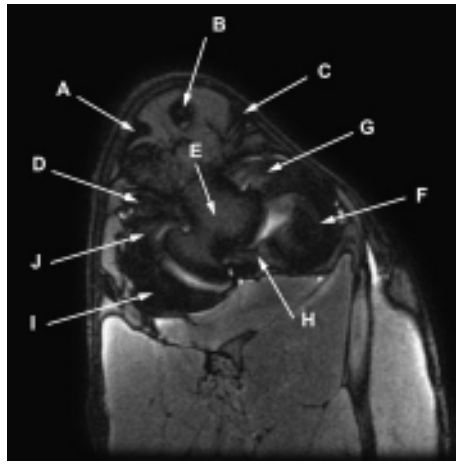

Figure 10.9 Transverse STIR image of an adult stifle. **A**, lateral patellar ligament; **B**, intermediate (middle) patellar ligament; **C**, medial patellar ligament; **D**, long digital extensor tendon; **E**, tibia; **F**, medial meniscus; **G**, cranial tibial ligament of the medial meniscus; **H**, caudal tibial ligament of the medial meniscus; **I**, lateral meniscus; **J**, cranial tibial ligament of the lateral meniscus.

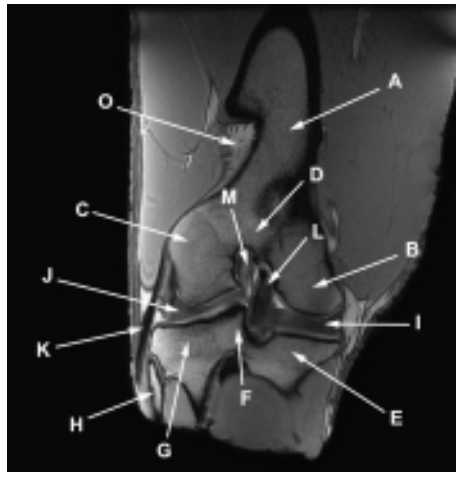

Figure 10.10 Frontal 3D T2* GRE image of an adult stifle. **A**, shaft (diaphysis) of femur; **B**, medial femoral condyle; **C**, lateral femoral epicondyle; **D**, intercondylar notch (fossa); **E**, medial tibial condyle; **F**, lateral intercondylar eminence and popliteal notch of the tibia; **G**, lateral tibial condyle; **H**, fibula; **I**, medial meniscus; **J**, lateral meniscus; **K**, lateral collateral ligament of the femorotibial joint showing origin on the lateral femoral epicondyle and its insertion on the lateral fibula condyle; **L**, caudal cruciate ligament showing origin on the intercondylar area of the medial femoral condyle and its insertion on the popliteal tibial notch; **M**, cranial cruciate ligament showing its origin on the intercondylar area of the lateral femoral condyle; **O**, origin of the superficial digital flexor tendon on the supracondylar femoral fossa.

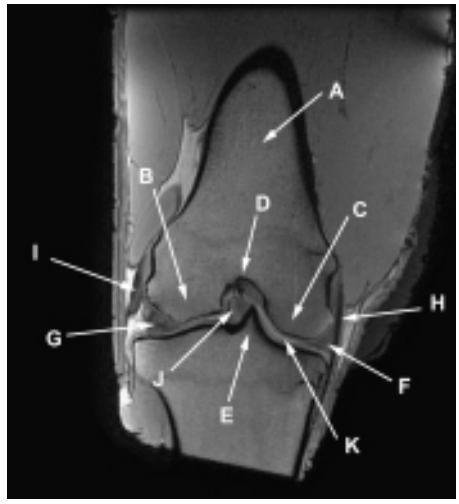

Figure 10.11 Frontal 3D T2* GRE image of an adult stifle. **A**, shaft (diaphysis) of femur; **B**, medial femoral condyle; **C**, lateral femoral epicondyle; **D**, intercondylar notch (fossa); **E**, medial intercondylar eminence; **F**, medial meniscus; **G**, lateral meniscus; **H**, medial collateral ligament of the femorotibial joint showing origin on the medial femoral epicondyle and its insertion on the medial tibial condyle; **I**, lateral collateral ligament of the femorotibial joint showing origin on the lateral femoral; **J**, cranial cruciate ligament showing its insertion on the lateral aspect of the tibial intercondylar eminence; **K**, femorotibial joint showing articular cartilage of the femur and tibia separated by synovial fluid.

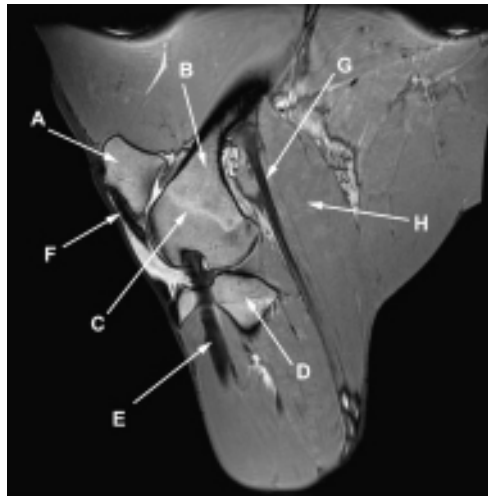

Figure 10.12 Sagittal 3D T2* GRE image of an adult stifle acquired using a custom-built jig to simulate weight bearing. **A**, patella; **B**, shaft (diaphysis) of femur; **C**, fused femoral growth; **D**, lateral tibial condyle; **E**, long digital extensor tendon showing origin in the extensor fossa of the lateral femoral condyle; **F**, lateral patellar ligament; **G**, superficial digital flexor tendon showing origin on the supracondylar femoral fossa; **H**, gastrocnemius muscle.

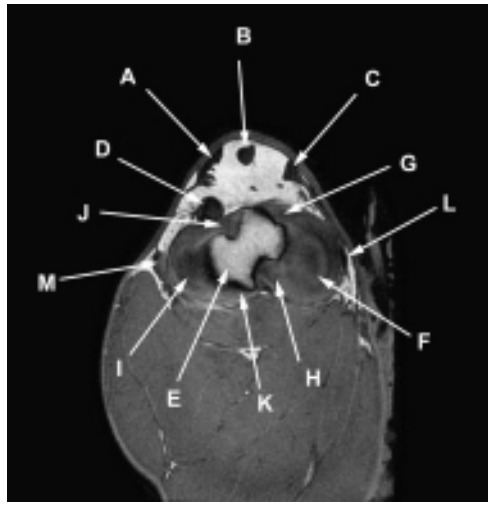

Figure 10.13 Transverse 3D T1 GRE image of an adult stifle acquired using a custom-built jig to simulate weight bearing. **A**, lateral patellar ligament; **B**, intermediate (middle) patellar ligament; **C**, medial patellar ligament; **D**, long digital extensor tendon; **E**, tibia; **F**, medial meniscus; **G**, cranial tibial ligament of the medial meniscus; **H**, caudal tibial ligament of the medial meniscus; **I**, lateral meniscus; **J**, cranial tibial ligament of the lateral meniscus; **K**, caudal tibial ligament of the lateral meniscus; **L**, medial collateral ligament of the femorotibial joint; **M**, lateral collateral ligament of the femorotibial joint.

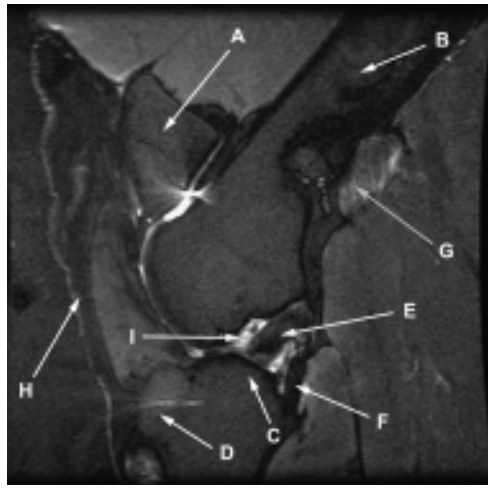

Figure 10.14 Sagittal STIR image of an adult stifle. **A**, patella; **B**, shaft (diaphysis) of femur; **C**, intercondylar region of the tibia; **D**, tibial tuberosity; **E**, cranial cruciate ligament showing insertion on the central intercondylar area of the tibia; **F**, caudal cruciate ligament showing insertion in the popliteal notch of the tibia; **G**, origin of the superficial digital flexor tendon in the supracondylar femoral fossa; **H**, intermediate (middle) patella ligament; **I**, synovial fluid within the femorotibial joint capsule.

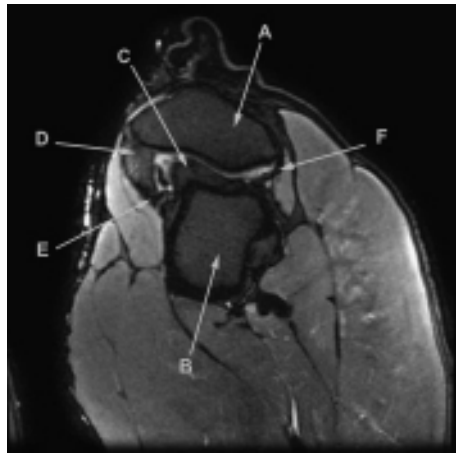

Figure 10.15 Transverse STIR image of an adult stifle. **A**, patella; **B**, shaft (diaphysis) of femur; **C**, proximal aspect of medial femoral trochlea; **D**, medial patellar fibrocartilage; **E**, medial femoropatellar ligament with origin on the medial aspect of the femur; **F**, lateral femoropatellar ligament with origin on the lateral aspect of the femur, inserting on the dorsolateral aspect of the patellar.

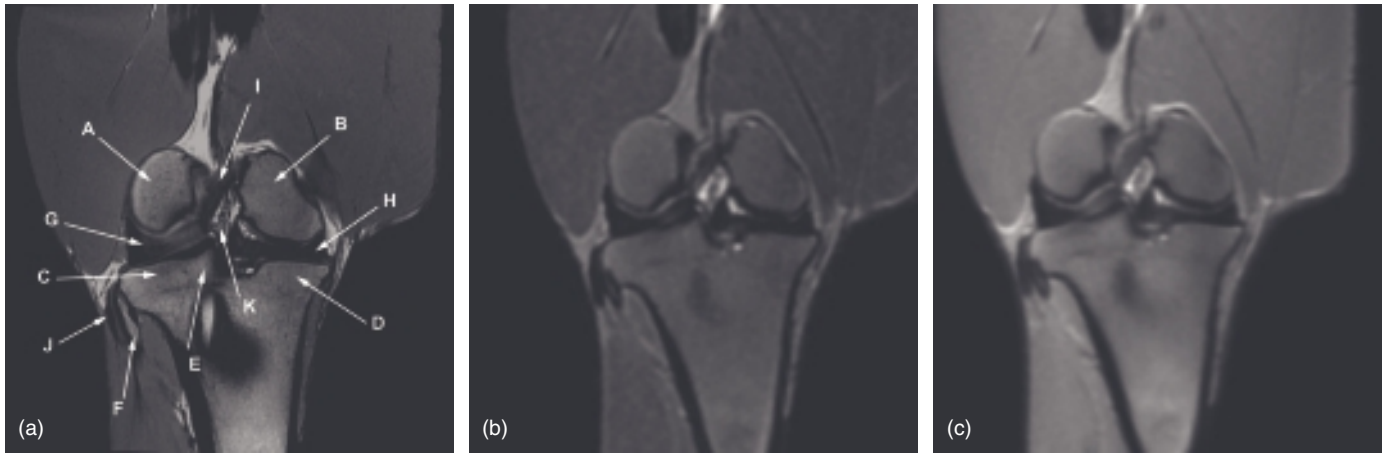

Figure 10.16 (a) Frontal 3D T2* GRE image of an adult stifle. **A**, lateral femoral condyle; **B**, medial femoral condyle; **C**, lateral tibial condyle; **D**, medial tibial condyle; **E**, tibial intercondylar eminence; **F**, fibula; **G**, lateral meniscus; **H**, medial meniscus; **I**, caudal femorominiscal ligament; **J**, lateral collateral ligament of the stifle (femorotibial) joint showing insertion on the fibula condyle; **K**, cranial cruciate ligament. (b) T2 fast spin-echo image of the same region. (c) Proton density image of the same region.

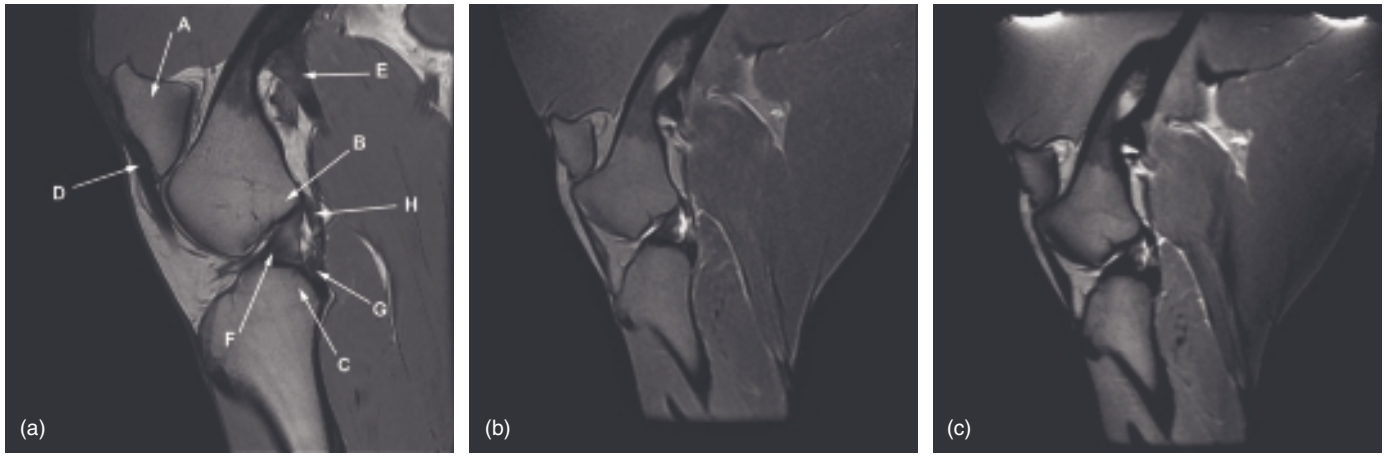

Figure 10.17 (a) Sagittal 3D T2* GRE image of an adult stifle. **A**, patella; **B**, intercondylar femoral notch (fossa); **C**, tibial intercondylar eminence and popliteal notch; **D**, intermediate (middle) patellar ligament showing origin on the dorsodistal aspect of the patellar; **E**, origin of the superficial digital flexor tendon on the supracondylar femoral fossa; **F**, cranial cruciate ligament; **G**, caudal cruciate ligament showing its insertion on the popliteal tibial notch; **H**, caudal meniscofemoral ligament. (b) T2 fast spin-echo image of the same region. (c) Proton density image of the same region.

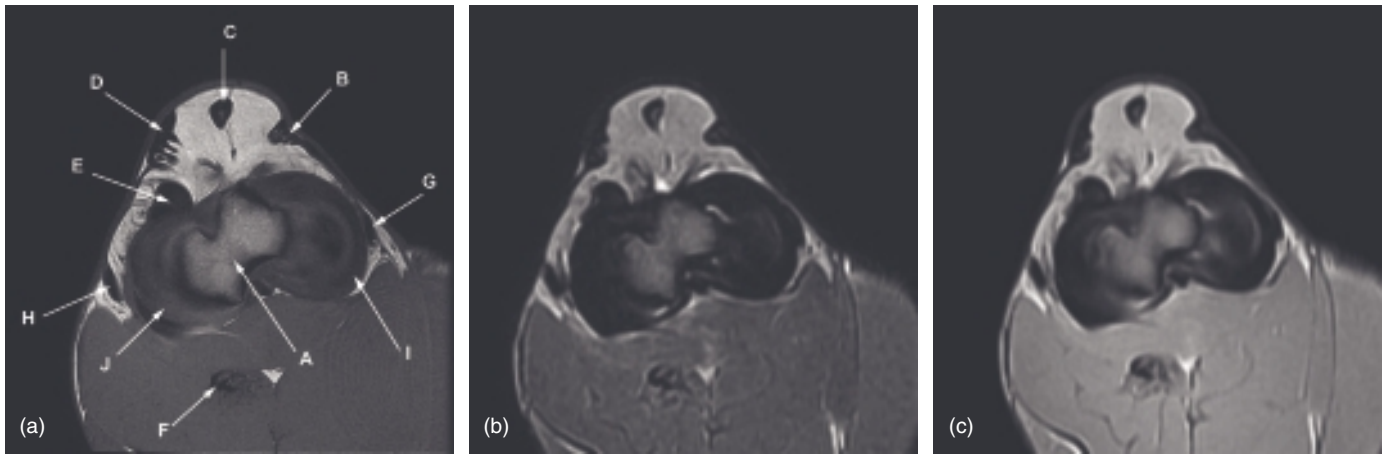

Figure 10.18 (a) Transverse 3D T1 weighted gradient echo image of an adult stifle. **A**, tibia; **B**, medial patella ligament (fossa); **C**, intermediate (middle) patellar ligament; **D**, lateral patella ligament; **E**, long digital extensor tendon; **F**, superficial digital extensor tendon; **G**, medial collateral ligament of the femorotibial joint; **H**, lateral collateral ligament of the femorotibial joint; **I**, medial meniscus; **J**, lateral meniscus. (b) T2 fast spin-echo image of the same region. (c) Proton density image of the same region.

larger cross-sectional area than the lateral collateral ligament. The ligaments should be well defined, of low signal intensity on all image sequences, generally surrounding by higher signal intensity fat-containing soft tissues. The contrast with the surrounding tissues is least marked on fat-suppressed images. The ligament margins may be slightly irregular, particularly in the mature horse. The medial, middle and lateral patellar ligaments are generally of homogeneous low signal intensity, and are clearly defined by contrast with adjacent fat and synovial fluid.

The cranial and caudal cruciate ligaments have homogeneous very low signal intensity on short τ inversion recovery (STIR), T2 and proton density (PD) images. On T2* images, the ligaments are of a relatively higher, but homogeneous signal intensity. The orientation of the ligaments leads to potential for magic angle effects, seen where the ligaments run at approximately 55° to the static magnetic field. These are most likely to occur on short TE (echo time) sequences therefore affecting T1-weighted and PD images in particular.

The medial and lateral menisci are generally of moderate signal intensity on T1 and PD, and low signal intensity on STIR and T2 fast spin-echo (FSE) images. On T1-weighted images, the signal intensity is similar to articular cartilage, but on other images they have lower signal than cartilage. The medial and lateral cranial meniscotibial ligaments, medial and lateral caudal meniscotibial ligament, meniscofemoral ligament, and lateral and medial femoropatellar ligaments have low signal intensity similar to the cruciate ligaments [6].

Synovial fluid is seen as high signal intensity on T2 FSE, T2* GRE (gradient recalled echo) and PD images, and as low signal intensity on T1-weighted images. There is considerable fat tissue surrounding the joints, particularly on the frontal and abaxial aspects. This fat tissue surrounds the patellar and collateral ligaments, giving clear contrast with the low signal intensity of the ligaments. The fat pads can be clearly defined and delineated

using a combination of fat-suppressed (where their signal intensity is low), T1 (where both fat is high signal intensity and synovial fluid is low signal intensity) and T2-weighted images (where both fat and synovial fluid have high signal intensity).

On T1-, PD-, T2- and T2*-weighted images without fat suppression, the cancellous bone has an intermediate to high signal intensity, representing the fat content of the bone. In the immature horse or pony, the physes of the distal femur and proximal tibia can be seen on T1-, PD- and T2*-weighted images as two undulating lines of high and low signal intensity adjacent to each other. On T2-weighted images, only the low signal intensity line appears clearly visible. On STIR images, active physes have high signal intensity relative to the low signal intensity of the surrounding cancellous bone. A physeal scar may be present in the adult, seen as a low signal intensity line on all sequences, i.e. less well-defined and frequently incomplete.

The subchondral bone should be of homogenous low signal intensity with a regular osteochondral junction and a smooth but slightly undulating endosteal border. In fat-suppressed images, the definition between the cortical and cancellous bones is indistinct. Cancellous bone is generally of heterogeneous signal intensity with a well-defined trabecular pattern on higher-resolution images. In fat-suppressed images, the cancellous bone has more homogeneous low signal intensity.

Muscle tissue is of intermediate to high signal intensity on proton density, moderate signal intensity on T2* and moderately low signal intensity on T1- and T2-weighted and STIR images. The boundaries of the muscles are seen as slightly higher signal intensity on T1-weighted and STIR images, slightly lower signal intensity on PD-weighted and are difficult to define on T2* images.

Immature (Figure 10.19)

In the immature horse, the ligaments and menisci tend to have relatively slightly higher and more heterogeneous signal intensity than in the adult. The margins of the cruciate ligaments tend to be clearer than in the adult. The undulating growth plates are clearly visible.

Normal variation

In a study using nine adult and nine immature joints from horses with no history of clinical signs of stifle pain, a range of minor variations was seen [5]. Small osteochondral defects were rare but seen in the femorotibial and femoropatellar joints of the nine immature ponies. These were more frequent in occurrence in the mature horses. Cartilage damage alone was more likely, including irregular cartilage surface, subchondral bone thickening and splits, with or without accompanying osseous pathology. Minor abnormal signal intensity (or abnormality) was seen in the meniscus of one horse, an osseous cystic-like lesion was seen in a different horse, while increased signal intensity in all sequences was detected in the distal third of the middle patellar ligament of a third horse. In the absence of clinical signs of stifle pain,

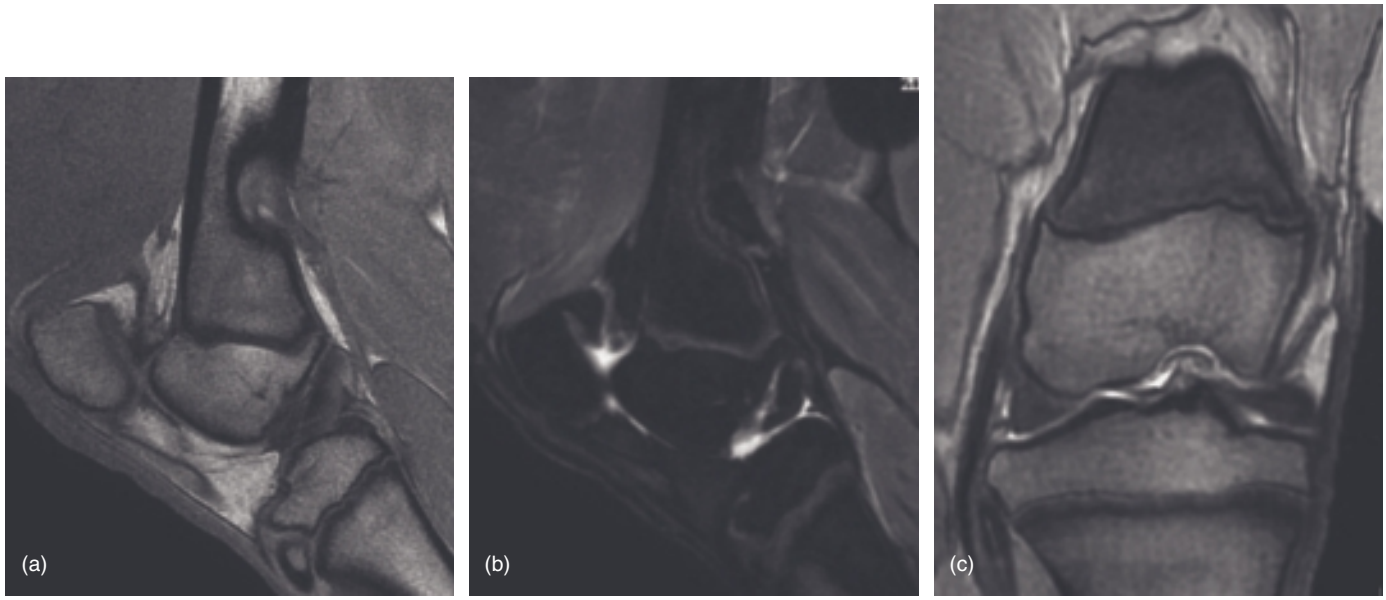

Figure 10.19 Images from a 12-month-old pony showing the open physes at this age. (a) Sagittal T1-weighted gradient-echo image. (b) Sagittal STIR image. (c) Frontal T2* gradient-echo image.

swelling or lameness, it is likely that these are incidental findings, although it is possible that these could ultimately progress to clinical problems. For the MR interpreter and clinician, it is important to be aware that these MR-detectable 'abnormalities' are not always associated with current clinical problems, so the findings on MRI should be interpreted in the context of the clinical picture.

REFERENCES

[1] Holcombe SJ, Bertone AL, Biller DS, Haider V. Magnetic resonance imaging of the equine stifle. *Vet Radiol Ultrasound* 1995; **36**: 119–25.
[2] Dyce KM, Sack WO, Wensing CJG. The stifle joint. In: *Veterinary Anatomy*, 2nd edn. Philadelphia, PA: WB Saunders, 1996, pp. 615–18.
[3] Judy CE, Saveraid T, Rick M, Herthel D. Magnetic resonance imaging of the equine stifle in a clinical setting. *Proceedings American College of Veterinary Surgeons Surgical Summit*, 2007.
[4] Judy CE. MRI of the equine stifle. *Proceedings 5th European Veterinary MRI Users Meeting*, 2009.
[5] Van der Straaten GO, Collins SN, Rijkenhuizen AB, Murray RC. Magnetic resonance imaging of the equine stifle: normal anatomy. *Proceedings Voorsjaarsdagen*, 2009.
[6] Gupte CM, Bull MJ, Murray RC, Amis AA. Comparative anatomy of the meniscofemoral ligament in humans and some domestic mammals. *Anat Histol Embryol* 2007; **36**: 47–52.

Chapter 11
The head

Russell Tucker and Shannon Holmes

OVERVIEW

The applications of magnetic resonance (MR) technology for examination of the musculoskeletal system have revolutionized the practice of equine lameness; however, equine head MR is currently less advanced [1]. The complexity of the equine skull anatomy makes it an ideal area to image in multi-planar cross-sections [2]. The initial experiences of equine neurologists, dentists and upper respiratory surgeons have been favourably similar to those in human and small animal MRI. The anatomic and physiologic information gained from the MR examinations of the head are superior to endoscopy, radiography and computed tomography (CT) for diagnosis, pre-surgical planning and improved prognostication. Although spatial resolution of high-detailed radiography and CT may be greater than MRI, the superior tissue contrast resolution of MRI provides more detailed information of the soft tissues, as well as the osseous structures of the skull and enables detection of lesions unrecognized with other imaging techniques.

For brain imaging, a clear advantage of MRI is the ability to differentiate grey matter from white matter and delineate which tissues are involved with pathologic conditions. MR imaging readily displays the mass effect from lesions within the brain parenchyma (intra-axial) or from lesions outside the brain parenchyma (extra-axial). Many intracranial lesions create perceptible abnormal brain tissue signal especially on fluid-sensitive sequences due to cellular destruction, inflammation and increased fluid accumulation. By comparing T1-weighted sequences before and after contrast administration, loss of normal vascular integrity and the blood–brain barrier can be concluded by the increased signal created by leakage of paramagnetic contrast agents. The pituitary gland, with normal uniform contrast enhancement, is especially well suited to evaluation by MRI. Additionally, the nasal cavity, sinuses, larynx and guttural pouches are well visualized and evaluated on MR examinations. Lesions of these areas, which create bony destruction or space-occupying masses, may be best delineated on MR examinations and yield a definitive diagnosis and prognosis or provide guidance for surgical intervention and biopsy.

The first reports of the cross-sectional anatomy of the equine brain, sinuses and nasal passages using MR examined normal anaesthetized neonatal foals and postmortem specimens of adult horses euthanized for

Equine MRI, edited by Rachel C. Murray.

medical reasons unrelated to diseases of the head. In foals, the major components of the brain and surrounding structures were identified and labelled in sagittal and transverse image planes. In isolated adult equine cadaver heads, MR images were correlated to anatomic preparations at identical tomographic slice planes, to illustrate the superior capability of MRI to identify important regions of the brain, sinuses and nasal passages. The foundation articles still serve as excellent references for detailed description of anatomic structures of the head [3–6]. Subsequently, limited case reports of MR use in equine brain and skull imaging have provided additional anatomic references and demonstrate superior tissue contrast of MR [7–10].

CHALLENGES WITH IMAGING OF THE HEAD

Although similar in principle and interpretation to small animal imaging [11, 12], there are multiple challenges when imaging equine patients. Adequate anaesthesia must be administered to maintain the patient in the MR gantry without detrimental patient motion. Conventional anaesthetic equipment may not be compatible with the magnetic field and can introduce unacceptable imaging artefacts (Figure 11.1). Any ferromagnetic orthopaedic or surgical implants also introduce magnetic susceptibility artefacts interfering with the MR imaging within the imaged region (Figure 11.2). Using non-ferromagnetic positioning devices, such as sponges, rope halters and sandbags, it is possible to stabilize the head to minimize patient motion (Figure 11.3). Respiratory and cardiac gating is also possible to help minimize patient motion introduced by normal physiologic oscillations caused by respiratory and cardiac activity (Figure 11.4).

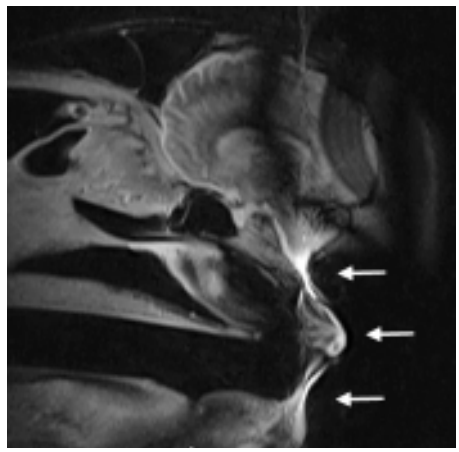

Figure 11.1 Metallic artefact created by a magnetic endotracheal tube. Gradient echo sagittal image obtained as a survey of the head for image planning. The white arrows demarcate a serpentine metallic artefact created by an endotracheal tube that is inappropriate for MR studies of the head. The endotracheal tube contains a small metallic spring. Note the greatest artefact is centred on the larynx and diminishes dorsally away from the tube.

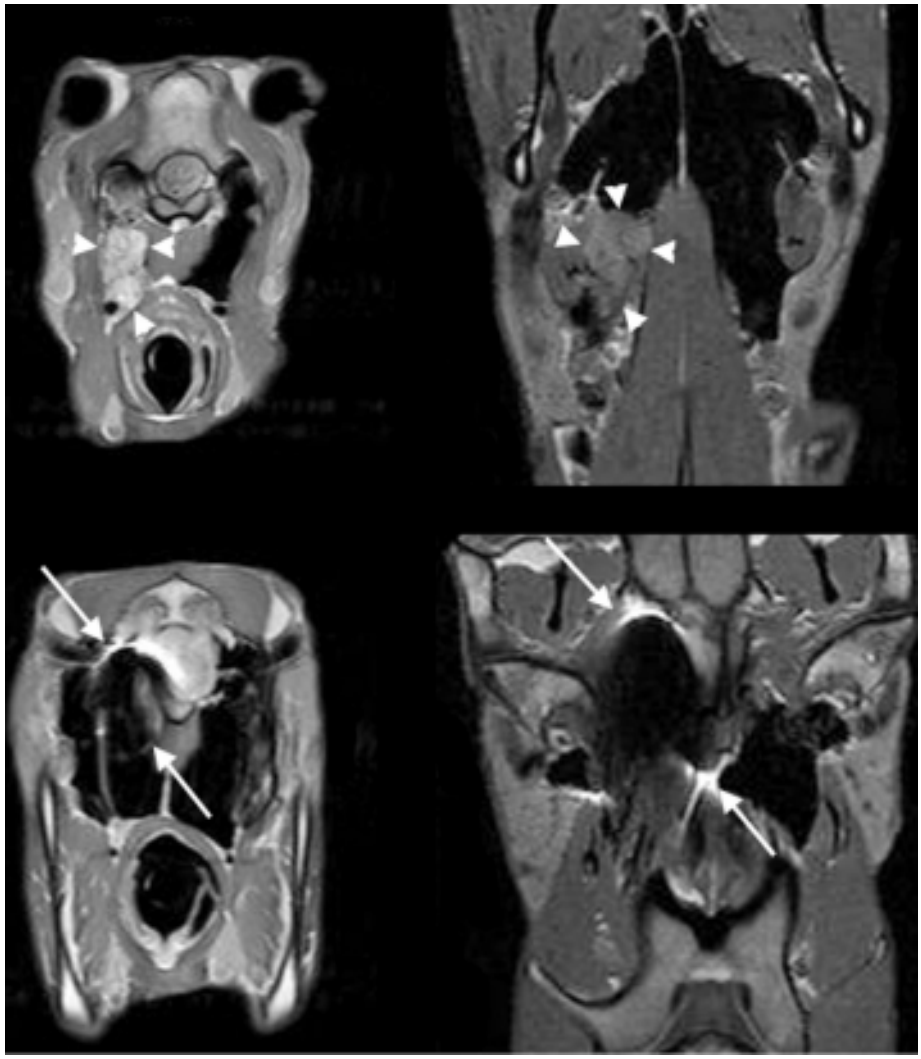

Figure 11.2 Metallic artefact created by prothrombic coils. T1-weighted post-contrast enhancement images in the transverse (left images) and dorsal (right images) planes. This patient was examined for persistent guttural pouch mycosis. The top images show the infectious tissue mass in the caudal recess of the medial guttural pouch (white arrowheads). The bottom images display an alternating hyperintense and hypointense signal artifact seen with ferromagnetic metallic implants (white arrows). In this case, the metallic implants were prothrombic coils placed to treat the guttural pouch infection.

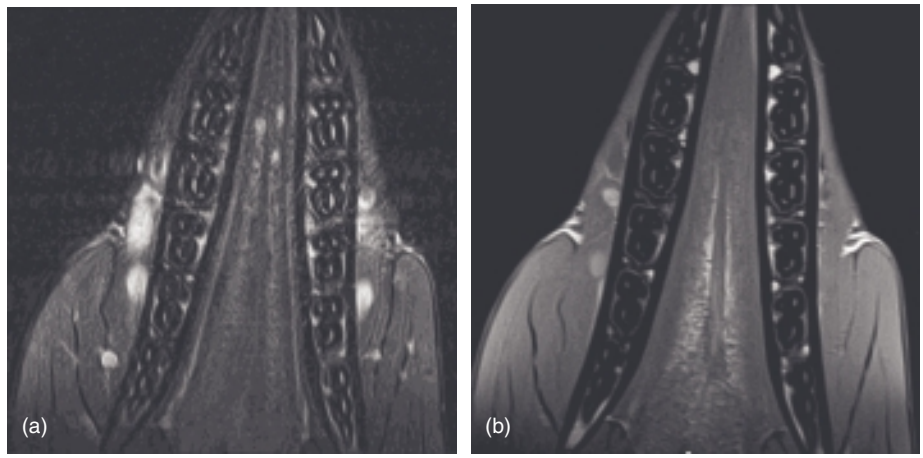

Figure 11.3 Motion due to incomplete skull stabilization. Short τ inversion recovery (STIR) (a) and T1-weighted (b) dorsal plane images of the mandible. (a) When the skull was not sufficiently stabilized, minor repetitive motion was experienced due to the vibration associated with the gradients. The margins of the mandible are blurred and there is exaggerated motion in the background projected in the phase encoding direction. (b) Following better head stabilization, the T1-weighted dorsal plane image of the mandible illustrates the motion artefact was eliminated.

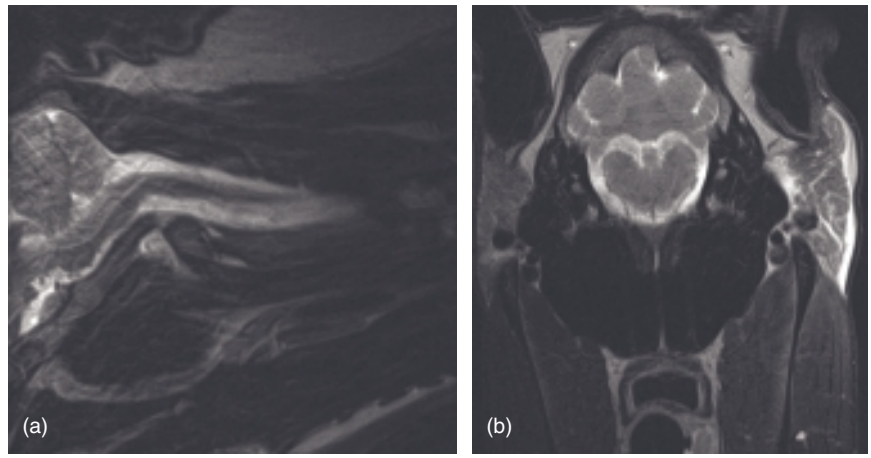

Figure 11.4 Motion associated with respiration. T2-weighted sagittal (a) and transverse (b) plane images of the caudal skull and proximal cervical spine. (a) This patient was imaged in lateral recumbency and the initial T2 sagittal image quality was compromised by artefact in the phase-encoding direction (dorsal-ventral direction). (b) Respiratory gating was used to obtain higher quality images without the detrimental motion artefact. In lateral recumbency, the expansion of the rib cage shifts the patient with each breath creating significant repetitive motion of the head and neck.

Unfortunately, gating techniques add to the imaging scan times and may prolong scans to unacceptable overall exam times; therefore, gated acquisitions are selectively employed only when other stabilization methods fail. Placement of the equine head into the MRI gantry can also be challenging. If the patient's head is not placed within the centre of the magnet gantry, the imaging field of view may cut off part of the region of interest and require repositioning of the patient further into the magnet centre (Figure 11.5). Finally, it is helpful to have an experienced MR operator perform the initial head and brain examinations to avoid many typical pitfalls and errors common to the equine head and skull imaging (Figure 11.6).

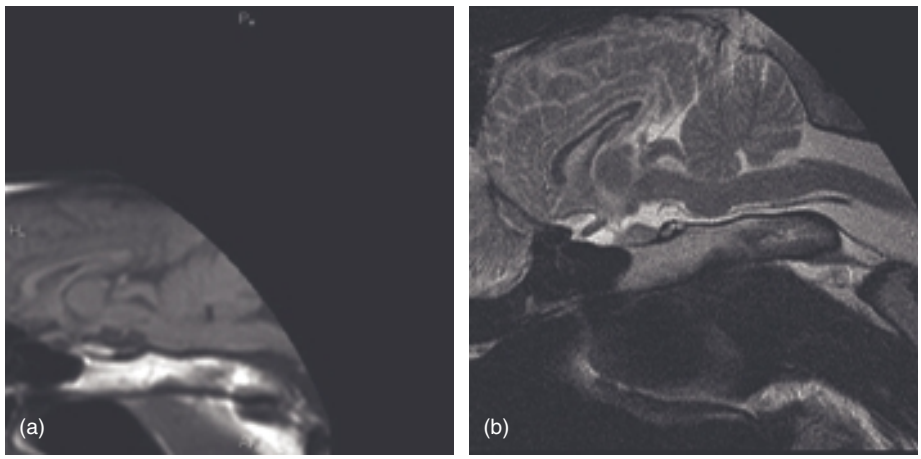

Figure 11.5 Artefact encountered at the edge of isocentre. Gradient-echo survey sagittal plane (a) and T2-weighted sagittal plane (b) images. In the initial survey image (a), the caudal aspect of the occipital lobe, cerebellum and spinal cord are excluded from the field of view. The curved edge is the limit of the imaging field. In this case, the head was initially positioned against the side of the magnet bore. (b) The entire brain was subsequently imaged when positioning sponges were used to shift the head into isocentre.

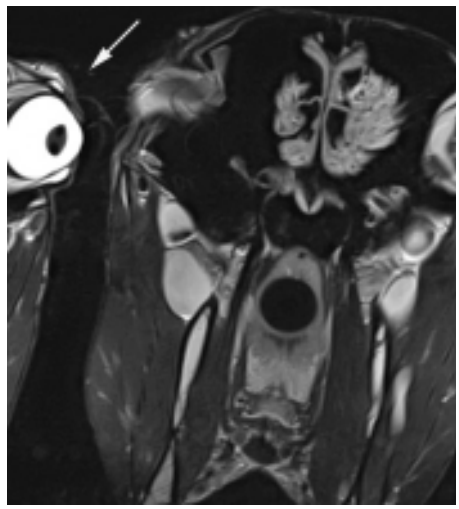

Figure 11.6 Aliasing artefact. T2-weighted transverse plane image. In the scan set-up, the anatomy on the right side of the image was excluded from the field of view but is displayed on the left side of the image (white arrow). This aliasing artefact is sometimes referred to as foldover or wrap artefact.

LIMITATIONS OF MRI IN THE HEAD

The limitations of MRI in the skull and brain must be appreciated whenever MR is being considered in equine patients. The large size and shape of the adult equine head and the inherent difficulty positioning the head within the gantry requires preplanning and forethought. Standard imaging protocols used for humans and small animals need to be adapted to cover the larger area of interest in equine patients, and scan times may be greatly prolonged. Increasing the slice thicknesses to cover a larger area will improve signal strength but will cause greater slice thickness averaging artefact. The larger air-filled cavities within the nasal sinus and guttural pouches can introduce air–soft tissue interface artefacts [13]. Finally, the cost and risk of MRI, must be acceptable relative to the potential information to be gained for each patient. Alternative imaging techniques, which may provide adequate diagnostic information, should be explored prior to MR examinations.

IMAGE ACQUISITION

For the most part, three standard anatomic planes relative to the head are commonly used when imaging any part of the equine head, including the brain, sinuses and nasal passages or the oral cavity and teeth [14]. The sagittal, transverse and dorsal anatomic planes have been described for the equine head and are most commonly positioned relative to the hard palate and base of the calvarium (Figure 11.7). Additional image planes can be obtained for further examination of structures if the standard image planes do not offer the optimal visualization of specific regions of interest. Proper placement of the image planes is essential to maintain anatomic symmetry to allow for critical comparison between left and right sides. Even slight obliquity will compromise interpretations and may lead to confusion and incorrect diagnosis (Figure 11.8).

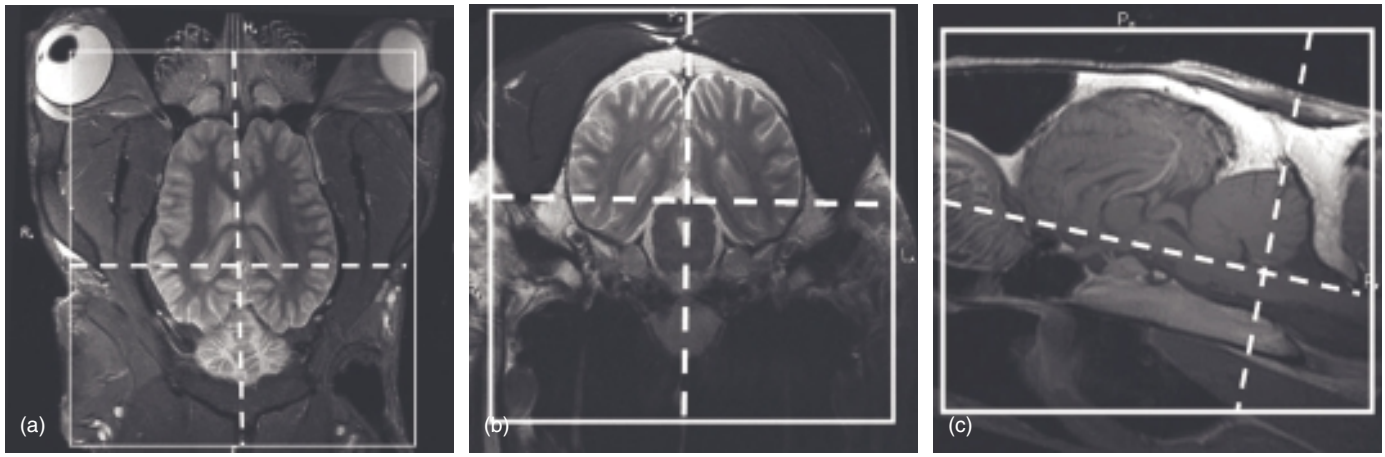

Figure 11.7 Brain imaging scan plans.The suggested fields of view (solid line box) and slice angle (dashed lines) are depicted for the transverse and sagittal planes on a STIR dorsal image (a), the sagittal and dorsal planes on a T2 transverse image (b) and the transverse and dorsal planes on a T1 sagittal image (c). It is critical to plan each imaging plane on two orthogonal planes. Consistency in planning relative to certain anatomical landmarks ensures image quality.

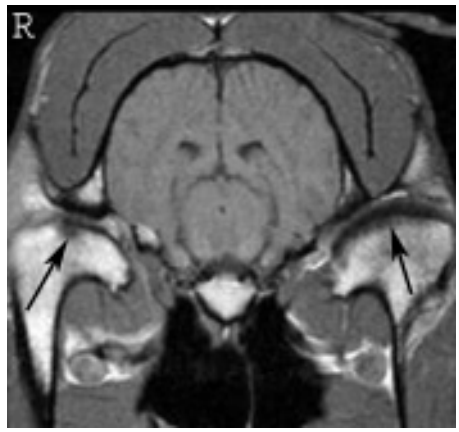

Figure 11.8 Anatomic asymmetry due to improper patient positioning. T1-weighted transverse plane image at the level of the temporomandibular joints. There is asymmetry of the joint surfaces between the right and left articular surfaces (black arrows). Better positioning of the head and more careful planning of the transverse image planes relative to the sagittal and dorsal images could improve transverse image symmetry. **R**, right side.

The initial set-up scan typically acquires two or three orthogonal image planes of the head to allow for planning the subsequent scan planes in proper slice orientation. Depending on the type of magnet and patient positioning, it is helpful to repeat the initial set-up scans to obtain perfect orientation of the three orthogonal planes relative to the head positioning. Time spent obtaining the perfect orientation on the initial sequences provides the most efficient reference images for subsequent sequences and reduces overall exam times. Prior practice of setting up the proper slice orientations on a cadaver specimen can improve operator experience and reduce clinical patient scan times.

NORMAL MR ANATOMY

The sagittal plane slices should be centred on the median anatomic plane and parallel to this section equally on left and right sides (Figure 11.9). The extent of the distances lateral to the median image plane will depend on the type of scan being performed and the desire to include the entire head or not. For equine brain scans, it is advised to image lateral enough to completely visualize the tympanic bulla and part of the external auditory canals. The thickness and number of slices are determined by the size of the area scanned and the acceptable scan times. The nature of the scan and the regions of interest will determine the rostal to caudal field of view (FOV) (Figures 11.10, 11.11, 11.12).

The transverse plane slices should be positioned to yield images that have perfect symmetry between the left and the right sides (Figure 11.13). For brain imaging, transverse slices should extend from the ethmoid turbinate to the foramen magnum (Figure 11.14). For imaging of the oral cavity and teeth, sinuses and nasal passages, or the airways and pharyngeal area,

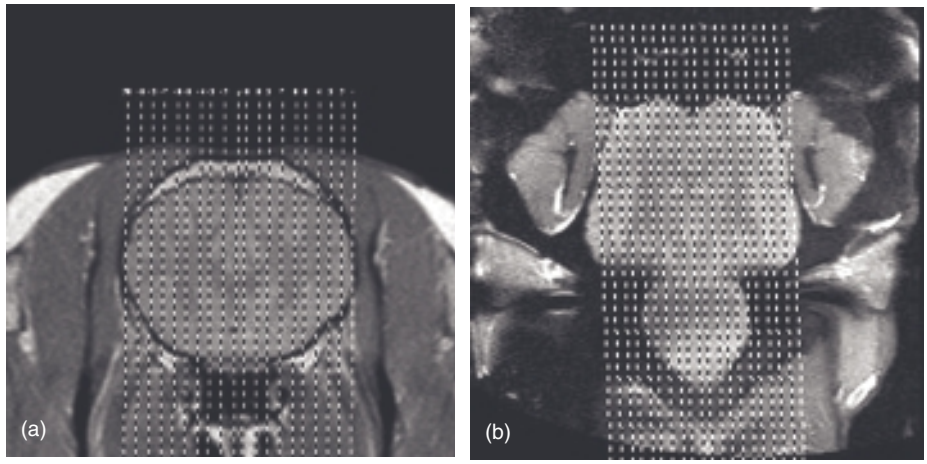

Figure 11.9 Sagittal slice planning on reference orthogonal images. Proton density transverse (a) and dorsal (b) images illustrating the orientation and plan for the sagittal image slices for brain imaging. Note the sagittal slices span the brain on both orthogonal images.

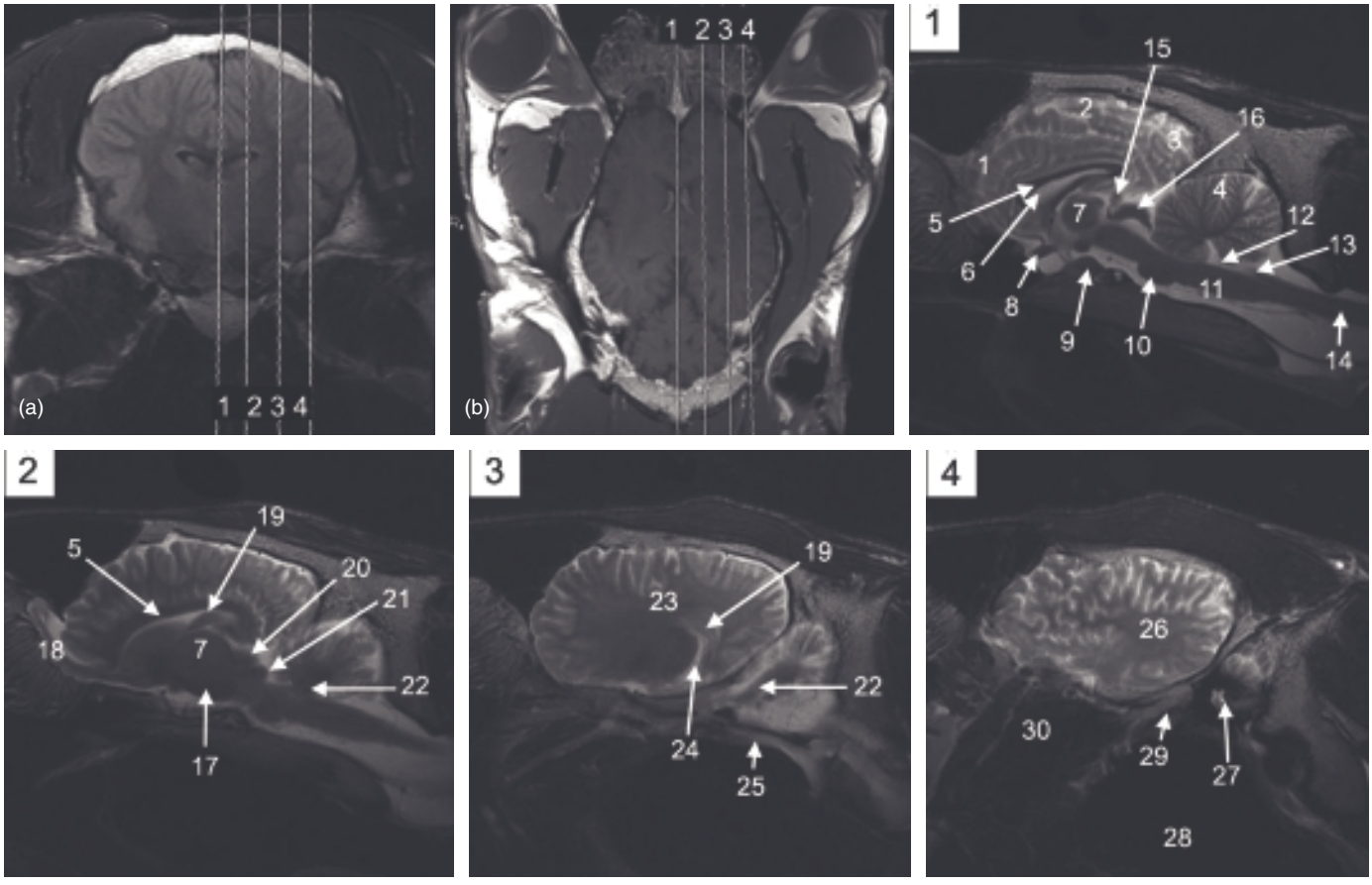

Figure 11.10 Sagittal plane intracranial anatomy. The reference images are a proton density-weighted transverse plane image (a) and T1-weighted post-contrast dorsal plane image (b). The labelled sagittal plane images 1–4 are T2-weighted and organized from midline to the lateral aspect of the cerebrum. Labelled structures: **1**, frontal lobe; **2**, parietal lobe; **3**, occipital lobe; **4**, cerebellum; **5**, corpus callosum; **6**, lateral ventricle (rostral); **7**, interthalamic adhesion; **8**, optic chiasm; **9**, pituitary gland; **10**, pons; **11**, medulla oblongata; **12**, fourth ventricle; **13**, obex; **14**, cervical spinal cord; **15**, pineal gland; **16**, colliculus; **17**, hypothalamus; **18**, olfactory lobe and recess; **19**, hippocampus; **20**, rostal colliculus; **21**, caudal colliculus; **22**, cerebellar peduncle; **23**, coronal radiation; **24**, lateral ventricle (caudal); **25**, internal jugular vein; **26**, temporal lobe; **27**, facial nerve; **28**, medial guttural pouch; **29**, trigeminal nerve; **30**, lateral pterygoid muscle.

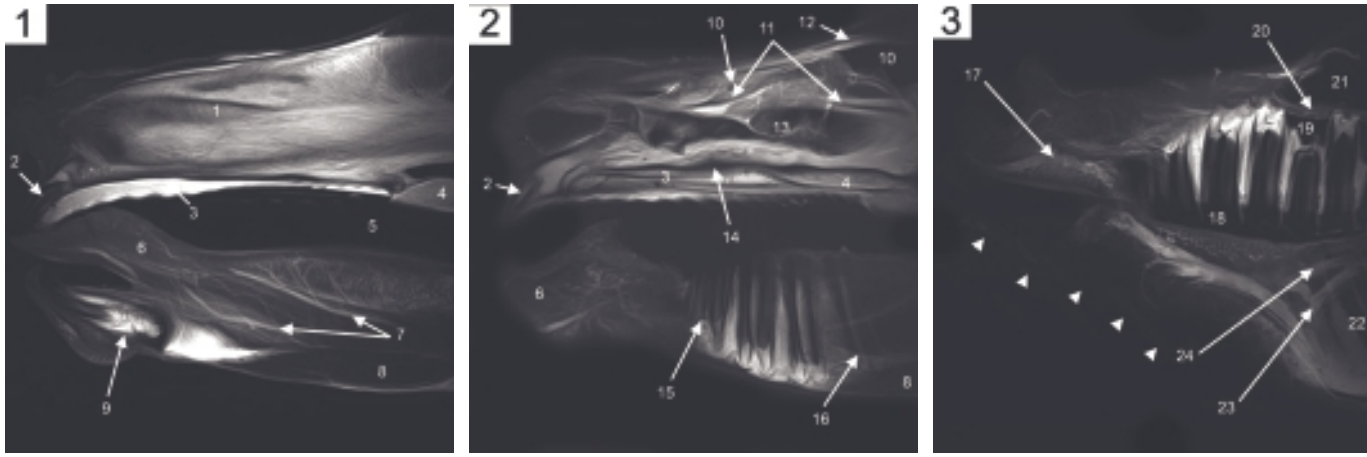

Figure 11.11 Sagittal plane MR anatomy of the rostral skull. T2-weighted sagittal images 1–3 (mid-sagittal to lateral) of the rostral sinuses and dentition. It is often necessary to examine the sinus and dentition in two fields of view for optimum image resolution. The arrow heads indicate a flow artefact. Labelled structures: **1**, nasal septum; **2**, maxillary incisor; **3**, hard palate; **4**, soft palate; **5**, oral cavity; **6**, tongue; **7**, lingual vein(s); **8**, geniohyoideus muscle; **9**, mandible; **10**, dorsal conchal sinus; **11**, middle nasal meatus; **12**, dorsal nasal meatus; **13**, ventral conchal sinus; **14**, ventral nasal meatus; **15**, mandibular second premolar roots; **16**, mandibular first molar roots (partial volume of the medial roots); **17**, maxillary vein; **18**, third maxillary premolar; **19**, rostral maxillary sinus; **20**, infraorbital canal and nerve; **21**, caudal maxillary sinus; **22**, masseter muscle; **23**, deep facial vein; **24**, buccal vein.

the transverse slices should be positioned to encompass at least a few additional slices rostral and caudal to the specific region of interest (Figure 11.15). It is helpful to maintain the same number and thickness of slices and the interslice spacing on transverse sequences to allow for critical comparison between sequences (Figures 11.16). Occasionally, such as with pituitary or inner ear imaging, it can be helpful to acquire thinner slices centred over the specific region of interest. There are signal to noise limits to how thin slices can be with most routine sequences, hence volume acquisitions or 3D protocols are used to generate thinner slices with reasonable signal to noise output and higher resolution.

The dorsal plane slices are positioned orthogonal to the sagittal and transverse image planes with some adaptation relative to the specific area of interest (Figure 11.17). If the brain or entire head is examined, then it is advised that the dorsal plane slices be positioned relative to the hard palate and base of calvarium (Figure 11.18). Due to slight angle differences in the orientation of the nasal passages and oral cavity, the larynx or pharyngeal regions, the optimal dorsal slice plane orientation can be adjusted separately for each of these regions (Figure 11.19).

Several major anatomic structures are illustrated on sagittal (Figure 11.10), transverse (Figure 11.14) and dorsal (Figure 11.18) images of the brain of an adult horse. The sagittal (Figures 11.11 and 11.12), transverse (Figures 11.14 and 11.15) and dorsal (Figures 11.18 and 11.19) sections of major anatomic structures of the oral and nasal cavities, sinuses, guttural pouches, larynx are illustrated for the rostal and caudal skull regions.

Normal anatomic variations have been noted in cross-sectional imaging of equine head exams. The nasal septum is often slightly deviated as a normal anatomic variant and not considered clinically significant (Figure 11.20). There is frequently mild asymmetry between the left and right frontal

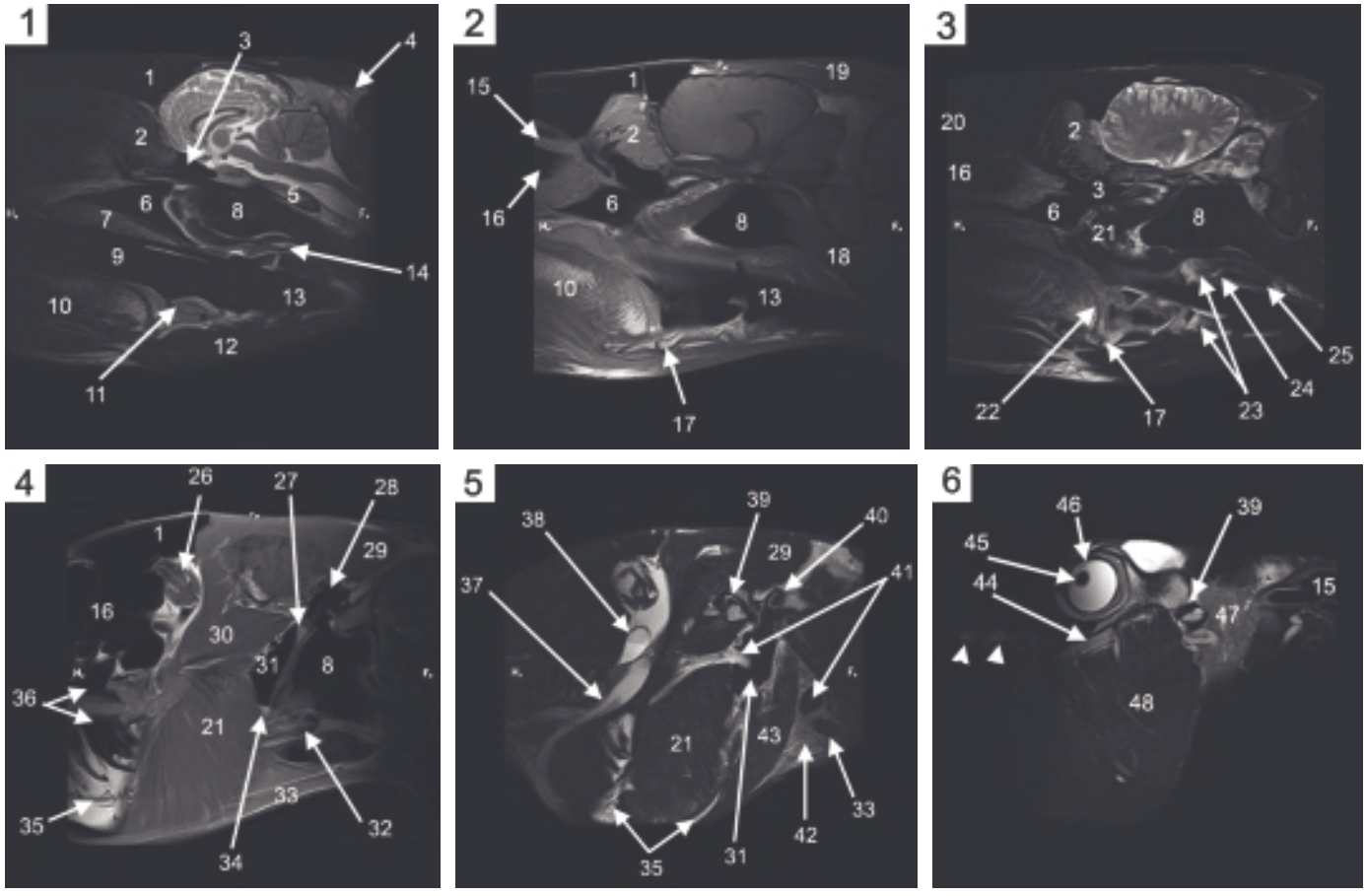

Figure 11.12 Sagittal plane MR anatomy of the caudal skull. The sagittal images begin on midline in image 1 and proceed through the skull in series to the lateral aspect of the skull (images 2–6). Images 2 and 4 are T1-weighted where as the remaining images are T2-weighted images. Labelled structures: **1**, frontal sinus; **2**, ethmoid turbinates; **3**, sphenopalatine sinus; **4**, occipital bone (pole); **5**, basisphenoid bone; **6**, nasopharynx; **7**, soft palate; **8**, medial guttural pouch; **9**, oropharynx; **10**, tongue; **11**, epiglottis; **12**, sternohyoideus muscle; **13**, tracheal lumen; **14**, oesophagus; **15**, middle nasal meatus; **16**, ventral conchal sinus; **17**, basihyoid bone with lingual process; **18**, longus capitis; **19**, temporal muscle; **20**, dorsal conchal sinus; **21**, medial pterygoid muscle; **22**, ceratohyoid bone; **23**, thyroid cartilage; **24**, arytenoid cartilage; **25**, cricoid cartilage; **26**, extraocular muscle and optic nerve; **27**, stylohyoid bone; **28**, tympanic bulla; **29**, temporal muscle; **30**, lateral pterygoid muscle; **31**, lateral guttural pouch; **32**, common carotid artery; **33**, lingofacial vein; **34**, retropharyngeal lymph node; **35**, mandible (mental nerve in #4); **36**, third maxillary and mandibular molars; **37**, deep facial vein; **38**, buccal vein; **39**, temporomandibular joint; **40**, external auditory meatus; **41**, maxillary vein; **42**, mandibular salivary gland; **43**, digastricus muscle; **44**, transverse facial artery; **45**, lens; **46**, iris; **47**, parotid salivary gland; **48**, masseter muscle.

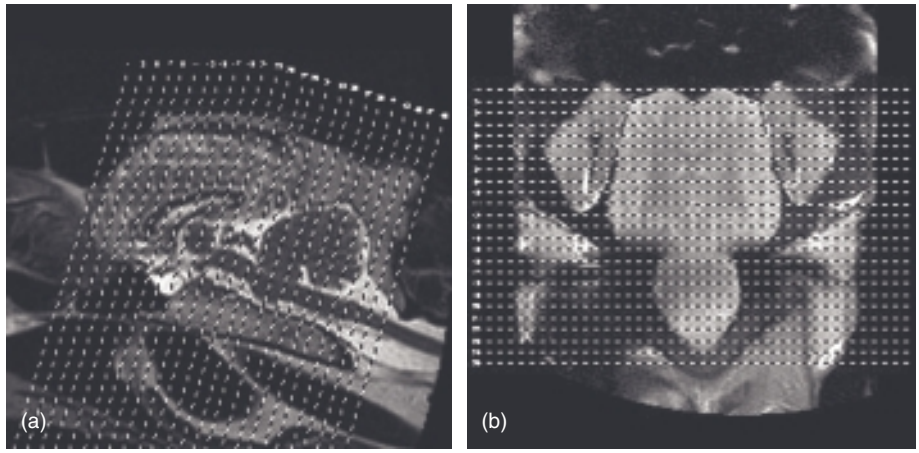

Figure 11.13 Transverse slice planning on reference orthogonal images. T2-weighted sagittal (a) and proton density dorsal (b) images illustrating the orientation and plan of the transverse slices for brain imaging. Note the transverse slices span the brain on both orthogonal images.

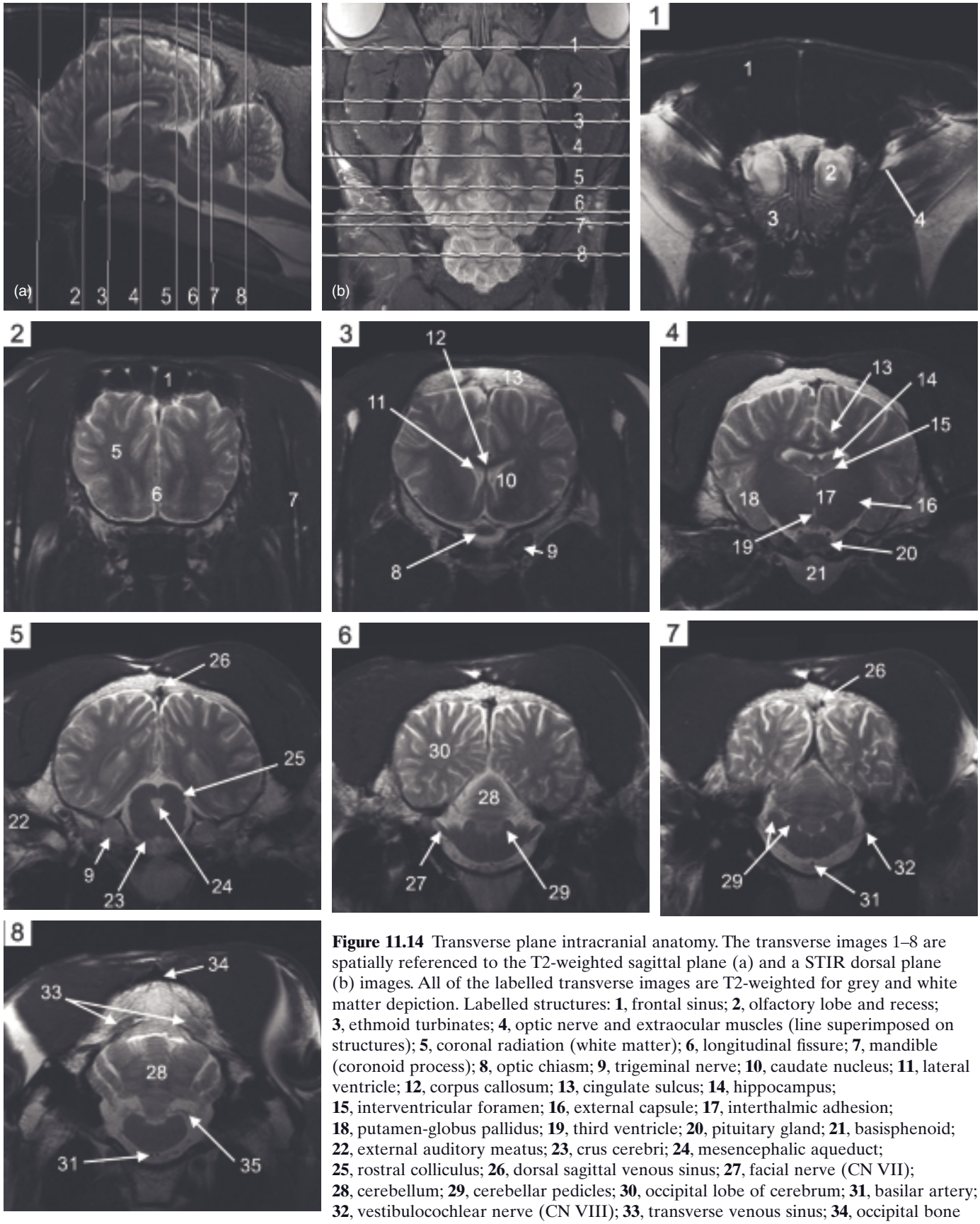

Figure 11.14 Transverse plane intracranial anatomy. The transverse images 1–8 are spatially referenced to the T2-weighted sagittal plane (a) and a STIR dorsal plane (b) images. All of the labelled transverse images are T2-weighted for grey and white matter depiction. Labelled structures: **1**, frontal sinus; **2**, olfactory lobe and recess; **3**, ethmoid turbinates; **4**, optic nerve and extraocular muscles (line superimposed on structures); **5**, coronal radiation (white matter); **6**, longitudinal fissure; **7**, mandible (coronoid process); **8**, optic chiasm; **9**, trigeminal nerve; **10**, caudate nucleus; **11**, lateral ventricle; **12**, corpus callosum; **13**, cingulate sulcus; **14**, hippocampus; **15**, interventricular foramen; **16**, external capsule; **17**, interthalmic adhesion; **18**, putamen-globus pallidus; **19**, third ventricle; **20**, pituitary gland; **21**, basisphenoid; **22**, external auditory meatus; **23**, crus cerebri; **24**, mesencephalic aqueduct; **25**, rostral colliculus; **26**, dorsal sagittal venous sinus; **27**, facial nerve (CN VII); **28**, cerebellum; **29**, cerebellar pedicles; **30**, occipital lobe of cerebrum; **31**, basilar artery; **32**, vestibulocochlear nerve (CN VIII); **33**, transverse venous sinus; **34**, occipital bone (pole); **35**, choroid plexus of the 4th ventricle.

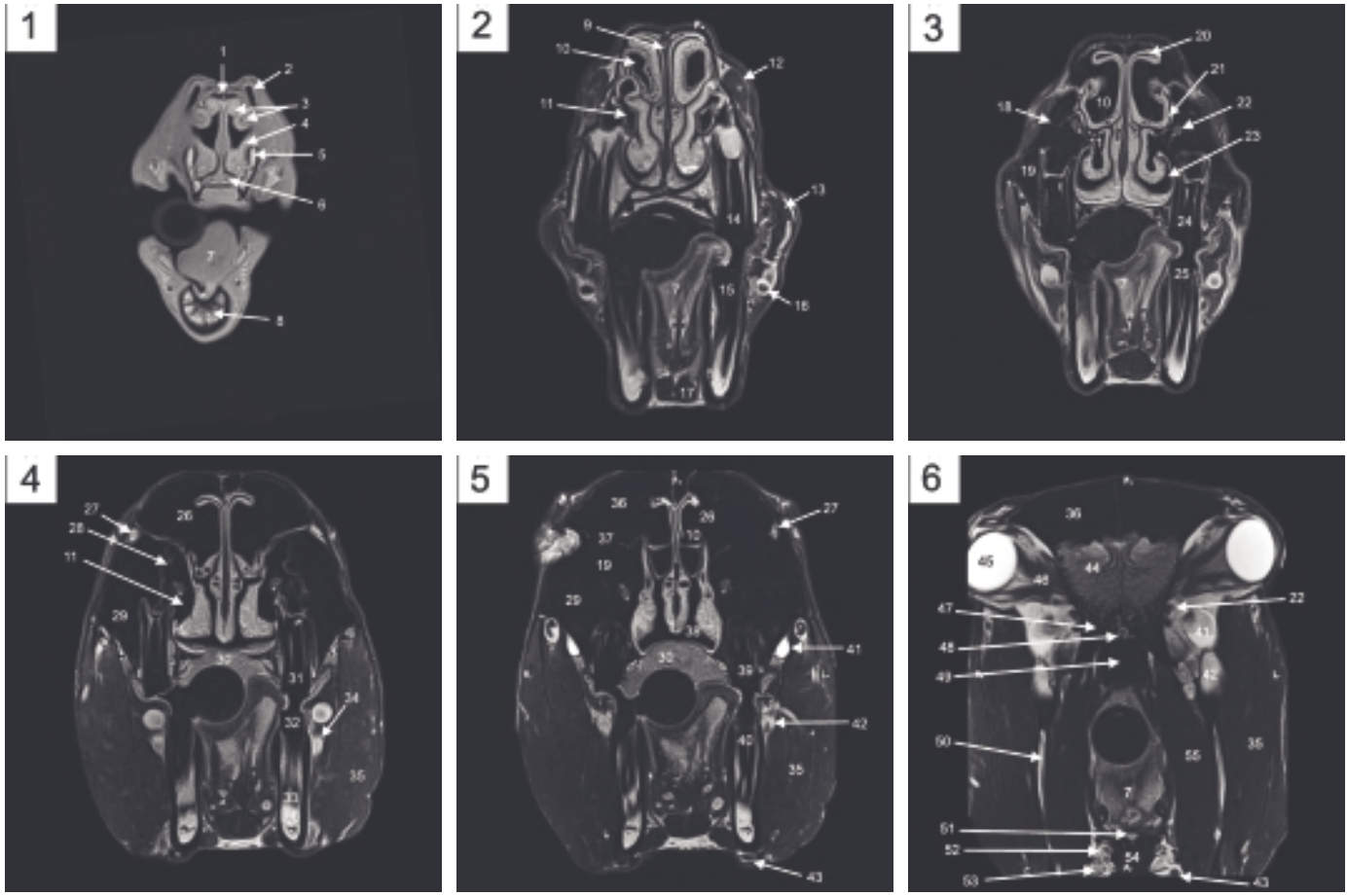

Figure 11.15 Transverse plane skull MR anatomy. Transverse plane images 1–10 are presented from rostral to caudal. Images 1 and 7 are T1-weighted; all other images are T2-weighted. Labelled structures: **1**, nasal bone; **2**, nasal diverticulum; **3**, dorsal conchal fold; **4**, ventral conchal fold; **5**, maxillary bone; **6**, palatine process of incisive bone; **7**, tongue; **8**, mandibular diastema; **9**, nasal septum; **10**, dorsal conchal sinus; **11**, ventral conchal sinus; **12**, superior labii levator muscle; **13**, buccinator muscle; **14**, third maxillary premolar; **15**, third mandibular premolar; **16**, facial vein; **17**, geniohyoid muscle; **18**, conchomaxillary opening; **19**, rostral maxillary sinus; **20**, dorsal nasal meatus; **21**, middle nasal meatus; **22**, infraorbital canal and nerve; **23**, ventral nasal meatus; **24**, first maxillary molar; **25**, fourth mandibular premolar; **26**, conchofrontal opening; **27**, nasolacrimal duct; **28**, conchomaxillary opening; **29**, caudal maxillary sinus; **30**, soft palate; **31**, second maxillary molar; **32**, third mandibular molar (crown); **33**, second mandibular molar (roots); **34**, buccal artery; **35**, masseter muscle; **36**, frontal sinus; **37**, frontomaxillary opening; **38**, nasal cavity; **39**, third maxillary molar; **40**, third mandibular molar; **41**, buccal vein; **42**, deep facial vein; **43**, facial vein; **44**, ethmoid turbinates; **45**, eye (vitreous); **46**, extraocular muscles and ocular nerve; **47**, sphenopalatine sinus; **48**, vomer; **49**, nasopharynx; **50**, mandible; **51**, lingual process of basihyoid bone; **52**, lingual vein; **53**, mandibular lymph nodes; **54**, omohyoid and sternohyoid muscles; **55**, medial pterygoid muscle; **56**, temporal muscle; **57**, zygomatic process; **58**, temporomandibular joint; **59**, mandibular condyle; **60**, lateral pterygoid process; **61**, basisphenoid bone; **62**, medial guttural pouch; **63**, lateral guttural pouch; **64**, stylohyoid bone; **65**, tracheal opening; **66**, parotid salivary gland; **67**, facial nerve; **68**, masseteric artery; **69**, longus capitis; **70**, retropharyngeal lymph node; **71**, common carotid artery; **72**, thyroid cartilage; **73**, dorsal cricoarytenoid muscle; **74**, corniculate process of the arytenoids; **75**, digastricus muscle; **76**, tympanic bulla; **77**, external auditory meatus; **78**, vestibulocochlear nerve; **79**, maxillary vein; **80**, external carotid artery; **81**, mandibular salivary gland; **82**, lingofacial vein; **83**, sternohyoideus muscle; **84**, transverse venous sinus with osseous tentorium; **85**, internal carotid artery; **86**, jugular process.

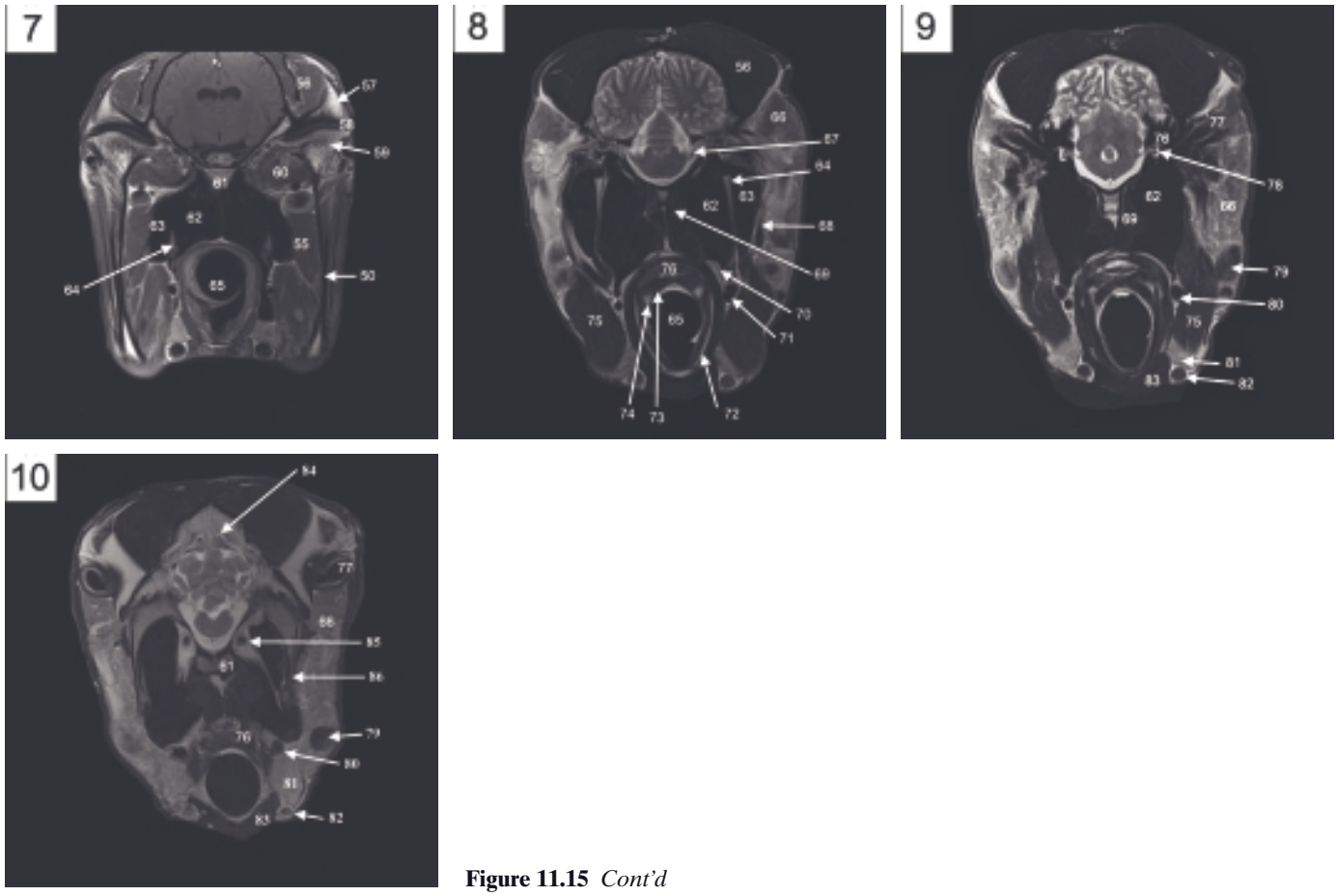

Figure 11.15 *Cont'd*

sinuses and within the guttural pouches. In these instances, there should be no adjacent abnormal tissue or mass effect creating the asymmetry or deviation, and the surrounding osseous margins and mucosal lining should be smooth and normal in signal intensity. In some horses, like other animals, there is often a small central hyperintensity within the normal pituitary gland, noted on T1-weighted sequences prior to contrast administration, thought to represent normal paramagnetic neurotransmitters and/or cholesterol byproducts (Figure 11.21). Due to the angle of the teeth relative to the axis of the rostral skull, care must be taken when evaluating the appearance of the teeth, especially adjacent tooth roots on transverse images. The most notable difference in imaging the foal head compared to the adult horse is the appearance of deciduous teeth and tooth buds (Figure 11.22).

The effects of positioning and prolonged anaesthesia cannot be ignored when evaluating equine head studies. Small amounts of homogeneous fluid, demonstrating a horizontal fluid–air interface, can be observed in the dependent aspects of the nasal cavity and sinuses (Figure 11.23). This may not always be symmetric between sides, but nonetheless should be small in volume and not associated with any other abnormal findings. If the horse is positioned in lateral recumbency, the dependent aspects of the sinuses and nasal passages can accumulate small amounts of free fluid and the venous structures on the dependent aspect of a lateral recumbent horse may become

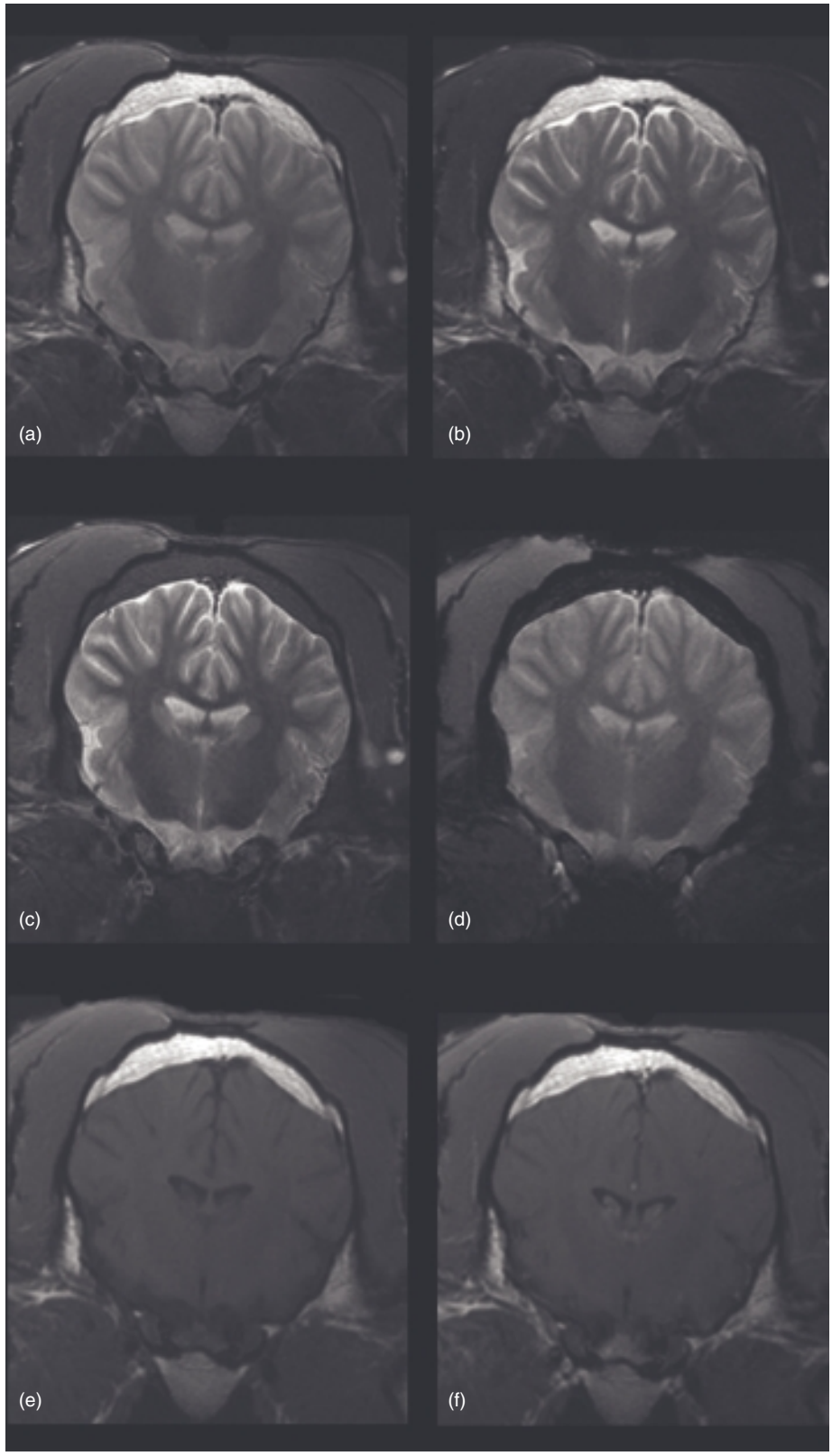

Figure 11.16 Normal brain contrast with routine sequences used to examine the intracranial structures. Transverse plane images at the level of the intrathalamic adhesion: (a), proton density (PD); (b), T2- weighted; (c), short τ inversion recovery (STIR); (d), gradient echo (GE); (e), T1-weighted; (f), T1-weighted post-contrast enhancement. The T2-weighted, PD-weighted and STIR images are high contrast sequences and depict the grey and white matter regions of the brain. The choroid plexus of the lateral ventricles have increased signal intensity on the post-contrast image (f), due to these structures being highly vascular.

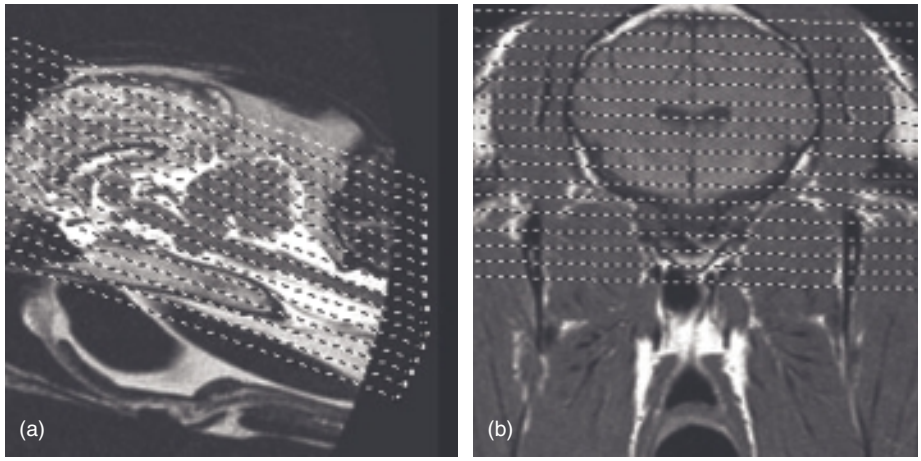

Figure 11.17 Dorsal slice planning on reference orthogonal images. T2-weighted sagittal (a) and T1-weighted transverse (b) images illustrating the orientation and plan for the dorsal image slices for brain imaging. Note the dorsal slices span the brain on both orthogonal images.

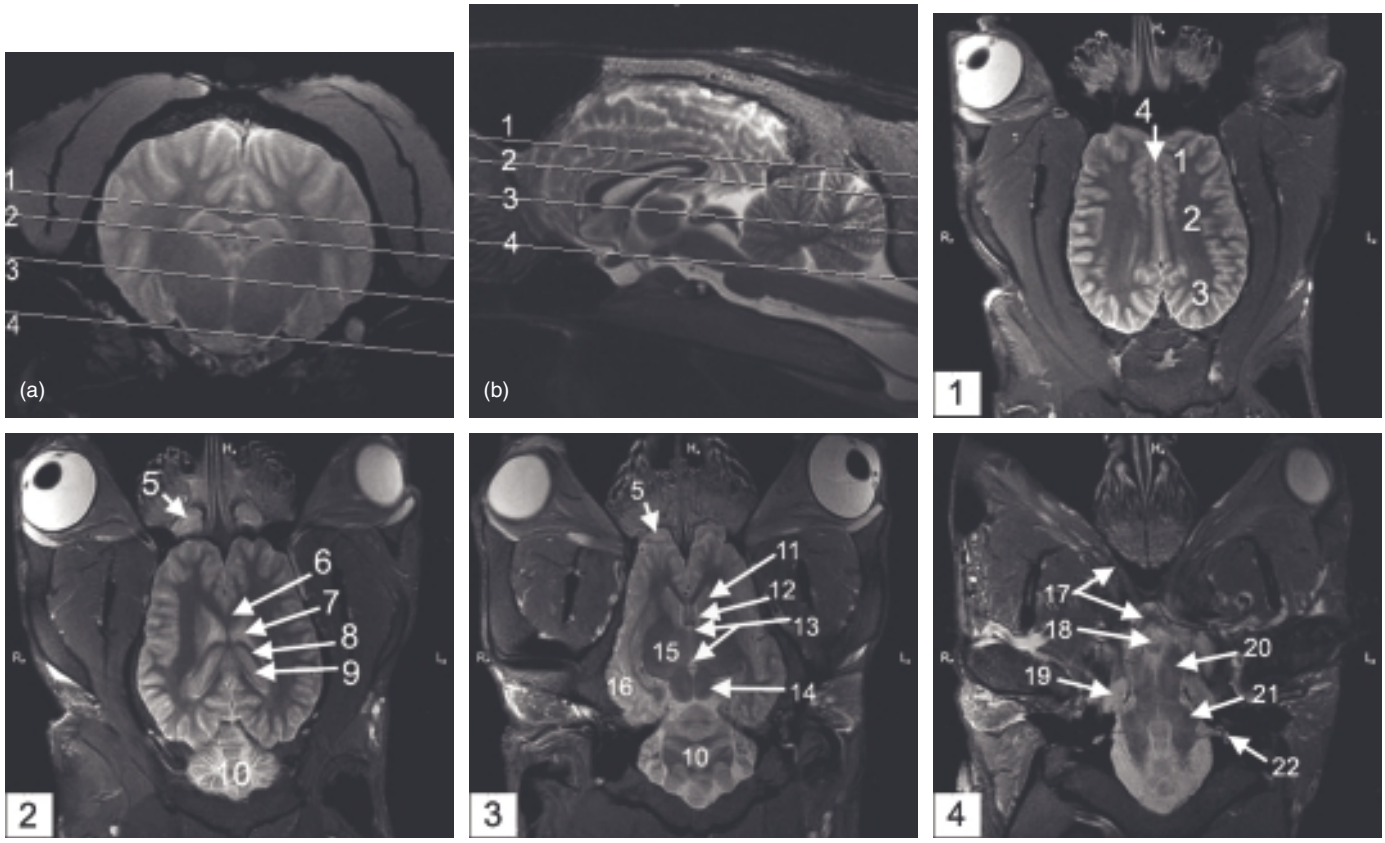

Figure 11.18 Dorsal plane intracranial anatomy. Gradient-echo transverse (a) and sagittal (b) images used for spatial referencing of the labelled STIR dorsal plane images 1–4. Labelled structures: **1**, frontal lobe; **2**, parietal lobe; **3**, occipital lobe; **4**, longitudinal fissure; **5**, olfactory lobe and recess; **6**, fornix; **7**, lateral ventricle; **8**, corpus callosum; **9**, hippocampus; **10**, cerebellum; **11**, caudate nucleus; **12**, interventricular foramen; **13**, third ventricle; **14**, rostral colliculus; **15**, thalmus at interthalamic adhesion; **16**, putamen/globus pallidus; **17**, optic chiasm and nerve; **18**, pituitary gland (partial volume); **19**, trigeminal nerve; **20**, crus cerebri; **21**, cerebellar pedicle; **22**, facial nerve.

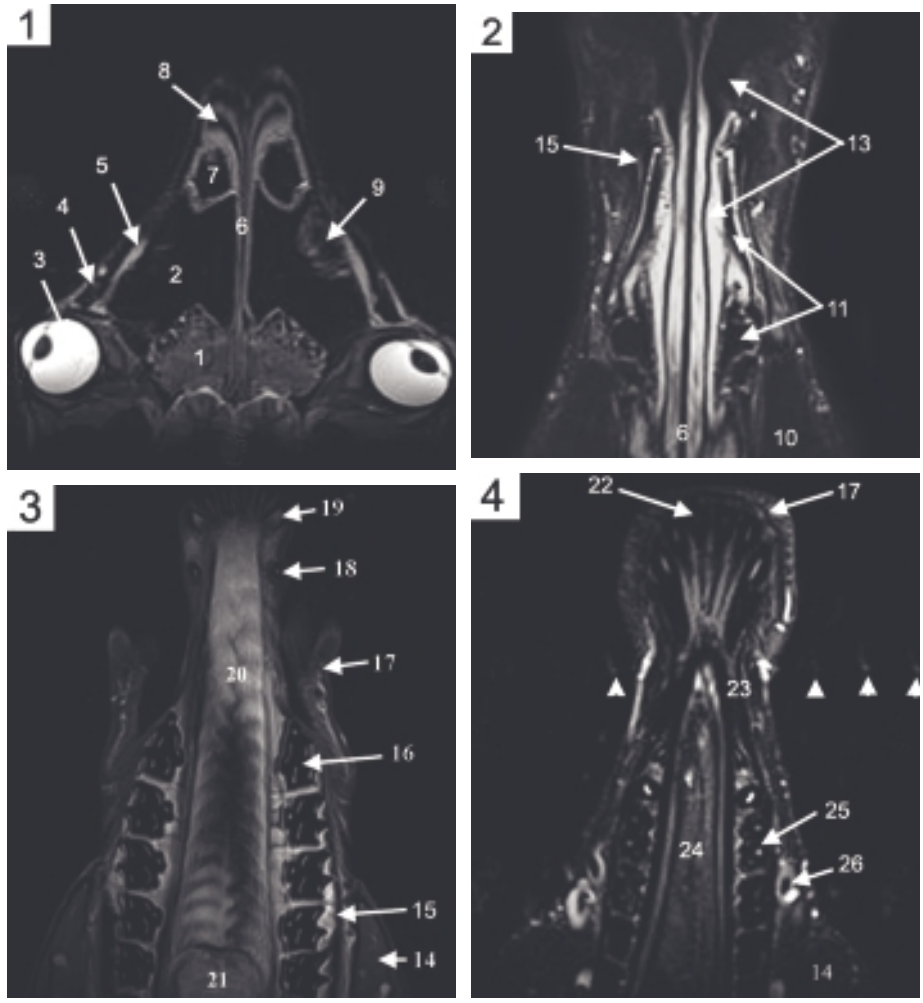

Figure 11.19 Dorsal plane MR anatomy of the skull. STIR (images 1–3) and T2-weighted (image 4) dorsal plane images, presented from dorsal to ventral. The arrow heads in image 4 denote blood flow artefact in the phase encoding direction (right to left). Labelled structures: **1**, ethmoid turbinates; **2**, frontal sinus; **3**, eye; **4**, caudal maxillary sinus; **5**, nasolacimal duct; **6**, nasal septum; **7**, dorsal conchal sinus; **8**, dorsal nasal meatus; **9**, middle nasal meatus (partial volume artefact); **10**, rostral maxillary sinus; **11**, ventral conchal sinus; **12**, nasal mucosa; **13**, common nasal meatus; **14**, superior labii levator muscle; **15**, maxillary bone; **16**, second maxillary premolar; **17**, lip; **18**, wolf tooth; **19**, third maxillary incisor; **20**, hard palate, **21**, soft palate; **22**, first mandibular incisor; **23**, mandibular diastema; **24**, tongue; **25**, third mandibular premolar; **26**, facial vein.

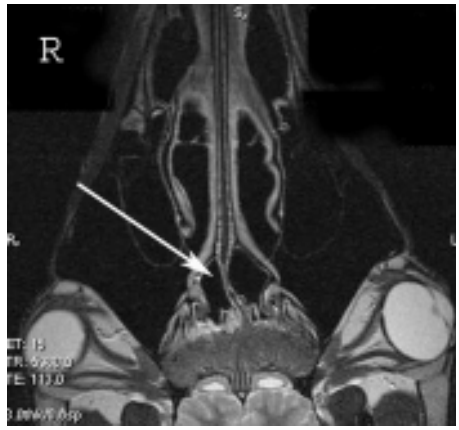

Figure 11.20 Normal variation – nasal septum deviation. T2-weighted dorsal image of the caudal nasal cavity. The nasal septum is deviated towards the right immediately rostal to the ethmoid turbinates (white arrow), a common incidental normal variation. Note the adjacent air-filled sinuses are well aerated with smooth mucosal surfaces and there is no abnormal mass or fluid accumulation. **R**, right side.

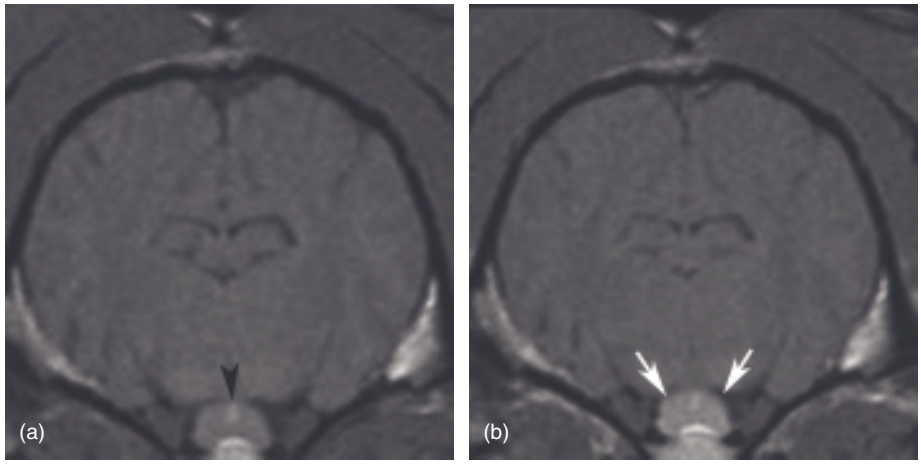

Figure 11.21 Normal variation – pituitary gland signal and enhancement. T1-weighted transverse images of the brain at the level of the pituitary gland pre-contrast (a) and post-contrast (b) administration. There is a central hyperintense signal present within the normal pituitary gland (black arrowhead) on the pre-contrast image. Following contrast, the remainder of the pituitary gland has uniform enhancement (white arrows).

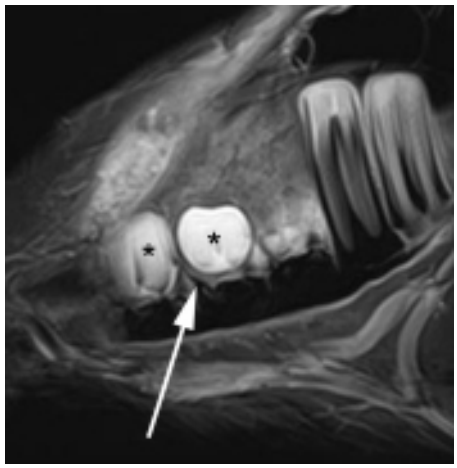

Figure 11.22 Normal variation – juvenile rostral mandible. T2-weighted sagittal image of the maxillary arcade of 1-month-old foal. The teeth buds of the 2nd and 3rd premolars are seen as nearly uniformly hyperintense structures located adjacent to the apices of the deciduous dentition. At this stage, the second molar is not completely mineralized; the crown is hyperintense relative to the hypointense crowns of the premolars and 1st molar.

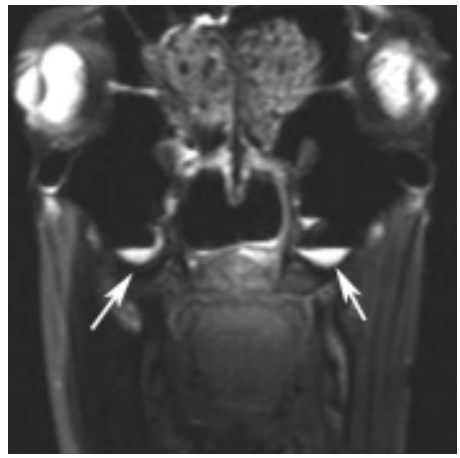

Figure 11.23 Normal variation – fluid in the nasal cavity. T2-weighted transverse image of the caudal nasal cavity and ethmoid turbinates. There is a small bilateral volume of homogenous hyperintense fluid accumulation in the dependent aspects of the caudal nasal cavity (white arrows). For this sequence, the isolated head was positioned in sternal recumbency creating the distinct air-fluid interface in the horizontal plane relative to gravity.

sluggish in flow and slightly engorged (Figure 11.24). Over time, the dependent superficial soft tissues can become oedematous and give the false impression of cellulitis (Figure 11.25). Additionally, the volumes of the normal air-filled guttural pouches are commonly asymmetric in anaesthetized horses positioned in lateral recumbency for any length of time (Figure 11.26). Care

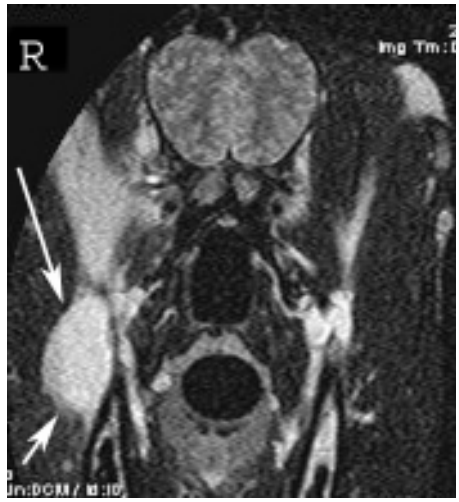

Figure 11.24 Normal variation – venous congestion. T2-weighted transverse image of the skull at the level of the frontal lobes. There is enlargement of the right buccal vein from venous congestion and sluggish flow in the dependent aspects of the skull (white arrows). The horse was in right lateral recumbency for imaging the head. **R**, right.

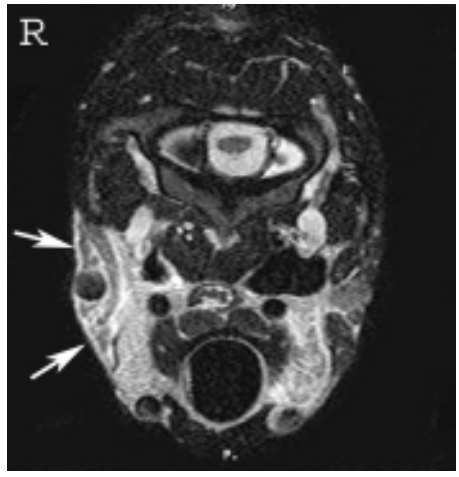

Figure 11.25 Normal variation – oedema. T2-weighted transverse image of the caudal skull at the level of the occipital-atlanto junction. There is diffuse hyperintense signal within the dependent tissues of the right side from venous congestion and edema after prolonged right lateral recumbency (white arrows). **R**, right.

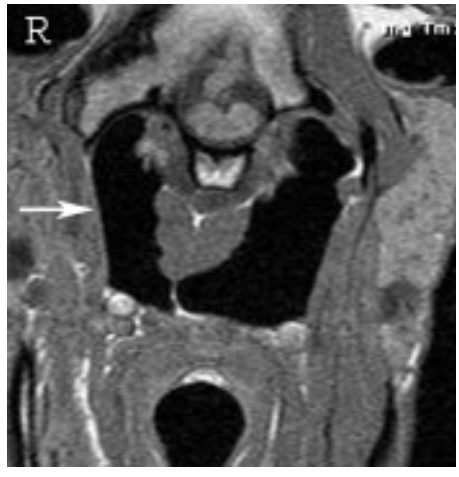

Figure 11.26 Normal variation – guttural pouch asymmetry. Proton density transverse image of the skull at the level of the guttural pouches. There is decreased volume of the dependent right side guttural pouch (white arrow). Note there is no abnormal tissue or signal within the guttural pouches or surrounding tissues. **R**, right.

must be exercised to not mistake such artefacts and incidental findings as representing true pathology.

REFERENCES

[1] Kraft SL, Gavin PR. Physical principles and technical considerations for equine computed tomography and magnetic resonance imaging. *Vet Clin N Am: Equine Pract* 2001; **17**: 115–30.
[2] Tucker RL, Ferrell EA. Computed tomography and magnetic resonance imaging of the equine head. *Vet Clin N Am: Equine Pract* 2001; **17**: 131–43.
[3] Chaffin MK, Walker MA, McArthur NH, Perris EE, Matthews NS. Magnetic resonance imaging of the brain of normal neonatal foals. *Vet Radiol Ultrasound* 1997; **38**: 102–11.
[4] Arencibia A, Vazquez JM, Jaber R *et al*. Magnetic resonance imaging and cross sectional anatomy of the normal equine sinuses and nasal passages. *Vet Radiol Ultrasound* 2000; **41**: 313–19.
[5] Arencibia A, Vazquez JM, Ramirez JA *et al*. Magnetic resonance imaging of the normal equine brain. *Vet Radiol Ultrasound* 2001; **42**: 405–8.
[6] Vazquez JM, Rivero M, Gil F *et al*. Magnetic resonance imaging of two normal equine brains and their associated structures. *Vet Rec* 2001; **148**: 229–32.
[7] Sanders SG, Tucker RL, Bagley RS, Gavin PR. Magnetic resonance imaging features of equine nigropallidal encephalomalacia. *Vet Radiol Ultrasound* 2001; **42**: 291–6.
[8] Ferrell EA, Gavin PR, Tucker RL, Sellon DC, Hines MT. Magnetic resonance for evaluation of neurologic disease in 12 horses. *Vet Radiol Ultrasound* 2002; **43**: 510–16.
[9] Spoormakers TJP, Ensink JM, Goehring LS *et al*. Brain abscesses as a metastatic manifestation of strangles: symptomatology and the use of magnetic resonance imaging as a diagnostic aid. *Equine Vet J* 2003; **35**: 146–51.
[10] Audigie F, Tapprest J, George C *et al*. Magnetic resonance imaging of a brain abscess in a 10 month old filly. *Vet Radiol Ultrasound* 2004; **45**: 210–15.
[11] Thomas CE, Kornegay JN, Burn RA *et al*. Magnetic resonance imaging – a general overview of principals and examples in veterinary neurodiagnosis. *Vet Radiol Ultrasound* 1993; **34**: 2–17.
[12] Leigh EJ, Mackillop E, Robertson ID, Hudson LC. Clinical anatomy of the canine brain using magnetic resonance imaging. *Vet Radiol Ultrasound* 2008; **49**: 113–21.
[13] Murray RC, Dyson SJ. Image interpretation and artifacts. *Clin Tech Equine Pract* 2007; **6**: 16–25.
[14] Tucker RL, Sampson SN. Magnetic resonance imaging protocols for the horse. *Clin Tech Equine Pract* 2007; **6**: 2–15.

Section C
Pathology

Chapter 12
The foot and pastern

Sue Dyson and Rachel Murray

INTRODUCTION

The aims of this chapter are to discuss briefly the indications for magnetic resonance imaging (MRI) of the foot and pastern, to review the current literature, to give an overview of the spectrum of injuries identified at the Animal Health Trust between January 2001 and December 2007 in horses undergoing either low-field or high-field MRI and to provide detailed descriptions of the lesions identified. Where applicable the current knowledge about the nature of these lesions is reviewed.

INDICATIONS FOR MAGNETIC RESONANCE IMAGING

Prior to consideration of MRI, all horses should be subjected to an in-depth lameness evaluation, including local analgesic techniques, high-quality radiography and, where appropriate, ultrasonography and nuclear scintigraphy. Magnetic resonance imaging is an expensive technique and is not required for the diagnosis of all causes of foot and pastern-related pain. However, in the absence of significant imaging findings, MRI is indicated even in the early stages of lameness. Early recognition of the cause of lameness may permit the most appropriate, targeted treatment. A reliable history of a recent, acute puncture wound to the foot is an exception, when MRI may be considered without previous in-depth evaluation.

Local analgesia should be used to define as objectively as possible the source or sources of pain, bearing in mind the current knowledge about the limitations of the majority of local analgesic techniques. Local analgesia is particularly important when acquiring low-field MR images, because the field of view is relatively small and if lameness is not abolished by palmar digital analgesia, then the pastern must be included in the examination. A number of abnormalities may be identified using MRI and interpretation of their relative significance can be facilitated by accurate localization of pain. Likewise the use of nuclear scintigraphy can help to determine the likely clinical significance of lesions identified using MRI, and in some horses may give information about both the nature of the pathological process and the prognosis.

Equine MRI, edited by Rachel C. Murray.

If a flexor cortex defect in the navicular bone is identified radiologically, it is likely that there is associated pathological change in at least the deep digital flexor tendon (DDFT) and such horses may not require MRI to give a prognosis. While MRI could give additional information, the prognosis for such lesions is extremely guarded, and the additional information obtained may have to be balanced against the cost.

SPECTRUM OF INJURY

Five hundred and eighty-four horses were examined at the Animal Health Trust during the study period using low- or high-field MRI, 568 with forelimb lameness and 16 with hind limb lameness. Pain was localized to the digit using local analgesic techniques. In addition to horses with negative imaging findings, horses with the following findings underwent MRI in order to determine better the nature and extent of pathological change:

- ill-defined osseous cyst-like lesions (OCLLs) in the spongiosa of the navicular bone without apparent communication with the flexor (palmar) cortex, or with equivocal radiolucent zones in the flexor cortex of the navicular bone associated with focal, moderate or intense increased radiopharmaceutical uptake (IRU)
- punctate focal core lesions in the DDFT in the pastern, with or without IRU in the region of the DDFT in pool phase scintigraphic images, or at its insertion in the distal phalanx in bone phase images
- enlargement of a collateral ligament (CL) of the distal interphalangeal (DIP) joint with or without change in echogenicity, or with focal IRU in the distal phalanx at the site of insertion of a CL of the DIP joint.

Horses with focal lesions in an oblique sesamoidean ligament (OSL), or a branch of the superficial digital flexor tendon (SDFT), which were considered insufficient to cause the degree of lameness, were also examined. Horses with a previously identified fracture of the distal phalanx or cartilage of the foot were evaluated if concurrent soft tissue pathology, which may influence treatment and prognosis, was suspected. Horses with periarticular new bone around the dorsal aspect of the proximal interphalangeal (PIP) joint which did not respond to intra-articular analgesia were also examined, because other lesions were thought likely be responsible for lameness.

The distribution of injuries is outlined in Table 12.1. This table reflects the cause or causes of lameness considered likely to be of most clinical importance based on the interpretation of the MR images in conjunction with the results of local analgesia (e.g. intra-articular analgesia of the DIP joint, intrathecal analgesia of the navicular bursa) and other imaging modalities (e.g. nuclear scintigraphy). Multiple injuries (i.e. several lesions likely to be contributing to pain and lameness), desmitis of a CL of the DIP joint and DDF tendonitis were the predominant injury categories.

All horses with a suspected lesion of the navicular bone, DDFT or a CL of the DIP joint based on conventional imaging techniques were determined to have much more severe lesions on MR images, often with lesions to other structures. A large proportion of lesions of the DDFT that extended proximal to the PIP joint were not detected ultrasonographically. Similarly,

Table 12.1 Distribution of injuries considered to be the primary cause of lameness based on magnetic resonance imaging, clinical findings, response to local analgesia and other imaging modalities in 584 horses with foot pain, January 2001–December 2007

Injured structure*	Number of horses (%)	Comments
Navicular bone	21 (3.6)	+ 31 horses with multiple injuries, 4 CL DIP joint
Navicular bone and DDFT	60 (10.3)	+ 60 horses with multiple injuries, 1 DSL
DSIL	20 (3.4)	+ 53 horses with multiple injuries, 5 navicular bone and DDFT, 1 navicular bone, 4 CL DIP joint, 1 distal phalanx
CSL	3 (0.5)	+ 57 with multiple injuries, 1 CL DIP joint
DDFT	89 (15.2)	+ 52 horses with multiple injuries, 3 primary distal phalanx pathology, 12 CL DIP joint
CL DIP joint	179 (30.1)	+ 106 horses with multiple injuries, 15 DDFT, 11 navicular bone and& DDFT, 4 primary distal phalanx pathology
SSL	2 (0.5)	
Multiple injuries	176 (30.1%)	
DIP joint	8 (1.4)	+ 10 horses with multiple injuries, 6 CL DIP joint, 1 DSIL
Primary injury of the middle and/or distal phalanges	25 (4.3)	Includes 5 with evidence of previous penetrating injury + 23 horses with multiple injuries, 10 CL DIP joint, 1 navicular bone and DDFT

DDFT, deep digital flexor tendon; CL, collateral ligament; CSL, collateral sesamoidean ligament; DSIL, distal sesamoidean impar ligament; DIP, distal interphalangeal; SSL, straight sesamoidean ligament.

ultrasonography failed to detect many lesions of the CLs of the DIP joint, the straight sesamoidean ligament (SSL) and the OSLs.

TYPES OF PATHOLOGICAL CHANGE

Navicular bone

Lesions of the navicular bone are seen alone, in conjunction with injuries of the DDFT, distal sesamoidean impar ligament (DSIL) or collateral sesamoidean ligament (CSL), or as a complex of injuries to multiple structures [1–7]. A comparison of MRI findings in control horses with no history of foot-related pain and horses with chronic palmar foot pain showed significant alterations of the podotrochlear (navicular) apparatus in the lame horses [8]. A comparative MRI and postmortem study showed good correlation between the lesions identified using MRI, gross [9] and histopathological findings [10]. The typical types of lesion identified are summarized in Table 12.2 and illustrated in Figures 12.1–12.8. We believe that there are a number of different pathological processes which can take place within the navicular bone and other components of the podotrochlear apparatus and the DDFT.

Table 12.2 Summary of magnetic resonance imaging abnormalities of the navicular bone

Distal border	Smooth extension of the distal border into the DSIL
	Entheseophyte formation
	Irregular thickness of distal cortex with mineralization extending proximally
	Enlargement of synovial invaginations
	Distal border fragment with no reaction in parent bone
	Distal border fragment with change in contour and signal intensity in adjacent navicular bone
Proximal border	Entheseophyte formation
	Endosteal mineralization
	Proximal border fragment
Flexor (palmar) border	Endosteal irregularity
	Increased thickness of flexor cortex
	Focal increased signal in flexor cortex in all image sequences
	Focal fluid accumulation palmar to bone consistent with fibrocartilage loss
	More extensive loss of fibrocartilage
	Linear increase in signal intensity through flexor cortex in STIR images
	Focal disruption of flexor cortex, with reaction (abnormal fluid and mineralisation) extending dorsally into the spongiosa
	Adhesions of DDFT
Dorsal border	Periarticular osteophyte formation
	Endosteal mineralization
Spongiosa/ medulla	Discrete osseous cyst-like lesions in the distal third of the bone
	Diffuse increased signal intensity on STIR images
	Focal increased signal on STIR images at insertion of CSL and/or origin of DSIL
	Linear increased signal on STIR images between insertion of CSL and origin of DSIL
	Focal or diffuse decreased signal intensity on T1- and T2-weighted images consistent with mineralization

Thickening of the flexor cortex

Some horses have no detectable structural change of the internal architecture of the flexor cortex of the navicular bone, but have significant thickening of the cortex, with or without endosteal irregularity, seen on T1- and T2-weighted images (Figure 12.1). This has usually been seen in association with distal or proximal extension of the flexor border, with associated abnormalities of the DSIL or CSL.

Degenerative lesions of the palmar cortex

Clinical experience with MRI in horses with foot pain provides support for the progression of many lesions from defects in the fibrocartilage of the distal half of the navicular bone centred around the sagittal ridge, into defects in the subchondral bone [11]. We have previously demonstrated that this site is prone to early degenerative changes, even in clinically sound horses [12]. Early clinical lesions are characterized on MR images by focal fluid accumulation dorsal to the DDFT, reflecting loss of fibrocartilage, and

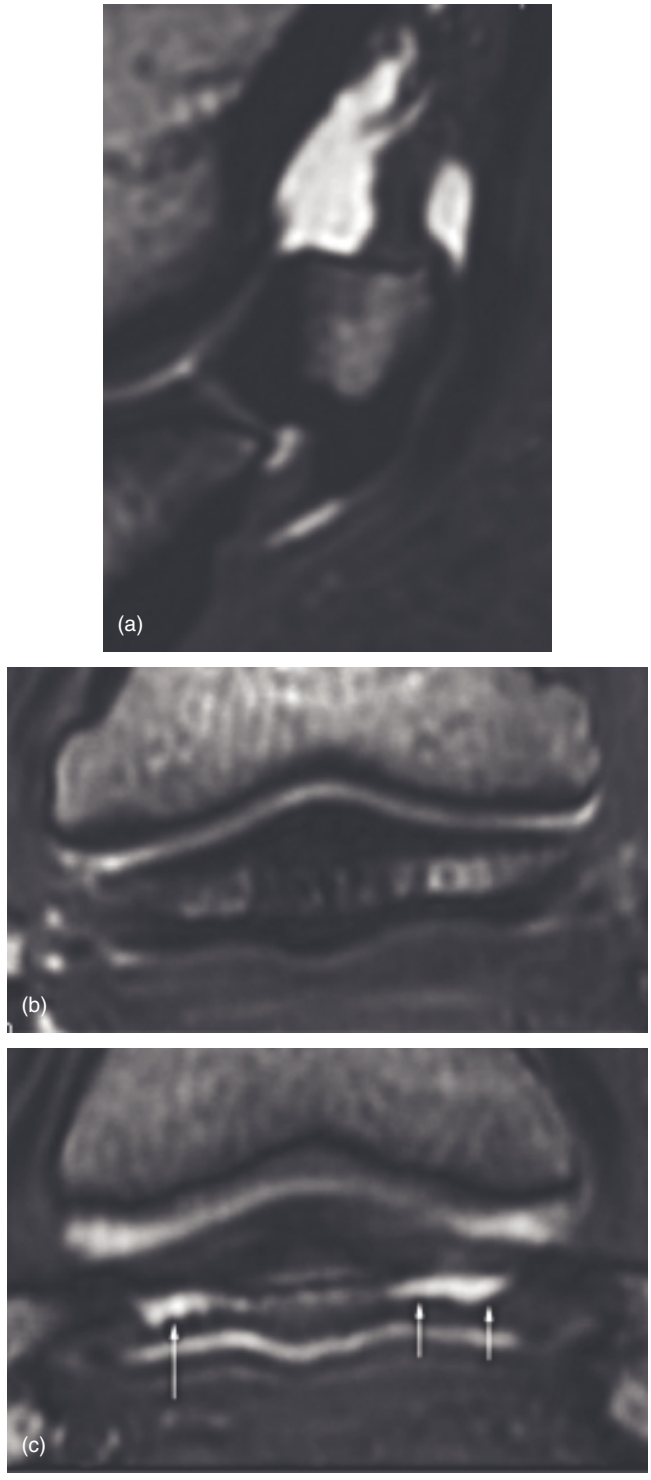

Figure 12.1 (a) Sagittal 3D T2* GRE high-field MR image of a navicular bone of a 4-year-old Warmblood. The dorsal, distal and palmar cortices of the navicular bone are thick. There is distal extension of the flexor cortex of the bone and a small entheseophyte on the proximal border of the bone. (b) Transverse 3D T2* GRE high-field MR image of the same navicular bone as in (a). The dorsal cortex of the navicular bone is thickened. (c) Transverse 3D T2* GRE high-field MR image of the same foot as in (a) and (b). The normal architecture of the distal sesamoidean impar ligament is disrupted with large areas of increased signal intensity (arrows).

focal increased signal intensity in fat-suppressed images in the flexor cortex (Figure 12.2). There may be endosteal irregularity of the flexor cortex of the bone (Figure 12.3). There is good correlation with increased radiopharmaceutical uptake in the navicular bone and these degenerative lesions [13, 14]. Less commonly acentric lesions occur in the proximal half of the flexor cortex of the navicular bone.

More advanced lesions have a focal area in the flexor cortex with increased signal intensity in T1- and T2-weighted images and in fat-suppressed images, often associated with an area of generalized reduced signal intensity in T1- and T2-weighted images in the spongiosa dorsal to

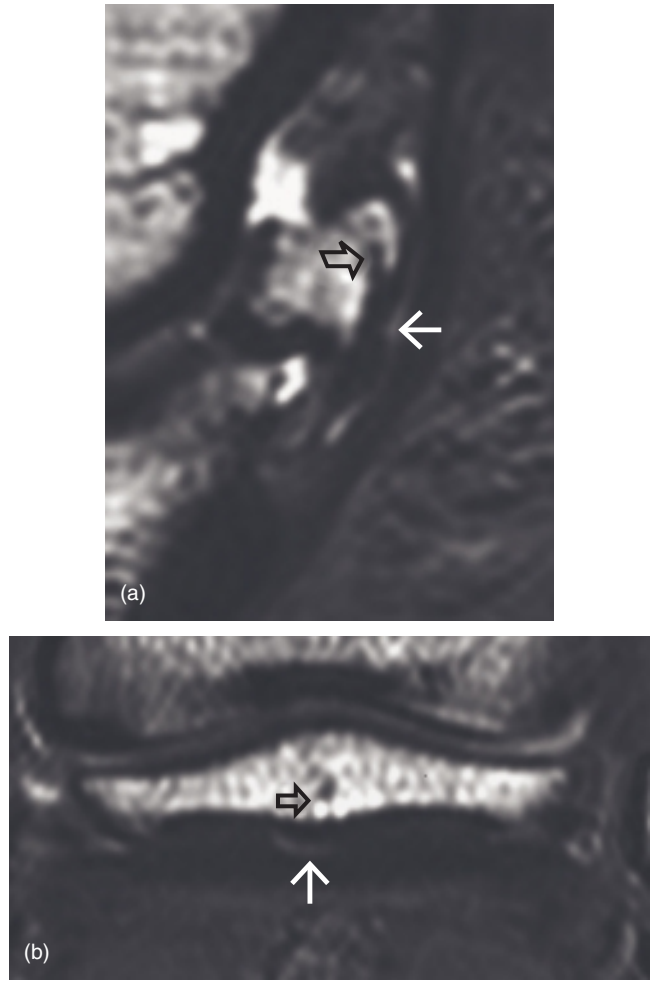

Figure 12.2 (a) Parasagittal 3D T2* GRE high-field MR image of a navicular bone. There is a partial thickness defect in the palmar cortex of the bone with focal fluid accumulation, reflecting loss of fibrocartilage (black arrow). There is irregular endosteal mineralization (open arrow). There was no significant radiological abnormality and radiopharmaceutical uptake was normal. (b) Transverse 3D T2* GRE high-field MR image of the navicular bone in (a). There is focal fluid accumulation palmar to the bone (arrow) reflecting fibrocartilage loss. Abaxial to this the deep digital flexor tendon is in close apposition to the bone and probably adherent. Dorsal to the fluid accumulation there is focal endosteal mineralization (open arrow).

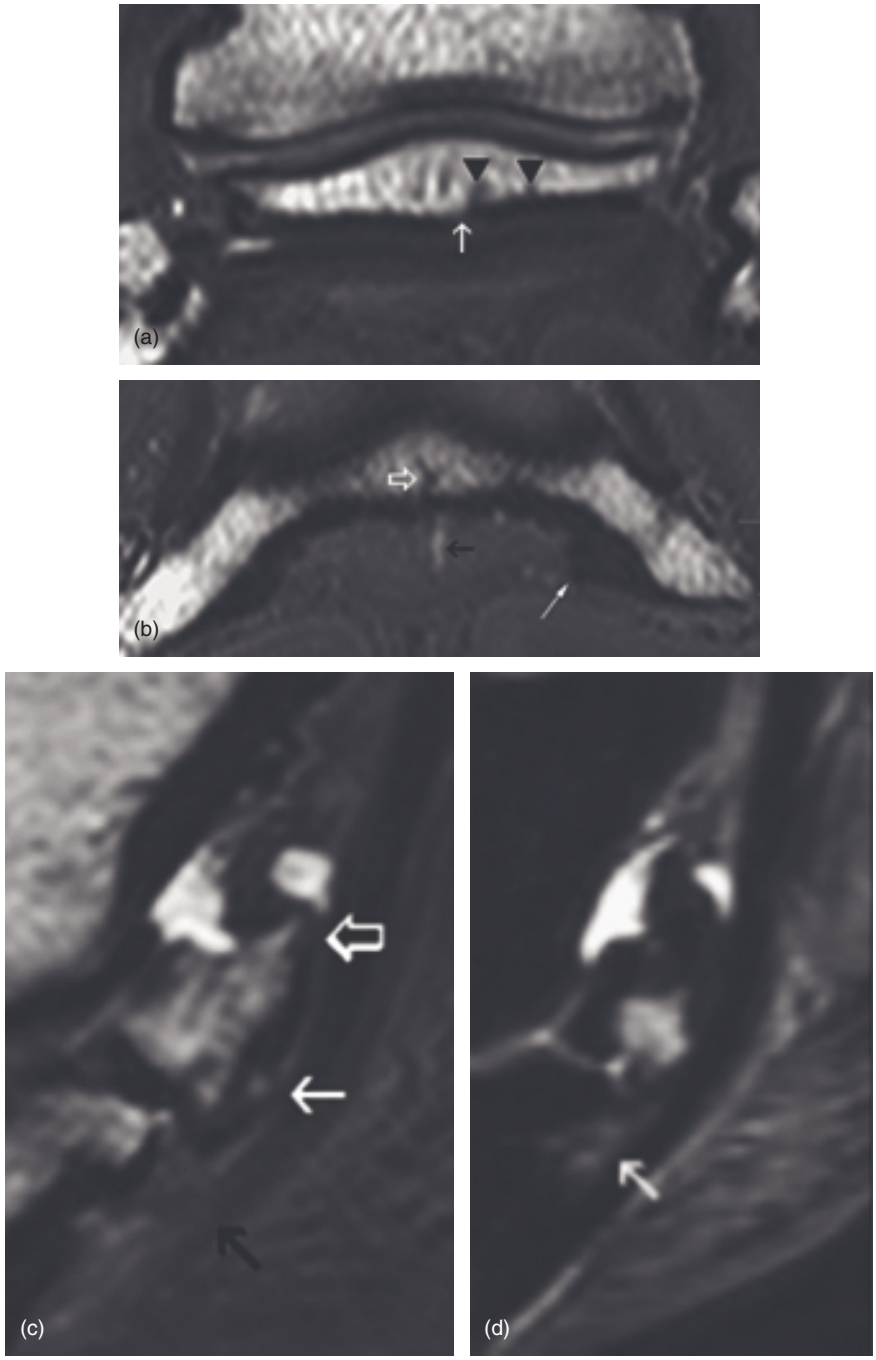

Figure 12.3 (a) Transverse 3D T2* GRE high-field MR image of a navicular bone. There is focal disruption of the palmar cortex of the bone just lateral to the sagittal ridge (white arrow). There is also mild endosteal irregularity laterally (arrow heads). In a palmaro 45° proximal–palmarodistal oblique radiographic view there was an extremely subtle area of reduced opacity within the palmar cortex coincident with this lesion, but it did not appear to penetrate the palmar aspect of the cortex. No other radiological abnormality was detected. There was focal moderately increased radiopharmaceutical uptake in the navicular bone.
(b) Transverse 3D T2* GRE high-field MR image of the foot in (a). Medial is to the right. There is complete loss of separation between the deep digital flexor tendon and the distal sesamoidean impar ligament. There is a linear region of increased signal intensity through both structures (black arrow). Dorsal to this there is mild endosteal irregularity of the palmar cortex of the distal phalanx (open arrow). There is entheseophyte formation on the axial aspect of the medial palmar process of the distal phalanx (white arrow). (c) Parasagittal 3D T2* GRE high-field MR image of the navicular bone in (a). There is a partial thickness defect in the palmar cortex of the navicular bone (white arrow). There is mild endosteal irregularity of the dorsal and palmar cortices of the navicular bone. Distal to the navicular bone there is loss of separation between the distal sesamoidean impar ligament and the deep digital flexor tendon (black arrow). There is also an entheseophyte extending into the collateral sesamoidean ligament (open arrow). (d) Parasagittal 2D STIR high-field MR image of the navicular bone in (a)–(c). There is a well-circumscribed region of hyperintense signal in the distal half of the bone. There is also increased signal intensity in the distal phalanx at the insertion of the distal sesamoidean impar ligament (arrow).

the flexor cortex lesion (Figure 12.4). There are frequently focal lesions of the DDFT, either sagittal plane splits or dorsal irregularities in the same sagittal plane as the flexor cortex defect. With advanced degenerative lesions of the flexor cortex there are often adhesions of the DDFT. Whether lesions

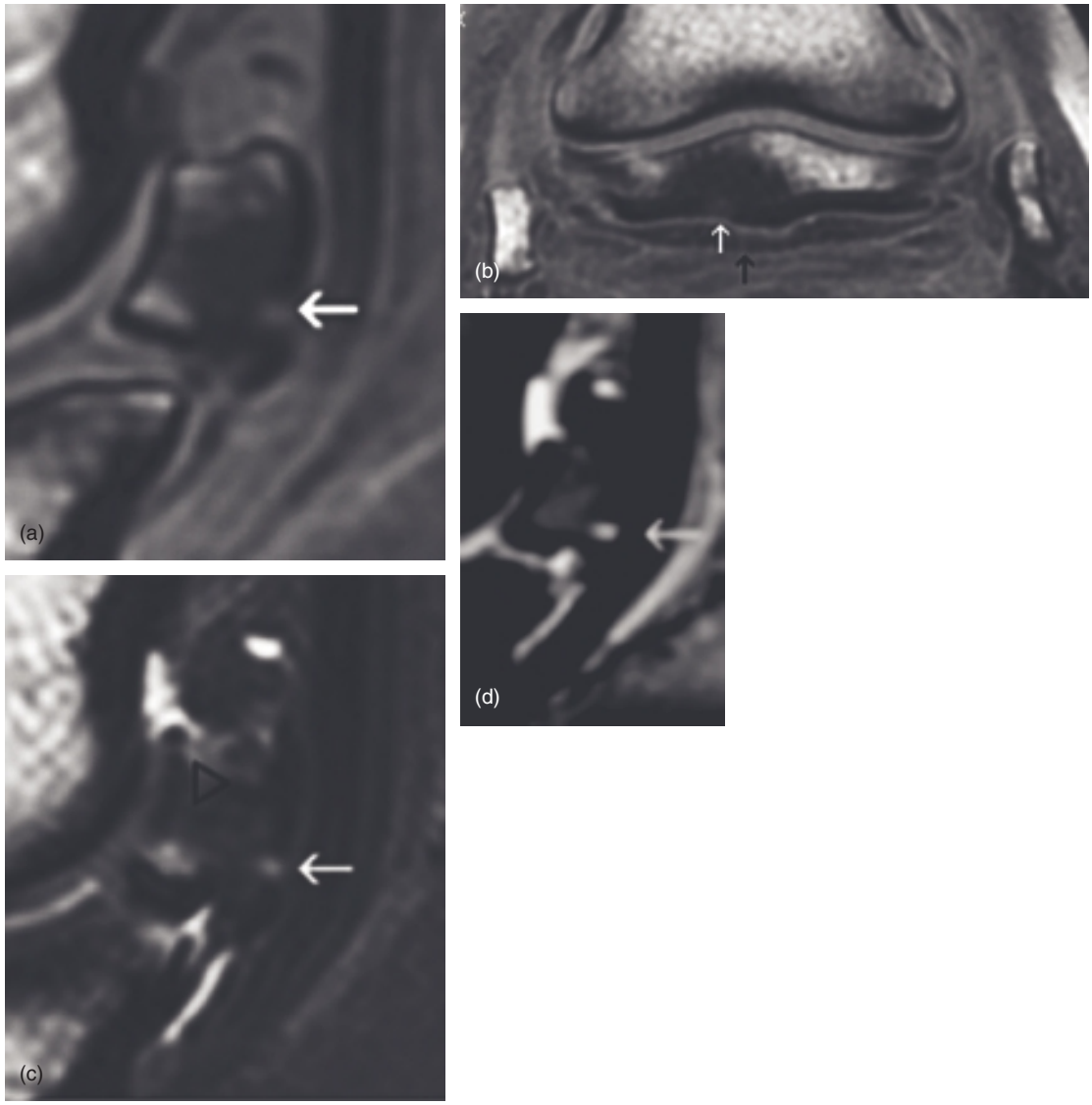

Figure 12.4 (a) Parasagittal 3D SPGR high-field MR image of a navicular bone. There is a full thickness defect in the palmar cortex of the bone (arrow). There is a diffuse area of reduced signal intensity within the spongiosa of the bone. On a palmaro 45° proximal–palmarodistal oblique radiographic view there was a focal area of subtle reduced opacity of the palmar cortex coincident with the defect in the MR image. No other radiological abnormality was detected. There was focal intense increased radiopharmaceutical uptake in the navicular bone. (b) Transverse 3D SPGR high-field MR image of the foot in (a). Medial is to the right. There is a full thickness defect of the palmar cortex of the navicular bone lateral to the sagittal ridge (white arrow); there is decreased signal intensity in the medulla in the lateral half of the bone. There is a sagittal plane split in the deep digital flexor tendon (black arrow). There is mild decreased signal intensity in the medial palmar process of the distal phalanx. (c) Parasagittal 3D T2* GRE high-field MR image of the navicular bone in (a) and (b). There is disruption of the flexor cortex (arrow) and focal increased signal intensity extending into the subchondral bone. Dorsally there is a diffuse area of intermediate signal intensity in the medulla. There is endosteal irregularity of the flexor cortex proximally (arrow head). (d) Parasagittal 2D STIR high-field MR image of the navicular bone in (a)–(c). There is focal disruption of the palmar cortex of the navicular bone with a focal area of hyperintense signal extending into the subchondral bone (arrow). There is a mild, diffuse increase in signal intensity in the medulla.

in the DDFT are primary or secondary to pre-existing damage of the fibrocartilage currently remains open to debate. However, recent postmortem evidence suggests that there may be non-age-related degenerative vascular and matrix changes in the dorsal aspect of the DDFT in both lame and clinically normal horses [15]. Although other authors have suggested that vascular occlusion and matrix changes in the DDFT may be age-related [16], the results of our study showed that the severity of these changes was greater in horses with palmar foot pain than in control horses. Minor fibrillation of the dorsal aspect of the DDFT was seen in both lame and control horses, whereas deep sagittal splits were only seen in lame horses. Complete occlusion of blood vessels, replacement of normal tendon architecture by focal fibroplasia and areas of fibrocartilaginous metaplasia were common in the lame horses. As these changes are predominantly seen in the intratendonous septa, there is a strong possibility that they predispose to the development of sagittal splits in the dorsal surface of the tendon along these septal planes. Sharp edges of splits in the DDFT extending from the dorsal surface may cause ulceration of the fibrocartilage of the navicular bone and thus predispose to lesions extending into the medulla.

Although historically navicular disease has been considered to be a bilateral condition with an insidious onset of lameness, lesions of the flexor border of the navicular bone may be unilateral or bilateral, and in some horses result in sudden onset of severe, unilateral lameness. Rarely, intense sclerosis of the medulla, characterized by diffuse low signal intensity throughout in both T1- and T2-weighted images has been seen in association with a defect in the flexor cortex [17].

Lesions restricted to the medulla

A group of horses has also been identified with no detectable abnormalities of the flexor fibrocartilage or cortex, but with diffuse abnormalities of the spongiosa (medulla) characterized by increased signal intensity in fat-suppressed images and reduced signal intensity in T1-weighted images (Figure 12.5). This

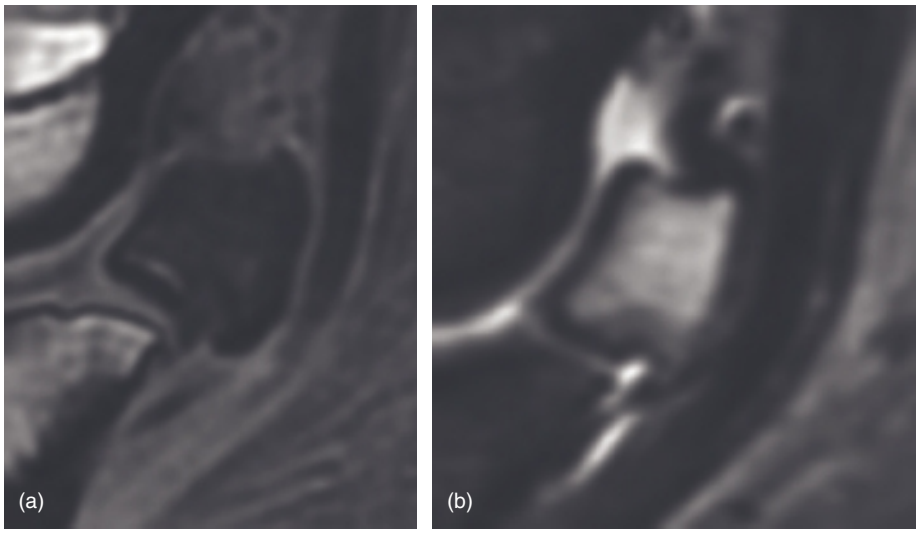

Figure 12.5 (a) Parasagittal 3D SPGR high-field MR image of a navicular bone. There is diffuse hypointense signal throughout most of the navicular bone. No significant radiological abnormality was detected; radiopharmaceutical uptake in the bone was marginally increased. (b) Parasagittal 2D STIR high-field MR image of the navicular bone in Figure 12.5a. There is diffuse hyperintense signal throughout the majority of the spongiosa of thee bone.

was not associated with significant IRU in seven of 11 horses and only mild IRU in the remaining four [14]. Postmortem examination of several horses has revealed evidence of early fat necrosis with a moth-eaten appearance of the trabeculae, with necrosis of bone edges. This may have a different aetiopathogenesis to the degenerative lesions of the flexor cortex described previously.

Increased signal intensity in the spongiosa in fat-suppressed images

Hyperintense signal in the spongiosa (medulla) of the navicular bone has been ascribed to the presence of oedema in the marrow spaces [3], but this was not validated postmortem. Further research is required to determine the true causes of this phenomenon. In our study of horses with chronic palmar foot pain, mild or moderate focal or generalized increased signal intensity in fat-suppressed images was associated with trabecular thinning and widened intertrabecular spaces [10]. Increased signal in fat suppressed images associated with irregularly decreased signal intensity in T1- and T2-weighted images was associated with generalized osteonecrosis and fibrosis, with irregular trabeculae, adjacent adipose tissue oedema and prominent capillary infiltration. A recent postmortem study of feet with advanced radiological abnormalities of the navicular bone demonstrated that increased signal intensity in fat-suppressed images correlated with areas of degenerate adipose tissues, with haemorrhage or replacement by fibrocollagenous material, or fluid-filled cystic spaces [18].

More recent data from horses with less advanced pathological change of the navicular bones detectable only using MRI revealed a spectrum of abnormalities associated with regions of high signal intensity in fat-suppressed images, including perivascular or interstitial oedema, enlarged bone spaces, fibrovascular tissue in bone spaces, medullary fibrosis, focal bone necrosis, marrow fat oedema and adipose tissue disruption (Dyson and Murray, unpublished data).

In some other horses, fluid-filled OCLLs have been seen in the distal aspect of the bone, apparently separate from synovial invaginations, and not associated with any detectable abnormality of the flexor aspect of the bone (Figure 12.6). Such lesions have not yet been characterized histologically and their aetiology remains speculative, although may be associated with lesions of the DSIL.

A linear band of increased signal intensity on fat-suppressed images in the palmar aspect of the spongiosa of the navicular bone has been seen in some horses with primary lesions of the DDFT [1], with no other structural abnormalities of the bone. Such increased signal intensity appears to be reversible and has not been seen at follow up examinations.

Altered signal intensity between the attachments of the CSL and the DSIL

A linear band of increased signal intensity is commonly seen extending from the insertion of the CSL to the origin of the DSIL in fat-suppressed images, with subtle reduced signal intensity in T1-weighted images (Figure 12.7). We

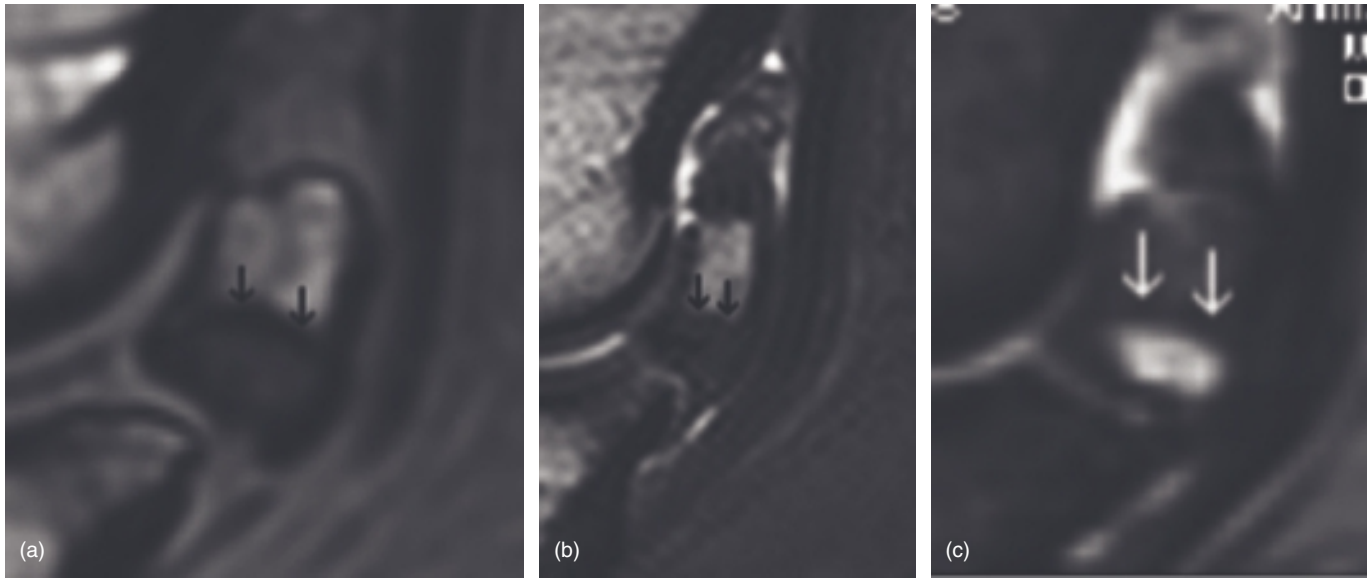

Figure 12.6 (a) Parasagittal 3D SPGR high-field MR image of a navicular bone. There is a mineralized band traversing from the dorsal to palmar cortices (arrows), distal to which is a diffuse area of intermediate signal intensity. There was a single axial discrete radiolucent zone proximal to the distal border of the bone and mild focal increased radiopharmaceutical uptake in the bone. (b) Parasagittal 3D T2* GRE high-field MR image of the navicular bone in Figure 12.6a. There is a similar mineralized band traversing from the dorsal to palmar cortices of the bone (arrows), distal to which is an area of intermediate signal intensity, consistent with proteinaceous fluid. (c) Parasagittal 2D STIR high-field MR image of the navicular bone in Figure 12.6a. There is a band of mineralization from the dorsal to palmar cortices (arrows), distal to which is a diffuse area of hyperintense signal.

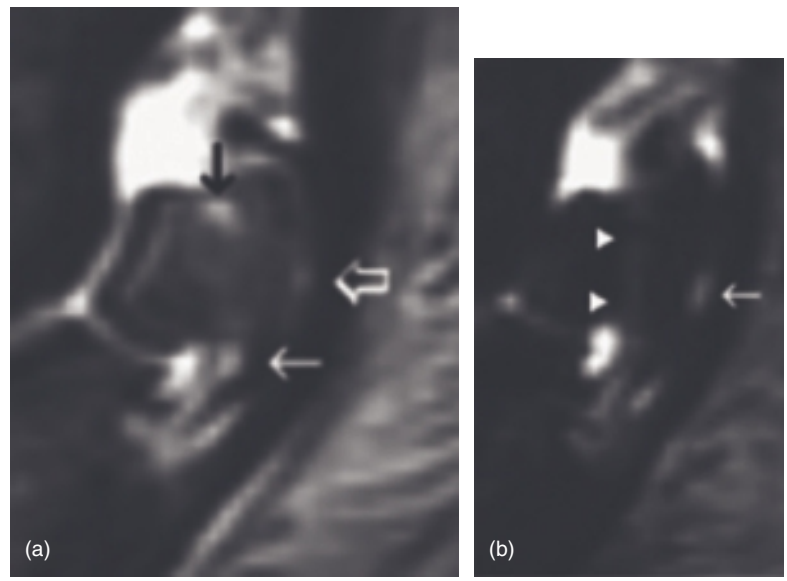

Figure 12.7 (a) Sagittal 2D STIR high-field MR image of a navicular bone. There is focal hyperintense signal immediately distal and dorsal to the insertion of the collateral sesamoidean ligament (black arrow). There is focal hyperintense signal proximal to and extending into the distal sesamoidean impar ligament (white arrow). There is a focal area of fluid accumulation palmar to the bone midway between the proximal and distal borders of the bone (open arrow), reflecting loss of or a depression in the fibrocartilage. (b) Sagittal 2D STIR high-field MR image of a navicular bone (the same as in Figures 12.2a and b). There is a linear band of high signal intensity extending between the insertion of the collateral sesamoidean ligament and the origin of the distal sesamoidean impar ligament (DSIL) (arrow heads). There is fluid accumulation palmar to the navicular bone (white arrow). There is also increased signal intensity in the DSIL throughout its length and at its insertion onto the distal phalanx.

believe that this represents abnormal stress in the podotrochlear apparatus. Focal increased signal intensity may be seen at either the insertion of the CSL or the origin of the DSIL (Figure 12.7). Presence of increased signal intensity was positively associated with lesions of the CSL and DSIL respectively [19].

Entheseous changes

The presence of entheseous new bone on the proximal border of the navicular bone, reflecting previous insertional desmopathy of the CSL is well documented radiologically [20, 21] and at postmortem examination [16, 22], in both clinically normal horses and horses with navicular disease. Its clinical significance remains uncertain, although more extensive new bone in this location tends to be associated with other signs of navicular disease [16, 20]. Recent experience with MRI has confirmed this [2] (Figure 12.3). Rarely, an avulsion fracture is identified at the insertion of the CSL into the navicular bone [11].

The degree of cortical irregularity on the distal border of the navicular bone is extremely variable, with mineralization sometimes extending through the distal half of the bone. There was a highly significant relationship between lesions of the DSIL and abnormalities of the distal border of the navicular bone [19]. There was also a positive correlation between IRU in the navicular bone and abnormalities of the distal border detected using MRI [14]. Thus these abnormalities seen on MR images are associated with altered bone modelling, either at these sites or elsewhere in the bone [14].

Mineralized and osseous fragments in the DSIL have also been recognized in both normal horses and in horses with navicular disease and their clinical significance remains difficult to determine. Fragments were unusual in sound horses undergoing pre-purchase radiological examination [23], although their true incidence may be underestimated by radiological examination compared with MRI or computed tomography. In two postmortem studies, fragments associated with a defect in the distal margin of the navicular bone were more common in horses with navicular disease than in age-matched controls [12, 16]. This has also been our clinical experience.

With computed or digital radiography it has become easier to detect distal border fragments radiologically [24]; however, experience with MRI indicates that their prevalence is higher than determined radiologically. These fragments are seen in either dorsal or sagittal images as discrete, rounded or oval-shaped areas of low signal intensity at the medial and/or lateral angle of the distal aspect of the navicular bone. Use of transverse images oriented parallel to the floor in a standing horse can be particularly useful to determine the presence of a fragment and its relationship with the parent bone. There may be a concave defect in a parent bone. Such fragments may be present without any other reaction in the navicular bone or in the DSIL or DDFT, and these may be clinically innocuous. However, there may be diffuse low signal intensity around the concave defect in the navicular bone in T1- and T2-weighted images extending a variable distance proximally, indicating abnormal mineralization (Figure 12.8a), and sometimes focal areas of increased signal intensity in fat-suppressed images. Such

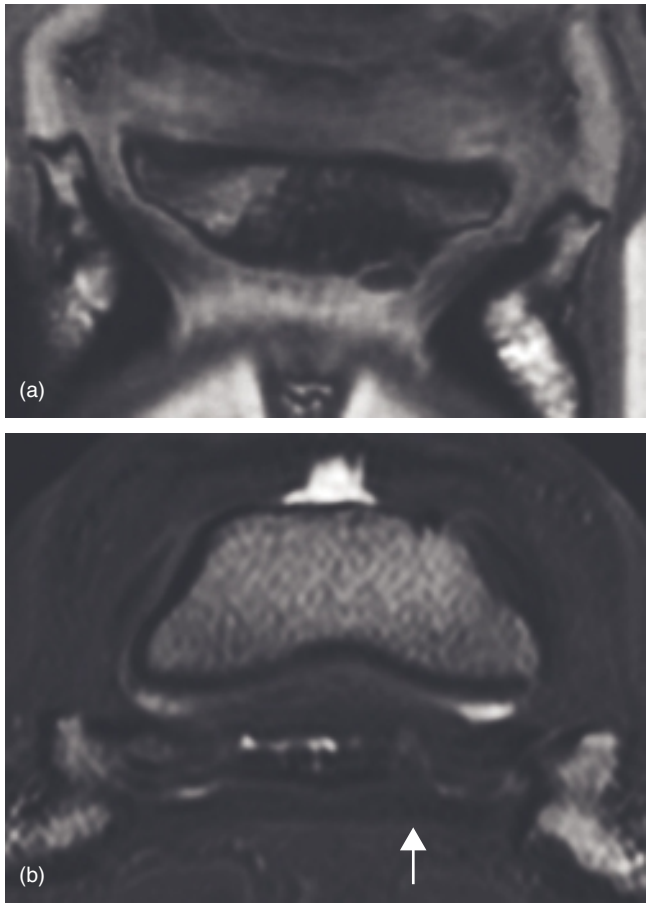

Figure 12.8 (a) Dorsal 3D T1-weighted spoiled gradient-echo high-field magnetic resonance image of a foot. Lateral is to the right. There is a well-circumscribed distal border fragment laterally. There is a concave defect in the lateral angle of the distal border of the navicular bone and marked osseous reaction in the distal half of the navicular bone characterized by reduced signal intensity. Note also modelling of the proximomedial aspect of the navicular bone. (b) Transverse 3D T2-weighted gradient-echo high-field magnetic resonance image of a foot, in which there was fragment distal to the lateral angle of the distal border of the navicular bone. Lateral is to the right. There is an adhesion of the deep digital flexor tendon to the distal border of the navicular bone at the site of the fragment (arrow). There is mild, diffuse decreased signal intensity in the medial palmar process of the distal phalanx.

reactions may reflect chronic instability between the fragment and the bone, which may be associated with pain. Focal adhesions between the fragment and the DDFT have been seen in a small number of horses associated with lameness (Figure 12.8b).

Periarticular osteophytes

Periarticular osteophytes on the dorsoproximal aspect of the navicular bone are most easily seen in T2-weighted sagittal MR images. They can be seen in conjunction with other abnormalities of the navicular bone, but may herald osteoarthritis of the DIP joint. Their presence should merit close scrutiny of the DIP joint.

The navicular bursa

The incidence and aetiology of primary bursitis of the navicular bursa is not known, nor is its relationship to the development of navicular disease. Villous hypertrophy, hyperplasia of synovial lining cells and venous congestion have been described in association with navicular disease, whereas the synovial membrane appeared uniform in six normal horses of undetermined age [25]. However, in another study comparing immature horses, horses with navicular disease and age-matched controls, three of 25 age-matched controls had evidence of asymptomatic chronic synovitis. In both the navicular disease group and the age-matched controls mild hyperplasia and hypertrophy was seen compared with immature horses up to 3 years of age [16]. In a more recent study, there was no evidence of acute inflammation within the navicular bursa in horses with palmar foot pain or age-matched control horses [11]; however, lame horses had marked chronic synovial proliferation compared with control horses [8, 12]. There was a positive association between abnormalities of the bursa and lesions of either the dorsal aspect of the DDFT or the flexor aspect of the navicular bone. Clinical experience with MRI has indicated that abnormal distension of the bursa is a frequent finding in lame horses, but is rarely seen in isolation [2]. Soft tissue proliferation within the bursa is frequently seen in association with lesions of the CSL, DDFT or DSIL.

Acute trauma to the navicular bone

Several horses have presented with acute onset, severe unilateral lameness with extensive increased signal intensity in fat-suppressed images in the navicular bone and in the palmar aspect of the distal phalanx, associated with a similar pattern of reduced signal intensity in T1-weighted images. This is thought to be due to acute bone trauma. This has been associated with IRU in the same areas. Generally lameness has ultimately resolved, albeit slowly.

One horse had acute onset severe lameness and diffuse increased signal intensity in the middle third of the bone in fat-suppressed images, and reduced signal intensity in T1-weighted images, associated with focal intense IRU. The horse never developed any radiological changes and made a complete recovery from this severe bone contusion or incomplete fracture.

Acute fracture of the navicular bone

MRI is usually not necessary for the diagnosis of navicular bone fractures, but can help to determine if there is associated damage to the DDFT, which may influence the decision as to whether to undertake surgical repair. Portions of the DDFT can become trapped in the fracture site.

Old fractures or congenital bipartite navicular bones

Several horses have been examined with radiological evidence of either an old fracture of the navicular bone or a congenital bipartite navicular bone. These horses have had sudden onset lameness, not associated with IRU in

the navicular bone. It was therefore considered likely that the navicular bone was not the source of pain causing lameness. Acute lesions of the DDFT have been identified using MRI, usually in the same sagittal plane as the defect in the navicular bone. The navicular bone has had no evidence of active bony reaction on MR images. It is considered that the DDFT injury probably occurs as a sequel to mild instability in the navicular bone or secondary to adhesions, but the bone is not the primary source of pain and lameness.

Distal sesamoidean impar ligament

Lesions of the DSIL are usually characterized by enlargement of the ligament, with larger areas of low signal intensity in T1-weighted images and high signal intensity in T2-weighted and fat-suppressed images compared with normal synovial interdigitations from the DIP joint (Figures 12.1, 12.9 and 12.10). There is sometimes loss of separation between the DSIL and

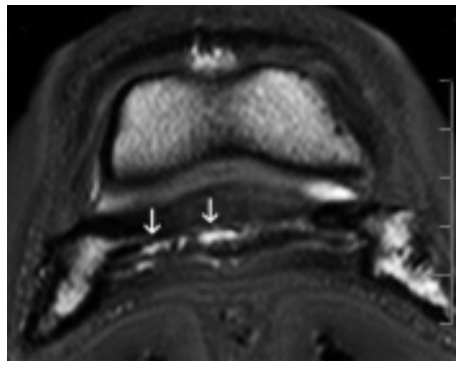

Figure 12.9 Transverse 3D T2* GRE high-field MR image of a foot. Lateral is to the left. There is disruption of the normal architecture of the distal sesamoidean impar ligament (DSIL) laterally (arrows) and slight swelling axially. The dorsal aspect of the deep digital flexor tendon (DDFT) has a slightly irregular border, especially laterally. At places there is loss of separation between the DSIL and the DDFT. There is focal mild decreased signal intensity in the palmar aspect of the lateral palmar process of the distal phalanx.

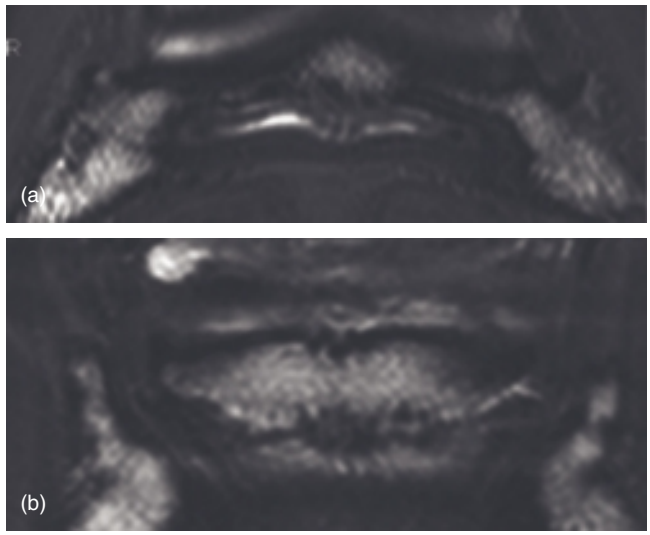

Figure 12.10 (a) Transverse 3D T2* GRE high-field MR image of a right front foot. The distal sesamoidean impar ligament (DSIL) is irregular, with tissue extending between it and the deep digital flexor tendon. Note also the cortical irregularity at the central region of insertion of the DSIL on the distal phalanx. (b) Dorsal 3D T2* GRE high-field MR image of the right front foot in (a). Note the cortical irregularity at the centre of the proximal and distal borders of the navicular bone.

the DDFT suggestive of adhesion formation. With acute injury there is sometimes increased signal intensity in fat-suppressed images at the ligament's origin in the navicular bone, or at the insertion on the distal phalanx, especially axially (Figures 12.3d and 12.7). Endosteal reaction at the insertion of the DSIL is common in normal horses, but cortical disruption or entheseophyte formation has only been seen in lame horses [11].

Chronic injuries are often associated with an increased number of variably sized cortical indentations into the navicular bone, with elongation of the flexor border of the bone, or marked endosteal irregularity at the insertion on the distal phalanx. Osseous cyst-like lesions at the insertion of the DSIL on the distal phalanx have been described in a small number of horses [26]. Lesions of the DSIL were seen in 38.2% of 264 horses undergoing high-field MRI, and were generally seen in association with lesions of the navicular bone involving the proximal or distal border of the navicular bone or the medulla [19]. Lesions of the DSIL were more frequent than those of the CSL, but appeared to be related. Increased signal intensity in fat-suppressed images in the navicular bone at the origin of the DSIL was likely to be seen in association with focal increased signal intensity in the navicular bone at the insertion of the CSL.

Lesions of both the DSIL and CSL were seen in association with lesions of the medulla of the navicular bone, predominantly linear increased signal intensity in fat-suppressed images extending through the middle third of the bone, from the insertion of the CSL to the origin of the DSIL. We speculate that such injuries reflect the lines of stress through the podotrochlear apparatus during extension of the DIP joint. Lesions of both the DSIL and CSL were also seen in association with lesions of the proximal and distal borders of the bone, such as entheseophyte formation, distal border fragments and abnormal mineralization extending from the border into the spongiosa, most commonly distally but also proximally (Figure 12.10). These abnormalities may be a more chronic response to overstress of the podotrochlear apparatus.

Lesions of the DSIL are much more difficult to identify in low-field images compared with high-field images because usually only a single image is available in any sequence due to the slice thickness. The slice obtained may be different in different sequences, making injury verification extremely difficult.

Histological changes include fibrocartilaginous metaplasia, focal vacuolar degeneration and increased vascularity in adjacent tissue [12]. At the intersection between the DSIL and DDFT, damage to arteriovenous complexes and changes at the bone ligament interface were demonstrated in horses with chronic palmar foot pain [27, 28].

Collateral sesamoidean ligament

Injuries of the CSL were rarely seen in isolation, with 75% occurring in hind limbs (one bilaterally). More commonly CSL injuries were seen in conjunction with other injuries of the podotrochlear apparatus, but were less common than injuries of the DSIL, occurring in only 10.5% of 264

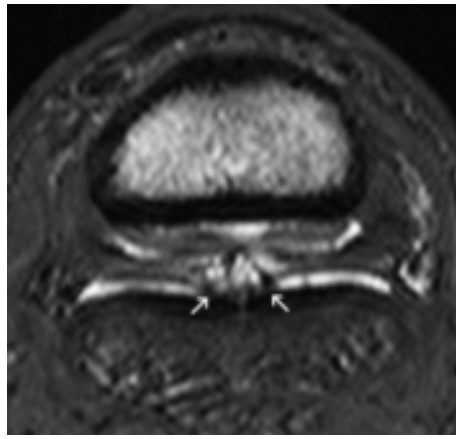

Figure 12.11 Transverse 3D T2*GRE high-field MR image of a foot at the level of the middle phalanx. The axial aspect of the collateral sesamoidean ligament is enlarged (arrows) and has hyperintense signal.

horses [19]. Acute injuries were characterized by enlargement of the ligament and increased signal intensity in all image sequences (Figure 12.11). There was often soft tissue proliferation in the adjacent palmar recess of the DIP joint and/or navicular bursa, which could be difficult to differentiate from periligamentous swelling. There was sometimes focal increased signal intensity in the navicular bone at the ligament's insertion in fat-suppressed images, or linear increased signal intensity extending through the bone to the origin of the DSIL. Diffuse increased signal intensity has also been described [29]. In more chronic injuries there was frequently loss of separation between the thickened CSL and the DDFT, often indicative of adhesion formation, with entheseophyte formation on the proximal border of the navicular bone. Isolated cases of cyst-like lesions associated with the CSL have also been seen [10]. Histologically fibrocartilaginous metaplasia has been the predominant change [12].

Deep digital flexor tendon

Lesions of the DDFT are common, occurring in 82.6% of limbs of 264 horses; however, some of these were isolated sagittal plane splits or minor dorsal irregularities of questionable clinical significance [19]. Lesions occurred most commonly at the level of the CSL (59.4%) and the navicular bone (59.0%). At the level of the proximal phalanx, core lesions predominated (90.3%), whereas at the level of the CSL and navicular bone sagittal plane splits, dorsal abrasions and focal core lesions were most common.

Primary lesions of the DDFT are defined as lesions that are the principal cause of lameness and usually comprise core lesions proximal (Figure 12.12a) or distal (Figures 12.12b and c) to the navicular bone. Primary lesions of the DDFT often involve principally one lobe and extend a variable distance proximodistally, anywhere from the proximal phalanx to the tendon's insertion on the distal phalanx [19, 30–32]. Occasionally lesions extend proximal to the metacarpophalangeal joint, but not all limbs were examined this far proximal.

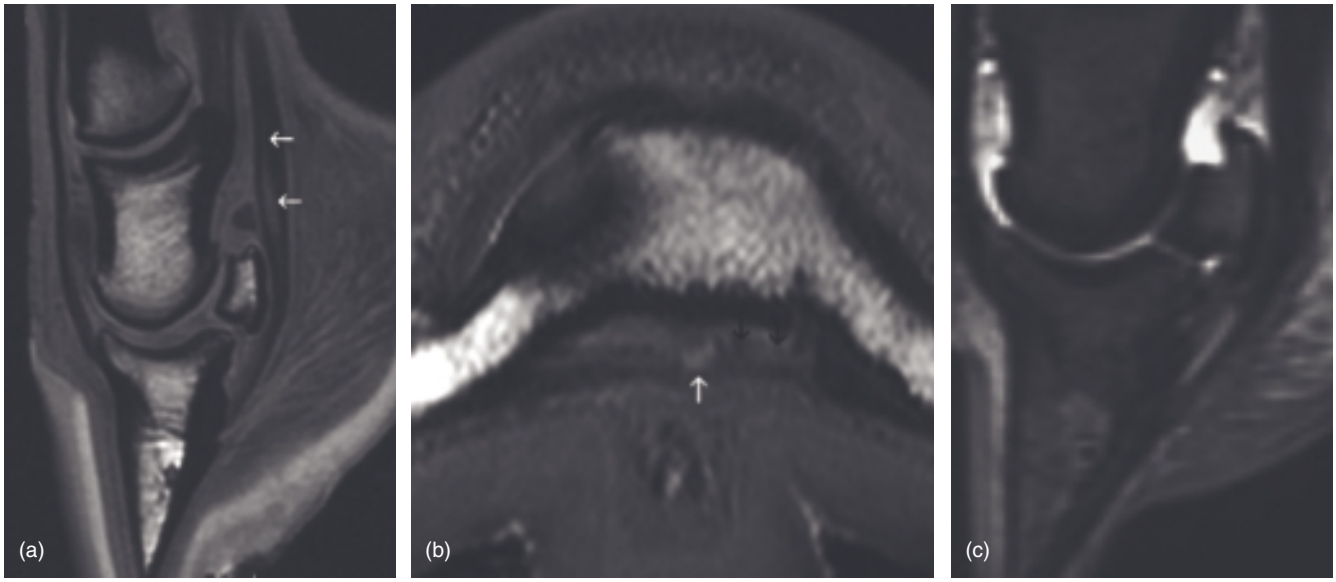

Figure 12.12 (a) Parasagittal 3D SPGR high-field MR image. There is an extensive core lesion characterized by increased signal intensity (arrows) in the enlarged deep digital flexor tendon (DDFT) proximal to the navicular bone. Note the convex dorsal border of the DDFT. (b) Transverse 3D T2* GRE high-field MR image of a foot. Medial is to the left. There is a focal core lesion in the axial aspect of the deep digital flexor tendon (DDFT) (white arrow). The lateral lobe of the DDFT is enlarged and has an irregular dorsal border (black arrows). There is mild endosteal irregularity of the distal phalanx at the insertion of the distal sesamoidean impar ligament, laterally more than medially. (c) Sagittal STIR high-field MR image of the same foot as (b). There is increased signal intensity in the distal aspect of the deep digital flexor tendon (DDFT), which is swollen. There is lack of separation between the DDFT and the distal sesamoidean impar ligament. There is mild diffuse increased signal intensity in the navicular bone. There is poor fat suppression especially in the distal aspect of the distal phalanx, probably because the foot was cold.

Acute inflammatory or necrotic lesions are seen on T1- and T2-weighted images and fat-suppressed images, whereas more chronic lesions with fibroplasia may only be seen in T1- and T2-weighted images. Lesions identified only in T1-weighted images may be degenerative or chronic with scarring or disruption of the normal collagen structure. Lesions confined to the insertion are often best identified in fat-suppressed images. Core lesions are frequently associated with swelling of the affected lobe, resulting in loss of the normal mediolateral symmetry [33]. There is often associated distension of the digital flexor tendon sheath (DFTS) and/or the navicular bursa, with or without soft tissue proliferation within the bursa.

Severe lesions involving the dorsal aspect of the tendon may be associated with adhesion formation between the DDFT and either the CSL and/or the DSIL. Such core lesions of the DDFT can also occur in conjunction with other soft tissue injuries contributing to lameness. These other lesions often occur on the ipsilateral side of the foot, suggesting that biomechanical forces contributed to injury. Histopathology of such lesions has revealed no evidence of inflammatory reaction, but extensive core necrosis in horses with lameness of less than 6 months' duration [34], whereas in horses with more chronic lameness the core lesions were predominantly fibroplasia and/or fibrocartilaginous metaplasia. Core necrosis was characterized by vacuoles in the fascicles which tended to coalesce with breakdown material in the vacuoles, and some 'floating' chondrocytes and fibroblasts within the

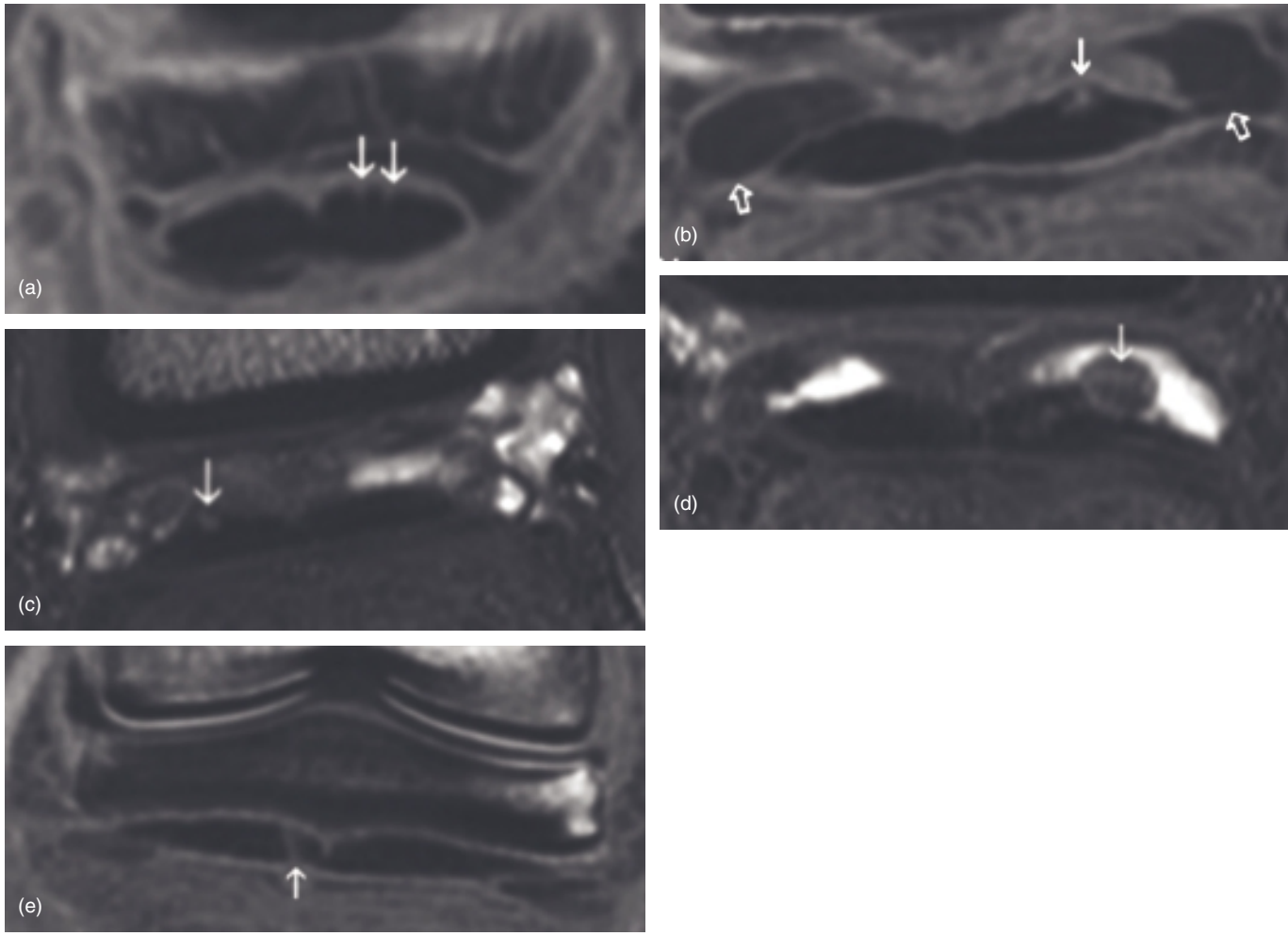

Figure 12.13 (a) Transverse 3D SPGR high-field MR image of a deep digital flexor tendon (DDFT) at the level of the proximal interphalangeal joint. Dorsal is proximal and medial is to the right. There is a dorsal abrasion of the medial lobe of the DDFT (arrows). Dorsal to the DDFT is the straight sesamoidean ligament, which has a heterogeneous architecture. (b) Transverse 3D SPGR high-field MR image of a deep digital flexor tendon (DDFT) at the level of the middle phalanx, with a dorsal core lesion of the medial lobe (arrow). Medial is to the right. Dorsal and abaxial to the DDFT, the navicular bursa is distended with hypointense fluid (open arrows). (c) Transverse 3D T2* GRE high-field MR image at the level of the middle phalanx and proximal recess of the navicular bursa. Lateral is to the left. Dorsal is to the top. There is a focal dorsal border lesion in the lateral lobe of the deep digital flexor tendon (arrow). Note also the proliferative synovium within the navicular bursa. (d) Transverse 3D T2* GRE high-field MR image at the level of the proximal recess of the navicular bursa. Lateral is to the right. There is an axial core lesion in the lateral lobe of the deep digital flexor tendon, with granulation tissue (arrow) dorsal to it in the navicular bursa. (e) Transverse 3D SPGR high-field MR image of a deep digital flexor tendon (DDFT) at the level of the navicular bone. Lateral is to the left. There is a parasagittal split (arrow) in the axial aspect of the lateral lobe of the DDFT.

vacuoles. There was some evidence of revascularization towards necrotic core lesions, especially those extending into the pastern.

Other DDFT lesion types identified using MRI include dorsal border irregularity and sagittal plane splits (Figures 12.13a–e). Such lesions occur with greatest frequency at the level of the CSL and the navicular bone [19]. In some horses different lesion types are seen at different levels of the tendon. Horses with lesions of both the navicular bone and the DDFT often have multifocal lesions involving the medial and lateral lobes of the DDFT, especially from the level of the proximal aspect of the navicular

bursa distally [19]. Lesions of the navicular bone are often in the same sagittal plane as the DDFT lesions. Defects in the flexor cortex of the navicular bone often have focal adhesions to the DDFT. Small focal adhesions may be more difficult to identify in low-field images because of the thicker slice thickness compared with high-field images. Use of additional higher resolution sequences at suspect locations can improve visualization. These DDFT lesions appear to be degenerative with vascular compromise, especially in the septae, and matrix changes with fibrocartilaginous metaplasia [15, 34, 35]. Histological examination has indicated that there is no evidence of any acute inflammatory response in these types of lesion.

Distal interphalangeal joint

Distension of the DIP joint capsule, with or without soft tissue proliferation, is a common non-specific finding in many lame horses and does not necessarily reflect primary DIP joint disease [2, 5]. The curved articular surfaces of the DIP joint and the effects of partial volume averaging make assessment of the articular cartilage challenging. Articular cartilage pathology in the horse is usually associated with focal decrease in signal intensity of the cartilage, or cartilage surface irregularity. Slight irregularity in the endosteal or chondral surfaces of the adjacent subchondral bone, or increased signal intensity of the subchondral bone in fat-suppressed images, may highlight an area of cartilage damage (Figure 12.14). Osteoarthritis of the DIP joint

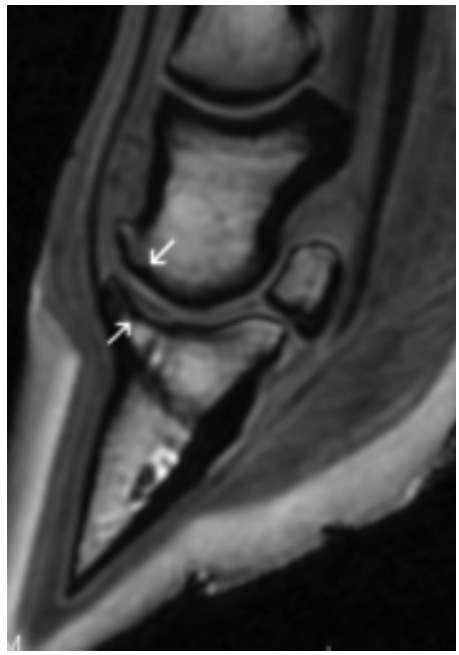

Figure 12.14 Sagittal 3D SPGR high-field MR image of a foot. There is irregular endosteal thickening of the subchondral bone of the middle and distal phalanges dorsally (arrows) reflecting osteoarthritis, possibly secondary to concurrent desmitis of the medial collateral ligament of the distal interphalangeal joint. Note also the slight modelling of the dorsal articular margins of the middle and distal phalanges.

can occur alone or in association with pathology of the navicular bone. It has also been seen as a sequel to severe injury of a CL of the DIP joint.

Articular cartilage is more difficult to evaluate in low-field images compared with high-field images, because of inferior resolution. However, if the images are obtained in a standing horse additional information may be acquired concerning joint space width. If there is extensive cartilage loss, joint space width may be narrowed. Abnormal joint space widening is sometimes seen in association with CL injury in both low- and high-field images. However, variation in joint space width must be interpreted with extreme care because it can be influenced quite markedly either by the way the horse is standing or by the way the limb is positioned with the horse under general anaesthesia.

Very focal OCLLs have been seen in the palmar aspect of the proximal articular surface of the distal phalanx, characterized in the acute stage by focal high signal intensity in T1- and T2-weighted images and fat-suppressed images within the subchondral and immediately adjacent cancellous bone, with reduced signal intensity in T1- and T2-weighted images in the surrounding trabecular bone of the distal phalanx (Figure 12.15). These lesions may be the result of acute subchondral bone trauma. More chronic OCLLs have been seen in the dorsal aspect of the distal phalanx approximately 1–2 cm palmar to the extensor process, characterized by a defect in the articular cartilage and subchondral bone extending into the trabecular bone (Figure 12.16).

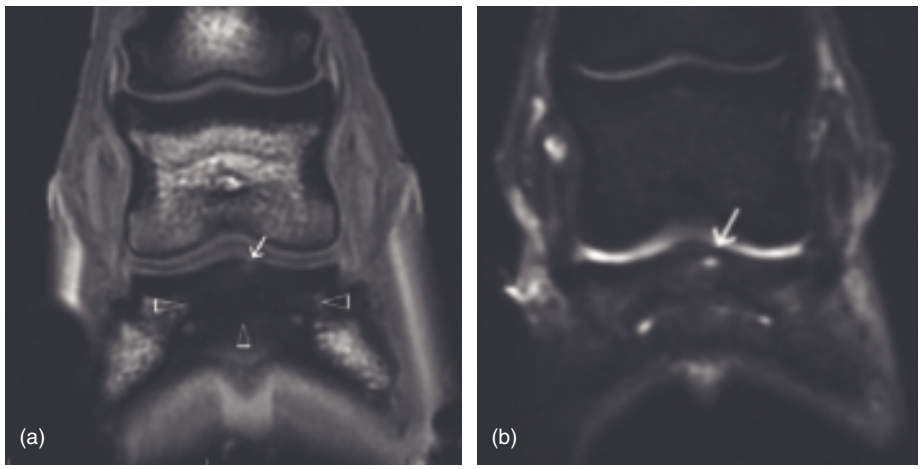

Figure 12.15 (a) Dorsal 3D SPGR high-field MR image of a foot. There is a focal axial defect in the subchondral bone of the distal phalanx (arrow), with diffuse decreased signal intensity in the underlying bone (arrow heads). This is an acutely developing osseous cyst-like lesion. There is signal void to the left of the image, a magnetic susceptibility artefact, the result of a small clench in the hoof wall. (b) Dorsal 2D STIR high-field MR image of the same foot as (a). There is a focal hyperintense signal in the axial aspect of the distal phalanx (arrow) and diffuse increased signal intensity distal and abaxial to this. To the left of the image there is signal void, a magnetic susceptibility artefact, the result of a small clench in the hoof wall.

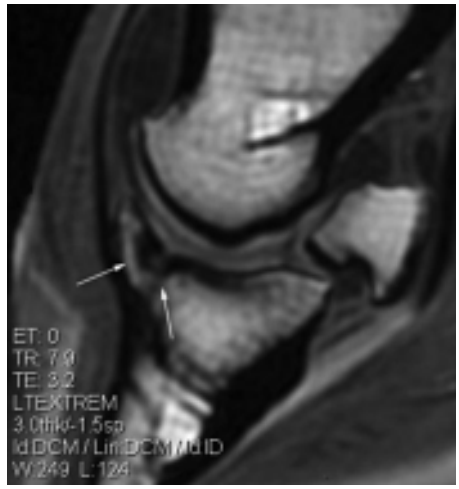

Figure 12.16 Sagittal SPGR parasagittal high-field MR image of a foot. There is a chronic osseous cyst-like lesion (OCLL) in the dorsal aspect of the distal phalanx (arrows). Note the flattening of the subchondral bone of the palmar distal aspect of the middle phalanx, a normal variant. Lameness was abolished by intra-articular analgesia and arthroscopic evaluation of the dorsal aspect of the distal interphalangeal joint confirmed a cartilage defect overlying the OCLL.

Collateral ligaments of the distal interphalangeal joint

Acute injury of a CL of the DIP joint is characterized by increased signal intensity in all image sequences, often with swelling of the CL and/or periligamentar tissues, whereas in more chronic injuries increased or heterogeneous signal intensity is sometimes seen only in T1- and T2*-weighted images (Figures 12.17–12.19) [24, 36–39]. Lesions identified only in T1-weighted images may be chronic or degenerative. Transverse images are the most sensitive, but careful image acquisition or image reformatting is sometimes necessary to compensate for obliquity during image acquisition. In some horses the entire cross-sectional area of the ligament has hyperintense signal, whereas in others only either the central region or the periphery of the ligament are abnormal. Lesions may be restricted to a portion of the proximodistal length of the ligament, or extend throughout its length. In some but not all horses, injuries can also be verified in dorsal (frontal) plane images. These images were the most sensitive for the identification of osseous cyst-like lesions at or close to the ligament's insertion (Figure 12.18e). The medial CL is more frequently injured than the lateral CL of the DIP joint [24]; however, both ligaments may be injured simultaneously. Therefore, although comparison between the medial and lateral ligaments can be useful, knowledge of their normal appearance is essential. In association with CL injury, synovial fluid from the DIP joint may be seen axial to the injured CL in transverse or dorsal plane T2-weighted images, abaxial to the middle phalanx.

Lesions are sometimes accompanied by endosteal and/or periosteal (entheseophyte formation) reaction at the origin on the middle phalanx or at the insertion on the distal phalanx. OCLLs have been seen at both the origin and insertion, but are more common at the insertion (Figures 12.18d and e) [24, 26]. Occasionally an OCLL is seen close to the insertion of a CL

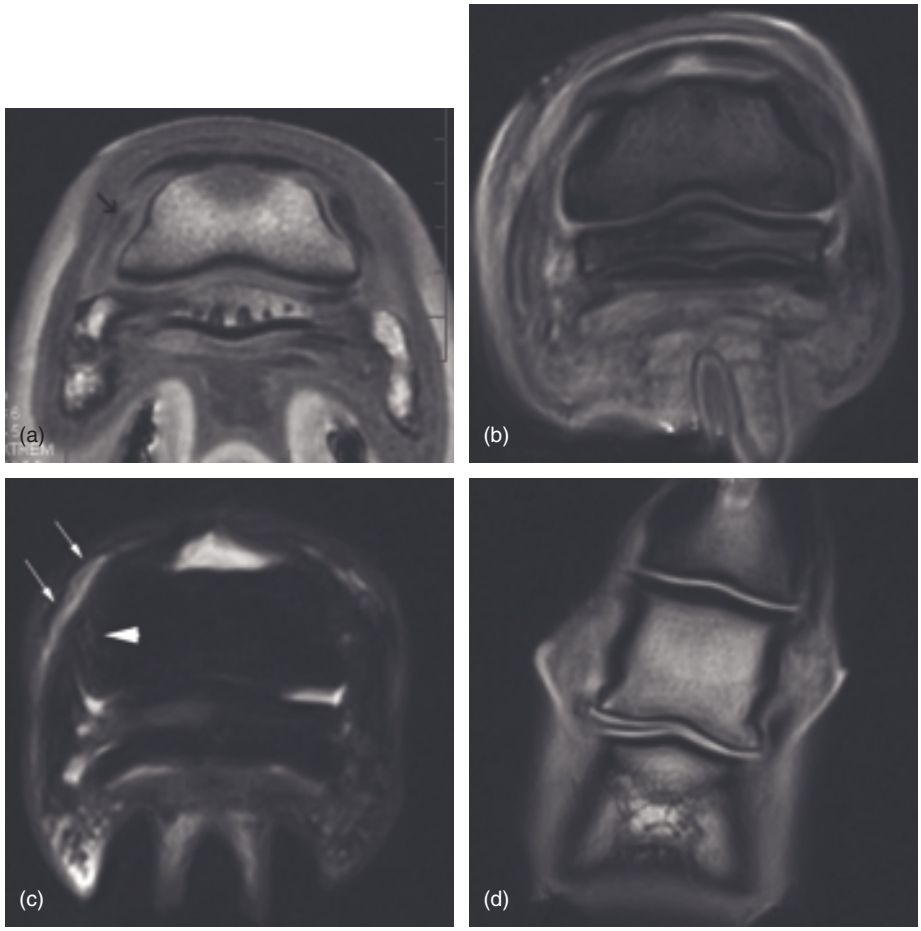

Figure 12.17 (a) Transverse 3D T1-weighted SPGR high-field MR image of the left front foot of a pony. Medial is to the left. The medial collateral ligament of the distal interphalangeal joint is enlarged, its margins are poorly defined and it has generalized increased signal intensity (arrow). (b) Transverse 2D T1-weighted GRE low-field MR image of a left front foot. Medial is to the left. The medial collateral ligament of the distal interphalangeal joint is ill-defined and has increased signal intensity. The overlying periligamentar soft tissues are thickened and also have increased signal intensity. There are areas of reduced signal intensity in the medial half of the navicular bone. (c) Transverse STIR fast spin-echo low-field MR image of the same foot as (b). Medial is to the left. There is diffuse increased signal intensity in the medial half of the navicular bone. There is mild increased signal intensity in the medial aspect of the middle phalanx (arrow head). There was also mild increased signal intensity in the dorsal medial aspect of the distal phalanx. This probably reflects bone trauma secondary to instability of the distal interphalangeal (DIP) joint. Note also the increased signal intensity in the periligamentar tissues abaxial to the medial collateral ligament of the DIP joint (arrows). (d) Dorsal T2-weighted 2D GRE low-field MR image of the same foot as (b)–(d). Medial is to the left. There is increased signal intensity in the medial collateral ligament (CL) of the distal interphalangeal (DIP) joint. The margins of the medial CL are poorly defined. There is abnormal widening of the medial aspect of the DIP joint space, reflecting joint instability.

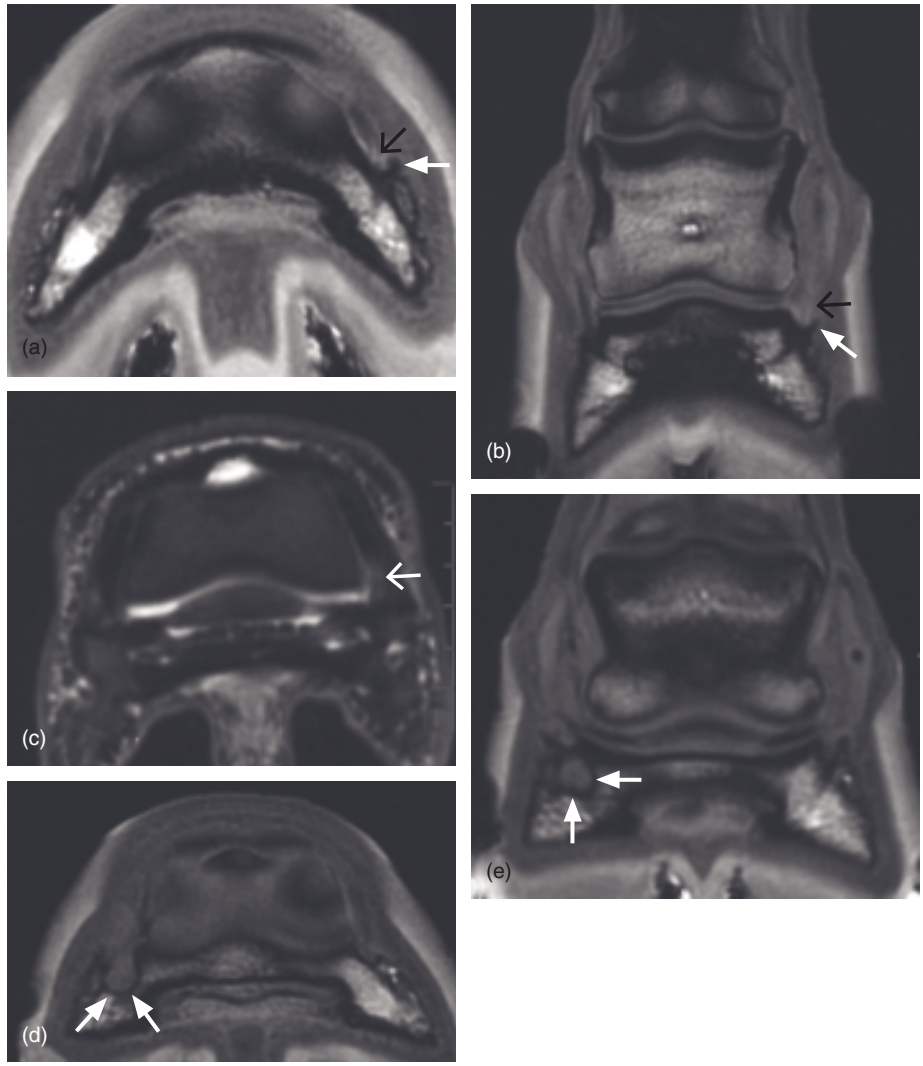

Figure 12.18 (a) Transverse 3D T1-weighted SPGR high-field MR image. Medial is to the right. There is increased signal intensity in the medial collateral ligament close to its insertion on the distal phalanx (black arrow). Note also the irregular cortical margin of the bone due to entheseophyte formation (white arrow). There is mild disruption of the overlying laminar architecture. There is endosteal and cortical irregularity of the palmar aspect of the distal phalanx and focal areas of reduced signal intensity in the distal sesamoidean impar ligament. (b) Dorsal 3D T1-weighted SPGR high-field MR image of the right front foot in (a). Medial is to the right. There is increased signal intensity in the medial collateral ligament of the distal interphalangeal joint close to its insertion (black arrow). Note also the bone spur (entheseophyte) on the ipsilateral aspect of the distal phalanx (white arrow). There is also mild diffuse decreased signal intensity in the axial aspect of the distal phalanx. (c) Transverse 2D STIR high-field MR image of the same foot as (a) and (b). Medial is to the right. There is increased signal intensity in the palmar axial aspect of the medial collateral ligament of the distal interphalangeal joint (arrow). (d) Transverse 3D SPGR high-field MR image of a foot. Medial is to the left. There is a large osseous cyst-like lesion (OCLL) in the medial aspect of the distal phalanx at the insertion of the medial collateral ligament (CL) of the distal interphalangeal (DIP) joint (arrows). The medial CL of the DIP joint was enlarged throughout its length, had poorly defined margins and had increased signal intensity in all image sequences. (e) Dorsal SPGR high-field MR image of the same foot as Figure 12.19d. Medial is to the left. There is a large OCLL in the medial aspect of the distal phalanx (arrows).

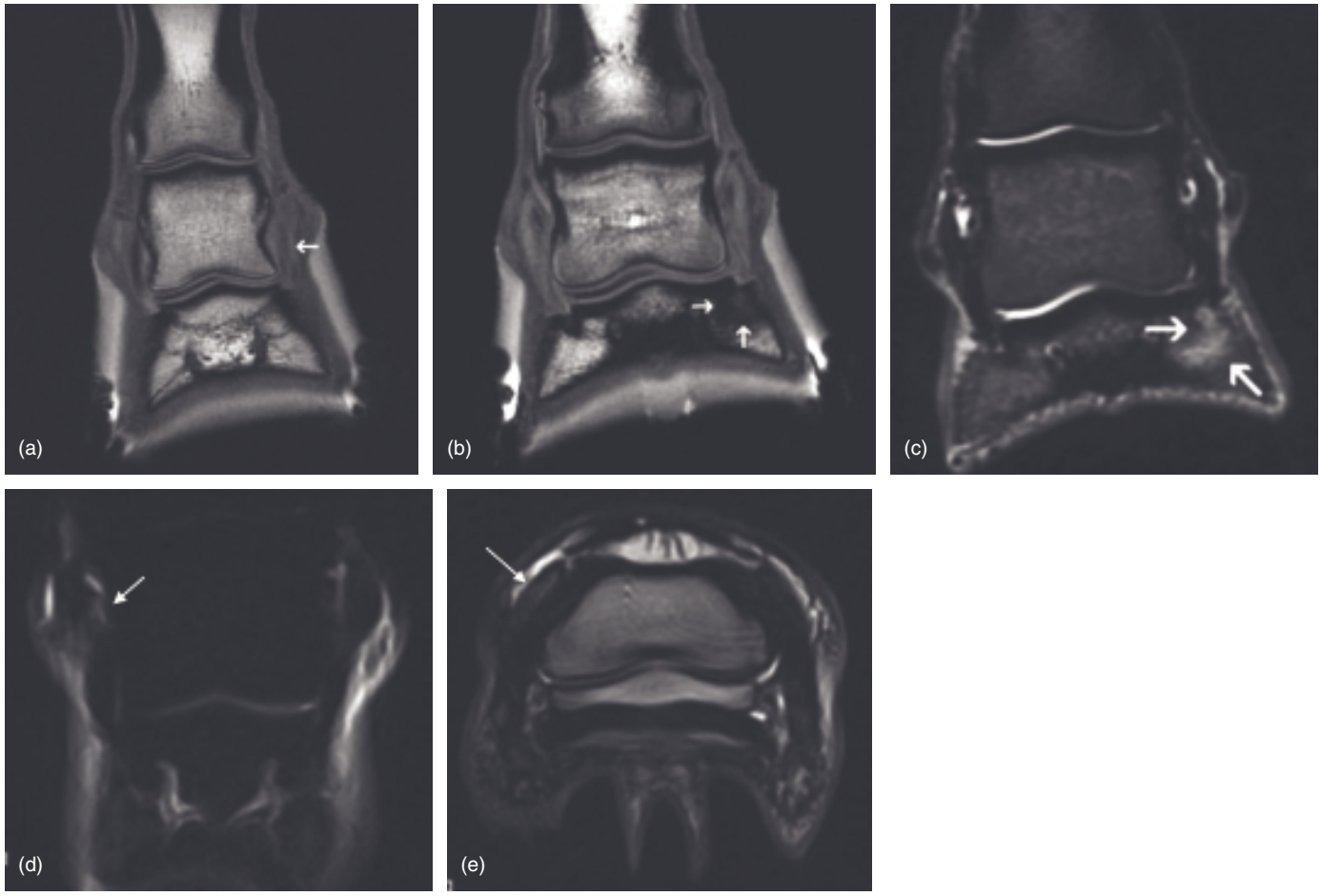

Figure 12.19 (a) Dorsal 3D SPGR high-field MR image of a right front foot. Medial is to the right. The medial collateral ligament of the distal interphalangeal joint is enlarged and has increased signal intensity (arrow). (b) Dorsal 3D SPGR high-field MR image of the same front foot as (a). Medial is to the right. There is reduced signal intensity (fluid and mineralisation) in the distal phalanx (arrows) in the region of insertion of the medial collateral ligament of the distal interphalangeal joint. (c) Dorsal 2D fast STIR high-field MR image of the right front foot as (a) and (b). Medial is to the right. There is an extensive area of increased signal intensity in the distal phalanx (arrows) that extends palmar to the region of insertion of the medial collateral ligament of the distal interphalangeal joint. (d) Dorsal STIR image of a foot from a horse which had been diagnosed with damage to the collateral ligament and periligamentar tissues on ultrasonographic examination. On MRI evaluation the horse was demonstrated to have damage to the chondrocoronal ligament (arrow). There is mild enlargement of the ipsilateral collateral ligament, but minimal alteration in signal intensity. (e) Transverse T2 fast spin-echo image of the same foot as (d) at the level of the navicular bone. Increased signal intensity is present in the chondrocoronal ligament (arrow). The ipsilateral cartilage of the foot has some irregularity of the margins and altered morphology with some disruption of the adjacent laminar junction.

without any detectable abnormality of the CL per se. In a small proportion of horses there are well-demarcated areas of increased signal intensity in fat-suppressed images in either the middle or distal phalanges (Figure 12.19), with decreased signal intensity on T1- and T2-weighted images, presumably reflecting secondary bone trauma, either immediately adjacent to the enthesis or more widespread. Occasionally there is malalignment of the middle and distal phalanges reflecting secondary subluxation of the DIP joint (Figure 12.17d), or there is evidence of secondary osteoarthritis of the DIP joint (Figure 12.14).

Interpretation of MR images of the lateral CL of the DIP joint obtained when the static magnetic field is perpendicular to the long axis of the limb is

potentially confounded by the magic angle effect, resulting in artefactual high signal intensity in T1- and T2-weighted gradient echo (GRE) and proton density (PD) sequences [40, 41]. The lateral CL ligament is susceptible to this artefact because it is at a more acute angle to the horizontal and thus the static magnetic field, B_0 and abduction of the limb in a standing horse can exacerbate this problem. There is also evidence that a potential for magic angle effect can occur near the origin of the ligaments on high-field images, so care with interpretation should be taken in both high- and low-field images. Confirmation of genuine abnormality requires identification of swelling of the ligament and/or periligamentar tissues, and increased signal intensity in long TE sequences, including T2 fast spin-echo (FSE) and/or fat-suppressed images, or complete disruption of the ligament's architecture reflecting partial rupture. Identification of associated osseous changes also helps.

The presence of IRU at the insertion of a CL of the DIP joint is highly supportive of CL injury [13]. There was an association between IRU and higher histological score in a comparative MRI, scintigraphy and postmortem study of 25 lame horses and 12 control horses [42].

A reasonable correlation between abnormalities detected using MRI and histopathological changes has been demonstrated [42]. However, 12 CLs appeared normal on MR images but were graded abnormal histologically, thus MRI may underestimate the presence of lesions. Lesions appeared to be degenerative, characterized in early lesions by linear pallor and hyalinization of collagen fibres, with transformation of fibroblasts into chondrocytes. There were areas of focal or diffuse fibrocartilaginous metaplasia. More severe lesions had extensive fibrocartilaginous metaplasia and development of multiple, intercommunicating fissures within the degenerate collagen, which contained chondrocytes and chondrones. Lesions were generally most severe towards the insertion of the ligament on the distal phalanx, and naturally occurring clefts between the ligament and the bone were identified. Lesions were associated with blood vessel occlusion in some limbs and attempts at revascularization. Adjacent osseous pathology was characterized by focal bone loss on the abaxial aspect of the cortex of the distal phalanx, with replacement by fibrous tissue, leading to the development of OCLLs. This study was biased by inclusion of horses with chronic lameness. More acute lesions may be more inflammatory in nature.

Injuries of the CLs of the DIP joint can occur as a primary cause of lameness, but may also be seen as part of a multiple injury complex (see section on Multiple injuries, below). In a series of 233 horses with CL injury, 109 had lameness associated with a primary injury of a CL, 40.4% of which had associated osseous pathology at the origin or insertion [24]. A further 113 horses had concurrent injuries, 85 of which were multiple injuries. Lesions have also been seen in association with delayed union fractures of the ipsilateral aspect of the distal phalanx, or evidence of trauma of an ipsilateral ossified cartilage of the foot.

Injuries of the CLs may be seen in association with injuries to the ipsilateral cartilage of the foot, the ligaments of the cartilages of the foot, and the palmar processes of the distal phalanx. Damage to the CLs may be confused with damage to the chondrocoronal ligament, which lies close to

the ligament (Figure 12.19). For assessment of the cartilages of the foot and its ligaments, and to differentiate these from collateral ligament lesions, a combination of T2 FSE, PD and STIR images is useful.

Middle and distal phalanges

Bone trauma may result in focal or diffuse areas of reduced signal intensity in T1- and T2-weighted images and increased signal intensity in fat suppressed images [5, 43] (Figures 12.17 and 12.20). A common site not necessarily associated with accompanying soft tissue lesions is the distal dorsal aspect of the middle phalanx (Figure 12.20). However, such lesions have also been seen in association with either CL injuries of the DIP joint, or lesions of the DDFT. Curiously such lesions have not necessarily been associated with IRU, in contrast to other areas of bone trauma. Primary bone trauma of the distal dorsal aspect of the middle phalanx usually has a fair prognosis, but the cortical and subchondral bone must be inspected carefully. Concomitant injury may adversely influence prognosis. Very severe trabecular lesions may progress to osteonecrosis, with a poorer prognosis.

Lesions involving a palmar process of the distal phalanx have been associated with both irregularity of the cortical margin and disruption of the adjacent laminar architecture. In a few horses with acute onset severe lameness, there has been generalized increased signal intensity in fat-suppressed images and hypointense signal in T1-weighted images throughout the proximal half of the distal phalanx, the navicular bone and parts of the distal aspect of the middle phalanx, presumably reflecting generalized bone trauma. This has been associated with corresponding IRU.

Osseous trauma in the distal phalanx distal to an extensively ossified cartilage of the foot has recently been identified in a small number of horses based on the results of nuclear scintigraphy and MRI (Figures 12.21a and b)

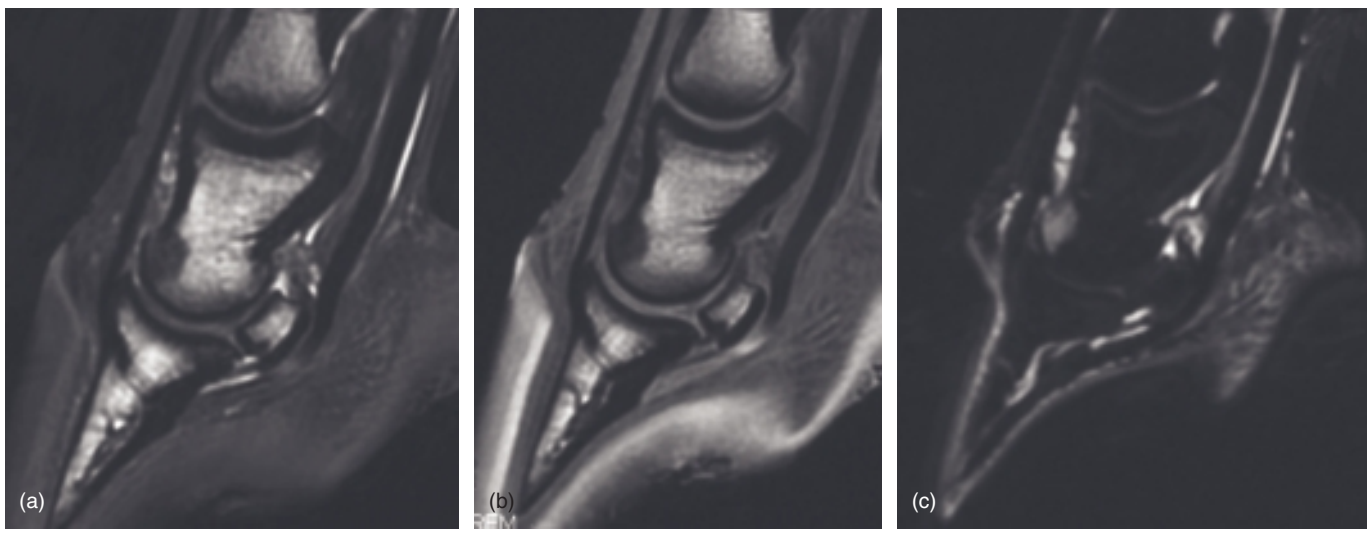

Figure 12.20 (a) Parasagittal 3D T2*GRE, (b) 3D SPGR, and (c) 2D STIR high-field MR images of a foot. In the SPGR and 3D T2* GRE sequences there is reduced signal intensity in the distal dorsal aspect of the middle phalanx, corresponding with a region of hyperintense signal in the STIR image. This pattern is typical of a bone contusion.

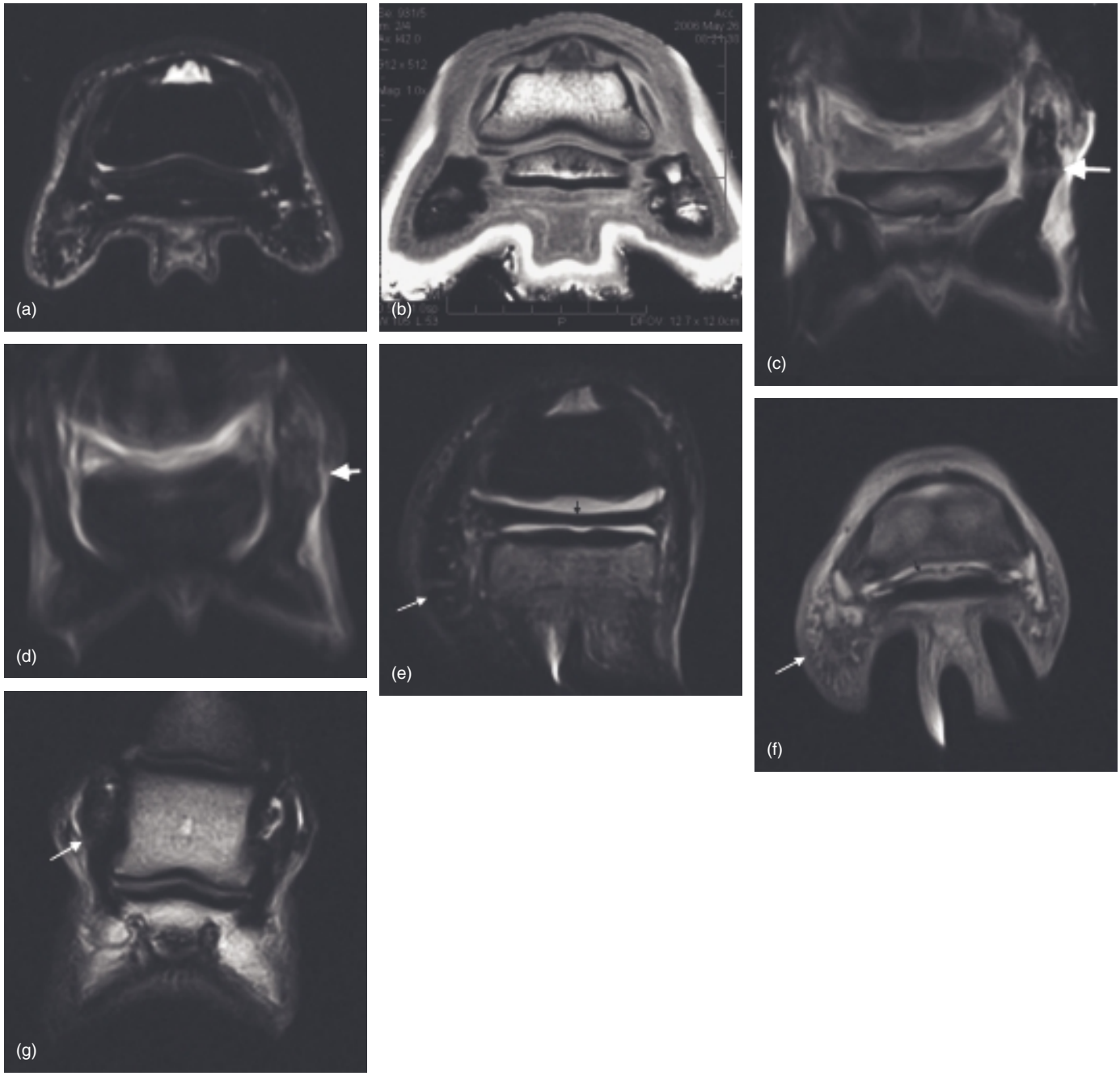

Figure 12.21 Transverse 2D STIR (a) and 3D T1-weighted gradient-echo (b) high-field magnetic resonance images of a right front foot. Lateral is to the left. There is increased signal intensity in the lateral palmar process in the STIR image and diffuse decreased signal intensity in the T1-weighted image in the lateral palmar process distal to the extensively ossified cartilage of the foot. This was associated with focal intense increased radiopharmaceutical uptake. This represents trauma to the distal phalanx distal to the base of the ossified cartilage. (c) Dorsal 3D T2-weighted GRE low-field MR image of a foot. Lateral is to the right. The lateral cartilage of the foot is ossified throughout its length and has a separate ossification centre proximally. There is mineralization of the base of the ossified cartilage and the distal phalanx characterized by reduced signal intensity. There is increased signal intensity in the region of the junction between the separate centres of ossification corresponding to a site of intense increased radiopharmaceutical uptake. This reflects bone trauma. (d) Dorsal fast spin-echo STIR low-field MR image of the same foot as (c). Lateral is to the right. There is increased signal intensity at the junction of the separate centres of ossification of the ossified lateral cartilage of the foot. (e) Transverse STIR image of a foot at the level of the collateral sesamoidean ligament (small black arrow), acquired standing. Although the images have been acquired with minimal obliquity there is marked asymmetry in the structure of the cartilages of the foot. The lateral cartilage (white arrow) is enlarged with irregular margins, axial soft tissue disruption and damage to the adjacent laminar structure. The cartilage has altered internal structure with increased vascularity and there is disruption of the chondrosesamoidean ligament. (f) Transverse proton density image of the same foot as (e), acquired at the level of the distal sesamoidean impar ligament (small black arrow) demonstrating the disruption of the laminae (white arrow) and modelling of the adjacent distal phalanx. (g) Dorsal T2 fast spin-echo image of the same foot as (e). The lateral chondrocoronal ligament is enlarged with increased signal intensity and irregular margins (arrow).

[24]. This has been characterized by increased signal intensity in the distal phalanx in fat-suppressed images and hypointense signal in T1-weighted images, associated with focal, moderate to intense IRU.

Mild, diffuse decreased signal intensity in T1- and T2-weighted images in the medial palmar process of the distal phalanx is a common finding of unlikely clinical significance [44]. Focal mineralization, characterized by more marked hypointense signal, is sometimes seen in one of the palmar processes of the distal phalanx associated with focal moderate to intense IRU (Figure 12.22). Other lesions include thickening of the axial cortex, the presence of an OCLL, an axial entheseophyte (one or two well-defined entheseophyte[s] at the axial aspect of the palmar process), a fracture, an axial defect in the palmar process and marked diffuse cortical irregularity. All these lesions occurred more frequently in the medial palmar process of the distal phalanx compared with laterally. Such lesions were usually seen in conjunction with other potential causes of lameness and their contribution to pain and lameness remains speculative. However, such abnormalities do have a higher prevalence in lame limbs compared with non-lame limbs.

Acute OCLLs are usually well demarcated, but may be surrounded by a diffuse region of bone with slightly reduced signal intensity in T1- and T2-weighted images. The content of the osseous cyst-like lesion usually has high signal intensity on fat-suppressed images, but may have intermediate signal intensity on T2-weighted images consistent with proteinaceous fluid. Osseous cyst-like lesions may occur in the subchondral bone, either in the middle or distal phalanges, at the origin or more commonly the insertion of a CL of the DIP joint, or at the insertion of the DSIL [5, 26].

The characteristics of a fracture depend on its chronicity. There is discontinuity of the homogeneous hypointense signal of cortical bone, with linear increased signal intensity in fat-suppressed images along the fracture

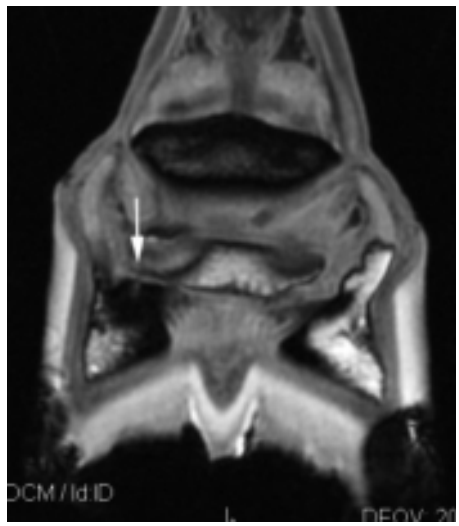

Figure 12.22 Dorsal T1-weighted spoiled gradient-echo high-field magnetic resonance images of a left front foot. Medial is to the left. There is a diffuse, marked decrease in signal intensity in part of the medial palmar process of the distal phalanx and a cortical defect (arrow).

line. There is often reduced signal intensity in T1- and T2-weighted images adjacent to the fracture, consistent with mineralization.

An abscess in the distal phalanx may occur as a sequel to a previous solar puncture injury (see section on Evidence of previous penetrating injury, below). There is a defect in the solar cortex, with a well-circumscribed area of loss of trabecular architecture of homogeneous intermediate signal intensity in the subcortical bone, consistent with proteinaceous fluid, surrounded by a diffuse area of decreased signal intensity in T1- and T2-weighted images [45].

Cartilages of the foot

Ossification of one or both cartilages of the foot was more prevalent in a group of horses with chronic palmar foot pain compared with age-matched control horses [8]. Mineralization within an ossified cartilage characterized by hypointense signal in T1-and T2-weighted images has been seen as an incidental finding. However, trauma to an ossified cartilage characterized by increased signal intensity in fat-suppressed images and reduced signal intensity in T1- and T2-weighted images has been seen at the base of an ossified cartilage, or at the junction of separate centres of ossification (Figure 12.21). This has been associated with focal moderate or intense IRU [24]. Occasionally this has been the only lesion identified using MRI, but more commonly this has been seen in association with a lesion of the ipsilateral CL of the DIP joint and sometimes also the chondrocoronal ligament.

Damage to the cartilaginous part of the cartilages of the foot is generally present in association with injury to the chondrocoronal and chondrosesamoidean ligaments, and does appear to represent a reason for lameness in the absence of other pathology (Figures 3.4, 12.19 and 12.21). There may also be laminar disruption or tearing adjacent to the distal portion of the cartilage.

Laminae

Abnormalities of the laminae were generally seen in horses in which other lesions were determined to be the primary source of pain, and included disruption of interlamellar alignment and separation of laminar layers by linear or focal decrease in signal intensity, consistent with gas accumulation. In some feet there was focal or more generalized disruption of the junction between the laminae and cortex of the distal phalanx, sometimes with an increased signal intensity in the area on both T1- and T2-weighted images. In association with local trauma, focal or linear haemosiderin accumulation was seen as a signal void.

We have little experience of the MRI findings in acute laminitis, although findings in horses with clinical signs for up to 14 days have been documented using a 4.7 Tesla magnet [46]. This obviously offers considerably greater image resolution than currently available in a clinical setting. With laminitis the ratio of the width of the laminae to the dermis was increased to>0.7. There was homogenous increased signal intensity within the corium and reduced vasculature within the corium, and loss of its normal architecture.

Within the laminae there were focal areas of either increased or decreased signal intensity and loss of detail of the laminar architecture. Separation between the laminae and the corium or between laminae was characterized by areas of low signal intensity.

The superiority of MRI over radiology for identification of abnormalities associated with chronic laminitis has been previously documented using a 1.5T magnet [47] (Figure 12.23). There was increased signal intensity in

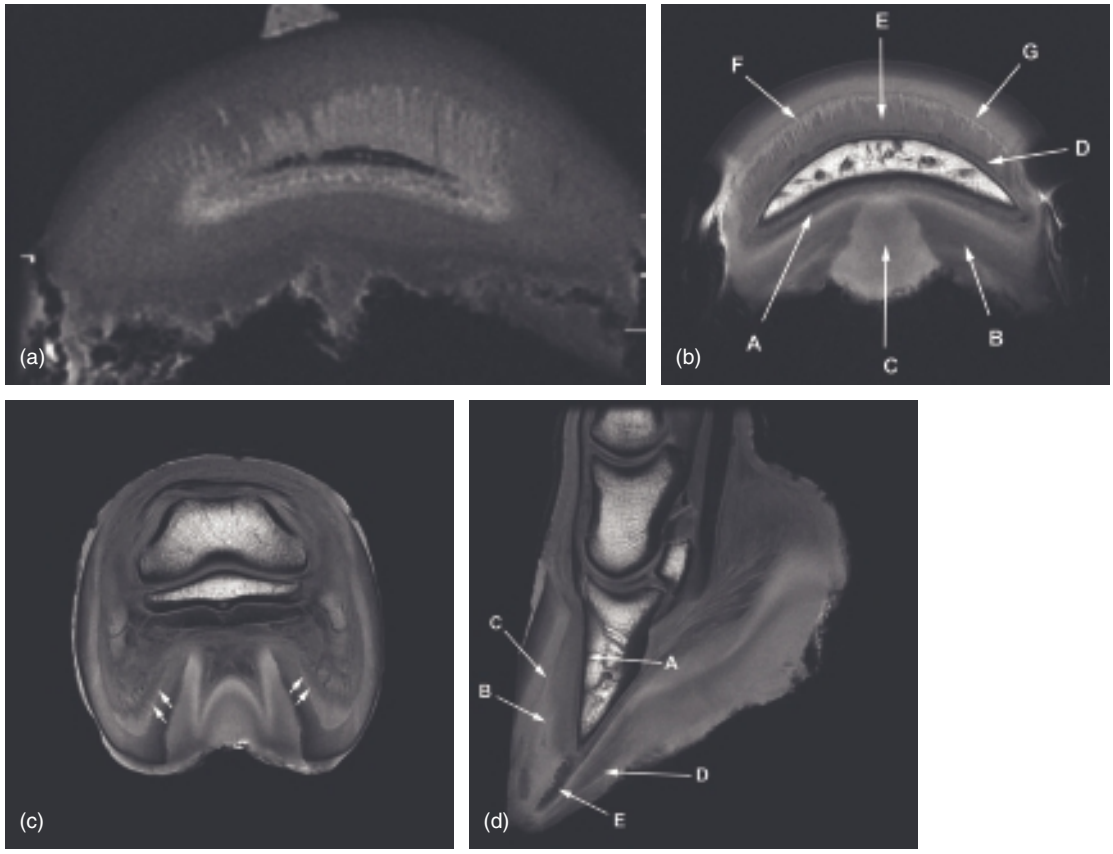

Figure 12.23 (a) Transverse T2* 3D GRE high-field MR image at of a foot at the tip of the distal phalanx from a pony with chronic laminitis. Dorsal is to the top and medial to the left. The dorsal margin of the distal phalanx is irregular. There is disruption of the alignment between the dermal and epidermal lamellae, especially medially. (b) High-resolution transverse 3D T1-weighted SPGR image of a chronic laminitic foot with dislocation of the distal phalanx. **A**, solar dermis vascular plexus; **B**, double (false) sole; **C**, apex of frog; **D**, lamellar vascular plexus; **E**, widened sublamellar dermis. Lamellar wedge, showing visible interdigitation between epidermal (hyperintense MR signal) and dermal lamellae (hypointense MR signal) following lamellar separation and distal phalanx dislocation. This is in marked contrast to the homogenous MR signal of the lamellar interface seen in a normal horse (see Figure 5.9); **G**, curvilinear hypointense feature at the dorsal margin of the lamellar interface, indicating lamellar separation and/or seroma. Image courtesy of Dr Simon Collins. (c) High-resolution transverse 3D T1-weighted SPGR image of a chronic laminitic foot with pronounced lamellar separation at the bars (arrows). Note visible interdigitation between epidermal (hyperintense signal) and dermal lamellae (hypointense signal) following dislocation of the distal phalanx. This is in marked contrast to the homogenous signal of the lamellar interface seen in a normal horse (see Figure 5.9). Image courtesy of Dr Simon Collins. (d) High-resolution sagittal 3D T1-weighted SPGR image of a chronic laminitic foot with rotational dislocation of the distal phalanx. **A**, note angular deviation between the dorsal surface of the hoof wall (viewed proximally) and the dorsal aspect of the distal phalanx; **B**, ectopic white line of the lamellar wedge (high signal intensity within the lamellar interface), and the widened sublamellar dermis proximally (moderate signal intensity); **C**, linear hypointense feature at margin of the lamellar interface, indicating lamellar separation and/or seroma formation; **D**, double (false) sole; **E**, low signal intensity track of solar abscessation passing through the widened white line at the hoof wall–sole junction. Image courtesy of Dr Simon Collins.

the dermal laminae in T1- and T2-weighted images, with disruption of the normal layered pattern and separation of the laminae (Figures 12.23a, c and f). There was disruption of the normal smooth interface between the parietal corium and the solar corium at the distal dorsal aspect of the distal phalanx. There was linear increased signal intensity in the parietal corium along the dorsal aspect of the distal phalanx seen in sagittal images. At the toe region there was clear separation of the dermal and epidermal lamellae seen as linear areas of high signal intensity perpendicular to the hoof wall in transverse T1- and T2-weighted images. Gas accumulation, characterized by focal well-circumscribed areas of low signal intensity in all image sequences, close to the toe of the distal phalanx was a common finding (Figure 12.23c). Abscess formation was characterized by a localized area of high signal intensity on T2-weighted images (Figures 12.23d and e) and less intense increased signal intensity on T1-weighted images, consistent with the presence of

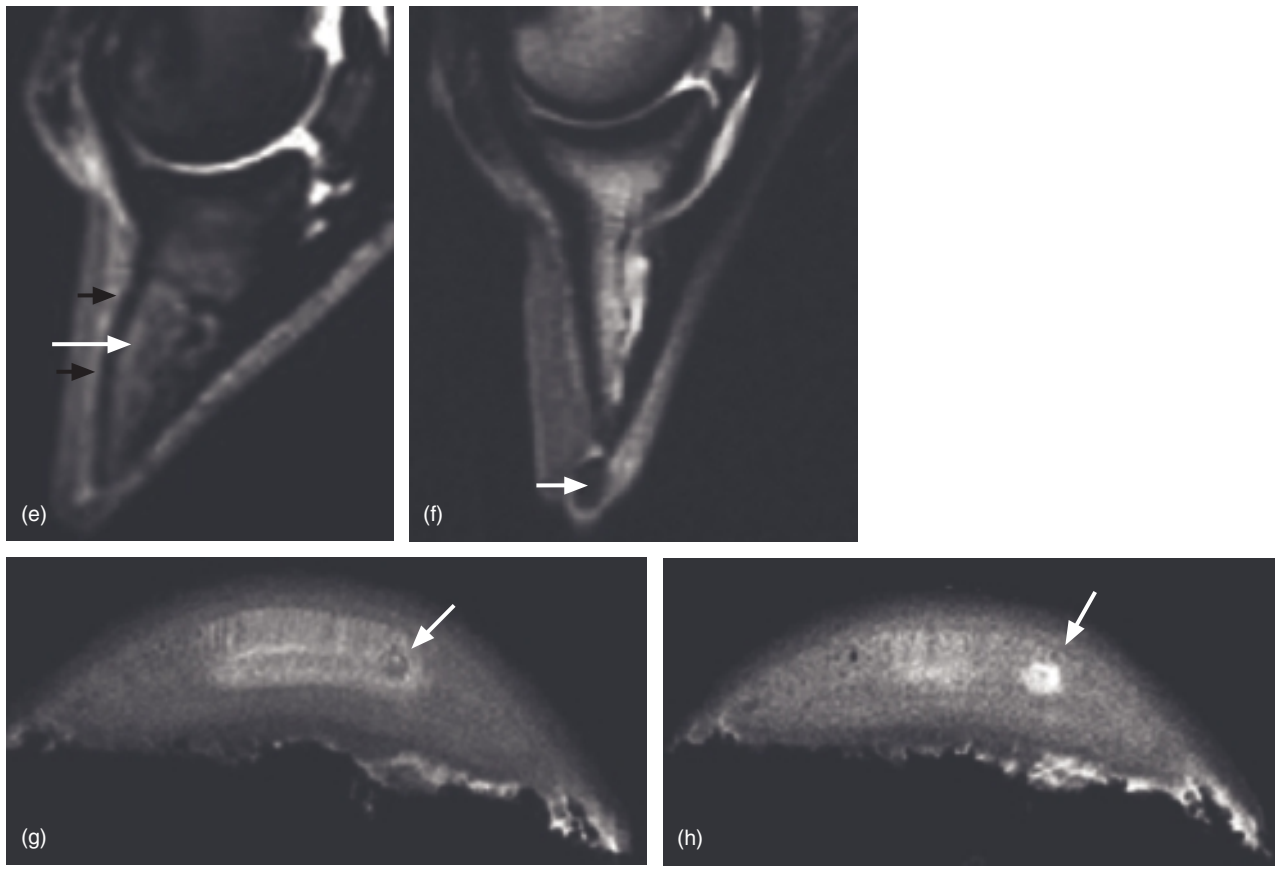

Figure 12.23 *Cont'd* (e) Sagittal 2D STIR high-field MR image at of a foot from a pony with chronic laminitis. Dorsal is to the left. There is increased signal intensity in the dorsal aspect of the distal phalanx (white arrow) and in the adjacent laminae (black arrows) reflecting fluid. (f) Sagittal 2D fast dual-echo high-field MR image of a foot from a pony with chronic laminitis. Dorsal is to the left. There is laminar disruption. There is a well-circumscribed area of low signal intensity in the laminae adjacent to the dorsodistal aspect of the distal phalanx consistent with gas. This is surrounded by a rim of high signal intensity consistent with fluid. (g) Transverse T2* 3D GRE high-field MR image of a foot from a pony with chronic laminitis. Dorsal is to the top and medial to the left. There is a circumscribed area of low signal intensity within the laminae consistent with gas. This is the same foot as (e). (h) Transverse T2* 3D GRE high-field MR image of a foot from a pony with chronic laminitis. Dorsal is to the top and medial to the left. There is a circumscribed area of high signal intensity within the laminae consistent with fluid. This is the same foot as in (d), slightly further distally, and these findings reflect abscess formation.

proteinaceous fluid. Irregularity of the dorsal and solar cortices of the distal phalanx was most obvious around the toe. Linear increased signal intensity in fat-suppressed images palmar to the dorsal cortex of the distal phalanx was a common finding, especially distally, seen best in sagittal images (Figure 12.23e). In some horses there was increased vascularity of the distal phalanx, with an increase in both number and size of vascular channels.

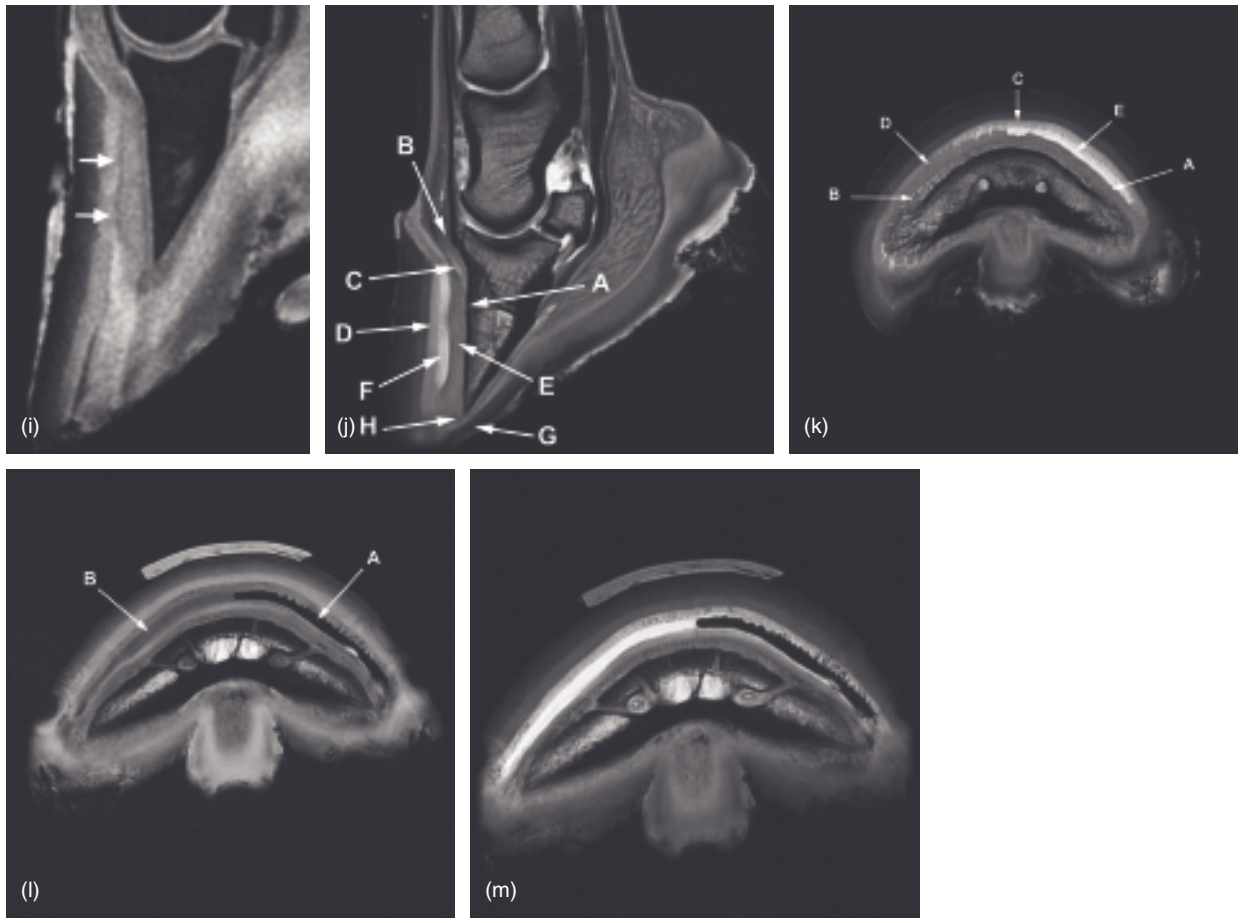

Figure 12.23 *Cont'd* (i) Sagittal fat saturated 3D SPGR high-field MR image of a foot from a pony with chronic laminitis. The foot is clearly very distorted in shape. There is laminar separation from the hoof wall (arrows) and linear low signal intensity consistent with gas. Note the increased dorsopalmar thickness of the laminae. (j) High-resolution sagittal 3D T2* GRE image of a foot with distal displacement (sinking) of the distal phalanx and pronounced lamellar separation. **A**, note parallel alignment between the dorsal surface of the hoof wall and the dorsal aspect of the distal phalanx; **B**, elongation and compression of the coronary dermis between the proximal border of the hoof wall and the extensor process of the distal phalanx ; **C**, linear hypointense feature at proximal margin of the lamellar interface, indicating lamellar separation and fluid infiltration; **D**, epidermal lamellae; **E**, dermal lamellae and sublamellar dermis; **F**, region of lamellar separation and fluid infiltration/seroma following distal displacement of the distal phalanx; **G**, flattening of the sole; **H**, compression of the solar dermis between the displaced distal phalanx and the sole. Image courtesy of Dr Simon Collins. (k) High-resolution transverse 3D T2* GRE image of a foot with distal displacement (sinking) of the distal phalanx and pronounced lamellar separation dorsally and medially. **A**, sublamellar dermis; **B**, lamellar vascular plexus; **C**, hyperintense signal of the separated epidermal lamellae; **D**, homogenous signal of the unaffected lamellar interface; **E**, region of lamellar separation and fluid infiltration/seroma following distal displacement of the distal phalanx. Image courtesy of Dr Simon Collins. (l) High-resolution transverse 3D T1 SPGR image of a catastrophic laminitic sinker foot acquired in lateral recumbency showing pronounced circumferential lamellar separation. Note the dorsal aspect of the hoof wall has been discriminated by Play-Doh. **A**, physical separation between epidermal and dermal lamellar; **B**, seroma and fluid infiltration following traumatic lamellar vascular damage. Image courtesy of Dr Simon Collins. (m) High-resolution transverse 3D T2* GRE image corresponding to (k). Image courtesy of Dr Simon Collins.

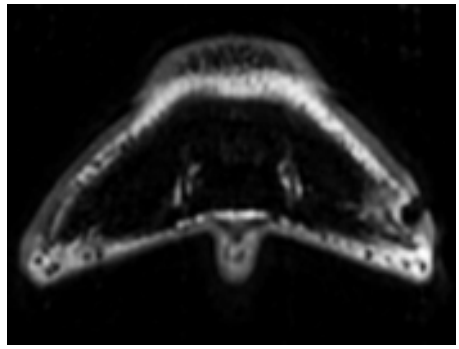

Figure 12.24 Transverse 2D STIR high-field MR image of a foot. Lateral is to the right. There is a well-circumscribed circular area of low signal intensity lateral to the lateral palmar process of the distal phalanx. There is a concave defect in the lateral cortex of the adjacent palmar process and increased signal intensity in the subcortical bone. This was associated with focal increased radiopharmaceutical uptake in the distal phalanx. This space-occupying lesion was fibrous tissue.

Space-occupying lesions

A keratoma is characterized by a smoothly demarcated area of hypointense signal in all image sequences, replacing the normal architecture of the corium and laminae. If close to the distal phalanx, there is an area of loss of normal bone architecture with a concave defect outlining the space-occupying mass, adjacent to which may be areas of high signal intensity in the trabecular bone in fat-suppressed images. Keratoma-like masses have been seen as incidental abnormalities when not immediately adjacent to the distal phalanx. A mass with identical appearance on MR images (Figure 12.24) proved to be fibroplasia when examined histologically, although very similar in appearance to a keratoma when surgically removed.

Evidence of previous penetrating injury

MR evidence of a previous penetrating injury is characterized by focal areas of hypointense signal in all image sequences traversing the soft tissues on the palmar aspect of the foot, which is typical of haemosiderin, gas or mineralization (Figure 12.25) [45, 48]. The presence of haemosiderin has been confirmed histologically. Soft tissue and osseous abnormalities have been identified in the same plane as the penetrating tract. Surprisingly, in chronic cases there is frequently no consistent evidence of infection, although abscess formation within the distal phalanx may occur (Figure 12.25). Where a horseshoe nail is positioned too close to or against the distal phalanx it is possible to see increased signal intensity on fat-suppressed images with decreased signal intensity on T1-weighted images in the affected region of the distal phalanx (Figure 12.25). There may be rapid resolution of pain in this type of penetration, but in more severe cases some horses have ultimately made a full functional recovery despite considerable traumatic damage to both soft tissue and osseous structures.

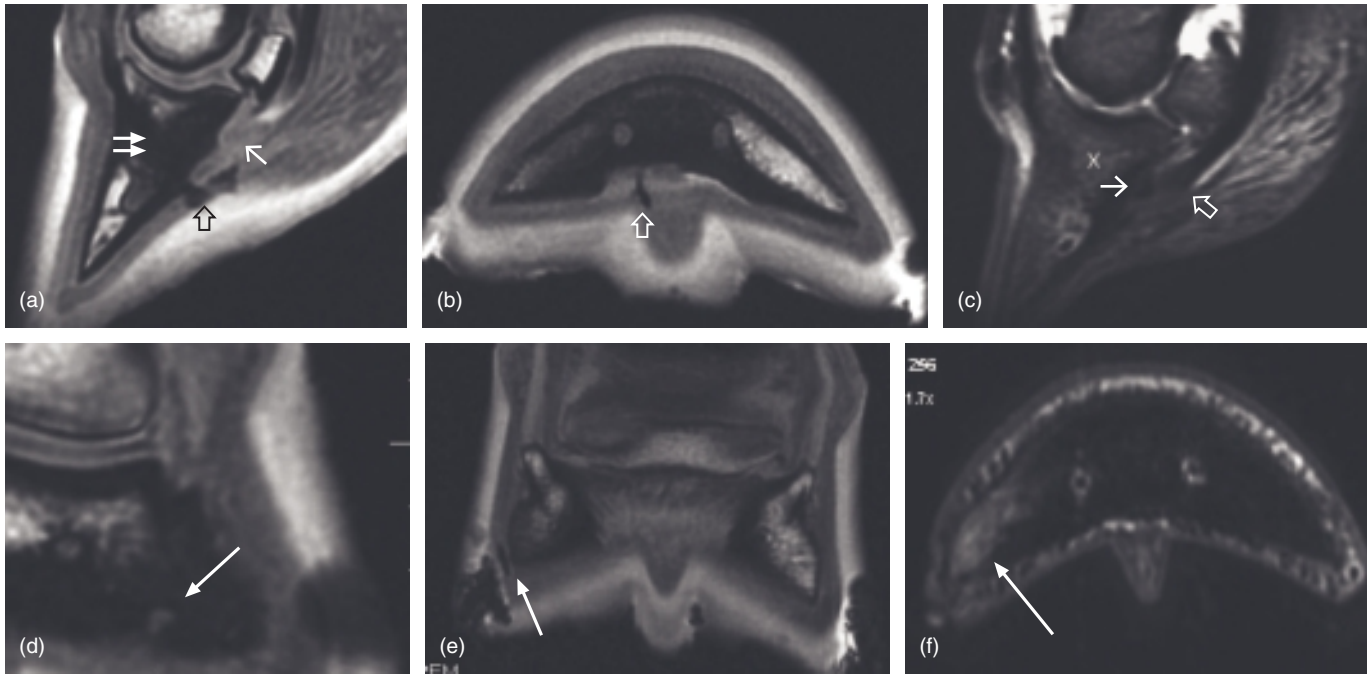

Figure 12.25 (a) Parasagittal 3D T1-weighted SPGR high-field MR image of a foot. There is evidence of a previous penetrating injury. Open arrow: focal lesions of low signal intensity in the laminae palmar and distal to the deep digital flexor tendon (DDFT) insertion, typical of haemosiderin in the puncture tract. Small arrow: enlargement and loss of architecture of the distal medial lobe of the DDFT. Double arrow: diffuse decreased signal intensity in the palmar and proximal aspect of the distal phalanx. The increased signal intensity of the DDFT distal to the navicular bone is partly due to the magic angle effect. (b) Transverse 3D T1-weighted SPGR high-field MR image of the same foot as (a). Medial is to the left. Arrow: focal area of decreased signal intensity in the deep digital flexor tendon and laminae. There is an irregular outline of the flexor cortex of the distal phalanx and generalized decreased signal intensity in the mid-body and medial aspect of the distal phalanx. (c) Parasagittal 2D T2-weighted STIR high-field MR image of the same foot as (a) and (b). Open arrow: enlargement, increased signal and loss of architecture of the deep digital flexor tendon (DDFT) from the level of the navicular bone to the tendon's insertion on the distal phalanx. Small arrow: area of decreased signal intensity in the dorsal aspect of the DDFT at the insertion on the distal phalanx. X: increased signal intensity in the cancellous bone in the palmar aspect of the distal phalanx. (d) Dorsal plane T1 gradient-echo image of the foot of a horse with a previous solar penetration at this location and recurrent pain. There is evidence of abscess formation within the distal phalanx (arrow). (e) Dorsal high-field T1-weighted image of the foot of a horse with a recent history of foot pain and no radiological abnormality. Medial is to the left. There is a linear area of low signal intensity in the laminae medially (arrow), indicative of either fluid, gas or haemosiderin. The adjacent area of the distal phalanx has decreased signal intensity which could be consistent with fluid or increased mineralization. (f) Transverse high-field STIR image of the distal phalanx in the same foot as (e). Medial is to the left. There is increased signal intensity medially (arrow), suggesting that there is fluid-based pathology not mineralization. This was the result of bone trauma, probably the result of a misdirected nail. The linear area of low signal intensity in the laminae reflected purulent material.

Quittor and other infections

Rarely, there is infection of a cartilage of the foot and surrounding soft tissues, so-called quittor. This is characterized by thickening of the affected cartilage of the foot, with poor demarcation of its margins and increased signal intensity in fat-suppressed images. There may be tracks of fluid (low signal intensity in T1-weighted images and high signal intensity on T2-weighted and fat-suppressed images) axial to the affected cartilage of the foot. There is thickening of the soft tissues abaxial to the cartilage of the foot.

Laminar infections are characterized by focal areas of low signal intensity in all image sequences, the result of gas accumulation.

Proximal interphalangeal joint

Significant lesions of the PIP joint were rare. A single horse had acute, severe lameness associated with a focal defect in the subchondral bone and overlying articular cartilage of the proximomedial aspect of the middle phalanx. Several horses with desmitis of a CL of the DIP joint also had ipsilateral lesions of the CL of the PIP joint. Several horses had quiescent OCLLs in the distal aspect of the proximal phalanx or the proximal aspect of the middle phalanx that were not considered likely to be contributing to lameness. Three horses with extensive dorsal enlargement of the dorsal articular margins of the PIP joint, which was identified radiologically, had no response to intra-articular analgesia. This was seen in association with chronic desmitis of the OSLs. All horses had no intra-articular pathology detectable using MRI and had other soft tissue lesions of the DDFT, CL of the DIP joint and CSL that were considered to be the principal cause of the current lameness.

Collateral ligaments of the proximal interphalangeal joint

To date we have primarily identified injuries of the CLs of the PIP joint in association with ipsilateral injury of the CL of the DIP joint. These have been characterized by enlargement of the affected ligament and increased signal intensity in both T1- and T2-weighted images.

Digital flexor tendon sheath

Distension of the digital flexor tendon sheath (DFTS) is a common non-specific finding, which is not necessarily of clinical significance. However, its presence merits close inspection of the DDFT and SDFT. Lesions of the DDFT are sometimes associated with adhesions between the tendon and the sheath wall.

Proximal and distal digital annular ligaments

To date we have only identified injuries of either the proximal or distal digital annular ligament in conjunction with other injuries (see section on Multiple injuries, below). However, primary desmitis of the distal digital annular ligament has been described either alone or in association with lesions of the DDFT within the adjacent DFTS [49]. Lesions were characterized by either diffuse or focal thickening of the distal digital annular ligament in the region of the PIP joint, with a variable increased signal intensity in T1- and T2-weighted images.

Straight sesamoidean ligament

Injuries of the SSL are uncommon and in our clinical population are usually seen in association with other lesions contributing to lameness [50]. Lesions occurred throughout the length of the ligament, in a contrast to a report in which a small number of horses had injuries close to the insertion of the

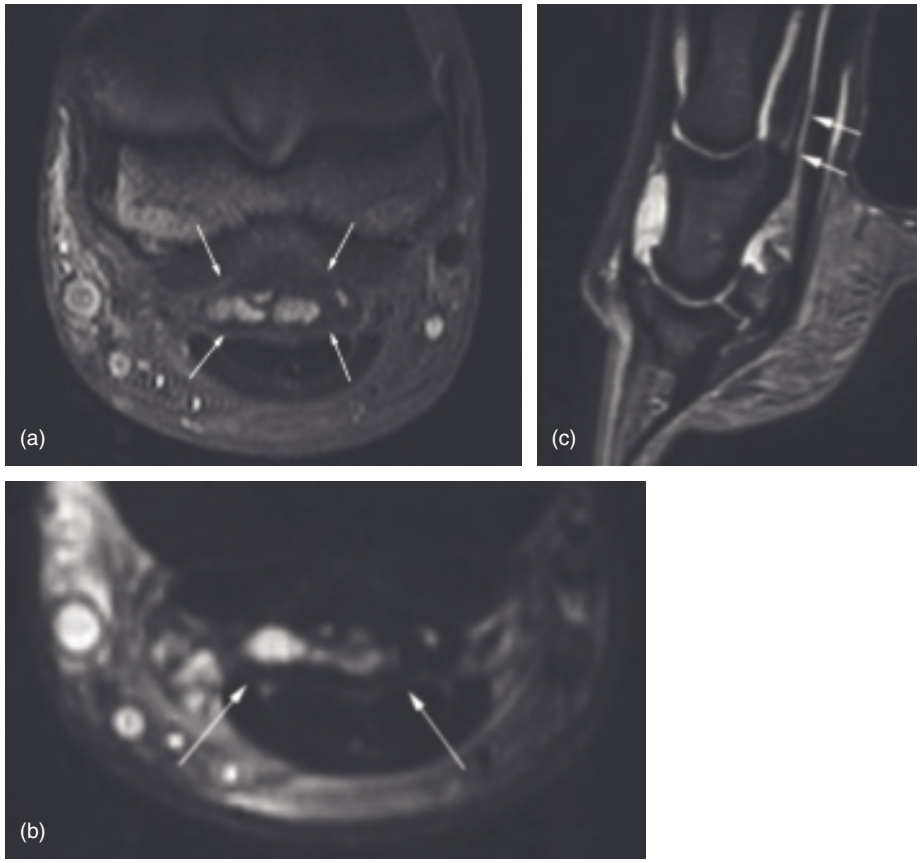

Figure 12.26 (a) Transverse 3D T1-weighted SPGR high-field MR image of the proximal aspect of the pastern. Medial is to the left. The straight sesamoidean ligament is enlarged and has large areas of increased signal intensity (arrows). (b) Transverse 2D STIR high-field MR image of the proximal aspect of the pastern as the same horse in (a). Medial is to the left. The straight sesamoidean ligament is enlarged and has focal areas of increased signal intensity (arrows). This injury was the primary cause of lameness. (c) Sagittal 2D STIR high-field MR image of the pastern region. The distal palmar aspect of the straight sesamoidean ligament has increased signal intensity (arrows).

SSL as the sole cause of lameness [51]. In our clinical population injuries of the SSL were associated with both increased cross-sectional area through most of the ligament and increased signal intensity (Figure 12.26) [50], whereas in previous descriptions an increase in size was not reported.

Oblique sesamoidean ligaments

Primary lesions of the OSLs have been described as the principal cause of lameness [51]. However, in our clinical population of horses undergoing MRI, lesions of one of the OSLs have been unusual as the sole cause of lameness, although lesions close to the origin on one of the proximal sesamoid bones were seen that were not identified ultrasonographically. Most lesions occurred in the proximal third of the ligament and were typified by enlargement of the ligament and increased signal intensity on T1- and T2-weighted images (Figure 12.27). Several horses have had a complex of straight, cruciate and oblique sesamoidean ligament injuries principally localized to the medial or

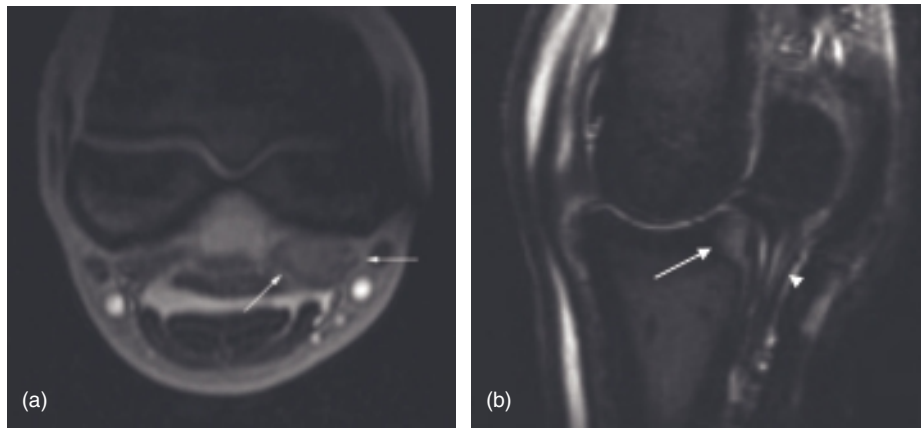

Figure 12.27 (a) Transverse 3D T2* GRE high-field MR image immediately distal to the proximal sesamoid bones. Medial is to the right. The medial oblique sesamoidean ligament is enlarged and has diffuse increased signal intensity (arrows). (b) Sagittal plane STIR image of the fetlock of a horse after traumatic injury, with damage to the collateral ligament and surrounding soft tissues. There is evidence of oblique and cruciate sesamoidean ligament injury with increased signal intensity in the palmaroproximal aspect of the proximal phalanx (arrow) near the insertion of the cruciate sesamoidean ligament, and increased signal intensity within the body of the oblique sesamoidean ligament (arrowhead). The apparent decrease in signal intensity in the distal aspect of the third metacarpal bone and the proximal sesamoid bone is because this slice was obtained close to or through the cortices of the bones.

lateral aspect of the limb. Associated damage to the ipsilateral branch of the suspensory ligament and/or ipsilateral proximal sesamoid bone is not unusual in horses working at speed. Care should be taken in the interpretation of MR images in which the static magnetic field is perpendicular to the long axis of the limb, because both the medial and lateral OSLs are susceptible to the magic angle effect, particularly near the origin [41].

Cruciate sesamoidean ligaments

Evaluation of the cruciate sesamoidean ligaments (CrSLs) is not easy because of their small size, and injury has usually been seen in association with lesions of the OSLs [50]. Injury was characterized by enlargement of the CrSLs, irregularity of the palmar border and increased signal intensity in T1- and T2-weighted images. Increased signal intensity in the bone at the origin and/or insertion on fat-suppressed images can be useful in identification of damage when the ligament body is difficult to visualize. The CrSLs may be easier to identify in parasagittal and transverse images obtained in a standing horse compared with a horse under general anaesthesia, because of the relative extension of the metacarpophalangeal (metatarsophalangeal) joint.

Superficial digital flexor tendon

Lesions of one of the branches of the SDFT characterized by increased signal intensity, with or without swelling, were invariably seen in association with a complex of soft tissue injuries.

Multiple injuries

In the clinical population at the Animal Health Trust undergoing MRI between January 2001 and December 2007, 30.1% of horses had injuries to multiple structures that were thought to be contributing to pain causing lameness, including variable combinations of injury to the CLs of the DIP and PIP joints, the DDFT, DSIL and CSL, the distal and proximal digital annular ligaments, the navicular bone, the DIP joint and the middle and distal phalanges (Figure 12.28) (Table 12.1). Less commonly there were lesions of the OSL, SSL or SDFT. Horses with multiple injuries often had lesions clustered towards one side of the limb, suggestive of generalized trauma to that region. Distension of the DIP joint and/or navicular bursa, with or without soft tissue proliferation, was a frequent non-specific finding in many horses irrespective of the primary injury site. Abnormalities of the distal phalanx and adjacent laminae consistent with chronic laminitis [47] were sometimes seen in addition to the lesions considered to be the primary cause of lameness.

In addition there were a significant number of other horses in which abnormalities of multiple structures were identified, but based on the MR signal characteristics, and the results of local analgesia and other imaging modalities, the principal cause of lameness was ascribed to one or two injured structures.

CONCLUSIONS

In the vast majority of horses examined using high-field MRI it has been possible to identify one or more lesions likely to be the cause of pain resulting in lameness. However, low grade signal abnormalities can be seen in some structures in clinically normal horses. It was clear that in some horses the development of relatively severe abnormalities had predated the onset of lameness. However, once pain causing lameness had been triggered it tended to be persistent. Moreover in some horses with bilateral lameness that was markedly asymmetrical in degree, very similar MRI abnormalities were identified bilaterally. In some unilaterally lame horses similar MRI lesions were also present bilaterally. Further information about the mediation of pain causing lameness is still required.

Comparison of signal intensity in T1- and T2-weighted and fat-suppressed images, together with the results of local analgesia and nuclear scintigraphy, can help to determine which injuries are most likely to be the major contributors to lameness. As subtle pathology may be more difficult to detect using low-field imaging with lower resolution images, in horses with only mild lameness it may be preferable to acquire high-field, high-resolution images.

The spectrum of injuries described is typical of the clinical population in a referral clinic in Great Britain with a high proportion of sports horses and general purpose riding horses. The proportion of each injury type may well be different in other countries dependent on the type or breed of horse, the discipline in which it is principally involved, environmental conditions, work surfaces and work programmes.

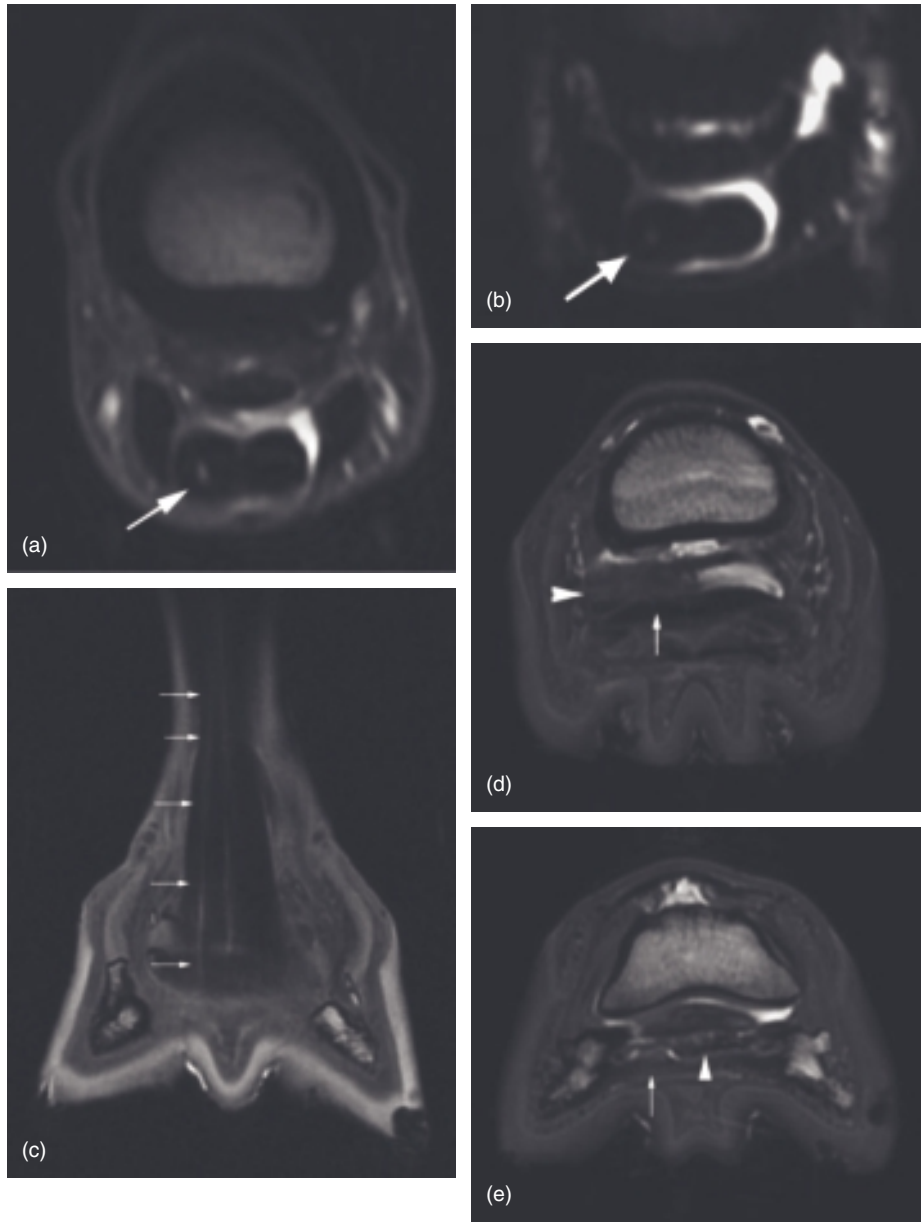

Figure 12.28 (a) Transverse 3D T2* gradient-echo high-field MR image of the proximal pastern region of a 5-year-old Thoroughbred event horse with left forelimb lameness improved by rest and markedly exacerbated by work. Lameness was improved by palmar digital nerve blocks and abolished by palmar (abaxial sesamoid) nerve blocks but not influenced by intra-articular analgesia of the distal interphalangeal joint. Medial is to the left. There is a large core lesion in the swollen medial lobe of the deep digital flexor tendon (arrow). This horse had multiple lesions contributing to pain and lameness, predominantly involving the medial aspect of the digit. (b) Transverse 2D STIR high-field MR image at the same level as in (a). There is high signal intensity in the core lesion of the medial lobe of the deep digital flexor tendon (DDFT) (arrow). A lesion of the medial lobe of the DDFT extended from the proximal aspect of the proximal phalanx to the tendon's insertion on the distal phalanx. (c) Dorsal 3D T1-weighted spoiled gradient-echo high-field MR image of the same foot as in (a) and (b). Medial is to the left. There is an extensive linear area of high signal intensity in the medial lobe of the deep digital flexor tendon (arrows). (d) Transverse 3D T2* gradient-echo high-field MR image of the same limb as (a)–(c), at the level of the proximal aspect of the navicular bursa. Medial is to the left. There is a dorsal split in the medial lobe of the deep digital flexor tendon (DDFT) (arrow), with soft tissue (arrow head) extending between the DDFT and the medial collateral sesamoidean ligament (CSL). The medial CSL is thickened. The lateral aspect of the navicular bursa is distended. (e) Transverse 3D T2* gradient-echo high-field MR image of the same limb as (a)–(d), distal to the navicular bone. Medial is to the left. The distal sesamoidean ligament is swollen (arrow head). There is soft tissue on the dorsal aspect of the deep digital flexor tendon medially (arrow). The medial collateral ligament of the distal interphalangeal joint has increased signal intensity and its margins are poorly defined. There is diffuse mild decreased signal intensity throughout the medial palmar process of the distal phalanx.

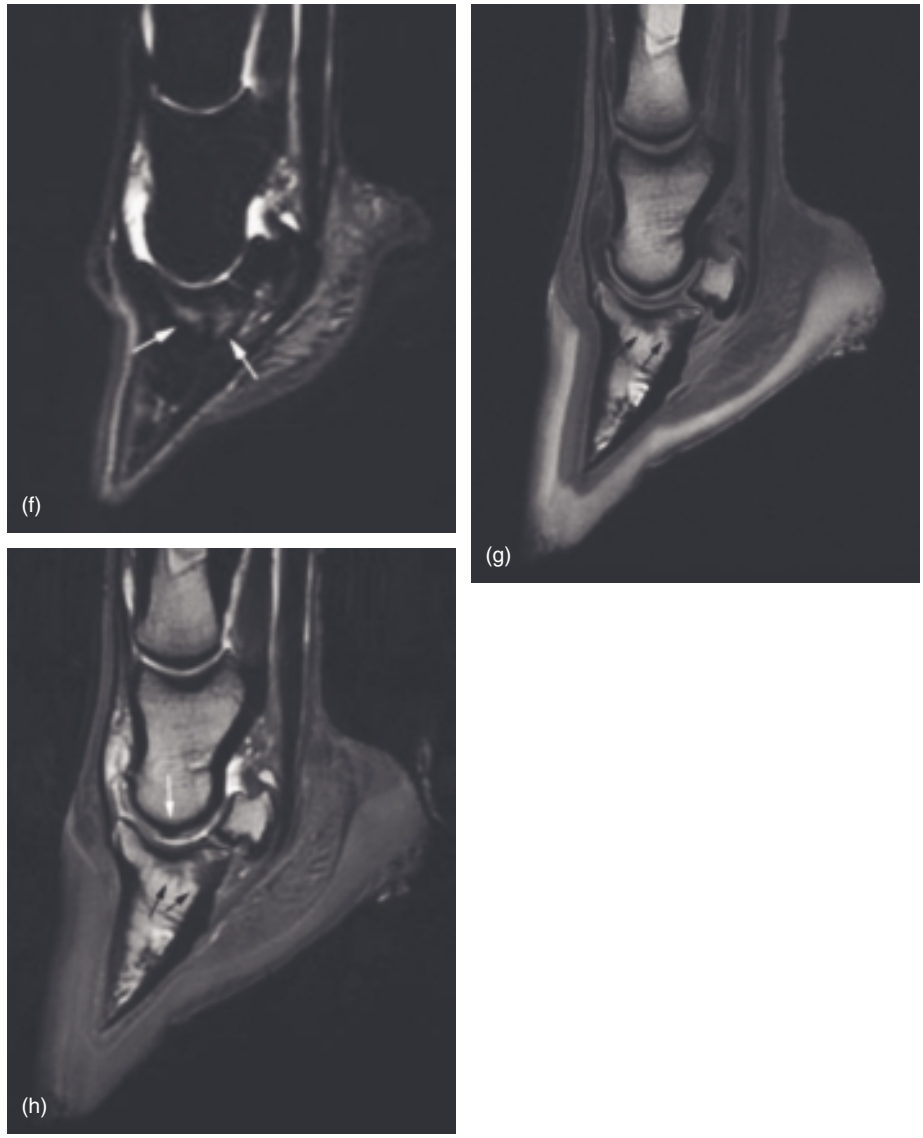

Figure 12.28 *Cont'd* (f) Sagittal 2D STIR high-field MR image of the same foot as in (a)–(e). Dorsal is to the left. There is increased signal intensity in the palmar half of the proximal aspect of the distal phalanx (arrows). There is increased signal intensity in the palmar aspect of the navicular bone. The dorsal and palmar recesses of the distal interphalangeal joint are distended. (g) Sagittal 3D T1-weighted spoiled gradient-echo high-field MR image of the same foot as in (a)–(f). Dorsal is to the right. There is reduced signal intensity in the palmar half of the proximal aspect of the distal phalanx (arrows) corresponding to the regions of high signal intensity seen in the STIR images. (h) Sagittal 3D T2* gradient-echo high-field MR image of the same foot as in (a)–(g). Dorsal is to the right. There is reduced signal intensity in the palmar half of the proximal aspect of the distal phalanx (black arrows) corresponding to the regions of high signal intensity seen in the STIR images. Note also the focal area of reduced signal intensity in the distal articular cartilage of the middle phalanx (white arrow).

REFERENCES

[1] Dyson S, Murray R, Schramme M, Branch M. Magnetic resonance imaging of the equine foot: 15 horses. *Equine Vet J* 2003; **35**: 18–26.
[2] Dyson S, Murray R, Schramme M. Lameness associated with foot pain: results of 199 horses (January 2001–December 2003) and response to treatment. *Equine Vet J* 2005; **37**: 113–21.
[3] Schneider R. Lameness problems in the foot: advances in diagnosis. Proceedings 13th Annual Congress American College of Veterinary Surgeons, *Washington DC, October 2003 (CD-Rom)*.
[4] Schneider R, Gavin P, Tucker R. What magnetic resonance imaging is teaching us about navicular disease. *Proc Am Assoc Equine Pract* 2003; **49**: 210–19.
[5] Dyson S, Murray R. Magnetic resonance imaging of the equine foot. *Clin Tech Equine Pract* 2007; **6**: 46–61.
[6] Sherlock C, Mair T, Blunden T. Deep erosions of the palmar aspect of the navicular bone diagnosed by standing magnetic resonance imaging. *Equine Vet J* 2008; **40**: 684–92.
[7] Sampson S, Schneider R, Gavin P, Ho C, Tucker R, Charles G. Magnetic resonance imaging findings in horses with recent onset navicular syndrome but without radiographic abnormalities. *Vet Radiol Ultrasound* 2009; **50**: 339–46.
[8] Murray R, Schramme M, Dyson S, Branch M, Blunden A. MRI characteristics of the foot in horses with palmar foot pain and control horses. *Vet Radiol Ultrasound* 2006; **47**: 1–16.
[9] Schramme M, Murray R, Blunden A, Dyson S. A comparison between MRI, pathology and radiology in 34 limbs with navicular syndrome and 25 control limbs. *Proc Am Assoc Equine Pract* 2005; **51**: 348–58.
[10] Murray R, Blunden A, Schramme M, Dyson S. How does magnetic resonance imaging represent histological findings in the equine digit? *Vet Radiol Ultrasound* 2006; **47**: 17–31.
[11] Dyson S, Murray R, Blunden T, Schramme M. Current concepts of navicular disease. *Equine Vet Educ* 2006; **18**: 45–56.
[12] Blunden A, Dyson S, Murray R, Schramme M. Histological findings in horses with chronic palmar foot pain and age-matched control horses. Part 1: the navicular bone and related structures. *Equine Vet J* 2006; **38**: 15–22.
[13] Dyson S, Murray R. Verification of scintigraphic imaging for injury diagnosis in 264 horses with foot pain. *Equine Vet J* 2007; **39**: 350–5.
[14] Dyson S, Murray R. Use of concurrent scintigraphic and magnetic resonance imaging evaluation to improve understanding of the pathogenesis of injury of the podotrochlear apparatus. *Equine Vet J* 2007; **39**: 365–9.
[15] Blunden A, Dyson S, Murray R, Schramme M. Histological findings in horses with chronic palmar foot pain and age-matched control horses. Part 2: the deep digital flexor tendon. *Equine Vet J* 2006; **38**: 23–7.
[16] Wright I, Kidd L, Thorp B. Gross, histological and histomorphometric features of the navicular bone and related structures in the horse. *Equine Vet J* 1998; **30**: 220–34.
[17] Barber M, Sampson S, Schneider R, Baszler T, Tucker R. Use of magnetic resonance imaging to diagnose distal sesamoid bone injury in a horse. *J Am Vet Med Assoc* 2006; **220**: 717–20.
[18] Busoni V, Heimann M, Trenteseaux J, Snaps F, Dondelinger R. Abnormal MRI findings in the deep digital flexor tendon and distal sesamoid bone in radiographically defined navicular disease – an in vitro study. *Vet Radiol Ultrasound* 2005; **46**: 279–86.
[19] Dyson S, Murray R. Magnetic resonance imaging of 264 horses with foot pain: the podotrochlear apparatus, the deep digital flexor tendon and the collateral ligaments of the distal interphalangeal joint. *Equine Vet J* 2007; **39**: 340–3.
[20] Verschooten F, Roels J, Lampu P, Desmet P, De Moor A, Picavet T. Radiographic measurements from the lateromedial projection of the equine foot with navicular disease. *Res Vet Sci* 1989; **46**: 15–21.
[21] Wright I. A study of 118 cases of navicular disease: radiological features. *Equine Vet J* 1993; **25**: 493–500.
[22] Pool R, Meagher D, Stover S. Pathophysiology of navicular syndrome. *Vet Clin N Am: Equine Pract* 1989; **5**: 109–29.

[23] Kaser-Hotz B, Ueltsch, G. Radiographic appearance of the navicular bone in sound horses. *Vet Radiol Ultrasound* 1992; **33**: 9–17.
[24] Dyson S, Murray R. Lameness and diagnostic imaging in the sports horse: recent advances related to the digit. *Proc Am Assoc Equine Pract* 2007; **53**: 262–75.
[25] Svalastoga E, Neilsen K. Navicular disease in the horse: the synovial membrane of bursa podotrochlearis. *Nord Vet Med* 1983; **35**: 28–30.
[26] Mair T, Sherlock C. Osseous cyst-like lesions in the feet of lame horses. *Equine Vet Educ* 2008; **20**: 47–56.
[27] Bowker R, Atkinson P, Atkinson T, Haut, R. Effect of contact stress in bones of the distal interphalangeal joint on microscopic changes in articular cartilage and ligaments. *Am J Vet Res* 2001; **62**: 414–24.
[28] Van Wulfen K. Normal anatomy of navicular bone suspensory ligaments and its relationship to navicular syndrome. MS thesis, Michigan State University, 1999.
[29] Kofler J, Kneissl S, Malleczek D. MRI and CT diagnosis of acute desmopathy of the lateral collateral sesamoidean ligament and long-term outcome in a horse. *The Vet J* 2007; **174**: 410–13.
[30] Dyson S, Murray R, Schramme M, Branch M. Lameness in 46 horses associated with deep digital flexor tendonitis in the digit: diagnosis confirmed with magnetic resonance imaging. *Equine Vet J* 2003; **35**: 681–90.
[31] Mair T, Kinns J, Jones R, Bolas N. Magnetic resonance imaging of the distal limb of the standing horse. *Equine Vet Educ* 2005; **17**: 74–82.
[32] Mair T, Kinns J. Deep digital flexor tendonitis in the equine foot diagnosed by low-field magnetic resonance imaging in the standing patient: 18 cases. *Vet Radiol Ultrasound* 2005; **46**: 458–66.
[33] Murray R, Roberts B, Schramme M, Dyson S, Branch M. Quantitative evaluation of equine deep digital flexor tendon morphology using magnetic resonance imaging. *Vet Radiol Ultrasound* 2004; **45**: 103–11.
[34] Blunden T, Dyson S, Murray R. Lesions of the deep digital flexor tendon: a correlative MRI and post mortem study in control and lame horses. *Equine Vet J* 2009; **41**: 25–33.
[35] Beck S, Blunden T, Dyson S, Murray R. Are matrix and vascular changes involved in the pathogenesis of deep digital flexor tendon injury in the horse? *The Vet J* doi:10.1016/j.tvjl2010.07.015.
[36] Dyson S, Murray R, Schramme M, Branch M. Collateral desmitis of the distal interphalangeal joint in 18 horses (2001–2002). *Equine Vet J* 2004; **36**: 160–6.
[37] Dyson S, Murray R. Collateral desmitis of the distal interphalangeal joint in 62 horses (January 2001–December 2003). *Proc Am Assoc Equine Pract* 2004; **50**: 248–56.
[38] Zubrod C, Farnsworth K, Tucker R, Ragle C. Injury of the collateral ligaments of the distal interphalangeal joint diagnosed by magnetic resonance imaging. *Vet Radiol Ultrasound* 2005; **46**: 11–16.
[39] Gutierrez S, White N, Werpy N *et al*. Magnetic resonance imaging findings of desmopathy of the collateral ligaments of the equine distal interphalangeal joint. *Vet Radiol Ultrasound* 2008; **50**: 21–31.
[40] Spriet M, Mai W, McKnight A. Asymmetric signal intensity in normal collateral ligaments of the distal interphalangeal joint in horses with a low field MRI system: a manifestation of the magic angle effect. *Vet Radiol Ultrasound* 2007; **48**: 95–100.
[41] Smith M, Dyson S, Murray R. Is a magic angle effect observed in the collateral ligaments of the distal interphalangeal joint or the oblique sesamoidean ligaments during standing low field magnetic resonance imaging? *Vet Radiol Ultrasound* 2008; **49**: 509–15.
[42] Dyson S, Blunden T, Murray R. The collateral ligaments of the distal interphalangeal joint: magnetic resonance imaging and post mortem observations in 25 lame horses and 12 control horses. *Equine Vet J* 2008; **40**: 538–44.
[43] Zubrod C, Schneider R, Tucker R, Gavin P, Ragle C, Farnsworth K. Diagnosis of subchondral bone damage using magnetic resonance imaging in eleven horses. *J Am Vet Med Assoc* 2004; **24**: 411–18.
[44] Nagy A, Dyson S, Murray R. A comparison between nuclear scintigraphy radiography, and magnetic resonance imaging of the palmar processes of the distal phalanx. *Equine Vet J* 2008; **40**: 57–63.

[45] Kristoffersen M, Dyson S, Murray R, Schramme M, Boado A. Magnetic resonance imaging and scintigraphic findings in 5 horses with obscure lameness associated with penetrating injuries. *Proc Am Assoc Equine Pract* 2004; **50**: 320–7.
[46] Arble J, Mattason J, Drost W *et al*. Magnetic resonance imaging of the initial active stage of equine laminitis at 4.7 tesla. *Vet Radiol Ultrasound* 2009; **50**: 3–12.
[47] Murray R, Dyson S, Schramme M, Branch M, Woods S. Magnetic resonance imaging of the equine digit with chronic laminitis. *Vet Radiol Ultrasound* 2003; **44**: 609–17.
[48] Boado A, Kristofferson M, Dyson S, Murray R. Magnetic resonance imaging to diagnose chronic penetrating wounds in the equine foot. *Equine Vet Educ* 2005; **17**: 62–8.
[49] Cohen J, Schneider R, Zubrod C, Sampson S, Tucker R. Desmitis of the distal digital annular ligament in seven horses: MRI diagnosis and surgical treatment. *Vet Surg* 2008; **37**: 336–44.
[50] Smith S, Dyson S, Murray R. Magnetic resonance imaging of distal sesamoidean ligament injury. *Vet Radiol Ultrasound* 2008; **49**: 516–28.
[51] Sampson S, Schneider R, Tucker R, Gavin P, Zubrod C, Ho C. Magnetic resonance imaging features of oblique and straight distal sesamoidean desmitis in 27 horses. *Vet Radiol Ultrasound* 2007; **48**: 303–11.

Chapter 13
The fetlock region

Sarah Powell

INTRODUCTION

Horses undergoing any activity may sustain an injury to the metacarpophalangeal/metatarsophalangeal (MCP/MTP) joint. However, horses that perform at maximum speeds, such as racing Thoroughbreds, high-level endurance horses and other disciplines necessitating repetitive maximum flexion and extension of the fetlock joint, such as show jumpers, are particularly prone to these injuries. Epidemiological studies of lameness in racing Thoroughbreds have found pain related to the fetlock region is the third most common cause of modified training days after dorsal metacarpal disease and inflammatory airway disease [1]. Pleasure horses and dressage horses are relatively under-represented – problems relating to the foot and subtarsal region predominating in these cases. The differences between disciplines are likely to relate to the age of the animals, the type of occupational training and associated differences in limb loading. The MCP/MTP joint will be referred to as the fetlock joint throughout this chapter, any differences between the fore and hind joints will be addressed in the text. The majority of the images presented in this chapter were acquired using a 0.27 T Hallmarq EQ2 dedicated equine magnetic resonance imaging (MRI) system.[1]

INDICATIONS AND CASE SELECTION

MRI of the fetlock region can be used as a method of further evaluating known or suspected pathology, localized to the region by diagnostic local analgesia. MRI may be used where other diagnostic imaging methods have failed to elucidate a cause for lameness related to this region or where further information may aid treatment or management protocols (Box 13.1). MRI is not a time- or cost-effective 'screening' modality; therefore it is imperative the site of pain is localized as far as possible. In cases where lameness is not improved following intra-articular analgesia of the fetlock joint and only partially abolished by a low 4- or 6-point nerve block it is essential that a lateral palmar/plantar nerve block is carried out to rule out

[1]Hallmarq Veterinary Imaging, Guilford, Surrey, UK. All comments on case selection, technical data, sequence selection and logistics of acquisition, relate to the use of this system unless otherwise stated.

Equine MRI, edited by Rachel C. Murray.

Box 13.1 Indications for MRI of the fetlock region

- Horses with pain responsive to intra-articular analgesia of the fetlock joint with normal or inconclusive ultrasonographic and radiographic findings.
- Horses with pain responsive to low four- or six-point nerve block with normal or inconclusive ultrasonographic and radiographic findings in whom the foot and proximal metacarpal/metatarsal structures hove been ruled out as a site of pain.
- Horses with pain related to fetlock region with inconclusive radiographic and ultrasonographic findings and abnormal increased radionuclide uptake in the fetlock region on scintigraphic images.
- To further evaluate the clinical relevance of radiographically and ultrasonographically evident pathology.
- To monitor healing of previously identified pathology.

subcarpal/subtarsal pain alleviated by proximal diffusion of the low 4- or 6-point nerve block. Knowledge of the pattern of response to diagnostic local analgesia can help to target the initial slice positioning in order to maximize the chance of detecting lesions. Communication between the veterinary surgeon requesting the MR examination and the individual acquiring the images will therefore maximize the likelihood of a successful examination. Not all horses are amenable to standing examinations, and examination of the hind limb is not without risk during limb and coil positioning, which is compounded by the relatively light sedation levels required compared to when imaging the feet.

PROTOCOLS

When imaging the fetlock a comprehensive set of sequences including T1-weighted gradient recalled echo (GRE), T2*-weighted GRE, T2 fast spin-echo (FSE) and fat-suppressed (short τ inversion recovery, STIR) sequences in three orthogonal and lesion oriented planes should be acquired. Where it is possible to acquire proton density (PD) images, these may provide additional information. In the standing sedated horse, the order in which these sequences are acquired should remain flexible, as selecting to run a sequence at a time appropriate to the sedation level will help to achieve a more time efficient examination. Sedation protocols vary between centres but the aim for all is to achieve adequate sedation with minimal movement for the duration of the examination. The foundation of the sedation protocol at our centre is romifidine hydrochloride (Sedivet 1.0% injection, Boehringer Ingleheim) at an initial dose of 5 mg/100 kg 5 minutes prior to the onset of positioning within the magnet. Anxious or difficult horses may require very small doses of detomidine/butorphanol in combination.

The horse must stand squarely all round to ensure equal loading of all four limbs. The head should be lightly rested and the horse encouraged to stand without support from the handler, as support will encourage him to lean. The coil should be secured to prevent slipping, but without excessive tension on the skin surface. After the initial sedation is administered the following 30 minutes are likely to yield images of the highest quality. In the initial stages, the horse may not yet be completely relaxed so time is best spent acquiring a T1-weighted frontal sequence which is less sensitive to motion and can be used to pilot the following transverse sequences. Later, as the horse relaxes, fat-suppressed, T2 FSE and T2* GRE sequences are acquired. As further sedation is given and/or the horse needs to urinate, the quality of the images will deteriorate as motion increases. For this reason, imaging both limbs within the same examination is not recommended; allowing the horse to relax in his stall prior to imaging the second limb will ensure the images are of comparable quality.

SLICE POSITIONING

Slice positioning should aim to evaluate the entire joint including distal third metatarsal bone, proximal phalanx and proximal sesamoid bones (PSBs) and the supporting soft tissues. The specific area of interest should also be taken into account; some studies may be biased towards, for example, the proximal phalanx if this is indicated clinically or on previous radiographs. It should be remembered that structures at the periphery of the field of view may be susceptible to the presence of artefacts, which confound interpretation, and abnormal signal patterns. Hyperintensity on STIR images, in particular, may be underestimated or missed completely in a structure not appearing in the centre of the image, or in the most proximal or distal slice of a sequence. Lesion-oriented slice positioning may be necessary to target areas of particular interest. For example, if a fissure in the sagittal groove is suspected a standard transverse sequence may not illustrate this as well as a transverse oblique or frontal oblique view (Figure 13.1).

OSSEOUS INJURY

Subchondral bone pathology of the distal third metacarpal bone/third metatarsal bone (MC3/MT3) condyles

Subchondral bone (SCB) pathology is an important cause of fetlock joint lameness and is thought to play a role in the pathogenesis of osteoarthritis (OA), osteochondral fragmentation, fractures and SCB necrosis, which represent the most common causes of fetlock lameness in all types of athletic horse [2]. In addition, bone-related injuries in the fetlock region represent the most common cause of distal limb catastrophic fracture of Thoroughbred racehorses seen on racecourses. Lateral condylar fractures of MC3, proximal phalangeal fractures and biaxial PSB fractures are the most common racing injury in National Hunt racing, turf flat racing and all-weather flat racing in the UK respectively [3]. Subchondral bone changes

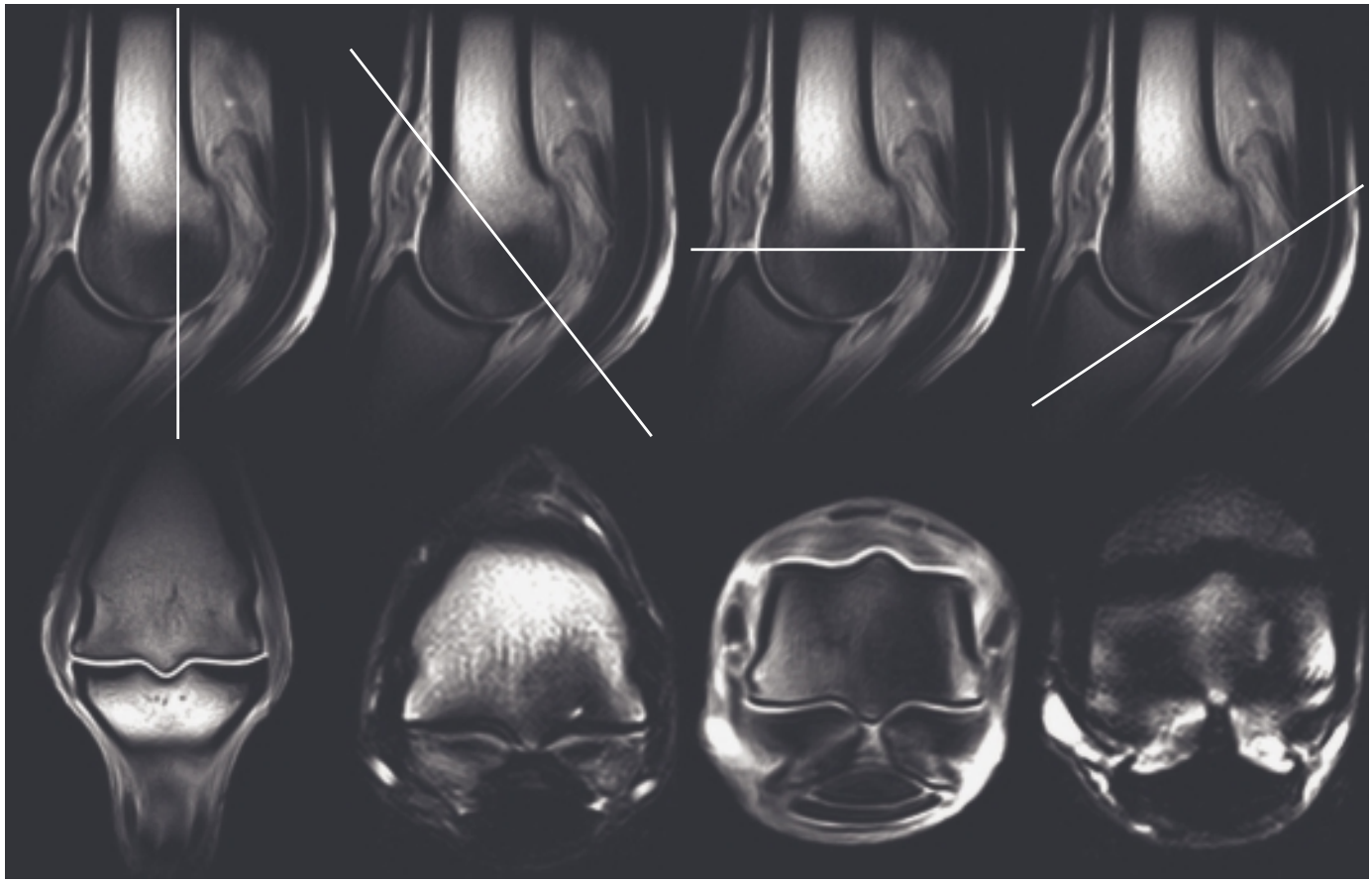

Figure 13.1 Slice orientation of routine examination of the distal metacarpal condyles. From top left – frontal, frontal oblique, transverse and transverse oblique views. Further orientations and a more distally centred pilot are required to fully evaluate the proximal phalanx.

seen as a consequence of repetitive microtrauma are more frequently seen, particularly in Thoroughbreds, than SCB changes resulting from a single supraphysiological-loading event [4, 5]. The latter are seen more commonly in event horses and show jumpers, where the location of the injury is often erratic. Injuries that result from accumulation of repetitive microtrauma, excessive loading and non-adaptive bone modelling occur at distinct anatomic locations which relate to the proposed load path running obliquely through the palmar/plantar apical region of MC3/MT3 to the dorsal proximal aspect of the distal epiphysis [6].

Condylar densification (sclerosis)

Alterations in density within the distal condyles of MC3/MT3 represent an adaptive response to loading. When a horse undergoes an athletic training programme, adaptive remodelling of the skeleton is initiated to accommodate these exercise-associated loads. This process is essential for conditioning the bone to further loading during exercise [7–9]. Extension of the fetlock joint in the sagittal plane around the distal aspect of the MC3/MT3 during maximal weight bearing hyperextends MC3/MT3 and the proximal

phalanx such that they approach right angles to each other. Contact is made between the palmar/plantar apical region of MC3/MT3, the PSBs and intersesamoidean ligament as the suspensory apparatus counters the loading and limits the range of extension. Extreme extension of the joint transfers loading to the proximal phalanx as it impinges on the dorsal articular aspect of MC3/MT3. The dynamics of this 'high-motion' joint are common to all horses, but it is the cyclic repetition of loading of the limbs of racing Thoroughbreds that lead to the common patterns of bone sclerosis seen both radiographically and on computed tomography (CT) and MR images [10, 11].

Regional variations in bone density of the distal condyles of MC3/MT3 have been shown to follow a distinct pattern [12] seen commonly on MR images. The bone is often more dense in the palmar/plantar regions of both medial and lateral condyles with a distinct zone of low-density bone within the medial and lateral parasagittal grooves separating the two condyles and the sagittal ridge. The lateral condyle is often, but not always, more dense than the medial. The density of the condyles generally decreases towards the dorsal aspect and is more evenly distributed across the width of the dorsal aspect of the condyle. The pattern and extent of subchondral bone densification in Thoroughbreds undergoing MRI examination while in full training varies between individuals and may reflect many factors, including age, conformation, training regime and training surfaces to name but a few. In our population of Thoroughbreds, some degree of increased densification of the palmar apical region is extremely common, and not always associated with clinical lameness (Figure 13.2a). In contrast, the densification pattern in non-competition horses rarely involves more than mild subchondral bone plate thickening (Figure 13.2b), which often does not extend into the trabecular bone. Less commonly, the dorsal region may be more severely affected and the palmar apical region relatively spared (Figure 13.3). Horses with densification of the palmar apical regions will often show varying degrees of densification of the PSBs (Figure 13.4). The densification of the PSB may be asymmetric; the most affected usually coinciding with the MC3/MT3 condyle with the greater degree of densification in the palmar/plantar apical region, indicating increased loading of this aspect of the joint. It is not uncommon in these cases to see additional pathology in the soft tissues supporting the ipsilateral or contralateral aspect of the joint, in particular the suspensory ligament branches (SLBs) and oblique distal sesamoidean ligaments. These soft tissue changes may not always be apparent ultrasonographically and may not be detectable clinically. The relevance and prevalence of apparently subclinical soft tissue pathology in the fetlock region of racing Thoroughbreds has not yet been established. Marked condylar densification patterns are often seen in the absence of any joint distension, other palpable abnormalities or pain related to joint flexion.

In more advanced cases, the pattern of densification may extend to include both palmar apical regions, the PSBs, the dorsal aspect of the condyles and the apposing surface of the dorsoproximal aspect of the proximal phalanx. In such cases, signs of chronic, proliferative synovitis are often apparent at the time of the clinical examination and on MR images.

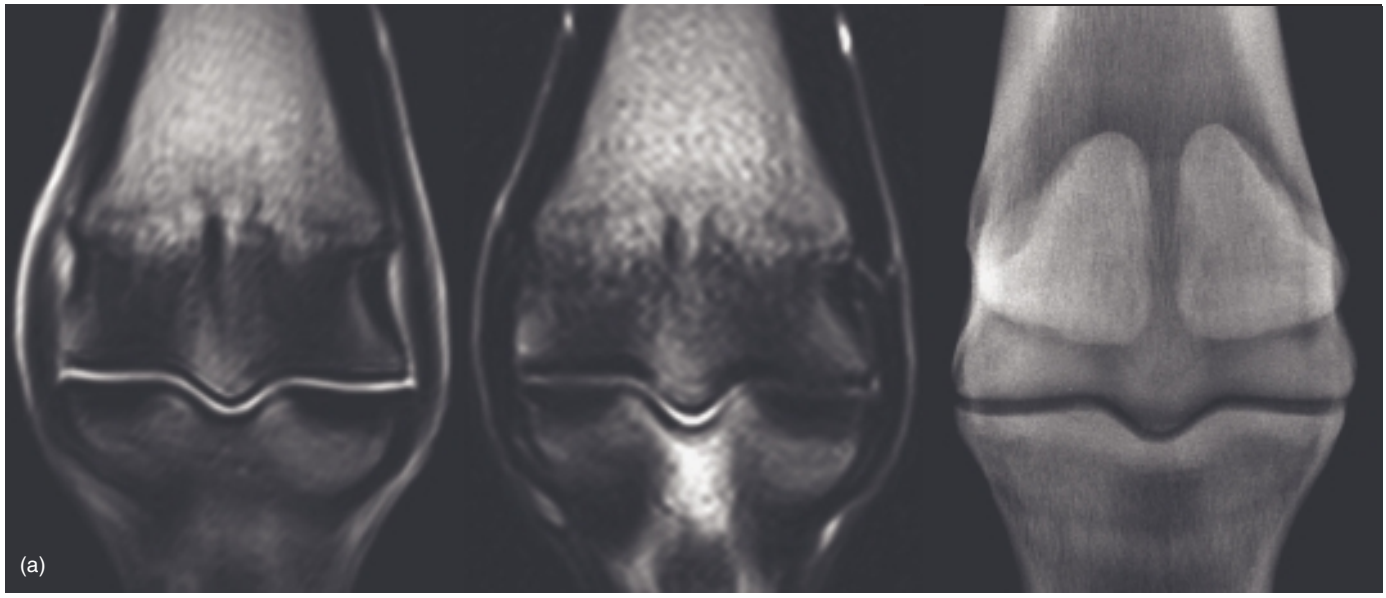

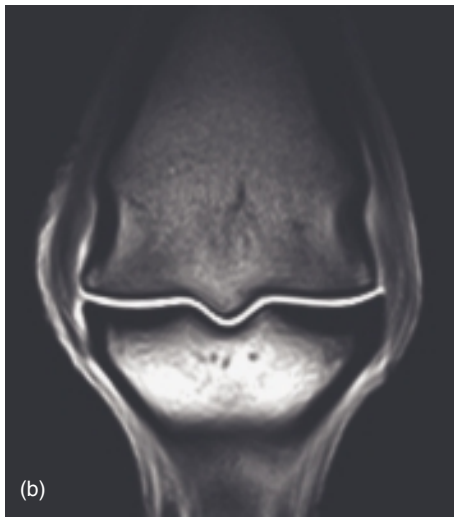

Figure 13.2 (a) T1 GRE (left) and T2 FSE (centre) frontal plane images and flexed dorsopalmar radiograph of the right fore fetlock joint of a 3-year-old flat racing Thoroughbred in full training with no history of fetlock pain. Medial is to the right. There is extensive, biaxially symmetric densification of the medial and lateral palmar metacarpal condyles and thickening of the SCB plate on the opposing surface of the proximal phalanx. (b) T1 GRE motion insensitive (MI) frontal image of a 6-year-old Thoroughbred that had never been in training and now used for low-level show jumping. There is no history of pain related to the fetlock joint. Note the minimal densification of the distal condyles of MC3 compared to those in Figure 13.1. There is mild thickening of the SCB plate of the proximal articular margins of the proximal phalanx.

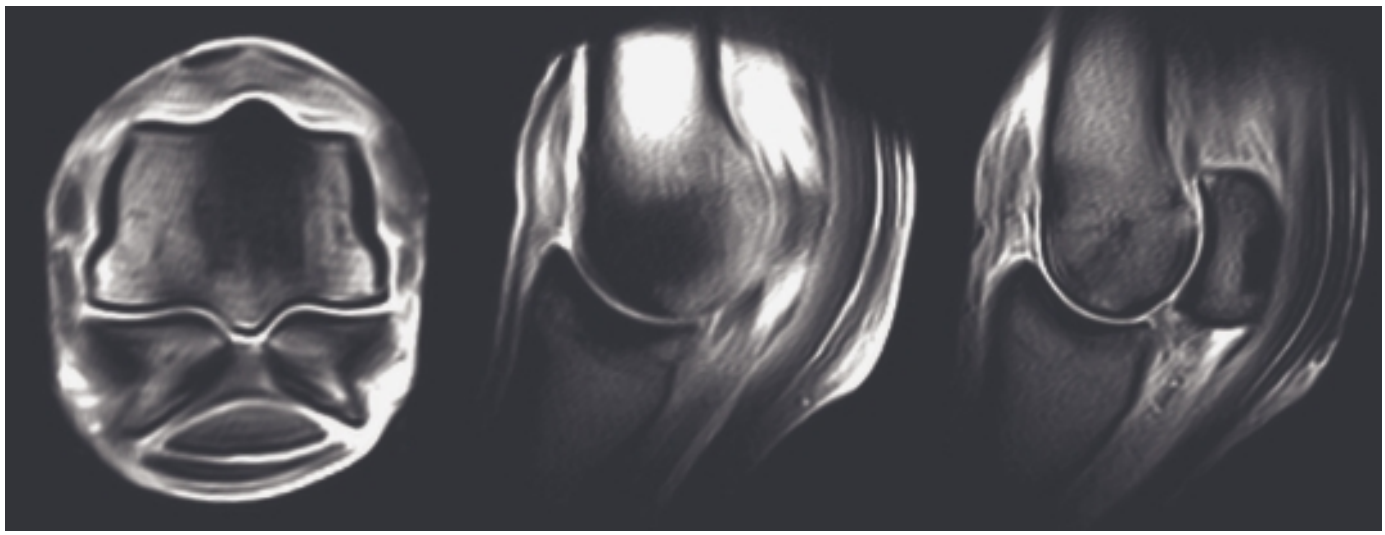

Figure 13.3 T1-weighted transverse, sagittal and parasagittal images of the left fore fetlock joint of a 3-year- old Thoroughbred in training with mild lameness related to the left fore fetlock joint. There is marked densification of the dorsal epiphyseal region of MC3. There is associated thickening of the SCB plate and modelling of the dorsal eminences of the dorsoproximal aspect of P1. The parasagittal image shows the palmar apical aspect of the metacarpal condyles and articular aspect of the PSBs are less affected in this case. This filly sustained a severely comminuted catastrophic fracture of the left fore proximal phalanx during a race 11 months later.

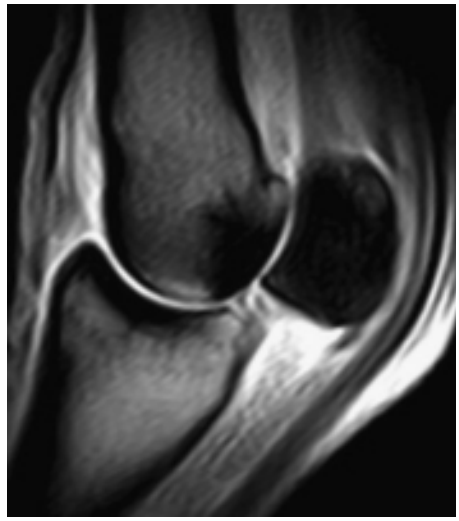

Figure 13.4 T1-weighted GRE MI parasagittal image of the left hind fetlock joint from a 3-year-old Thoroughbred in training with lameness arising from the left hind fetlock joint. There is marked densification of the lateral PSB in association with moderated densification of the plantar apical region and mild thickening of the dorsal epiphyseal region and proximal articular margin of the proximal phalanx. This colt also had a lateral suspensory ligament branch injury in this limb.

As with all types of pathology, it is important to use several sequence types to achieve a full and accurate evaluation of the MC3/MT3 condyles. Areas of bone sclerosis appear hypointense on all MR sequences. T1-weighted sequences are relatively easy to acquire in the higher joints of standing horses, yet they yield only part of the information regarding the type of pathology present in the bone and do not allow the differentiation of hypointensity due to bone densification and hypointensity due to the presence of fluid as these have similar intensities on T1 sequences (Figure 13.5a). Fat-suppressed or STIR sequences do not allow the identification of bone sclerosis as the signal from adipose tissue is suppressed, appearing hypointense and thus similar in intensity to areas of bone sclerosis. The most useful sequences are those in which adipose tissue appears hyperintense. In T2-weighted and PD sequences the relative loss of adipose tissue in densified trabecular bone renders this area hypointense relative to the surrounding bone. The phase cancellation artefact seen on T2*-weighted GRE sequences obtained using the dedicated equine standing MRI system [1] can provide an indication of increased fluid content within the trabecular bone (see Chapter 4) (Figure 13.5b) [13]. This finding can then be confirmed on fat-suppressed images (Figure 13.5c). However, in the absence of diagnostic quality STIR sequences, this artefact provides strong indication of fluid-based bone pathology. T2* hypointensity may also represent haemorrhage within the trabecular bone, though this has yet to be detected histologically in association with this combination of sequence intensities. The normal appearance of the distal metacarpal condyles on STIR and T2 FSE sequences is represented in Figure 13.5d.

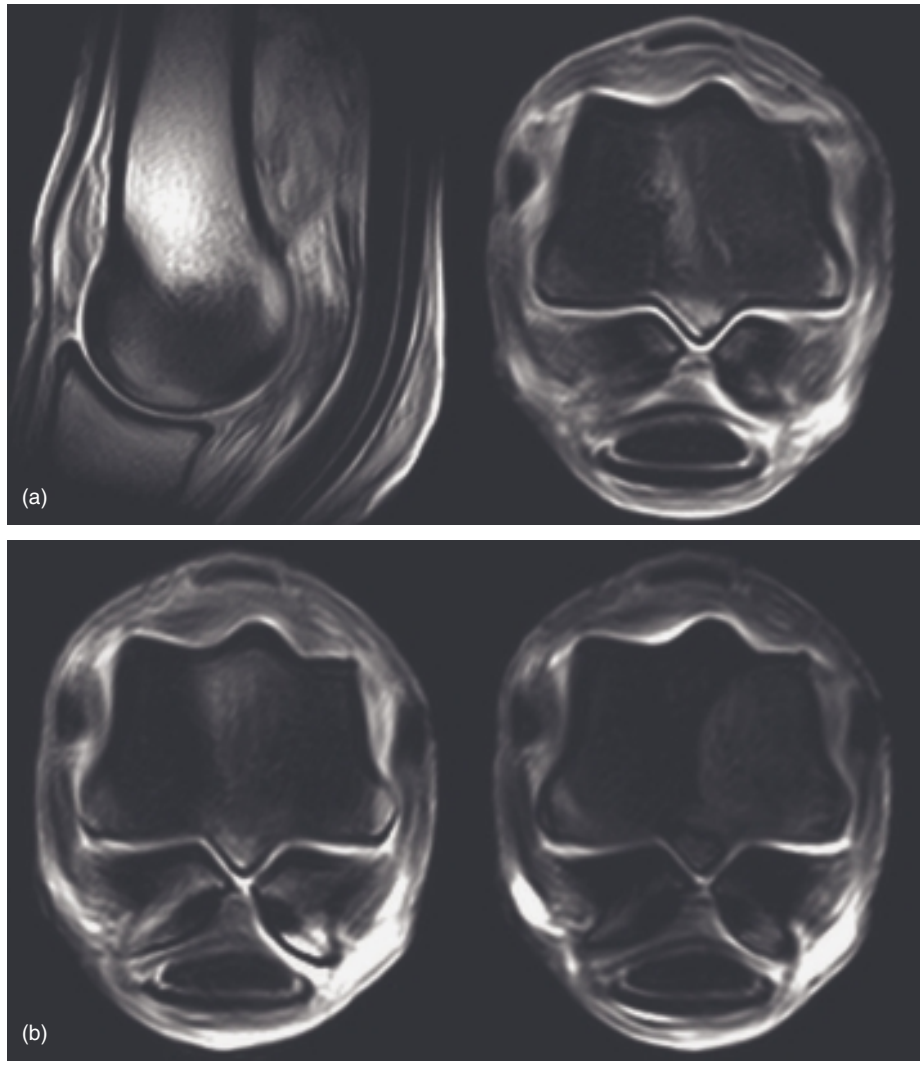

Figure 13.5 Images of the distal metatarsal condyle of the left hind limb of a 3-year-old TB colt with lameness attributable to both hind fetlock joints. The colt had had 26 starts. Lateral is to the right in the transverse image. (a) T1-weighted GRE sagittal (left) and transverse (right) plantar apical bone densification is present, extending to the dorsal epiphyseal region. The medial condyle appears of lower signal intensity compared to the right. On T1-weighted sequences alone this could represent differential densification of the medial and lateral condyles or that varying degrees of fluid are present in the lateral condyle compared to the medial. (b) Slice-matched T1-weighted GRE (left) and T2*-weighted GRE (right) transverse images, 5 mm distal to (a). The decrease in signal intensity in the distal condyles appears relatively uniform medial to lateral on the T1-weighted image. In the T2*-weighted image the condyles appear markedly different with increased signal intensity in the lateral condyle. This combination of T1 and T2* appearance is likely to represent that fluid is present in the lateral condyle. The hypointense medial condyle on both the T1 and T2* images may represent either bone sclerosis or the presence of fluid, which may appear hypointense if the amount of fluid is equal to the amount of fat in this region.

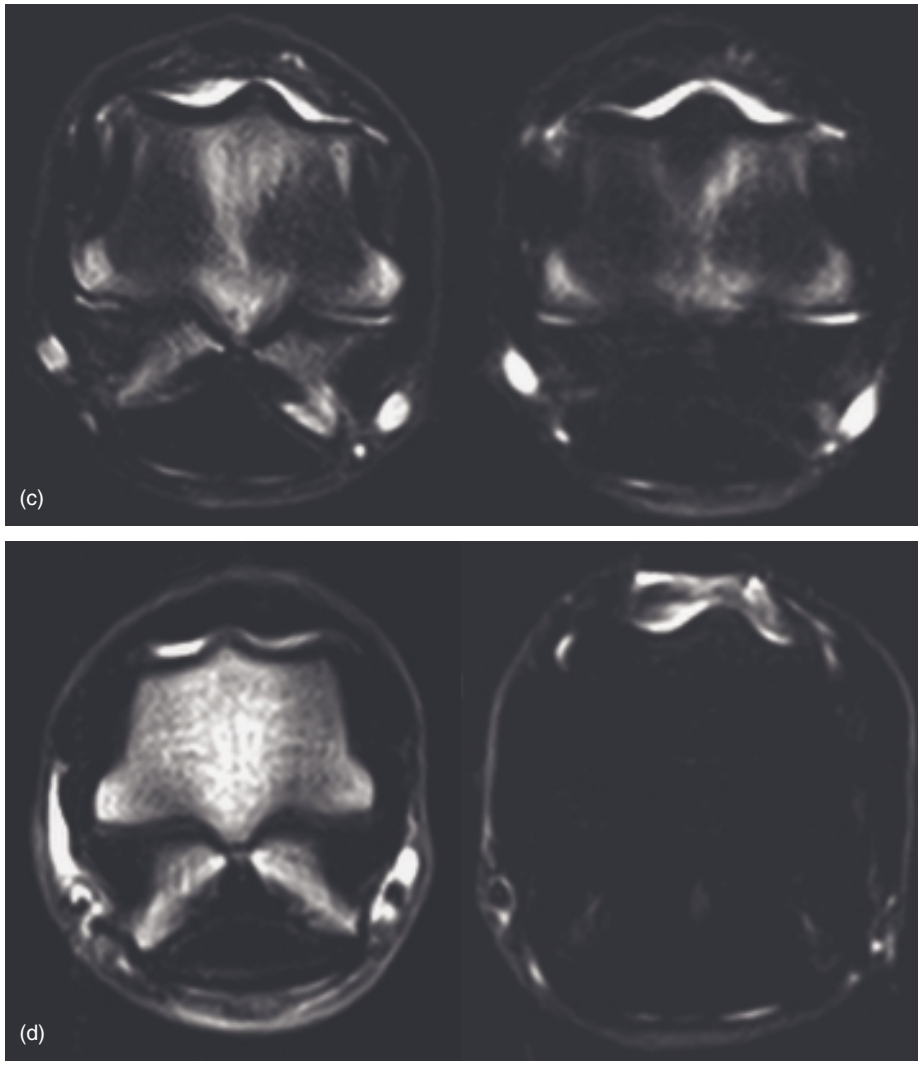

Figure 13.5 *Cont'd* (c) T2 FSE (left) and STIR FSE (right) slice-matched transverse images illustrating both fluid and bone densification are present. The T2 FSE confirms biaxial condylar densification is present but the slice matched STIR FSE image shows marked generalized increased signal intensity within the surrounding cancellous bone, particularly in the lateral parasagittal groove. The combination of intensities of the condylar regions on T2* and STIR images indicate the degree of fluid is equal to the degree of fat in the medial condyle while the degree of fluid exceeds the degree of fat in the lateral condyle. Note the relative appearances of the PSBs; they appear generally low signal intensity in the STIR image ruling out lack of fat suppression as a cause for the hyperintensity of the condyles. (d) T2 FSE (left) and STIR FSE (right) slice-matched reference images of the distal metatarsal condyles in a horse with no history of pain arising from the left hind fetlock joint. There is minimal SCB densification within the plantar apical region of the metatarsal condyles and no increase in signal in this region in the STIR FSE image.

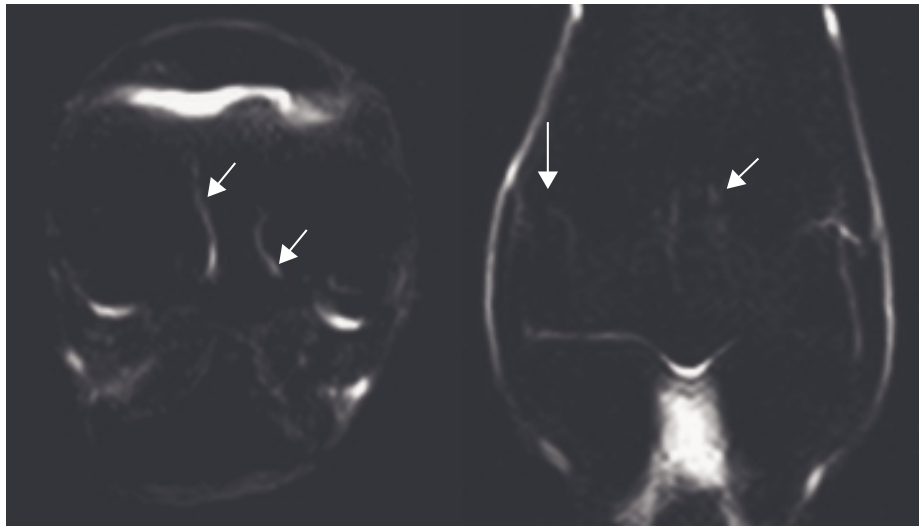

Figure 13.6 STIR FSE transverse (left) and frontal (right) images of the distal metacarpal region at the level of the distal metacarpal physis. The linear areas of signal hyperintensity running palmarodorsally in the transverse image represent nutrient vessels of the metacarpal condyles. These vessels are variably distinct and may be more numerous and larger diameter in horses with metacarpal disease. They should not be confused with fissure fractures of the palmar apical surface of the condyle. In the frontal image vessels can also be seen entering the distal metacarpal condyles via the collateral fossae.

Hyperintensity within the distal MC3/MT3 condyles

VASCULAR PATTERN

Normal areas of increased signal intensity may be seen in the region of the distal MC3/MT3 physis due to the presence of nutrient vessels and should not be misinterpreted as pathology. Vessels appear as well-defined hyperintense lines emanating from the palmaroproximal aspect of the sagittal grooves coursing dorsally and from the collateral fossae coursing axially. They are distinguishable by their position and relative appearance on a combination of sequences. The relative size and number of vascular channels may depend on the age of the horse and also the presence of any pathology. For example, horses with clinical signs of capsulitis / synovitis with joint distension and increased heat in the overlying subcutaneous tissues may show an increase in number and size of the vessels in this region (Figure 13.6). Very mild STIR hyperintensity may be seen in the distal MC3/MT3 physeal region in young horses in the absence of lameness likely due to the relatively increased vascularity of this region compared to the surrounding bone.

Subchondral bone injuries and the presence of bone marrow oedema-type signal patterns

Since the introduction of MRI in human sports medicine many reports have described occult bone injuries [14], otherwise known as 'bone bruises' [15]. The term 'bone bruise', defined as a transient increase in bone marrow water

content with hyperaemia, trabecular microdamage and increased bone mineral metabolism following trauma, was used to indicate the traumatic origin of the characteristic signal pattern of intraosseous T2-weighted fat suppressed and STIR hyperintensity with corresponding T1 hypointensity.

Bone marrow oedema (BMO) is a term used to describe the replacement of bone marrow fat by material containing H+ ions, in the form of water [16] and not restricted to traumatic aetiologies. The H+ may be contained within cells, but in some situations may be free – for example in intraosseous necrosis or haemorrhage. Increasingly, however, bone 'bruise' and BMO [17] have been used by clinicians as generic diagnostic terms for what is an imaging observation with a wide diagnostic differential, both traumatic and non-traumatic in origin. These include avascular necrosis [18], osteochondral defects [19], neoplasia [20], metabolic disease [21], infection [22] and arthritis [23]. Therefore, for want a better phrase, BMO is often used as shorthand to describe the appearance of bone on MR images, but it must be borne in mind that the appearance is not always related to the presence of oedema. Bone marrow lesions (BML) and bone marrow oedema-type (BMO-t) signal pattern have been suggested as more appropriate terms.

BMO or BMO-t signal patterns have been reported in horses undergoing MRI [24, 25] and the characteristic appearance has also been shown histologically to represent a number of pathologies in our equine patients [26].

SCB injury due to a single supraphysiologic loading event

In human imaging, distinct patterns of BMO have been shown to correlate with specific mechanisms of injury in the knee following acute traumatic events – the patterns of ligamentous disruption and BMO depending on the type and direction of force causing the injury [27, 28]. The dynamic motion of the equine fetlock joint during loading is almost entirely in the sagittal plane and the majority of BMO-t signal patterns related to repetitive load injuries are also seen at consistent and predetermined sites. There are cases, however, where the location of the injury appears erratic and likely to be due to abnormal location, direction and magnitude of a single loading event. In particular, BMO-t signal may be seen on the medial or lateral aspect of the distal MC3/MT3 condyles as the result of an impaction injury, in conjunction with a collateral ligament injury on the opposite side of the joint (a distraction-type injury). This mechanism is well documented in varus and valgus injuries of the distal femoral condyles and collateral ligaments of the human knee [28]. The ligament may suffer mild or complete tearing and the bone injury on the impaction side of the joint can range from focal to more generalized 'bruising'. Subcutaneous oedema is often present on the distraction aspect of the joint (Figure 13.7).

Focal SCB injury due to repetitive joint loading

SCB lesions in the distal metacarpal or metatarsal condyles are difficult to definitively diagnose radiographically and are traditionally diagnosed using

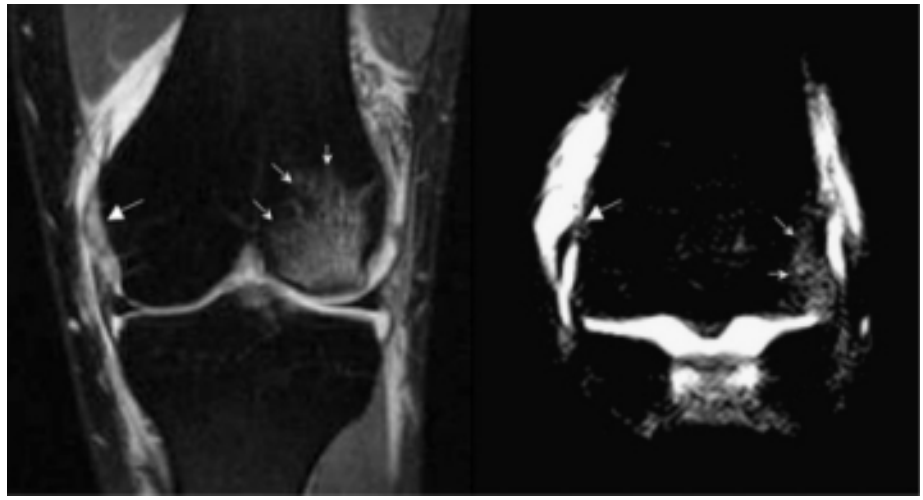

Figure 13.7 T2 fat-suppressed coronal image of a human knee joint (left). There is hyperintensity within the femoral attachment of the medial collateral ligament (large white arrow) due to a distraction injury causing partial avulsion of the ligament and hyperintensity within the lateral femoral condyle (small white arrows) due to an impaction injury on the opposite side of the joint. A similar pattern is seen in the STIR FSE frontal image (right) of the right fore fetlock joint of a Grand Prix show jumper with sudden onset severe lameness during a competition. Here there is hyperintensity within the proximal attachment of the lateral collateral ligament with associated subcutaneous oedema and hyperintensity within the medial aspect of the joint, which is thought to have occurred due to a varus injury.

scintigraphic assessment. However, the anatomic detail afforded by MRI allows greater differentiation of the structures involved to determine the precise localization of lesions and identify lesions before they are visible radiographically. Arthroscopic evaluation of the overlying articular cartilage is difficult in the majority of cases due to their anatomic location on the palmar or plantar aspect of the articular surface of the condyles. When it can be visualized at surgery or at postmortem, overlying articular cartilage may appear thin, discoloured or mildly fibrillated. The appearance of the articular surface on MR images may greatly underestimate the degree of SCB pathology, particularly using low-resolution images. Follow-up MRI can prove a useful tool in monitoring these lesions though this may depend largely on the severity of the initial injury, the presence or absence of damage to the overlying articular cartilage and the time interval between examinations (Figures 13.8a–c). A proportion retains a focal area that appears hyperintense on all sequences on the margin of the condylar surface with the joint space, even when imaged many months later. These may represent cases where SCB necrosis and/or full-thickness cartilage defects are present. Horses with these findings may return to training following a period of rest, though recurrent lameness is often seen, necessitating further periods of rest and/or intra-articular medication.

Distal metacarpal/metatarsal subchondral stress reaction

Stress reaction of the distal MC3/MT3 is commonly seen in the racing or endurance horse. These cases are often presented for lameness investigation

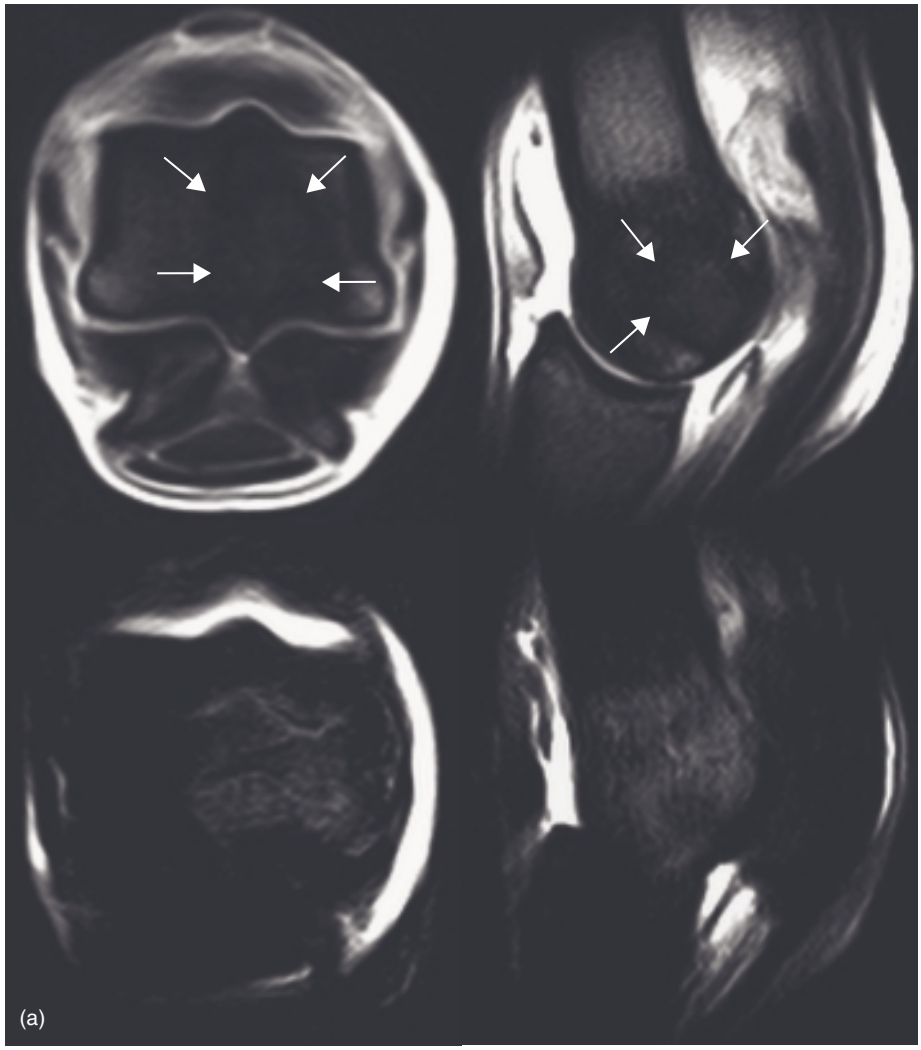

Figure 13.8 (a) T2* GRE transverse, T2* GRE sagittal images (top) and slice-matched STIR images (bottom) from the initial examination of the left fore limb of a 2-year-old Thoroughbred markedly lame after galloping. The left fore fetlock joint was moderately distended and an 80% improvement of the lameness was seen following intra-articular analgesia of the fetlock joint. Anaesthesia of the lateral branches of the palmar and palmar metacarpal nerves just proximal to the fetlock joint rendered the horse sound. Radiographic examination revealed moderate, bilateral densification of the MC3 condyles. Ultrasonographic assessment of the joint was largely unremarkable. The area of T2* hyperintensity in the lateral condyle surrounded by a hypointense rim is formed due to the phase cancellation artefact. There is corresponding STIR hyperintensity more generally within the lateral metacarpal condyle. Note the swelling of the soft tissues on the lateral aspect of the metacarpophalangeal joint and the distension of the dorsal recess of the joint.

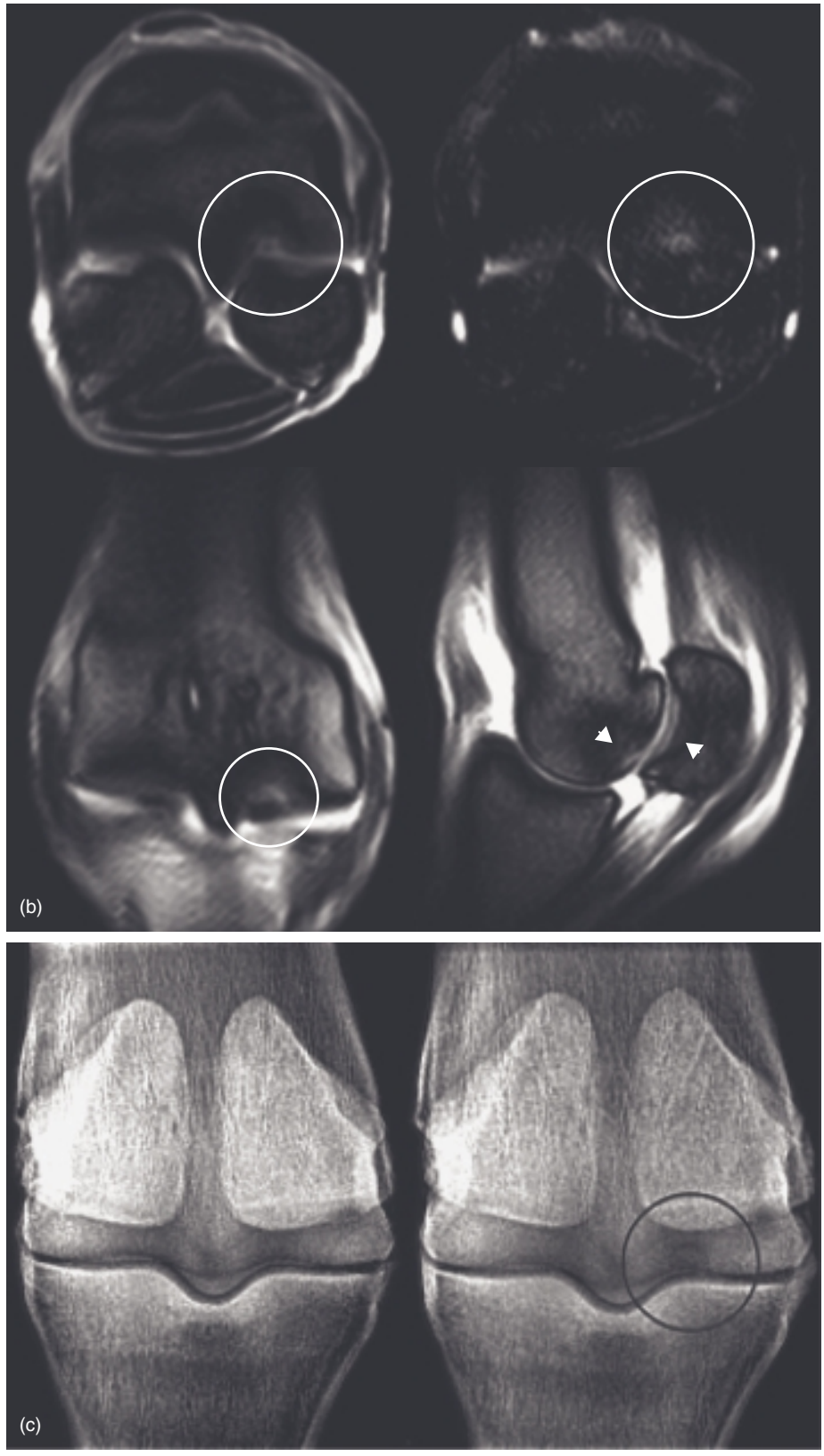

Figure 13.8 *Cont'd* (b) Follow-up images taken following 8 weeks of box rest. The filly was now sound at the trot. The previous hyperintensity in the lateral condyle has resolved considerably to leave a focal area of altered signal intensity on T2* GRE (transverse top left, frontal bottom left, sagittal bottom right) and increased signal in the lateral parasagittal groove on STIR FSE images (top right) (circles, arrows). There is a corresponding increase in signal on the articular border of the lateral proximal sesamoid bone, although these areas do not appose each other in the standing horse. The soft tissue swelling has resolved although the joint remained persistently mildly distended. Note the large vascular channel present in the distal metacarpal physeal region of this chronically distended joint. (c) Flexed dorsopalmar radiographs of the left fore fetlock. The image on the left was taken at the time of the initial examination. To the right is the radiograph taken 8 weeks later. This projection is often difficult to interpret and perceived pathology can be angle dependent and complicated by the relatively lucent areas of the sagittal grooves surrounded by the more radiodense condyles. In the follow-up radiograph there appears to be a well-defined, crescent-shaped radiolucent area in the lateral sagittal groove (circle). A SCB lesion in the lateral sagittal groove is suspected. This is supported by the follow-up MR images in Figure 13.11b.

Figure 13.9 STIR FSE sagittal images of the left metatarsophalangeal joint of a 2-year-old Thoroughbred racehorse. The trainer reported deterioration in hind limb action shortly after the horse commenced fast canter work. Radiographs were unremarkable. The image on the left was taken from the initial examination, which revealed relatively mild subchondral bone sclerosis but marked, generalized STIR hyperintensity over the whole distal metatarsal condyle was present. This had resolved 8 weeks later (right). Similar signal changes were seen in the contralateral limb. As no SCB fissuring or focal STIR hyperintensity was visible emanating from the region of the sagittal groove, this filly was treated with a course of non-steroidal anti-inflammatories and continued in ridden walking and trotting exercise during the recuperation period. The metatarsophalangeal joint has required subsequent intra-articular medications but the filly was subsequently campaigned successfully during her 2- and 3-year-old career.

due to perceived poor performance by the rider, in particular lack of hind limb impulsion. An obvious lameness may not be visible when trotted in hand, though horses with bilateral MT3 subchondral stress reactions almost invariably exhibit a short striding 'plaiting' hind limb action. In the early stages, subchondral stress reactions are almost impossible to identify radiographically and diagnosis is usually made on bone phase scintigraphic images where marked increased radionuclide uptake can be seen in the affected condyle. MRI has advantages over scintigraphy as it allows assessment of articular cartilage integrity and the degree of condylar sclerosis, which may have management and prognostic implications. STIR and T2* hyperintensity indicates fluid in the extracellular spaces, which in severe cases may include the entire distal condyle but is usually bounded proximally by the distal MT3 physis (Figure 13.9). Spin-echo sequences are necessary to reveal the degree of concurrent condylar sclerosis.

End-stage SCB injury

End-stage SCB injury represents a progression from the cumulative microdamage of non-adaptive stress injury to necrosis and collapse of the SCB. In many cases the overlying articular cartilage is compromised,

although this can range from thinning and discolouration to full-thickness cartilage erosions, which are consistently located on the plantar/palmar aspect of the distal MC3/MT3 condyles. The lateral condyle is more commonly affected in the hind limb, while the medial and lateral condyles are more equally represented in the forelimb. Biaxial and bilateral lesions are not uncommon, particularly in the hind limb. Lesions are often visible as crescent shaped lucencies on dorsolateral proximal-plantaromedial distal, dorsomedial proximal-plantarolateral oblique and flexed plantaro/palmarodorsal radiographic projections [29, 30] and have marked focal increase in radionuclide uptake on scintigraphic images. The lesions have a characteristic appearance on MR images with focal hyperintensity on all sequences within the subchondral bone of the palmar/plantar apical region surrounded by a combination of trabecular bone sclerosis (T1/T2 FSE and STIR hypointensity) and the presence of trabecular fluid (STIR hyperintensity (Figure 13.10a–d). The gross appearance in the most severe cases is of focal full-thickness erosions of the articular cartilage overlying necrotic SCB. Horses with bilateral changes are often reported to have appeared 'sound' prior to the examination, the trainer reporting a recent history of progressive 'loss of action' rather than overt lameness.

Detection of pre-fracture pathology in the fetlock joint

Perhaps the 'Holy Grail' of Thoroughbred fetlock MRI is the ability to predict which horses are at risk of developing complete fractures. This is problematic in that most horses sustaining condylar fractures have pre-existing SCB damage within the distal MC3/MT3 condyles [31] but may not have a history of overt fetlock lameness and therefore may not have warranted investigation prior to sustaining the injury. However, with the introduction of MRI systems that allow horses to be imaged standing, increasing numbers of racehorses are being imaged while in full training, which would once have been unfeasible due to the potential risks of general anaesthesia. Data are now being compiled on the MRI appearance of the distal MC3/MT3 condyles in many clinical contexts, including horses with no history of lameness related to the fetlock joint, those with low-grade lameness with equivocal radiographic findings and horses with sudden onset lameness after fast work. It is vital that an in-depth knowledge of the case including a full history of the lameness, clinical appearance of the joint, the results of any diagnostic local analgesia and radiographic findings are available from the attending veterinary surgeon. Under these circumstances it is possible in certain cases to identify animals at an increased risk of sustaining complete condylar fractures should the horse remain in full training.

Condylar fissure fractures

Fissuring of the articular cartilage and underlying SCB within the sagittal grooves of the distal metacarpal condyles represents non-adaptive remodelling and results from the coalescence of microfractures and subsequent failure of the SCB. These lesions can be difficult to fully evaluate using

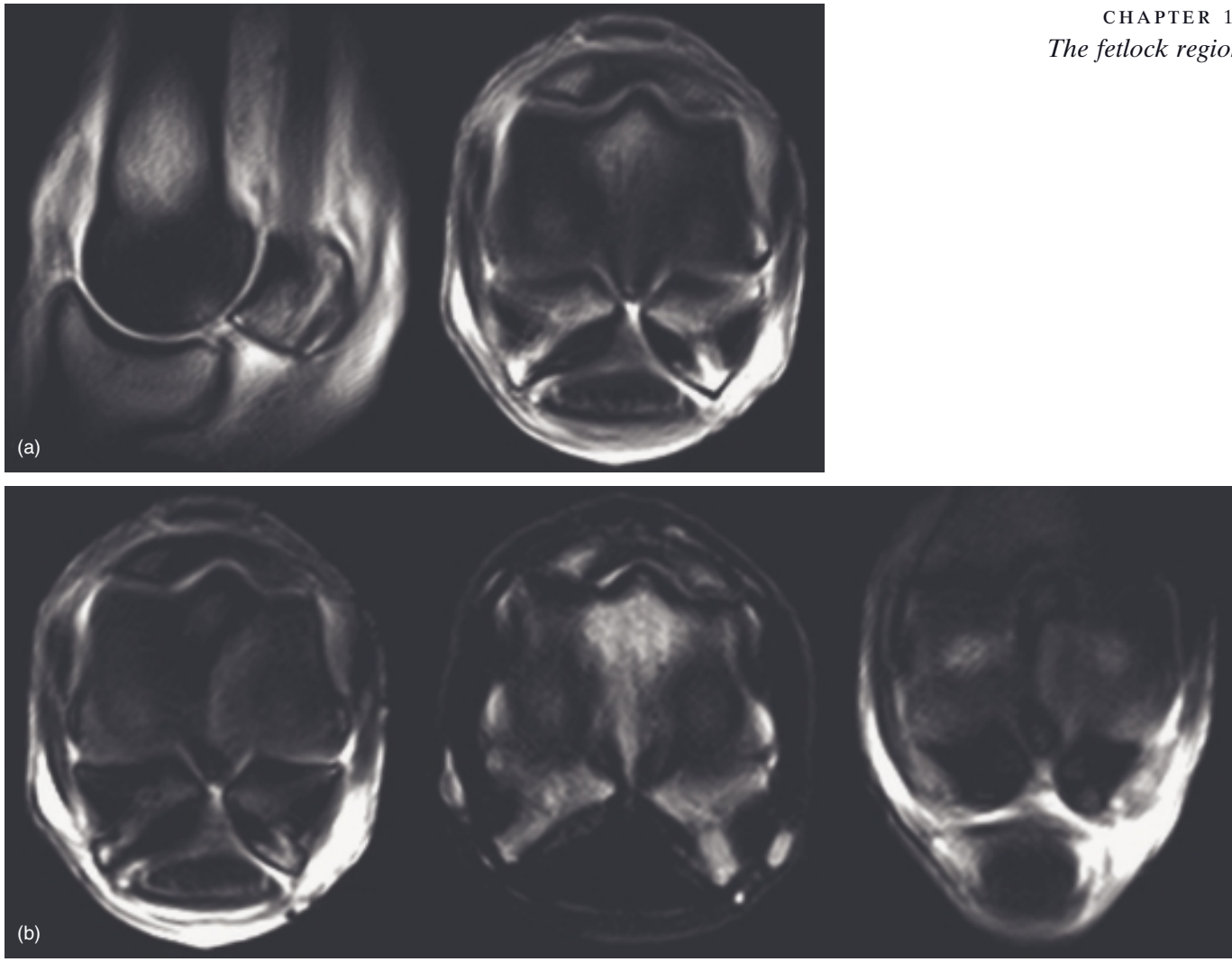

Figure 13.10 Images of the right hind fetlock of a 4-year-old flat racing Thoroughbred gelding with right hind lameness, significantly improved following intra-articular analgesia of the right hind fetlock joint. The horse had 34 starts over a 2-year period. There was moderate distension of both hind fetlock joints detectable on clinical examination. Distal limb flexion exacerbated the lameness. Radiographs had marked sclerosis of the distal metatarsal condyles with a radiolucent area on the plantar apical region of the lateral condyle. There was focal increased radiopharmaceutical uptake present biaxially and bilaterally in the plantar aspect of the distal condyles of MT3. (a) T1-weighted parasagittal (left) and transverse (right) MR images of the right hind. The parasagittal image shows focal increase in signal associated with the articular margin of the plantar apical region of the lateral condyle surrounded by low signal intensity, which is extensive throughout the distal metatarsal condyles. The transverse image shows the change is biaxial. Densification of the dorsoproximal articular margin of the proximal phalanx can also be seen in this transverse image. The proximal sesamoid bones have relatively mild densification. (b) T2* GRE (left), T2 FSE (centre) transverse and T2* GRE frontal oblique images of the left hind (lateral is to the right). The T2 FSE illustrates there is a hypointense sclerotic margin around the defects, which appear hyperintense on all sequences. The T2*-weighted image shows the cancellous bone of the lateral condyle is hyperintense compared with the medial condyle extending from the lateral sagittal groove to include the sagittal ridge. The transverse oblique view is useful for fully evaluating the sagittal ridge in this region, which again appears hyperintense. (c) STIR FSE frontal (left) and STIR FSE transverse (right) images. There is dramatic increase in signal within the cancellous bone particularly of the lateral condyle in addition to the focal increase in signal at the site of the SCB defects. (d) Postmortem appearance of the distal metatarsal condyles of the right hind limb of a Thoroughbred racehorse in training with end-stage subchondral bone disease similar to that in (a)–(c). Photograph courtesy of Rob Pilsworth.

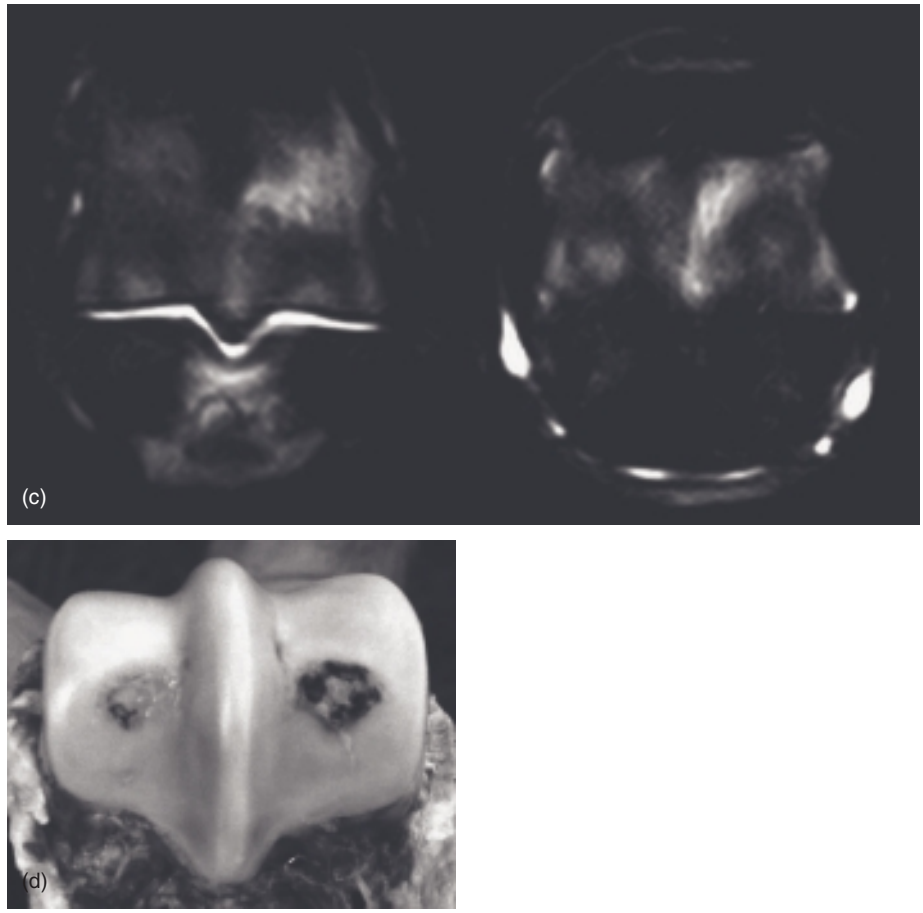

Figure 13.10 *Cont'd*

established imaging techniques. Repeated radiographic views are often necessary and the appearance of potential lesions may be angle dependent and not repeatable on subsequent views. Scintigraphic evaluation of the region is highly sensitive but relatively non-specific. MRI can assist in further quantifying an inconclusive radiographic study (Figures 13.11a–d). When fissuring of the articular cartilage and underlying subchondral bone is present, often in the sagittal groove, the MRI appearance is of linear marked hyperintensity on all sequences commonly surrounded by hypointense, sclerotic trabecular bone of the distal MC3/MT3 condyle.

Though clearly an abnormal and highly concerning finding, some horses train successfully despite the presence of radiographically evident condylar fissures and this finding in isolation on MR images does not necessarily preclude the horse from continuing in training, particularly if not associated with lameness. However, the linear marked hyperintensity of the fissure may be surrounded by generalized STIR hyperintensity extending proximally into the cancellous bone of the condyle. This diffuse STIR hyperintensity is currently thought to be associated with more 'active' changes within the condyle and initial work suggests these cases are at high risk of the incomplete fissure propagating to complete condylar fracture should the horse continue in full training. A number of Thoroughbreds in full race training

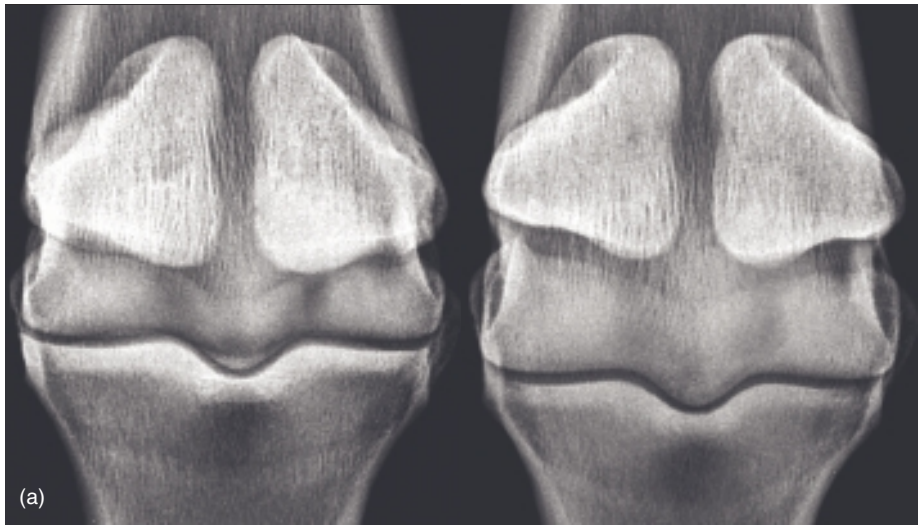

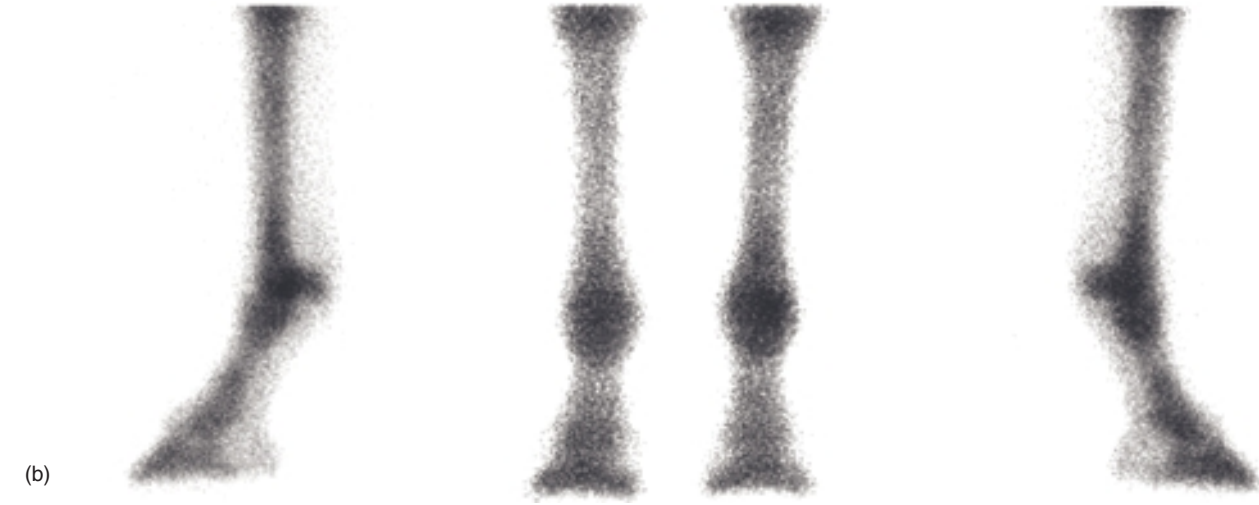

Figure 13.11 Images of a 6-year-old chaser with left fore lameness after schooling over fences and abolished by intra-articular analgesia of the left fore fetlock joint. Radiographic examination indicated some sclerosis of the distal metacarpal condyles and proximal sesamoid bones with a linear radiolucent area within the lateral sagittal groove, surrounded by more radiodense cancellous bone. There was moderate, focal increased radiopharmaceutical uptake in the lateral condyle of the left fore fetlock joint. (a) The initial flexed dorsopalmar view (left) appears to show a linear radiolucent area within the lateral sagittal groove (arrow). When this projection is repeated with the limb in a greater degree of flexion (right), the radiolucent area appears more diffuse and is surrounded by more radiodense cancellous bone. (b) Scintigraphic images of the front fetlocks of the horse in Figures 13.12a–f, taken 3 hours after intravenous injection with technetium^{99}-MDP. There is moderate, focal increased radionuclide uptake in the lateral condyle of the left fore fetlock joint. This is not a dramatic example and many horses with this degree of uptake may not be prevented from continuing in training. Scintigraphic evaluation of these cases is extremely sensitive but does not permit the specificity afforded by an MRI examination of the region. Compare these images with those in Figure 13.12b, which represents a different disease entity with different management and therapeutic options. (c) T1 GRE (top left) and STIR FSE (top right) frontal images and T1 GRE (bottom left) and STIR FSE (bottom right) transverse images of the left fore fetlock joint. Lateral is to the right. The T1-weighted images show hypointensity within both distal metacarpal condyles, more marked on the lateral aspect of the joint (black arrows). A linear hyperintensity is present in the lateral sagittal groove of MC3 (white arrow heads). Diffuse hyperintensity within the lateral distal metacarpal condyle is visible on STIR images (white arrows). The lateral proximal sesamoid bone is also hyperintense when compared to the medial proximal sesamoid bone. The linear area of increased signal intensity represents a fissure fracture within the lateral sagittal groove, which may have been present for some time and, when seen in isolation, does not necessarily preclude the horse from continuing in training. The more generalized increase in signal intensity within the lateral metacarpal condyle surrounding the fissure is concerning when seen in combination with a fissure and it is recommended that horses showing this pattern do not continue in full work. (d) The horse was euthanased 7 days after the MRI examination for an unrelated problem. Postmortem examination revealed a full thickness fissure was present in the articular cartilage within the lateral sagittal groove of the distal metacarpal condyle. Photograph courtesy of Marcus Head.

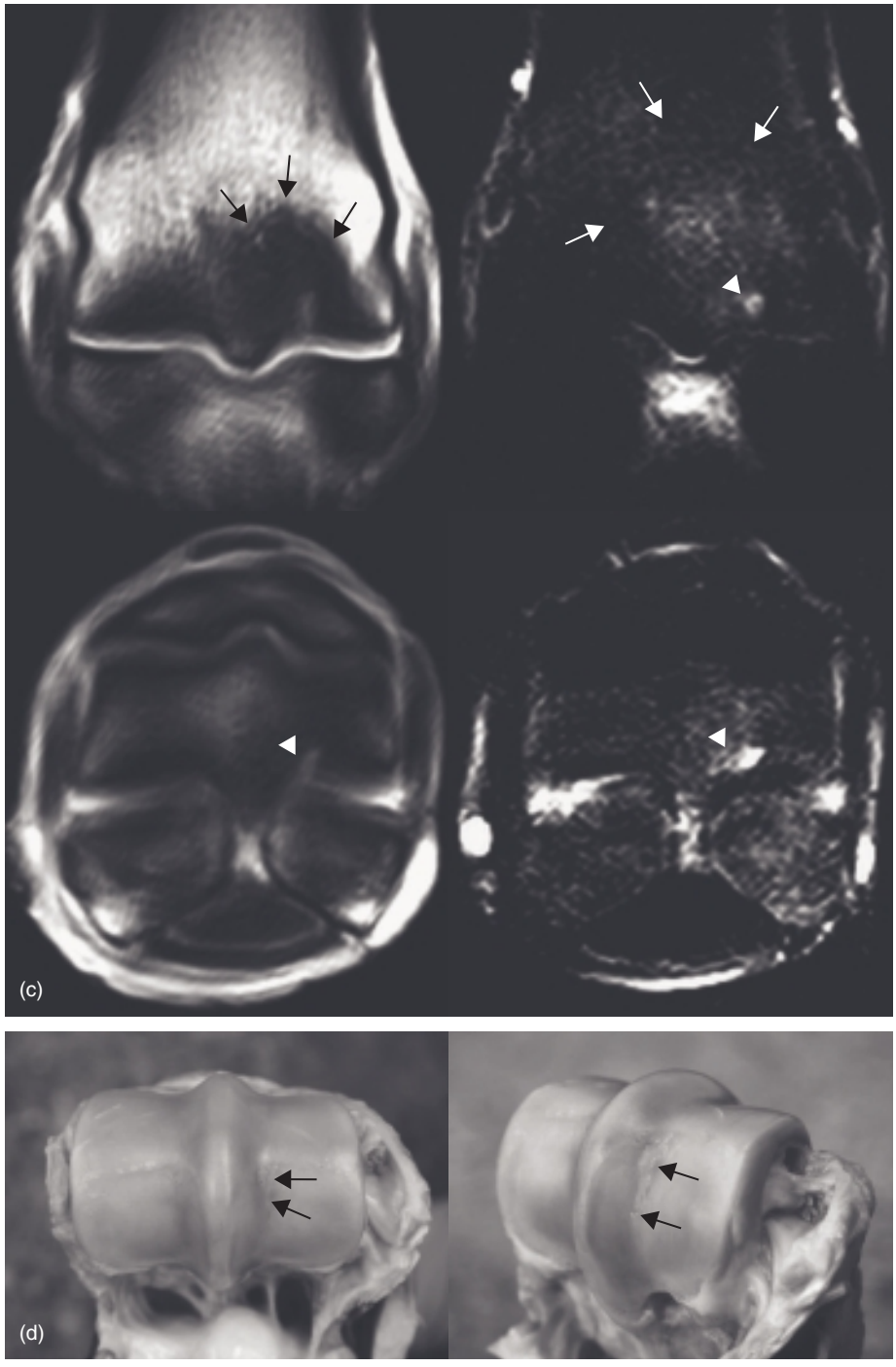

Figure 13.11 *Cont'd*

with radiographically apparent condylar fissures, but without lameness related to the fetlock joint, have undergone MR examination at our centre and have not shown diffuse STIR hyperintensity out-with the linear hyperintensity of the fissure (Figure 13.12).

When imaging the fetlock with this type of injury in mind lesion-orientated slice positioning is essential. It is useful to start with a frontal image parallel to the long axis of the third metacarpal bone prior to targeted oblique transverse and oblique frontal sequences, which should be piloted from an orthogonal sequence rather than the pilot study to maximize the likelihood of small lesions being visible (Figure 13.13). However, decisions regarding the management of these cases should never rely on the interpretation of MR images alone and must be done in conjunction with a firm knowledge of the case, including the radiographic/scintigraphic findings, and only following extensive discussion with the attending veterinary surgeon.

'Pre-fracture' pathology of the distal metacarpal condyles in the absence of condylar fissuring

Dramatic STIR hyperintensity on MR images may be seen in horses with fetlock lameness first noticed after fast work and in the absence of overt, radiographically evident fracture pathology (Figure 13.14). These patterns closely resemble the MR appearance of horses imaged shortly after sustaining complete condylar fractures (Figure 13.15), with marked hyperintensity on STIR images uniaxially in the affected condyle with a well-defined margin. These cases represent excellent candidates for MRI as, with unremarkable

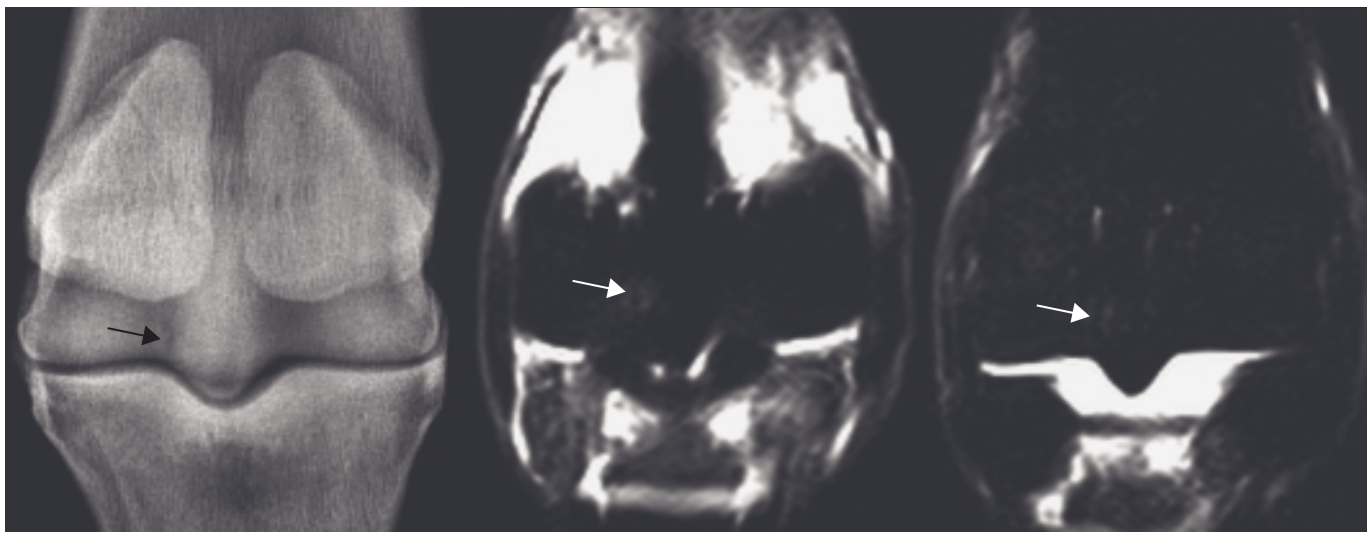

Figure 13.12 Flexed DP radiograph of a 3-year-old-filly in full race training (left). A linear radiolucency representing a condylar fissure fracture is present in the lateral sagittal groove (black arrow). STIR FSE frontal images (centre and right) show very focal hyperintensity corresponding with the fissure. The surrounding trabecular bone is hypointense. This fissure had been detectable radiographically for several months, during which the filly trained and raced successfully. No lameness related to the joint was present at the time of the MRI examination.

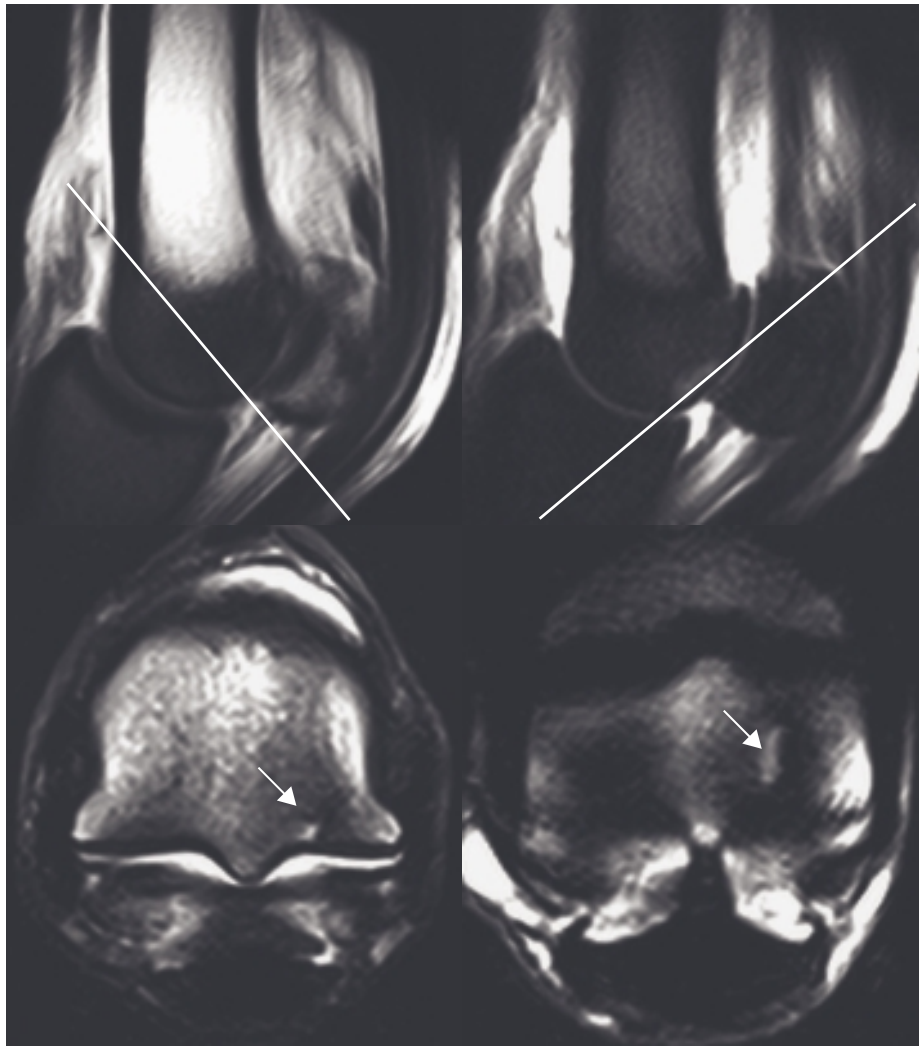

Figure 13.13 T2 FSE oblique frontal (bottom left) and oblique transverse images (slice positioning is indicated in the corresponding sagittal images). The lesion-oriented sequences are essential to assess the full extent of the pathology and to aid detection of more subtle lesions.

radiographs and a good response to intra-articular medication, horses may be allowed to continue in full training leading to catastrophic fracture. Cases with this MR appearance may not have shown fetlock lameness in the past and the joint may be unremarkable when examined clinically. When this appearance is seen the animal should be box rested for 4–8 weeks prior to repeating the radiographs and/or MR examination and further management dictated by the appearance of the condyle at that time.

Monitoring of stress injuries with MRI

MRI is the modality of choice in human stress fracture imaging for both the detection of stress injuries and to monitor healing. The increased radionuclide uptake on bone phase scintigraphy images persists long after healing of the stress fracture has occurred and is known to lag behind the resolution of abnormal signal on MR images. A classification has been proposed using

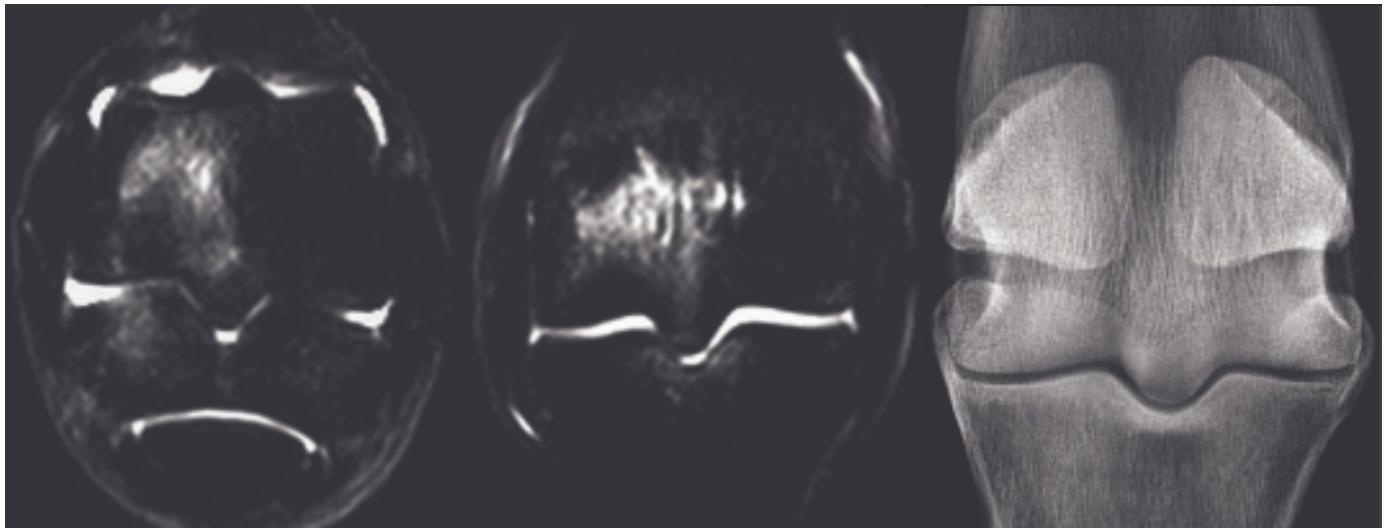

Figure 13.14 STIR FSE transverse (left) and frontal (centre) MR images and flexed DP radiograph (right) of a 3-year-old-colt showing marked right fore lameness after galloping. There was no recent history of fetlock joint lameness. The joint was medicated and the colt presented for MR examination 3 days later. The lameness had improved significantly when presented for MRI. Dramatic STIR hyperintensity is present in the lateral metacarpal condyle. There is also hyperintensity within the lateral PSB and the articular groove of the proximal phalanx. The flexed DP radiograph was taken at the time of the MR examination and was largely remarkable. No fissuring of the articular surface was evident on either MR or radiographic images. There is relatively mild sclerosis of the trabecular bone in the palmar apical region of the lateral condyle. In the absence of the additional information afforded by the MRI examination and the improvement in the lameness following joint medication this joint may have returned to canter work with insufficient time for the bone injury to heal.

bone scan and MRI data to predict time to healing of stress fracture in human athletes [32]. Early work in racehorses suggests correlations with humans may exist with the appearance of stress injuries during healing, though time to resolution of interosseous hyperintensity and the correlation of this with degree of lameness remain unknown at present.

In certain instances, incomplete condylar stress fractures may be treated conservatively rather than undergoing surgical fixation. This can be successful with horses returning to race successfully. However, some horses may show recurrent lameness and radiographs may indicate non-healing of the fracture at the joint margin. MRI examination of horse with non-healing fractures can aid surgical planning, as it is possible to assess the most proximal extent of the non-union and the junction with healed bone (Figure 13.16).

Injuries to the proximal phalanx

Osteochondral fragmentation of the dorsoproximal aspect of the proximal phalanx

Osteochondral lesions of the dorsal articular margin of the proximal phalanx are a frequent occurrence and may be diagnosed radiographically. They may be detected as an 'incidental' finding, seen when evaluating the joint for other reasons. In certain cases, a horse may exhibit fetlock-related lameness (typically a forelimb) with mild distension of the joint and pain when digital pressure is applied to the dorsoproximal aspect of the proximal phalanx,

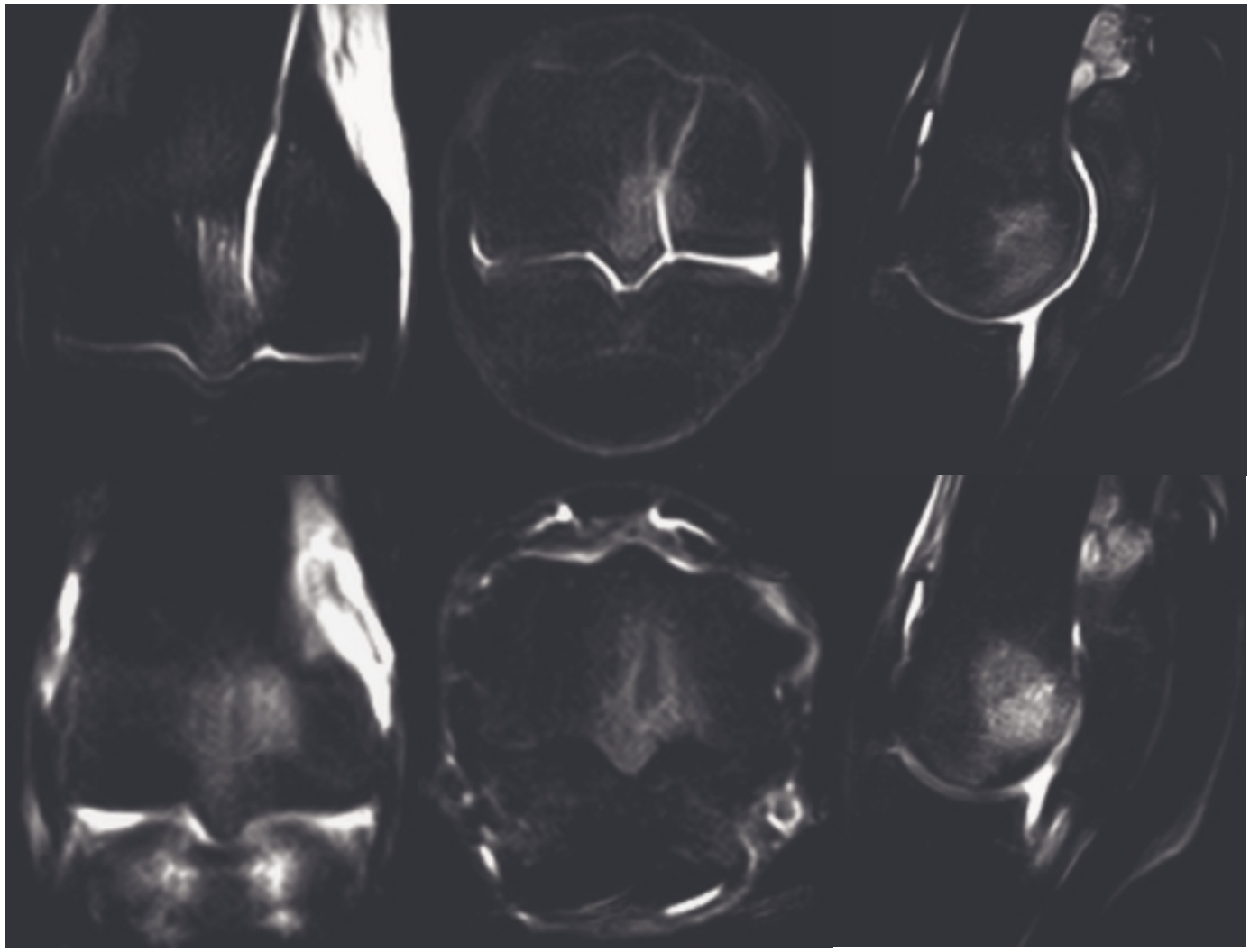

Figure 13.15 Top: STIR FSE frontal (left) transverse (centre) and sagittal (right) images of a 3-year-old Thoroughbred which sustained a complete, displaced lateral condylar fracture of the left fore fetlock joint while galloping 2 hours previously. The fracture line can be seen extending from the lateral sagittal groove travelling in a dorsoproximal direction where it becomes comminuted. The extremely hyperintense fracture line is surrounded by a relatively less intense increase in signal in the subchondral bone. Bottom: A similar pattern and intensity of signal is seen in these images from a 3-year-old colt showing left fore lameness after galloping, which was significantly improved by intra-articular analgesia of the left fore fetlock joint and abolished after a low 4-point nerve block. The signal intensity within the palmar aspect of the lateral sagittal groove corresponds well with those of the complete fracture.

and with forced flexion of the joint but without conclusive radiographic findings. MRI may be used to assist the differentiation of horses developing osteochondral fragmentation from those developing short, incomplete sagittal dorsoproximal fractures of the proximal phalanx, which have a similar clinical presentation (Figure 13.17a and b).

Visualizing dorsal and palmar/plantar articular margin fragments on standing MRI examinations can be difficult and small fragments may be missed entirely depending on the selected sequences, surrounding soft tissues, slice thickness and slice position. In standing horses, slice positions

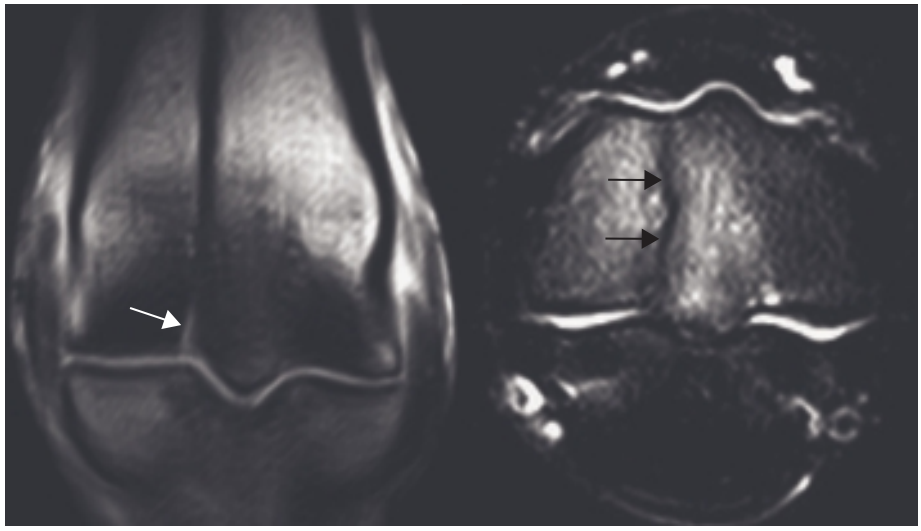

Figure 13.16 T1 frontal (left) and STIR transverse (right) MR images of the left hind fetlock joint a 6-year-old flat race horse which sustained an incomplete medial condylar fracture the previous season. The fracture was treated conservatively but lameness returned at the start of canter work the following year. A standing MRI examination was carried out to assess the extent of the non-union and assist in surgical planning. There is a linear T1 hyperintensity in the medial sagittal groove in the non-healed articular aspect of the previous fracture line surrounded by hypointense trabecular bone densification. The more proximal fracture line has healed appropriately, seen as T1 hypointensity (black arrows). The fracture line shows the same signal pattern on STIR images though generalized bone marrow oedema-type signal is seen in the medial two-thirds of the bone, which extended just proximal to the distal metatarsal physis. It was elected that a single lag screw was sufficient to stabilize the fracture line, which was placed under standing sedation. The horse returned to racing 4 months after surgery and had 16 starts in the following two seasons.

in frontal and transverse planes should be piloted using a T1 sagittal sequence (useful as it renders the joint capsule and synovium as hyperintense relative to the cortical bone) rather than the original pilot scan, which is unlikely to transect the area of interest.

Short, incomplete sagittal fractures of the dorsoproximal aspect of the proximal phalanx

Proximal phalanx fractures are the most common cause of catastrophic distal limb fracture during turf flat racing in the UK and are traditionally considered to arise from the intermittent nature of maximal loading and high absolute load values during galloping leading to a single supraphysiological loading event [3, 4, 33]. Though this is the likely aetiopathogenesis in the majority of cases, some reports have suggested that a number of proximal phalanx fractures may be stress related and secondary to non-adaptive bone modelling resulting from repetitive overload of the joint [34, 35]. A number of MRI examinations of racehorses with fetlock joint lameness at our centre have revealed BMO-t signal patterns thought to represent pro-dromal stress fractures of the proximal phalanx in the absence of a fracture line at the joint surface – supporting this pathway to injury in

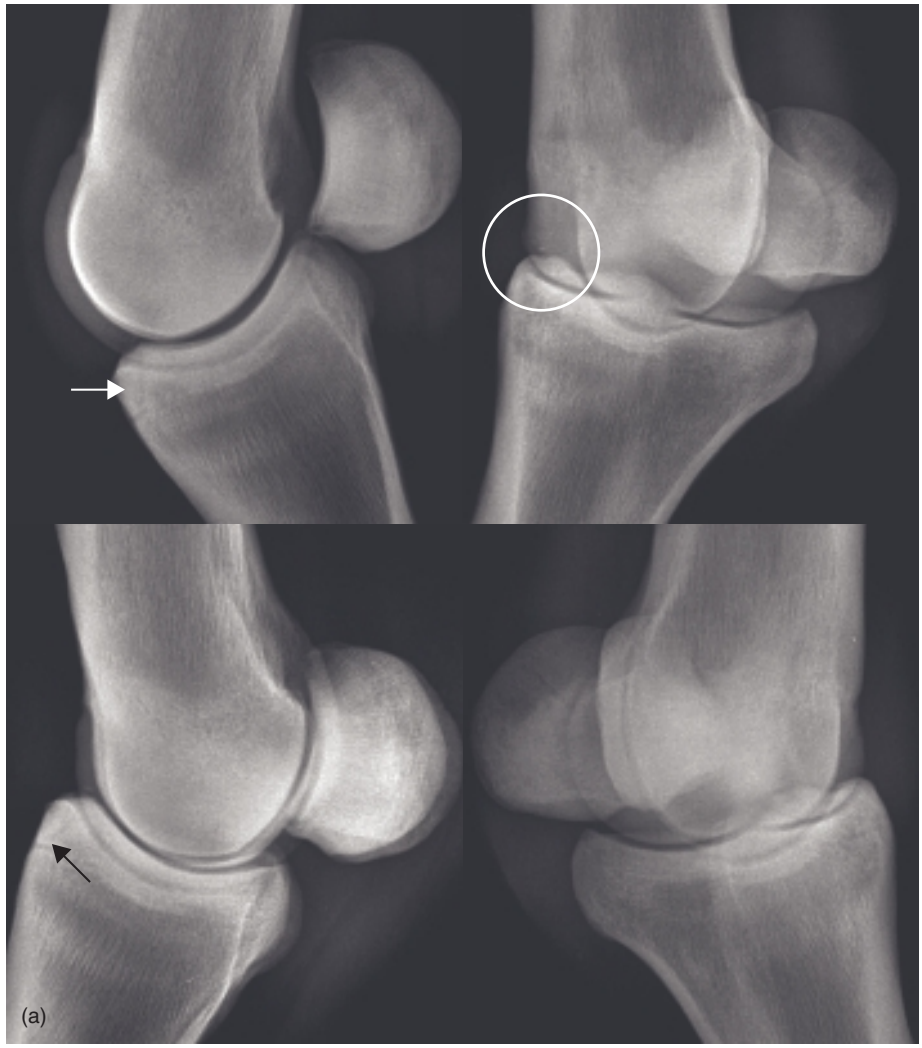

Figure 13.17 (a) Selected radiographs T1 GRE, T2 FSE and STIR GRE parasagittal images of the left fore fetlock joint of a 3-year-old Thoroughbred filly with left forelimb lameness after galloping and a recent history of mild distension of the joint. There was pain on palpation of the dorsoproximal aspect of the proximal phalanx when examined the same day as the onset of lameness. Flexion of the left fore fetlock joint exacerbated the lameness. On the day the initial radiographs were taken the filly had been box rested for 4 days and appeared sound. There was now no resentment of forced flexion of the joint and no pain could be elicited when firm digital pressure was applied to the dorsoproximal aspect of the proximal phalanx. Radiographic examination revealed a small osteochondral fragment which can be seen on the dorsomedial eminence of the proximal phalanx (circled). A radiolucent line in the dorsoproximal aspect of the proximal phalanx running in the frontal plane could also be seen on L-M and flexed L-M views (arrows) but was not consistently repeatable on further projections. When stall rested for one week the filly rapidly became sound, only to show lameness again on commencing walking and trotting exercise. (b) MR images demonstrate that the radiolucent line seen radiographically is not artefactual and correlates with an area of low signal intensity on T1-weighted GRE images, intermediate signal intensity delineated by a hypointense margin on T2 FSE images and increased signal intensity on STIR GRE images, representing a non-displaced large osteochondral fragment of the dorsomedial eminence of the proximal phalanx. MR images allow definitive localization of the lesion.

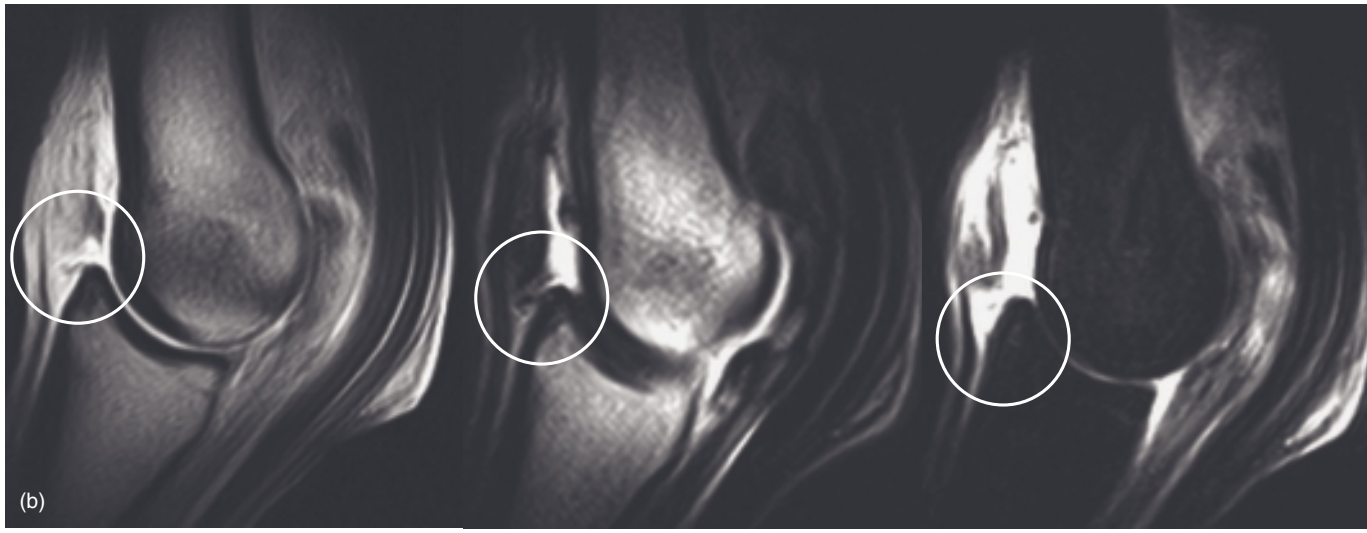

Figure 13.17 *Cont'd*

the Thoroughbred racehorse [36]. Importantly, these horses showed very mild, transient lameness not associated with recent galloping exercise and underwent MRI on the basis of a positive response to pressure applied to the dorsoproximal aspect of the proximal phalanx. Radiography and scintigraphy have a well-defined role in forming a diagnosis, although standing MRI plays a useful role in investigating horses presenting with pain in this region, but with unremarkable or inconclusive radiographic findings, and with early detection, some catastrophic injuries may be prevented.

Radiographically silent dorsoproximal proximal phalanx stress injuries can appear dramatic on MR images with the BMO-t signal pattern extending across the entire articular surface and distally into the trabecular bone (Figures 13.18a and b). However, not all cases are so dramatic and some are only readily detectable on sagittal views. More subtle lesions require careful slice positioning, and sequences oriented in the transverse and frontal planes may be difficult to interpret due to the overlap of the sagittal ridge of MC3/MT3 and the sagittal groove of the first phalanx or joint space/capsule respectively. For this reason, volume averaging or movement artefact may prevent detection of subtle lesions. In the sagittal plane the dorsal cortical bone and subchondral bone of the articular aspect are more easily evaluated. T1-weighted sequences demonstrate this type of pathology less dramatically than T2* and fat-suppressed sequences and, again, early or subtle lesions may be missed if a comprehensive set of sequences is not acquired (Figure 13.19a and b). Short, incomplete sagittal fractures can heal in the absence of surgical fixation, though a number may represent from lameness due to non-healing of the joint margin. These show a similar signal pattern to those with stress injuries without overt fracture of the cortical bone, but an area of trabecular bone densification is seen indicative of the age of the lesion. In these cases the non-union at the joint surface appears hyperintense on all sequences, which is rarely seen in radiographically occult lesions (Figure 13.20).

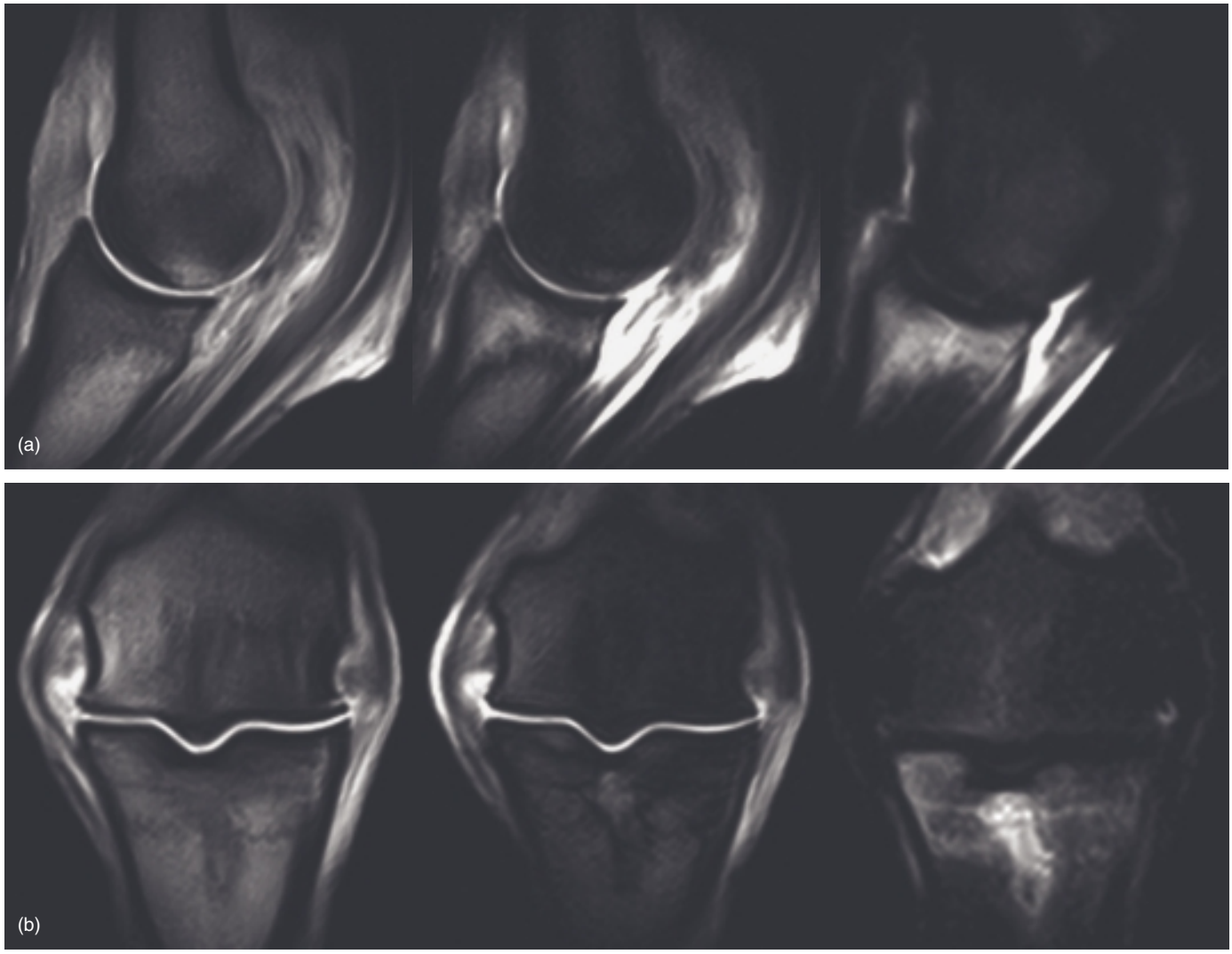

Figure 13.18 (a) T1 GRE, T2* GRE and STIR FSE sagittal images of the right fore fetlock joint of a 3-year-old racing Thoroughbred with mild right fore lameness. There was mild resentment to digital palpation of the dorsoproximal aspect of the first phalanx and mild distension of the fetlock joint. Radiographs showed modelling of the dorsoproximal aspect of the first phalanx with mild periosteal reaction of the dorsal cortex. On MRI, the dorsoproximal aspect of the first phalanx appears hypointense on T1-weighted images and hyperintense in T2* GRE and STIR FSE sequences. In this case the palmar apical region of the medial metacarpal condyle also appears to have moderate STIR and T2* hyperintensity. (b) T1 GRE, T2* GRE and STIR FSE frontal images of the fetlock joint. There is thickening of the subchondral bone plate in the sagittal groove of the first phalanx and the sagittal ridge of the metacarpal condyle. The cancellous bone of the proximal phalanx is hypointense on the T1 image and hyperintense on the T2* and STIR FSE. The horse was removed from training and underwent 6 weeks of box rest followed by 6 weeks of walking exercise. Follow-up radiographs at that point showed more extensive periosteal new bone on the dorsoproximal aspect of the proximal phalanx.

Figure 13.19 (a) T1, T2* and STIR FSE sagittal (top) and transverse (bottom) MR images of 3-year-old Thoroughbred in training with mild right fore lameness when examined prior to galloping. There was minimal joint distension, and a mild response to digital palpation of the dorsoproximal aspect of the first phalanx. The lameness was abolished following intra-articular analgesia of the right fore fetlock joint. Initial radiographs were unremarkable. There is mild signal hypointensity in the dorsoproximal aspect of the proximal phalanx on the T1-weighted image and focal signal hyperintensity on T2* and STIR FSE images. There was marked, focal increased uptake of the radionuclide in the dorsoproximal aspect of the proximal phalanx corresponding with the area of signal change on MR images. This horse underwent 4 weeks of box rest followed by 4 weeks of walking exercise prior to re-entering training. (b) Lateral scintigraphy image of the right fore fetlock and dorsopalmar view of both front fetlocks taken from the horse in (a). There is marked focal increased uptake of the radionuclide in the dorsoproximal aspect of the proximal phalanx corresponding with the area of signal change on MR images.

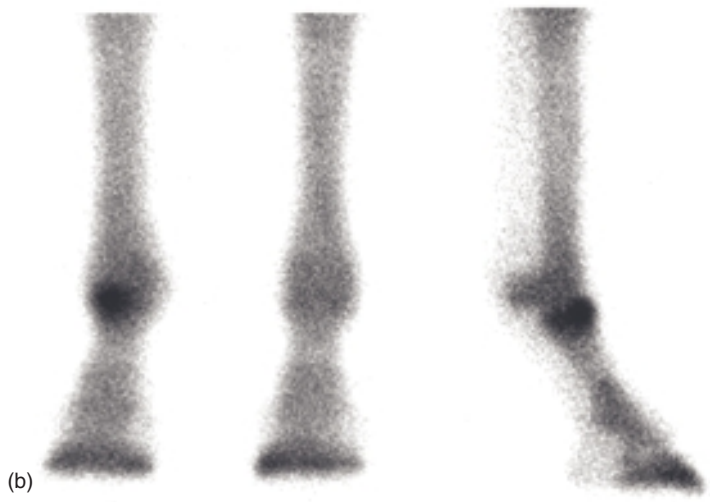

Figure 13.19 *Cont'd*

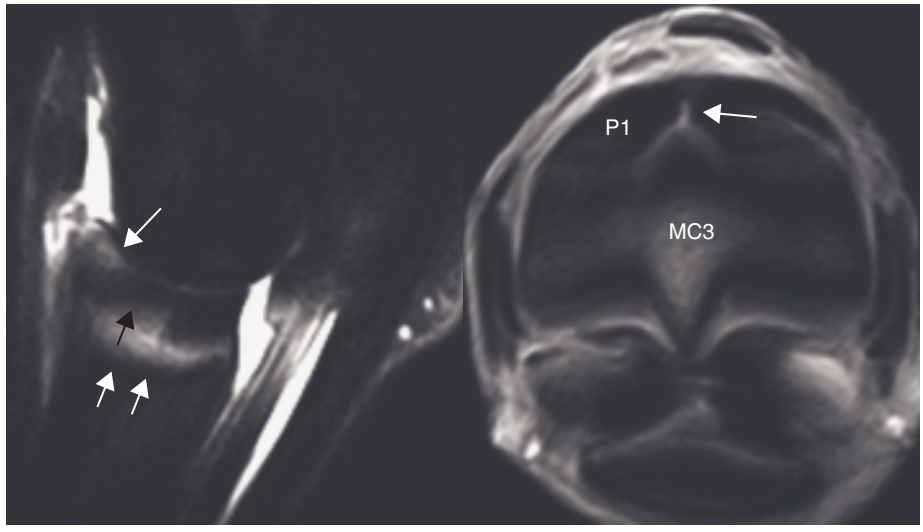

Figure13.20 STIR FSE sagittal (left) and T1 transverse (right) MR images of the right fore fetlock joint of a 3-year-old colt that sustained a short incomplete sagittal proximal phalanx fracture 6 months earlier and was treated conservatively. The colt re-entered training to show recurrent right forelimb lameness (abolished by intra-articular analgesia of the joint) at the onset of fast canter work. The STIR image shows dramatic hyperintensity in the proximal aspect of P1 (open white arrows) that showed BMO-t pattern on other sequences and in which a region of hypointense bone is present (black arrow) representing sclerosis at the site of the old fracture. STIR and T1 hyperintensity is present at the dorsoproximal articular margin of P1 indicating a reinjury or non-union of the previous fracture at this site (closed white arrows).

Osteochondrosis of the sagittal ridge of the third metacarpal bone

Osteochondrosis lesions of the fetlock joint are most commonly seen on the dorsal sagittal ridge of the MC3/MT3 [37]. Clinically silent cases may be detected on pre-sale radiographs in yearlings but they are also in young Thoroughbreds early in training (Figure 13.21a and b) and are detected best on T1 and T2* sequences, where they appear focally hyperintense and

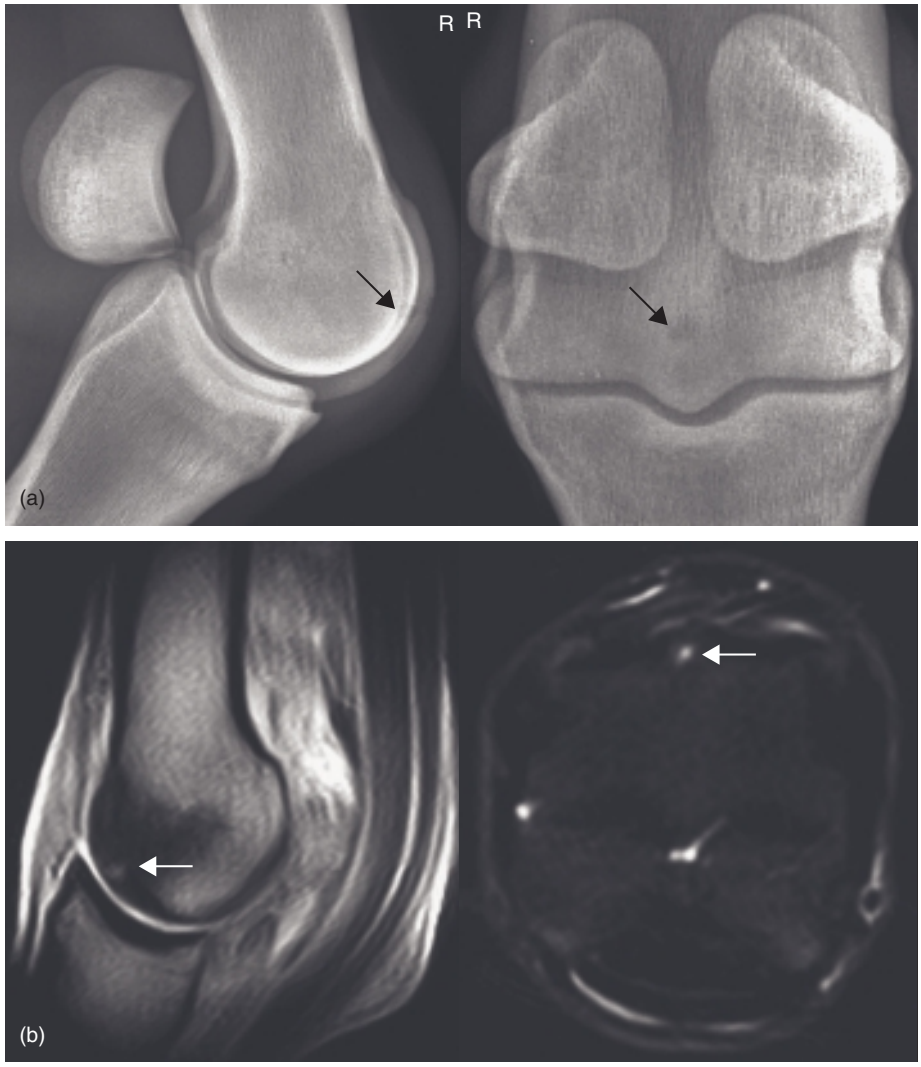

Figure 13.21 (a) Flexed lateromedial and flexed dorsopalmar view of the right fore fetlock of a 2-year-old Thoroughbred in training with right fore lameness abolished by intra-articular analgesia of the fetlock joint. There is a focal radiolucency within the dorsal aspect of the sagittal ridge. (b) T1 GRE sagittal and STIR FSE transverse image of the right fore fetlock of 2-year-old Thoroughbred in training with right fore lameness abolished by intra-articular analgesia of the fetlock joint. Radiographs had a focal radiolucency within the dorsal aspect of the sagittal ridge. There is focal signal hyperintensity on all sequences on the dorsodistal aspect of the sagittal ridge surrounded by hypointensity of the dorsal epiphyseal physis.

may be surrounded by areas of hypointense trabecular bone. In standing horses the slice thickness and sensitivity to motion of STIR sequences may lead to lesions of small size going undetected.

Osseous cyst-like lesions

Osseous cyst-like lesions may be seen in yearlings or in young Thoroughbreds in early training as a possible manifestation of ostoechondrosis, and in older horses following trauma to the joint. Most are diagnosed radiographically but in some cases MRI may help to assess their accessibility at surgery. In cysts thought to be traumatic in origin, the appearance is of focal hyperintensity on all sequences at the articular margin surrounded by extensive hyperintense signal on fat-suppressed images in the surrounding trabecular bone. As the lesion matures, and in those with a developmental aetiology without associated lameness, the hyperintensity is limited to within the margins of the cyst-like lesion itself rather than extending into the surrounding bone (Figure 13.22a and b).

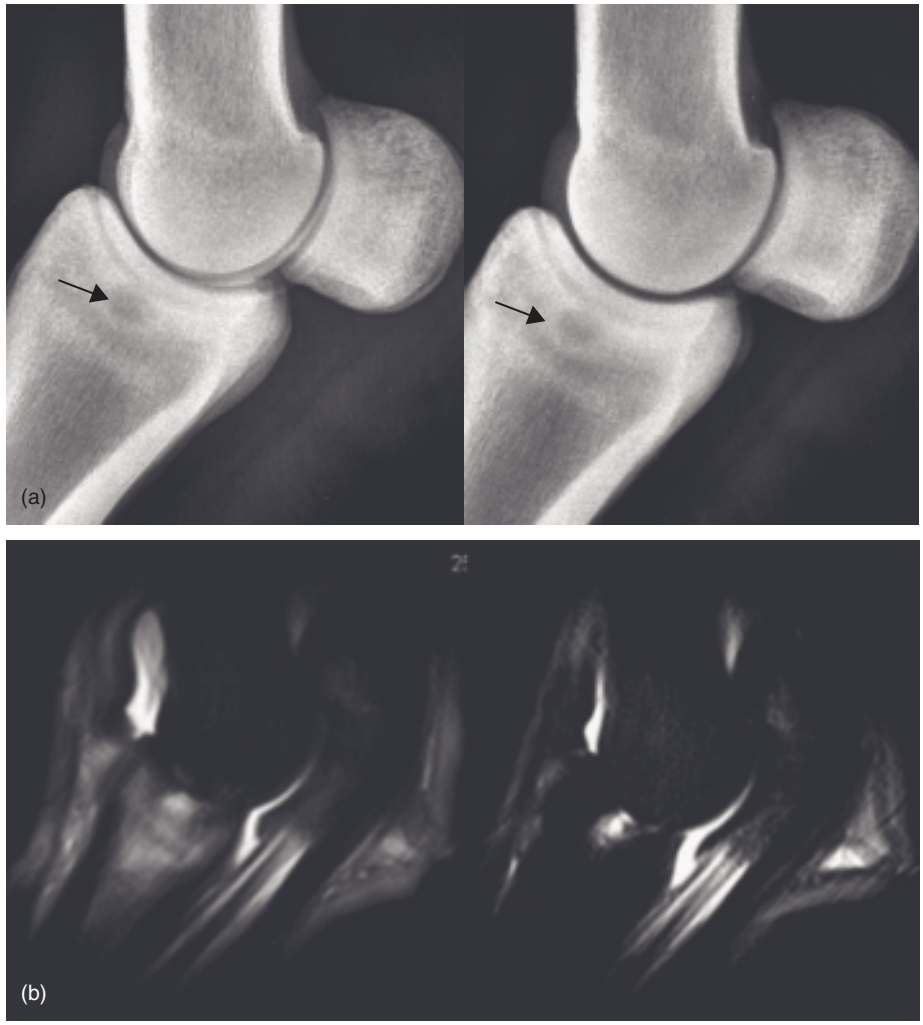

Figure 13.22 (a) LM radiographs of the left fore fetlock joint of a 12-year-old Cob mare with sudden onset severe lameness and marked swelling around the fetlock joint following turnout. The image on the left was taken at the time of the initial examination 3 weeks after the onset of lameness. There is a radiolucent area at the proximal articular aspect of the proximal phalanx (arrow). The image on the right was taken 7 months later at which time the pony was paddock sound. The SC cyst-like lesion has a slightly more defined margin on the follow-up radiograph. (b) STIR FSE sagittal images of the left fore fetlock joint of the horse in (a). Left: STIR image obtained at the initial examination 3 weeks after the onset of lameness. Right: STIR image obtained 7 months later at which time the pony was paddock sound. Radiographically, the osseous cyst-like lesion has a slightly more defined margin on the follow-up radiograph, but the MR images show resolution of the generalised STIR hyperintensity throughout the proximal aspect of the proximal phalanx to leave a well-defined focal hyperintense region. The distension of the dorsal recess of the joint has also resolved. The MR images afford more information than radiographic examination regarding the resolution of the bone injury.

Evaluating the soft tissue structures supporting the fetlock joint in standing horses can be problematic. Slice thickness and motion artefact can make differentiation of individual structures difficult. Reduction of slice thickness is possible, although the trade-off of an increased acquisition time is prohibitive. Image quality greatly influences the ability to appreciate tissue margins and the presence of signal abnormalities, which may lead to lesions being missed or misdiagnoses being made. Problems differentiating specific structures also arise as, for example, the superficial and deep parts of the collateral ligaments of the fetlock joint may appear isointense with the collateral sesamoidean ligaments, the extensor branches of the suspensory ligament, the metacarpo/metatarsophalangeal fascia and the skin in some sequences. The close proximity of the synovial membrane can further confound interpretation as volume averaging may result in apparent changes in signal within the margins of adjacent structures. However, in co-operative patients, diagnostic quality images can be obtained and can yield more information on known lesions or detect some undiagnosed ultrasonographically leading to more appropriate treatment and management.

There are limited data available regarding the incidence of soft tissue-related injuries of the fetlock joint in racehorses as the nature of these injuries rarely requires immediate euthanasia and may only become clinically apparent in the days following the race. For this reason morbidity due to injury to the soft tissues surrounding the fetlock joint may be underestimated in studies documenting relative risk and proportion of musculoskeletal injuries relating to the soft tissues [4].

Synovitis/capsulitis

Damage to the synovial attachments of the fetlock joint is frequently seen in young racehorses, usually as faster work is introduced to the training regime. There may be subcutaneous oedema and hyperaemia associated with the area of damage. These cases often present with mild lameness, mild joint distension, increased temperature of the joint surface and resentment to forced joint flexion, which exacerbates the lameness. Soft tissue oedema may be seen and aids visualization of the lesions (Figure 13.23).

Chronic proliferative synovitis

Chronic proliferative synovitis (CPS) results from repetitive injury of the dorsal aspect of the fetlock joint leading to thickening of the bi-lobed synovial pad located dorsally on the sagittal ridge of MC3/MT3 [38, 39]. Diagnosis is often based on clinical findings, ultrasonography and radiography but may be seen in horses undergoing MRI examination to investigate concurrent pathology within the joint. CPS is commonly seen in association with erosions of the proximodorsal margin of the metacarpal condyle, the degree of which is not always fully appreciated radiographically and may be more fully evaluated on MR images (Figure 13.24a–c).

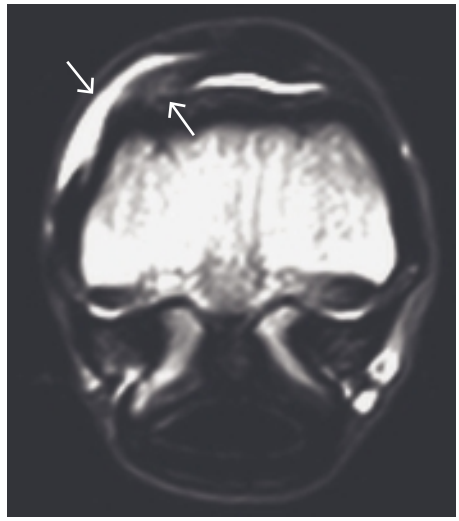

Figure 13.23 T2 FSE transverse image of the right fore fetlock joint of a 2-year-old-colt with right fore lameness abolished by intra-articular analgesia. The colt had galloped the previous day and appeared sound that evening. The following day there was filling over the subcutaneous tissue (left arrow) over the dorsolateral aspect of the joint and moderate joint distension had developed. Radiographs were unremarkable. Focal T2 FSE and STIR hyperintensity was detected in the dorsolateral capsular attachment (right arrow). There is also cortical hyperintensity and endosteal irregularity of the dorsal cortex at this level.

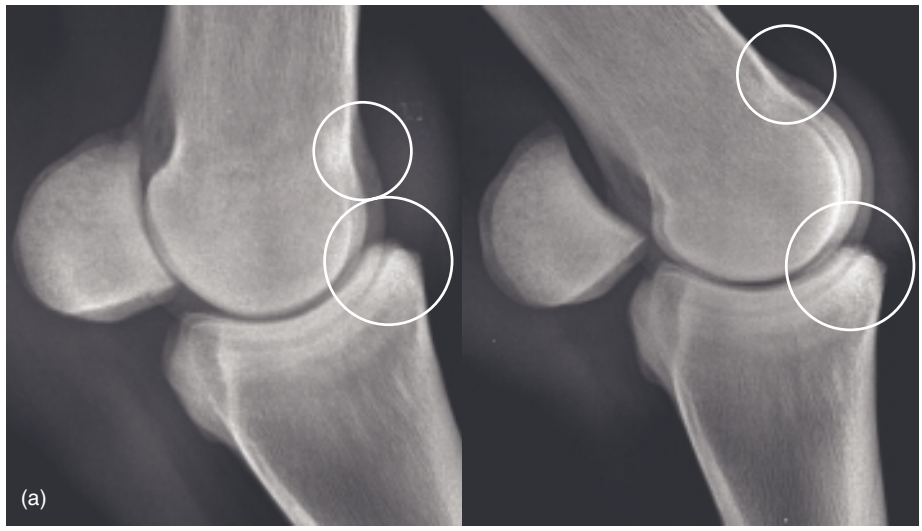

Figure 13.24 (a) Flexed (left) and standing (right) lateromedial radiographs of the right hind fetlock joint from a 4-year-old Thoroughbred with a history of bilateral hind limb lameness related to both metatarsophalngeal joints, which had been repeatedly medicated. There was palpable thickening of the soft tissues on the dorsal aspect of the joints and mild resentment to forced flexion. Irregularity of the dorsal sagittal ridge is present with a focal radiolucent area (small circles), which may indicate an erosive lesion is present. There is also densification and modelling of the dorsal articular margin of the proximal phalanx (large circles). This combination of radiographic changes is commonly seen in horses with chronic proliferative synovitis as these regions impinge upon each other during hyperextension of the joint at galloping speeds.

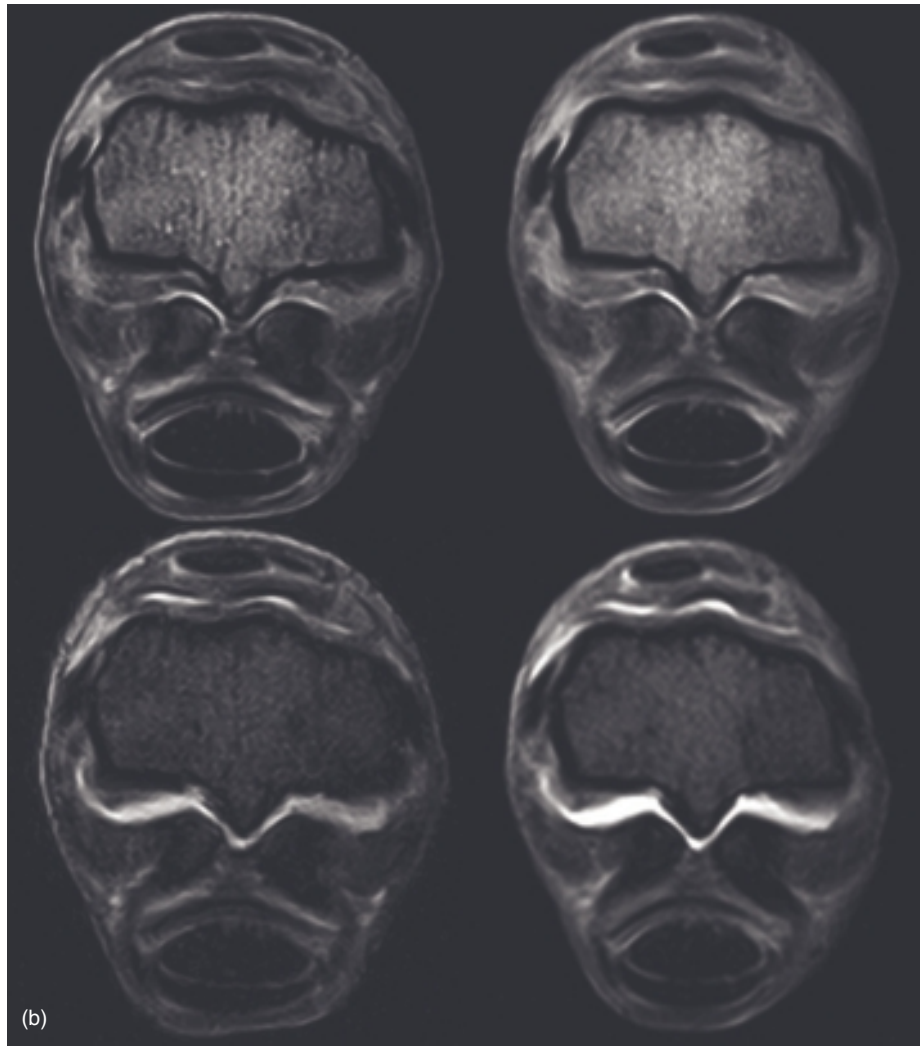

Figure 13.24 *Cont'd* (b) T1 GRE (top) and T2* GRE (bottom) transverse images of the right hind fetlock joint of a 4-year-old Thoroughbred with a history of bilateral fore limb lameness related to both hind fetlock joints, which had been repeatedly medicated (see (a)). The images to the right were taken with the horse under standing sedation with a slice thickness of 5 mm and an image matrix size of 256 x 256. The images to the left were obtained postmortem and are high-resolution images with a slice thickness of 1.09 mm and an image matrix size of 512 x 512. Despite the standing images showing less detail than those taken of the cadaver specimen, the low signal intensity within the fibrocartilage on the dorsal aspect of the metacarpal condyles and associated endosteal changes can still be seen. There is also fibrillation of the dorsal margin of the deep digital flexor tendon (DDFT) at this level, which is only possible to see in standing horses when motion is at an absolute minimum. (c) Postmortem specimen of the right metacarpophalangeal joint. There is extensive erosion of the dorsoproximal aspect of the metacarpal condyles and thickening and discolouration of the proximodorsal synovial fold. The articular cartilage is discoloured, thin and numerous wear lines are present. Photograph courtesy of Katherine Whitwell.

The collateral ligaments of the fetlock joint

When imaging the collateral ligaments of the fetlock joint in the standing horse it is essential that placement of the limb within the isocentre of the magnet is optimized. If positioning is compromised, or the coil is placed too tightly around the limb, distortion of tissue margins and signal drop-out may occur. This may have only minimal affect on the interpretation of the deeper structures but will prevent adequate assessment of the superficial soft tissue structures. The phase-encoding direction should be oriented to prevent flow artefact travelling through the area of interest (see Chapter 4).

Subtle changes in the ligaments may be difficult to detect with certainty in the standing horse and more severe cases are easily detected ultrasonographically. In some horses the degree of lameness observed cannot be fully explained by mild changes seen ultrasonographically, which may indicate that insertional bone pathology is present (Figures 13.25a–c) or a concurrent impaction injury on the opposite side of the joint (Figure 13.8). The signal changes of STIR and T2 FSE hyperintensity are usually found at the proximal and distal aspect of the ligament due to the distractive nature of the injury. Subcutaneous oedema may be present in more severe or acute cases. Enlargement of the ligament is not consistently seen in mild cases (Figure 13.26).

Suspensory ligament branch lesions

Suspensory ligament branch injuries may be detected using MRI when they are not apparent ultrasonographically. Thoroughbred racehorses of 2 and 3 years of age frequently show increased signal intensity within the suspensory ligament branches on fat-suppressed and T2 FSE sequences, which may be of no apparent clinical significance and is not usually associated with increase in size of the ligaments or a painful response of firm digital palpation of the region. It is not yet known if this represents an adaptive remodelling response of the immature ligamentous tissue to cyclical loading at faster gaits or early accumulation of microdamage (degeneration), a failure of adaptation which may predispose to injury later in life (Figure 13.27).

In some cases a clear difference is seen between the medial and lateral suspensory ligament branches on MR images not appreciable ultrasonographically (Figure 13.28). The axial aspect of the branches at their insertion on to the abaxial margin of the PSB is sometimes difficult to assess as general loss of echogenicity in this region may be attributed to an off-incidence artefact with the ligament fibres. In some cases, T2 FSE and STIR hyperintensity can be seen on MR images despite an apparently normal ultrasonographic appearance (Figure 13.29).

Distal sesamoidean ligament injuries

The distal sesamoidean ligaments (DSLs) originate from the base of the PSBs and function as a continuation of the suspensory ligament, to stabilize and prevent excessive hyper-extension the MCP/MTP during weight-bearing [40]. Traditionally assessed ultrasonographically, recent studies have revealed

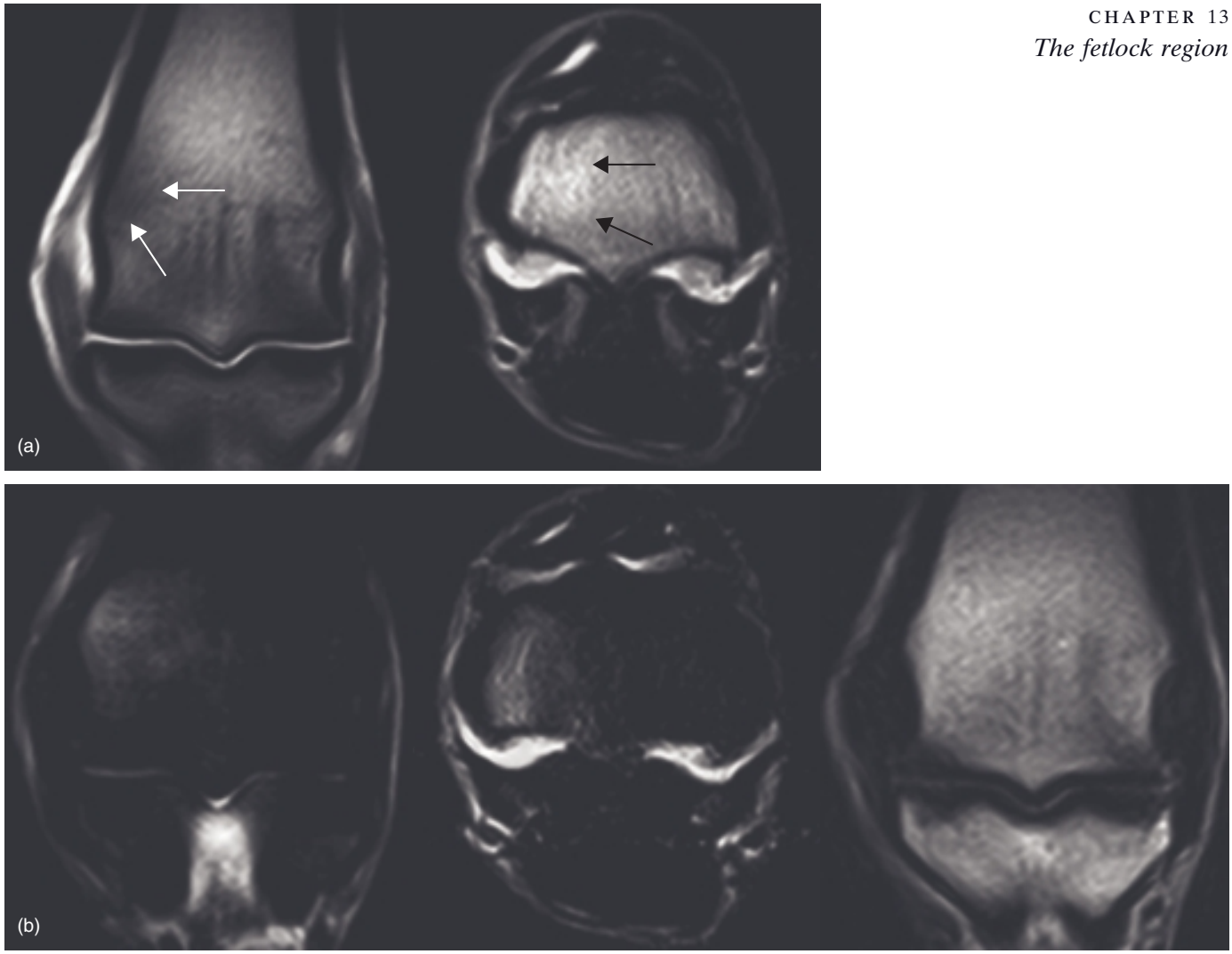

Figure 13.25 Images of a 9-year-old show jumper with a history of mild, variable right fore lameness. Sudden onset, severe left fore lameness had occurred recently during a competition. Swelling was palpable over the lateral aspect of the joint and there was mild resentment of firm flexion of the joint. There was increased radiopharmaceutical uptake in the palmarolateral aspect of the distal metacarpus. (a) T1-weighted frontal (left) and T2 FSE transverse (right) images. There is thickening of the subchondral bone plates in the proximopalmar articular surfaces of the first phalanx, mild decrease in signal intensity within the distal metacarpal condyles and mild decrease in signal intensity on the endosteal surface of the lateral cortex of the third metacarpal bone in the region of the distal metacarpal physis (white arrows) at the site of the proximal insertion of the lateral superficial collateral ligament, correlating with mild increased signal intensity on the T2 FSE transverse image (black arrows). (b) STIR FSE frontal (left) transverse (centre) images and T2 FSE frontal image (right) of the right fore fetlock joint. Increased signal intensity in the lateral aspect of the metacarpal condyle is clearly visible in the fat-suppressed images. The lateral collateral ligament of the fetlock joint appears enlarged, although of uniform low signal intensity on fat-suppressed and T2 FSE sequences. Despite the apparent enlargement of the lateral collateral ligament in both frontal and transverse STIR FSE and T2 FSE images the echogenicity, longitudinal fibre pattern and cross-sectional area were unremarkable ultrasonographically. This apparent enlargement was due to thickening of the subcutaneous tissues, which are not well differentiated on MR images.

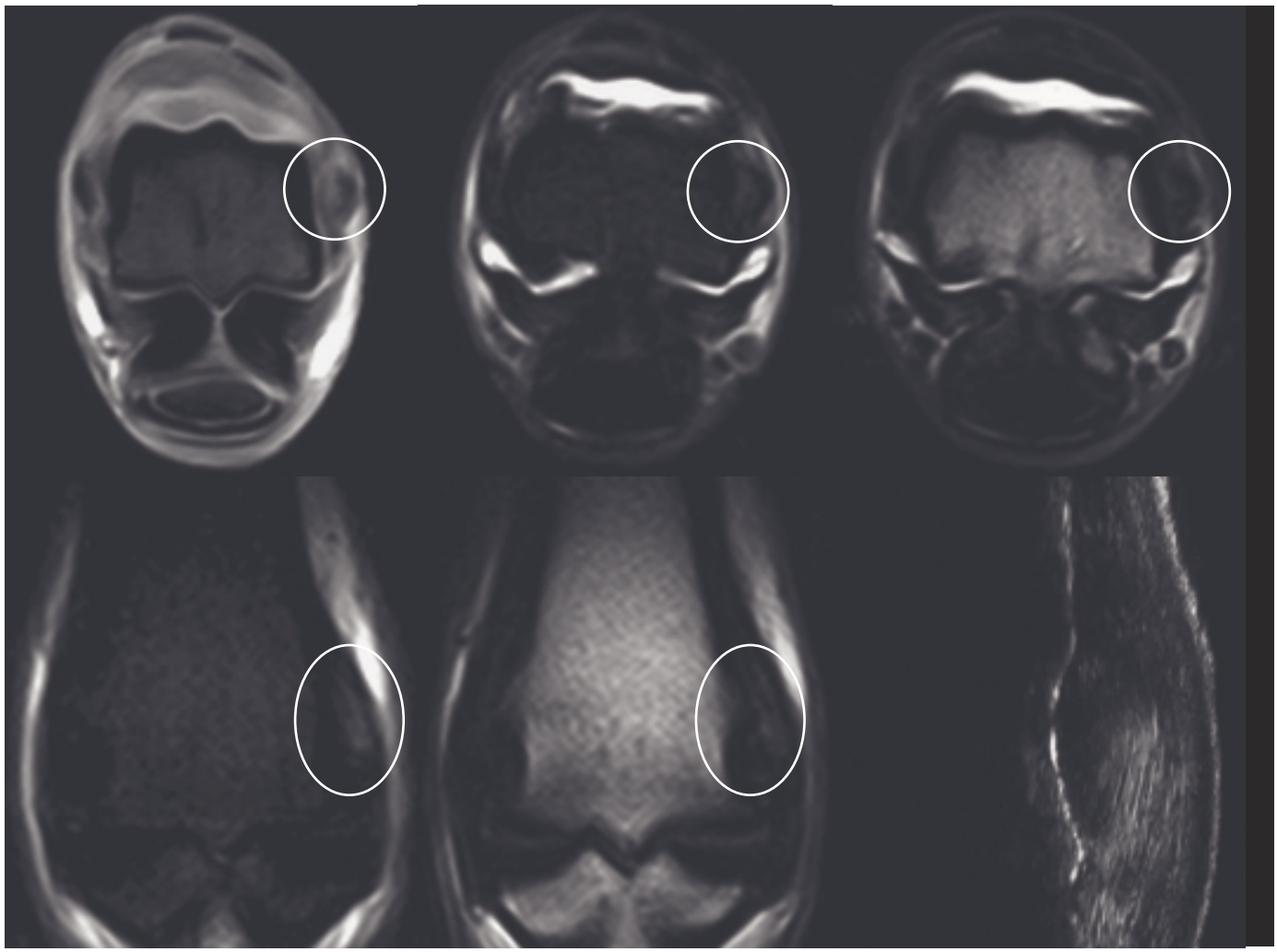

Figure 13.26 MR images of the left fore fetlock joint of a 12-year-old pony gelding whose left fore limb was caught in fencing. The T2* GRE transverse image (top left) shows increased signal intensity within the lateral collateral ligament (circled). T2*-weighted sequences of the collateral ligaments of the fetlock joints should be interpreted with care as they are prone to motion artefact and do not afford adequate differentiation of tissue margins in many cases. STIR FSE transverse image (top centre) and T2 FSE transverse image (top right) of the same joint with increased signal intensity within the superficial part of the lateral collateral ligament (circled). STIR FSE and T2 FSE frontal images (bottom left and bottom right) confirm this finding. Initially, ultrasonography of the collateral ligaments was unremarkable. A repeat ultrasonographic examination 8 weeks later revealed enlargement and disruption to the longitudinal fibre pattern in the region if the area of increased signal intensity on the MR images (bottom right).

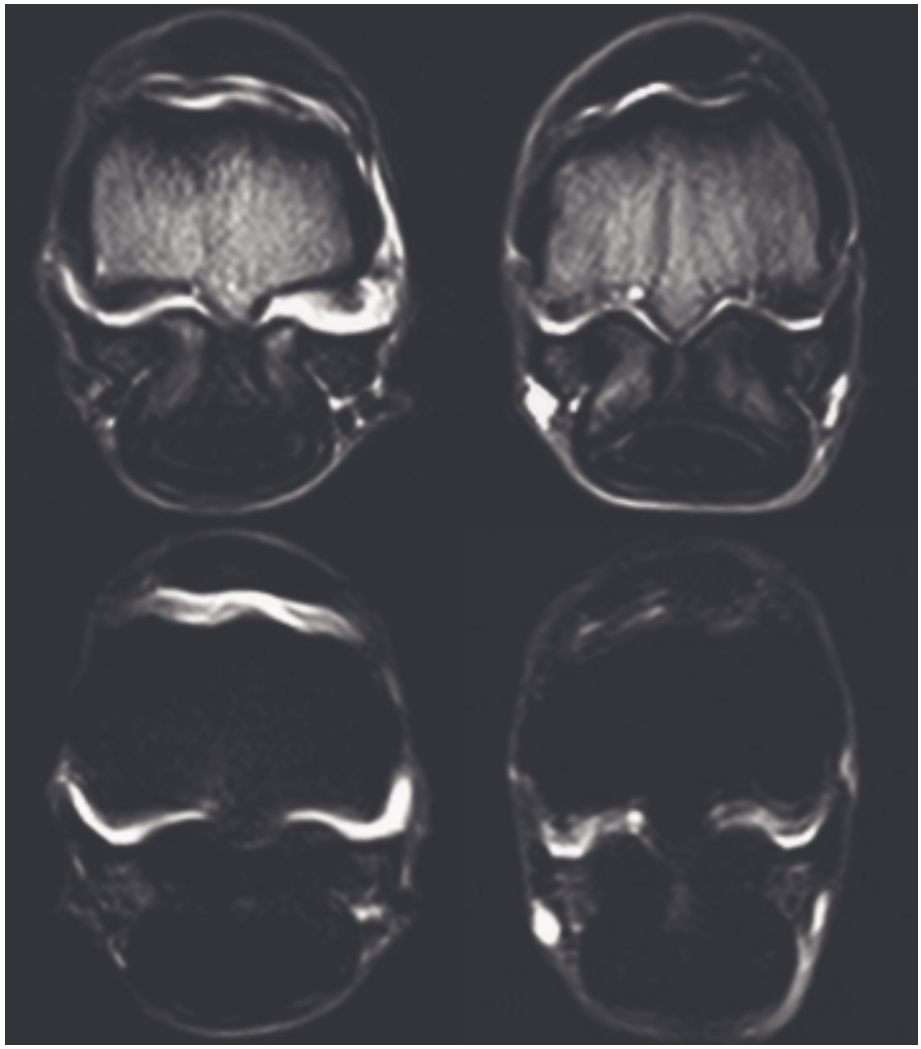

Figure 13.27 T2 FSE transverse (top) and STIR FSE transverse (bottom) images of the left and right metacarpophalangeal joints of a 2-year-old Thoroughbred filly with a history of left fore lameness. There is biaxial, bilateral signal hyperintensity within the suspensory ligament branches just proximal to the insertion on the PSB. Though this was not thought to be primarily responsible for the current lameness in the left fore limb it may be a contributing factor. This appearance of the ligaments can be seen in horses with no history of fetlock joint lameness. In this case there were also generalized increase in signal on fat-suppressed images within the PSB and distal metacarpal condyles in addition to changes associated with dorsal erosive lesions and modelling changes to the dorsal articular margin of the proximal phalanx.

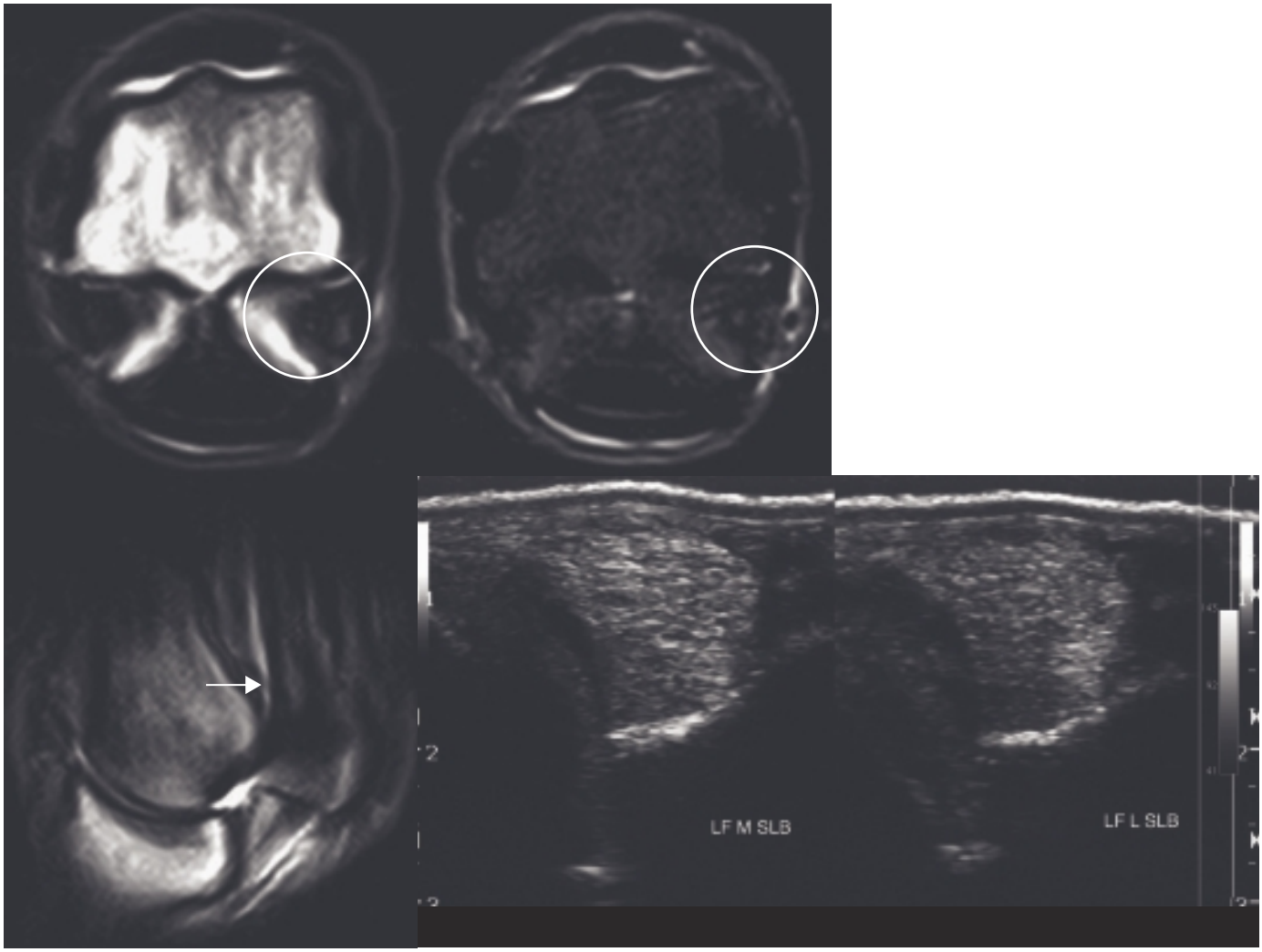

Figure 13.28 T2 FSE transverse (top left) and parasagittal (bottom left) images of the left metacarpophalangeal joint of a 3-year-old Thoroughbred in training with a history of left fore lameness improved by intra-articular analgesia of the left fore fetlock joint and abolished following a low 4-point nerve block. There is a well-defined increase in signal intensity on T2 FSE transverse and sagittal images within the medial SLB (circle and arrow), which is not clearly visible on ultrasonographic images. There was similar, though less marked increase in signal on fat suppressed images. In the absence of a pain response to palpation of the branch and any palpable heat or swelling of the region it is unlikely that this is a major contributor to the fetlock pain in this individual.

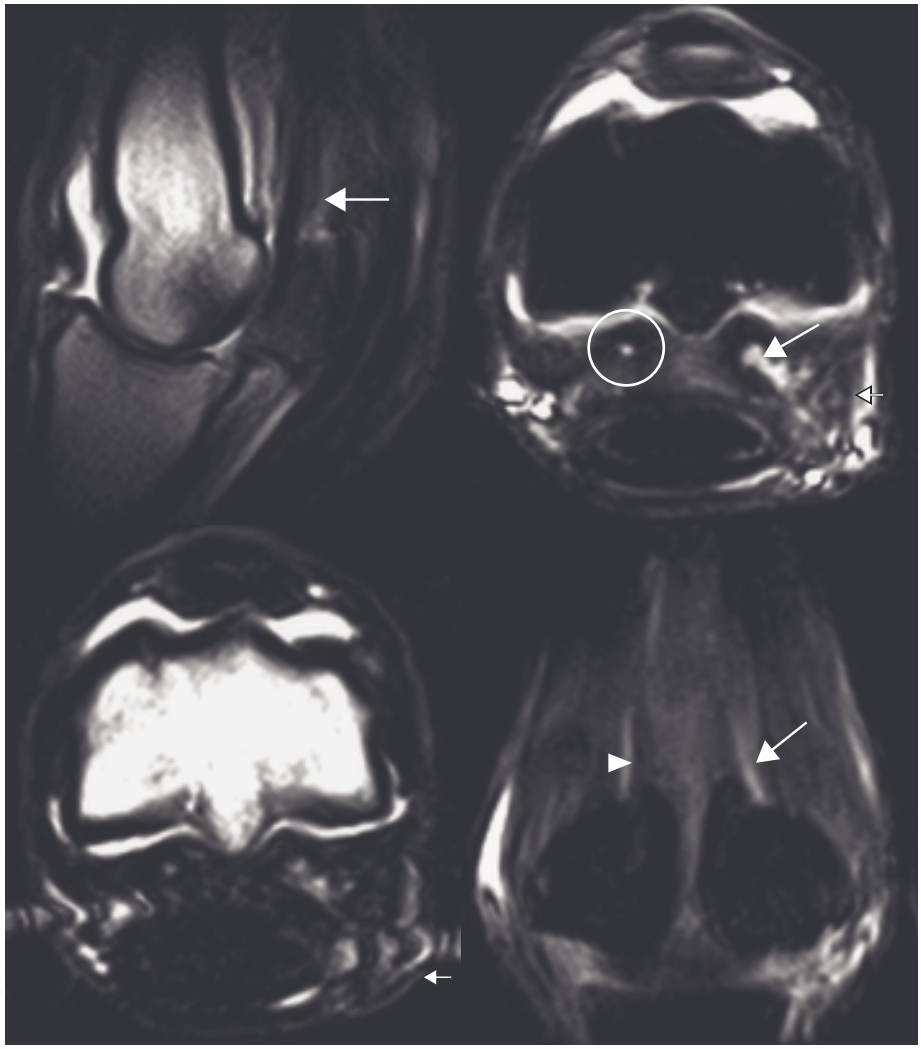

Figure 13.29 T2 FSE sag (top left) and STIR GRE transverse (top right) images of a 3-year-old Thoroughbred with a severe, longstanding injury to the lateral suspensory ligament branch (large white arrow) with marked periligamentous fibrosis (small white arrow). An axial core lesion in the medial branch (circled and arrowhead) was not clearly visible on ultrasonographic images and was not associated with any increase in size of the branch.

the limitations of this technique for evaluating these structures [41, 42]. However, injuries not detectable ultrasonographically may be part of a complex of lesions leading to lameness rather than being the primary cause.

The oblique DSLs are prone to the magic angle effect [43] and sequences with long effective echo times such as T2 FSE and STIR FSE are necessary to prevent misdiagnoses, particularly in the proximal portion of the ligaments, due to fibre divergence and partial volume effect. Care should be taken to ensure the limb is positioned symmetrically within the magnet and the RF coil should be fitted without excessive compression on the skin as this may cause signal hyperintensity in the associated tissues.

Transverse sequences alone may be used to evaluate the oblique and cruciate ligaments, though transverse and sagittal sequences are recommended for evaluation of the straight DSL. It is necessary to pilot the transverse sequences from a transverse oblique slice through the base of the sesamoids to maximize slice symmetry and minimize the appearance of artefacts (Figure 13.30a).

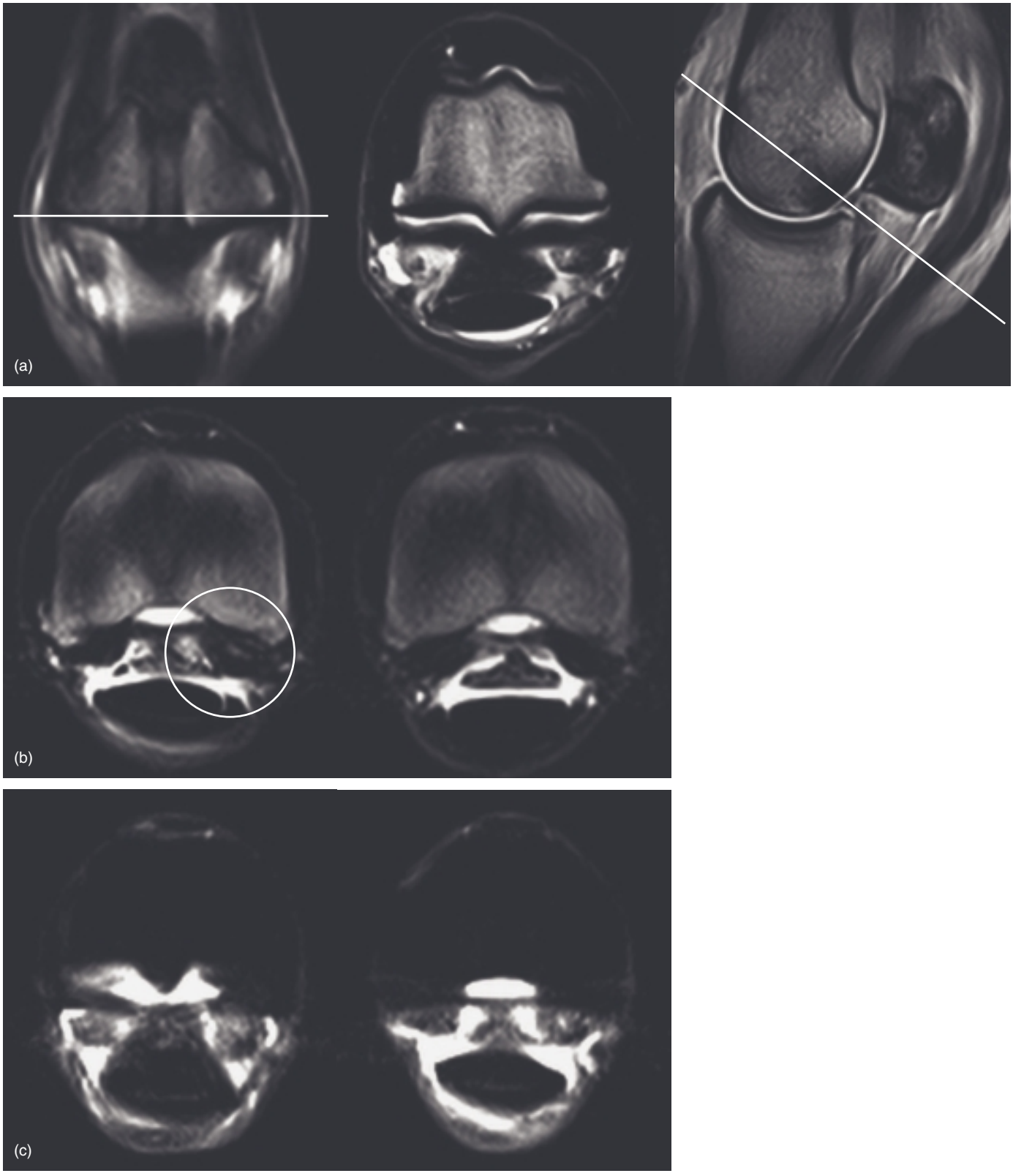

Figure 13.30 (a) Transverse slices to visualize the ODSL can be piloted from a transverse oblique slice (above top left) and from a sagittal slice (above bottom left) to ensure symmetric positioning (above right). (b) T2 FSE transverse MR images of the right fore MCP joint (left) and left fore MCP for comparison (right). There is signal hyperintensity within the medial oblique distal sesamoidean ligament just distal to the origin on the base of the medial proximal sesamoid bone. This change continued for a distance of 1.5 cm distal to the origin. These changes correlated well with the ultrasonographic appearance of the ligaments. (c) STIR FSE transverse MR images of the right fore fetlock joint. The image to the left is just distal to the origin of the ODSL on the base of the proximal sesamoid bones. The image to the right is 5 mm distal to this. The medial ODSL appears increased in size with poorly defined margins. There is a central region of signal hyperintensity. Although T1 and T2* images can be misleading, T2FSE and STIR sequences frequently correlate well with ultrasonographic findings.

Studies have shown the medial and lateral ODSL may be asymmetric (the LODSL being greater in cross-sectional area and signal intensity ratio compared to the MODSL), although left/right asymmetry is rarely seen in normal ligaments, the most common site of injury in the ODSL is within the proximal third, whereas the distal portion is more commonly affected in SDSL injuries. Injured ligaments show an increase in size and signal intensity. The cruciate distal sesamoidean ligaments (CDSL) are less frequently affected [44]. There is generally loss of definition of the margins of the ligaments and hyperintensity of the peri-ligamentous tissue on T2* and STIR sequences, representing oedema, where injuries are seen (Figure 13.30b and c). Recent diagnostic nerve blocks placed at the level of the base of the PSBs should be taken into account during interpretation.

REFERENCES

[1] Bailey CJ, Read SW, Hodgeson DR. Flat, hurdle and steeplechase racing risk factors for musculoskeletal injury. *Equine Vet J* 1998; **30**: 498–503.
[2] Kawcak CE. The role of subchondral bone in joint disease: a review. *Equine Vet J* 2001; **33**: 120–6.
[3] Parkin TDH, Cleg PD, French WP. Risk of fatal distal limb fracture among Thoroughbreds involved in the five types of racing in the United Kingdom. *Vet Rec* 2004; **154**(16): 493–7.
[4] Stover SM, Murray A. The Californian Post Mortem Program: leading the yay. *Vet Clin North Am Equine Practice* 2008; **24**(1): 21–36.
[5] Brama PAJ, Karssenberg D, Barneveld A. Contact areas and pressure distribution on the proximal articular surface of the proximal phalanx under sagittal plane loading. *Equine Vet J* 2001; **33**: 26–32.
[6] Riggs CM, Whitehouse GH, Boyde A. Pathology of the distal condyles of the third metacarpal and third metatarsal bones of the horse. *Equine Vet J* 1999; **31**: 140–8.
[7] Norrdin RW, Kawcak CE, Capwell BA. Subchondral bone failure in an equine model of overload arthrosis. *Bone* 1998; **22**: 133–9.
[8] Firth EC, Rogers CW. Musculoskeletal responses of 2 year old TB horses to early training. Conclusions. *N Z Vet J* 2005; **53**: 377–83.
[9] Reilly GC, Currey JD, Goodship AE. Exercise of young TB horses increases the impact strength of the third metacarpal bone. *J Orthop Res* 1997; **15**: 862–8.
[10] Riggs CM. Structural variation of the distal condyles of the third metacarpal and third metatarsal bones in the horse. *Equine Vet J* 1999; **31**: 130–9.
[11] Rubio-Martinez. Structural characterization of the SCB in the distal aspect of the third metacarpal bones from Thoroughbred racehorses via micro-CT. *Am J Vet Res* 2008; **69**(11): 1413–22.
[12] McGibbon CA, Bencardino J, Palmar WE. Subchondral bone and cartilage thickness from MRI: effect of chemical shift artifact. *MAGMA* 2003; **16**: 1–9.
[13] Riggs CM, Whitehouse GH, Boyde A. Structural variation of the distal condyles of the third metacarpal and metatarsal bones in the horse. *Equine Vet J* 1999; **31**(2): 130–9.
[14] Berger PE, Ofstein RA, Jackson DW, Morrison DS, Silvino N, Amador R. MRI demonstration of radiographically occult fractures: what have we been missing? *Radiographics* 1989; **9**(3): 403–7.
[15] Yao L, Lee JK. Occult intraosseous fracture: detection with MR imaging. *Radiology* 1988; **167**(3): 749–51.
[16] Peterfy CG. MRI of the wrist in early rheumatoid arthritis. *Ann Rheum Dis* 2004; **63**(5): 473–7.
[17] Alanen V, Taimela S, Kinnunen J, Koskinen SK, Karaharju E. Incidence and clinical significance of bone bruises after supination injury of the ankle. A double-blind, prospective study. *J Bone Joint Surg* 1998; **80**(3): 513–15.
[18] Bluemke DA, Zerhouni EA. MRI of avascular necrosis of bone. *Top Magn Reson Imaging* 1996; **8**(4): 231–46.

[19] DeSmet AA, Fisher DR, Burnstein MI *et al*. Value of MR imaging in staging osteochondral lesions of the talus: results in 14 patients. *Am J Radiology* 1990; **154**: 555–60.
[20] Shankman S, Cisa J, Present D. Tumors of the ankle and foot. *Magn Reson Imaging Clin N Am* 1994; **2**(1): 139–53.
[21] Chung C, Yu JS, Becker W. Pagets disease of the calcaneus: findings on MR imaging. *Foot Ankle Int* 1998; **19**(4): 225–8.
[22] Craig JG, Amin MB, Wu K *et al*. Osteomyelitis of the diabetic foot: MR imaging-pathologic correlation. *Radiology* 1997; **203**(3): 849–55.
[23] Schweitzer ME, Haims AH, Morrison WB. MR imaging of ankle marrow. *Foot Ankle Clin* 2000; **5**(1): 63–82.
[24] Dyson S, Murray R, Schramme M, Branch M. Magnetic resonance imaging of the equine digit: 15 cases. *Equine Vet J* 2003; **35**(1): 18–26.
[25] Powell SE, Ramzan PH, Head MJ, Shepherd MC, Baldwin GI, Steven WN. Standing magnetic resonance imaging detection of bone marrow oedema-type signal pattern associated with subcarpal pain in 8 racehorses: a prospective study. *Equine Vet J* 2010; **42**: 10–17.
[26] Murray RC, Blunden TS, Schramme MC, Dyson SJ. How does magnetic resonance imaging represent histologic findings in the equine digit? *Vet Radiol & Ultrasound* 2006; **20**: S121–S134.
[27] Saunders TG, Medynski MA, Feller JF. Bone contusion patterns of the knee at MR imaging: footprints of the mechanism of injury. *Radiographics* 2000; **20**: S135–S151.
[28] Schweitzer ME, Tran D, Deely DM, Hume EL. Medial collateral ligament injuries: evaluation of multiple signs, prevalence and location of associated bone bruises, and assessment with MR imaging. *Radiology* 1995; **194**: 825–9.
[29] Hornof W, O'Brien T. Radiographic evaluation of the palmar aspect of the equine metacarpal condyles: a new projection. *Vet Radiol & Ultrasound* 1980; **21**: 161.
[30] Pilsworth R, Hopes R, Greet TR. A flexed dorsopalmar projection of the equine fetlock in demonstrating lesion of the distal third MC3. *Vet Rec* 1988; **122**(14): 332–3.
[31] Riggs CM, Whitehouse GH, Boyde A. Pathology of the distal condyles of the third metacarpal and third metatarsal bones of the horse. *Equine Vet J* 1999; **31**: 140–8.
[32] Bertone AL. Distal limb: fetlock and pastern. In: Hinchcliff KW, Kaneps AJ, Geor RJ (eds) *Equine Sports Medicine and Surgery*. Philadelphia, PA: Saunders, 2004.
[33] Arendt EA, Griffiths HJ. The use of MR imaging in the assessment and clinical management of stress reactions of bone in high-performance athletes. *Clin Sports Med* 1997; **16**: 291–306.
[34] Shepherd MC, Meehan J. The European Thoroughbred. In: Dyson SJ, Pilsworth RC, Twardock AR, Martinelli MJ. *Equine Scintigraphy*. Suffolk, Equine Veterinary Journal, 2003, pp. 117–49.
[35] Bailey RE, Dyson SJ, Pardin TD. Focal increased radiopharmaceutical uptake in the dorsoproximal diaphyseal region of the equine proximal phalanx. *Vet Radiol & Ultrasound* 2007; **48**(5): 460–6.
[36] Ramzan PHL, Powell SE. Proximal phalangeal fracture as stress injuries? Clinical and imaging features of suspected prodromal fracture in the proximal phalanx in three Thoroughbred racehorses. *Equine Vet J* 2010; **42**: 164–9.
[37] Yovich JR. Osteochondritis dissecans of the sagittal ridge of the third metacarpal and metatarsal bones in horses. *J Am Vet Med Assoc* 1985; **186**: 1186.
[38] Dabareiner RM, White NA, Sullins KE. Metacarpophalangeal joint synovial pad fibrotic proliferation in 63 horses. *Vet Surg* 1999; **25**: 199.
[39] Kannegieter NJ. Chronic proliferative synovitis of the equine metacarpophalangeal join. *Vet Rec* 1990; **127**: 8–10.
[40] Denoix J-M. Functional anatomy of the tendons and ligaments of the distal limb. *Vet Clin North Am: Equine Pract* 1994; **10**: 273–322.
[41] Sampson S, Schneider R, Tucker R, Gavin P, Zubrod C, Ho C. Magnetic resonance imaging features of the oblique and straight distal sesamoidean desmitis in 27 horses. *Vet Radiol Ultrasound* 2007; **48**: 303–11.
[42] Schneider R, Tucker R, Habegger S, Brown J, Leathers C. Desmitis of the straight sesamoidean ligament in horses: 9 cases (1995–1997). *J Am Vet Med Assoc* 2003; **222**: 973–7.

[43] Smith M, Dyson S, Murray R. Is the magic angle effect observed in the collateral ligaments of the distal interphalangeal joint or the oblique distal sesamoidean ligaments during standing magnetic resonance imaging? *Vet Radiol & Ultrasound* 2008; **49**: 509–15.
[44] Smith S, Dyson S, Murray R. Magnetic resonance imaging of distal sesamoidean ligament injury. *Vet Radiol & Ultrasound* 2008; **49**: 516–28.

Chapter 14
The metacarpal/metatarsal region

Matthew Brokken, Russell Tucker and Rachel Murray

INTRODUCTION

Injuries in the metacarpal and metatarsal region are a common cause of lameness in the equine athlete. Some lameness problems in the metacarpus/metatarsus have been difficult to diagnose accurately because affected horses frequently do not have clinical signs that allow lameness to be localized to this area [1, 2]. Many pathologic processes have been described, including:

- avulsion of the origin of the suspensory ligament [3–5]
- palmar or plantar proximal cortical stress fractures [6]
- proximal suspensory desmitis [7–9]
- desmitis of the accessory ligament of the deep digital flexor tendon (ALDDFT) [10, 11]
- fractures of the proximal aspect of the splint bones [12]
- superficial and deep digital flexor tendonitis [13, 14].

Examination of the metacarpal/metatarsal region with radiography and/or nuclear scintigraphy is helpful in detecting changes within bone, such as avulsion injuries, splint bone exostoses and cortical stress fractures. Ultrasound is useful in detecting fibre disruption and thickening within the tendons and ligaments. However, detection of abnormalities, specifically desmitis of the ALDDFT and proximal suspensory ligament (PSL), has not been possible in some horses with either ultrasound or nuclear scintigraphy [2]. Magnetic resonance imaging (MRI) has been used in horses with lameness problems that cannot be diagnosed from other imaging techniques [15–18]. MRI is useful for evaluating bone and soft tissues in equine and human patients [15–23]. There has been limited information about the use of MRI for metacarpal/metatarsal injuries in the horse [20, 24–28]. However, the use of MRI for this region is increasing due to the difficulty completely evaluating this area with other imaging modalities. Sectional images allow accurate assessment of both size and signal within the PSL and ALDDFT as well as the relationship between the PSL and the second and fourth metacarpal/metatarsal bones (Figure 14.1).

It is especially important that horses have an adequate lameness examination with diagnostic local analgesia performed prior to MR examination. The localization of metacarpal and metatarsal lameness is accomplished by observing improvement in the lameness after diagnostic local analgesia. There are multiple techniques for desensitizing the proximal aspect of the palmar metacarpus and plantar metatarsus [29–33]. However, there is confusion interpreting the results of subcarpal and subtarsal analgesia due to the

Equine MRI, edited by Rachel C. Murray.

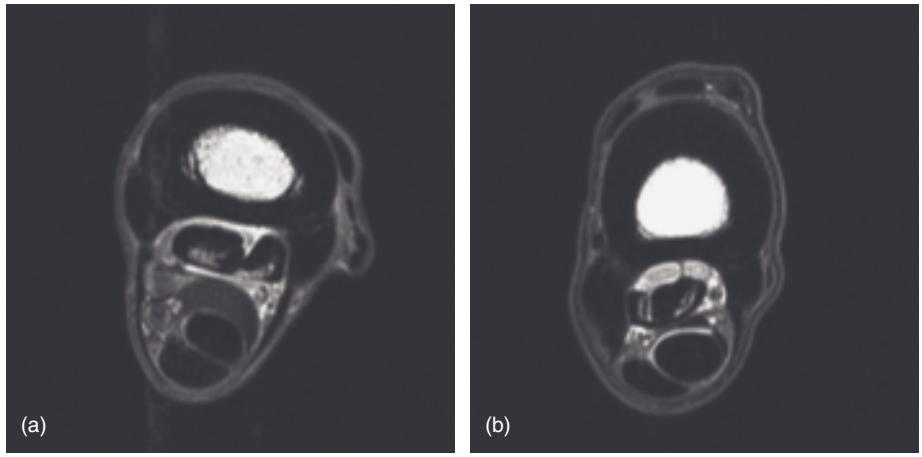

Figure 14.1 Transverse high-field proton density images of the normal proximal metacarpus (a) and metatarsus (b). These images illustrate the ability of MR to clearly differentiate between structures.

lack of specificity of local analgesic techniques [30, 33]. The majority of horses do not block completely sound with local analgesia of the proximal metacarpus/metatarsus [27]. This is most likely related to the nature of the block where the efficacy depends on local diffusion throughout the region. It is also possible that the horses do not block completely sound due to other concurrent lameness issues (i.e. osteoarthritis of the lower hock joints). As described elsewhere [30, 33], the possibility of desensitizing the carpometacarpal and middle carpal joints with subcarpal analgesia is present, as is the potential for diffusion from intra-articular analgesia, and should be considered when evaluating horses with lameness in this region.

SPECIFIC INJURIES

Magnetic resonance imaging allows evaluation of both the soft tissues and osseous structures in this region, including evaluation of the origin and insertion of ligaments. Abnormalities can be observed in the suspensory ligament, including its origin on the proximal third metacarpal/metatarsal bone, body, branches and insertion on the proximal sesamoid bones. The entire length of the ALDDFT can be evaluated, with damage potentially being detected in the proximal part of the ligament; an area that can be difficult to evaluate with ultrasonography. Proximal flexor tendon injuries and the relationship of the suspensory ligament to the axial surface of the second and fourth metacarpal/metatarsal bones can also be evaluated, along with interosseous ligament injury. In addition, the presence and type of osseous pathology in the second, third and fourth metatarsal bones may be determined using MRI.

Suspensory ligament

Injury to the suspensory ligament (SL) can take place at any site along the ligament's length. The proximal third of the ligament has been described as

a common site for injury in horses [2]. MR imaging allows evaluation of the suspensory ligament, its distal attachment to the proximal sesamoid bones and its proximal attachment primarily to the third metacarpal/metatarsal bone. The MR appearance of the normal suspensory ligament is described in Chapter 7. This section will discuss the MR appearance of injuries of the suspensory ligament with particular emphasis on the proximal portion.

MR abnormalities in the SL are commonly characterized by an increase in signal and/or size of the ligament (Figure 14.2). There can also be a decrease in signal of the normal muscle tissue of the ligament (Figure 14.3).

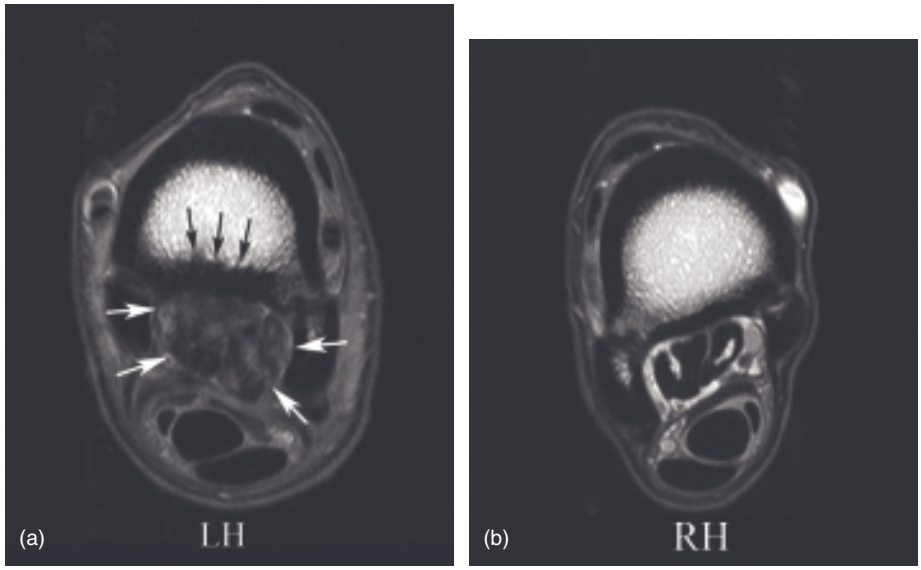

Figure 14.2 (a) Transverse high-field proton density image of a horse with severe enlargement and abnormal high signal intensity in the left hind limb proximal suspensory ligament (white arrows). At the suspensory attachment to the third metatarsal bone this horse also has reduced signal intensity on T1, T2 and proton density images with endosteal irregularity (black arrows). The normal right hind limb (b) is shown for comparison.

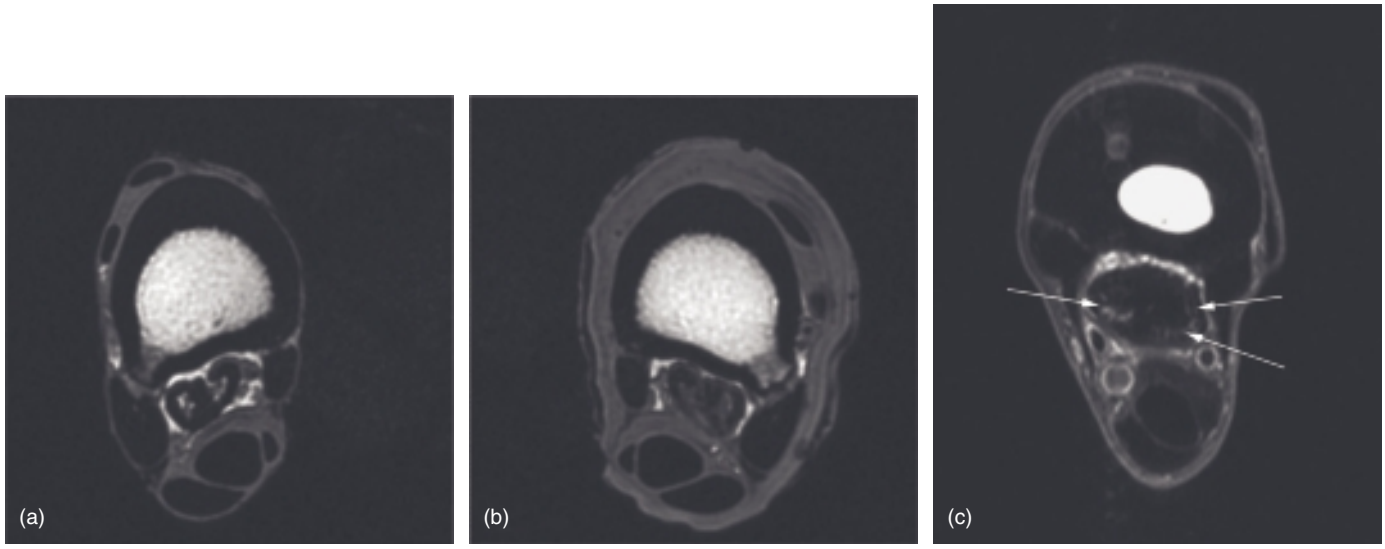

Figure 14.3 (a, b) Transverse high-field T1 gradient-echo images of the proximal metatarsal region in a horse with chronic unilateral proximal suspensory damage and low-grade lameness. In the normal limb (a) there is clear definition of the muscular and ligamentar tissues with high signal intensity in the muscle. In the abnormal limb (b) the suspensory ligament is enlarged with decreased signal intensity within the muscle tissue and loss of some clarity of the margin between the muscular and ligamentar tissues. These findings are characteristic of chronic damage and scarring. (c) Transverse high-field proton density image of a different horse with marked enlargement of the forelimb suspensory ligament with decreased signal intensity of the muscular tissue (arrows).

The transverse proton density (PD) weighted images are useful in detecting enlargement and abnormal morphology of the PSL, although use of T2-weighted and STIR sequences may be particularly useful to detect the presence of fluid and a comparison of T1-, T2- or T2*-weighted and STIR images may give a guide to the relative presence of muscular tissue, fluid-based and structural pathology. Due to the normal variation of the high signal suspensory ligament muscle fibres, systematic comparison with the contralateral limb is important to identify mild signal changes (Figures 14.4 and 14.5).

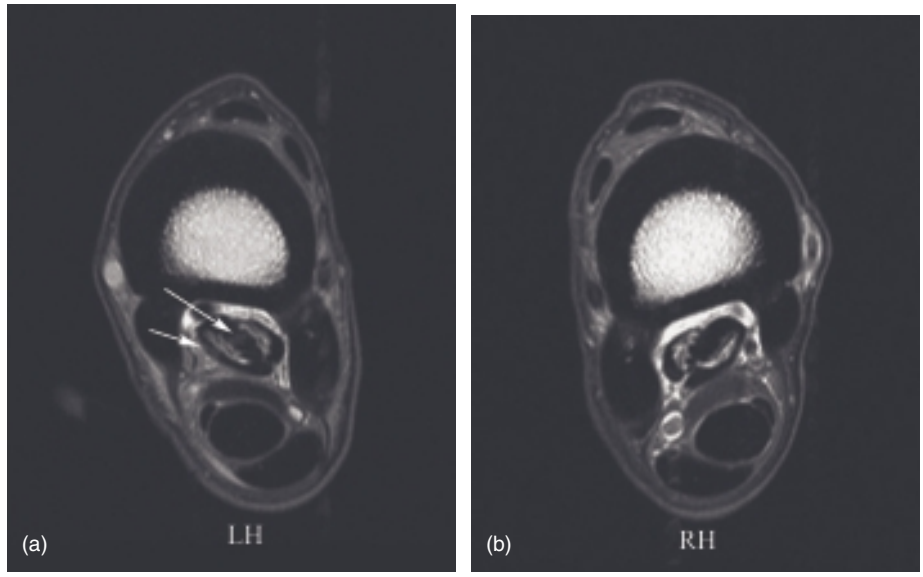

Figure 14.4 Left hind (a) and right hind (b) transverse high-field proton density images of a horse with subtle increased signal intensity within the left hind proximal suspensory ligament (arrows). This illustrates the importance of contralateral limb comparison for subtle injuries.

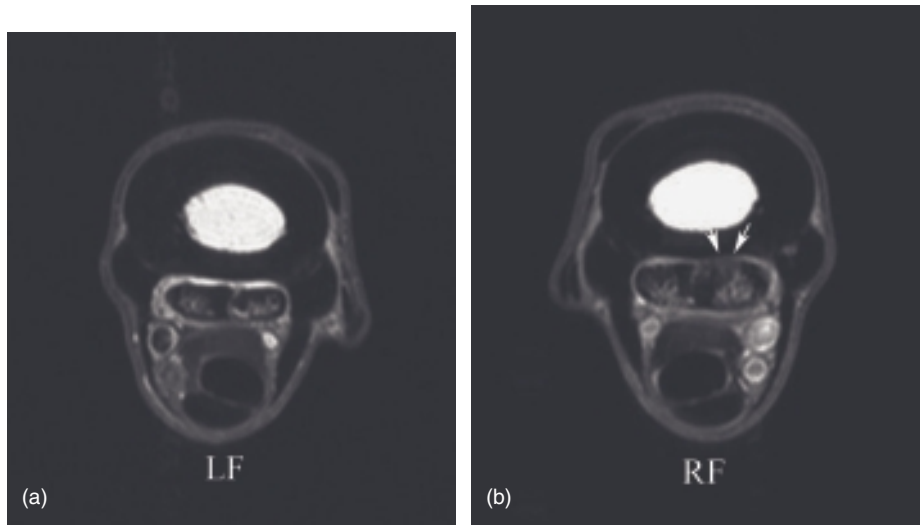

Figure 14.5 Left (a) and right (b) fore transverse high-field proton density images of a horse with a focal region of increased signal intensity in the dorsal aspect of the right fore proximal suspensory ligament (arrows).

The degree of damage to the SL is based on signal intensity, size and loss of distinct borders of the ligament. In a recent study conducted at the authors' institution [27], the majority of the horses with forelimb proximal suspensory desmitis noted on MR had regions of high signal and enlargement present within the ligament (Figure 14.6). There was one horse that did have enlargement with a decrease in the normal high signal of the muscle fibres within the forelimb PSL on all sequences with irregularity of the ligament's borders. This finding has also been observed in subsequent cases imaged at the authors' institution (Figure 14.3). In the hind limb, we have identified some horses with only enlargement of the ligament without evidence of increased signal intensity. We have also found that, in general, the MR lesions in the hind limb PSL were subjectively milder than those in the forelimb; nine out of 13 horses were subjectively graded as mild [27] (Figures 14.7 and 14.8).

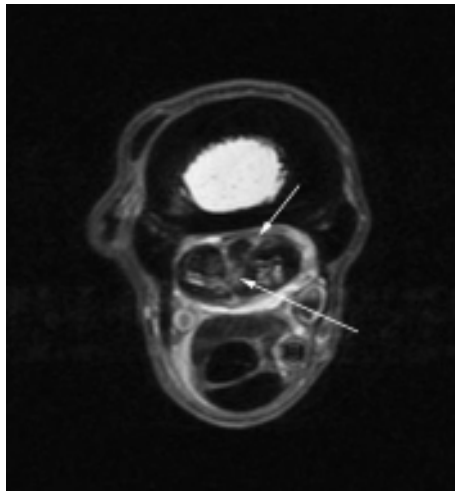

Figure 14.6 Transverse high-field proton density image of a horse with enlargement and increased signal intensity (arrows) of the forelimb proximal suspensory ligament.

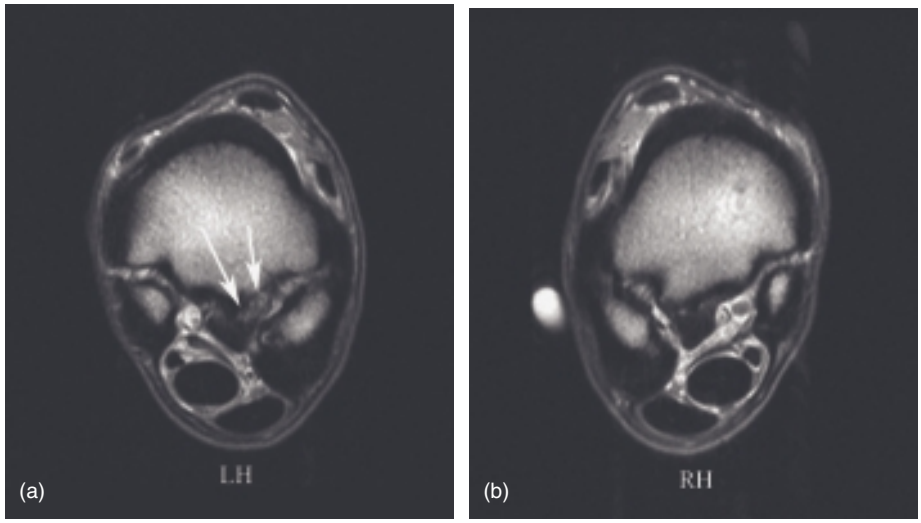

Figure 14.7 Left hind (a) and right hind (b) transverse high-field proton density images of a horse with increased signal intensity in the left hind proximal suspensory ligament (arrows).

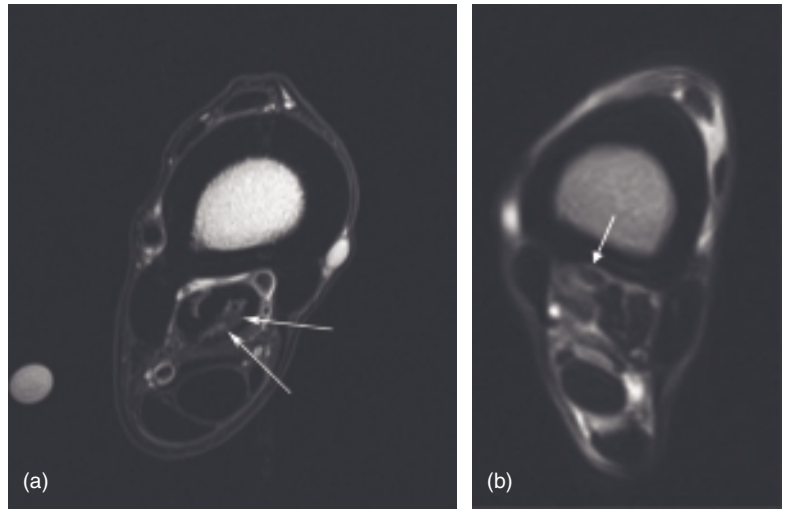

Figure 14.8 Damage to a single lobe of the suspensory ligament. (a) Transverse high-field proton density image of a horse with mild increased signal intensity in the medial aspect of the hind limb proximal suspensory ligament (arrows). (b) Transverse low-field T1-weighted image of the proximal metatarsal region obtained standing in a horse with damage to the medial lobe of the suspensory ligament (arrow) seen as generalized increase in signal intensity, loss of normal architecture and increased size.

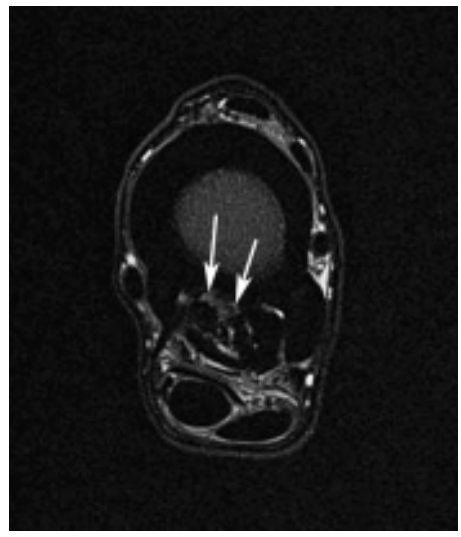

Figure 14.9 Transverse high-field STIR image of a horse with increased signal intensity in the hind limb proximal suspensory ligament indicating damage to the ligament (arrows).

Normal ligaments are characterized by lower signal on all MR sequences; an increase in signal intensity occurs in areas of ligamentous damage (Figure 14.9). In horses, increased tendon or ligament signal has been shown to represent increased cellularity and vascularity [34]. High signal in abnormal superficial digital flexor tendons has been shown to be due to haemorrhage along with fibre pattern disruption, hyperplastic granulation tissue, immature collagen and hypercellularity [24, 35]. The exact cause of increased signal in the damaged equine SL has not been documented. Horses with a decrease in the normal muscle tissue signal within the PSL with ligamentous

enlargement most likely indicates a chronic injury that has been replaced with mature scar tissue [24, 35, 36]. A chronic, scarred ligament may be difficult to distinguish from a healed ligament because the signal intensity will be similar [36]. This fact emphasizes the careful and systematic examination of both limbs as an internal comparison to detect subtle differences on MR images (Figure 14.3).

Although enlargement may be present in many horses, measurements, both thickness and cross-sectional area, do not, at this time, always allow abnormal ligaments to be detected from the normal population. The large variation in horse size does not allow clear limits to be established for these parameters at this time. Normal thickness of the PSL in a Warmblood breed, for example, is outside of the range of normal for Quarter Horses. As important, there is a large variation in ligament size even within individuals of the same breed [19].

Proximal suspensory ligament origin

Horses can have damage to the proximal suspensory ligament alone or in combination with osseous pathology at the ligament's origin. In addition, we have also identified horses with primary osseous injury at the origin of the PSL with little or no ligamentous pathology. In horses with osseous injury, the palmar/plantar medullary cavity and endosteum of the third metacarpal/metatarsal bone have low signal intensity on PD-, T1- and T2-weighted sequences and/or high signal intensity on the fat-suppressed sequences with high signal intensity possibly with a margin of low signal intensity on T2* gradient-echo images if there is phase cancellation artefact (Figures 14.10 and 14.11).

The transverse PD-, T2- and T2*-weighted sequences are helpful in identifying abnormal low signal (sclerosis) in the third metacarpal/metatarsal bone at the PSL attachment (Figure 14.12). Low signal on PD-, T1- and T2-weighted images in the third metacarpus/metatarsus at the PSL attachment may indicate increased bone density and may be a sign of chronic injury [37] (Figure 14.13). In a recent study, low signal at the attachment

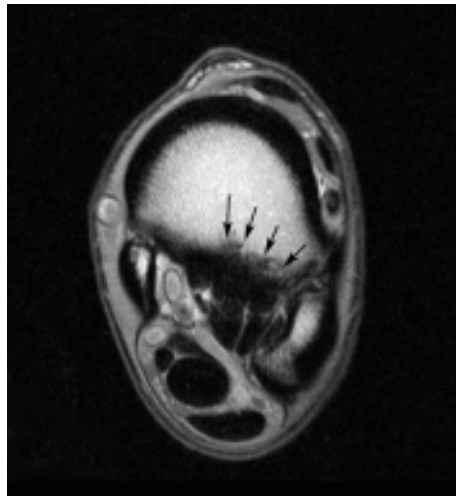

Figure 14.10 Transverse high-field proton density image of a horse with enlargement of the hind limb proximal suspensory ligament and concurrent low signal intensity (sclerosis) in the third metatarsal bone (arrows).

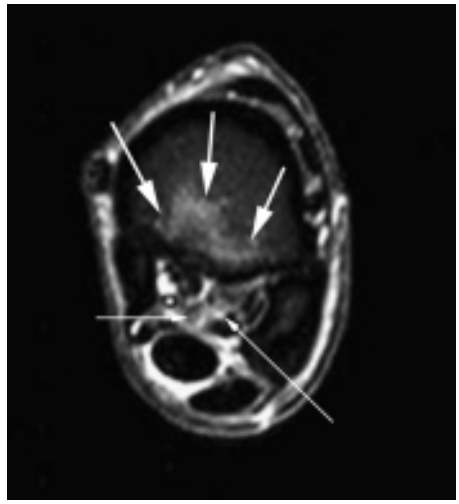

Figure 14.11 Transverse high-field STIR image of a horse with an abnormal amount of high signal in the proximal third metatarsal bone at the proximal suspensory ligament attachment (large arrows). There is also damage to the proximal suspensory ligament in the same region (smaller arrows).

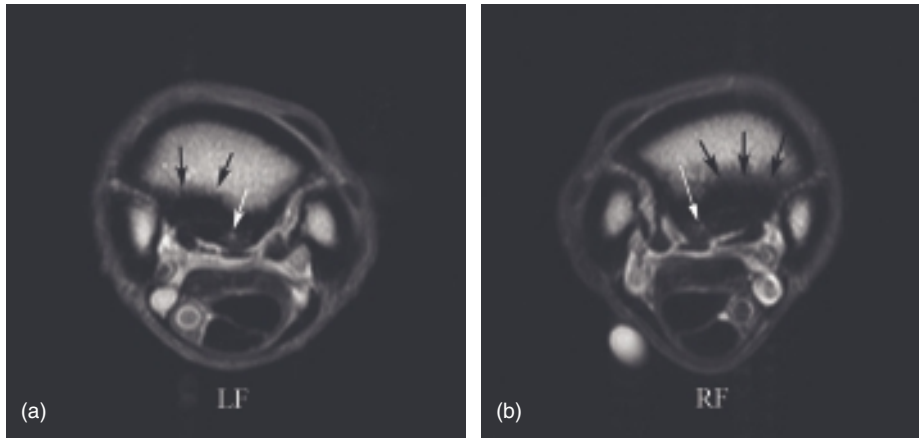

Figure 14.12 Left front (a) and right front (b) transverse high-field proton density images of a horse with bilateral proximal suspensory desmitis. There is increased signal intensity within the ligament (white arrows) as well as reduced signal intensity in the third metacarpal bone at the suspensory attachment (black arrows).

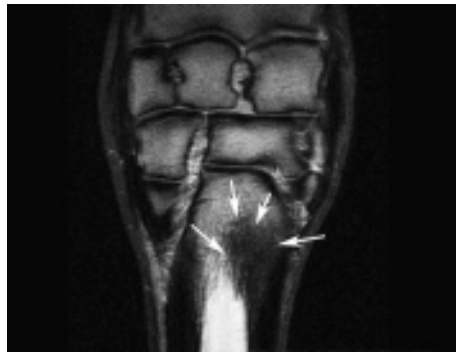

Figure 14.13 Dorsal high-field proton density image of the same horse in Figure 14.12 illustrating the low signal intensity present in the third metacarpal bone at the proximal suspensory attachment (arrows).

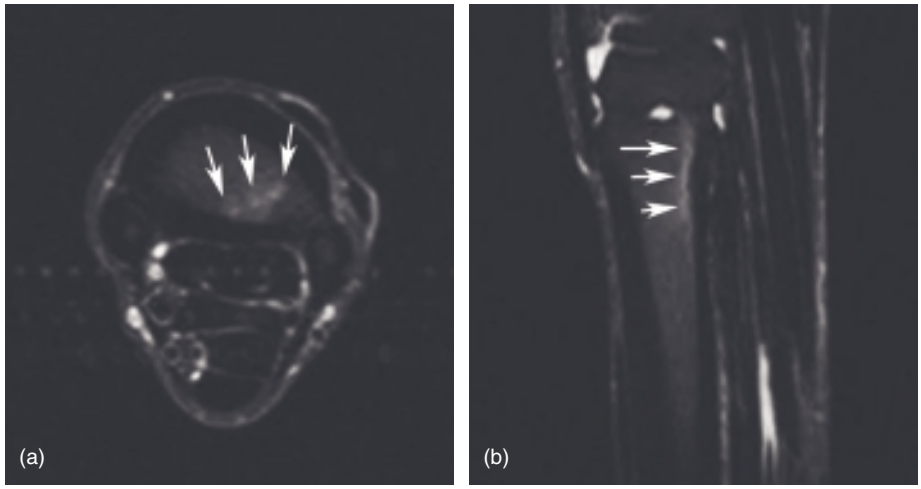

Figure 14.14 Transverse (a) and sagittal (b) high-field STIR images of a horse with increased signal in the third metacarpal bone in the region of the proximal suspensory ligament attachment (arrows). There is also mild increased signal intensity and enlargement within the suspensory ligament.

of the PSL was more common in the forelimb than the hind limb (6 of 10 horses with forelimb PSL desmitis) [27]. Three of these horses also had high signal intensity in this area on fat-suppressed sequences. In horses doing fast work (including race, endurance and cutting horses) presented for MRI soon after lameness has been detected, increased signal intensity on fat-suppressed images in the palmar third metacarpal bone in the region of the origin of the suspensory ligament may be a more frequent finding (Edmonds P *et al*., personal communication, 2009) [38]. In comparison, five of 13 horses with PSL desmitis in the hind limb had low PD signal at the PSL attachment to the third metatarsal bone. Only one of these horses had high signal present on fat-suppressed sequences at the attachment of the PSL to the third metatarsal bone.

The fat-suppressed sequences are most useful in identifying high signal within the bone at the PSL attachment (Figure 14.14). When horses are imaged standing, if STIR images cannot be obtained, use of T2* gradient-echo sequences can be useful in detection of fluid due to the patterns seen in relation to fat–water phase cancellation artefact. The high signal present on fat-suppressed sequences in the third metacarpus/metatarsus at the PSL attachment is most likely due to the bone's response to tearing of the PSL fibre insertions (Sharpey's fibres). The damaged bone will then have high signal indicative of fluid, inflammation or oedema. This bone oedema or bone contusion has not been studied histologically at the PSL attachment in horses, but previous studies of other anatomic areas describe microfractures of trabecular bone, haemorrhage, bone marrow fibrosis and necrosis, and accumulation of extracellular fluid [34, 36, 39, 40]. The higher signal may also indicate a more acute injury to the PSL attachment. In our study [27], four of five horses with high signal within the proximal metacarpus/metatarsus had lameness less than 2 months in

duration. Bone injuries in this location have been previously recognized with nuclear scintigraphy [41], and reportedly correlate well with MR findings [2].

Some horses that have high signal in the proximal third metacarpus/metatarsus on fat-suppressed sequences will also have low signal intensity on the PD-weighted and T2-weighted image sequences. In these horses, the low signal may represent osteonecrosis and fibrosis [34] during the early stages of injury. Injury to the ligament and its osseous attachment may indicate different aetiologies in these horses, which may influence the treatment that is prescribed. Specific treatments for injuries identified in the metacarpal/metatarsal region will be discussed in Chapter 22.

Suspensory ligament adhesions to the second and fourth metacarpal/metatarsal bones

MR examination of the metacarpal region allows clear visualization of the axial surface of the second and fourth metacarpal/metatarsal bones and their relationship with the SL [16] (Figure 14.15). Exostoses involving the splint bones are common in horses and can be the result of direct trauma or secondary to desmitis of the interosseous ligament, which connects the splint bones to the third metacarpal/metatarsal bone. Ultrasonography of the SL in the area of an exostosis can be difficult due to the inability to maintain surface contact and acoustic shadowing caused by mineralization and refraction artefacts caused by the margins of the splint bones, flexor tendons and vasculature [16].

Magnetic resonance imaging allows accurate evaluation of the splint bones and regions of desmitis in the SL associated with adhesions (Figure 14.16). The MR appearance of adhesions between the SL and the splint bones in the metacarpal region has been described in a report of four horses [16].

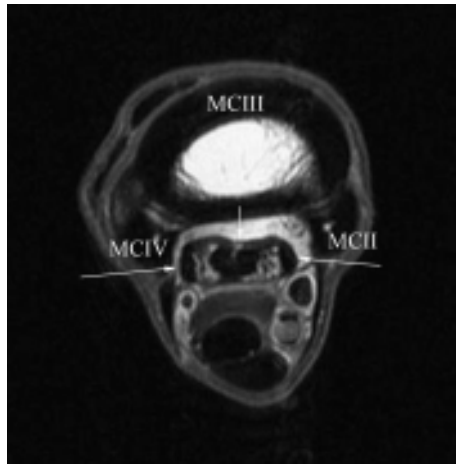

Figure 14.15 Transverse high-field proton density image of the proximal metacarpal region illustrating the normal appearance of the second and fourth metacarpal bones (MCII and MCIV) and the normal high signal intensity border of the suspensory ligament (arrows). (MCIII) Third metacarpal bone.

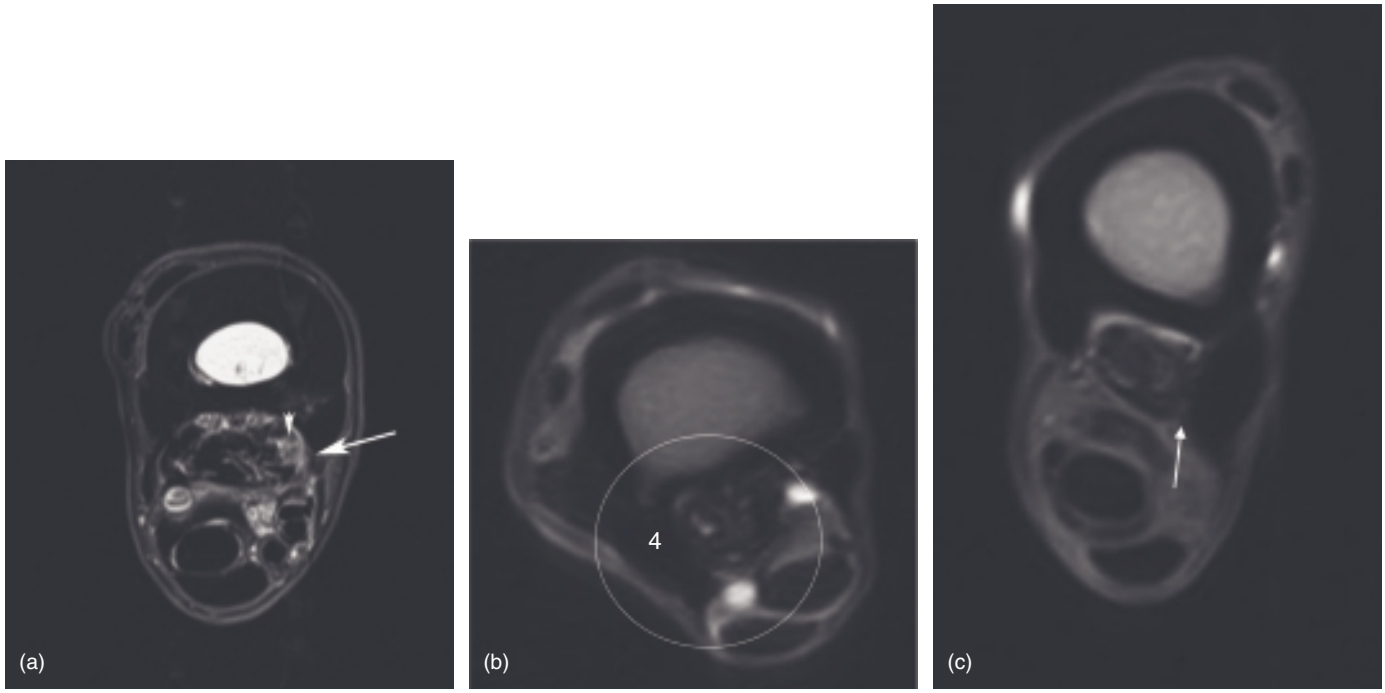

Figure 14.16 Adhesions between the suspensory ligament and small metacarpal/metatarsal bones. (a) Transverse high-field proton density image of a horse with an adhesion of the medial aspect of the suspensory ligament to the second metacarpal bone (large arrow). Adjacent to the adhesion, there is abnormal high signal intensity within the suspensory ligament indicating desmitis (small arrow). There is flow artefact from the medial metacarpal artery contributing to the increased signal. (b) Transverse low-field T2* gradient-echo images of the metatarsal region obtained standing. There is damage to the lateral lobe of the suspensory ligament with marked enlargement and loss of normal architecture, and marked adhesion formation between the ligament and the fourth metatarsal bone (circle). There is a reactive exostosis of the fourth metatarsal bone that had increased signal intensity on STIR images. **4**, fourth metatarsal bone. (c) Transverse low-field T2* gradient-echo images of the metatarsal region obtained standing in a different horse. There is a mild adhesion (arrow) between the abnormal suspensory ligament and the fourth metatarsal bone. There was enlargement and heterogeneous increase in signal intensity in the lateral lobe of the suspensory ligament further proximally.

The suspected cause of the suspensory desmitis is the adhesion of the SL to the exostosis. The adhesion results in tearing of the ligamentous fibres leading to inflammation and lameness. This is illustrated by the fact that the high signal within the SL extends distally from the site of the adhesion because the ligament is loaded from distal to proximal. Several horses do have exostoses present on the abaxial border of the splint bones and these are the most noticeable on palpation but, due to their location, are not associated with the SL (Figure 14.17). It is the axial proliferation of the splint bones that are involved with adhesions and the size of this proliferation does not seem to correlate with lameness or the presence of adhesions to the SL (Figures 14.18 and 14.19). In a recent report, the second metacarpal exostoses were all considered to be small on the basis of palpation and radiography [16].

The SL has a clearly defined, high signal connective tissue border throughout its length in the metacarpus/metatarsus (Figure 14.15). The MR appearance of a splint bone adhesion is characterized by low signal interruption of the normal high signal border of the suspensory ligament (Figure 14.20). Adjacent to this adhesion, the SL will have varying degrees of high signal within the ligament, indicative of damage, and may also be thickened at this location (Figure 14.16).

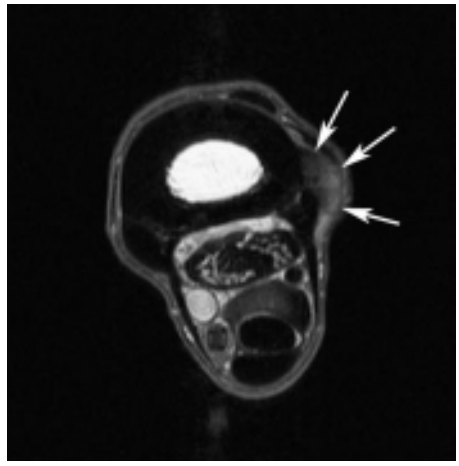

Figure 14.17 Transverse high-field proton density image of a horse with exostosis on the abaxial margin of the fourth metacarpal bone (arrows). The exostosis has a higher signal intensity than the normal low signal intensity of the fourth metacarpal bone, indicating poorly organized bone with some disruption of the overlying soft tissues.

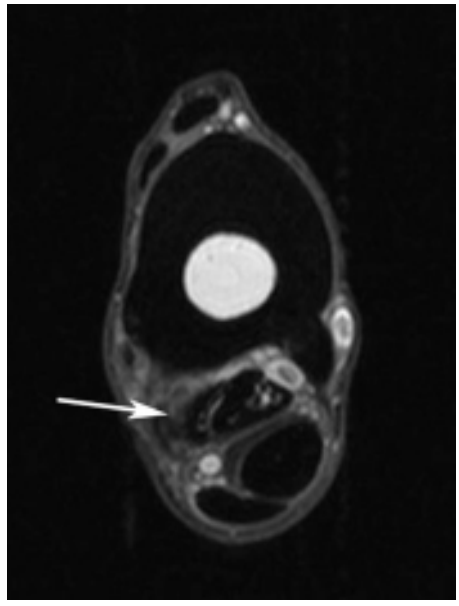

Figure 14.18 Transverse high-field proton density image of a horse with an adhesion between the suspensory ligament and a small fourth metatarsal bone exostosis (arrow).

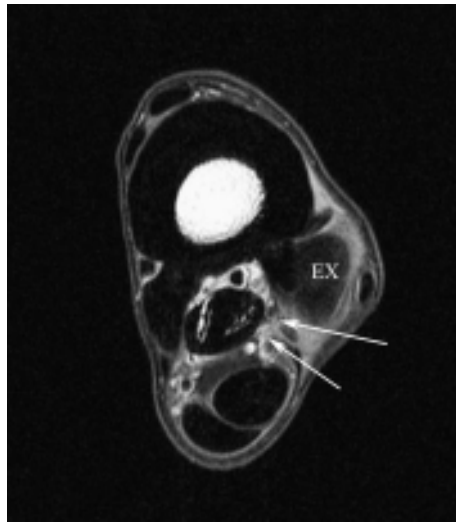

Figure 14.19 Transverse high-field proton density image of a horse with a large exostosis of the second metatarsal bone (EX) and an adhesion to the plantaro-medial aspect of the suspensory ligament (arrows).

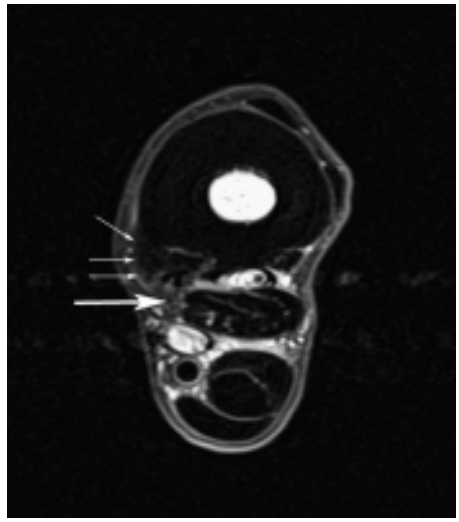

Figure 14.20 Transverse high-field proton density image of a horse with an adhesion from the second metacarpal bone to the suspensory ligament (large arrow). This horse also has an abaxial exostosis of the second metacarpal bone (small arrows).

ALDDFT

In a recent study evaluating horses with lameness localized to the proximal metacarpal region with diagnostic local analgesia and that had MRI performed, the most common MR finding was desmitis of the ALDDFT [27]. This is in contrast to previous reports that do not mention desmitis of the ALDDFT when discussing pathologic processes in the proximal metacarpal region [2]. Another report by Dyson [10], discusses ALDDFT desmitis in which the region was localized primarily by palpation and all injuries were diagnosed with ultrasound. This illustrates the utility of MRI for detection of subtle lesions before they can be detected via palpation or are present sonographically.

The normal ALDDFT has clear margins and homogenous low signal on all sequences. However, as the forelimb ALDDFT extends more proximal to its third carpal bone attachment, the overall signal intensity increases to intermediate signal. This change in signal intensity occurs approximately at the level of the PSL attachment to the third metacarpal bone. Injury to the ALDDFT is characterized on MR images by abnormal signal, enlargement and/or irregularity of the border of the ligament (Figure 14.21). The transverse PD-weighted sequences are most useful in determining alterations in signal and shape of the ALDDFT. The PD-weighted sequences provide good anatomic detail of the ALDDFT with minimal interference from vessel flow artefact. Comparison with the contralateral limb allows detection of subtle changes in signal and size of the ALDDFT (Figures 14.22 and 14.23). In the horses with ALDDFT injuries that we have imaged, all have had enlargement and abnormal high signal in part of the ligament (Figure 14.24).

Previous reports discuss that ALDDFT injuries were primarily in the distal aspect of the ligament [10]. With MRI, we have found that in the majority of horses with damage to the ALDDFT, the damage is localized to

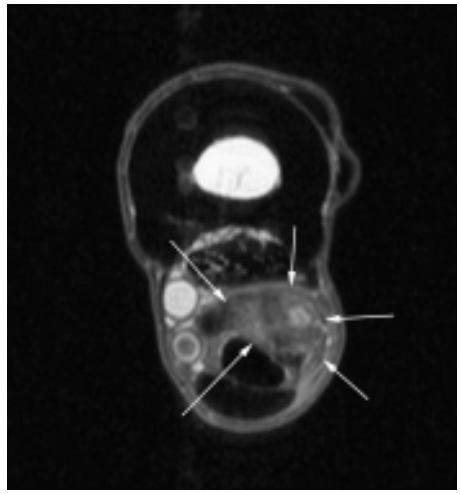

Figure 14.21 Transverse high-field proton density image of a horse with severe enlargement and high signal intensity in the accessory ligament of the deep digital flexor tendon of the proximal metacarpal region (arrows).

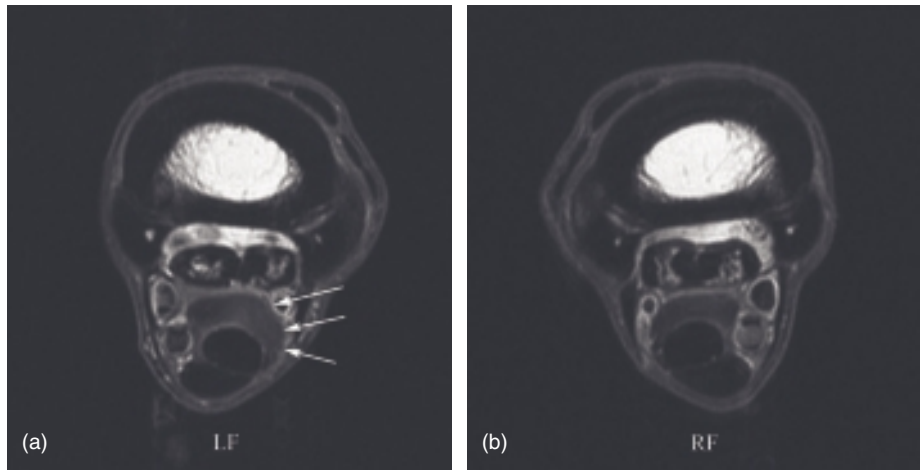

Figure 14.22 Left front (a) and right front (b) transverse high-field proton density images of a horse with subtle enlargement and increased signal in the lateral aspect of the accessory ligament of the left deep digital flexor tendon (arrows).

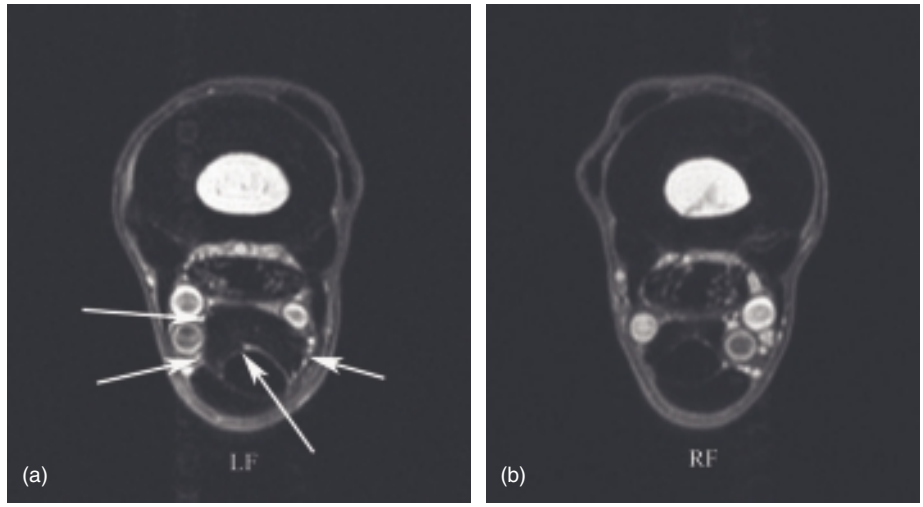

Figure 14.23 Left front (a) and right front (b) transverse high-field proton density images of a horse with enlargement of the accessory ligament of the left deep digital flexor tendon (arrows). Just proximal to this region of enlargement, there was abnormal high signal intensity in the ligament. These images illustrate the importance of contralateral limb comparison for evaluation of this anatomic region.

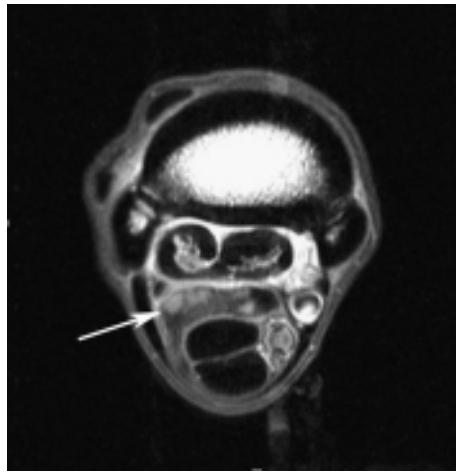

Figure 14.24 Transverse high-field proton density image of a horse with enlargement and abnormal high signal intensity (arrow) within the accessory ligament of the deep digital flexor tendon in the proximal metacarpal region.

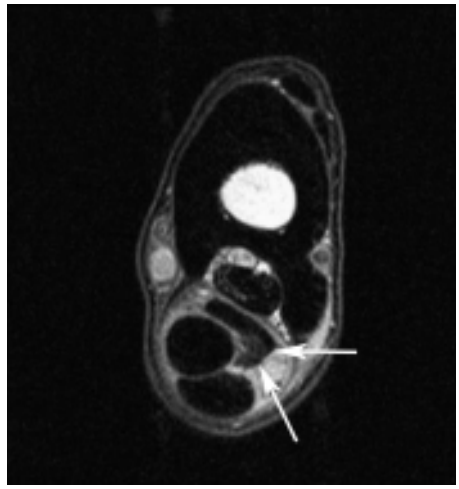

Figure 14.25 Transverse high-field proton density image of a horse with enlargement and abnormal high signal intensity (arrows) within the hind limb accessory ligament of the deep digital flexor tendon.

the proximal portion of the ligament [27] (1–4 cm distal to the carpometacarpal joint), an area that is difficult to evaluate with ultrasound.

A recent report by Dyson discusses injury to the hind limb ALDDFT [42]. This condition is much less common than in the forelimb and the MR appearance of this injury has not been officially documented but has been observed by the authors in some horses (Figure 14.25). Dyson describes two clinical manifestations of hind limb ALDDFT injury: acute onset lameness and postural abnormalities. The acute onset lameness cases would appear to most likely benefit the most from MRI. As for the forelimb ALDDFT, injury to the hind limb ALDDFT causes enlargement and increased signal within the ligament.

Horses with desmitis of the ALDDFT must be differentiated from horses with proximal suspensory desmitis or injury of the attachment of the PSL to the third metacarpal/metatarsal bone. This is important because making a specific diagnosis allows appropriate treatment recommendations for individual horses (see Chapter 22).

Interosseous ligament injury

Damage to the articulation between the second and third, or third and fourth metacarpal or metatarsal bones may be seen on MRI as irregularity of the periosteal and/or endosteal aspects of the cortex and enthesiophyte formation at the origin and insertion of the interosseous ligaments (Figure 14.26). Where there is synostosis further distally, in horses with pain localized to this area there may be cortical and ligamentar irregularity further proximally, often with increased signal intensity on fat-suppressed images. Syndesmopathy is not uncommonly observed in the medial interosseous ligament and articulation between the second and third metacarpal bones of endurance and race horses with lameness localized to this region, with or without concurrent proximal palmar metacarpal bone pathology or bruising (Figure 14.27). In some cases, there may be an apparent incomplete fracture surrounded by sclerotic-type bone, extending into the third metacarpal bone from the articulation.

Osseous injury

There have been some horses that respond to proximal metacarpal/metacarpal analgesia that have osseous abnormalities not associated with the PSL attachment. These include bone injury to the proximal splint bones [26], proximal third metacarpal/metacarpal bone (Figure 14.28), proximal third metacarpal

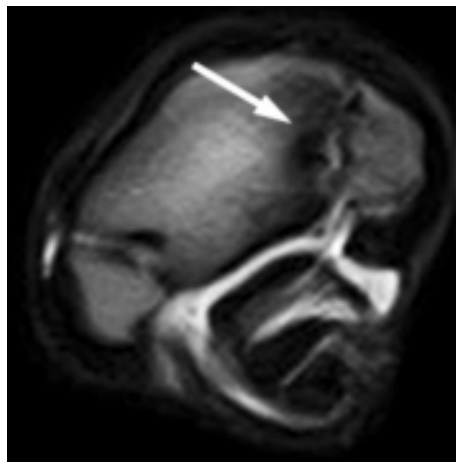

Figure 14.26 Transverse T2* gradient-echo low-field image of the proximal metacarpus obtained standing in a horse with pain localized to this region. There is evidence of medial metacarpal interosseous ligament injury (arrow) seen as irregularity of the endosteal and periosteal aspects of the cortex at the origin and insertion of the ligament, along with loss of normal ligament architecture.

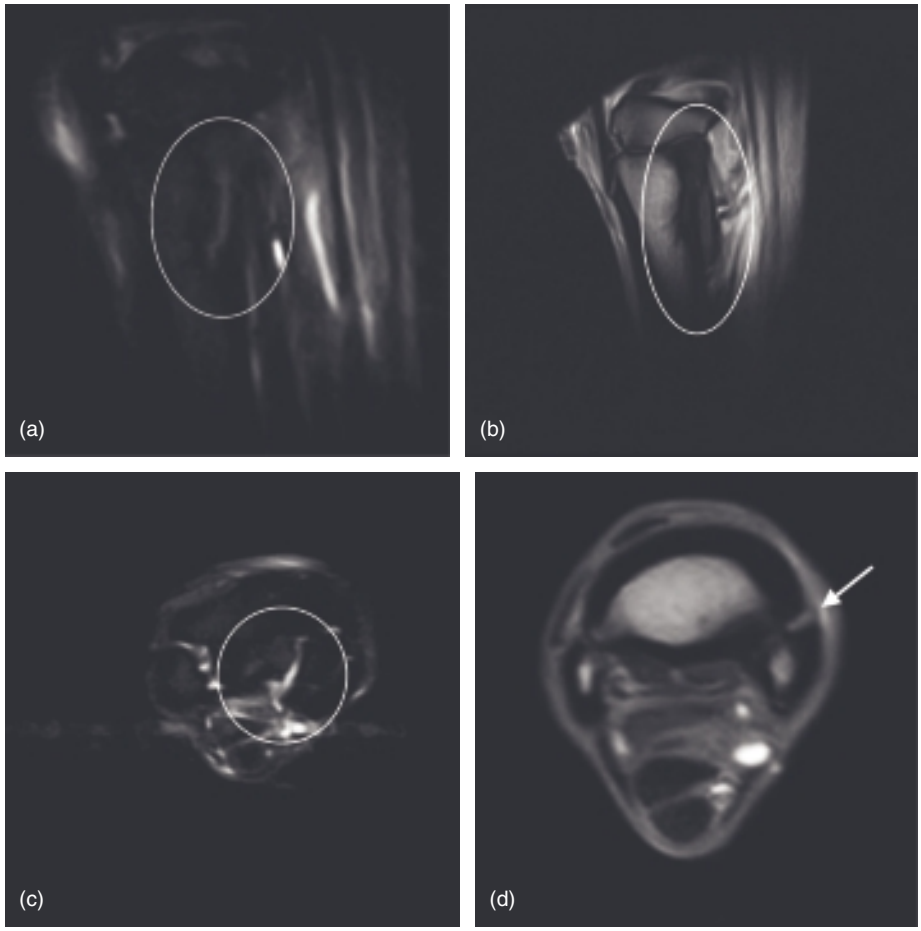

Figure 14.27 (a) Sagittal STIR, (b) sagittal T2* gradient-echo (GRE), (c) transverse STIR and (d) transverse T1 GRE MR images obtained standing in a 12-year-old Arabian endurance horse with a 1-month history of lameness. There is evidence of bone trauma (circle) in the palmar medial aspect of the third metacarpal bone and its articulation with the second metacarpal bone, seen as high signal intensity on STIR images and high signal intensity with a hypointense margin on T2* GRE images due to the fat–water phase cancellation artefact. Image (d) shows there is concurrent medial syndesmopathy located further distally (arrow). This horse also had mild proximal suspensory desmitis affecting the medial lobe.

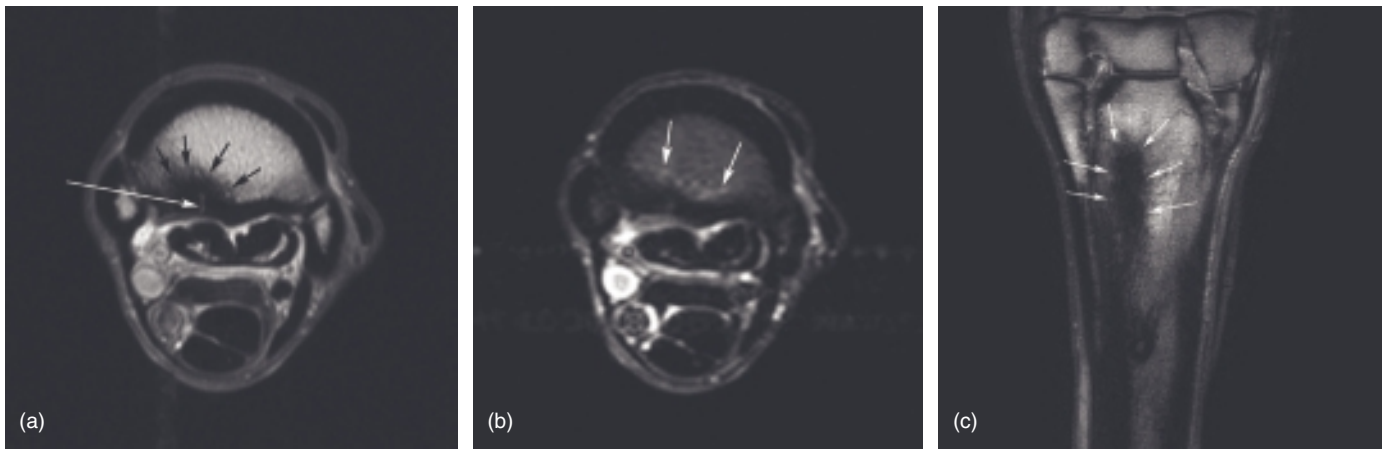

Figure 14.28 Transverse high-field proton density (a), STIR (b), and dorsal proton density images (c) of a horse with low signal intensity on proton density-, T1- and T2-weighted images and high signal intensity on fat-suppressed images within the palmar aspect of the third metacarpal bone. There is a high signal intensity line in the palmar aspect of the third metacarpal bone (white arrow in image (a)) suggestive of a fracture of the palmar cortex.

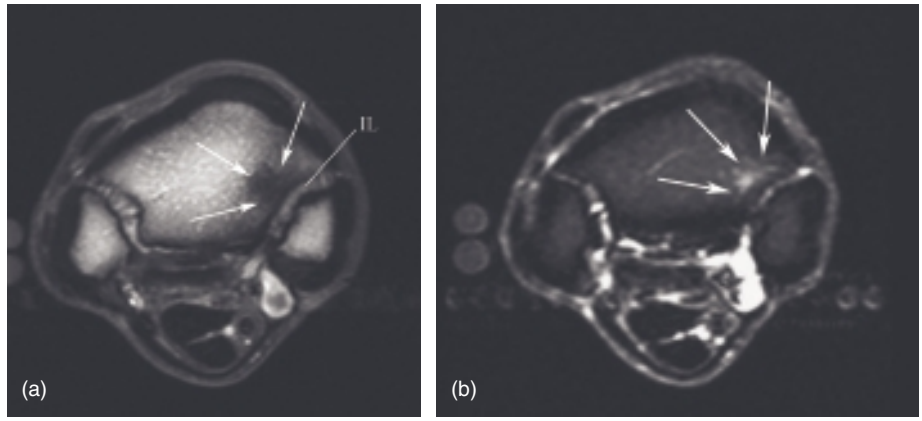

Figure 14.29 Transverse high-field proton density image (a) of a horse with low signal intensity in the region of the interosseous ligament in the proximal third metacarpus (arrows). Transverse STIR image (b) of the same horse with abnormal high signal in the proximal third metacarpal bone corresponding to the region of low signal intensity on the proton density sequence (arrows).

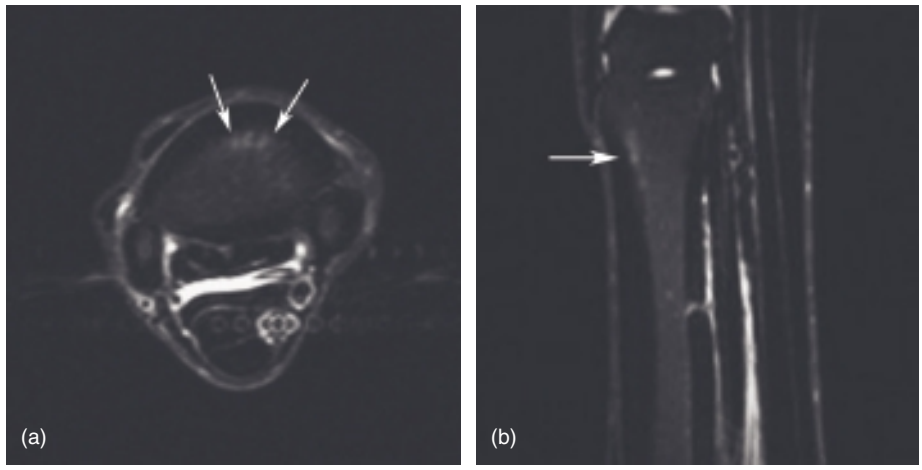

Figure 14.30 Transverse (a) and sagittal (b) high-field STIR images of a horse with abnormal high signal intensity in the proximal third metacarpal bone (arrows). The horse was used for jumping and trauma was suspected as the most likely cause.

bone in the region of interosseous ligament [27] (Figure 14.29) and dorsal third metacarpal/metatarsal bone [26] (Figure 14.30). The exact cause of some of these lesions is unknown but is most likely due to trauma.

In horses undergoing strenuous fast exercise, including endurance, racing and cutting horses, it is not uncommon to detect proximal palmar metacarpal bone pathology proximal to, at, and distal to the origin of the suspensory ligament [41–43]. In a series of 50 endurance horses undergoing low-field MRI, 21% had proximal palmar metacarpal osseous pathology. Of these, 81% had evidence of bone bruising/trauma with increased signal intensity on STIR and T2-weighted images, decreased signal intensity on T1-weighted images and increased signal intensity with a hypointense rim (due to fat–water cancellation artefact) on T2* gradient echo (GRE) images from the standing Hallmarq system. Other than bone bruising, 9% had evidence

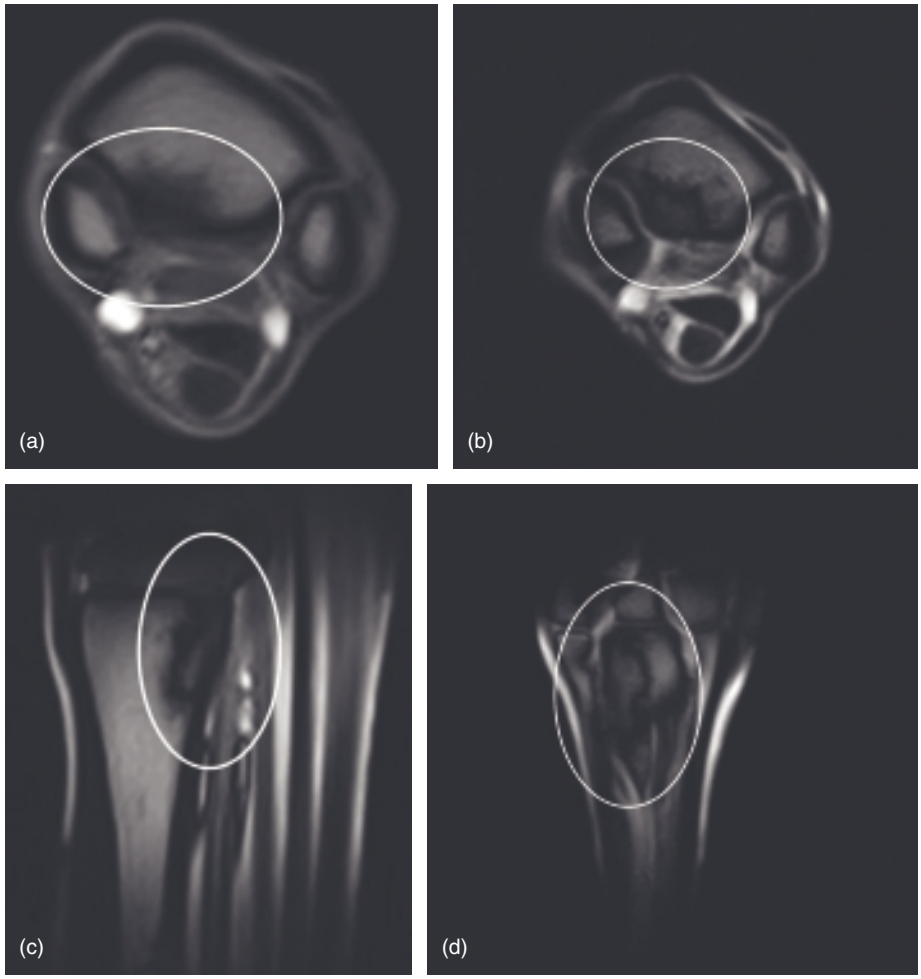

Figure 14.31 (a) Transverse T1-weighted, (b) transverse T2* gradient-echo (GRE), (c) sagittal T2* GRE and (d) dorsal T2* GRE MR images obtained standing in a 10-year-old Arabian endurance horse with grade 4/5 lameness and pain on palpation in the region of the medial origin of the suspensory ligament. There is decreased signal intensity on T1-weighted images, with increased signal intensity on T2* images in the palmaromedial aspect of the third metacarpal bone. The hypointense margin on T2* GRE images is due to a fat–water cancellation artefact.

of incomplete fracture and 10% had other lesions [43]. Damage is more frequently located on the medial aspect of the metacarpus, and may be seen in conjunction with medial interosseous ligament pathology. In the series of endurance horses reported, 62% of pathology involved the medial aspect, 29% medial and lateral, and 9% only involved the lateral aspect. A similar pattern appears to be seen in young racehorses [38]. This severe bone bruising-type change on MRI is often associated with an acute onset, moderate to severe lameness that improves with subcarpal analgesia, with or without SL damage or pain on palpation of the area (Figures 14.27 and 14.31). A more chronic, low-grade history of lameness appears more likely to be associated with lower signal intensity on fat-suppressed images, but there may be cortical thickening, periosteal and/or endosteal irregularity. These changes may also be associated with changes in the SL or interosseous ligament(s) (Figure 14.27).

Flexor tendons

Injuries to the flexor tendons in the metacarpal/metatarsal region are commonly diagnosed via palpation and ultrasonography. The use of MRI has been performed to evaluate horses with tendonitis of the superficial digital flexor tendon [24]. We have imaged a small number of horses with primary tendonitis of the deep or superficial digital flexor tendons in which the horses did not have clinical signs that would localize the injury to this anatomic area (Figures 14.32 and 14.33). These horses did respond to subcarpal/subtarsal analgesia. We have also noticed subtle tendonitis lesions in horses with more significant injuries to other structures in the area (i.e. PSL, ALDDFT).

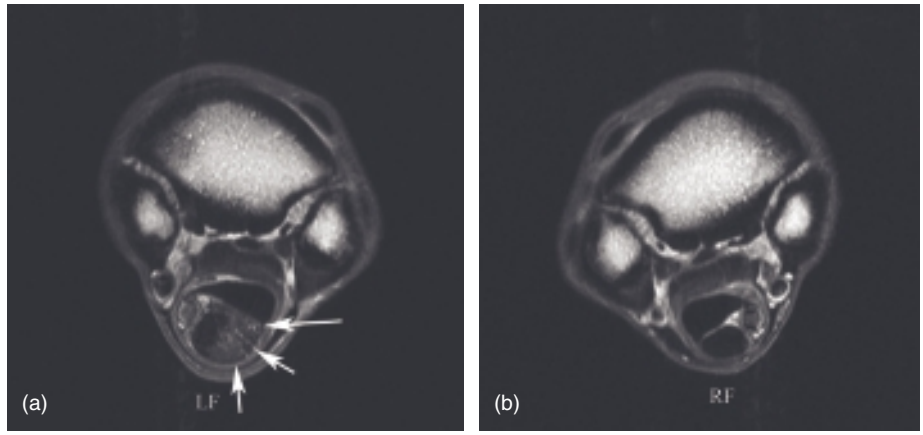

Figure 14.32 Left (a) and right (b) front transverse high-field proton density images of a horse with enlargement and increased signal intensity in the left front superficial digital flexor tendon (arrows). The area of injury is at the level of the attachment of the proximal suspensory ligament to the third metacarpal bone.

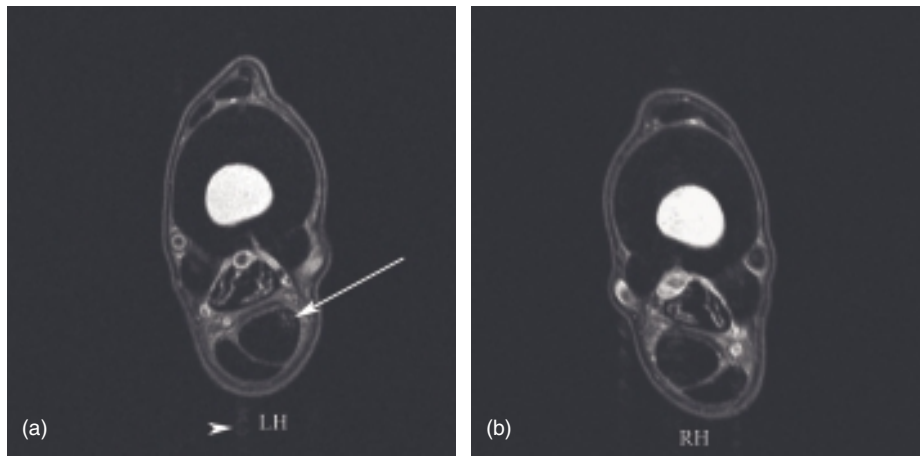

Figure 14.33 Left and right hind transverse high-field proton density images of a horse with subtle increased signal intensity in the left hind deep digital flexor tendon (arrow). Note the presence of the vessel flow artefact (arrowhead).

Negative findings

In a recent proceeding publication, the authors noted that 16% (4/25) of horses that were imaged with a high-field magnet in the proximal metatarsal region did not have any abnormalities [26]. We found that one horse out of 45 (2%) did not have significant MR findings in the proximal metatarsal region that would contribute to lameness [27]. The exact reason for this is unknown but it may be due to our inexperience to recognize subtle changes or confusing results from diagnostic analgesia. Further research in this region is warranted into the pathology and appearance of the proximal metacarpal/metatarsal region.

REFERENCES

[1] Dyson S. Some observations on lameness associated with pain in the proximal metacarpal region. *Equine Vet J* (*Suppl.*) 1988; **6**: 43–52.
[2] Dyson S. Proximal metacarpal and metatarsal pain: a diagnostic challenge. *Equine Vet Educ* 2003; **15**: 134–8.
[3] Bramlage LR, Gabel AA, Hackett RP. Avulsion fractures of the origin of the suspensory ligament in the horse. *J Am Vet Med Assoc* 1980; **176**: 1004–10.
[4] Booth TM. Proximal suspensory ligament desmitis with suspensory ligament avulsion fractures. *Equine Vet Educ* 2003; **15**: 132–3.
[5] Launois T, Desbrosse F, Perrin R. Percutaneous osteostixis as treatment for avulsion fractures of the palmar/plantar third metacarpal/metatarsal bone cortex at the origin of the suspensory ligament in 29 cases. *Equine Vet Educ* 2003; **15**: 126–38.
[6] Ross M, Ford T, Orsini P. Incomplete longitudinal fracture of the proximal palmar cortex of the third metacarpal bone in horses. *Vet Surg* 1988; **17**: 82–6.
[7] Dyson S. Proximal suspensory desmitis-clinical, ultrasonographic and radiographic features. *Equine Vet J* 1991; **23**: 25–31.
[8] Dyson S. Proximal suspensory desmitis in the hindlimb: 42 cases. *Br Vet J* 1994; **150**: 279–91.
[9] Dyson SJ, Arthur RM, Palmer SE, Richardson D. Suspensory ligament desmitis. *Vet Clin N Am: Equine Pract* 1995; **11**: 177–215.
[10] Dyson S. Desmitis of the accessory ligament of the deep digital flexor tendon: 27 cases (1986–1990). *Equine Vet J* 1991; **23**: 438–44.
[11] McDiarmid A. Eighteen cases of desmitis of the accessory ligament of the deep digital flexor tendon. *Equine Vet J* 1994; **6**: 49–56.
[12] Peterson R, Pascoe J, Wheat J. Surgical management of proximal splint bone fractures in the horse. *Vet Surg* 1987; **16**: 367–72.
[13] Reef V, Sertich P, Turner R. Musculoskeletal ultrasonography. In: Reef VB (ed.) *Equine Diagnostic Ultrasound*. Philadelphia, PA: WB Saunders, 1998, pp. 39–187.
[14] Genovese R, Rantanen N. The deep digital flexor tendon, carpal sheath, and accessory ligament of the deep digital flexor tendon (inferior check ligament). In: Rantanen NW, McKinnon AO (eds) *Equine Diagnostic Ultrasonography*. Baltimore, MD: Williams & Wilkins, 1998, pp. 399–445.
[15] Zubrod CJ, Schneider RK, Tucker RL, Gavin PR, Ragle CA, Farnsworth KD. Use of magnetic resonance imaging for identifying subchondral bone damage in horses: 11 cases (1999–2003). *J Am Vet Med Assoc* 2004; **224**: 411–18.
[16] Zubrod CJ, Schneider RK, Tucker RL. Use of magnetic resonance imaging to identify suspensory desmitis and adhesions between exostoses of the second metacarpal bone and the suspensory ligament in four horses. *J Am Vet Med Assoc* 2004; **224**: 1815–20.
[17] Sampson SN, Schneider RK, Tucker RL, Gavin PR, Zubrod CJ, Ho CP. Magnetic resonance imaging features of oblique and straight distal sesamoidean desmitis in 27 horses. *Vet Radiol & Ultrasound* 2007; **48**: 303–11.
[18] Cohen JM, Schneider RK, Zubrod CJ, Sampson SN, Tucker RL. Desmitis of the distal digital annular ligament in seven horses: MRI diagnosis and surgical treatment. *Vet Surg* 2008; **37**: 336–44.

[19] Bischofberger AS, Konar M, Ohlerth S *et al*. Magnetic resonance imaging, ultrasonography and histology of the suspensory ligament origin: a comparative study of normal anatomy of Warmblood horses. *Equine Vet J* 2006; **38**: 508–16.
[20] Sampson SN, Tucker RL. Magnetic resonance imaging of the proximal metacarpal and metatarsal regions. *Clin Tech in Eq Pract* 2007; **6**: 78–85.
[21] Turner D, Prodromos C, Petaxnick J, Clark J. Acute injury of the ligaments of the knee: Magnetic resonance evaluation. *Radiology* 1985; **154**: 717–22.
[22] Lynch T, Crues J, Morgan F, Sheehan W, Harter L, Ryu R. Bone abnormalities of the knee: prevalence and significance of MR imaging. *Radiology* 1989; **171**: 761–6.
[23] Drape J, Silbermann-Hoffman O, Houvet P *et al*. Complications of flexor tendon repair in the hand: MR imaging assessment. *Radiology* 1996; **198**: 219–24.
[24] Kasashima Y, Kuwano A, Katayama Y, Taura Y, Yoshihara T. Magnetic resonance imaging application to live horse for diagnosis of tendinitis. *J Vet Med Sci* 2002; **64**: 577–82.
[25] Redding WR. The use of MRI in the diagnosis of proximal plantar pain in 17 cases. *Proc Am College of Vet Surg* 2006; **41**: 147–8.
[26] Redding WR, Schramme MC. Comparison of ultrasound and MRI in the diagnosis of proximal plantar metatarsal pain in 25 horses. *Proc Am College of Vet Surg* 2007; **42**: 112–15.
[27] Brokken MT, Schneider RK, Sampson SN, Tucker RL, Gavin PG, Ho CP. Magnetic resonance imaging features of proximal metacarpal and metatarsal injuries in the horse. *Vet Radiol & Ultrasound* 2007; **48**: 507–17.
[28] Coudry V, Denoix J-M, Didierlaurent D, Rossignol F, Audigie F. Use of magnetic resonance imaging to diagnose the cause of proximal metacarpal pain in a standardbred trotter. *Vet Record* 2008; **162**: 790–2.
[29] Wheat J, Jones K. Selected techniques of regional anesthesia. *Vet Clin North Am*: *Large Anim Pract* 1981; **3**: 223–46.
[30] Ford T, Ross M, Orsini P. A comparison of methods for proximal palmar metacarpal analgesia in horses. *Vet Surg* 1989; **18**: 146–50.
[31] Stashak T. Examination for lameness. In: Stashak TS (ed.) *Adams' Lameness in Horses*. St Louis, MO: Lippincott Williams & Wilkins, 2002, pp. 113–83.
[32] Castro F, Schumacher J, Pauwels F, Blackford J. A new approach for perineural injection of the lateral palmar nerve in the horse. *Vet Surg* 2005; **34**: 539–42.
[33] Dyson S, Romero J. An investigation of injection techniques for local analgesia of the equine distal tarsus and proximal metatarsus. *Equine Vet J* 1993; **25**: 30–5.
[34] Murray R, Blunden T, Schramme M, Dyson S. How does magnetic resonance imaging represent histologic findings in the equine digit? *Vet Radiol & Ultrasound* 2006; **47**: 17–31.
[35] Crass J, Genovese R, Render J, Bellon E. Magnetic resonance, ultrasound and histopathologic correlation of actue and healing tendon injuries. *Vet Radiol & Ultrasound* 1992; **33**: 206–13.
[36] Rubin D. Magnetic resonance imaging: practical considerations. In: Resnick D, Kransdorf MJ (eds) *Bone and Joint Imaging*. Philadelphia, PA: Elsevier Inc, 2004, pp. 118–32.
[37] Barber M, Sampson S, Schneider R, Baszler T, Tucker R. Use of magnetic resonance imaging to diagnose distal sesamoid bone injury in a horse. *J Am Vet Med Assoc* 2006; **229**: 117–20.
[38] Powell SE, Ramzan PHL, Head MJ, Shepherd MC, Baldwin GI, Steven WN. Standing magnetic resonance imaging detection of bone marrow oedema-type signal pattern associated with subcarpal pain in 8 racehorses: a prospective study. *Equine Vet J* 2010; **42**: 10–17.
[39] Zanetti M, Bruder E, Romero J, Hodler J. Bone marrow edema pattern in osteoarthritic knees: correlation between MR imaging and histologic findings. *Radiology* 2000; **215**: 835–40.
[40] Martig S, Boisclair J, Konar M, Spreng D, Lang J. MRI characteristics and histology of bone marrow lesions in dogs with experimentally induced osteoarthritis. *Vet Radiol & Ultrasound* 2007; **48**: 105–12.
[41] Young R, O'Brien T, Craychee T. Examination procedures for the diagnosis of suspensory desmitis in the horse. *Proc Am Ass Equine Practnrs* 1990; **35**: 233–41.

[42] Eliashar E, Dyson SJ, Archer RM, Singer ER, Smith RKW. Two clinical manifestations of desmopathy of the accessory ligament of the deep digital flexor tendon in the hindlimb of 23 horses. *Equine Vet J* 2005; **37**: 495–500.
[43] Murray RC. The role of MRI in race and endurance horse injuries. *Hallmarq European MRI User Meeting*, 2009.

Chapter 15
The carpal region

Sarah Powell and Rachel Murray

INTRODUCTION

Carpal lameness may occur in horses of all breeds and disciplines but is most prevalent in racehorses. Repetitive impact loading of the dorsal load path of the carpus during training and racing leads to adaptive modelling and, in time, non-adaptive subchondral bone sclerosis, particularly in the third and radial carpal bones. This may result in osteochondral fragmentation, osteoarthritis and carpal bone fractures. Repetitive overload injury can occur in other sports, particularly endurance racing and eventing. Carpal lameness may also result from trauma events, which may occur while jumping fences and through falls or kick injuries. While many of these injuries can be evaluated sufficiently well using radiography, ultrasonography and scintigraphy, magnetic resonance imaging (MRI) of the equine carpus has been described [1, 2] and may be useful to further evaluate certain pathologic conditions.

INDICATIONS FOR MRI OF THE CARPAL REGION

Once lameness has been localized to the carpal region, further evaluation of the pathology involved is usually adequately achieved using radiography, ultrasonography and scintigraphy, although some ligamentous and osteochondral lesions can be missed without MRI. In addition, the extent of injury may be shown further by use of MRI. In racehorses, it is unusual to have clinically significant carpal lameness in the absence of radiographic and scintigraphic findings, although this can occur, and in horses doing other sports MRI may demonstrate pathology in the absence of positive findings with other imaging. Magnetic resonance imaging of the carpus may be particularly useful in horses whose degree of lameness does not correlate with the findings of conventional imaging modalities, or where the pattern of diagnostic local analgesia is inconclusive. For example, defining the site of pain and associated pathology in horses equally responsive to middle carpal joint and subcarpal analgesia is problematic in the absence of conclusive radiographic and ultrasonographic findings, and may be elucidated using MRI [3]. MRI may also be used to further evaluate known pathology prior to surgery such as carpal bone fractures and carpal sepsis, where a focus of infection within the bone is suspected.

Equine MRI, edited by Rachel C. Murray.

IMAGE ACQUISITION

It is recommended that T1, T2 (T2*) and fat-suppressed images of the region are used, and proton density (PD) may also be useful. Comparison of T1, T2 and fat-suppressed images is important to differentiate active osseous lesions from adaptive remodelling. To evaluate the soft tissues of the carpal region, often transverse images are the most useful, although dorsal/frontal images are important for evaluation of origin and insertion regions.

Images of the carpus can be obtained both standing and under general anaesthesia. For evaluation of severe injury or for monitoring of injury in the carpus, obtaining images in the standing horse may give considerable advantages.

OSSEOUS PATHOLOGY

Carpal bone sclerosis and bone 'oedema'

Carpal bone sclerosis has been well documented in the third carpal bone of Thoroughbred racehorses [4, 5] but may be seen in any of the bones of the middle carpal and antebrachiocarpal joints. Extensive sclerosis may lead to resorption and regions of necrosis, which can potentially be seen on MR images before radiographic changes are evident. Some degree of carpal bone sclerosis is to be expected when imaging Thoroughbreds in training and is not always associated with clinical lameness. Horses with third carpal bone sclerosis very commonly have corresponding changes in the radial carpal bone [6] and, less commonly, in the intermediate carpal bone on MR images (Figure 15.1). MRI can be useful to differentiate whether this increased bone density is associated with osteochondral damage at or adjacent to the articular surface, presence of trabecular damage, necrosis or other bone pathology, or adjacent ligamentar or capsular damage (Figure 15.2). The adjacent tissues should therefore be carefully evaluated. The margins between the area of increased bone density and surrounding trabecular bone may also provide some indication of the ongoing activity.

For horses with decreased signal intensity on T1, T2 and fat-suppressed images, it is likely that there is primarily increased bone density. For horses with increased bone density, this usually indicates a load path that may be affected by the conformation, foot balance or direction of training, which may assist in recommendations for management in cases of repetitive overloading. Where there is hypointense signal on T1-weighted images, but an area of increased signal intensity on T2-weighted and fat-suppressed images, then this indicates associated bone damage. The margin between the subchondral bone and cartilage should be carefully evaluated for presence of an irregular osteochondral interface and associated cartilage damage.

Studies involving human patients with osteoarthritis of the knee suggest there is correlation between the presence of bone oedema and the occurrence of pain [7, 8]. In addition, in many cases the size of the bone oedema lesion appears to correlate with the degree of pain and the presence or

absence of partial and full-thickness cartilage defects. The sclerotic changes seen in Figures 15.1 are usually bilateral and it may be difficult to determine why lameness predominates in one limb. However, if increased signal intensity is seen within the subchondral or trabecular bone on fat-suppressed images, the degree of this change often correlates with the degree of lameness (Figures 15.3 and 15.4). In our populations this also appears to be true, not just for carpal bone disease, but also in the fetlock and subcarpal region.

Carpal bone fractures

Carpal osteochondral fragments are most likely to occur on the dorsal aspect and are seen as separate focal areas of low signal intensity, which may have either smooth or irregular margins, usually with a clear defect in

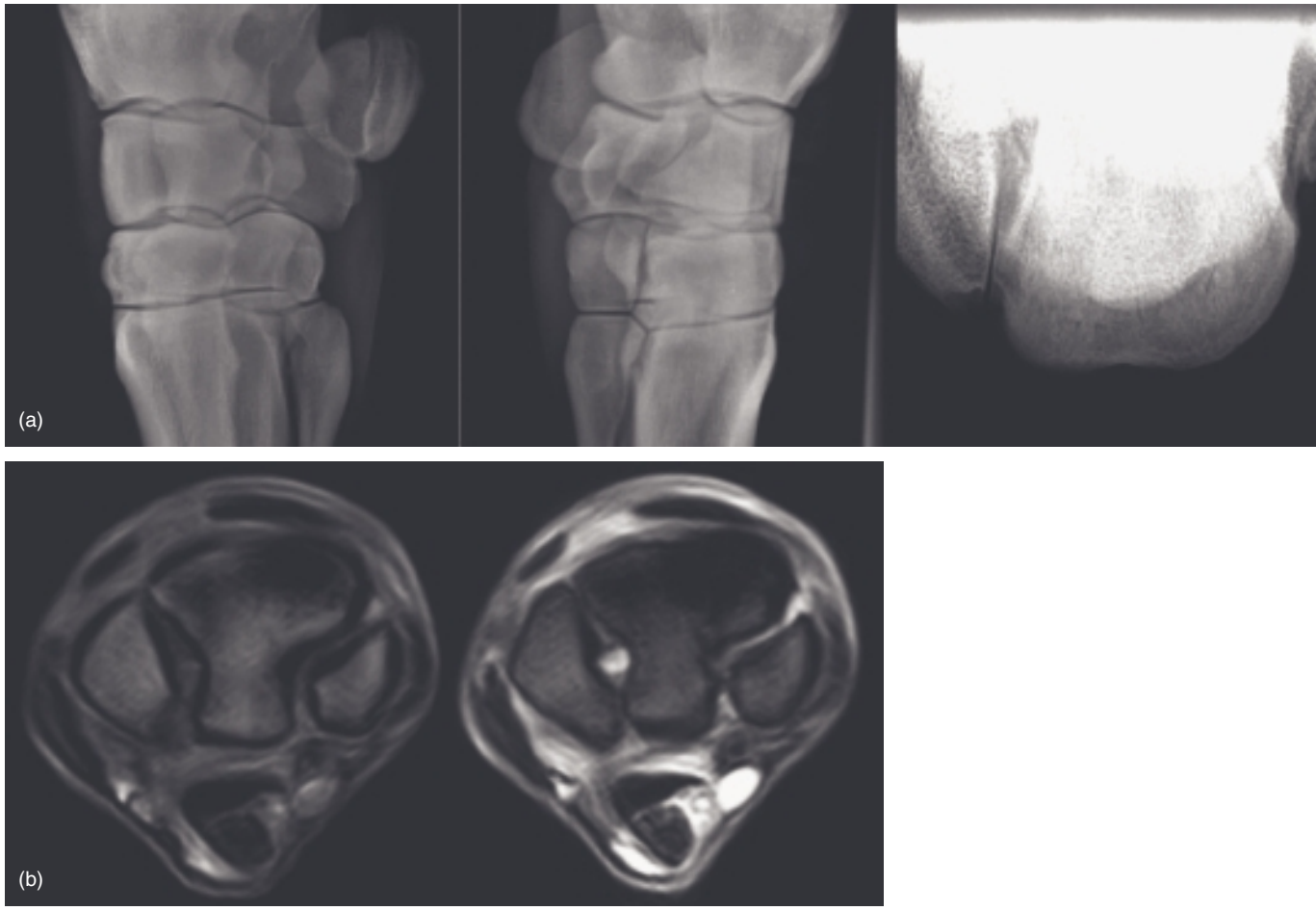

Figure 15.1 (a) DMPLO (left) DLPMO (centre) and DPrDDiO (right) radiographs of an unraced 2-year-old Thoroughbred with moderate right fore lameness improved following intra-articular medication of the middle carpal joint. The middle and antebrachiocarpal joints were distended. There is mild increased bone mineral density of the radial facet of the third carpal bone. Magnetic resonance imaging was carried out, which revealed a more marked degree of densification of the third, radial and intermediate carpal bones than was appreciable radiographically. (b) Low-field T1-weighted GRE (left) and T2*-weighted GRE (right) images of the right carpus at the level of the third carpal bone, obtained in a standing horse. Medial is to the right. There is marked low signal intensity emanating from the radial facet of the third carpal bone extending to the level of the carpometacarpal joint.

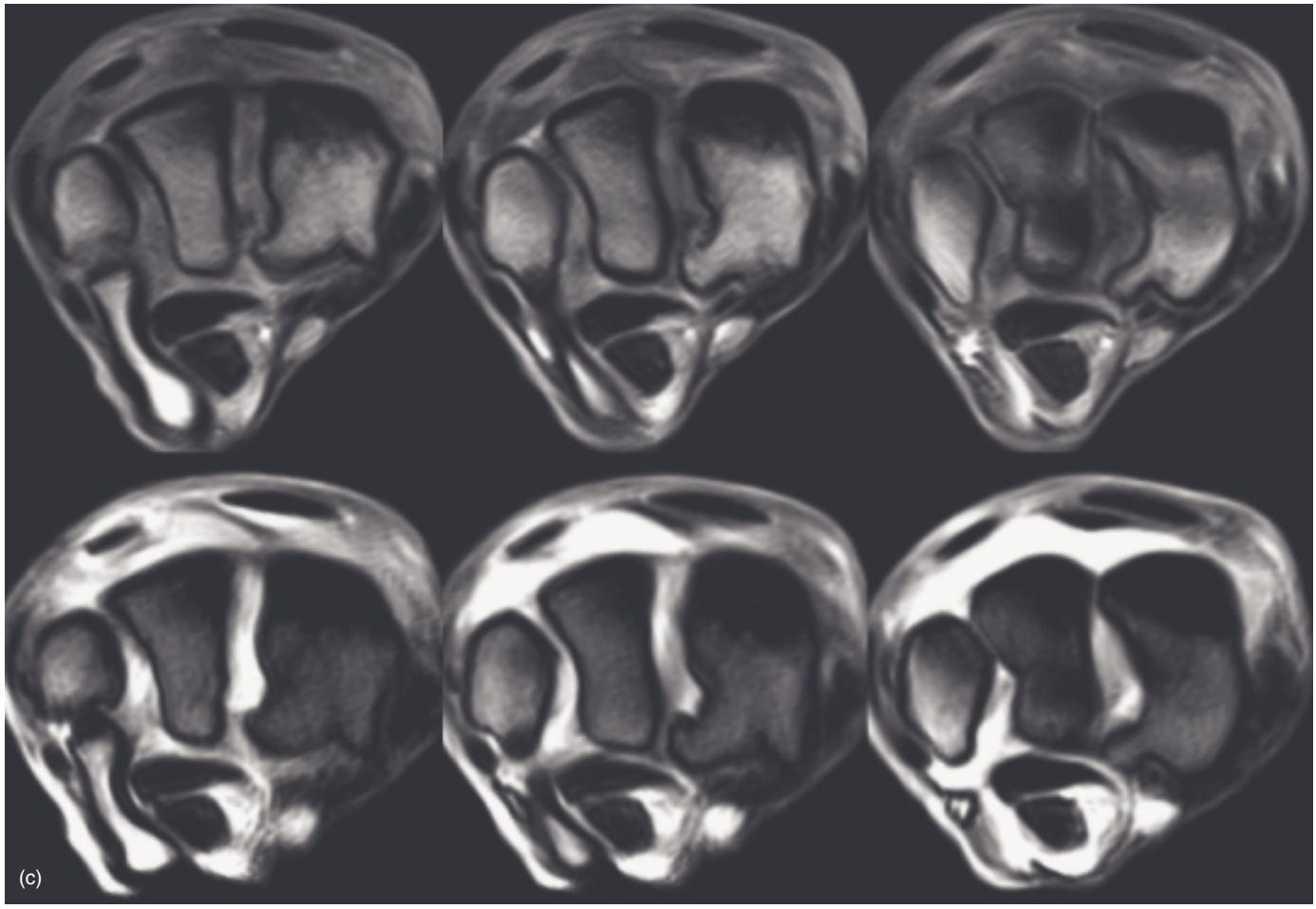

Figure 15.1 *Cont'd* (c) Low-field T1-weighted GRE (top) and T2*-weighted GRE (bottom) images through the proximal row of carpal bones moving distally from left to right, obtained in a standing horse. Medial is to the right. The degree of distension of the middle carpal joint can be seen on these T2*-weighted images where fluid appears bright, though the capsular attachments are indistinct.

the parent bone and thickened irregular subchondral and cancellous bone (seen as homogeneous or heterogeneous low signal intensity on T1- and T2-weighted images) at the site (Figure 15.5). In acute or active damage, there is likely to be evidence of pathology in the parent bone with markedly reduced signal intensity in all sequences (sclerosis) and/or increased signal intensity on fat suppressed images with reduced signal intensity on T1-weighted images.

Severe carpal bone fractures may be seen as a disruption of the cortical surface and linear increased signal intensity on T2-weighted images in the fracture gap associated with accumulated blood, fluid and debris. In the acute fracture, there is likely to be associated increased signal intensity on fat-suppressed images within the adjacent bone, reflecting osseous pathology at the site (Figures 15.6 and 15.7), although in the peracute case it is possible for this to be absent.

Carpal bone fractures may be difficult to assess radiographically due to the complex nature of the carpal joints and overlay of joint margins. In

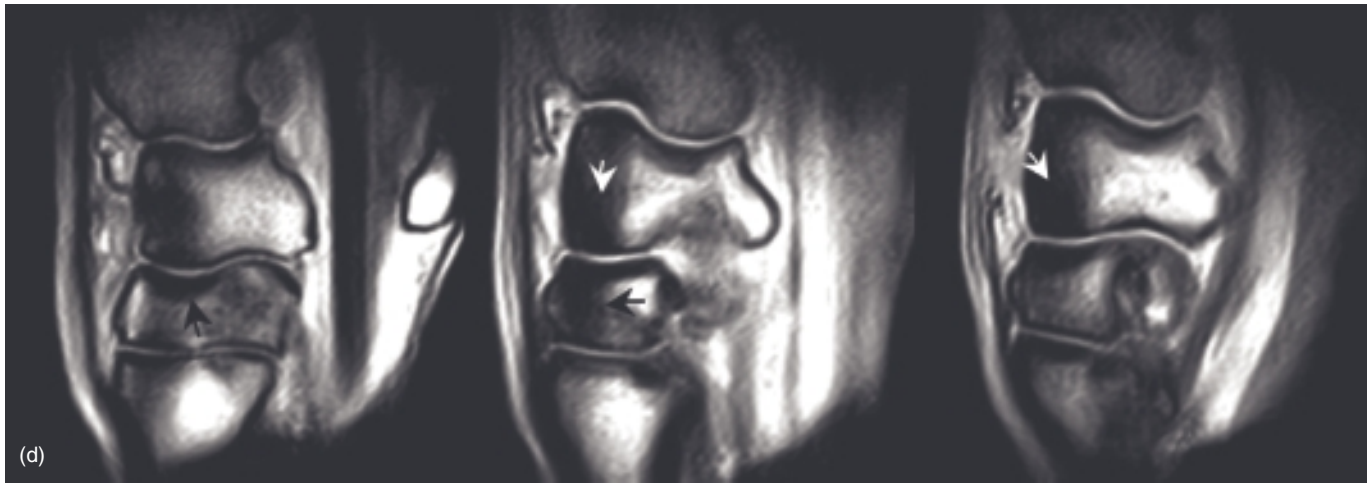

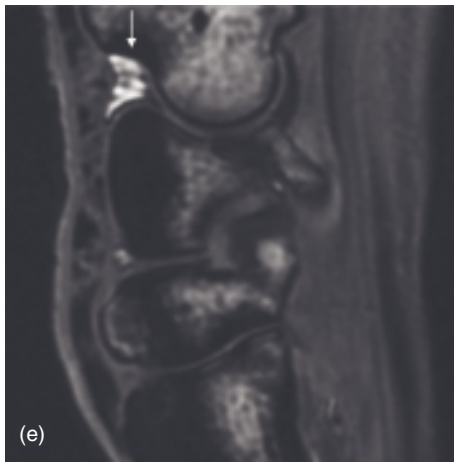

Figure 15.1 *Cont'd* (d) Low-field T1-weighted GRE sagittal images of the carpus moving medially from left to right obtained in a standing horse. The image to the left shows thickening of the subchondral bone plate of the intermediate facet of the third carpal bone, which becomes more extensive at the level of the radial facet (centre) where the low signal extends to the carpometacarpal joint (black arrows). There is marked densification of the intermediate carpal bone and radial carpal bone (white arrows). (e) High-field T1-weighted sagittal image of the carpus. There is marked sclerosis, seen as low signal intensity on T1, T2, T2* and fat-suppressed images, running in a load plane marked by the white arrow. This is seen affecting the distal radius, radial carpal bone, medial facet of the third carpal bone and proximal third metacarpal bone in the same plane.

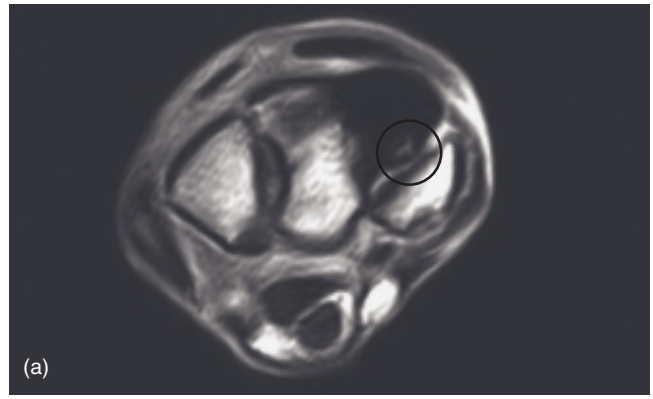

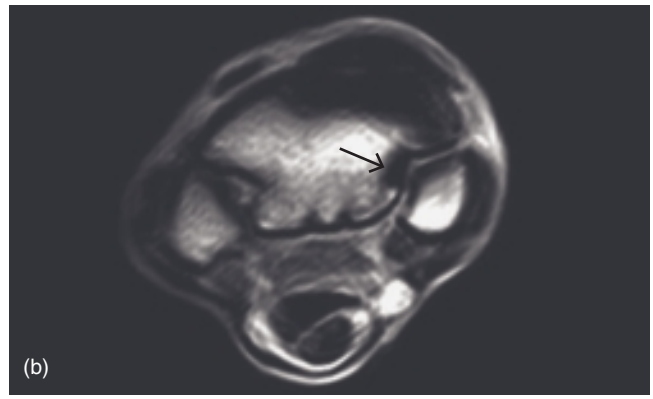

Figure 15.2 T1-weighted GRE transverse images at the level of the distal aspect of the third carpal bone (a) and proximal third metacarpal bone (b) taken from the right fore limb of a 4-year-old Thoroughbred in training with pain related to the carpal region. The lameness was not completely abolished following intra-articular analgesia of the middle and antebrachiocarpal joints. There is marked bone mineral densification extending from the radial facet of the third carpal bone to the level of the carpometacarpal joint. The dorsoproximal aspect of the third metacarpal bone also shows similar loading associated densification. In addition there is a focal signal hyperintensity at the insertion of the intercarpal ligament on the third carpal bone (circled) and thickening of the cortical bone at the insertion of the interosseous ligament between the second and third metacarpal bones (arrow).

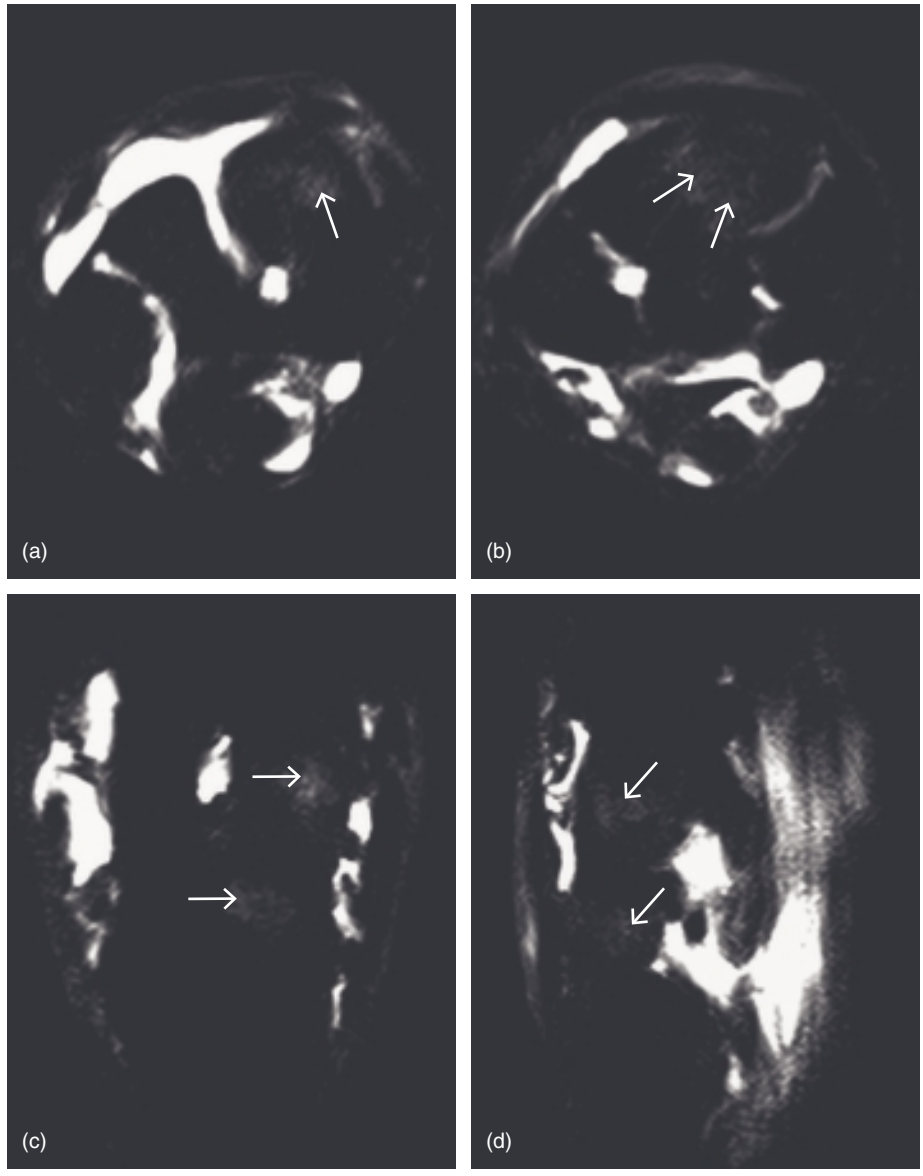

Figure 15.3 STIR transverse (a and b), sagittal (d) and frontal (c) images of the right carpus in a 3-year-old Thoroughbred in training with right fore lameness partially improved by intra-articular analgesia of the middle and antebrachiocarpal joints. The degree of sclerosis of the third, radial and intermediate carpal bones was comparable in both left and right forelimbs. However, in the right forelimb only, there was generalized increased signal intensity on STIR images within the radial and third carpal bones (arrows). This represents a case where the hyperintensity does not appear to involve the cortical bone.

traumatic, comminuted injuries, multiple projections are required to fully assess the location and number of fragments (Figure 15.6). MRI examination of such cases may be helpful to assist in surgical planning.

It is important to evaluate the carpus in all three planes in cases of suspected fracture. Damage to adjacent soft tissues should be evaluated in carpal fractures. The intercarpal ligament, collateral ligament, joint capsule and carpal canal should be assessed for damage. The articular surface, and articular cartilage integrity should also be evaluated where possible.

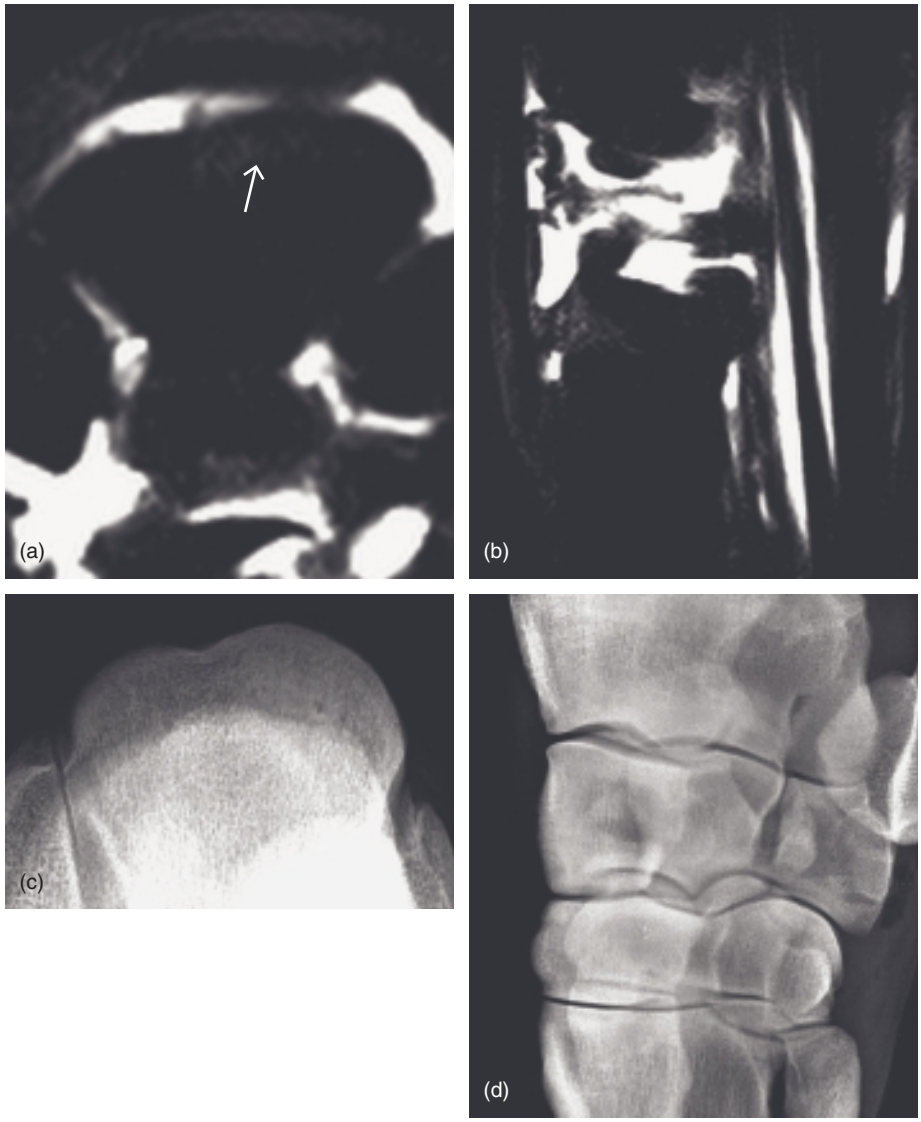

Figure 15.4 STIR transverse (a) and sagittal (b) images of the third carpal bone taken from a 3-year-old racehorse with lameness abolished by intra-articular analgesia of the middle carpal joint. There is signal hyperintensity within the subchondral and cortical bone in association with the capsular attachment (arrow), which is thickened. DLPMO (d) and DPrDDiO (c) view of the third carpal bone of the same horse.

Monitoring fracture healing

Healing of incomplete fractures may be seen initially as resolution of increased signal intensity on fat-suppressed images. This increased signal intensity is likely to become increasingly more limited to the area around the fracture line and may be followed by gradual loss of the fracture line.

OSTEOCHONDRAL PATHOLOGY

Where it is possible to evaluate the entire surface of the articular cartilage, this should be done. However, if MRI is undertaken under weight-bearing conditions, or for the palmar aspect even during flexion, it may not be possible to separate the articular surface sufficiently to evaluate the cartilage surface.

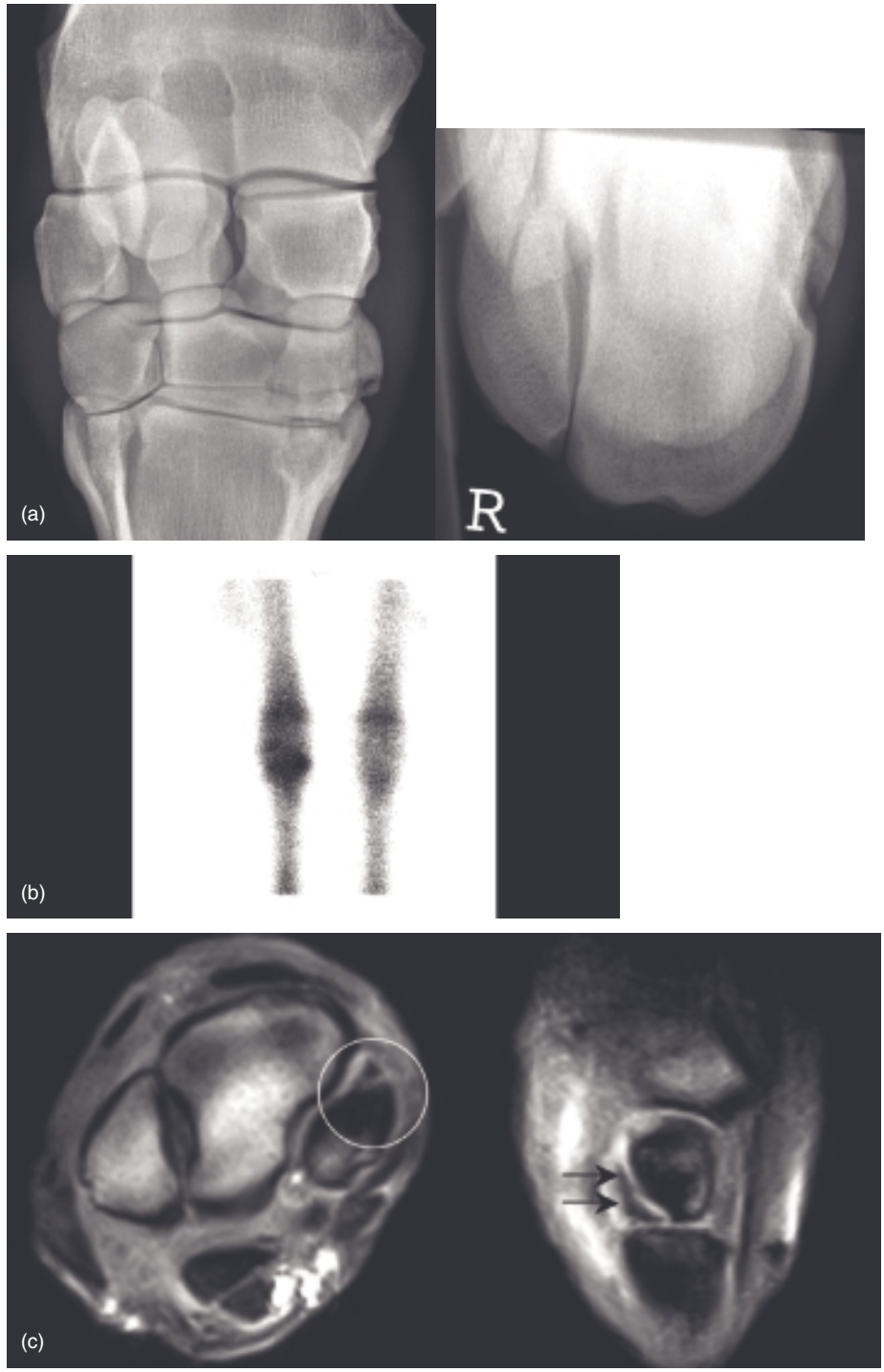

Figure 15.5 Minimally displaced fracture. (a) Radiographs of a 7-year-old event horse with right fore lameness after falling at a fence 6 weeks previously. The right fore carpus was painful to flex and the middle carpal joint was moderately distended. Lameness was improved following intra-articular analgesia of the middle carpal joint. There is an irregular margin to the abaxial aspect of the second carpal bone. The activity of this change was assessed scintigraphically (see (b)). (b) Dorsopalmar bone phase scintigraphic image of both carpi. There is a focal region of abnormal increased uptake in the region of the second carpal bone. (c) T1 GRE transverse (left) and sagittal (right) images of the right carpus. Medial is to the right on the transverse image, palmar is to the right on the sagittal image. There is a complete, minimally displaced dorsal plane fracture of the second carpal bone with extensive second carpal bone sclerosis. After assessment of the fracture on MR images it was elected to treat the horse conservatively with intra-articular medications. The horse has no pain related to the right carpus 2 years after the initial injury, though it is no longer used for jumping.

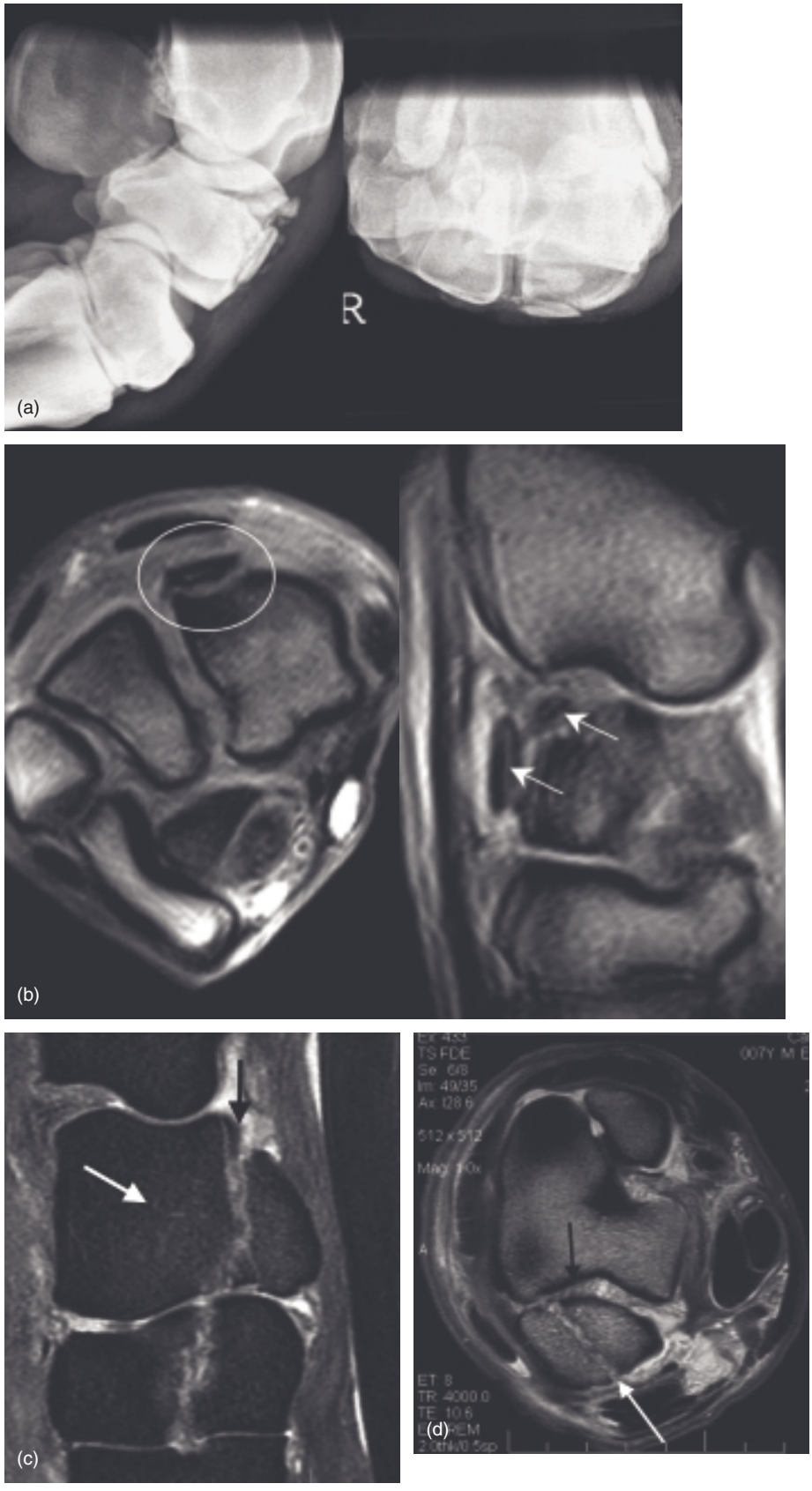

Figure 15.6 Fractures. (a) Radiographs of a 14-year-old endurance horse who sustained a comminuted fracture of the radial carpal bone during a ride the previous day. There are multiple displaced fragments clearly visible radiographically. However, a non-displaced dorsal plane fracture of the palmar aspect of the radiocarpal bone was suspected on the initial radiographs. An MRI examination was carried out to determine the relative positions of the fragments and to rule out further pathology within the carpus. (b) Low-field T1 GRE transverse (left) and dorsal plane (right) images of the right fore carpus. There is a large dorsal plane fracture visible with several fragments located in a more palmar position. (c) High-field sagittal fat-saturated image of the carpus. There is linear marked increase in signal intensity representing fracture lines (black arrow). Adjacent to these, within the bones, there is increased signal intensity representative of adjacent bone damage/pathology (white arrow). (d) High-field transverse plane image of the carpus. There is a fracture of the fourth carpal bone (white arrow). The adjacent intercarpal ligament (black arrow) should be evaluated if there is a nearby fracture.

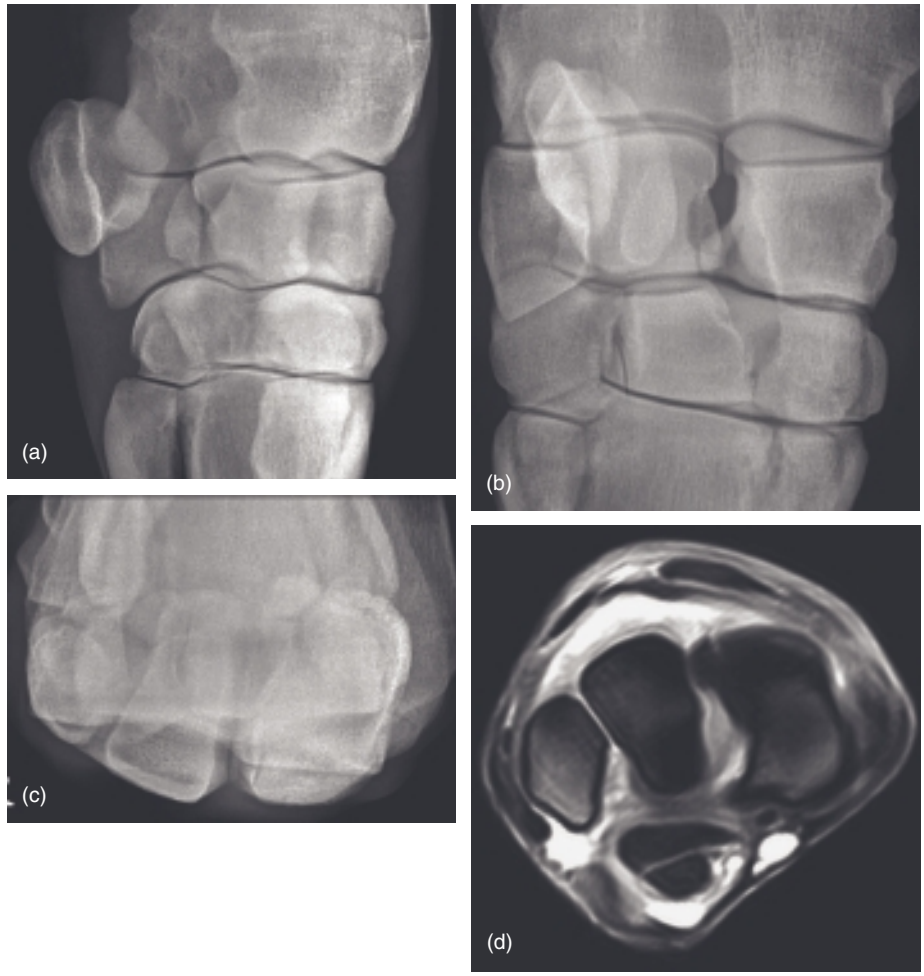

Figure 15.7 Fractures. (a, b and c) Selected radiographs of a 2-year-old racing Thoroughbred with right fore lameness significantly improved following intra-articular analgesia of the right fore middle carpal joint. There is focal radiolucent area in the distal articular margin of the radiocarpal bone on the DLPMO projection. On the proximal row skyline view (right) a linear radiolucency is present dorsomedially. (d) T2*-weighted GRE transverse image of the right fore carpus. Medial is to the right. There is marked densification of the dorsal aspect of the radiocarpal bone with focal linear increased signal intensity on the dorsomedial aspect representing a minimally displaced sagittal fracture of the radial carpal bone is visible. (c) T2*-weighted GRE (left) and STIR FSE (centre and right) transverse images. Medial is to the right. The radiolucent line seen radiographically is confirmed as a fracture line, seen clearly on the T2*-weighted image (circled). The STIR FSE image shows generalized signal hyperintensity axially within the radial carpal bone (arrow) in addition to a more focal increase at the fracture site (circled).

It is therefore essential to fully evaluate the subchondral bone, which may provide indicators of articular cartilage integrity. Where there is subchondral or cancellous bone damage, increased signal intensity on fat-suppressed images or irregularity of the osteochondral margin, concurrent articular cartilage damage should be considered.

Subchondral bone fractures may be seen as linear high signal intensity surrounded by a small area of relatively lower increased signal intensity on fat-suppressed images and a linear low signal intensity with surrounding low signal intensity on T1-weighted images (Figures 15.7 and 15.8). An irregular

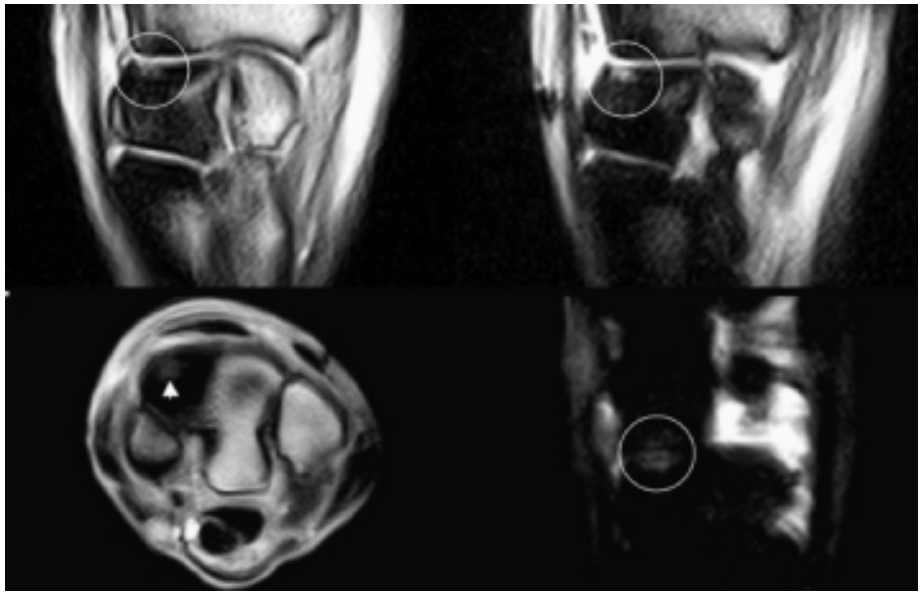

Figure 15.8 Clockwise from top left: T1 sagittal, T2* sagittal, STIR frontal and T1 transverse MR images at the level of the radial facet of the third carpal bone of the left fore limb of a 2-year-old Thoroughbred with left fore lameness abolished following intra-articular analgesia of the middle carpal joint. A focal region of hyperintensity on all sequences is present in the subchondral cortical bone of the medial facet of the third carpal bone.

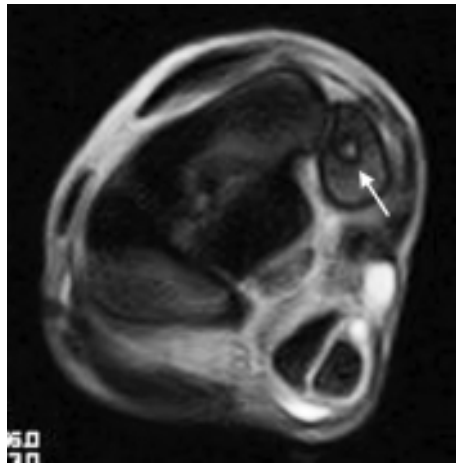

Figure 15.9 Transverse T2* gradient-echo image of the carpus obtained standing. There is an osseous cyst-like lesion (arrow) in the ulnar carpal bone of a limb without lameness.

roughened articular and/or endosteal surface to subchondral bone, evident on T1- and T2-weighted images, or a roughened articular surface on fat-suppressed images may indicate subchondral bone irregularity or damage. Osseous cyst-like lesions may be seen as focal high signal intensity in the subchondral and cancellous bone on T1 and T2 fat-suppressed images, with/without alteration in overlying cartilage signal (Figure 15.9).

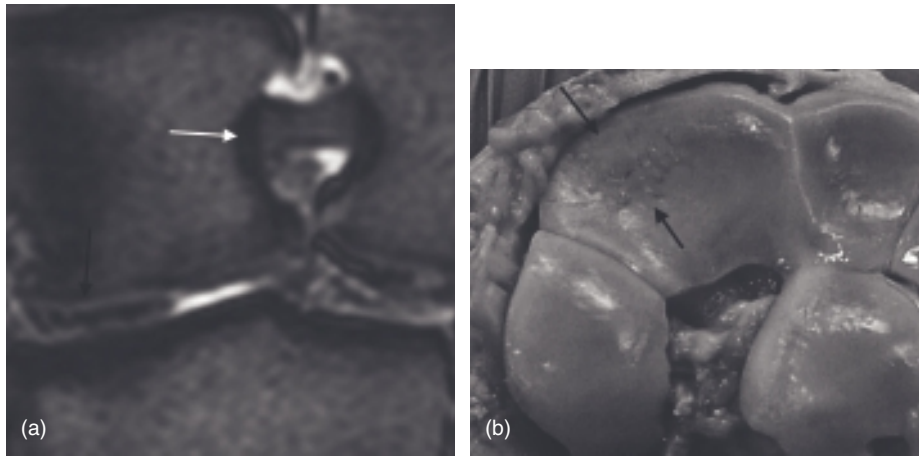

Figure 15.10 (a) High-field sagittal plane image of the carpus. There is marked cartilage irregularity seen on the dorsal aspect of the articular surface of the third carpal bone (black arrow). The white arrow identifies the intercarpal ligament between the radial and intermediate carpal bones. (b) Photograph of the articular cartilage on the surface of the third carpal bone obtained at the same location. There is cartilage irregularity and pitting (arrows), supporting the findings in (a).

It is possible to detect articular cartilage cracks and fibrillation on high-field images, and if severe, this may be seen on low-field images. Linear low signal intensity running through the cartilage on T1-weighted images with altered signal intensity on T2 may indicate cracks, while an irregular cartilage surface is likely to reflect fibrillation, and cartilage defects can also be detected (Figure 15.10). Altered cartilage signal intensity without loss generally reflects cartilage alteration (composition).

JOINT CAPSULE/SYNOVIAL PATHOLOGY

Distension of the joint, with increased volume of fluid (low signal T1, high signal T2) should be assessed. In acute haemarthrosis, the synovial fluid has relatively higher signal intensity on T1- and lower signal intensity on T2-weighted images than would normally be expected. Inflamed, oedematous synovium retains similar signal intensity to the surrounding synovial fluid. Hyperplastic, fibrotic synovium can be seen as a ragged surface protruding into joint fluid of intermediate signal intensity, so higher than the synovial fluid on T1- and lower than the synovial fluid on T2-weighted images. Damage to the joint capsule may be detected as loss of continuity, thickening or alteration in signal intensity, and enthesiophyte formation at the origin or insertion may indicate chronic damage. Enthesiophytes have low signal (T1 and T2) continuation of bone adjacent to the linear low signal intensity of the ligament. Osteophytes are seen as altered bone contour at the margins of the joint.

Certain disease entities of the proximal metacarpal region are included here as important differential diagnoses in horses with apparent carpal pain. Lack of specificity of diagnostic local analgesia of the carpal and subcarpal region can make it difficult to determine whether lameness is arising from the proximal metacarpal region or carpus [9]. MRI offers advantages over radiography and ultrasonography when investigating suspected carpal and subcarpal lameness [10–12]. Avulsion at the origin of the suspensory ligament and fatigue injuries of the palmaroproximal cortex of the third metacarpal bone are important differential diagnoses in cases of lameness arising from the proximal metacarpal region, which may not always be readily apparent radiographically. However, stress reactions and stress fractures of the proximal metacarpal region are dramatic when seen on MR images even in the absence of conclusive radiographic and ultrasonographic findings [13] (Figures 15.11 and 15.12).

These stress reactions, once considered the preserve of the Thoroughbred racehorse, have been detected on MRI in our clinic in horses competing in those disciplines where maximum speed or repetitive high-speed movements are involved, such as endurance and reining horses. There is commonly a combination of pathologies detected in these horses, for example many will have varying degrees of change within the proximal suspensory ligament and/or syndesmosis between the second and third metatarsal bones. The advantage of MRI over scintigraphic imaging of stress reactions/fracture of the proximal metacarpal bone is that both soft tissue and bone pathology can be evaluated – and subsequently monitored if necessary – rather than just the bone or soft tissue component in isolation. The cases usually present with moderate lameness equally but incompletely responsive to diagnostic local analgesia of the middle carpal and subcarpal regions. There is not always pain on digital palpation of the proximal suspensory ligament; however, percussion of the region can elicit a painful response in some cases. Radiographs of the carpus and subcarpal region in the early stages and ultrasonography of the proximal suspensory ligament often do not show sufficient change to account for the degree of lameness. Even in the presence of marked bone marrow oedema-type signal pattern in the proximal palmar metacarpus, an overt breach of the palmar cortical bone or fracture line may not be detected. This may be due to the horse being imaged prior to overt fracture taking place (i.e. at the stress reaction stage) or due to volume averaging and movement artefact confounding visualization of the fracture. When seen, a cortical fracture is often hyperintense on all sequences in the early stages, progressing to hypointense with time and healing. Care should be taken to differentiate between palmar cortical stress fractures and avulsion fractures, and also to assess the presence or absence of suspensory ligament desmitis. Cases where bone changes predominate and the suspensory ligament is relatively spared appear to have a better prognosis for return to full athletic function than those with concurrent, significant ligamentous damage.

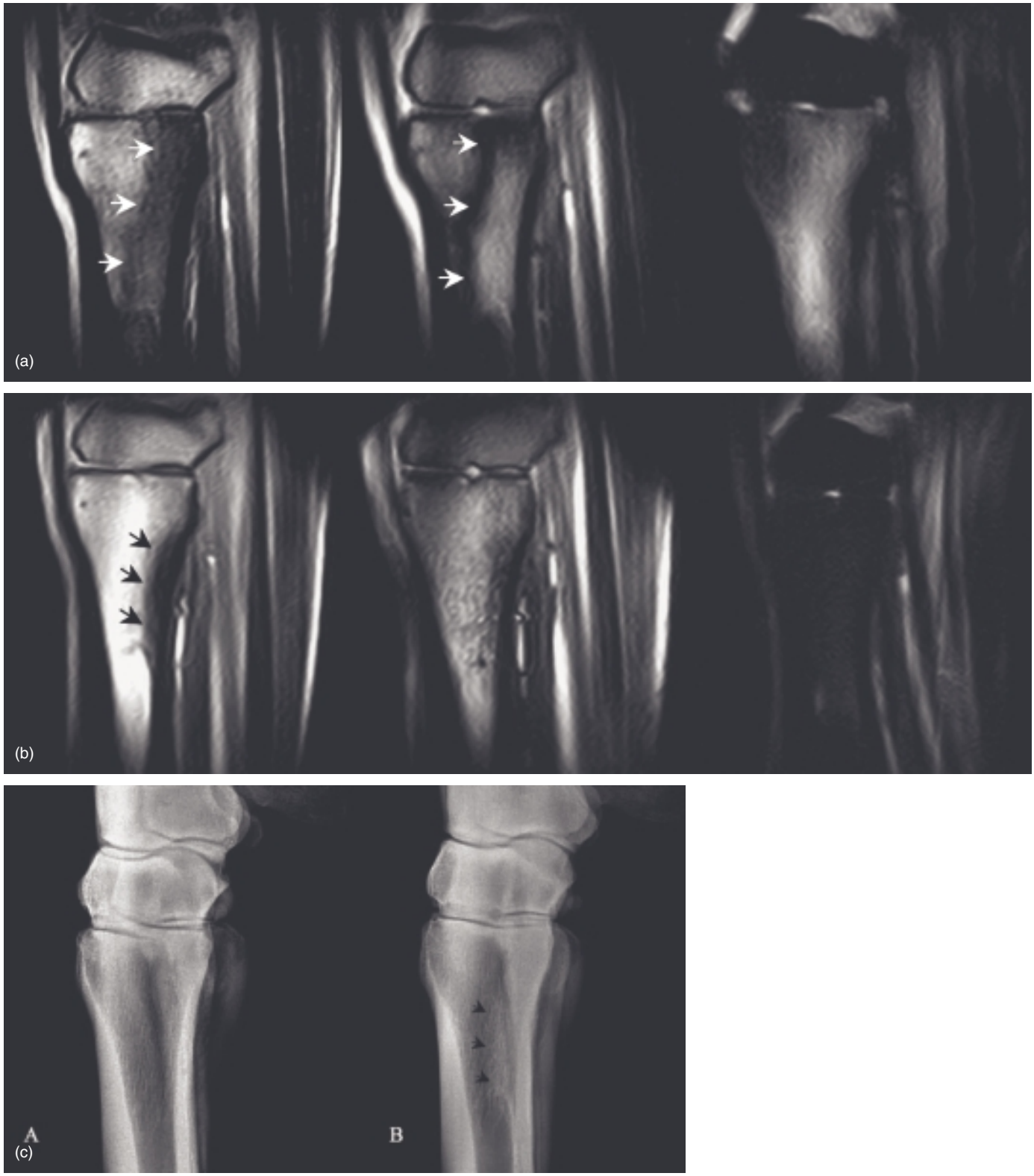

Figure 15.11 (a) T1, T2* and STIR sagittal images of a 7-year-old steeplechaser with marked right fore lameness of 10 days' duration. On initial presentation the lameness had improved significantly following intra-articular analgesia of the right middle carpal joint. Initial radiographs of the carpus and proximal metacarpus were unremarkable (c) A. A slight, transient response to medication of the middle carpal joint was observed prompting an MR examination. Signal hypointensity is seen on T1-weighted images within the proximal palmar metacarpal region corresponding with a region of marked hyperintensity on T2* and STIR images. A phase cancellation artefact is present in the T2*-weighted image which delineates the area of fluid signal in the palmar aspect of the third metacarpal bone. (b) T1, T2* and STIR sagittal images of the horse in Figure 15.8a at 3 months post injury. The hyperintensity on T2* and STIR images has resolved although an endosteal reaction is now present on the palmar cortex of the third metacarpal bone (black arrows), which was also visible radiographically at this stage. (c) Lateromedial radiographs of the right carpus taken at the time of the initial lameness (A) and 3 months later (B) show development of endosteal reaction of the palmar cortex of the third metacarpal bone (black arrows).

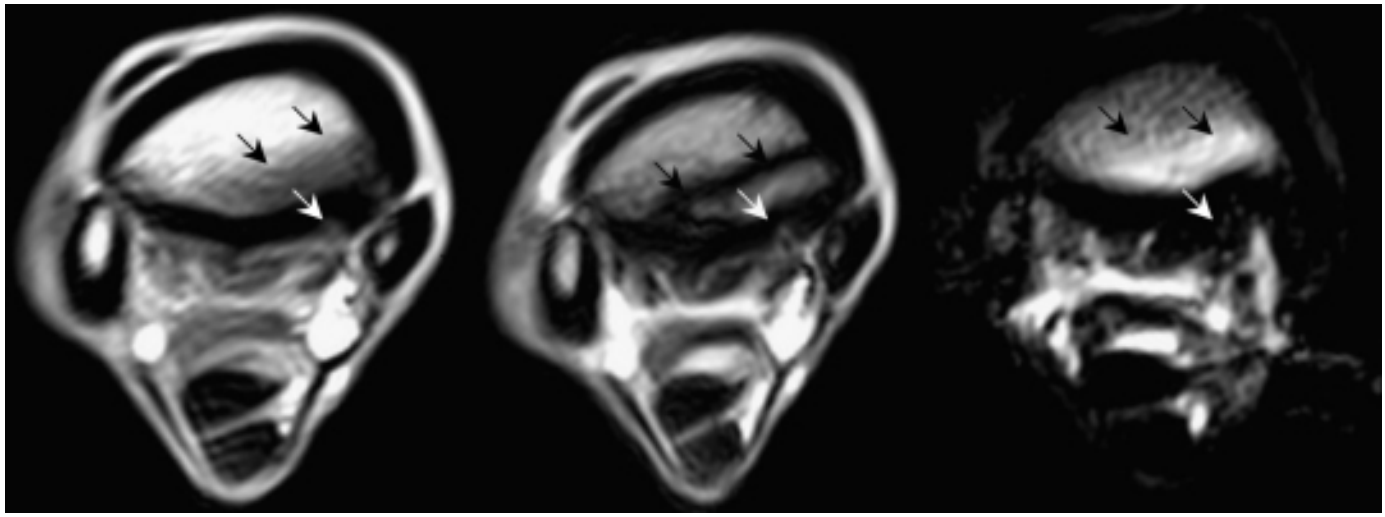

Figure 15.12 T1, T2* and STIR transverse images of the proximal metacarpal region of a 2-year-old Thoroughbred in training with lameness equally responsive to middle carpal joint and subcarpal analgesia. There is signal hypointensity on T1-weighted images and corresponding signal hyperintensity on T2*- and STIR-weighted images within the trabecular bone of the palmaroproximal aspect of the third metacarpal bone (black arrows). Focal signal hyperintesity is visible within the cortical bone in association with the origin of the medial lobe of the suspensory ligament (white arrows) suggestive of a breach of the cortical bone not visible radiographically representing a radiographically occult palmar cortical stress fracture of the third metacarpal bone.

LIGAMENTAR PATHOLOGY

Carpal joint

Intercarpal ligament injury

Intercarpal ligament damage is seen as loss of the linear structure of the ligaments with or without alteration of the cortical bone at the origin or insertion. Occasionally there may be widening of the gap between the adjacent carpal bones. Ligament disruption can be seen as increased signal intensity on T2-weighted images, either within the ligament structure or due to increased synovial infiltration in the area due to ligament disruption, in which case the synovial infiltration is seen as low signal intensity on T1-weighted images. Osseous damage at the origin or insertion may be observed as irregularity of the periosteal or endosteal margin of the cortex, and in some cases there may be an extensive endosteal reaction (Figure 15.13).

COLLATERAL LIGAMENTS

Damage to the collateral ligaments can be detected as increased size or distortion of ligament shape, disruption of ligament continuity or alteration in the periligamentar tissues. Generalized or marked increase in signal intensity within the ligament is likely to be significant, although there is sometimes some mild signal heterogeneity within a normal ligament. The bone at the origin and insertion sites should be evaluated for enthesiophyte formation, endosteal or periosteal irregularity, or altered signal intensity on

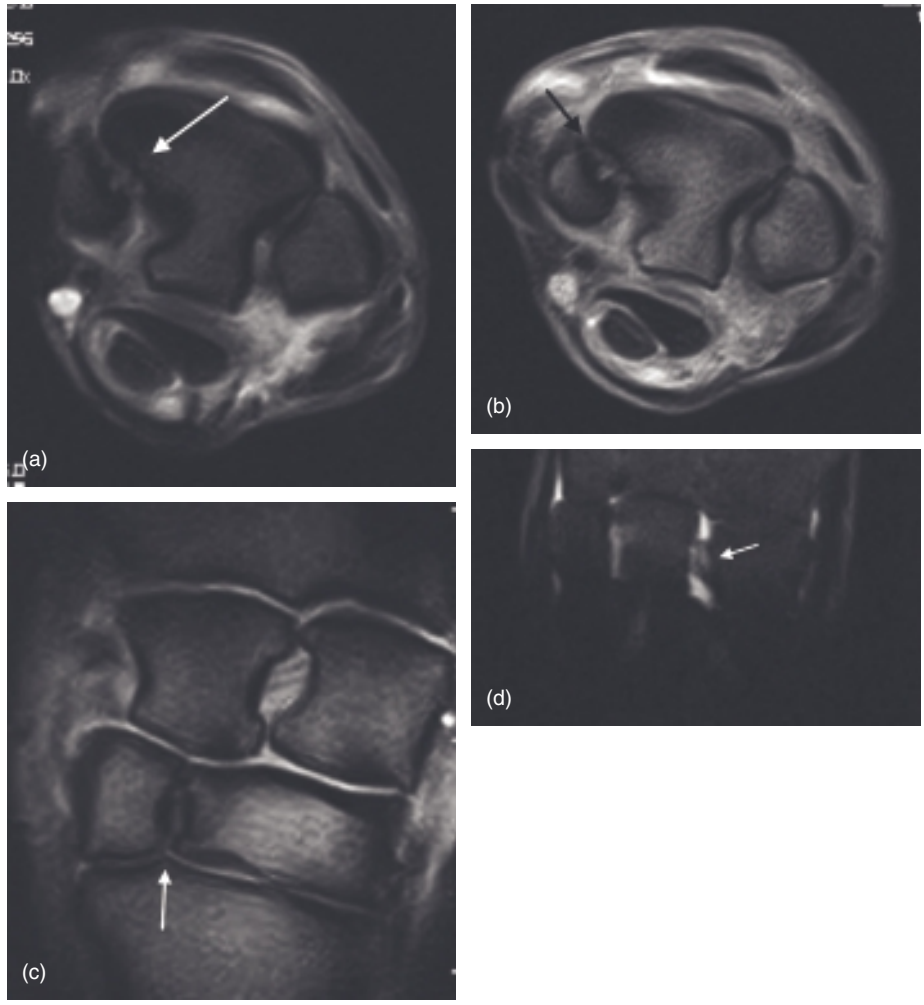

Figure 15.13 Intercarpal ligament damage. (a) Transverse plane T2* gradient-echo image obtained standing. There is a marked endosteal and periosteal irregularity at the origin and insertion of the intercarpal ligament (arrow) between the second and third carpal bones. There is also disruption of the normal ligamentar structure. (b) Transverse plane T1-weighted image obtained standing in the same horse, at the same location as (a), with the intercarpal ligament marked with an arrow. (c) Dorsal plane T1-weighted image of the distal row of carpal bones obtained standing. There is irregularity of the cortical bone at the origin and insertion of the ligament between the third and fourth carpal bones. (d) Dorsal plane STIR image of the carpus obtained in a standing horse. There is high signal intensity in the intercarpal ligament between the radial and intermediate carpal bones (arrow). There is also some increase in signal intensity within the lateral aspect of the intermediate carpal bone near the insertion of the ligament to the ulnar carpal bone. (Image for Figure 15.13d courtesy of Dr Meredith Smith)

different images sequences, particularly an increase in signal intensity on fat-suppressed images.

INTEROSSEOUS LIGAMENT INJURY

Damage to the interosseous ligaments between the metacarpal bones may occur alone, in conjunction with damage to the intercarpal ligaments or in conjunction with suspensory ligament injury. This is most easily detected as alteration in the bone at the origin and insertion, with endosteal and/or periosteal irregularity. There may be thickening of the cortex with increased density of the adjacent cancellous bone with or without evidence of active trabecular damage seen as increased signal intensity on fat suppressed images (Figure 15.2).

Carpal canal

Accessory ligament of the deep digital flexor tendon (ALDDFT)

Damage to the ALDDFT may be seen as enlargement of the ligament and loss of normal structure, usually with increased signal intensity on T1- and/or T2-weighted images, depending on the stage of the damage. There may consequently be loss of separation between the ALDDFT and the suspensory ligament distal to the carpus. However, in some cases the damage to the ligament is limited to the level of the carpus making ultrasonographic evaluation difficult and limiting diagnosis to MRI. There may be irregularity of the palmar aspect of the third carpal bone where it originates from this bone and the palmar carpal ligament.

Superficial digital flexor tendon (SDFT)/deep digital flexor tendon (DDFT)

Evaluating the tendons at the level of the carpal canal can provide some challenges as there is frequently residual muscular tissue present. As this may cause confusion, comparison with the contralateral limb is recommended. Enlargement of the tendon may be associated with pathology or tears proximal or distal to the level evaluated (Figure 15.14).

Suspensory ligament

Damage to the suspensory ligament frequently occurs concurrently with carpal changes. In some cases, there may be evidence of compression overloading injury on the medial side of the carpus occurring at the same time as a lateral lobe injury to the suspensory ligament, possibly indicating compression overload on the medial aspect with tensile overload on the lateral aspect, which may be related to conformation or gait. In a number of horses with suspensory ligament damage, there is evidence of carpometacarpal osteochondral damage and damage to the middle carpal joint may also occur.

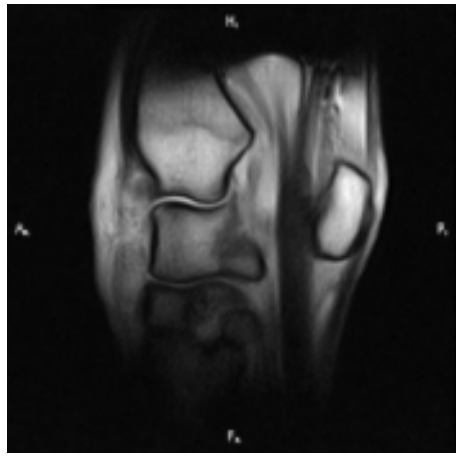

Figure 15.14 Low-field sagittal plane T1-weighted image of the carpus. There is enlargement of the deep digital flexor tendon adjacent to the accessory carpal bone. This may be indicative of pathology at either this level, or at a level proximal or distal to the enlargement. This horse had a tear in the musculotendonous junction proximal to the level of the carpus. Note also the marked antebrachiocarpal and middle carpal joint effusion. (Image courtesy of Dr Meredith Smith)

REFERENCES

[1] Kaser-Hotz B, Sartoretti-Schefer S, Weiss R. Computed tomography and magnetic resonance imaging of the normal equine carpus. *Vet Radiol Ultrasound* 1994; **35**: 457–61.

[2] Murray RC. Magnetic resonance imaging of the equine carpus. *Clin Tech Equine Pract* 2007; **6**: 86–95.

[3] Powell SE, Baldwin GI, Ramzan PHL, Shepherd MC, Head MJ. Standing MRI examination assists the differentiation of proximal palmar metacarpal pain from middle carpal joint pain in the racing Thoroughbred: 25 cases. *Proceedings of the 47th British Equine Veterinary Association Congress*, 2008. Newmarket: Equine Veterinary Journal, p. 146.

[4] Secombe CJ, Firth, EC, Perkins NR, Anderson BH. Pathophysiology and diagnosis of third carpal bone disease in horses: a review. *N Z Vet J* 2002; **50**(1): 2–8.

[5] Firth EC, Delahunt J, Wichtel JW. Galloping exercise induces regional changes in bone density within the third and radial carpal bones of Thoroughbred horses. *Equine Vet J* 1999; **31**: 111–15.

[6] Anastasiou A, Skioldebrand E, Ekman S *et al*. Ex vivo magnetic resonance imaging of the distal row of equine carpal bones: assessment of bone sclerosis and cartilage damage. *Vet Radiol Ultrasound* 2003; **44**: 501–12.

[7] Sowers MF, Hayes C, Jamadar D *et al*. MR-detected subchondral bone marrow and cartilage defect characteristics associated with pain and X-ray-defined knee osteoarthritis. *Osteoarthr Cartilage* 2003; **11**(6): 387–93.

[8] Hayes CW, Jamadar DA, Welch GW *et al*. Osteoarthritis of the knee: comparison of MR imaging findings with radiographic severity measurements and pain in middle-aged women. *Radiol* 2005; **237**(3): 998–1007.

[9] Dyson S. Some observations on lameness associated with pain in the proximal metacarpal region. *Equine Vet J (Suppl.)* 1988; **6**: 43–52.

[10] Zubrod CJ, Schneider RK, Tucker RL. Use of magnetic resonance imaging to identify suspensory desmitis and adhesions between exostoses of the second metacarpal bone and the suspensory ligament in four horses. *J Am Vet Med Assoc* 2004; **224**(11): 1815–20.

[11] Boegard T. Radiography and bone scintigraphy in osteoarthritis of the knee – comparison with MR imaging. *Acta Radiol Suppl* 1998; **418**: 7–37.

[12] Brokken MT, Schneider RK, Sampson SN, Tucker RL, Gavin PR, Ho CP. Magnetic resonance imaging features of proximal metacarpal and metatarsal injuries in the horse. *Vet Radiol Ultrasound* 2007; **48**(6): 507–51.
[13] Powell SE, Ramzan PHL, Shepherd MC, Head MH, Baldwin G, Steven WN. Standing magnetic resonance imaging detection of bone marrow oedema-type signal pattern associated with subcarpal pain in 8 racehorses: a prospective study. *Equine Vet J* 2010; **42**(1): 10–17.

Chapter 16
The distal tarsal region

Sue Dyson

INTRODUCTION

The use of magnetic resonance imaging (MRI) of the hock region is technically challenging for both acquiring diagnostic images and interpreting them, and therefore should only be performed when essential. However, other imaging modalities have potential limitations. Radiography is insensitive for detection of early abnormalities consistent with osteoarthritis, and cannot detect bone contusions and early entheseous changes. Ultrasonography of the tarsal and proximal metatarsal regions is not easy and, even with a skilled operator, results may be negative despite the presence of soft tissue injury. The medial and lateral extremities of the suspensory ligament (SL) can be difficult to evaluate, because of the limited window of access. Overlying blood vessels may create artefacts that prohibit accurate evaluation of the architecture of the suspensory ligament. Ultrasonography is relatively insensitive for the detection of adhesions of the proximal aspect of the suspensory ligament to the second, third or fourth metatarsal bones. We have previously demonstrated in the digit that lesions of the deep digital flexor tendon (DDFT), oblique and straight sesamoidean ligaments and the collateral ligaments of the interphalangeal joints may be present on MR images, but could not be identified ultrasonographically [1]. Nuclear scintigraphy can highlight the presence of abnormal bone modelling but gives limited information about the nature of osseous pathology.

We have previously demonstrated the superior ability of MRI to detect osteochondral pathology and intertarsal ligament injury in the equine tarsus [2–4]. In tarsi from horses with no history of hind limb lameness, exercised at a low level, there is a repeatable subchondral bone thickness pattern from medially to laterally and proximally to distally [5]. In horses with a history of distal tarsal joint pain this normal pattern was lost [6]. There was a high degree of individual variation in thickness from medially to laterally. In tarsi from horses with a history of tarsal pain and radiological changes ($n = 16$), 100% of tarsi had abnormalities visible on MR images, including alteration of the chondro-osseous margins, the deep margin of the subchondral bone, lesions in the articular cartilage, intertarsal ligament injury, mineralization or cyst formation in the cancellous bone, periarticular osteophytes and entheseous new bone at capsular attachments [4, 7]. In tarsi from horses with a history of tarsal pain and no radiological changes ($n = 3$), all tarsi

Equine MRI, edited by Rachel C. Murray.

had abnormalities visible on MR images involving the subchondral bone, the intertarsal ligaments or periarticular new bone.

Radiographs, MR images and histological sections were analysed subjectively for osteochondral abnormalities and sensitivity and specificity tests were carried out using histology as the gold standard [4, 7]. Lesions affecting bone, cartilage and ligaments detected on MR images were confirmed by gross postmortem examination and histology. Homogeneous increased signal intensity of the intertarsal ligaments and loss of normal ligament shape on both T1- and T2-weighted images was associated with loss of normal shape, definition and arrangement of ligament fibres seen histologically. An increased area of low signal intensity in adjacent bone on MR images was associated with increased dense bone histologically. Loss of joint space definition with some remaining irregular regions of high signal intensity on MR images was associated with cartilage erosion and loss of joint space, with some remaining pockets of degenerate cartilage on gross postmortem examination, and histology.

Magnetic resonance imaging was 100% sensitive and specific at detecting severe osteophyte formation medially, focal osteochondral junction defects at the midline, complete articular cartilage and joint space loss laterally, and an abnormally increased area of dense bone dorsally on the lateral aspect with no trabeculae still visible. Magnetic resonance imaging was more sensitive and specific than radiology for detection of all types of pathology, including intertarsal ligament pathology, cartilage erosion, osseous cyst-like lesions (OCLLs) and subchondral bone irregularity.

The purpose of this chapter is to illustrate the different types of lesion that can be identified using MRI in the distal aspect of the equine tarsus and proximal metatarsal region, with reference to both cadaver studies and clinical experience. Examples of both low-field and high-field MR images are provided for comparison.

INDICATIONS FOR MAGNETIC RESONANCE IMAGING

Magnetic resonance imaging of the distal hock joints and proximal metatarsal region is indicated if pain has been localized to the area using local analgesic techniques, but the results of imaging using radiography, ultrasonography and scintigraphy have negative or equivocal results, are inconsistent with the degree of lameness and/or there has been a poor response to treatment. Local analgesic techniques in this region are not entirely specific. Intra-articular analgesia of the tarsometatarsal (TMT) joint has the potential to improve pain associated with proximal suspensory desmitis. Proximal suspensory desmitis and TMT joint pain may coexist [8]. Pain associated with proximal suspensory desmitis is not reliably abolished by a variety of techniques for subtarsal analgesia. However, proximal diffusion of local anaesthetic solution may result in alleviation of lameness associated with distal hock joint pain after subtarsal analgesia. In some horses with proximal suspensory desmitis, perineural analgesia of the tibial nerve is required to abolish lameness. Distal hock joint pain is not

necessarily abolished by intra-articular analgesia of the TMT and centrodistal joints, and perineural analgesia of the fibular and tibial nerves may be required. MRI may be necessary to explain the reason for increased radiopharmaceutical uptake in the absence of associated radiological abnormalities. There are close anatomical and clinical relationships between the proximal aspect of the SL, the DDFT and their accessory ligaments, and the distal aspect of the tarsus. We therefore believe that there is merit in combining examination of both the distal aspect of the hock and the proximal metatarsal region.

ABNORMALITIES

Intertarsal interosseous ligament injury

Experience to date indicates that lesions of the centrodistal interosseous ligament occur more commonly than at other sites. Acute injuries are characterized by focal or generalized increased signal intensity on T1- and T2-weighted images, with loss of the normal architecture of the ligament, sometimes with poorly defined margins (Figures 16.1–16.4). In more chronic lesions there may be increased thickness of the adjacent cortical and subchondral bone, with an irregular deep border to this bone (Figures 16.3b and c). In advanced lesions there may be replacement of ligamentous tissue by osseous tissue and loss of the cortical bone. Homogeneous increased signal intensity of the interosseous ligaments and loss of normal ligament shape on both T1- and T2-weighted images was associated with loss of normal shape, definition and

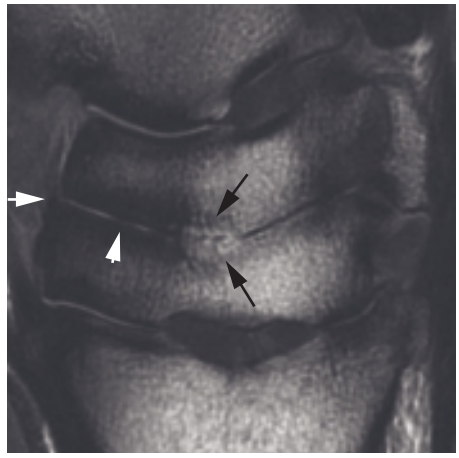

Figure 16.1 Sagittal 3D T1-weighted gradient-echo high-field MR image of a tarsus. Dorsal is to the left. There is increased signal intensity in the centrodistal intertarsal ligament, with loss of ligament and altered cortical bone architecture (black arrows). There is a small osteophyte on the dorsoproximal aspect of the third tarsal bone (white arrow). There is mild irregularity of the deep margin of the subchondral bone of the distal aspect of the central tarsal bone and the proximal aspect of the third metatarsal bone. There are focal areas of decreased signal intensity in the articular cartilage of the centrodistal joint dorsal to the centrodistal intertarsal ligament (arrowhead). There is loss of joint space plantar to the centrodistal intertarsal ligament. These abnormalities are consistent with osteoarthritis.

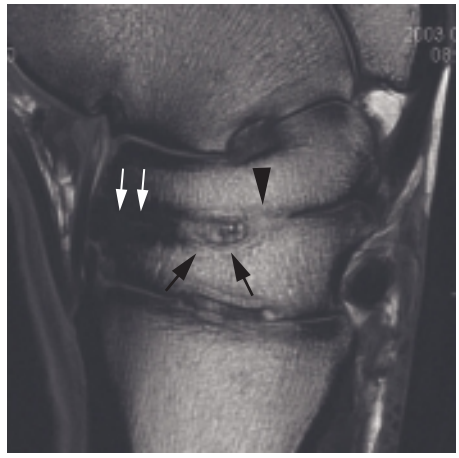

Figure 16.2 Sagittal 3D T1-weighted gradient-echo high-field MR image of a tarsus. Dorsal is to the left. There is increased signal intensity in the centrodistal intertarsal ligament (black arrows), plantar to which there is partial fusion of the centrodistal joint (arrowhead). Dorsal to the intertarsal ligament there is increased thickness of the subchondral bone of the distal aspect of the central tarsal bone and the proximal aspect of the third tarsal bone, with irregular narrowing of the centrodistal joint space (white arrows). There is periarticular osteophyte formation on the dorsal aspects of the centrodistal and tarsometatarsal joints. These abnormalities are consistent with osteoarthritis.

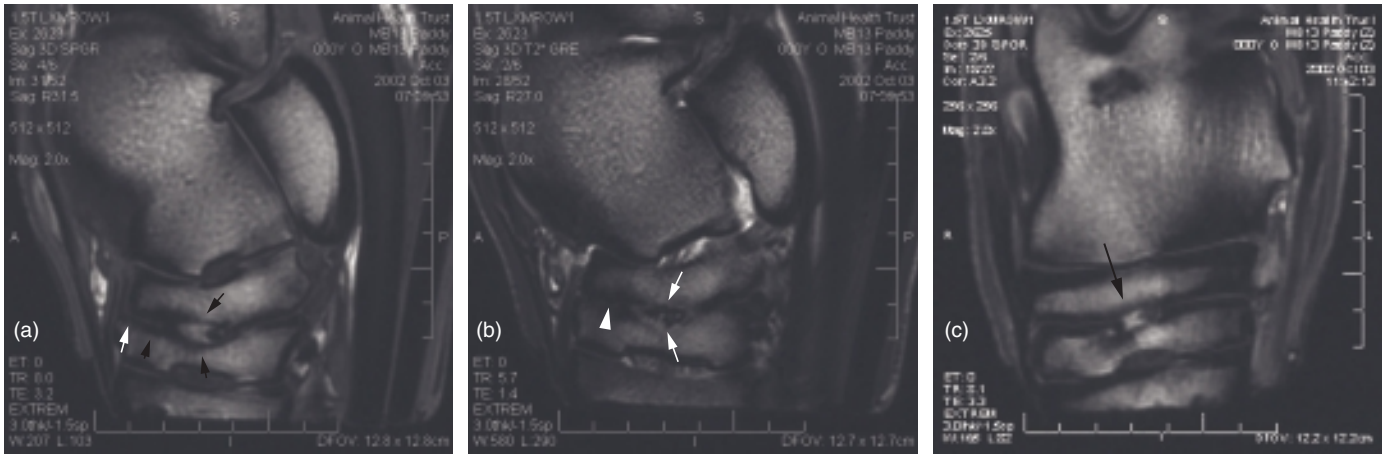

Figure 16.3 (a) Parasagittal 3D T1-weighted spoiled gradient-echo high-field MR image of a hock of a 9-year-old Warmblood dressage horse with performance problems that were partially improved by intra-articular analgesia of the centrodistal and tarsometatarsal joints. The horse also had sacroiliac joint region pain. Dorsal is to the left. There is diffuse increased signal intensity in the centrodistal intertarsal ligament (black arrows). Dorsal to the intertarsal ligament there is focal decreased signal intensity in the centrodistal joint articular cartilage (arrowhead) and an irregular chondral margin of the subchondral bone of the proximodorsal aspect of the third tarsal bone (white arrow). There was subtle joint space narrowing detected radiologically and mild focal increased radiopharmaceutical uptake in the region of the centrodistal intertarsal ligament. Histological examination of the centrodistal intertarsal ligament confirmed loss of normal ligament fibre architecture. (b) Parasagittal 3D T2* gradient-echo high-field MR image of the same hock as in (a). Dorsal is to the left. There is reduced signal intensity in the region of the centrodistal intertarsal ligament (arrows). The deep margin of the subchondral bone of the distal dorsal aspect of the central tarsal bone is irregular. The centrodistal joint space is poorly defined dorsally with some focal areas of increased signal intensity (arrowhead). (c) Dorsal 3D T1-weighted gradient-echo high-field MR image of the same tarsus. Medial is to the left. There is increased signal intensity in the centrodistal intertarsal ligament (black arrow) and an irregular deep margin of the distal subchondral bone of the central tarsal bone laterally.

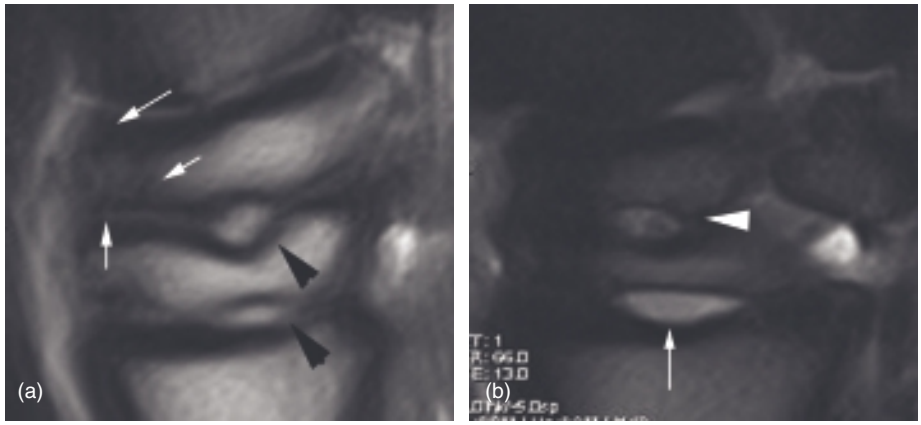

Figure 16.4 (a) Parasagittal T1-weighted gradient-echo motion-insensitive low-field MR image of the left tarsus of a mature riding horse with lameness improved by intra-articular analgesia of the tarsometatarsal (TMT) joint. Dorsal is to the left. There is diffuse increased signal intensity in the centrodistal (CD) and TMT intertarsal ligaments (arrowheads). The chondral margins of the subchondral bone on the dorsal aspect of the CD joint are irregular (white arrow), as are the deep margins of the subchondral bone of the central tarsal bone proximally and distally (white arrows). There was no detectable radiological abnormality. (b) Parasagittal T2-weighted gradient-echo motion-insensitive low-field MR image of the same hock as in (a). Dorsal is to the left. There is diffuse increase in signal intensity in the tarsometatarsal intertarsal ligament (arrow); the CD intertarsal ligament has a patchy increase in signal intensity. There is a very irregular deep border of the subchondral bone of the proximal and distal aspects of the central and third tarsal bones dorsally.

arrangement of ligament fibres seen histologically [4]. An increased area of low signal intensity in adjacent bone on MR images was associated with increased dense bone histologically.

We speculate that interosseous ligament injury may create low-grade instability and predispose to the development of osteoarthritis. Most severe abnormalities of the interosseous ligaments have been seen in association with advanced osteoarthritis.

Osteoarthritis of the centrodistal and tarsometatarsal joints

The features used to identify evidence of osteoarthritis of the distal hock joints are summarized in Table 16.1 and illustrated in Figures 16.1–16.5. The greater the number and severity of changes identified, the more likely they are to be of clinical significance.

We have previously documented the superiority of MRI for detection of early abnormalities associated with osteoarthritis in the equine tarsus compared with radiology [3, 4]. However, there appears to be overlap between lesions that can be found in both clinically normal horses and those with distal hock joint pain. Abnormalities seen on MR images from horses with a history of distal tarsal pain that had no radiological evidence of pathology were much less severe than those seen on images of tarsi with radiological evidence of pathology. Some of the abnormalities (e.g. mild abnormalities of intertarsal ligament, small osteophytes) detected in tarsi

Table 16.1 Criteria to assess the distal hock joints using magnetic resonance imaging

Structure	Properties	Normal	Abnormal
Proximal/distal articular cartilage	Signal intensity	Homogenous high signal	Heterogeneous signal
			Focal loss of signal
			Diffuse loss of signal
	Structure	Regular osteochondral junction	Complete loss of cartilage/joint space
			Irregular osteochondral junction
Proximal/distal subchondral bone	Signal intensity	Homogenous low signal	Heterogeneous signal
			Focal increase in intensity
			Diffuse increase in intensity
	Structure	Regular osteochondral junction	Irregular osteochondral junction
		Regular deep border	Irregular deep border
Cortical bone	Signal intensity	Homogenous low signal	Heterogeneous signal
			Focal increase in intensity
			Diffuse increase in intensity
	Structure	Uniform layer of dense bone	Increased dense bone dorsally
			Presence of osteophytes
			Bone bridging joint space
Cancellous bone	Signal intensity	Heterogeneous signal	Increased intensity on fat-suppressed images
			Increased area of low signal
	Structure	Visible trabecular pattern	Loss of trabecular pattern
Interosseous ligaments	Signal intensity	Heterogeneous signal	Increased signal intensity
			Reduced signal intensity
			Homogeneous signal
	Structure of bone surrounding ligament	Homogenous low signal	Increased area of low signal
		Regular border	Focal increase in signal intensity
			Irregular border

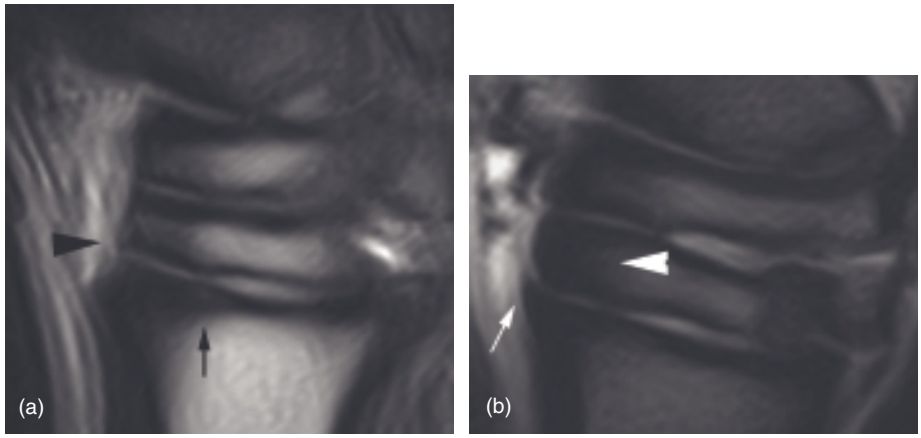

Figure 16.5 (a) Parasagittal T1-weighted gradient-echo motion-insensitive low-field MR image of an 8-year-old event horse with lameness improved by intra-articular analgesia of the tarsometatarsal joint. There is a small osteophyte on the distal dorsal aspect of the third tarsal bone (arrowhead). The deep border of the subchondral bone of the third tarsal bone is irregular dorsally. There is a focal area of increased signal intensity in the subchondral bone of the proximal aspect of the third metatarsal bone (arrow). No significant radiological abnormality was detected. (b) Dorsal T2-weighted gradient-echo motion-insensitive low-field MR image of the same hock as in (a). Lateral is to the left. There is a periarticular osteophyte on the proximolateral aspect of the third metatarsal bone (arrow). There is diffuse decreased signal intensity throughout the cancellous bone of the lateral aspect of the third tarsal bone (arrowhead).

from horses with no history of hind limb lameness were of similar severity to those in painful tarsi with no radiological changes. However, cartilage abnormalities were not seen in painful tarsi with no radiological changes. In contrast, seven normal tarsi had focal cartilage signal intensity abnormalities and seven had diffuse reduction in cartilage signal intensity. Mildly irregular deep subchondral bone borders were seen in all three tarsi with a history of pain and no radiological changes. Irregular deep subchondral bone borders were not observed in normal tarsi. These results suggest that perhaps mild cartilage abnormalities are not painful, but that mild subchondral bone abnormalities are. However, the small group size ($n = 3$) means that this group might not be an accurate representation of the population of horses with pain without radiological changes. Thus the identification of low-grade abnormalities on MR images does not necessarily implicate them as a current source of pain.

Subchondral bone trauma

Subchondral bone trauma is characterized by a region of high signal intensity in fat-suppressed images, together with a corresponding area of reduced signal intensity on T1- and T2-weighted images. Such lesions have been seen in a variety of locations within the talus, central, third and fourth tarsal bones, and the proximal aspect of the third metatarsal bone. Lesions in the proximoplantar aspect of the third metatarsal bone may reflect an entheseous reaction at the origin of the SL (Figure 16.6).

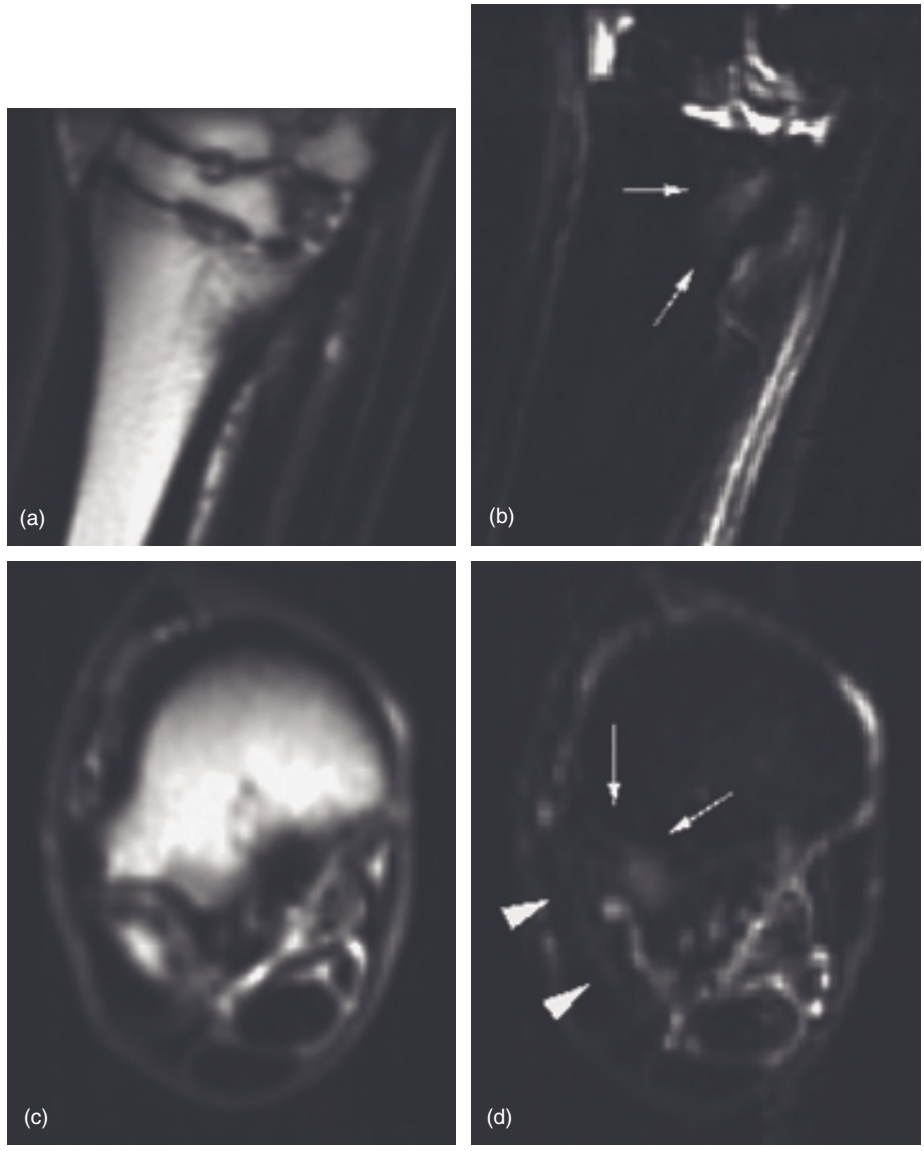

Figure 16.6 (a) Sagittal fast spin-echo (FSE) high-field MR image of the proximal metatarsal region of a 4-year-old Thoroughbred racehorse with severe persistent lameness improved by subtarsal analgesia or intra-articular analgesia of the tarsometatarsal joint. Dorsal is to the left. There is ill-defined reduced signal intensity on the endosteal aspect of the proximoplantar aspect of the third metatarsal bone at the origin of the suspensory ligament. There were only minor alterations in signal intensity in the suspensory ligament itself. No ultrasonographic or radiological abnormalities were detectable; however, there was focal intense increased radiopharmaceutical uptake in the proximoplantar aspect of the third metatarsal bone. (b) Sagittal 2D STIR high-field MR image of the proximal metatarsal region of the same limb as in (a). Dorsal is to the left. There is increased signal intensity in the proximoplantar aspect of the third metatarsal bone (arrows), coincident with the decreased signal intensity seen in (a). (c) Transverse T1-weighted FSE high-field MR image of the proximal metatarsal region of the same limb as in (a) and (b). Lateral is to the left. There is reduced signal intensity in the plantarolateral aspect of the third metatarsal bone. (d) Transverse 2D STIR high-field MR image of the proximal metatarsal region of the same limb as in (a)–(c). Lateral is to the left. There is increased signal intensity in the plantarolateral aspect of the third metatarsal bone (arrows), corresponding with the area of reduced signal intensity seen in (c). These signal abnormalities are consistent with bone trauma at the enthesis of the suspensory ligament. There is also increased signal intensity in the axial aspect of the fourth metatarsal bone (arrowheads) consistent with bone trauma at the enthesis of the interosseous ligament.

Fracture

Incomplete fractures of the third or central tarsal bone may not be detectable radiologically and probably reflect a stress-related bone injury in young Thoroughbred racehorses. A fracture is identified as a line of high signal intensity in all image sequences surrounded by an area of decreased signal intensity (Figure 16.7).

Interosseous ligament injury (syndesmopathy)

The degree of variability in the articulations between the second and third, and fourth and third metatarsal bones has not yet been definitively established. In some horses the space between the bones has appeared widened in association with increased signal intensity in the interosseous ligament (Figure 16.8). There may be increased signal intensity in fat-suppressed images in the subcortical bone of the affected bones (Figure 16.6c). In other horses there has been endosteal irregularity adjacent to the insertion of the interosseous ligament. The role of these lesions in relation to pain and lameness has yet to be established.

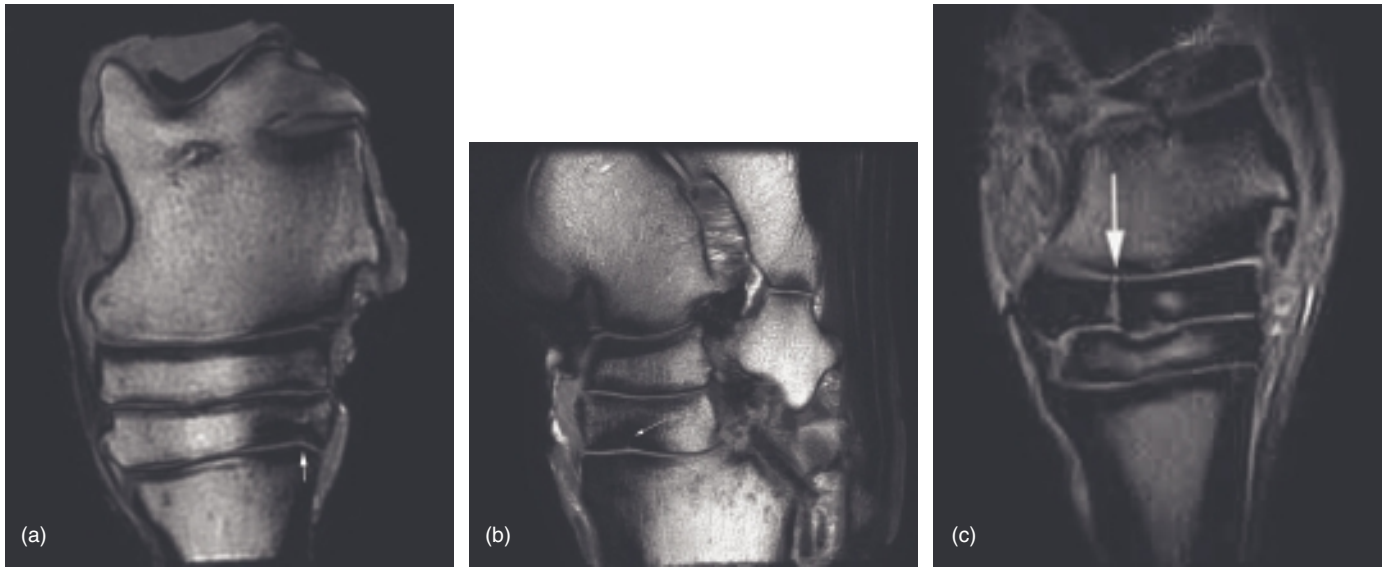

Figure 16.7 (a) Dorsal 3D T1-weighted spoiled gradient-echo high-field MR image of a hock of a 3-year-old Thoroughbred flat racehorse. Lateral is to the right. There is abnormal thickness of the distal subchondral bone of the third tarsal bone laterally. There is a small hyperintense line at the distal aspect of the third tarsal bone, which represents an incomplete fracture. (b) Lateral parasagittal 3D spoiled gradient-echo high-field MR image of the same hock as in (a). Dorsal is to the left. There is abnormal thickness of the distal subchondral bone of the third tarsal bone and the proximal subchondral bone of the third metatarsal bone. There is a short hyperintense line in the distal aspect of the third tarsal bone, an incomplete fracture (arrow). (c) Dorsal T1-weighted gradient-echo image of a 7-year-old roping horse with a 2-month history chronic intermittent lameness and recent more severe acute lameness following competition. A complete sagittal fracture can be identified as a linear area of hyperintensity (arrow) extending from the proximal margin of the central tarsal bone to the distal margin. This finding is surrounded by extensive sclerosis characterized by low signal intensity in the trabecular bone. Mild increased signal intensity was present on STIR images indicating fluid surrounding the fracture. Image courtesy of Dr Natasha Werpy.

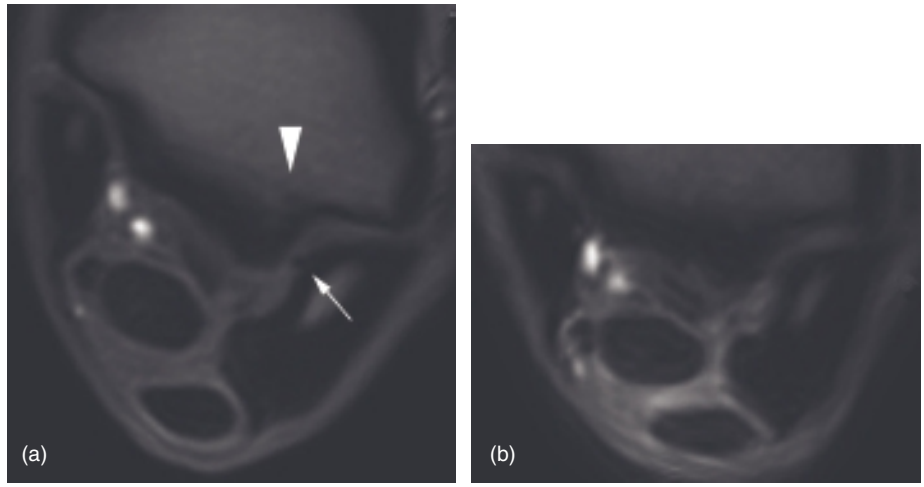

Figure 16.8 (a) Transverse T1-weighted gradient-echo motion-insensitive low-field MR image of the proximal metatarsal region of an 11-year-old Grand Prix showjumper, the same limb as in Figures 16.9a–c. Lateral is to the right. The space between the fourth and third metatarsal bones is abnormally wide. Note also slight cortical irregularity on the axial aspect of the fourth metatarsal bone (white arrow) and mild endosteal irregularity on the opposing aspect of the third metatarsal bone (white arrowhead) reflecting syndesmopathy. The plantar cortex of the third metatarsal bone is also thickened, associated with chronic proximal suspensory desmitis. (b) Transverse T2* gradient-echo motion-insensitive low-field MR image of the proximal metatarsal region of the same limb as in (a). Lateral is to the right. The space between the fourth and third metatarsal bones is abnormally wide. The plantar cortex of the third metatarsal bone is also thickened due to endosteal and periosteal (entheseous) new bone associated with chronic proximal suspensory desmitis.

Proximal suspensory desmitis

Evaluation of the SL using MRI is not easy because of the presence of muscle and adipose tissue in variable patterns and amounts in the central portion of the medial and lateral lobes of the ligament, resulting in well-demarcated areas of high signal intensity in T1, T2 and to a lesser extent fat-suppressed images [9, 10]. Loss of mediolateral symmetry in size, increased signal intensity around the periphery of each lobe of the SL and increased area of high signal intensity are characteristic lesions (Figures 16.9 and 16.10). There may be periligamentar tissue immediately surrounding the ligament, often of intermediate signal intensity (Figure 16.11). Occasionally there may be replacement of the central region of high signal intensity by a region of low signal intensity due to fibrous repair tissue [11] (Figure 16.11).

Acute entheseous reaction is seen as an area of increased signal intensity in fat-suppressed images in the cancellous bone dorsal to the origin of the SL on the plantar cortex of the third metatarsal bone, with corresponding areas of reduced signal intensity in T1- and T2-weighted images [12] (Figure 16.6). This may be seen alone or in conjunction with lesions of the SL per se. Chronic entheseous reaction is characterized by periosteal new bone on the proximoplantar aspect of the third metatarsal bone, seen as

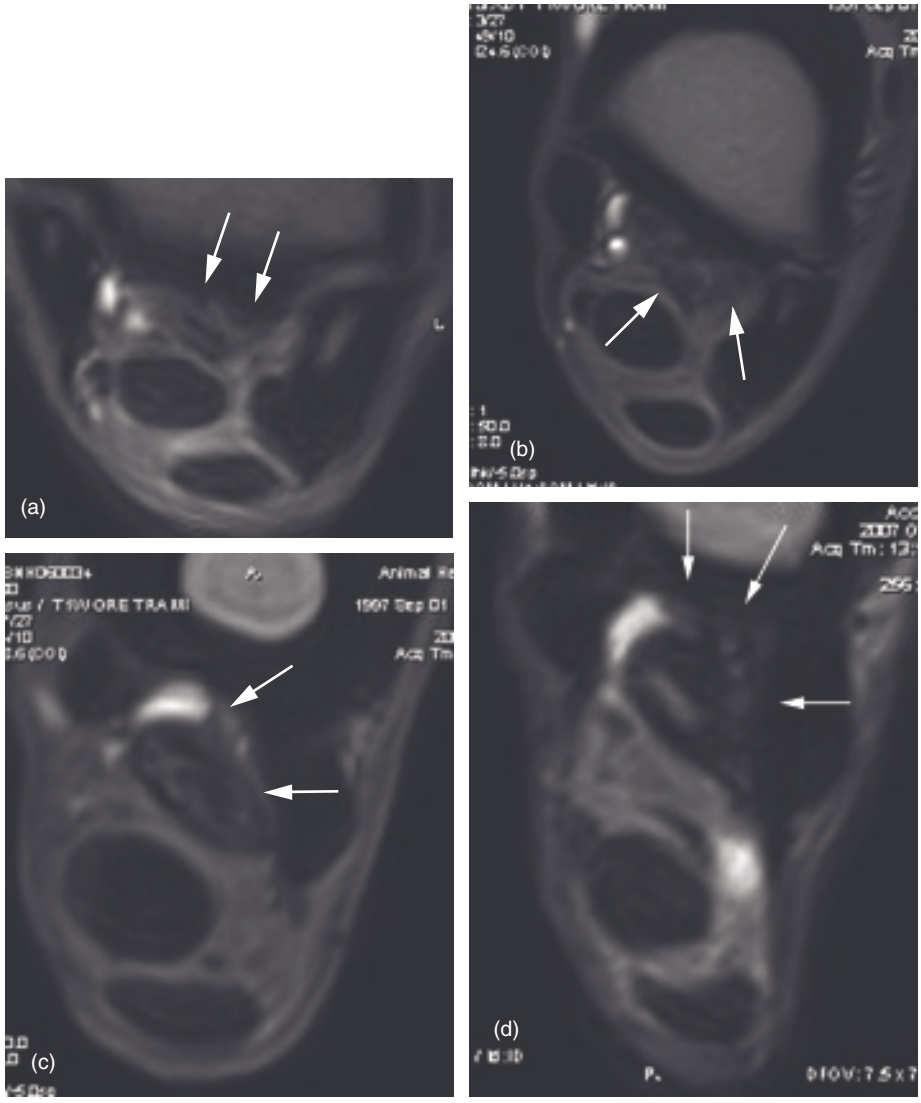

Figure 16.9 (a) Transverse T2-weighted gradient-echo motion-insensitive low-field MR image of the proximal metatarsal region of an 11-year-old Grand Prix showjumper, with lameness substantially improved by subtarsal analgesia of the deep branch of the lateral plantar nerve. Lateral is to the right. There is an irregular plantar cortex of the third metatarsal bone laterally (arrows). The suspensory ligament has a diffuse increase in signal intensity and is enlarged laterally. Only minor structural changes of the suspensory ligament were identified ultrasonographically, which did not seem consistent with the degree of lameness. No significant radiological abnormality was detected and radiopharmaceutical uptake was normal. (b) Transverse T1-weighted gradient-echo motion-insensitive low-field MR image of the proximal metatarsal region of the same limb as in (a), slightly further distally. The lateral lobe of the suspensory ligament is enlarged (arrows), and its periphery has increased signal intensity. (c) Transverse T1-weighted gradient-echo motion-insensitive low-field MR image of the proximal metatarsal region of the same limb as in (a) and (b), slightly further distal to (b). There are substantial adhesions between the suspensory ligament and the plantar aspect of the third metatarsal bone and the axial aspect of the fourth metatarsal bone. (d) Transverse T2-weighted gradient-echo motion-insensitive low-field MR image of the proximal metatarsal region of a 6-year-old dressage horse with lameness improved by subtarsal analgesia of the deep branch of the lateral plantar nerve. Lateral is to the right. There are extensive adhesions between the suspensory ligament and the plantar cortex of the third metatarsal bone and the axial aspect of the fourth metatarsal bone. There were no detectable ultrasonographic abnormalities of the suspensory ligament. No significant radiological abnormality was detectable and radiopharmaceutical uptake was within the normal range.

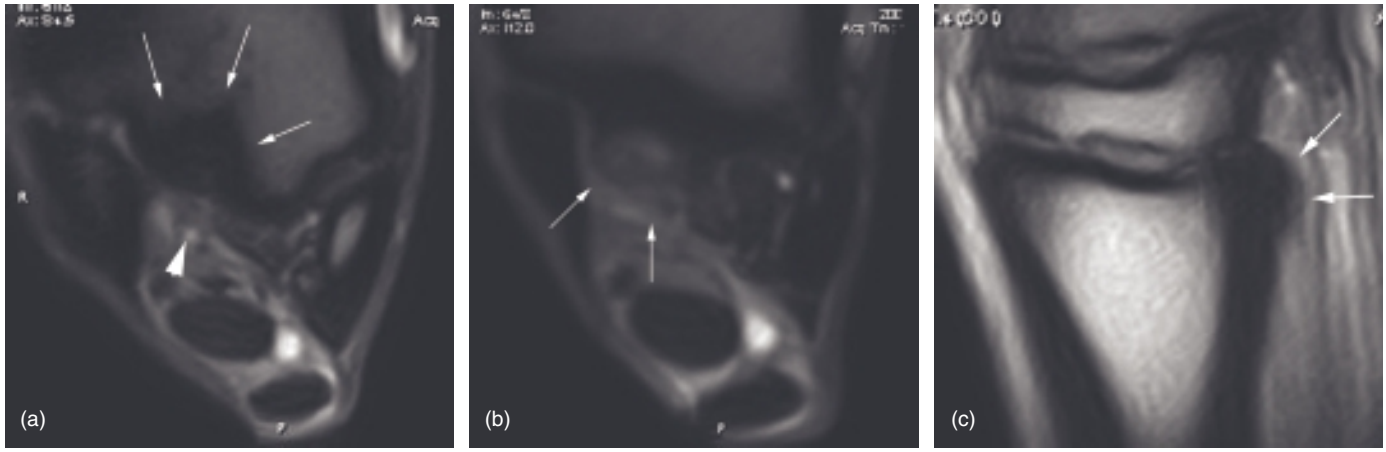

Figure 16.10 (a) Transverse T2-weighted gradient-echo motion-insensitive low-field MR image of the proximal metatarsal region of a 9-year-old showjumper with lameness substantially improved by subtarsal analgesia of the deep branch of the lateral plantar nerve. Medial is to the left. The plantar cortex of the third metatarsal bone was thickened, with marked endosteal reaction especially medially (arrows). There is increased signal intensity in the medial lobe of the suspensory ligament (arrowhead). It was difficult to acquire diagnostic quality ultrasonographic images, and no abnormality could be identified consistent with the degree of lameness. There was mild subcortical increased radiopacity of the proximoplantar aspect of the third metatarsal bone seen radiologically. There was moderate focal increased radiopharmaceutical uptake in the proximoplantar aspect of the third metatarsal bone. (b) Transverse T2-weighted gradient-echo motion-insensitive low-field MR image of the proximal metatarsal region of the same limb as in (a). Medial is to the left. The plantar cortex of the third metatarsal bone is abnormally thick, especially medially. The medial lobe of the suspensory ligament has diffuse increased signal intensity (arrows). (c) Medial parasagittal T1-weighted gradient-echo motion-insensitive low-field MR image of the proximal metatarsal region of the same limb as in (a). Dorsal is to the left. There is entheseous new bone on the proximoplantar aspect of the third metatarsal bone (arrows).

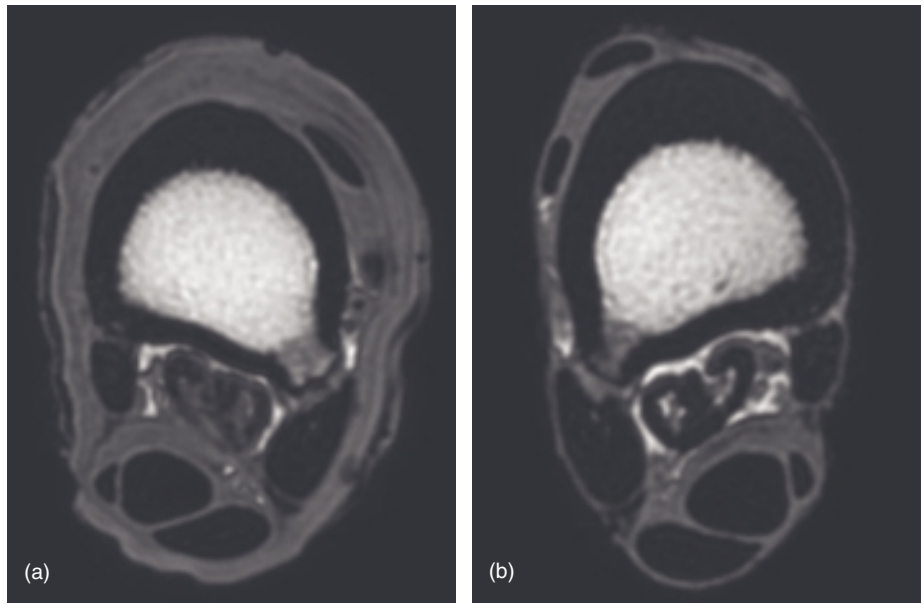

Figure 16.11 (a) Transverse T1-weighted gradient-echo high-field MR image of the left proximal metatarsal region of a 12-year-old Warmblood dressage horse with left hind limb lameness. Medial is to the left. Both lobes of the suspensory ligament are enlarged; there is heterogeneous signal intensity in the peripheral ligamentous tissue. Compare with the uniform low signal intensity of the superficial and deep digital flexor tendons. There is reduced signal intensity in the central areas of each lobe (compare with (b)). There is periligamentar tissue of intermediate signal intensity especially on the plantar and medial aspects of the suspensory ligament. (b) Transverse T1-weighted gradient-echo high-field MR image of the right proximal metatarsal region of a 12-year-old Warmblood dressage horse with left hind limb lameness at the same level as in (a). Medial is to the right. The peripheral ligamentous tissue of the suspensory ligament is of uniform low signal intensity, isointense to the superficial and deep digital flexor tendons. There are areas of high and intermediate signal intensity within the central areas of each lobe. Compare with (a). The margins of the suspensory ligament are more clearly defined.

irregular areas of low signal intensity plantar to the normal straight contour of the third metatarsal bone on T1- and T2-weighted images (Figure 16.10) or endosteal new bone seen as an irregular deep margin to the cortical bone on T1 and T2 weighted images (Fig. 16.10). Adhesions of the injured lobe of the SL to the second or fourth metatarsal bone and /or third metatarsal bone are seen as loss of separation between the SL and the bone or a band of tissue of low signal intensity extending from the SL to the bone (Figure 16.9).

In a series of 16 horses with hindlimb lameness improved by subtarsal analgesia, proximal suspensory desmitis was identified using high-field MRI in 13 horses, 11 of which had both enlargement of the SL and altered signal intensity [11]. In two horses there was enlargement of the SL but no change in signal intensity. Five of the 13 horses had osseous changes at the origin of the SL, characterized by decreased signal intensity in T1- and T2-weighted images. One of the five horses had corresponding increased signal intensity in STIR images. One horse had a lesion of the DDFT in the proximal metatarsal region and in two horses there was no satisfactory explanation for the lameness. The distal hock joints were not examined.

Twenty-five horses with a positive response to perineural analgesia of the deep branch of the lateral plantar nerve underwent high-field MRI at North Carolina State University [13]. Six horses had proximal suspensory desmitis, generally characterized by increased signal intensity in the collagenous part of the ligament. Seven horses had proximal suspensory desmitis with associated osseous changes, four with endosteal reaction of the plantar cortex of the third metatarsal bone, two with increased signal intensity in fat-suppressed images in the proximal aspect of the fourth metatarsal bone or in the fourth tarsal bone, and one horse with a dorsal cortex abnormality. Of the 13 horses with suspensory abnormalities, two had alterations in signal intensity within the central muscular tissue and the surrounding collagenous tissue. Most lesions (10) were located centrally, but two horses had lesions restricted to the abaxial aspect of the lateral lobe of the SL.

Eight horses had primary osseous abnormalities, including an exostosis on the fourth metatarsal bone with adhesion to the SL in two horses; increased signal intensity in fat-suppressed images of the central and third tarsal bones associated with the intertarsal ligament attachments; fracture of the plantar aspect of the third and fourth tarsal bones; an OCLL in the central tarsal bone; osteoarthritis of the centrodistal joint; and a diffuse endosteal reaction in the dorsomedial aspect of the third metatarsal bone and increased signal intensity in fat-suppressed images. In four horses no lesion was found to explain the lameness, although there were mild shape and size changes of the proximal aspect of the SL. Ultrasonographic images of the SL were available for 23 horses, in only 10 of which was there agreement between ultrasonography and MRI (nine positive and one negative).

Seventeen horses with proximal metatarsal region pain, defined as substantial improvement following perineural analgesia of the deep branch of the lateral plantar nerve, were examined at the Animal Health Trust using either high-field or low-field MRI. Intra-articular analgesia of the tarsometatarsal

joint produced no change, or a lesser response. Ultrasonographic examination had been inconclusive in the majority of horses. Fifteen horses had evidence of proximal suspensory desmitis and one horse had desmitis of the accessory ligament of the DDFT (S Dyson and R Murray, unpublished data). In 11 horses both the medial and lateral lobes of the SL had abnormalities, whereas in three horses lesions were restricted to the lateral lobe and in one horse to the medial lobe. Adhesions to the plantar cortex of the third metatarsal bone or to the axial aspect of either the second or fourth metatarsal bone were identified in four horses. Eight horses had endosteal reaction at the origin of the ligament on the third metatarsal bone and three horses had entheseous new bone on the plantar cortex. Evidence of low-grade osteoarthritis of the centrodistal and or tarsometatarsal joints was seen in three horses. Three horses had abnormal widening of the syndesmosis between the second and third or fourth and third metatarsal bones, with associated increased signal intensity. In one horse only osseous pathology was identified, with a diffuse area of reduced signal intensity in the proximal plantar medial aspect of the third metatarsal bone in T1- and T2-weighted images.

Desmitis of the accessory ligament of the deep digital flexor tendon

Injuries of the accessory ligament of the DDFT in the hind limb are unusual, in contrast to the forelimb. One horse had a lesion extending from the origin on the plantar aspect of the distal hock to the proximal metatarsal region characterized by enlargement of the ligament and increased signal intensity in all image series, in addition to increased signal intensity at the origin of the accessory ligament of the SL.

REFERENCES

[1] Dyson S, Murray R. Lameness and diagnostic imaging in the sports horse: recent advances related to the digit. *Proc Am Assoc Equine Pract* 2007; **53**: 262–75.
[2] Branch M, Murray R, Dyson S, Goodship A. Can we visualise pathology of the distal tarsal joints using magnetic resonance imaging? *Proceedings 42nd British Equine Veterinary Association Congress*, 2003. Newmarket: Equine Veterinary Journal, p. 297.
[3] Branch M, Murray R, Dyson S, Goodship A. Magnetic resonance imaging of distal tarsal osteochondral structure: normal variation or pathological change? *Proc Am Assoc Equine Pract Focus on Joints Meeting*, 2004, pp. 28–41.
[4] Branch M. How is adaptive change related to pathology in the equine distal tarsal osteochondral unit? PhD thesis, University of London, 2005.
[5] Branch M, Murray R, Dyson S, Goodship A. Is there a characteristic distal tarsal subchondral bone plate thickness pattern in horses with no history of hindlimb lameness? *Equine Vet J* 2005; **37**: 450–5.
[6] Branch M, Murray R, Dyson S, Goodship A. Alteration of distal tarsal subchondral bone thickness pattern in horses with tarsal pain. *Equine Vet J* 2007; **39**: 101–5.
[7] Branch M, Murray R, Dyson S, Goodship A. Magnetic resonance imaging of the equine tarsus. *Clin Tech Equine Pract* 2007; **6**: 96–102.
[8] Dyson S. Diagnosis and management of common suspensory lesions in the forelimbs and hindlimbs of sports horses. *Clin Tech Equine Pract* 2007; **6**: 179–88.
[9] Bischofberger A, Konar M, Ohlerth S *et al*. Magnetic resonance imaging, ultrasonography and histology of the suspensory ligament origin: a comparative study of normal anatomy of Warmbloods. *Equine Vet J* 2006; **38**: 508–19.

[10] Sampson S, Tucker R. Magnetic resonance imaging of the proximal metacarpal and metatarsal regions. *Clin Tech Equine Pract* 2007; **6**: 78–85.
[11] Brokken T, Schneider R, Sampson S, Tucker R, Gavin P, Ho C. Magnetic resonance imaging features of proximal metacarpal and metatarsal injuries in the horse. *Vet Radiol Ultrasound* 2007; **48**: 507–17.
[12] Dyson S. Proximal metacarpal and metatarsal pain: a diagnostic challenge. *Equine Vet Educ* 2006; **15**: 134–42.
[13] Redding R, Schramme M. Comparison of ultrasound and MRI in the diagnosis of proximal plantar metatarsal pain in 25 horses. *Proc Am Coll Vet Surgeons* (CD-Rom), 2007.

Chapter 17
The proximal tarsal region

Rachel Murray, Natasha Werpy, Fabrice Audigié, Jean-Marie Denoix, Matthew Brokken and Thorben Schulze

INTRODUCTION

Imaging of the proximal tarsus can be achieved in both standing and anaesthetized horses. The height of the horse and the amount of hind end musculature determines which magnet configuration will produce the best images of this region. A horse with short limbs and wide, well-muscled quarters may be more difficult to fit into the long, narrow bore of some high-field magnets under general anaesthesia. In the same way, the side of the lateral recumbency should be considered because it is generally easier to bring the proximal tarsus of the lower hind limb closer to the isocentre of the magnet compared with the upper one. Well developed hind limb musculature can prevent the limb from being placed far enough into the bore to allow the tarsus to be positioned at the isocentre of the magnet. The tarsus of a horse with this body type (or stature) is more easily positioned in a standing system. In contrast, for a narrow horse with long limbs, the height of the tarsus and width between the limbs may make it more difficult to image this region within a standing system. The degree of sway in the proximal aspect of the limbs in a standing, sedated horse is often substantially greater than in the distal aspect of the limbs. This degree of sway can produce significant motion artefact and can make it frustrating to acquire images of the proximal tarsus. Therefore, selection of sedation and patient handling is particularly important when acquiring images of the proximal tarsus using the standing system.

Soft tissue and osseous abnormalities of the proximal tarsus can be assessed using MRI, and it may be possible to identify lesions that have not been detected using other imaging modalities.

OSSEOUS PATHOLOGY

Fracture

Fractures of the talus, calcaneus and distal tibia can be identified on magnetic resonance images of the proximal tarsus. Fractures may be visualized as sharp, well-defined linear areas of increased or decreased signal intensity with loss of the normal bone contour. These findings can extend through the cortical, subchondral and cancellous bone. Displacement of the fracture can result in defects in the osseous margins. In acute fractures, increased signal

Equine MRI, edited by Rachel C. Murray.

intensity on fat-suppressed images is evident in the bone surrounding the fracture. Displaced, complete fractures are generally evident on radiographs. In these cases, magnetic resonance imaging (MRI) may not be required to reach a diagnosis. However, a non-displaced fracture may be difficult to visualize on radiographs until there is osseous remodelling around the fracture line. MRI is useful for identification of non-displaced fractures when pain is localized to this region with marked radiopharmaceutical uptake and no radiographic evidence of a fracture (Figure 17.1).

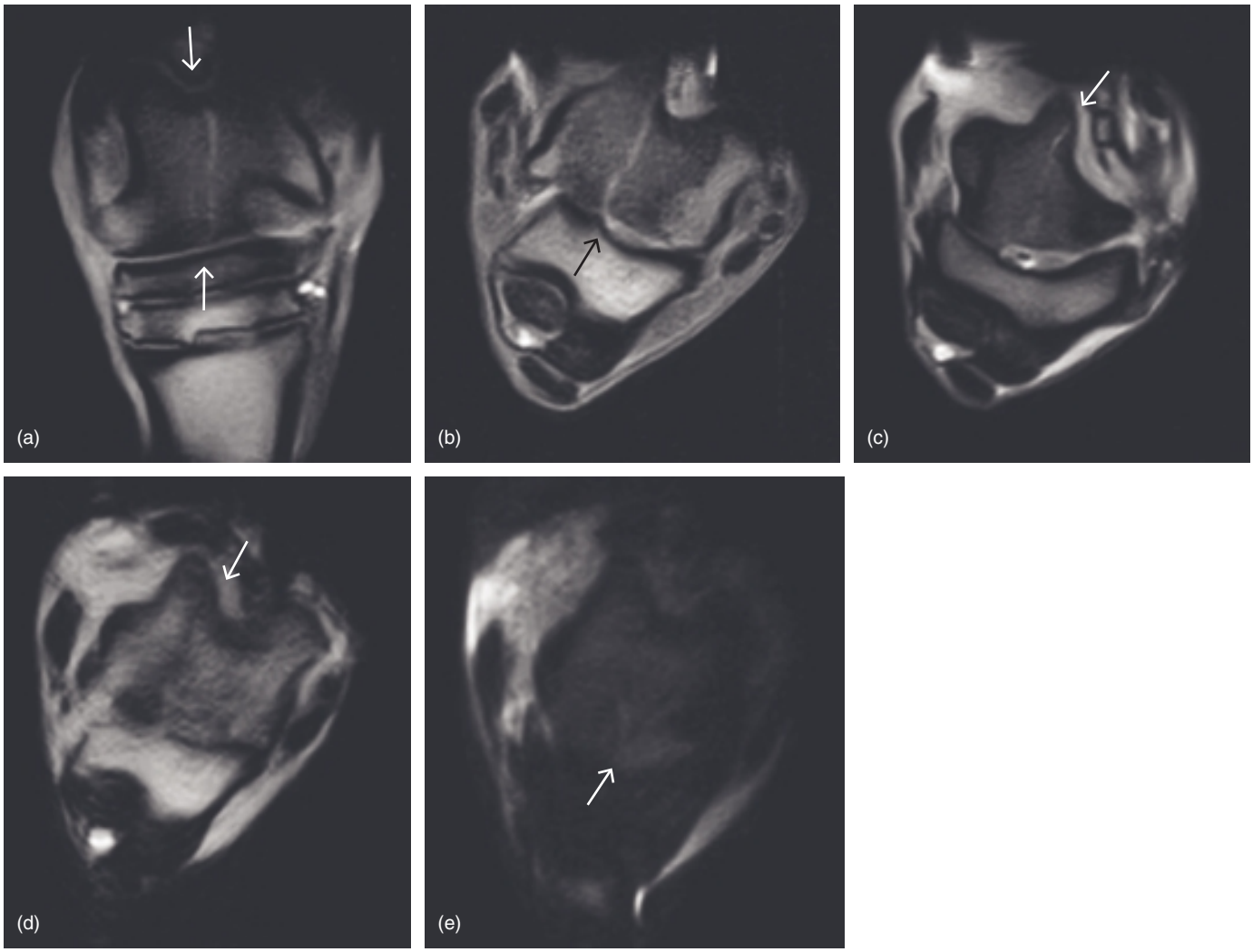

Figure 17.1 Talus fracture. (a) Dorsal and (b) transverse T1-weighted and (c) transverse T2* gradient-echo, (d) T2 FSE and (e) STIR images of the left tarsus of a 12-year-old Arabian endurance horse that had pulled up non-weight bearing lame after an endurance ride, 3 weeks previously. Radiographs were equivocal on initial evaluation but there was greatly increased radiopharmaceutical uptake in the talus. MR images were obtained standing using a 0.27T MR imaging system, demonstrating a minimally displaced complete sagittal fracture of the talus (arrows). The fracture line itself is seen as high signal intensity on T1-weighted images, bounded by low signal intensity representing bone oedema/damage. On T2* gradient-echo images the fracture line is seen as high signal intensity surrounded by moderately high signal intensity within the adjacent bone with a boundary of low signal intensity due to a fat–water cancellation artefact. On T2 FSE images, it is more difficult to see the fracture line, which is represented by lower signal intensity than the surrounding bone, but the absence of low signal intensity in the surrounding bone confirms that the low signal intensity boundary seen on T2* gradient-echo images represents an artefact and not sclerosis. On STIR images, there is generalized increase in signal intensity within the talus clearly defining bone oedema/pathology but it is relatively difficult to define a fracture line.

Fractures occurring in regions with/of extensive sclerosis are easily identified on many different sequences. Acute non-displaced fractures surrounded by fluid in the absence of sclerosis are most easily identified on T1-weighted images as a linear hyperintense line bordered by low signal intensity fluid. A fracture line can be obscured by surrounding high signal intensity on fat-suppressed images, although high signal highlights the presence of bone damage. In general, careful evaluation of the cortical and compact bone on all sequences will reveal the presence of a fracture.

Following identification of a fracture, it is important to evaluate all the associated soft tissue structures and not be misled into considering solely osseous injury. Assessment of the adjacent soft tissue structures including tendon, ligament and joint capsule attachments is necessary to determine the complete extent of the injury.

Bone trauma/bruising/contusion

Where there has been trauma to the tarsal bones without macroscopic fracture, there may be osseous damage related to trabecular microfracture, bone oedema and increased blood flow. This condition is know as bone bruising or contusion and is demonstrated as high signal intensity on fat-suppressed images with a concurrent low signal intensity on T1-weighted and sometimes T2*-weighted images dependent on the sequence parameters and relative fluid/fat content (see fat–water cancellation artefact). High signal intensity can be identified on T2-weighted images at the site of injury, depending on sequence parameters. This may affect more than one bone or joint, and adjacent soft tissues and joints should be evaluated (Figures 17.2 and 17.3). Haemarthrosis may occur concurrently and can be identified as

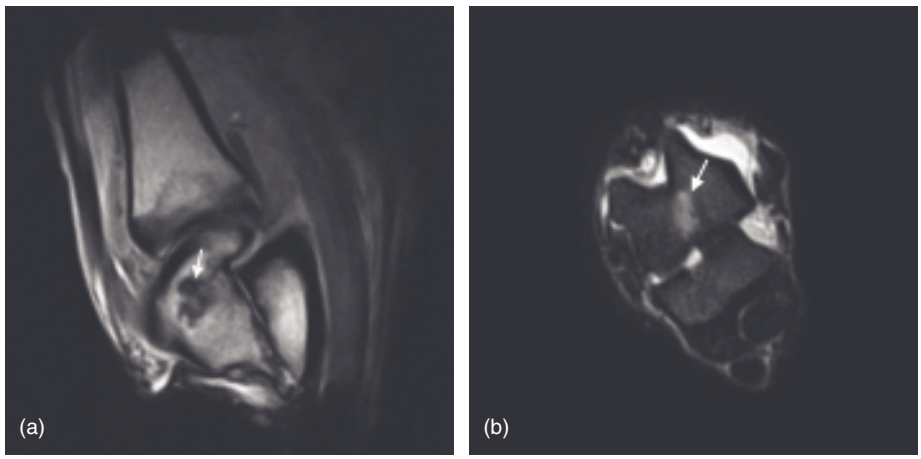

Figure 17.2 Focal talus pathology. (a) Sagittal T1-weighted and (b) transverse STIR low field images from a 3-year-old racehorse with acute lameness following competition. Low signal intensity can be identified in the talus on the T1-weighted image with corresponding increased signal intensity in the same area of the talus on the STIR image (white arrows). These findings represent fluid within the talus indicating oedema, contusion and/or osteonecrosis. There is also synovitis of the tibiotarsal joint characterized by increased fluid. This finding is best demonstrated on the STIR transverse image.

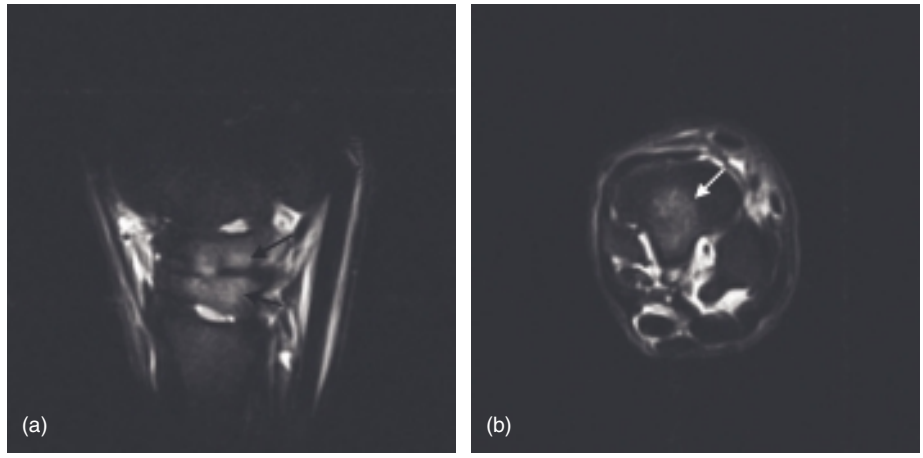

Figure 17.3 Tarsal bone trauma/contusion. (a) Sagittal and (b) transverse STIR images from a 9-year-old Warmblood jumper with an acute grade 3/5 lameness following competition. These images demonstrate increased signal intensity in the central and third tarsal bones (arrows). This pattern represents diffuse fluid accumulation and is consistent with trauma. In this case, the lameness gradually improved over a 6-month time period and the horse returned to full work after that time. Osteophytosis on the dorsal proximal aspect of the third metatarsus can be identified on the sagittal image.

layering of different signal intensities in the joint. Red blood cells will settle in the dependent portion of the joint and will be covered by a serum layer. Bone bruising representing strain-related trabecular and cortical damage may occur adjacent to a ligament enthesis where there has been partial avulsion or excessive strain, so associated ligaments and periligamentar tissues should be assessed for damage. Ligament strain may result in secondary joint instability, so other articular ligaments, associated tendons and the articular surface should be assessed (Figures 17.4 and 17.5).

Where there is damage to an adjacent tendon, tendon sheath or bursa, then there may be concurrent bone bruising within the local bone if the damaged ligament or tendon is abrading the bone and causing secondary trauma. Bone bruising can result from biomechanical damage at the time of the original trauma or from altered biomechanics following an injury, resulting from tendon or ligament damage. Alternatively, bone contusion can be seen in association with adjacent inflammation (Figure 17.6).

When evaluating a bone contusion on MR images, a more severe focus of injury within the bone can be surrounded by diffuse changes resulting in increased signal intensity on fat-suppressed images. The entire region of increased signal intensity indicates osseous injury of various degrees. The severity of the injury generally correlates with the amount of signal increase on fat-suppressed images.

Osseous cyst-like lesions

Osseous cyst-like lesions (OCLLs) may be incidental or of clinical significance. They often have intermediate signal intensity surrounded by low

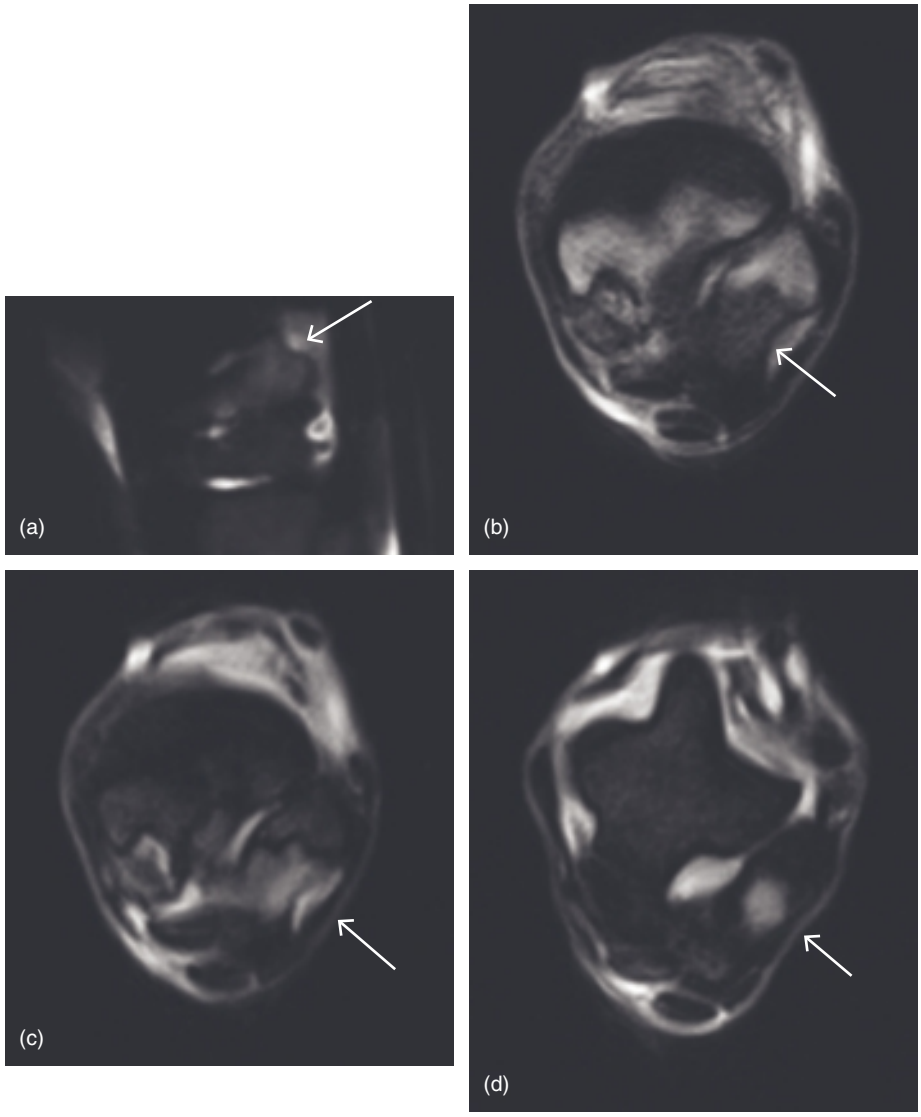

Figure 17.4 Bone bruising/trauma of calcaneus, central and fourth tarsal bones. (a) Sagittal STIR, (b) transverse T1-weighted and (c) T2* gradient-echo at the level of the central tarsal bone, and (d) at the level of the calcaneus images of the left tarsus of a 5-year-old flat racehorse with moderate to severe lameness following racing, 10 days prior to MRI. The lameness was localized to the tarsal region, radiographs were equivocal but there was generalized increase in radiopharmaceutical uptake, particularly towards the lateral aspect, so images were obtained standing using a 0.27 T MR imaging system. There is evidence of bone bruising in the plantar part of the central tarsal bone and its articulation with the fourth tarsal bone, and in the fourth tarsal bone and calcaneus (arrows). Bone bruising is seen as high signal intensity on STIR images and low signal intensity on T1-weighted images. On the T2* gradient-echo images, the fat–water cancellation artefact results in high signal intensity where there is very high water content, with a hypointense rim where there is equal fat and water content. The lack of a low signal intensity margin on T1-weighted images confirms that the signal intensity pattern on the T2* gradient-echo scan represents an artefact and not bone sclerosis.

signal intensity sclerosis. Well-circumscribed cysts without alterations in signal intensity in the surrounding bone are more likely to be incidental (Figure 17.7) in contrast to cyst-like lesions with irregular or poorly circumscribed margins and alterations in signal intensity in the surrounding bone. There is insufficient information available at this time to determine whether apparently incidental OCLLs can progress and become clinically significant. Reaction of the bone surrounding an OCCL, as demonstrated by the presence of fluid or extensive sclerosis, represents more significant bone damage and may be suggestive of pain (Figure 17.8). Where there is a query about clinical significance in a horse with unilateral lameness, there is value to assessing the contralateral limb for the presence and nature of any OCLLs.

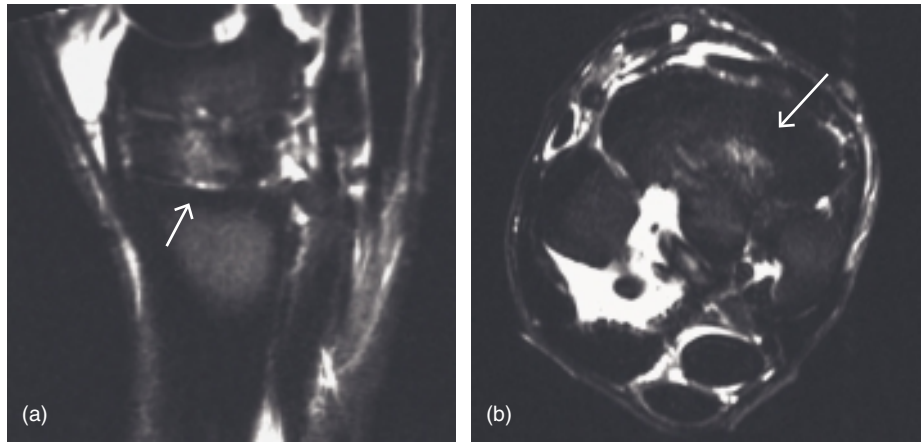

Figure 17.5 Tarsal bone oedema. (a) Sagittal and (b) transverse high-field STIR images of the tarsus from a 10-year-old Quarter Horse gelding who presented with a history of right hind limb lameness of 2 months duration that manifested as 'hopping' when he was cantered on the right lead. There is increased signal intensity in the third tarsal bone, consistent with tarsal bone bruising (arrows). This horse was 2/5 lame in the right hind limb and 3/5 after distal limb flexion, and the gait abnormality was abolished following anaesthesia of the deep branch of the lateral plantar nerve. Radiographs of the tarsus showed slight joint space narrowing and osteophyte formation at the margins of the distal intertarsal and tarsometatarsal joints. Following MRI, lameness was treated by injection of the tarsometatarsal joints with 6mg of triamcinolone each and the horse was confined to a stall with light hand walking only for 2 months. The horse resumed normal exercise 3 months after MRI. Images courtesy of Dr Michael Schramme, North Carolina State University.

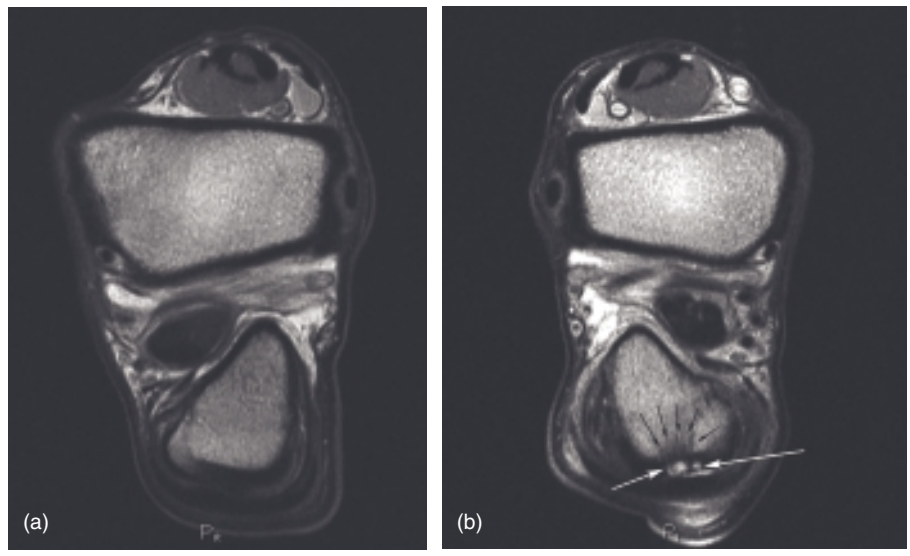

Figure 17.6 Calcaneal bursitis. High-field MR images of the tarsal region in a 6-year-old Selle Francais gelding with chronic problems in the right calcaneal bursa. There is calcaneal bursitis and osteitis of the tuber calcis. (a) Transverse proton density image of the normal left calcaneus. (b) Transverse proton density image of the right tarsus. There are focal regions of high signal intensity over the point of the calcaneus (white arrows) with sclerosis (black arrows). (c) Sagittal proton density image of the normal left tarsus in the region of the calcaneus. (d) Sagittal proton density image of the left normal tarsus in the region of the sustentaculum tali. (e) Sagittal proton density image of the right tarsus in the region of the calcaneus. There is effusion of the calcaneal bursae (gastrocnemius calcaneal bursa and intertendinous calcaneal bursa) (arrows). (f) Sagittal proton density image of the right hind in the region of the sustentaculum tali. There is increased signal in the calcaneus (arrow). (g) Sagittal T2 FSE image of the tarsus in the same plane as (e), demonstrating increased fluid within the calcaneal bursa. (h) Sagittal STIR image of the normal left tarsus. (i) Sagittal STIR image of the right tarsus showing increased signal in the calcaneus (arrow).

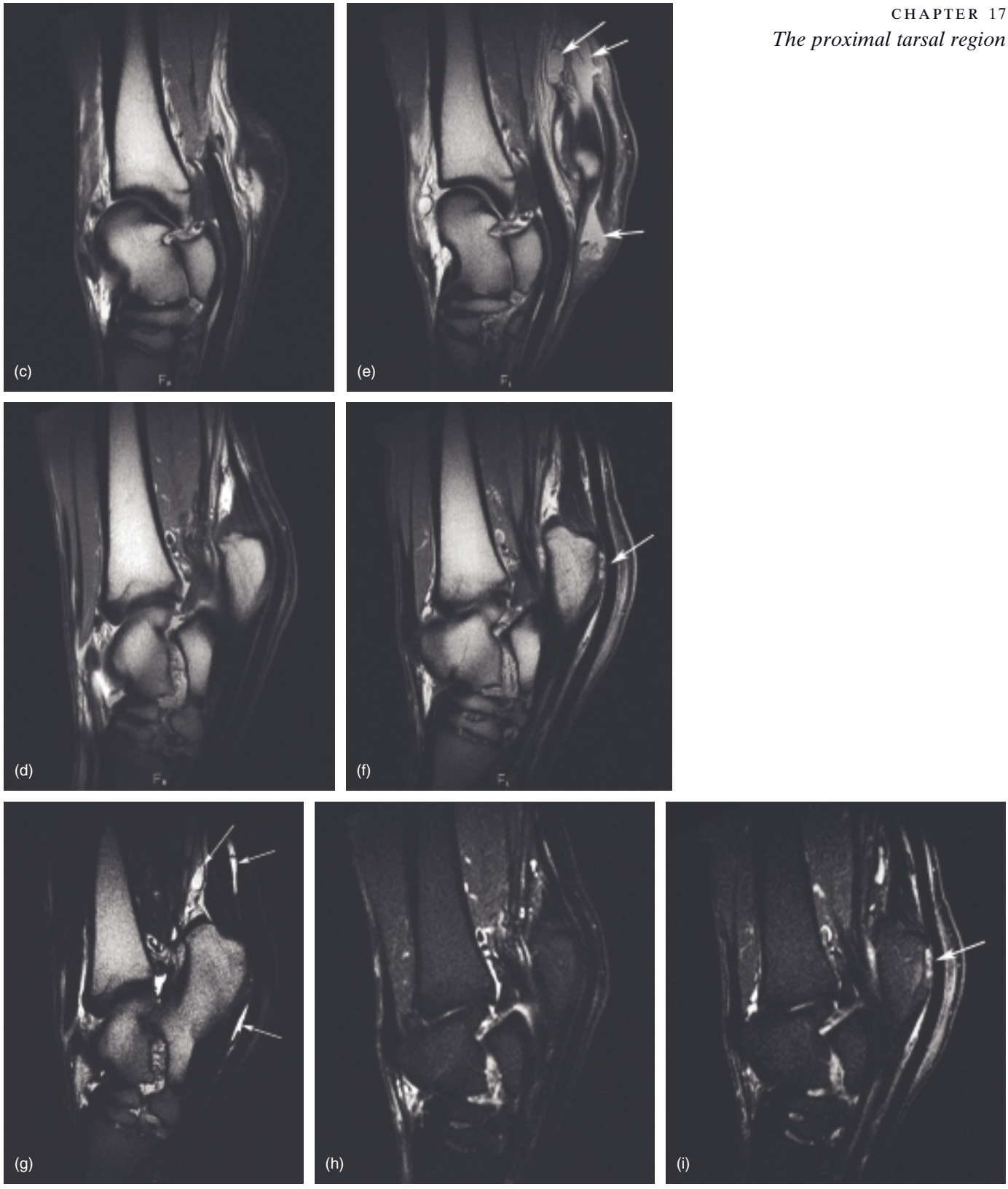

Figure 17.6 *Cont'd*

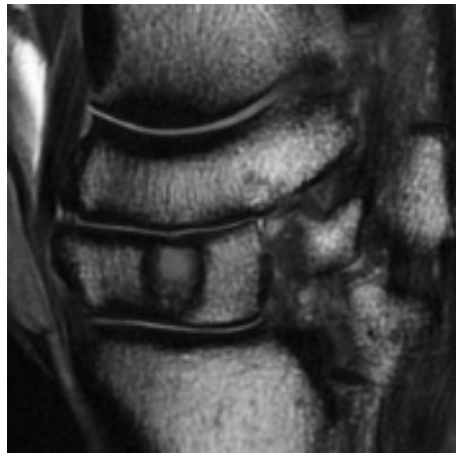

Figure 17.7 Osseous cyst-like lesion (OCLL) in the third tarsal bone. High-field sagittal plane 3D T1 gradient-echo MR image of an OCLL within the third tarsal bone of a 6-year-old Thoroughbred National Hunt racehorse. The horse had no history of tarsal lameness, and the cyst-like lesion was found as an incidental finding. There is slight indentation of the articular surface within the centrodistal joint, but no evidence of osteoarthritic changes.

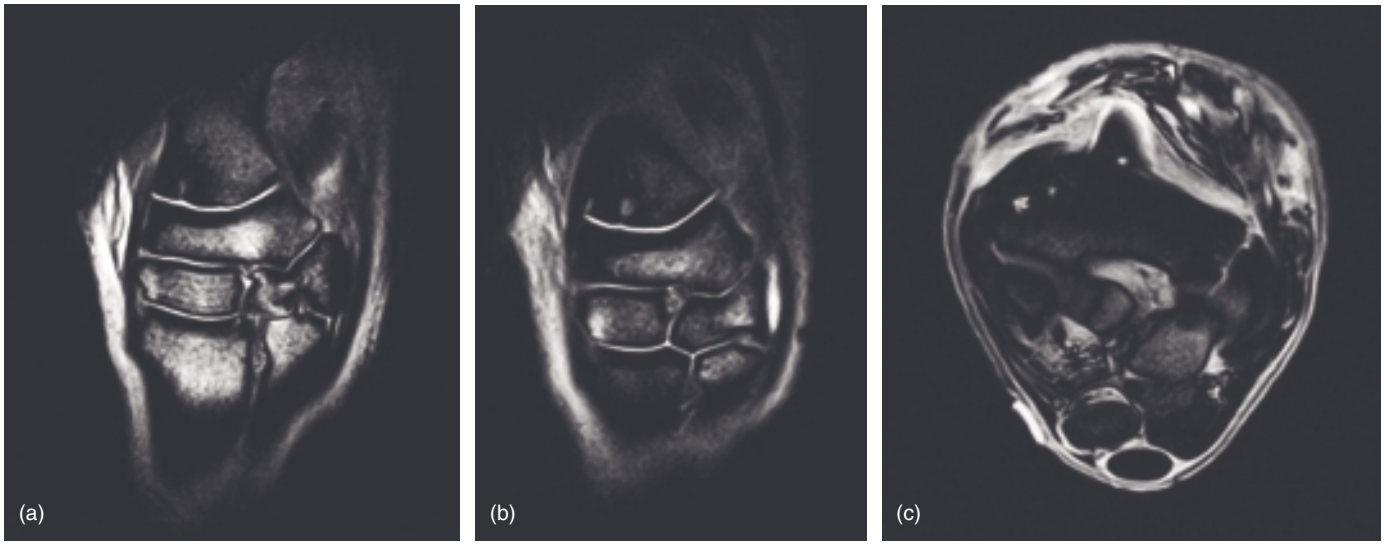

Figure 17.8 Osseous cyst-like lesions (OCLLs) in the talus. (a, b) Low-field sagittal and (c) transverse 3D T1 gradient-echo MR images of the left tarsus of a 4-year-old Warmblood mare with left hind lameness localized partially to the tarsus, a positive flexion test and a history of stumbling with this limb. There are multiple OCLLs in the talus, with evidence of communication with the articular surface. There is indentation of the articular surface and corresponding change in the opposing articular surface. There is irregular increase in trabecular bone density surrounding the cyst-like lesions. The horse had multiple osteochondrosis type lesions in other joints and was ultimately euthanized.

Osseous cyst-like lesions can be associated with subchondral bone trauma or lysis at the articular surface (Figure 17.9). Where an OCLL occurs adjacent to an articular surface, it is important to evaluate the articular surface for defects in the cartilage and subchondral bone, lack of joint congruency and any associated osteoarthritic changes (Figure 17.10). These

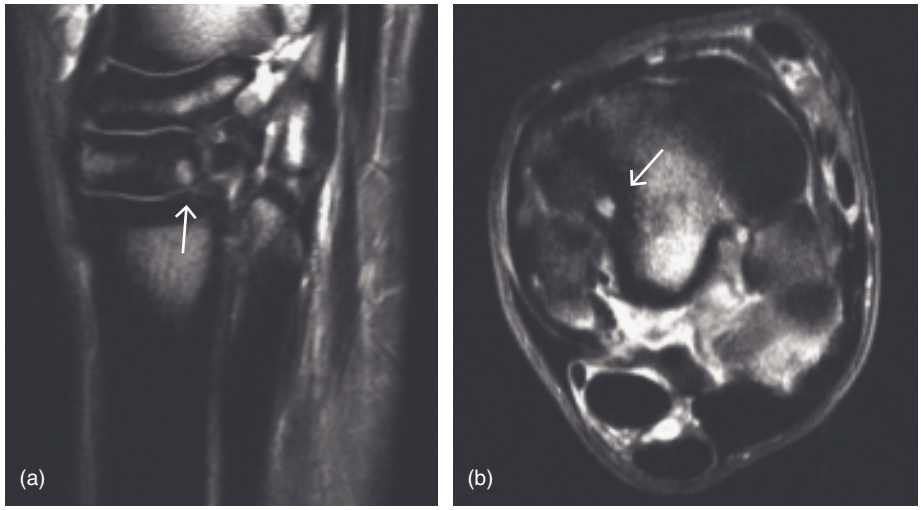

Figure 17.9 Osseous cyst-like lesions (OCLLs) in the third tarsal bone. (a) High-field sagittal and (b) transverse proton density images of the tarsus of a 5-year-old Quarter Horse mare used for Western pleasure riding, who had been lame in the left hind limb for the previous year. There is an OCLL in the plantarodistal aspect of the third tarsal bone, with irregular increase in trabecular bone density in the surrounding bone (arrow). Following MRI, lameness responded temporarily to intra-articular medication with triamcinolone and hyaluronic acid. Images courtesy of Dr Michael Schramme, North Carolina State University.

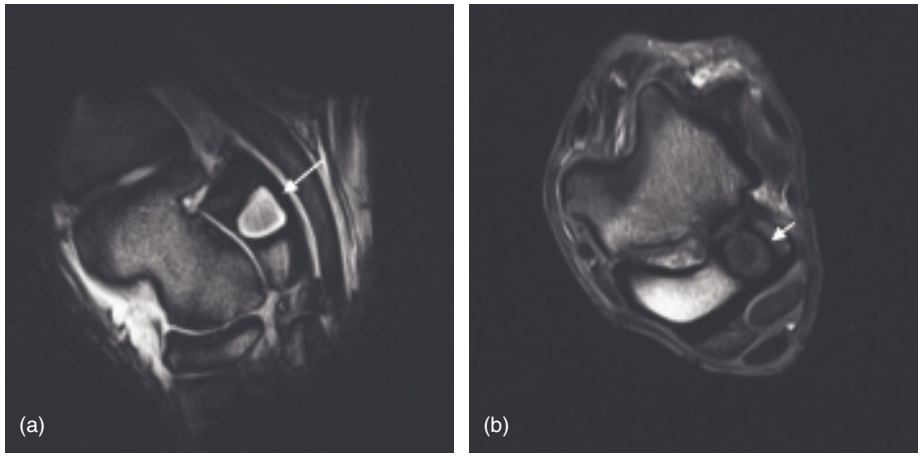

Figure 17.10 Calcaneal cyst. (a) Low field sagittal T2*-weighted gradient-echo image and (b) transverse T1-weighted gradient-echo image (b) from a 10-year-old Warmblood dressage horse with a grade 3/5 lameness localized to the tarsus. A large osseous cyst-like lesion can be identified in the calcaneus characterized by focal trabecular bone loss surrounded by sclerosis (arrows). The cyst could be identified on radiographs. However, potential communication with the talocalcaneal joint was determined using MRI. A focal defect in the subchondral bone of the calcaneus at the dorsal aspect of the cyst can be identified on the transverse image. The opposing surface of the talus is irregular indicating focal subchondral bone injury. The area of abnormality in the talus is bordered by sclerosis (within the trabecular bone).

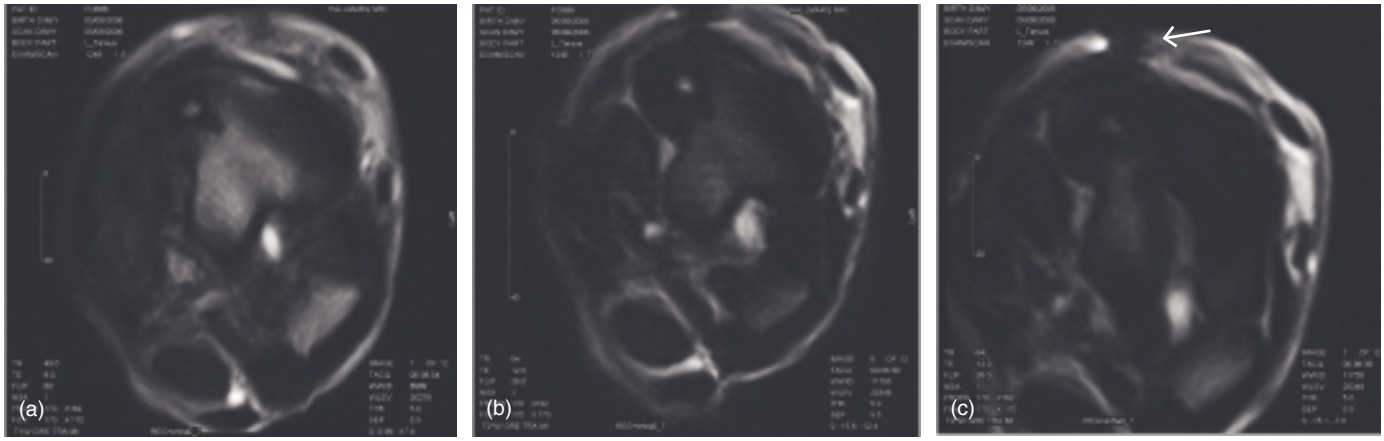

Figure 17.11 Focal osseous damage and abscessation. (a) Low field transverse T1 and (b, c) T2* gradient-echo images of the left tarsus, obtained standing in a 9-year-old part bred Arab mare with a history of an acute onset left hind limb lameness 3 months prior to the MRI. The limb was positive to flexion and had a stringhalt-like action. Tibial and fibular analgesia and tarsometatarsal joint analgesia were both positive. On scintigraphic examination there was increased radiopharmaceutical uptake in the tarsus. MR imaging was performed to determine what abnormality was present in the tarsal region. There is a focal area of increased signal intensity on T1 and T2* (and STIR) images in the third tarsal bone, which is surrounded by heterogeneous lower signal intensity with irregular, poorly defined margins. There is an area of low signal intensity in the overlying soft tissues, seen most clearly on gradient-echo sequences (arrow). This finding is consistent with haemosiderin deposition, and is considered suggestive of previous penetration or trauma to this region. A diagnosis of focal osseous damage and abscessation was made.

should be differentiated from focal abscess formation, containing high signal intensity proteinaceous fluid (Figure 17.11).

INFECTION

Osteomyelitis, Sequestrum

Bone adjacent to a focus of infection may have increased signal intensity on fat-suppressed images (Figure 17.12). This finding may represent a manifestation of local inflammation or be indicative of secondary bone infection. Definitive osseous infection generally has a mottled, inhomogeneous increase in signal intensity on PD, T2 and fat-suppressed images with a corresponding loss of the fat signal on T1-weighted images. The signal pattern is the result of granulation tissue formation and proteinaceous fluid accumulation. Low signal intensity indicating the replacement of fat with cancellous sclerosis can occur in chronic stages. Osteomyelitis may result from haematogenous seeding or from contiguous spread through a wound or penetrating injury. Osteitis occurs when the infection is limited to the cortex. On MR images, osteitis appears as increased signal intensity and disruption of the cortex, and may have adjacent periostitis.

In haematogenous seeding, there may be focal abscess formation in the cortical or cancellous bone, or the infection may be limited to the medullary bone. Focal abscess formation will have well demarcated high signal intensity on T2-weighted and fat-supressed images and may have a low signal intensity sclerotic rim (Figure 17.11). Increased signal intensity can be seen in the bone surrounding the abscess on fat-suppressed images indicating

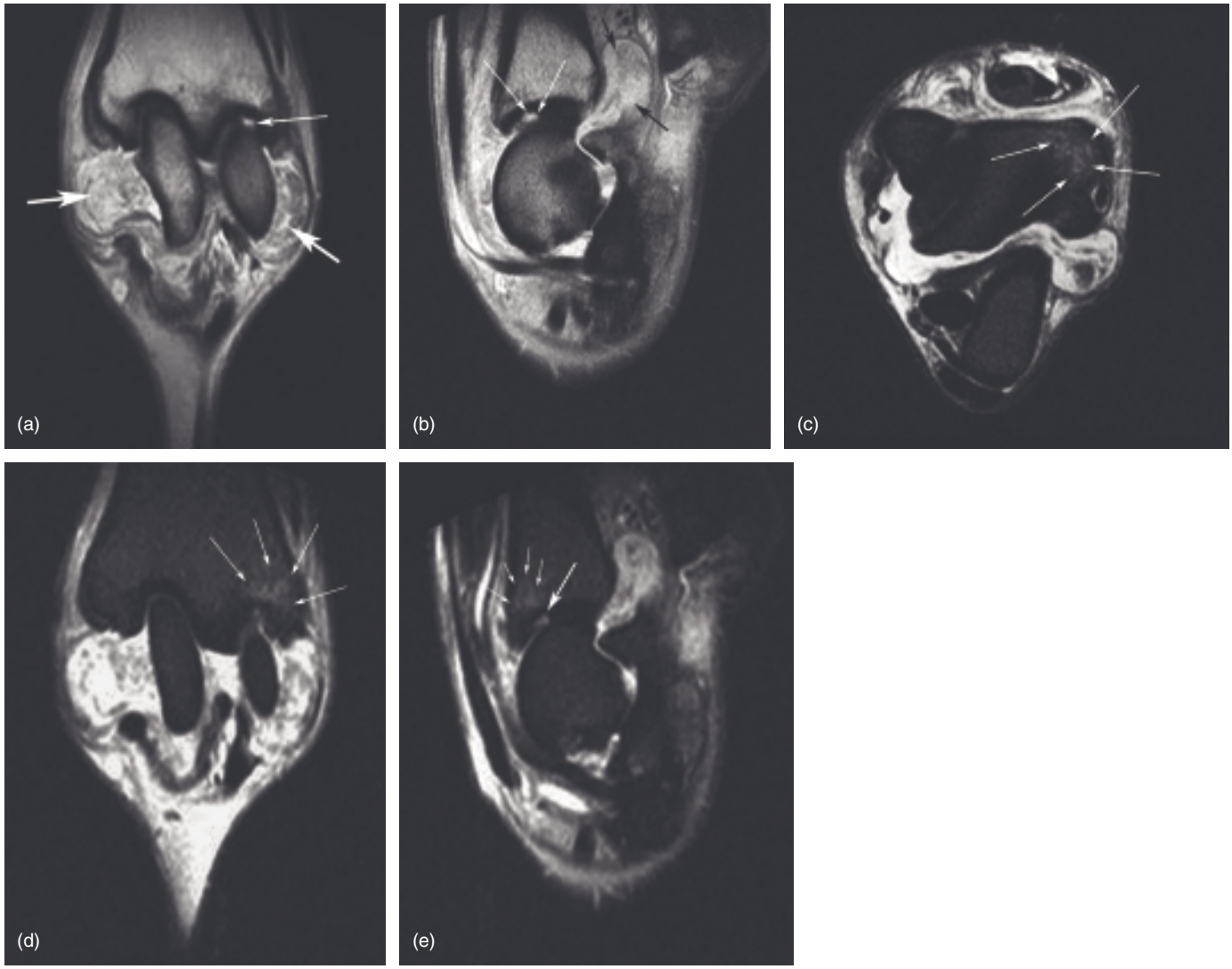

Figure 17.12 Septic tarsocrural joint. High-field MR images from a Thoroughbred racehorse that developed acute swelling and lameness while confined to a stall, diagnosed as sepsis of the tarsocrural joint. Synovial fluid analysis was consistent with infection. (a) Dorsal proton density (PD) image of the tarsus with increased fluid/fibrin in the tarsocrural joint (large arrows). There is a focal region of high signal intensity in the tarsocrural articular suface adjacent to the lateral trochlear ridge (small arrow). (b) Sagittal PD image of the tarsus. There is increased signal intensity in the subchondral bone adjacent to the articular surface consistent with an osteochondral defect (white arrows). Note the increased fluid in the plantar pouch of the tarsocrural joint (black arrows). (c) Transverse STIR image of the tarsus at the level of the distal tibia. There is increased signal intensity in the subchondral bone of the lateral aspect of the distal tibia (arrows). (d) Dorsal STIR image of the tarsus. There is increased signal intensity in the subchondral bone of the lateral aspect of the distal tibia (arrows). (e) Sagittal STIR image of the tarsus. There is increased signal intensity in the subchondral bone of the lateral aspect of the distal tibia (small arrows). There is also a focal region of abnormal high signal in the subchondral bone near the articular surface of the tarsocrural joint (large arrow).

diffuse inflammation. In a foal the physes and articular surfaces should be closely evaluated (Figures 17.13 and 17.14).

When there has been contiguous spread or penetration, there is likely to be overlying soft tissue swelling, with increased signal intensity in these soft tissues on PD, T2 and fat-suppressed images. There may be thickening and separation of the periosteum with reactive bone formation. The cortex is likely to be affected or disrupted, particularly with a penetrating injury.

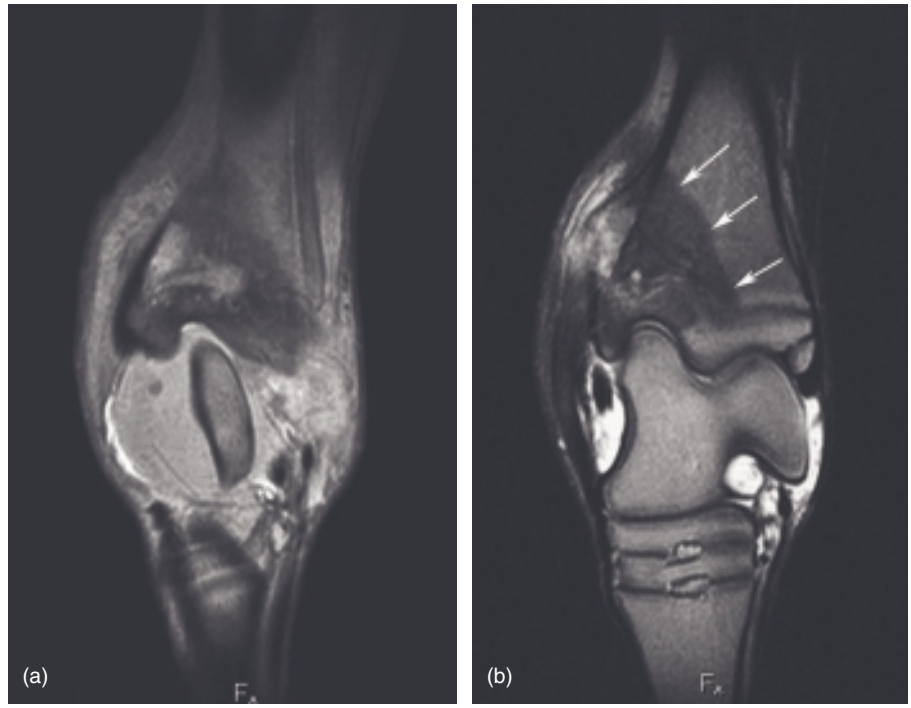

Figure 17.13 Septic physitis. High-field MR images from a foal with rhodococcus pneumonia and septic physitis. (a) Dorsal proton density (PD) image of a foal with increased signal intensity in the medial aspect of the distal tibia. (b) Dorsal PD image of a foal with sclerosis (arrows) and increased abnormal signal intensity surrounding the medial physis of the distal tibia. A sequestrum was present in the right distal tibia. Note the swelling overlying the abnormality.

In cases with osteomyelitis secondary to a penetrating wound or injury, haemosiderin may be present in the soft tissues as a result of previous haemorrhage (Figure 17.11). Even if there is no known history of a penetrating wound, the presence of haemosiderin in the soft tissues would be suggestive of trauma or infection necessitating careful evaluation of all adjacent osseous and soft tissue structures. Where osteomyelitis occurs adjacent to a joint, synovial changes reflecting synovial sepsis should be assessed.

Sequestra are usually of low to intermediate signal intensity on T1- and T2-weighted sequences. A sequestrum is surrounded by increased signal intensity on PD, T2 and STIR sequences resulting from the presence of proteinaceous fluid or granulation tissue (Figure 4.18). The margins of a sequestrum will appear clearly separated from the parent bone, which generally has irregular margins. Sequestra do not exhibit contrast enhancement, so administration of intravenous gadolinium contrast may be useful to support the diagnosis of sequestrum formation.

Synovial sepsis

In acute synovial sepsis, the inflamed and hyperaemic synovium may appear indistinguishable from the synovial fluid. Therefore, effusion of the tarsocrural joint and/or proximal intertarsal (talocalcaneoquartal) joint is the most apparent finding. Immediately following the acute stages, fibrotic synovium

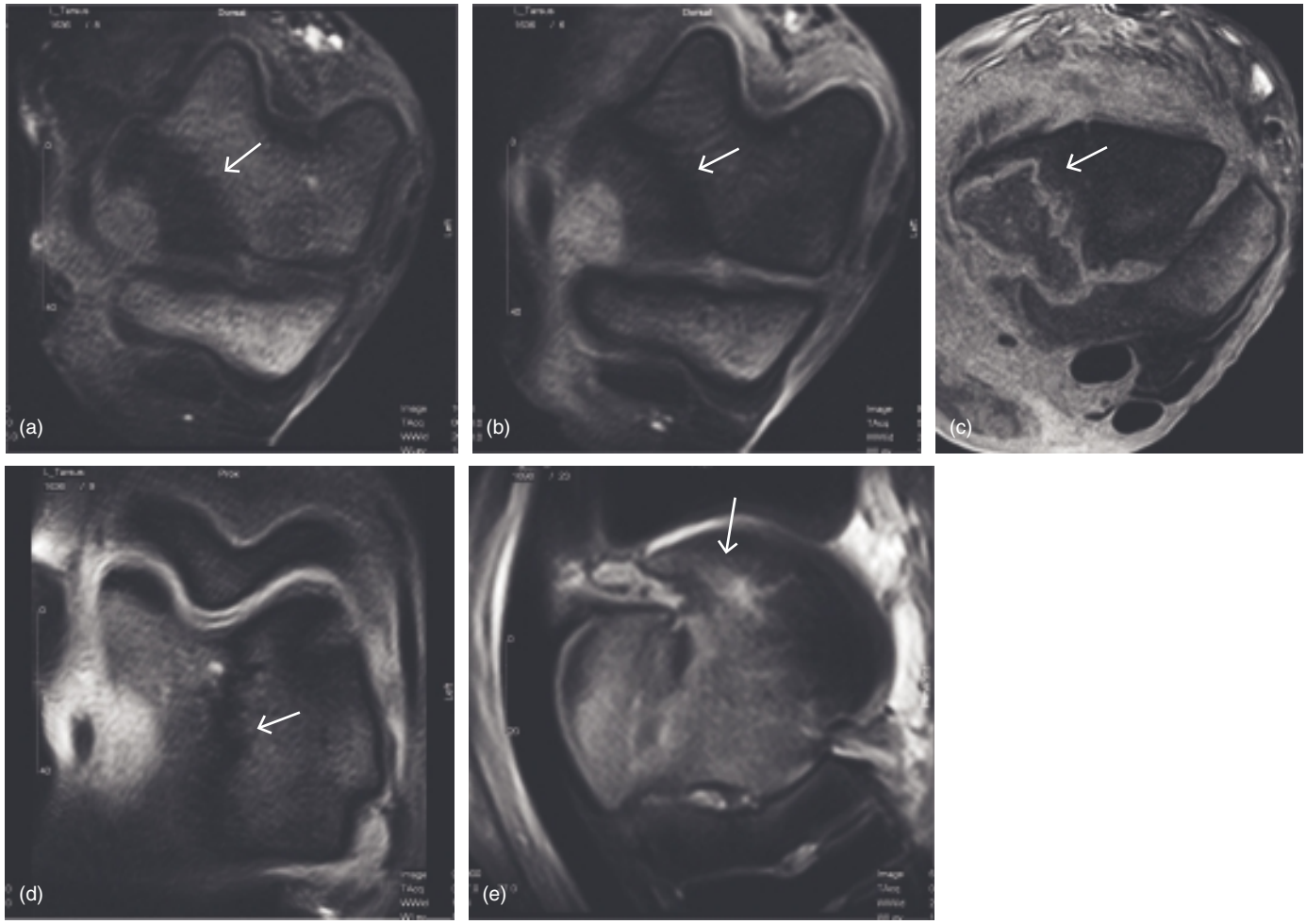

Figure 17.14 Osteomyelitis and sequestrum formation in a foal. Low-field MR images of the left tarsus of a 5-week-old Warmblood foal, obtained under sedation. The foal presented for lameness and swelling of the tarsocrural joint. Joint sepsis was diagnosed, which was treated with lavage and antimicrobial therapy. Rhodococcus equi was cultured so treatment with erythromycin and rifampicin was started. The foal stabilized for approximately 10 days, then lameness recurred. MR examination revealed severe osteomyelitis, necrosis and sequestrum formation in the medial aspect of the talus. (a) Transverse plane T1-weighted and (b) T2* gradient-echo image showing the trochlear ridges of the talus, (c) transverse plane T1-weighted image through the talocalcaneal joint, (d) dorsal plane T2* gradient-echo image, and (e) sagittal plane STIR image of the talus. Disruption of the normal signal intensity pattern in the talus is present, with poor definition of the contour of the medial side of the talus. There is generalized increase in signal intensity of the talus on STIR and T2* images, with decreased signal intensity on T1-weighted images, indicating increased water content associated with severe bone pathology. The low signal intensity seen at the margin of the high signal in the T2* gradient-echo images is a manifestation of a fat–water cancellation artefact and not sclerosis. The sequestrum and its involucrum are clearly outlined in (c). A very poor prognosis was given, and the foal was euthanized. The diagnosis was confirmed on necropsy examination.

and fibrin strands can be identified within the joint characterized by intermediate signal intensity in contrast to the adjacent synovial fluid which has low signal intensity on T1-weighted images and high signal intensity on T2-weighted and fat-suppressed images (Figure 17.12). Thickening of the joint capsule can be identified in acute and chronic cases of sepsis. The signal pattern of the joint capsule will change over time as fluid is replaced by fibrosis. Haemorrhage into the joint results in an increased cellular and protein content of the synovial fluid. The increased cells and protein alter the signal intensity of the synovial fluid resulting in increased signal intensity on T1- and

reduced signal intensity on T2-weighted images compared with a normal joint. However, it is difficult to differentiate between traumatic and septic synovitis, so use of joint aspirates is essential. The adjacent soft tissues structures should be evaluated for involvement, including articular cartilage, bone, tendon and ligament.

OSTEOCHONDRAL PATHOLOGY

Damage to subchondral bone can often be visualized radiographically, ultrasonographically or by alteration in radiopharmaceutical uptake on scintigraphic examination. However, more subtle changes or damage limited to the articular cartilage is more readily visualized and better characterized using MRI, even if lesions may retrospectively be detected on other imaging modalities (Figure 17.15). MRI also has the advantage of allowing the evaluation of articular cartilage that cannot be examined ultrasonographically, such as the tibial cochlea or the talocalcaneal joint surfaces.

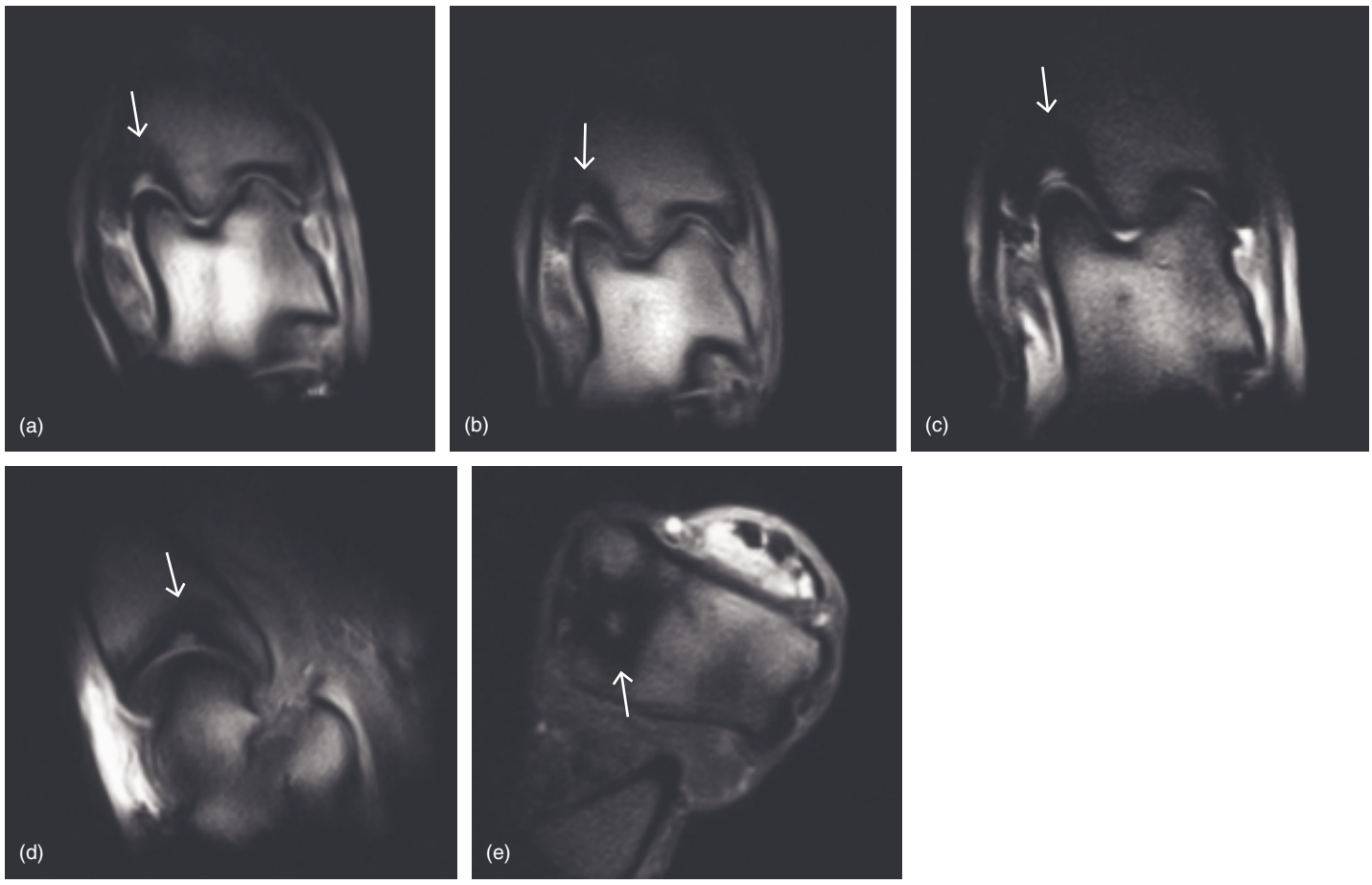

Figure 17.15 Subchondral bone pathology. Low-field MR images acquired standing, of an 11-year-old Warmblood mare with a 2-year history of right hind limb lameness that was localized to the tarsal region. Initial radiographic examination was unrewarding. MR images revealed an osseous cyst-like lesion in the distal tibia at the articulation with the trochlear ridge of the talus seen as high signal intensity in the subchondral bone on both T1- and T2-weighted images surrounding by low signal intensity thickened subchondral or sclerotic bone with irregular margins (arrows). Repeated radiographic examination demonstrated the presence of the cystic lesion surrounded by a marked increase in trabecular density with irregular margins. (a and b) T1 gradient-echo dorsal plane image; (c) T2 FSE dorsal plane image; (d) T1 gradient-echo sagittal plane image; (e) T1 gradient-echo transverse plane image at the level of the distal tibia.

The clarity of the articular cartilage and its interfaces with the synovial fluid and the subchondral bone is greatly improved when images are obtained perpendicular to the relevant part of the articular surface (Figure 17.16). Evaluation of the articular cartilage should be done in conjunction with assessment of slice positioning to determine the validity of any findings. Alteration in cartilage signal intensity is indicative of altered composition, while loss of normal contour indicates cartilage loss, abrasion or disruption (fraying, fibrillation, thinning or defect). Cartilage damage can be easier to identify if there is adjacent damage to the subchondral bone. Subchondral bone damage can be identified as altered signal intensity, irregularity of the osteochondral or endosteal aspect or defect of the osteochondral margin. The extent of bone damage should be evaluated using fat suppressed images to determine the affected area of bone and likely severity of damage (Figure 17.17). This may also be indicated by the degree of loss of joint space (Figure 17.18).

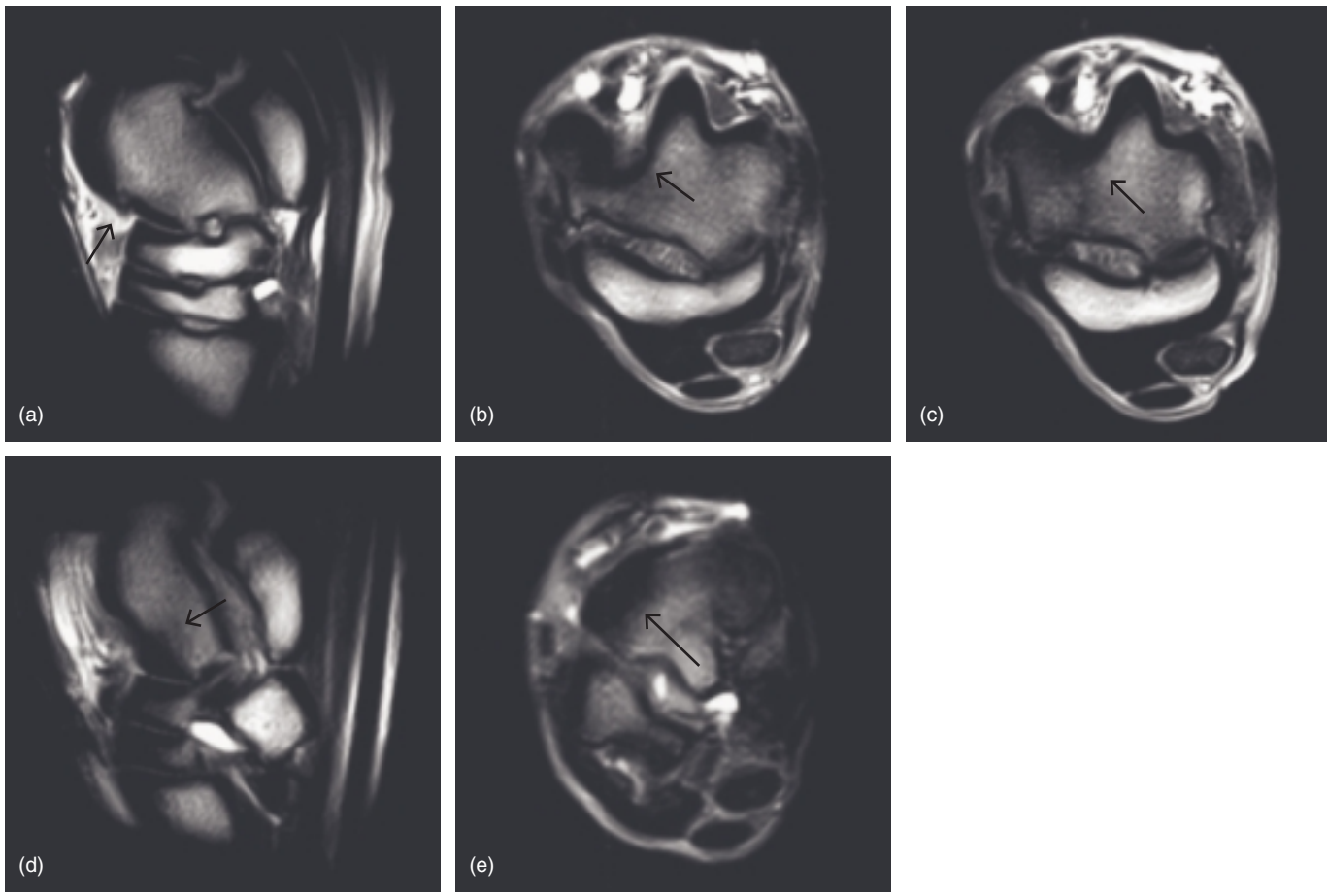

Figure 17.16 Osteochondral pathology. Low-field images of the right tarsus of a 7-year-old Warmblood mare used for medium level dressage and jumping, with a 2.5-month history of lameness, obtained standing. (a) T1-weighted sagittal plane image, (b and c) transverse images and (d) lateral sagittal plane image. There is osteochondral irregularity in the distal aspect of the lateral trochlear ridge with corresponding change in the central tarsal bone articulation (arrows). The lameness was not affected by intertarsal joint or proximal suspensory blocks, but improved significantly with intra-articular analgesia of the tarsocrural joint and was eliminated by a tibial and peroneal block. Radiographic examination was equivocal. Arthroscopic examination revealed a one cent size cartilage defect on the talus. Post-operative management included treatment with IRAP and Tildren, and physical rehabilitation. The horse returned to full soundness and its previous level of athletic function in 3 months and has stayed in full athletic function.

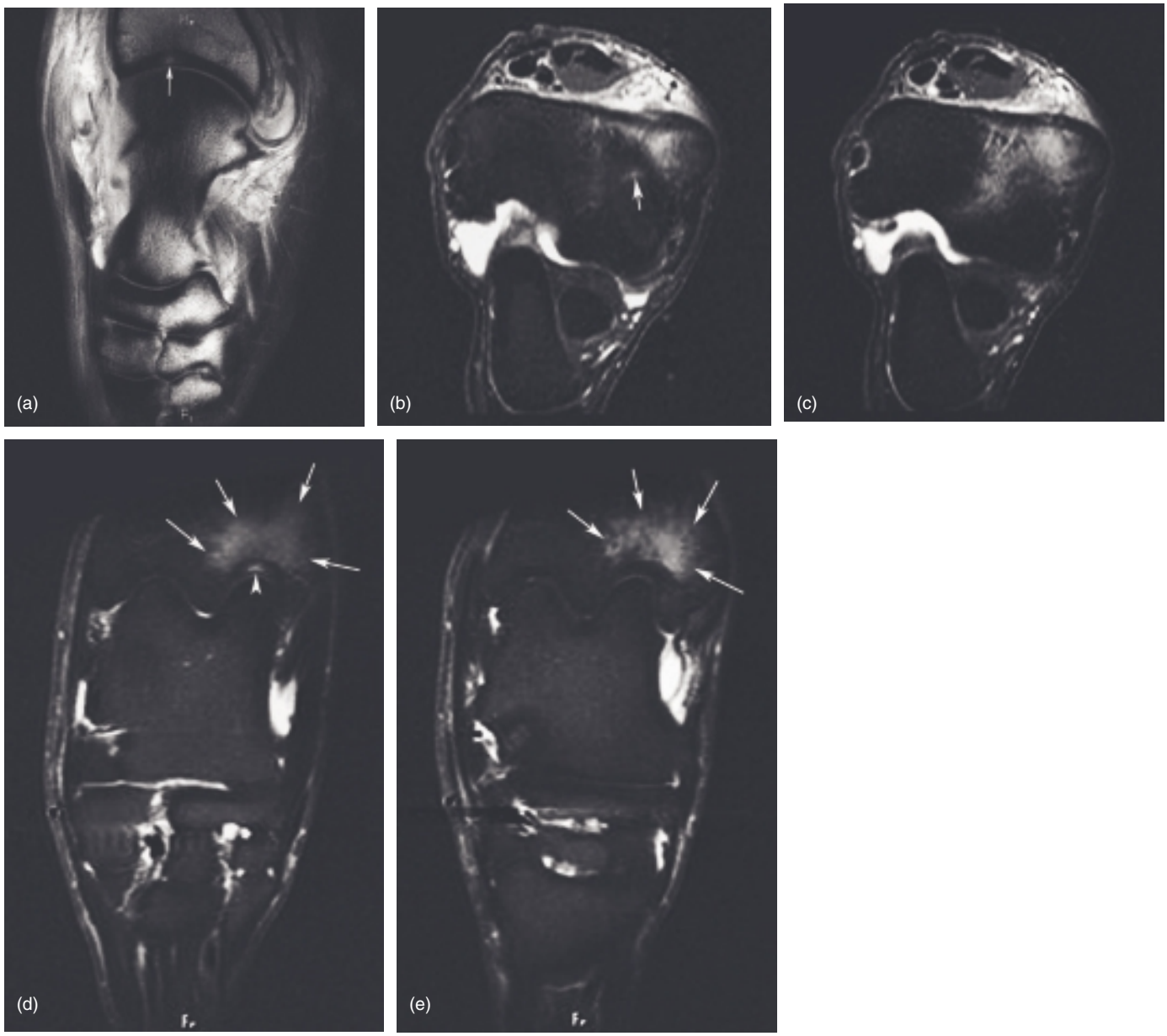

Figure 17.17 Focal subchondral bone damage. High-field MR images of the right tarsus of an 11-year-old Oldenburg dressage horse with lameness of one week duration, diagnosed as having focal osseous injury and adjacent osteochondral abnormality. (a) Sagittal plane proton density image. There is a focal region of increased signal intensity in the subchondral bone adjacent to the articular surface of the disto-medial tibia (arrow). (b) Transverse plane STIR image. There is diffuse increased signal intensity in the subchondral bone of the medial aspect of the distal tibia. A focal region of high signal intensity is present near the tarsocrural articular surface (arrow). At arthroscopy, a focal region of cartilage damage could not be identified. (c) Transverse plane STIR image. There is increased signal intensity in the medial aspect of the distal tibia, which is consistent with some type of osseous injury. (d) Dorsal plane STIR image. There is diffuse increased signal intensity in the medial aspect of the distal tibia (arrows) as well as a focal region of increased signal intensity in the subchondral bone adjacent to the tarsocrural joint (arrowhead). (e) Dorsal plane STIR image. There is diffuse increased signal intensity in the subchondral bone of the medial aspect of the distal tibia (arrows).

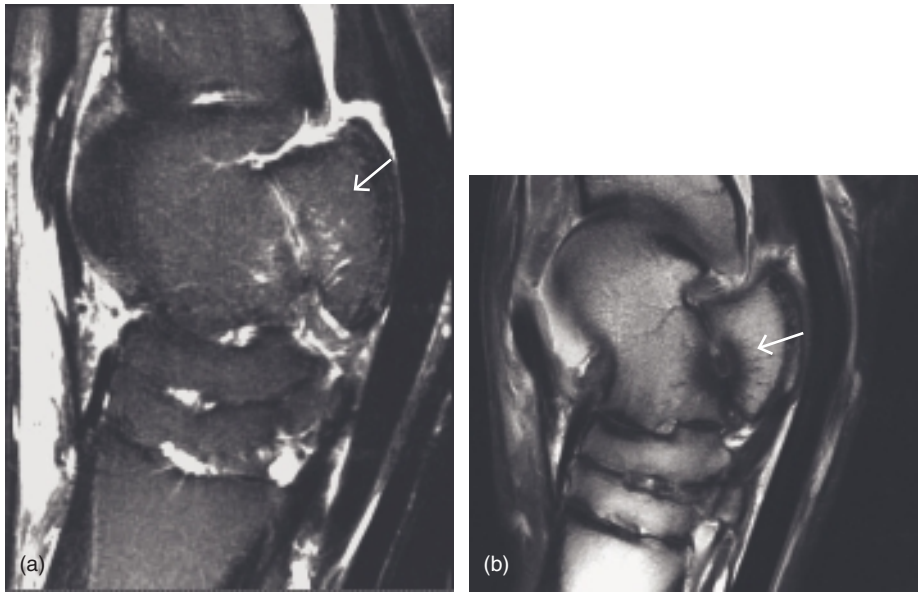

Figure 17.18 Talocalcaneal joint pathology. Sagittal plane STIR (a) and proton density (b) images of the left tarsus of a 7-year-old Thoroughbred gelding who suffered a puncture wound to the lateral aspect of the hock 4 months previously. Joint fluid analysis was negative for the presence of sepsis but the joint remained swollen and painful. On presentation the horse was lame at a walk, with marked tarsocrural joint effusion. Radiographs showed evidence of new bone formation at the attachement sites of the medial collateral ligament of the tarsocrural joint, the plantar ligament, the dorsal tarsal ligament and the joint margins of the distal tarsal joints. Ultrasonography revealed thickening of the medial collateral ligament with areas of decreased echogenicity as well as severe thickening of the joint capsule and synovial membrane. Analysis of tibiotarsal joint fluid revealed a total protein concentration of 3.8 g/dl, a leukocyte count of 190 cell/µl. A differential count revealed 25% large mononuclear cells, 68% intact neutrophils and 7% small mononuclear cells. MR images revealed increased signal intensity on STIR images and decreased signal intensity on proton density images in the talus and calcaneus at the talocalcaneal articulation (arrows). Joint space narrowing and loss was present. A diagnosis of talocalcaneal joint pathology with joint space loss and adjacent bone oedema was made. After MRI, the tibiotarsal joint was injected with hyaluronic acid and 10mg triamcinolone acetonide. The distal intertarsal and tarsometatarsal joints were injected with 40mg methylprednisolone each. The horse remained lame and was retired from showing. Images courtesy of Dr. Michael Schramme, North Carolina State University.

LIGAMENT PATHOLOGY

The ligaments supporting the tarsal joints include the collateral and plantar ligaments, in addition to the intertarsal ligaments. On MR images, ligament damage is seen as increased signal intensity, altered ligament margins or architecture, loss of continuity (seen as complete loss of continuity in the case of a rupture), alteration in size or length, or changes in the bone at the origin or insertion. If there is secondary joint instability, then there may be acute or chronic changes to the joint congruency and the articular surface. If joint luxation or subluxation is identified, then the associated soft tissues and ligaments should be carefully evaluated for damage, as should the tissues of the articular surface, including the subchondral bone (Figure 17.19).

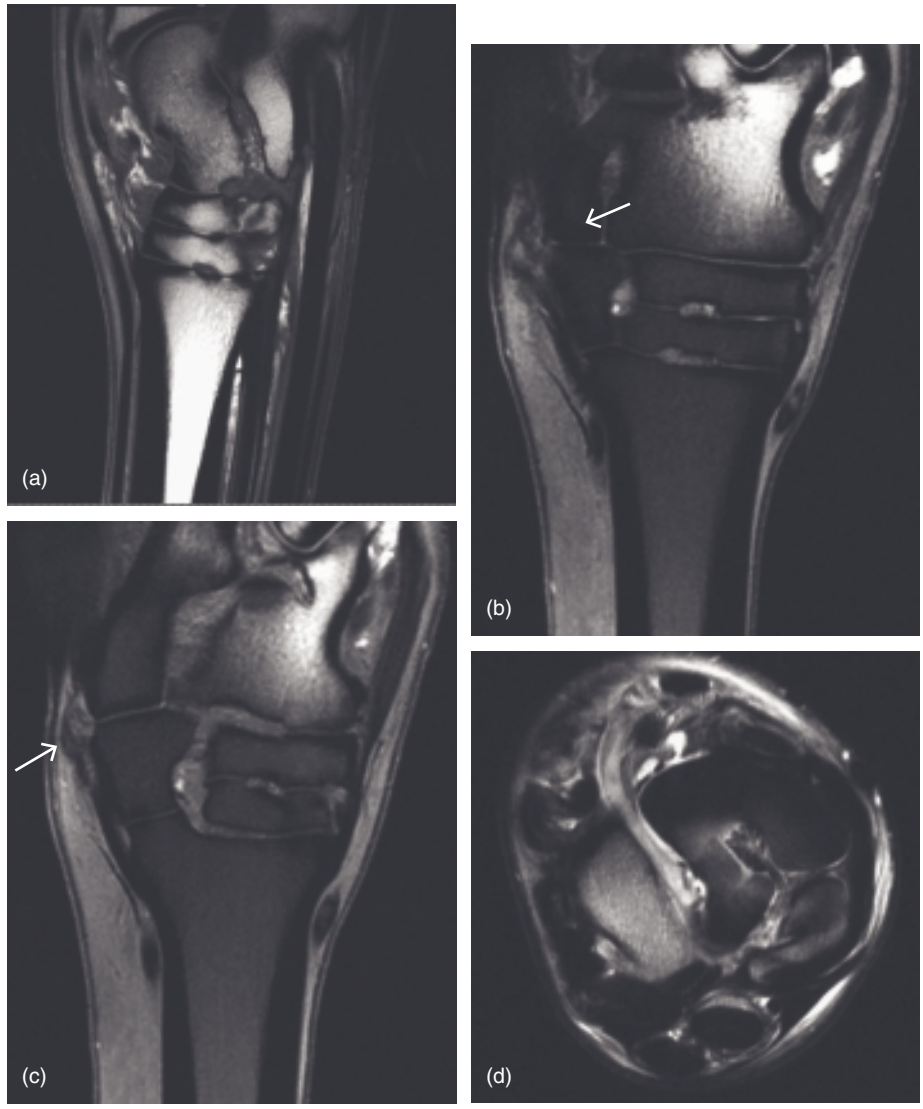

Figure 17.19 Proximal intertarsal joint subluxation. (a) Sagittal and (b and c) dorsal plane T1-weighted and (d) transverse plane proton density high-field MR images of the right tarsus of a 6-year-old Quarter Horse stallion who presented with a suspected tarsal subluxation after catching his foot in the stall door guard rails. Proximal intertarsal joint subluxation was confirmed radiographically but MRI was considered useful to show the presence of possible soft tissue disruption. There is disruption of lateral collateral ligament continuity and loss of normal architecture as the ligament traverses the proximal intertarsal joint (arrow), with a heterogeneous increase in signal intensity within the ligament and periosteal irregularity on the lateral aspect of the fourth tarsal bone. There is also some loss of normal architecture in the dorsal soft tissues. A diagnosis of lateral collateral ligament disruption over the lateral surface of the fourth tarsal bone and disruption of the dorsal connective tissues over the proximal intertarsal joint was made. The stallion regained full breeding soundness after prolonged cast immobilization and stall rest. Images courtesy of Dr Michael Schramme, North Carolina State University.

It is important to consider magic angle effect on ligament signal intensity. In both the standing horse with a transverse orientation static magnetic field, and for the limb under general anaesthesia with either the magnetic field oriented longitudinally to the limb axis for high-field machines or transversally for open low-field ones, the tarsal ligaments can be subject to magic angle effect. Ligaments with increased signal intensity on short TE sequences that are not oriented perpendicular or parallel to the long axis of the limb should be measured relative to the main magnetic field to determine if they are susceptible to magic angle effect. This effect can make it difficult to evaluate the ligaments of the tarsus because its appearance can overlap with certain types of injury. Therefore, it is important to assess not only the signal intensity of the ligament, but also the size and margins (Figure 17.20). The ligaments themselves may be difficult to visualize or interpret, therefore it is important to evaluate the bone at the origin and

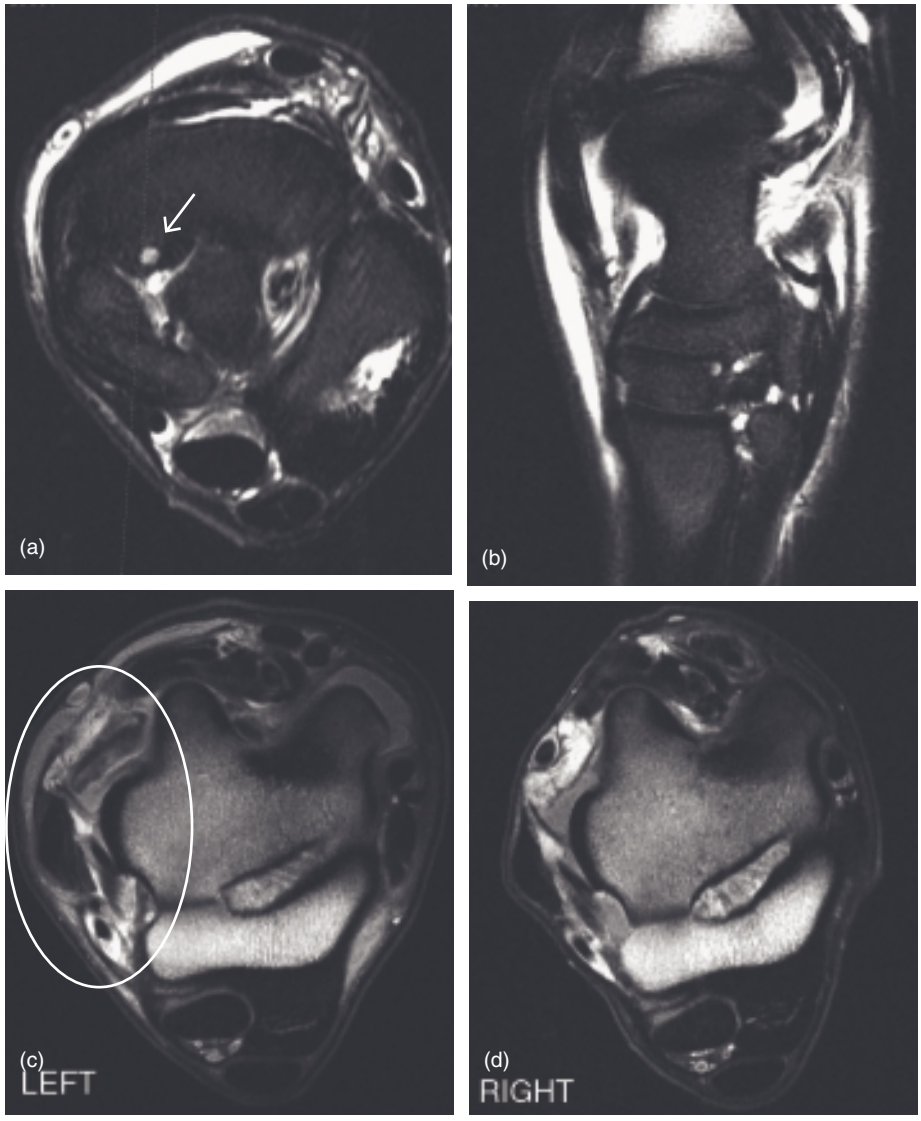

Figure 17.20 Medial collateral ligament damage. (a) Transverse and (b) corresponding dorsal plane STIR images, and (c) transverse plane proton density images of the left tarsus of a 4-year-old Westphalian gelding with a left hind limb lameness of 3 months' duration. The horse had sustained a fall in a paddock and become instantly toe-touching lame at a walk. His tarsocrural joint was very swollen but swelling and lameness reduced with stall rest, only to return intermittently on limited turn-out. On presentation he was 3/5 lame at the trot in his left hind limb. Radiographs were within normal limits but ultrasonography showed a thickened medial collateral ligament. On MR images, there is an osseous cyst-like lesion within the palmaromedial aspect of the third tarsal bone (arrow). The medial collateral ligaments of the left tarsus have a greater cross-sectional area than the lateral, and there is higher signal intensity in the palmar half of the tendon with evidence of chronic synovitis (circled). He was stall rested with physical therapy but lameness did not resolve. The normal right tarsus is shown as a comparison (d). Images courtesy of Dr Michael Schramme, North Carolina State University.

insertion of all ligaments. Any cortical irregularity, either periosteal or endosteal, may be indicative of increased ligament strain. Irregularity of the subchondral bone at the origin and insertion of the intertarsal ligaments may also be indicative of ligament pathology, as would osteoarthritic changes around the ligament insertion.

Damage to the collateral ligaments are often most clearly defined on transverse images, particularly through an accurate assessment of their size and shape. In contrast, their continuity may be best followed on frontal plane images oriented parallel to the suspected ligament portion (Figures 17.21 and 17.22). The different branches of the collateral ligaments should be examined throughout their length for swelling, increase in signal intensity, irregularity of the ligament margins or disruption of periligamentar tissues (Figure 17.23), and the bone at all insertion sites should be examined. The plantar ligaments can be most easily evaluated in transverse and sagittal plane images, and damage may be seen as swelling, increased signal intensity and loss of separation from adjacent structures, representing swelling or periligamentous thickening (Figure 17.24). Enthesiophyte formation or avulsion fractures appear most likely to occur associated with the collateral ligaments of the tarsus (Figure 17.22). Increased signal intensity at the origin or insertion on fat-suppressed images indicates bone pathology, which is often associated with ligament strains, with or without associated ligament damage.

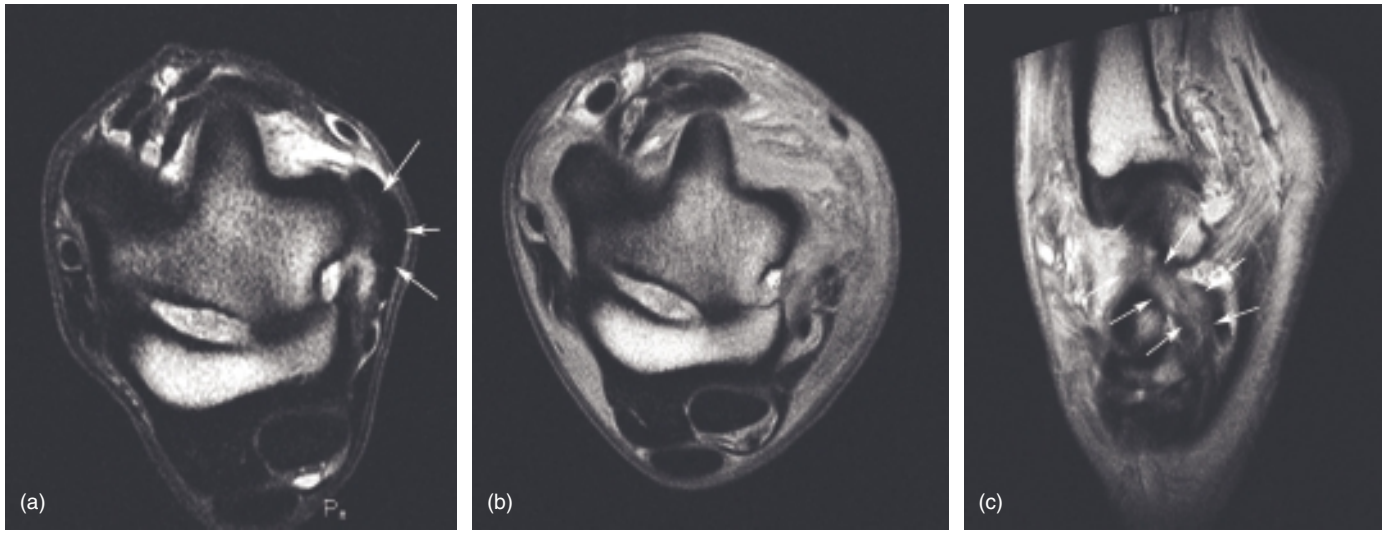

Figure 17.21 Severe medial collateral ligament damage. High-field images of the right tarsus of a horse with recent medial collateral ligament injury, and the normal contralateral limb. There is severe disruption of the right medial collateral ligament and effusion in the tarsocrural joint. (a) Transverse proton density (PD) image of a normal medial collateral ligament in the left tarsus (arrows). (b) Transverse PD image of the right tarsus with severe disruption of the medial collateral ligament. (c) Sagittal PD image of the right tarsus with severe disruption of the proximal attachment of the medial collateral ligament. Arrows delineate the distal portion of the ligament.

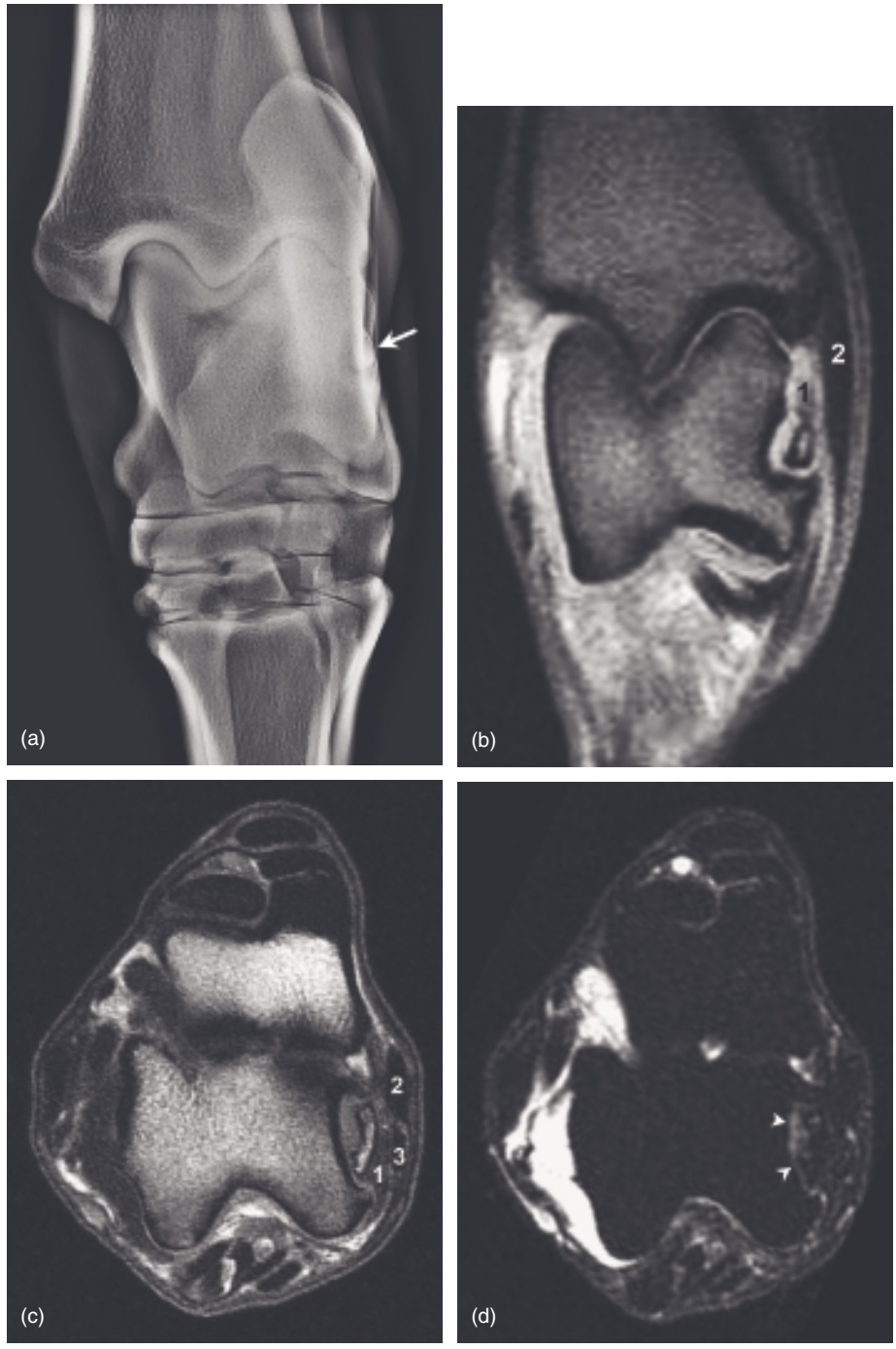

Figure 17.22 Lateral collateral ligament damage and partial avulsion. Images from a 6-year-old show jumper Selle-Français stallion with a history of poor hind limb propulsion. (a) Dorso-plantar radiographic projection of the left tarsus. A bony fragment (arrow) surrounded by a radiolucent area can be seen at the lateral aspect of the tarsus. (b–d) Low-field MR images of the tarsus, obtained under general anaesthesia: (b) dorsal gradient echo T1-weighted; (c) transverse spin-echo T1-weighted; and (d) STIR images. The osseous fragment is located in the distal attachment of the short lateral collateral ligament (1) at the deep aspect of the long lateral collateral ligament (2) and of the lateral digital extensor tendon (3). This avulsion fracture is associated with a shape alteration of the lateral aspect of the talus. In contrast, no damage in the adjacent deep part of the talus can be visualized which may account for the low clinical significance of this injury. A slight increase in signal intensity of the short lateral collateral ligament can also be observed. The tissue located at the deep aspect of the bony fragment presents a brighter signal compared with that of the collateral ligament which may be indicative of fibrous scar tissue.

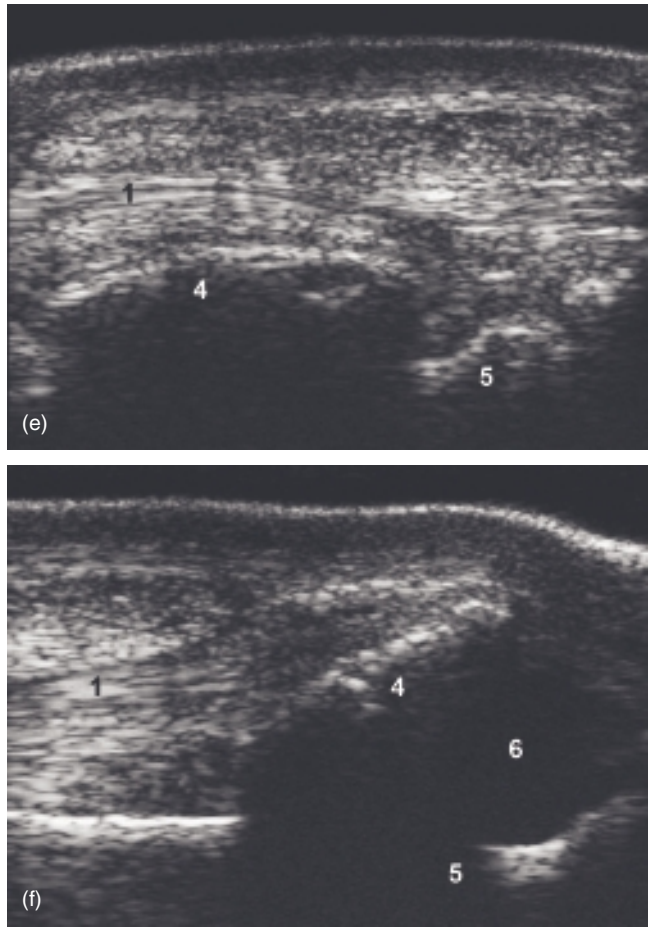

Figure 17.22 *Cont'd* (e) Longitudinal ultrasonographic scan of the short lateral collateral ligament at the lateral aspect of the talus (weight-bearing limb – dorsal is to the left): the avulsion fragment (4) is clearly visualized between this ligament and the talus (5). (f) Longitudinal ultrasonographic scan of the short lateral collateral ligament at the lateral aspect of the talus (non weight-bearing limb, flexed hock); flexion of the tarsus creates tension in the short lateral collateral ligament inducing displacement of the bony fragment. This movement is associated with synovial fluid accumulation at the deep aspect of the bony fragment (6). This fluid accumulation may be the reason for the bright line visible at the lateral aspect of the cortical bone of the talus on the STIR image (d, arrowhead).

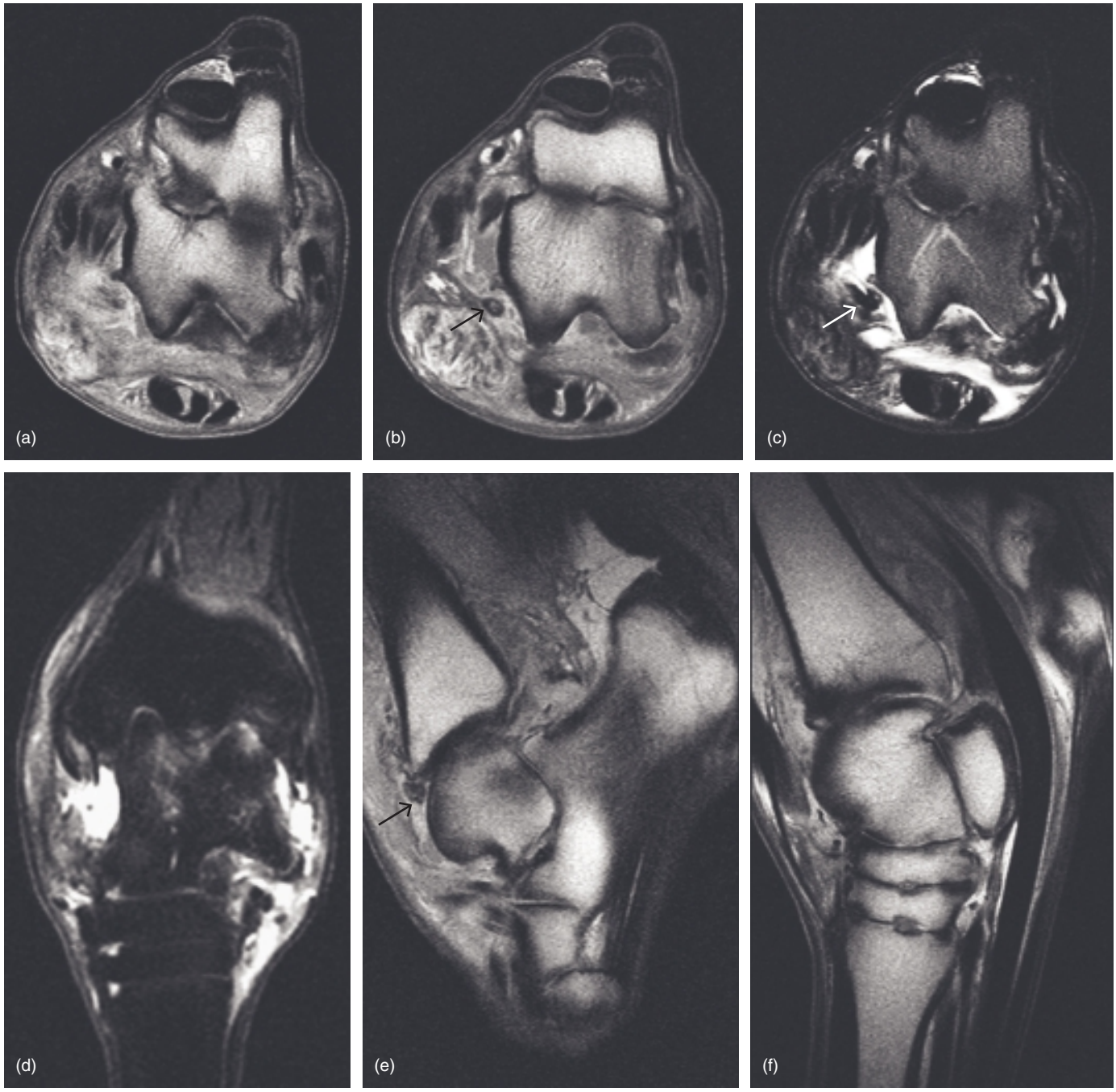

Figure 17.23 Short collateral ligament damage and severe joint pathology. Low-field MR images of the tarsus of an 11-year-old French Warmblood show jumper with severe left hind limb lameness, obtained under general anaesthesia. There is severe chronic synovitis and synovial proliferation and thickening of the short medial collateral ligament seen on transverse spin-echo T1-weighted (a and b) and T2 FSE (c) images of the tarsus. The talus has periarticular bone remodelling with signal alterations in the trochlear, and poor definition of the articular cartilage. A focal signal abnormality (arrows) in the dorsomedial aspect of the synovial membrane is consistent with either a small osseous fragment or mineralization of the synovial membrane, seen on radiographic images. There is severe pathology of the talus, seen as high signal intensity on STIR images (d). Sagittal plane spin-echo T1-weighted images through the lateral (e) and medial (f) trochlear ridges showing osteochondral disruption and irregularity.

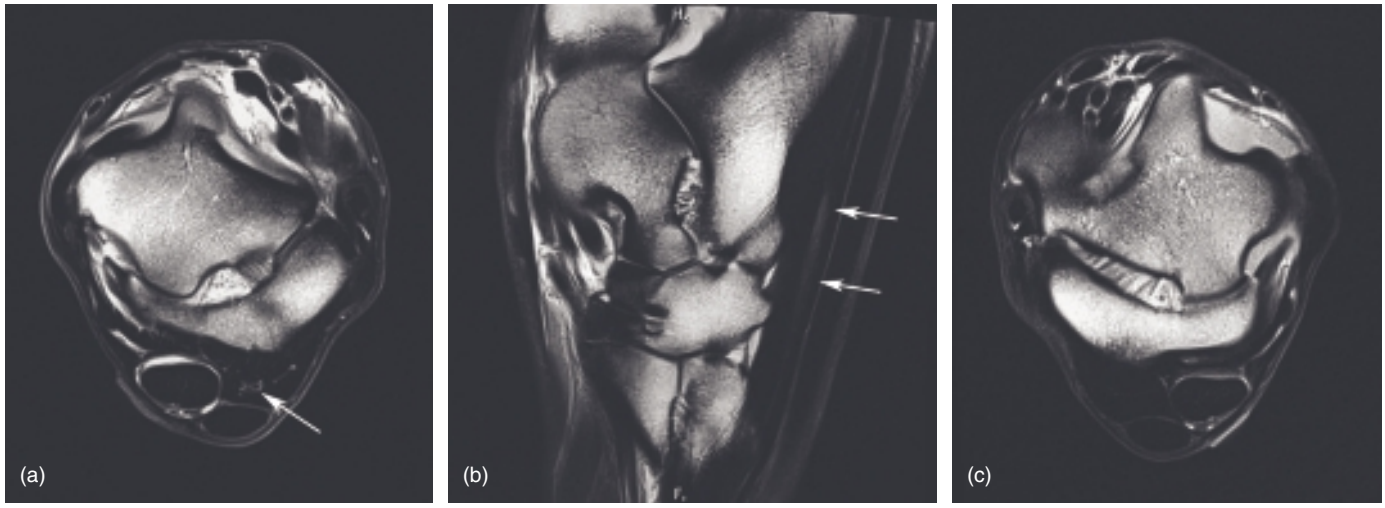

Figure 17.24 Long plantar ligament damage. High-field MR images of the tarsus from a horse that had been lame in the left hind limb for several months and responded to intra-articular analgesia of the distal tarsal joints. Injections of anti-inflammatory medication had not improved the lameness. (a) Transverse proton density (PD) image of the left tarsus showing injury to the long plantar ligament. There is abnormal increased signal within the ligament (arrow). (b) Sagittal PD image of the left tarsus showing injury to the long plantar ligament. There is abnormal increased signal within the ligament (arrows). (c) Transverse PD image of the right tarsus (normal long plantar ligament).

TENDON PATHOLOGY AND TARSAL SHEATH

Tendon damage can be detected as a loss of continuity, swelling or enlargement, increase in signal intensity in various sequences or disruption, thickening and inflammation of the peritendonous structures (Figure 17.25). In horses with a proximal plantar swelling of the hock, MR examination is useful for differentiating distension of different sheaths or bursae (including the plantar tarsal sheath, the gastrocnemius or the superficial digital flexor tendon bursae and the subcutaneous calcaneal bursa), and for performing a thorough evaluation of the injured anatomical structures.

In cases with plantar tarsal sheath effusion, damage to the deep digital flexor tendon as it traverses the sustentaculum tali should be evaluated carefully and ideally using images acquired perpendicular to the tendon at this level, in addition to standard imaging planes (Figures 17.25–17.28). Such perpendicular images are also particularly useful for an accurate assessment of the thickness of the fibrocartilage covering the plantar aspect of the sustentaculum tali to detect thinning or ulceration of this structure. Thickening of the mesotendon and of parietal and tendinous layers of the synovial membrane of the tarsal sheath is better characterized using a combination of transverse T1- and T2-weighted sequences.

The presence of adjacent bone damage should also be assessed, including on fat-suppressed images. Bone remodelling at the enthesis of the flexor retinaculum and alterations of the plantar aspect of the sustentaculum tali extending in some cases more deeply in its cancellous bone may also be observed. In chronic tarsal sheath effusion, extensive bony proliferation of the distal aspect of the sustentaculum tali can be visualized in long-standing cases (Figure 17.26). Damage to the accessory ligament of the deep digital flexor tendon may be observed as enlargement with or without increase in signal intensity and loss of separation from the adjacent tissues.

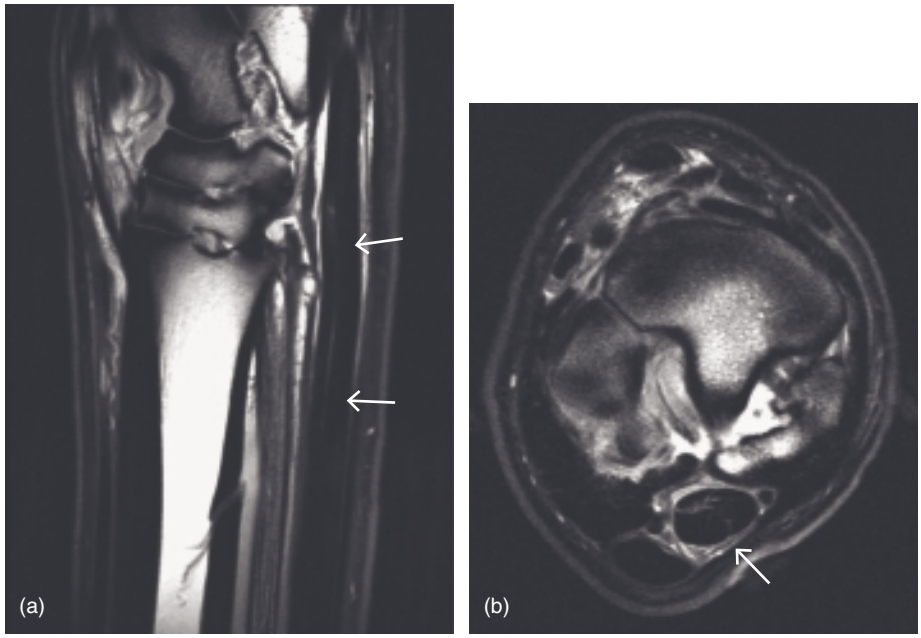

Figure 17.25 Damage to the deep digital flexor tendon (DDFT). High-field MR image showing DDFT damage at the level of the tarsus in a 6-year-old Friesian gelding. The horse had a 3-month history of right hind limb lameness, which was worse under saddle. Intra-articular medication of the distal tarsal joints failed to improve the lameness. On presentation the horse was 2/5 lame in the right hind limb. Distal limb flexion exacerbated the lameness to 3/5. While the lameness was not improved by a low 6-point block or intra-articular anesthesia of the tarsometatarsal joint, it was abolished by both anaesthesia of the deep branch of the lateral plantar nerve and intrathecal anaesthesia of the tarsal sheath. Ultrasonography indicated a heterogenous echogenicity of the DDFT at the level of the head of the fourth metatarsal bone. MR images show high signal intensity within the DDFT on sagittal (a) and transverse (b) proton density images, which was also noted on T2 and STIR images. After MRI, the right tarsal sheath was injected with hyaluronic acid and 10mg triamcinolone. The horse was rested for 4 months and was then gradually returned successfully to exercise. Images courtesy of Dr Michael Schramme, North Caroline State University.

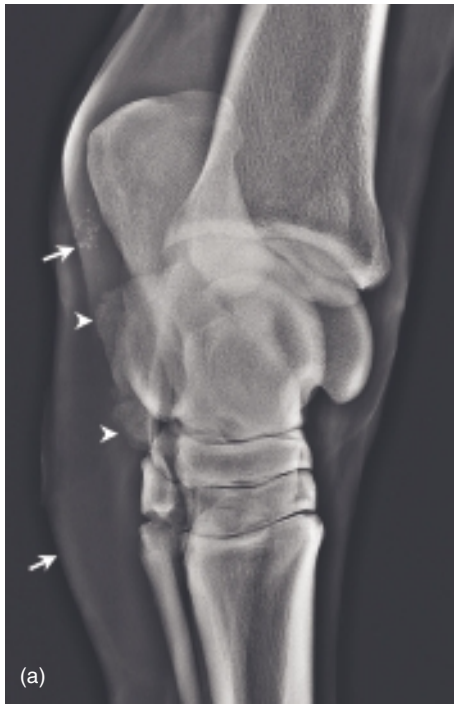
(a)

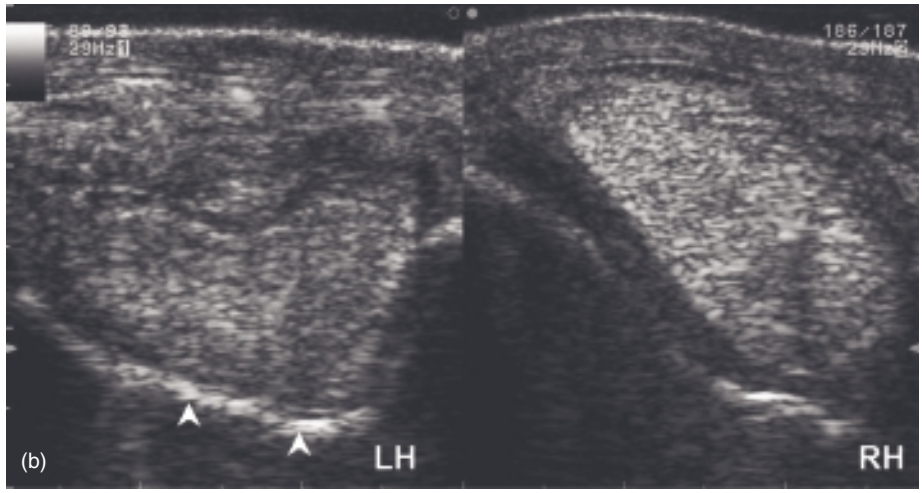
(b)
LH
RH

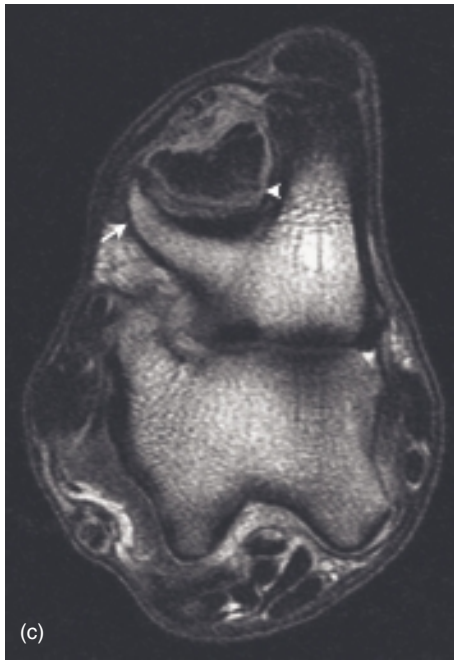
(c)

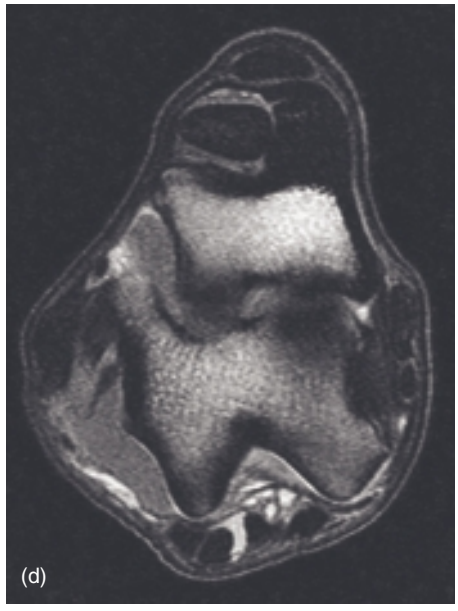
(d)

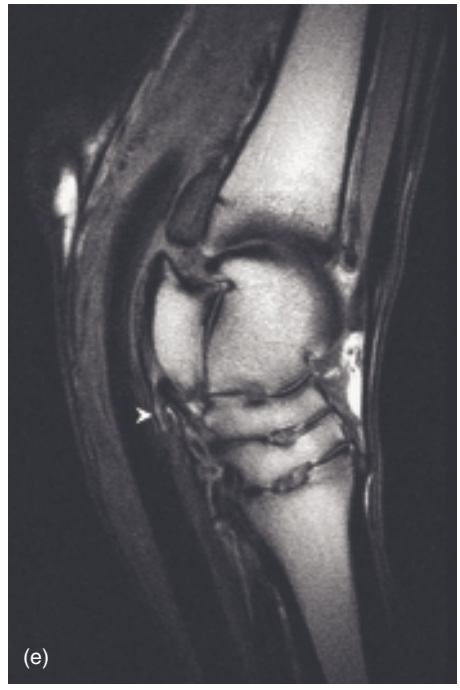
(e)

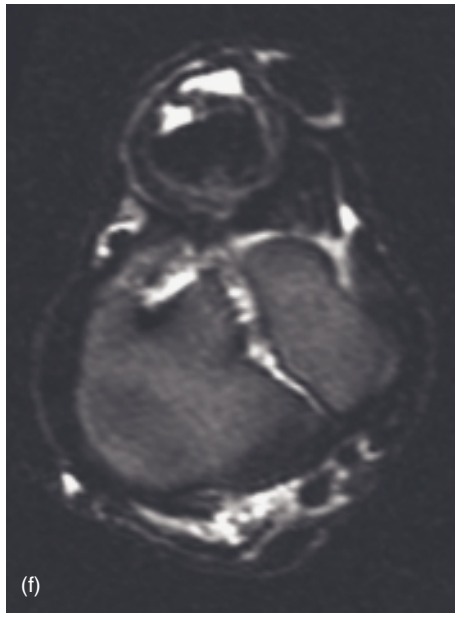
(f)

Figure 17.26 Tarsal sheath and sustentaculum tali pathology. Low-field MR images obtained under general anaesthesia in an 8-year-old show jumper Selle-Français gelding presenting with a marked left tarsal sheath effusion and a moderate lameness of this hind limb. (a) Dorsomedial-plantarolateral radiographic projection of the tarsus. The thickening and mineralization of the soft tissues can be clearly visualized (arrows). Extensive bony proliferation of the sustentaculum tali at its medial and distal borders is also present (arrowheads). (b) Transverse ultrasonographic scans of left and right hind limbs performed at the level of the sustentaculum tali showing a severe left lateral digital flexor tendonitis (medial is to the left) with an abnormal V shape of the tendon and a slight decrease of echogenicity. There is also marked thinning of the fibrocartilage covering the plantar groove of the sustentaculum tali (arrowheads). The synovial membrane proliferation is visible at the plantar aspect of the tendon. (c) Transverse spin-echo T1-weighted image of the lame hind limb showing a thinning and signal abnormalities of the fibrocartilaginous groove of the sustentaculum tali compared to a reference image (d) and an increased signal of the dorsal aspect of the lateral digital flexor tendon (arrowhead). There is also obvious remodelling of the medial border of the sustentaculum tali (arrow). (e) Longitudinal spin-echo T1-weighted image of the lame hind limb. The tarsal sheath effusion and the large bony proliferation at the disto-plantar aspect of the sustentaculum tali (arrow) are clearly visualized. (f) Transverse T2-weighted image demonstrating fluid accumulation in the tarsal sheath with a thickening of its mesotendon and synovial membrane hyperplasia.

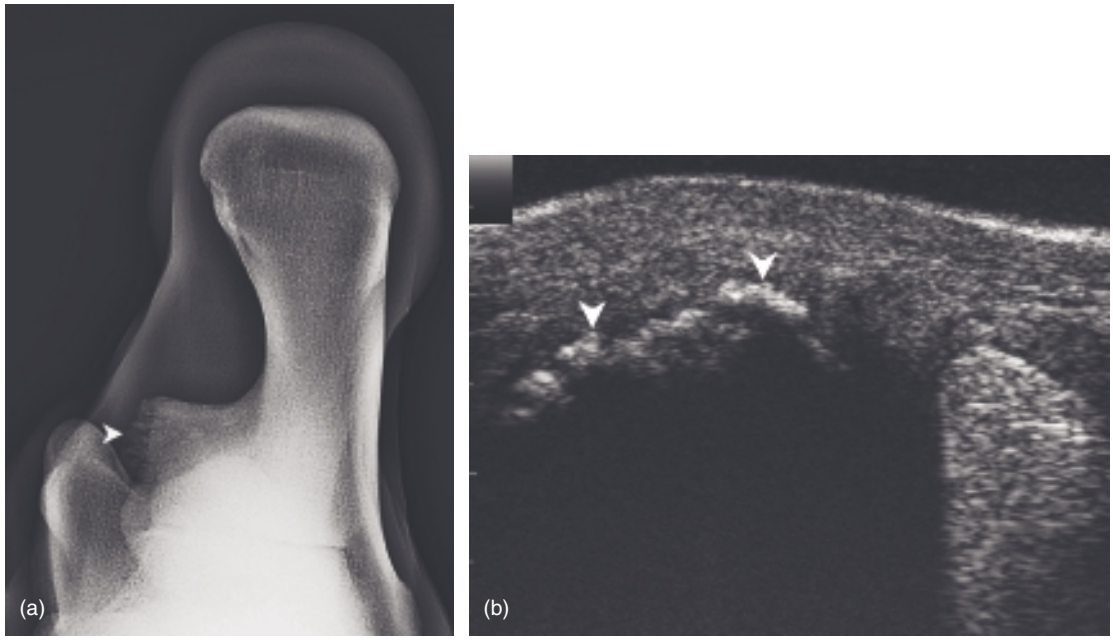

Figure 17.27 Tarsal sheath pathology. Low-field MR images obtained under general anaesthesia in a 10-year-old pleasure horse, presenting with a moderate right tarsal sheath effusion and a severe chronic lameness of this hind limb. (a) Skyline radiographic view of the tarsus demonstrating marked bony proliferation at the medial aspect of the sustentaculum tali (arrowhead). (b) This remodelling was also visualized using a transverse ultrasonographic scan performed at the medial aspect of the tarsus (arrowheads, dorsal is to the left). This appears as an ill-defined hypointense signal area on spin echo T1-weighted images (c, arrowheads). (c) An abnormal hypointense signal is also present in the adjacent medial part of the sustentaculum tali. Another area of diffuse hypointense signal is also visualized in the sagittal part of the calcaneus (arrows). (d) Transverse STIR and corresponding T1-weighted (e) images showing signal alterations of the plantar groove of the sustentaculum tali (arrows) and a large bruising of the calcaneus. Due to the thin dark line (arrowheads) extending from the dorsal aspect of the calcaneus to its plantar alteration (arrow) among the bone oedema-like lesion on the STIR image, a diagnosis of sagittal plane fatigue fracture of the body of the calcaneus was considered. (f) Longitudinal spin-echo T1-weighted images. The marked focal signal abnormality of the plantar aspect of the sustentaculum tali (ulceration of the flexor surface) is associated with a concurrent focal dorsal damage of the lateral digital flexor tendon (arrowhead). (g) Longitudinal ultrasonographic scan of the lateral digital flexor tendon as it traverses the sustentaculum tali (proximal is to the left). The ulceration of the plantar groove of the sustentaculum tali is clearly identified (arrowheads).

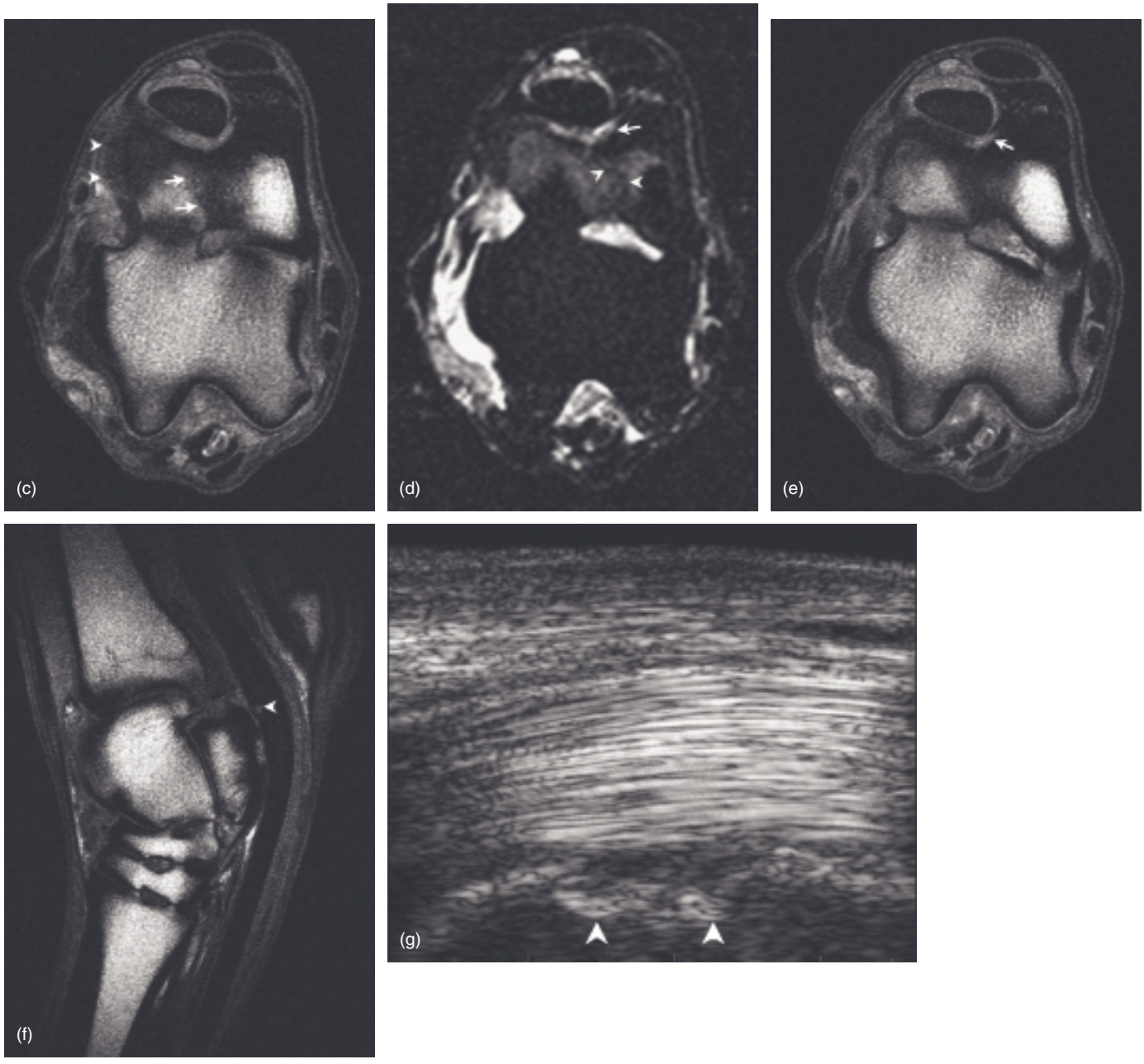

Figure 17.27 *Cont'd*

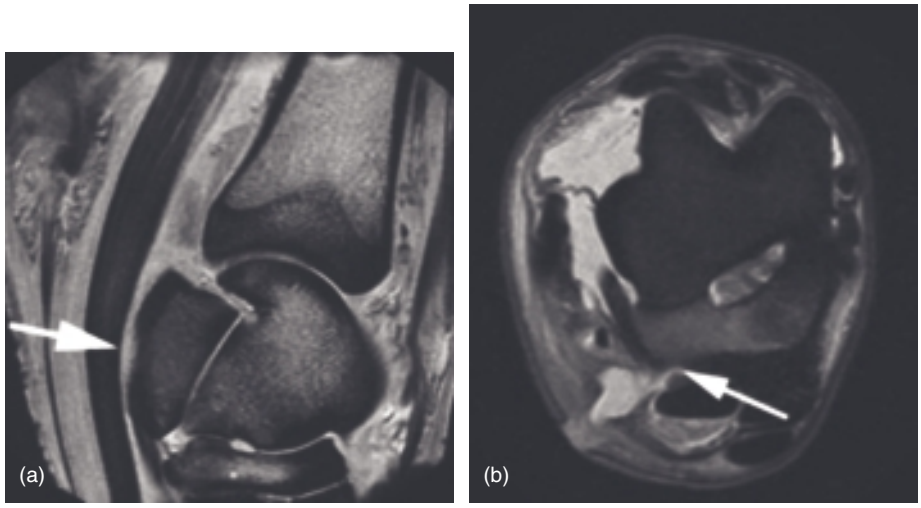

Figure 17.28 Sustentaculum tali osteomyelitis. Sagittal T1-weighted gradient-echo image (a) and transverse STIR image (b) from an 11-year-old Quarter Horse gelding that had sustained a penetrating wound to the tarsus, treated by lavage and systemic antibiotics over several weeks. The lameness continued to progress. MRI images demonstrate bone lysis on the palmar aspect of the sustentaculum tali. There is extensive fluid in the calcaneus characterized by increased signal intensity on STIR images. These findings are consistent with osteomyelitis. The site of the penetrating wound can be identified on the STIR transverse image characterized by disruption of the fascial planes. There is extensive cellulitis surrounding the site of the penetrating wound. Proliferative tenosynovitis can be identified in the tendon sheath, surrounding the deep digital flexor tendon. There is moderate synovitis of the tibiotarsal joint characterized by increased fluid. The horse was euthanized due to a poor prognosis.

CALCANEAL BURSA

Acute damage to the calcaneal bursa may be seen as increased fluid content with minimal alteration in signal intensity, thickening and inflammation of the synovial membrane. Chronic damage is characterized by increased amounts of soft tissue within the bursa, indicating fibrotic synovial proliferation and thickening and scarring of the synovial membrane. Fibrotic synovial proliferation can result in pockets of fluid in the bursa adjacent to a particular location of damage. On fat-suppressed images, there may be increased signal intensity in the adjacent bone, indicative of either direct damage as a result of trauma or secondary to inflammatory changes in the adjacent bursa (Figure 17.6).

Chapter 18
The stifle

Carter Judy

INTRODUCTION

Magnetic resonance imaging (MRI) of the equine stifle is currently one of the most challenging anatomical locations on the horse to image. Limitations in scanner design and the unique anatomy of the horse have made imaging of this region difficult in the best of circumstances.

PATIENT AND SCANNER PREPARATION

Imaging of the equine stifle is not for the faint of heart. It requires utilizing the available equipment at the edge of its design specifications. It requires positioning of the patient within the confines of a relatively small gantry (70 cm) and placing the stifle within the useful magnetic field. Many horses will not be able to be imaged due to limitations of the currently available scanners.

Prior to anaesthesia and imaging, horses are screened by weight, 'femur length' as measured from the apex of the patella to the greater trochanter of the femur, 'tibial length' as measured from the apex of the patella to the point of the hock, and 'pelvic measurement' as measured from tuber coxae to tuber coxae over the dorsum. A review of successful MRI examinations revealed that all horses with femur lengths greater than 44 cm, tibial lengths greater than 44 cm and pelvic measurements less than 62 cm have the best results in that the entire stifle is successfully imaged [1]. Partial examination of the stifle is possible if one of these measurements is non-compliant, but if more than one is outside these parameters, imaging of the stifle has not been possible. The best candidate for imaging of the stifle is a horse with long limbs and a narrow pelvis. Ironically a petite Quarter Horse weighing 400 kg is more difficult to image than a long limbed Thoroughbred or Warmblood weighing upwards of 535 kg.

Currently MRI images are obtained using a Siemens Magnetom Espree[1] with a field strength of 1.5 Tesla. Prior to introducing the horse into the magnet, the attached MRI table[1] with integrated spine coil[1] is pre-positioned into the bore of the magnet. The centre of the magnetic field is noted. The horse is anaesthetized into general anaesthesia and placed in lateral recumbency with the stifle to be imaged on the down side (i.e. if the right stifle is

[1]Siemens Medical, 51 Valley Stream Parkway, Malvern, PA, USA.

Equine MRI, edited by Rachel C. Murray.

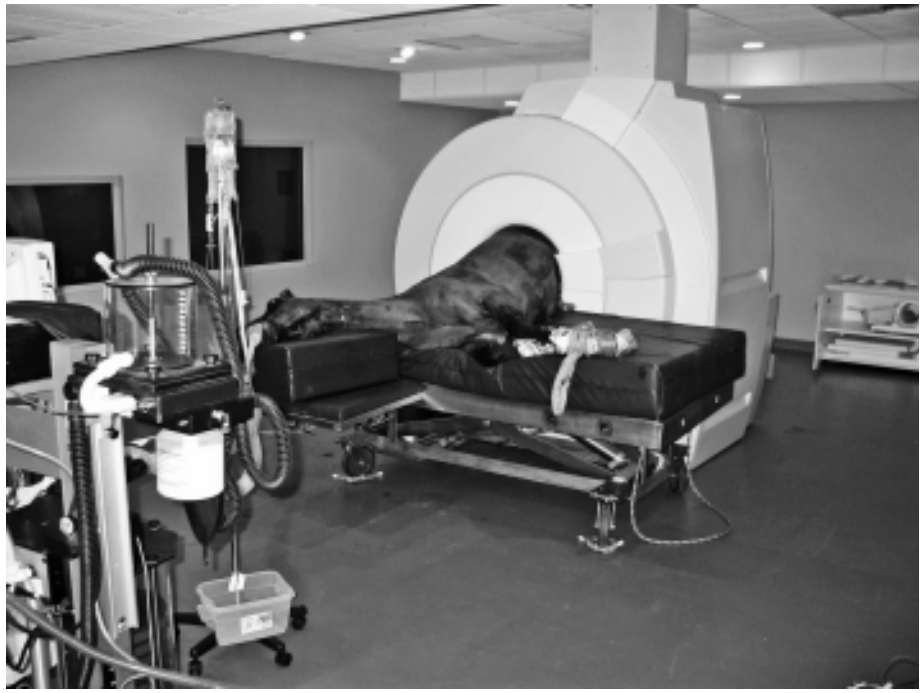

Figure 18.1 A 502 kg American Quarter Horse undergoing MRI examination of the left stifle.

to be imaged then the horse is placed in right lateral recumbency). The horse is placed on a separate MRI-compatible movable table[2] and placed adjacent to the bore of the magnet. The horse is then manually positioned into the magnet as far as possible. Ropes and padding are used to stabilize the limb to prevent further movement. A body matrix coil[1] is placed medially over the stifle to be imaged to create a parallel imaging array with the integrated spine coil within the MRI table that was pre-positioned. Use of the integrated body coil[1] is possible, but image quality is compromised. Figure 18.1 illustrates a 502 kg quarter horse within the magnet undergoing MRI evaluation of the left stifle.

IMAGING SEQUENCES

A combination of a body matrix coil[1] and the integrated spine coil[1] are used in parallel to acquire the signal. Images are obtained in multiple planes using multiple acquisition sequences. A routine examination of the stifle would include the following scanning sequences and positions:

- single plane localizer
- three plane localizer (frontal, sagittal, axial)
- proton density and T2-weighted dual echo – axial
- proton density and T2-weighted dual echo – sagittal
- proton density and T2-weighted dual echo – frontal plane

[2]Shank's Veterinary Equipment, 505 E. Old Mill Street, Milledgeville, IL, USA.

- T2 STIR (short τ inversion recovery) – axial
- T2 STIR – sagittal
- T2 STIR – frontal
- T1-weighted VIBE (volume interpolated gradient echo) fat saturated – axial
- T1-weighted VIBE fat saturated – sagittal
- T1-weighted VIBE fat saturated – frontal.

Additional sequences that have been used to further clarify pathology include:

- T2 MEDIC (multi-echo data image combination) water excitation – multiple planes
- T2 CISS (true FISP dual excitation) – multiple planes
- proton density fat saturated – multiple planes.

Contrast enhancement has been also used to further clarify pathological lesions within the stifle. Intravenous administration of 0.05–0.1 ml/kg of Gadopentatate dimeglumine contrast (Magnevist)[3] at the end of the routine examination followed by one minute of perfusion time then re-examination using the T1-weighted VIBE fat-saturated imaging protocols has produced the most useful information (Judy CE *et al*., in preparation).

The average time required to produce 14 sequences is 45 minutes for one stifle. Currently, imaging of a single stifle is performed since imaging the opposite stifle would require a change in recumbency and would compromise the anaesthetic condition of the patient.

INDICATIONS

Imaging of the stifle with MRI should be considered when a horse's lameness has been localized to the stifle. This may be determined by a detailed lameness exam with careful inspection and manipulation, by elimination of the lameness with intra-articular anaesthesia or by localization to the stifle with a diagnostic modality such as nuclear scintigraphy. Some pathological conditions of the stifle may not improve with intra-articular anaesthesia, as many structures that are affected may be extra-articular. MRI should be considered only after other diagnostic modalities have been unable to identify the cause of the problem. In some cases another diagnostic modality will be suggestive of, but not definitive for a problem in the stifle and MRI can be a useful tool to clarify a diagnosis.

The decision between exploratory arthroscopy of the stifle and MRI evaluation should be based on several factors. First and foremost should be to determine if MRI is feasible using the available technology. If an intra-articular lesion is suspected based on clinical evaluation, exploratory arthroscopy may provide a good way to evaluate and treat areas that are accessible with the arthroscope. However, there are many structures that are only partially visible (medial meniscus, cruciate ligaments) and others that are not visible at all (collateral ligaments, patellar ligaments,

[3]Magnevist brand gadopentetate dimeglumine – medication package insert – June 2007, Bayer Health Care Pharmaceuticals Inc, Wayne, NJ, USA.

subchondral bone) with an arthroscope. In addition, there are many operable lesions that are discovered via MRI of the stifle that result in a more complete surgical plan based on the results of the MRI examination. MRI provides a much more thorough evaluation of the stifle when the patient can be properly imaged, but will not provide the opportunity to treat the lesion during the same examination as an arthroscopic examination will.

MRI STIFLE PATHOLOGY

Imaging of the stifle with MRI has provided further insight into the pathology of this anatomic region. Injuries that have been difficult to image using other modalities such as radiography, ultrasound, nuclear scintigraphy and diagnostic arthroscopy can be readily visualized with MRI.

Examples of abnormalities that have been found to date include:

- cranial cruciate desmitis
- medial meniscal injury
- osteochondral fragmentation
- bone oedema – tibia, femur and patella
- cartilage erosions/disruption
- subchondral bone cysts
- synovitis/synovial effusion.

Due to the relatively low number of horses that have had the stifle imaged with MRI, undoubtedly this partial list will continue to grow as more horses have this imaging modality performed.

Cruciate ligaments

Parasagittal and frontal plane images have proved the most effective for diagnosing injuries to this ligament. Comparison with the caudal cruciate ligament provides an excellent internal reference for degree of signal increase on axial images as well as frontal images. Both ligaments should normally appear hypointense on all sequences when not injured and of relatively similar size. Care should be taken when interpreting the signal of the cranial cruciate ligament on T1-weighted images as it tends to run at 55° off B_0 within a cylindrical, closed magnet with the horse in lateral recumbency. This causes a magic angle artefact with artefactual increase in internal signal. Therefore evaluating internal signal of this ligament solely on T1-weighted images should be performed with caution.

Thickening and enlargement of the cranial cruciate ligament with an increase in internal signal on proton density (PD) and T1-weighted images has been the most consistent finding when this injury is encountered. T2-weighted images and T2-weighted STIR images would be expected to also have increased signal in more acute injuries; however, this has not been observed to date. This is likely due to the fact that most horses currently undergoing MRI evaluation of the stifle for this injury have experienced a prolonged course of lameness and the acute aspects have subsided by the time the horse is imaged. Figures 18.2 and 18.3 depict a chronic cranial cruciate ligament desmitis.

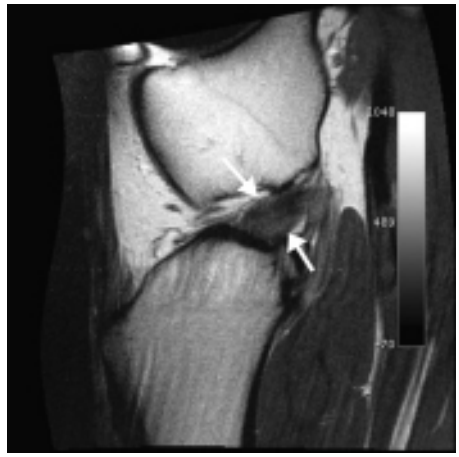

Figure 18.2 Proton density parasagittal plane MRI of the cranial cruciate ligament demonstrating a chronic cranial cruciate desmitis from a 13-year-old Arabian endurance horse. The ligament is demarcated by the white arrows. Note the increase in internal signal and moderate thickening and enlargement of the ligament.

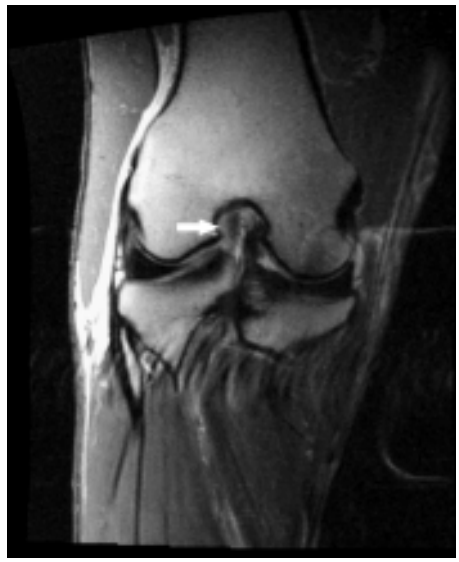

Figure 18.3 Proton density frontal plane MRI of the cranial cruciate ligament demonstrating a chronic cranial cruciate desmitis from a 13-year-old Arabian endurance horse. The white arrow is marking the cranial cruciate ligament. Note the increase in internal signal and moderate thickening and enlargement of the cranial cruciate ligament.

Secondary MRI signs of cranial cruciate ligament injury occur with a varying degree of sensitivity and specificity. These are the result of damage to the support structures of the stifle and secondary instability and inflammation. These include joint effusion of one or all of the compartments of the stifle and bone oedema adjacent to the origin or insertion of the ligament.

Concomitant injury to the medial meniscus is reported to occur simultaneously with most cranial cruciate ligament injuries in the horse [1]. This has not been directly observed to date with MRI. This is most likely the

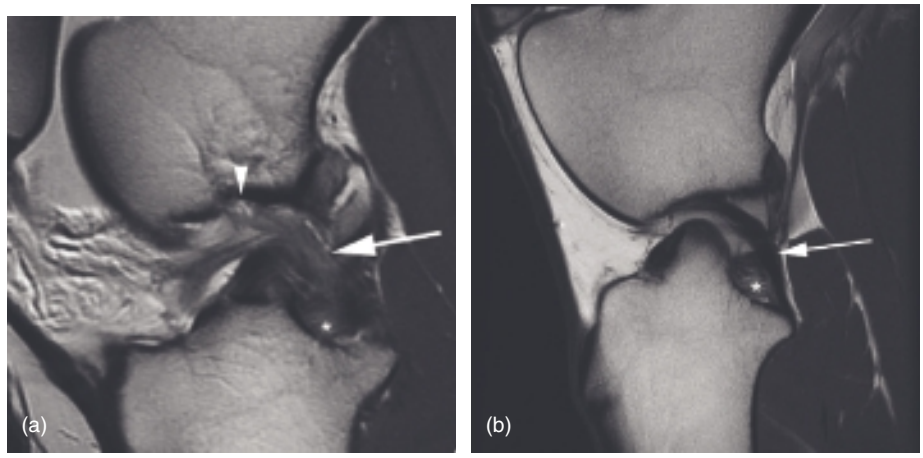

Figure 18.4 Sagittal proton density image from a 6-year-old Warmblood mare that became acutely lame after slipping and falling (a). The caudal cruciate ligament is thickened and inflamed (arrow). There is a partial tear affecting the central aspect of the ligament origin (arrowhead). The normal insertion of the caudal ligament (*) of the medial meniscus can be identified cranial to the caudal cruciate ligament. A normal image is provided for comparison (b). The caudal cruciate ligament (arrow) has well-defined margins with low signal intensity on proton density images. Images courtesy of Dr Natasha Werpy.

result of the relative low numbers of horses imaged and the relative degree of rarity of this type of injury. Caudal cruciate ligament may also occur, with or without concurrent meniscal damage (Figure 18.4).

Medial meniscal injury

Disruption of the medial meniscus is readily visible with MRI. Frontal and parasagittal images are the most effective for evaluating the meniscus. Axial images can be useful as well but rely on excellent positioning for a proper evaluation. An advantage of MRI is its ability to evaluate the entire meniscus and to visualize lesions that do not reach the articular surface, which would therefore not be visible by arthroscopic evaluation or ultrasound examination.

The normal meniscus on a parasagittal and frontal plane image has a hypointense triangular appearance that is well defined. An increase in internal signal or anatomical disruption is indicative of damage to this structure. The most common disruptions are on PD and T2-weighted images. An internal meniscal signal extending to the articular surface is indicative of a tear, but should be correlated with other MRI findings within the stifle such as enlargement of the meniscus and effusion of the medial femerotibial compartment. An isolated fissure of the ligament without other signs may be the result of collagen degeneration rather than a distinct injury. Often extrusion of the medial meniscus in a medial direction will be present. Figures 18.5–18.7 demonstrate a medial meniscal desmitis with an associated subchondral defect and secondary medial femerotibial compartment effusion. Meniscal tears are also shown in Figures 10.3 and 10.4.

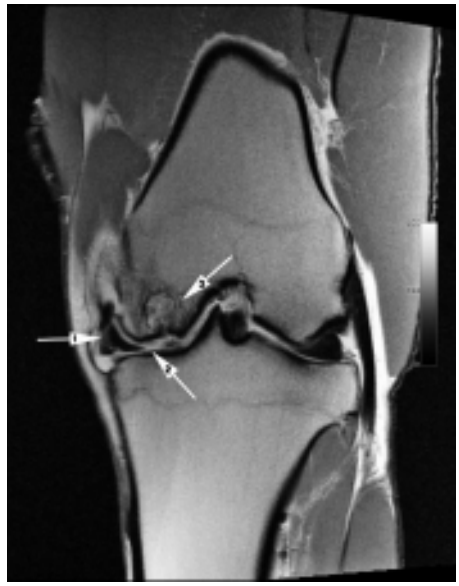

Figure 18.5 Proton density frontal plane MRI demonstrating a medial meniscal tear and subchondral bone cyst from a 12-year-old American Quarter Horse. Arrow 1 depicts extrusion of the medial meniscus and a heterogeneous signal within the meniscus indicating disruption of the collagen fibres. Arrow 2 shows a void of in the meniscus with meniscal tissue on either side of the arrow. Arrow 3 depicts a subchondral bone cyst.

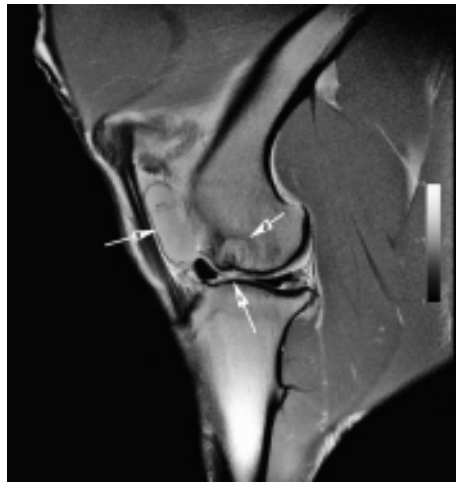

Figure 18.6 Proton density parasagittal plane MRI demonstrating a medial meniscal tear and subchondral bone cyst from a 12-year-old American Quarter Horse. Arrow 1 depicts the disruption of the meniscus, loss of articular cartilage and heterogeneous signal within the meniscus. An associated subchondral bone cyst is also present (arrow 2) along with a moderate amount of joint effusion (arrow 3).

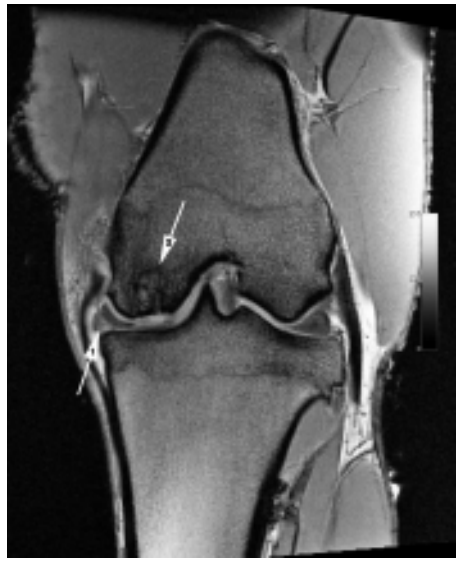

Figure 18.7 T2 FISP frontal plane MRI demonstrating a medial meniscal tear and subchondral bone cyst from a 12-year-old American Quarter Horse. Note the extrusion of the medial meniscus, the heterogeneous signal within the medial aspect of the meniscus (arrow 1). This sequence shows a marked change in signal within the medial aspect of the meniscus. An associated subchondral bone cyst is also present (arrow 2).

Damage to the meniscal ligaments can occur with or without meniscal damage. These ligaments include the cranial tibial meniscal ligament (Figure 10.2), caudal ligament of the meniscus (Figure 18.4) and meniscofemoral ligament (Figure 10.4).

Osteochondral fragmentation

Osteochondrosis dissecans (OCD) is the most common irregularity identified to date in equine MRI of the stifle. This is much more readily visible on MRI compared with traditional radiography. MRI allows a more detailed evaluation of OCD lesions and can identify occult and subtle pathology that has not been identified previously. In addition, pathology of the underlying bone and adjacent articular surfaces can be readily identified. Most horses diagnosed with OCD of the trochlear ridges of the femur via MRI have normal radiographs at the time of examination.

OCD lesions appear as irregularities of the lateral trochlear ridge, medial trochlear ridge or intercondylar groove of the distal femoral condyle. In some cases an irregularity of the articular surface of the patella will be noted as well. Typically OCD lesions have altered signal intensity within the cartilage and subchondral bone relative to the marrow. This signal intensity tends to be hyperintense on T2 STIR images and hypointense on T1-weighted VIBE fat-saturated and PD images. A high signal fluid line on T2-weighted images in the subchondral bone has been correlated with instability of the osteochondral fragment during arthroscopy. Additional pathology in the underlying subchondral bone and trabecular bone can be seen as a distinct hyperintense signal on T2 STIR images and has been noted to contrast enhance when intravenous contrast is administered[3]. Figures 18.8–18.10 demonstrate examples of osteochondrosis of the stifle joint.

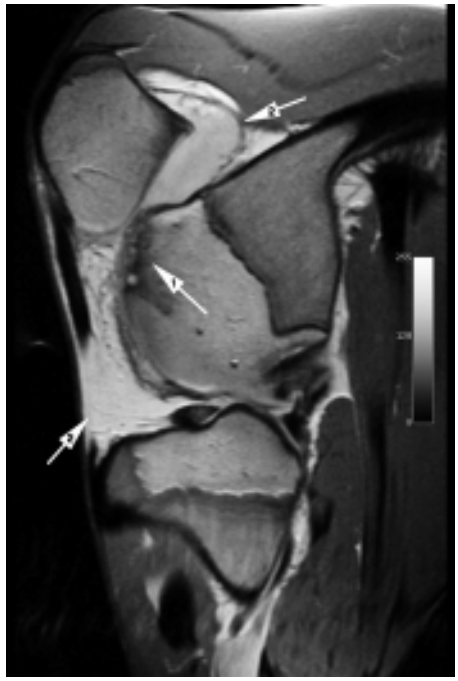

Figure 18.8 Proton density parasagittal plane MRI demonstrating an osteochondrosis dissecans (OCD) lesion of the lateral ridge of the trochlea of the femur in an 18-month-old Thoroughbred. Note the disruption of the articular surface with heterogeneous signal in the underlying subchondral bone consistent with sclerosis and oedema (arrow 1). The articular cartilage is mottled with regions of hyperintensity directly underneath the articular cartilage consistent with loose fragmentation (arrow 1). Associated moderate joint effusion of the femeropatellar compartment of the stifle is also present (arrows 2).

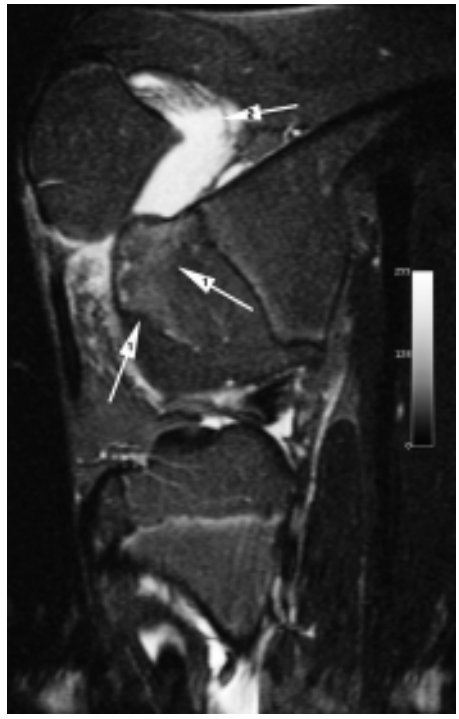

Figure 18.9 T2 STIR parasagittal plane MRI demonstrating an OCD lesion of the lateral ridge of the trochlea of the femur in an 18-month-old Thoroughbred. Note the disruption of the articular surface with a high signal in the underlying subchondral bone consistent with bone edema (arrows 1). Directly beneath the articular cartilage is a band of high signal denoting a region of detached cartilage. Associated moderate joint effusion of the femeropatellar compartment of the stifle is also present (arrow 2).

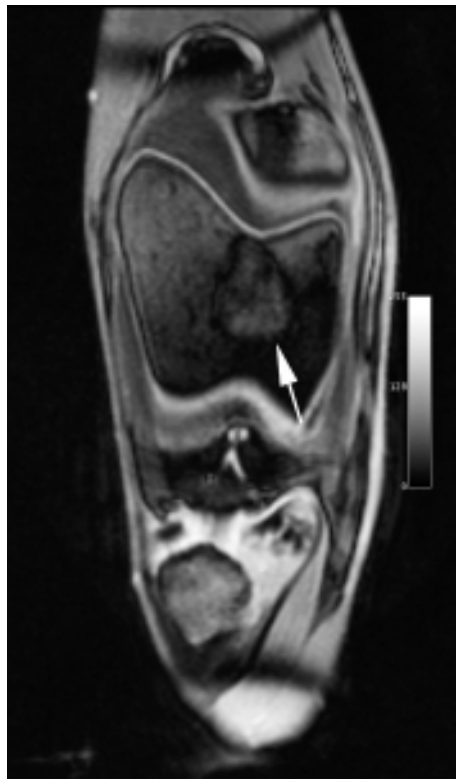

Figure 18.10 Proton density frontal plane MRI demonstrating an OCD lesion of the inter-trochlear groove of the distal femur in a 16-month-old Thoroughbred. Note the region of heterogeneous signal (arrow).

Bone oedema (contusion)

MRI allows the accurate imaging of previously unidentified bone marrow oedema. Routine imaging techniques such as radiography and ultrasound are unable to identify this pathological process. Nuclear scintigraphy has been shown to correlate very well with increased bone oedema on MRI [2]. This oedema may be the result of many potential pathological processes including trauma (acute and stress related), arthritis, avascular necrosis, osteomyelitis and bone tumour. The most common causes are trauma, arthritis and osteomyelitis.

The presence of increased free water within the bone will appear hyperintense on both T2 STIR and fat-suppressed images (PD and T1 VIBE). Since the primary cause of fluid accumulation in the extracellular marrow is capillary leakage, post-contrast[3] images will also show a hyperintense region as well. Typically this oedema begins in the subchondral regions of the bone and radiates deeper into the marrow cavity. Figures 18.11–18.13 demonstrate examples of bone oedema within the stifle.

Bone oedema will often been found in conjunction with other pathological process within the stifle. OCD fragmentation, cruciate ligament injury, cartilage erosions and subchondral cystic lesions invariably have a mild to moderate bone oedema associated with them.

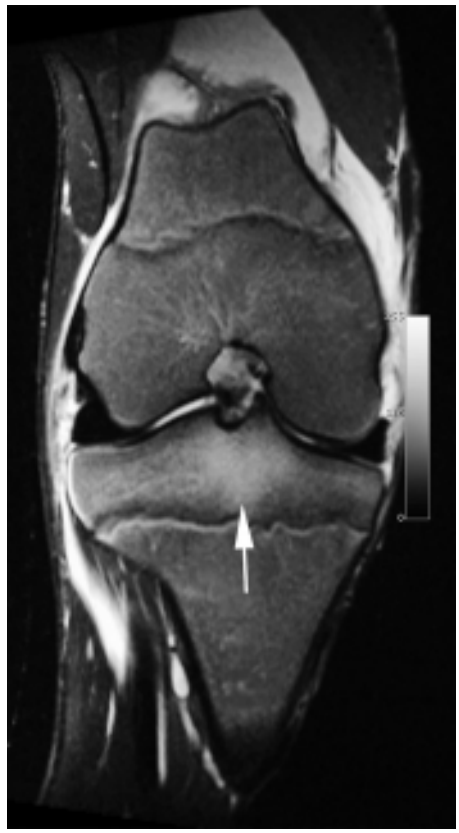

Figure 18.11 T2 STIR frontal plane MRI demonstrating marked bone oedema of the proximal central epiphysis of the tibia in a 26-month-old Thoroughbred. Note the homogenous diffuse hyperintense region in the central aspect of the proximal epiphysis (arrow).

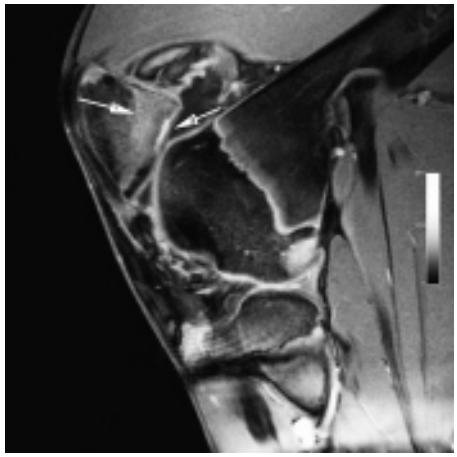

Figure 18.12 T1 VIBE fat-saturated post-intravenous contrast (gadopentetate dimeglumine[3]) parasagittal plane MRI of a 2-year-old Warmblood. Note the region of contrast enhancement diffusely throughout the patella (arrow 1). The articular cartilage of the patella is also contrast enhancing (arrow 2).

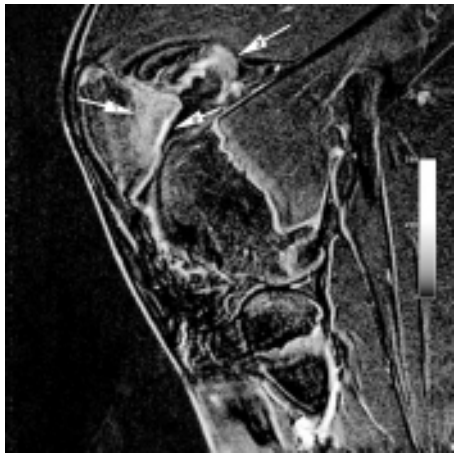

Figure 18.13 T1 VIBE fat-saturated post-intravenous contrast (gadopentate dimeglumine[3]) parasagittal plane subtraction MRI of the same 2-year-old Warmblood as in Figure 18.12. Subtracting the pre- and post-contrast T1 VIBE fat-saturated images from each other created this image. The subtraction demonstrates only the location of contrast within the tissues. Note the region of contrast enhancement diffusely throughout the patella (arrow 1). The articular cartilage is also contrast enhancing along the articular surface of the patella (arrow 2). There is marked increase in contrast uptake in the synovial lining of the supra-patellar recess consistent with marked synovitis (arrow 3).

Cartilage erosions

Cartilage erosions and damage not related to OCD fragmentation is readily visible using MRI evaluation. MRI provides appropriate in-plane resolution and tissue contrast to detect focal cartilage lesions and subchondral bony abnormalities prior to appearance on radiographs. In addition, MRI allows evaluation of cartilage in regions not observable using current arthroscopic techniques.

The signal characteristics of articular cartilage are dependent on the pulse sequence used, cellular composition of the collagen, proteoglycans and free water, and the orientation of the collagen within the cartilage matrix. Disruptions of the cartilage are readily noticeable as a change in the signal characteristics in the anticipated, regular appearing cartilage on either side of the erosion or tear. Proton density fat-saturated images and T1 VIBE fat-saturated pre- and post-contrast,[3] along with the corresponding subtraction images, have provided very good evaluation of the articular cartilage and the presence of apparent erosions. Invariably, secondary signs of pathology including adjacent bone oedema and an increase in the amount of intra-articular fluid almost always accompany these erosions. Figures 18.14 and 18.15 demonstrate images of cartilage damage.

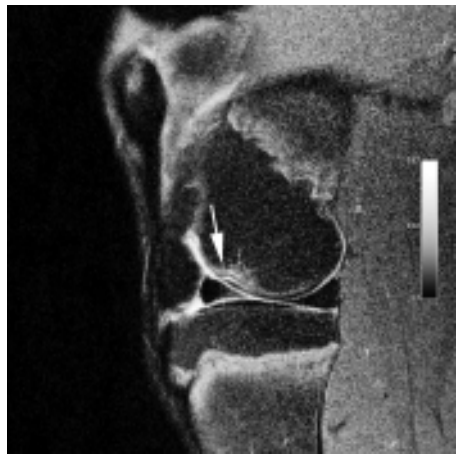

Figure 18.14 Proton density fat-saturated parasagittal MRI demonstrating a cartilage erosion with mild subchondral bone edema in a 3-year-old American Quarter Horse (arrow).

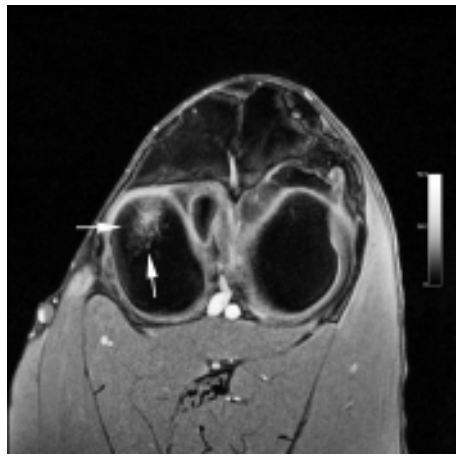

Figure 18.15 T1 VIBE fat-saturated post-intravenous contrast (gadopentetate dimeglumine[3]) axial plane MRI showing contrast uptake in the region of the medial condyle in a 3-year-old American Quarter Horse. The arrows delineate the location of the contrast enhancement.

Subchondral bone cysts

Subchondral cystic lesions of the medial femoral condyle are typically diagnosed relatively easily using radiography. However, occult lesions have been identified in multiple horses that have not been visualized using digital or computerized radiography before and after MRI examination. Evaluation of the adjacent meniscus can also be determined more completely with MRI evaluation.

Subchondral cystic lesions of the medial femoral condyle typically appear within the middle of the articular surface of the femoral condyle. The contents of the cyst typically have a heterogeneous signal with the majority of the cyst being hyperintense with small focal regions of hypointensity throughout on proton density, T2-weighted, T1 VIBE fat saturated, and T2 STIR images. Most cysts have an inward-collapsing articular surface and disruption of the adjacent subchondral bone. These cysts will have a region of hypointensity immediately surrounding the region of hyperinstensity, which corresponds to sclerosis of the bone. Surrounding this sclerosis is often a region of diffuse bone oedema on T2 STIR images. In most horses, there is a region of focal fluid accumulation with the joint space adjacent to the cyst. Figures 18.16–18.18 demonstrate a severe bone cyst of the medial femoral condyle.

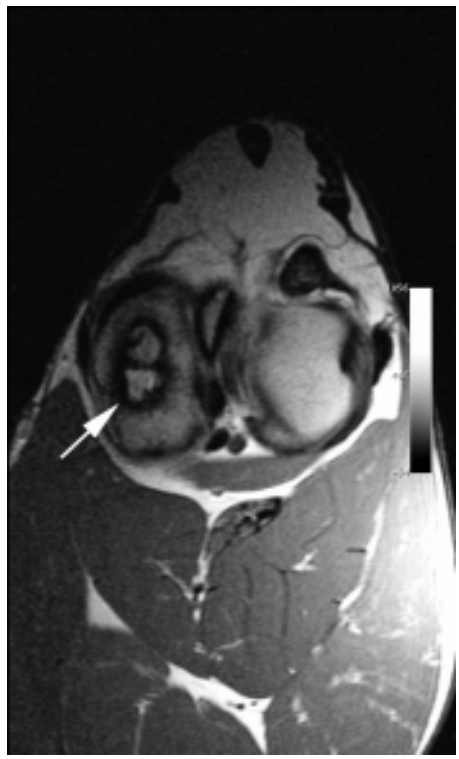

Figure 18.16 Proton density axial plane MRI demonstrating a severe subchondral bone cyst in a 5-year-old American Quarter Horse. Notice the region of heterogeneous hyperintense signal consistent with fluid-filled tissue surrounded by a distinct region of hypointense signal consistent with bone sclerosis (arrow).

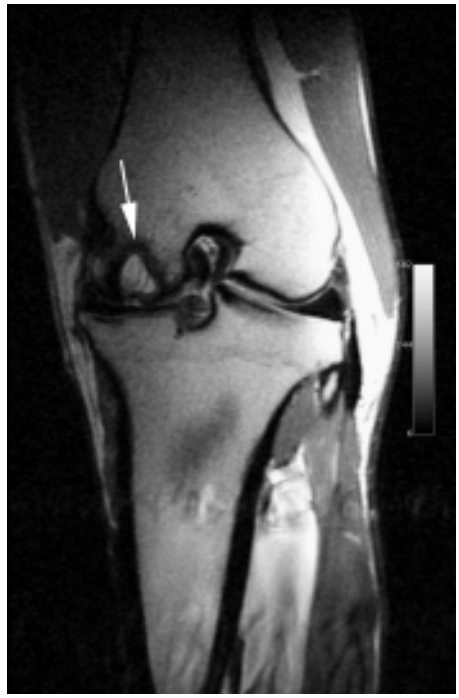

Figure 18.17 Proton density frontal plane MRI demonstrating a severe subchondral bone cyst in a 5-year-old American Quarter Horse. Notice the region of heterogeneous hyperintense signal consistent with fluid-filled tissue surrounded by a distinct region of hypointense signal consistent with bone sclerosis. Along the articular surface of the cyst is a small region of fluid signal adjacent to meniscus demonstrating disruption of the articular cartilage. The medial meniscus is intact.

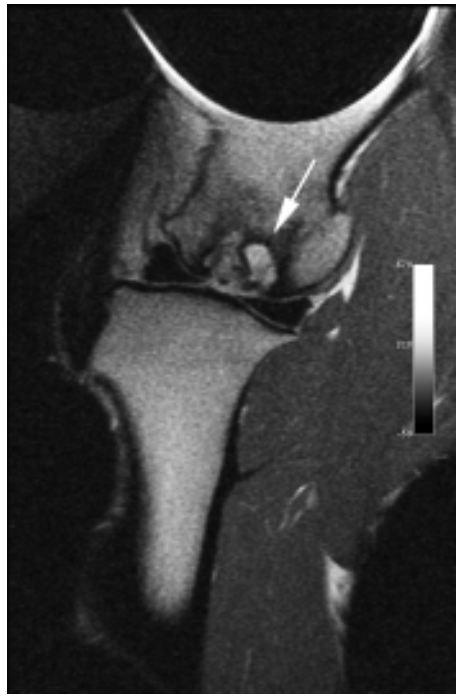

Figure 18.18 Proton density parasagittal plane MRI demonstrating a severe subchondral bone cyst in a 5-year-old American Quarter Horse. Notice the region of heterogeneous hyperintense signal consistent with fluid-filled tissue surrounded by a distinct region of hypointense signal consistent with bone sclerosis (arrow). This image demonstrates the artefact often noted in stifle MRI with a distinct region of no signal where the anatomical region is no longer in the useful magnetic field. This is demonstrated by the region of no signal (black) at the top of the image.

Synovitis/synovial effusion

Synovitis and synovial effusion of the stifle joint compartments accompanies many of the conditions that occur within the stifle. They are often a secondary finding and their presence often supports the primary diagnosis. Primary traumatic synovitis with synovial effusion is relatively rare. Infections synovitis can be a primary cause of stifle lameness and shares may of the nonspecific findings of synovitis and synovial effusion.

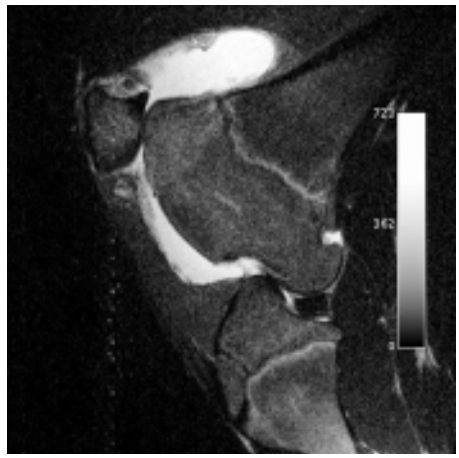

Figure 18.19 T2 STIR sagittal plane MRI demonstrating severe joint effusion of the femeropatellar compartment of the stifle in a 4-year-old Wamblood. The hyperintense region adjacent to the patella is excessive fluid within the joint.

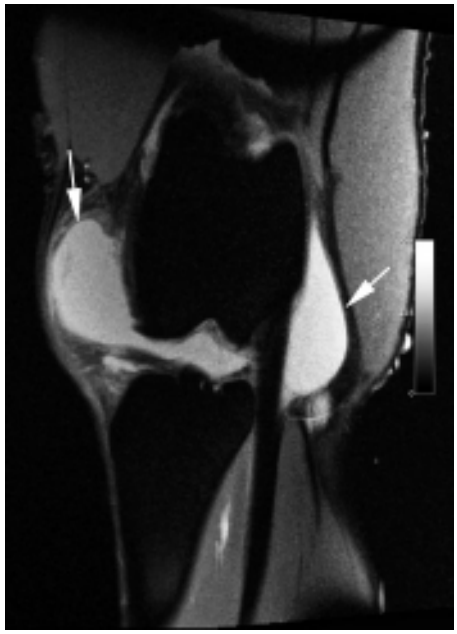

Figure 18.20 T2 MEDIC water excitation frontal plane MRI demonstrating severe joint effusion of the medial and lateral femerotibial compartments of the stifle in a 12-year-old Wamblood (arrows).

Increase in fluid within the synovial space as viewed on T2-weighted, T2 STIR and PD images is indicative of synovial effusion. This is demonstrated in Figures 18.19 and 18.20. Synovial proliferation and joint capsule thickening will be present on PD, T2-weighted and T2 STIR images. T1-weighted VIBE fat-saturated post-intravenous contrast[3] injection reveals synovial inflammation the best. The capillary leakage associated with the inflammatory process allows an increase in the extravascular distribution of the

contrast agent, which is easily visualized using pre- and post-contrast subtraction techniques (images). Figure 18.13 demonstrates the contrast enhancement in the synovium consistent with synovitis.

Septic synovitis shares the same characteristics as traumatic synovitis and the signal characteristics are indistinguishable. Careful correlation with clinical signs, laboratory findings and joint aspirates should be made to clarify the diagnosis if a septic joint is suspected.

CONCLUSION

MRI of the equine stifle is in its infancy in relation to the anatomical locations lower on the limb [3]. Current limitations in scanner design have limited the use of this technology to date. As scanners continue to progress and techniques evolve, imaging of the equine stifle will provide an unparalleled evaluation of the stifle in the future.

REFERENCES

[1] Judy C, Saveraid T, Rick M, Herthel, D. Magnetic resonance imaging of the equine stifle in a clinical setting. Proceedings of American College of Veterinary Surgeons Surgical Summit, Chicago, IL, 17–21 October 2007.

[2] Judy C, Saveraid T, Rick M, Herthel D. Correlation of nuclear scintigraphic and magnetic resonance imaging in equine clinical orthopedic cases. Proceedings of American College of Veterinary Surgeons Surgical Summit, Chicago, IL, 17–21 October 2007.

[3] Holcombe S, Bertone A, Biller D, Haider V. Magnetic resonance imaging of the equine stifle. *Vet Radiol Ultrasound* 1995; **36**(2): 119–25.

Chapter 19
The head

Russell Tucker, Katherine Garrett, Stephen Reed and Rachel Murray

INTRODUCTION

Equine neurologic examinations and neurologic diseases have been well described; however, lesions within the brain and skull were a diagnostic challenge because of limited imaging options, especially for soft tissues, prior to the use of magnetic resonance imaging (MRI) for many brain and skull disorders [1–6]. The initial reports of the use of MRI in describing the normal anatomy of neonatal foals and adult horses, limited accounts of MRI use in clinical patients and subsequent guidelines on scanning protocols for the brain and head regions serve as excellent references for appropriate clinical applications [5–16]. With the increasing availability of MR facilities and the acceptance of the diagnostic advantages of MRI for several forms of head and brain pathology in horses, the clinical applications continue to expand.

MRI examinations generate a diverse spectrum of image sequences providing superior soft tissue contrast, acquisition of multiplanar cross-sectional images, and the ability to use intravenous contrast to illustrate breakdown of the blood–brain barrier and highlight specific types of pathology. With experience, the osseous structures of the head and calvarium can also be critically examined and allow accurate characterization of destructive, proliferative and traumatic lesions. As with all imaging modalities, it is important that the findings on MRI are interpreted in conjunction with the clinical presentation, neurologic exam, blood work and cerebrospinal fluid (CSF) analysis.

The following cases demonstrate advantages of MR imaging in several pathologic conditions commonly encountered in equine practice. It should be noted that the selected images for these cases were chosen to illustrate the lesions detected on one or more of the acquired sequences and image planes. In the actual clinical setting, reviewers of the MRI examinations would have the opportunity to scroll through the entire image sets, and cross-reference between sequences and scan planes.

PITUITARY ABNORMALITIES

In our experience, pituitary abnormalities are not unusual. Patients may present with endocrinological abnormalities or because of blindness related to compression of the optic chiasm and nerves [17].

Equine MRI, edited by Rachel C. Murray.

The MR features that are of particular use in detection of pituitary lesions include the following.

SIZE AND SHAPE OF THE PITUITARY

In normal horses, the size of the pituitary gland is reported as being 8–10 mm dorso-ventrally, and 18–25 mm transversely and rostro-caudally [18]. Retrospective MR measurements of the pituitary gland in heads of normal horses ranged from 5 to 8 mm dorso-ventrally, 12 to 14 mm transversely and 11 to 14 mm rostrocaudally (Murray R and Dyson S, unpublished data; Saveraid T and Tucker R, unpublished data). The size of the pituitary masses in the horses below was considerably greater, both on MR evaluation and gross examination. With enlargement and compression, the normal pituitary shape may be altered. However, pituitary dysfunction in the absence of neurological abnormality may not be associated with enlargement.

SIGNAL INTENSITY AND HOMOGENEITY IN THE PITUITARY

Signal heterogeneity and increased signal intensity on T2-weighted images may be indications of abnormality. However, similar to other species, a central region of hyperintensity has been noted in some normal horses on T1 pre-contrast images thought to represent neurotransmitters and cholesterol content.

CONTRAST ENHANCEMENT PATTERN

Uniform contrast enhancement is considered normal, and heterogeneous contrast enhancement can be indicative of pathology. Thin-slice dynamic pituitary contrast protocols have not yet been explored in equine patients, but may provide useful information undetected on conventional brain imaging sequences.

SHAPE AND SIGNAL INTENSITY WITHIN THE ADJACENT STRUCTURES, PARTICULARLY THE OPTIC NERVES AND CHIASM

The optic nerves and chiasm may be compressed to an abnormal, flattened shape, and may be partly displaced. Increased signal intensity of adjacent structures on T2 and FLAIR (fluid attenuated inversion recovery)-weighted sequences is indicative of oedema and inflammation. Evidence of haemorrhage and haemosiderin within these tissues is most obvious on T2* gradient-echo images.

The following cases illustrate two types of pituitary masses and the MR findings.

Case 1

A 13-year-old Thoroughbred mare presented with decreased mentation, poor appetite, weight loss and absence of normal oestrus cycles. The

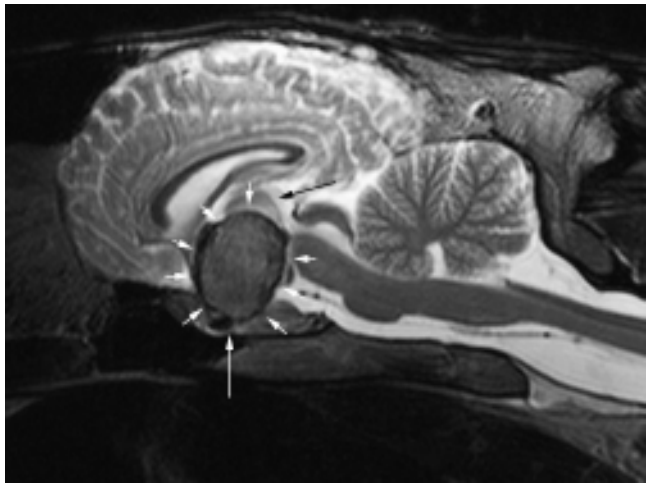

Figure 19.1 T2-weighted turbo spin-echo mid-sagittal plane image of a mass (short white arrows) within and dorsal to the sella turcica. Note the compression of the optic chiasm by the mass (long white arrow) and displacement of the interthalamic adhesion dorsally (black arrow). The mass has heterogeneous T2 signal intensity and the rim of hypointensity characterizes intracellular haemosiderin.

decreased mentation had progressed to prolonged periods of somnolence, slow circling behaviour and an apparent decrease in vision. The mare had decreased menace and pupillary light responses and demonstrated slight weakness on a tail pull test. An anatomic diagnosis of a central nervous system (CNS) lesion rostral to the foramen magnum was made. Endogenous adrenocorticotropic hormone, triiodothyronine (T3) and thyroxine (T4) levels were normal. An MRI examination was undertaken in an attempt to find the cause of the neurologic signs and to further investigate a possible pituitary lesion.

There was a mass centred on the median plane ventral to the diencephalon (Figure 19.1). The ventral aspect of the mass was within the sella turcica. The mass displaced the interthalamic adhesion dorsally, compressed the left and right sides of the thalamus and hypothalamus and distorted the third ventricle. The lateral ventricles were mildly dilated, likely due to the compression of the third ventricle obstructing the flow of CSF. A portion of the pituitary distinct from the mass can be identified in the caudal and ventral parts of the sella turcica.

The mass was between the optic tracts and immediately caudal to the optic chiasm, which was compressed and displaced. The mass was isointense to the surrounding brain parenchyma on T1 images with an inner rim of low signal intensity (Figure 19.2a). The mass had mild heterogeneous contrast enhancement (Figure 19.2b). The mass had isointense to hypointense heterogeneous T2 signal intensity with an inner rim of low T2 signal intensity and an outer rim of high signal intensity on T2-weighted and FLAIR sequences. In the region of the thalamus and hypothalamus surrounding the mass, there was moderate to high signal intensity representing inflammation and oedema on T2-weighted and FLAIR sequences (Figure 19.3a). On a T2*-weighted

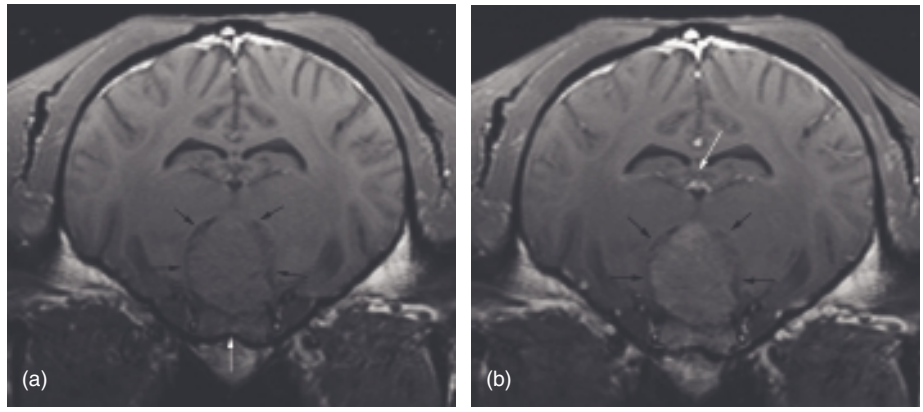

Figure 19.2 (a) T1-weighted spin-echo transverse plane image of a pituitary adenoma at the level of the sella turcica (black arrows). The adenoma is isointense to grey matter. It is within and dorsal to the sella turcica with normal pituitary tissue (white arrow) ventral to the mass. The rim of low signal around the adenoma represents intracellular haemosiderin from chronic haemorrhage. (b) Post gadolinium administration T1-weighted spin-echo transverse plane image at the same location as (a). Note the mild amount of contrast enhancement heterogeneously in the adenoma (black arrows) as well enhancement in the normal pituitary tissue. This sequence was obtained 5 minutes after intravenous administration of contrast material. Normal contrast enhancement is seen within the choroid plexus in the lateral and third ventricles (white arrow).

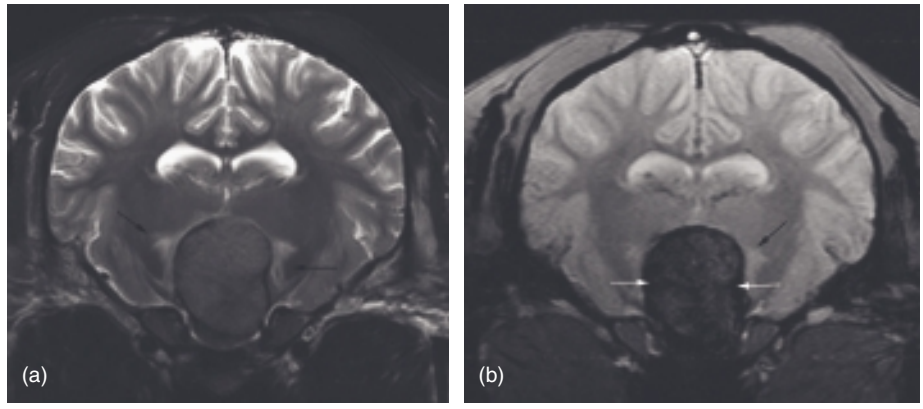

Figure 19.3 (a) T2-weighted turbo spin-echo transverse image 7 mm rostral to Figures 19.2a and b. The mass is characterized by heterogeneous T2 signal intensity. Hyperintensity is seen within the thalamus and hypothalamus (black arrows) representing oedema of the brain parenchyma secondary to mass effect and compression by the adenoma. The rim of low signal intensity surrounding the mass represents intracellular haemosiderin from chronic haemorrhage. (b) Gradient-echo transverse image at the same level. Areas of hypointensity around and within the adenoma (white arrows) characterize areas of magnetic field inhomogeneity due to breakdown products of haemorrhage. Hyperintensity surrounding the mass is also apparent on this sequence (black arrow).

gradient-echo sequence there were areas of moderate magnetic susceptibility artefact within the mass consistent with focal haemorrhage (Figure 19.3b).

This horse was treated with pergolide and cyproheptadine in an attempt to ameliorate the signs of pituitary pars intermedias dysfunction and improvement was seen for a brief period of time. The horse's condition then deteriorated over the following 6 weeks with progressive anorexia, weight

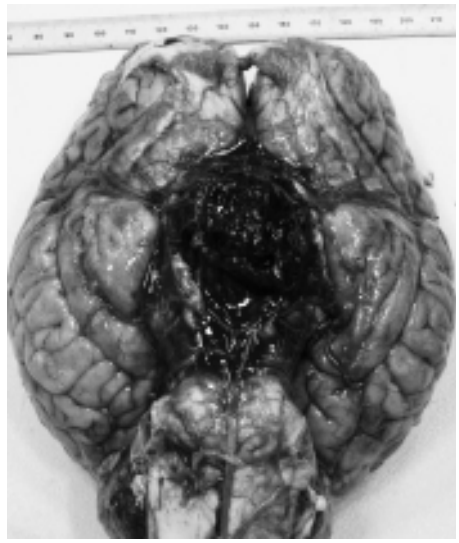

Figure 19.4 Ventral view of brain at postmortem examination after removal from the calvarium. The large pituitary mass noted on MR images in Figures 19.1–19.3 is apparent and appears grossly haemorrhagic.

loss and depression despite aggressive supportive care. The failure to respond to treatment was likely due to the secondary involvement of the brainstem. The mare was euthanized and necropsy confirmed a large pituitary mass with histologic features consistent with a pituitary macroadenoma of the pars intermedia (Figure 19.4). There was some normal pars intermedia tissue, which was compressed by the mass.

Case 2

An 11-year-old, three-quarter Thoroughbred gelding was presented for sudden onset blindness, with circling or standing in a corner of the stable and markedly reduced menace and pupillary light reflexes. Ophthalmoscopic examination of the eyes revealed no abnormality and central blindness was diagnosed. On MR examination, there was marked enlargement of the pituitary gland. The pituitary gland measured 20 mm in a dorsoventral direction, 19 mm transversely and 26 mm in a rostral to caudal direction. The enlarged pituitary was noted to be impinging on the optic chiasm, rostral to the pituitary gland. There was uniform low signal intensity throughout the pituitary gland on images in all three planes, indicating a homogeneous, solid mass without oedema, inflammation or old haemorrhage (Figure 19.5a). The optic chiasm, positioned dorsal and rostral to the pituitary gland, had increased signal intensity on T2-weighted images and loss of normal shape (Figure 19.5b). The pituitary mass and impingement on adjacent structures was best demonstrated by the sagittal images.

The owner elected for euthanasia following the MR findings, and the horse underwent necropsy examination. Gross dissection of the head revealed symmetrical enlargement of the pituitary tumour to 30 mm in its longest direction, with elevation and compression of the overlying hypothalamus and moulding of the optic chiasm. Histological examination determined the

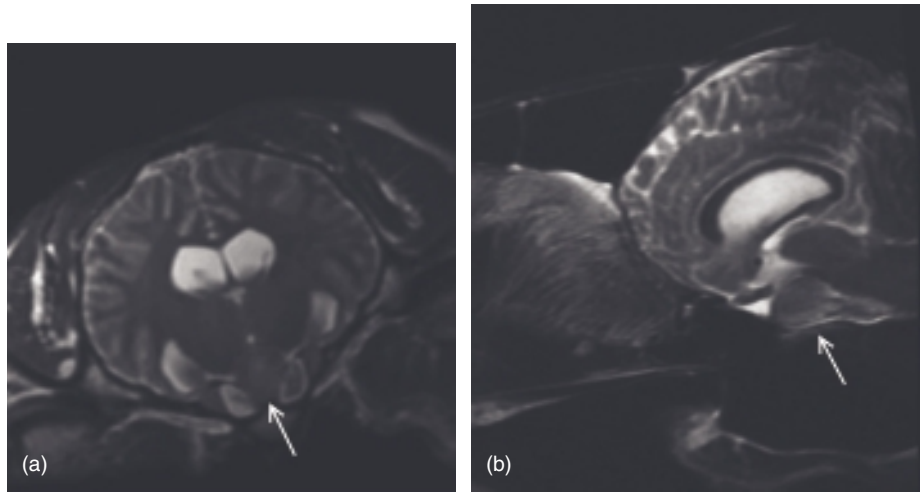

Figure 19.5 (a) Transverse T2 fast spin-echo image through the pituitary of a horse presenting with sudden onset blindness. There is marked enlargement of the pituitary gland (arrow) with compression of surrounding structures, including the optic chiasm but little alteration in signal intensity. Necropsy examination confirmed a chromophobe adenoma of the pars distalis with congestion of the optic chiasm, multifocal mild perivascular haemorrhage, and oedema and spongiosis of the neuropil, consistent with a reaction to compression. (b) Sagittal T2 fast spin-echo image of the same horse as in (a). There is enlargement of the pituitary gland with compression of the optic chiasm, which has altered signal intensity and morphology (arrow).

presence of a chromophobe adenoma of the pars distalis of the pituitary gland. There was congestion in the optic chiasm, with multifocal mild perivascular haemorrhage. In the area of indentation by the tumour there was oedema and spongiosis of the neuropil, consistent with a reaction to compression. Compressive pathology affecting the optic chiasm and hypothalmic region overlying the tumour accounts for the clinical signs of sudden onset central blindness seen in this horse. A chromophobe adenoma is relatively infrequent in horses compared with an adenoma of the pars intermedia. These tumours are endocrinologically inactive and have clinical signs directly referable to compression of overlying structures of the brain [19].

INFLAMMATORY DISEASE

Various types of inflammatory lesions may occur in the CNS tissues. The oedema and inflammation tend to create increased signal intensity on T2-weighted and FLAIR images and decreased signal intensity on T1-weighted images. Mass effect from inflammatory disease is inconsistent. Contrast enhancement is also variable. Lesions are often multifocal and may be seen in tissues other than the CNS, so surrounding musculature and tissues should be assessed carefully for similar lesions or additional abnormalities. Evaluation of CSF can provide useful evidence of ongoing inflammatory changes. Where there is a brain abscess, findings are likely to include a mass effect and a surrounding oedema with peripheral enhancement. With meningitis, there is typically avid enhancement of the meninges and adjacent tissues [11].

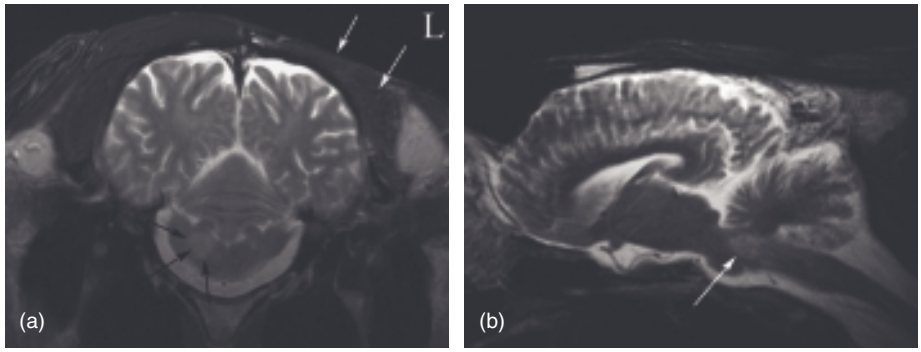

Figure 19.6 (a) T2-weighted turbo spin-echo transverse plane image of the brain at the level of the caudal pons. There is focal hyperintensity in the brainstem in the area of the nuclei of the seventh and eighth cranial nerves (black arrows). There is marked atrophy of the masseter and temporalis muscles (white arrows). **L**, left side.
(b) T2-weighted turbo spin-echo paramedian sagittal image of the brain to the right of the median plane. The T2 hyperintensity seen in (a) is seen ventral to the cerebellum in the caudal pons (white arrow). There is a small amount of fluid in the frontal sinus secondary to dorsal recumbency.

Case 3

An 18-year-old Thoroughbred gelding became ataxic 9 months prior to presentation. Two months prior to presentation, he started to exhibit weight loss, dysphagia and facial muscle wasting. He had been treated for equine protozoal myelitis (EPM) twice prior to presentation. This horse exhibited grade 3/4 ataxia in all limbs. He also had atrophy of the left facial muscles as well as the left temporalis and masseter muscles, muzzle deviation to the right side, and difficulty moving food to the pharynx with normal tongue tone, prehension and ability to swallow. These neurologic signs suggested multifocal disease with involvement of cranial nerves V, VII, IX and X, as well as the cervical spinal cord and brainstem. Equine protozoal myelitis Western blot was weakly positive on the CSF and positive on serum.

On the T2-weighted and FLAIR sequences there was hyperintensity consistent with inflammation and oedema throughout the right side of the medulla and caudal pons in areas including the nuclei of cranial nerves V, VII, VIII and XII (Figure 19.6). These areas were isointense or slightly hypointense to brain parenchyma on T1-weighted images and did not enhance following contrast administration. There was marked atrophy of the left temporalis muscle likely secondary to involvement of the trigeminal nerve. These MRI findings are consistent with those seen in a previously reported case of EPM [20].

Nitazoxanide, vitamin E and flunixin meglumine were administered. Supportive care including intravenous fluid therapy and enteral feeding via nasogastric tube was also performed. The horse became progressively more depressed and developed pleuropneumonia a week after admission, likely secondary to aspiration due to dysphagia. The following day he became acutely more ataxic, was unable to rise and died.

On postmortem examination, neuronal degeneration, inflammation and protozoal organisms consistent with *Sarcocystis neurona* were identified in the nuclei and nerves of cranial nerves V, VII and VIII. The left masseter muscle had evidence of denervation atrophy and the left cranial nerve VII had mild atrophy. Mild inflammation with occasional protozoa was seen in the cranial cervical and thoracic spinal cord.

TRAUMA

In patients with a history of head trauma, disruption of the musculoskeletal structures of the head should be carefully assessed, and the CNS evaluated for evidence of oedema, inflammation and haemorrhage. In these areas there is likely to be increased signal intensity on T2-weighted images and increased contrast enhancement within brain parenchyma. Fractures and osseous injuries can be subtle on MRI exams if not largely displaced. In cases of known or suspected trauma, cortical bone continuity should be closely evaluated for minimally displaced fractures. T1 and proton density (PD) sequences are often most helpful for evaluating osseous trauma. Osteomyelitis will have increased signal of T2 and FLAIR sequences and typically displays marked contrast enhancement. In recent head trauma, haemorrhage can be seen with different signal intensity patterns depending on the haemorrhage age and the changing magnetic properties of degrading haemoglobin. In horses with past head trauma, evidence of haemosiderin as a magnetic susceptibility artefact on T2* gradient-echo images may remain in the tissues for years after the event. In some cases, there may be no known history of trauma, but the horse may present with blindness, nasal or aural haemorrhage or neurologic signs and evidence of trauma are discovered on MR examination (Figure 19.7).

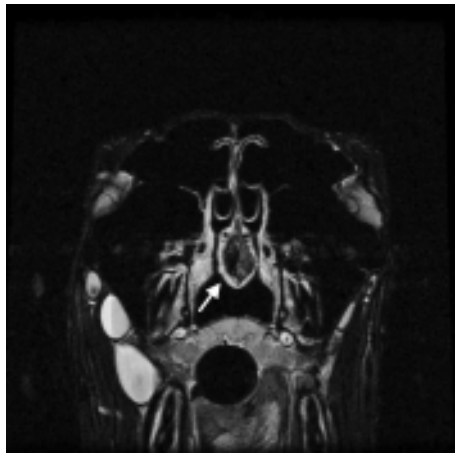

Figure 19.7 Transverse T2 fast spin-echo image of the caudal nasal septum in a horse with a history of sudden onset blindness, epistaxis and possible head trauma. MR examination revealed damage to the caudal nasal septum, fractured vomer, damage to the roof of the sphenopalatine sinus, and damage to the optic chiasm and nerves (arrow).

Case 4

A 4-month-old Thoroughbred colt was normal when turned out in a pasture but was found recumbent with signs of obvious head trauma 2 hours later. The foal was seizing, stuporous and unable to rise. Skull radiographs outlined fractures of the frontal bone and fluid within the frontal sinus.

MRI of the brain performed approximately 3 hours after the presumed traumatic event revealed a comminuted depression fracture of the right frontal bone with fragments in the sinus as well as within the right frontal lobe (Figure 19.8). There was a fracture of the frontal sinus septum. Within the right frontal sinus and subcutaneous tissues in the region of the frontal bone fracture, there was fluid of moderate T1 and T2 signal intensity as well as areas of magnetic susceptibility artefacts on a T2*-weighted gradient-echo sequence indicative of air and haemorrhage in the sinus. The left frontal and both sides of the sphenopalatine sinuses contained air ventrally (due to positioning in dorsal recumbency) and fluid of low T2 and high T1 signal intensity with some areas of magnetic susceptibility artefact on a T2*-weighted gradient echo sequence also suggestive of haemorrhage. The nasal mucosa was thickened secondary to inflammation.

There was an area of haemorrhage in the frontal lobe with T1 signal isointense to the brain parenchyma and low T2 signal with a rim of high T2 signal, consistent with an acute haematoma. The hemorrhage between the occipital lobes represents a contrecoup lesion (Figure 19.9). Smaller areas of haemorrhage were seen on T2*-weighted gradient echo images surrounding the brainstem (Figure 19.10).

Surgical removal of the fracture fragments was attempted following the MRI examination through the frontal sinus. Multiple bony fragments were

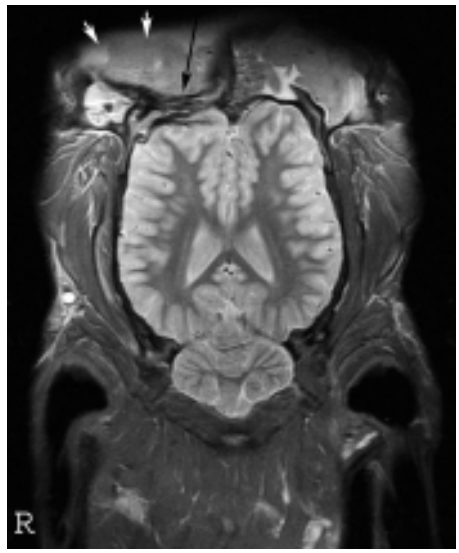

Figure 19.8 STIR turbo spin-echo dorsal image of the brain at the level of the frontal sinus. The left frontal bone is intact while multiple fracture fragments of the right frontal bone are present, some within the frontal lobe (black arrow). Fluid of mixed signal intensity is present in the frontal sinus (white arrows). **R**, right side.

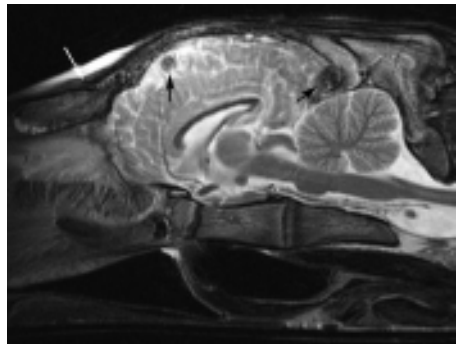

Figure 19.9 T2-weighted turbo spin-echo mid-sagittal image of the brain. Hypointense areas of magnetic susceptibility artefact are present in the frontal and occipital lobes of the brain indicating areas of haemorrhage (black arrows). There is hyperintensity in the subcutaneous tissues as well as fractures of the frontal bone (white arrow). Low T2 signal fluid is seen in the frontal and sphenopalatine sinuses.

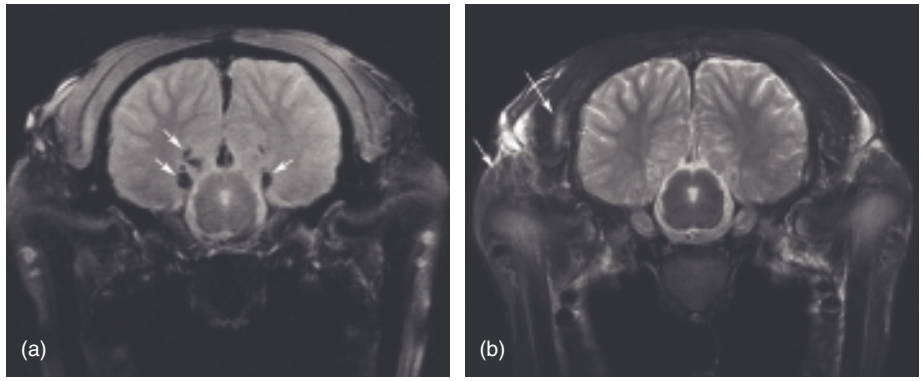

Figure 19.10 (a) Gradient-echo transverse image of the brain at the level of the mesencephalic aqueduct. Multiple small magnetic susceptibility artefacts are present with the internal capsule as well as in the longitudinal fissure representing areas of hemorrhage (white arrows). The areas of haemorrhage are more obvious than in (b). (b) T2-weighted turbo spin-echo transverse image at the same location as (a). There is also evidence of external soft tissue injury from trauma (white arrows).

removed. The foal recovered from anaesthesia but remained recumbent as a result of the severe head trauma and died 2 days after surgery. In this case, MRI affected the treatment plan but was unable to improve outcome.

CONGENITAL CNS ABNORMALITY

Many forms of congenital problems can be diagnosed with MRI. Brain and skull malformations are most obvious if the exam is performed in proper acquisition and orientation to permit critical side-to-side and patient-to-patient comparisons. The soft tissue contrast of MRI allows the relative percentages of grey and white matter and the overall shape and size of the brain tissues to be carefully accessed. Examples of congenital hydrocephalus and hypoplasia are occasionally encountered.

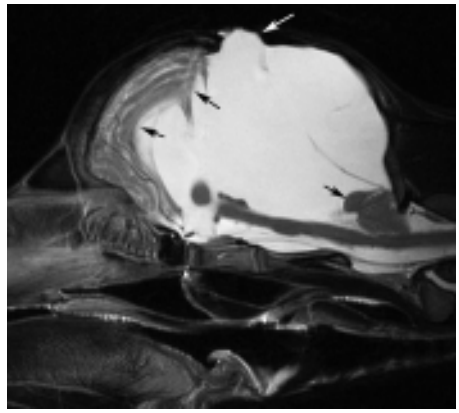

Figure 19.11 T2-weighted turbo spin-echo mid-sagittal image of the brain in a case of severe communicating hydrocephalus. The cerebrum and cerebellum are compressed (black arrows). The fontanelle is open with meningocele formation (white arrow).

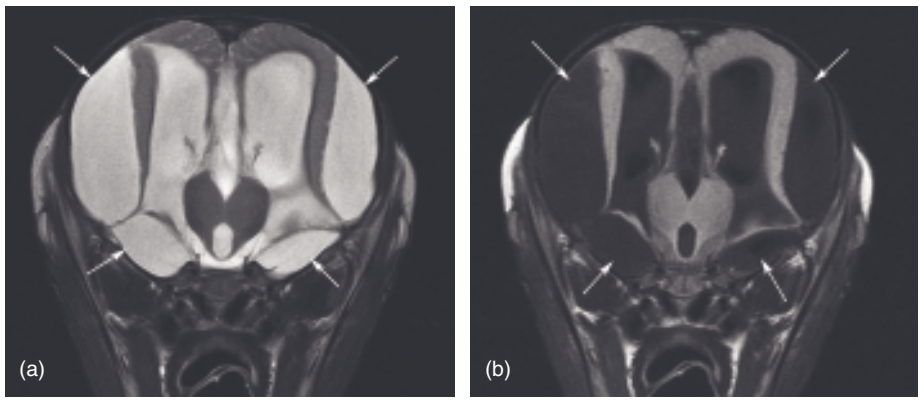

Figure 19.12 T2-weighted turbo spin-echo (a) and FLAIR (b) transverse images of the brain at the level of the thalamus. The lateral and third ventricles are massively dilated with excessive cerebrospinal fluid also present outside of the brain (white arrows).

Case 5

A 1-month-old Quarter Horse filly was noticed by the owners to have a dome-shaped head, blindness and obtundation. A congenital brain lesion was suspected.

MRI images showed severe communicating hydrocephalus with a specific location of obstruction not identified. The lateral ventricles, third ventricle, and fourth ventricle were enlarged and filled with low T1, high T2 signal fluid consistent with CSF (Figure 19.11). The calvarium was enlarged and there was a large amount of fluid surrounding the brain (Figure 19.12). The parenchyma of the cerebral hemispheres was thinned and the cerebellum compressed and herniated into the foramen magnum. There was a meningocele and an open fontanelle at the junction of the left and right frontal and parietal bones.

Treatment was not pursued although the possibility of placement of a ventriculoperitoneal shut was discussed with the owners. The foal at 8 months old continued to have severely impaired vision.

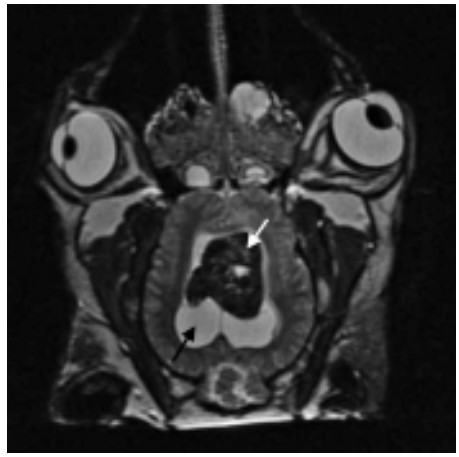

Figure 19.13 Dorsal T2 fast spin-echo image of a horse with a history of intermittent seizures. MR examination demonstrated a large cholesterol granuloma (white arrow) and secondary hydrocephalus (black arrow). The cholesterol granuloma derives from the choroid plexus and has heterogeneous signal intensity throughout.

CNS MASSES

CNS masses are usually well characterized using MRI (Figure 19.13). The precise location (extra-axial or intra-axial) and the number of masses are important features to aid in diagnoses. The MRI features of neoplasia are variable but frequently lead to mass effect and surrounding oedema. The contrast enhancement characteristics are dependent on the tumour type and location. Some tumours, such as meningiomas and choroid plexus tumours, usually have avid, uniform contrast enhancement and typical locations. Intra-axial tumours and abscesses may share common MRI characteristics; however, abscesses tend to be thicker-walled and may demonstrate peripheral 'rim'enhancement. Age and duration of clinical presentation should be considered when evaluating potential brain disorders. If the mass effect is significant, foraminal herniation or optic chiasm compression can occur and should be carefully scrutinized.

OCULAR AND OPTIC NERVE MASSES

Ocular and optic nerve abnormalities may occur secondary to trauma, infection of adjacent structures, degeneration or neoplasia. Neoplasia may result in secondary compression of the optic structures, or may derive from these structures themselves (Figures 19.14, 19.15 and 19.16).

NEURODEGENERATIVE LESIONS

Nigropallidal encephalomalacia from chronic ingestion of Yellow Star thistle have been described with characteristic MR findings in specific nuclei location in horses [9]. Other neurodegenerative lesions may be diffuse in distribution and therefore not as easily detected on MRI exams. More experience is needed to determine if characteristic findings are present in other neurodegenerative diseases in horses.

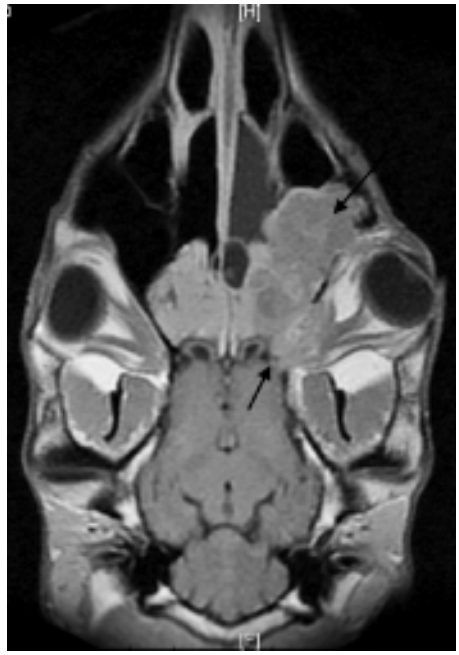

Figure 19.14 Dorsal T1 fast spin-echo image post-contrast administration in a horse with progressive left-sided blindness. There is an infiltrative adenocarcinoma (arrow) originating from the ethmoidal region, extending into the orbit and compressing the optic nerve. Image courtesy of Henrik Nyberg.

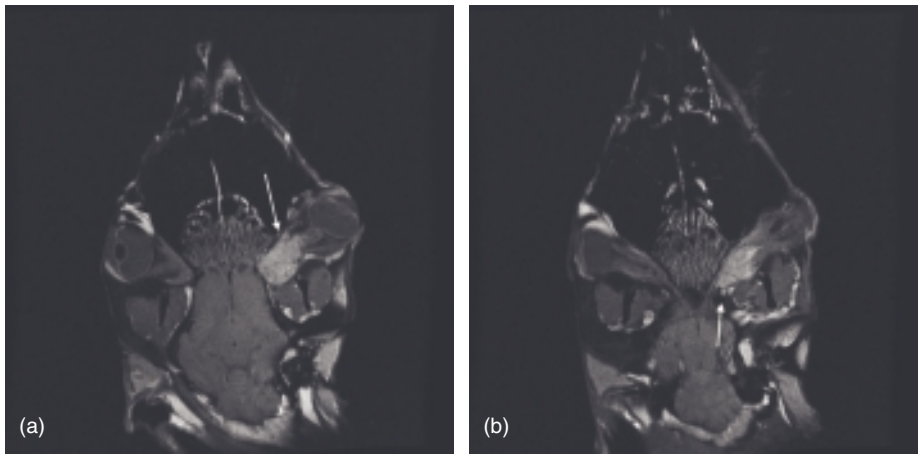

Figure 19.15 Dorsal T1 fast spin-echo images post-contrast administration of a 16-year-old horse presenting with exophthalmos and blindness of the left eye. (a) There is a welldefined orbital soft tissue mass (arrow) which is associated with the optic nerve and shows dense contrast enhancement. (b) The mass tapers towards the caudal margin (arrow). This is characteristic of a meningioma arising from the optic nerve sheath.

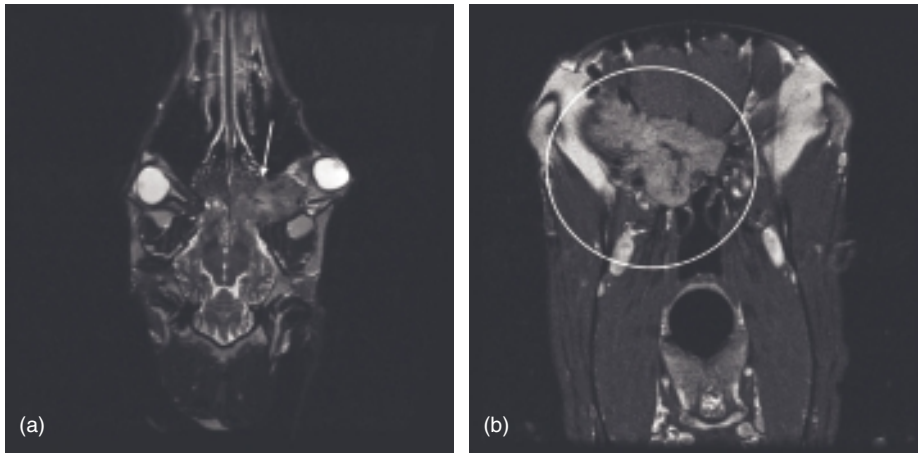

Figure 19.16 Dorsal T2 fast spin-echo image (a) and transverse T1 fast spin-echo image post-contrast administration (b) of a 27-year-old horse with left ocular muscle atrophy and exophthalmos. There is a destructive retrobulbar mass on the left side (arrow) which is invading the cribriform plate and the olfactory lobe of the brain (circle), as well as involving the optic nerve and chiasm. There is considerable enhancement following contrast administration. These findings are consistent with an agressive neoplastic lesion, most likely squamous cell carcinoma or a soft tissue sarcoma.

SINUS AND NASAL SEPTUM

Lesions within the sinuses and nasal septum are frequently encountered and there is excellent contrast of several types of nasal pathology with the air-filled sinuses. Mass effect causing pronounced deviation (Figure 19.17) and erosions of turbinates and nasal septum are noted with expansive nasal cysts, neoplasia and progressive haematomas. Fluid accumulations are common and purulent effusions tend to have intermediate signal on T1- and T2-weighted sequences. Erosion through the cribiform plate and into the olfactory lobes creates abnormal meningial and brain parenchymal signal and abnormal contrast enhancement. Expansive nasal cysts can be erosive or non-erosive and can be difficult to differentiate from some neoplasia (Figure 19.18). Internal contents vary from uniform fluid signal to mixed fluid and tissue signal and warrant biopsy for definitive diagnosis.

SINUS MASSES

Case 6

A 9-year-old Thoroughbred mare had a right-sided ethmoid haematoma 2 years prior to presentation, which was treated successfully at that time with intralesional formalin injection. Prior to current presentation, the owner noticed right-sided epistaxis. Upper airway endoscopy revealed a left-sided ethmoid mass consistent with an ethmoid haematoma and a small swelling

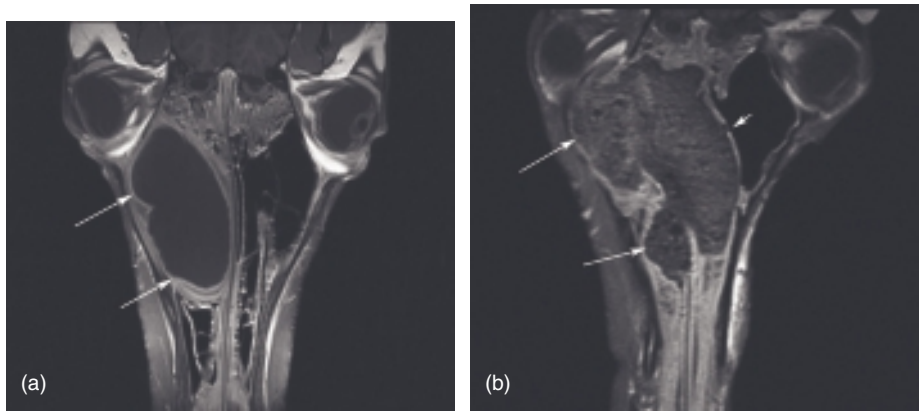

Figure 19.17 (a) T1-weighted spin-echo dorsal image of the sinonasal region at the level of the orbits obtained 5 minutes after intravenous contrast administration. There is an oval hypointensity within the frontal and maxillary sinuses consistent with fluid and the lining of the fluid-filled structure undergoes contrast enhancement (white arrows). The bony margins of the sinus cavity are intact with slight deviation of the nasal septum. Histologic examination confirmed the diagnosis of a sinonasal cyst. (b) T1-weighted spin-echo dorsal image of the sinonasal region at the level of the orbits obtained 5 minutes after intravenous contrast administration. There is a large mass of mixed signal intensity within the frontal and maxillary sinuses (large white arrows) with areas of signal void consistent with air. The mass extends to the left side of the median plane and displaces the nasal septum to the left (small white arrow). The margins of the mass undergo contrast enhancement. Surgical exploration revealed feed material within the sinus and sinusitis secondary to an oronasal fistula.

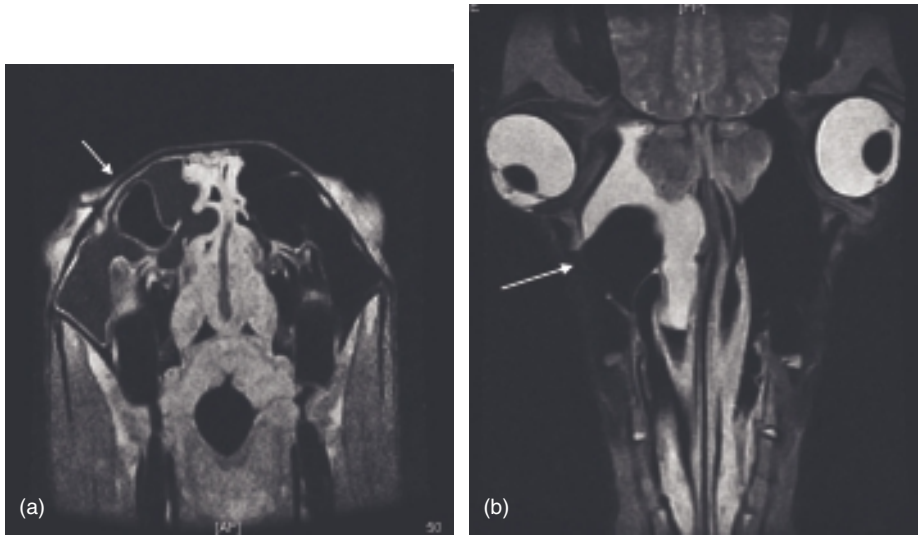

Figure 19.18 Tranverse T1 fast spin-echo image post-contrast administration (a) and dorsal T2 fast spin-echo (b) images from an 8-year-old pony with a history of respiratory infection followed by intermittent right-sided nasal discharge and coughing that did not respond to medical treatment. MR images demonstrate a well-circumscribed sinus cyst and surrounding sinusitis (arrow). The mucosal lining of the sinus and of the cyst both enhance with contrast administration. Following surgical resection there was complete clinical recovery. Images courtesy of Henrik Nyberg.

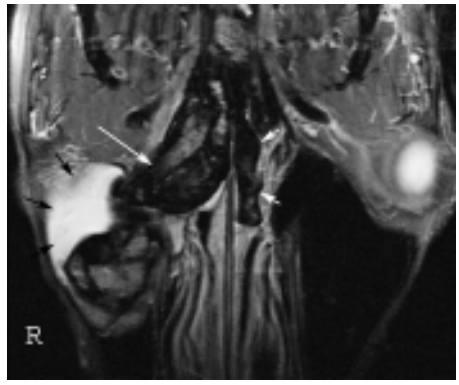

Figure 19.19 STIR turbo spin-echo dorsal image of the ethmoid and maxillary sinus region ventral to the eyes. A large mass of heterogeneous low signal intensity is in the right ethmoid region and maxillary sinus (large white arrows). The mass is surrounded by hyperintense fluid (black arrows). A smaller mass of similar signal intensity is present in the left ethmoid region (small white arrows). **R**, right side.

covered with normal mucosa in the right ethmoid region. Radiography of the sinus area showed a soft tissue opacity in the right maxillary sinus.

MRI revealed there was a mass present in the right sphenopalatine and maxillary sinuses involving the ethmoid labyrinth (Figure 19.19). The mass had heterogeneous signal intensity on T1- and T2-weighted images (Figure 19.20a). On a T2*-weighted gradient-echo sequence, the mass was nearly completely characterized by a magnetic susceptibility artefact, suggesting that the mass contained large amounts of iron from haemorrhage (Figure 19.20b). The mixed T1 and T2 signal characteristics indicated that the haemorrhage was chronic and ongoing. The mass surrounded but did not invade

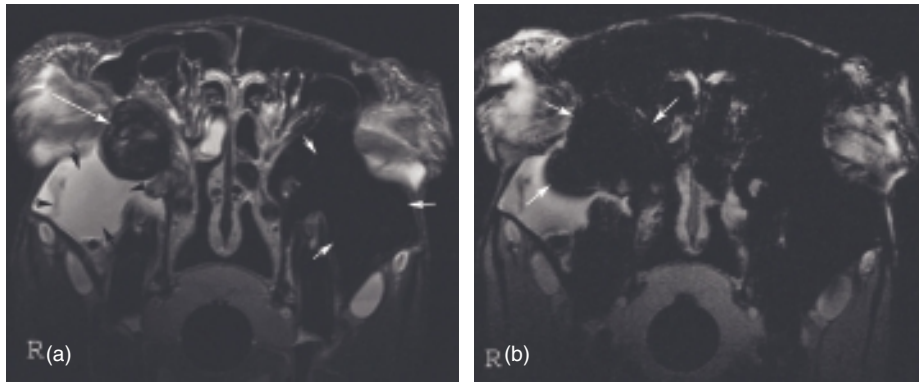

Figure 19.20 (a) T2-weighted turbo spin-echo transverse image caudal to the orbit. The left caudal maxillary sinus is filled with air (small white arrows). The right caudal maxillary sinus contains a mass of heterogeneous low signal intensity (large white arrow) surrounded by fluid of high signal intensity (black arrows). **R**, right side. (b) Gradient-echo transverse image at the same level as (a). The large magnetic susceptibility artefact in the region of the sinus mass indicates that the mass contains byproducts of haemorrhage (white arrows). **R**, right side.

the right molar teeth. The nasal septum was very slightly displaced to the left side at the level of the orbit. The mass was surrounded by a high T2 and low T1 signal intensity substance that filled the maxillary sinus, consistent with fluid. Rostrally, this fluid contained an area of moderate to low T2 signal, indicating an area of increased protein content. The mass did not enhance following contrast administration. There was a smaller mass in the area of the left ethmoid labyrinth with similar signal characteristics as the mass on the right side.

The right-sided mass involving the frontal, maxillary and sphenopalatine sinus was surgically resected via a frontal nasal bone flap and the left-sided mass was injected intralesionally with formalin. Histology of the mass confirmed the diagnosis of ethmoid haematoma. Follow-up upper airway endoscopy showed resolution of the left-sided ethmoid haematoma and the mare remained asymptomatic.

SPHENOPALATINE SINUSITIS

Although the majority of sinus pathology is recognized in the larger frontal and maxillary sinuses, pathology in the spheno-palatine sinuses and subsequent distension and destruction can lead to visual disturbances and progressively defective vision, blindness and optic atrophy [21]. In humans, MRI or computed tomography (CT) are regarded as important in the diagnosis of the condition. Clinical and ophthalmic examination may reveal sudden onset partial or complete blindness, intermittent visual disturbance and/or optic atrophy. This condition has been reported in both foals and adult horses. MR features include increased signal intensity fluid within the sinus on both T1- and T2-weighted images, consistent with proteinaceous fluid. There may be disruption of the midline septum and of the bony roof of the sinus with dorsal expansion of the sinus into the overlying tissues, and/or evidence of communication between the sinus and dorsal tissues. This may be associated

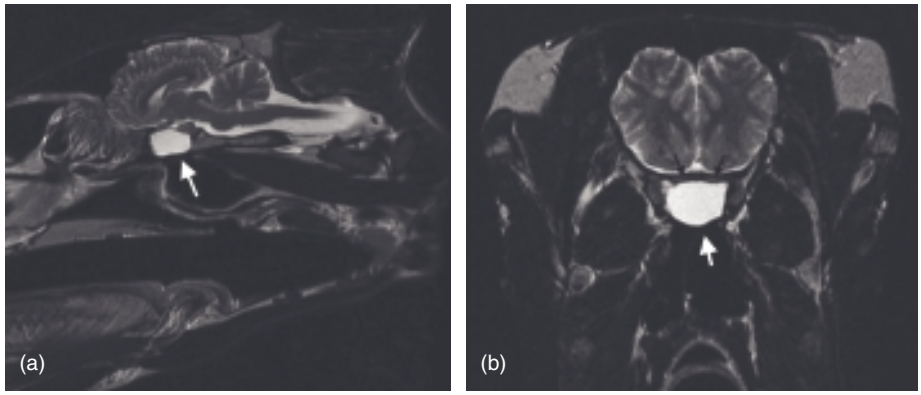

Figure 19.21 Sphenopalatine sinusitis in a horse with a history of intermittent blindness: Sagittal (a) and transverse (b) T2 fast spin-echo images of the sphenopalatine sinus (white arrow), which contains material of high signal intensity material on T2 and intermediate signal intensity on T1. There is poor definition of the dorsal wall and dorsoventral compression of the optic nerves (small black arrows). Following unsuccessful attempts to manage the sphenopalatine sinusitis medically or via drainage of the sinus, necropsy examination revealed purulent fluid within the sinus with erosion of the dorsal wall and active Wallerian degeneration of the optic nerves and chiasm.

with compression of the adjacent optic nerve with altered signal intensity consistent with degeneration or oedema. There may also be visible compression of the pituitary gland (Figure 19.21).

MR FEATURES OF LARYNGEAL ABNORMALITIES

Laryngeal abnormalities may be detected with MRI; however, the presence of the endotracheal tube distorts the laryngeal structures and dynamic MR examination to observe laryngeal motility and co-ordination is not practical in most clinical conditions. Endoscopy and ultrasonography may be better options if functional rather than structural abnormalities are suspected. However, lesions surrounding or invading into the laryngeal region can be well defined with MRI, offering a tentative diagnosis and providing surgical guidance.

Case 7

A yearling Thoroughbred colt presented with abnormal findings on upper airway endoscopy performed as part of a pre-purchase examination. Laryngeal palpation revealed an abnormal space on the right side of the larynx between the cricoid and thyroid cartilages and upper airway endoscopy showed rostral displacement of the palatopharyngeal arch. Ultrasonographic examination of the right side of the larynx detected an absence of the cricothyroid articulation and the dorsal aspect of the thyroid cartilage extended dorsal to the muscular process of the arytenoid. High-speed treadmill endoscopic examination showed bilateral axial deviation of the aryepiglottic folds and rostral displacement of the palatopharyngeal arch. Laryngeal dysplasia secondary to fourth branchial arch abnormality was suspected.

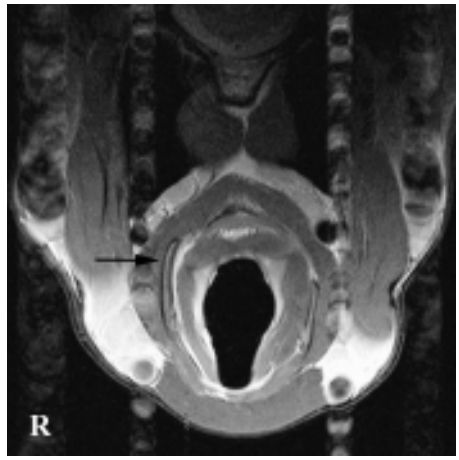

Figure 19.22 Proton density-weighted turbo spin-echo transverse image of the larynx at the level of the arytenoid cartilages. The right thyroid lamina extends dorsal to the arytenoid cartilage (black arrow) while the dorsal extent of the normal left thyroid lamina is ventral to the muscular process of the arytenoid cartilage. **R**, right side.

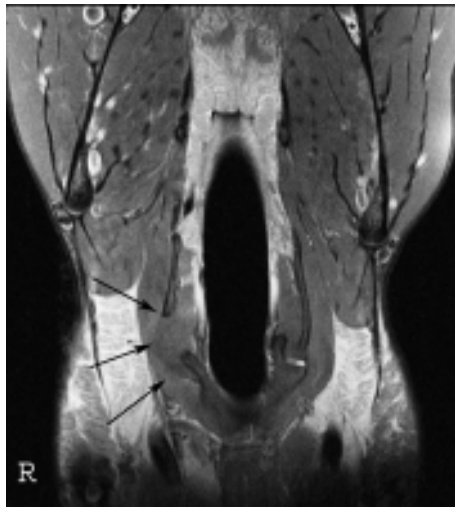

Figure 19.23 STIR turbo spin-echo dorsal image of the larynx at the level of the cricothyroid articulation. The left side of the larynx is normal; the right side is abnormal. The right cricothyroid articulation is absent with the loss of the caudal cornu of the thyroid cartilage and articular process of the cricoid cartilage. The right cricoarytenoideus lateralis muscle is interposed between the thyroid and cricoid cartilages on the right (black arrows). The normal left cricoartytenoideus lateralis muscle is located deep to the thyroid cartilage. **R**, right side.

The MR images displayed multiple anatomic abnormalities of the right side of the larynx. The lamina of the thyroid cartilage extended dorsal to the muscular process of the arytenoid and the caudal cornu was absent (Figure 19.22). There was no cricothyroid articulation and no articular process on the cricoid cartilage (Figure 19.23). The cricoarytenoideus lateralis muscle was located caudal to instead of deep to the thyroid lamina. The right cricopharyngeus muscle was smaller than the left cricopharyngeus muscle. These findings were consistent with postmortem examination of previous cases of fourth branchial arch abnormality [22].

Laser cauterization of the palatopharyngeal arch and bilateral laser ventriculocordectomy were performed to attempt to decrease the impedance to airflow through the larynx. The owner was advised that the laser treatment would not resolve the underlying anatomic abnormalities. A previous report concluded that rostral displacement of the palatopharyngeal arch treated with laser cauterization carried a poor prognosis [23]. The lack of success in these cases is likely due to the spectrum of underlying structural deformities of the larynx impairing function which remain untreated.

Throat and cranial cervical masses may be detected on MRI if lesions are cranial enough to be positioned within the gantry for imaging. The superior soft tissue contrast with MRI is useful in differentiating normal from abnormal thyroid tissue and evaluating retro-pharyngeal lymphadenopathy. Abscesses or neoplasia are usually well delineated from surrounding normal tissues and have similar MR features and characteristics as when located in other body areas.

Case 8

A 2-year-old Quarter Horse filly was referred for evaluation of a large fluctuant swelling in the throat latch region 1 month prior to presentation. The referring veterinarian lanced the mass and a large quantity of fluid drained from it. Following the surgical drainage, an abnormal upper respiratory noise was heard when the horse was re-introduced to work. Upper airway endoscopy revealed grade IV/IV right-sided arytenoid hemiplegia. Ultrasound examination showed a mass containing multiple small anechoic cyst-like structures dorsal to the trachea and larynx.

MR images delineated a right-sided mass located dorsolateral to the cranial trachea (Figure 19.24). The mass displaced the right lobe of the thyroid gland ventrally and was in contact with the caudal right aspect of the cricoid cartilage. The mass was bounded on the right by the linguofacial

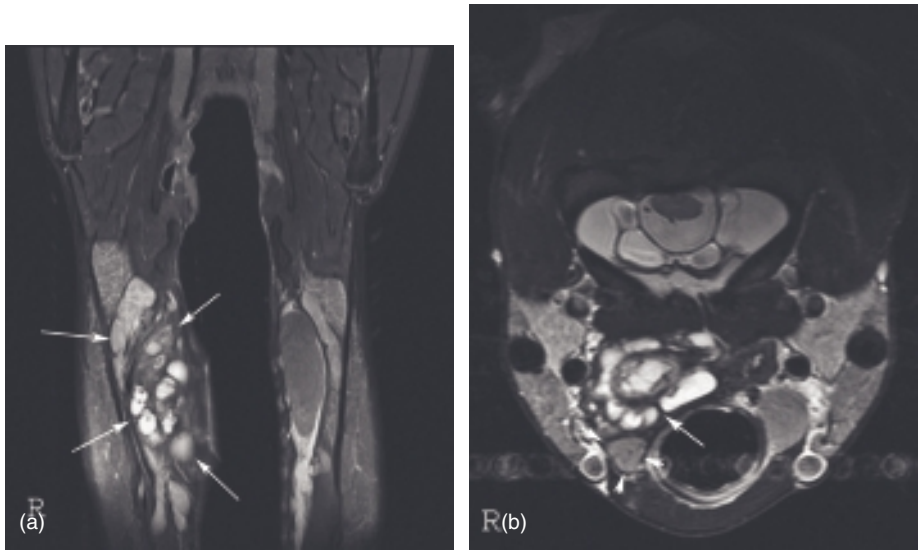

Figure 19.24 (a) STIR turbo spin-echo dorsal image of the throat region at the level of the trachea. There is a multilobulated cystic mass adjacent to the trachea (white arrows). **R**, right side. (b) T2-weighted turbo spin-echo transverse image of the mass noted in (a) at the level of the second tracheal ring. The multilobulated cystic mass is located between the trachea, oesophagus and parotid salivary gland (large white arrow). The right lobe of the thyroid is displaced ventrally by the mass (small white arrows). **R**, right side. Histopathology resolved the mass to be an epithelial cyst.

vein, external carotid artery and parotid salivary gland, on the left by the oesophagus, dorsally and caudally by the longus capitis muscle, ventrally by the trachea and right lobe of the thyroid gland, and cranially by the larynx. The mass consisted of multiple cyst-like structures separated by septae of low T2 and T1 signal. The contents of the cyst-like structures varied from homogeneous high T2 signal to heterogeneous low to high T2 signal and had uniformly low T1 signal. These findings indicated a multilobulated cystic mass. Although the right recurrent laryngeal nerve was not identified on the images, the anatomic location of the mass and clinical signs strongly suggested that the mass may have been compromising the nerve function.

The mass was surgically resected. At surgery, the mass was located on the dorsal to right dorsal aspect of the trachea immediately caudal to the cricoid cartilage in the area of the right recurrent laryngeal nerve. It was not attached to the thyroid gland. The mass was palpably firm, well encapsulated, with no significant vascular supply. Fluid within the mass was noted to be serosanguinous in nature.

Histologic examination of the mass confirmed a diagnosis of an epithelial cyst composed of multiple cystic structures. The right arytenoid paralysis did not resolve after the mass was removed so a neuromuscular pedicle graft was performed 2 months later. Nine months after the neuromuscular pedicle graft, the owner reported that the horse was being used successfully for her intended use.

GUTTURAL POUCH AND EAR INFECTIONS

MRI provides useful information in cases of known or suspected guttural pouch and ear pathologies. The capability to evaluate the entire ear anatomy including the external auditory canals, tympanic bullae and membranes, and the inner ear structures is extremely valuable. Infections of the ear are typically characterized by abnormal fluid accumulations and inflammatory reactions (Figure 19.25). Inner ear infections will alter the normal fluid signal

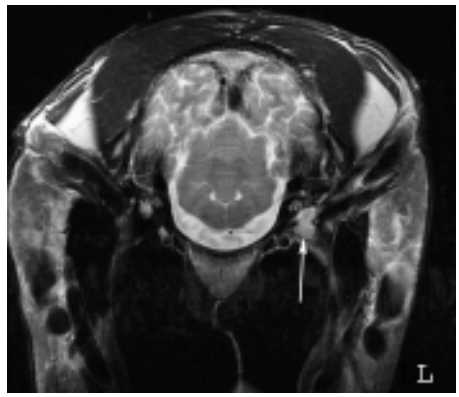

Figure 19.25 T2-weighted turbo spin-echo transverse image of the skull at the level of the tympanic bulla. There is moderate signal intensity within the tympanic bulla consistent with otitis media (white arrow). This horse presented with a head tilt and left-sided facial nerve paralysis. The clinical signs improved after fenestration of the tympanic membrane to allow drainage and long-term antimicrobial therapy. **L**, left side.

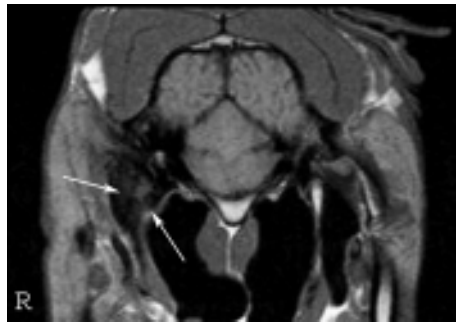

Figure 19.26 Proton density turbo spin-echo transverse images of the skull at the level of the guttural pouches in an adult horse that presented with clinical signs of right-sided vestibular disease. Endoscopy had revealed a thickened right stylohyoid bone and thickening of the guttural lining. MR images illustrated the extensive unilateral temporohyoid osteoarthropathy and guttural pouch involvement (white arrows). The left stylohyoid bone and surrounding guttural pouches are normal for comparison. **R**, right side.

within the semi-circular canals and may demonstrate abnormal signal in the surrounding brain parenchyma and meningial contrast enhancement.

For cases of guttural pouch mycosis and stylohyoid osteoarthropathy, the abnormal thickening and signal of the stylohyoid bone and mucosal proliferation can be visualized. Symmetric slice positioning is crucial to allow for side-to-side comparison (Figure 19.26). Abnormal fluid accumulation and contrast enhancement is typical of active infection and inflammation; however, long-standing infections may show minimal post-contrast enhancement.

SUMMARY

MRI can provide useful information on a variety of conditions present in the equine head, although like other imaging technologies, MRI does not provide all the answers. Computed tomography may be a more practical option for evaluation of osseous or dental structures alone because it outlines the mineralized tissues more clearly, but it does not provide as much information on the associated soft tissues. Prior to performing MRI for head exams, more conventional diagnostics such as radiology, ultrasonography and endoscopy should be considered. Inconclusive results or the absence of abnormal findings using these less-costly imaging technologies support the recommendation for further imaging with MRI. As with other species, electrical disturbances in the brain without structural abnormality will not be detected with MRI. Many horses with a history of seizures have no or equivocal findings on MR imaging of the brain. However, MR imaging is useful to rule out structural lesions and provide further information for decision making about case management.

General MRI characteristics of most lesions in the head of horses parallel findings in human and small animal patients; however, the size and unique anatomic features make equine brain and skull imaging more challenging.

With more clinical experience in horses, the distinct advantages and limitations of equine head MRI will become better resolved and the appropriate applications for MRI imaging for disorders of the head can be confidently offered.

REFERENCES

[1] Reed SM (ed). Neurologic diseases. *Vet Clin N Am: Equine Pract* 1987; **3**: 255–440.
[2] Mayhew IG. *Large Animal Neurology: handbook for veterinary clinicians*. Philadelphia, PA: Lea and Febiger, 1989.
[3] Loftstedt J, Collatos C. Selected neurologic and muscular diseases. Reed SM (ed.) Neurologic diseases. *Vet Clin N Am: Equine Pract* 1997; **13**: 1–106.
[4] MacKay RJ. Neurologic disorders in neonatal foals. *Vet Clin N Am: Equine Pract* 2005; **21**: 387–406.
[5] Diver TJ. Structural and functional diseases of the equine brain. *Clin Tech Equine Pract* 2006; **5**: 67–73.
[6] Diver TJ, Ducharme NG, de Lahunta A, Irby NL, Scrivani PV. Temporohyoid Osteopathy. *Clin Techn Equine Pract* 2006; **5**: 17–23.
[7] Tucker RL, Ferrell EA. Computed tomography and magnetic resonance imaging of the equine head. *Vet Clin N Am: Equine Pract* 2001; **17**: 131–43.
[8] Ferrell EA, Gavin PR, Tucker RL, Sellon DC, Hines MT. Magnetic resonance for evaluation of neurologic disease in 12 horses. *Vet Radiol Ultrasound* 2002; **43**: 510–16.
[9] Sanders SG, Tucker RL, Bagley RS, Gavin PR. Magnetic resonance imaging features of equine nigropallidal encephalomalacia. *Vet Radiol Ultrasound* 2001; **42**: 291–6.
[10] Spoormakers TJP, Ensink JM, Goehring LS *et al*. Brain abscesses as a metastatic manifestation of strangles: symptomatology and the use of magnetic resonance imaging as a diagnostic aid. *Equine Vet J* 2003; **35**: 118–20.
[11] Audigie F, Tapprest J, George C *et al*. Magnetic resonance imaging of a brain abscess in a 10 month old filly. *Vet Radiol Ultrasound* 2004; **45**: 210–15.
[12] Vazquez JM, Rivero M, Gil F *et al*. Magnetic resonance imaging of two normal equine brains and their associated structures. *Vet Rec* 2001; **148**: 229–32.
[13] Chaffin MK, Walker MA, McArthur NH, Perris EE, Matthews NS. Magnetic resonance imaging of the brain of normal neonatal foals. *Vet Radiol Ultrasound* 1997; **38**: 102–11.
[14] Arencibia A, Vazquez JM, Jaber R *et al*. Magnetic resonance imaging and cross sectional anatomy of the normal equine sinuses and nasal passages. *Vet Radiol Ultrasound* 2000; **41**: 313–19.
[15] Arencibia A, Vazquez JM, Ramirez JA *et al*. Magnetic resonance imaging of the normal equine brain. *Vet Radiol Ultrasound* 2001; **42**: 405–8.
[16] Tucker RL, Sampson SN. Magnetic resonance imaging protocols for the horse. *Clin Tech Equine Pract* 2007; **6**: 2–15.
[17] Wallace M, Crisman M, Pickett J, Carrig C, Sponenburg D. Central blindness associated with a pituitary adenoma in a horse. *Equine Pract* 1996; **18**(8): 8–13.
[18] Venzke WG. Equine endocrinology. In: Getty R (ed.) *Sisson and Grossman's The Anatomy of the Domestic Animals*. Philadelphia, PA: WB Saunders, 1975.
[19] Capen CC. Tumors of endocrine glands. In: Moulton JE (ed.) *Tumors in Domestic Animals*, 3rd edn. Berkeley, CA: University of California Press, 1990, pp. 553–629.
[20] Javsicas LH, Watson E, MacKay RJ. What is your neurologic diagnosis? Equine protozoal myeloencephalitis. *J Am Vet Med Assoc* 2004; **232**: 201–4.
[21] Barnett KC, Blunden AS, Dyson SJ, Whitwell KE, Carson D, Murray R. Blindness, optic atrophy and sinusitis in the horse. *Vet Ophthalmol* 2008; **11**(Suppl. 1): 20–6.
[22] Lane JG. Fourth branchial arch defects in Thoroughbred horses: a review of 60 cases. Paper presented at the Second World Equine Airways Symposium, 2001.
[23] Blikslager AT, Tate LP, Tudor R. Transendoscopic laser treatment of rostral displacement of the palatopharyngeal arch in four horses. *J Clin Laser Med Surg* 1999; **17**: 49–52.

Section D
Clinical management and outcome

Chapter 20
The foot and pastern

Andrew Bathe

INTRODUCTION

There is no doubt that magnetic resonance imaging (MRI) has revolutionized our understanding of disease processes in the feet. Older papers on the treatment of problems in the navicular and coffin joint region lacked the ability to have accurate characterization of the pathology that was present and thus do not tend to provide accurate information on how to treat lesions in these areas.

However, we are still in the relatively early days of MRI and on a learning curve, with differences in diagnostic criteria between different clinicians. Multiple potential lesions can be identified and the difficulty is often in determining which are clinically significant. There is now increasing scientific rigour in the interpretation and understanding of the normal range of appearance and of the different types of pathology that can be seen. An understanding of the different artefacts that can be created is developing and this is helping to decrease the incidence of false-positive diagnoses. MRI started off being used on more severe, chronic cases, a significant portion of which stood no chance of returning to athletic use and many of which were subject to euthanasia. The increase in use of MRI and the increasing access to it, especially with the advent of standing low-field units, has meant that it is being used earlier in the course of lameness and on mild cases. This is leading to higher success rates in the treatment of many of the conditions that have been identified and more positive feedback from clients.

When trying to determine the optimum form of treatment of the newly recognized conditions in the relatively inaccessible region of the foot, we need to remember that there remains uncertainty as to the best form of treatment of well-defined soft tissue injuries in other more accessible regions such as the metacarpus. The basic principles of treatment of injuries of the foot are the same for the majority of conditions, consisting of initial rest, controlled exercise and corrective farriery to optimize the biomechanical forces within the foot. Overall there is a lack of evidence-based medicine, but MRI has now been employed long enough for there to be case series being published with sufficient numbers and long-term follow-up to provide some useful information when selecting treatment options. We are still in the early days, however, and all those involved in the diagnosis and treatment of horses using MRI should be encouraged to collate their results to improve the evidence base available to us.

Equine MRI, edited by Rachel C. Murray.

DEEP DIGITAL FLEXOR TENDON INJURIES

Injuries to the deep digital flexor tendon (DDFT) have only been accurately documented with the use of MRI [1], as ultrasonography does not allow visualization of the entire tendon. Injuries can occur alone, in association with navicular bone pathology or as part of multiple injuries. Combined injuries are discussed in the section on navicular disease. As with any tendon injury the basic treatment requirement is for rest and controlled exercise. Prompt diagnosis is important in preventing ongoing exercise and preventing further tendon damage, and thus MRI should optimally be employed at an early stage in a horse presenting with clinical signs consistent with a DDFT injury.

Dyson *et al*. [2] described the outcome for conservatively managed DDFT injuries, as part of a larger group of horses with foot pain. Horses received box rest and controlled walking exercise for up to 1 hour per day, for a minimum of 6 months. Corrective trimming and shoeing was performed on an individual basis. Thirteen out of 47 (28%) horses with primary DDFT injuries and long-term follow-up returned to full function; 19% were sound but had not resumed full work; while 53% had persistent or recurrent lameness. Prognosis was worst for horses with combined navicular bone and DDFT injuries. Five horses with primary DDFT injuries had follow-up MRI with four reportedly showing a decrease in lesion size, but this was only evident in T1-weighted images. Some horses received medication of the digital flexor tendon sheath or navicular bursa with hyaluronan, with or without corticosteroids, and a few received shockwave treatment, but no specific follow-up information was presented because of the small number involved.

Schramme [3], as part of a review of treatment of DDFT injuries, described the use of a foot-pastern cast with a heel wedge or wedged-heel shoes, aiming to decrease the strain in the healing DDFT. He reported that some horses actually showed deterioration in the degree of lameness, and the majority of clinicians do not seem to consider that there is any appreciable benefit in wedging the heel.

Boswell (Boswell J, personal communication, 2009) reported on a case series of 67 cases of DDFT injuries diagnosed over a 5-year period in a private practice, using a standing low-field magnet. Horses with other conditions such as navicular bone changes were excluded. Long-term follow-up was available on 55 cases, but only 14 of these (25%) returned to full work following rest and controlled exercise for 3–48 months. There was no difference between parasagittal splits and core lesions in their return to full work, although the former were slightly more likely to achieve soundness. There was no difference in outcome for lesions proximal or distal to the navicular bone. These results support the poor prognosis with conservative management reported by Dyson *et al*. [2].

In my opinion it is logical to shoe to the conformation of the individual horse, rather than following a formula. The exercise plane should be determined depending on the duration of the problem and the severity of the lameness, as well as the severity of the lesion on MRI. An acute onset, severe

lameness should be managed with strict box rest and then controlled walking exercise, and will have a poorer prognosis and longer convalescent period if unrestricted exercise is allowed. Conversely in cases that present with a more low-grade, recurrent lameness, or in chronic cases, I believe that there is little benefit in prolonged box rest and horses seem to manage better with small paddock turn-out.

Because of the poor prognosis with conservative treatment alone, many forms of injectable biological compounds have been used in treating these injuries [3] – as they have in the palmar metacarpal region. Core lesions are considered more amenable to intralesional injection as the therapeutic compounds are more likely to be contained, but there are difficulties in accurately targeting the lesion. Many lesions are on the margin of the tendon, and some clinicians consider that intrasynovial medication may have benefits [3]. Lesions proximal to the navicular bone can be injected using endoscopic visualization via the digital tendon sheath and/or navicular bursa, which can be combined with ultrasonography. Even if the lesion is not fully appreciable on ultrasonography, it is useful to assist in guiding the region of injection – based on localization from the MRI findings.

Puchalski *et al*. [4] combined ultrasound guidance with computed tomography (CT) confirmation of positioning to inject DDFT lesions positioned between the navicular bone and coronary band. Anderson *et al*. [5] described a technique for the injection of the insertion of the DDFT using radiographic guidance, in a similar fashion to injection of the navicular bursa. A 20 G 8.9 cm spinal needle was inserted in the depression between the heel bulbs, at the level of the coronary band. The needle is advanced dorsad and angled distally at around 10°, until the distal phalanx is contacted. Lateromedial and dorsoproximal-palmarodistal oblique radiographic projections are then obtained to check accurate placement. This was a cadaver study and a weight-bearing position was simulated, but practically this would probably be most easily performed using a Hickman block and partially flexed position. In the study, successful injection of dye into the target region was obtained in all 10 cadaver limbs, but all limbs also showed staining of adjacent structures such as the impar ligament and navicular bursa. This injection technique has the benefit of not requiring general anaesthesia, but it would be difficult to accurately target the majority of lesions found at this level and thus I would consider it a regional injection technique. Ultrasonography through the frog can be used to monitor needle insertion through the frog into the distal portion of the DDFT (Figure 20.1) and we have used this on a small number of clinical cases (Bathe AP, Powell SE, unpublished observations 2009). No complications have been noted with this technique and injection into a lesion can be monitored.

Various products have been studied in the metacarpal region, or used empirically in the metacarpal and foot regions. Insulin-like growth factor-1 [6] has been studied experimentally, but has not found general clinical acceptance and no benefit was noted following injection in a small number of cases of DDFT lesions proximal to the navicular bone (Bladon B, personal communication, 2009). Porcine urinary bladder matrix (UBM) [7] remains popular with some clinicians but there is a lack of scientific validation of its

Figure 20.1 Ultrasonographically guided injection of bone marrow concentrate into an insertional DDFT lesion using a solar approach.

effects in horses and some horses do seem to have transient but marked adverse reactions. A series of 12 horses with DDFT lesions proximal to the navicular bone were injected with 1–3 ml of UBM using ultrasound and CT guidance [4]. One horse had an injection reaction, but 11 out of 12 improved at re-examination. Five out of 12 were re-examined more than 6 months after injection and all had improved to less than grade 1/5 lameness. These results are difficult to compare to other studies that assess return to function. Adipose-derived nucleated cell fractions have been shown to have some mild beneficial effects in a collagenase model of tendonitis [8], but are generally considered to be inferior to bone marrow-derived mesenchymal stem cells [9, 10].

Smith [11] reported on nine cases from North Carolina State University that had autologous mesenchymal stem cells implanted into the injured DDFT or the navicular bursa at the end of surgery, but showed no difference in outcome compared to surgery alone. Platelet-rich plasma [12, 13] has had a resurgence in popularity as commercial kits make production significantly easier. It is most commonly used in ligament injuries, although there is now evidence that it may be beneficial in tendon injuries [14]. Bone marrow concentrate [15] combines growth factors and some mesenchymal stem cells. It has the practical advantage of being able to be produced patient-side. It does not have the purity and cell numbers of cultured stem cells, but there is work to suggest that bone marrow mononuclear cells and cultured bone marrow mesenchymal cells have similar regenerative capabilities [16].

While the principles of intralesional treatments are attractive, there is currently no convincing evidence of clinical benefit. There is some logic to the use of intrabursal hyaluronan in cases with marginal tears within the navicular bursa, but clinically the anti-inflammatory effect of hyaluronan alone seems to be limited, and it is more usually combined with corticosteroids. Corticosteroids are generally considered detrimental to healing in the

early stages of tendon injury. Bell *et al*. [17] reported on navicular bursa medication with corticosteroids in horses with foot pain that underwent MRI examination. Twenty-one horses had DDFT tears, and 67% of these returned to intended use for a median period of 6 months, despite concurrent navicular pathology. In my opinion there can be a role for intrabursal corticosteroid treatment in horses with residual lameness after an appropriate period of rest, especially if the MRI appearance is supportive of a lack of lesion activity and the presence of navicular bursitis.

Endoscopic assessment and treatment of lesions of the DDFT in the navicular bursa was described by Smith *et al*. [18]. Under general anaesthesia the bursae were evaluated using either the technique originally described by Wright *et al*. [19] for treatment of septic navicular bursae or a transthecal approach, using more proximal portals, through the distal reflection of the digital flexor tendon sheath and the palmar surface of the T-ligament [20]. In the original series of 20 cases, all horses blocked to palmar digital analgesia and/or intrathecal analgesia of the navicular bursa. Only four horses were examined with MRI and six with CT. DDFT lesions were seen in all cases and through a contralateral instrument portal torn and fibrillated tissue was removed using a combination of hand and motorized equipment. Postoperatively horses received box rest and controlled walking exercise for a minimum of 2 months. No postoperative complications were noted and nine out of 15 (60%) horses with follow-up of more than 6 months were sound and in full work. The mechanical removal of damaged tendon tissue was considered to allow healing to take place.

Smith [11] reported on a larger case series of 105 cases as a multi-centre study. Ninety-one out of 105 (87%) cases and 96 out of 115 (83%) bursae were found to have abnormalities on endoscopic evaluation, with 92 dorsal border DDFT lesions being identified, 13 of which had concurrent navicular fibrocartilage lesions. Of these, 81 had tearing; 15 granulomas; six parasagittal splits; and five minor fibrillation. Long-term follow-up was available on 65 horses, with 54% being back in full work and 37% having persistent or recurrent lameness. Extensive tearing carried a significantly poorer prognosis than mild tearing, but there was no influence on outcome of combination injuries as determined on MRI, or the presence of adhesions. There was a trend towards poorer prognosis with lameness of more than 3 months duration. This study is to be commended because of its multi-centre nature and large case numbers. The results are certainly significantly better than the published results for conservative management [2], but as only a few cases within the series had pre-operative MRI it is difficult to correlate results with case series based on MRI diagnoses. Other surgeons have noted increased severity of lameness after surgery and have seen considerable fibrosis developing postoperatively on follow-up MRI scans (Boswell, personal communication, 2009).

It is relatively technically demanding to perform the surgery well and there is a learning curve associated with it. The transthecal approach tends to provide improved visualization compared with the standard approach. There is certainly a rationale for performing the procedure. Very mild cases or those with parasagittal splits may not require surgery, but it should be

noted that other lesions may be noted at endoscopy that were not evident on MRI – particularly in low-field systems. Surgery on severe cases with marked lameness, pathology and combination injuries will inherently carry a poor prognosis. Optimal case selection needs to be defined but this surgical procedure offers a potentially beneficial form of treatment for intrabursal DDFT lesions.

Palmar digital neurectomy may have a role in the management of persistent lameness from DDFT lesions that have received an appropriate period of rest and rehabilitation. In my opinion acute severe DDFT injuries are a contraindication to performing a neurectomy because of the significant risk of developing rupture of the DDFT. I am aware of cases that underwent neurectomy and which were able to return to exercise in the short term, but which have subsequently damaged the DDFT further and have needed to be retired. Follow-up MRI after conservative management may be beneficial in case selection, and postoperative scans can be used to monitor the appearance of the DFFT after neurectomy (Werpy N, personal communication, 2006), again trying to prevent cases progressing to tendon rupture.

COLLATERAL DESMOPATHY OF THE DISTAL INTERPHALANGEAL JOINT

This is a common cause of lameness arising from the foot. MRI is essential for an accurate and complete diagnosis, although it is one of the easier conditions to over-diagnose because of the magic angle effect and artefacts from oblique positioning. Early case series [21] were based on ultrasonographic diagnosis. Fortunately there are now some recent case series based on MRI diagnoses. Gutierrez-Nibeyro *et al*. [22] described the treatment and outcome in 20 horses diagnosed with low-field standing MRI. Dakin *et al*. [23] wrote up 289 horses diagnosed with high-field MRI, with follow-up data on 182.

Management involves rest and controlled exercise; however, the prognosis with this is not encouraging. Dyson [2] reported only five out of 17 (29%) cases with follow-up returning to full work for a minimum of 6 months, after a minimum of 6 months of controlled exercise. The period of rest may need to be very prolonged. The later study from the same group [23] showed that 44% of the horses took longer than 18 months to come sound. Controlled exercise consisted of box rest and controlled walking exercise, starting at 15 minutes twice a day and building up to 1 hour daily, predominantly in straight lines. Gutierrez-Nibeyro *et al*. [22] had a less rigorous approach, consisting of either 4–8 weeks of box rest, followed by 4–12 weeks of hand walking, and then paddock turn-out if still lame; or 12 weeks of paddock turn-out for mild to moderate cases. The mean convalescent period for cases with an excellent outcome was 29 weeks, whereas for those with a poor outcome it was 33 weeks. The controlled exercise regime should be tailored to the severity of the desmopathy and the clinical signs, as described in both papers, but also the temperament of the horse needs to be considered. Even if there is residual lameness it may be more prudent to allow controlled turn-out rather than continued attempts at controlled

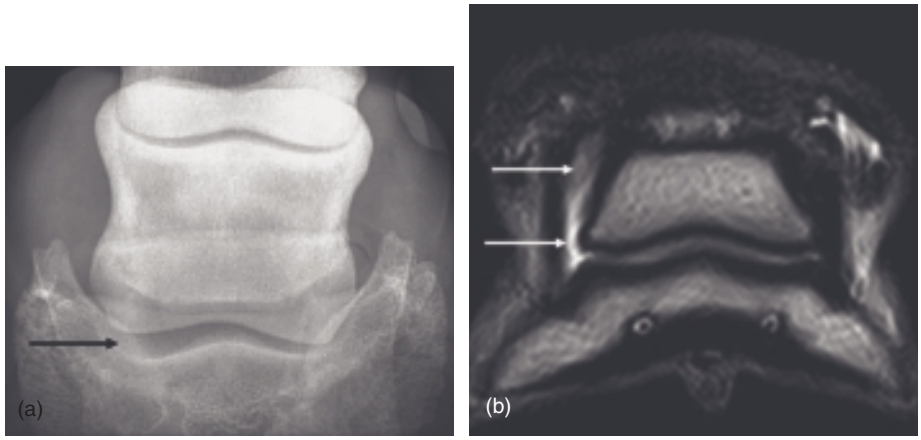

Figure 20.2 Severe medial collateral ligament injury. (a) Stressed dorsoproximal-palmarodistal oblique radiograph showing widening of medial joint space (arrow). (b) Dorsal T2 FSE image showing marked increased signal intensity in the axial portion of the medial collateral ligament (arrows).

walking, especially if the horse is becoming fractious to handle or if it is box-walking excessively.

Corrective farriery is logical, although there is no proof that any method of trimming or shoeing is superior to another. The feet can either be trimmed and shod as deemed appropriate for the individual [23] or shod with half-round shoes, wide webbed shoes or bar shoes [22]. As ever, the most important factor is correct trimming and balancing of the feet, rather than the specific shoe that is applied [24]. Severe collateral ligament injuries with instability of the distal interphalangeal joint (Figure 20.2) may benefit from a foot cast to improve stability and thus comfort, for 4–6 weeks [22, 25].

The poor prognosis with conservative treatment alone has encouraged clinicians to employ other treatments in an attempt to improve the outlook. Dakin *et al*. [23] reported that only 31% of horses with collateral ligament desmopathy, with or without associated osseous abnormality, returned to full work for a minimum of 6 months. The prognosis for cases with other soft tissue and osseous changes in addition to the desmopathy was poorer, with a 15% return to full function. In this series 57 horses received treatment to the ligament with extracorporeal shockwave therapy (ESWT) or radial pressure wave therapy (RPWT) (three treatments at 2-weekly intervals; 1000 shocks per ligament; 3.5 bar). The method of treatment was not specified in the paper but it is normally directed distally from the coronary band (Figure 20.3). The insertion of the ligaments is not readily accessible, and care needs to be taken to orientate the applicator appropriately. For desmopathy cases alone, the outcome with conservative management alone was 13%, and this improved to 25% with shockwave therapy. This difference was not statistically significant, which led the authors to conclude that there was no effect on outcome, even though the statistical power of the study was limited and thus there may have been a clinical effect. There was no effect of shockwave on outcome when cases with other pathologies were included. Gutierrez-Nibeyro *et al*. [22] used focused ESWT (three to seven treatments at 2-weekly intervals; 1500 pulses per ligament; 20 mm convex

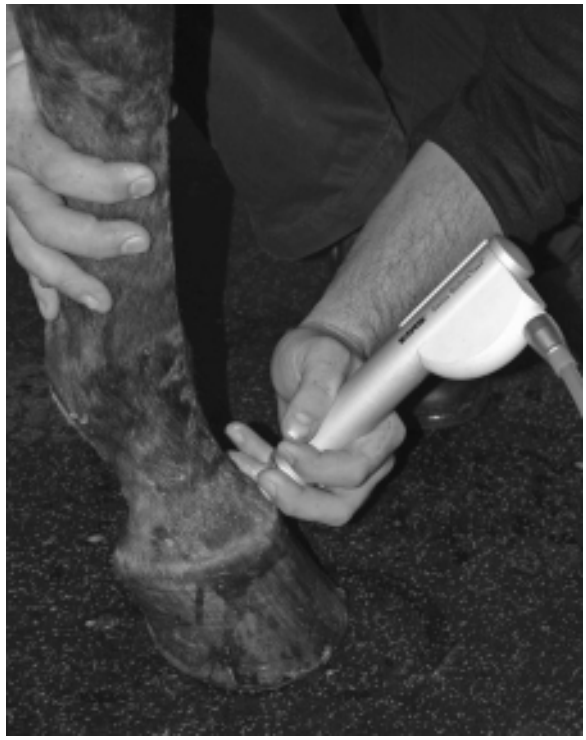

Figure 20.3 Shockwave therapy of a distal interphalangeal joint collateral ligament injury.

applicator handpiece; 0.15 mJ/mm^2) on 13 cases, 54% of which returned to full work. Their overall success rate was 60%, with a minimum follow-up period of 9 months, so there is no evidence from their work of a benefit from ESWT. Sixty-two per cent of their cases with concomitant DDFT lesions returned to full work, which was considerably better than the results of Dakin *et al*. [23] for combination injuries.

Gutierrez-Nibeyro *et al*. [22] treated half of their cases with intra-articular hyaluronan (20 mg) and triamcinolone (6 mg) into the distal interphalangeal joint. The outcome was not significantly different compared with those not receiving intra-articular medication (Gutierrez-Nibeyro SD, personal communication, 2009).

Dakin *et al*. [23] reported on a small numbers of cases that received either intravenous infusion of tiludronate if there was evidence of bone inflammation, or intra-articular medication with hyaluronan and triamcinolone if there was marked synovitis of the distal interphalangeal joint. These treatments are logical but there is insufficient evidence to know if they are beneficial. There are concerns about the use of corticosteroids in acute injuries as diffusion to the ligament may impair soft tissue healing. Martinelli (personal communication, 2009) has used autologous conditioned serum (ACS) (Irap) [26] injected intra-articularly into the distal interphalangeal joint. This product contains anti-inflammatory cytokines, including interleukin-1 receptor antagonist, and several growth factors, including insulin-like growth factor-1, platelet-derived growth factor and transforming growth factor-beta-1. The aim is to minimize inflammation within the joint but also to

promote soft tissue healing. The protocol is 4–8 weeks of alternating shockwave and ACS, or 8–10 weeks for an insertional desmopathy. The results have been very encouraging with a success rate of 84% in over 30 cases with long-term follow-up (Martinelli MJ, personal communication, 2009). I tend to use ACS and shockwave together, with an initial injection of ACS into the affected ligament, followed by five intra-articular injections at weekly intervals. Radial shockwave is administered three times at weekly intervals. On a small case series with long-term follow-up, 75% have returned to full work. This form of treatment certainly seems to justify continued study.

Palmar digital neurectomy can be an option for treatment if there is a failure to adequately respond to conservative or medical management. Dakin *et al*. [23] included four cases, all of which returned to their previous function, remaining sound for a minimum of 12 months and up to 4 years. Based on this and my own experience, palmar digital neurectomy can be a safe procedure to perform, but it is not appropriate for acute injuries.

The presence of collateral ligament (CL)-related osseous injury [3] did not influence the outcome compared to CL injury alone in the thorough study by Dakin *et al*. [23]. Only three horses out of 12 with osseous cyst-like lesions (OCLLs) at the origin or insertion of the ligament returned to full work. Smith *et al*. [27] described surgical treatment of radiographically diagnosed OCLLs at the insertion of the CL by surgical curettage and packing with an autogenous cancellous bone graft. One out of three cases returned to full work, but the other two were subject to euthanasia.

CL desmopathy can be a frustrating condition to treat. The differences in outcome between the case series described by Dakin *et al*. [23] and Gutierrez-Nibeyro *et al*. [22] is interesting. The injuries are recorded to be of longer duration in the latter paper, and they also report of median lameness at presentation of grade 3/5. The degree of lameness is unfortunately not reported in the former paper, but is unlikely to be more severe than that. Differences between the caseloads are the most likely reason for the inconsistencies between the papers. My clinical impression is that the prognosis for acute cases, with an early diagnosis and appropriate management, is better than the more chronic cases that have been reported in the literature.

NAVICULAR DISEASE

Lameness associated with the navicular bone has been much better characterized since the advent of MRI, and the involvement of the surrounding soft tissues can now be evaluated in clinical cases [2]. Older papers on navicular disease or navicular syndrome would have included many cases that may well now be diagnosed as DDFT or CL injuries, and thus there is a need to revisit the efficacy of treatments in the face of more accurate characterization. Dyson *et al*. [2] in a study of 199 horses with foot pain undergoing MRI found only 5% to have navicular bone changes in isolation, while 14% had both navicular and DDFT changes, 11% had damage to the distal sesamoidean impar ligament (DSIL) and 17% had multiple injuries – the majority of which are likely to have navicular involvement. The prognosis for return to full function was very poor, with only 22% of cases of navicular pathology

alone returning to full work, and only 5% of cases of navicular and DDFT pathology had a successful outcome. Sherlock *et al*. [28] reported 16 cases of deep erosions of the palmar aspect of the navicular bone diagnosed with standing MRI. Only one of these (6%) returned to full work, while 44% were capable of working at a lower level and 44% were subject to euthanasia.

An initial period of rest is necessary if there is an acute onset severe lameness or MRI evidence of significant acute soft tissue involvement. Controlled exercise is necessary, but generally excessive restriction of exercise is counter-productive in primary bone pathology. Horses will often do better with small paddock turn-out.

Corrective shoeing is used to try and optimize the biomechanical forces acting through the navicular region, and decrease the load through the DDFT. Correct trimming of the foot is vital, taking into consideration mediolateral as well as dorsopalmar balance. Egg bar shoes, natural balance shoes and wedging of the heels are commonly used. The theory behind these was recently reviewed by Rijkenhuizen [29], but my practical experience is that it is important to find what suits the individual horse, and close collaboration with the farrier is essential. There do seem to be geographic and breed differences, with heel wedges being commonly used in the USA, especially in Quarter Horses. In the UK they are less popular and often only used as a temporary measure, because in the relatively weak-heeled Thoroughbred they can lead to crushing of the heels. An *in vitro* study by Weaver *et al*. [30] topographically mapped the pressure distribution across the palmar surface of the navicular bone and showed that heel wedges tended to increase the pressure on the major loading areas where navicular pathology is most common.

Supportive medical therapy with non-steroidal anti-inflammatory drugs (NSAIDs), most commonly phenylbutazone, is commonly employed. This can be helpful acutely and to allow a gradual reintroduction to exercise. It can be an effective form of long-term treatment in low-grade lameness in non-competition horses or for sports where medication control rules do not preclude NSAIDs. Isoxuprine is now rarely used in the treatment of navicular disease, and the pathologies identified on MRI do not seem to support the use of vasodilators. Tiludronate, a nonamino-bisphosphonate that regulates bone metabolism through an inhibition of bone resorption, has been licensed in Europe for the treatment of navicular disease.

Denoix *et al*. [31] reported on a double-blind placebo-controlled trial in a total of 73 horses, with dosages of 0.5 mg/kg and 1 mg/kg compared. Diagnosis was based on a positive palmar digital nerve block and positive radiographic findings. MRI was not undertaken, so the precise nature of the pathology is uncertain. There was little evidence of efficacy at the lower dose rate. Of 12 cases with lameness of less than 6 months' duration, 75% returned to a normal level of activity by 6 months after a single treatment, compared with 25% for the placebo group. No significant difference was evident up to 2 months after treatment, and continuing to increase the plane of exercise seemed to be an important part of the treatment in this study. The chronic cases showed no significant differences in any of the efficacy criteria evaluated after a single treatment, but five out of eight horses were reported to have responded positively after multiple treatments.

In a small study of clinical cases identified with a variety of types of navicular pathology on MRI and treated with a single intravenous infusion of tiludronate, eight out of 12 (67%) returned to full function on long-term follow-up (Bathe AP, Hilton RL, unpublished observations, 2009). This is encouraging given that the majority had associated soft tissue damage as well. Active cystic lesions on the palmar aspect of the navicular bone can respond temporarily to tiludronate. The precise mode of action for this drug to be effective is uncertain, as histologic studies of advanced navicular disease with severe radiographic changes and increased signal in fat-suppressed images showed degenerative changes. Although 'bone oedema' is a popular term for increased signal on fat-suppressed images it is often inaccurate, as a variety of pathologies can be present [32]. Some horses have increased signal intensity on fat-suppressed images in navicular bone in association with, and in the plane of, a DDFT lesion, possibly representing bone trauma at time of injury/secondary to DDFT lesion or associated flexor cortex pathology. This MRI signal and pain often resolves with rest and progressive healing of the DDFT lesion. Overall it is difficult to predict which cases will respond well to tiludronate treatment, but this does appear to be a useful product.

Intra-articular medication of the distal interphalangeal joint has been commonly used for the treatment of navicular disease. There is logic for this approach in primary bone disease, as the synovial invaginations of the distal interphalangeal joint into the distal border of the navicular bone will allow for ready diffusion of corticosteroid into the bone. However, the increasing recognition of navicular bursal pathology supports more specific treatment into the bursa.

Verschooten *et al*. [33] reported on 161 horses with clinical and radiographic signs of navicular disease, with 60% responding positively for a period of 2 months or more, but the clinical effect rapidly diminished after this time. Dabareiner *et al*. [34] reported on 25 cases of navicular area pain, which had been non-responsive to corrective farriery and systemic NSAIDs. Eighteen (72%) cases had not significantly responded to intra-articular medication of the distal interphalangeal joint with corticosteroids and hyaluronan. The average duration of lameness prior to treatment was 9.3 months. The bursa was medicated with triamcinolone (6 mg) or methylprednisolone (40 mg), hyaluronan and amikacin under radiographic guidance. Eighty per cent returned to full function within 2 weeks of treatment and remained free of lameness for a mean of 4.6 months. Fifty-six per cent were still being used for their intended purpose 1–3 months after treatment. Five horses received multiple treatments and three sustained severe DDFT damage or rupture.

The use of MRI to identify significant tendonous pathology could reduce the risk of this complication. Bell *et al*. [35] reported on 23 cases of foot pain evaluated with MRI and treated with intrabursal injections. All cases blocked to a palmar digital block and 64% had no obvious radiographic abnormalities. MRI findings included DDFT changes in 60%; flexor cortex bone or fibrocartilage changes in 43% and distal interphalangeal joint collateral desmopathy in 54%. Adhesions were very commonly diagnosed, although it should be noted that the distinction between tissue apposition

and adhesion is often extremely difficult on MRI. Distension of the bursa with saline prior to imaging can improve the accuracy of this diagnosis.

Cases were treated with medication of the navicular bursa with triamcinolone (range 4–25 mg, median 15 mg), amikacin and hyaluronan in 51%. The lameness resolved within 2–4 weeks in 74% of horses, and they returned to full function. Median duration of soundness was 6 months. Five horses received multiple treatments. Hyaluronan treatment had no significant effect on outcome. Triamcinolone doses less than 10mg had a significantly poorer outcome, which is interesting as a large number of clinicians would consider this to be a high dose for such a small synovial structure. Poor prognostic indicators on MRI were flexor cortex erosions and adhesions between the navicular bone and DDFT. The presence of navicular bursitis was a positive prognostic indicator, which is both logical and a useful criteria for selecting cases for intrathecal medications.

Extracorporeal shockwave therapy has been used in the management of navicular disease, using both focused and radial systems. McClure *et al*. [36] reported on the results of one treatment with focused ESWT under general anaesthesia in 27 horses. Sixty-seven per cent of the cases improved by one lameness grade, and those judged to have flexor cortex erosions or adhesions did not respond so well. The majority of clinicians would treat the horse standing under sedation, with the approach through the heel bulbs considered more likely to allow penetration of the shockwaves. Because of the depth of the target tissue, focused shockwave would more logically be employed in comparison with radial. The results in my hands have been somewhat disappointing, using either system. Despite the widespread use of shockwave in orthopaedic practice, there does not seem to be much use of it for this application. The mode of action is more likely to be analgesic [37] rather than disease modifying.

Surgical treatment in the form of navicular suspensory (collateral sesamoidean) desmotomy has been previously described [38], but has not found widespread clinical acceptance. There would be a logical use of the technique in cases of desmopathy of the collateral sesamoidean ligament but marked fibrosis and adhesion can be identified on follow-up MRI examinations after this surgical procedure (Werpy N, personal communication, 2006; Murray R, personal communication, 2009), which does not tend to encourage its use.

Decompressive drilling of the navicular bone was developed by Kirker-Head (personal communication, 2002), based on the hypothesis that this would be analgesic by relieving the high intra-osseous pressure noted in navicular disease [39]. Decompression surgery may also expedite balanced navicular bone remodelling by opening up channels for vascular in-growth and by stimulating the natural processes of repair. The proximal aspect of the navicular bone is visualized by an arthoscopic approach to the palmar aspect of the distal interphalangeal joint, and a contralateral instrument portal is used to introduce the drill bit. This is combined with fluoroscopic guidance (Figure 20.4) to make three 2.7mm drill tracts into the medulla of the navicular bone. Jenner [40] studied this experimentally. An *in vitro* study demonstrated an approximately 20% reduction in breaking strength following decompressive drilling. In an *in vivo* study using healthy horses, there

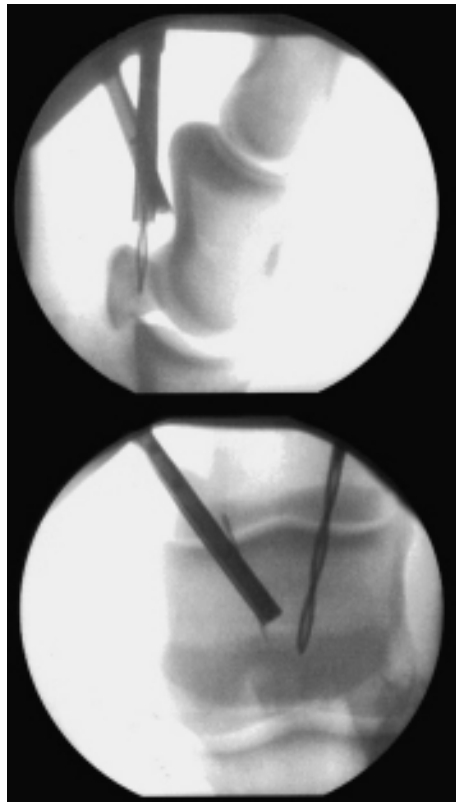

Figure 20.4 Dorsopalmar and lateromedial fluoroscopic intraoperative views showing arthroscope and drill bit during decompressive drilling of navicular bone.

was a significantly reduced intraosseous pressure in response to a stress test. The tracts filled with fibrous tissue by 12 weeks and no significant lameness was induced.

I have used this procedure on two cases of very severe navicular disease. One had a very large flexor cortex erosion and returned to low level dressage use, having been 4/5 lame. The other was an international showjumper and was also 4/5 lame and underwent MRI, which revealed marked navicular bone oedema and associated dorsal DDFT pathology, as well as mild CL desmopathy. The horse was given a hopeless prognosis based on the MRI findings but the owner was keen to pursue treatment. The horse returned to showjumping one year later, but a year later suffered from low-grade lameness again. A palmar digital neurectomy was performed at this stage and the horse is still competing internationally 3 years later. The technique is somewhat technically challenging and requires careful patient selection. Logically, the technique holds the most potential benefit for horses whose navicular bones are free from significant degenerative changes and whose adnexal structures are lacking in pathology. MRI will facilitate optimal patient selection.

Endoscopy of the navicular bursa can be employed in cases of navicular disease, but is most applicable for cases with significant DDFT involvement, as previously discussed. My experience of debriding large flexor cortex erosions has been poor. Adhesions between the navicular bone and DDFT have associated fibrocartilage loss. Adhesions more proximally within the

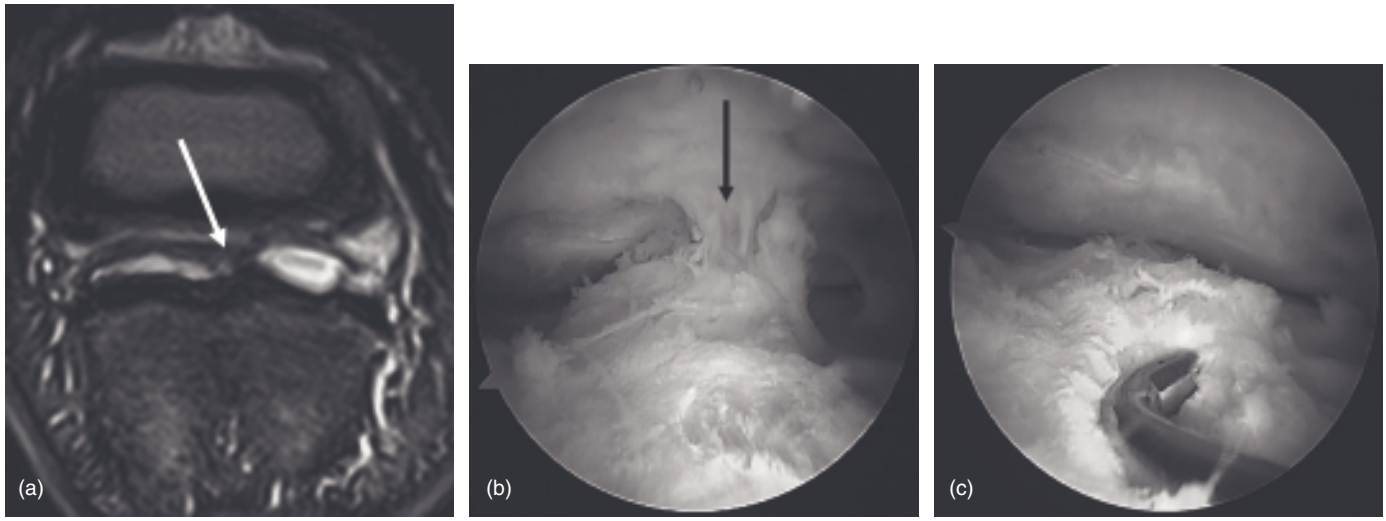

Figure 20.5 Intrabursal adhesions between the DDFT and collateral sesamoidean ligament. (a) Transverse T2 FSE image showing a low signal intensity filling defect (arrow) between the DDFT and collateral sesamoidean ligament. (b) Endoscopic view of the adhesion (arrow). (c) Endoscopic view after surgical resection of the adhesion.

bursa, such as between the suspensory ligament and DDFT, are more amenable to surgical intervention (Figure 20.5). A combination of sharp dissection, motorised synovial resectors and radiofrequency electrosurgical devices can be used to break down adhesions, with the transthecal approach being the most useful.

Palmar digital neurectomy remains a useful method of managing persistent navicular region pain. My experience has been that there has been an increase in the number of horses undergoing this procedure now that MRI can be used to select out cases of severe DDFT involvement, as rupture of this structure used to be the most common significant postoperative complication. Severe navicular bone involvement or persistent pain from a DSIL injury would be positive indicators for surgery for me. A number of different techniques have been described [41, 42]. If pain on palpation of the transected nerve ends develops postoperatively then local infiltration of corticosteroids seems to prevent this developing to a long-term problem.

DISTAL INTERPHALANGEAL JOINT

Distal interphalangeal joint pain is still a common clinical diagnosis, often with no appreciable radiographic or MRI findings, and frequently representing synovitis or early osteoarthritis. These can respond well to intra-articular medication with corticosteroids, but we need to be cognisant of the fact that some of these cases will represent the early stages of a significant disease process, which may become apparent later. Intra-articular medication of an acute onset lameness localized to this area may not be advisable without prior MRI examination, because the non-specificity of the block may well mean that there could be a DDFT or CL injury.

Dyson *et al.* [2] recorded only five distal interphalangeal joint injuries out of 199 cases of foot pain undergoing MRI. Cartilage lesions within the distal interphalangeal joint are very difficult to evaluate accurately because

the cartilage is thin relative to the spatial resolution of clinical MRI, and the joint surface is curved leading to volume averaging effects. Thus if pathology is severe enough to be evident on MRI it is likely to be clinically significant. The cartilage defects are rarely in a surgically accessible site, and thus medical treatment is appropriate. Triamcinolone is considered to be chondroprotective in equine osteoarthritis [43], especially in comparison with methylprednisolone [44], and is widely used clinically. An alternative approach is to attempt to induce an anabolic effect in the cartilage using ACS. Weinberger (personal communication, 2009) has treated a large number of horses, with reportedly good success rates. I have had success with this in cases that have been previously been non-responsive to corticosteroids, and in my opinion this is the current treatment of choice for acute injuries. Approximately six injections should be administered at weekly intervals, and the horse kept in light walking exercise. The period of controlled exercise depends on the persistence of lameness. Medication with corticosteroids can be helpful as the horse comes back into work. Intra-articular treatment with mesenchymal stem cells or adipose-derived nucleated cell fractions is heavily marketed in some quarters, but there remains little objective evidence of benefit.

Subchondral cyst-like lesions within the distal or middle phalanx are uncommon but readily identified on MRI. They may not always be clinically significant or associated with pain, so management may not be necessary. However, in the absence of pain it is possible that they could be related to joint instability and increased risk of other damage, so management of the joint may be indicated even in the absence of pain. Clinically significant subchondral cyst-like lesions can be treated conservatively or medically with intra-articular corticosteroids. They are generally not easily approached to allow intra-lesional medication with corticosteroids. Story and Bramlage [45] reported on 11 cases treated using arthroscopic debridement, with an age range of 16–33 months. Access can be challenging but 10 out of 11 cases were successful. Lesions of the extensor process can be identified and are more easily accessible arthroscopically (Figure 20.6). Extra-articular approaches can be used, but infection remains a concern with such an approach.

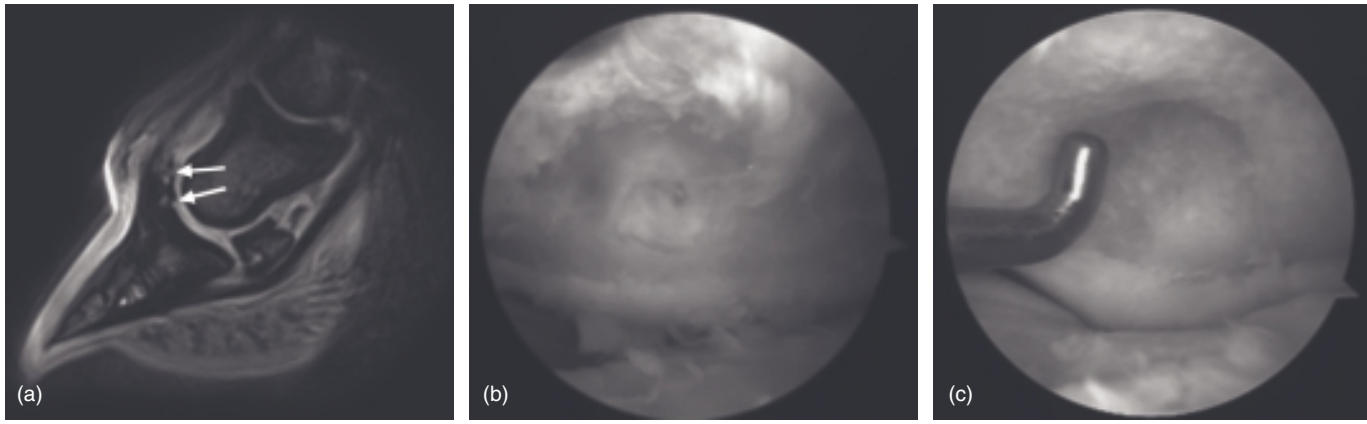

Figure 20.6 Subchondral cystic lesions (arrow) in the extensor process of the distal phalanx. (a) Sagittal T2* GRE image. (b) Endoscopic view at the start of debridement. (c) Endoscopic view at the end of debridement.

BONE TRAUMA/BRUISING

Dyson *et al*. [2] noted that 7% of their cases of foot pain evaluated with MRI had primary injuries of the middle or distal phalanx, characterized by an increased signal intensity in fat-suppressed images, as well as decreased signal intensity in the cancellous bone in T1- and T2-weighted images. In cases where this represents true bone trauma/bruising there is a good prognosis with controlled exercise. Tiludronate treatment may be logical in non-responsive cases. Olive *et al*. [46] reported bone marrow lesions in the middle phalanx of seven horses identified on standing MRI. Five were reported to have returned to work satisfactorily, although in two of these it was retrospectively considered that the bone bruise was an incidental finding. Two horses were retired, one of which had an associated osteoarthritis of the proximal interphalangeal joint (PIP).

MISCELLANEOUS CONDITIONS OF THE FOOT

Ossification of the cartilages of the feet and fractures of the ossified cartilages can be identified on MRI, as well as radiography and scintigraphy [47]. There is normally a good response to conservative treatment. In non-responsive or recurrent cases local medication with corticosteroids can be beneficial (Powell SE, personal communication, 2009). Marked local soft tissue proliferation can be identified on MRI. MRI is also helpful to rule out the concurrent presence of CL desmopathy.

Keratomas can be clearly identified on MRI and the multi-slice imaging can be helpful in the surgical planning for more complex tumours (Figure 20.7). Surgical removal of standard lesions can be performed in standard fashion by resecting a strip of hoof wall (Figure 20.8). The outcome is normally good, with a low risk of recurrence.

Laminitis can be identified on MRI [48, 49] and enhanced evaluation of laminar gas and fluid, and of distal phalanx changes may be helpful in a complex case. A review of the treatment of laminitis is outside the scope of

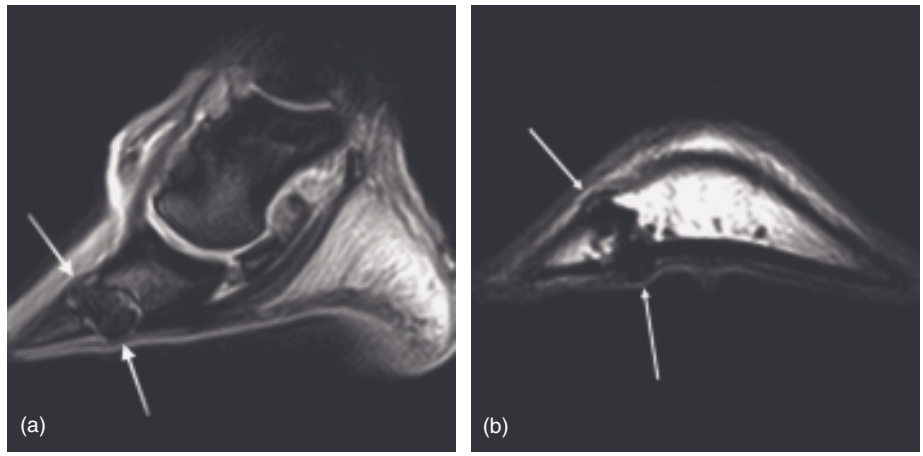

Figure 20.7 Keratoma (arrow) within the distal phalanx, extending to both dorsal and solar surfaces. (a) T2* GRE parasagittal image and (b) dorsal T2 FSE image showing a discrete area of hypointensity within the distal phalanx.

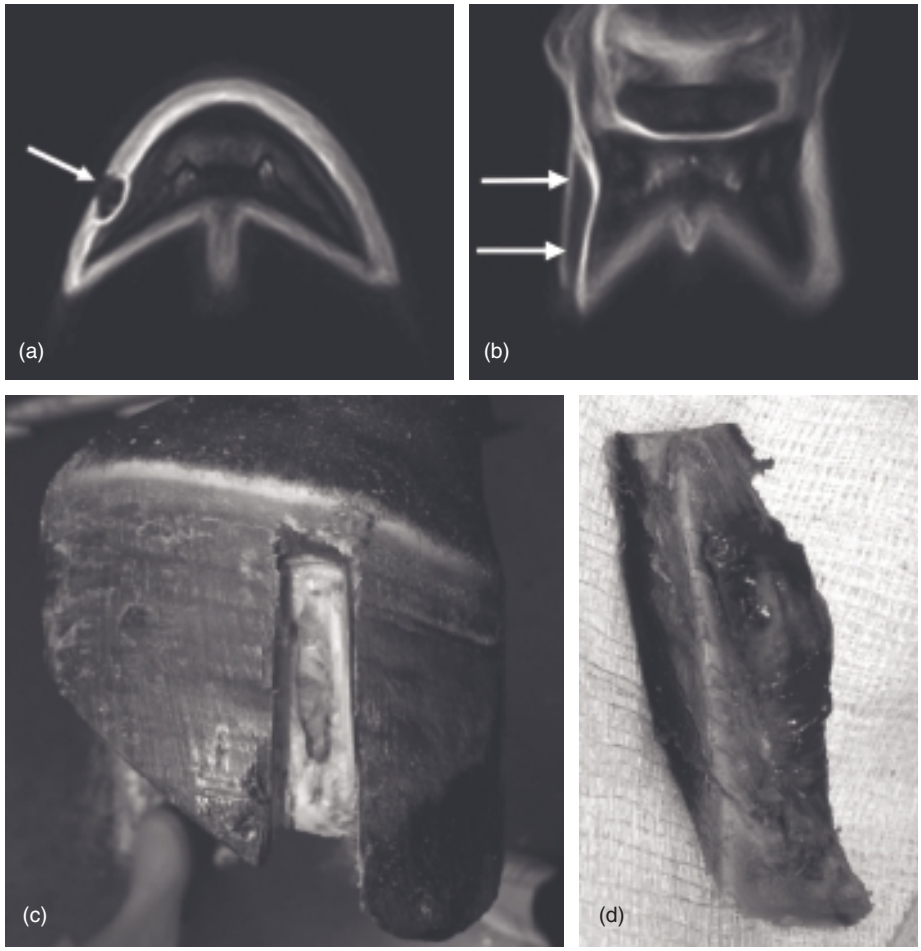

Figure 20.8 Keratoma in hoof wall. (a) Transverse T2* GRE and (b) dorsal T2* GRE images showing a hypointense mass (arrows) within lamellae. (c) Postoperative view after stripping hoof wall. (d) Keratoma visible on resected portion of hoof wall.

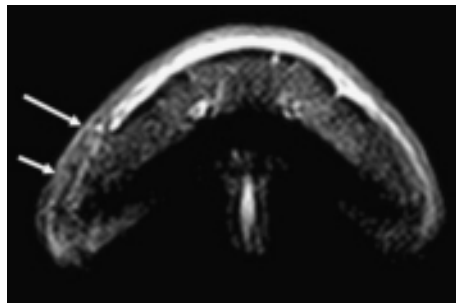

Figure 20.9 Transverse plane STIR image of a foot with focal laminitis and pedal osteitis in an endurance horse. There is hyperintense signal within the pedal bone and disorganized laminae on the lateral aspect (arrows).

this chapter. Focal, traumatic laminitis can also be identified, especially in endurance horses (Figure 20.9). This usually responds to rest and corrective shoeing.

Foot penetrations can be further evaluated with MRI. The precise identification of soft tissue pathology and a three-dimensional appreciation of bone pathology can be extremely helpful in the evaluation and surgical

planning of complex acute cases (Figures 20.10 and 20.11). MRI can also be invaluable in assessing more chronic problems after penetration (Figures 20.12 and 20.13). Kinns and Mair [50] described the identification of DDFT lesions in three horses evaluated with standing MRI that had persistent lameness 2 weeks after injury, with no evidence of synovial sepsis. All three horses were reported to come sound after a prolonged period of rest. Boado *et al*. [51] and Kristoffersen *et al*. [52] described use of MRI to diagnose penetrating injury to the foot in two and five cases of chronic foot lameness respectively. Of these seven horses, only one was reported to have resolution of lameness.

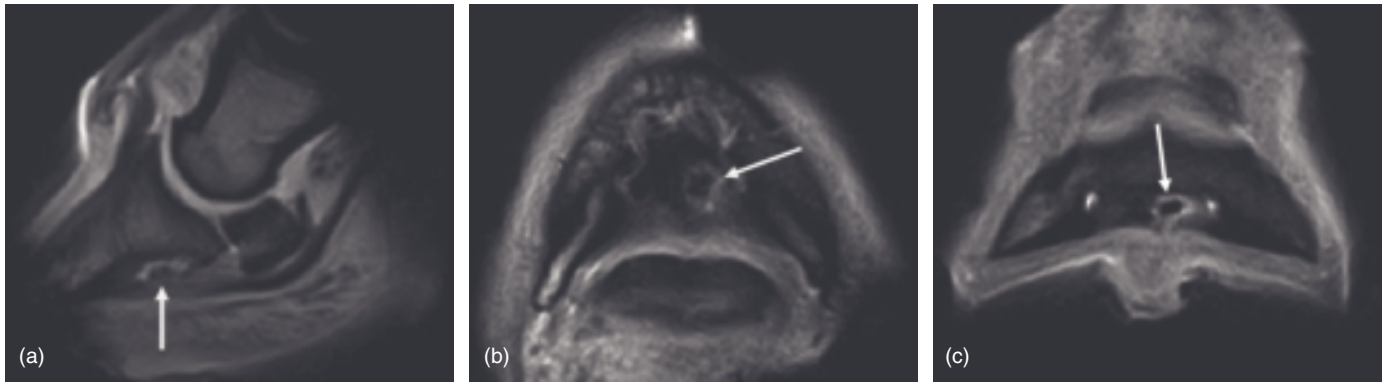

Figure 20.10 (a) Sagittal, (b) transverse and (c) dorsal (frontal) T2-weighted images of a foot with sequestrum formation at the insertion of the DDFT into the distal phalanx following a solar penetration.

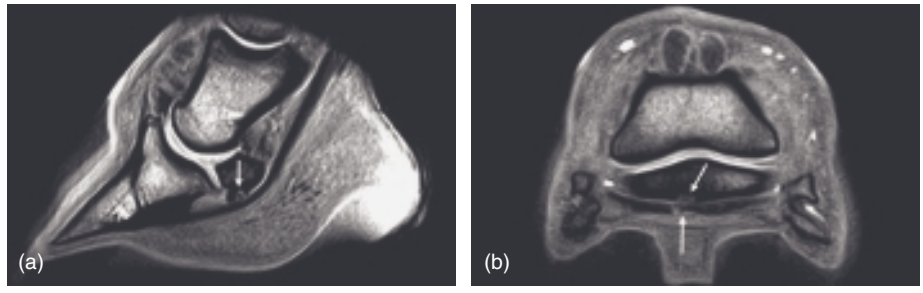

Figure 20.11 (a) Sagittal and (b) transverse T1-weighted images of a foot. There is hypointense signal in the navicular bone and a traumatic defect in the DDFT and navicular bone (arrows) following a solar penetration, which, interestingly, did not develop bursal sepsis.

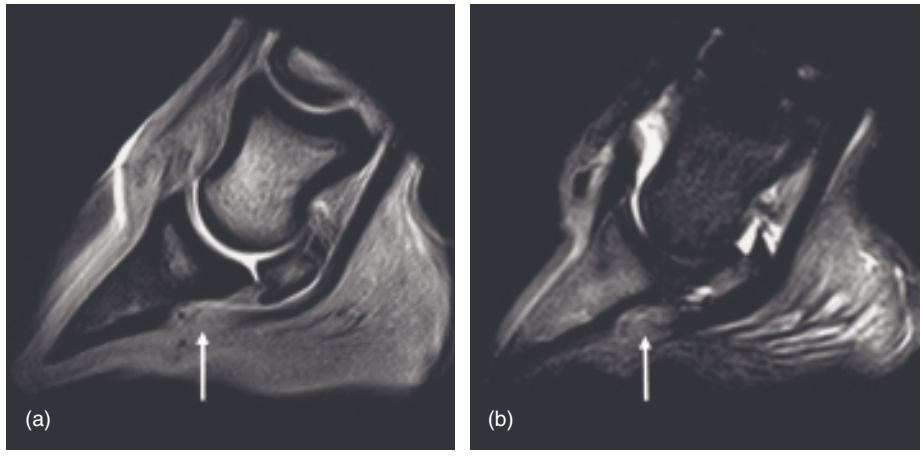

Figure 20.12 DDFT insertional tendinitis subsequent to a solar penetration. (a) Sagittal T1-weighted image showing high signal intensity in the DDFT (arrow) and low signal intensity in the distal phalanx. (b) Transverse STIR image showing hyperintense signal in DDFT insertion (arrow) and distal phalanx.

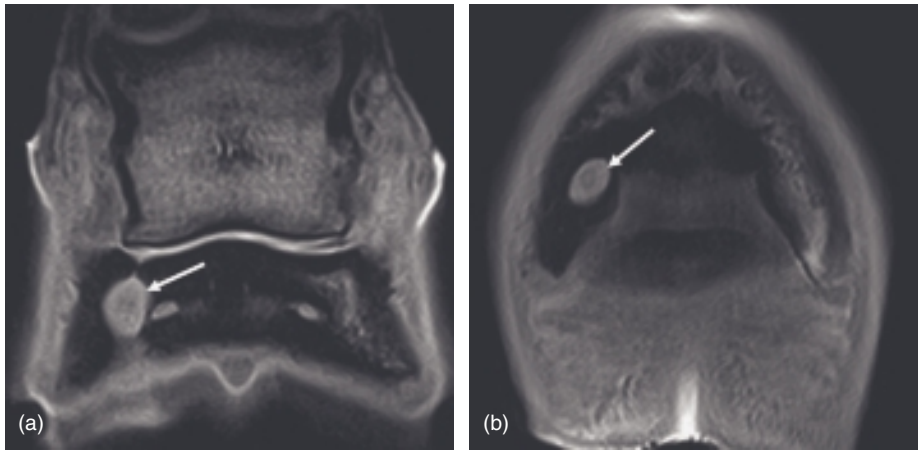

Figure 20.13 Granuloma affecting the distal phalanx. (a) Dorsal plane T2* GRE image showing a well-circumscribed hyperintense mass in the distal phalanx. (b) Transverse plane T2* GRE image showing hypointense signal intensity in the distal phalanx surrounding a well-circumscribed hyperintense mass.

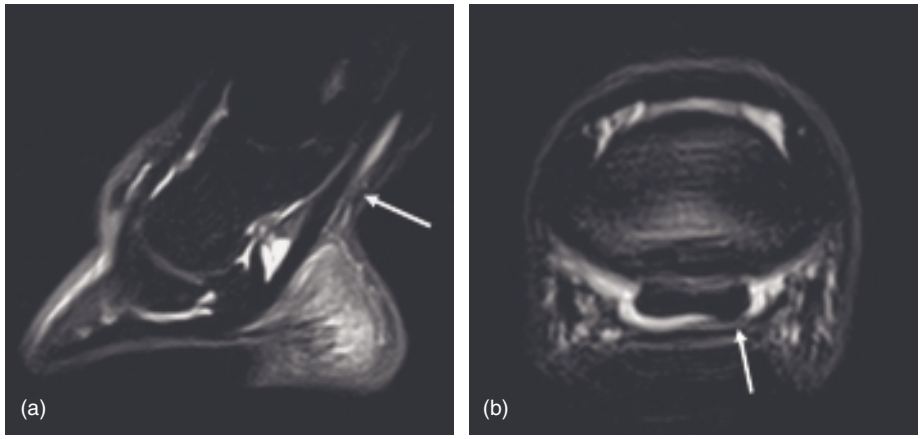

Figure 20.14 Adhesion to the DDFT, not diagnosed on ultrasonography, following more proximal pastern laceration. (a) Sagittal STIR and (b) transverse T2 FSE image showing adhesion (arrows) between distal digital annular ligament and DDFT.

PASTERN

Zubrod and Barrett [53] reviewed the MRI aspects of soft tissue injuries in the pastern region, affecting the collateral ligaments of the PIP, the oblique and straight distal sesamoidean ligaments, the SDFT branches, and the proximal and distal annular ligaments. The DDFT obviously continues up into the pastern and proximal lesions may be evaluated with both MRI and ultrasound. The same considerations for treatment of these tendon and ligament injuries exist as discussed earlier, and some may be amenable to intralesional injection or tenoscopic evaluation/debridement. In my opinion MRI is particularly helpful in allowing more accurate identification of pathology in the proximal portion of the oblique distal sesamoidean ligament and the palmar and plantar ligaments of the pastern, allowing accurate targeting of shockwave therapy and intralesional medication.

Adhesions can occur secondary to injuries in the pastern region, and these can be amenable to surgical treatment (Figure 20.14). Cohen *et al.* [54] described MRI diagnosis and surgical treatment of seven cases of desmitis of the distal digital annular ligament. There was a positive response to palmar digital nerve blocks, and the desmitis was considered a primary

condition in all cases. Surgical transaction was undertaken using a hook knife under tenoscopic visualization. Seventy-one per cent were reported to come sound. This condition has been rarely diagnosed as a significant lesion elsewhere, and it remains to be seen if this is an under-diagnosed problem. In our clinic we have had good responses to conservative management and intrathecal medication with corticosteroids (Head M, personal communication, 2009).

ACKNOWLEDGEMENT

Thanks to Sarah Powell for supplying the majority of the images.

REFERENCES

[1] Dyson S, Murray R, Schramme M, Branch M. Lameness in 46 horses associated with deep digital flexor tendonitis in the digit: diagnosis confirmed with magnetic resonance imaging. *Equine Vet J* 2003; **35**: 681–90.
[2] Dyson S, Murray R, Schramme M. Lameness associated with foot pain: results of magnetic resonance imaging in 199 horses (January 2001–December 2003) and response to treatment. *Equine Vet J* 2005; **37**: 113–21.
[3] Schramme MC. Treatment of deep digital flexor tendonitis in the foot. *Equine Vet Educ* 2008; **20**: 389–91.
[4] Puchalski SM, Snyder JR, Hornof WJ, Macdonald MH, Galuppo LD. Contrast-enhanced computed tomography of the equine distal extremity. *AAEP Proc* 2005; **51**: 389–94.
[5] Anderson JDC, Puchalski SM, Larson RF, Delco ML, Snyder JR. Injection of the insertion of the deep digital flexor tendon in horses using radiographic guidance. *Equine Vet Educ* 2008; **20**: 383–8.
[6] Dahlgren LA, Van der Meulen MC, Bertram JE, Starrak GS, Nixon AJ. Insulin-like growth factor-1 improves cellular and molecular aspects of healing in collagenase-induced model of flexor tendonitis. *J Orthop* 2002; **209**: 10–19.
[7] Mitchell RD. Treatment of tendon and ligament injuries with UBM powder (ACell-Vet). *Proc Am Coll Vet Surg* 2004; **14**: 190–3.
[8] Nixon AJ, Dahlgren LA, Haupt JL, Yeager AE, Ward DL. Effect of adipose-derived nucleated cell fractions on tendon repair in horses with collagenase-induced tendinitis. *Am J Vet Res* 2008; **69**: 928–37.
[9] Smith RKW, Korda M, Blunn GW, Goodship AE. Isolation and implantation of autologous equine mesenchymal stem cells from bone marrow into superficial digital flexor tendon as a potential novel treatment. *Equine Vet J* 2003; **35**: 99–102.
[10] Taylor SE, Smith RKW, Clegg PD. Mesenchymal stem cell therapy in equine musculoskeletal disease:scientific fact or clinic fiction. *Equine Vet J* 2007; **39**: 172–80.
[11] Smith MRW, Wright IM, Smith RKW, Bladon B, Schramme MC. Treatment options for DDFT lesions: evidence based results. *Proceedings European College Veterinary Surgeons 18th Annual Scientific Meeting* 2009, pp. 211–14.
[12] Schnabel L, Mohammed HO, Miller BJ *et al*. Platelet rich plasma (PRP) enhances anabolic gene expression patterns in flexor digitorum superficialis tendons. *J Orthop Res* 2006; **25**: 230–40.
[13] Waselau M, Sutter WW, Genovese RL, Bertone AL. Intralesional injection of platelet-rich plasma followed by controlled exercise for treatment of midbody suspensory ligament desmitis in Standardbred racehorses. *J Am Vet Med Ass* 2008; **232**: 1515–20.
[14] Bosch G, van Schie HT, de Groot MW *et al*. Effects of platelet-rich plasma on the quality of repair of mechanically induced core lesions in equine superficial digital flexor tendons: A placebo-controlled experimental study. *J Orthop Res* 2010; **28**: 211–17.
[15] Nixon AJ. Stem cells for cartilage repair. *ACVS Proc* 2007; 31–5.

[16] Crovace A, Lacitignola L, Francioso E, Rossi G. Histology and immunohistochemistry study of ovine tendon grafted with cBMSCs and BMMNCs after collagenase-induced tendinitis. *Vet Comp Ortho Traum* 2008; **21**: 329–36.
[17] Bell CD, Howard RD, Taylor DS, Voss ED, Werpy NM. Outcomes of podotrochlear (navicular) bursa injections for signs of foot pain in horses evaluated via magnetic resonance imaging: 23 cases (2005–2007). *J Am Vet Med Assoc* 2009; **1**: 920–5.
[18] Smith MR, Wright IM, Smith RK. Endoscopic assessment and treatment of lesions of the deep digital flexor tendon in the navicular bursae of 20 lame horses. *Equine Vet J* 2007; **39**: 18–24.
[19] Wright IM, Phillips TJ, Walmsley JP. Endoscopy of the navicular bursa; a new technique for treatment of contaminated and septic bursae. *Equine Vet J* 1999; **31**: 5–11.
[20] McIlwraith CW, Nixon A, Wright IM, Boening J. *Diagnosis and Surgical Arthroscopy in the Horse*, 3rd edn. Philadelphia, PA: Mosby, 2005, pp. 347–65.
[21] Turner TA, Sage AM. Desmitis of the distal inerphalangeal collateral ligaments: 22 cases. *Proc Am Ass Equine Practnrs* 2002; **48**: 343–6.
[22] Gutierrez-Nibeyro SD, White NA 2nd, Werpy NM *et al*. Magnetic resonance imaging findings of desmopathy of the collateral ligaments of the equine distal interphalangeal joint. *Vet Radiol Ultrasound* 2009; **50**: 21–31.
[23] Dakin SG, Dyson SJ, Murray RC, Newton R. Osseous abnormalities associated with collateral desmopathy off the distal interphangel joint. Part 2: Treatment and outcome. *Equine Vet J* 2009; **41**: 1–5.
[24] Bathe AP. Chronic foot lameness. In: Curtis S (ed.) *Corrective Farriery: a textbook of remedial horseshoeing Volume I*. Newmarket: R&W Publications, 2002, pp. 81–104.
[25] Martinelli MJ, Schramme MC. Collateral desmitis of the distal interphalangeal joint. *Proc Am Coll Vet Surg* 2007; 94–8.
[26] Frisbie DD, Kawcak CE, Werpy NM, Park RD, McIlwraith CW. Biochemical, and histologic effects of intra-articular administration of autologous conditioned serum in horses with experimentally induced osteoarthritis. *Am J Vet Res* 2007; **68**: 290–6.
[27] Smith MRW, Crowe OC, Ellson C *et al*. Surgical treatment of osseous cyst-like lesions in the distal phalanx arising from collateral ligament insertional injury. *Equine Vet Ed* 2005; **17**: 195–200.
[28] Sherlock C, Mair T, Blunden T. Deep erosions of the palmar aspect of the navicular bone diagnosed by standing magnetic resonance imaging. *Equine Vet J* 2009; **40**: 684–92.
[29] Rijkenhuizen ABM. Navicular disease: a review of what's new. *Equine Vet J* 2006; **38**: 82–8.
[30] Weaver MP, Shaw DJ, Munaiwa G, FitzPatrick DP, Bellenger DR. Pressure distribution between the deep digital flexor tendon and the navicular bone, and the effect of raising the heels in vitro. *Vet Comp Orthop Traumatol* 2009; **22**: 278–82.
[31] Denoix JM, Thibaud D, Riccio B. Tiludronate as a new therapeutic agent in the treatment of navicular disease: a double-blind placebo-controlled clinical trial. *Equine Vet J* 2003; **35**: 407–13.
[32] Busoni V, Heimann M, Trenteseaux J, Snaps F, Dondelinger R. Abnormal MRI findings in the deep digital flexor tendon and distal sesamoid bone in radiographically defined navicular disease – an in vitro study. *Vet Radiol Ultrasound* 2005; **46**: 279–86.
[33] Verschooten F, Desmet P, Peremans K, Picavet T. Navicular disease in the horse: The effect of controlled intrabursal corticoid injection. *Equine Vet Science* 1990; **11**: 316–20.
[34] Dabareiner RM, Kent Carter G, Honnas CM. Injection of corticosteroids, hyaluronate and amikacin into the navicular bursa in horses with signs of navicular area pain unresponsive to other treatments: 25 cases (1999–2002). *J Am Vet Med Ass* 2003; **223**: 1469–74.
[35] Bell CD, Howard RD, Scott Taylor D, Voss ED, Werpy NM. Outcomes of podotrochlear (navicular) bursa injections for signs of foot pain in horses evaluated via magnetic resonance imaging: 23 cases (2005–2007). *J Am Vet Med Ass* 2009; **234**: 920–5.
[36] McClure S. Extracorporeal shockwave therapy. *Proc Am Coll Vet Soc* 2003.

[37] Bolt DM, Burba DJ, Hubert JD *et al*. Determination of functional and morphologic changes in palmar digital nerves after nonfocused extracorporeal shockwave treatment in horses. *Am J Vet Res* 2004; **65**: 1714–18.
[38] Wright IM. A study of 118 cases of navicular disease: treatment by navicular suspensory desmotomy. *Equine Vet J* 1993; **25**: 501–9.
[39] Pleasant RS, Baker GJ, Foreman JH, Eurell JA, Losonsky JM. Intraosseous pressure and pathologic changes in horses with navicular disease. *Am J Vet Res* 1993; **54**: 7–12.
[40] Jenner F. Navicular disease with core decompression – a new approach. *Proc Euro Coll Vet Soc* 2007; 110–11.
[41] Maher O, Davis DM, Drake C *et al*. Pull-through technique for palmar digital neurectomy: 41 horses (1998–2004). *Vet Surg* 2007; **37**: 87–93.
[42] Harris JM, Kennedy MA. Modified posterior digital neurectomy for management of chronic heel pain in horses. *Proc Am Assoc Equine Pract* 1994; 99–100
[43] Frisbie DD, Kawcak CE, Trotter GW, Powers BE, Walton RM, McIlwraith CW. Effects of triamcinolone acetonide on an in vivo equine osteochondral fragment exercise model. *Equine Vet J* 1997; **29**: 349–59.
[44] Frisbie DD, Kawcak CE, Baxter GM *et al*. Effects of 6alpha-methylprednisolone acetate on an equine osteochondral fragment exercise model. *Am J Vet Res* 1998; **59**: 1619–28.
[45] Story MR, Bramlage LR. Arthroscopic debridement of subchondral bone cysts in the distal phalanx of 11 horses (1994–2000). *Equine Vet J* 2004; **36**: 356–60.
[46] Olive J, Mair TS, Charles B. Use of standing low-field magnetic resonance imaging to diagnose middle phalanx bone marrow lesions in horses. *Equine Vet Ed* 2009; **21**: 116–23.
[47] Dakin SG, Robson KE, Dyson SJ. Fractures of ossified cartilages of the foot: 10 cases. *Equine Vet Ed* 2006; **18**: 130–8.
[48] Murray RC, Dyson SJ, Schramme MC, Branch M, Woods S. Magnetic resonance imaging of the equine digit with chronic laminitis. *Vet Radiol Ultrasound* 2003; **44**: 609–17.
[49] Arble JB, Mattoon JS, Drost WT *et al*. Magnetic resonance imaging of the initial active stage of equine laminitis at 4.7 T. *Vet Radiol Ultrasound* 2009; **50**: 3–12.
[50] Kinns J, Mair TS. Use of magnetic resonance imaging to assess soft tissue damage in the foot following penetrating injury in 3 horses. *Equine Vet Ed* 2005; **17**: 69–73.
[51] Boado A, Kristoffersen M, Dyson S, Murray R. Use of nuclear scintigraphy and magnetic resonance imaging to diagnose chronic penetrating wounds in the equine foot. *Equine Vet Educ* 2005; **17**: 62–8.
[52] Kristoffersen M, Dyson S, Murray R, Schramme M, Boado A. Magnetic resonance imaging and scintigraphic findings in five horses with obscure foot lameness associated with penetrating injuries. *Proc AAEP* 2004; **50**: 320–7.
[53] Zubrod CJ, Barrett MF. Magnetic Resonance Imaging of tendon and ligament injuries. *Clin Tech Eq Pract* 2007; **64**: 217–29.
[54] Cohen JM, Schneider RK, Zubrod CJ, Sampson SN, Tucker RL. Desmitis of the distal digital annular ligament in 7 horses: MRI diagnosis and surgical treatment. *Vet Surg* 2008; **37**: 336–44.

Chapter 21
The fetlock region

21A General

Sue Dyson

INTRODUCTION

The purpose of magnetic resonance imaging (MRI) is to determine the diagnosis for the pain causing lameness, in order to tailor treatment accordingly and establish as accurate a prognosis as possible. Currently knowledge relating to injuries of the fetlock region that are only detectable using MRI is extremely limited [1–7]. This chapter provides a preliminary overview of such injuries based on experience at the Animal Health Trust and a review of the sparse literature.

SELECTION OF HORSES TO UNDERGO MRI OF THE FETLOCK REGION AT THE ANIMAL HEALTH TRUST

The fetlock region is more accessible than the foot for imaging using radiography, ultrasonography, nuclear scintigraphy, arthroscopy and endoscopy, thus the indications for MRI are fewer than in the foot. The primary circumstance when MRI is indicated is if:

1 pain has been localized to the fetlock region using perineural analgesia (i.e. abolition of lameness or significant improvement in lameness by perineural analgesia of the palmar/plantar [at the junction of the proximal three-quarters and distal one-quarter of the metacarpal region] and palmar/plantar metatarsal nerves), or by intrasynovial analgesia of the metacarpophangeal (MCP) (or metatarsophalangeal [MTP]) joint or the digital flexor tendon sheath (DFTS); and

2 there are no radiological or ultrasonographic abnormalities sufficient to explain the degree of lameness; and

3 there is no effusion in the joint (effusion may indicate that arthroscopy is likely to be useful) or arthroscopic evaluation revealed no abnormality; and

4 there is no effusion in the DFTS, warranting endoscopic exploration.

In some instances MRI may give additional information prior to or instead of tenoscopic evaluation of the DFTS.

It should be recognized that palmar (plantar) nerve blocks performed at the level of the base of the proximal sesamoid bones have the potential to influence fetlock region pain. Intra-articular analgesia may also influence

Equine MRI, edited by Rachel C. Murray.

extra-articular structures, such as the proximal aspect of the oblique sesamoidean ligaments (OSLs) and the suspensory ligament (SL) branches. Intrathecal analgesia of the DFTS can influence adjacent structures such as the OSLs or straight sesamoidean ligament (SSL). MRI may also be indicated if there is effusion in the DFTS, but no other detectable ultrasonographic abnormality. While endoscopic evaluation of the DFTS may reveal surface defects of the superficial digital flexor tendon (SDFT), deep digital flexor tendon (DDFT) or manica flexoria, abnormalities of the internal architecture of these structures may only be detected using MRI. Occasionally, in very thick-skinned cob-type horses, it may be physically impossible to image the palmar soft tissue structures ultrasonographically and MRI may be indicated.

SPECTRUM OF INJURY

Between January 2001 and July 2008 102 horses have undergone either high-field or low-field examination of the fetlock region at the Animal Health Trust, approximately half of which also underwent examination of the digit because of suspected concurrent injuries. Injuries included stress-related bone injury in young Thoroughbred racehorses, defined as acute if there was evidence of increased signal intensity in the bone in fat-suppressed images ($n = 9$) or chronic ($n = 10$), and one horse had a transverse fracture of the distal aspect of the third metacarpal bone. Six mature sports horses had acute subchondral bone trauma, including two with concurrent insertional desmopathy of a SL branch and six had chronic subchondral bone trauma, including one with desmitis of an OSL. A further two horses had an incomplete fracture of the proximal aspect of the proximal phalanx (both suspected radiologically, but not confirmed). Two horses had SDFT injury within the DFTS and a third had desmitis of the plantar annular ligament (PlAL) and associated injury of the SDFT. One horse, examined at the owner's request, had dorsal abrasions of the DDFT in the proximal pastern region and distension of the DFTS. One horse had desmitis of the proximal digital annular ligament and one had lesions of the SDFT and DDFT associated with a fibrous mass on the plantar aspect of the proximal pastern. Sixty-one additional horses had injuries of the OSL ($n = 26$, including two with injuries of the SSL and one with injury to a SL branch), SSL ($n = 33$) or cruciate sesamoidean ligament ($n = 3$, including two with injuries of the OSL). In only two horses was an injury to a distal sesamoidean ligament the sole cause of lameness; five horses had injuries of more than one distal sesamoidean ligament and/or a SL branch as the principal cause of lameness; the majority had other lesions in the digit contributing to lameness.

OTHER DOCUMENTED LESIONS IN THE FETLOCK

Magnetic resonance imaging has also been used to diagnose osteoarthritis of the MCP/MTP joint [6] (often associated with obvious radiological abnormalities), osseous cyst-like lesions (OCLLs) [6] and injury of the collateral ligaments (CLs) of the MCP or MTP joint [4]. Other lesions that

have been identified in horses examined using MRI postmortem, but which were not identified premortem using conventional imaging modalities, include intersesamoidean ligament injury and abnormalities of the proximal sesamoid bones (PSBs) (Smith M, personal communication, 2009).

OPTIONS FOR CLINICAL MANAGEMENT

Stress-related bone injury in young Thoroughbred racehorses

Although nine horses were classified as having acute injuries, the majority of these had evidence of abnormal mineralization of the condyles of the third metacarpal/metatarsal bone, reflecting previous bone injury. The majority of horses with both acute and chronic subchondral bone injuries had shown intermittent lameness of variable severity for several months and had failed to respond previously to intra-articular medication with triamcinolone and hyaluronan. One horse with relatively acute lameness had a suspected condylar fracture based on MRI examination, not previously detected radiologically. Radiological reassessment after 21 days revealed an incomplete fracture.

The majority of horses were treated by box rest and a prolonged ascending walking exercise programme with systemic treatment with aspirin or tiludronate. Two horses underwent arthroscopic evaluation of the joint, but no visible lesions were identified. The majority of horses were never able to withstand full training. This is consistent with a previous report of two racehorses with condylar pathology, both of which improved with rest but had chronic recurrent lameness when training was resumed [1]. In the current series, two horses have undergone follow-up MRI and major lesions have persisted. One horse with bilateral hind limb lameness, which was maintained in training, sustained a catastrophic hind limb lateral condylar fracture.

Based on the results of a single Standardbred racehorse in which a radiolucent lesion was identified in the palmar aspect of a condyle of the third metacarpal bone, there may be a role for arthroscopic debridement if a focal articular cartilage and subchondral bone defect was identified [8]. It is interesting to speculate whether earlier recognition of subchondral bone injury and initiation of rest at that stage would influence the prognosis.

Subchondral bone trauma in mature horses

In mature sports horses with evidence of acute subchondral bone trauma of either the distal aspect of the third metacarpal (metatarsal) bone or, less commonly, the proximal aspect of the proximal phalanx, treatment comprised box rest and controlled walking exercise for 3–6 months. The duration related to time taken for lameness to resolve. Some horses received a single intravenous infusion of tiludronate. The majority of horses had no evidence of joint effusion or cartilage pathology and therefore did not receive intra-articular medication. Horses with associated increased radiopharmaceutical uptake (IRU) underwent follow-up scintigraphic examination at 3 months and there was marked reduction in IRU. In contrast to the young

Thoroughbred racehorses, in the majority of horses there was slow but complete resolution of lameness and horses were able to return to full athletic function. Two mature sports horses with acute subchondral bone injury have been previously documented, one of which underwent arthroscopic evaluation because the bone lesion appeared to communicate with the joint [1]. An area of fibrillated cartilage overlying defective subchondral bone was identified and curettaged. Both horses were able to resume light work by 6 months after diagnosis, but both had recurrent lameness due to unrelated causes.

Horses with focal areas of marked reduced signal intensity in both T1- and T2-weighted images consistent with mineralization and no detectable abnormalities in fat-suppressed images were classified as having chronic subchondral bone injury. These horses usually had normal radiopharmaceutical uptake. One horse underwent arthroscopic exploration with negative results. These horses were treated similarly to those with acute injuries, but the majority had persistent lameness.

In the mature horses examined at the Animal Health Trust using high-field or low-field MRI, the majority had no definitive abnormalities of the articular cartilage, although some had focal areas of increased signal intensity in all image sequences in the adjacent subchondral bone. This is in contrast to the results of Sherlock *et al*. [6], who recorded the presence of cartilage abnormalities in nine of 13 horses with subchondral bone injury in the fetlock identified using low-field MRI. However, the lesions in the subchondral bone of the third metacarpal/metatarsal condyles and the proximal aspect of the proximal phalanx were similar, although five horses also had evidence of CL injury. Follow-up information was available for 11 horses, six of which were sound and in full work in a variety of disciplines after an unspecified period of rest and a variety of treatments including non-steroidal anti-inflammatory drugs, extracorporeal shockwave therapy, intra-articular medication with corticosteroids, hyaluronan or interleukin-1 receptor antagonist and remedial farriery. The results in this study did not show any difference in response to treatment between horses with or without increased signal intensity in STIR images, in contrast to experience at the Animal Health Trust.

Incomplete fractures of the proximal phalanx

Two horses with an incomplete fracture of the proximal aspect of the proximal phalanx were managed conservatively by box rest and a controlled ascending exercise programme over 3 months. Follow-up scintigraphic examination revealed marked reduction in IRU. Both horses returned to full athletic function, subsequently competing internationally in show jumping and eventing respectively.

Superficial and deep digital flexor tendon injury

One racehorse with SDF tendonitis underwent follow-up MR examination after 6 months; abnormal signal intensity in T1-weighted images persisted. The horse resumed training, but subsequently changed trainers and was lost

to follow-up. An international level show jumper with fibrillation of the dorsal aspect of the DDFT underwent endoscopic debridement (as recommended before MRI), followed by intrathecal medication using hyaluronan, and returned to full athletic function. A pony with PlAL desmitis and SDF tendonitis was treated by desmotomy of the PlAL; the DFTS was explored endoscopically but no abnormality was seen. Lameness has persisted. This is consistent with previously documented results for treatment of PlAL injury [9]. Horses with desmitis of the proximal digital annular ligament or SDFT and DDFT lesions associated with overlying fibrous tissue had persistent lameness, despite prolonged periods (>9 months) of rest, controlled exercise and physiotherapy.

Distal sesamoidean ligament injury

Although injuries of a distal sesamoidean ligament were common, in only two horses was the injury the sole cause of lameness. One horse with a severe injury of the SSL underwent endoscopic inspection of the DFTS and ultrasound-guided injection of cultured mesenchymal stem cells. Lameness persisted and the horse was retired as a broodmare. One horse with a proximal OSL injury was able to return to full athletic function after a 6-month rest and controlled exercise rehabilitation programme. Three horses with combined lesions of the OSL and cruciate sesamoidean ligament (CrSL) or OSL and SL branch have been treated by rest, controlled exercise and radial pressure wave therapy and are now in moderate work, but have not yet returned to full athletic function.

In contrast, 27 horses have been documented with primary injuries of the OSL ($n = 18$), SSL ($n = 3$) or a combination of OSL and SSL injury ($n = 6$) [5]. All horses underwent a box rest and controlled walking exercise programme over 6 months. Ultrasound-guided ligament splitting was performed in two horses. Telephone follow–up information was available for 21 horses, 76% of which returned to full athletic function in a variety of disciplines. There was a trend for horses with lameness of less than 4 months' duration to do better than horses with lameness of longer duration, and for horses with lesions graded as mild or moderate to do better than those with severe lesions. These results compare favourably with previous reports of injuries of the OSLs diagnosed ultrasonographically. It is currently not known whether injuries that are not detectable ultrasonographically, but which are identified using MRI, are less severe than a lesion seen ultrasonographically, and therefore more likely to respond to treatment.

Currently there is no documented follow-up of the management of either OCLLs of primary CL injury of the fetlock diagnosed using MRI.

REFERENCES

[1] Zubrod C, Schneider R, Tucker R, Gavin P, Ragle C, Farnsworth K. Diagnosis of subchondral bone damage using magnetic resonance imaging in eleven horses. *J Am Vet Med Assoc* 2004; **24**: 411–18.

[2] Dyson S, Murray R. Osseous trauma in the fetlock region of mature sports horses. *Proc Am Assoc Equine Pract* 2006; **52**: 450–6.

[3] Dyson S, Murray R. Magnetic resonance imaging of the equine fetlock joint. *Clin Tech Equine Pract* 2007; **6**: 62–77.
[4] Schramme M, Redding R. Early diagnosis of joint disease. *Proc Vet Orthopaedic Soc*, Keystone, 2006, pp. 61–2.
[5] Sampson S, Schneider R, Tucker R, Gavin P, Zubrod C, Ho C. Magnetic resonance imaging features of oblique and straight distal sesamoidean desmitis in 27 horses. *Vet Radiol Ultrasound* 2007; **48**: 303–11.
[6] Sherlock C, Mair T, ter Braake F. Subchondral bone damage in the fetlock region diagnosed using low-field magnetic resonance imaging in standing horses. *Vet Radiol Ultrasound* 2009; **50**: 13–20.
[7] Smith S, Dyson S, Murray R. Magnetic resonance imaging of distal sesamoidean ligament injury. *Vet Radiol Ultrasound* 2008; **49**: 516–28.
[8] Byron C, Goetz T. Arthroscopic debridement of a palmar third metacarpal condyle subchondral bone injury in a Standardbred. *Equine Vet Educ* 2007; **19**: 344–50.
[9] Owen R, Dyson S, Parkin T, Singer E, Kristoffersen M, Mair T. A retrospective study of palmar (plantar) annular ligament injury in 71 horses: 2001–2006. *Equine Vet J* 2008; **40**: 237–44.

21B Thoroughbred racehorses

Sarah Powell

INTRODUCTION

Between June 2006 and June 2009 146 horses have undergone standing MRI of the fetlock region at Rossdales Equine Diagnostic Centre. Of these, 107 were Thoroughbred horses used for racing (flat and over fences), 84 of which have remained under the care of the practice and are available to follow-up. Maximum follow-up is 144 weeks, with a minimum of 2 weeks. Mean follow-up is 74 weeks and median follow-up is 18 weeks. The reason for these 84 horses undergoing MRI was to further evaluate known or suspected pathology in the region of the metacarpophalangeal or metatarsophalangeal joint. No horses had been diagnosed with a definitive, causative lesion on other imaging modalities, including radiography and ultrasonography and in some cases scintigraphy. All horses showed mild or moderate lameness (grade 1–3/5), which had been localized to the fetlock joint by diagnostic local anaesthesia in 81 of 84 horses within 1 week of MR imaging. Three of 84 horses did not undergo diagnostic local analgesia due to the presence of a marked pain response when digital pressure was applied to the dorsoproximal aspect of the proximal phalanx. The majority of horses had a history of fetlock lameness unresponsive to intra-articular low-dose corticosteroid medication. A number had a recent history of marked lameness seen after fast work, with or without a previous history of fetlock lameness. Others had a recent history of fetlock lameness with no previously reported lameness related to the fetlock joint.

LESIONS DETECTED

There are a number of lesions that may be considered to be the primary cause of lameness in Thoroughbred racehorses undergoing MRI examination of the fetlock region with equivocal radiographic, ultrasonographic and nuclear scintigraphic images. The spectrum of lesions detected in these 84 racehorses included:

- subchondral bone injury of the distal metacarpal or metatarsal condyles (including bone mineral densification/subchondral stress reaction/subchondral stress fracture and overt cortical stress fracture and subchondral bone necrosis)

Equine MRI, edited by Rachel C. Murray.

- soft tissue injuries (suspensory ligament branch injuries/oblique distal sesamoidean ligament injuries/synovial and capsular injuries)
- cartilage lesions (articular/dorsal fibrocartilage erosions)
- injuries to the proximal phalanx (prodromal stress fractures/non-healing fracture/bone 'contusions'/dorsoproximal fragmentation)
- injuries to the proximal sesamoid bones.

Many had multiple pathologies, in which case the diagnosis was based on the lesion considered most likely to be of primary significance. In two cases the cause of lameness was not elucidated.

Stress injuries

Twenty-six of the 84 horses (30.9%) had subchondral bone changes consistent with a spectrum of stress injury to the distal third metacarpal/metatarsal condyles. This was seen as bone marrow oedema-type (BMO-t) signal pattern (T1 hypointensity, T2* and short τ inversion recovery [STIR] hyperintensity) within the cancellous bone of the palmar/plantar apical region. Fifteen of the 26 were classified as stress reaction with no evidence of cortical stress fracture and 11 of the 26 were classified as stress reaction with the presence of cortical stress fracture within the region of the sagittal groove. Of these 11 cases with breach of the cortical bone on MR images, this diagnosis could not be made with certainty from the radiographs taken at the time of the MRI examination. Five of these horses showed a clear linear lucency consistent with the presence of an incomplete condylar stress fracture when follow-up radiographs were taken between 3 and 4 weeks after the MRI examination. Six of the 84 horses had focal subchondral bone injuries close to the joint margin with no surrounding stress reaction within the cancellous bone. These were often at more variable sites within the joint rather than within the sagittal grooves of the palmar apical region.

Six of the 84 horses had radiographically evident condylar fissure fractures within the distal third metacarpal/metatarsal condyles (five forelimbs, one hind limb). These had been diagnosed previously and the horses had been trained and raced successfully despite the presence of these fissures. All of these cases had been managed with corticosteroid medication of the joint containing the fissure. MRI was undertaken in these cases due to a recent history of more marked lameness unresponsive to corticosteroid medication. Of these cases, four were considered 'active' fissures due to the presence of marked BMO-t signal pattern in the cancellous bone surrounding the fissure. These horses were considered at risk of sustaining complete fractures should they continue in training. Two of the 6 were classified as 'inactive' fissures, and not considered the primary cause of lameness.

Subchondral bone necrosis

Five of the 84 horses were found to have end-stage subchondral bone disease (one unilateral forelimb, four bilateral hind limbs) due to the presence of subchondral bone necrosis and loss of subchondral support to the cartilage leading to palmar cortical fragmentation.

Dorsal epiphyseal erosive lesions

Six of the 84 horses were found to have severe erosions of the fibrocartilage in the dorsal epiphyseal region of the joint. These cases had marked subchondral bone densification within the cancellous bone. Two of the six had marked BMO-t signal pattern within the dorsal aspect of the distal metacarpal/metatarsal condyles. In four of the six horses the bone and cartilage changes extended over the dorsal aspect of the sagittal ridge.

Pathology in the proximal phalanx

Thirteen of the 84 horses (14.3%) were found to have injuries to the proximal phalanx. Of these 10 were classified as incomplete sagittal fractures. Two of the 10 had no signal abnormalities in the cortical bone but marked bone oedema-type signal pattern in the cancellous bone and were therefore classified as stress reactions which were thought to represent prodromal stress fractures [1]. Eight of the 10 had cortical fractures and all of these cases had evidence of pre-existing pathology in the form of thickening of the subchondral bone plate of the dorsoproximal articular angle of the proximal phalanx. Two of the 13 cases were classified as bone 'contusions' of the proximal articular surface of the proximal phalanx. One horse had a large non-displaced fragment of the dorsomedial eminence of the proximal phalanx not visible radiographically. Of the six (of 10) horses diagnosed with sagittal fractures that underwent repeat radiography 4 weeks after the MRI examination, four showed periosteal new bone formation on the dorsoproximal aspect of the proximal phalanx.

Pathology in the proximal sesamoid bones

In five of the 84 horses the primary cause of lameness was found to be the medial or lateral proximal sesamoid bone; two of the five had non-displaced fractures of the medial proximal sesamoid bone, one had BMO-t signal within the medial proximal sesamoid bone and one had desmitis of the intersesamoidean ligament with marked changes at the insertion of the ligament on the axial border of the lateral proximal sesamoid bone. All five horses showed abnormal bone mineral densification of the affected proximal sesamoid bone.

Soft tissue lesions

Nine of the 84 horses were found to have significant soft tissue lesions not visible or underestimated on ultrasonographic examinations prior to the MRI examination and considered to be the primary cause of lameness. These included suspensory ligament branch injury ($n = 1$), villonodular synovitis ($n = 2$), chronic proliferitive synovitis ($n = 3$), oblique distal sesamoidean ligament injuries ($n = 3$).

TREATMENT AND FOLLOW-UP

Only horses that remained under the care of Rossdale & Partners were included in these figures. Follow-up consisted of conversations with the

treating Rossdale & Partners veterinary surgeon and/or via clinical case records. Racing performance was obtained from the *Racing Post* website. Six horses had been euthanized due to persistent fetlock lameness. Three were euthanized due to unrelated causes. Twelve have been retired from racing either to stud or to be retrained for other disciplines. Sixty-three of the 84 (75%) horses that underwent MRI examination remained in training or pre-training yards; 38 of the 84 (45%) returned to racing. Thirty-eight of the 63 (60%) that remained in training returned to racing. Thirteen of 26 (50%) horses with metatarsophalangeal joint lameness and 25 of 58 (43%) with metacarpophalangeal joint lameness have raced since the MRI examination. The mean return to racing in forelimb injuries was 7 weeks. The mean return to racing in hind limb injuries was 15 weeks.

Horses considered at imminent risk of sustaining complete fractures of the proximal phalanx ($n = 10$) or palmar/plantar metacarpal/metatarsal condyles ($n = 14$) were box rested for 4–6 weeks prior to undergoing repeat radiography. Several of these horses underwent intra-articular medication of the joint prior to undergoing the period of box rest. Two horses underwent surgical lag screw fixation of an incomplete lateral condylar stress fracture of the forelimb under standing sedation. Two horses underwent surgical lag screw fixation of the medial condyle of the hind limb. Six of 11 (55%) horses with pre-fracture changes of the condyle have returned to racing (mean 26 weeks). Of six horses with fissure fractures three have returned to racing (mean 19 weeks). Horses with focal subchondral bone injuries not consistent with imminent risk of fracture ($n = 6$) were treated with variable amounts of rest and intra-articular medication with corticosteroid/IRAP depending on the proximity of racing. Of these, two (33%) have returned to racing (mean 10 weeks).

Horses with mild generalized BMO-t signal pattern within the condyles not considered at imminent risk of fracture ($n = 15$) were continued in walking exercise. The majority were treated with corticosteroid medication of the joint(s) with or without intravenous infusion or injection of bisphosphonate tiludronate (Tildren). A number were given short courses of oral phenylbutasone (Bute). Of these 15, nine (60%) have returned to racing (mean 26 weeks).

Horses with end-stage subchondral bone disease ($n = 5$) with the presence of subchondral bone necrosis and palmar cortical fragmentation were treated with an extended period of rest and intra-articular corticosteroid medication. All have received subsequent corticosteroid medications. One that had bilateral/biaxial MRI findings consistent with plantar cortical subchondral bone necrosis and collapse of the overlying cortical bone in the metatarsal condyles returned to racing at 53 weeks post-MRI and has continued to race with some success (total follow up 112 weeks).

Dorsal erosions of the distal metacarpal/metacarsal condyles ($n = 6$) were treated with either corticosteroid medication of the joint or IRAP therapy or a combination of both. One (16%) returned to racing after 20 weeks.

Horses with soft tissue injuries were treated with intra-articular corticosteroid or IRAP medication. Several horses underwent an initial corticosteroid medication prior to undergoing a course of IRAP therapy. Three horses had a course of three extracorporeal shockwave therapy due to the

presence of suspensory ligament branch injury or oblique distal sesamoidean ligament injury. Four of 11 (36%) horses diagnosed with soft tissue injuries returned to racing (mean 14 weeks).

MONITORING FETLOCK PATHOLOGY ON MRI – GENERAL OBSERVATIONS

Sixteen of 84 horses underwent repeat MRI examination of the same site between 8 and 20 weeks after the initial scan. The majority of these were carried out to monitor the resolution of BMO-t signal pattern within the distal metacarpal/metatarsal condyles. Generally speaking, BMO-t signal seen in cases diagnosed with subchondral stress reaction of the condyles with minimal radiographic change initially and at follow-up, which had only a recent history of fetlock lameness, was seen to resolve on follow-up MR images as the horses returned to soundness – although concurrent bone mineral densification patterns remained static or worsened during that time. Those that subsequently developed radiographic signs of focal subchondral bone injuries showed a significant reduction in BMO-t signal within the cancellous bone with time, although a focal region, hyperintense on all sequences, often remained at the joint margin likely to represent bone necrosis subsequent to the initial insult. Sagittal fractures of the proximal phalanx heal to leave marked hypointensity on T1-weighted images within the proximal aspect of the proximal phalanx. The BMO-t signal has been observed to resolve completely on follow-up MR images. In non-healing sagittal fractures a linear area of hyperintensity on all sequences remains at the dorsal articular margin. Resolution of soft tissue injuries on MR images appears to lag behind resolution of clinical lameness.

DISCUSSION

The horses included here represent a relatively specific group of Thoroughbred horses used for racing aged between 2 and 5 years, which underwent MRI examination of the fetlock region because other imaging had not revealed a definitive cause of lameness. The majority of horses had some degree of radiographic abnormality of the proximal phalanx or distal metacarpal/metatarsal condyles. However, the radiographs were either inconclusive or not thought to explain the degree of lameness. In this group, 49 out of 84 (58%) were diagnosed with condylar pathology as the primary cause of lameness. Of these, 22 (45%) have returned to racing. Other reports concerned with outcome of horses with condylar pathology detected on MRI consist of few cases [2] and data specific for Thoroughbreds are yet to be available. Figures from The Animal Health Trust included here support the conclusion that the majority show recurrent lameness.

Patterns of abnormal bone mineral densification of the distal metacarpal and metatarsal condyles are virtually ubiquitous in Thoroughbred racehorses (and other horses competing at maximum speeds). Normal loading-related densification patterns are yet to be established. Many cases also show multiple regions of cortical and cancellous bone-related change, and

mixed bone mineral densification and fluid signal patterns, indicating both chronic and acute pathology. In some cases this can confound the differentiation of significant pathology from more benign, loading-related changes. Many cases undergo multiple treatments preventing useful comparisons between treatments. Meaningful follow-up with respect to return to racing is confounded by inherent variables between cases. The time from initial injury to return to racing may be influenced by many factors, including subsequent related or unrelated lameness and the time of year the injury is sustained, making this an unreliable assessment of the true convalescence period for specific pathologies detected on MRI. It is also worth bearing in mind that a return to racing does not infer a complete resolution of the lameness.

REFERENCES

[1] Ramzan PHL, Powell SE. Clinical and imaging features of suspected prodromal fracture of the proximal phalanx in three Thoroughbred racehorses. *Equine Vet J* 2010; **42**: 164–9.

[2] Zubrod C, Schneider R, Tucker R, Gavin P, Ragle C, Farnsworth K. Diagnosis of subchondral bone damage using magnetic resonance imaging in eleven horses. *J Am Vet Med Assoc* 2004; **24**: 411–18.

Chapter 22
The metacarpal/metatarsal region

22A US perspective

Matthew Brokken and Russell Tucker

INTRODUCTION

There has been a wealth of information documenting treatment and outcome of metacarpal/metatarsal injuries diagnosed with ultrasonography, radiography and nuclear scintigraphy [1–10]. However, information regarding treatment and follow-up for horses with metacarpal/metatarsal injuries diagnosed with high-field magnetic resonance imaging (MRI) is extremely limited [11, 12]. This chapter will discuss common treatments for metacarpal/metatarsal injuries and the use of MRI to help determine which treatment(s) will be the most effective at returning horses to performance.

FORELIMB PROXIMAL SUSPENSORY DESMITIS

Most horses with injury to the forelimb proximal supensory ligament (PSL) have a good prognosis for return to performance with an adequate rest and controlled exercise programme. Some reports state that the prognosis for return to full athletic function is 90% for acute injuries [9]. However, with chronic forelimb suspensory injuries it can be more difficult to achieve a successful outcome. Crowe *et al*. [13] reported that 53% of horses with lameness for over 3 months returned to performance 6 months following treatment with radial pressure wave therapy. In a study evaluating desmoplasty and fasciotomy of the PSL, three of four horses with chronic desmitis returned to full work [8]. Some have also recommended the use of osteostixis for those horses with osseous abnormalities at the PSL [14].

The use of autologous cell-based therapy for suspensory injuries has also been recently advocated [15–17]. The most popular include platelet-rich plasma and mesenchymal stem cells (bone-marrow derived and adipose derived). Research demonstrating their clinical effectiveness is lagging behind their availability to equine veterinarians; however, some initial reports have been favourable. The purpose of these therapies is to promote early granulation of defects, optimize collagen type I production, and minimize scar tissue formation [15]. Further research is needed in this area regarding treatment of horses with PSL injury diagnosed with MRI. The extent of injury may be less severe than those horses diagnosed with ultrasound and it is

Equine MRI, edited by Rachel C. Murray.

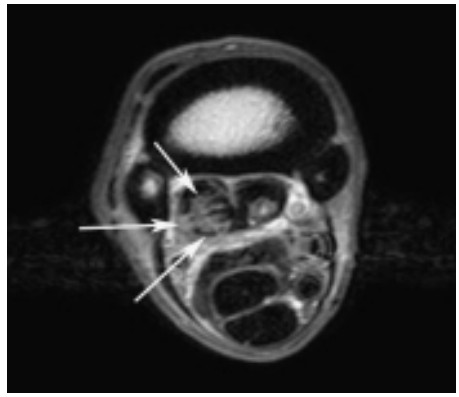

Figure 22.1 Transverse proton density image of a horse with proximal suspensory desmitis (arrows). This horse was placed in a 6-month rest and rehabilitation programme and returned to its previous level of performance.

unknown if these horses will respond to a greater degree to the regenerative therapies.

The authors have had success placing horses with forelimb PSL injuries in a 6-month rest and rehabilitation programme (Figure 22.1). The programme begins with horses confined to a box stall with 5–10 minutes of hand walking daily that is slowly increased to 30–40 minutes. After 60 days, horses are turned out in a small paddock and also begin trotting, starting with 5 minutes and increasing to 15–20 minutes a day. If the horses are trotting sound after 4 months, the level of exercise is increased to walk-trotting under saddle. Repeat ultrasound evaluations are encouraged if the injury was originally diagnosed with ultrsonography. Horses are not turned out in a large field and are not returned to regular training until 6 months from the start of the programme. Some horses receive peri-ligamentous injection of a combination of isoflupredone acetate, betamethasone sodium phosphate and acetate, and polysulfated glycosaminoglycans with the goal of decreasing inflammation prior to starting the rehabilitation programme.

Eighty per cent of horses with forelimb proximal suspensory desmitis identified with high-field MRI returned to the same or higher level of performance than before their injury [12]. All of these horses were placed in a 6-month rest and rehabilitation programme. One horse in this study did have ligament-splitting surgery on the PSL due to the severe fibre disruption and lack of response to conservative therapy. This horse returned to a higher level of performance than before the injury. Two horses remained lame with lameness attributable to the PSL. There was no correlation between the severity of MR findings and prognosis for the horses to return their intended use. Accurate diagnosis with MRI will help in determining a prognosis for athletic horses in the future.

HIND LIMB PROXIMAL SUSPENSORY DESMITIS

Most horses with acute proximal suspensory desmitis of the forelimb respond well to stall rest and a regime of controlled exercise for 6 months.

However, in the hind limb, the prognosis is much lower and in a large number of horses lameness persists or reoccurs with exercise. To date, a wide variety of treatments have been used for hind limb suspensory ligament injuries, including rest and controlled exercise [3, 5], internal blistering [18], peri-lesional autogenous bone marrow injection [19], extracorporeal shock and radial wave therapy [13, 20], percutaneous osteostixis [14], tibial neurectomy [21], fasciotomy with neurectomy [10], and desmoplasty and fasciotomy [8]. The number and variety of treatments demonstrate the difficulty in healing this area and returning these horses to their intended use.

Treatment of hind limb PSL desmitis remains a frustrating condition for equine veterinarians due to the persistence or recurrence of lameness with exercise. Estimates of horses that return to performance without residual lameness from hind limb proximal suspensory ligament desmitis range from 14 to 58% [5, 13, 22].

Extracorporeal shockwave (ESWT) or radial pressure wave therapy (RPWT) has had varying success in some horses with PSL injury [13, 23]. In the report by Crowe *et al*. [13], 41% of horses with lameness greater than 3 months were sound and returned to work 6 months after treatment with radial pressure wave therapy. In a study with collagenase-induced suspensory desmitis, treatment of affected ligaments with ESWT resulted in significantly greater decreases in ligament area, area of the lesion within the ligament and proportion of the ligament affected by the lesions than that of controls [23]. However, this study was performed on collagenase-induced injury in the suspensory body and not the proximal aspect of the ligament.

Some have hypothesized that the poor prognosis and persistent lameness is due to a compartment syndrome from the enlarged PSL causing compression on the plantar metatarsal nerves due to the restriction from the inelastic plantar metatarsal fascia [10] (Figure 22.2). Pathologic examination of the deep branch of the lateral plantar nerve in horses with proximal suspensory

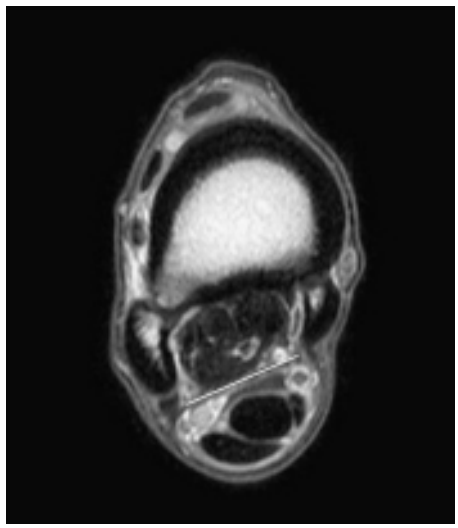

Figure 22.2 Transverse proton density image of a horse with hind limb proximal suspensory desmitis. The white line depicts the region of the plantar metatarsal fascia. Note that the region the suspensory ligament has to expand is limited by the fascia and the metatarsal bones.

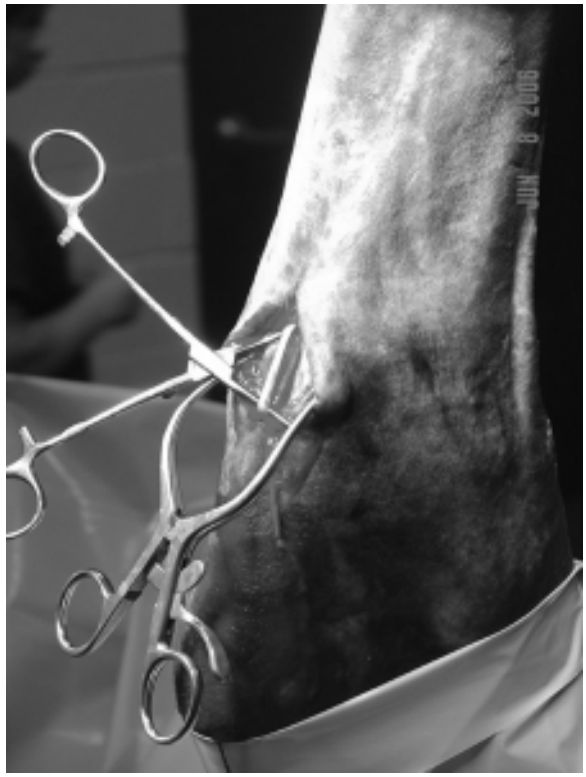

Figure 22.3 Intra-operative image of the deep branch of the lateral plantar nerve before transection (between haemostats). Image courtesy of Dr Chad J. Zubrod, Oakridge Equine Hospital, Edmond, OK.

desmitis revealed evidence of chronic nerve compression [24]. The section of nerve removed was proximal to the restricting deep plantar fascia however; lameness was resolved in over half of the horses with just removal of the nerve without fasciotomy of the plantar metatarsal fascia (Figure 22.3).

Recently, new surgical procedures have been aimed at decompression, desensitization and promoting angiogenesis of the injured PSL [8, 10]. The desmoplasty and fasciotomy procedure described by Hewes *et al*. [8] involves ultrasound guidance of a scalpel blade or ligament knife to the core lesion and proximal-to-distal movement of the blade. At the PSL origin, the blade was advanced through the core lesion to score the bone surface. Desmoplasty and fasciotomy allowed 20 of 23 horses (85%) with hind limb proximal suspensory desmitis to return to full work after a rest and rehabilitation programme [8]. All these horses had ultrasonographic evidence of core lesions and follow-up was not available in seven other horses in which the procedure was performed.

The most popular surgical procedure of late has been plantar metatarsal neurectomy and fasciotomy as described by Bathe [10]. It is believed that the thick plantar metatarsal fascia restricts the expansion of the injured PSL leading to a local compartment syndrome and compression of the plantar metatarsal nerves. The premise for developing this surgical procedure was

that persistent lameness is due to both compartment syndrome and chronic local nerve irritation. In horses with desmitis of the PSL without other adjacent abnormalities, neurectomy and faciotomy alone are performed. In horses with severe ultrasonographic abnormalities in the ligament, these horses are injected with some type of autologous cell-based therapy in addition to the surgery. In horses with abnormalities in the ligament and its osseous insertion, osteostixis is performed as well as surgery. Bathe [10] reports success rates of 79% in horses that underwent neurectomy and fasciotomy alone. With cell-based injections and surgery, the success rate was reported to be 84%. Only 55% of those horses with ligament and osseous damage returned after surgery. The surgery is contraindicated in horses with straight hind limb conformation or excessive extension in the metatarsophalangeal joints [9].

In a study by Brokken *et al*. [12] examining horses with hind limb PSL injuries diagnosed with MRI, nine of 13 (69%) horses were able to return to their intended use. Eleven of the horses were placed in a 6-month rest and rehabilitation programme as described for the forelimb. Two of these horses were treated with fasciotomy and neurectomy of the deep branch of the lateral plantar nerve then placed in rest and rehabilitation programmes. Both of these horses had chronic lamenesses that had not responded to other conservative treatments and had severe lesions with marked enlargement and high signal on MR images. One of the two horses that underwent fasciotomy and neurectomy surgery was performing at a higher level than before the injury and the other horse was still lame at the time of follow-up.

SUSPENSORY LIGAMENT ADHESIONS TO SPLINT EXOSTOSES

Axial exostoses of the small metacarpal/metatarsal (splint) bones can result in adhesions to the suspensory ligament and associated desmitis. Most horses with splint exostosis have lameness that is mild and that usually improves with rest or decreased level of exercise [25, 26]. However, in some horses lameness persists and these horses may be sensitive to digital pressure over the affected area. Zubrod *et al*. [11] reports that suspensory desmitis is the result of adhesion of the suspensory ligament to the exostosis. The adhesion then results in abnormal tensile strain within the ligament, causing tearing of the ligament fibres leading to inflammation. Characterization of the adhesion and the extent of desmitis was easily discernable with the use of a high-field strength magnet.

Treatment involves surgical removal of the splint exostosis as well as the adhesions to the suspensory ligament. Prognosis after surgical removal and resolution of the suspensory desmitis is good. All four horses with MR evidence of adhesions from a second metacarpal bone exostosis to the suspensory ligament returned to their intended use with surgical removal of the exostosis and a 6-month rest and rehabilitation programme [11]. The programme consisted of stall rest for 60 days with hand-walking started 2 weeks after surgery. After 60 days, horses began light jogging in hand and were turned out to a small paddock (30×30 feet). Horses were not allowed

to return to training or turned out into a large field for free exercise until 6 months from the start of the programme.

ACCESSORY LIGAMENT OF THE DEEP DIGITAL FLEXOR TENDON

Injury to the forelimb accessory ligament of the deep digital flexor tendon (ALDDFT) has been recognized as a cause of lameness in horses [4, 6]. There has been a wide success rate of horses that return to their previous level of performance following conservative management with one success rate of 18% [27] and another with a complete functional recovery of 76% [4]. The long-term prognosis for horses with desmitis of the ALDDFT has been stated to be guarded, with 43% of horses returning to their previous level of performance [6]. Injury to the hind limb ALDDFT has been recently described by Eliashar *et al*. [28] in a case report of 23 horses. These horses were all diagnosed with ultrasonographic examination. Seventy-three per cent of horses with acute onset unilateral lameness and 90% of horses with insidious or sudden onset of postural abnormality returned to previous work.

Most horses with injury to the ALDDFT are treated conservatively with rest and controlled exercise with or without the addition of ESWT and/or injection of anti-inflammatory medications around the ligament. In a recent study conducted by the authors, the most common finding of horses with lameness localized to the proximal metacarpal region and then imaged with high-field strength MR, was ALDDFT desmitis (59%) [12]. Treatment of the horses diagnosed with ALDDFT desmitis was determined by the severity and duration of the injury. Horses with acute lesions and mild MR abnormalities were placed in rest and rehabilitation programmes similar to the horses with PSL injuries. Some of these horses had the area around the injured ALDDFT injected with a combination of isoflupredone acetate, betamethasone sodium phosphate and acetate, and polysulfated glycosaminoglycans prior to starting the rest and rehabilitation programme. Horses with moderate or severe MR changes or chronic lameness that had not responded to conservative treatment had ALDDFT desmotomy performed. The premise behind ALDDFT desmotomy is to eliminate the chronic tearing that occurs in the injured ligament and to create a functionally longer ligament when it heals [29]. In the study by Brokken *et al*. [12], five of eight horses (63%) with ALDDFT desmotomy returned to their intended use. The success of this procedure in these horses further supports the importance of making an accurate diagnosis with the aid of MR imaging. Horses with desmitis of the ALDDFT have a surgical option that is not appropriate for horses with PSL injury.

CONCLUSIONS

The use of MRI may allow earlier detection of injuries in the metacarpal/metatarsal region as well as more accurate characterization of the nature of

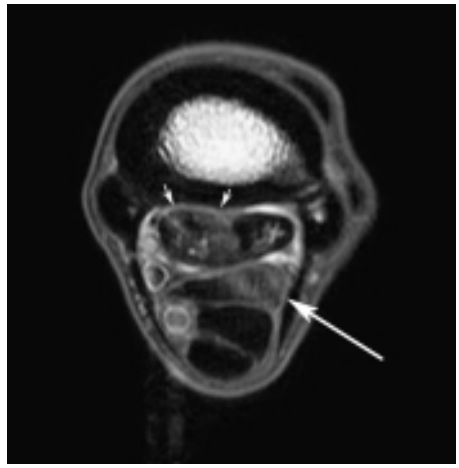

Figure 22.4 Transverse proton density image of a horse with damage to the proximal suspensory ligament (small arrows) as well as the accessory ligament of the deep digital flexor tendon (large arrow).

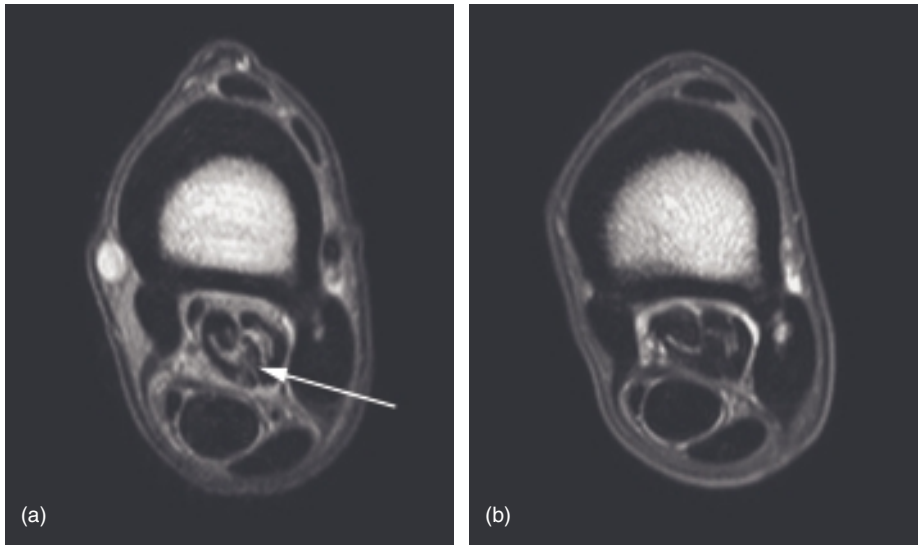

Figure 22.5 Transverse proton density images of a horse with proximal suspensory desmitis (a) and follow-up MR examination after 7 months of a rest and rehabilitation programme (b). The region of high signal intensity has been replaced with low signal intensity tissue within the ligament.

the injury, be it primarily ligamentous, osseous or a combination (Figure 22.4). This knowledge will help determine what the optimal treatment for each horse should be. Follow-up MR examinations have been performed on only a very small number of horses to determine the appearance of healed or healing injuries in the metacarpal/metatarsal region (Figure 22.5). Characterization of the injuries leading to more appropriate treatment and then accurate, long-term follow-up on the horses is needed to establish a prognosis for the different injuries. This information may also provide insight into the methodology of injury as well as guide treatment.

REFERENCES

[1] Bramlage LR, Gabel AA, Hackett RP. Avulsion fractures of the origin of the suspensory ligament in the horse. *J Am Vet Med Assoc* 1980; **176**: 1004–10.
[2] Dyson S. Some observations on lameness associated with pain in the proximal metacarpal region. *Equine Vet J* 1988; **6**(Suppl.): 43–52.
[3] Dyson S. Proximal suspensory desmitis-clinical, ultrasonographic and radiographic features. *Equine Vet J* 1991; **23**: 25–31.
[4] Dyson S. Desmitis of the accessory ligament of the deep digital flexor tendon: 27 cases (1986–1990). *Equine Vet J* 1991; **23**: 438–44.
[5] Dyson S. Proximal suspensory desmitis in the hindlimb: 42 cases. *Br Vet J* 1994; **150**: 279–91.
[6] McDiarmid A. Eighteen cases of desmitis of the accessory ligament of the deep digital flexor tendon. *Equine Vet J* 1994; **6**: 49–56.
[7] Dyson S. Proximal metacarpal and metatarsal pain: a diagnostic challenge. *Equine Vet Educ* 2003; **15**: 134–8.
[8] Hewes CA, White NA. Outcome of desmoplasty and fasciotomy for desmitis involving the origin of the suspensory ligament in horses: 27 cases (1995–2004). *J Am Vet Med Assoc* 2006; **229**: 407–12.
[9] Dyson S. Diagnosis and management of common suspensory lesions in the forelimbs and hindlimbs of sport horses. *Clin Tech Equine Pract* 2007; **6**: 179–88.
[10] Bathe AP. Plantar metatarsal neurectomy and fasciotomy for the treatment of hindlimb proximal suspensory desmitis. *Proc Am College of Vet Surg* 2007; **42**: 116–17.
[11] Zubrod CJ, Schneider RK, Tucker RL. Use of magnetic resonance imaging to identify suspensory desmitis and adhesions between exostoses of the second metacarpal bone and the suspensory ligament in four horses. *J Am Vet Med Assoc* 2004; **224**: 1815–20.
[12] Brokken MT, Schneider RK, Sampson SN, Tucker RL, Gavin PG, Ho CP. Magnetic resonance imaging features of proximal metacarpal and metatarsal injuries in the horse. *Vet Radiol Ultrasound* 2007; **48**: 507–17.
[13] Crowe OM, Dyson SJ, Wright IM, Schramme MC, Smith RKW. Treatment of chronic or recurrent proximal suspensory desmitis using radial pressure wave therapy in the horse. *Equine Vet J* 2004; **36**: 313–16.
[14] Launois T, Desbrosse F, Perrin R. Percutaneous osteostixis as treatment for avulsion fractures of the palmar/plantar third metacarpal/metatarsal bone cortex at the origin of the suspensory ligament in 29 cases. *Equine Vet Educ* 2003; **15**: 126–38.
[15] Sutter WW. Autologous cell-based therapy for tendon and ligament injuries. *Clin Tech Equine Pract* 2007; **6**: 198–208.
[16] Arguelles D, Carmona JU, Climent F, Munoz E, Prades M. Autologous platelet concentrates as a treatment for musculoskeletal lesions in five horses. *Vet Rec* 2008; **162**: 208–11.
[17] Waselau M, Sutter WW, Genovese RL, Bertone AL. Intralesional injection of platelet-rich plasma followed by controlled exercise for treatment of midbody suspensory ligament desmitis in standardbred racehorses. *J Am Vet Med Assoc* 2008; **232**: 1515–20.
[18] Marks D, Mackay-Smith MP, Leslie JA, Soule SG. Lameness resulting from high suspensory disease (HSD) in the horse. *Proc Am Assoc Equine Pract* 1981; **24**: 493–7.
[19] Herthel DJ. Enhanced suspensory ligament healing in 100 horses by stem cells and other bone marrow components. *Proc Am Assoc Equine Pract* 2001; **47**: 319–21.
[20] McClure SR, VanSickle D, Evans R, Reinertson EL, Moran L. The effects of extracorporeal shock-wave therapy on the ultrasonographic and histologic appearance of collagenase-induced equine forelimb suspensory ligament desmitis. *Ultrasound Med Biol* 2005; **30**: 461–7.
[21] Dyson S. Proximal suspensory desmitis in the forelimb and hindlimb. *Proc Am Assoc Equine Pract* 2000; **46**: 137–41.
[22] Dyson S. Suspensory apparatus. In: Rantanen NW, McKinnon AO (eds) *Equine Diagnostic Ultrasonography*. Baltimore, MD: Williams & Wilkins, 1998, pp. 447–73.
[23] Caminoto EH, Alves AG, Amorim RL, Thomassian A, Hussni CA, Nicoletti JM. Ultrastructural and immunocytochemical evaluation of the effects of extracorporeal

shock wave treatment in the hind limbs of horses with experimentally induced suspensory ligament desmitis. *Am J Vet Res* 2005; **66**: 892–6.
[24] Toth F, Schumacher J, Schramme M, Holder T, Adair HS, Donnell RL. Compressive damage to the deep branch of the lateral plantar nerve associated with lameness caused by proximal suspensory desmitis. *Vet Surg* 2008; **37**: 328–35.
[25] Frank ER. Splints. In: Frank ER (ed.) *Veterinary Surgery*. Minneapolis, MN: Burgess Publishing, 1964, pp. 195–6.
[26] Goble DO. The small metacarpal and metatarsal bones. In: Mansmann RA, McAllister ES (eds). *Equine Medicine and Surgery*. Santa Barbara, CA: American Veterinary Publications, 1982, pp. 1115–20.
[27] Van den Belt A, Becker C, Dik K. Desmitis of the accessory ligament of the deep digital flexor tendon in the horse: clinical and ultrasonographic features-a report of 24 cases. *J Vet Med Series A* 1993; **40**: 492–500.
[28] Eliashar E, Dyson SJ, Archer RM, Singer ER, Smith RKW. Two clinical manifestations of desmopathy of the accessory ligament of the deep digital flexor tendon in the hindlimb of 23 horses. *Equine Vet J* 2005; **37**: 495–500.
[29] Becker CK, Savelberg HH, Buchner HH, Barneveld A. Effects of experimental desmotomy on material properties and histomorphologic and ultrasonographic features of the accessory ligament of the deep digital flexor tendon in clinically normal horses. *Am J Vet Res* 1998; **59**: 352–8.

22B UK perspective

Sue Dyson

Between January 2003 and February 2008 63 horses underwent high-field ($n = 10$) or low-field standing ($n = 53$) magnetic resonance imaging (MRI) of the proximal half of the metacarpal ($n = 42$) or metatarsal ($n = 21$) regions and distal carpus or tarsus at the Centre for Equine Studies of the Animal Health Trust. Horses were selected for examination based on a positive response (at least 80% improvement in lameness) to perineural analgesia of the palmar metacarpal nerves (subcarpal) (2×2 ml mepivacaine) or the ulnar nerve (10 ml mepivacaine) in forelimbs; in hind limbs lameness was substantially improved by perineural analgesia of the deep branch of the lateral plantar nerve (3 ml mepivacaine) or the tibial nerve (20 ml mepivacaine). Response to subcarpal and subtarsal analgesia was assessed 10 minutes after injection; response to ulnar or tibial nerve blocks was assessed after 20 minutes. In some horses mild improvement in lameness was seen after intra-articular analgesia of the middle carpal or tarsometatarsal joints, evaluated at 10 minutes after injection. The results of radiographic and ultrasonographic examinations of the carpal and proximal metacarpal regions and tarsal and proximal metatarsal regions did not satisfactorily explain the degree of lameness.

Horses had been lame for 0.75 to 12 months prior to examination, with a mean duration of 2.7 months. There were 34 racehorses, mostly flat racehorses, and 29 non-racehorses (dressage, showjumping, eventing, endurance and general purpose horses). Racehorses ranged in age from 1 to 8 years (mean 2.8 years); non-racehorses ranged from 4 to 15 years (mean 10 years).

Forty-two horses had unilateral or bilateral forelimb lameness, and 21 horses had hind limb lameness. The results of MRI are summarized in Table 22.1. Suspensory ligament injuries alone or in combination with other soft tissue or osseous injuries were the most common in both forelimbs ($n = 21$) and hind limbs ($n = 19$).

Horses were treated by various combinations of box rest and controlled walking exercise and extracorporeal shockwave therapy (ESWT) or radial pressure wave therapy (RPWT), local infiltration with corticosteroids, intra-articular medication with corticosteroids and hyaluronan, and spa therapy. A small proportion of horses received treatment with platelet-rich plasma ($n = 1$), tiludronate ($n = 1$) or surgery ($n = 2$). Follow-up information was

Equine MRI, edited by Rachel C. Murray.

Table 22.1 Summary of injury diagnosis in 63 horses with proximal metacarpal or metatarsal region pain examined using magnetic resonance imaging

Principle injured structure	Forelimbs	Hind limbs
Suspensory ligament*	21	19
Accessory ligament of the deep digital flexor tendon (ALDDFT)	6	1
Third metacarpal (MCIII) or metatarsal bone	2	1
Abnormal mineralization of the carpal bones and proximal MCIII	6	
Intercarpal ligament injury or interosseous ligament injury (MCII & III or MTIV & III)	5	
Osteoarthritis of carpometacarpal joint	1	
Exostosis on MCII, III, or IV	1	

* In addition, two horses had abnormal mineralization of carpal bones, five had abnormal signal intensity of the ALDDFT, one horse had syndesmopathy of the articulation between MCIII and MCIV, and one horse had low-grade osteoarthritis of the tarsometatarsal joint.

acquired by a standardized telephone questionnaire. Many horses were also reassessed by the referring veterinary surgeon.

Thirteen horses were lost to follow-up. Follow-up information was available for 50 horses, three of which were only in light work. Success was classified as return to full athletic function for at least 4 months. The duration of time in full work at the time of follow-up ranged from 4 to 24 months. Of 22 racehorses, 12 were sound and in full work and 10 had persistent or recurrent lameness. Of 25 non-racehorses, nine were in full work and 16 were lame. Of 33 horses with forelimb lameness, 17 were in full work and 16 had persistent or recurrent lameness. Of 14 horses with hind limb lameness, six were sound and in full work and eight had persistent or recurrent lameness.

22C Thoroughbred racehorses

Sarah Powell

Between June 2006 and August 2009, 153 Thoroughbred horses used for racing (mainly flat racing) have undergone low-field magnetic resonance imaging of the subcarpal region at Rossdales Diagnostic Centre. In the majority of cases the middle carpal joint was also imaged. Ninety-eight were imaged to investigate lameness that could not be adequately localized to either the middle carpal joint or subcarpal region by any other means, including radiography/ultrasonography and diagnostic local analgesia. The remainder underwent magnetic resonance imaging (MRI) examination to further evaluate known pathology, such as to assess the bone involvement of suspensory ligament injury, to investigate the presence of adhesion formation between the suspensory ligament and the second or fourth metacarpal bones suspected ultrasonographically or to get baseline images of lesions with a view to monitoring these as the horse returned to exercise. In those that underwent scintigraphic examination of the carpal and subcarpal regions, hyperintensity within the cuboidal bones of the carpus and/or the palmar proximal third metacarpal bone correlated anatomically with the presence of an abnormal increased radionuclide uptake (IRU) in bone phase images. However, the resolution of this abnormal IRU was observed to lag behind the resolution of fluid signal on MRI images in all those cases that were re-imaged.

Perhaps the most useful outcome of MR imaging of the subcarpal region in these cases has been the ability to identify those horses with findings consistent with bone stress reactions in the palmar proximal metacarpus [1]. With adaptive/degenerative changes common in the carpal bones and the heterogenous appearance of the suspensory ligament ultrasonographically, these horses would previously had been 'speculatively' diagnosed as either having middle carpal joint disease or suspensory ligament desmitis – based on any radiographic or ultrasonographic findings. The interpretation of diagnostic local anaesthesia may be confounded by overlap of structures desensitized by intra-articular analgesia of the middle carpal joint and by lateral palmar or subcarpal anaesthesia. For this reason the results are often inconclusive for differentiation of several disease entities. MRI has enabled us to definitively diagnose stress injuries – as scintigraphy had done before – but with the added benefit of definitive anatomic localization of bone activity and a concurrent appraisal of the soft tissue structures.

Equine MRI, edited by Rachel C. Murray.

The benefit of this in the racehorse lies in the potential to minimize days lost from training – a universal aim in those working with the breed. An unnecessary loss of training days may occur with an erroneous diagnosis of suspensory ligament desmitis. Management of a significant suspensory ligament injury is approached with more caution than a primarily bone stress-related injury, particularly in more mature horses. A suspensory injury generally requires 4–6 weeks' box rest and a gradual rehabilitation incorporating hand-walking or horse-walker exercise followed by a gradual return to full training with regular ultrasonographic evaluations of the suspensory ligament. By contrast, bone stress injuries thought not to have progressed to cortical stress fracture on MR images are kept in walking exercise from the time of the diagnosis, with a more rapid return to full training and a better short- to mid-term prognosis to return to full atheletic function. Those horses where breach of the palmar cortical bone is seen on the MR images are box rested until sound (usually 2–4 weeks) with a relatively rapid reintroduction of exercise following this initial rest period.

A low number of horses with bone stress reaction in the absence of cortical stress fracture were variably treated with intravenous bisphosphonates, with no significant advantage perceived by the treating clinicians.

Racehorses with a primary diagnosis of suspensory ligament pathology are treated with extracorporeal shockwave therapy (ESWT) or local infiltration of low-dose corticosteroids depending on the nature of the lesion, severity of lameness. A relatively common finding in 2-year-old racing Thoroughbreds is an apparent generalized enlargement of the muscular component of the suspensory ligament in the absence of any other changes, which has been observed to resolve in cases undergoing repeat scanning as 3-year-olds. This is speculated to represent a loading response of the muscle fascicles as a response to early training. Whether this predisposes to future overt suspensory ligament disease is unknown. In horses with an MRI diagnosis of bone stress injury to the proximal third metacarpal bone, it is not uncommon to see changes consistent with mild suspensory ligament desmitis, such as enlargement of the proximal third and loss of definition of the muscular and ligamentous components of the suspensory ligament. This is perhaps to be expected in what is likely to be a 'syndrome' of changes due to repetitive overload of the region – this does not appear though to be limiting and, again, these horses do not appear to go on to develop clinically relevant suspensory disease subsequently in their 3- or 4-year-old careers. The same is true when imaging the metacarpophalangeal joint, where abnormal signal patterns are frequently seen in the suspensory ligament branches – these horses, with few exceptions, rarely go on to develop clinically detectable branch injuries.

Horses with adhesion formation or periligamentous fibrosis between the suspensory ligament and second or fourth metacapal bones but without significant suspensory ligament pathology detected on MR images were treated with local infiltration of low-dose corticosteroid and continued in walking and trotting exercise for a 2-week period prior to resuming full training. Of those that have remained under the care of the treating

clinicians ($n = 6$) all have returned to racing (follow-up 8–26 months) and none has required further medication at that site.

Horses with changes to the syndesmosis between the second and third metacarpal bones (with or without the presence of bone stress reaction in the palmar proximal third metacarpal bone) are also treated with local infiltration of low-dose corticosteroid. Though no detailed follow-up has been done at this stage, anecdotally racehorses with bone stress reaction in the palmar proximal third metacarpal bone in association with changes at the syndesmosis of the second and third metacarpal bones diagnosed on MRI (i.e. those appearing to repetitively and excessively load the medial aspect of the forelimb) may be predisposed to go on to develop clinically relevant middle carpal joint pathology and many require middle carpal joint medications during their 3- and 4-year-old campaigns. However, the proximal metacarpal region rarely requires further attention.

In summary, the most significant advantage of MR imaging of the subcarpal region in the racing Thoroughbred appears to be teasing apart those with bone stress reactions/stress injuries from those with clinically relevant proximal suspensory and middle carpal joint disease. The former appear to require a less extensive period out of full training from the time of the MRI diagnosis and are afforded a more favourable prognosis for a subsequent return to racing. Horses with tissue adhesions and syndesmosis-related pathology can, in many cases, remain in ridden exercise and return to fast work relatively soon. Those with a primary diagnosis of suspensory ligament pathology or those with signal changes consistent with fluid present in the cuboidal bones of the carpus require a more extended period of rest and may require attention to these areas in the future.

It should be remembered that although pathology detected in the suspensory ligament and its enthesis may be assumed relatively benign in young flat racehorses, the career span of these animals is often only 2–3 years and these findings may go on to cause performance-limiting lameness should these horses be retrained for other disciplines requiring greater longevity.

REFERENCE

[1] Powell SE, Ramzan PHL, Head MJ, Shepherd MC, Baldwin GI, Steven WN. Standing magnetic resonance imaging detection of bone marrow oedema-type signal pattern associated with subcarpal pain in 8 racehorses: A prospective study. *Equine Vet J* 2010; **42**: 10–17.

Chapter 23
The carpus

23A Osseous injury

Sarah Powell

INTRODUCTION

Between June 2006 and August 2009 56 horses underwent magnetic resonance imaging (MRI) of the carpus at Rossdales Diagnostic Centre. Of these, 39 were Thoroughbred horses used for racing and 17 were competition or pleasure horses. Thoroughbred racehorses that underwent imaging of the middle carpal joint and subcarpal region as part of an investigation into the differentiation of subcarpal and carpal pain, which had a final diagnosis of proximal metacarpal injury, are not include here and are discussed elsewhere in the text. In all horses included here, the lameness had been localized to the joint by diagnostic local analgesia, with the exception of those horses with clear localizing signs, for example in the case of fractures.

The primary reason for MRI evaluation of the carpus in the Thoroughbred group was to more fully assess the extent of pathology seen radiographically, particularly in the case of bone mineral densification of the third and radial carpal bones. Six horses in the Thoroughbred group underwent MRI examination to assess radiographically evident fractures of the third, radial or intermediate carpal bones prior to surgery. Four Thoroughbred racehorses underwent magnetic resonance imaging specifically to assess the soft tissue structure of the carpus due to assumed injury; these horses had all undergone an ultrasonographic examination prior to the MRI. All 39 horses had been radiographed prior to the examination and 17 underwent scintigraphic evaluation of the carpi prior to or following the MRI. All horses had been in full training just prior to the MRI examination.

The primary reason for MRI evaluation of the carpus in the competition and pleasure horse group was to more fully evaluate bone changes seen or suspected radiographically or to further localize changes seen scintigraphically. Three horses underwent MRI examination due to suspected soft tissue injury. Of the 17 horses, eight underwent scintigraphic examination prior or subsequent to the MRI examination, all were radiographed prior to the MRI examination and three underwent an ultrasonographic examination.

Equine MRI, edited by Rachel C. Murray.

Bone mineral densification of the carpal bones

Of the Thoroughbred group, without exception, some degree of bone mineral densification, seen as T1 gradient echo (GRE), T2* GRE and T2 fast spin-echo (FSE) hypointensity of the carpal bones, was detected; it was graded mild, moderate or severe. The most common finding was densification of the radial facet of the third carpal bone and, in the vast majority of cases, was present in conjunction with densification of the radial carpal bone. In a lower number of cases densification in the intermediate carpal bone was present. Densification was often seen in the absence of any overt fluid distension of the carpal joints, though in many cases mild thickening of the soft tissue structures over the dorsomedial aspect of the carpus was detected clinically. In the majority of cases radiographic assessment of the extent of densification of the third and radial carpal bones was underestimated radiographically when compared with the MR images. Cases with mild or moderate densification in the absence of any hyperintensity within the trabecular or subchondral bone of the carpal bones were usually treated with intra-articular corticosteroid (triamcinolone [Adcortyl]) and sodium hyaluronan, and continued in full training. Of 18 racehorses with a primary diagnosis of densification in the absence of short τ inversion recovery (STIR) hyperintensity within the carpal bones and no concurrent soft tissue injury, 12 have returned to racing. A high proportion had been treated previously and also required maintenance medications following the MRI. An intra-articular course of autologous conditioned serum (IRAP) was used in eight cases, although these horses had also been treated with corticosteroid medication prior to or following the diagnosis. Horses undergoing a repeat MRI scan did not show a significant reduction in the degree or extent of densification on the follow-up images, and the majority deteriorated further with time. However, all horses undergoing repeat scanning had remained in some degree of exercise.

STIR hyperintensity within the carpal bone(s): generalized

In eight cases generalized STIR hyperintensity was seen within the trabecular bone of the third and/or radial carpal bones. This was seen in conjunction with a normal signal intensity of the surrounding cuboidal bones and, therefore, not considered to represent poor fat suppression. Of these eight cases five had undergone bone-phase scintigraphic assessment of the carpi prior to or following the MRI examination, and in all cases some degree of increased uptake of the radionuclide was detected, although in some this was more easily localized specifically on MRI than on scintigraphic images. Of horses with mild to moderate generalized uptake in the radial and third carpal bones (this change was not seen in only one case in the intermediate carpal bone), all had associated densification within the affected carpal bones. These cases were medicated with intra-articular corticosteroid (triamcinolone [Adcortyl]) and were variably rested between 1 week and

3 months. Five received intravenous injections of the bisphosphonate tiludronate (Tildren). Four were re-presented for MRI examination of the carpi between 3 months and 14 months after the initial examination, and the STIR hyperintensity had resolved, though the densification had either remained static or deteriorated further.

STIR hyperintensity within the carpal bones(s): focal

In four cases focal STIR hyperintensity was seen associated with the subchondral bone of the dorsal aspect of the third or radial carpal bones but in the absence of any associated T1 or T2* hyperintensity. These horses all showed a moderate degree of lameness at the time of the initial examination and had responded transiently to intra-articular corticosteroid medication. They were treated with intra-articular corticosteroid medication and advised to remain out of training for a variable period. Of these cases, three had undergone a bone scan examination of the carpi, which revealed moderate focal increased uptake of the radionuclide within the dorsal aspect of the third or radial carpal bones. One horse, which remained in training, sustained a radiographically evident osteochondral fragment from the dorsodistal aspect of the radial carpal bone at the site of the previously detect STIR hyperintensity 5 weeks following the MRI examination. Three of the four horses have returned to racing since the initial MRI examination.

Focal STIR hyperintensity within the carpal bones associated with focal T1 and T2* hyperintensity at the joint margin

A further four cases had STIR hyperintensity adjacent to the joint margin, which also appeared hyperintense on T1 and T2* images. This was often seen in conjunction with narrowing of the joint space and loss of definition or signal changes within the overlying articular cartilage. These horses often had a history of moderate lameness, which had been refractory or incompletely responsive to intra-articular corticosteroid medication. In all cases some degree of soft tissue thickening or joint distension could be detected over the dorsomedial aspect of the affected carpus. In three cases the signal changes were associated with the radial facet of the third carpal bone and in one case both the radial facet of the third carpal bone and the opposing articular surface of the radial carpal bone were affected. In one case, haemosiderin deposits seen on the MR images indicated that a previous arthroscopic procedure to the middle carpal joint had been carried out. One case underwent computed tomographic (CT) imaging of the affected carpus under general anaesthesia prior to undergoing arthroscopic surgery, which showed a similar distribution of pathologic change. It was considered that the CT did not significantly improve the diagnostic assessment above and beyond that of the MRI findings in this case. Two horses underwent arthroscopic examination and subsequent debridement of the lesions. This revealed osteochondral defects consistent with the location and size of the signal changes seen on MRI. The two horses that were not investigated surgically underwent a single corticosteroid medication followed by a course

of autologous conditioned serum (IRAP). One of the four cases has returned successfully to racing, though this horse has received multiple joint medications. Two were retired to stud due to persistent lameness related to the carpus and one is still convalescing from surgery.

Comminuted carpal bone fractures

Six horses underwent MRI examination to further assess fractures of the carpal bones. Of these, four had comminuted fractures of the radial carpal bone, one had a comminuted fracture of the second carpal bone and one had a non-displaced sagittal fracture of the intermediate facet of the radial carpal bone. MRI was considered superior to radiography for assessment of the number and relative positions of the fracture fragments in cases with comminution, and to allow decision making in relation to surgical intervention. One case of comminuted radial carpal bone fracture underwent a CT examination of the fracture prior to surgery. The CT images revealed the same degree and relative positions of the comminuted fragments of the radial carpal bone; however, a bone fragment from the palmar aspect of the third carpal bone, clearly visible on the CT images, was not visible on the MR images taken from the horse under standing sedation. Of the four horses with comminuted radial carpal bone fractures one was euthanized and three were retired from racing. The comminuted fracture of the second carpal bone was treated with intra-articular corticosteroid medication and has returned to racing. The horse with the sagittal radial carpal bone fracture has never raced, though the reason for this is unknown.

23B Soft tissue injury

Rachel Murray

In the racehorse, the majority of injuries seen appear to relate to bone and articular cartilage pathology. For non-racing horses, similar osseous lesions may also been seen in horses that are undertaking high-intensity repetitive loading, including the sports of endurance or eventing. Injuries in the carpal region are frequently associated with lesions detected in the proximal metacarpal region and may be difficult to separate from proximal metacarpal pathology, including damage to the intermetacarpal interosseous ligaments and accessory ligament of the deep digital flexor tendon (ALDDFT). Although structures within the carpal canal extend into the proximal metacarpal region, it is possible for magnetic resonance imaging (MRI) to detect pathology that is isolated to the level of the carpus. Treatment and follow-up for the proximal metacarpal region is covered in Chapter 22.

The intra-articular soft tissues of the carpus include the intercarpal ligaments and joint capsule, which may be defined using MRI. Use of MR arthrography to better define the palmar anatomy has been reported and was suggested to add additional information that could be used for arthroscopic guidance [1]. Damage to the joint capsule and synovium may occur with other pathological change, which is likely to determine the method of management and outcome.

The intercarpal ligaments provide stabilization and energy dissipation for the carpal bones [2]. Intercarpal ligament damage can be seen in both racing and sport horses, in addition to pleasure horses with a history of trauma. Damage to the intercarpal ligaments can be recognized using MRI (Figures 23.1 and 23.2; and see 15.13). Damage to these ligaments may occur alone or in conjunction with other joint pathology. It has been reported that damage to the dorsomedial intercarpal ligament or the medial palmar intercarpal ligament did not correlate with cartilage pathology or osteochondral fragmentation [3]. However, it has been suggested that in young racehorses, damage to the palmar intercarpal ligaments may be a fatigue-type injury analogous to carpal osteochondral damage [4].

In a report of postoperative follow-up in 42 racehorses undergoing arthroscopy of the middle carpal joint, postoperative performance was most correlated with subchondral bone pathology, but damage to more than one-third of the medial intercarpal ligament had a significant detrimental effect

Equine MRI, edited by Rachel C. Murray.

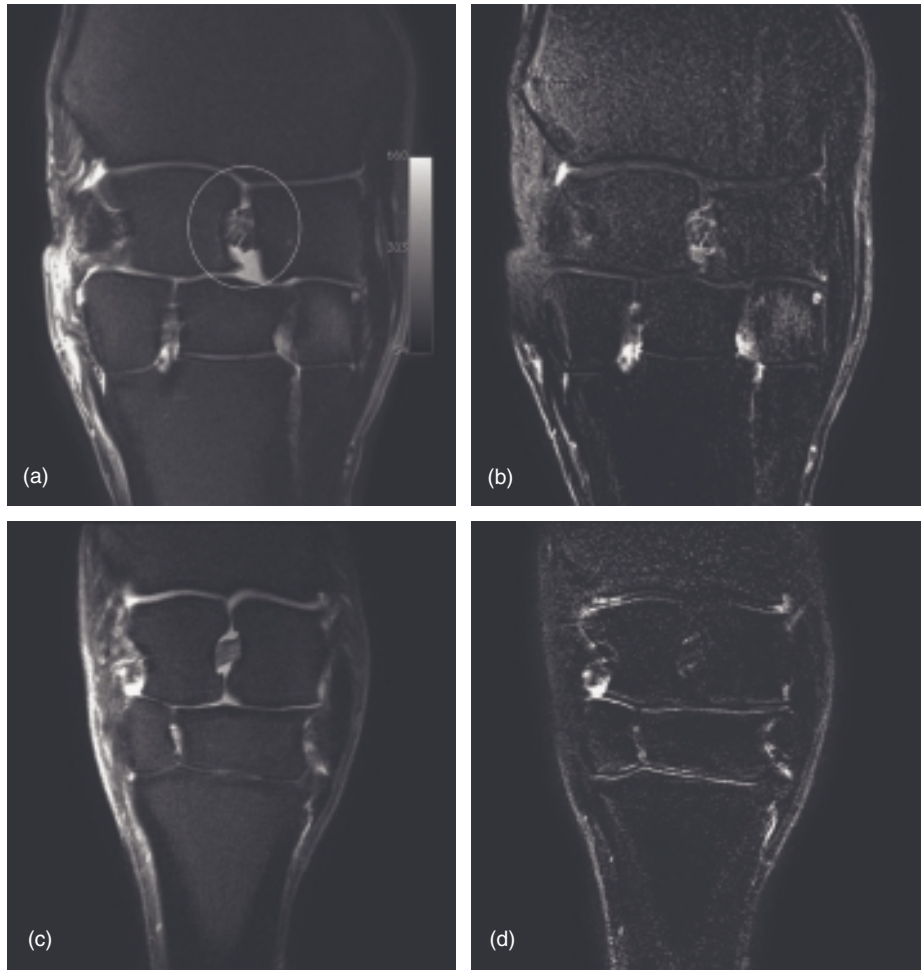

Figure 23.1 Images of the carpus from a 12-year-old Quarter Horse gelding used for barrel racing with a history of acute onset lameness localized to the carpus with intra-articular analgesia, but radiographic examination was inconclusive. (a) Proton density fat-saturated dorsal image. The inter-carpal ligament between the radial and intermediate carpal bones has increased signal intensity with loss of ligamentous integrity (circle). Along the medial aspect of the intermediate carpal bone at the attachment of this ligament, a region of mild increased signal intensity is apparent, beginning at the ligament and extending towards the middle carpal joint distally. (b) A post-contrast T1 VIBE fat-saturated subtraction image at the same location reveals moderate contrast enhancement of the ligament consistent with acute inflammation. (c and d) The contralateral limb is provided as a normal comparison: (c) proton density fat-saturated; and (d) T1 VIBE fat-saturated post-contrast subtraction. This ligament was visualized on arthroscopic evaluation of the joint and confirmed to be a grade 3 tear. The horse is currently in rehabilitation. Images courtesy of Dr Carter Judy.

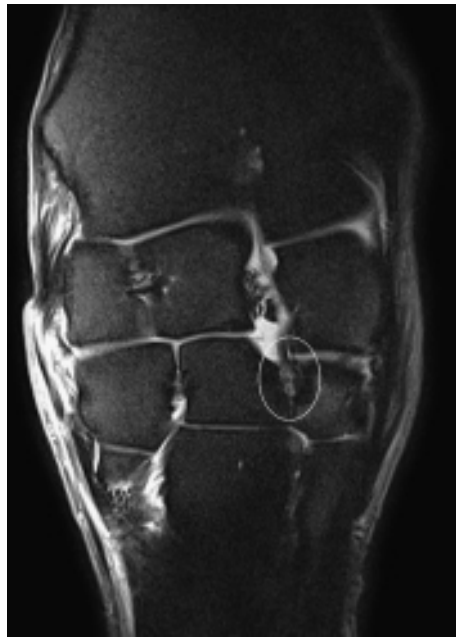

Figure 23.2 Proton density fat-saturated dorsal image of the carpus from a 3-year-old Thoroughbred gelding used in flat racing. The horse had acute onset lameness localized to the carpus with intra-articular analgesia and no significant radiographic abnormalities. The inter-carpal ligament between the third and second carpal bones has increased signal intensity with loss of ligamentous integrity (circle). This ligament was not grossly visible during arthroscopic evaluation of the joint. Several osteochondral fragments were removed from the distal radial and intermediate carpal bones. The horse has returned to training and raced successfully. Image courtesy of Dr Carter Judy.

on performance [5]. Of 37 horses diagnosed with lameness associated with avulsion of the lateral palmar intercarpal ligament from the ulnar carpal bone, 91% of horses treated by arthroscopic fragment removal returned to work and were eight times more likely to return to work than those treated conservatively [6].

At this stage, there is limited long-term follow-up information on large numbers of horses with a diagnosis of damage to other intercarpal ligaments using MRI. However, information from clinics using both high- and low-field imaging for diagnosis of intercarpal ligament injury indicates that in the absence of other joint pathology, there can be a reasonable prognosis for return to function for horses with damage to the ligament between the second and third carpal bones or third and fourth carpal bones (Judy C, personal communication, 2009; Murray, unpublished data) (see Figures 15.13, 23.1 and 23.2). Where there is concurrent damage to other structures, including osteochondral disruption and sclerosis, then recovery may be less successful. Management options that have been used include arthroscopic debridement with removal of any associated fragments, shockwave therapy, intra-articular medication (including corticosteroid, hyaluronic acid or regenerative techniques), systemic administration of non-steroidal anti-inflammatory drugs (NSAIDs) and/or chondroprotective agents, physiotherapy and rest. Administration of tiludronate has also been used in some horses with concurrent osseous damage.

REFERENCES

[1] Getman LM, McKnight AL, Richardson DW. Comparison of magnetic resonance contrast arthrography and arthroscopic anatomy of the equine palmar lateral outpouching of the middle carpal joint. *Vet Radiol Ultrasound* 2007; **48**(6): 493–500.

[2] Whitton RC, Rose RJ. The intercarpal ligaments of the equine midcarpal joint. Part 2: The role of the palmar intercarpal ligaments in the restraint of dorsal displacement of the proximal row of carpal bones. *Vet Surg* 1997; **26**(5): 367–73.

[3] Whitton RC, Kannegieter NJ, Rose RJ. The intercarpal ligaments of the equine midcarpal joint. Part 3: Clinical observations in 32 racing horses with midcarpal joint disease. *Vet Surg* 1997; **26**(5): 374–81.

[4] Phillips TJ, Wright IM. Observations on the anatomy and pathology of the palmar intercarpal ligaments in the middle carpal joints of thoroughbred racehorses. *Equine Vet J* 1994; **26**(6): 486–91.

[5] Whitton RC, Kannegieter NJ, Rose RJ. Postoperative performance of racing horses with tearing of the medial palmar intercarpal ligament. *Aust Vet J* 1999; **77**(11): 713–17.

[6] Beinlich CP, Nixon AJ. Prevalence and response to surgical treatment of lateral palmar intercarpal ligament avulsion in horses: 37 cases (1990–2001). *J Am Vet Med Assoc* 2005; **226**(5): 760–6.

Chapter 24
The tarsus

Tim Mair and Ceri Sherlock

INTRODUCTION

There is limited information available concerning the clinical management of diseases of the equine tarsus following diagnosis using magnetic resonance imaging (MRI). MRI of the hock region is technically challenging, and the use of conventional imaging modalities (radiography, ultrasonography and nuclear scintigraphy) is well established. However, conventional imaging techniques have limitations, and it is likely that MRI will become more widely used in the evaluation of the tarsus in the future. This chapter reviews the treatments and outcomes of the more common conditions affecting the equine tarsus and discusses potential roles of MRI in the management of these diseases.

OSTEOARTHRITIS OF THE DISTAL TARSAL JOINTS

Osteoarthritis of the distal tarsal joints is a common cause of hind limb lameness in horses of all ages and in horses performing in all disciplines [1, 2], and is the most common cause of lameness associated with the tarsus [3–10]. MRI of horses with tarsal pain frequently shows alteration of the chondro-osseous margins, changes to the endosteal surface of subchondral bone, articular cartilage damage, intertarsal ligament injury, mineralization and cyst development in the cancellous bone, periarticular osteophyte formation and enthesious new bone at capsular attachments [11, 12] (see Figure 17.15). MRI was found to be more sensitive and specific than radiography at detecting pathological changes confirmed at postmortem in these studies.

Despite the fact that osteoarthritis of the distal hock joints is a common disorder, there are very few published studies that assess or compare the efficacies of different treatment options. Corrective shoeing to ensure correct mediolateral balance, and adjusting the break-over by shortening the toe, squaring and rolling the toe of the shoe, or setting the shoe back from the toe have been recommended. A lateral trailer or lateral extension of the shoe provides symptomatic relief in some horses [6]. Horses with distal tarsal osteoarthritis usually benefit from being kept in regular work. Maintaining muscular fitness and proprioceptive conditioning may support

Equine MRI, edited by Rachel C. Murray. © 2011 by Blackwell Publishing Ltd.

joint stability and normal loading patterns, and has been shown to provide a protective effect in ponies [13]. In severe osteoarthritis a decrease in workload may be necessary [14].

Some early encouraging results with extracorporeal shockwave therapy (ESWT) have been reported [15, 16], but there is little long-term follow-up information. Potential analgesic effects of this treatment may give it some value as a short-term treatment [14].

In horses demonstrating mild to moderate lameness, phenylbutazone or flunixin, or a combination, may be effective in conjunction with corrective farriery and controlled exercise [17, 18]. Lameness generally recurs if the drug treatment is withdrawn. A topically administered non-steroidal anti-inflammatory drug (NSAID), diclofenac liposomal cream, is now approved in the United States for the treatment of horses with osteoarthritis. This formulation provides enhanced local delivery without achieving clinically important blood concentrations of the drug, thus alleviating the adverse effects of systemically administered NSAIDs. Diclofenac liposomal cream was shown to improve clinical signs of naturally occurring osteoarthritis in horses in a double-blind controlled clinical study [19] as well as improving clinical signs and modifying the disease process in an experimental model of carpal osteoarthritis in horses [20].

Intra-articular injection of corticosteroids (e.g. triamcinolone acetonide 3–12 mg per joint or methylprednisolone acetate 30–60 mg per joint) into the affected joint(s) can be beneficial in many cases, but the clinical improvement may only be temporary (usually lasting several weeks to several months); some clinicians believe that combining corticosteroids with hyaluron produces a longer-lasting effect. A positive response to intra-articular analgesia should be established prior to intra-articular medication. The tarsometatarsal and centrodistal joints of both limbs may be treated simultaneously, although care must be taken not to exceed a potentially toxic total dose of corticosteroids. Injection of the tarsometatarsal joint is technically easier and safer than injecting the centrodistal joint, so medication of the tarsometatarsal joint alone offers many practical advantages over medicating both joints separately. However, these authors still recommend medication of both joints if intra-articular analgesia of both joints is required to abolish the lameness. After injection, horses should ideally be rested for 2 to 3 days, after which work can be resumed.

A positive response rate to intra-articular medication with corticosteroids was reported to be 38% in one study [21] and 52% in another [22]; in the latter study a positive response was defined as the ability of horses to return to their previous level of exercise, whereas 70% of cases showed some degree of improvement in the lameness. The duration and degree of lameness does not appear to affect the response rate to intra-articular medication with corticosteroids. However, the severity of radiographic changes may affect the response rate, but there are conflicting results in two published series. Cases with moderate to severe radiographic changes tended to show a positive long-term response to treatment in one study [21], whereas in another study, cases with less marked changes affecting the tarsometatarsal joint were found to be more likely to respond well to treatment [22].

Both intra-articular and intravenous hyaluronan (hyaluronic acid) and intra-articular polysulphated glycosaminoglycans (PSGAG) can provide temporary relief of lameness, although definitive data from controlled clinical trials are lacking. These drugs are commonly administered in conjunction with other therapies [18]. Anecdotally, reports suggest that PSGAG may be more effective than hyaluronan in treating osteoarthritis, whereas hyaluronan may be more effective in acute synovitis. However, it was recently reported that hyaluronan has a superior effect on decreasing the degree of articular cartilage fibrillation and that PSGAGs have a superior effect to reduce synovial membrane and soft tissue inflammation [23, 24].

Oral compounds sold as supplements for osteoarthritis usually contain components of cartilage and precursor molecules such as chondroitin sulphate and glucosamine hydrochloride, plus antioxidants and free radical scavengers [18]. These agents may be beneficial as adjunctive treatments, although evidence of their efficacy is very limited [25].

In addition to articular cartilage damage, bone remodelling changes involving cortical, subchondral and cancellous bone may play an important role in this disease [26]. Tiludronate is a member of the bisphosphonate class of drugs that inhibit bone resorption (via inhibition of osteoclasts). In a double-blind placebo-controlled trial of tiludronate treatment of 109 horses with bone spavin, the tiludronate-treated horses were significantly less lame than the placebo horses at 120 days after treatment [27].

Arthrodesis can be undertaken in situations where medical treatment is unsuccessful or in cases where the disease process has progressed so far that medical treatment is no longer effective [28]. Options for arthrodesis of the distal tarsal joints include surgical arthrodesis using a variety of techniques [29–37], laser-facilitated arthrodesis using the neodymium: yttrium-aluminium-garnet (Nd:YAG) or 980 nm diode laser [38–40], chemical arthrodesis by the intra-articular injection of monoiodoacetate (MIA) [41–44] or alcohol. A recent retrospective study of 54 horses treated by surgery revealed that 59% of horses returned to their previous level of performance and a further 11% improved after surgery [37]. Comparison of the laser-facilitated arthrodesis with the three drill tract intra-articular drilling technique in normal horses showed less lameness postoperatively with the laser procedure [40]. Although there were promising early results, MIA has been abandoned by many clinicians due to the severe postoperative pain experienced by some horses and other complications.

Increased intraosseous pressure (>45 mm Hg) has been recorded in horses with distal tarsal osteoarthritis. Subchondral fenestration reduces this pressure and may be helpful in relieving pain [45]. In one study, 25 of 38 horses (66%) returned to their intended use after subchondral fenestration, which is comparable to the success rate of other surgical procedures.

Partial tibial neurectomy and neurectomy of the deep peroneal nerve have been used to treat horses with distal tarsal osteoarthritis [46]. The technique resulted in 19 of 23 horses (83%) becoming sound for 2 months and 14 of 23 (61%) remaining sound for 12 to 36 months. The effect of the surgery is almost immediate, but the surgical technique is challenging and not widely utilized.

OSTEOARTHRITIS OF THE TALOCALCANEAL JOINT

Osteoarthritis of the talocalcaneal joint (Figure 24.1; and see Figure 17.18) is an unusual cause of moderate to severe hind limb lameness in mature horses and is usually of sudden onset [47, 48]. In a review of 14 horses affected by talocalcaneal osteoarthritis, conservative treatment (including rest, intra-articular corticosteroids, hyaluronic acid or PSGAG) produced poor results, and all horses remained lame [48]. Surgical arthrodesis of the talocalcaneal joint in 8 horses has been reported to result in significant improvement in the degree of lameness in all horses [48, 49].

DESMITIS OF THE COLLATERAL LIGAMENTS

Although tarsal collateral ligament desmitis (see Figures 17.20–17.23) has been described occasionally in the veterinary literature [50–53], it has recently been noted that it may occur more frequently than previously reported; collateral desmitis was the most common tendon/ligament injury associated with the tarsus in a large group of horses (26/128 horses) undergoing ultrasonography for evaluation of the tarsus [50]. The medial tarsal collateral ligaments (18 horses) were more commonly affected than the lateral tarsal collateral ligaments (8 horses) [50]. Tarsal collateral ligament injuries solely affecting the ligament have been identified but they have also been reported in combination with osseous lesions at the ligament's insertion or origin [50, 51, 54, 55]. Injuries of the collateral ligaments can vary from partial ligament fibre disruption to complete rupture and dislocation of the affected joint [56–59]. Mild ligament lesions may not be obviously evident in horses [60]. MRI has been utilized in horses with tarsal collateral ligament desmitis. It is considered the gold standard for assessment of soft tissue injuries and joint injuries in humans [61–63] as it provides tomographical images that allow concurrent assessment of osseous and soft tissue structures [64].

Treatment modalities that may enhance the normal repair of the damaged ligaments include shockwave therapy [65], therapeutic ultrasonography [66] or intra-lesional injection with autologous bone marrow [67], growth factors [68], purified mesenchymal stem cells [69] or gene therapy [70]; however, evidence of the efficacy of these treatments is lacking. Surgical intervention in horses with ligament injuries is rarely performed because of their high weight and unpredictable temperaments; attempts have been predominantly unrewarding [56], although there are some reports of encouraging results in small numbers of horses with polypropylene mesh repairs in the fetlock joints [71]. Suture reconstruction has been reported in foals [58, 72] but is not recommended for desmopathies affecting only a proportion of the ligament [57]. More recently, reconstruction using small intestinal submucosa of experimentally induced metacarpophalangeal collateral ligament transection has been reported [73]. This demonstrated less laxity at 8 weeks compared with a sham treatment; however, the repair was only 38% the strength of an uninjured collateral ligament at this time period.

Conservative treatment (stall rest, cold hosing, bandaging, and topical and systemic anti-inflammatories) is an effective regime for ligament

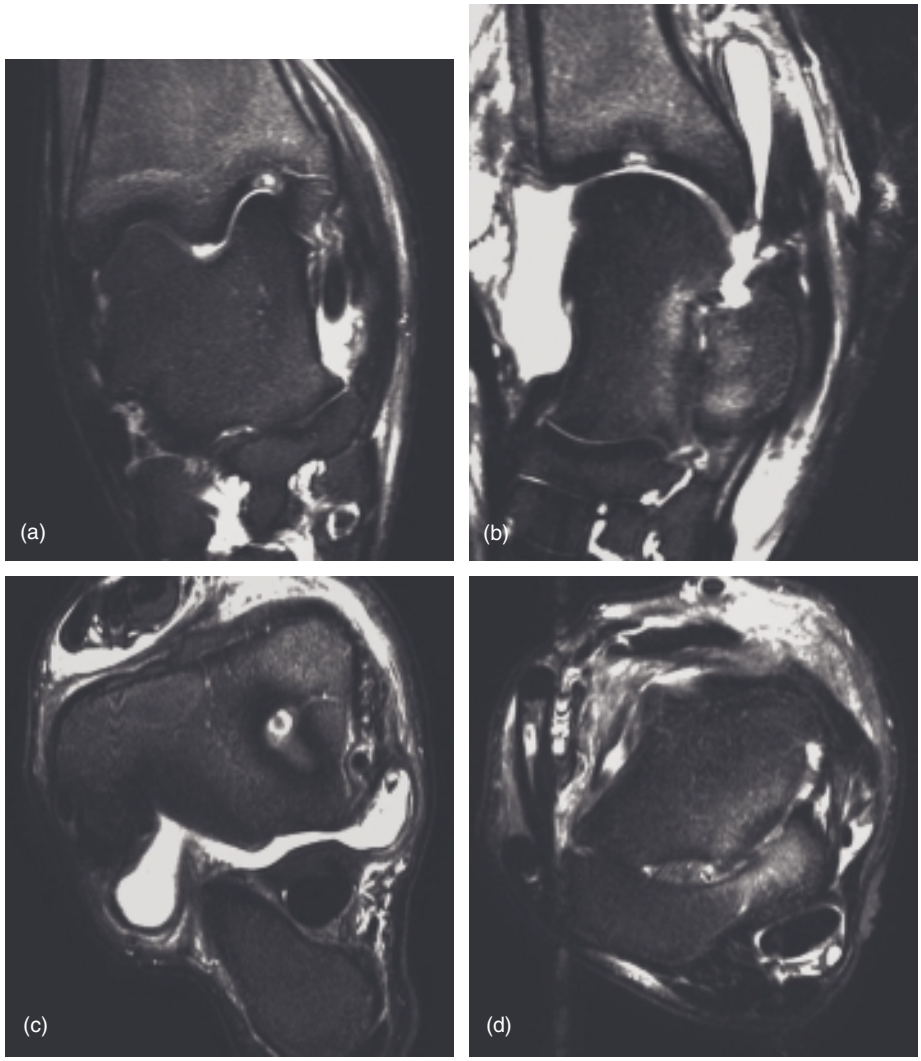

Figure 24.1 Talocalcaneal cyst and oedema. Dorsal plane (a), sagittal plane (b) and transverse plane STIR images at the level of the distal tibia (c), and talocalcaneal joint (d) of a 9-year-old Walking horse gelding with severe left hind limb lameness of 5 weeks' duration. The horse had a longer history of tarsocrural joint effusion that had previously been treated with intra-articular injections. Five weeks previously however, he became severely lame in the right hind limb and the right hock became very swollen and painful to palpation. The referring veterinary surgeon's radiographs revealed periosteal proliferation of the distal tibia and a possible cystic lesion within the distal tibia. On presentation the gelding was markedly lame at a walk. On flexion of the tarsus, he became non-weight-bearing for a short period of time. Radiographs of the right tarsus revealed periosteal proliferation at the level of the distal medial tibia and medial talus as well as osteoarthritis of the distal intertarsal and tarsometatarsal joints. Joint fluid analysis was suggestive of joint effusion with mild neutrophilic inflammation but not sepsis. The MR images showed a subchondral cystic lesion in the distal medial tibia at the articulation with the medial trochlear ridge of the talus, with surrounding increase in signal intensity. There is also increase in STIR signal intensity on the plantaromedial aspect of the talus and in both the talus and calcaneus adjacent to the medial part of the talocalcaneal joint. The horse was treated with antibiotics, anti-inflammatory medication and intramuscular Adequan. After 8 weeks, the joint was injected with corticosteroids and hyaluronic acid. He was confined to his stall for 4 months. On re-evaluation he was 2/5 lame at the trot in the same limb and still positive to upper limb flexion, yet walking comfortably and with a much improved range of joint motion. Radiographs at that time revealed evidence of talocalcaneal osteoarthritis. Images courtesy of Dr Michael Schramme, North Carolina State University.

injuries, and immobilization remains the mainstay of therapy [59, 74]. Conservative immobilization and rehabilitation are also recognized management regimes for ligament laxity in humans [75]. However, the severity of ligamentous damage as well as any concurrent damage to other components of the joints affect the management and ultimate prognosis of the horse [56]. Severe desmitis causing joint instability may also require more intensive joint immobilization through casting, splinting or Robert Jones banding.

Reports suggest that collateral ligament desmopathy in other joints demonstrates a poor prognosis for return to athleticism [57, 59, 74, 76]. In addition to the predisposition to osteoarthritis, desmitis may predispose to reinjury [75].

DESMITIS OF THE INTERTARSAL LIGAMENTS

Using MRI, desmitis of the intertarsal ligaments may be detectable as acute/active ligament pathology or chronic change with evidence of cortical and subchondral bone changes at the origin and insertion. There may also be associated osteoarthritic changes.

In the acute stages, management of intertarsal ligament damage should be aimed at stabilization of the joint. Loads on the affected ligament and joint should be minimized by limiting motion as far as possible to a normal plane and avoiding rotation. Associated synovitis and joint pain should also be managed. Where accessible, the use of ESWT may be an option, although there is no record of efficacy at this location. It is possible that tiludronate could be of benefit in the presence of associated bone damage and pain, but there does not appear to be documented evidence of effectiveness. In chronic intertarsal ligament desmitis, management will need to include treatment of any associated osteoarthritis of the distal tarsal joints.

LUXATION OF THE TARSUS

Luxations and subluxations of the tarsus are rare, but usually occur at the tarsometatarsal, centrodistal or talocalcaneal-centroquatral joints, or less commonly at the tarsocrural joint (with the tibia generally displaced distocranially) (see Figure 17.19). There will be loss of integrity of one or more ligaments due to rupture or severe strain, and there may be an associated fracture [77]. Open reduction and internal fixation is necessary if fractures are present [33].

Surgical arthrodesis is considered the treatment of choice for luxations of the distal hock joints [33, 78]; however, closed reduction and external coaption alone can also be successful, especially if pasture soundness is acceptable [79]. A full-limb cast should be applied for 3 months with several cast changes during that time. Tarsocrural joint luxations carry a poorer prognosis for athletic soundness because of associated joint and ligament damage [33, 80, 81]. Reduction may be difficult or impossible to achieve in some cases.

CUNEAN TENDONITIS AND BURSITIS

Cunean tendonitis and bursitis have been reported in Standardbred racehorses, especially 2- and 3-year olds, and the tendon may appear painful in some horses with distal tarsal osteoarthritis [82, 83]. Rest or decreased exercise regimens, with NSAID medication is generally effective at alleviating tendonitis. Cryotherapy has also been reported [84].

IDIOPATHIC TARSAL SYNOVITIS

Idiopathic tarsal synovitis is most common in young horses and causes distension of the tarsocrural joint without associated lameness [85, 86]. In many cases the cause cannot be identified, although an underlying osteochondrosis or chip fracture may be detectable on MRI even if this is not observed on radiography and ultrasonography. No treatment is required, although drainage followed by intra-articular medication with corticosteroids or atropine and pressure bandaging has been recommended if cosmetic correction is required [87].

OSTEOCHONDROSIS

Surgical treatment is often recommended for horses destined for athletic careers even if the animal is not lame at the time of diagnosis [33, 88–94]. When performed in young horses, the prognosis after arthroscopic surgery in terms of future athletic soundness is excellent, and it is also reasonably good for the resolution of synovial effusion [94]. In Warmbloods at least, surgery in foals before 5 months of age would be inappropriate because of the ability of some osteochondrosis lesions to heal spontaneously [88].

In one large study, 140 of 183 horses (76.5%) treated for osteochondrosis of the tarsocrural joint by arthroscopic surgery raced or returned to their intended use [89]. In another study [95], the performances of 64 Thoroughbreds and 45 Standardbreds treated by arthroscopic surgery for tarsocrural osteochondrosis prior to 2 years of age were compared with other foals from the dams of surgically treated horses. For the Thoroughbreds, 43% of those that had surgery raced as 2-year-olds and 78% raced as 3-year-olds, compared with 48% and 72% of the siblings that raced at the same ages. For the Standardbreds, 22% of those that had surgery raced as 2-year-olds and 43% raced as 3-year-olds, compared with 42% and 50% of the siblings. The median number of starts for surgically treated horses was lower than siblings for all groups except 3-year-old Thoroughbreds. There was a tendency for horses with multiple lesions to be less likely to race than horses with only a single lesion.

Conservative management of horses with tarsocrural osteochondrosis has also been used, with variable success rates, for example 47% for return to performance [96]. However, it is generally accepted that the prognosis for racing soundness is poorer in horses treated conservatively than horses treated by surgery [97–100].

OSSEOUS CYST-LIKE LESIONS AND SUBCHONDRAL BONE CYSTS

Osseous cyst-like lesions and subchondral bone cysts are poorly described in the equine tarsus, but have been reported in the medial malleolus, intertrochlear groove and lateral trochlear ridge of the talus, lateral malleolus, distal intermediate ridge and distal medial aspect of the tibia [101–103] (Figure 24.1; and see Figures 17.7–17.10). Diagnosis by MRI has been reported [103]. Surgical treatment by debridement was reported to be successful with return to soundness in four of six horses (67%), whereas five conservatively treated horses continued to exhibit lameness (although two were sufficiently sound for light pleasure riding) [102]. Subsequent development of osteoarthritis was documented in one horse with a subchondral lesion of the talus [103]. Injection of the cyst with corticosteroids has been described to be a viable alternative treatment to surgical debridement of subchondral bone cysts [104, 105]; however, there is currently limited information on this type of treatment for osseous cysts of the tarsus.

TARSAL FRACTURES

Distal tibia: malleolar fractures

Fractures of the malleolus [51–54, 106–109] are often associated with avulsion of the short collateral ligaments and are frequently comminuted [108]. Associated ligament damage may be detected using MRI. Conservative treatment has been successful for small or non-displaced malleolar fractures [54]; however, surgical intervention may result in a shorter convalescence [2]. Surgical removal of small fragments has been recommended for multiple fragments and those smaller than 3×1 cm. Fragments larger than 3 cm can be reattached to the parent bone [109]. The prognosis for return to function after malleolar fractures is variable [109]. A fair to good prognosis is reported after surgical treatment [109]; 81% of horses with lateral malleolar fractures treated by fragment removal returned to athleticism [53] and 100% of five horses with either medial or lateral malleolar fractures returned to athleticism [54]. Horses with multiple fragments treated conservatively appear more likely to develop osteoarthritic changes within the tarsocrural joint [110].

Talus

Trochlear ridges of the talus

Arthroscopic removal of trochlear ridge fracture fragments is the preferred method of fragment removal [108, 109]. Larger fragments may necessitate removal via an arthrotomy directly over the lesion [111]. Large fragments (larger than the distal third to half of the ridge) may also be repaired through interfragmentary compression with 3.5 mm cortical screws or small cannulated screws placed in lag fashion, providing anatomic reconstruction can be achieved [109]. Absorbable polydioxanone pins and cannulated screws have also been used to achieve interfragmentary compression [109].

Fractures of the central and distal medial trochlear ridge are often larger and therefore lag screw fixation is recommended [109]. Horses that undergo prompt surgical treatment have minimal soft tissue injury and degenerative joint disease, and with those fragments smaller than 3 cm have a favourable prognosis [109].

Fractures of the distal lateral or medial aspect of the body of the talus

Conservative treatment is normally unsuccessful. Large fragments can be stabilized with interfragmentary compression with 3.5 mm cortical screw placed in lag fashion. Resolution of tarsocrural effusion and return to athleticism is favourable [33].

Sagittal fractures of the talus

Horses with incomplete sagittal fractures can be treated conservatively and may require 7–8 months or more to return to athleticism [112]. Lag screw fixation (4.5 mm or 5.5 mm cortical screws) under arthroscopic guidance to achieve anatomic reduction is the treatment of choice for complete fractures [109]. The fractures can be repaired from either the medial or lateral aspect of the joint; however, the medial fragment is generally smaller [109, 113]. Horses require 8–12 weeks of stall rest and radiographic evaluation of healing prior to return to work. If the fractures are severely comminuted, they are normally considered inoperable as there is joint instability and severe soft tissue damage [109].

Conservative therapy for incomplete sagittal fractures yields a good prognosis (64% of race horses returned to athleticism [112]) (Figure 24.2). The prognosis for simple sagittal talus fractures repaired by lag screw fixation to achieve anatomic reduction also appears favourable [109].

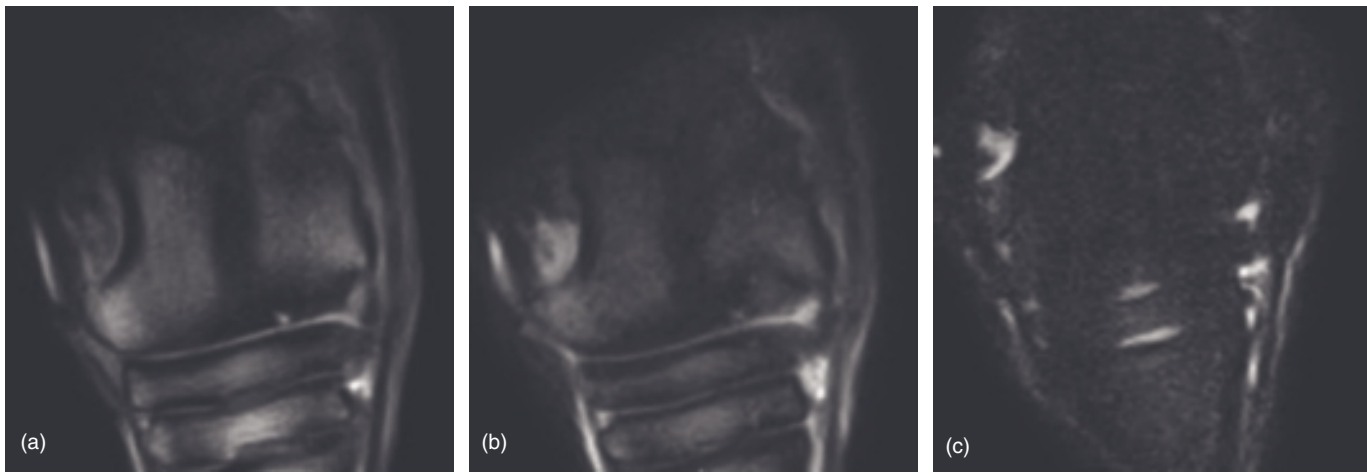

Figure 24.2 Dorsal T1-weighted (a), T2* gradient echo (b) and STIR images (c) of follow-up scans on the left tarsus of a 12-year-old Arabian endurance horse 6 months following a minimally displaced sagittal plane fracture of the talus. The horse had been managed conservatively with box rest. At this point the horse was weight-bearing and walking comfortably on the limb. Compared with the initial images (see Figure 17.1), the low signal intensity on T1-weighted images is limited to very close to the fracture line. The fracture line itself is only seen as a clear entity at the distal extent of the fracture. On T2* gradient-echo images, there is no evidence of increased signal intensity and there is only a region of low signal intensity immediately adjacent to the fracture line. This previous high signal intensity on STIR images in the talus is completely absent at 6 months.

Calcaneus

Small fragments from the calcaneus that are not associated with synovial structures can either be left to heal conservatively or be removed via a direct approach if they are infected. Larger fragments should be repaired using lag screw fixation.

Transverse fractures of the shaft of the calcaneus should be stabilized by application of wires and plates using tension band principles. Plates should preferably be placed on the plantaro-lateral side of the bone to avoid disruption of the soft tissues on the plantar calcaneus [114]. The prognosis for return to athleticism is considered guarded [109, 114, 115]. Comminuted fractures that involve the body and sustentaculum tali but not the tuber calcaneus can be treated conservatively, as periarticular tissues generally maintain acceptable anatomic alignment [109].

The surgical approach to the sustentaculum tali depends on the involvement of the tarsal sheath as well as the location of the fracture fragment. Fracture fragment removal may be achieved tenoscopically, via tenovaginotomy or via a direct approach to the fragment if it is outside the tendon sheath [116].

Even with immediate treatment, horses with open sustentaculum tali fractures have been reported to have a guarded prognosis and horses with delayed treatment have a grave prognosis [115, 118, 119]; however, more recently, a 60% return to athleticism was reported in sustentaculum tali fractures treated aggressively surgically [116].

Fractures of the small tarsal bones

Fractures of the central and third tarsal bone can be treated surgically or conservatively and controversy exists regarding the most appropriate treatment [120–123]. Conservative treatment with stall rest has been successful; however, return to athleticism may be prolonged (8–10 months) and osteoarthritis is frequently a consequence, although osteoarthritis itself can also be a consequence of surgical treatment [120, 123–125]. Surgical treatment involves lag screw fixation (3.5 mm or 4.5 mm cortical screws) through stab incisions under radiographic or fluoroscopic guidance followed by 4–6 months' rest. Preoperative planning is essential as central tarsal bones may have comminuted fragments that displace on screw placement [125] and the likelihood of comminution has been suggested as a reason for improved long-term results using internal fixation for central tarsal bone fractures [123]. Arthrodesis of the small tarsal joints has also been utilized as a surgical option in horses with fracture fragments that are too small to allow internal fixation or horses with chronic fractures that have caused secondary osteoarthritis in these joints.

Third tarsal bone fractures appear to have a better prognosis for return to function than central tarsal bone fractures [123] and this may be associated with the absence of communication with the tarsocrural joint and the decreased likelihood of comminution of this bone. Prognosis for return to athleticism is variable; however, most commonly it appears to be

approximately 70% and ranges from 40 to 92% irrespective of conservative or surgical management [120, 122, 123, 126].

TARSAL BONE TRAUMA/BRUISE

The authors have experience of a limited number of lame horses with evidence of a 'bone bruise' pattern affecting the tarsal bones, especially the fourth tarsal bone, central tarsal bone or calcaneus, diagnosed by MRI (see Figures 17.4 and 17.5). These lesions may occur in association with osteoarthritis of the centrodistal or tarsometatarsal joints or of the talocalcaneal joint, or they may occur as an isolated lesion. It has been assumed that most horses presenting with bone bruise patterns in the tarsal bones in the absence of osteoarthritis are induced either by repetitive biomechanical stress or an acute episode of trauma; some cases may have associated soft tissue damage. Our limited experience suggests that many of these horses with acute bone trauma will improve following a period of rest and controlled exercise. Tiludronate may also be helpful in these cases. However, if this altered signal intensity is related to adjacent joint pathology, then outcome may be poor.

ASEPTIC CALCANEAL BURSITIS

Aseptic calcaneal bursitis presents as lameness associated with distension of the bursae; the lameness improves following intrathecal local analgesia. It has been associated with a number of underlying lesions, including osteolytic lesions of the calcaneal tuber [128, 129] (see Figure 17.6), tearing of the retinacular insertions of the superficial digital flexor tendon, superficial digital tendonitis and traumatic fragmentation of the calcaneus [94]. Osteolytic lesions of the calcaneal tuber occur at the proximal plantar margin and/or apex, and may be avulsion injuries of the plantar ligament or gastrocnemius tendon. Surgical removal of degenerate bone and debridement (via bursoscopy) has been reported to have been successful in allowing a small number of affected horses to return to soundness [94]. Partial tears of the medial or lateral retinacular insertions of the superficial digital flexor tendon have been identified in some horses with lameness that improves following intrathecal analgesia of the distended calcaneal bursa. The lesions can be identified by tenoscopy and are reported to benefit from surgical debridement [94]. Closed intrathecal fragmentation of the calcaneal tuber frequently results in secondary calcaneal bursitis. Fragments may be removed surgically via bursoscopy and the fracture debrided with curettes [94].

SEPTIC CALCANEAL BURSITIS

Treatment of septic calcaneal bursitis involves broad spectrum systemic antibiotics with or without intravenous regional perfusion and repeated surgical lavage/debridement of the affected bursae (which can be performed via bursoscopy or via needle lavage under ultrasound guidance) [94, 127–130]. Sequestrae and bone fragments should be surgically removed, and

areas of osteomyelitis debrided and curetted. The long-term prognosis of septic calcaneal bursitis varies depending on which bursae are affected and whether or not there is associated calcaneal bone damage. In one retrospective study of septic calcaneal bursitis in 24 horses, the prognosis for septic subcutaneous calcaneal bursitis (without involvement of the deeper bursae) was shown to be excellent (six of six cases made a successful recovery) [128]. The outcome for horses with infection of the deeper calcaneal bursae, but without osseous damage, was good (six of eight, [75%] survived), but the outcome for cases of septic bursitis with bone involvement was poorer (four of nine [44%] survived).

TENOSYNOVITIS OF THE DEEP DIGITAL FLEXOR TENDON SHEATH (TARSAL SHEATH)

Mild bilateral distension of the tarsal sheath not associated with lameness may be observed, especially in young horses; this condition is usually transient and does not require specific therapy [127]. More severe distension of the tarsal sheath is due to inflammation of the sheath (aseptic tenosynovitis) and may be associated with damage to the deep digital flexor tendon (DDFT) (lateral digital flexor tendon), the mesotendon attachments of the DDFT within the sheath and/or the sustentaculum tali [118, 127, 131–133] (see Figures 17.26 and 17.27). The cause is assumed to be chronic low-grade trauma that causes damage to the tendon or sheath, and/or bony changes to the sustentaculum tali, which irritate the sheath. Fractures of the sustentaculum tali may also cause tenosynovitis. Other causes may include mineralization of the sheath, adhesions, tendovaginal masses, bony exostoses, intersynovial communication with the tarsocrural joint or calcaneal bursa [118, 119, 127, 133, 134].

Cases that have bony involvement are usually chronically lame, whereas some horses with chronic tenosynovitis without associated bone or tendon damage may remain sound. In sound horses no treatment may be required, and affected horses can often be worked as normal. Persistent or recurrent low-grade lameness associated with distension of the tarsal sheath may respond to reduced exercise/rest and medical treatment (including systemic and topical NSAIDs, intra-thecal medication of the sheath with hyaluronan, PSGAGs or corticosteroids).

Tarsal sheath tenoscopy is indicated in chronic cases of tenosynovitis that respond poorly to medical therapy [94]. Tenoscopy permits debridement of masses and adhesions, debridement of DDFT tears, removal of mineralized masses within the sheath, and removal of fragments and bony proliferations of the sustentaculum tali [94, 119, 135, 136]. Postoperatively, some horses may show considerable pain, requiring medication with NSAIDs and epidurally administered morphine/detomidine [94]. Postoperative medication of the sheath with hyaluronan may be beneficial. There are no long-term follow-up studies of horses treated tenoscopically for aseptic tenosynovitis of the tarsal sheath, but it is recognized that some horses will be improved following surgery (including synovectomy and mass removal), depending on the nature and extent of the lesions present in the sheath [94].

Chronic degenerative changes of the sustentaculum tali and overlying DDFT have a guarded prognosis for resuming normal work [33].

SEPTIC TENOSYNOVITIS OF THE TARSAL SHEATH

Septic tenosynovitis usually occurs secondary to wounds, but may rarely occur following bacteraemic spread of infection from another site in the body [137]. As a result of its protected location, the tarsal sheath is not as commonly affected as some other tendon sheaths, such as the digital flexor tendon sheath [138–140]. Wounds to the calcaneus and sustentaculum tali may be complicated by concurrent osteomyelitis and septic tenosynovitis [117, 135–141]. Treatment includes wound debridement, systemic and intrathecal antibiotics, intravenous regional perfusion of antibiotics, lavage, and tenoscopic debridement and lavage [94, 136–139, 142–145]. Horses with simple septic tenosynovitis have a good prognosis for return to athletic function with prompt and aggressive therapy. However, horses with associated tendon injury, joint sepsis or significant pannus formation within the tarsal sheath have a poorer prognosis for long-term soundness [145]. Concurrent osteomyelitis of the sustentaculum tali is considered a serious complication and carries a more guarded prognosis [135, 141]; however, affected horses can make a full recovery with return to their previous use [117].

EXTENSOR TENDON LACERATIONS

The long-term prognosis is variable depending on the extent of the wound and the involvement of other structures. However, in most reports, a fair to good prognosis for soundness is reported with around 75% of horses becoming sound [146–149]. Long-term loss of extensor function does not appear to seriously affect the gait, although in some studies, a better outcome has been reported for partial disruption compared to complete laceration of the extensor tendons [150, 151]. Common complications of this type of injury include exuberant granulation tissue and sequestration.

SEPTIC ARTHRITIS/OSTEOMYELITIS

Septic arthritis (most commonly of the tarsocrural joint) (see Figure 17.12) is common in adult horses following wounds to the tarsal region [152], and in foals secondary to haematogenous spread of bacteria ('joint ill') or secondary to an extension of septic physitis (see Figure 17.13). It can also arise iatrogenically following intra-articular medication [153] and surgery, including arthroscopic surgery [154]. Concurrent osteomyelitis of the tarsal bones may occur, especially in foals with joint ill [155] (see Figure 17.14).

Treatments include wound debridement, intra-articular and systemic antibiotics, joint lavage, and arthroscopic lavage and debridement [94, 143, 156]. Constant-rate infusion systems can be used to continuously deliver antibiotics into the affected joint [144, 157]. Gentamicin-impregnated collagen sponges may also be safely implanted into the tarsocrural joint to provide a rapid, yet short-lived release of intra-articular gentamicin [158].

Gentamicin-impregnated polymethylmethacrylate beads placed in a drill tract across the affected joint have been used successfully to treat horses with sepsis of the small tarsal joints [159]. The prognosis for adult horses with septic arthritis of the tarsocrural joint is good, with over 80% returning to their previous level of performance [139]; the prognosis for foals with septic arthritis is less favourable [139], and the prognosis for ability to race is unfavourable [160]. The prognosis in foals is affected by numerous factors, such as multiple joint involvement and multisystem disease. Associated osteomyelitis or septic physitis in foals may require surgical debridement.

INCOMPLETE OSSIFICATION OF THE TARSAL BONES

Incomplete ossification of the tarsal bones is a problem of premature or dysmature newborn foals; however, clinical signs may not be evident until later in life [161]. The condition commonly presents as an angular limb deformity (especially valgus deformity), and is associated with radiographic evidence of incomplete ossification of the central and/or third tarsal bones, with or without collapse of the affected bones. Collapse typically leads to fragmentation of the dorsal aspect of the tarsal bones. The degree of collapse of the dorsal aspect of the affected bones can be graded as type 1 (<30% collapse of the dorsal aspect of the bone compared with the height of the plantar aspect) or type 2 (>30% collapse). MRI may add additional information in relation to conformation of the tarsal bones, their articulations and degree of fragmentation. Collapse of the tarsal bones frequently leads to degenerative joint disease, and the long-term prognosis for foals with type 2 collapse is significantly poorer than foals with type 1 collapse [162].

Treatment of incomplete ossification of the tarsal bones should be aimed at maintaining the true longitudinal axis of the affected limb so that ossification can proceed without further distortion of the cartilaginous templates. Stall confinement, and splints or tube casts can be used to reduce the compressive forces acting on the dorsal aspects of the tarsal bones [162]. Older foals with valgus deformity can be treated with hemicircumferential periosteal transection and stripping, or with growth plate retardation techniques [163, 164].

REFERENCES

[1] Stashak TS. Bone spavin (osteoarthritis or degenerative joint disease of the distal tarsal joints). In: Stashak TS (ed.). *Adam's Lameness in Horses*, 4th edn. Philadelphia, PA: Lea & Febiger, 1987, pp. 694–704.
[2] Dabareiner RM, Carter GK, Dyson SJ. The tarsus. In: Ross MW, Dyson SJ (eds). *Diagnosis and Management of Lameness in the Horse*. Philadelphia, PA: Saunders, 2003, pp. 440–9
[3] Vaughan JT. Analysis of lameness in the pelvic limb and selected cases. *Proc Am Assoc Equine Pract* 1965; **11**: 223.
[4] Gill HE. Diagnosis and treatment of hock lameness. *Proc Am Assoc Equine Pract* 1973; **19**: 257–62.
[5] O'Brien T. Radiographic interpretation of the equine tarsus. *Proc Am Assoc Equine Pract* 1973; **19**: 289–300.
[6] Moyer W. Bone spavin: a clinical review. *J Equine Med Surg* 1978; **2**: 362–71.

[7] Baxter GM, Dechant JE, Southwood LL. Diagnosis of distal tarsal osteoarthritis. *Compend Contin Educ Pract Vet* 2003; **25**: 138–47.
[8] Eksell P, Uhlhorn H, Carlsten J. Evaluation of different projections for radiographic detection of tarsal degenerative joint disease in Icelandic horses. *Vet Radiol Ultrasound* 1999; **40**: 228–32.
[9] Gabel AA. Prevention, diagnosis and treatment of inflammation of the distal hock. *Proc Am Assoc Equine Pract* 1983; **28**: 287–98.
[10] Bjornsdottir S, Axelsson M, Eksell P, Sigurdsson H, Carlsten J. Radiographic and clinical survey of degenerative joint disease in the distal tarsal and fetlock joints in Icelandic horses. *Equine Vet J* 2000; **32**: 268–72.
[11] Branch M, Murray R, Dyson S, Goodship A. Alteration of distal tarsal subchondral bone thickness pattern in horses with tarsal pain. *Equine Vet J* 2007; **39**: 101–5.
[12] Branch M, Murray R, Dyson S, Goodship A. Magnetic resonance imaging of the equine tarsus. *Clin Tech Equine Pract* 2007; **6**: 96–102.
[13] Back W, Remmen JL, Knaap J, de Koning JJ. Effect of lateral heel wedges on sagittal and transverse plane kinematics of trotting Shetland ponies and the influence of feeding and training regimes. *Equine Vet J* 2003; **35**: 606–12.
[14] Baxter GM. Review of methods to manage horses with advanced distal tarsal osteoarthritis. *Proc Am Assoc Equine Pract* 2004; **50**: 299–305.
[15] McCarroll D, McClure S. Extracorporeal shock wave therapy for treatment of osteoarthritis of the tarsometatarsal and distal intertarsal joints of the horse. *Proc Am Assoc Equine Pract* 2000; **46**: 200–2.
[16] Schnewlin M, Lischer C. Extracorporeal shock wave therapy in veterinary medicine. *Schweiz Arch Tierheilkd* 2001; **143**: 227.
[17] Lees P, Creed RFS, Gerring EEL *et al*. Biochemical and haematological effects of phenylbutazone in horses. *Equine Vet J* 1983; **15**: 158–67.
[18] Goodrich LR, Nixon AJ. Medical treatment of osteoarthritis in the horse – a review. *Vet J* 2006; **171**: 51–69.
[19] Lynn RC, Hepler DI, Kelch WJ, Bertone JJ, Smith BL, Vatistas NJ. Double-blinded placebo-controlled clinical field trial to evaluate the safety and efficacy of topically applied 1% diclofenac liposomal cream for the relief of lameness in horses. *Vet Ther* 2004; **5**: 128–38.
[20] Frisbie DD, McIlwraith CW, Kawkak CE, Werpy NM, Pearce GL. Evaluation of topically administered liposomal cream for treatment of horses with experimentally induced osteoarthritis. *Am J Vet Res* 2009; **70**: 210–15.
[21] Labens R, Mellor DJ, Voute LC. Retrospective study of the effect of intra-articular treatment of osteoarthritis of the distal tarsal joints in 51 horses. *Vet Rec* 2007; **161**: 611–16.
[22] Byam-Cook KL, Singer ER. Is there a relationship between clinical presentation, diagnostic and radiographic findings and outcome in horses with osteoarthritis of the small tarsal joints? *Equine Vet J* 2009; **41**: 118–23.
[23] Frisbie DD, Kawkak CE, McIlwraith CW, Werpy NM. Evaluation of polysulfated glycosaminoglycan or sodium hyaluronan administered intra-articularly for treatment of horses with experimentally induced osteoarthritis. *Am J Vet Res* 2009; **70**: 203–9.
[24] Caron JP, Kaneene JB, Miller R. Results of a survey of equine practitioners on the use and perceived efficacy of polysulfated glycosaminoglycans. *J Am Vet Med Assoc* 1996; **209**: 1564–8.
[25] Hanson RR. Oral glycosaminoglycans in treatment of degenerative joint disease in horses. *Equine Pract* 1996; **18**: 18–22.
[26] Branch MV, Murray RC, Dyson SJ, Goodship AE. Is there a characteristic distal tarsal subchondral bone plate thickness pattern in horses with no history of hindlimb lameness? *Equine Vet J* 2005; **37**: 450–5.
[27] Gough MR, Thibaud D, Smith RKW. Tiludronate infusion in the treatment of bone spavin: a double blind placebo-controlled trial. *Equine Vet J* 2010; **42**: 381–7.
[28] McIlwraith CW, Bramlage LR. Surgical treatment of joint injury. In: McIlwraith CW, Trotter GW (eds). *Joint Disease in the Horse*. Philadelphia, PA: WB Saunders, 1996, pp. 292–317.
[29] Adams OR. Surgical arthrodesis for treatment of bone spavin. *J Am Vet Med Assoc* 1970; **157**: 1480–5.

[30] Edwards GB. Surgical arthrodesis for the treatment of bone spavin in 20 horses. *Equine Vet J* 1982; **14**: 117–21.
[31] Barber SM. Arthrodesis of the distal intertarsal and tarsometatarsal joints in the horse. *Vet Surg* 1984; **4**: 227–35.
[32] Wyn-Jones G, May SA. Surgical arthrodesis for the treatment of osteoarthrosis of the proximal intertarsal, distal intertarsal, and tarsometatarsal joints in 30 horses: a comparison of 4 different techniques. *Equine Vet J* 1986; **18**: 59–64.
[33] Auer JA. Tarsus. In: Auer JA, Stick JA (eds). *Equine Surgery*, 3rd edn. Philadelphia, PA: Saunders, 2006, pp. 1288–307.
[34] Mackay RCJ, Liddell WA. Arthrodesis on the treatment of bone spavin. *Equine Vet J* 1972; **4**: 34–6.
[35] Sonnichsen HV, Svalastoga E. Surgical treatment of bone spavin in the horse. *Equine Pract* 1985; **7**: 6.
[36] Archer RM, Schneider RK, Lindsay WA, Wilson JW. Arthrodesis of the equine distal tarsal joints by perforated stainless steel cylinders. *Equine Vet J* 1989; **6**: 125–30.
[37] Dechant JE, Baxter GM, Southwood LL *et al*. Use of a three-drill-tract technique for arthrodesis of the distal tarsal joints in horses with distal tarsal osteoarthritis: 54 cases (1990–1999). *J Am Vet Med Assoc* 2003; **223**: 1800–5.
[38] Hague BA, Guccione A. Laser-facilitated arthrodesis of the distal tarsal joints. *Clin Tech Equine Pract* 2002; **1**: 32–5.
[39] Hague BA, Guccione A. Clinical impressions of a new technique utilizing a Nd:YAG laser to arthrodese the distal tarsal joints. *Vet Surg* 2000; **29**: 464.
[40] Scruton C, Baxter GM, Frisbie DD. Comparison of intra-articular drilling and diode laser treatment for arthrodesis of the distal tarsal joints in normal horses. *Vet Surg* 2003; **32**: 495.
[41] Bohanon TC, Schneider RK, Weisbrode SE. Fusion of the distal intertarsal and tarsometatarsal joints in the horse using intra-articular sodium monoiodoacetate. *Equine Vet J* 1991; **23**: 289–95.
[42] Bohanon TC. Chemical fusion of the distal tarsal joints with sodium monoiodoacetate in 38 horses clinically affected with bone spavin. *Vet Surg* 1995; **24**: 421.
[43] Williams JM, Brandt KD. Immobilization ameliorates chemically-induced articular cartilage damage. *Arthritis Rheum* 1984; **27**: 208.
[44] Sammmut EB, Kannegieter NJ. Use of sodium monoiodoacetate to fuse the distal hock joints in horses. *Aust Vet J* 1995; **72**: 25–8.
[45] Kristoffersen K. Investigations of aseptic hock diseases in the horse. PhD thesis, Royal Veterinary Agricultural University, Copenhagen, Denmark, 1981.
[46] Inschoot J, Steenhaut M, DeMoor A. Partial tibial neurectomy and neurectomy of the deep peroneal nerve as a treatment of bone spavin in 24 horses. *Equine Pract* 1995; **17**: 8–13.
[47] White NA, Turner TA. Hock lameness associated with degeneration of the talocalcaneal articulation: report of two cases. *Vet Med Small Anim Clin* 1980; **75**: 678–81.
[48] Smith RK, Dyson SJ, Schramme MC *et al*. Ostearthritis of the talocalcaneal joint in 18 horses. *Equine Vet J* 2005; **37**: 166–71.
[49] Pauwels DT, Adams SB, Blevins WB. Arthrodesis of the talocalcaneal joint of two horses with talocalcaneal osteoarthritis. *Vet Comp Orthop Traumatol* 2005; **18**: 7–12.
[50] Whitcomb M. Ultrasonography of the equine tarsus. *Proc Am Assoc Equine Pract* 2006; **52**: 13–30.
[51] Boero M, Kneller S, Baker G, Metcalf M, Twardock A. Clinical, radiographic, and scintigraphic findings associated with enthesitis of the lateral collateral ligaments of the tarsocrural joint in standardbred racehorses. *Equine Vet J* 1988; **6**(Suppl.): 53–9.
[52] Bramlage L. Traumatic and developmental lesions of the tarsus. *Proc Am Assoc Equine Pract* 2006; **52**: 1–4.
[53] Wright I. Fractures of the lateral malleolus of the tibia in 16 horses. *Equine Vet J* 1992; **24**: 424–9.
[54] Jakovljevic S, Gibbs C, Yeats J. Traumatic fractures of the equine hock: a report of 13 cases. *Equine Vet J* 1982; **14**: 62–8.
[55] Phillips T. Unusual hock problems. *Proc Am Assoc Equine Pract* 1986; **32**: 663–7.

[56] McIlwraith C. Specific disease of joints: sprains and luxations, meniscal tears, and osteochondral fragmentation. In: Stashak T (ed.). *Adams' Lameness in Horses*, 5th edn. Philadelphia,PA: Lea & Febiger, 2002, pp. 518–33.
[57] Desmaizieres L-M, Cauvin E. Carpal collateral ligament desmopathy in three horses. *Vet Rec* 2005; **157**: 197–201.
[58] Rodgerson D, Spirito M. Repair of collateral ligament instability in 2 foals by using suture anchors. *Can Vet J* 2001; **42**: 557–60.
[59] Yovich J, Turner A, Stashak T, McIlwraith C. Luxation of the metacarpophalangeal and metatarsophalangeal joints in horses. *Equine Vet J* 1987; **19**: 295–8.
[60] Cauvin E, Munroe G, Boyd J, Paterson C. Ultrasonographic examination of the femorotibial articulation in horses: imaging of the cranial and caudal aspects. *Equine Vet J* 1996; **28**: 285–96.
[61] Mackenzie R, Palmar C, Lomas D, Dixon A. Magnetic resonance imaging of the knee: diagnostic performance studies. *Clin Radiol* 1996; **51**: 251–7.
[62] Schneck C, Mesgarzadeh M, Bonakdarpour A. MR imaging of the most commonly injured ankle ligaments. II. Ligament injuries. *Radiol* 1992; **184**: 507–12.
[63] Schneck C, Mesgarzadeh M, Bonakdarpour A, Ross G. MR imaging of the most commonly injured ankle ligaments. I. Normal anatomy. *Radiol* 1992; **184**: 499–506.
[64] Murray R, Mair T. Use of magnetic resonance imaging in lameness diagnosis in the horse. *In Pract* 2005; **27**: 70–8.
[65] Caminoto E, Alves A, Amorim R, Thomassian A, Hussni C, Nicoletti J. Ultrastructural and immunocytochemical evaluation of the effects of extracorporeal shock wave treatment in the hind limbs of horses with experimentally induced suspensory ligament desmitis. *Am J Vet Res* 2005; **66**: 892–6.
[66] Leung M, Ng G, Yip K. Therapeutic ultrasound enhances medial collateral ligament repair in rats. *Ultrasound Med Biol* 2006; **32**: 449–52.
[67] Herthel D. Enhanced suspensory ligament healing in 100 horses by stem cell and othe bone narrow components. *Proc Am Assoc Equine Pract* 2001; **47**: 319–21.
[68] Dahlgren L, Rosenbusch R, Booth L. Development of an in vitro model for the study of the response of equine tendon fibroblasts to injury and medication. *Vet Comp Orthop Traumatol* 1997; **10**: 6–11.
[69] Smith R, Korda M, Blunn G. Isolation of autolougous equine mesenchymal stem cells from bone marrow into the superficial digital flexor tendon as a potential novel treatment. *Equine Vet J* 2003; **35**: 99–102.
[70] Woo S, Hildebrand K, Watanabe N. Tissue engineering of ligament and tendon healing. *Clin Orthop* 1999; **367S**: S312–S323.
[71] van der Harst M, Rijkenhuizen A. The use of a polypropylene mesh for treatment of ruptured collateral ligaments of the equine metacarpophalangeal joint: a report of 2 cases. *Vet Q* 2000; **22**: 57–60.
[72] Sanders-Shamis M, Gabel A. Surgical reconstruction of a ruptured medial collateral ligament in a foal. *J Am Vet Med Assoc* 1988; **193**: 80–2.
[73] Bertone A, Goin S, Kamei S *et al*. Metacarpophalangeal collateral ligamant reconstruction using small intestinal submucosa in an equine model. *J Biomed Mater Res* 2008; **84A**: 219–29.
[74] Kawcak C, Trotter G. Other joint conditions. In: Ross M, Dyson S (eds). *Diagnosis and Management of Lameness in the Horse*. Philadelphia, PA: WB Saunders, 2003, pp. 610–13.
[75] Kaeding C, Pedroza A, Parker RD, Spindler KP, McCarty EC, Andrish JT. Intraarticular findings in the reconstructed multiligament-injured knee. *Arthroscopy* 2005; **21**: 424–30.
[76] Chopin J, Wright J, Melville L, Robinson W. Lateral collateral ligament avulsion of the humeroradial joint in a horse. *Vet Radiol Ultrasound* 1997; **38**: 50–4.
[77] Wheat JD, Rhode EA. Luxation and fracture of the hock of the horse. *J Am Vet Med Assoc* 1964; **145**: 341–4.
[78] Dowling BA, Dart AJ, Hodgson DR. Surgical treatment of tarsometatarsal joint luxation in a miniature horse foal. *Aust Vet J* 2000; **78**: 683–4.
[79] Moll HD, Slone DE, Humburg JM, Jagar JE. Traumatic tarsal luxation repaired in three horses without internal fixation in three horses and three ponies. *J Am Vet Med Assoc* 1987; **190**: 297–300.

[80] Reeves MJ, Trotter GW. Tarsocrural joint luxation in a horse. *J Am Vet Med Assoc* 1991; **199**: 1051–3.
[81] Laing JA, Caves SF, Rawlinson RJ. Successful treatment of a tarsocrural joint luxation in a pony. *Aust Vet J* 1992; **69**: 200–1.
[82] Gabel AA. Diagnosis, relative incidence, and probable cause of cunean tendon bursitis-tarsitis of Standardbred horses. *J Am Vet Med Assoc* 1979; **175**: 1079–85.
[83] Gabel AA. Treatment and prognbosis for cunean tendon bursitis-tarsitis of Standardbred horses. *J Am Vet Med Assoc* 1979; **175**: 1086–8.
[84] Jacobs KM, Oliver TPS. Cryotherapy. In: Ross MW, Dyson SJ (eds). *Diagnosis and Management of Lameness in the Horse*. Philadelphia, PA: WB Saunders, 2003, pp. 7802.
[85] Van Pelt RW. Intra-articular injection of 6 alpha-methyl 17 alpha-hydroxyprogesterone acetate in tarsal hydrarthrosis (bog spavin) in the horse. *J Am Vet Med Assoc* 1967; **151**: 1159–71.
[86] Rooney JR. Bog spavin and tibiotarsal lesions in the horse. *Mod Vet Pract* 1973; **54**: 43–4.
[87] Van Pelt RW, Riley WF. Therapeutic management of tarsal hydarthrosis (bog spavin) in the horse by intra-articular injection of prednisolone. *J Am Vet Med Assoc* 1967; **151**: 328–38.
[88] Dik KJ, Emerink E, van Weeran PR. Radiographic development of osteochondral abnormalities in the hock and stifle of Dutch Warmblood foals from age 1 to 11 months. *Equine Vet J* 1999; **31**(Suppl. 1): 9–15.
[89] McIlwraith CW, Foerner JJ, Davis DM. Osteochondritis dissecans of the tarsocrural joint: results of treatment with arthroscopic surgery. *Equine Vet J* 1991; **23**: 155–62.
[90] Lindsell CE, Hilbert BJ, McGill CA. A retrospective clinical study of osteochondrosis dissecans in 21 horses. *Aust Vet J* 1983; **60**: 291–3.
[91] Olsson I, Pettersson H, Stromberg B. The prognosis of treated osteochondrosis in the hock joint of Standardbreds. *Svensk Veterinartidning* 1983; **35**(Suppl 3): 70–1.
[92] Hoppe F, Philipsson J. Racing performance of trotting horses with osteochondrosis of the hock. *Svensk Veterinartidning* 1984; **36**: 285–8.
[93] Sonnichsen HV, Hansen SF. Osteochondrosis dissecans in the tbiotarsal joint. Results by surgical treatment. *Nord Vet Med* 1985; **37**: 136–9.
[94] McIlwraith CW, Nixon AJ, Wright IM, Boening KJ. *Diagnostic and Surgical Arthroscopy in the Horse*, 3rd edn. Edinburgh: Mosby, 2005.
[95] Beard WL, Bramlage LR, Schneider RK, Embertson RM. Postoperative racing performance in standardbreds and thoroughbreds with osteochondrosis of the tarsocrural joint: 109 cases (1984–1990). *J Am Vet Med Assoc* 1994; **204**: 1655–9.
[96] Rose JA, Sande RD, Rose EM. Results of conservative management of osteochondrosis in the horse. *Proc Am Assoc Equine Pract* 1985; **31**: 617–26.
[97] DeMoor A, Verschooten F, Desmet P, Steenhaut M, Hoorens J, Wolf G. Osteochondrosis dissecans of the tbiotarsal joint in the horse. *Equine Vet J* 1972; **4**: 139–43.
[98] Stromberg B, Rejno S. Osteochondrosis in the horse. I. A clinical and radiological investigation of osteochondrosis dissecans of the knee and hock joint. *Acta Radiol* 1978; **358**(Suppl): 139–52.
[99] Trotter GW, McIlwraith CW. Osteochondrosis dissecans and subchondral cystic lesions and their relationship to osteochondrosis in the horse. *J Equine Vet Sci* 1981; **1**: 157–62.
[100] Laws EG, Richardson DW, Ross MW, Moyer W. Racing performance of Standardbreds after conservative and surgical treatment for tarsocrural osteochondrosis. *Equine Vet J* 1993; **25**: 199–202.
[101] Simpson CM, Lumsden JM. Unusual osteochondral lesions of the talus in a horse. *Aust Vet J* 2001; **79**: 752–5.
[102] Garcia-Lopez JM, Kirker-Head CA. Occult subchondral osseous cyst-like lesions of the equine tarsocrural joint. *Vet Surg* 2004; **33**: 557–64.
[103] Zubrod CJ, Schneider RK, Tucker RL, Gavin POR, Ragle CA, Farnsworth KD. Use of magnetic resonance imaging for identifying subchondral bone damage in horses: 11 cases (1999–2003). *J Am Vet Med Assoc* 2004; **224**: 411–18.
[104] Foerner JJ, Rick MC, Juzwiak JS *et al*. Injection of equine subchondral bone cysts with triamcinolone: 73 horses (1999–2005). *Proc Am Assoc Equine Practnrs* 2006; **52**: 412–13.

[105] Wallis TW, Goodrich LR, McIlwraith CW *et al*. Arthroscopic injection of corticosteroids into the fibrous tissue of subchondral cystic lesions of the medial femoral condyle in horses: a retrospective study of 52 cases (2001–2006). *Equine Vet J* 2008; **40**: 461–7.
[106] Dyce K, Sack W, Wensing C. In: *Textbook of Veterinary Anatomy*, 2nd edn. Philadelphia, PA: WB Saunders, 1996, pp. 611–30.
[107] Updike S. Functional anatomy of the equine tarsocrural collateral ligamants. *Am Vet Res* 1984; **45**: 867–74.
[108] Bohanon T. The tarsus. In: Auer J, Stick J (eds). *Equine Surgery*, 2 edn. Philadelphia, PA: WB Saunders, 1999, pp. 848–62.
[109] Nixon A. Fractures and luxations of the hock. In: Nixon A (ed.). *Equine Fracture Repair*. Philadelphia, PA: WB Saunders, 1996, pp. 259–72.
[110] Foerner J. Surgical treatment of selected musculoskeletal disorders of the rear limb. In: Auer J (ed.). *Equine Surgery*, 2nd edn. Philadelphia, PA: WB Saunders, 1992, pp. 848–62.
[111] Bolt D, Williams J, Burba D. Traumatic injuries of the large tarsal bones in horses. *Compend Contin Educ Pract Vet* 2002; **24**: 724–33.
[112] Davidson E, Ross M, Parente E. Incomplete sagittal fractures of the talus in 11 racehorses: outcome. *Equine Vet J* 2005; **37**: 457–61.
[113] Meagher D, Mackey V. Lag screw fixation of a sagittal fracture of the talus in the horse. *J Equine Vet Sci* 1990; **10**: 108–12.
[114] Ferguson J, Presnell K. Tension band plating of a fracture equine fibular tarsal bone. *Can Vet J* 1976; **17**: 314–17.
[115] Jones R. The diagnosis and treatment of avulsion fracture of the sustentaculum tali in a horse. *Can Vet J* 1976; **17**: 287–90.
[116] Scott E. Surgical repair of a dislocated superficial digital flexor tendon and fractured fibular in a horse. *J Am Vet Med Assoc* 1983; **183**: 322–3.
[117] Hand D, Watkins J, Honnas C, Kemper D. Osteomyelitis of the sustentaculum tali in horses: 10 cases (1992–1998). *J Am Vet Med Assoc* 2001; **219**: 431–5.
[118] Edwards G. Changed in the sustentaculum tali associated with distension of the tarsal sheath (thorough-pin). *Equine Vet J* 1978; **10**: 97–102.
[119] Welch R, Auer J, Watkins J, Baird A. Surgical treatment of tarsal sheath effusion associated with an exostosis on the calcaneus of a horse. *J Am Vet Med Assoc* 1990; **196**: 1992–4.
[120] Tulamo R, Bramlage L, Gabel A. Fractures of the central and third tarsal bone in horses. *J Am Vet Med Assoc* 1983; **182**: 1234–8.
[121] Martin F, Herthel D. Central tarsal bone fractures in 5 horses: report on the use of a cannulated compression bone screw. *Equine Pract* 1992; **14**: 23–7.
[122] Elce Y, Ross M, Woodford A, Arensberg C. A review of central and third tarsal bone slab fractures in 57 horses. *Proc Am Assoc Equine Pract* 2001; **47**: 488–90.
[123] Murphey E, Schneider R, Adams S, Santschi E, Stick J, Ruggles A. Long-term outcome of horses with a slab fracture of the central or third tarsal bone treated conservatively: 25 cases (1976–1993). *J Am Vet Med Assoc* 2000; **216**: 1949–54.
[124] Ramey, D. Use of lag screw fixation for repair of a central tarsal bone fracture in a horse. *J Am Vet Med Assoc* 1988; **15**: 10.
[125] Kelmer G, Wilson D, Essman S. Computed tomography assisted repair of a central tarsal bone slab fracture in a horse. *Equine Vet Educ* 2008; **20**: 284–7.
[126] Winberg F, Pettersson H. Outcome and racing performance after internal fixation of third and central tarsal bone slab fractures in horses: a review of 20 cases. *Acta Vet Scand* 1999; **40**: 172–80.
[127] Dik KJ, Leitch M. Soft tissue injuries of the tarsus. *Vet Clin N Am: Equine Pract* 1995; **11**: 235–47.
[128] Post EM, Singer ER, Clegg PD, Smith RK, Cripps PJ. Retospective study of 24 cases of calcaneal bursitis in the horse. *Equine Vet J* 2003; **35**: 662–8.
[129] Bassage LH, Garcia-Lopez J, Currid EM. Osteolytic lesions of the tuber calcanei in two horses. *J Am Vet Med Assoc* 2000; **217**: 710–16.
[130] Ingle-Fehr JE, Baxter GM. Endoscopy of the calcaneal bursa in horses. *Vet Surg* 1998; **27**: 561–7.
[131] Van Pelt RW, Riley WF, Tillotson PJ. Tenosynovitis of the deep digital flexor tendon in horses. *Can Vet J* 1969; **10**: 235–43.

[132] Van Pelt RW. Inflammation of the tarsal synovial sheath (Thoroughpin) in horses. *J Am Vet Med Assoc* 1969; **155**: 1481–8.
[133] Dik KJ, Merkens HW. Unilateral distension of the tarsal sheath in the horse: a report of 11 cases. *Equine Vet J* 1987; **19**: 307–13.
[134] Hago BED, Vaughan LC. Use of contrast radiography in the investigation of tenosynovitis and bursitis in horses. *Equine Vet J* 1986; **18**: 102–6.
[135] MacDonald MH, Honnas CM, Meagher DM. Osteomyelitis of the calcaneus in horses: 28 cases. *J Am Vet Med Assoc* 1989; **194**: 1317–23.
[136] Cauvin ER, Tapprest J, Munroe GA, May SA, Schramme MC. Endoscopic examination of the tarsal sheath of the lateral digital flexor tendon in horses. *Equine Vet J* 1999; **27**: 348–55.
[137] Archer DC, Clegg PD, Edwards GB. Septic tenosynovitis of the tarsal sheath of an Arab gelding with suspected sepsis of the lateral digital flexor tendon subsequent to bacterial peritonitis. *Vet Rec* 2004; **155**: 485–9.
[138] Honnas CM, Schumacher J, Cohen ND, Watkins JP, Taylor TS. Septic tenosynovitis in horses: 25 cases (1983–1989). *J Am Vet Med Assoc* 1991; **199**: 1616–22.
[139] Schneider RK, Bramlage LR, Moore RM, Mecklenburg LM, Kohn CW, Gabel AA. A retrospective study of 192 horses affected with septic arthritis/tenosynovitis. *Equine Vet J* 1992; **24**: 436–42.
[140] Jann H, Pasquini C. Wounds of the distal limb complicated by involvement of deep structures. *Vet Clin N Am: Equine Pract* 2005; **21**: 145–65.
[141] Santschi EM, Adams SB, Fessler JF, Widmer WR. Treatment of bacterial tarsal tenosynovitis and osteitis of the sustentaculum tali of the calcaneus in five horses. *Equine Vet J* 1997; **29**: 244–7.
[142] Schneider RK, Bramlage LR, Mecklenburg LM, Moore RM, Gabel AA. Open drainage, intra-articular and systemic antibiotics in the treatment of septic arthritis/tenosynovitisin horses. *Equine Vet J* 1992; **24**: 443–9.
[143] Ter Braake F. Direct endoscopic approach improves prognosis of septic synovitis in the horse. *Tijdschr Diergeneeskd* 2002; **127**: 444–9.
[144] Meagher DT, Latimer FG, Sutter WW, Saville WJ. Evaluation of a balloon constant rate infusion system for treatment of septic arthritis, septic tenosynovitis, and contaminated synovial wounds: 23 cases (2002–2005). *J Am Vet Med Assoc* 2006; **228**: 1930–4.
[145] Wereszka MM, White NA, Furr MO. Factors associated with outcome following treatment of horses with septic tenosynovitis: 51 cases (1986–2003). *J Am Vet Med Assoc* 2007; **230**: 1195–200.
[146] Baxter GM. Retrospective study of lower limb wounds involving tendons, tendon sheaths or joints in horses. *Proc Am Assoc Equine Pract* 1987; **33**: 715–28.
[147] Foland JW, Trotter GW, Stashak TS, McIlwraith CW, Turner AS, Aanes WA. Traumatic injuries involving tendons of the distal limbs in horses: a retrospective study of 55 cases. *Equine Vet J* 1991; **23**: 422–5.
[148] Belknap JK, Baxter GM, Nickels FA. Extensor tendon laceration in horses: 50 cases (1982–1988). *J Am Vet Med Assoc* 1993; **203**: 428–31.
[149] Mespoulhès-Rivière C, Martens A, Bogaert L, Wilderjans H. Factors affecting outcome of extensor tendon lacerations in the distal limb of horses. A retrospective study of 156 cases (1994–2003). *Vet Comp Orthop Traumatol* 2008; **21**: 358–64.
[150] Gasthuys F, Van Brantegem L, Vlaminck L. Retrospective study of tendon wounds of the distal limb segments in horses. *Vlaams Diergeneesk Tijdschrift* 1998; **67**: 172–80.
[151] Jansson N. Digital extensor tendon lacerations in horses: a retrospective evaluation in 22 cases. *J Equine Vet Sci* 1995; **15**: 537–40.
[152] Gibson KT, McIlwraith CW, Turner AS, Stashak TS, Aanes WA, Trotter GW. Open joint injuries in horses: 58 cases (1980–1986). *J Am Vet Med Assoc* 1989; **194**: 398–404.
[153] Lapointe JM, Laverty S, Lavoie JP. Septic arthritis in 15 standardbred racehorses after intra-articular injection. *Equine Vet J* 1992; **24**: 412–14.
[154] Olds AM, Stewart AA, Freeman DE, Schaeffer DJ. Evaluation of the rate of development of septic arthritis after elective arthroscopy in horses: 7 cases (1994–2003). *J Am Vet Med Assoc* 2006; **229**: 1949–54.
[155] Firth EC, Goedegebuure SA, Dik KJ, Poulos PW. Tarsal osteomyelitis in foals. *Vet Rec* 1985; **116**: 261–6.

[156] Meijer MC, van Weeren PR, Rijkenhuizen AB. Clinical experiences of treating septic arthritis by repeated joint lavage: a series of 39 cases. *J Vet Med A Physiol Pathol Clin Med* 2000; **47**: 351–65.
[157] Lescun TB, Adams SB, Wu CC, Bill RP, Van Sickle DC. Effects of continuous intra-articular infusion of gentamicin on synovial membrane and articular cartilage in the tarsocrural joint of horses. *Am J Vet Res* 2002; **63**: 683–7.
[158] Ivester KM, Adams SB, Moore GE, Van Sickle DC, Lescun TB. Gentamicin concentrations in synovial fluid obtained from the tarsocrural joints of horses after implantation of gentamicin-impregnated collagen sponges. *Am J Vet Res* 2006; **67**: 1519–26.
[159] Booth TM, Butson RJ, Clegg PD, Schramme MC, Smith RK. Treatment of sepsis in the small tarsal joints of 11 horses with gentamicin-impregnated polymethylmethacrylate beads. *Vet Rec* 2001; **148**: 376–80.
[160] Steel CM, Hunt AR, Adams PL *et al*. Factors associated with prognosis for survival and athletic use in foals with septic arthritis: 93 cases (1987–1994). *J Am Vet Med Assoc* 1999; **215**: 973–7.
[161] Leitch M. Musculoskeletal disorders in neonatal foals. *Vet Clin N Am: Equine Pract* 1985; **1**: 189–207.
[162] Dutton DM, Watkins JP, Walker M, Honnas CM. Incomplete ossification of the tarsal bones in foals: 22 cases (1998–1996). *J Am Vet Med Assoc* 1998; **213**: 1590–4.
[163] Dutton DM, Watkins JP, Honnas CM, Hague BA. Treatment response and athletic outcome of foals with tarsal valgus deformities: 39 cases (1988–1997). *J Am Vet Med Assoc* 1999; **215**: 1481–4.
[164] Witte S, Thorpe PE, Hunt RJ, Spirito MA, Rodgerson DH. A lag-screw technique for bridging of the medial aspect of the distal tibial physis in horses. *J Am Vet Med Assoc* 2004; **225**: 1581–3.

Chapter 25
The head

Russell Tucker, Katherine Garrett, Stephen Reed and Rachel Murray

Since magnetic resonance imaging (MRI) of the equine head has only come into common clinical use relatively recently, there is a paucity of objective data concerning how imaging findings have affected treatment and outcome. However, one of the major benefits of performing an MRI examination is the ability to formulate a more specific diagnosis. In the authors' experience, this has allowed more targeted and efficient treatments in most cases and has helped direct patient management with owners in many cases. For horses with neurologic disease, management can be difficult and potentially dangerous, so achieving a specific diagnosis at an early stage can be extremely helpful for an owner in the decision-making process. The ability to give an accurate diagnosis and guide prognosis is essential, especially when euthanasia is the appropriate option for management.

MRI has proven to be of great diagnostic value for structural diseases of the equine brain [1, 2]. Within the central nervous system, localization of a lesion to the area rostral to the foramen magnum is a useful tool to explain the clinical signs and often helps develop a list of differential diagnoses. Lesions typically affecting this area include a space-occupying lesion, inflammatory encephalitis or meningitis (viral, bacterial or protozoal), trauma, intoxication, hypoxic insult, metabolic disease or congenital malformation. Other lesions often identified within the head of the horse include sinus masses, dental disease, trauma and congenital malformations. Further refinement of the list of differential diagnoses can be based on signalment, history, clinical signs and clinical pathologic data, but a definitive diagnosis may remain elusive. Recognition of a lesion using MRI will often narrow the differential diagnosis list.

Understanding the nature of a space-occupying lesion may be helpful in guiding treatment. For example, recognition of a mass lesion as an abscess will guide treatment to include appropriate antimicrobials, anti-inflammatory agents and establishment of drainage when possible. The extent of a neoplastic mass can be characterized more accurately and the feasibility of surgical intervention can be determined using the MRI examination to assist with surgical planning. Follow-up MRI examination may be used to assess response to treatment. Restoration or partial recovery of normal neurologic functions can be a slow process in successfully treated neoplastic and infectious conditions. Follow-up MRI examinations can be useful to reveal recurrent or non-responsive disease progression and allow clinicians and

Equine MRI, edited by Rachel C. Murray.

owners to make educated decisions about alternative therapy options or humane euthanasia when appropriate. Alternatively, repeat MRI examinations demonstrating reduction or resolution of neoplastic and infectious conditions can provide encouraging information in spite of delayed neurologic recovery and persistent neurologic deficits.

In cases of sinus masses, radiography often reveals soft tissue opacity in a sinus, but MRI can assist in determination of the type of mass present within the sinus and its extent. Conditions as diverse as bacterial sinusitis secondary to oro-nasal fistula, ethmoid haematoma and sinus cyst appear similar on radiographs, but have very different prognoses (see Figure 19.17). The additional information gained from MRI examination has enabled clinicians to formulate a more complete surgical plan and discuss options and potential outcomes with clients more accurately. Masses within the sinuses that invade into the sphenopalatine sinus or involve adjacent tooth roots can be better characterized by MRI examinations and this added information may alter the surgical approach and prognosis. In addition to loss of bone and erosion of tooth roots, often apparent on radiography or computed tomography (CT), MRI can detect inflammation of the dental nerves and pulp cavities, periodontal membranes and of the mucosal lining of surrounding nasal sinuses.

Diagnosis of equine protozoal encephalomyelitis based on antibody titres in blood and cerebrospinal fluid (CSF) can be unreliable [3, 4] but MRI may prove to be a valuable diagnostic aid in cases where clinical signs are referrable to the brainstem, cranial nerves or cerebrum. When equine protozoal myelitis (EPM) is suspected, treatment can be instituted using anti-protozoal medications [5]. Other encephalitides are treated with anti-inflammatory and antimicrobial therapies and supportive care.

In cases of trauma, MRI can provide additional information that can guide decision making as to the feasibility of surgical intervention. Radiographs of the skull can be challenging to interpret and non-displaced fractures may be difficult to identify, especially in the acute stages. MRI allows a more complete assessment of both the bony and soft tissue structures involved, which is particularly useful as the sinonasal region or brain parenchyma may be involved or additional fractures may be present (Figure 25.1)

Nigropallidal encephalomalacia has been diagnosed using MRI in two horses in the literature [6]. Treatment was not pursued and the horses were euthanized. Even with a precise diagnosis, there is no specific treatment and the prognosis is poor [7].

Otitis media may present as facial nerve paralysis or with signs of vestibular disease. MRI enables the differentiation of this condition from others affecting the cranial nerves and brainstem (see Figure 19.26). Once diagnosed, appropriate treatment with antimicrobial drugs can be instituted. Follow-up examinations allow for monitoring of response to therapeutic intervention or the need for a more aggressive treatment. Fenestration of the tympanic membrane can assist with drainage in cases of otitis media as well.

Temporohyoid osteoarthropathy in adult horses is often associated with vestibular syndrome; however, some affected horses may also demonstrate

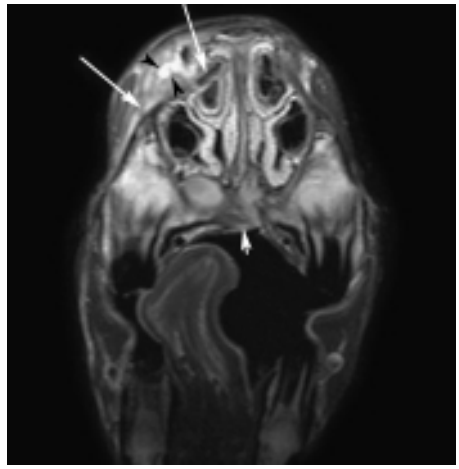

Figure 25.1 T2-weighted turbo spin-echo transverse image of the skull at the level of premolar 3. Fracture of the nasal bone was identified with radiographic images and confirmed on MRI (large white arrows). Hyperintense signal consistent with inflammatory fluid is present in the area of the nasal bone fracture (black arrowheads). MRI also identified fracture of the hard palate which was not visible on radiographic images (small white arrow).

facial nerve paralysis, dysphagia, head shaking, pain on chewing or with palpation of this area and behaviour problems (see Figure 19.26). The underlying cause is unknown but is suspected to be inflammation secondary to inner or middle ear infection [8]. Clinical signs are most often unilateral, although on CT or MRI evidence of bilateral disease may be identified. Treatment of temporohyoid osteoarthropathy can be either medical or surgical. In the authors' opinion surgical correction results in much more rapid outcome of the problem. At least partial medical management is required for all cases that involve facial nerve paralysis with loss of tear production and exposure keratitis [8]. Surgical intervention involves either a stylohyoidectomy or a ceratohyoidectomy.

Congenital malformations may initially manifest themselves similarly to acquired conditions. For example, foals with hydrocephalus may appear similar to those with hypoxic-ischaemic encephalopathy and a horse with laryngeal dysplasia may present as a horse with laryngeal hemiplegia. Obtaining the correct diagnosis often changes the treatment plan and prognosis. Treatment options are limited in many cases of congenital malformations, but a foal with hydrocephalus was treated with a ventriculoperitoneal shunt. Cystic remnants of embryonic structures in the cranial neck have been treated with surgical resection [9, 10].

In the future, correlation of MRI findings to gross pathological examination will be valuable in furthering our understanding of the significance of various MRI lesions. Hopefully this will enable us to recognize lesions at earlier stages, offer better treatment options and improve patient outcomes. Additional clinical experience with equine MRI of the head will undoubtedly lead to improved techniques for obtaining images as well as improved diagnostic ability.

REFERENCES

[1] Ferrell EA, Gavin PR, Tucker RL, Sellon DC, Hines MT. Magnetic resonance for evaluation of neurologic disease in 12 horses. *Vet Radioi Ultrasound* 2002; **43**: 510–16.
[2] Divers TJ. Structural and functional diseases of the equine brain. *Clin Tech Equine Pract* 2006; **5**: 67–73.
[3] Dabey JP, Lindsay DS, Saville WJ *et al*. A review of Sarcocystis neurona and equine protozoal myeloencephalitis (EPM). *Vet Parasitol* 2001; **95**: 89–131.
[4] Furr M. Immunity, pathophysiology, and diagnosis of equine protozoal myeloencephalitis. *Clin Tech Equine Pract* 2006; **5**: 3–8.
[5] MacKay RJ. Equine protozoal myeloencephalitis: treatment, prognosis and prevention. *Clin Tech Equine Pract* 2006; **5**: 9–16.
[6] Sanders SG, Tucker RL, Bagley RS, Gavin PR. Magnetic resonance imaging features of equine nigropallidal encephalomalacia. *Vet Radiol Ultrasound* 2001; **42**: 291–6.
[7] Talcott P. Nigropallidal encephalomalacia. In: Robinson NE (ed.) *Current Therapy in Equine Medicine 5*. St Louis, MO: Saunders, 2003, pp. 780–1.
[8] Divers TJ, Ducharme NG, de Lahunta A *et al*. Temporohyoid osteoarthropathy. *Clin Tech Equine Pract* 2006; **5**: 17–23.
[9] Field JR, Trout D, Physick-Sheard PW. Ablation of a congenital neck mass in a foal. *Can Vet J* 1990; **31**: 643–4.
[10] Hance SR, Robertson JT, Wicks JR. Branchial cyst in a filly. *Equine Vet J* 1992; **24**: 329–31.

Index

Note to index: *tables* are indicated throughout. *Figures* may be accessed directly *(italics)*, or from their text page entries

Equine MRI, edited by Rachel C. Murray. © 2011 by Blackwell Publishing Ltd.